

Polymer–carbon nanotube composites

Preparation, properties and
applications

Edited by Tony McNally and Petra Pötschke

Polymer–carbon nanotube composites

Related titles:

Polymer nanocomposites: Physical properties and applications
(ISBN 978-1-84569-672-6)

This comprehensive book covers the physical properties of polymer nanocomposites, which are defined as polymer matrices that are reinforced with nano-scale fillers. Understanding the physical properties of polymer nanocomposites is a key factor in gaining wider uptake of the materials in new applications. The book is divided into sections covering polymer/nanoparticle composites, polymer/nanoplatelet composites and polymer/nanotube composites. It finishes with a comprehensive section on applications including electrical, mechanical and thermal properties of high-performance polymer composite bipolar plates for fuel cells, electrospun polymer nanocomposite fibres and polymeric/inorganic nanocomposites: fabrication and applications in multiple bioimaging.

Fatigue life prediction of composites and composite structures
(ISBN 978-1-84569-525-5)

This important book addresses the highly topical subject of fatigue life prediction of composites and composite structures. Fatigue is the progressive and localised structural damage that occurs when a material is subjected to cyclic loading. The use of composites is growing in structural applications and they are replacing traditional materials, primarily metals. Many of the composites being used have only recently been developed and there are uncertainties about the long-term performance of these composites and how they will perform under cyclic fatigue loadings. The book will provide a comprehensive review of fatigue damage and fatigue life modelling.

Creep and fatigue in polymer matrix composites
(ISBN 978-1-84569-656-6)

This authoritative book reviews the experimental and theoretical approaches to creep and fatigue of polymer matrix composites in the context of durability. Part I focuses on viscoelastic and viscoplastic modelling. Part II covers environmental effects and stress corrosion while Part III analyses creep rupture and damage interaction. Part IV investigates fatigue modelling and characterisation and Part V covers the monitoring of creep and fatigue.

Details of these and other Woodhead Publishing materials books can be obtained by:

- visiting our web site at www.woodheadpublishing.com
- contacting Customer Services (e-mail: sales@woodheadpublishing.com; fax: +44 (0) 1223 832819; tel.: +44 (0) 1223 499140 ext. 130; address: Woodhead Publishing Limited, 80 High Street, Sawston, Cambridge CB22 3HJ, UK)

If you would like to receive information on forthcoming titles, please send your address details to: Francis Dodds (address, tel. and fax as above; e-mail: francis.dodds@woodheadpublishing.com). Please confirm which subject areas you are interested in.

Polymer–carbon nanotube composites

Preparation, properties and
applications

Edited by
Tony McNally and Petra Pötschke



Oxford Cambridge Philadelphia New Delhi

Published by Woodhead Publishing Limited,
80 High Street, Sawston, Cambridge CB22 3HJ, UK
www.woodheadpublishing.com

Woodhead Publishing, 1518 Walnut Street, Suite 1100, Philadelphia,
PA 19102-3406, USA

Woodhead Publishing India Private Limited, G-2, Vardaan House,
7/28 Ansari Road, Daryaganj, New Delhi – 110002, India
www.woodheadpublishingindia.com

First published 2011, Woodhead Publishing Limited
© Woodhead Publishing Limited, 2011
The authors have asserted their moral rights.

This book contains information obtained from authentic and highly regarded sources. Reprinted material is quoted with permission, and sources are indicated. Reasonable efforts have been made to publish reliable data and information, but the authors and the publisher cannot assume responsibility for the validity of all materials. Neither the authors nor the publisher, nor anyone else associated with this publication, shall be liable for any loss, damage or liability directly or indirectly caused or alleged to be caused by this book.

Neither this book nor any part may be reproduced or transmitted in any form or by any means, electronic or mechanical, including photocopying, microfilming and recording, or by any information storage or retrieval system, without permission in writing from Woodhead Publishing Limited.

The consent of Woodhead Publishing Limited does not extend to copying for general distribution, for promotion, for creating new works, or for resale. Specific permission must be obtained in writing from Woodhead Publishing Limited for such copying.

Trademark notice: Product or corporate names may be trademarks or registered trademarks, and are used only for identification and explanation, without intent to infringe.

British Library Cataloguing in Publication Data
A catalogue record for this book is available from the British Library.

ISBN 978-1-84569-761-7 (print)
ISBN 978-0-85709-139-0 (online)

The publisher's policy is to use permanent paper from mills that operate a sustainable forestry policy, and which has been manufactured from pulp which is processed using acid-free and elemental chlorine-free practices. Furthermore, the publisher ensures that the text paper and cover board used have met acceptable environmental accreditation standards.

Typeset by RefineCatch Limited, Bungay, Suffolk, UK
Printed by TJI Digital, Padstow, Cornwall, UK

Contents

<i>Contributor contact details</i>	<i>xv</i>
<i>Introduction to polymer–carbon nanotube composites</i>	<i>xxi</i>
T. McNALLY, Queen's University Belfast, UK and P. PÖTSCHKE, Leibniz Institute of Polymer Research Dresden, Germany	
<i>References</i>	<i>xxvi</i>
 Part I Preparation and processing of polymer–carbon nanotube composites	 1
1 Polyolefin–carbon nanotube composites by <i>in-situ</i> polymerization	3
W. KAMINSKY, University of Hamburg, Germany	
1.1 Introduction	3
1.2 <i>In-situ</i> polymerization techniques for polyolefin–CNT composites	5
1.3 Polymer architecture by metallocene catalysis	7
1.4 Polyethylene–CNT composites	9
1.5 Polypropylene–CNT composites	11
1.6 Conclusion and future trends	21
1.7 References	22
2 Surface treatment of carbon nanotubes via plasma technology	25
B. RUELLE, C. BITTENCOURT and P. DUBOIS, University of Mons and Materia Nova Research Centre, Belgium	
2.1 Introduction	25
2.2 Carbon nanotube surface chemistry and solution-based functionalization	27
2.3 Plasma treatment of carbon nanotubes	33
2.4 Summary	48
2.5 References	49

vi	Contents	
3	Functionalization of carbon nanotubes for polymer nanocomposites	55
	Y.-K. YANG, Hubei University, P. R. China, X.-L. XIE, Huazhong University of Science and Technology, P. R. China and Y.-W. MAI, The University of Sydney, Australia	
3.1	Introduction	55
3.2	Non-covalent functionalization of carbon nanotubes with polymers	57
3.3	Covalent functionalization of carbon nanotubes with polymers	64
3.4	Conclusion	80
3.5	Acknowledgements	81
3.6	References	81
4	Influence of material and processing parameters on carbon nanotube dispersion in polymer melts	92
	G. R. KASALI WAL, T. VILLMOW, S. PEGEL and P. PÖTSCHKE, Leibniz Institute of Polymer Research Dresden, Germany	
4.1	Introduction	92
4.2	Fundamentals of melt mixing and filler dispersion	94
4.3	Review of the literature	97
4.4	Batch compounding using small-scale mixers	101
4.5	Continuous melt mixing using extruders	118
4.6	Conclusion and future trends	127
4.7	Acknowledgements	129
4.8	References	129
5	High-shear melt processing of polymer–carbon nanotube composites	133
	Y. LI and H. SHIMIZU, National Institute of Advanced Industrial Science and Technology (AIST), Japan	
5.1	Introduction	133
5.2	High-shear processing technique	135
5.3	Polymer nanoblends by high-shear processing	136
5.4	Polymer–carbon nanotube (CNT) nanocomposites by high-shear processing	139
5.5	Conclusion and future trends	151
5.6	References	152
6	Injection moulding of polymer–carbon nanotube composites	155
	C. Y. LEW, C. DEWAGHE and M. CLAES, Nanocyl S.A., Belgium	
6.1	Introduction	155
6.2	Background	156

6.3	Experiment design and materials	159
6.4	Analysis	165
6.5	Conclusion	188
6.6	References	191
6.7	Appendix: list of units	192
7	Elastomer–carbon nanotube composites	193
	J. FRITZSCHE, H. LORENZ and M. KLÜPPEL, German Institute of Rubber Technology, Germany and A. DAS, R. JURK, K. W. STÖCKELHUBER and G. HEINRICH, Leibniz Institute of Polymer Research Dresden, Germany	
7.1	Introduction	193
7.2	Processing	195
7.3	Structure–property relationships	202
7.4	Systems with ionic liquids for increased coupling activity	210
7.5	Hybrid systems based on silica filler	216
7.6	Conclusion	225
7.7	References	226
8	Epoxy–carbon nanotube composites	230
	J. M. KENNY, Institute of Polymer Science and Technology (ICTP-CSIC), Spain and L. VALENTINI, D. PUGLIA and A. TERENCE, University of Perugia, Italy	
8.1	Introduction	230
8.2	Experimental materials and methods	231
8.3	Chemorheological approach	234
8.4	Chemorheological analysis of epoxy–CNTs systems	240
8.5	Properties of epoxy–CNT composites	252
8.6	Conclusion and future trends	256
8.7	References	256
Part II	Properties and characterization of polymer–carbon nanotube composites	263
9	Quantification of dispersion and distribution of carbon nanotubes in polymer composites using microscopy techniques	265
	S. PEGEL, T. VILLMOW and P. PÖTSCHKE, Leibniz Institute of Polymer Research Dresden, Germany	
9.1	Introduction	265
9.2	Light microscopy	269
9.3	Transmission electron microscopy	276
9.4	Conclusion and future trends	291

viii	Contents	
9.5	References	291
9.6	Appendix: list of abbreviations	293
10	Influence of thermo-rheological history on electrical and rheological properties of polymer–carbon nanotube composites	295
	I. ALIG, D. LELLINGER and T. SKIPA, German Polymer Institute, Germany	
10.1	Introduction	295
10.2	Background	299
10.3	Measuring techniques and materials	308
10.4	Destruction and formation of electrical and rheological networks	312
10.5	Influence of processing history	321
10.6	Conclusion	323
10.7	Acknowledgements	324
10.8	References	324
11	Electromagnetic properties of polymer–carbon nanotube composites	329
	F. NANNI and M. VALENTINI, INSTM–University of Rome ‘Tor Vergata’, Italy	
11.1	Introduction	329
11.2	Electromagnetic wave absorbing CNT composites	332
11.3	Electromagnetic shielding CNT composites	336
11.4	Other CNT composites’ electromagnetic applications	340
11.5	Conclusion	342
11.6	References	343
12	Mechanical properties of polymer–polymer-grafted carbon nanotube composites	347
	S. H. GOH, National University of Singapore, Singapore	
12.1	Introduction	347
12.2	Grafting of polymers onto CNTs	349
12.3	Fabrication of composites	352
12.4	Mechanical properties of polymer composites containing polymer-grafted CNTs	353
12.5	Conclusion	368
12.6	References	369
13	Multiscale modeling of polymer–carbon nanotube composites	376
	G. M. ODEGARD, Michigan Technological University, USA	
13.1	Introduction	376

13.2	Computational modeling tools	377
13.3	Equivalent-continuum modeling concepts	379
13.4	Specific equivalent-continuum modeling methods	388
13.5	Example: polymer–carbon nanotube composite	390
13.6	Conclusion and future trends	394
13.7	Sources of further information	395
13.8	References	396
14	Raman spectroscopy of polymer–carbon nanotube composites	400
	H. D. WAGNER, Weizmann Institute of Science, Israel	
14.1	Introduction	400
14.2	The Raman effect: basic principles	401
14.3	Molecules and fibers under strain: how the Raman spectrum is affected	402
14.4	Raman signature of carbon nanotubes	403
14.5	Usefulness of Raman spectroscopy in nanotube-based composites	405
14.6	Conclusion	421
14.7	Acknowledgements	422
14.8	References	422
15	Rheology of polymer–carbon nanotube composites melts	428
	M. R. NOBILE, University of Salerno, Italy	
15.1	Introduction	428
15.2	Linear rheological properties of polymer–carbon nanotube (CNT) composites	429
15.3	Non-linear rheological properties of polymer–carbon nanotube (CNT) composites	448
15.4	Flow-induced crystallization in polymer–carbon nanotube (CNT) composites	463
15.5	Conclusion	470
15.6	References	471
16	Thermal degradation of polymer–carbon nanotube composites	482
	S. P. SU and Y. H. XU, Hunan Normal University, P. R. China and C. A. WILKIE, Marquette University, USA	
16.1	Introduction	482
16.2	Mechanisms of thermal degradation/stability improvement by CNTs	483
16.3	The thermal degradation of polymer–CNT composites	486
16.4	Future trends	501

x	Contents	
16.5	Conclusion	502
16.6	References	503
16.7	Appendix: symbols and abbreviations	509
17	Polyolefin–carbon nanotube composites	511
	M. MORCOM and G. SIMON, Monash University, Australia	
17.1	Introduction	511
17.2	Processing methods used in CNT–polyolefin nanocomposites	512
17.3	Mechanical properties of CNT–polyolefin nanocomposites	518
17.4	Crystallinity of polyolefin–CNT blends	526
17.5	Rheological properties of CNT–polyolefin blends	530
17.6	Electrical properties of CNT–polyolefin blends	532
17.7	Wear behaviour of polyolefin–CNT composites	533
17.8	Thermal conductivity of polyolefin–CNT composites	533
17.9	Thermal degradation and flame-retardant properties	534
17.10	Conclusion and future trends	537
17.11	References	537
18	Composites of poly(ethylene terephthalate) and multi-walled carbon nanotubes	545
	K. MCCROSSAN, C. MCCLORY, B. MAYORAL, D. THOMPSON, D. MCCONNELL and T. McNALLY, Queen's University Belfast, UK and M. MURPHY, T. NICHOLSON, D. MARTIN and P. HALLEY, The University of Queensland, Australia	
18.1	Introduction	545
18.2	Poly(ethylene terephthalate)–MWCNT composites: a literature survey	547
18.3	Poly(ethylene terephthalate)–MWCNT melt processing and bulk material properties	551
18.4	Changes in crystalline structure and crystal conformation	554
18.5	Thermal stability of PET–MWCNT composites	577
18.6	Formation of CNT networks in PET: rheological and electrical percolation	579
18.7	Conclusion and future trends	582
18.8	Acknowledgements	583
18.9	References	583
19	Carbon nanotubes in multiphase polymer blends	587
	A. GÖLDEL and P. PÖTSCHKE, Leibniz Institute of Polymer Research Dresden, Germany	
19.1	Introduction	587
19.2	Current state of melt mixing polymer blends with nanotubes	588

19.3	Localization of CNTs in polymer blends during melt mixing	595
19.4	Tailoring the localization of CNTs	611
19.5	Utilization of selective localization: double percolated polycarbonate–acrylonitrile butadiene styrene (PC–ABS)–CNT blends	613
19.6	Conclusion and future trends	615
19.7	Acknowledgements	616
19.8	References	617
19.9	Appendix: list of abbreviations	619
20	Toxicity and regulatory perspectives of carbon nanotubes	621
	D. MARTIN and R. F. MINCHIN, The University of Queensland, Australia and M. BELKINA, A. MILEV and G. S. KAMALI KANNANGARA, University of Western Sydney, Australia	
20.1	Toxic effects of nanomaterials and nanoparticles: public perception and the necessary ‘risk-versus-reward’ debate	621
20.2	Toxicology of carbon nanotubes in comparison to other particulate materials	623
20.3	Comparisons between carbon nanotubes and asbestos: a summary of respiratory studies	624
20.4	Toxicity of carbon nanotubes	628
20.5	Influence of the parameters of carbon nanotubes on their toxicity	630
20.6	Future biological applications of carbon nanotubes	643
20.7	Future trends	644
20.8	Conclusion	647
20.9	References	648
Part III	Applications of polymer–carbon nanotube composites	655
21	The use of polymer–carbon nanotube composites in fibres	657
	H. DENG and Q. FU, Sichuan University, P. R. China and E. BILOTTI and T. PEIJS, Queen Mary University of London, UK	
21.1	Introduction	657
21.2	Preparation of polymer–CNT fibres	658
21.3	Orientation of CNTs and polymer	659
21.4	Mechanical properties of polymer–CNT fibres	662
21.5	A theoretical approach to reinforcement efficiency of CNTs	665
21.6	Electrical properties of polymer–CNT fibres	667

21.7	Sensing properties of polymer–CNT fibres	669
21.8	Conclusion and future trends	670
21.9	References	672
22	Biomedical/bioengineering applications of carbon nanotube-based nanocomposites	676
	N. DUNNE and C. MITCHELL, Queen's University Belfast, UK	
22.1	Introduction to biomaterials and implants	676
22.2	Orthopaedic implants	677
22.3	Nanomaterials in medicine	680
22.4	Load-bearing implants for orthopaedic applications	686
22.5	Carbon nanotubes in dentistry	693
22.6	Carbon nanotubes and dental restorative materials	695
22.7	Carbon nanotubes in periodontal dentistry	696
22.8	Carbon nanotubes and denture-based resin	697
22.9	Carbon nanotubes and targeted drug delivery for oral cancer	699
22.10	Carbon nanotubes used for monitoring biological systems	699
22.11	Carbon nanotube biosensors	701
22.12	Bioactivity of carbon nanotubes	703
22.13	Regulation of occupational exposure to carbon nanotubes	706
22.14	Conclusion	707
22.15	References	708
23	Fire-retardant applications of polymer–carbon nanotubes composites: improved barrier effect and synergism	718
	C. DEWAGHE, C. Y. LEW and M. CLAES, Nanocyl S. A., Belgium and P. DUBOIS, University of Mons, Belgium	
23.1	Introduction	718
23.2	Fire protection mechanisms	727
23.3	Using carbon nanotubes to develop fire-retardant solutions	730
23.4	Synergism	734
23.5	Carbon nanotubes in flame-resistant coatings	739
23.6	Conclusion	743
23.7	References	744
24	Polymer–carbon nanotube composites for flame-retardant cable applications	746
	G. BEYER, Kabelwerk Eupen AG, Belgium	
24.1	Introduction	746
24.2	Carbon nanotube-based nanocomposites	748

24.3	Cable with the multi-walled carbon nanotube (MWCNT)–organoclay–aluminium trihydrate (ATH) flame-retardant system	752
24.4	Conclusion	758
24.5	References	758
25	Polymer–carbon nanotube conductive nanocomposites for sensing J.-F. FELLER, M. CASTRO and B. KUMAR, University of South Brittany (UBS), France	760
25.1	Introduction	760
25.2	Basic concepts of conductive polymer nanocomposites	761
25.3	Carbon nanotube (CNT) conductive polymer nanocomposite (CPC) transducers' fabrication	769
25.4	Sensing properties and applications of CNT conductive polymer nanocomposites	780
25.5	Conclusion	794
25.6	Acknowledgements	795
25.7	References	795
	<i>Index</i>	805

Contributor contact details

(* = main contact)

Editors

T. McNally
School of Mechanical and Aerospace
Engineering
Queen's University Belfast
BT9 5AH
UK

P. Pötschke
Department of Polymer Reactions and
Blends
Leibniz-Institut für Polymerforschung
Dresden e.V. (Leibniz Institute of
Polymer Research Dresden)
Hohe Str. 6
D-01069 Dresden
Germany

Chapter 1

W. Kaminsky
Institute for Technical and
Macromolecular Chemistry
University of Hamburg
Bundesstr. 45
D-20146 Hamburg
Germany
E-mail: kaminsky@chemie.uni-
hamburg.de

Chapter 2

B. Ruelle, C. Bittencourt and
P. Dubois*
Centre of Innovation and Research in
Materials and Polymers
(CIRMAP)
University of Mons and Materia Nova
Research Centre
Place du Parc 20
B 7000 Mons
Belgium
E-mail: philippe.dubois@umons.ac.be

Chapter 3

Y.-K. Yang
Ministry of Education Key Laboratory
for Green Preparation and
Application of Functional Materials
and Faculty of Materials Science
and Engineering
Hubei University
Wuhan 430062
P. R. China
E-mail: yingkuiyang@gmail.com

X.-L. Xie
State Key Laboratory of Materials
Processing and Die & Mould
Technology
School of Chemistry and Chemical
Engineering
Huazhong University of Science and
Technology
Wuhan 430074
P. R. China
E-mail: xlxie@mail.hust.edu.cn

Y.-W. Mai*
Centre for Advanced Materials
Technology (CAMT)
School of Aerospace, Mechanical and
Mechatronic Engineering J07
The University of Sydney
Sydney
NSW 2006
Australia
E-mail: yiu-wing.mai@sydney.edu.au

Chapter 4

G. R. Kasaliwal*, T. Villmow,
S. Pegel and P. Pötschke
Department of Polymer Reactions and
Blends
Leibniz-Institut für Polymerforschung
Dresden e.V. (Leibniz Institute of
Polymer Research Dresden)
Hohe Str. 6
D-01069 Dresden
Germany
E-mail: kasaliwal@ipfdd.de; villmow@
ipfdd.de; pegel@ipfdd.de; poe@
ipfdd.de

Chapter 5

Y. Li and H. Shimizu
Nanotechnology Research Institute

National Institute of Advanced
Industrial Science and Technology
(AIST)
Tsukuba Central 5
1-1-1 Higashi
Tsukuba
Ibaraki 305-8565
Japan
E-mail: yongjin-li@aist.go.jp
shimizu-hiro@aist.go.jp

Chapter 6

C. Y. Lew*, C. Dewaghe and
M. Claes
R&D Department
Nanocyl S.A.
4 Rue de l'Essor
5060 Sambreville
Belgium
E-mail: andy.lew@nanocyl.com
mclaes@nanocyl.com

Chapter 7

J. Fritzsche, H. Lorenz and
M. Klüppel*
Deutsches Institut für
Kautschuktechnologie e.V.
(German Institute of Rubber
Technology)
Eupener Straße 33
D-30519 Hannover
Germany
E-mail: Manfred.Klueppel@
DIKautschuk.de

A. Das, R. Jurk, K. W. Stöckelhuber
and G. Heinrich
Leibniz-Institut für Polymerforschung
Dresden e.V. (Leibniz Institute of
Polymer Research Dresden)
Hohe Str. 6
D-01069 Dresden
Germany

Chapter 8

J. M. Kenny*

Institute of Polymer Science and
Technology (ICTP-CSIC)

Juan de la Cierva 3

28006 Madrid

Spain

E-mail: kenny@ictp.csic.es

and

European Center for Nanostructured
Polymers (ECNP)

L. Valentini, D. Puglia and A. Terenzi
Civil and Environmental Engineering

Department

University of Perugia

Loc. Pentima Bassa 21

05100 Terni

Italy

Chapter 9

S. Pegel*, T. Villmow and P. Pötschke

Department of Polymer Reactions and
Blends

Leibniz-Institut für Polymerforschung

Dresden e.V. (Leibniz Institute of
Polymer Research Dresden)

Hohe Str. 6

D-01069 Dresden

Germany

E-mail: pegel@ipfdd.de; villmow@
ipfdd.de; poe@ipfdd.de

Chapter 10

I. Alig*, D. Lellinger and T. Skipa

Deutsches Kunststoff-Institut

(German Polymer Institute)

Schlossgartenstraße 6

D-64289 Darmstadt

Germany

E-mail: ialig@dkl.tu-darmstadt.de

Chapter 11

F. Nanni* and M. Valentini

INSTM – Italian Interuniversity

Consortium on Material Science
and Technology

Research Unit of University of Rome
‘Tor Vergata’

Department of Sciences and Chemical
Technologies

Via della Ricerca Scientifica 1

00133 Rome

Italy

E-mail: fnanni@ing.uniroma2.it

Chapter 12

S. H. Goh

Department of Chemistry

National University of Singapore

3 Science Drive 3

Singapore 117543

Singapore

E-mail: chmgohsh@nus.edu.sg

Chapter 13

G. M. Odegard

Department of Mechanical

Engineering–Engineering
Mechanics

Michigan Technological University

Houghton

MI 49931

USA

E-mail: gmodegar@mtu.edu

Chapter 14

H. D. Wagner

Department of Materials and
Interfaces

Weizmann Institute of Science
Rehovot 76100
Israel
E-mail: daniel.wagner@weizmann.ac.il

VIC 3800
Australia
E-mail: mel@morcom.com.au; george.
simon@eng.monash.edu.au

Chapter 15

M. R. Nobile
Department of Chemical and Food
Engineering
Research Centre for Nanomaterials
and Nanotechnology at Salerno
(Nanomates)
University of Salerno
Fisciano 84084
Italy
E-mail: mrmobile@unisa.it

Chapter 16

S. P. Su* and Y. H. Xu
College of Chemistry and Chemical
Engineering
Hunan Normal University
Changsha
Hunan 410081
P. R. China
E-mail: sushengpei@gmail.com

C. A. Wilkie
Marquette University
PO Box 1881
Milwaukee
WI 53201
USA
E-mail: charles.wilkie@marquette.edu

Chapter 17

M. Morcom and G. Simon
Department of Materials Engineering
Monash University
Wellington Road
Clayton

Chapter 18

K. McCrossan, C. McClory,
B. Mayoral, D. Thompson,
D. McConnell and T. McNally*
School of Mechanical and Aerospace
Engineering
Queen's University Belfast
Belfast
BT9 5AH
UK

M. Murphy, T. Nicholson, D. Martin
and P. Halley
Centre for High Performance
Polymers
The University of Queensland
Brisbane
QLD 4072
Australia

D. Martin and P. Halley
Australian Institute for Bioengineering
& Nanotechnology
The University of Queensland
Brisbane
QLD 4072
Australia

Chapter 19

A. Gödel* and P. Pötschke
Department of Polymer Reactions and
Blends
Leibniz-Institut für Polymerforschung
Dresden e.V. (Leibniz Institute of
Polymer Research Dresden)
Hohe Str. 6

01069 Dresden
Germany
E-mail: goeldel@ipfdd.de; poe@ipfdd.de

Chapter 20

D. Martin*
Australian Institute for Bioengineering
& Nanotechnology
The University of Queensland
Brisbane
QLD 4072
Australia
E-mail: darren.martin@uq.edu.au

R. F. Minchin
School of Biomedical Sciences
The University of Queensland
Brisbane
QLD 4072
Australia

M. Belkina, A. Milev and
G. S. Kamali Kannangara
ARC Centre of Excellence for
Functional Nanomaterials
Locked Bag 1797
University of Western Sydney
Penrith South
DC 1797
Australia

Chapter 21

H. Deng* and Q. Fu
College of Polymer Science and
Engineering
State Key Laboratory of Polymer
Materials Engineering
Sichuan University
24 South Section-1
Yihuan Road
Chengdu

610065 Sichuan
P. R. China
E-mail: huadeng@scu.edu.cn

E. Bilotti and T. Peijs*
Queen Mary University of London
Centre for Materials Research
and
School of Engineering and Materials
Science
Mile End Road
London
E1 4NS
UK

T. Peijs
Eindhoven University of Technology
Eindhoven Polymer Laboratories
5600 MB Eindhoven
The Netherlands
E-mail: t.peijs@qmul.ac.uk

Chapter 22

N. Dunne*
School of Mechanical & Aerospace
Engineering
Queen's University Belfast
Ashby Building
Stranmillis Road
Belfast
BT9 5AH
UK
E-mail: n.dunne@qub.ac.uk

C. Mitchell
School of Medicine, Dentistry and
Biomedical Sciences
Queen's University Belfast
Grosvenor Rd
Belfast
BT12 6BP
UK
E-mail: c.mitchell@qub.ac.uk

Chapter 23

C. Dewaghe*, C. Y. Lew and
M. Claes
R&D Department
Nanocyl S.A.
4 Rue de l'Essor
5060 Sambreville
Belgium
E-mail: cdewaghe@nanocyl.com
mclaes@nanocyl.com

P. Dubois
Polymer Materials and Composites
Services
University of Mons
Place du Parc 20
7000 Mons
Belgium
E-mail: philippe.dubois@materianova.be

Chapter 24

G. Beyer
Kabelwerk Eupen AG
Malmedyer Straat 9
B-4700 Eupen
Belgium
E-mail: gbeyer@euregio.net

Chapter 25

J.-F. Feller*, M. Castro and
B. Kumar
Smart Plastics Group
Laboratory of Materials Engineering
of Brittany (LIMAT^B)
University of South Brittany (UBS)
Christiaan Huygens Research Centre
Saint-Maude Street
56321 Lorient
France
E-mail: jean-francois.feller@univ-ubs.
fr; mickael.castro@univ-ubs.fr;
bijandra.kumar@univ-ubs.fr

Introduction to polymer–carbon nanotube composites

T. McNALLY, Queen's University Belfast, UK and P. PÖTSCHKE,
Leibniz Institute of Polymer Research Dresden, Germany

It is now well accepted that tubular structures of carbon, or carbon nanotubes (CNTs) existed for some time prior to their clear identification using microscopic techniques by Iijima in 1991 (Iijima, 1991) and to the subsequent reports on the predicted electronic structure of a fullerene tubule and large-scale synthesis of multi-walled CNTs (MWCNTs) in 1992 (Ebbesen and Ajayan, 1992; Mintmire *et al.*, 1992), and the synthesis of single-walled CNTs (SWCNTs) by two independent groups the following year (Bethune *et al.*, 1993; Iijima and Ichihashi, 1993). Raudushkevish and Lukyanovich in 1952 referred to 'carbon tubes' and Oberlin, Endo and Koyama in 1976 to 'hollow carbon fibres' and presented the first microscopic images at low magnification in which the hollow but not tubular structure of MWCNTs could be seen (Raudushkevish and Lukyanovich, 1952; Oberlin *et al.*, 1976). In 1978, the term 'nanotubes' was used for the first time in the context of carbon nanotubes (Wiles and Abrahamson, 1978). In 1987, Hyperion Catalysis International (of Cambridge, MA, USA) started to publish a series of patents with regard to the production of 'nanofibrils' and their use in masterbatches with polymers (Tennent, 1987). Moreover, CNTs were found in 2006 in ancient Damascus sabres used during the Crusades more than 400 years ago, most possibly formed as a consequence of the sophisticated thermo-mechanical treatment of forging and annealing applied by craftsmen to refine the steel to its exceptional quality (Reibold *et al.*, 2006). It is also most likely that Thomas Edison, when developing the light bulb circa 1880, using carbonised bamboo, produced similar carbon structures (Edison, 1879). The unique electrical, mechanical and thermal properties of CNTs have now been widely documented and, as was the case with other nanoparticles, the first large-scale commercial exploitation of carbon nanotubes will be as a functional filler for polymeric materials. The potential of CNTs to achieve electrically dissipative or conductive composites was first demonstrated by Hyperion Catalysis International in their masterbatches containing MWCNTs. The first reference to the potential of CNTs as mechanically reinforcing fillers for polymers was made indirectly by Ajayan *et al.* in 1994 (Ajayan *et al.*, 1994) and directly in 1998 by Wagner *et al.* working on a composite of MWCNTs with an UV cured *in-situ* polymerised urethane–diacrylate oligomer and again in 1998 by the same group (Lourie *et al.*, 1998) and Schadler *et al.* (Schadler *et al.*, 1998), both studying epoxy–MWCNT composites. Since then, there has been exponential growth in the study of composites of CNTs

with both thermosetting and thermoplastic polymers. A limited number of review articles have been published on this topic: by way of example, see (Breuer and Sundararaj, 2004; Moniruzzaman and Winey, 2006; Du *et al.*, 2007; Ahir *et al.*, 2008; Li *et al.*, 2008; McClory *et al.*, 2009; Byrne and Gun'ko, 2010; Spitalskya *et al.*, 2010). Most have focused on specific aspects of polymer–CNT composites, such as on elastomer–CNT composites (Bokobza, 2007) and mechanical properties of polymer–CNT composites (Coleman *et al.*, 2006).

However, at the time of compiling this text, no book had been published to date which describes comprehensively the preparation, properties, characterisation and applications of polymer–CNT composites. Therefore, we have attempted to provide a detailed account of the relevant topics and associated challenges in the field of polymer–CNT composites, with a particular emphasis on the state of the art at this time, through contributions from many of the leading researchers in this field. To this end, the book has been sub-divided into three parts.

Part I (Chapters 1–8) focuses on the preparation and processing of polymer–CNT composites. Specifically, in Chapters 2–4, the synthesis of polymer–CNT composites using non-melt mixing methods is described. In Chapter 1, Kaminsky reports on the *in situ* polymerisation techniques which can be readily employed to prepare polyolefin–CNT composites with MWCNT loading up to 25 wt%. The author describes how MAO catalyst can be anchored covalently to the surface of CNTs and ethylene or propylene polymerised from the surface. This approach yields good interfacial adhesion between the polymer and CNTs and the resultant composites have enhanced mechanical properties and thermal stability relative to the neat polymer. In Chapter 2, Dubois and co-workers describe the use of plasma technology to surface-treat CNTs prior to incorporation into a polymer matrix. Most interestingly, the authors report a plasma post-discharge treatment which avoids CNT degradation. Using this technique, they were able to graft amine groups onto the surface of CNTs which in turn were used as initiating sites for the ring opening polymerisation of ϵ -caprolactone. In Chapter 3, Mai and co-workers summarise the various methodologies available for the non-covalent and covalent functionalisation of CNTs for polymer nanocomposites. In particular, the authors emphasise the role of CNT functionalisation in dispersion of CNTs in polymer matrices and interfacial interaction between polymer and CNT, both important factors in obtaining efficient stress transfer from the polymer to the CNTs and achieving a reinforcing effect. Chapters 4 and 5 focus on the melt mixing/extrusion of polymer–CNT composites. In Chapter 4, Pötschke and co-workers describe how material and processing parameters influence CNT dispersion in polymer melts. The authors discuss both batch mixing using small-scale mixers and continuous melt mixing using twin-screw extrusion of different polymer–CNT systems. They report how polymer type, melt viscosity, polymer molecular weight, screw speed, processing temperature and residence time affect CNT dispersion. In Chapter 5, Li and Shimizu describe the application of very high shear ($>1000 \text{ sec}^{-1}$) melt processing of polymer–CNT composites. The authors

demonstrated the effectiveness of high shear melt mixing in achieving CNT dispersion in both a homopolymer and a polymer–polymer blend. Secondary melt processing and shaping of polymer–CNT composites, such as injection moulding, have hitherto not been studied in detail. In Chapter 6, Lew and Claes report on the relationship between polymer–CNT composite properties, including electrical conductivity and surface finish as a function of varying injection moulding parameters, such as injection melt temperature and injection speed. Chapters 1–6 focus on the preparation and processing of thermoplastic CNT composites, however the remaining two chapters in Part I, Chapters 7 and 8, describe the preparation and properties of elastomer– and thermoset–CNT composites, respectively. In Chapter 7, Klüppel and co-workers describe the preparation of elastomer–CNT and elastomer hybrid filler composites, highlighting the importance of adding a pre-dispersing agent to aid CNT dispersion. The authors also report the dielectric, electrical and thermal conductivity, mechanical and fracture properties of the resultant composites. In Chapter 8, Kenny and co-workers present a chemo-rheological approach and analysis of a number of epoxy–CNT systems where the effect of CNT type (SWCNT, DWCNT and MWCNT) and functionality on composite properties, including cure kinetics, was examined.

In Part II (Chapters 9–20) the properties of a number of different polymer–CNT systems (Chapters 9, 10, 11, 12, 16) and two of the principal techniques employed to characterise polymer–CNT composites (Chapters 14 and 15) are described. The remaining chapters focus on multi-scale modelling of polymer–CNT composites (Chapter 13), detailed studies of specific polymer–CNT composite systems (Chapters 17, 18 and 19) and, most timely, on the toxicity of CNTs (Chapter 20). As is widely accepted, the key challenge to fully exploiting polymer–CNT composites is achieving highly dispersed and distributed CNTs in the polymer matrix, the extent of which is in many instances the key factor to optimising composite properties. In Chapter 9, Pötschke and co-workers describe the quantification of CNT dispersion and distribution using extensive microscopic techniques. Furthermore, the authors provide a methodology to determine the spatial distribution and orientation of CNTs in a polymer matrix. Alig and co-workers in Chapter 10 discuss the inter-relationship between thermo-rheological history, CNT network structure and composite properties. Using well-defined shear-flow conditions and in-line measurements, the authors describe the influence of processing history on CNT network formation and destruction, electrical conductivity, and viscoelastic properties of CNT-filled polymer melts. In Chapter 11, Nanni and Valentini describe the underlying theory and electromagnetic properties of polymer–CNT composites. Goh, in Chapter 12, provides an introduction to the ‘grafting-to’ and ‘grafting-from’ methods for grafting polymers onto the surface of CNTs and a detailed review of the mechanical properties of a range of polymer–CNT composite systems reinforced with polymer-grafted CNTs. In Chapter 13, Odegard describes a general framework for multi-scale modelling of CNT composites, a topic hitherto poorly

described in the literature due to multi-scale modelling approaches that incorporate both molecular- and continuum-level simulations being relatively new, limited experimental validation of the models available and the limitations of molecular dynamics simulations of polymers over long time scales. The author discusses the fundamental aspects of efficient and accurate modelling techniques and provides a review of current state-of-the-art modelling approaches and applies one such model to predict the modulus of CNT-filled polyethylene. Two key characterisation tools, Raman spectroscopy and melt rheology, have been used to study the structure–property relationships of polymer–CNT composites. In Chapter 14, Wagner describes the application of Raman spectroscopy to the study of polymer–CNT interactions and demonstrates the usefulness of the Raman signature of CNTs as a detector device for the presence of bulk matrix defects, the occurrence of polymer phase transitions, and the change in CNT orientation with respect to an applied stress. Nobile, in Chapter 15, demonstrates the effectiveness of rheology measurements in understanding the linear and non-linear viscoelastic behaviour of polymer–CNT composites. The effect of CNT dispersion, aspect ratio, and alignment on the rheology of polymer–CNT composites is discussed. The rheological behaviour of polymer–CNT composite melts in shear and uniaxial elongational flows and the role of MWCNTs in flow-induced crystallisation of polymer–CNT composites are reported. The thermal degradation/stability of polymer–CNT composites plays a crucial role in their melt processing and ultimately application. In Chapter 16, Su and co-workers review the mechanisms of thermal degradation improvement of polymers afforded by CNT addition and discuss the thermal degradation of a range of polymer–CNT composites. Morcom and Simon in Chapter 17 provide a detailed review of polyolefin–CNT composites. The authors discuss a wide range of processing methods used to prepare polyolefin–CNT composites and review the effect of CNT addition on polyolefin crystallinity as well as the mechanical, rheological, electrical, thermal, and wear properties of this family of composites. In Chapter 18, McNally and co-workers describe the preparation of composites of poly(ethylene terephthalate) (PET), an important engineering polymer, with MWCNTs. The authors report the electrical and rheological percolation of these composites as a function of CNT loading. They also provide the results of a detailed study of the crystallisation behaviour of PET on CNT addition, using a combination of differential scanning calorimetry and Fourier transfer infrared and Raman spectroscopy. Gödel and Pötschke, in Chapter 19, describe the localisation of CNTs in polymer blends during melt mixing. The authors discuss tailoring the localisation of CNTs and highlight the factors which influence transfer and localisation of CNTs and other nano-scale fillers. The impact of selective localisation of CNTs on polymer blend rheology and morphology is also described. The potential toxicity of CNTs and CNT composites continues to be a controversial topic with several conflicting reports published to date. As there may be many possible bioengineering and biomedical applications of polymer–CNT composites, the toxicity of CNTs is

currently of immense interest. In Chapter 20, Martin and co-workers describe the toxicology of CNTs compared with other particulate materials and compare CNTs and asbestos, from respiratory exposure studies. The authors discuss the toxicity of CNTs and the parameters that influence their toxicity, including aspect ratio, level of CNT aggregation, surface chemistry and defects, and CNT impurity.

Finally, in Part III (Chapters 21–25), some of the more technologically interesting applications of polymer–CNT composites are discussed. In Chapter 21, Peijs and co-workers describe the production of polymer–CNT composite fibres and the orientation of CNTs and polymer during fibre production. The authors also report the electrical, mechanical and sensing properties of polymer–CNT fibres. Dunne and Mitchell in Chapter 22 provide a comprehensive review of the biomedical and bioengineering applications of polymer–CNT composites, with a particular emphasis on joint replacement surgery and dentistry. Initially, the use of CNTs in orthopaedic implants and dentistry, including in dental restorative materials, periodontal dentistry and denture base resins, is discussed. The authors then discuss the use of CNTs in regenerative medicine and tissue engineering, including targeted drug delivery systems, monitoring biological systems and biosensors. In Chapter 23, Dewaghe and co-workers describe the fire-retardant applications of polymer–CNT composites. The authors discuss fire testing, fire protection mechanisms, and the role CNTs can play in fire retardation, including the impact of CNTs on heat release rate and the influence of CNT dispersion. They also report, using examples, on the synergism between CNTs and ammonium phosphate in intumescent systems, and the use of CNTs in flame-resistant coatings. Beyer, in Chapter 24, describes the use of polymer–CNT composites in cable applications, with particular focus on the flammability of composites of LLDPE with MWCNTs, and EVA with MWCNTs and with a hybrid filler system based on MWCNTs and a nanoclay. The crack density and surface characteristics of charred MWCNT compounds are also assessed. In Chapter 25, Feller and co-workers discuss the concept of sensing with conductive polymer–CNT composites. The authors describe the synthesis, fabrication, characterisation and structure-sensing properties of polymer–CNT composites. Using examples, the authors also demonstrate the use of these composite materials in temperature, stress and chemical sensing applications.

It was the intention of the editors when compiling this book to address as many of the issues and topics associated with polymer–CNT composites as possible. Specifically, each contributor, a leading researcher in the field, was invited to include a review of the current-state-of-the-art of the relevant topic covered in their chapter and, where applicable, include new results. To the best of our knowledge, this is the first comprehensive text to be published which solely focuses not only on specific polymer–CNT composite systems but also on general relationships, characterisation and the properties of polymer–CNT composites. Many key challenges remain, all highlighted throughout the book, which must be addressed if polymer–CNT composites are to find widespread commercial application.

References

- Ahir, S.V., Huang, Y.Y., Terentjev, E.M. (2008) 'Polymers with aligned carbon nanotubes: Active composite materials', *Polymer*, 49(18), 3841–3854.
- Ajayan, P.M., Stephan, O., Colliex, C., Trauth, D. (1994) 'Aligned carbon nanotube arrays formed by cutting a polymer resin-nanotube composite', *Science*, 265(5176), 1212–1214.
- Bethune, D.S., Kiang, C.H., de Vries, M.S., Groman, G., Savoy, R., Vasequez, J., Beyers, R. (1993) 'Cobalt-catalysed growth of carbon nanotubes with single-atomic-layer walls', *Nature*, 363, 605–607.
- Bokobza, L. (2007) 'Multiwall carbon nanotube elastomeric composites: a review', *Polymer*, 48, 4907–4920.
- Breuer, O., Sundararaj, U. (2004) 'Big returns from small fibers: a review of polymer/carbon nanotube composites', *Polymer Composites*, 25, 630–645.
- Byrne, M.T., Gun'ko, Y.K. (2010) 'Recent advances in research on carbon nanotube–polymer composites', *Advanced Materials*, 22, 1672–1688.
- Coleman, J., Khan, U., Blau, W.J., Gun'ko, Y.K. (2006) 'Small but strong: a review of the mechanical properties of carbon nanotube–polymer composites', *Carbon*, 44(9), 1624–1652.
- Du, J.-H., Bai J., Cheng H.-M. (2007) 'The present status and key problems of carbon nanotubes based polymer composites' *eXPRESS Polymer Letters*, 1(5), 253–273.
- Ebbesen, T.W., Ajayan, P.M. (1992) 'Large-scale synthesis of carbon nanotubes', *Nature*, 358, 220–221.
- Edison, T. (1879) 'Electrical lamp', US Patent 223 898.
- Iijima, S. (1991) 'Helical microtubules of graphitic carbon', *Nature*, 354, 56–58.
- Iijima, S., Ichihashi, T. (1993) 'Single-shell carbon nanotubes of 1-nm diameter', *Nature*, 363, 603–605.
- Li, C., Thostenson, E.T., Chou, T.-W. (2008) 'Sensors and actuators based on carbon nanotubes and their composites: a review', *Composite Science & Technology*, 68(6), 1227–1249.
- Lourie, O., Cox, D.M., Wagner, H.D. (1998) 'Transmission electron microscopy observations of fracture of single-wall carbon nanotubes under axial tension', *Applied Physics Letters*, 73(24), 3527–3529.
- McClory, C., Chin, S.J., McNally, T. (2009) 'Polymer carbon nanotube composites', *Australian Journal of Chemistry*, 62(8), 762–785.
- Mintmire, J.W., Dunlap, B.I., White, C.T. (1992) 'Are fullerene tubules metallic?', *Physical Review Letters*, 68(5), 631–634.
- Moniruzzaman, M., Winey, K. (2006) 'Polymer nanocomposites containing carbon nanotubes', *Macromolecules*, 39(16), 5194–5205.
- Oberlin, A., Endo, M., Koyama, T. (1976) 'Filamentous growth of carbon through benzene decomposition', *Journal of Crystal Growth*, 32(3), 335–349.
- Raudushkevish, L.V., Lukyanovich, V.M. (1952) 'O strukture ugleroda, obrazujucesja pri termiceskom razlozenii okisi ugleroda na zeleznom kontakte', *Zurn Fisis Chim*, 28(26), 88–95.
- Reibold, M., Paufler, P., Levin, A.A., Kochmann, W., Pätzke N., Meyer, D.C. (2006) 'Carbon nanotubes in an old Damascus sabre', *Nature*, 444, 286.
- Schadler, L.S., Giannaris, S.C., Ajayan, P.M. (1998) 'Load transfer in carbon nanotube epoxy composites', *Applied Physics Letters*, 73(26), 3842–3844.

- Spitalskya, Z., Tasis, D., Papagelis, K., Galiotis, C. (2010) 'Carbon nanotube-polymer composites: chemistry, processing, mechanical and electrical properties', *Progress in Polymer Science*, 35, 357–401.
- Tennent, H.G. (1987) 'Carbon fibrils: method for producing same and compositions containing same,' US Patent 4 663 230.
- Wagner, H.D., Lourie, O., Feldman, Y., Tenne, R. (1998) 'Stress-induced fragmentation of multiwall carbon nanotubes in a polymer matrix', *Applied Physics Letters*, 72(2), 188–190.
- Wiles, P.G., Abrahamson, J. (1978) 'Carbon fibre layers on arc electrodes – I: their properties and cool-down behaviour', *Carbon*, 16, 341–349.

Polyolefin–carbon nanotube composites by *in-situ* polymerization

W. KAMINSKY, University of Hamburg, Germany

Abstract: The *in-situ* polymerization of olefins such as ethylene and propylene (PP) in the presence of carbon nanotubes (CNTs) is one of the most efficient and versatile ways to synthesize polyolefine nanocomposites. Since a good interfacial adhesion between polyolefin matrix and carbon nanotubes is crucial for successful preparation, the polymerizations were performed with methylaluminoxane (MAO) anchored covalently to the surface of the nanotubes. Thus, a heterogeneous co-catalyst is formed and the polymerization starts with the addition of ethylene or propylene directly on the tube surface. The resulting nanocomposites contain 0.1–25.0 wt% of homogeneous distributed CNT and a good separation of the individual tubes. They show better crystallization temperatures, temperature stability and mechanical properties than unfilled polyolefins.

Key words: *in-situ* polymerization, metallocene catalysts, polyethylene composites, polyolefins, polypropylene composites.

1.1 Introduction

Polyolefins such as polyethylene (PE) and polypropylene (PP) are the biggest group of polymers with a high growth rate potential, due to their versatile properties, their easy tailored microstructure, and their low costs (Galli and Vecellio, 2004). In 2009, about 120 million tons of polyolefins were produced worldwide (Kaminsky, 2008). Temperature stability, the stiffness, and electric conductivity can be increased by the incorporation of nanoparticles and nanotubes (Moniruzzaman and Winey, 2006; Ajayan and Tour, 2007). The uniform dispersion of the carbon nanotubes (CNTs) in the polymer matrices is required to enhance the good physical and mechanical properties of the composite material. Various techniques to prepare nanocomposites have been studied, such as ultrasonication in combination with solution blending (Barrau *et al.*, 2003; Okamoto *et al.*, 2008), melt blending (Bhattacharyya *et al.*, 2003; Wu *et al.*, 2008), and *in-situ* polymerization (Bonduel *et al.*, 2005; Wiemann *et al.*, 2005; Jeong *et al.*, 2008).

If nanocomposites are prepared via solution blending, the filler is mixed with a polymer in solution. In addition to mechanical mixing, ultrasound can be used to separate the filler particles. When the dispersion is satisfactory, the solvent is evaporated to yield the filled polymer. This method is suitable for systems that consist of a polymer which is soluble in common solvents (Andrews *et al.*, 1999) and also where the nanofiller can be dispersed well. Polyethylene or highly tactic

polypropylene, especially with high molecular masses, is not a good soluble in most low boiling organic solvents, which makes this method problematic for the preparation of PE-CNT- or PP-CNT-based nanocomposites.

In the case of a melt-compounding technique, molten polymer and the nanofillers are mixed intensively under the exposure of shear forces. Different kinds of mixing devices, such as a twin-screw extruder, are available for this task. It is important that the shear forces exerted by the mixer are sufficient to tear the individual particles apart. Especially in the case of carbon nanotubes (CNT), this can be a serious problem because they have a high tendency to agglomerate due to a very high surface energy. This method is not suitable for highly viscous melts of polymers because the mixing is not optimum and the high shear forces can lead to a partial degradation of the polymer itself. A good dispersion of CNT in polyolefin matrices can only be achieved by simple melt-compounding at low filler contents and low molecular masses and an accordingly low viscosity of its melt (Alexandre *et al.*, 2001).

A wide variety of polymer carbon nanotube composites have been prepared by *in-situ* polymerization using epoxy resins, polyesters, polyurethanes, polyacrylates, polyamides, and polyolefins as the matrix (Harris *et al.*, 2004; Coleman *et al.*, 2006; Tasis *et al.*, 2006).

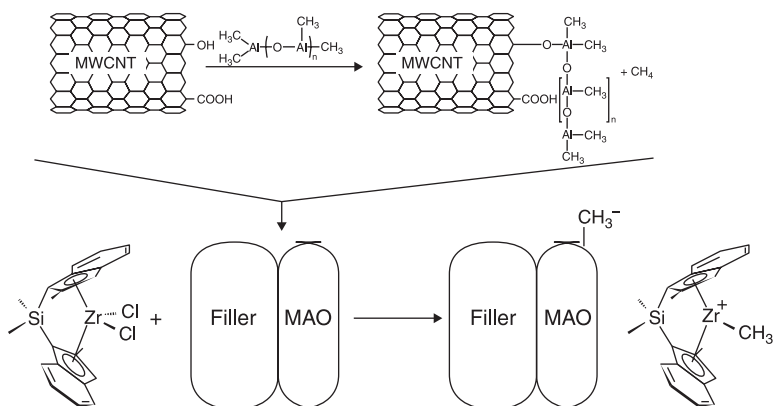
For polyolefin nanocomposites, the *in-situ* polymerization of polyolefins in the presence of CNT is one of the most efficient and versatile ways to synthesize nanocomposites. Metallocene-methylaluminoxane (MAO) catalysts allow the tailoring of the polymer microstructure, tacticity, and stereoregularity, by the utilization of a metallocene with a suitable ligand structure (Brintzinger *et al.*, 1995; Kaminsky, 2004). Polypropylene with an isotactic, syndiotactic, or atactic configuration can be obtained by using C_{2-} , C_{2v-} , or C_{s-} symmetric zirconocenes (Ewen *et al.*, 1988; Resconi *et al.*, 2000). These catalysts are also excellent tools in the production of copolymers. Metallocene-MAO catalysts are highly active in the production of precisely designed polyolefins and engineering plastics (Coates, 2000; Scheirs and Kaminsky, 2000; Razavi and Thewalt, 2006) and also permit the control of the molecular masses.

The forces necessary to separate the CNT agglomerates into individual particles by melt-compounding or solution blending are applied during the compounding process, while during *in-situ* polymerization they can be applied beforehand. The *in-situ* polymerization provides the possibility of a previous CNT separation during the 'pre-treatment' in a low viscosity medium like toluene at a comparatively low energy input (e.g. by ultrasound). The matrix is synthesized afterwards in the presence of the (already separated) nanotubes. The resulting nanocomposites are generally indicated by a good separation, homogeneous distribution, and a good wetting with polymer (Andrews *et al.*, 1999; Dong *et al.*, 2006; Funck and Kaminsky, 2007). Theoretically, it should be possible to produce a nanocomposite with any molecular weight at any filler content desired. But there are some polymer fiber agglomerizations which occur when high molecular weight polyolefins are synthesized.

1.2 *In-situ* polymerization techniques for polyolefin-CNT composites

Metallocene-MAO and other single site catalysts are soluble in hydrocarbons and therefore, they can perfectly cover the surface of carbon nanotubes, especially if the surface of multi-walled carbon nanotubes (MWCNTs) shows defects. In a first step, MAO as co-catalyst can be adsorbed or anchored on the surface of MWCNT to change the surface to a hydrophobic one (Fig. 1.1). The absorption of MAO is increased if the carbon nanotubes are oxidized with the formation of hydroxyl and carboxy groups. These groups can react with MAO by the formation of covalent oxygen aluminum bond, without deactivation effects on the catalyst. Excess MAO is washed out. As a second step, the metallocene is added to form catalytically active polymerization sites on the nanosurface (Funck and Kaminsky, 2007). The metallocene, together with MAO, forms an ion pair as active site with an anionic MAO and a cationic metallocene. The cations are sitting outside on the nano surface and through the positive load prevent the aggregation of the tubes. This is one reason why there is such a good dispersion of the fillers in polyolefins obtained by *in-situ* polymerization with metallocene catalysts. The thickness of the polymer coat, formed by the addition of ethylene or propylene, depends on the polymerization time and the pressure of the monomer. The *in-situ* polymerization leads to polymer-encapsulated carbon nanotubes.

At the beginning of an experiment, single-walled carbon nanotubes or oxidized multi-walled CNT (2–20 walls, average outer diameter 15 nm, length up to 50 μm supplied by Nanocyl S.A., Sambreville, Belgium) were sonicated in a toluene suspension, using a Sonopuls homogenizer HD 2200 equipped with a KE 76 sonotrode. The amplitude (10–50%) and the sonication time (5–120 min) were varied to achieve an optimum distribution of fillers in the polymer. The sonicated



1.1 Formation of active sites for polymerization on the surface of MWCNTs.

fillers were then either introduced directly into the toluene-charged reactor (without pre-reaction) or stirred with 2 ml of MAO solution (equivalent to 200 mg MAO) for 24 hours (with pre-reaction). MAO was purchased from Crompton as a 10 wt% solution in toluene. After it was filtered over a D4 fritted glass filter, toluene and trimethylaluminum were removed under reduced pressure. The MAO was used as a 100 mg/mL freshly prepared solution in dry toluene. Triisobutylaluminium (TIBA) was obtained from Aldrich and used as a 1 mol/L solution in toluene. The metallocene catalysts such as [rac-dimethylsilylbis(2-methyl-4-(1-naphyl)indenyl)zirconium dichloride] (see Fig. 1.4 (c)) were purchased from Boulder Scientific. The concentration of the solution was 5 mmol/L.

All polymerizations were carried out in a 1-litre glass reactor (from Büchi AG, Ulster, Switzerland) that was heated to 90°C for 1 hour and then flushed with argon. The reactor was charged with 200 ml of toluene and heated to 30°C polymerization temperature. In the case of the polymerizations without pre-reaction, MAO and the fillers were introduced into the reactor immediately after sonication, and the dispersion was then saturated with ethylene or propylene at the desired pressure using a mass-flow controller (from Brooks Instruments, 5850 series). The reaction was started by an injection of the metallocene about 10^{-6} mol zirconocene, Al:Zr = 3500 to 7000. In case of the polymerizations with pre-reaction, 2 ml of TIBA solution (1 mmol/ml toluene) were added to the toluene before saturation with propylene. The pre-activated catalyst (filler/MAO/metallocene) was injected into the reactor when saturation was completed using a pressure lock. Polymerizations were typically quenched after 45 min by adding 5 ml of ethanol. All polymers were stirred with a quenching solution (water, ethanol, hydrochloric acid) overnight, filtered, washed and dried under vacuum at 60°C. In this way, polyolefin-carbon nanotube composites with 0.5–50 wt% filler content were obtained.

Melting temperatures, T_m , were determined by differential scanning calorimetry (DSC) with a DSC 821e (from Mettler-Toledo) from the second heating cycle at a heating rate of 20 K/min. Crystallization temperatures, T_c , were determined by DSC from the cooling curve (cooling rate 10 K/min) after complete melting at 200°C for 5 min. All crystallinities were calculated from the melting peak of the second heat of the basis of a crystallization enthalpy of 207 J/g for 100% crystalline isotactic polypropylene (Wang *et al.*, 2001). The half-time of crystallization ($\tau_{0.5}$) was determined by isothermal DSC experiments. The samples were quenched to the desired isothermal crystallization temperature (cooling rate 40 K/min) after they were entirely molten at 200°C for 5 min. Electron microscopy was performed on a Leo 1530 FE-REM (SEM) and on a JEOL JEM-1011 (TEM). For studies of morphology, composite cryofractures were used. Gel permeation chromatography was carried out with a Waters GPC 2000 Alliance system equipped with a refractive index detector, viscosimetric detector, and a set of three columns, Styragel type. The particle size for each column was 10 μm , and the pore

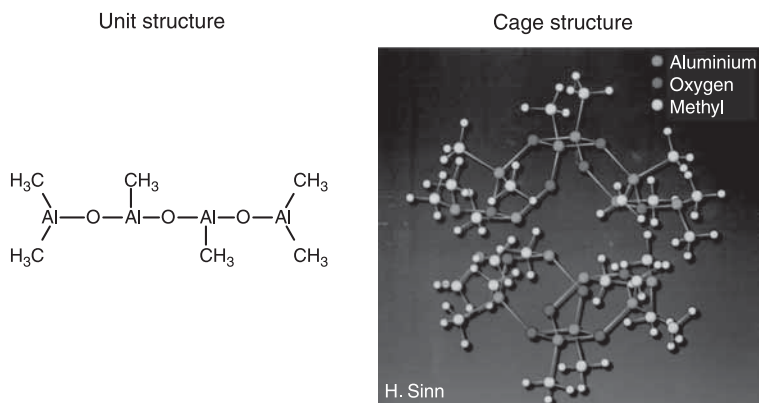
sizes were 10^3 Å (HT3), 10^4 Å (HT4), and 10^6 Å (Hto). 1,2,4-Trichlorobenzene was used as solvent. The analyses were performed at 140 °C and 1.0 mL/min.

1.3 Polymer architecture by metallocene catalysis

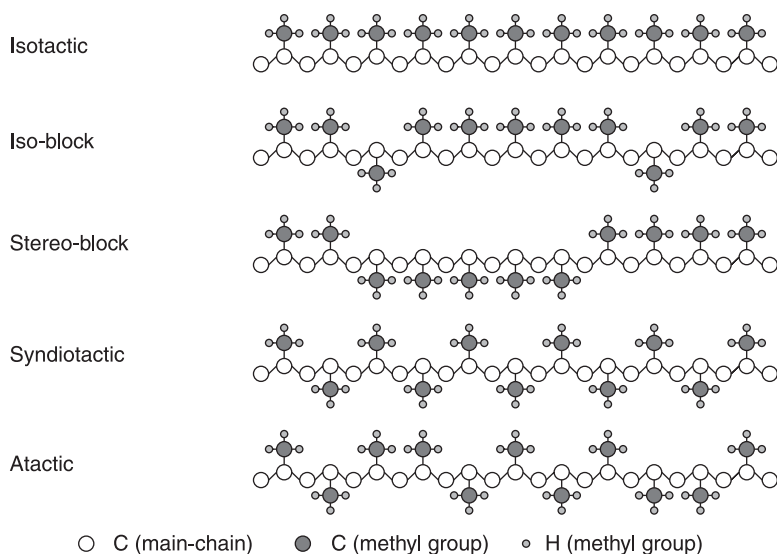
In comparison to Ziegler-Natta catalysts, metallocene-MAO catalysts show only one type of active site and their chemical structure can easily be changed. These properties allow one to accurately predict the properties of the resulting polyolefins by knowing the structure of the catalyst used during their manufacture and to control the resulting molecular weight and distribution, comonomer content and tacticity by careful selection of the appropriate reactor conditions. In addition, their catalytic activity is 10–100 times higher than that of the classic Ziegler-Natta systems.

A key factor in the activation of metallocenes is the co-catalyst. MAO is a mixture of different structures in which the unit $\text{Al}_4\text{O}_3(\text{CH}_3)_6$ is the main product (Fig. 1.2). The compound is electronically unsaturated (Fig. 1.2) as a Lewis acid and forms bigger cages or clusters such as from 3 or 4 units and separation of trimethylaluminum as condensation reactions (Sinn, 1995; Koide and Barron, 1996).

It is generally assumed that the function of MAO is first to undergo a fast ligand exchange reaction with the metallocene dichloride, thus rendering the metallocene methyl and dimethyl aluminium compounds. In a further step, either Cl^- or CH_3^- is abstracted from the metallocene compound by an Al-centre in MAO, thus forming a metallocene cation and a MAO anion (Sishta *et al.*, 1992). The alkylated metallocene cation represents the active centre. Meanwhile, other weakly coordinating cocatalysts, such as tetra(perfluorophenyl)borate anions $[(\text{C}_6\text{F}_5)_4\text{B}]^-$, have successfully been applied to the activation of metallocenes (Duchateau and Bochmann, 1997; Sishta *et al.*, 1992).



1.2 Structure of methylaluminoxane (MAO) (Sinn, 1995).



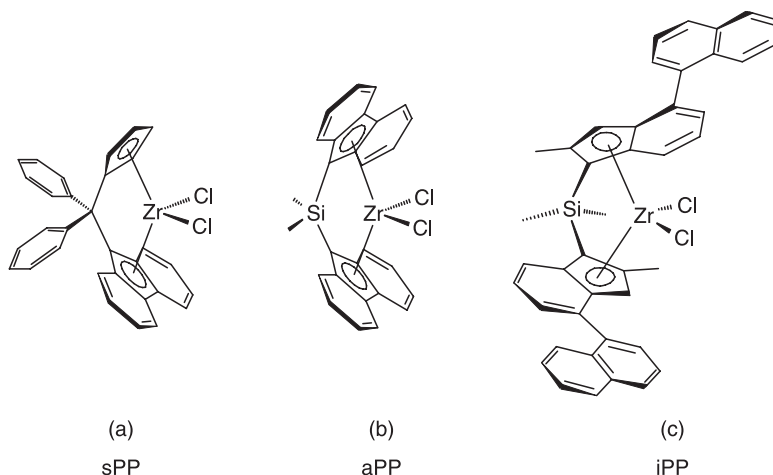
1.3 Microstructures of PPs that can be obtained by different metallocene catalysts. The hydrogen atoms of the backbone are not included.

Using metallocene catalysts it is possible to produce polyolefins with a narrow molecular weight distribution ($M_w:M_n = 2$) and high activities. The catalyst of bis(cyclopentadienyl) zirconiumdichloride (Cp_2ZrCl_2)/MAO produces 95 °C polyethylene with an activity of 40 million g PE/g Zr · h. Polypropylenes, with different microstructures and characteristics, can be custom-made just by varying the ligands on metallocene (Fig. 1.3).

The different microstructures are shown in Fig. 1.4. Bridged fluorene-cyclopentadienyl catalysts (a) with a C_s -symmetry produces a syndiotactic polypropylene, C_1 -symmetric catalysts such as bisfluorenyl (b), or unbridged bis(cyclopentadienyl) zirconocenes produce atactic polypropylenes and C_2 -symmetric metallocenes such as bridged and substituted bis(indenyl) complexes (c), produce isotactic polypropylenes.

Isoblock and stereoblock structures are obtained if insertions happen by higher temperatures or by different substitutions of the metallocene structure. By combining different olefins and cycloolefins with one another, the range of characteristics can be further broadened (Kaminsky, 1998).

Copolymers, block copolymers, and long-chained copolymers such as ethylene/propylene copolymers, ethylene/norbornene-, propylene norbornene copolymers are of interest because of their high melting and glass transition points up to 200 °C (Kaminsky *et al.*, 2004; Arriola *et al.*, 2006). Long-chain branched polyethylenes can be obtained with a crystallizing polyethylene backbone chain



1.4 Structures of zirconocenes used as catalyst components for olefin polymerization. The C_s -symmetric catalyst $[\text{Ph}_2\text{C}(\text{Cp})(\text{Flu})]\text{ZrCl}_2/\text{MAO}$ (a) produces syndiotactic poly(propylene) (sPP); the C_1 -symmetric catalyst $[\text{Me}_2\text{Si}(\text{Flu})_2]\text{ZrCl}_2/\text{MAO}$ (b) atactic poly(propylene) (aPP); and the C_2 -symmetric catalyst $\text{rac}[\text{Me}_2\text{Si}(2\text{-Me}_4\text{-(1-Naph)-1-Ind)}_2]\text{ZrCl}_2/\text{MAO}$ (c) isotactic poly(propylene) (iPP).

and oligoethylene or oligopropylene side chains. The oligopropylene side chain can have iso-, syndio-, or atactic microstructures. In the case of long-chain branched polypropylenes, the variety is even higher (Arikan *et al.*, 2007). All these homo- and copolymers can be synthesized by *in-situ* polymerization to coat carbon single- and carbon multi-walled nanotubes.

1.4 Polyethylene–CNT composites

Polyethylene multi-walled carbon nanotube–polyethylene composites (PE–MWCNT) were prepared by *in-situ* polymerization with different metallocene catalysts. Park *et al.* (2008) used biscyclopentadienyl zirconiumdichloride (Cp_2ZrCl_2) as the catalyst. The content of MWCNT in the polymer was varied between 1 and 5 wt%. The electrical, thermo- and dynamic mechanical properties are of great interest (Yang *et al.*, 2007). Low amounts of MWCN can reduce the electrostatic load of polyethylene films drastically.

We investigated PE–MWCNT composites synthesized by the highly active zirconocene b (see Fig. 1.4). For the *in-situ* polymerization, oxidized MWCNTs were used (Table 1.1). PE–MWCNT composites can be produced with very high activities; 20,000 kg of polymer is obtained in one hour with one mol of the zirconium complex. As suspected, the activity decreases with an increasing amount of tubes in the starting suspension from 29,000 kg PE/mol Zr·h (pure PE) down to 4700 kg PE/mol Zr·h (18.4 wt% of CNT in PE). There is nearly no effect

Table 1.1 Synthesis of PE–MWCNT composites by 30°C in toluene using $[\text{Ph}_2\text{C}(\text{Cp})(\text{Flu})]\text{ZrCl}_2/\text{MAO}$ (structure (a) in Fig. 1.4)

mg CNT in suspension	wt% CNT in polymer	Activity kg PE/mol Zr-h	Molecular weight of PE (g/mol)	Melting point (°C)	Crystallization temperature (°C)
0	0	29 000	800 000	139.0	107.3
20	0.6	23 000	990 000	139.8	115.5
35	0.8	23 500	850 000	138.2	116.6
90	1.0	21 000	810 000	139.2	115.9
100	1.6	20 000	750 000	138.7	116.8
150	3.3	5 900	780 000	136.5	116.9
190	5.8	6 800	650 000	136.2	117.4
190	8.6	5 100	880 000	135.7	116.9
200	10.0	6 000	780 000	136.7	115.7
200	18.4	4 700	740 000	136.6	115.4

Table 1.2 Specific conductivity of PE/CNT composites depending on the filler content

Material	Specific electric conductivity (S/cm)
Pure PE	10^{-13}
PE/0.6 CNT	8×10^{-11}
PE/0.8 CNT	10^{-6}
PE/1.6 CNT	10^{-4}
PE/3.3 CNT	6×10^{-3}

of increasing CNT content on the molecular weight of the polyethylene. The molecular weight is high, about 700 000–900 000. Compared to pure PE, the nanocomposites show a decrease of 1 or 2 °C in the melting point. Only the crystallization temperature shows a significant effect. Small amounts (less than 1 wt% of CNT) are sufficient to increase the crystallization temperature by 10 °C. The tubes act as nucleation agents.

All PE–MWCNT composites are characterized by the strong increase in the tensile strength; the content of 1 wt% of MWCNT results in a tensile strength of 20 MPa while this value is only 5 MPa for pure PE, 10 wt% of MWCNT gives 47 MPa. Even higher is the effect for the electric conductivity (Table 1.2). For these measurements, plates of 1 mm thickness were pressed from the PE–CNT composite materials. The voltage used was 85 V.

The influence of the carbon nanotubes on the specific conductivity is low if the content is less than 0.6 wt%. If the content is more than 0.8 wt%, the conductivity increases more than 100 000 times.

1.5 Polypropylene–CNT composites

For the synthesis of polypropylene (PP)–CNT composites, double-walled (DWCNTs) and multi-walled carbon nanotubes (MWCNTs) were used. Composites were obtained with a matrix of isotactic polypropylene (iPP), ultra high molecular weight isotactic PP and syndiotactic PP (sPP) depending on the metallocene structure (for the metallocene structures, see Fig. 1.3).

1.5.1 Isotactic PP–CNT composites

Table 1.3 shows the most important polymerization conditions and properties of iPP/DWCNT composites. Zirconocene was used, dimethylsilyl(bis-2-methylindenyl)zirconiumdichloride $[\text{Me}_2\text{Si}(2\text{-Me-Ind})_2]\text{ZrCl}_2$.

The polymerization activity as well as the molecular mass of the obtained iPP matrix does not depend a lot on the filler content. Activities up to 27 000 kg PP/mol cat·h·[P] and molecular weights of the iPP of 380 000 were achieved. Surprisingly, the melting point of the iPP increased with increasing amounts of DWCNT. The double-walled carbon nanotubes not only increase the crystallization rate as found for PE–CNT composites, but also the tacticity of the polypropylene is increased. Less mis-insertion occurs. The crystallization temperature of highly filled PP is about 15 °C higher than that of pure iPP.

Similar results were obtained with MWCNT as fillers (Table 1.4) and the synthesis of high molecular weight iPP. The polymerization activities and the molecular weights of the iPP measured by viscosity do not depend greatly on the MWCNT content in the polymer.

The molecular weight (viscosity average) of the pure high molecular weight iPP is $M_v = 1\,400\,000$ g/mol for a metallocene catalyst with a typical polydispersity

Table 1.3 *In-situ* polymerization of iPP/DWCNT composites depending on the filler content; catalyst $[\text{Me}_2\text{Si}(2\text{-Me-Ind})_2]\text{ZrCl}_2/\text{MAO}$ (zirconocene structure in Fig. 1.1)

DWCNT content in the polymer (wt%)	Polymerization activity (kg iPP/mol Zr·h·[P])	Molecular mass g/mol	iPP melting temperature (°C)	Crystallization temperature (°C)
0	28 000	313 000	149.8	109.9
0.05	26 000	296 000	152.9	116.9
0.3	25 000	343 000	153.9	120.8
0.4	21 000	398 000	156.1	121.7
0.9	25 000	199 000	155.6	121.9
1.8	27 000	386 000	154.3	122.9
2.3	26 000	386 000	157.5	123.9
6.3	25 000	384 000	155.8	125.5
7.6	24 000	372 000	160.4	124.2

Table 1.4 *In-situ* polymerization of iPP/MWCNT composites depending on the filler content, catalyst $\text{Me}_2\text{Si}(2\text{-Me}_4\text{-(1-naph)-1-Ind)}_2\text{ZrCl}_2/\text{MAO}$ (structure (c) in Fig. 1.4)

MWCNT content in the polymer (wt%)	Polymerization activity (kg iPP/mol Zr-h-[P])	Molecular weight (Mv)	iPP melting temp. (°C)	iPP crystallization temperature (°C)
0	not detected	1 870 000	160.2	112.5
0.2	5 500	1 840 000	160.0	117.8
0.5	4 800	1 720 000	161.6	118.9
0.9	4 300	1 910 000	161.3	120.0
1.6	3 800	1 840 000	160.9	123.7
2.2	7 600	2 330 000	162.2	123.4
3.7	4 200	1 590 000	161.3	124.9
4.6	3 500	1 310 000	161.2	125.2
5.6	2 900	1 500 000	161.8	124.2
11.1	4 850	1 840 000	160.4	124.7

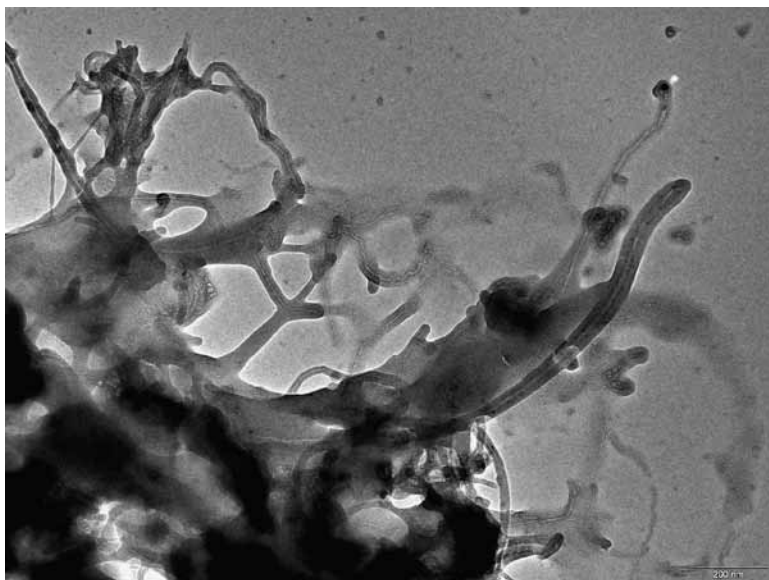
of two. The polymer matrix of the composites discussed here have a molecular weight in the range of $M_v = 1\,300\,000\text{--}1\,900\,000\text{ g/mol}$.

The wide scattering is probably a result of CNT remaining during the viscometric and GPC analyses. The polypropylene also shows for this catalyst a characteristic percentage of isotactic pentads of $97 \pm 2\%$. The supported MAO is sterically hindered and, due to the removal of solved MAO, the Al:Zr ratio is not optimal. However, the polymerization activity is determined to an average quantity of $5000\text{ kg}_{\text{Pol}}/(\text{mol}_{\text{Zr}}/\text{h} \times \text{mol}_{\text{Mon}}/\text{l})$.

To reinforce high and ultra-high molecular mass polypropylene with nanotubes through *in-situ* polymerization, a CNT pre-treatment that avoids the uncontrolled gelation of the polymer inside the reactor is necessary. This task is accomplished by linking the co-catalyst covalently to the nanotube surfaces.

To prevent the PP from forming an unwanted gel, the growing polymer strings must entwine themselves around the nanotubes. Therefore, the polymerization must take place directly and only on the CNT surfaces. To force the catalyst to form the active complex only with the inhibited MAO, immobilized on the CNT, no dissolved MAO must be left in the reactor. Consequently, any unreacted and dissolved co-catalyst is removed by a filtration and washing procedure (Kaminsky *et al.*, 2008).

The resulting and extremely strong nanocomposites were obtained in powder form while the high molecular weight iPP becomes insoluble during the polymerization process and tends to accumulate as a block around the stirrer. The obtained pure iPP normally must be cut off the stirrer in one piece and has a fibrous surface structure after drying. It is a great advantage that CNT-high molecular weight iPP can be obtained in powder form and this makes the processing easier.

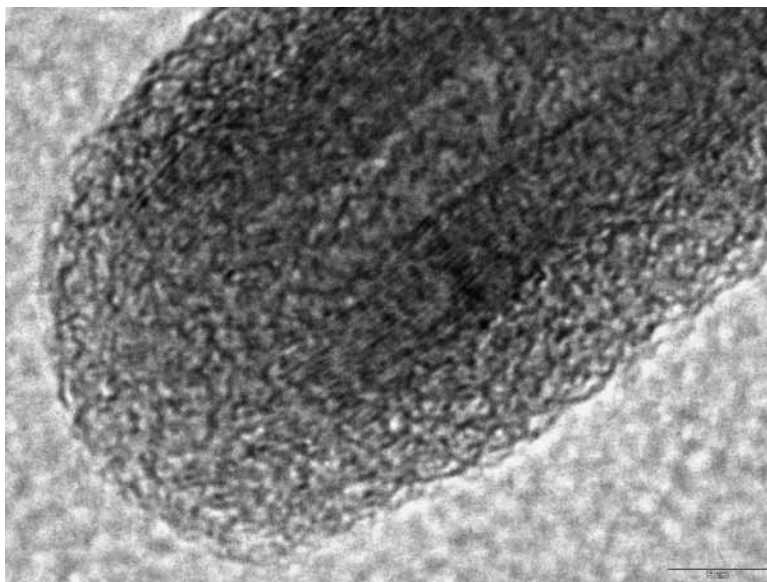


1.5 TEM micrograph of an iPP/MWCNT nanocomposite. The tubes are covered by thin film of iPP (8–10 nm), magnification 100000.

The morphology of the iPP–CNT nanocomposites was investigated by using scanning electron microscopy (SEM), while transmission electron microscopy (TEM) was used to prove the coating ability of the pre-treatment discussed here and the encapsulation of individual tubes (Fig. 1.5).

As expected, the polymer grows directly on the tube surface, which led to very good coverage and wetting of individual CNTs with a thin PP layer. The encapsulation is almost complete and nearly every tube is affected. It is also obvious that almost every nanotube is coated with about 10 nm *in-situ* grown polypropylene film and that there is a good attraction on the tubes. Even the small agglomerate on the lower left side is permeated with polymer and seems to be widening by the growth of the polymer chains. Figure 1.6 shows a detailed TEM micrograph of a funnel-shape opened MWCNT. The nanotube consists of 20 walls and is layered by an 8 nm thick *in-situ* grown PP film. The opened cap is covered, too.

The morphology of nanocomposites prepared by *in-situ* polymerization is, in comparison to those produced by melt-compounding, generally indicated by a good CNT separation, homogeneous distribution in the matrix, and a good polymer wetting, which in turn indicates a tight adhesion. Especially the pre-treatment discussed here led to an encapsulation of the tubes with a homogeneous iPP layer. SEM micrography taken from cryofractures of different high molecular weight iPP–MWCNT nanocomposites shows no pull-out effect.



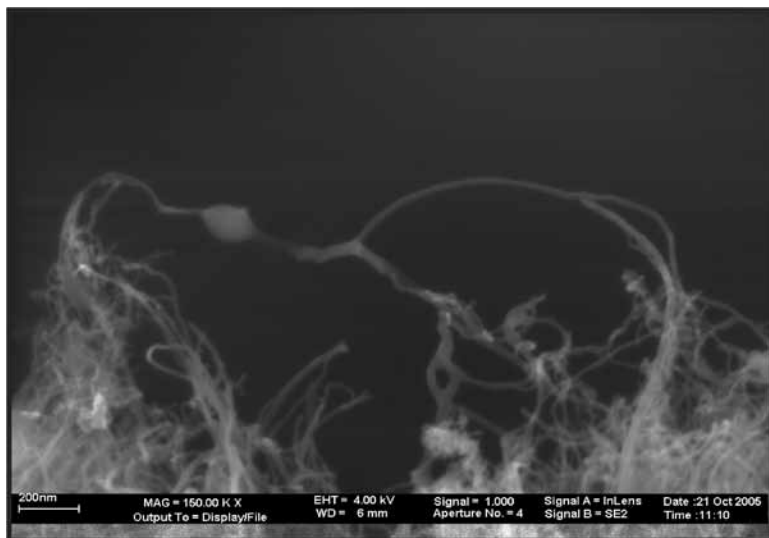
1.6 Detailed TEM micrograph of an opened MWCNT, covered by an 8 nm thick iPP layer, magnification 1 600 000.

If the polymerization time is reduced to some seconds by adding only traces of propylene, it can be seen where there are active sites on the surface of MWCNT formed by defects and anchoring the MAO–metallocene catalyst. Only at some parts of the tube does the polymerization form a ball of polypropylene (Fig. 1.7). The same can be found at the end of the tube (Kaminsky and Funck, 2008).

As previously discussed, a homogeneous distribution and a good interfacial adhesion are crucial for the successful preparation of nanocomposites. The main challenge in this context is to avoid the slipping of the polymer off the nanotubes (pull-out) under mechanical stress.

The differently loaded nanocomposites were examined according to their crystallization behavior which plays an important role during the processing of polymeric materials. It is known that CNTs act as nucleating agents (Valentini *et al.*, 2003; Wang *et al.*, 2006), therefore improvements in the crystallization behavior were expected.

Important parameters for the characterization of the crystallization behavior are the crystallization temperature (T_c), the melting temperature (T_m), and the half-time of crystallization ($\tau_{0.5}$). The melting temperature (see Table 1.4) is not influenced by the presence of nanotubes or their amount. The average melting temperature is $160 \pm 1^\circ\text{C}$. Also, the crystallinity is not affected by the CNT, i.e. in the range of $45 \pm 4\%$. In contrast to T_m , the effect on the crystallization temperature (T_c) is emphasized more. Pure high molecular mass iPP has a T_c of



1.7 SEM micrograph of MWCNT with a ball of iPP at an active site after 20 min polymerization time, magnification 150000.

about 118 °C. The addition of only 0.9 wt% MWCNT led to an increase in crystallization temperature by 5 °C. At higher filler contents the crystallization temperature rises rapidly by up to 7 or 8 °C above the one of pure iPP, leveling at a MWCNT content of about 3 wt%.

1.5.2 Syndiotactic PP–CNT composites

Syndiotactic PP is more flexible than isotactic PP and has therefore a potential for films and other applications. sPP–CNT nanocomposites can even expand these applications.

Different pre-treatments before polymerization were necessary to achieve a homogeneous distribution of the MWCNT. Preliminary experiments had shown that MWCNTs stayed aggregated if not treated with ultrasound prior to the polymerization. The effect of different ultrasonic amplitudes (which are a measure of the energy input) and various sonification times was investigated.

For experiments without pre-reaction, the MWCNTs were treated with ultrasound in a toluene suspension for 15 minutes prior to the polymerization. The amplitude was varied from 10 to 30%, and no pre-reaction with MAO was carried out. A higher ultrasonic amplitude led to a slightly better dispersion of the nanotubes. It was still not very good after treatment with an amplitude of 30%, however (Kaminsky and Wiemann, 2006).

The activity (Table 1.5) does not show any significant dependence on the amplitude used for the sonication of the fillers. It is 3500 to 4000 kg_{Pol}/(mol_{Zr}·h·[P])

Table 1.5 Activities of propylene polymerization after different pre-treatments of the MWCNTs, catalyst $[(p\text{-MePh})_2\text{C}(\text{Cp})(2,7\text{-bis-}t\text{BuFluo})]\text{ZrCl}_2/\text{MAO}$ (compare structure (a) in Fig. 1.4)

Pre-reaction time (h)	Amplitude (%)	Sonication time (min)	Activity (kg sPP/Zr·h·[P])	sPP molecular weight (g/mol)
0	10	15	3 700	280 000
0	20	15	3 900	275 000
0	30	15	3 800	270 000
24	10	15	2 600	290 000
24	20	15	2 600	290 000
24	30	15	2 600	285 000
24	10	30	2 900	295 000
24	10	60	2 600	315 000
24	10	120	2 900	310 000

and, therefore, in the range of the activities for the polymerizations without MWCNTs ($4300 \text{ kg}_{\text{PP}}/(\text{mol}_{\text{Zr}} \cdot \text{h} \cdot [\text{P}])$).

To improve the homogeneity of the dispersion, polymerizations were carried out after the same ultrasonic treatments, but this time a pre-reaction of the MWCNTs with MAO for approximately 24 hours was performed. The improvement of the dispersion with rising ultrasonic amplitude was somewhat more pronounced when the sPP-MWCNT nanocomposites were prepared with pre-reaction than when they were prepared without pre-reaction.

What is clearly more important than the effect of the amplitude is the effect of the pre-reaction with MAO on the dispersion. Obviously, the pre-reaction leads to a better distribution of the nanotubes in the sPP-matrix. This effect is probably due to the hydroxyl groups and other defects present on the surface of the MWCNTs. As described, they can react with the MAO, thus anchoring the co-catalyst to the surface of the nanotubes. This would, on one hand, prevent the nanotubes from reagglomerating after the ultrasonic treatment because of repulsive forces between the MAO ions. On the other hand, it would lead to the polymer formation directly on the surface of the fillers. The growing polymer chains would then separate the MWCNTs from each other during the polymerization.

In addition to the effect of the amplitude, the effect of the sonication time of the nanotubes on their distribution in the polymer matrix was investigated. The amplitude was set to 10% and the sonication times were 15, 30, 60 and 120 minutes. From Table 1.5, it can be seen that a longer sonication time generally improves the dispersion. The most homogeneous distribution is achieved for the sPP-MWCNT composite after sonication of the nanotubes for 120 minutes. This sPP-MWCNT nanocomposite contains 0.5 wt% of nanotubes as compared to 0.8 wt%, 0.4 wt%, and 0.8 wt% for the samples that had been sonicated

for 60, 20, and 15 minutes, respectively. The activities were still around $2500 \text{ kg}_{\text{Pol}}/(\text{mol}_{\text{Zr}} \cdot \text{h} \cdot [\text{P}])$.

For the subsequent polymerizations, an ultrasonic amplitude of 10% and a sonication time of 60 minutes were chosen as a compromise between a dispersion as homogeneous as possible and the possible damage of the nanotubes due to high amplitudes or long sonication times (Lu *et al.*, 1996). A series of sPP–MWCNT nanocomposites with filler contents between 0.1 and 0.9 wt% was prepared.

The quality of the adhesion of the matrix sPP to MWCNTs was estimated by SEM. There is an excellent dispersion of all individual tubes in the polymer matrix, no bundles are present. Moreover, no pull-out of nanotubes out of the polymer matrix is observed. This is proof of a very good adhesion of the polymer matrix to the nanotube surface because otherwise MWCNTs pointing straight out of the polymer surface and holes where they could have been pulled out of the polymer should have been observed. The carbon nanotubes were wet well, which also is a sign of a good adhesion between the components of the nanocomposite.

The molecular weights of the sPP–MWCNT nanocomposites were elevated slightly with regard to the pure sPP. There is almost no dependence on the molecular weights of sPP and the preparation technique (see Table 1.5). The molecular weight varies between 270 000 and 315 000 and is slightly higher for polymerizations with pre-reaction time. For neat sPP, a value of 310 000 g/mol synthesized by the same metallocene catalyst (Kaminsky *et al.*, 2006) was found. These materials were also characterized with respect to their crystallization behavior, their thermal degradation, their electrical properties, and their tensile properties (see next section).

1.5.3 Properties of polypropylene–CNT composites

The differently loaded syndio- and isotactic polypropylene–CNT nanocomposites were examined with regard to their degradation, tensile strength, crystallization properties, and selected mechanical properties. The results for the different filler contents of MWCNT in a syndiotactic PP matrix are summarized in Table 1.6.

The melting temperatures of the sPP–MWCNT composites are compared with pure sPP and increased slightly with the filler content. In the composites the melting temperatures lay at least two or four degrees above those of the neat sPP.

The crystallinity increased slightly with respect to the pure polymer as well. In this case, no trend regarding the dependence on the filler content is observed. All crystallinities were calculated from the melting peak of the second heat on the basis of a crystallization enthalpy of 164 J/g for the 100% crystalline material (Wang *et al.*, 2001).

A more pronounced effect of the filler content was observed for the crystallization temperatures. All crystallization temperatures of sPP–MWCNT were located above the crystallization temperature of pure sPP (96 °C). Already at a filler content as low as 0.1 weight-%, the crystallization temperature was

Table 1.6 Properties of some sPP/MWCNT composites

Filler content (wt%)	0	0.1	0.5	0.9
Melting temperature (°C)	140	142	144	144
Crystallinity (%)	27.0	27.5	27.5	29.5
Crystallization temperature (°C)	96	103	105	111
Rate constant at 122°C of crystallization (10 ⁻⁴ min ⁻¹)	7.5	88	n.d.	n.d.
Half-time of crystallization at 122°C (min)	16.6	5.3	2.3	n.d.
Degradation temperature (°C)	412	421	420	423
Tensile strength (MPa)	17.5	19.1	19.2	18.7

n.d. = not detected.

raised by 5°C in comparison to that of neat sPP. This effect is even more pronounced at higher filler contents. The nanocomposites containing 0.9% MWCNTs exhibit a crystallization temperature of 111°C which is 15°C higher than that of pure sPP. The rise in the crystallization temperature upon incorporation of carbon nanotubes is an indication of the nucleating ability of the MWCNTs.

Agreement exists about the fact that the crystallization temperature of PP is raised by the addition of carbon nanotubes. The extent of the increase shows great differences, however. The crystallization temperature of iPP–MWCNT films obtained by solution casting is raised to higher values by about 8°C upon addition of 0.5 wt% of carbon nanotubes (Sandler *et al.*, 2003). In contrast to that, the addition of 0.5 wt% single-walled carbon nanotubes (SWCNTs) to PP–EPDM blends by melt-compounding led to a rise in crystallization temperature of 4°C only. At higher filler loadings, even a lowering of the T_c is found (Valentini *et al.*, 2003). In iPP–SWCNT nanocomposites that had been prepared by solution blending of PP and SWCNT modified with octadecylamine, a filler content of 1.8 wt% SWCNTs was necessary to reach a 5°C increase in crystallization temperature. The peak sharpened when SWCNTs were present.

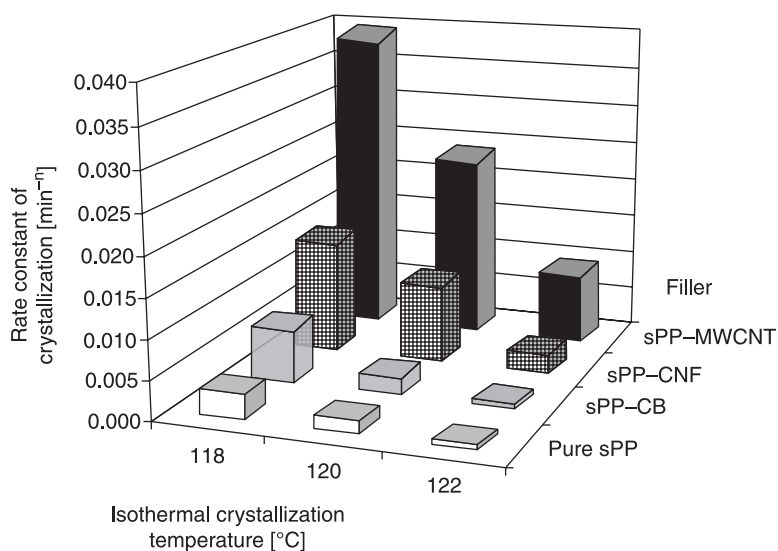
A melt-compounded sample of PP–SWCNT was subjected to isothermal and non-isothermal crystallization. The crystallization temperature of the composite containing 0.8 wt% SWCNT is raised by 11°C as compared to the neat polymer (Bhattacharyya *et al.*, 2003). The differences in the effect of comparable amounts of carbon nanotubes are probably due to differences in the homogeneity of the dispersion in the polymer matrix and to the different types of nanotubes used.

In our work, an enhancement of the crystallization temperature of 5 to 15°C of the sPP–MWCNT nanocomposites in comparison to the pure polymer could be achieved. At a filler content of 0.5 wt% of MWCNTs, the crystallization temperature was raised by 10°C which is more of an increase than in the publications cited above, even though the cooling rate was the same in all experiments. One possible reason for this is the different preparation method used in this work which could have led to a better dispersion of the nanotubes.

The half-time of crystallization (see Table 1.6) is the time needed for 50% of the crystallizable material to crystallize from the melt. Generally, the half-times of crystallization depend on the (isothermal) crystallization temperature and on the amount of filler incorporated and increase with increasing temperatures which could be confirmed for all the materials investigated. This was significantly lower for the sPP–MWCNT nanocomposites than for the pristine polymer which is due to the nucleation of crystallite growth from the MWCNT surface.

The comparison of the nanocomposites with different filler contents shows that the crystallization at a certain isothermal crystallization temperature proceeded faster when more MWCNTs were incorporated in the polymer. If one looks at the half-time of crystallization at 122 °C, for example, it can easily be seen that it was significantly reduced when more carbon nanotubes were present. The half-time of crystallization at this temperature was 15 minutes for the pure polymer. When only 0.1 wt% of carbon nanotubes were incorporated, it was lowered to one third of that value, accordingly, to only 5 minutes. When the percentage of MWCNTs was raised to 0.5 wt%, the half-time of crystallization is reduced by roughly three minutes to 2.3 minutes. The nanocomposite with a filler loading of 0.9 wt% crystallizes too fast to allow for the determination of the half-time of crystallization possible at this crystallization temperature.

In Fig. 1.8, the rate of the half-time crystallization is compared for sPP with different fillers and at different isothermal crystallization temperatures. The filler



1.8 Influence of the type of filler and the isothermal crystallization temperature on the rate of the half-time crystallization of sPP composites.

content is 0.1 wt%. It can be seen that the rate constant of crystallization of pure sPP is always the lowest compared to the nanocomposites.

With respect to the filler type, MWCNTs show the strongest nucleating ability again. The constant rate of crystallization for the pure sPP ($7.5 \times 10^{-4} \text{ min}^{-1}$) is multiplied to more than the tenfold value ($8.8 \times 10^{-3} \text{ min}^{-1}$) in the presence of the carbon nanotubes. Carbon nanofibers and carbon black show a much smaller effect but still act as nucleating agents for sPP. Lozano and Barrera (2001) and Sandler *et al.* (2003) have reported an increase in crystallization temperature and an acceleration of the crystallization upon addition of CNFs or CNTs to iPP. The extent to which the properties were enhanced and the influence of the filler content were discussed controversially, though. This could be the result of differences in the homogeneities of the nanocomposites as well as the different types of nanotubes and preparation methods used.

The degradation of the neat polymer and the nanocomposites containing MWCNTs was investigated using TGA. Experiments were performed at a heating rate of $5^\circ\text{C}/\text{min}$. The results are shown in Table 1.6. The mass loss of the nanocomposites with different filler loadings and the pure polymer are presented depending on the temperature.

The degradation temperature of a composite filled by 0.1 wt% of MWCNT is 9°C higher than that of neat sPP. Higher amounts of the tubes have no significant influence. The presence of the nanofillers generally enhanced the yield strength of the pure sPP (17.5 Mpa) slightly in all investigated cases. The tensile strength increased for the syndiotactic PP by low filler contents up to 10%. The effects of high molecular weight isotactic PP-MWCNT composites on the crystallization behavior and mechanical properties are similar to that of the composites with a syndiotactic PP matrix.

As previously mentioned, the melting temperature is not influenced by the presence of nanotubes or their amount. The average melting temperature is $160 \pm 1^\circ\text{C}$. Also, the crystallinity is not affected by the CNT and lies in the range of $45 \pm 4\%$. In contrast to the melting temperature, the effect on the crystallization temperature is stronger. Pure high molecular weight iPP has a crystallization temperature of about 118°C . The addition of only 0.9 wt% MWCNT led to an increase in crystallization temperature to 123°C .

Pristine high molecular weight iPP does not crystallize or it takes too long to provide reliable results at temperatures above 130°C . Compared with sPP (96°C), this temperature is much higher. Generally, iPP-MWCNT composites crystallize much faster than sPP-CNT composites.

The half-time of crystallization for high molecular weight iPP-MWCNT composites is significantly reduced by low amounts of nanotubes. At 135°C , it is 4.5 min for a composite with 0.9 wt% filler content. The same composite requires 6.3 min at 137°C and does not crystallize at 139°C . When 2.2 wt% of MWCNT are incorporated, the time is reduced to only 2.4 min at 135°C and to 4.1 min at 137°C . This nanocomposite crystallizes even at higher temperatures (7.1 min at

Table 1.7 Dynamic mechanical measurements of high molecular weight iPP–MWCNT composites

MWCNT (wt %)	Deflection at 23 °C (μm)	Temperature stability (°C)
0.0	–487.8	48.7
0.9	–406.5	60.4
1.6	n.d.	69.5
2.3	–286.8	71.5
3.7	230.5	n.d.

n.d. = not detected.

139 °C and 8.1 min at 140 °C). When the percentage of MWCNT rises to more than 3%, no significant reduction of the half-time is obtained.

Selected high molecular weight iPP–MWCNT composites were analyzed by dynamic mechanical analysis (DMA) (Kaminsky *et al.*, 2009). Samples of the same form were pressed down by a constant force, the deflection was measured and also the temperature where the deflection was not reversible (Table 1.7).

Neat iPP shows a high deflection of –487.8 μm . The form stability can be increased by 100% if 3.7 wt% of MWCNT is incorporated into the polymer matrix by *in-situ* polymerization. The nanocomposite material becomes much stiffer. Also the temperature stability increases for the nanocomposites. While this temperature is 48.7 °C for neat iPP, it can be increased by 22 °C to a value of 71.5 °C for a composite with 2.3 wt% of CNT.

1.6 Conclusion and future trends

In-situ polymerization offers a way to prepare CNT containing nanocomposites even with a high molecular weight polyolefin matrix. This makes *in-situ* polymerization one of the most efficient and versatile methods to synthesize nanocomposites.

Generally, a very good separation, homogeneous distribution and an excellent wetting of the nanotubes with polyethylene or polypropylene can be achieved. The polymerization takes place directly on the CNT surface which in turn led to an encapsulation of the nanotubes with about 10 nm thick polymer film. The thickness of the polymer cover can be varied by the polymerization time, the ethylene or propylene pressure, and the catalyst concentration.

The crystallization temperature is raised up to 7 or 8 °C above that of pure iPP at a MWCNT content of 3 wt% or higher or by 15 °C of pure sPP at a MWCNT content of 0.9 wt%. This reduces the beat times for an injection molding machine to form articles from sPP–MWCNT composites up to a factor of 20 and greatly increases the economy of the process. The CNT nanocomposites show exciting

mechanical and electric properties. Some 2 to 3 wt% of MWCNT are sufficient to increase the conductivity 10^8 times and the stiffness and form stability by 100%. A big market for these composite materials could be the automotive and the electronic industries. Cars should weigh less and then they need less gasoline in the same way.

This can be achieved by using polyolefin–CNT composites. Important for the stiffness and the temperature stability are the aspect ratio and the filler content. The aspect ratio is the length of the tube divided by the diameter of the tube. This must be at least 10,000 to have the wanted properties. For an injection molding machine, the only way to produce cheap autobodies, the length of a fiber cannot be much longer than 1 mm. Otherwise, the nozzle will be blocked. These properties are given for multi-walled carbon nanotube reinforced polymers. For North America, Sinclair (2001) forecast a large demand of polyolefin nanocomposites in the near future. Through *in-situ* polymerization, excellent dispersed CNT-composite materials can be produced and should stimulate an interesting next decade for the polyolefin industry.

1.7 References

- Ajayan PM, Tour JM (2007) Material science: nanotube composites, *Nature*, 447, 1064–1068.
- Alexandre M, Pluta M, Dubois P, Jérôme R (2001) Metallocene catalyzed polymerization of ethylene in the presence of graphite, synthesis and characterization of the composites, *Macromol. Chem. Phys.*, 202, 2239–2246.
- Andrews R, Jaques D, Rao AM, Rantel T, Derbyshire F, Chen Y, Chen J, Haddon RC (1999) Nanotube composite carbon fibers, *Appl. Phys. Letters*, 75, 1329–1331.
- Arikan B, Stadler FJ, Kaschta J, Münstedt H, Kaminsky W (2007) Synthesis and characterization of novel ethene-graft-ethene/propene copolymers, *Macromol. Rapid Comm.*, 28, 1472–1478.
- Arriola DJ, Carnahan EM, Hustad PD, Kuhlman RL, Wenzel TT (2006) Catalytic production of olefin block copolymers via chain shuttling polymerization, *Science*, 312, 714–719.
- Barrau S, Demont P, Perez E, Peigney A, Laurent C, Lacabanne C (2003) Effect of palmitic acid on the electrical conductivity of carbon nanotubes–epoxy resin composites, *Macromolecules*, 36, 9678–9680.
- Bhattacharyya AR, Sreekumar TV, Liu T, Kumar S, Ericson LM, Hauge RH, Smalley RE (2003) Crystallization and orientation studies in polypropylene/single wall carbon nanotube composite, *Polymer*, 44, 2373–2377.
- Bonduel D, Mainil M, Alexandre M, Monteverdeb F, Dubois P (2005) Supported coordination polymerization: a unique way to potent polyolefin carbon nanotube nanocomposites, *Chem. Commun.*, 2005, 781–783.
- Brintzinger HH, Fischer, J, Mühlaupt R, Rieger B, Waymouth R (1995) Stereospecific olefin polymerization with chiral metallocene catalysts, *Angewandte Chem. Int. Ed. Engl.*, 34, 1143–1170.
- Coates GW (2000) The discovery of metallocene catalysts and their present state of the art, *J. Rev.*, 100, 1223–1252.
- Coleman JN, Khan U, Gunko YK (2006) Mechanical reinforcement of polymers using carbon nanotubes, *Adv. Mater.*, 18, 689–706.

- Dong X, Wang L, Liang G, Sun T, Zhao Z, Yu H (2006) Preparation of nanopolyethylene wire with carbon nanotubes supported Cp_2ZrCl_2 catalyst, *J. App. Polym. Sci.*, 101, 1291–1294.
- Duchateau R, Lancaster SJ, Thornton-Pett M, Bochmann M (1997) Synthesis of cyclopentadienyl, indenyl, and fluorenylbis(pentafluorophenyl)boranes as ligands in titanium and zirconium half sandwich complexes, *Organometallics*, 16, 4995–5005.
- Ewen J, Jones R L, Razavi A (1998) Syndiospecific propylene polymerization with group IVB metallocenes, *J. Am. Chem. Soc.*, 110, 6255–6256.
- Funck A, Kaminsky W (2007) Polypropylene carbon nanotube composites by in situ polymerization, *Composite Sci. Techn.*, 67, 906–915.
- Galli P, Vecellio G (2004) Polyolefins: the most promising large-volume materials for the 21st century. *J. Polym. Sci., Part A : Polym. Chem.*, 42, 396–411.
- Harris PJF (2004) Carbon nanotube composites, *Int. Mater Rev.*, 49, 31–43.
- Jeong J, Lee H, Kang S, Tan L, Baek J (2008) Nylon 610 functionalized multiwalled carbon nanotube composite prepared from in-situ interfacial polymerization, *J. Polym. Sci.*, 108, 1506–1513.
- Jordan RF, Dasher WE, Echols SF (1986) Reactive cationic dicyclopentadienyl zirconium (iv) complexes, *J. Am. Chem. Soc.*, 108, 1718–1719.
- Kaminsky W (1998) Highly active metallocene catalysts for olefin polymerization, *J. Chem. Soc. Dalton Trans.*, 1998, 1413–1418.
- Kaminsky W (2004) The discovery of metallocene catalysts and their present state of the art, *J. Polym. Sci. Part A Polym. Chem.*, 42, 3911–3921.
- Kaminsky W (2008) Trends in polyolefin chemistry, *Macromol. Chem. Phys.*, 209, 459–466.
- Kaminsky W, Funck A (2008) Insitu polymerization of olefins with nanoparticles by metallocene catalysis, *Macromol. Symp.*, 260, 1–8.
- Kaminsky W, Funck A, Haehnsen H (2009) New application for metallocene catalysts in olefin polymerization, *Dalton Transactions*, 41, 8803–8810.
- Kaminsky W, Funck A, Klinken C (2008) Insitu polymerization of olefins with nanoparticles or fibers by metallocene catalysts, *Top. Catal.*, 48, 84–90.
- Kaminsky W, Funck A, Wiemann K (2006) Nanocomposites by in-situ polymerization of olefins with metallocene catalysts, *Macromol. Symp.*, 239, 1–6.
- Kaminsky W, Tran PD, Werner R (2004) New polymers by copolymerization of ethylene and norbornene with metallocene catalysts, *Macromol. Symp.*, 213, 101–108.
- Kaminsky W, Wiemann K (2006) Polypropene nanocomposites by metallocene/MAO catalysts, *Composite Interfaces*, 13, 365–375.
- Koide Y, Barron A R (1996) Polyketone polymers prepared using a palladium/aluminoxane catalyst, *Macromolecules*, 29, 1110–1118.
- Lozano K, Barrera EV (2001) Nanofiber reinforced thermoplastic composites: thermoanalytical and mechanical analysis, *J. Appl. Polym. Sci.*, 79, 125–133.
- Lu KL, Lago RM, Chen YK, Gree MLH, Harris GJF, Tsang SC (1996) Mechanical damage of carbon nanotubes by ultrasound, *Carbon*, 34, 814–816.
- McMahon CN, Barron AR (1998) Synthesis of a base-stabilized alumoxane, preferential hydrolysis of an aluminumamido over an aluminum alkyl, *J. Chem. Soc. Dalton Trans.*, 3703–3704.
- Moniruzzaman M, Winey KI (2006) Covalent integration of functionalized single wall nanotubes into nylon 6,10 via interfacial in-situ polycondensation, *Macromolecules*, 39, 5194–5205.

- Okamoto M, Fujigaya T, Nakashima N (2008) Individual dissolution of single-walled carbon nanotubes by using polybenzimidazole, and high effective reinforcement of their composite films, *Adv. Funct. Mater.*, 18, 1776–1782.
- Park S, Yoon SW, Choi H, Lee JS, Cho WK, Kim J, Park HJ, Yun WS, Choi CH, Do Y, Choi JS (2008) Pristine multiwalled carbon nanotube/polyethylene nanocomposites by immobilized catalysts, *Chem. of Materials.*, 20, 4588–4594.
- Razavi A, Thewalt U (2006) Site selective ligand modification and tactic variation in polypropylene chains produced with metallocene catalysts, *Coord. Chem. Rev.*, 250, 155–16.
- Resconi L, Cavallo L, Fait A, Piemontesi F (2000) Selectivity in propene polymerization with metallocene catalysts, *Chem. Reviews*, 100, 1253–1345.
- Sandler I, Broza KG, Nolte M, Schulte K, Lam YM, Shaffer SP (2003) Crystallization of carbon nanotube and nanofiber polypropylene composites, *J. Macromol. Sci B*, 42, 479–488.
- Scheirs J, Kaminsky W (2000) *Metallocene Based Polyolefins*, Vols I and II, Chichester: John Wiley & Sons, Ltd.
- Sinclair KG (2001) Future trends in polyolefin materials, *Macromol. Symp.*, 173, 237–261.
- Sinn H (1995) Proposals for structure and effect of methylalumoxane based on mass balances and phase separation experiments, *Macromol. Symp.*, 97, 27–52.
- Sishta C, Hathorn RM, Marks TJ (1992) Group 4 metallocene-alumoxane olefin polymerization catalysts. CPMA-NMR spectroscopic observation of cation-like zirconocene alkyls, *J. Am. Chem. Soc.*, 114, 1112–1114.
- Tasis D, Tagmatarchis N, Bianco A, Prato M (2006) Chemistry of carbon nanotubes, *Chem. Rev.*, 106, 1105–1136.
- Valentini L, Biagiotti I, Kenny JM, Manchado MAL (2003) Physical and mechanical behavior of single walled carbon nanotube/polypropylene/ethylene-propylene-diene rubber nano composites, *J. Appl. Polym. Sci.*, 89, 2657–2663.
- Wang B, Sun G, Liu J, He X, Li J (2006) Crystallization behavior of carbon nanotubes-filled polyamide 1010, *J. Appl. Polym. Sci.*, 100, 3794–3800.
- Wang ZG, Wang XH, Hsiao BS, Philips RA, Medellin-Rodriguez FJ, Srinivas S, Wang H, Han CC (2001) Structure and morphology development in syndiotactic polypropylene during isothermal crystallization and subsequent melting, *J. Polym. Sci, B*, 39, 2982–2995.
- Wiemann K, Kaminsky W, Gojny FH, Schulte K (2005) Synthesis and properties of syndiotactic polypropylene/carbon nanofiber and nanotube composites prepared by in-situ polymerization with metallocene/MAO catalysts, *Macromol. Chem. Phys.*, 206, 1472–1478.
- Wu D, Sun Y, Wu L, Zhang M (2008) Linear viscoelastic properties and crystallization behavior of multi-walled carbon nanotube/polypropylene composites, *J. Appl. Polym. Sci.*, 108, 1506–1513.
- Yang B, Pramoda KP, Xu GQ, Goh SH (2007) Mechanical reinforcement of polyethylene using polyethylene-grafted multiwalled carbon nanotubes, *Adv. Funct. Mater.*, 17, 2062–2069.

Surface treatment of carbon nanotubes via plasma technology

B. RUELLE, C. BITTENCOURT and P. DUBOIS,
University of Mons and Materia Nova Research Centre, Belgium

Abstract: The chapter begins by discussing carbon nanotube (CNT) surface chemistry and solution-based functionalization. It then reviews promising alternative ways to modify the CNT surface through plasma processes. Plasma treatments have the advantage of being non-polluting and provide a wide range of grafted functional groups, depending on the plasma parameters such as power, gases used, duration of treatment and gas pressure. However, the interaction of high energy particles with the CNT surface can induce damage in the CNT structure. A plasma post-discharge treatment, which can prevent the degradation of CNTs, is presented.

Key words: carbon nanotubes, functionalization, plasma, post-discharge treatment.

2.1 Introduction

Since their observation by Iijima (1991), carbon nanotubes (CNTs) have attracted the attention of many researchers due to their outstanding properties (Thostenson *et al.*, 2001). Their unique physical properties result from their structure, which at atomic scale can be thought of as a hexagonal sheet of carbon atoms rolled into a seamless one-dimensional cylindrical shape. Besides their extremely small (nanometric) size, their excellent electrical and thermal conducting performances, combined with their strong toughness and transverse flexibility make them promising for use in a wide variety of applications such as electronic components, chemical and biological sensors, chemical and genetic probes, field emission tips or mechanical memories (Collins and Avouris, 2000). Carbon nanotubes are thus expected to expand their unique properties in multidisciplinary fields and should play a key role in nanotechnology.

Characterized by both high aspect ratio (length-to-diameter) and low density, this allotropic variety of carbon is an ideal candidate to be used as filler materials in composites. In fact, CNTs can provide a three-dimensional conductive network through the polymer matrix with exceedingly low percolation thresholds (Kilbride *et al.*, 2002). Furthermore, it has been suggested that their high thermal conductivity can be exploited to make thermally conductive composites (Bagchi and Nomura, 2006). In addition, the mechanical enhancement of polymer materials using CNTs as reinforcing nanofillers will be exploited in the very near future (Wang *et al.*, 2008).

A key parameter for producing high quality nanocomposite materials with improved physical properties is the homogeneous dispersion of the individual CNTs. Unfortunately, the CNTs tend to form large bundles thermodynamically stabilized by van der Waals forces and physical entanglements between the tubes, which occur during their synthesis. The presence of these aggregates in addition to the CNT's low solubility in water and organic solvents represent a drawback for the engineering of CNT in polymer nanocomposites. It has been reported that the homogeneous dispersion of CNTs is relatively difficult to achieve in the large majority of polymers (Andrews and Weisenberger, 2004).

The chemical functionalization of the CNT sidewalls, i.e. the CNT surface-anchoring of functional (reactive) groups, represents a solution for the tuning of interactions between CNTs and the host polymer matrix, improving their dispersion ability (Hirsch and Vostrowsky, 2005). This surface modification can be divided into two main approaches.

First is the *non-covalent functionalization*, used in different techniques such as the addition of surfactants (Hirsch, 2002), polymer wrapping (Liu, 2005) or polymerization-filling technique (PFT) (Bonduel *et al.*, 2005), which allows the unaltered CNTs to preserve their physical properties. However, the interaction between the wrapping molecules and the nanotubes remains generally weak, limiting the efficiency of the property transfer between the nanotubes and the host polymer, in particular, there may be a low load transfer for mechanical properties.

The other approach relies upon the *covalent grafting* of functional chemical groups along the CNT sidewalls. These chemical functions can be used as anchoring sites for polymer chains (Hirsch and Vostrowsky, 2005) and to improve the interaction with the polymer matrix (Thostenson *et al.*, 2005). The covalent bonding between CNTs and the polymer chains ensures an optimal interfacial strength and thus a better load transfer. Nevertheless, the covalent functionalization can influence the CNTs' properties, depending on the nature and density of the functional sites. Indeed, the functionalization can take place on already existing CNT structural defects, or active sites can be created by grafting chemical functions. In the latter case, functionalization can degrade the CNTs' physical properties if the density of the active site is significant, leading to damaged CNT structure (Fu *et al.*, 2001). The majority of developed covalent sidewall functionalizations are carried out in organic solvent. Nevertheless, as the CNT surface is largely inert, rather harsh conditions are needed for wet chemical functionalization of CNTs, which rarely results in a controlled covalent functionalization process (Hirsch and Vostrowsky, 2005).

To overcome these drawbacks, 'dry' processes are being developed. For example, the ball-milling of CNTs in a reactive atmosphere was shown to functionalize nanotubes with different chemical groups, such as amides, amines, carbonyls and thiols, for instance, depending on the reactant gas (Konya *et al.*, 2002). Using this method, CNTs are broken, and dangling bonds are formed on their newly created extremities that can then react with a selected gas. A relatively long period of time, a minimum of 24 hours, is usually necessary to

graft a significant amount of functional groups onto CNTs. However, the average length of the CNTs decreases as the treatment time increases and some amorphous carbon was also observed after the breaking process (Ma *et al.*, 2008). Another drawback of this technique is the presence of functional groups exclusively at the ends of cup-stacked carbon nanotubes.

Alternative 'dry' approaches to chemical modification of CNTs using plasma discharges have been also proposed and developed. Considered the fourth state of matter, plasma is an ionized gas that constitutes a highly unusual and highly reactive chemical environment. Plasma treatments have evolved into a valuable technique to modify material surface properties without altering the bulk properties, allowing their use in various applications such as plasma cleaning, plasma sterilization or biomedical applications (D'Agostino *et al.*, 2005). Recently, plasmas were also applied to modify the surface properties of CNTs. Characterized by a relatively low reaction time, surface plasma treatment is an environmentally friendly process without any use of organic solvents. The plasma technique allows the grafting of a wide range of different functional groups on the CNT surface depending on plasma parameters such as power applied to the discharge, nature of the gas used, duration of treatment and gas pressure.

2.2 Carbon nanotube surface chemistry and solution-based functionalization

As mentioned above, even though chemical functionalization displays some drawbacks, it still represents a very important method investigated by several research groups. Hereafter are discussed some important results recently reported in the literature.

Actually, the chemical functionalization of CNTs via covalent grafting reaction can be divided into: (a) end-caps and 'defect groups' chemistry; and (b) sidewall functionalization.

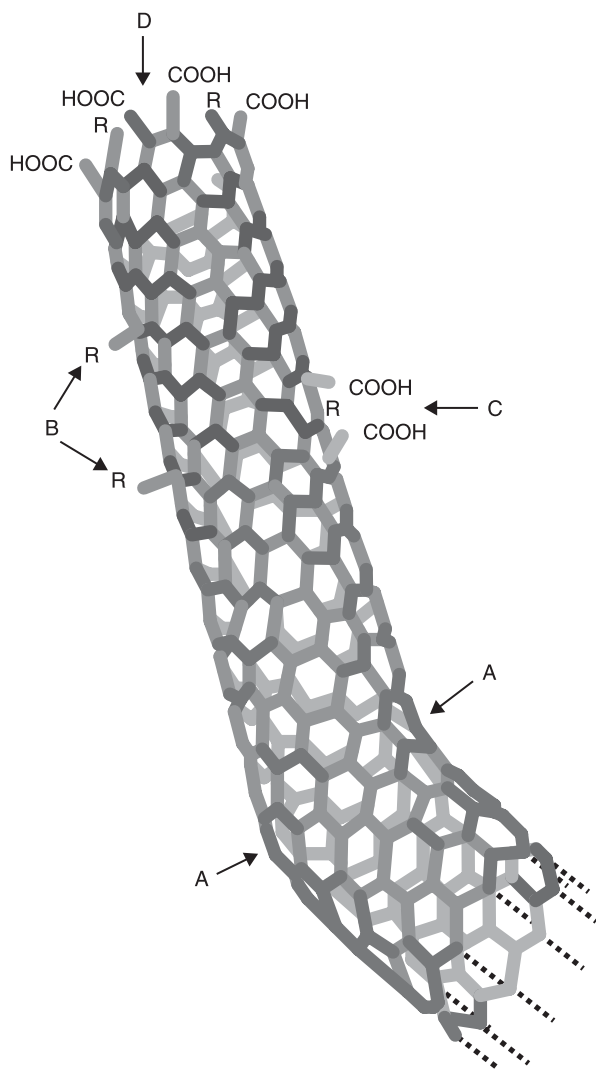
2.2.1 End-caps and defect-sites chemistry

Functionalization via 'end-caps and defect-site' chemistry consists of grafting functional groups directly on the already existing defects in the structure of CNTs using wet chemistry. Carbon nanotubes are in general described as perfect graphite sheets rolled into nanocylinders. In reality, CNTs present structural defects: typically, ca. 1–3% of the carbon atoms of a nanotube are located at a defect site (Hu *et al.*, 2001).

The end-caps of nanotubes are composed of highly curved fullerene-like hemispheres, which are much more reactive when compared to the sidewalls (Sinnott, 2002). The sidewalls themselves contain defect-sites such as pentagon-heptagon pairs called Stone-Wales defects, sp^3 -hybridized defects or holes in the carbon sheet (Charlier, 2002). The most frequently encountered type of defect is

the Stone-Wales (or 7–5–5–7) defect, which leads to a local deformation of the nanotube curvature. Grafting reactions are most favored at the carbon–carbon double bonds in these positions. The different defects commonly observed in CNTs are shown in Fig. 2.1 (Hirsch, 2002).

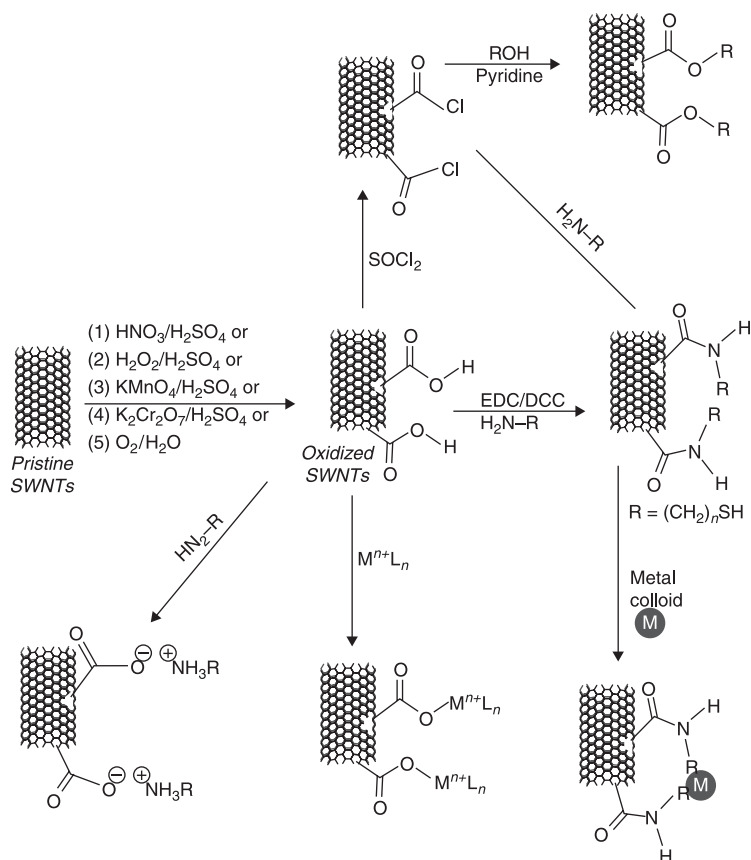
Frequently, the techniques applied for the purification of the raw material, such as acid oxidation, induce the opening of the tube caps as well as the formation



2.1 Typical defects along a single-wall CNT: (A) five- and seven-membered rings forming a bend in the tube; (B) dangling bonds; (C) hole in the carbon framework; and (D) open end of CNT terminated with -COOH groups (Hirsch, 2002).

of holes in the sidewalls. These vacancies and tube extremities are therefore functionalized with oxygenated functional groups such as carboxylic acid, ketone, alcohol and ester groups (Chen *et al.*, 1998). The introduced carboxyl groups can present useful sites for further modifications in organic solvents such as the coupling of molecules through the creation of amide or ester bonds. Figure 2.2 represents common functionalization routes on single-wall CNT ends and defect-sites through solution-based chemistry (Banerjee *et al.*, 2005).

Using solution-based chemistry, nanotubes can be grafted with a wide range of functional moieties via amidation or esterification reactions, for which bifunctional molecules are often utilized as linkers/coupling agents. This method was used to graft amine moieties onto carbon nanotubes via the reaction with diamines such as triethylenetetramine (Gojny *et al.*, 2003), ethylenediamine (Meng *et al.*, 2008) or 1,6-hexamethylenediamine (Li *et al.*, 2007). Another approach involves the reduction of the carboxyl groups to hydroxyls, followed by transformation into amino groups



2.2 Some representative functionalization reactions at CNT ends and defect-sites (Banerjee *et al.*, 2005). SWNTs, single-walled nanotubes.

via phthalimide coupling and hydrolysis (Ramanathan *et al.*, 2005). Gromov *et al.* (2005) have developed two other approaches, using amino-decarboxylation substitution, to make primary amino groups directly attach onto the carbon nanotube surface. The carboxylic groups, the majority grafted at the open ends of CNTs, are replaced with amino groups via Hofmann rearrangement of carboxylic amide or via Curtius reaction of carboxylic acid chloride with sodium azide.

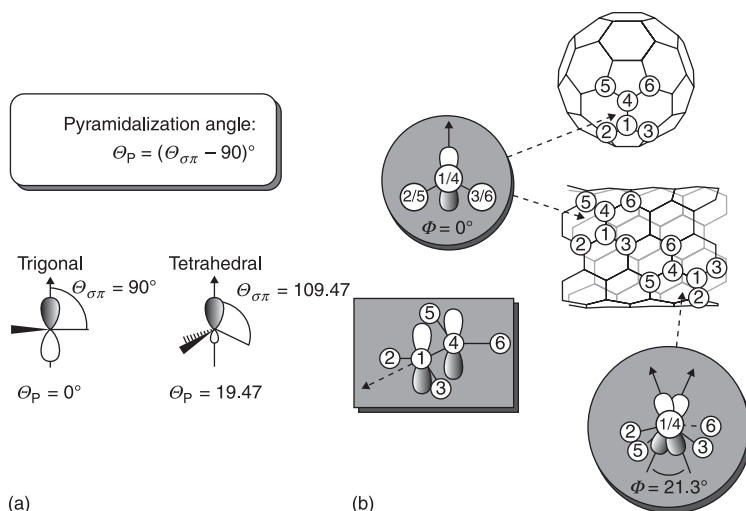
One advantage of the defect-site chemistry is that functionalized carbon nanotubes mostly retain their pristine electronic and mechanical properties (Zhang *et al.*, 2003). However, as mentioned earlier, the spatial distribution of grafted functions is not homogeneous. In fact, the majority of carboxylic groups, used as anchoring sites, are localized at the extremities of the carbon nanotubes.

2.2.2 Sidewall functionalization

The other approach for covalent grafting reactions is the ‘sidewall functionalization’, which consists of grafting chemical groups through covalent reactions onto the π -conjugated skeleton of CNTs (Hirsch, 2002). Unlike defect-site chemistry, which takes advantage of defects already present in the CNT structure, the direct covalent sidewall functionalization is associated with a change in hybridization from sp^2 to sp^3 . This simultaneous loss of conjugation of CNTs influences their physical properties, and more particularly their electrical conductivity, depending on the density of functionalization.

First, covalent sidewall functionalization was carried out on the basis of well-developed grafting chemistry on fullerenes whose reactivity depends strongly on the curvature of the carbon framework. However, the sidewall reaction chemistry of CNTs differs from that of fullerenes as the chemical reactivity in carbon systems arises from two factors that induce local strain: the pyramidalization at the carbon atoms and the π -orbital misalignment between adjacent pairs of conjugated carbon atoms (Chen *et al.*, 2003). The fullerene structures and the CNT end-caps present a pronounced pyramidalization of the carbon atoms further improving chemical reactions. In the CNT sidewalls, the pyramidalization strain is not as acute and, thus, π -orbital misalignment has a greater influence on sidewall chemical reactivity (Hamon *et al.*, 2001). In Fig. 2.3, the reactivity of the C–C bond in CNT structure is presented in function of its angle to the tube circumference. Because the deformation energy of sp^2 bond is inversely proportional to the diameter of the CNT, nanotubes with a smaller diameter have higher reactivity (Hirsch, 2002).

However, whereas the nanotube end-caps are quite reactive due to their fullerene-like structure, even taking into account the folding of the graphene sheet, the reactivity of CNT sidewalls remains low and sidewall-functionalization is only successful if a highly reactive reagent is used. As mentioned, an additional constraint on sidewall functionalization is the tendency of CNTs to form bundles, which limits the available nanotube surface for the grafting of chemical reagents.

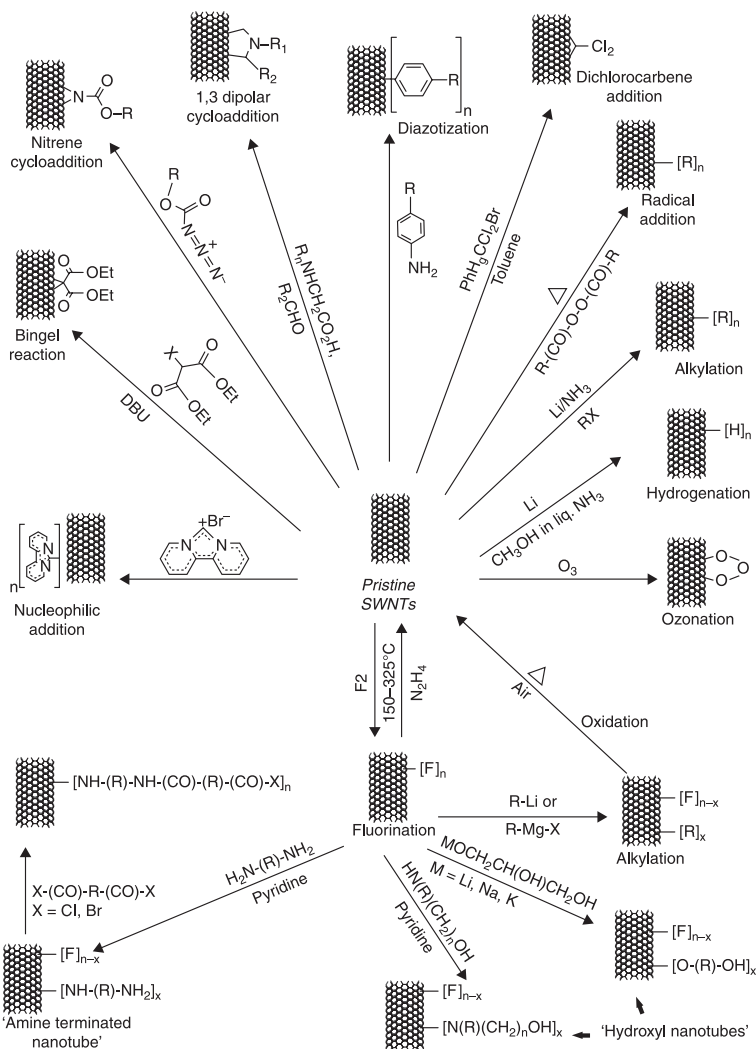


2.3 Pyramidalization angles (θ_P) and the π -orbital misalignment angles (Φ) along C1–C4 in the CNT framework and its capping fullerene C_{60} (Hirsch and Vostrowsky, 2005).

Typically, the covalent sidewall functionalization is carried out in organic solvent, which allows the utilization of the sonication process to improve the dispersion of CNTs and, thus, to increase the available surface of carbon nanotubes. However, precipitation immediately occurs when this process is interrupted (Tasis *et al.*, 2006). The required reactive species such as carbenes, nitrenes or radicals are in general made available through thermally activated reactions (Balasubramanian and Burghard, 2005). Normally, the grafting reaction can be initiated exclusively on the intact sidewall or in parallel at defect-sites. The most common sidewall functionalizations using organic solvents, such as carbene (Lee *et al.*, 2001) or nitrene (Holzinger *et al.*, 2004) [2+1] in cycloaddition reactions or radical additions via diazonium salts (Bahr *et al.*, 2001), are shown in Fig. 2.4.

The first sidewall functionalization studied was the fluorination of CNTs. Carbon nanotubes were fluorinated using fluorine in the range between room temperature and 600°C (Mickelson *et al.*, 1998). This reaction is very useful because further nucleophilic substitutions can easily be accomplished and make possible a flexible approach to provide the CNT sidewalls with various types of functional groups (Khabashesku *et al.*, 2002).

Among these reactions, several diamines are reported to react with ‘fluoronanotubes’ via nucleophilic substitution reactions (Stevens *et al.*, 2003), leading to the formation of amino-functionalized CNTs. However, if bifunctional reagents such as diamines with sufficiently long carbon chains are used, the nanotubes can be covalently cross-linked with each other. Modification with amino-containing substituents was developed using photolysis of acetonitrile



2.4 Representative covalent sidewall functionalization reactions of CNTs as carried out in organic solvents (Banerjee *et al.*, 2005).

(Nakamura *et al.*, 2008). The 1,3-dipolar cycloaddition reaction can be also used to graft linkers, with amino groups at their ends, uniformly distributed along the sidewalls (Pantarotto *et al.*, 2003).

As discussed before, the carbon nanotube covalent functionalizations carried out in organic solvent present some drawbacks. The need to agitate carbon nanotubes by sonication to improve their dispersion in organic solvents can trigger severe damage to the tube walls and the average length of CNTs can be reduced

(Monthieux *et al.*, 2001). Moreover, certain highly reactive chemical products also involve harsh conditions causing detrimental damage to the tips and sidewalls of CNTs, which decreases their stability and can cut them into short pieces (Liu *et al.*, 1998). In addition, the solvent functionalization process generally requires time-consuming multistep reactions. Finally, the use of organic solvent pollutes and is difficult to upgrade for industrial processes.

In the next section, the use of plasmas as an optimal alternative for grafting functional groups at the CNT surface will be presented and discussed.

2.3 Plasma treatment of carbon nanotubes

2.3.1 Introduction to plasma: the fourth state of matter

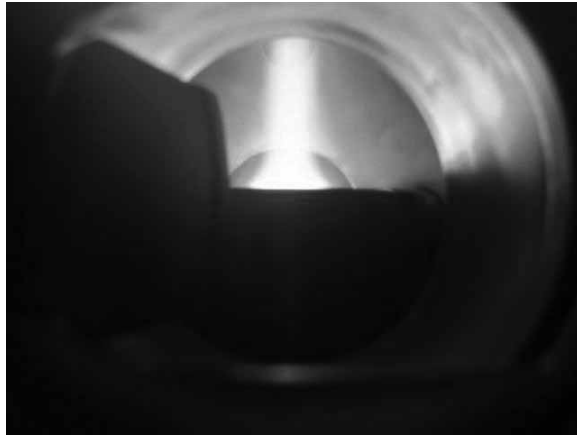
Plasma is physically defined as an ionized gas with an equal number of positively and negatively charged particles. It consists of free electrons, ions, radicals, UV radiation and various highly excited neutral and charged species (Chapman, 1980). The entire plasma is electrically neutral; however, the displacement of the species is controlled by electric and magnetic fields. According to the gas temperature, the plasma can be classified into thermal plasma, which is characterized by being fully ionized (gas temperature T_g = electron temperature T_e), or non-thermal (or cold) plasma where the gas is only partially ionized (T_g is much lower than T_e).

Thermal plasma implies that the temperature of all active species (electrons, ions and neutral species) is the same. This is true for stars, for example, as well as for fusion plasma. High temperatures are required to form these equilibrium plasmas, typically ranging from 4000K to 20000K (Bogaerts *et al.*, 2002).

In the non-thermal or cold plasmas, the temperature of neutral and positively charged species is low, with the electrons having a much higher temperature than the other particles because they are light and easily accelerated by the applied electromagnetic field. As a result, the plasma is in the non-equilibrium state and the reactions may proceed at low temperature. Indeed, the electrons can reach temperatures of 10^4 – 10^5 K (1–9 eV) while the temperature of the gas can be as low as room temperature (Grill, 1994). Figure 2.5 shows the image of a cold plasma discharge.

2.3.2 Characteristics and principal applications of plasma

To reach the plasma state of atoms and molecules, energy for the ionization must be input into the atoms and the molecules from an external energy source. The ionization occurs when an atom or a molecule gains enough energy from the excitation source or via collisions with other particles. There are many kinds of plasma sources differing greatly from one another. The electrically induced discharge in gas is the most common method for plasma ignition because of



2.5 Radio frequency cathodic magnetron sputtering of titanium target in an argon plasma.

handling convenience. Direct current (DC) discharges, pulsed DC discharges, radio frequency (RF) discharges (13.56 MHz) and microwave (μ -wave) discharges (2.45 GHz) represent the plasma categorization based on electric apparatuses (Denes and Manolache, 2004). These are the common standard frequencies used for RF, and μ -wave plasmas are authorized frequencies for industrial, scientific and medical applications worldwide in order to avoid interfering with telecommunication. The basic feature of a variety of electrical discharges is that they produce plasmas in which the majority of the electrical energy primarily goes into the production of energetic electrons, instead of heating the entire gas stream (Fridman *et al.*, 2005). These energetic electrons induce ionization, excitation and molecular fragmentation of the background gas molecules to produce excited species that create a ‘chemically-rich’ environment. Due to their essential role, the electrons are therefore considered to be the primary agents in the plasma.

Plasma processes provide a cost-effective and environmentally friendly alternative to many important industrial processes because this reliable method produces no waste products and in most cases exposes operators to no significant hazards. Plasmas thus find well-established use in industrial applications, however, they are also gaining more interest in the field of life sciences, related to environmental issues (Hammer, 1999) and biomedical applications (Frauchiger *et al.*, 2004). Recently, the production of CNTs via plasma-enhanced chemical vapor deposition has been reported as well (Boskovic *et al.*, 2005).

Gas discharge plasmas are used in a large variety of applications requiring surface modification. Plasma processing is generally used for film deposition and may also be used for resistant materials development (McOmber and Nair, 1991). Surface modification by plasmas also plays a crucial role in the microelectronics industry, in the microfabrication of integrated circuits and in materials technology

(Hino and Akiba, 2000). Actually, the versatility of plasma technologies stems from its many advantages: different sizes, shapes, geometries and type of materials can be treated, surface topography and bulk properties are usually not affected and they exhibit high reproducibility. For surface modification, plasma approaches can be classified into different categories: plasma etching (Inoue and Kajikawa, 2003), plasma polymerization and plasma functionalization (Chu *et al.*, 2002) based on the outcomes of plasma interactions. Etching, deposition or grafting of chemical groups can dominate in modifications of the material's surface, depending on various factors such as the gas used, the nature of the surface and the plasma parameters.

Plasma etching occurs when the surface material removal effect, due to ions and active neutral species as well as vacuum ultraviolet radiation, is prominent in the modification effect. During this process, the plasma generates volatile etched products from the chemical reactions between the elements present on the material surface and the plasma species.

In the plasma polymerization process, the plasma interacts with organic molecules (monomers) and involves their fragmentation and subsequent deposition. The plasma polymer formed thus is deposited in the form of a thin film. Notwithstanding the use of the word polymer, 'plasma polymer' refers to a new class of material that has little in common with the conventional polymer. In the case of the plasma polymer, the chains are short and randomly branched and terminate with a high degree of cross-linking, and are not constituted by regularly repeating units.

Plasma treatment using gases such as O_2 , N_2 , NH_3 or CF_4 allows reactive chemical functionalities to be inserted onto the material's surface. Compared with other chemical modification methods, plasma-induced functionalization presents interesting characteristics such as being a solvent-free and time-efficient technique. Moreover, this treatment allows the grafting of a wide range of different functional groups depending on plasma parameters such as power, nature of the gas used and its pressure, duration of treatment, etc. This method also provides the possibility of scaling up to produce large quantities necessary for commercial use. Plasma treatment is widely used for surface activation of various materials, ranging from organic polymers to ceramics and metals. In this field, we can cite the polymer surface functionalization in pulsed and continuous nitrogen microwave plasma, under admixture of hydrogen (Meyer-Plath *et al.*, 2003). This process makes it possible to graft nitrogen functional groups onto polystyrene with a high selectivity in primary amine groups.

2.3.3 Plasma-based treatment of carbon nanotubes

The surface modification of carbon nanotubes can be carried out through a wide range of plasma processes. In addition to the already cited advantages of plasma treatments, the number of functional groups grafted on the CNT surface can also

be tailored. This is an important characteristic of this type of surface treatment since having saturation of these groups on the surface can alter the electronic conductivity of nanotube materials.

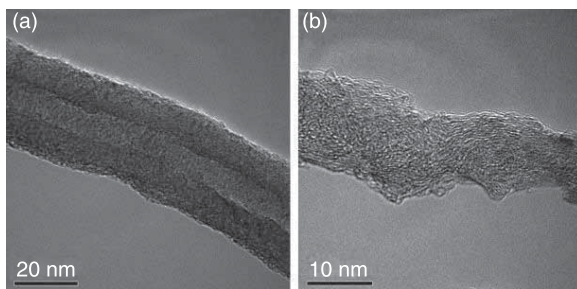
To facilitate the discussion, we will classify the plasma treatment of CNTs into: (1) CNT surface etching, which is generally carried out via an argon (Ar) plasma treatment; (2) coating of CNTs through plasma polymerization; and (3) plasma functionalization, which allows the grafting of reactive functional groups on to CNT surfaces and opens the way to a wide variety of subsequent chemical reactions.

Carbon nanotube surface etching

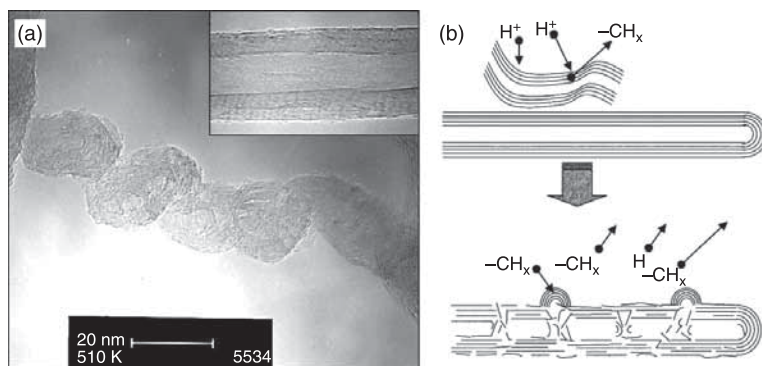
The plasma surface modification of CNTs is a non-reactive treatment when Ar gas is used. The effects of argon RF plasma treatment on the surface of vertically grown CNTs have been investigated. The inert Ar plasma produces an efficient etching and cleaning process of CNT films, causing structural changes in the CNTs and leading to an increase in their field emission ability (Ahn *et al.*, 2003). An observed improvement in gas ionization in comparison with that of untreated aligned CNTs was also observed after Ar RF plasma treatment (Yan *et al.*, 2005). The Ar plasma was also used to activate the CNT surface, allowing the subsequent grafting of maleic anhydride (Tseng *et al.*, 2007) or 1-vinylimidazole (Yan *et al.*, 2007).

Nevertheless, the destruction of carbon nanotube sidewalls was observed after treatment with an Ar-non reactive μ -wave plasma (Qin and Hu, 2008). Figure 2.6 shows high resolution transmission electronic microscopy (HRTEM) images of multi-wall CNTs recorded before and after Ar μ -wave plasma treatment. We can observe that ion bombardment and irradiation in Ar plasma deform the graphite walls and destroy the CNT layered structure; a reduction in the power supplied to the plasma or in the treatment duration can reduce the destruction of sidewalls.

Hydrogenation of CNT films through H_2 RF plasma processes improved the CNT field emission properties via creation of defects along the CNT structure (Yu



2.6 HRTEM images of MWNTs (a) before and (b) after Ar microwave plasma treatment for 3 minutes (Qin and Hu, 2008).



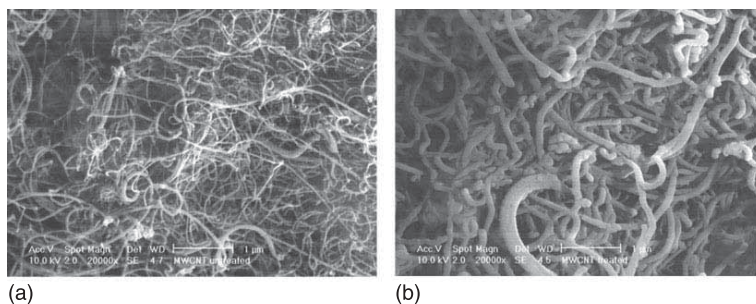
2.7 HRTEM images of a formed nodular CNT and an untreated CNT in the insert (a) and schematic diagram of the formation of nodular CNTs (b) (Zhang *et al.*, 2004).

et al., 2004; Feng *et al.*, 2007). The enhancement of emission properties was attributed to apparition of nodular CNTs due to bending of graphene sheets along the CNT wall (Fig. 2.7 (a)) (Zhang *et al.*, 2004). During the H_2 RF plasma treatment, it was suggested that hydrogen ions bombarding the tube sidewall remove carbon atoms from the CNT surface under $-CH_x$ radical forms. Meanwhile, a small fraction of $-CH_x$ redeposited on the remaining CNT surface induces the formation of nanoscale particles with an onion-like structure distributed along the tubes (Fig. 2.7 (b)). The improvement of the emission characteristics was attributed to the change in the electronic (formation of sp^3 defects in sp^2 graphite network) and/or geometrical CNT structure (Zhang *et al.*, 2004).

Vertically aligned CNTs were hydrogenated in a $H_2 + Ar$ pulsed dc plasma, and correlations between the plasma characteristics and the CNT surface chemistry were discussed (Jones *et al.*, 2008). Actually, scanning electron microscope (SEM) morphological analysis of CNTs treated in this way showed the etching of the tangled nanotubes and the ‘welding’ of nanoparticles. The extent of the etching effect was correlated with the quantity of plasma-excited hydrogen H^* interacting with CNTs.

Plasma polymerization

The plasma polymerization process has been used to coat CNTs with plasma polymer films. Several examples are reported in the literature. A plasma polymerization method spraying a mixture of aniline and CNTs was developed to deposit plasma polyaniline onto CNTs leading to the formation of composite films with improved electrical properties in comparison to neat plasma (Nastase *et al.*, 2006). Chen *et al.* (2001) developed an approach based on RF plasma activation, followed by chemical reactions between derivatized dextran- and



2.8 SEM images of multi-walled CNTs before treatment (a) and after MMA plasma polymerization treatment (b) (Gorga *et al.*, 2006).

plasma-generated functional groups such as aldehyde groups from acetaldehyde and amino groups from ethylenediamine. The resulting polysaccharide-grafted CNTs proved highly hydrophilic.

Multi-walled CNTs were also modified using plasma polymerization with ethylene glycol (EG) as the monomer (Avila-Orta *et al.*, 2009). The plasma-polymerized EG-coated CNTs showed very stable dispersion with water, methanol and ethylene glycol, confirming the hydrophilic behavior of the treated CNTs. This plasma polymerization technique was successfully used to produce a plasma poly(methyl methacrylate) (PMMA) coating on CNTs (Gorga *et al.*, 2006). Excellent suspensions of CNTs were achieved in toluene after plasma treatment, and plasma PMMA coating was observed using SEM (Fig. 2.8). The coated CNTs were incorporated into the PMMA matrix via melt mixing and the mechanical properties of the nanocomposites formed in this way were determined with tensile measurements. The CNT coating slightly improved the load transfer from the PMMA matrix to the nanotubes, over the uncoated CNTs, but it did not significantly influence the dispersion of CNTs. The mechanical properties were not dramatically improved.

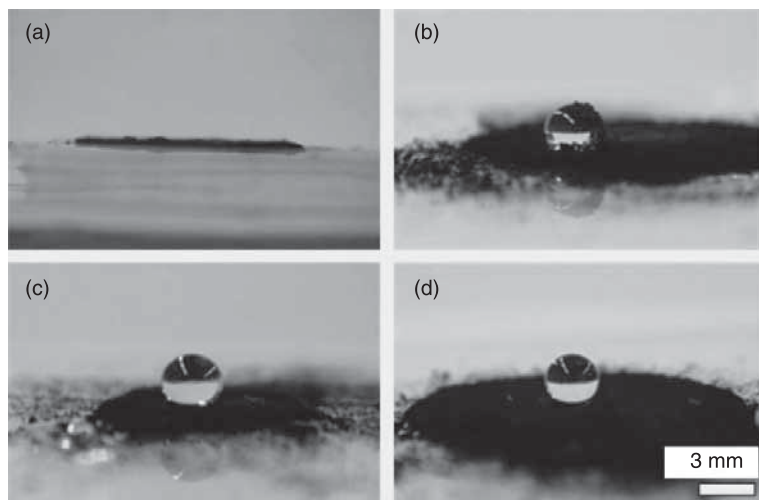
Styrene plasma was also reported to deposit polystyrene (PS) plasma polymer coating onto multi-walled CNTs (Felten *et al.*, 2007). It was shown that polystyrene nanocomposite filled with plasma PS-coated CNTs presented better mechanical properties than the ones filled with unmodified CNTs (Shi and He, 2004).

Plasma chemical functionalization

CNT sidewalls can be fluorinated via CF_4 plasma treatment (Plank *et al.*, 2003). Fluorination is one of the most effective modifications of the CNT surface and makes possible a wide range of subsequent derivatization reactions (Lee *et al.*, 2003). It has been observed that bundles of pristine CNTs can be transformed into unroped fluorinated CNTs without structural deformation (Valentini *et al.*, 2005). Moreover, unlike other fluorination procedures, the CF_4 plasma treatment was

demonstrated to enhance the reactivity of fluoronanotubes with aliphatic amines at room temperature. Two minutes of CF_4 plasma treatment was reported to increase the field emission current (Zhu *et al.*, 2005). Fluorine atoms were grafted on the CNT sidewalls when these were exposed to a CF_4 plasma that had been generated in a surface wave microwave plasma reactor (Kalita *et al.*, 2008). The amount of grafted fluorine (up to 24 atomic %) was determined by X-ray Photoelectron Spectroscopy (XPS) and Raman studies revealed a structure change in the treated CNTs. HRTEM showed modification of the outer wall with fluorine incorporation while the inside walls remained unaffected. Super-hydrophobic CNTs were obtained by NF_3 glow-discharge plasma supplied by alternating current (AC) power (Hong *et al.*, 2006). The treatment time to obtain hydrophobic CNT powders was shorter than 1 minute. Figure 2.9 illustrates liquid droplets on CNT cushions of about 1 mm thickness. Figure 2.9 (a) was taken after a water droplet fell onto untreated CNTs. The other photographs (Figs 2.9 (b)–(d)) show respectively the droplets of polyethylene glycol (PEG), glycerol and water placed on CNTs that had been exposed for 10 minutes to NF_3 plasma treatment. These images reveal a significant enhancement of the hydrophobicity.

The grafting of oxygen-containing groups using plasma processes has been extensively reported. Hydroxyl, carbonyl and carboxyl groups were grafted onto CNTs via O_2 and CO_2 RF plasma in order to form polar groups that could improve the overall adhesion of CNTs to a polyamid matrix (Bubert *et al.*, 2003). Oxygen concentration of up to 14% was determined by XPS, which was considered by the



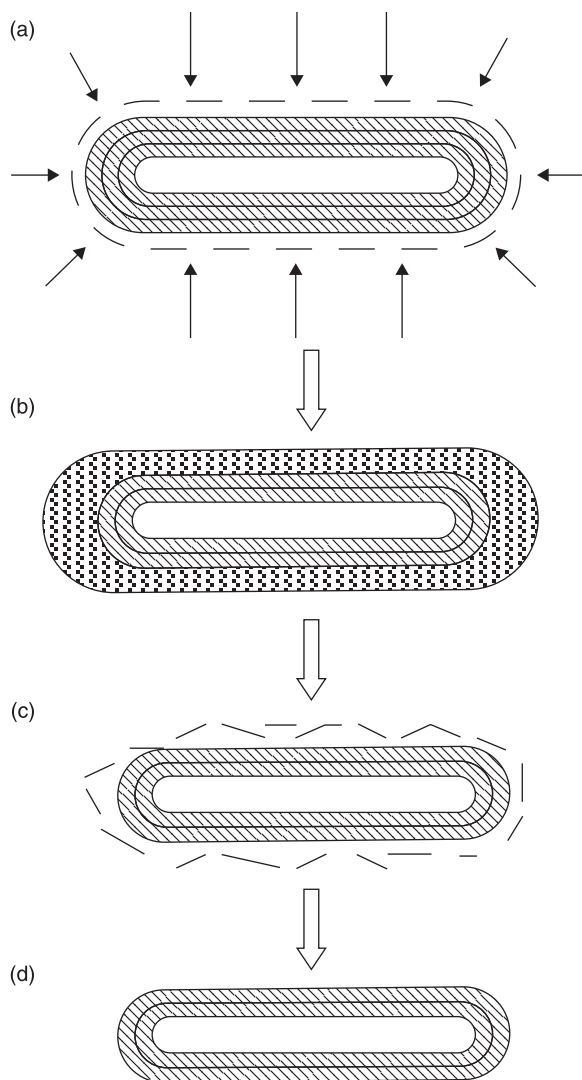
2.9 Photographic images of liquid droplets. Untreated CNT powder (a) completely absorbed liquid droplets and (b)–(d) the droplets of PEG, glycerol and distilled water on 10-min plasma treated CNTs, respectively (Hong *et al.*, 2006).

authors as equivalent to a complete saturation of the outer CNT surface. The efficiency of oxygen grafting in function of plasma frequency (RF or μ -wave) was determined through contact angle measurement, showing that μ -wave plasma treatment leads to better wettability (Chirila *et al.*, 2005). Other plasma processes were proposed to readily functionalize CNTs with oxygenated groups such as air-atmospheric pressure dielectric barrier discharge (Okpalugo *et al.*, 2005) or air μ -wave oven-generated plasma (Hojati-Talemi *et al.*, 2009).

Zschoerper *et al.* (2009) have characterized Ar/O₂ and Ar/H₂O RF plasma-treated CNTs by XPS. To overcome the limitations of XPS analysis in distinguishing between functional groups with similar binding energies, alcohol, keto/aldehyde and carboxyl groups were tagged using derivatization techniques with fluorine-containing reagents. Trifluoroacetic anhydride (TFAA) was used for the derivatization of alcohol groups, (trifluoromethyl)phenylhydrazine (TFMPH) for keto/aldehyde groups and trifluoroethanol for carboxyl groups through reactions carried out in the saturated vapor phase. Despite the fact that the total oxygen content is almost identical, variations in different functional group concentration are observed in the function of treatment parameters such as pressure or treatment time. Based on this work, CNT bucky papers were modified using Ar/O₂ plasma and thereafter melt-mixed into polycarbonate (Pötschke *et al.*, 2009). Carboxylic acid and ester groups were formed on the CNT surface, allowing better macrodispersion and better phase adhesion to the matrix, as showed by morphological investigations.

A flexible amperometric biosensor based on O₂ RF plasma-functionalized CNTs films on polydimethylsiloxane substrates has been developed (Lee *et al.*, 2009). The plasma-treated samples presented better glucose response than non-treated ones, showing their potential application as biosensors. The O₂ RF plasma treatment was also found to improve the sensing potential of CNTs to detect NO₂ (Ionescu *et al.*, 2006) or to clean CNT surfaces by removing amorphous carbon (Rawat *et al.*, 2006). In fact, it has been observed that purification of carbon nanotube powder can be attained after CNT treatment in glow discharges (RF or μ -wave). Amorphous carbon domains are eliminated and the impurities are removed by ion bombardment and irradiation in an O₂ RF plasma (Xu *et al.*, 2007). However, it was also reported that the average diameter of multi-walled CNTs decreases with treatment duration. Figure 2.10 shows a three-step model proposed to explain this decrease. First, ion bombardment causes the creation of vacancies and interstitials in CNTs; the superficial structure, including the amorphous carbon that was produced, is thus lost. In a second step, the ion beams continue to react with amorphous carbon until they are peeled totally away from the CNTs. Finally, the oxidation of amorphous carbon in CO₂ occurs, inducing the decrease of the CNT's average diameter.

Plasma-oxidized CNTs were reported to present improved dispersion in epoxy resin in comparison with non-treated CNTs (Kim *et al.*, 2006). The epoxy nanocomposites filled with plasma-modified CNTs exhibited higher storage and



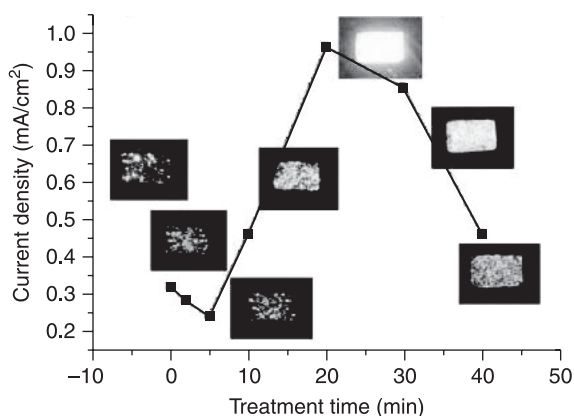
2.10 Proposed model for the transformation process of the multi-walled CNTs under O_2 plasma treatment. (a) Oxygen functional groups are grafted by O_2 plasma; (b) defects and carbon nanowires are created by ion bombardment, losing the superficial structure; (c) ions continue to react with amorphous carbon which are peeled totally from the carbon nanotubes; (d) amorphous carbon is oxidized under O_2 plasma which forms carbon dioxide, the diameter of the multi-walled carbon nanotubes decreases due to the disappearance of the outer wall (Xu *et al.*, 2007).

loss moduli than CNT/epoxy nanocomposites as well as improved tensile strength and elongation at break due to better dispersion and stronger interaction between the CNTs and the polymer matrix.

Felten *et al.* showed that cluster dispersion on thermal evaporation coating of CNTs with various metals can be tuned by increasing the cluster nucleation density through the formation of interaction sites when CNTs are treated in an O₂ RF plasma (Felten *et al.*, 2007). The same effect was also observed when the CNTs were exposed to an NH₃ RF plasma before the metal coating.

The nitrogen-containing groups can be grafted through plasma treatment if gases, such as N₂, N₂/H₂ or NH₃, are used. The treatment of multi-walled CNTs in an N₂/Ar RF plasma was shown to be an effective procedure to enhance the field emission characteristics of CNTs due to the doping of the CNT structure with N atoms (Gohel *et al.*, 2005). The N1s core level peak was fitted with components at 398.2, 398.6, 399.7 and 400.8 eV, which corresponds to C-N, C≡N (sp³ bonding), C=N (sp² bonding) and NO. The field emission properties of screen-printed CNT films were also improved after NH₃ or N₂ RF plasma treatment (Feng *et al.*, 2007). For the CNT films treated by N₂ plasma, the emission current density and fluorescent photos at 6.4 V/μm clearly demonstrated the influence of the treatment time on field emission properties (Fig. 2.11).

The improvement of the field emission properties was attributed to the change in CNT morphology after plasma treatment with the formation of nano-protuberances, i.e. 'multi-tip' CNTs. The dependence of the emission current with treatment duration showed an optimum after 20 minutes of treatment. Prolonged treatment was shown to reduce the field emission properties that were associated with the destruction of CNTs and nano-protuberances.



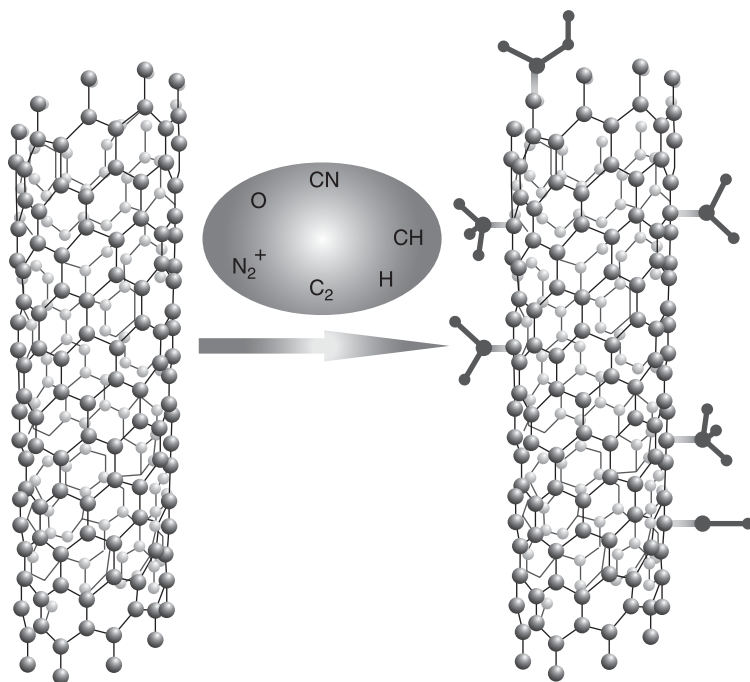
2.11 The emission current density and fluorescent photos of the CNT films at 6.4 V/μm after various N₂ plasma treatment times (Feng *et al.*, 2007).

The N_2 RF plasma treatment was also used to improve the Pt catalyst deposition at the CNT surface, resulting in an enhancement of the electrochemical activity (Kim *et al.*, 2008).

Bystrzejewski *et al.* reported the treatment of single-walled CNTs in a DC hollow cathode glow discharge (HCGD) (Bystrzejewski *et al.*, 2009). Various gases (N_2 , H_2O , $N_2 + H_2O$ and $NH_3 + H_2O$) were used to functionalize CNTs. The N_2 and/or H_2O plasma treatment resulted in the presence of amorphous carbon species at the CNT surface while the use of $NH_3 + H_2O$ yielded a very clean product consisting of functionalized CNTs. *In-situ* optical emission studies showed that the functionalization occurs via radical addition channels with the initial assistance of N_2^+ radical ions. The N_2^+ bombardment breaks the C–C bonds on the CNT surface, after which other chemical radicals are subsequently added and quenched (Fig. 2.12).

An NH_3 μ -wave plasma treatment has been also used to enhance the solubility of CNTs (Wu *et al.*, 2007). The introduction of polar functional groups increases the hydrophilicity of CNTs, making the application of CNTs in the immobilization of biomolecules and construction of biosensors more convenient.

The studies cited above demonstrate the wide range of plasma processes that can be used to modify the CNT surface. The excited species such as electrons,



2.12 Radical addition yielding functional groups ($-CH_3$, $-CN$, $-OH$, $-NH_2$, ...) covalently attached to CNT sidewall (Bystrzejewski *et al.*, 2009).

ions and radicals within plasma interact with the surface of CNTs and break the C=C bonds, which promotes the creation of active sites to bind functional groups as well as some physical modification of the CNT surface. Moreover, it was also reported that UV photons interact with CNTs and create active sites on their sidewalls, however, they can at the same time promote the defunctionalization of moieties grafted onto CNTs (Khare *et al.*, 2002). Due to the interaction of the different plasma reactive species with CNTs, the grafting of functional groups can therefore occur through different simultaneous reactions. This wide range of interactions involves a lack of control on the grafting of wanted chemical function and makes it difficult to determine the weight of each functional mechanism. Moreover, prolonged plasma treatments promote damage of CNTs, resulting in diminution of their diameter with destruction of the outer wall, the forming of onion-like structures, or even their complete destruction.

Plasma post-discharge treatment of carbon nanotubes

To prevent the unwanted effects of plasma functionalization, a solution was proposed by Ruelle *et al.* (2007). These authors proposed avoiding the functionalization of CNTs directly inside the plasma where the density of high energy ions is very high, and instead, placing the CNTs outside the discharge production zone to reduce the detrimental effects associated with ion bombardment and irradiation. In this approach, radicals are the most important reactive species to graft functional groups onto the CNT surface. In this case, the application of microwave discharge sources for the production of intense beams of atomic, radical and metastable species is well established. For example, carbon nanotubes have been hydrogenated by atomic hydrogen generated in a H₂ microwave plasma (Wu *et al.*, 2007). In this type of functionalization, the exact location of the sample and its distance from the plasma discharge zone become a key factor in determining the density of functionalization. Khare *et al.* studied the exposition of SWNTs to microwave-generated N₂ plasma, by placing CNTs at different distances from discharge (Khare *et al.*, 2005). At the shortest distance (1cm), they observed the highest concentration in nitrogen groups but also a loss of integrity of SWNTs due to highly reactive species, like N₂⁺. At intermediate distances, the incorporation of nitrogen, but also a high quantity of oxygen, onto the CNTs is obtained while functionalization was not observed for the maximal distance of 7 cm due to total recombination of atomic nitrogen before arriving at the CNT surface. It is thus important to place CNTs outside the glow discharge zone at an optimal distance to avoid interaction with highly reactive ions and UV photons. In this treatment configuration, radicals become the most important reactive species for the grafting of functional groups onto carbon nanotubes. The efficiency of this approach depends on the density of the radicals produced.

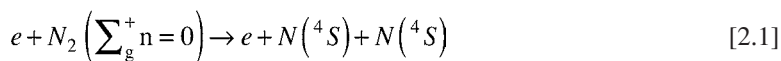
In this context, a surface wave discharge set-up was developed (Godfroid *et al.*, 2003). The microwave-induced plasmas present a higher density of electrons in



2.13 An Ar + N₂ microwave discharge sustained by a surface wave launched on the quartz tube. A high quantity of atomic nitrogen is produced in this plasma discharge (Ruelle, 2009).

comparison with other type of plasmas, such as RF plasmas, for instance, because electrons are more easily created with microwaves (at the same power).

The high electron density of the μ -wave-induced plasmas is the key parameter in the creation of atomic nitrogen in Ar + N₂ microwave plasma (Fig. 2.13). Godfroid *et al.* have demonstrated that production of atomic nitrogen in Ar + N₂ μ -wave discharge is achieved through two electronic mechanisms (Godfroid *et al.*, 2005). The first is dissociation by direct electronic impact, which is achieved by collision between a nitrogen molecule and an electron:



This reaction leads to the production of atomic nitrogen in the fundamental state N(⁴S).

The second is called dissociative recombination and is achieved by recombination between an electron and an ionized nitrogen molecule:

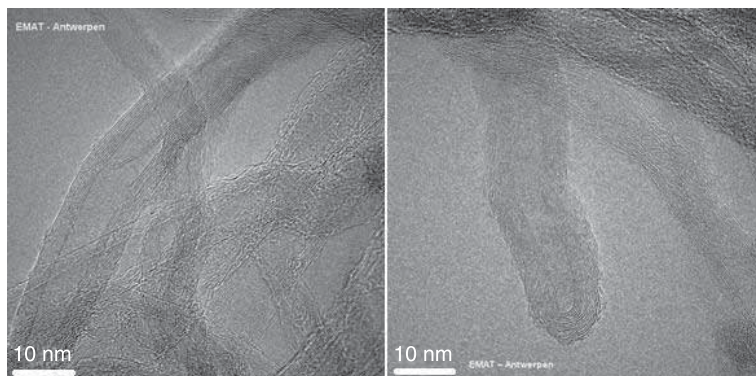


Finally, the set-up and parameters of the microwave discharge were studied to find the higher nitrogen dissociation rate (Godfroid *et al.*, 2003). The most influential parameters proved to be the power supply pulse, the dilution of N₂ in Ar and the total gas flow, which makes it possible to achieve a high homolytic dissociation up to 40% of the molecular N₂.

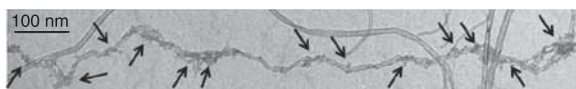
The CNTs were thus treated in the post-discharge of an Ar + N₂ microwave plasma sustained by a surface wave launched in a quartz tube via a surfaguide supplied by a 2.45 GHz microwave generator, which can be pulsed (Ruelle *et al.*, 2007). In this plasma-induced functionalization, the plasma was not used to directly interact with the surface of CNTs but as a source of atomic nitrogen N• reactive flow. It is important to note that the discharge tube and the post-discharge chamber are separated by a diaphragm that consists of an aluminium ring with a circular aperture whose diameter measures a few millimetres. This diaphragm plays two roles in the post-discharge treatment. First, the separation between the plasma set-up and the post-discharge protects the samples placed in the post-discharge from irradiation of high-energy particles from μ -wave plasma. Moreover, the average distance of 40 cm between the end of the discharge tube and the sample holder promotes the interaction of CNTs with atomic nitrogen species that have enough mean lifetime to reach the sample holder, in contrast to other reactive species.

High resolution photoelectron spectroscopy analysis showed that by exposing multi-walled CNTs to atomic nitrogen N• generated in the μ -wave plasma, nitrogen chemical groups were grafted onto the CNT surface, altering the density of electronic states (Ruelle *et al.*, 2008). High-resolution TEM and SEM images revealed that the atomic nitrogen exposition did not damage the surface of the CNTs (Fig. 2.14). The absence of damage in the structure of carbon nanotubes after the plasma treatment also indicated that nitrogen group grafting resulted only from chemical reaction between CNT surfaces and atomic nitrogen species, without the side-effects of irradiation or high energy particle interaction at the CNT surface.

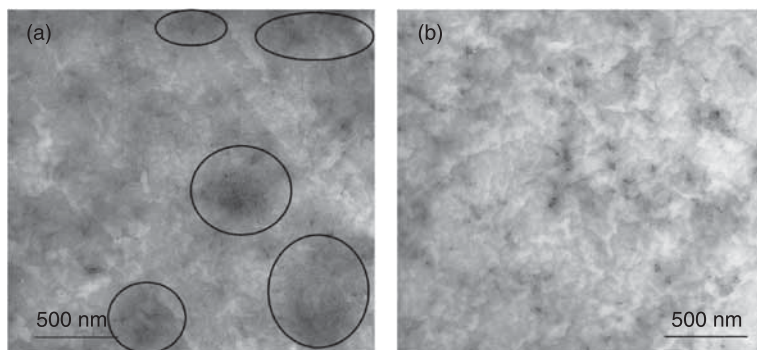
With the addition of H₂ in the post-discharge, an efficient and selective grafting of primary amine groups was developed. Actually, two-thirds of grafted nitrogenated functional groups were primary amine groups, as determined by



2.14 HRTEM images of CNTs treated in the post-discharge chamber of Ar + N₂ μ -wave plasma (Ruelle *et al.*, 2008).



2.15 TEM image of one CNT with PCL islets resembling a pearl-necklace structure (Ruelle, 2009).



2.16 TEM images of PCL nanocomposites filled with (a) 3 wt% CNTs and (b) 3 wt% CNT-g-PCL nanohybrids. CNTs remain agglomerated (black circles) in the CNTs-filled PCL nanocomposites while very small bundles are observed (circled) when PCL is filled with CNT-g-PCL nanohybrids (Ruelle, 2009).

XPS after (trifluoromethyl)benzaldehyde derivative reaction (Ruelle, 2009). These grafted amine groups have been used as initiation sites for promoting the ring opening polymerization (ROP) of ϵ -caprolactone (ϵ -CL) yielding polyester-grafted CNT nanohybrids (Ruelle *et al.*, 2007). The morphology of the recovered nanohybrids has been characterized by TEM, showing that PCL islets, and so the initiator primary amines were homogeneously dispersed along the CNT sidewalls (Fig. 2.15). Moreover, the nanohybrids displayed the best dispersion ability in chloroform, a good PCL solvent, in comparison to pristine and amino-CNTs.

The CNT-g-PCL nanohybrids, mixed with free PCL chains, presented a high degree of CNT pre-disaggregation and were thus used as nanofillers in PCL; pristine and amino-CNT-filled nanocomposites were also prepared as comparative materials. TEM images showed that slightly disrupted CNT bundles are present in the CNT-filled PCL nanocomposites while CNTs are homogeneously dispersed when CNT-g-PCL nanohybrids are used (Fig. 2.16). Electrical conductivity measurements of the PCL nanocomposites showed a similar percolation threshold (~ 0.35 wt%) for each PCL nanocomposite, corresponding to a theoretical value for optimal dispersion of CNTs, which is equal to the inverse of CNT aspect ratio.

The different nanofillers (CNTs, amino-CNTs and CNT-g-PCL nanohybrids) were also dispersed in a high-density polyethylene (HDPE) matrix. TEM analysis

indicated that CNTs and amino-CNTs were poorly dispersed in HDPE while CNT-g-PCL were more homogeneously dispersed, even though PCL and HDPE are known to be non-miscible polymers. Electrical measurements confirmed these observations, showing an electrical percolation threshold of 2.5 wt% for CNTs and amino-CNT-filled HDPE nanocomposites and 1.1 wt% for samples filled with a CNT-g-PCL nanohybrid.

The grafting of primary amine groups on the CNT surface did not influence the dispersion ability of CNTs in PCL and HDPE matrices. However, the electrical measurements showed that the electrical conductivity of amino-CNTs was higher than that of pristine CNTs; functionalization can be used to improve the electrical conductivity. This last result confirmed that the CNT structure is preserved after CNT functionalization in the microwave plasma post-discharge.

2.4 Summary

Offering both a high aspect ratio (length-to-diameter) and a low density, CNTs show strong application potential as advanced filler materials to replace or complement the conventional nanofillers, such as nanoclays, in the fabrication of multifunctional polymer nanocomposites. In this field, the degree of dispersion of the individual CNTs is an essential parameter to produce nanocomposite materials with enhanced properties. In order to homogeneously disperse CNTs throughout polymer matrices, the CNT entanglements and bundles, stabilized by intermolecular van der Waals forces, must be disrupted. One of the most reported techniques to overcome these drawbacks is the surface modification of CNTs. In this context, solvent-based covalent functionalizations are well reported in the literature. Nevertheless, this type of functionalization presents different drawbacks, such as CNT insolubility, which can limit control over the grafting of the functional group onto the CNT surface.

Plasma processes constitute a promising alternative for surface modification. Plasma treatments have the advantage of being non-polluting and provide a wide range of different functional groups depending on plasma parameters such as power, type of gas used, treatment duration and gas pressure.

Generally, CNTs are placed inside the plasma, where their surface interacts with plasma-excited species such as radicals, electrons, ions and UV radiation which induces the breaking of C–C bonds and the creation of active sites for bonding of functional groups on the CNT surface.

Argon and hydrogen plasmas are reported to etch CNT surface and end-caps, improving their field emission properties. When organic monomers are introduced in the plasma, CNTs are coated with plasma polymer films. This results in the pre-disaggregation of CNT bundles, which can be well dispersed in polymer matrices. Fluorinated, oxygenated and nitrogenated gases were also used to generate functional groups at the CNT surface. This surface modification of CNTs opens the way for compatibilization with polymer matrices or for further

attachment of other molecules in order to form polymer nanohybrids. Nevertheless, total control over the grafting of functional groups on the CNT surface is difficult to achieve when CNTs are treated directly in the plasma discharge chamber.

To prevent the degradation of the CNTs during plasma treatment, it was proposed to use plasma discharges as a source of reactive species, such as radicals, which can interact with the CNT surface outside the plasma discharge, avoiding structural damage and destruction due to high energy species bombardment. This process can be considered as a 'dry' chemical reaction at the CNT surface. The grafted functional groups can be used as initiator sites for polymerization, yielding CNT nanohybrids that can be introduced into polymer matrices, forming high-performance polymer nanocomposites and nanohybrids.

2.5 References

- Ahn K. S., Kim J. S., Kim C. O. and Hong J. P. (2003) 'Non-reactive RF treatment of multiwall carbon nanotube with inert argon plasma for enhanced field emission', *Carbon*, 41, 2481–2485.
- Andrews R. and Weisenberger M. C. (2004) 'Carbon nanotube polymer composites', *Curr. Opin. Solid State Mater. Sci.*, 8, 31–37.
- Avila-Orta C. A., Cruz-Delgado V. J., Neira-Velazquez M. G., Hernandez-Hernandez E., Mendez-Padilla M. G., and Medellin-Rodriguez F. J. (2009) 'Surface modification of carbon nanotubes with ethylene glycol plasma', *Carbon*, 47, 1916–1921.
- Bagchi A. and Nomura S. (2006) 'On the effective thermal conductivity of carbon nanotube reinforced polymer composites', *Compos. Sci. Technol.*, 66, 1703–1712.
- Bahr J. L., Yang J., Kosynkin D. V., Bronikowski M. J., Smalley R. E. and Tour J. M. (2001) 'Functionalization of carbon nanotubes by electrochemical reduction of aryl diazonium salts: a bucky paper electrode', *J. Am. Chem. Soc.*, 123, 6536–6542.
- Balasubramanian K. and Burghard M. (2005) 'Chemically functionalized carbon nanotubes', *Small*, 1, 180–192.
- Banerjee S., Hemraj-Benny T. and Wong S. S. (2005) 'Covalent surface chemistry of single-walled carbon nanotubes', *Adv. Mater.*, 17, 17–29.
- Bogaerts A., Neyts E., Gijbels R. and van der Mullen J. (2002) 'Gas discharge plasmas and their applications', *Spectrochimica Acta B*, 57, 609–658.
- Bonduel D., Mainil M., Alexandre M., Monteverde F. and Dubois Ph. (2005) 'Supported coordination polymerization: a unique way to potent polyolefin carbon nanotube nanocomposites', *Chem. Commun.*, 781–783.
- Boskovic B. O., Golovko V. B., Cantoro M., Kleinsorge B., Chuang A. T. H., Ducati C., Hofmann S., Robertson J. and Johnson B. F. G. (2005) 'Low temperature synthesis of carbon nanofibres on carbon fibre matrices', *Carbon*, 43, 2643–2648.
- Bubert H., Haiber S., Brandl W., Marginean G., Heintze M. and Brüser V. (2003) 'Characterization of the uppermost layer of plasma-treated carbon nanotubes', *Diam. Rel. Mater.*, 12, 811–815.
- Bystrejewski M., Rummeli M. H., Gemming T., Pichler T., Huczko A. and Lange H. (2009) 'Functionalizing single-wall carbon nanotubes in hollow cathode glow discharges', *Plasma Chem. Plasma Process.*, 29, 79–90.
- Chapman B. (1980) *Glow Discharge Processes*, New York: Wiley Interscience.
- Charlier J.-C. (2002) 'Defects in carbon nanotubes', *Acc. Chem. Res.*, 35, 1063–1069.

- Chen J., Hamon M. A., Hu H., Chen Y., Rao A. M., Eklund P. C. and Haddon R. C. (1998) 'Solution properties of single-walled carbon nanotubes', *Science*, 282, 95–98.
- Chen Q. D., Dai L. M., Gao M., Huang S. M. and Mau A. (2001) 'Plasma activation of carbon nanotubes for chemical modification', *J. Phys. Chem. B*, 105, 618–622.
- Chen Z., Thiel W. and Hirsch A. (2003) 'Reactivity of the convex and concave surfaces of single-walled carbon nanotubes (SWCNTs) towards addition reactions: dependence on the carbon-atom pyramidalization', *Chem. Phys. Chem.*, 4, 93–97.
- Chirila V., Marginean G. and Brandl W. (2005) 'Effect of the oxygen plasma treatment parameters on the carbon nanotubes' surface properties', *Surf. Coat. Technol.*, 200, 548–551.
- Chu P. K., Chen J. Y., Wang L. P. and Huang N. (2002) 'Plasma-surface modification of biomaterials', *Mater. Sci. and Eng. R*, 36, 143–206.
- Collins P. G. and Avouris P. (2000) 'Nanotubes for electronics', *Sci. Am.*, 283, 62–69.
- D'Agostino R., Favia P., Oehr C. and Wertheimer M. R. (2005) 'Low-temperature plasma processing of materials: past, present and future', *Plasma Process Polym.*, 2, 7–15.
- Denes F. S. and Manolache S. (2004) 'Macromolecular plasma-chemistry: an emerging field of polymer science', *Prog. Polym. Sci.*, 29, 815–885.
- Felten A., Bittencourt C., Colomer J.-F., Van Tendeloo G. and Pireaux J.-J. (2007) 'Nucleation of metal clusters on plasma treated multi wall carbon nanotubes', *Carbon*, 45, 110–116.
- Feng T., Zhang J., Li Q., Wang X., Yu K. and Zou S. (2007) 'Effects of plasma treatment on microstructure and electron field emission properties of screen-printed carbon nanotube films', *Physica E*, 36, 28–33.
- Frauchiger V. M., Schlottig F., Gasser B. and Textor M. (2004) 'Anodic plasma-chemical treatment of CP titanium surfaces for biomedical applications', *Biomaterials*, 25, 593–606.
- Fridman A., Chirokov A. and Gutsol A. (2005) 'Non-thermal atmospheric pressure discharges', *J. Phys. D: Appl. Phys.*, 38, R1–R24.
- Fu K., Huang W., Lin Y., Riddle L. A., Carroll D. L. and Sun Y. P. (2001) 'Defunctionalization of functionalized carbon nanotubes', *Nano. Lett.*, 1(8), 439–441.
- Godfroid T., Dauchot J.-P. and Hecq M. (2003) 'Atomic nitrogen source for reactive magnetron sputtering', *Surf. Coat. Technol.*, 174–175, 1276–1281.
- Godfroid T., Dauchot J.-P. and Hecq M. (2005) 'Effect of plasma temperature and plasma pulsation frequency on atomic nitrogen production', *Surf. Coat. Technol.*, 200, 649–654.
- Gohel A., Chin K. C., Zhu Y. W., Sow C. H. and Wee A. T. S. (2005) 'Field emission properties of N₂ and Ar plasma-treated multi-wall carbon nanotubes', *Carbon*, 43, 2530–2535.
- Gojny F.H., Nastalczyk J., Roslaniec Z. and Schulte K. (2003) 'Surface modified multi-walled carbon nanotubes in CNT/epoxy-composites', *Chem. Phys. Lett.*, 370, 820–824.
- Gorga R. E., Lau K. K. S., Gleason K. K. and Cohen R. E. (2006) 'The importance of interfacial design at the carbon nanotube/polymer composite interface', *J. Appl. Polym. Sci.*, 102, 1413–1418.
- Grill A. (1994) *Cold Plasma in Materials Fabrication*, Boca Raton, FL: IEEE Press.
- Gromov A., Dittmer S., Svensson J., Nerushev O. A., Perez-Garcia S. A., Licea-Jiménez L., Rychwalski R. and Campbell E. E. B. (2005) 'Covalent amino-functionalisation of single-wall carbon nanotubes', *J. Mater. Chem.*, 15, 3334–3339.
- Hammer T. (1999) 'Application of plasma technology in environment', *Contrib. Plasma Phys.*, 39, 441–462.

- Hamon M. A., Itkis M. E., Niyogi S., Alvaraez T., Kuper C., Menon M. and Haddon R. C. (2001) 'Effect of rehybridization on the electronic structure of single-walled carbon nanotubes', *J. Am. Chem. Soc.*, 123, 11292–11293.
- Hino T. and Akiba M. (2000) 'Japanese development of fusion reaction plasma components', *Fus. Eng. Des.*, 49–50, 97–105.
- Hirsch A. (2002) 'Functionalization of single-walled carbon nanotubes', *Angew. Chem. Int. Ed.*, 41, 1853–1859.
- Hirsch A. and Vostrowsky O. (2005) 'Functionalization of carbon nanotubes', *Top. Curr. Chem.*, 245, 193–237.
- Hojati-Talemi P., Cervini R. and Simon G. P. (2009) 'Effect of different microwave-based treatments on multi-walled carbon nanotubes', *J. Nanopart. Res.*, DOI 10.1007/s11051-009-9609-y.
- Holzinger M., Steinmetz J., Samaille D., Glerup M., Paillet M., Bernier P., Ley L. and Graupner R. (2004) '2+1 Cycloaddition for cross-linking SWCNT', *Carbon*, 42, 941–947.
- Hong Y. C., Shin D. H., Cho S. C. and Uhm H. S. (2006) 'Surface transformation of carbon nanotube powder into super-hydrophobic and measurement of wettability', *Chem. Phys. Lett.*, 427, 390–393.
- Hu H., Bhowmik P., Zhao B., Hamon M. A., Itkis M. E. and Haddon R. C. (2001) 'Determination of the acidic sites of purified single-walled carbon nanotubes by acid-base titration', *Chem. Phys. Lett.*, 345, 25–28.
- Iijima S. (1991) 'Helical microtubules of graphite carbon', *Nature*, 354, 56–58.
- Inoue S. and Kajikawa K. (2003) 'Inductivity coupled plasma etching to fabricate the nonlinear optical polymer photonic crystal waveguides', *Mat. Sci. Eng. B*, 103, 170–178.
- Ionescu R., Espinosa E.H., Sotter E., Llobet E., Vilanova X., Correig X., Felten A., Bittencourt C., Van Lier G., Charlier J.-C. and Pireaux J. J. (2006) 'Oxygen functionalisation of MWNT and their use as gas sensitive thick-film layers', *Sensors and Actuators B*, 113, 36–46.
- Jones J. G., Waite A. R., Muratore C. and Voevodin A. A. (2008) 'Nitrogen and hydrogen plasma treatments of multiwalled carbon nanotubes', *J. Vac. Sci. Technol. B*, 26(3), 995–1000.
- Kalita G., Adhikari S., Aryal H. R., Ghimre D. C., Afre R., Soga T., Sharon M. and Umeno M. (2008) 'Fluorination of multi-walled carbon nanotubes (MWNTs) via surface wave microwave (SW-MW) plasma treatment', *Physica E*, 41, 299–303.
- Khabashesku V. N., Billups W. E. and Margrave J. L. (2002) 'Fluorination of single-wall carbon nanotubes and subsequent derivatization reactions', *Acc. Chem. Res.*, 35, 1087–1095.
- Khare B. N., Meyyappan M., Cassell A. M., Nguyen C. V. and Han J. (2002) 'Functionalization of carbon nanotubes using atomic hydrogen from a glow discharge', *Nano. Lett.*, 2, 73–77.
- Khare B., Wilhite P., Tran B., Teixeira E., Fresquez K., Mvondo D. N., Bauschlicher C. and Meyyappan M. (2005) 'Functionalization of carbon nanotubes via nitrogen glow discharge', *J. Phys. Chem. B*, 109, 23466–23472.
- Kilbride B. E., Coleman J. N., Frayssé J., Fournet P., Cadek M. and Drury A. (2002) 'Experimental observation of scaling laws for alternating current and direct current conductivity in polymer-carbon nanotube composite thin films', *J. Appl. Phys.*, 92, 4024–4030.
- Kim J. A., Seong D. G., Kang T. J. and Youn J. R. (2006) 'Effects of surface modification on rheological and mechanical properties of CNT/epoxy composites', *Carbon*, 44, 1898–1905.

- Kim S., Jung Y. and Park S.-J. (2008) 'Preparation and electrochemical behaviors of platinum nanocluster catalysts deposited on plasma-treated carbon nanotube supports', *Coll. Surf. A: Physicochem. Eng. Aspects*, 313–314, 189–192.
- Konya Z., Vesselenyi I., Niesz K., Kukovecz A., Demortier A., Fonseca A., Delhalle J., Mekhalif Z., Nagy J. B., Koos A. A., Osvath Z., Kocsonya A., Biro L. P. and Kiricsi I. (2002) 'Large scale production of short functionalized carbon nanotubes', *Chem. Phys. Lett.*, 360, 429–435.
- Lee J.-Y., Park E.-J., Lee C.-J., Kim S.-W., Pak J. J. and Min N. K. (2009) 'Flexible electrochemical biosensors based on O₂ plasma functionalized MWCNT', *Thin Solid Films*, 517, 3883–3887.
- Lee W. H., Kim S. J., Lee W. J., Lee J. G., Haddon R. C. and Reucroft P. J. (2001) 'X-ray photoelectron spectroscopic studies of surface modified single-walled carbon nanotube material', *Appl. Surf. Sci.*, 181, 121–127.
- Lee Y. S., Cho T. H., Lee B. K., Rho J. S., An K. H. and Lee Y. H. (2003) 'Surface properties of fluorinated single-walled carbon nanotubes', *J. Fluor. Chem.*, 120, 99–104.
- Li J., Fang Z. P., Tong L. F., Gu A. J. and Liu F. (2007) 'Improving dispersion of multiwalled carbon nanotubes in polyamide 6 composites through amino-functionalization', *J. Appl. Polym. Sci.*, 106, 2898–2906.
- Liu J., Rinzler A. G., Dai H., Hafner J. H., Bradley R. K., Boul P. J., Lu A., Iverson T., Shelimov K., Huffman C. B., Rodriguez-Marcias F., Shon Y.-S., Lee T. R., Colbert D. T. and Smalley R. E. (1998) 'Fullerene pipes', *Science*, 280, 1253.
- Liu P. (2005) 'Modifications of carbon nanotubes with polymers', *Eur. Polym. J.*, 41, 2693–2703.
- Ma P. C., Tang B. Z. and Kim J.-K. (2008) 'Conversion of semiconducting behavior of carbon nanotubes using ball milling', *Chem. Phys. Lett.*, 458, 166–169.
- McOmber J. I. and Nair R. S. (1991) 'Development of a process to achieve residue-free photoresist removal after high-dose ion implantation', *Nucl. Instrum. Meth. Phys. Resear. B*, 55, 281–286.
- Meng H., Sui G. X., Fang P. F. and Yang R. (2008) 'Effects of acid- and diamine-modified MWNTs on the mechanical properties and crystallization behavior of polyamide 6', *Polym.*, 49, 610–620.
- Meyer-Plath A. A., Finke B., Schröder K. and Ohl A. (2003) 'Pulsed and CW microwave plasma excitation for surface functionalization in nitrogen-containing gases', *Surf. Coat. Technol.*, 174–175, 877–881.
- Mickelson E. T., Huffman C. B., Rinzler A. G., Smalley R. E., Hauge R. H. and Margrave J. L. (1998) 'Fluorination of single-wall carbon nanotubes', *Chem. Phys. Lett.*, 296, 188–194.
- Monthieux M., Smith B. W., Burtiaux B., Claye A., Fischer J. E. and Luzzi D. E. (2001) 'Sensitivity of single-wall carbon nanotubes to chemical processing: an electron microscopy investigation', *Carbon*, 39, 1251–1272.
- Nakamura T., Ohana T., Ishihara M., Hasegawa M. and Koga Y. (2008) 'Photochemical modification of single-walled carbon nanotubes with amino functionalities and their metal nanoparticles attachment', *Diam. Rel. Mater.*, 17, 559–562.
- Nastase C., Nastase F., Vaseashta A. and Stamatini I. (2006) 'Nanocomposites based on functionalized nanotubes in polyaniline matrix by plasma polymerization', *Prog. Solid State Chem.*, 34, 181–189.
- Niyogi S., Hamon M. A., Hu H., Zhao B., Bhowmik P., Sen R., Itkis M. E. and Haddon R. C. (2002) 'Chemistry of single-walled carbon nanotubes', *Acc. Chem. Res.*, 35, 1105–1113.

- Okpalugo T. I. T., Papakonstantinou P., Murphy H., McLaughlin J. and Brown N. M. D. (2005) 'Oxidative functionalization of carbon nanotubes in atmospheric pressure filamentary dielectric barrier discharge (APDBD)', *Carbon*, 43, 2951–2959.
- Pantarotto D., Partidos C. D., Graff R., Hoebeke J., Briand J.-P., Prato M. and Bianco A. (2003) 'Synthesis, structural characterization and immunological properties of carbon nanotubes functionalized with peptides', *J. Am. Chem. Soc.*, 125, 6160–6164.
- Plank N., Jiang L. and Cheung R. (2003) 'Fluorination of carbon nanotubes in CF plasma', *Appl. Phys. Lett.*, 83, 2426.
- Pötschke P., Zschoerper N. P., Moller B. P. and Vohrer U. (2009) 'Plasma functionalization of multiwalled carbon nanotube bucky papers and the effect on properties of melt-mixed composites with polycarbonate', *Macromol. Rapid Comm.*, 30, 1828–1833.
- Qin Y. and Hu M. (2008) 'Effects of microwave plasma treatment on the field emission properties of printed carbon nanotubes/Ag nano-particles films', *Appl. Surf. Sc.*, 254, 1757–1762.
- Ramanathan T., Fischer F. T., Ruoff R. S. and Brinson L. C. (2005) 'Amino-functionalized carbon nanotubes for binding to polymers and biological systems', *Chem. Mater.*, 17, 1290–1295.
- Rawat D. S., Taylor N., Talapatra S., Dhali S. K., Ajayan P. M. and Migone A. D. (2006) 'Effect of surface cleaning and functionalization of nanotubes on gas adsorption', *Phys. Rev. B*, 74, 113403.
- Ruelle B. (2009) 'Functionalization of carbon nanotubes via plasma post-discharge surface treatment: Implication as nanofiller in polymeric matrices', PhD thesis, University of Mons.
- Ruelle B., Felten A., Ghijsen J., Drube W., Johnson R. L., Liang D., Erni R., Van Tendeloo G., Dubois Ph., Hecq M. and Bittencourt C. (2008) 'Functionalization of MWCNTs with atomic nitrogen: electronic structure', *J. Phys. D Appl. Phys.*, 41, 045202.
- Ruelle B., Peeterbroeck S., Gouttebaron R., Godfroid T., Monteverde F., Dauchot J.-P., Alexandre M., Hecq M. and Dubois Ph. (2007) 'Functionalization of carbon nanotubes by atomic nitrogen formed in a microwave plasma Ar + N₂ and subsequent poly(ϵ -caprolactone) grafting', *J. Mater. Chem.*, 17, 157–159.
- Shi D. and He P. (2004) 'Surface modifications of nanoparticles and nanotubes by plasma polymerization', *Rev. Adv. Mater. Sci.*, 7, 97–107.
- Sinnott S. B. (2002) 'Chemical functionalization of carbon nanotubes', *J. Nanosci. Nanotechnol.*, 2, 113–123.
- Stevens J. L., Huang A. Y., Peng H., Chiang I. W., Khabashesku V. N. and Margrave J. L. (2003) 'Sidewall amino-functionalization of single-walled carbon nanotubes through fluorination and subsequent reactions with terminal diamines', *Nano. Lett.*, 3, 331–336.
- Tasis D., Tagmatarchis N., Bianco A. and Prato M. (2006) 'Chemistry of carbon nanotubes', *Chem. Rev.*, 106, 1105–1136.
- Thostenson E., Li C. and Chou T. W. (2005) 'Nanocomposites in context', *Compos. Sci. Technol.*, 65, 491–516.
- Thostenson E., Ren Z. and Chou T.W. (2001) 'Advances in the science and technology of carbon nanotubes and their composites: a review', *Compos. Sci. Technol.*, 61, 1899–1912.
- Tseng C. H., Wang C. C. and Chen C. Y. (2007) 'Functionalizing carbon nanotubes by plasma modification for the preparation of covalent-integrated epoxy composites', *Chem. Mater.*, 19 (2), 308–315.
- Valentini L., Puglia D., Armentano I. and Kenny J. M. (2005) 'Sidewall functionalization of single-walled carbon nanotubes through CF₄ plasma treatment and subsequent reaction with aliphatic amines', *Chem. Phys. Lett.*, 403, 385–389.

- Wang W., Ciselli P., Kuznetsov E., Peijs T. and Barber A. H. (2008) 'Effective reinforcement in carbon nanotube-polymer composites', *Philos. Trans. Roy. Soc. A*, 366, 1613–1626.
- Wu Z., Xu Y., Zhang X., Shen G. and Yu R. (2007) 'Microwave plasma treated carbon nanotubes and their electrochemical biosensing application', *Talanta*, 72, 1336–1341.
- Xu T., Yang J., Liu J. and Fu Q. (2007) 'Surface modification of multi-walled carbon nanotubes by O₂ plasma', *Appl. Surf. Sci.*, 253, 8945–8951.
- Yan B., Qian K., Zhang Y. and Xu D. (2005) 'Effects of argon plasma treating on surface morphology and gas ionization property of carbon nanotubes', *Physica E*, 28, 88–92.
- Yan Y. H., Cui J., Chan-Park M. B., Wang X. and Wu Q. Y. (2007) 'Systematic studies of covalent functionalization of carbon nanotubes via argon plasma-assisted UV grafting', *Nanotechnol.*, 18, 1–7.
- Yu K., Zhu Z., Zhang Y., Li Q., Wang W., Luo L., Yu X., Ma H., Li Z. and Feng T. (2004) 'Change of surface morphology and field emission property of carbon nanotube films treated using a hydrogen plasma', *Appl. Surf. Sci.*, 225, 380–388.
- Zhang J., Feng T., Yu W., Liu X., Wang X. and Li Q. (2004) 'Enhancement of field emission from hydrogen plasma processed carbon nanotubes', *Diam. Rel. Mater.*, 13, 54–59.
- Zhang J., Zou H., Qing Q., Yang Y., Li Q., Liu Z., Guo X. and Du Z. (2003) 'Effect of chemical oxidation on the structure of single-walled carbon nanotubes', *J. Phys. Chem. B*, 107, 3712–3718.
- Zhu Y. W., Cheong F. C., Yu T., Xu X. J., Lim C. T., Thong J. T. L., Shen Z. X., Ong C. K., Liu Y. J., Wee A. T. S. and Sow C. H. (2005) 'Effects of CF₄ plasma on the field emission properties of aligned multi-wall carbon nanotube films', *Carbon*, 43, 395–400.
- Zschoerper N. P., Katzenmaier V., Vohrer U., Haupt M., Oehr C. and Hirth T. (2009) 'Analytical investigation of the composition of plasma-induced functional groups on carbon nanotube sheets', *Carbon*, 47, 2174–2185.

Functionalization of carbon nanotubes for polymer nanocomposites

Y.-K. YANG, Hubei University, P. R. China, X.-L. XIE, Huazhong University of Science and Technology, P. R. China and Y.-W. MAI, The University of Sydney, Australia

Abstract: Carbon nanotubes (CNTs) are excellent candidates for substituting or complementing conventional nanofillers in the fabrication of multifunctional polymer nanocomposites owing to their unique electronic, thermal and mechanical properties. The critical challenge is to uniformly disperse and exfoliate CNTs into polymers to achieve good matrix/nanotube adhesion that maximizes the transfer of the nanotube properties to the polymer matrix. However, many potential applications have been prevented due to the poor dispersion of CNTs and the weak matrix/CNT interface interaction. Functionalization of CNTs provides an effective means to optimize the physical–mechanical properties of polymer–CNT nanocomposites. In this chapter, we summarize various functionalization techniques, including non-covalent and covalent methodologies, with particular emphasis on the dispersion of CNTs and the interface interaction in polymer–CNT nanocomposites.

Key words: carbon nanotubes, dispersion, functionalization, interface adhesion, polymer nanocomposites.

3.1 Introduction

Carbon nanotubes (CNTs) are all-carbon macromolecules which consist of one or more graphene sheets seamlessly wrapped into cylinder-shaped tubes, corresponding to single-walled carbon nanotubes (SWNTs) or multi-walled carbon nanotubes (MWNTs), respectively.^{1–3} The pseudo one-dimensional nanostructures endow them with high surface area, large aspect ratio and unusual physicochemical properties such as excellent electrical and thermal conductivities and mechanical strength.^{4–6} CNTs have been considered as ideal nano-fillers and functional additives in high-performance polymer-based nanocomposites to improve the matrix properties and enable novel functionalities.^{7–9} Impressive progress has been made in these directions. For example, adding 1 wt% MWNTs in ultra-high molecular weight polyethylene (UHMWPE) film results in an increase of strain energy density and ductility by 150% and 140%, respectively.¹⁰ Elastic stiffness and tensile strength are similarly increased by 42% and 25%, respectively, for polystyrene (PS)–MWNT composites containing 1 wt% MWNTs.¹¹ It is found that epoxy composites show an increase of ~120% in thermal conductivity at 1 wt% SWNT loading.¹² Yu *et al.*¹³ recently prepared

novel segregated-network CNT–polymer composites by mixing poly(vinyl acetate) (PVAc) emulsion with a gum arabic-stabilized CNTs aqueous solution. It is found that PVAc–CNT composites show a sharp increase in electrical conductivity, while their thermal conductivity and thermal energy are kept insensitive to filler loading. This work makes possible the preparation of polymer nanocomposites with a higher thermoelectric performance and further development of lightweight, low-cost, and non-toxic composites for future thermo-electric applications.

However, nano-sized CNTs are intrinsically insoluble and have a strong tendency to aggregate in solvents and polymers because of the strong van der Waals forces and electrostatic interactions.¹⁴ Therefore, realistic applications of polymer–CNT nanocomposites have been significantly less than their anticipated high potential, due to the poor dispersion and compatibility of CNTs in polymers and the weak interface bonding between polymer and CNTs. Dispersion is a fundamental issue for particulate-reinforced polymer composites.¹⁵ It is imperative that homogeneous dispersion of CNTs not only transfers the external load to the nanotubes, but also minimizes the stress concentration sites and obtains a more uniform stress distribution.^{16–18} The interfacial adhesion between CNTs and polymer is also critical to optimize the mechanical and other functional properties of the composites. It is widely recognized that the efficient load transfer depends on the strong interfacial bonding between the host matrix and the fillers used.^{16–19} Herein lies the critical challenge to transfer the excellent properties of CNTs. To the host polymer via optimal methodologies during processing of the composites. Generally, improved strategies are to functionalize the CNTs with polymers. Frankland *et al.*²⁰ used molecular simulation to analyze the shear strength of polymer–SWNT interface, and predicted that it would increase by an order of magnitude owing to the chemical bonding between SWNTs and polymer with ~0.3% grafting density. Graff *et al.*²¹ improved the dispersibility of SWNTs in epoxy matrices by functionalizing the nanotubes with protein concanavalin. Incorporation of 1 wt% fluorinated-SWNTs in poly(ethylene oxide) showed increases of 145% in tensile modulus and 300% in yield strength.²² Recently, O'Connor *et al.*²³ used Kevlar-functionalized MWNTs as additives to reinforce commercially available polyvinyl acetate, and obtained improvements of 80% in tensile strength and 173% in Young's modulus at very low loading (0.25–0.5 wt%) of MWNTs.

To date, several reviews have been published on functionalization methods for CNTs,^{24–27} which conceptually fall into two groups: non-covalent and covalent functionalization. The first group involves non-covalent wrapping or adsorption of functional molecules which can be either small organic molecules such as surfactants or various species of macromolecules. The second group involves chemical bonding between functional molecules and CNTs via versatile reactions onto the graphitic surface of the CNTs. From a materials' chemistry perspective, both methodologies are equally important to the development and applications of

materials that contain CNTs, regardless of the functionalization means of attaching the chemical handles to CNTs. Previous reviews have mainly focused on the methodologies to functionalize CNTs with small organic molecules and polymers.^{24–27} However, this chapter is a critical review of the most significant results of polymer–CNT composites containing polymer-functionalized CNTs in the past decade, with special emphases on the dispersion of CNTs, polymer–CNT interface bonding and final properties of the resultant nanocomposites.

3.2 Non-covalent functionalization of carbon nanotubes with polymers

CNTs are non-covalently functionalized by polymers employing π - π stacking, and electrostatic and hydrophobic interactions. This type of functionalization can be divided into two methods: *in-situ* polymerization and physical mixing. The former polymerizes the monomer in the presence of pristine or purified CNTs, and can be carried out in the presence and/or absence of solvent. The latter involves direct mixing of the CNTs with a preformed polymer through solution or melt processing. Periodically functionalized CNTs can be achieved by helical wrapping of general polymers, or by forming nanohybrid shish-kebabs of crystalline polymers. During processing, some additives such as surfactants are sometimes used to assist dispersion of CNTs in polymers.

3.2.1 *In-situ* polymerization

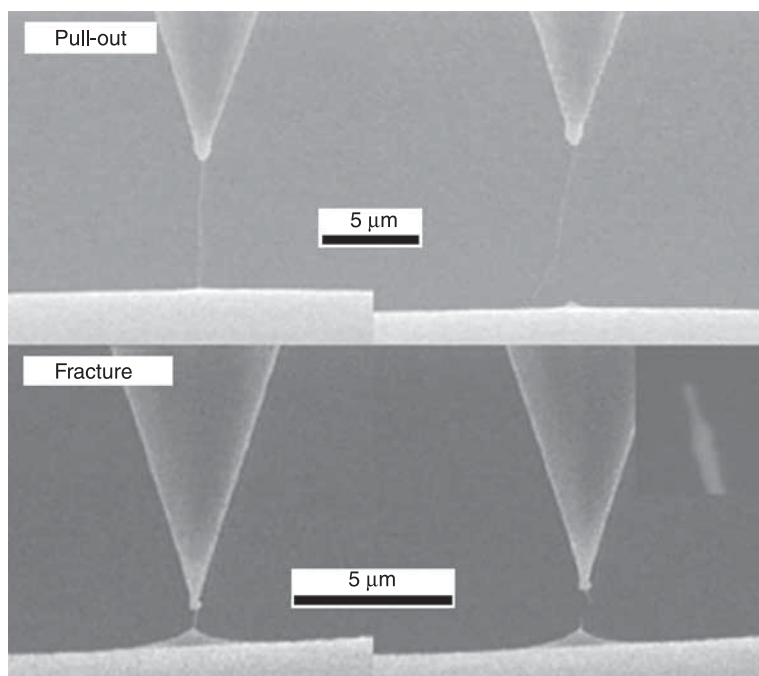
The general procedures of *in-situ* polymerization are to disperse pristine CNTs or purified CNTs in monomer or mixture of monomer and solvent, followed by polymerizing the monomer to prepare polymer–CNT composites. Clayton *et al.*²⁸ prepared poly(methyl methacrylate)–SWNT (PMMA–SWNT) composite films by *in-situ* free radical polymerization that was triggered by heat, ultraviolet (UV) light and gamma radiation, respectively. The resultant composite films upon evaporation of methylene chloride show enhanced transparency with respect to the melt-blended composites due to the improved dispersion of CNTs. Putz *et al.*²⁹ showed the clear evidence of cohesive interaction between SWNTs and PMMA chains, leading to an increase in the low-temperature elastic modulus of ~10% beyond that of pure PMMA at less than 0.1 wt% SWNTs. Recently, Zhang *et al.*³⁰ obtained PMMA–MWNT composite fibers by infiltration of MMA into aligned MWNT aerogel fibers at room temperature with subsequent *in-situ* polymerization at 50 °C. They found that PMMA fills the space of MWNTs and exhibits local order. When compared to the control PMMA, PMMA–MWNT fibers with 15 wt% MWNTs exhibit a 16-fold and a 49-fold increase in tensile strength and Young's modulus, respectively.

In-situ polymerization was also applied to prepare polymer–CNT composites by a step-growth mechanism, except for a commonly known chain reaction such

as the above free radical polymerization. For instance, poly(*p*-phenylene benzobisoxazole) (PBO)–SWNT composites were synthesized in the presence of SWNTs in poly(phosphoric acid) (PPA), using typical PBO polymerization conditions, then PBO–SWNT fibers were spun from their liquid crystalline solutions using dry-jet wet spinning.³¹ The addition of 10 wt% SWNTs increases the tensile strength of PBO fiber by ~50% and reduces shrinkage and high-temperature creep. Zhao *et al.*³² ultrasonically pre-dispersed MWNTs into the polymerizable master solution followed by *in-situ* hydrolytic polymerization of the caprolactam monomer to achieve the homogeneous dispersion of MWNTs in polyamide 6 (PA6) matrices. They found that adding 0.5 wt% MWNTs has little effect on the molecular weight of PA6, and the tensile strength and storage modulus of PA6–MWNT composites are slightly improved, however, MWNTs clearly influence the crystallization and glass transition behavior.

In some cases, acid oxidation or organic modification has been used to chemically pretreat CNTs before *in-situ* polymerization of the monomer. Velasco-Santos *et al.*³³ prepared PMMA nanocomposites by *in-situ* polymerization of MMA in the presence of pristine MWNTs (*p*-MWNTs) and functionalized-MWNTs (*f*-MWNTs) containing carboxylic groups, respectively. Both Raman and infrared spectra prove the interaction between PMMA and *f*-MWNT, which effectively improves the mechanical load transfer with respect to PMMA–*p*-MWNT. The storage modulus of PMMA–*f*-MWNT with only 1 wt% *f*-MWNTs is increased by an outstanding 1,135% at 90 °C and the glass transition temperature (T_g) is exceptionally raised by ~40 °C. In evaluating the force required to pull out each nanotube from the polymer matrix, Barber *et al.*³⁴ found that the interfacial strength between MWNTs and matrix increases dramatically when the surface of MWNTs is chemically modified. Figure 3.1 shows a transition from pull-out to fracture at a critical embedded length as an individual nanotube is pulled from the polymer matrix. This indicates that a smaller critical length and a larger pull-out force are required when using the chemically modified MWNTs instead of the unmodified tubes. These observations imply that the ability of load transfer of CNTs can be significantly enhanced by using pre-modified rather than pristine CNTs in the preparation of polymer–CNT composites.

Apart from the aforementioned work, surfactant-assisted processing of CNTs is also used to improve dispersion and interfacial bonding of CNTs with polymer, where surfactants are the third component functioning as dispersants. In general, surfactant-assisted dispersion of CNTs is conducted in an aqueous medium with the aid of ultrasonication. Ultrasonication action offers mechanical energy to weaken the van der Waals forces between CNT bundles to exfoliate CNTs into small ropes or even individual CNTs, while the surfactant organic molecules are physically absorbed onto the external surface of the CNTs, resulting in the formation of a stable CNT colloidal system induced by electrostatic and/or steric repulsion.^{35–38} Once monomers are added to a homogeneous CNT colloid stabilized by surfactant molecules under ultrasonication, then *in-situ* polymerization



3.1 A transition from pull-out to fracture occurs at a critical nanotube embedded length, with chemically modified nanotubes showing a smaller critical length than the unmodified nanotubes. (Reproduced with permission from ref. 34. Copyright 2006 Wiley-VCH Verlag GmbH & Co. KGaA.)

(so-called emulsion polymerization) is carried out to achieve an emulsion-like solution as a result of a mixture of CNTs and polymer particles. Finally, the resultant colloidal solution is dried (prior to demulsifying if needed), to obtain a composite in a solid state, where the dispersion and debundling of CNTs are expected to remain in the polymer matrix. Barraza *et al.*³⁹ prepared thermo-plastic PS–SWNT and elastomeric poly(styrene-*co*-isoprene) (PSI)–SWNT composites in the presence of cetyltrimethylammonium bromide (CTAB) as a cationic surfactant. They found that the adsorbed polymer layers on SWNTs are conducive to the dispersion of SWNTs. Raman spectra of PS–SWNT and PSI–SWNT hybrids suggest that the strong interaction between SWNTs and the matrix contributes to a reduced vibrational freedom of polymer chains. Xia *et al.*⁴⁰ developed a novel ultrasonically initiated emulsion polymerization approach to prepare PMMA–MWNT and poly(*n*-butyl acrylate) (PBA)–MWNT composites without any chemical initiator. Based on a combination effect of sonication, such as dispersion, pulverizing, activation and initiation, the aggregation and entanglement of MWNTs in aqueous solution can be broken down, consequently resulting in a uniform dispersion of MWNTs in both PMMA and PBA matrices.

Further, incorporation of PBA-encapsulated MWNTs into a nylon 6 matrix effectively improves the interface adhesion; the yield strength and Young's modulus increase by about 30% and 35% at only 1 wt% loading, respectively.

Some researchers believe that CNTs can partially participate in polymerization to form a strong chemical bonding between CNTs and the matrix. Some suggested that π -bonds in CNTs are initiated by AIBN to generate radicals on the surface of CNTs followed by growing the polymer chains.^{41–43} Others proposed that some polymer chains may be covalently attached to CNTs by an additional mechanism of macromolecular radicals,^{44–46} where the CNTs act as terminal agents. In most cases, the formation of chemical linkage between CNTs and polymer is difficult in such polymerization systems. But it is widely recognized that *in-situ* polymerization is not only a significantly important method that allows better dispersion of CNTs in a polymer matrix, but is a very convenient processing technique to produce polymer nanocomposites with high CNTs loadings. This methodology has shown very good miscibility with most monomers, especially for the preparation of insoluble and thermally unstable polymers.¹⁶

3.2.2 Polymer wrapping

Unlike *in-situ* polymerization of monomer in the presence of CNTs, polymer wrapping directly mixes the pre-synthesized polymer and CNTs by mechanical blending. In this regard, the dispersion and debundling of CNTs in the polymer matrix are achieved by the non-covalent interaction between them such as van der Waals forces, hydrophobic and electrostatic interactions as well as special π - π stacking and CH- π interactions. Researchers used polymer wrapping to fabricate polymer–CNT composites through two methodologies, including solution blending and melt compounding. Solution processing is the most common method that is generally performed by dispersing CNTs in a suitable solvent or polymer solution, followed by mixing and then precipitating from their non-solvent or evaporating the solvent to obtain the polymer–CNT composites. In solution processing, high-power ultrasonication in combination with mechanical agitation is often required to accelerate the deaggregation and exfoliation of nanotube bundles since it is difficult to directly disperse CNTs in solvent using simple stirring. Coleman *et al.*⁴⁷ prepared a suspension of poly(vinyl alcohol) (PVA)–MWNT by ultrasonication, and cast them onto a polished Teflon disk followed by evaporation of the solvent at 60°C in an oven. The final free-standing PVA–MWNT films show increases in Young's modulus, tensile strength and toughness by 3.7, 4.3 and 1.7 times at less than 1 wt% nanotubes compared to the parent PVA. It is believed that the PVA-nanotube interaction is completely non-covalent as a result of the van der Waals forces. A 78% increase in tensile modulus for PVA–SWNT films was reported by Liu *et al.*⁴⁸ when adding 0.8 wt% SWNTs modified by multi-hydroxyl groups to the PVA matrix by simple mixing. Recently, Wang *et al.*⁴⁹ prepared polyelectrolyte–MWNT core-shell nanocomposites by alternately assembling poly(aniline-co-*o*-anisidine) and

poly(sodium 4-styrenesulfonate) ionomers to the carboxylated-MWNTs. The wrapped polyelectrolyte improves the dispersibility and stability of MWNTs in solution. The conductivity of the nanocomposites increases to 4.2 S/cm by 3 orders of magnitude from 0.004 S/cm of pure polyelectrolyte. These results indicate that the use of surface-modified CNTs can increase the capability of polymer wrapping to enhance the dispersion and interfacial bonding between the components.

CNTs are well known to be π -conjugated, quasi-one-dimensional structures consisting of rolled-up graphene sheets. Hence, conjugated polymer–CNT composites are desirable due to the relatively strong π - π non-covalent interaction between them. Tang *et al.*⁵⁰ first reported that CNTs were helically wrapped by poly(phenylacetylene) (PPA) chains to endow them with good solubility in organic solvents. Poly(phenylene vinylene) (PPV) derivatives that consist of rigid aromatic phenyl and flexible aliphatic vinyl groups in their main chains, acting as typical conjugated polymers, are more widely studied owing to the great promise of their CNT composites in photoelectric applications.^{51–54} Curran *et al.*⁵¹ prepared poly(*m*-phenylenevinylene-*co*-2,5-dioctoxy-*p*-phenylenevinylene) (PmPV)–MWNT composites by mixing MWNTs with PmPV in toluene. It is found that the electrical conductivity of PmPV is increased by up to eight orders of magnitude, and MWNTs act as nanometric heat sinks to prevent the build-up of large thermal effects. Considering the luminescent property of PmPV, Star *et al.*⁵² used PmPV–CNT composites to fabricate an optoelectronic memory device. The resultant device reveals a photogating effect on charge transport which can rectify or amplify the current flow through the tubes.⁵³ Recently, Tchoul *et al.*⁵⁴ prepared PS–SWNT composites by rapid evaporation of chloroform solutions of PmPV-functionalized SWNTs and polystyrene. It is found that PmPV is a good stabilizing agent for dispersion of SWNTs, and the resulting composites show a higher electrical conductivity and lower percolation threshold than those of PS-containing acid-oxidized SWNTs in the absence of PmPV.

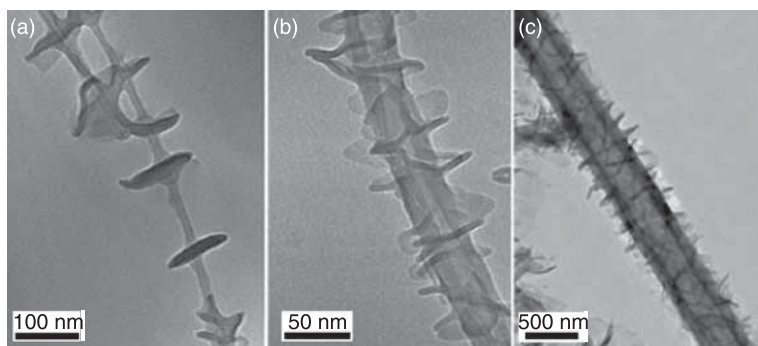
Other polymers such as non-conjugated poly(allylamine),⁵⁵ poly(L-lysine),⁵⁶ Nafion⁵⁷ and polyethylenimine,⁵⁸ poly(*o*-toluidine),⁵⁹ pyrene-labeled hydroxypropyl cellulose⁶⁰ and poly(thiophene)s,⁶¹ were successfully applied to functionalize CNTs by polymer wrapping. These results show that such structural polymers can afford well-dispersed CNT solutions, thereby their composites, even with an extremely low polymer concentration in some cases, result in improved mechanical and electrical properties. Recent theoretical simulation⁶² and experimental observations^{63,64} suggest that wrapping or coating is a ‘general phenomenon’ occurring between polymers and CNTs regardless of the preparation methods of solution processing and melt-shear mixing.

Melt processing is an alternative that is especially beneficial to insoluble polymers, and it is mainly conducted with high shear forces at a given temperature that is above the melting point or glass transition temperature of the polymer used. Liu *et al.*^{65,66} prepared MWNT-reinforced PA6 nanocomposites by the simple melt-compounding method. It is found that the elastic modulus and yield strength

of PA6–MWNT (2 wt%) composites are increased greatly with respect to those of pure PA6 by about 214% and 162%, respectively, which are due to the uniform dispersion of MWNTs throughout the PA6 matrix and the strong interfacial bonding between nanotubes and matrix. Interestingly, only α -form crystals are observed for PA6–MWNT composites quite different from those observed in PA6–clay nanocomposites. However, in most cases, melt processing inevitably encounters such difficulties as poor dispersibility, low CNT loading in the polymer matrix due to the high melting viscosities, and unexpected polymer degradation, although it is most compatible with current industrial processing techniques.

3.2.3 Nanohybrid shish-kebabs (NHSK): periodically functionalized CNTs

Cadek *et al.*⁶⁷ reported that Young's modulus of PVA is increased by a factor of 2 at less than 1 wt% MWNTs loading when crystalline polymers wrap around the nanotubes surface. Using non-crystalline polymers towards similar MWNTs, however, results in much lower levels of reinforcement. This finding clearly implies that well-ordered polymer coating is extremely important to effective load transfer of composites. Polymers with high affinity for physisorption or wrapping on CNTs are in principle good candidates to promote enhanced interfacial bonding between the matrix and CNTs. This non-covalent interaction also retains the structural integrity of CNTs.^{68,69} Therefore, using crystalline polymers to functionalize CNTs via CNT-induced crystallization seems an ideal method since they possess better mechanical properties than those of non-crystalline polymers. In this regard, Li *et al.*⁷⁰ reported some significant results. They first used a polymer solution crystallization technique to achieve periodically decorated CNTs.^{71–74} In detail, CNTs were first dispersed in a given solvent under ultrasonication followed by mixing with a solution of polymer, and the resulting polymer–CNT dilute solution was then brought to the crystallization temperature (T_c), at which point the polymer crystallizes on the surface of the nanotubes to generate polymer–CNT nanohybrids. Both PE and Nylon 66 were successfully applied to functionalize SWNTs and MWNTs and even vapor-grown carbon nanofibers (CNFs). It is found that CNTs are periodically decorated with polymer lamellar crystals to form nano-hybrid shish-kebab (NHSK) structures (Fig. 3.2). The NHSK structural parameters can be readily adjusted by controlling crystallization conditions; the periodicity of polymer lamellae varies from 20 to 150 nm and the kebabs are ~5–10 nm thick along CNTs with a lateral size of ~20 nm to micrometers.⁷² This provides a unique opportunity to control the functionalization degree of CNTs. It is of great interest that the formation conditions of NHSK depend on the structures of CNTs used, probably offering an opportunity for separation of CNTs. Accordingly, the NHSK formation is attributed to a heterogeneous nucleation mechanism of size-dependent soft epitaxy. Such functionalized-MWNTs can be easily dispersed in solution, and can also be used as precursors to prepare polymer–CNT nanocomposites with excellent dispersion.



3.2 TEM images of (a) PE–MWNT-10, (b) PE–MWNT-25 and (c) PE/CNF NHSK structures produced by crystallization of PE in *p*-xylene for 0.5 h at 103, 97, and 97°C. PE, MWNT, and CNF concentrations are 0.01, 0.002, and 0.002 wt%, respectively. (Reprinted with permission from ref. 72. Copyright 2006 American Chemical Society.)

Periodically functionalized CNTs is an attractive field of research, similar PE NHSK structures are achieved by combining the polymerization-filling technique with tandem copolymerization catalysis of ethylene in the presence of metallocene catalyst-treated MWNTs.^{75,76} Recently, Fu *et al.*^{77–79} reported that fine NHSK superstructures could be directly achieved in injection-molded bars of high-density PE (HDPE) or linear low-density PE (LLDPE)–MWNT composites prepared by a so-called dynamic packing injection molding (DPIM) technique. It is noted that the NHSK structures can confer significant mechanical reinforcement. The oriented HDPE–MWNT composites have their tensile strength increased by 150 and 270% and Young's modulus enhanced by 130 and 180%, with respect to the oriented pure HDPE and the isotropic composite at the same MWNTs loading (5 wt%), respectively. Both tensile strength and elongation-at-break of LLDPE are also improved by adding LLDPE-decorated MWNTs. These studies may open up a convenient gateway to achieve directly well-defined NHSK structures in simple injection-molding for reinforcement of polymer composites.

3.2.4 Supercritical CO₂ technology

Supercritical (SC) fluids have a promising future in materials synthesis and processing due to such excellent properties as near-zero surface tension, high diffusivity, low viscosity and ease of control, and hence they have been widely applied to prepare polymer-based materials.⁸⁰ Among the supercritical fluids, supercritical carbon dioxide (SC CO₂) is the most popular due to its non-flammability, non-toxicity, low cost and high compatibility with many organic solvents. Recently, the supercritical CO₂ technique has shown intriguing advantages in the synthesis of CNT-based composites with metal, metal oxide and polymer.⁸¹

In addition to polymer solution crystallization and DPIM methods as summarized in Section 3.2.3, SC-CO₂-induced polymer epitaxy on CNTs has been used to form the NHSK structures. Xu *et al.*^{82,83} employed a SC-CO₂ antisolvent-induced polymer epitaxy (SAIPE) method to aid PE epitaxy growth along CNTs form an NHSK structure under different experimental conditions. They found that the periodicity of PE lamellae, lateral size and kebabs' thickness of NHSK varied by the change of solvent, concentrations of PE and CNTs, and SC-CO₂ pressure. Functionalized SWNTs with PVA and PEG are well dispersed in aqueous solutions and have potential applications in biologically relevant systems.⁸³

Dai *et al.*⁸⁴ first dispersed MWNTs into an ethanol solution of 2,4-hexadiyne-1,6-diol (HDiD), and then introduced CO₂ up to a desired pressure, followed by heating the mixture up to 200 °C for polymerization of HDiD to give poly(HDiD)–MWNT composites. It is found that the solvent power of ethanol for HDiD is reduced due to the anti-solvent effect of CO₂, resulting in the adsorption of HDiD on the outer surface of CNTs. In contrast, the CO₂–ethanol mixture under the experimental conditions has near-zero surface tension and larger diffusivity, leading to the diffusion of HDiD molecules into the interior cavities of CNTs. Thus, it can be deduced that MWNTs were synchronously filled and coated by poly(HDiD) to form the multi-component composites which possess optical properties originated from poly(HDiD). Wang *et al.*⁸⁵ directly coated MWNTs with fluorinated graft poly(methyl vinyl ether-*alt*-maleic anhydride) in SC-CO₂ under 100–170 bar at 40 °C, resulting in the formation of quasi one-dimensional nano-structures with conducting cores and insulating surfaces with an average thickness of ~2 nm. Later, Yue *et al.*⁸⁶ prepared PMMA–SWNT composites in SC-CO₂ by copolymerizing methyl methacrylate (MMA) monomers with acrylated-modified SWNTs. It is shown that SC-CO₂ increases the diffusivity of monomer, and facilitates the growth of tethered PMMA chains near the entanglement area and interstitial space of the nanotube bundles, yielding partial debundling and disentanglement of SWNT bundles and improved dispersion in PMMA.

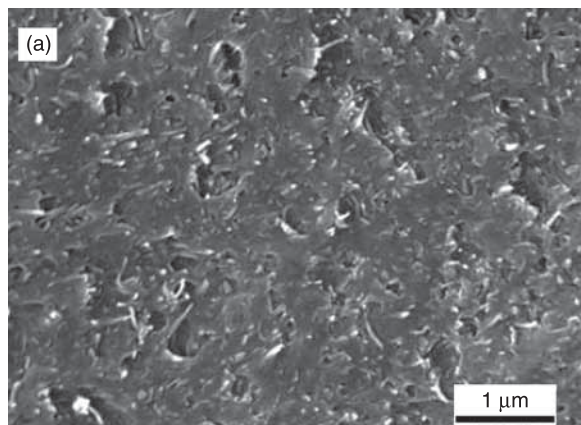
3.3 Covalent functionalization of carbon nanotubes with polymers

Covalent grafting of polymer chains to CNTs can be performed by either 'grafting-from' or 'grafting-to' strategies.^{87–89} The 'grafting-from' technique involves chemical attachment of functional groups to CNTs to form the CNT-supported macro-initiators, followed by surface-initiated polymerization of monomers to yield the tethered polymer chains. In general, initiators are linked to CNTs by employing the derivation reaction of CNT-bound carboxylic acid groups or direct addition of reagents to the surface of CNTs. By comparison, 'grafting-to' is concerned with immobilization of preformed functional polymers onto the surface of CNTs that are pristine, purified, oxidized or pre-functionalized.

3.3.1 Grafting-from methodology

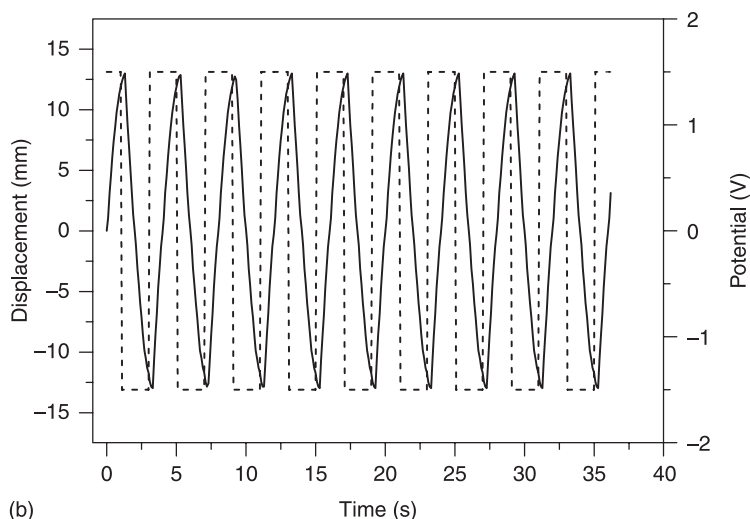
Conventional free radical polymerization

Xie *et al.*⁹⁰ attached allylamine functional molecules to MWNTs by acylation-amidation to generate allyl-modified MWNTs, followed by conventional free radical polymerization of styrene to yield PS-grafted MWNTs (MWNT-*g*-PS) with a hairy rod nanostructure. It is found that 1 of every 100 carbon atoms in MWNTs is grafted by PS, forming a uniform thin shell (ca. 8–10 nm) on the outer wall. MWNT-*g*-PS shows enhanced thermal stability and T_g as compared to pure PS, and MWNTs are uniformly dispersed in the polymer matrix. Also, they prepared water-soluble poly(sodium 4-styrenesulfonate-*co*-acrylic acid)-grafted MWNTs (MWNT-*g*-PSA) by an analogous method.⁹¹ The MWNT-*g*-PSA modified glassy carbon electrode was found to show strong electron transfer capability, high electrochemical activity and catalytic ability, which could be used in sensitive, selective, rapid and simultaneous monitoring of biomolecules. Further, MWNT-*g*-PSA incorporated into the mixed ionic membrane of PSA and PVA was used as an electromechanical actuator.⁹² As expected, MWNT-*g*-PSA is homogeneously dispersed in the PSA–PVA membrane (Fig. 3.3 (a)), thereby the electric conductivity increases by several orders of magnitude to 1.44×10^{-4} from 7.53×10^{-13} S/cm of the PSA–PVA membrane. MWNT-*g*-PSA strengthens the PSA–PVA membrane from 14.4 to 32.7 MPa with a loading up to 20 wt%, and it also enhances the fracture toughness by 34.8%. A steady relationship of time-dependent displacement under a repeated square wave input is clearly visible



3.3 (a) SEM image of cryo-fractured MWNT-*g*-PSA reinforced PSA–PVA membranes at 20 wt% loading. (b) Time-dependent displacement of composite actuator (20 wt% MWNT-*g*-PSA) under repeated stimulation at an applied square-wave electric potential of (\pm) 1.5 V with a frequency of 0.25 Hz. (Reprinted with permission from ref. 92. Copyright 2009 American Chemical Society.)

(Continued)



(b)

3.3 Continued.

(Fig. 3.3 (b)). A similar mechanism was employed by Shim *et al.*^{93,94} to prepare MWNT-g-PS in the presence of AIBN as a free radical initiator. Recently, a novel composite of MWNTs and molecularly imprinted polymers (MIPs) was also prepared by copolymerization of methacrylic acid and trimethylolpropane trimethacrylate in the presence of dopamine as a template molecule.⁹⁵ It is found that the vinyl groups modified on the surface of MWNTs are a key factor for forming the composite of MIPs and MWNTs. Besides, Li *et al.*⁹⁶ chemically attached α -alkene groups to SWNTs, and then copolymerized them with ethylene to produce SWNT-g-PE composites in the presence of a metallocene catalyst. The interaction between two components and dispersion of SWNTs in PE matrix are clearly improved, leading to expected results that the thermal stability and mechanical properties (tensile strength, modulus and elongation-at-break) of SWNT-g-PE are higher than those of PE and PE-SWNTs mixture with the same loading of SWNTs.

Controlled/living radical polymerization (CLRP)

Of all the CLRP techniques, atom transfer radical polymerization (ATRP) was first applied to synthesize polymer-grafted CNTs via a 'grafting-from' approach. The key is to introduce ATRP initiators onto the surface of CNTs. Yao *et al.*⁹⁷ initially functionalized SWNTs by 1,3-dipolar cycloaddition reaction for attaching phenols, which further reacted with 2-bromoisobutyryl bromide to achieve the SWNT-supported ATRP initiators. These initiators were active in polymerization of methyl methacrylate and *tert*-butyl acrylate from the surface of SWNTs. Later,

Baskaran *et al.*,⁹⁸ Kong *et al.*⁹⁹ and Qin *et al.*¹⁰⁰ simultaneously and independently reported their results on polymer-grafted CNTs using ATRP, in which either SWNTs or MWNTs were functionalized by ATRP initiators via subsequent acylation-esterification prior to polymer grafting. Homo, block, and copolymer brushes were chemically linked to CNTs at levels up to 90 wt% from the TGA results. The average thickness (or the amount) of polymer grafted onto CNTs varies with the feed ratio of monomer to the CNT-supported macro-initiators and reaction time. Therefore, the ATRP process from the surface of CNTs is still living. As is well known, dispersion of CNTs into solvents before functionalization is difficult even after ultrasonication; however, polymer-grafted CNTs are soluble in given solvents which are compatible with the parent polymers. Moreover, all functionalized-CNTs show enhanced T_g and T_d (decomposition temperature) compared to pure polymers due to the high thermal conductivity of CNTs and the constraint effect of grafted polymer chains. Wang *et al.*¹⁰¹ used ATRP to synthesize MWNT-*g*-PMMA including 10 wt% MWNTs, and then blended with poly(styrene-*co*-acrylonitrile) (SAN) by solution processing. Upon addition of MWNT-*g*-PMMA with an effective MWNT loading of 1 wt%, the storage modulus at 40 °C, Young's modulus, tensile strength, ultimate strain, and toughness of SAN-MWNT-*g*-PMMA composites are increased by up to 90, 51, 99, 184 and 614%, respectively, compared to pristine SAN. Such simultaneous improvements of a polymer using rigid fillers are rarely observed. These results are due to the uniform dispersion of CNTs and strong CNT-matrix interaction since PMMA is miscible with SAN. Shi *et al.*¹⁰² reported ATRP of *n*-butyl methacrylate (BMA) from MWNTs to produce MWNT-*g*-PBMA, in which the relative amount of PBMA was determined by TGA to be ~16 wt%. Incorporating MWNT-*g*-PBMA (0.2 wt% MWNTs) in a PVC matrix leads to increases in storage modulus (at 35 °C), Young's modulus, yield stress, tensile strength, ultimate strain and toughness by 83, 40, 74, 84, 38 and 145%, respectively, compared to PVC. The miscibility between PVC and grafted-PBMA enables the homogeneous dispersion of MWNTs, and also improves the efficiency of load transfer from matrix to nanotubes, as a result of the enhanced mechanical performance.

Polymer chains can grow from the dithioester-modified CNTs in a controlled process by a reversible addition-fragmentation chain transfer (RAFT) mechanism. Similar to ATRP, RAFT agents are anchored onto the surface of CNTs by derivation reaction of the CNT-bound carboxylic groups before surface-initiation polymerization of monomer. Using this method, various polymers such as PS,^{103,104} PMMA,¹⁰⁵ water-soluble poly(*N*-(2-hydroxypropyl)-methacrylamide)¹⁰⁶ and poly(2-hydroxyethyl methacrylate) (PHEMA)¹⁰⁷ and poly(acryl amide) (PAM),¹⁰⁸ thermoresponsive poly(*N*-isopropylacrylamide) (PNIPAM)^{109,110} and their block polymers have been successfully attached to the surface of CNTs, resulting in the formation of core-shell nanostructures, with polymer as the brush-like or hairy shell, and CNTs as the hard backbone. The shell thickness or content of grafted polymers on CNTs can be well controlled by changing the reaction parameters of RAFT polymerization. The

covalent bonding of polymers to CNTs dramatically improves the solubility and stability of MWNTs in solvents. It is noted that the PNIPAM shell of MWNT-g-PNIPAM shows reversible response to temperature as a result of switching between hydrophilicity and hydrophobicity, which should have potential applications in smart sensors and probes.¹⁰⁹ Moreover, using a suitable content of MWNT-g-PS as lubricant additives can effectively improve the anti-wear property of the base lubricant, because the long PS chains prevent MWNTs from flocculating in the base lubricant due to their improved dispersibility.¹⁰⁴

In addition to ATRP and RAFT, another important CLRP technique of nitroxide-mediated polymerization (NMP) has been applied to functionalize CNTs with various polymers. Zhao *et al.*¹¹¹ prepared poly(4-vinylpyridine)-grafted MWNTs (MWNT-g-P4VP) and poly(sodium 4-styrenesulfonate)-grafted MWNTs (MWNT-g-PSS) by surface-mediated NMP of monomers from the surface of MWNTs that were initially functionalized by TEMPO (2,2,6,6-tetramethylpiperidiny-1-oxyl) functional groups. It is found that MWNT-g-P4VP shows good solubility in acidic aqueous solutions, but tends to aggregate in neutral or basic solutions, due to the presence of basic pyridine units. By comparison, MWNT-g-PSS is stable in aqueous solutions throughout the pH range 1 to 14. They also prepared MWNT-g-(PS-*b*-P4VP) by further polymerization of MWNT-g-PS with 4-vinylpyridine.¹¹² Changing the grafted polymer shell from PS to PS-*b*-P4VP results in an obvious change of solubility. In the work of Dehonor *et al.*,¹¹³ PS brushes bonded covalently to N-doped MWNTs were also synthesized by a ‘grafting-from’ route using NMP. Datsyuk *et al.*¹¹⁴ developed a two-step route to prepare block polymers grafted double-walled carbon nanotubes (DWNTs) without chemical pre-treatment. PAA or PS short chains were first polymerized in the presence of NMP initiators to form stable nitroxide radicals around DWNTs, and then these active sites reinitiated polymerization of methyl acrylate (MA) to yield amphiphilic DWNT-g-(PAA-*b*-PMA) and DWNT-g-(PS-*b*-PMA), respectively. These grafted block copolymers promote the dispersion of CNTs and improve their surface bonding with various polymer matrices.

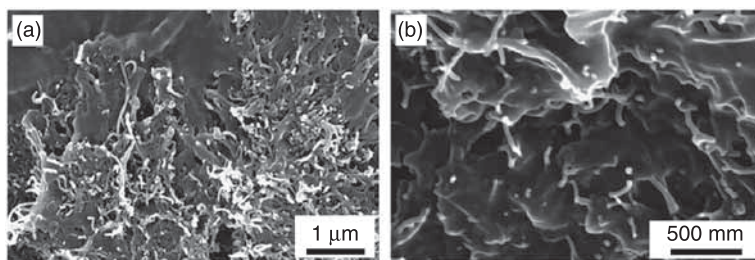
As reported above, surface-mediated CLRP techniques not only control the amount and thickness of versatile grafted-polymers on CNTs, but also produce block copolymers with multifunctional components. Such functionalized-CNTs with tailor-made structures and properties are important for improving the dispersibility, compatibility and miscibility of CNTs in polymer matrices and their interface bonding to enhance the effectiveness of load transfer from the matrix to CNTs. Moreover, these cases may open up a path to fabricating novel CNT-based devices and sensors.

Ring-opening polymerization (ROP)

Hydroxyl-functionalized CNTs have been widely used as initiating species for ROP of ϵ -caprolactone^{115–117} and L-lactide^{118–120} monomers to achieve biodegradable

polymers grafted CNTs and even hyperbranched polymers grafted CNTs.¹²¹ The amount of grafted polymers can be controlled by adjusting the feed ratio of monomer to the CNT-supported macro-initiators.^{115,119,121} The grafted poly(ϵ -caprolactone) (PCL) retains the biodegradability of conventional PCL that can be enzymatically biodegraded, and CNTs retain their tubelike morphologies.¹¹⁵ By adding 1 wt% MWNT-g-PLLA (effective MWNTs: ~ 0.7 wt%), the tensile modulus of PLLA increases from 2,463 to 4,710 MPa, and the strength from 56.4 to 85.6 MPa, resulting in 91 and 52% improvements, respectively.¹¹⁸ The Flory-Huggins interaction parameter (B) is estimated to be $96.6 \text{ cal}\cdot\text{cm}^{-3}$ for PLLA-MWNT-g-PLLA composite, which suggests that MWNTs are highly compatible with PLLA after functionalization.¹¹⁸ Further, the activation energy of PLLA-MWNT-g-PLLA is higher than that of PLLA-MWNT composites, leading to the higher thermal stability for the former.¹¹⁹ Also, all mechanical properties of PLLA-MWNT-g-PLLA composites are superior to those of PLLA-MWNT composites because of the better dispersion of MWNT-g-PLLA in the PLLA matrix in conjunction with stronger interface adhesion and higher miscibility between MWNT-g-PLLA and PLLA compared to MWNTs and PLLA.^{118,119} Figure 3.4 compares SEM images of PLLA-MWNT-g-PLLA and PLLA-MWNT composites containing similar loading (2 wt%) of MWNTs. Most MWNTs aggregate in PLLA-MWNT composites (Fig. 3.4 (a)); however, after functionalization, MWNTs are uniformly embedded in PLLA matrix for PLLA-MWNT-g-PLLA (Fig. 3.4 (b)). These results indicate the potential application of biocompatible polymers functionalized CNTs in bio-nanomaterials, biomedicine, artificial organs and bones.^{115–120}

Covalent functionalization of CNTs with polyamide 6 (PA 6) was accomplished by anionic ROP of ϵ -caprolactam in the presence of ϵ -caprolactam grafted CNTs as initiators and sodium ϵ -caprolactamates as catalysts.^{122,123} It is found that the CNT-initiated anionic ROP shows high efficiency under low reaction temperature (170°C) and short reaction time (6 h), with the final products having a limited amount of grafted-PA 6 (65 wt%). The functionalized nanotubes are soluble in formic acid and *m*-cresol, which may prove to be new avenues for homogeneous dispersion of CNTs in PA 6 to form high-quality nanocomposite materials.



3.4 SEM images of (a) PLLA-MWNT and (b) PLLA-MWNT-g-PLLA composites at the same MWNT loading of 2 wt%. (Reprinted with permission from ref. 119. Copyright 2007 Elsevier.)

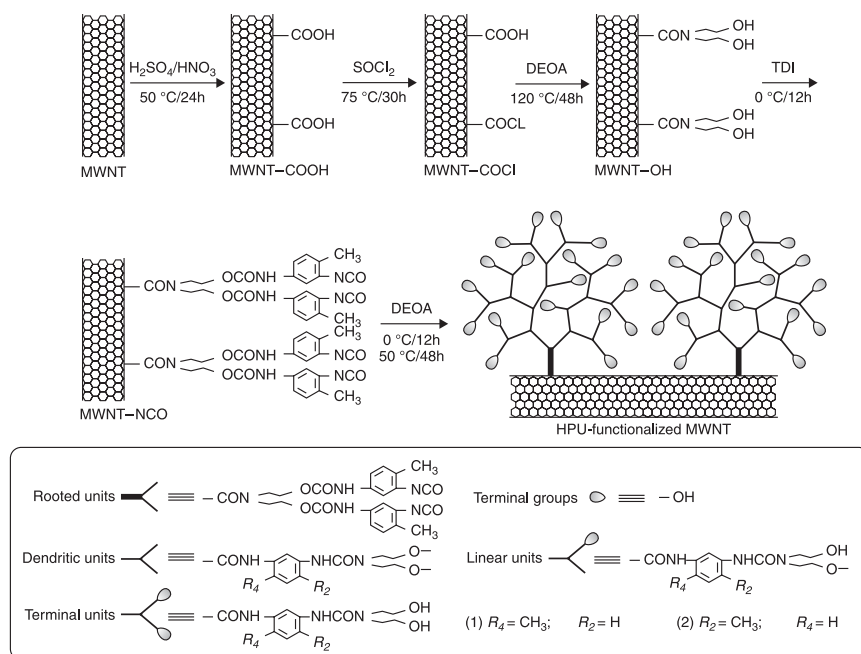
Epoxy resin as an important thermosetting material has also been applied to fabricate high-performance nanocomposites with CNTs. Zhu *et al.*¹²⁴ pretreated SWNTs through acid oxidation and subsequent fluorination to generate carboxyl and fluorine groups on the surface of SWNTs. Epoxy composites containing 1 wt% SWNTs were then processed by dispersing the functionalized nanotubes in dimethyl formamide (DMF) and mixing with epoxy monomer and diamine hardener. SWNTs are observed to be highly dispersed and well embedded in epoxy composites due to the formation of strong covalent bonds with the defect sites of SWNTs, where epoxy ring-opening esterification with carboxyl and amine curing reaction with fluorine groups proceed. Hence, epoxy–SWNT composites with respect to neat epoxy show a 30% increase in modulus and an 18% increase in tensile strength, respectively. Bae *et al.*¹²⁵ and Bekyarova *et al.*¹²⁶ also found that surface treatment of CNTs with acid oxidation promotes homogeneous dispersion of CNTs in epoxy resin and provides strong interaction with matrices through chemical bonding of ring-opening esterification, and thus enhances the overall mechanical properties. Tseng *et al.*¹²⁷ prepared covalent-integrated epoxy composites using plasma-treated CNTs. Integration of CNTs into a thermosetting epoxy matrix was also achieved by coupling nanotubes with silanes containing epoxy groups and then observing the subsequent reaction with the epoxy monomer and diamine hardener.¹²⁸ It is found that modifying the CNT surface with siloxanes significantly improves the dispersion of CNTs in epoxy matrix and enhances their interfacial adhesion due to covalent linkage CNTs with epoxy through ring-opening. As a result, composites containing siloxane-CNTs yield better thermal stability, higher flexural modulus and improved strength and fracture resistance than those containing untreated CNTs.

A fully integrated SWNT–epoxy composite was also prepared via chemically attaching amino groups to SWNTs followed by reacting with epoxy resin and curing agent.¹²⁹ In the SWNT-reinforced epoxy polymer composites, SWNTs are covalently integrated into the epoxy matrix through ring-opening reaction of epoxy groups during epoxy curing, and hence become part of the cross-linked structures rather than separate components. The resulting composites thus show dramatic improvement in their mechanical properties better than those of pure epoxy resin. Young's modulus increases from 2,026 to 2,650 MPa at just 1 wt% functionalized SWNTs, giving more than 30% improvement. At the same loading, the tensile strength is 25% higher than neat epoxy when compared to untreated SWNT–epoxies. A recent result reported by Liu *et al.*¹³⁰ also confirms that epoxy composites containing covalently modified MWNTs possess greater storage modulus relative to the noncovalent system.

Condensation polymerization

Different to the chain reaction mechanism of conventional or living radical polymerization, condensation polymerization belongs in general to the

step-growth reaction. This technique has been mainly used to prepare polyesters, polyamides and polyurethanes functionalized CNTs so far. Xie *et al.*^{131,132} developed an *in-situ* polycondensation method to functionalize MWNTs with hyperbranched poly(urea-urethane) (HPU) and linear photoresponsive polyurethane with azo pendant groups. As shown in Fig. 3.5, MWNTs were pretreated with acyl chloride followed by reacting with diethanolamine to form multiple hydroxyl groups, which were further used as active species for reacting diisocyanates with diethanolamine or diols containing azo-benzene, resulting in the formation of grafted hyperbranched polymers or linear polymers from the surface of MWNTs. The amount or thickness of the polymer shell is adjustable by changing the feed ratio of monomers to MWNTs. It is noted that the modified MWNTs containing azobenzene show reversible photoisomerism behavior in solutions; and the responsive rate constant can be effectively controlled by adjusting the main-chain flexibility of grafted polyurethanes.¹³³ This may play a crucial role in developing novel high-performance optic and photonic nano-devices. A similar methodology was used to attach polyurea, polyurethane^{134,135} and polycaprolactone polyurethane¹³⁶ onto CNTs terminated with hydroxyl or amino groups. As a result, SWNT-g-PU improves the dispersion of SWNTs in



3.5 Schematic representation of synthesizing hyperbranched poly(urea-urethane)s-grafted MWNTs by surface-mediated *in-situ* polycondensation. (Reprinted with permission from ref 132. Copyright 2007 American Chemical Society.)

PU matrix and strengthens the interfacial interaction between the matrix and SWNTs. Consequently, SWNT-g-PU has a remarkable reinforcing effect over pristine SWNTs. Also, incorporating SWNT-g-PU into the PU matrix improves the phase separation and the degree of crystallization of PCL soft segment.¹³⁶

Recently, Zhou *et al.*¹³⁷ first reacted oligo-hydroxyamide (oHA) with acyl chloride modified MWNTs to obtain oligo-hydroxyamide (oHA)-grafted MWNTs (MWNT-oHA), which has a remarkable solubility in polar solvents and a good thermal stability. MWNT-oHA was then covalently incorporated with poly(*p*-phenylene benzobisoxazole) (PBO) via *in-situ* condensation reaction. Using a dry-jet wet-spinning technique, continuous MWNT-PBO composite fibers were finally fabricated with different MWNT loadings. As expected, MWNT-PBO fibers relative to pure PBO fibers show overall increases in tensile modulus and strength, thermal stability and electrical conductivity, due to their excellent dispersion and high alignment of MWNTs in PBO matrix and their enhanced interfacial interaction. Baek *et al.*^{138–140} have developed a direct Friedel-Crafts acylation for functionalization of CNTs and carbon nanofibers (CNF) in a polyphosphoric acid (PPA)–phosphorous pentoxide (P₂O₅) medium. Various benzoic acid monomers have been selected to prepare linear or hyperbranched poly(ether-ketone)s (PEKs) grafted MWNTs (MWNT-g-PEK). This method shows a strong driving force to build extremely high-molecular weight PEKs directly from the carboxylic groups instead of the expensive and corrosive acid chloride groups. Accordingly, the proposed strategy could be an ideal chemical functionalization method for CNTs for the fabrication of polymer nanocomposites.

Other polymerization methods

As shown in the above sections, strong interfacial bonding and homogeneous dispersion are critical to take full advantage of the excellent properties of CNTs for the reinforcement of polymer matrices. Hence, researchers attempt at all times to find versatile suitable approaches to functionalize CNTs. Liu *et al.*¹⁴¹ prepared a styrenic polymer composite containing well-dispersed MWNTs by anionic polymerization of a nanotube-bound *p*-methylstyrene. Initially, MWNTs were first modified by ligand-exchange reaction of ferrocene, and then monolithiated by *tert*butyl-lithium and followed by termination with *p*-chloromethylstyrene (*p*MS). The *p*MS-terminated species on MWNTs were finally functionalized with living polystyryl-lithium anions via anionic polymerization, forming MWNT-g-PS that is soluble in common organic solvents. Based on the anionic mechanism, PS¹⁴² and PMMA¹⁴³ were also chemically grown from the surface of SWNTs.

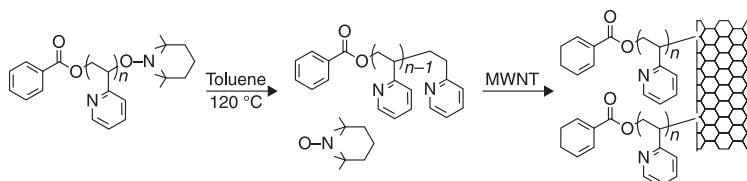
Zhang *et al.*¹⁴⁴ developed an electrografting method for functionalization of CNTs. In their work, SWNTs and *N*-succinimidyl acrylate (NSA) were pre-dispersed in room-temperature ionic liquids (RTILs) by a combination of grinding and mixing, yielding a black gel for use as the RTIL-supported 3D SWNTs electrode. Once an electrochemical reaction occurred, poly(*N*-succin-imidyl

acrylate)s were *in-situ* grafted onto SWNTs. Therefore, large quantities of SWNTs were considerably untangled in RTILs so as to greatly increase the effective area of the electrode. It is thought that the application of the RTIL-supported CNTs electrode can realize the homogeneous electrochemical functionalization of SWNTs in large quantities. Tasis *et al.*¹⁴⁵ reported a ceric ion-induced redox radical polymerization technique for the preparation of water-soluble polyacrylamide grafted CNTs. In this work, carbinol groups, thermally generated from organic peroxides and methanol, were covalently attached to CNTs. Then, these carbinol groups provided initiating sites for surface-mediated polymerization of acrylamide. Recently, Priftis *et al.*¹⁴⁶ functionalized CNTs with PLLA and PCL by a two-step process, whereby CNTs were first modified with titanium alkoxide catalysts through a Diels-Alder cycloaddition, followed by surface initiated titanium-mediated coordination polymerizations of L-lactide and ϵ -caprolactone monomers.

3.3.2 Grafting-to methodology

Macromolecular radical coupling

Ni and Sinnott¹⁴⁷ used classical molecular dynamics simulations to predict a pathway to the chemical functionalization of CNTs by coupling either radicals or their fragments to the nanotube walls. Recently, density functional theory calculations were also used by Galano to model the potential ability of CNTs to act as free-radical scavengers.¹⁴⁸ Experimentally, Lou *et al.*¹⁴⁹ demonstrated the coupling reaction of sp^2 -hybridized carbons of CNTs with TEMPO-end-capped poly(2-vinylpyridine) (P2VP) that was pre-synthesized by a nitroxide-mediated polymerization (NMP) method. Figure 3.6 shows the direct covalent attachment of macro-molecular radicals, released by thermolysis of P2VP chains terminated with TEMPO radical-stabilizing group, to the surface of pristine MWNTs. The resultant MWNT-g-P2VP is easily dispersible in organic solvents and acidic water in contrast to neat MWNTs. P2VP chains form a shell around CNTs and their grafting ratio can be adjusted to some extent in the range of 6~12%. The same



3.6 Heating of TEMPO-end-capped P2VP chains causes TEMPO groups to dissociate, resulting in the formation of MWNT-g-P2VP by macromolecular radical coupling. (Reproduced with permission from ref. 149. Copyright 2004 Wiley-VCH Verlag GmbH & Co. KGaA.)

approach was used for the grafting of PS, PCL, and PCL-*b*-PS copolymer onto MWNTs as a result of the addition reaction of the parent polymeric radicals.¹⁵⁰ It is found that the grafting density of polymers (12~30%) can easily be controlled by tailoring the molecular weight of polymers prior to functionalization. NMP techniques have been used to synthesize a variety of polymers,¹⁵¹ thus, all these polymers should be grafted onto CNTs by a radical addition mechanism.

Wu *et al.*¹⁵² found that bromine-terminated PS synthesized by ATRP was also directly reacted with MWNTs under ATRP conditions using CuBr/2,2'-bi-pyridine as catalysts, yielding MWNT-*g*-PS by a macromolecular radical coupling mechanism. Grafting PMMA onto MWNTs was performed by emulsion polymerization of MMA monomers in the presence of nanotubes in micelles.¹⁵³ Incorporation of MWNT-*g*-PMMA (39 wt% PMMA) into commercial PMMA leads to an improved nanotube-matrix bonding and uniform nanotube dispersion in the matrix. The applied tensile load on the PMMA–MWNT-*g*-PMMA composites is effectively transferred to MWNT-*g*-PMMA. The storage modulus at 20 °C is greatly enhanced by 1,100% from ~2.5 GPa for pure PMMA to ~31 GPa for the PMMA composites containing 20 wt% MWNT-*g*-PMMA.

McIntosh *et al.*¹⁵⁴ prepared PP–SWNT composites by melt compounding with and without benzoyl peroxide (BPO) initiators. During the high shear and high temperature phase of processing, free radicals upon decomposition of BPO can initiate PP chains to generate polymer radicals, which further allow covalent linkage with SWNTs. The resulting fibers made from PP–SWNTs show improved interfacial bonding and some alignment with BPO present serving as a free radical initiator. Accordingly, their mechanical properties increase by 82.9, 89.8, 72.3, and 173.1% in tensile strength, and by 69.2, 99.7, 137.2, and 133.7% in elastic modulus, respectively, corresponding to SWNTs loadings of 2.5, 5, 7.5, and 10 wt%. These mechanical properties are highly superior to those of pure PP fibers and PP–SWNT fibers without BPO under comparable SWNTs loading. It is suggested that free radicals scavenge protons from the PP matrix, providing active sites for direct covalent bonding of SWNTs and their ropes. In contrast to conventional matrix and reinforcing filler type of composite, such functionalized composites could be viewed as a material consisting of macromolecules, which are supported by a strong interface between SWNTs and surrounding matrix via covalent linkage. This type of fully integrated composites with CNTs will result in more efficient load transfer and provide better mechanical reinforcement.

Cycloaddition of polymers to CNTs

Cycloaddition of azides by thermolysis to strained-double-bonds of fullerenes has been widely used in solution to synthesize polymeric fullerenes.¹⁵⁵ Since CNTs contain a similar double bond in their backbone, the same principle should be applicable for functionalization of CNTs. In recent years, nitrene cycloaddition of azides has been effectively employed to functionalize CNTs by thermolysis in

solution¹⁵⁶ and photolysis under UV irradiation.¹⁵⁷ Qin *et al.*¹⁵⁸ reported the grafting of PS chains to SWNTs by a two-step process, where PS-Br obtained by ATRP was converted to PS-N₃ with sodium azide in DMF, followed by performing cycloaddition of PS-N₃ to SWNTs in 1,2-dichlorobenzene (DCB) at 130 °C in a nitrogen atmosphere for 60 h. The resultant SWNT-g-PS contains 85 wt% PS and 15 wt% SWNTs, corresponding to 1 PS chain per 48 SWNT carbons. SWNT-g-PS can be diffused into individual SWNT and very small bundles in solvents. Li *et al.*¹⁵⁹ employed disubstituted polyacetylenes that were terminated by halogen atoms at the ends of their alkyl pendants to react with sodium azide so as to yield azido-functionalized polymers. Polyacetylene chains were then attached to the SWNT side-walls in high-boiling-point solvent of DCB by a cycloaddition reaction of azido groups with the strained double bonds. The resultant SWNT-g-polyacetylenes can be soluble in common solvents, emit intense visible lights and strongly attenuate the power of harsh laser pulses.

In contrast to the direct attachment of azido-functionalized polymers to CNTs, covalent functionalization of alkyne-decorated SWNTs with well-defined, azido-end-capped PS chains was accomplished by the Cu(I)-catalyzed [3+2] Huisgen cycloaddition,¹⁶⁰ in which alkyne-decorated SWNTs were obtained by the reaction of pristine SWNTs with *p*-aminophenyl propargyl ether using a solvent-free diazotization and coupling procedure. This type of Huisgen cyclo-addition was highly efficient to prepare soluble polymer-nanotube conjugates, even at relatively low temperatures (60 °C) and short reaction times (24 hours). The final SWNT-g-PS has a grafting density of 1 PS chain per 200~700 SWNT carbons, corresponding to roughly 45 wt% PS within them by TGA measurement. These materials exhibit high dispersibility, stability and solubility in organic solvents of polymers.

Acylation-esterification/amidation of CNT-bound carboxyl groups

It is well known that various functional groups, such as carboxyl, hydroxyl, ketone and ester groups, are frequently formed on the surface of CNTs during oxidation treatment by strong acids for the purpose of purification, cutting and functionalization. Among them, CNT-bound carboxyl groups have attracted more attention due to their relatively higher reactivity and intrinsic multifunctionality towards chemical reactions. Chen *et al.*¹⁶¹ prepared soluble CNTs for the first time by an acylation-amidation process, where SWNT-bound carboxyl groups were treated with acyl chloride followed by reacting with octadecylamine (ODA) to achieve SWNT-g-ODA. Poly(*m*-aminobenzene sulfonic acid) (PABS)-grafted SWNTs (SWNT-g-PABS) was obtained by the same research team using a combination of acylation and amidation of acid-oxidized SWNTs.^{162–164} SWNT-g-PABS containing 17 wt% nanotubes is quite soluble in water and gives several orders of magnitude increase in electrical conductivity over pure PABS.¹⁶² Compared to the purified SWNTs, devices fabricated with SWNT-g-PABS show

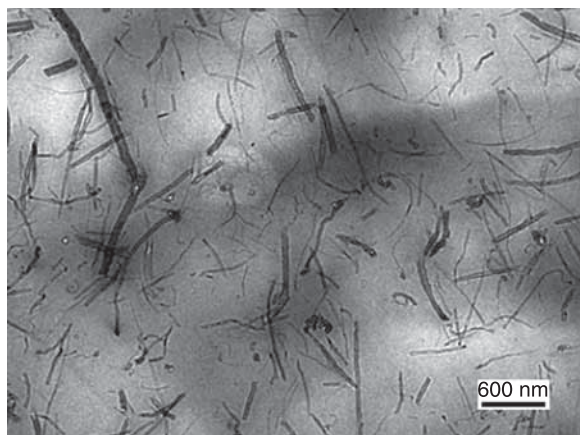
more than twice the higher resistance change upon exposure to NH_3 due to the improved sensor performance.¹⁶³ Further, SWNT-*g*-PABS is used as a supporting scaffold for the growth of artificial bone material. It is found that hydroxyapatite (HA) can nucleate and crystallize on the surface of SWNT-*g*-PABS, and its film can be mineralized resulting in the well-aligned plate-shaped HA crystals.¹⁶⁴ Recently, Zhang *et al.*¹⁶⁵ prepared interlinked MWNTs with polyamines via reaction of the acyl-activated MWNTs with amino-functionalized alternating polyketones. The amount of polymer bonded to MWNT is estimated to be ~40 wt% by TGA analysis. Though cross-linked MWNTs are insoluble in any solvent, they can be melt-blended into low-density polyethylene (LDPE). However, the final LDPE composites containing functionalized-MWNTs show comparable mechanical properties to those obtained by simple blending of ‘uncross-linked’ nanotubes with LDPE. Thus, the enhancement of mechanical properties of LDPE matrix is not realized, probably due to the poor dispersion of cross-linked fillers when using melt blending. In the recent work of Ma *et al.*,¹⁶⁶ flame-retardant poly(diaminodiphenyl methane spirocyclic pentaerythritol bisphosphonate) (PDSPB) was grafted onto the surface of acyl-activated MWNTs to obtain MWNT-*g*-PDSPB, and then integrated into ABS resin via melt blending to produce ABS–MWNT-*g*-PDSPB nanocomposites. MWNT-*g*-PDSPB (65 wt% grafting) was soluble and stable in polar solvents. MWNT-*g*-PDSPB can form structural networks at very low loading (0.2 wt%), lower than unmodified-MWNTs (1.0 wt%) as indicated by their linear viscoelastic behavior; better flame retardance is also observed for ABS–MWNT-*g*-PDSPB composites. These findings are due to better dispersion of MWNT-*g*-PDSPB relative to unmodified-MWNTs in ABS matrix.

Similarly, oxidized-CNTs can react with hydroxyl-terminated polymers via an acylation-esterification process. Here, carboxyl groups attached to CNTs are converted to acyl chlorides by treatment with thionyl chloride. The acyl-activated CNTs are then susceptible to reaction with the hydroxyl groups of polymers to produce polymer-grafted CNTs via ester linkages. By using this process, PEG has been used to prepare water-soluble SWNTs.¹⁶⁷ Sun *et al.*¹⁶⁸ and Tao *et al.*¹⁶⁹ reported the functionalization of CNTs with various lipophilic and hydrophilic dendrons under the same reaction conditions. The experimental results suggest that there are no significant differences between amidation and esterification reactions regardless of SWNTs or MWNTs.¹⁶⁸ In the work of Hill and co-workers,¹⁷⁰ poly(styrene-*co-p*-(4-(4'-vinylphenyl)-3-oxabutanol)) (PSV) with medium molecular weight ($M_w=5,500$ g/mol) was used to functionalize SWNTs and MWNTs by this acylation-esterification process. The resulting PSV-functionalized CNTs are soluble in common solvents, and are further applied to fabricate PS–CNT composite films by means of a wet-casting method. The homogeneous dispersion of PSV-functionalized CNTs in a PS matrix promises that CNTs solubilization will enable the preparation of desirable polymeric composites.

Condensation between oxidized CNTs and polymers

Unlike the two-step process of esterification or amidation towards acyl-activated-CNTs, carboxylic acid-functionalized CNTs after oxidation can directly react with amino- and/or hydroxyl-terminated polymers by one-step condensation to produce polymer-grafted CNTs via covalent amide or ester linkages. Sun *et al.* grafted poly(propionylethylenimine-co-ethylenimine) (PPEI-EI)¹⁷¹ and PEG¹⁷² onto oxidized-SWNTs by [1-ethyl-3-(dimethylamino) propyl] carbodiimide hydrochloride (EDC) activated condensation in an aqueous KH_2PO_4 buffer solution. The nanotube-bound carboxylic acids were also targeted for esterification reactions with pendant hydroxyl groups in the derivatized polyimide using *N,N'*-dicyclohexylcarbodiimide (DCC) activated condensation in organic solvent.¹⁷³ Resonance Raman measurements indicate good dispersion of the functionalized samples as reflected by the overwhelming luminescence interference since such interference cannot be found in a simple polymer-nanotube mixture. The same approach was applied to graft PVA to SWNTs and MWNTs in the presence of DCC in highly polar dimethyl sulphoxide (DMSO).¹⁷⁴ The resultant PVA-grafted nanotubes are soluble in highly polar solvents such as DMSO and water, thereby allow the intimate mixing of nanotubes with polymer matrix by wet-casting. The PVA composite films containg PVA-grafted nanotubes are of high optical quality without any observable phase separation. CNTs within the films are as well dispersed as in solution (Fig. 3.7), indicating that functionalization of CNTs by the matrix polymer is effective in the homogeneous dispersion of nanotube to fabricate high-quality nano-composites.

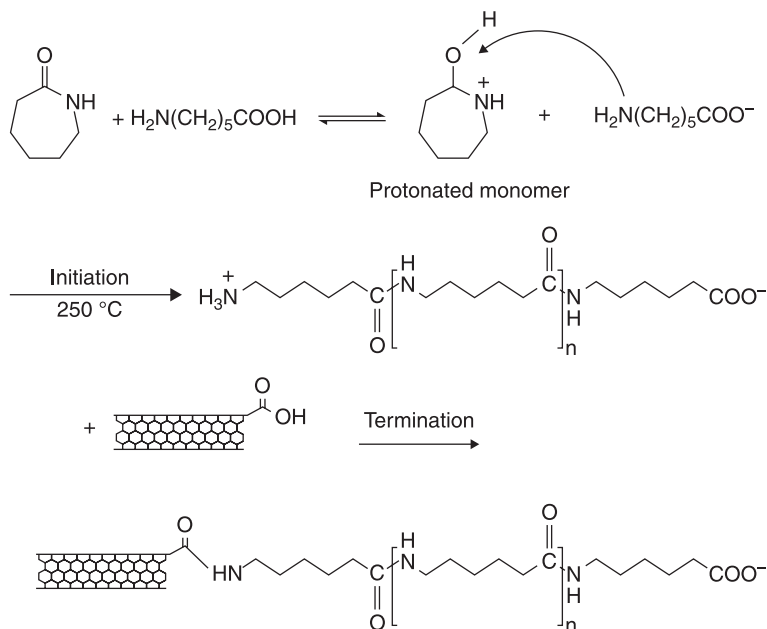
In addition to the functionalization of CNTs by carbodiimide-activated condensation, some investigators have found that the surface carboxyl groups of



3.7 TEM image of PVA-MWNT-*g*-PVA films from cross-sectional microtome. (Reprinted with permission from ref. 174. Copyright 2003 American Chemical Society.)

oxidized CNTs can react directly with polymers containing amino- and/or hydroxyl groups through thermally induced condensation at high temperature in a one-step process. In the work of Ge *et al.*,¹⁷⁵ the carboxylic acid-functionalized MWNTs (MWNT-COOH) were initially dispersed in a solution of aromatic polyetherimide with the aid of sonication, followed by removing the solvents from suspension. Finally, interfacial grafting reaction occurred in between MWNTs and the terminal amino groups of polyetherimide at 150–160 °C for 96 h under N₂ protection without any catalysts or force fields. The tensile strength and modulus of pure polyetherimide film were ~121 MPa and ~2.9 GPa with an elongation-at-break of 16%. However, the tensile strength and modulus of polyetherimide composite films grafted with 0.14, 25, 38 wt% MWNT-COOH increased to ~131, 186, 194 MPa and ~3.7, 4.1, 4.4 GPa, respectively, with corresponding elongations-at-break of 10, 8 and 7%. It is suggested that the covalent interfaces between nanotubes and polyetherimide chains play an important role in improving the mechanical performance.

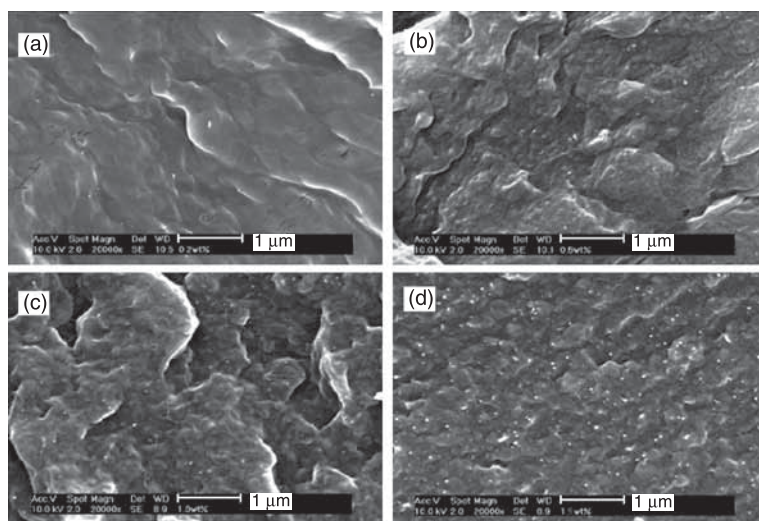
Gao *et al.*^{176,177} reported a way to fabricate PA6-SWNT composites by ring-opening polymerization of caprolactam monomers using 6-aminocaproic acid as an initiator in the presence of oxidized SWNTs (SWNT-COOH). As shown in Fig. 3.8, PA6 chains can be chemically linked to SWNTs through condensation



3.8 Synthesis of PA6-SWNT composites by ring-opening polymerization of caprolactam using 6-aminocaproic acid as an initiator in the presence of oxidized SWNTs. (Reprinted with permission from ref. 176. Copyright 2005 American Chemical Society.)

reactions between carboxyl groups around SWNTs and the terminal amino groups of PA6 at 250 °C, where caprolactam also acts as an excellent dispersant for SWNT-COOH. Continuous fibers are then drawn from PA6–SWNT composites using a custom-made spinneret assembly. SWNTs are uniformly diffused into PA6 matrix with different SWNTs loading (Fig. 3.9), and show improved mechanical properties for PA6 nanocomposites. As compared with pure PA6, incorporating 1.5 wt% oxidized-SWNTs (3~4% carboxyl groups) into PA6 matrix results in increases from 40.9 MPa to 75.1 MPa in tensile strength, from 440 MPa to 1,200 MPa in Young's modulus, corresponding to enhancements of 2.7 and 1.9 times, respectively.¹⁷⁶

The mechanical properties of PA6–SWNT composite fibers are highly dependent on the density of the carboxylic acid functional groups attached to SWNTs.¹⁷⁷ At similar SWNT loading (0.5 wt%), the composite fibers fabricated using SWNTs with 0, 4.2, 6.0 and 6.8% carboxyl groups show tensile strengths of 69.1, 83.4, 88.6, and 98.5 MPa, respectively, which are clearly stronger than the pure PA6 fiber (40.9 MPa). It can be concluded that the tensile strength of PA6–SWNT fibers increases with the coverage density of carboxyl groups attached to SWNTs. The same tendency for Young's modulus increase is also observed for the composite fibers concerning the concentration of carboxylic acid groups. For example, PA6–SWNT fiber prepared with SWNTs containing 6.8% carboxyl groups shows a Young's modulus of 1,500 MPa, an increase of ~2.6



3.9 SEM cross-sectional fracture images of PA6–SWNT composite fibers prepared with SWNT loading of (a) 0.2; (b) 0.5; (c) 1.0 and (d) 1.5 wt%. The oxidized-SWNTs contain 3–4% carboxylic-acid sites, and the bright regions in these images are attributed to SWNTs as a result of high conductivity. (Reprinted with permission from ref. 176. Copyright 2005 American Chemical Society).

times in comparison with that of the composite fiber from unmodified SWNTs (575 MPa). However, the break strain of the composite fibers is nearly independent of the amount of the carboxyl groups and lower than that of pure PA6 fiber. Moreover, it is found that replacement of SWNT–COOH by SWNT–CONH₂ in the PA6–SWNT fibers entices grafting longer PA chains to SWNTs as a result of changes in condensation reaction, thereby resulting in different composite morphology and mechanical performance.¹⁷⁷ At the same nanotube loading (0.5 wt%), PA6–SWNT fiber containing SWNT–CONH₂ has a higher tensile strength and break strain, but a lower Young's modulus relative to the fiber fabricated using SWNT–COOH under comparable coverage density of functional groups (4.2%). These results indicate that the fiber reinforced by SWNT–COOH is stiffer, while that containing SWNT–CONH₂ is tougher (measured by area under the stress–strain curve).

The work reported by Gao *et al.*^{176,177} clearly proves again that polymers attached to CNTs can effectively enhance CNT–matrix interfacial bonding and improve their compatibility; thereby allowing homogeneous dispersion of CNTs in the polymer matrix and resulting in an increased ability of load transfer from the matrix to nanotubes. Such polymer nanocomposites with CNTs are expected to possess excellent mechanical performance, thermal stability and electrical properties. Besides, both coverage density and the nature of functional groups bound onto CNTs influence the linkage reaction between CNTs and matrix, and hence the CNT–matrix interfacial interaction, composite morphology and final material properties.

3.4 Conclusion

Polymer–CNT nanocomposites possess desirable combined properties that cannot be found in individual components. From a structural viewpoint, there are three main system requirements for the effective improvement of polymers with CNTs. First, smaller diameters of CNTs (or CNT bundles) are required to produce a higher packing density. Second, a homogeneous dispersion of CNTs in the polymer matrix is necessary to avoid unreinforced regions and thereby obtain a uniform stress distribution throughout the composite. Finally, a strong matrix–nanotube interfacial bonding is desirable to effectively transfer the load from the matrix to CNTs. Apart from the first point, the latter two points can be achieved by maximizing the matrix–CNT physical contact or by constructing chemical linkages between the nanotubes and matrix. Non-covalent functionalization of CNTs is mainly based on the physical interactions of van der Waals forces or π – π stacking between two components, which are chiefly controlled by thermodynamics. This method offers a possibility to exfoliate the nanotubes into smaller bundles and even individual CNTs without causing any obvious structural damages to CNTs in solution and polymer matrix. However, the interface adhesion between the wrapping molecule and nanotube is weak, based on physical forces,

thus the efficiency of load transfer is low in the composites. In contrast, covalent functionalization involves direct chemical attachment of functional groups to the π -conjugated skeleton of CNTs by virtue of grafting-from or grafting-to strategies. The grafted chains can be imagined as being entangled with the matrix polymer chains acting as bridges between CNTs and the matrix, and become an integral part of the polymer matrix. Therefore, CNTs with covalently attached polymers are superior in improving the material performance of polymers. However, the chemically functionalized CNTs inevitably result in the loss of their intrinsic structures, even if the evidence collected implies that CNTs can tolerate a limited number of structural defects before CNT-based materials lose their electronic and mechanical properties. Hence, how to functionalize CNTs without damaging their intrinsic structures is a great challenge for future research.

3.5 Acknowledgements

The authors acknowledge financial support from the Outstanding Youth Fund of the National Natural Science Foundation of China (50825301), the National Natural Science Foundation of China (20804014, 51073050) and the Program for Excellent Middle-Aged and Young Talents of Hubei Provincial Department of Education (Q20091005).

3.6 References

- 1 S. Iijima, Helical microtubules of graphitic carbon, *Nature*, **1991**, 354, 56–58.
- 2 S. Iijima, T. Ichihashi, Single-shell carbon nanotubes of 1-nm diameter, *Nature*, **1993**, 363, 603–604.
- 3 D.S. Bethune, C.H. Kiang, M.S. de Vries, G. Gorman, R. Savoy, J. Vazquez, R. Beyers, Cobalt-catalysed growth of carbon nanotubes with single-atomic-layer walls, *Nature*, **1993**, 363, 605–607.
- 4 P.M. Ajayan, Nanotubes from carbon, *Chem. Rev.*, **1999**, 99, 1787–1799.
- 5 V.N. Popov, Carbon nanotubes: properties and application, *Mater. Sci. Eng. R*, **2004**, 43, 61–102.
- 6 V. Sgobba, D.M. Guldi, Carbon nanotubes-electronic/electrochemical properties and application for nanoelectronics and photonics, *Chem. Soc. Rev.*, **2009**, 38, 165–184.
- 7 R.H. Baughman, A.A. Zakhidov, W.A. de Heer, Carbon nanotubes: the route toward applications, *Science*, **2002**, 297, 787–792.
- 8 M. Moniruzzaman, K.I. Winey, Polymer nanocomposites containing carbon nanotubes, *Macromolecules*, **2006**, 39, 5194–5205.
- 9 A.B. Kaiser, Electronic transport properties of conducting polymers and carbon nanotubes, *Rep. Prog. Phys.*, **2001**, 64, 1–49.
- 10 S.L. Ruan, P. Gao, X.G. Yang, T.X. Yu, Toughening high performance ultrahigh molecular weight polyethylene using multiwalled carbon nanotubes, *Polymer*, **2003**, 44, 5643–54.
- 11 D. Qian, E.C. Dickey, R. Andrews, T. Rantell, Load transfer and deformation mechanisms in carbon nanotube-polystyrene composites, *Appl. Phys. Lett.*, **2000**, 76, 2868–2870.

- 12 J. Hone, M.C. Llaguno, M.J. Bierck, A.T. Johnson, B. Batlogg, Z. Benes, J.E. Fischer, Thermal properties of carbon nanotubes and nanotube-based materials, *Appl. Phys. A.*, **2002**, 74, 339–343.
- 13 C. Yu, Y.S. Kim, D. Kim, J.C. Grunlan, Thermoelectric behavior of segregated-network polymer nanocomposites, *Nano. Lett.*, **2008**, 8, 4428–4432.
- 14 B.I. Kharisov, O.V. Kharissova, H.L. Gutierrez, U.O. Méndez, Recent advances on the soluble carbon nanotubes, *Ind. Eng. Chem. Res.*, **2009**, 48, 572–590.
- 15 S.C. Tjong, Structural and mechanical properties of polymer nanocomposites, *Mater. Sci. Eng. R.*, **2006**, 53, 73–197.
- 16 J.N. Coleman, U. Khan, Y.K. Gun'ko, Mechanical reinforcement of polymers using carbon nanotubes, *Adv. Mater.*, **2006**, 18, 689–706.
- 17 X.L. Xie, Y.-W. Mai, X.P. Zhou, Dispersion and alignment of carbon nanotubes in polymer matrix: a review, *Mater. Sci. Eng. R.*, **2005**, 49, 89–112.
- 18 N. Grossiord, J. Loos, O. Regev, C.E. Koning, Toolbox for dispersing carbon nanotubes into polymers to get conductive nanocomposites, *Chem. Mater.*, **2006**, 18, 1089–1099.
- 19 J.N. Coleman, U. Khan, W.J. Blau, Y.K. Gun'ko, Small but strong: a review of the mechanical properties of carbon nanotube-polymer composites, *Carbon*, **2006**, 44, 1624–1652.
- 20 S.J.V. Frankland, A. Caglar, D.W. Brenner, M. Griebel, Molecular simulation of the influence of chemical cross-links on the shear strength of carbon nanotube-polymer interfaces, *J. Phys. Chem. B*, **2002**, 106, 3046–3048.
- 21 R.A. Graff, J.P. Swanson, P.W. Barone, S. Baik, D.A. Heller, M.S. Strano, Achieving individual-nanotube dispersion at high loading in single-walled carbon nanotube composites, *Adv. Mater.*, **2005**, 17, 980–984.
- 22 H. Geng, R. Rosen, B. Zheng, H. Shimoda, L. Fleming, J. Liu, Q. Zhao, Fabrication and properties of composites of poly(ethylene oxide) and functionalized carbon nanotubes, *Adv. Mater.*, **2002**, 14, 1387–1390.
- 23 I. O'Connor, H. Hayden, S. O'Connor, J.N. Coleman, Y. K. Gun'ko, Polymer reinforcement with kevlar-coated carbon nanotubes, *J. Phys. Chem. C*, **2009**, 113, 20184–20192.
- 24 D. Tasis, N. Tagmatarchis, A. Bianco, M. Prato, Chemistry of carbon nanotubes, *Chem. Rev.*, **2006**, 106, 1105–1136.
- 25 D.A. Britz, A.N. Khlobystov, Noncovalent interactions of molecules with single walled carbon nanotubes, *Chem. Soc. Rev.*, **2006**, 35, 637–659.
- 26 X. Peng, S.S. Wong, Functional covalent chemistry of carbon nanotube surfaces, *Adv. Mater.*, **2009**, 21, 625–642.
- 27 P. Singh, S. Campidelli, S. Giordani, D. Bonifazi, A. Bianco, M. Prato, Organic functionalisation and characterisation of single-walled carbon nanotubes, *Chem. Soc. Rev.*, **2009**, 38, 2214–2230.
- 28 L.M. Clayton, A.K. Sikder, A. Kumar, M. Cinke, M. Meyyappan, T.G. Gerasimov, J.P. Harmon, Transparent poly(methyl methacrylate)/single-walled carbon nanotube (PMMA/SWNT) composite films with increased dielectric constants, *Adv. Funct. Mater.*, **2005**, 15, 101–106.
- 29 K.W. Putz, C.A. Mitchell, R. Krishnamoorti, P.F. Green, Elastic modulus of single-walled carbon nanotube/poly(methyl methacrylate) nanocomposites, *J. Polym. Sci. Part B: Polym. Phys.*, **2004**, 42, 2286–2293.
- 30 S. J. Zhang, L. J. Zhu, C.P. Wong, S. Kumar, Polymer-infiltrated aligned carbon nanotube fibers by *in situ* polymerization, *Macromol. Rapid Commun.*, **2009**, 30, 1936–1939.

- 31 S. Kumar, T.D. Dang, F.E. Arnold, A.R. Bhattacharyya, B.G. Min, X. Zhang, R.A. Vaia, C. Park, W.W. Adams, R.H. Hauge, R.E. Smalley, S. Ramesh, P.A. Willis, Synthesis, structure, and properties of PBO/SWNT composites, *Macromolecules*, **2002**, 35, 9039–9043.
- 32 C. Zhao, G. Hu, R. Justice, D.W. Schaefer, S. Zhang, M. Yang, C.C. Han, Synthesis and characterization of multi-walled carbon nanotubes reinforced polyamide 6 via in-situ polymerization, *Polymer*, **2005**, 46, 5125–5132.
- 33 C. Velasco-Santos, A.L. Martínez-Hernández, F.T. Fisher, R. Ruoff, V.M. Castaño, Improvement of thermal and mechanical properties of carbon nanotube composites through chemical functionalization, *Chem. Mater.*, **2003**, 15, 4470–4475.
- 34 A.H. Barber, S.R. Cohen, A. Eitan, L.S. Schadler, H.D. Wagner, Fracture transitions at a carbon-nanotube/polymer interface, *Adv. Mater.*, **2006**, 18, 83–87.
- 35 H. Wang, W. Zhou, D.L. Ho, K.I. Winey, J.E. Fischer, C.J. Glinka, E.K. Hobbie, Dispersing single-walled carbon nanotubes with surfactants: a small angle neutron scattering study, *Nano Lett.*, **2004**, 4, 1789–1793.
- 36 K. Yurekli, C.A. Mitchell, R. Krishnamoorti, Small-angle neutron scattering from surfactant-assisted aqueous dispersions of carbon nanotubes, *J. Am. Chem. Soc.*, **2004**, 126, 9902–9903.
- 37 N. Grossiord, P. van der Schoot, J. Meuldijk, C. E. Koning, Determination of the surface coverage of exfoliated carbon nanotubes by surfactant molecules in aqueous solution, *Langmuir*, **2007**, 23, 3646–3653.
- 38 N.R. Tummala, A. Striolo, SDS surfactants on carbon nanotubes: aggregate morphology, *ACS Nano*, **2009**, 3, 595–602.
- 39 H.J. Barraza, F. Pompeo, E.A. O'Rear, D.E. Resasco, SWNT-filled thermoplastic and elastomeric composites prepared by mini emulsion polymerization, *Nano. Lett.*, **2002**, 2, 797–802.
- 40 H. Xia, Q. Wang, G. Qiu, Polymer-encapsulated carbon nanotubes prepared through ultrasonically initiated in situ emulsion polymerization, *Chem. Mater.*, **2003**, 15, 3879–3886.
- 41 Z. Jia, Z. Wang, C. Xu, J. Liang, B. Wei, D. Wu, S. Zhu, Study on poly(methyl methacrylate): carbon nanotube composites, *Mater. Sci. Eng. A*, **1999**, 271, 395–400.
- 42 S. J. Park, M.S. Cho, S.T. Lim, H.J. Choi, M.S. Jhon, Synthesis and dispersion characteristics of multi-walled carbon nanotube composites with poly(methyl methacrylate) prepared by in-situ bulk polymerization, *Macromol. Rapid Commun.*, **2003**, 24, 1070–1073.
- 43 J.H. Sung, H.S. Kim, H.J. Jin, H.J. Choi, I.J. Chin, Nanofibrous membranes prepared by multiwalled carbon nanotube/poly(methyl methacrylate) composites, *Macromolecules*, **2004**, 37, 9899–9902.
- 44 S. Qin, D. Qin, W.T. Ford, J.E. Herrera, D.E. Resasco, S.M. Bachilo, R.B. Weisman, Solubilization and purification of single-wall carbon nanotubes in water by in situ radical polymerization of sodium 4-styrenesulfonate, *Macromolecules*, **2004**, 37, 3965–3967.
- 45 S. Qin, D. Qin, W.T. Ford, J.E. Herrera, D.E. Resasco, Grafting of poly(4-vinylpyridine) to single-walled carbon nanotubes and assembly of multilayer films, *Macromolecules*, **2004**, 37, 9963–9967.
- 46 X. Kan, Y. Zhao, Z. Geng, Z. Wang, J.J. Zhu, Composites of multiwalled carbon nanotubes and molecularly imprinted polymers for dopamine recognition, *J. Phys. Chem. C*, **2008**, 112, 4849–4854.
- 47 J.N. Coleman, M. Cadek, R. Blake, V. Nicolosi, K.P. Ryan, C. Belton, A. Fonseca, J.B. Nagy, Y.K. Gun'ko, W.J. Blau, High performance nanotube-reinforced plastics:

- understanding the mechanism of strength increase, *Adv. Funct. Mater.*, **2004**, 14, 791–798.
- 48 L. Liu, A.H. Barber, S. Nuriel, H.D. Wagner, Mechanical properties of functionalized single-walled carbon-nanotube/poly(vinyl alcohol) nanocomposites, *Adv. Funct. Mater.*, **2005**, 15, 975–980.
 - 49 F. Wang, G. Wang, S. Yang, C. Li, Layer-by-layer assembly of aqueous dispersible, highly conductive poly(aniline-co-*o*-anisidine)/poly(sodium 4-styrenesulfonate)/MWNTs core-shell nanocomposites, *Langmuir*, **2008**, 24, 5825–5831.
 - 50 B.Z. Tang, H. Xu, Preparation, alignment, and optical properties of soluble poly(phenylacetylene)-wrapped carbon nanotubes, *Macromolecules*, **1999**, 32, 2569–2576.
 - 51 S.A. Curran, P.M. Ajayan, W.J. Blau, D.L. Carroll, J.N. Coleman, A.B. Dalton, A.P. Davey, A. Drury, B. McCarthy, A composite from poly(*m*-phenylenevinylene-co-2,5-diethoxy-*p*-phenylenevinylene) and carbon nanotubes: a novel material for molecular optoelectronics, *Adv. Mater.*, **1998**, 10, 1091–1093.
 - 52 A. Star, Y. Lu, K. Bradley, G. Grüner, Nanotube optoelectronic memory devices, *Nano. Lett.*, **2004**, 4, 1587–1591.
 - 53 D.W. Steuerman, A. Star, R. Narizzano, H. Choi, R.S. Ries, C. Nicolini, J.F. Stoddart, J.R. Heath, Interactions between conjugated polymers and single-walled carbon nanotubes, *J. Phys. Chem. B*, **2002**, 106, 3124–3130.
 - 54 M.N. Tchoul, W.T. Ford, M.L.P. Ha, I. Chavez-Sumarriva, B.P. Grady, G. Lolli, D. E. Resasco, S. Arepalli, Composites of single-walled carbon nanotubes and polystyrene: preparation and electrical conductivity, *Chem. Mater.*, **2008**, 20, 3120–3126.
 - 55 J.B. Kim, T. Premkumar, K. Lee, K.E. Geckeler, A facile approach to single-wall carbon nanotube/poly(allylamine) nanocomposites, *Macromol. Rapid Commun.*, **2007**, 28, 276–280.
 - 56 J.B. Kim, T. Premkumar, O. Giani, J.J. Robin, F. Schue, K.E. Geckeler, A mechanochemical approach to nanocomposites using single-wall carbon nanotubes and poly(L-lysine), *Macromol. Rapid Commun.*, **2007**, 28, 767–771.
 - 57 R. Kannan, B.A. Kakade, V.K. Pillai, Polymer electrolyte fuel cells using nafion-based composite membranes with functionalized carbon nanotubes, *Angew. Chem. Int. Ed.*, **2008**, 47, 2653–2656.
 - 58 M. Shim, T. Ozel, A. Gaur, C. Wang, Insights on charge transfer doping and intrinsic phonon line shape of carbon nanotubes by simple polymer adsorption, *J. Am. Chem. Soc.*, **2006**, 128, 7522–7530.
 - 59 V. Bavastrello, S. Carrara, M.K. Ram, C. Nicolini, Optical and electrochemical properties of poly(*o*-toluidine) multiwalled carbon nanotubes composite Langmuir-Schaefer films, *Langmuir*, **2004**, 20, 969–973.
 - 60 Q. Yang, L. Shuai, J. Zhou, F. Lu, X. Pan, Functionalization of multiwalled carbon nanotubes by pyrene-labeled hydroxypropyl cellulose, *J. Phys. Chem. B*, **2008**, 112, 12934–12939.
 - 61 K.K. Kim, S.M. Yoon, J.Y. Choi, J. Lee, B.K. Kim, J.M. Kim, J.H. Lee, U. Paik, M.H. Park, C.W. Yang, K.H. An, Y. Chung, Y.H. Lee, Design of dispersants for the dispersion of carbon nanotubes in an organic solvent, *Adv. Funct. Mater.*, **2007**, 17, 1775–1783.
 - 62 I. Gurevitch, S. Srebnik, Monte Carlo simulation of polymer wrapping of nanotubes, *Chem. Phys. Lett.*, **2007**, 444, 96–100.
 - 63 W. Yi, A. Malkovskiy, Q. Chu, A.P. Sokolov, M.L. Colon, M. Meador, Y. Pang, Wrapping of single-walled carbon nanotubes by a π -conjugated polymer: the role of

- polymer conformation-controlled size selectivity, *J. Phys. Chem. B*, **2008**, 112, 12263–12269.
- 64 D. Baskaran, J.W. Mays, M.S. Bratcher, Noncovalent and nonspecific molecular interactions of polymers with multiwalled carbon nanotubes, *Chem. Mater.*, **2005**, 17, 3389–3397.
- 65 W.D. Zhang, L. Shen, I.Y. Phang, T. Liu, Carbon nanotubes reinforced Nylon-6 composite prepared by simple melt-compounding, *Macromolecules*, **2004**, 37, 256–259.
- 66 T. Liu, I.Y. Phang, L. Shen, S.Y. Chow, W.D. Zhang, Morphology and mechanical properties of multiwalled carbon nanotubes reinforced Nylon-6 composites, *Macromolecules*, **2004**, 37, 7214–7222.
- 67 M. Cadek, J.N. Coleman, V. Barron, K. Hedicke, W.J. Blau, Morphological and mechanical properties of carbon-nanotube-reinforced semicrystalline and amorphous polymer composites, *Appl. Phys. Lett.* **2002**, 81, 5123–5125.
- 68 M. Shim, A. Javey, N.W.S. Kam, H. Dai, Polymer functionalization for air-stable π -type carbon nanotube field-effect transistors, *J. Am. Chem. Soc.*, **2001**, 123, 11512–11513.
- 69 T. Ozel, A. Gaur, J.A. Rogers, M. Shim, Polymer electrolyte gating of carbon nanotube network transistors, *Nano. Lett.*, **2005**, 5, 905–911.
- 70 L. Li, B. Li, M.A. Hood, C.Y. Li, Carbon nanotubes induced polymer crystallization: the formation of nanohybrid shish-kebabs, *Polymer*, **2009**, 50, 953–965.
- 71 C.Y. Li, L. Li, W. Cai, S.L. Kodjie, K.K. Tenneti, Nanohybrid shish-kebabs: periodically functionalized carbon nanotubes, *Adv. Mater.*, **2005**, 17, 1198–1202.
- 72 L. Li, C.Y. Li, C. Ni, Polymer crystallization-driven, periodic patterning on carbon nanotubes, *J. Am. Chem. Soc.*, **2006**, 128, 1692–1699.
- 73 S.L. Kodjie, L. Li, B. Li, W. Cai, C.Y. Li, M.K. Ting, Morphology and crystallization behavior of HDPE/CNT nanocomposite, *J. Macromol. Sci. Phys.*, **2006**, 45, 231–245.
- 74 L. Li, C.Y. Li, C. Ni, L. Rong, B. Hsiao, Structure and crystallization behavior of Nylon 66/multi-walled carbon nanotube nanocomposites at low carbon nanotube contents, *Polymer*, **2007**, 48, 3452–3460.
- 75 D. Bonduel, S. Bredeau, M. Alexandre, F. Monteverde, P. Dubois, Supported metallocene catalysis as an efficient tool for the preparation of polyethylene/carbon nanotube nanocomposites: effect of the catalytic system on the coating morphology, *J. Mater. Chem.*, **2007**, 17, 2359–2366.
- 76 A. Toti, G. Giambastiani, C. Bianchini, A. Meli, S. Bredeau, Ph. Dubois, D. Bonduel, M. Claes, Tandem action of early-late transition metal catalysts for the surface coating of multiwalled carbon nanotubes with linear low-density polyethylene, *Chem. Mater.*, **2008**, 20, 3092–3098.
- 77 K. Wang, F. Chen, Q. Zhang, Q. Fu, Shish-kebab of polyolefin by ‘melt manipulation’ strategy in injection-molding: a convenience pathway from fundament to application, *Polymer*, **2008**, 49, 4745–4755.
- 78 S. Liang, K. Wang, D. Chen, Q. Zhang, R. Du, Q. Fu, Shear enhanced interfacial interaction between carbon nanotubes and polyethylene and formation of nanohybrid shish-kebabs, *Polymer*, **2008**, 49, 4925–4929.
- 79 J. Yang, C. Wang, K. Wang, Q. Zhang, F. Chen, R. Du, Q. Fu, Direct formation of nanohybrid shish-kebab in the injection molded bar of polyethylene/multiwalled carbon nanotubes composite, *Macromolecules*, **2009**, 42, 7016–7023.
- 80 A.I. Cooper, Recent developments in materials synthesis and processing using supercritical CO₂, *Adv. Mater.*, **2001**, 13, 1111–1114.

- 81 Z. Liu, B. Han, Synthesis of carbon-nanotube composites using supercritical fluids and their potential applications, *Adv. Mater.*, **2009**, 21, 825–829.
- 82 Z. Zhang, Q. Xu, Z. Chen, J. Yue, Nanohybrid shish-kebabs: supercritical CO₂-induced PE epitaxy on carbon nanotubes, *Macromolecules*, **2008**, 41, 2868–2873.
- 83 F. Zhang, H. Zhang, Z. Zhang, Z. Chen, Q. Xu, Modification of carbon nanotubes: water-soluble polymers nanocrystal wrapping to periodic patterning with assistance of supercritical CO₂, *Macromolecules*, **2008**, 41, 4519–4523.
- 84 X. Dai, Z. Liu, B. Han, Z. Sun, Y. Wang, J. Xu, X. Guo, N. Zhao, J. Chen, Carbon nanotube/poly(2,4-hexadiyne-1,6-diol) nanocomposites prepared with the aid of supercritical CO₂, *Chem. Commun.*, **2004**, 2190–2191.
- 85 J. Wang, A.N. Khlobystov, W. Wang, S.M. Howdle, M. Poliakoff, Coating carbon nanotubes with polymer in supercritical carbon dioxide, *Chem. Commun.*, **2006**, 1670–1672.
- 86 B.H. Yue, Y.B. Wang, C.Y. Huang, R. Pfeffer, Z. Iqbal, Polymeric nanocomposites of functionalized carbon nanotubes synthesized in supercritical CO₂, *J. Nanosci. Nanotech.*, **2007**, 7, 994–1000.
- 87 N. Tsubokawa, Preparation and properties of polymer-grafted carbon nanotubes and nanofibers, *Polym. J.*, **2005**, 37, 637–655.
- 88 Y.L. Zhao, J.F. Stoddart, Noncovalent functionalization of single-walled carbon nanotubes, *Acc. Chem. Res.*, **2009**, 42, 1161–1171.
- 89 Z. Spitsky, D. Tasis, K. Papagelis, C. Galiotis, Carbon nanotube-polymer composites: chemistry, processing, mechanical and electrical properties, *Prog. Polym. Sci.*, **2010**, 35, 357–401.
- 90 Y.K. Yang, X.L. Xie, J.G. Wu, Y.-W. Mai, Synthesis and self-assembly of polystyrene-grafted multiwalled carbon nanotubes with a hairy-rod nanostructure, *J. Polym. Sci., Part A: Polym. Chem.* **2006**, 44, 3869–3881.
- 91 F.P. Du, K.B. Wu, Y.K. Yang, L. Liu, T. Gan, X.L. Xie, Synthesis and electrochemical probing of water-soluble poly(sodium 4-styrenesulfonate-co-acrylic acid)-grafted multiwalled carbon nanotubes, *Nanotechnology*, **2008**, 19: 085716.
- 92 F.P. Du, C.Y. Tang, X.L. Xie, X.P. Zhou, L. Tan, Carbon nanotube enhanced gripping in polymer-based actuators, *J. Phys. Chem. C*, **2009**, 113, 7223–7226.
- 93 J.U. Ha, M. Kim, J. Lee, S. Choe, I.W. Cheong, S.E. Shim, A novel synthesis of polymer brush on multiwall carbon nanotubes bearing terminal monomeric unit, *J. Polym. Sci., Part A: Polym. Chem.*, **2006**, 44, 6394–6401.
- 94 M. Kim, C.K. Hong, S. Choe, S.E. Shim, Synthesis of polystyrene brush on multiwalled carbon nanotubes treated with kmno₄ in the presence of a phase-transfer catalyst, *J. Polym. Sci., Part A: Polym. Chem.*, **2007**, 45, 4413–4420.
- 95 X. Kan, Y. Zhao, Z. Geng, Z. Wang, J.J. Zhu, Composites of multiwalled carbon nanotubes and molecularly imprinted polymers for dopamine recognition, *J. Phys. Chem. C*, **2008**, 112, 4849–4854.
- 96 S. Li, H. Chen, W. Bi, J. Zhou, Y. Wang, J. Li, W. Cheng, M. Li, L. Li, T. Tang, Synthesis and characterization of polyethylene chains grafted onto the sidewalls of single-walled carbon nanotubes via copolymerization, *J. Polym. Sci., Part. A: Polym. Chem.*, **2007**, 45, 5459–5469.
- 97 Z. Yao, N. Braid, G.A. Botton, A. Adronov, Polymerization from the surface of single-walled carbon nanotubes-reparation and characterization of nanocomposites, *J. Am. Chem. Soc.*, **2003**, 125, 16015–16024.
- 98 D. Baskaran, J.W. Mays, M.S. Bratcher, Polymer-grafted multiwalled carbon nanotubes through surface-initiated polymerization, *Angew. Chem. Int. Ed.*, **2004**, 43, 2138–2142.

- 99 H. Kong, C. Gao, D. Yan, Controlled functionalization of multiwalled carbon nanotubes by in situ atom transfer radical polymerization, *J. Am. Chem. Soc.*, **2004**, 126, 412–413.
- 100 S. Qin, D. Qin, W.T. Ford, D.E. Resasco, J.E. Herrera, Polymer brushes on single-walled carbon nanotubes by atom transfer radical polymerization of *n*-butyl methacrylate, *J. Am. Chem. Soc.*, **2004**, 126, 170–176.
- 101 M. Wang, K.P. Pramoda, S.H. Goh, Enhancement of the mechanical properties of poly(styrene-*co*-acrylonitrile) with poly(methyl methacrylate)-grafted multiwalled carbon nanotubes, *Polymer*, **2005**, 46, 11510–11516.
- 102 J.H. Shi, B.X. Yang, K.P. Pramoda, S.H. Goh, Enhancement of the mechanical performance of poly(vinyl chloride) using poly(*n*-butyl methacrylate)-grafted multiwalled carbon nanotubes, *Nanotechnology*, **2007**, 18, 375704.
- 103 J. Cui, W.P. Wang, Y.Z. You, C. Liu, P. Wang, Functionalization of multiwalled carbon nanotubes by reversible addition fragmentation chain-transfer polymerization, *Polymer*, **2004**, 45, 8717–8721.
- 104 X.W. Pei, W.M. Liu, J.C. Hao, Functionalization of multiwalled carbon nanotube via surface reversible addition fragmentation chain transfer polymerization and as lubricant additives, *J. Polym. Sci., Part A: Polym. Chem.*, **2008**, 46, 3014–3023.
- 105 G. Xu, W.T. Wu, Y. Wang, W. Pang, Q. Zhu, P. Wang, Y. You, Constructing polymer brushes on multiwalled carbon nanotubes by in situ reversible addition fragmentation chain transfer polymerization, *Polymer*, **2006**, 47, 5909–5918.
- 106 C.Y. Hong, Y.Z. You, C.Y. Pan, Functionalized multi-walled carbon nanotubes with poly(*N*-(2-hydroxypropyl)methacrylamide) by RAFT polymerization, *J. Polym. Sci., Part A: Polym. Chem.*, **2006**, 44, 2419–2427.
- 107 X. Pei, J. Hao, W. Liu, Preparation and characterization of carbon nanotubes-polymer/Ag hybrid nanocomposites via surface RAFT polymerization, *J. Phys. Chem. C*, **2007**, 111, 2947–2952.
- 108 G.J. Wang, S.Z. Huang, Y. Wang, L. Liu, J. Qiu, Y. Li, Synthesis of water-soluble single-walled carbon nanotubes by RAFT polymerization, *Polymer*, **2007**, 48, 728–733.
- 109 C.Y. Hong, Y.Z. You, C.Y. Pan, Synthesis of water-soluble multiwalled carbon nanotubes with grafted temperature-responsive shells by surface raft polymerization, *Chem. Mater.*, **2005**, 17, 2247–2254.
- 110 G. Xu, W.T. Wu, Y. Wang, W. Pang, P. Wang, Q. Zhu, F. Lu, Synthesis and characterization of water-soluble multiwalled carbon nanotubes grafted by a thermoresponsive polymer, *Nanotechnology*, **2006**, 17, 2458–2465.
- 111 X. Zhao, W. Lin, N. Song, X. Chen, X. Fan, Q. Zhou, Water soluble multi-walled carbon nanotubes prepared via nitroxide-mediated radical polymerization, *J. Mater. Chem.*, **2006**, 16, 4619–4625.
- 112 X.D. Zhao, X.H. Fan, X.F. Chen, C.P. Chai, Q.F. Zhou, Surface modification of multiwalled carbon nanotubes via nitroxide-mediated radical polymerization, *J. Polym. Sci., Part A: Polym. Chem.*, **2006**, 44, 4656–4667.
- 113 M. Dehonor, K. Masenelli-Varlot, A. González-Montiel, C. Gauthier, J.Y. Cavaillé, H. Terrones, M. Terrones, Nanotube brushes: polystyrene grafted covalently on CN_x nanotubes by nitroxide-mediated radical polymerization, *Chem. Commun.*, **2005**, 5349–5351.
- 114 V. Datsyuk, C. Guerret-Piécourt, S. Dagréou, L. Billon, J.C. Dupin, E. Flahaut, A. Peigney, C. Laurent, Double walled carbon nanotube/polymer composites via in-situ nitroxide mediated polymerisation of amphiphilic block copolymers, *Carbon*, **2005**, 43, 873–876.

- 115 H. Zeng, C. Gao, D. Yan, Poly(ϵ -caprolactone)-functionalized carbon nanotubes and their biodegradation properties, *Adv. Funct. Mater.*, **2006**, 16, 812–818.
- 116 F. Buffa, H. Hu, D.E. Resasco, Side-wall functionalization of single-walled carbon nanotubes with 4-hydroxymethylaniline followed by polymerization of ϵ -caprolactone, *Macromolecules*, **2005**, 38, 8258–8263.
- 117 Y.K. Yang, C.P. Tsui, C.Y. Tang, S.Q. Qiu, Q. Zhao, X.J. Cheng, Z.G. Sun, R.K.Y. Li, X.L. Xie, Functionalization of carbon nanotubes with biodegradable supramolecular polypseudorotaxanes from grafted-poly(ϵ -caprolactone) and α -cyclodextrins, *Eur. Polym. J.*, **2010**, 46, 145–155.
- 118 G.X. Chen, H.S. Kim, B.H. Park, J.S. Yoon, Synthesis of poly(l-lactide)-functionalized multiwalled carbon nanotubes by ring-opening polymerization, *Macromol. Chem. Phys.*, **2007**, 208, 389–398.
- 119 H.S. Kim, B.H. Park, J.S. Yoon, H.J. Jin, Thermal and electrical properties of poly (L-lactide)-graft-multiwalled carbon nanotube composites, *Eur. Polym. J.*, **2007**, 43, 1729–1735.
- 120 J. Feng, W. Cai, J. Sui, Z. Li, J. Wan, A.N. Chakoli, Poly(L-lactide) brushes on magnetic multiwalled carbon nanotubes by in-situ ring-opening polymerization, *Polymer*, **2008**, 49, 4989–4994.
- 121 Y. Xu, C. Gao, H. Kong, D. Yan, Y.Z. Jin, P.C.P. Watts, Growing multihydroxyl hyperbranched polymers on the surfaces of carbon nanotubes by in situ ring-opening polymerization, *Macromolecules*, **2004**, 37, 8846–8853.
- 122 L. Qu, L.M. Veca, Y. Lin, A. Kitaygorodskiy, B. Chen, A.M. McCall, J.W. Connell, Y.P. Sun, Soluble Nylon-functionalized carbon nanotubes from anionic ring-opening polymerization from nanotube surface, *Macromolecules*, **2005**, 38, 10328–10331.
- 123 M. Yang, Y. Gao, H. Li, A. Adronov, Functionalization of multiwalled carbon nanotubes with polyamide 6 by anionic ring-opening polymerization, *Carbon*, **2007**, 45, 2327–2333.
- 124 J. Zhu, J.D. Kim, H. Peng, J.L. Margrave, V.N. Khabashesku, E.V. Barrera, Improving the dispersion and integration of single-walled carbon nanotubes in epoxy composites through functionalization, *Nano. Lett.*, **2003**, 3, 1107–1113.
- 125 J. Bae, J. Jang, S.H. Yoon, Cure behavior of the liquid-crystalline epoxy/carbon nanotube system and the effect of surface treatment of carbon fillers on cure reaction, *Macromol. Chem. Phys.*, **2002**, 203, 2196–2204.
- 126 E. Bekyarova, E.T. Thostenson, A. Yu, M.E. Itkis, D. Fakhrutdinov, T.W. Chou, R.C. Haddon, Functionalized single-walled carbon nanotubes for carbon fiber-epoxy composites, *J. Phys. Chem. C*, **2007**, 111, 17865–17871.
- 127 C.H. Tseng, C.C. Wang, C.Y. Chen, Functionalizing carbon nanotubes by plasma modification for the preparation of covalent-integrated epoxy composites, *Chem. Mater.*, **2007**, 19, 308–315.
- 128 P.C. Ma, J.K. Kim, B.Z. Tang, Effects of silane functionalization on the properties of carbon nanotube/epoxy nanocomposites, *Compos. Sci. Technol.*, **2007**, 67, 2965–2972.
- 129 J. Zhu, H. Peng, F. Rodriguez-Macias, J.L. Margrave, V.N. Khabashesku, A.M. Iman, K. Lozano, E.V. Barrera, Reinforcing epoxy polymer composites through covalent integration of functionalized nanotubes, *Adv. Funct. Mater.*, **2004**, 14, 643–648.
- 130 L. Liu, K.C. Etika, K.S. Liao, L.A. Hess, D.E. Bergbreiter, J.C. Grunlan, Comparison of covalently and noncovalently functionalized carbon nanotubes in epoxy, *Macromol. Rapid Commun.*, **2009**, 30, 627–632.

- 131 Y.K. Yang, X.L. Xie, J.G. Wu, Z.F. Yang, X.T. Wang, Y.-W. Mai, Multiwalled carbon nanotubes functionalized by hyperbranched poly(urea-urethane)s by a one-pot polycondensation, *Macromol. Rapid Commun.*, **2006**, 27, 1695–1701.
- 132 Y.K. Yang, X.L. Xie, Z.F. Yang, X.T. Wang, W. Cui, J.Y. Yang, Y.-W. Mai, Controlled synthesis and novel solution rheology of hyperbranched poly(urea-urethane)-functionalized multiwalled carbon nanotubes, *Macromolecules*, **2007**, 40, 5858–5867.
- 133 Y.K. Yang, X.T. Wang, L. Liu, X.L. Xie, Z.F. Yang, R.K.Y. Li, Y.-W. Mai, Structures and photoresponsive behaviors of multiwalled carbon nanotubes grafted by polyurethanes containing azobenzene side-chains, *J. Phys. Chem. C*, **2007**, 111, 11231–11239.
- 134 C. Gao, Y.Z. Jin, H. Kong, R.L.D. Whitby, S.F.A. Acquah, G.Y. Chen, H. Qian, A. Hartschuh, S.R.P. Silva, S. Henley, P. Fearon, H.W. Kroto, D.R.M. Walton, Polyurea-functionalized multiwalled carbon nanotubes: synthesis, morphology, and Raman spectroscopy, *J. Phys. Chem. B*, **2005**, 109, 11925–11932.
- 135 X. Chen, X. Chen, M. Lin, W. Zhong, X. Chen, Z. Chen, Functionalized multi-walled carbon nanotubes prepared by in-situ polycondensation of polyurethane, *Macromol. Chem. Phys.*, **2007**, 208, 964–972.
- 136 H. Xia, M. Song, Preparation and characterisation of polyurethane grafted single-walled carbon nanotubes and derived polyurethane nanocomposites, *J. Mater. Chem.*, **2006**, 16, 1843–1851.
- 137 C. Zhou, S. Wang, Y. Zhang, Q. Zhuang, Z. Han, In situ preparation and continuous fiber spinning of poly(*p*-phenylene benzobisoxazole) composites with oligo-hydroxyamide-functionalized multi-walled carbon nanotubes, *Polymer*, **2008**, 49, 2520–2530.
- 138 S.J. Oh, H.J. Lee, D.K. Keum, S.W. Lee, D.H. Wang, S.Y. Park, L.S. Tan, J.B. Baek, Multiwalled carbon nanotubes and nanofibers grafted with polyetherketones in mild and viscous polymeric acid, *Polymer*, **2006**, 47, 1132–1140.
- 139 J.Y. Choi, S.J. Oh, H.J. Lee, D.H. Wang, L.S. Tan, J.B. Baek, In-situ grafting of hyperbranched poly(ether ketone)s onto multiwalled carbon nanotubes via the $A_3 + B_2$ approach, *Macromolecules*, **2007**, 40, 4474–4480.
- 140 I.Y. Jeon, L.S. Tan, J.B. Baek, Nanocomposites derived from in situ grafting of linear and hyperbranched poly(ether-ketone)s containing flexible oxyethylene spacers onto the surface of multiwalled carbon nanotubes, *J. Polym. Sci., Part A: Polym. Chem.*, **2008**, 46, 3471–3481.
- 141 I.C. Liu, H.M. Huang, C.Y. Chang, H.C. Tsai, C.H. Hsu, R.C.C. Tsiang, Preparing a styrenic polymer composite containing well-dispersed carbon nanotubes: anionic polymerization of a nanotube-bound *p*-methylstyrene, *Macromolecules*, **2004**, 37, 283–287.
- 142 G. Viswanathan, N. Chakrapani, H. Yang, B. Wei, H. Chung, K. Cho, C.Y. Ryu, P.M. Ajayan, Single-step in situ synthesis of polymer-grafted single-wall nanotube composites, *J. Am. Chem. Soc.*, **2003**, 125, 9258–9259.
- 143 F. Liang, J.M. Beach, K. Kobashi, A.K. Sadana, Y.I. Vega-Cantu, J.M. Tour, W.E. Billups, In-situ polymerization initiated by single-walled carbon nanotube salts, *Chem. Mater.*, **2006**, 18, 4764–4767.
- 144 Y. Zhang, Y. Shen, J. Li, L. Niu, S. Dong, A. Ivaska, Electrochemical functionalization of single-walled carbon nanotubes in large quantities at a room-temperature ionic liquid supported three-dimensional network electrode, *Langmuir*, **2005**, 21, 4797–4800.
- 145 D. Tasis, K. Papagelis, M. Prato, I. Kallitsis, C. Galiotis, Water-soluble carbon nanotubes by redox radical polymerization, *Macromol. Rapid Commun.*, **2007**, 28, 1553–1558.

- 146 D. Priftis, N. Petzetakis, G. Sakellariou, M. Pitsikalis, D. Baskaran, J.W. Mays, N. Hadjichristidis, Surface-initiated titanium-mediated coordination polymerization from catalyst-functionalized single and multiwalled carbon nanotubes, *Macromolecules*, **2009**, 42, 3340–3346.
- 147 B. Ni, S.B. Sinnott, Chemical functionalization of carbon nanotubes through energetic radical collisions, *Phys. Rev. B*, **2000**, 61, R16343–R16346.
- 148 A. Galano, Carbon nanotubes as free-radical scavengers, *J. Phys. Chem. C*, **2008**, 112, 8922–8927.
- 149 X. Lou, C. Detrebleur, C. Pagnouille, R. Jérôme, V. Bocharova, A. Kiriy, M. Stamm, Surface modification of multiwalled carbon nanotubes by poly(2-vinylpyridine): dispersion, selective deposition, and decoration of the nanotubes, *Adv. Mater.*, **2004**, 16, 2123–2127.
- 150 X. Lou, C. Detrebleur, V. Sciannamea, C. Pagnouille, R. Jérôme, Grafting of alkoxyamine end-capped (co)polymers onto multi-walled carbon nanotubes, *Polymer*, **2004**, 45, 6097–6102.
- 151 C.J. Hawker, A.W. Bosman, E. Harth, New polymer synthesis by nitroxide mediated living radical polymerizations, *Chem. Rev.*, **2001**, 101, 3661–3688.
- 152 H.X. Wu, R. Tong, X.Q. Qiu, H.F. Yang, Y.H. Lin, R.F. Cai, S.X. Qian, Functionalization of multiwalled carbon nanotubes with polystyrene under atom transfer radical polymerization conditions, *Carbon*, **2007**, 45, 152–159.
- 153 G.L. Hwang, Y.T. Shieh, K.C. Hwang, Efficient load transfer to polymer-grafted multiwalled carbon nanotubes in polymer composites, *Adv. Funct. Mater.*, **2004**, 14, 487–491.
- 154 D. McIntosh, V.N. Khabashesku, E.V. Barrera, Benzoyl peroxide initiated in situ functionalization, processing, and mechanical properties of single-walled carbon nanotube-polypropylene composite fibers, *J. Phys. Chem. C*, **2007**, 111, 1592–1600.
- 155 C.J. Hawker, A simple and versatile method for the synthesis of C60 copolymers, *Macromolecules*, **1994**, 27, 4836–4837.
- 156 M. Holzinger, O. Vostrowsky, A. Hirsch, F. Hennrich, M. Kappes, R. Weiss, F. Jellen, Sidewall functionalization of carbon nanotubes, *Angew. Chem. Int. Ed.*, **2001**, 40, 4002–4005.
- 157 K.M. Lee, L. Li, L. Dai, Asymmetric end-functionalization of multi-walled carbon nanotubes, *J. Am. Chem. Soc.*, **2005**, 127, 4122–4123.
- 158 S. Qin, D. Qin, W.T. Ford, D.E. Resasco, J.E. Herrera, Functionalization of single-walled carbon nanotubes with polystyrene via grafting to and grafting from methods, *Macromolecules*, **2004**, 37, 752–757.
- 159 Z. Li, Y. Dong, M. Hussler, J.W.Y. Lam, Y.P. Dong, L. Wu, K.S. Wong, B. Z. Tang, Synthesis of, light emission from, and optical power limiting in soluble single-walled carbon nanotubes functionalized by disubstituted polyacetylenes, *J. Phys. Chem. B*, **2006**, 110, 2302–2309.
- 160 H. Li, F. Cheng, A.M. Duft, A. Adronov, Functionalization of single-walled carbon nanotubes with well-defined polystyrene by ‘click’ coupling, *J. Am. Chem. Soc.*, **2005**, 127, 14518–14524.
- 161 J. Chen, M.A. Hamon, H. Hu, Y. Chen, A.M. Rao, P.C. Eklund, R.C. Haddon, Solution properties of single-walled carbon nanotubes, *Science*, **1998**, 95–98.
- 162 B. Zhao, H. Hu, R.C. Haddon, Synthesis and properties of a water-soluble single-walled carbon nanotubes-poly(*m*-aminobenzene sulfonic acid) graft copolymer, *Adv. Funct. Mater.*, **2004**, 14, 71–76.

- 163 E. Bekyarova, M. Davis, T. Burch, M.E. Itkis, B. Zhao, S. Sunshine, R.C. Haddon, Chemically functionalized single-walled carbon nanotubes as ammonia sensors, *J. Phys. Chem. B*, **2004**, 108, 19717–19720.
- 164 B. Zhao, H. Hu, S.K. Mandal, R.C. Haddon, A bone mimic based on the self-assembly of hydroxyapatite on chemically functionalized single-walled carbon nanotubes, *Chem. Mater.*, **2005**, 17, 3235–3241.
- 165 Y. Zhang, A.A. Broekhuis, M.C.A. Stuart, T. Fernandez, P. Landaluce, D. Fausti, P. Rudolf, F. Picchioni, Cross-linking of multiwalled carbon nanotubes with polymeric amines, *Macromolecules*, **2008**, 41, 6141–6146.
- 166 H.Y. Ma, L.F. Tong, Z.B. Xu, Z.P. Fang, Functionalizing carbon nanotubes by grafting on intumescent flame retardant: nanocomposite synthesis, morphology, rheology, and flammability, *Adv. Funct. Mater.*, **2008**, 18, 414–421.
- 167 B. Zhao, H. Hu, A. Yu, D. Perea, R.C. Haddon, Synthesis and characterization of water soluble single-walled carbon nanotube graft copolymers, *J. Am. Chem. Soc.*, **2005**, 127, 8197–8203.
- 168 Y.P. Sun, W. Huang, Y. Lin, K. Fu, A. Kitaygorodskiy, L.A. Riddle, Y.J. Yu, D.L. Carroll, Soluble dendron-functionalized carbon nanotubes: preparation, characterization, and properties, *Chem. Mater.*, **2001**, 13, 2864–2869.
- 169 L. Tao, G. Chen, G. Mantovani, S. Yorkb, D.M. Haddleton, Modification of multi-wall carbon nanotube surfaces with poly(amidoamine) dendrons: synthesis and metal templating, *Chem. Commun.*, **2006**, 4949–4951.
- 170 D.E. Hill, Y. Lin, A.M. Rao, L.F. Allard, Y.P. Sun, Functionalization of carbon nanotubes with polystyrene, *Macromolecules*, **2002**, 35, 9466–9471.
- 171 Y. Lin, D.E. Hill, J. Bentley, L.F. Allard, Y.P. Sun, Characterization of functionalized single-walled carbon nanotubes at individual nanotube-thin bundle level, *J. Phys. Chem. B*, **2003**, 107, 10453–10457.
- 172 W. Huang, S. Fernando, L.F. Allard, Y.P. Sun, Solubilization of single-walled carbon nanotubes with diamine-terminated oligomeric poly(ethylene glycol) in different functionalization reactions, *Nano. Lett.*, **2003**, 3, 565–568.
- 173 D. Hill, Y. Lin, L. Qu, A. Kitaygorodskiy, J.W. Connell, L.F. Allard, Y.P. Sun, Functionalization of carbon nanotubes with derivatized polyimide, *Macromolecules*, **2005**, 38, 7670–7675.
- 174 Y. Lin, B. Zhou, K. A.S. Fernando, P. Liu, L.F. Allard, Y.P. Sun, Polymeric carbon nanocomposites from carbon nanotubes functionalized with matrix polymer, *Macromolecules*, **2003**, 36, 7199–7204.
- 175 J.J. Ge, D. Zhang, Q. Li, H. Hou, M.J. Graham, L. Dai, F.W. Harris, S.Z.D. Cheng, Multiwalled carbon nanotubes with chemically grafted polyetherimides, *J. Am. Chem. Soc.*, **2005**, 127, 9984–9985.
- 176 J. Gao, M.E. Itkis, A. Yu, E. Bekyarova, B. Zhao, R.C. Haddon, Continuous spinning of a single-walled carbon nanotube-nylon composite fiber, *J. Am. Chem. Soc.*, **2005**, 127, 3847–3854.
- 177 J. Gao, B. Zhao, M.E. Itkis, E. Bekyarova, H. Hu, V. Kranak, A. Yu, R.C. Haddon, Chemical engineering of the single-walled carbon nanotube-nylon 6 interface, *J. Am. Chem. Soc.*, **2006**, 128, 7492–7496.

Influence of material and processing parameters on carbon nanotube dispersion in polymer melts

G. R. KASALIWAL, T. VILLMOW,
S. PEGEL and P. PÖTSCHKE, Leibniz Institute of
Polymer Research Dresden, Germany

Abstract: Melt processing of polymer–carbon nanotube (CNT) composites is of great industrial importance for the large-scale production of composite materials and desired products. The properties of these composites greatly depend on the quality of CNT dispersion. In this chapter, a broad overview of the influence of material and processing parameters on the dispersion of multi-walled CNTs in thermoplastic polymer matrices during melt processing is provided. The results discussed here are based on small-scale batch mixers as well as on laboratory-scale continuous extruders. To analyse and quantify the state of dispersion, microscopic methods were applied.

Key words: dispersion, dispersion analysis, melt mixing, multi-walled carbon nanotubes.

4.1 Introduction

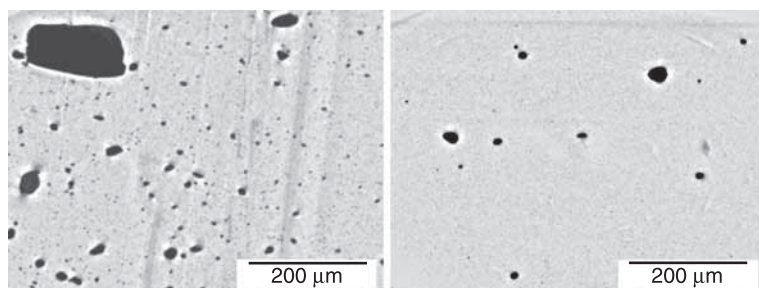
In the past few decades, extensive research and development have been carried out in the field of polymer composite production. On an industrial scale, melt processing has become the method of choice to incorporate colour pigments or reinforcement particles, for instance. Nowadays, a wide variety of melt compounding technology is available which is applicable to polymer-CNT composite production. In comparison to other composite production methods such as solvent casting, melt mixing is fast, economic, and relatively environmentally friendly. Melt processing extruders can produce composites from a few kilograms to a few tons per hour depending on their size and demand. For this purpose, single (direct incorporation) and multi-step (masterbatch dilution) processing routes mostly on continuously working compounders are employed. However, for smaller batches or special matrix systems, discontinuous processes are also used. The melt mixed composites can be directly processed to the desired products by means of injection or compression moulding, profile extrusion, blow moulding, and fibre spinning.

On an industrial scale, mostly multi-walled CNTs (MWCNTs) are used and therefore, this chapter focuses on MWCNTs which are introduced, for instance, to obtain electrically and thermally conductive and/or mechanically reinforced materials. However, achievement of the desired properties, especially mechanical enhancement of these composites, greatly depends on the extent of CNT

dispersion and distribution in the polymer matrix. Agglomerates above a certain size may act as stress concentrators and induce cracks and fracture.

The term ‘dispersion’ describes the process during which the smallest dispersible unit of an agglomerate is separated from it and is mixed in the host matrix system but is also used to characterize the achieved state of CNT separation. In our case, the smallest dispersible unit is an individual carbon nanotube in a polymer matrix. A good distribution is achieved when all available CNTs are uniformly arranged in the host matrix. During melt processing, the shear forces generated inside a mixing unit are supposed to cause dispersion and distribution of the CNTs in the polymer matrix. Practically, however, the aim of good dispersion and distribution cannot be achieved in all cases and in several scientific reports it is reported that complete dispersion of CNT agglomerates in polymer melts is difficult. Quite often the presence of undispersed agglomerates in composite materials is reported (Du *et al.*, 2004; Takase, 2007; Baets *et al.*, 2008; Masuda and Torkelson, 2008; Kasaliwal *et al.*, 2009; Micusik *et al.*, 2009; Prashantha *et al.*, 2009). The choice of processing conditions and base materials seems to have a big impact on dispersion. For example, in Fig. 4.1, several undispersed agglomerates can be seen in optical micrographs of polycarbonate with 1 wt% MWCNTs which are processed at different mixing speeds.

The difficulties in dispersing CNT in polymer melts are usually caused by strong van der Waals interactions, often in combination with physical entanglements between neighbouring tubes. The strength of van der Waals interactions in turn depends on the distance between the nanotubes and the physical or chemical nature of the surrounding medium. The entanglements and thus the agglomerate structure among other things depend on the structure of the support material and the catalyst arrangement. Especially in the case of fluidized bed materials for large-scale production, curved, entangled, and intertwined tubes can be generated due to imperfect growth. Such kinds of ‘as-produced’ CNT materials with primary agglomerates of high cohesive strength can make the preparation of composites a very interesting and challenging technological task.



4.1 Optical micrographs of polycarbonate melt compounded with 1 wt% MWNT under different conditions.

This chapter aims to provide an overview of the factors that can influence dispersion of MWCNTs during melt processing and is divided into five main sections. After the introduction, the second section deals with fundamental aspects of filler dispersion, as it is necessary to have an insight into the dispersion process. The state of the art of melt-processed polymer–MWCNT composites, along with the different methods that are employed to access filler dispersion, is discussed in the third section. The fourth section is based on small-scale lab studies on melt-processed composites where the influences of variation in material properties and in technological parameters such as mixing speed, temperature, and time on CNT dispersion are discussed, mainly for polycarbonate-based composites. Beside direct incorporation of MWCNTs in polymers for composite manufacturing, the masterbatch dilution method is also briefly considered. The fifth section deals with continuous melt mixing using a co-rotating twin-screw extruder, in which the influence of processing parameters such as screw profile, residence time, mixing speed, and throughput on CNT dispersion during masterbatch production and its dilution is reported on the examples of poly(caprolactone) and poly(carbonate).

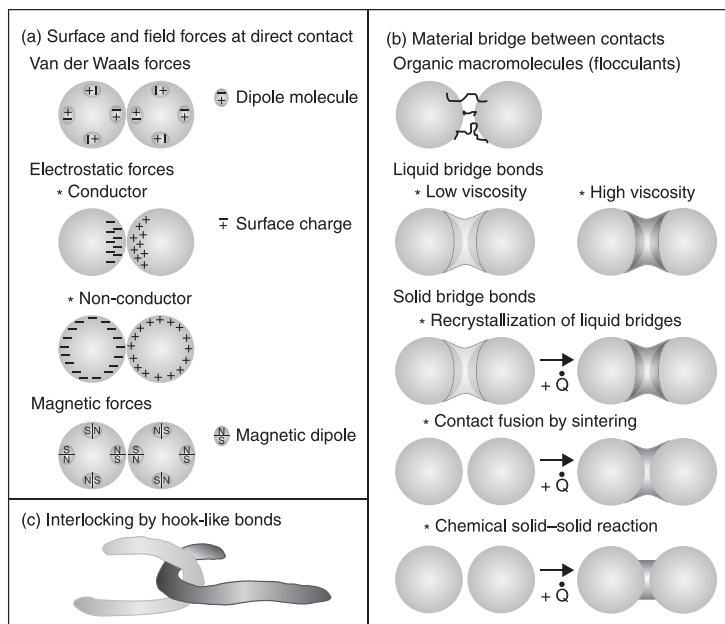
4.2 Fundamentals of melt mixing and filler dispersion

Generally, the problem of polymer–CNT composite production can be considered as a homogenization task where filler particles have to be distributed within a viscous medium. In the case of weak interactions between individual CNTs, this process can be classified as distributive mixing. However, as mentioned in the introduction, most CNT materials are delivered as primary agglomerates with remarkable strength. To achieve homogeneous CNT dispersion in polymer composites, the mixing process has to involve a dispersive component. More precisely, this means the mechanical agitation of the MWCNTs agglomerates has to enable their breakdown in size. Principally, the disintegration or dispersion of primary agglomerates can proceed by removal of individual MWCNTs from the agglomerate surface (erosion) or agglomerate breakage (rupture).

A simple theoretical model which is widely used in the literature considers the balance of external stress and agglomerate strength. Agglomerate breakage is assumed to take place if the stress generated by the polymer flow exceeds the agglomerate strength. To estimate the cohesive strength of agglomerates made up of convex-shaped particles, equations like the one proposed by Rumpf (Rumpf, 1970) can be used:

$$\sigma = (1 - \varepsilon) \cdot k \cdot \frac{F}{A} \quad [4.1]$$

The inter-particle adhesive forces (F) along with porosity (ε), the coordination number of particles forming the agglomerate (k) and the surface area of particles forming the agglomerates (A) are responsible for the cohesive strength of agglomerates. The inter-particle adhesive forces which hold particles together result in agglomerate formation and its growth and can be classified into three

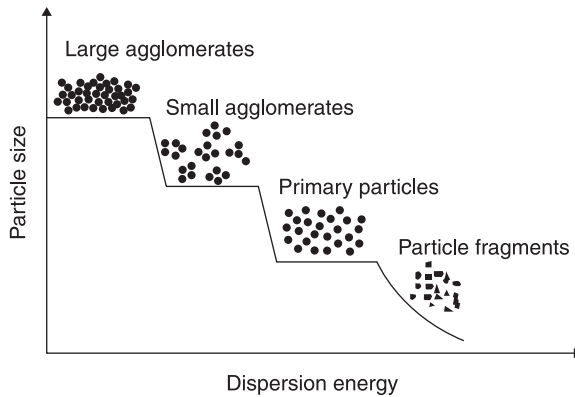


4.2 Illustration of different categories of particle adhesion. (Reprinted from Tomas, 2007, with permission from Elsevier.)

main categories. They are, namely, surface and field forces, material bridges, and interlocking (Rumpf, 1970; Schubert, 1979), schematically shown in Fig. 4.2.

A high cohesive strength of agglomerates results in higher resistance against particle separation and dispersion in the matrix system. In the case of dry fillers, surface and field forces are predominantly responsible for the agglomerate strength, whereas for partially wetted or infiltrated agglomerates, liquid bridges are the main influence. Although the forces like van der Waals are considered very weak intermolecular forces, they become quite significant at the nanoscale due to the very high specific surface area of the material. For instance, as the particle size decreases, van der Waals forces exceed the gravitational forces by several orders of magnitude (Tomas and Kleinschmidt, 2009). Further, if liquid bridges are formed between incomplete wet primary particles in partially infiltrated agglomerates, the agglomerate strength increases tremendously. However, if the agglomerates are fully infiltrated, then agglomerate strength becomes negligible (Schubert, 1979).

To achieve uniform dispersion of filler agglomerates in a polymer melt, it is necessary to overcome their agglomerate strength. During melt processing, shear and elongational stresses generated inside a mixing unit provide the required energy for the size reduction of filler agglomerates. In Fig. 4.3, a scheme describing the reduction in the particle size versus the required energy is shown. Large



4.3 Schematic showing reduction in particle size with increasing dispersion energy. (Reprinted from Wang, 2003, with permission from Elsevier.)

agglomerates are broken down into smaller ones and then to primary particles as the dispersion energy increases. If the applied energy is too high, the particles can be damaged (as e.g. breakage of nanotubes).

The process of size reduction of filler agglomerates as shown in Fig. 4.3 consists of several stages during dispersive melt mixing operations. These stages are, namely, filler incorporation (in melt), wetting and infiltration of filler (by polymer melt), followed by dispersion, distribution, and flocculation (of filler in the polymer melt). In a melt mixing operation, all these stages, briefly described in the following, run parallel to each other.

As the filler is incorporated in a polymer melt, the filler surface comes into contact with the melt and the melt wets the filler surface. Wetting of a surface is defined as the replacement of a solid–air interface with a solid–liquid interface (Parfitt, 1973). Wetting can be further classified into three types, namely, adhesional, immersional, and spreading wetting. A solid is regarded as completely wet with a liquid if the contact angle is zero (Jaycock, 1973).

As soon as the filler surface is wetted, the melt infiltrates into the filler agglomerate. It is reported in the literature that material parameters like porosity or packing density of agglomerates, melt viscosity, melt molecular weight, and branching of the polymer can significantly affect melt infiltration into agglomerates and thereby the dispersion of agglomerates. Yamada *et al.* (1997, 1998) found that a matrix with a lower melt viscosity infiltrates faster into agglomerates of carbon black (CB) than a high melt viscosity matrix, and, below a critical packing density, agglomerates exhibited high erosion rates. Similar findings have been reported for CaCO_3 agglomerates by Levresse *et al.* (1999). While studying the intercalation of nano-clay in polystyrene by annealing, Vaia *et al.* (1995) reported faster intercalation when using a matrix with lower molecular weight and melt viscosity.

Furthermore, Roland *et al.* (2004) reported that dispersion of CB was worse in branched poly(isobutylene) than in linear poly(isobutylene) even when applying high shear stresses.

Following the stage of melt infiltration, the particles are subjected to dispersion. In this stage, the size of filler agglomerates is reduced which is attributed to the two main dispersion mechanisms of rupture and erosion. Rupture mechanism is a fast process during which the large agglomerates are broken down into smaller ones in a short time. In erosion, large agglomerates are reduced to smaller ones by the removal of single particles, aggregates, or fragments and clusters from the surface which needs a comparatively much longer time. The critical shear stress required for dispersion by the erosion process is much lower than the one required for the rupture process. The ratio of applied shear stress and cohesive strength of agglomerates could be decisive in governing the speed of agglomerate dispersion. Thus, the step of filler dispersion is considered to be very important as it determines the rate at which size reduction of the filler in the polymer melt occurs (Manas-Zloczower, 1994).

These dispersion mechanisms have been extensively investigated for fillers such as carbon black (CB), silica, calcium carbonate (CaCO_3), etc. and are reported in the literature (e.g. Bolen and Colwell, 1958; Kao and Mason, 1975; Powell and Mason, 1982; Shiga and Furuta, 1985; Rwei *et al.*, 1990; Rwei *et al.*, 1991; Rwei *et al.*, 1992; Hansen *et al.*, 1998). Furthermore, several models are proposed to describe the dispersion mechanism as in e.g. (Tadmor, 1976; Manas-Zloczower *et al.*, 1982; Manas-Zloczower and Feke, 1989; Coran and Donnet, 1992; Seyvet and Navard, 2001; Potente *et al.*, 2002; Lozano *et al.*, 2003; Kasaliwal *et al.*, 2010a).

As the mixing process continues, the particles separated from agglomerates are distributed in the polymer matrix. If the melt state is maintained for a long time, it is possible that the well-distributed particles can flocculate to form clusters; this process is also known as secondary agglomeration. This effect is quite well known for epoxy and elastomer systems, but seldom addressed for much higher viscous thermoplastic melts (Lellinger *et al.*, 2008; Pegel *et al.*, 2008, see also Chapter 7).

4.3 Review of the literature

Due to the high relevance to industrial applications, melt processing of polymer-MWCNT composites is being extensively investigated and reported in the literature. Nevertheless, comprehensive and reliable studies on relationships between processing and structure of polymer-CNT composites can rarely be found. Many studies simply focus on reporting about the physical properties of the manufactured composites and interpret the results with qualitative statements about CNT dispersion.

Morphological investigations are usually based on microscopic methods such as light microscopy (LM), scanning electron microscopy (SEM), atomic force microscopy (AFM), and transmission electron microscopy (TEM), to characterize

the state of dispersion. Nevertheless, apart from a few examples available in the literature, these tools are seldom used to systematically investigate the influence of processing conditions on the state of dispersion. Accessing the quality of filler dispersion is very important to differentiate the impact of different processing conditions on dispersion; but in most cases this is only done qualitatively and not by using quantitative techniques. In the following, some examples from the literature are discussed where such tools were used to draw useful conclusions on parameters influencing the state of dispersion.

For instance, Leer *et al.* (2006) discussed the state of MWCNT dispersion in systems based on polycarbonate produced using a micro-single screw extruder. Based on optical micrographs analysed using a normalized grey scale distribution, they found that longer compounding time achieved by up to three processing cycles yielded better MWCNT dispersion. Andrews *et al.* (2002) characterized the state of dispersion of MWCNTs in polypropylene by applying LM and introducing a dispersion index based on an assignment of appearance on a scale between 1 and 10. They reported that the state of dispersion improved drastically as the mixing energy was increased during melt compounding in a batch mixer by increasing either mixing speed or mixing time. Further, from TEM investigations on nanotubes extracted from the composite, they concluded progressive tube shortening with increasing mixing energy. Lin *et al.* (2006) investigated the state of MWCNT dispersion in polycarbonate for composites produced by a masterbatch dilution step in different lab-scale mixers. They applied TEM investigations to qualitatively characterize the state of MWCNT dispersion and recommended a mixer with the best mixing efficiency. In addition, tubes extracted from the composites were observed using AFM and their length distribution was evaluated in order to quantify the effect of breakage, which was found to be small and similar for all mixers.

A detailed study was reported by Kasaliwal *et al.* (2009) where mixing conditions were varied for polycarbonate with MWCNT using a factorial design. The effects of melt temperature and mixing speed on dispersion were assessed by a dispersion index obtained from LM images.

Villmow *et al.* (2008b) studied the influence of MWCNT content, screw profile, temperature profile, and rotation speed during twin-screw extrusion using a Berstorff ZE 25 extruder on the dispersion of poly(lactic acid) (PLA) masterbatches containing 15 and 7.5 wt% MWCNTs and samples diluted from these. From LM, a dispersion index and the number of agglomerates per mm² were assessed and TEM was used to study MWCNT dispersion and network formation at the sub-micron scale. High rotation speed (500 rpm) that still ensures a certain residence time of the melt, combined with a screw profile containing mainly mixing elements was found to be highly convenient to disperse and distribute the MWCNT in the PLA matrix as well as during masterbatch production as the dilution step. The temperature profile showed less influence. Nonetheless, an increasing temperature profile resulted in slightly better nanotube dispersion.

The morphological characterization of composites using microscopy techniques gives a direct visual impression of the state of CNT dispersion, even if a 3D structure is visualized using 2D images. Nevertheless, these methods have certain advantages and drawbacks. LM is the easiest method and gives an excellent overview of the micron-scale state of dispersion but has limitations in accessing submicron-size particles. SEM and AFM give general overviews of the state of dispersion on both micron and submicron scale. TEM gives an excellent insight into the state of filler dispersion and distribution on the submicron scale. However, due to time-consuming sample preparation, TEM is only rarely performed. Nevertheless, with the help of proper image-processing techniques and different statistical approaches, valuable quantitative analysis, even deducing on the 3D structure, can be performed to characterize the state of dispersion at all length scales. In this regard, Chapter 9 of this book provides a useful overview of the application of image analysis methods for the quantitative description of dispersion, distribution, and orientation of nanotubes.

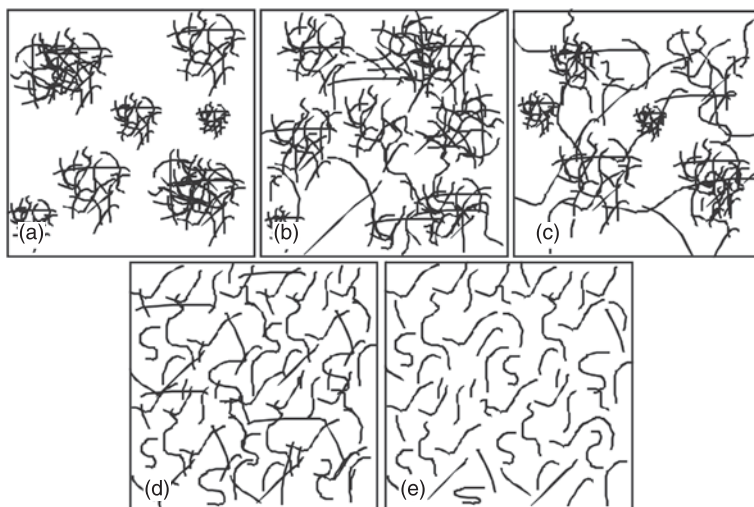
Apart from morphological investigation, changes in composite properties are often used to characterize the quality of CNT dispersion. Of these indirect methods, especially melt rheological and electrical resistivity measurements are quite commonly employed. Melt rheology reflects the state of network formation between the nanotubes and polymer chains which enhance elastic properties and induces changes in the melt viscosity of the matrix polymer especially at low frequencies/shear rates as described in detail in Chapter 15 of this book. In addition, several examples (Pötschke *et al.*, 2002; Du *et al.*, 2004; Huang *et al.*, 2006; Fan and Advani, 2007) can be referred to. As well as oscillatory and steady state measurements in shear, creep recovery experiments are found to give sensitive information about the state of dispersion. At longer recovery times, higher storage compliance is observed for systems which are better dispersed (Triebel *et al.*, 2010).

Quite often also, electrical percolation thresholds or achieved conductivity values are used as a measure of the state of dispersion. At a given CNT content, as soon as enough separated tubes become available for electrical network formation, percolation occurs. As more nanotubes are involved in the network, conductivity of the composites further increases before levelling off. Thus, an increase in electrical conductivity can be correlated with an improvement in dispersion, at least in a certain range. An example using dielectric spectroscopy is given by Pötschke *et al.* (2003), where polycarbonate-based composites were processed in a small-scale mixer under different mixing speeds and times and, depending on these conditions, the MWCNTs were either percolated or not. The influence of mixing conditions was great near the percolation threshold and diminished with increasing nanotube concentration. Also the study by Kasaliwal *et al.* (2009) considers the effect of mixing conditions on the electrical behaviour and relates the resistivity to the macro dispersion index assessed by quantitative analysis of LM micrographs. Interestingly, even at quite low dispersion indices,

the composites with only 1 wt% MWCNT were already conductive. This indicates that also bad dispersion states despite big agglomerates may lead to composites with high conductivities. Electrically conductive networks needed for electrical percolation can be formed at lower CNT amounts at better dispersion but can also be formed from connected agglomerates. Different possible scenarios are illustrated in Fig. 4.4. Thus, the use of electrical percolation or electrical values is equivocal for assessing the state of dispersion.

Based on former investigations with CB, Le *et al.* (2009) presented an online technique to characterize the state of CNT dispersion during compounding with rubber (see also Le *et al.* 2004). Here the electrical conductance is directly measured in a batch mixer. The trends in on-line conductance followed the values measured off-line and were closely related to the state of dispersion observed microscopically.

Another method used in the literature is Raman imaging, where the intensity of the G-band was recorded for $40 \times 40 \mu\text{m}$ spots and the standard deviation of that map was correlated to the quality of the CNT dispersion (Du *et al.*, 2004). Thereby, differences in dispersion of wet and dried SWCNT in PMMA could be assessed. Some authors have employed wide angle X-ray scattering (WAXS) (McNally *et al.*, 2005) and small angle X-ray scattering (SAXS) (Pujari *et al.*, 2009) investigations to characterize the state of MWCNT dispersion. Brühwiler *et al.*



4.4 Sketches hypothesizing different arrangements of nanotubes and their agglomerates illustrating percolated (b, c, d) and not percolated (a, e) structures: (a) highly agglomerated structure; (b) cluster-cluster percolation; (c) network consisting of small agglomerates and dispersed nanotubes; (d) network of well-dispersed nanotubes; (e) completely dispersed nanotubes not forming a network.

(2010) recently presented another example using SAXS, where on injection-moulded plates position-resolved average SAXS intensities were obtained for different scattering vectors q . The homogeneity of the intensity distribution sensitive to nanotubes was assigned to the nanotube dispersion, showing agglomerates of MWCNT in PC at higher loadings. Recently, in some reports, differential scanning calorimetry (DSC) was used to qualitatively differentiate states of dispersion. The nucleation action of nanotubes in a crystallizable polymer matrix is proportional to the amount of nanotube surface. Thus, at better dispersions, a higher surface is available for crystallization and the melting enthalpy was found to be higher (Masuda and Torkelson, 2008; Villmow *et al.*, 2008b; Pujari *et al.*, 2009).

4.4 Batch compounding using small-scale mixers

Batch compounding in small-scale mixers is very helpful in determining the factors that can influence CNT dispersion. The main advantage of using small-scale mixers is that a small material amount is needed and these mixers can be easily handled. Thus, a broad variety of mixtures and processing parameters can be investigated over short time scales. In this section some important relationships between different melt processing conditions as well as the choice of base materials on the CNT dispersion are summarized. The results obtained are helpful for understanding the scientific background about ongoing dispersion processes and to have guidelines for larger mixing scales.

The results presented originate from experiments using a DACA microcompounder. The assembly represents a conical twin screw extruder but has a bypass and a chamber volume of only 4.5 cm³. The design of this kind of compounder allows the variation of the technological parameters' mixing time, speed and temperature.

To obtain empirical relationships or to rate the quality of different composites, the state of CNT dispersion has been investigated by means of LM and TEM. As described in Chapter 9, thin sections were prepared from extruded strands and at least six light micrographs have been used to evaluate the area ratio of undispersed agglomerates A_A (area of agglomerates related to the image area) and the degree of dispersion D_{LM} . From at least five TEM images the degree of dispersion D_{TEM} as well as the distribution coefficient Q_p were derived. For some sets, the particle size distribution (number of agglomerates in different size classes) was evaluated and the mean circle equivalent diameter x_{50} was determined.

4.4.1 Processing of polycarbonate with different multi-walled carbon nanotube (MWCNT) materials

The properties of MWCNT materials produced by different manufacturers can vary significantly. This variation is mainly concerning their purity, packing density or porosity of agglomerates, length and diameter distribution of tubes, size

Table 4.1 Characteristic features of MWCNTs from different manufacturers

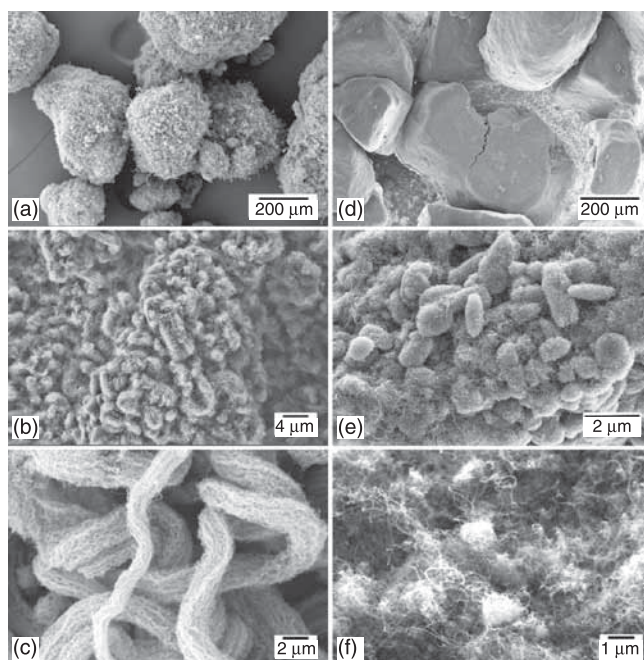
	Nanocyl 7000	Baytubes C150 HP	Ts-Na	Baytubes C150 P	FutureCarbon	Graphistrength C100
Carbon purity* (%)	90	99	>80%	95	90	90
Tube lengths* (μm)	1–1.5	1–10				0.1–10
Tube diameters* (nm)	9.5	1–15	<10	5–20		10–20
Bulk density* (kg/m^3)	66			130–150	28	50–150
Packing density	0.05	0.2	0.06			
Agglomerate size† (x_{90} , x_{50}) (μm)	Over 675,‡	610, 282		485, 314 ²	62, 29 ²	501, 302 ²

* Manufacturer's datasheets. † From Krause *et al.* (2010). ‡ Not measurable. Blank space: data unavailable. Ts-Na = Tsinghua-Nafine Nano-Powder Commercialization Engineering Center, Beijing, China.

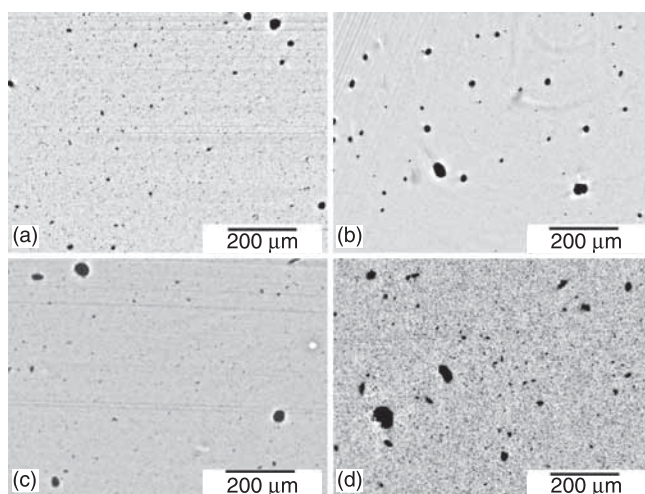
distribution of produced agglomerates, or structure of the agglomerates themselves. In Table 4.1, some of these characteristic features of MWCNT materials from different manufacturers are summarized. In Fig. 4.5, SEM micrographs of two of these as-received materials are shown which differ in agglomerate size, surface roughness, and substructure. When looking inside the fractured surface of agglomerates, in both materials, a substructure was observed revealing smaller agglomerates. The size of these small agglomerates could be dependent on the length of the nanotubes. At higher magnifications, the agglomerates can appear to have a combed yarn structure (as in Fig. 4.6 (a) for Nanocyl NC 7000) or they can indicate a bird's nest structure (as in case of Fig. 4.6 (b) for Baytubes® C150 HP).

MWCNT materials, namely, Nanocyl NC7000, Baytubes® C150 HP, and Ts-Na (two lots, delivered at different dates), were melt compounded with polycarbonate under identical conditions using the DACA microcompounder. Representative LM and TEM micrographs of these composites are shown in Figs 4.6 and 4.7, respectively. Such images were analysed to obtain the degrees of dispersion D_{LM} and D_{TEM} as well as the distribution coefficient Q_p . The corresponding results are summarized in Table 4.2 (for details, see Chapter 9).

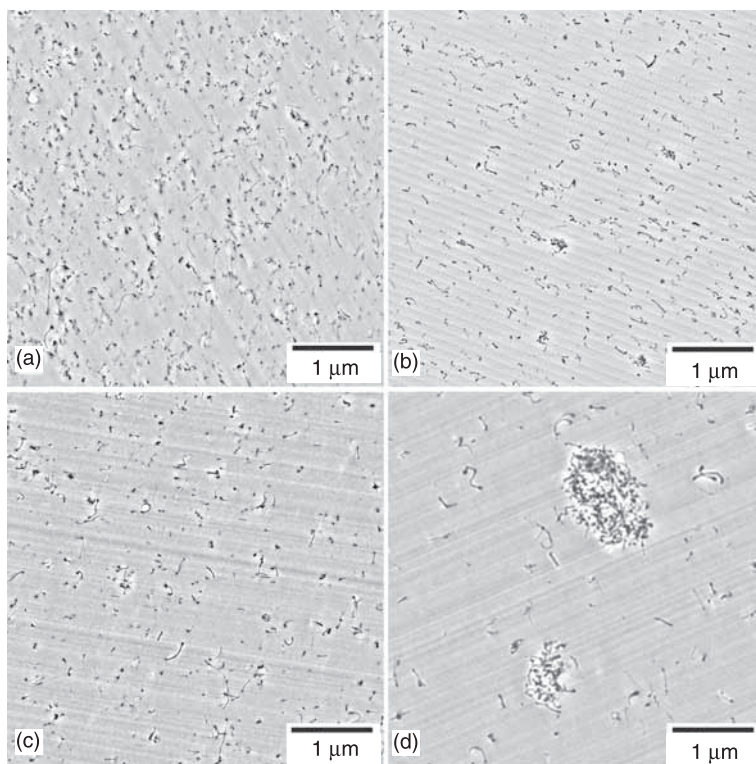
The microscopy images and the analysis indicate that Nanocyl NC7000 can be better dispersed than the other CNT materials, whereas the second lot of Ts-Na showed the worst dispersion. The reason for better dispersability of a nanotube material cannot be attributed to one specific factor but it is collectively based on several factors such as differences in internal morphology (see Fig. 4.5), packing



4.5 SEM images of MWCNT materials from different manufacturers shown at different magnifications: (a, b, c) Nanocyl NC 7000 (from Nanocyl S.A., Sambreville, Belgium); (d, e, f) Baytubes C150 HP (from Bayer MaterialScience AG, Leverkusen, Germany) (reproduced from Villmow *et al.*, 2010).



4.6 Optical micrographs of PC composites containing 1 wt% MWCNT melt compounded in a DACA microcompounder at 280°C, 50 rpm, 15 min.: (a) Nanocyl NC 7000; (b) Baytubes C150 HP; (c) Ts-Na (1st lot); (d) Ts-Na (2nd lot), section thickness 15 μm.



4.7 TEM images of PC composites containing 1 wt% MWNT: (a) Nanocyl NC 7000; (b) Baytubes C150 HP; (c) Ts-Na (1st lot); (d) Ts-Na (2nd lot); (a, c, and d reproduced from Pegel *et al.*, 2008).

Table 4.2 Quantification of the state of MWCNT dispersion (from Figs 4.6 and 4.7) using degrees of dispersion D_{LM} and D_{TEM} and distribution coefficient Q_p (based on TEM)

MWNT type	D_{LM}^*	D_{TEM}	Q_p
Nanocyl NC7000	0.73 ± 0.16	0.84 ± 0.28	1.06 ± 0.01
Baytubes C150 HP	0.68 ± 0.09	0.33 ± 0.06	1.16 ± 0.01
Ts-Na (1st lot)	0.80 ± 0.15	0.37 ± 0.14	1.13 ± 0.03
Ts-Na (2nd lot)	0.55 ± 0.26	0.16 ± 0.08	1.28 ± 0.12

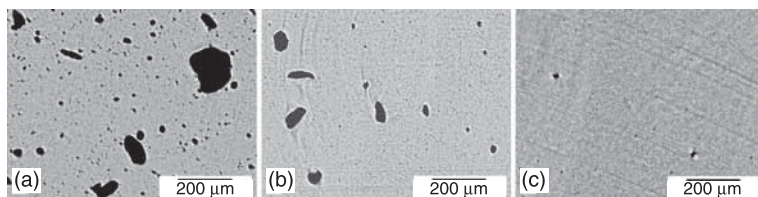
* For the calculation of degree of dispersion, packing density values of MWCNT as given in Table 4.1 are used.

density, and tube dimensions which depend on synthesis conditions. Slight deviations in manufacturing conditions during synthesis can significantly affect the dispersability as evidenced in the two lots of Ts-Na where identical morphological features of the single nanotubes (length and diameter) were found (Pegel *et al.* 2008). Possibly,

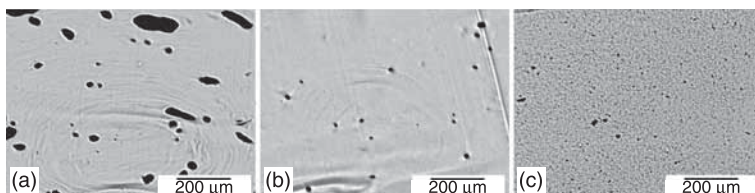
small differences in the content of impurities and available surface groups due to changed nanotube growth conditions may also be contributory factors.

Interestingly, this sensitivity of dispersability and dispersion obtained on the characteristic features of the starting primary nanotube agglomerates is rarely discussed in the literature. Even the variation in diameter or the length of nanotubes might influence their dispersability. To address this issue in more detail, polycarbonate was melt compounded with 1 wt% of different MWCNT materials from the same producer, having approximately the same tube length but varying in the tube diameter (from ca. 5 to 10 nm), using the DACA microcompounder. As illustrated in Fig. 4.8, the dispersion of the MWCNT improves as the MWCNT diameter (measured using TEM investigations) is increased, indicating better dispersability of the thicker tubes. As thinner MWCNTs are less stiff than thicker ones, they are able to be much more entangled with neighbouring tubes and develop stronger van der Waals interactions. In addition, as per the Rumpf equation (Rumpf, 1970), the strength of agglomerates is inversely proportional to the radius of the constituting tube, thinner tubes form agglomerates with higher strength.

The lengths of MWCNTs can be varied either during synthesis or during post-treatment. For the latter case, ball milling is quite often used. To study the effect of variation in MWCNT length on dispersion, MWCNT NC 7000 as delivered was subjected to ball milling for different times and these materials were melt compounded with PC. Optical micrographs of composites with 4 wt% nanotubes are shown in Fig. 4.9. The agglomerate area and size significantly decreased with shortening the tubes, whereas at the highest milling time a huge number of very small agglomerates were observed. It has to be taken into account that during ball milling also a compaction of agglomerates can occur, so that possibly the remaining smaller agglomerates are much more compacted and more difficult to disperse into single tubes on the sub-micron scale. This is indicated by the fact that the better dispersed ball milled nanotubes showed worse electrical properties than the untreated ones. An additional effect may arise from surface groups generated by the ball milling shortening.



4.8 Optical micrographs of PC with 1 wt% MWCNT having different external diameter distributions (material and data supplied by Nanocyl S.A.); (a) 5.4 ± 1.6 nm, C purity 89%, $A_A = 8.03\%$; (b) 6.9 ± 1.9 nm, C purity 98.7%, $A_A = 1.8\%$; (c) 9.9 ± 4.1 nm, C purity 90%, $A_A = 0.3\%$. Composites produced at 280°C, 50 rpm, 15 minutes, section thickness 15 μm . A_A , area ratio.



4.9 Optical micrographs of PC with 4 wt% MWCNT based on Nanocyl N7000; (a) Nanocyl NC 7000, length x_{50} 1300 nm, $A_A = 5.87\%$; (b) ball milling for 3 hours, length x_{50} 360 nm, $A_A = 0.856\%$; (c) ball milling for 10 hours, length x_{50} 200 nm, $A_A = 1.32\%$. Composites produced at 280°C, 50 rpm, 15 minutes, section thickness 5 μm .

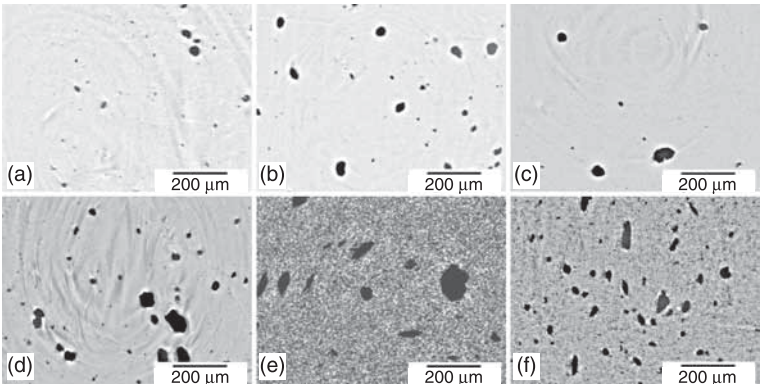
A qualitative improvement in dispersion was also reported when using shear pulverized versus as produced MWCNTs in melt compounding with polypropylene (Masuda and Torkelson, 2008; Pujari *et al.*, 2009).

4.4.2 Dispersability of MWCNTs in different polymers

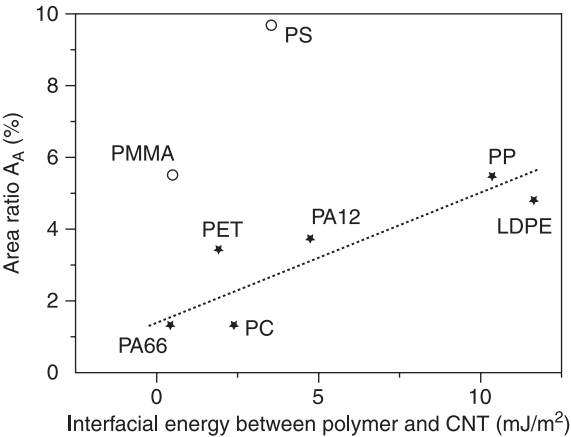
Polymers differ in several ways, such as chemical structure of the backbone chain, side groups, their amorphous or crystalline nature, surface energies, etc. Even for a given polymer, there could be variations in matrix molecular weight and therefore in melt viscosity at a given temperature. Collectively, these factors have an impact on CNT dispersion in different matrices. It can be assumed that the state of macrodispersion of nanotubes does not change upon solidification, even if in partially crystalline polymers changes in the nanoarrangement may occur. In this study, different polymers such as polypropylene (PP), poly methyl methacrylate (PMMA), polycarbonate, polystyrene (PS), polyamide 66 (PA66), polyamide 12 (PA12), low density polyethylene (LDPE), and poly(ethylene terephthalate) (PET) were melt compounded with 1 vol.% MWCNT (Nanocyl NC 7000, sieved agglomerate size fraction of 100–200 μm). To achieve similar applied shear stresses during compounding, the mixing temperature of each polymer was adjusted in a way that, at a given shear rate (of 300 rad/s), the melt viscosity was the same (500 Pas). Optical micrographs illustrating the state of MWCNT agglomerate dispersion in these polymers are shown in Fig. 4.10.

Although the applied shear stress was the same in all cases, tremendous differences in the agglomerate dispersion were observed. Apart from melt viscosity, interfacial energy between polymer and nanotubes is a property that may influence MWCNT dispersion. In order to verify that possible influence, the agglomerate area ratio is plotted versus interfacial energy (taken from the literature¹) in

¹ The interfacial energies were calculated by harmonic mean equation. Surface energies and their polar and dispersive parts were taken from <http://www.surface-tension.de/solid-surface-energy.htm>. The surface energy values of CNT are taken from Barber *et al.* (2004) and were assumed to be independent of temperature.



4.10 Optical micrographs of 1 vol% MWCNT composites produced by using (a) PA66 (265°C); (b) PET (290°C); (c) PC (300°C); (d) PA12 (220°C); (e) PP (200°C); and (f) LDPE (170°C). Composites produced at 100 rpm, 5 min., processing temperature indicated beside the name of the polymer, section thickness 20 μm.



4.11 Area ratio of undispersed CNT agglomerates A_A versus interfacial energy (dotted line is only a guide).

Fig. 4.11. Interestingly, no simple relationship is found, even if there is a general tendency for the area ratio to increase with interfacial energy. Excluding PMMA and PS, the tendency is clearer.

So far, the deviation of PS and PMMA is not easily explainable but may be attributed to the high stiffness of PS chains or the bulky methyl methacrylate side groups in PMMA, which hinder the infiltration of these polymer melts into the primary agglomerates. These results indicate that interfacial energy may not be the only influencing factor (next to viscosity) on macro scale dispersion. Possibly,

in addition, chemical affinity and steric aspects of molecular structure have to be considered.

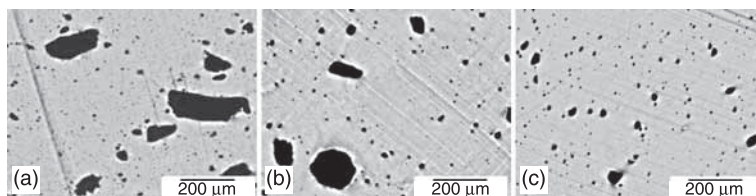
4.4.3 Incorporation of MWCNTs in polycarbonates with different melt viscosities

During melt compounding, the shear stresses applied to the primary agglomerates are important for their dispersion. Increasing melt viscosity results in higher shear stresses on agglomerates and can lead to faster size reduction of fillers as compared to low viscosity matrices. Several studies concerning the influence of polymer matrix viscosity on the dispersion of layered silicates (nanoclay) support this argument (Fornes *et al.*, 2001; Gianelli *et al.*, 2005; Chu *et al.*, 2007).

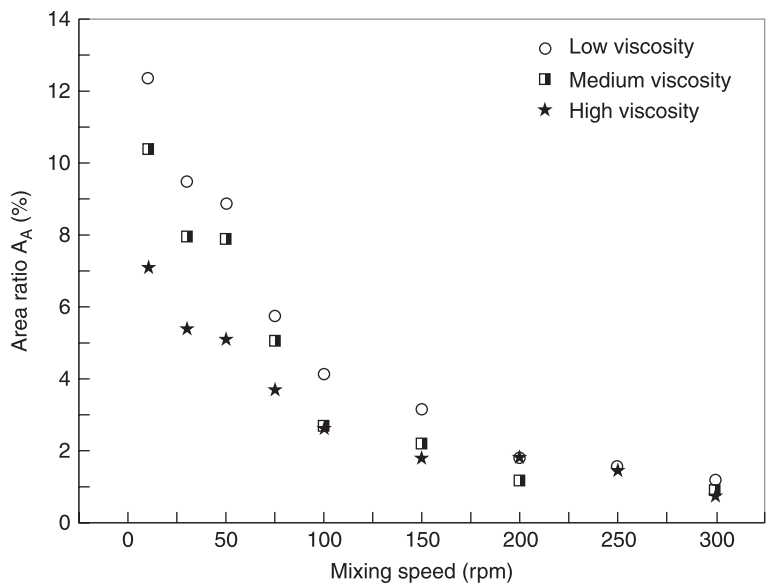
In composites with carbon nanotubes, in addition, the internal porous structure of the primary agglomerates has to be considered, in which the stage of melt infiltration is very important. Infiltration is enhanced when using low viscosity polymer melts. If the melt infiltration is suitable, the agglomerates can be significantly weakened and thus lower shear stresses are needed for their dispersion. Infiltrated agglomerate surface layers enhance the peripheral erosion of agglomerates. Thus, the effects of high and low viscosity counteract on the generation of high stresses and enabling good infiltration, and that balance is also dependent on the nanotube agglomerate structure.

In order to investigate the influence of matrix viscosity on dispersion, three polycarbonates of different molecular weight and thereby melt viscosity at a given temperature were melt mixed with 1 wt% Baytubes® C150 HP. Different mixing speeds were employed to generate different applied shear stresses on filler agglomerates. In Fig. 4.12, optical micrographs of some of these composites are shown.

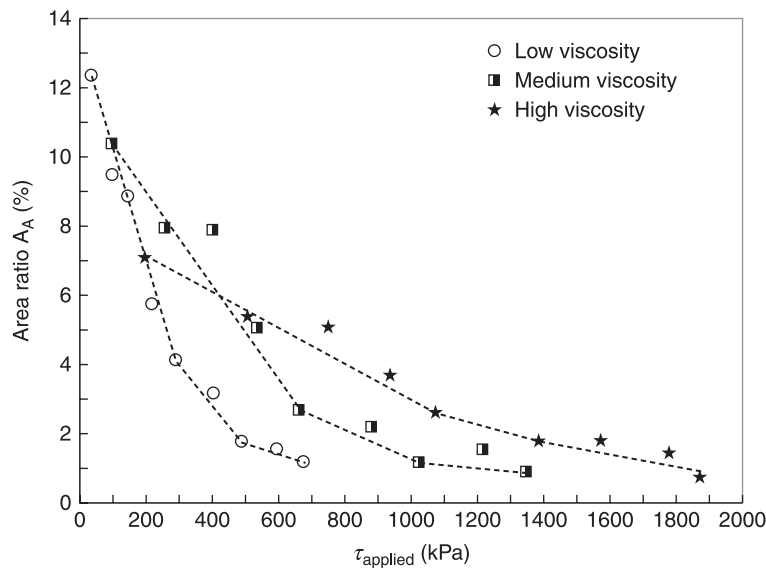
In Figs 4.13 and 4.14, the agglomerate area ratio of these composites (prepared at different mixing speeds) is plotted versus mixing speed and applied shear stress, respectively. At lower mixing speeds up to 150 rpm, dispersion is better in the high viscous matrix than in lower viscosity matrices as applied shear stresses are higher.



4.12 Optical micrographs of polycarbonate with 1 wt% MWCNT (Baytubes C150 HP) where the polycarbonate differs in melt viscosity; (a) low melt viscosity (Makrolon 2205); (b) medium melt viscosity (Makrolon 2600); (c) high melt viscosity (Makrolon 3108). Composites prepared at 280°C, 50 rpm, 5 min., section thickness 20 μm.



4.13 Area ratio A_A vs. mixing speed for composites of PCs with different viscosity and 1 wt% Baytubes C150 HP (adapted from Kasaliwal *et al.*, 2010b).



4.14 Area ratio A_A vs. applied shear stress for composites of PCs with different viscosity and 1 wt% Baytubes C150 HP (adapted from Kasaliwal *et al.*, 2010b).

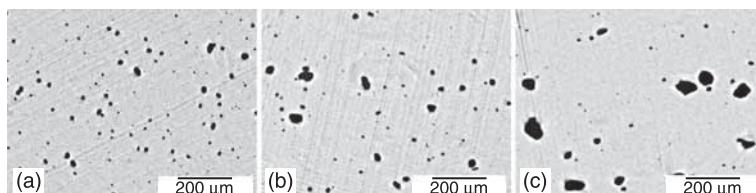
However, as the mixing speed increases, differences in the state of dispersion narrow and vanish at high mixing speeds, although big differences in applied shear stress exist. When plotting the area ratio versus the applied shear stress, it becomes obvious that (above 400 kPa) to generate a certain agglomerate area higher stresses were applied for the high viscous matrix. To generate the same (low) agglomerate ratio, much less shear stress was needed in the case of low viscous matrix, indicating the important role of the infiltration process in these composites.

In a rubber MWCNT system, Le *et al.* (2009) mentioned similar observations whereas lowering of the melt viscosity of natural rubber till an optimum level was found to improve the nanotube dispersion.

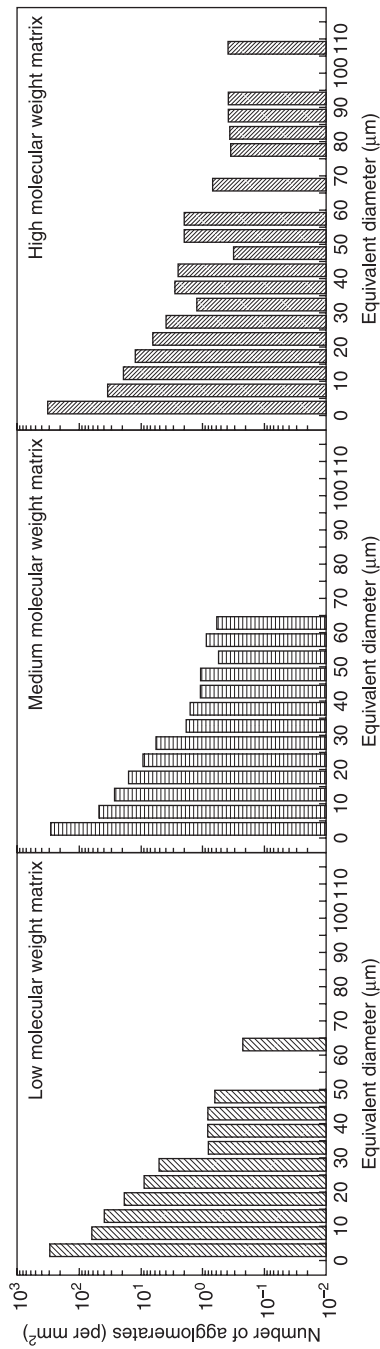
4.4.4 Incorporation of MWCNTs in polycarbonates with different molecular weights

Even if the matrix molecular weight is related to the melt viscosity of polymers, it was important to know in context with the important agglomerate infiltration step whether there is an additional influence of molecular weight besides viscosity on dispersion. To observe that effect on MWCNT dispersion, it is necessary to adjust the temperature of the given polymer to have similar melt viscosities. Therefore, the three polycarbonates used previously were now melt compounded at temperatures adjusted to generate the same melt viscosity. Thereby, comparable shear stresses were applied from the different polycarbonates on the primary agglomerates. As illustrated in Figs 4.15 and 4.16, with increasing molecular weight also the size of undispersed agglomerates increases.

The results show that the molecular weight of matrix clearly has an additional influence on the size of undispersed agglomerates whereby low molecular weight results in smaller and less numerous particles. This can be attributed to the much faster infiltration of polymer chains with lower molecular weight into the filler agglomerates thereby making them weaker and facilitating the dispersion process.



4.15 Optical micrographs of polycarbonate with 1 wt% MWCNT (Baytubes C150 HP) where the polycarbonate differs in molecular weight but shows the same melt viscosity: (a) low molecular weight (Makrolon 2205, 260°C); (b) medium molecular weight (Makrolon 2600, 290°C); (c) high molecular weight (Makrolon 3108, 310°C). Composites prepared at 100 rpm, 5 min., temperatures adjusted to obtain a zero shear viscosity of about 500 Pas, section thickness 20 μm.

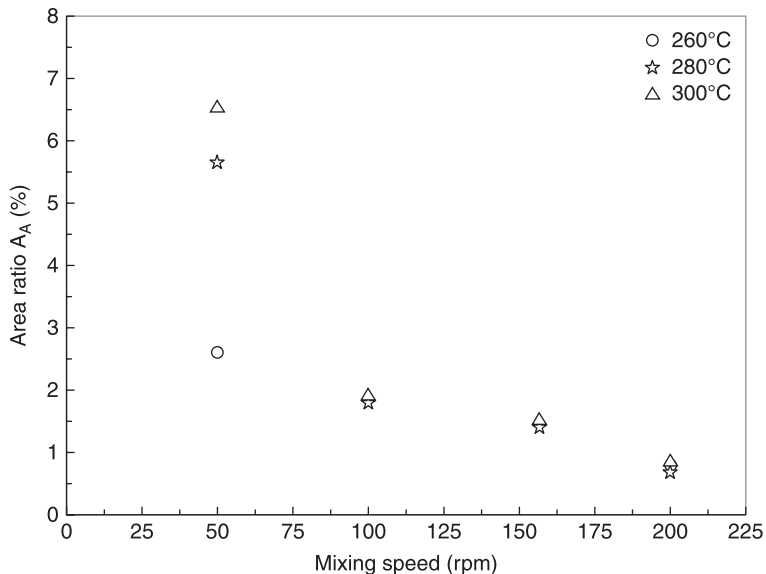


4.16 Particle size distribution in composites of polycarbonate with 1 wt% MWCNT (Baytubes C150 HP) where the polycarbonates differ in molecular weight but have the same melt viscosity (adapted from Kasaliwal *et al.*, 2010b).

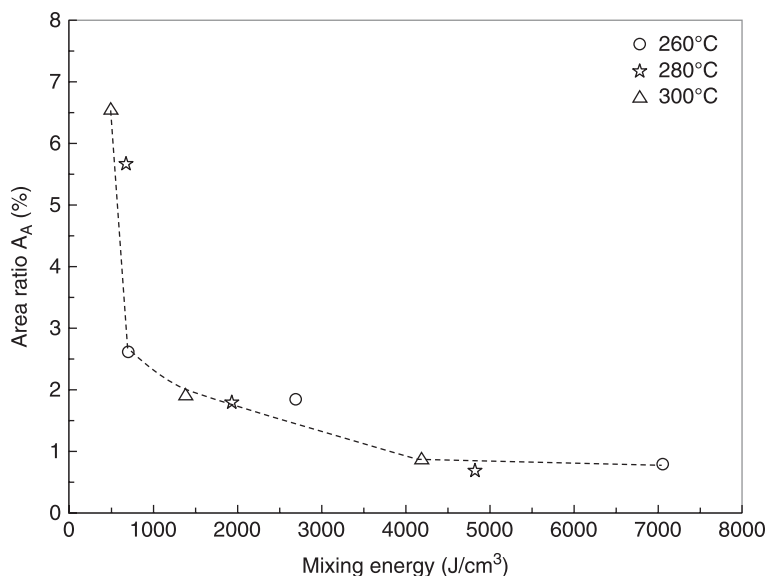
4.4.5 Influence of processing parameters on the dispersion of MWCNTs in polycarbonate

In small-scale batch mixing, the important process parameters that can be varied are rotation speed, mixing time, melt temperature, and degree of filling. These parameters affect the shear rate, residence time, melt viscosity, and by that shear stresses or mixing energy provided to the system. For a given system, varying mixing conditions therefore is expected to influence the dispersion kinetics and the final dispersion state of primary nanotube agglomerates.

To observe the effects of variation in technological parameters, polycarbonate (medium viscosity, Makrolon 2600) was melt compounded with 1 wt% MWCNTs (Baytubes® C150 HP) by varying melt temperature and mixing speed at a constant mixing time of 5 min (Kasaliwal *et al.*, 2009). In Fig. 4.17, the remaining agglomerate area ratio A_A (based on sections with 20 μm thickness) is plotted versus mixing speed, for composites prepared at three melt temperatures. In composites prepared at low mixing speed better dispersion is observed when mixing temperature is low or melt viscosity is high. In composites prepared at high speeds, dispersion is the same regardless of applied mixing temperature or melt viscosity. In Fig. 4.18, the area ratio A_A is plotted versus mixing energy indicating that a common dependency is received for all three temperatures. With increasing mixing energy, the area ratio first decreases significantly but above about 4000 J/cm^3 the curve levels off, and further increase in mixing energy does not seem to enhance dispersion further. The



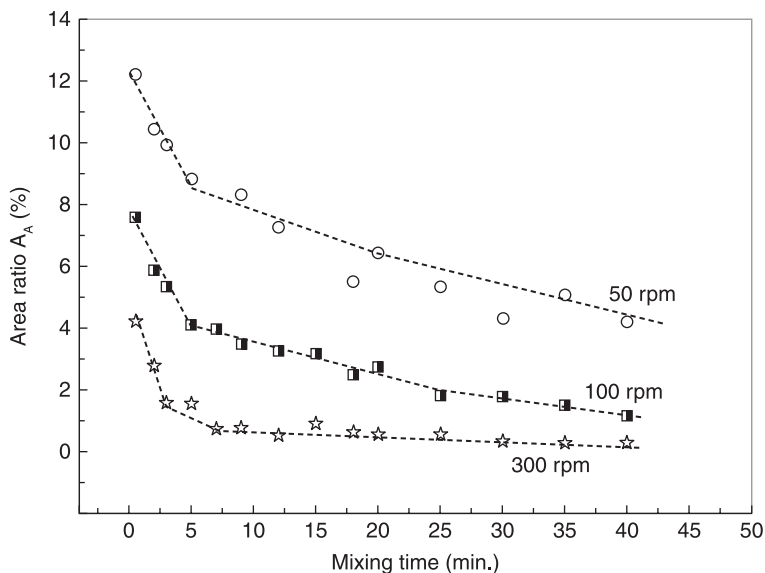
4.17 Area ratio A_A vs. mixing speed for composites of PC with 1 wt% Baytubes C150 HP produced at different temperatures (adapted from Kasaliwal *et al.*, 2009).



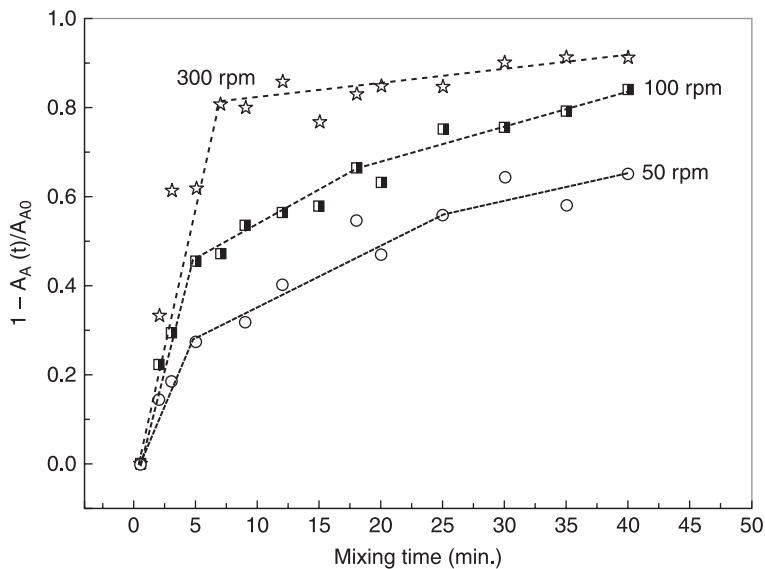
4.18 Area ratio A_A vs. mixing energy for composites of PC with 1 wt% Baytubes C150 HP produced at different temperatures (adapted from Kasaliwal *et al.*, 2009).

results correspond to those mentioned in Section 4.4.4: at low speeds, agglomerate dispersion is shear stress-driven and at high speeds similar dispersions are achieved irrespective of the melt temperature or viscosity.

In any melt mixing process the agglomerates can undergo dispersion by both rupture and erosion mechanisms, whereas the extent of these mechanisms might vary depending upon the mixing conditions employed. To investigate the share of both mechanisms a kinetic study (14 mixing times between 0.5 and 40 min.) was performed using a low viscous PC (Makrolon 2205) and 1 wt% Baytubes® C 150 HP, applying three mixing speeds (50, 100, and 300 rpm) at a melt temperature of 280°C (Kasaliwal *et al.*, 2010a). The area ratio of undispersed agglomerates A_A was plotted versus mixing time (Fig. 4.19) and shows a dramatic increase with mixing speed and time. The dispersion kinetics as assessed by plotting the relative change of area ratio related to the area ratio at 0.5 min., versus mixing time (Fig. 4.20) reveals faster and higher relative changes at higher mixing speed. However, with progressing MWCNT dispersion the rate slows down and under the conditions selected it was not possible to get complete dispersion at macro scale. At high mixing speeds and prolonged mixing time, usually small agglomerates are observed, which are difficult to disperse. From theoretical calculations it can be concluded that smaller agglomerates have higher agglomerate strength than the larger ones (Kasaliwal *et al.*, 2010a) and therefore are more difficult to disperse. The remaining agglomerates may be related to the internal structure of the primary



4.19 Area ratio A_A vs. mixing time at different mixing speeds for composites of PC with 1 wt% Baytubes C150 HP (reproduced from Kasaliwal *et al.*, 2010a).



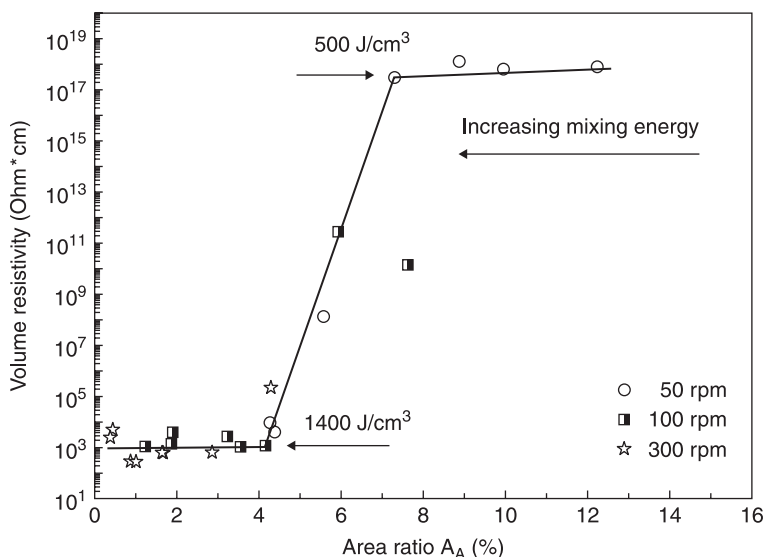
4.20 Relative change in the area ratio A_A vs. mixing time for composites of PC with 1 wt% Baytubes C150 HP (reproduced from Kasaliwal *et al.*, 2010a).

agglomerates as illustrated in Fig. 4.5, where denser small agglomerates in the size range of 1–10 μm were observed within the big agglomerates.

Further mathematical treatment of these values using a model developed by Kasaliwal *et al.* (2010a) resulted in the conclusion that, at high speed (300 rpm), the fast dispersion is governed by the rupture-dominant mechanism, whereas at low speeds (50 and 100 rpm), the slower dispersion is governed by both rupture- and erosion-dominant mechanisms.

In addition, electrical resistivity of all samples was measured. When plotting resistivity versus the remaining agglomerate ratio (see Fig. 4.21), two plateaus and a transition range between low and high resistivity were found, indicating dispersion-dependent percolation behaviour.

At agglomerate area ratios above 7%, corresponding to low mixing energies, the amount of dispersed nanotubes is not high enough for percolation and electrical resistivity of the composites is altogether dominated by the matrix system. When a sufficient amount of dispersed nanotubes is generated, in our case between 7% and 4% of the remaining agglomerates, percolation occurs and in that small concentration range the resistivity decreases by more than 12 decades depending on the state of dispersion. Below approximately 4%, no additional changes in resistivity were observed, even if the area ratio goes down to nearly 0.2%; the electrical resistivity is dominated by the nanotubes. This is a very interesting finding since it is commonly assumed that the electrical resistivity decreases with increasing filler dispersion (see discussion in Section 4.3). However, these results clearly indicate that this assumption holds only in a limited transition range.



4.21 Volume resistivity vs. area ratio A_A for composites of PC with 1 wt% Baytubes C150 HP (reproduced from Kasaliwal *et al.*, 2010a).

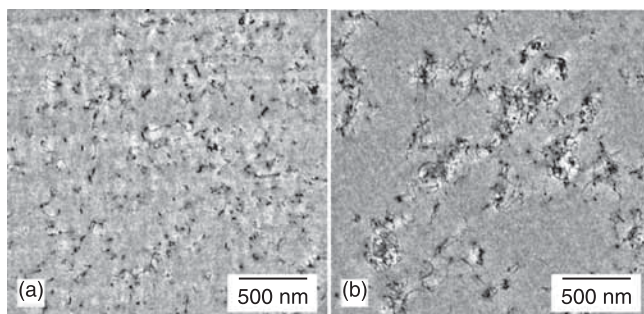
4.4.6 Masterbatch dilution

When using masterbatches for the production of composite materials, the quality of dispersion within the masterbatch is an important prerequisite for achieving good dispersion in the diluted composites. In a good masterbatch it is expected that all of the primary nanotube agglomerates will be dispersed into single tubes and wetted by polymer. When a masterbatch contains uninfiltated, large remaining agglomerates, it is quite difficult to disperse them in the dilution step (compare, e.g. Mičušík *et al.*, 2009), whereas infiltrated smaller agglomerates may be dispersed at that stage. As agglomerates are subjected to shearing twice, first, during masterbatch production and, second, during dilution, in most cases better dispersion is observed in diluted composites.

During masterbatch dilution, an already existing percolated nanotube network can be extended by the incorporation of additional polymer chains or by rupture and erosion processes, as previously described. For this, miscibility between the polymer chains in the masterbatch and the diluting polymer is required; otherwise a phase-separated structure can be formed between a masterbatch phase and a non-filled polymer phase. As in many cases the nature of the polymer used in the masterbatch is not known, the addition of non-matching dilution polymer may lead to non-homogeneous materials.

In principle, the effects of mixing conditions on dispersion are similar to the ones observed during direct incorporation of MWCNTs in melt compounding. Distinct from direct incorporation, the ‘primary agglomerates’ which should be dispersed are now the masterbatch with already infiltrated polymer chains. Thus, the effects discussed in context with wetting and infiltration of the polymer melt into primary agglomerates do not play a major role. As a general effect, it is found that higher shear forces (achieved by lower temperature or higher rotation speed) improve dispersion.

For instance, in Fig. 4.22, TEM images of polycarbonate–MWCNT composites produced from a masterbatch (from Hyperion Cat. Inc., USA) with 15 wt%



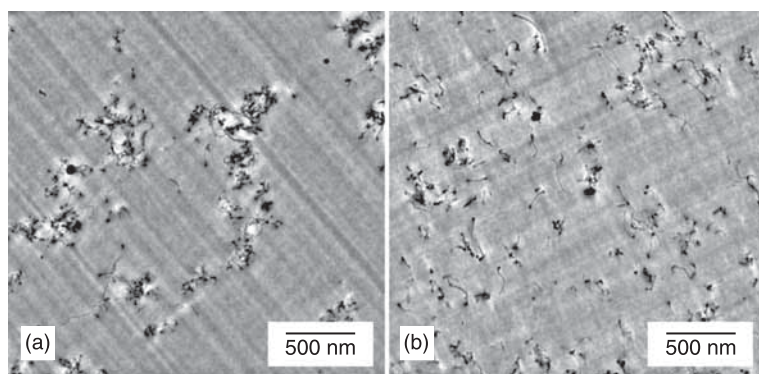
4.22 Polycarbonate with 0.875 wt% CNT composites diluted from a masterbatch containing 15 wt% MWCNT under different dilution conditions: (a) 250°C, 50 rpm, 15 min.; (b) 300°C, 50 rpm, 15 min. (reproduced from Pegel *et al.*, 2008).

MWCNTs at two different temperatures and low mixing speed are shown. In the sample produced at 250°C, better dispersion is observed as compared to that diluted at 300°C, which may be assigned to higher shear stresses at the lower mixing temperature. It should be emphasized that both samples were completely free of primary agglomerates as checked by LM investigations.

4.4.7 The effect of secondary agglomeration

In the dispersion at the nanoscale, another effect has to be considered which is well known for the formation of electrical pathways in epoxy systems, but not much regarded in thermoplastic melts. This is the effect of secondary agglomeration, also called flocculation or clustering. It occurs between well-separated nanotubes due to long-range interactions between the nanotubes in the liquid and strongly depends on the matrix viscosity. For melts with well-dispersed nanotubes, a shear-induced insulator–conductor transition was described by Skipa *et al.* (2010), using time-resolved measurements of electrical conductivity under steady shear and in the quiescent melt. These effects were assigned to the agglomeration of nanotubes under steady shear and the formation of an electrical conductive network of interconnected agglomerates (Alig *et al.*, 2008; Skipa *et al.*, 2010), however, without morphological investigations.

The effect of secondary agglomeration could be visualized using TEM after subjecting the composite shown in Fig. 4.22 to a second mixing cycle at 300°C and different mixing speeds (Pegel *et al.*, 2008). At 300°C, the previously nicely dispersed composite (Fig. 4.22 (a)) now develops small secondary agglomerates, the size of which is bigger in the case of a lower mixing speed (Fig. 4.23 (a)) than for a higher mixing speed (Fig. 4.23 (b)).



4.23 Secondary agglomeration of MWNT in the polycarbonate melt processed from the state shown in Fig. 4.22 (a) in a second step at (a) 300°C, 50 rpm, 5 min; (b) 300°C, 250 rpm, 5 min (reproduced from Pegel *et al.*, 2008).

The effect of secondary agglomeration can also be seen when looking at the morphology of injection-moulded parts produced under different injection-moulding conditions (Villmow *et al.*, 2008a). This was illustrated by TEM images of injection-moulded plates of polycarbonate with 2 and 5 wt% MWCNTs when investigating the morphology in different depths from the surface. In the inner part, especially when high melt temperatures had been used during moulding, secondary agglomerates could be seen.

4.5 Continuous melt mixing using extruders

In the previous section, results obtained by small-scale batch mixing of polymer–MWCNT composites using microcompounders were discussed. These processing–property relationships can be applied to a certain amount also to melt processing using continuous melt mixing processes like twin-screw extrusion, which is highly relevant to industrial manufacturing of composite materials and parts. As CNT producers increase their manufacturing capacities and the prices of CNT drop, industrial applications of melt mixed composites gain more importance. In that context, investigations on influencing factors in laboratory-scale twin-screw extrusion (Villmow *et al.*, 2008b) and injection moulding (Lellinger *et al.*, 2008; Villmow *et al.*, 2008a) have started to attract attention.

From small-scale mixing it was concluded that high screw speed and long residence time result in better dispersion of MWCNTs within polymer matrices. Previous investigations on PLA (Villmow *et al.*, 2008b), using a twin-screw extruder, also indicated that higher mixing speeds (100 rpm vs. 500 rpm) were favourable in masterbatch production and dilution. However, in comparison to small-scale mixing, the melt mixing using continuous processes provides new challenges. The residence time of polymer melt during twin-screw extrusion is a complex function of rotation speed, throughput, and screw configuration and cannot be adjusted independently. The interaction between different processing parameters leads to complex functions of shear conditions and residence time, thus affecting CNT dispersion. In this section, the influence of extrusion conditions using a co-rotating intermeshing twin-screw extruder (ZE25, from Berstorff, Germany) on the macroscopic MWCNT dispersion is discussed for masterbatches based on poly (caprolactone) (PCL) and their diluted composites.

4.5.1 Preparation of masterbatches: influence of screw configuration on residence time and MWCNT dispersion

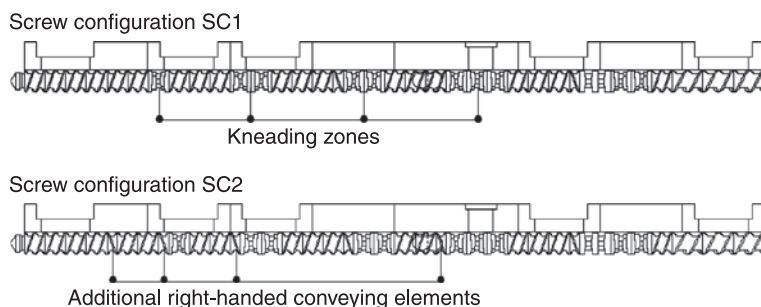
Twin-screw extruders provide a modular assembly, and especially the extrusion screw can be varied in nearly endless configurations. This machine consists of different numbers of conveying, kneading, and mixing elements, resulting in different flow and shear conditions. For this study, masterbatches containing

7.5 wt% MWCNTs (Nanocyl NC 7000, from Nanocyl S.A. Belgium) based on PCL (CAPA 6800, from Perstorp, UK) were produced, using five different screw configurations. Two classes of screw configurations were used; whereas dispersive screws favour the break-up of cohesive agglomerates, distributive screws increase the homogeneity of the mixture by continuously generating new interfacial area.

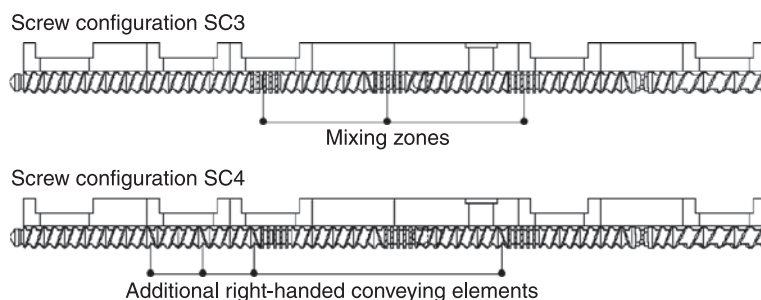
The two dispersive screw configurations (SC1 and SC2, see Fig. 4.24) used in the present study contain kneading and conveying elements. For these screws, the number of kneading blocks is the same, but the number of right-handed conveying elements was varied to control the minimum residence time during extrusion. The kneading blocks consisted of five kneading discs with a positive (45°) staggering angle. Both screws were designed to have a length to diameter ratio (L/D) of 36.

Three distributive screw configurations were designed based on the dispersive ones. In SC3, the number and location of conveying elements of screw configuration SC1 were maintained but the kneading elements were substituted by mixing elements. Screw configuration SC4 was designed to have additional right-handed conveying elements compared to SC3 (Fig. 4.25).

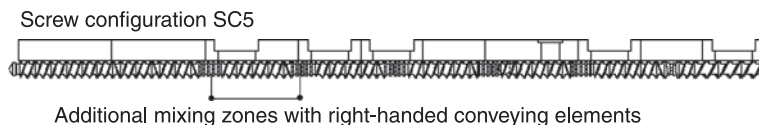
The fifth screw profile was based on SC4, but having an extended L/D of 48. Additionally, this screw configuration contains two extra mixing zones to have



4.24 Dispersive screw configurations SC1 and SC2 (adapted from Villmow *et al.*, 2010).



4.25 Distributive screw configurations SC3 and SC4 (adapted from Villmow *et al.*, 2010).



4.26 Distributive screw configuration SC5 (adapted from Villmow *et al.*, 2010).

five in total (Fig. 4.26). Each mixing zone consisted of mixing elements having five discs, whereas each had 10 cogs. All experiments were performed at a mean barrel temperature of 200 °C.

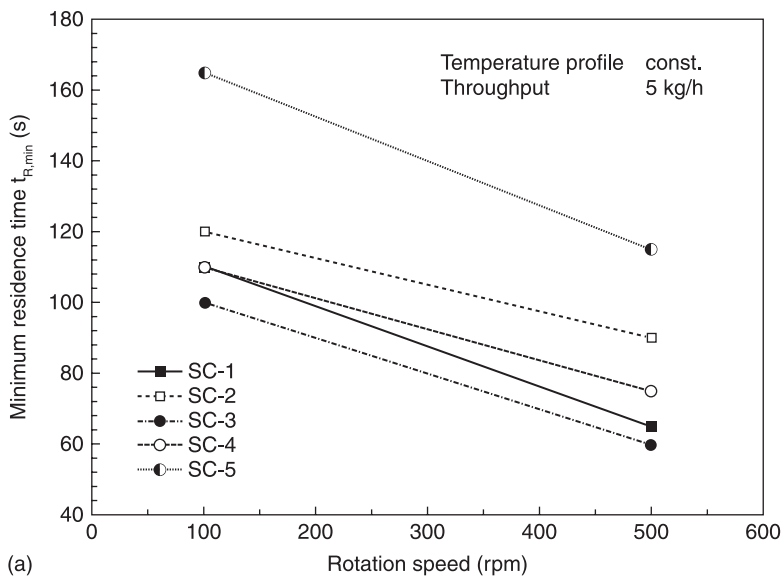
The minimum residence time $t_{R,min}$ was measured based on the first appearance of a change in colour of the extrudate after the addition of five black granules with 7.5 wt% MWCNT.

The use of kneading elements results in longer minimum residence times, as these elements exhibit an active (conveying or stuffing) effect in comparison to mixing elements that act neutrally regarding their conveying behaviour. This effect is independent from rotation speed and throughput. The further addition of back conveying elements (SC2 and SC4) leads to a significant increase in $t_{R,min}$ for both types of mixing. The gain in $t_{R,min}$ is thereby in the range of 10 to 30 seconds depending on the mixing speed. Besides the number of back conveying elements, $t_{R,min}$ strongly depends on L/D of the processing unit. Thus, SC5 exhibits the longest $t_{R,min}$ determined in the frame of this study.

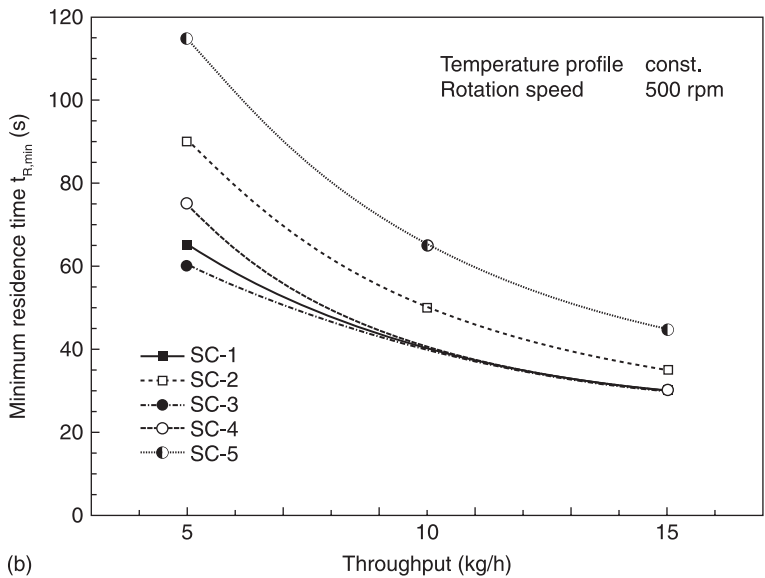
The influence of mixing speed and throughput on $t_{R,min}$ using different screw configurations is shown in Fig. 4.27. As an increase of mixing speed leads to higher conveying velocity and decreased filling degree of the screws, shorter $t_{R,min}$ were observed. Increasing the rotation speed from 100 to 500 rpm results in a decrease in $t_{R,min}$ in the range of 30 to 50 seconds. Furthermore, the use of an extended screw (SC5) increased $t_{R,min}$ by about 50% for both investigated mixing speeds. The influence of throughput on the $t_{R,min}$ was investigated in the range between 5 and 15 kg/h, by maintaining constant rotation speed of 500 rpm. The $t_{R,min}$ decreases exponentially with increasing throughput and was approximately halved when comparing the values determined for 5 and 15 kg/h.

The investigation of macro dispersion from LM investigations (sample thickness 2.5 μm , particles > 5 μm regarded) reveals an exponential decrease of the area ratio A_A of undispersed MWCNT agglomerates with increasing residence time $t_{R,min}$ for both types of mixing (dispersive or distributive) as illustrated in Fig. 4.28. For comparable residence times, better MWCNTs dispersions were observed for distributive mixing in comparison to dispersive mixing.

The exponential decrease of A_A with residence time results in a plateau level (at about 2%) when using distributive screw configurations, which was not observed for the dispersive screw configurations. Interestingly, even when applying long residence times (low throughputs), remaining primary agglomerates in the range of 70 to 100 μm were observed, as shown in Fig. 4.29 (b) for SC5. The particle

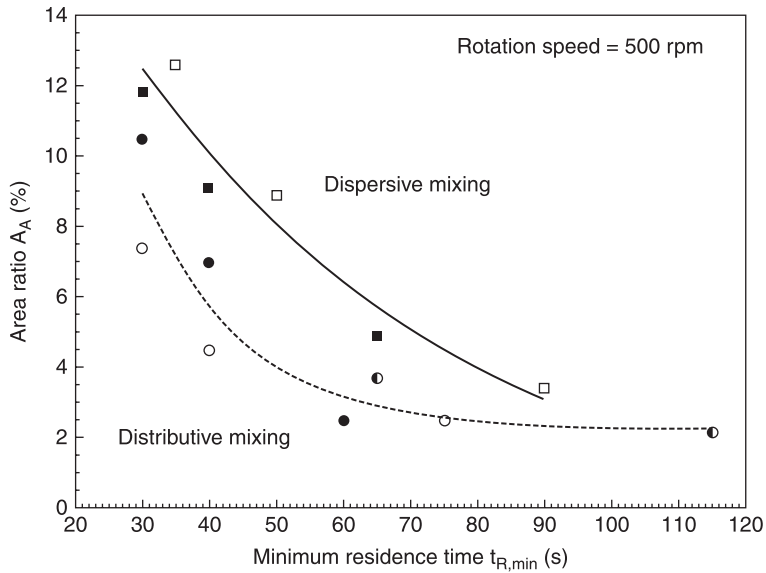


(a)



(b)

4.27 Minimum residence time $t_{R,min}$ of PCL depending on processing parameters and screw configurations: (a) versus rotation speed; (b) versus throughput (adapted from Villmow *et al.*, 2010).

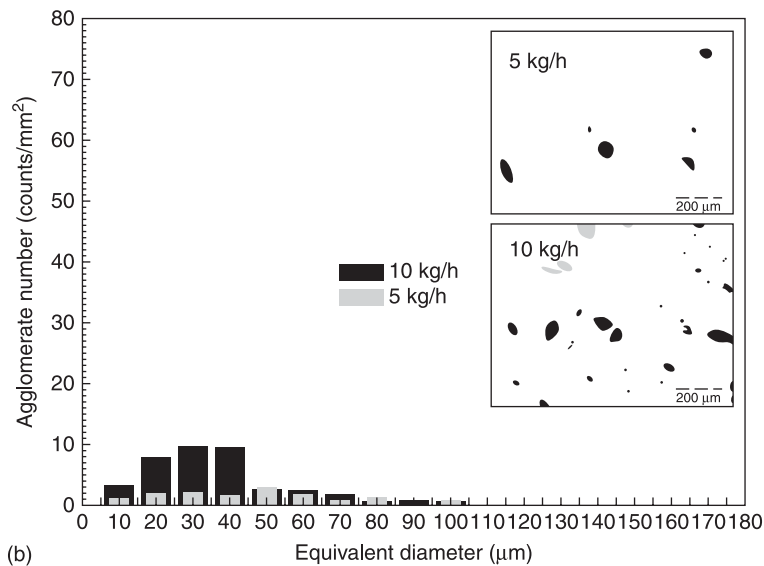
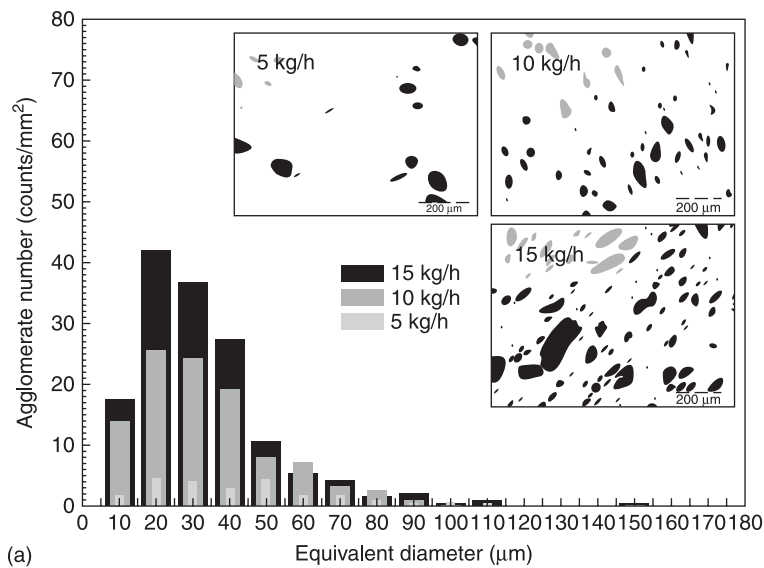


4.28 Dependence of the agglomerate area ratio A_A on the minimum residence time $t_{R,min}$ in PCL masterbatches with 7.5 wt% MWCNT (adapted from Villmow *et al.*, 2010).

size distributions for the composites also indicate that these large particles were present under all conditions investigated as shown in Fig. 4.29 for composites produced with SC2 and SC5.

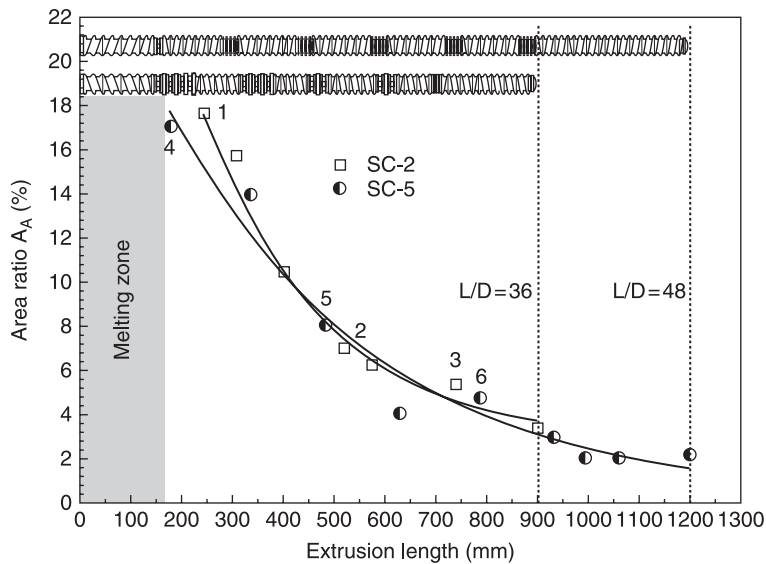
In addition, investigation of the morphology development along the length of the screw during extrusion was performed, giving additional information concerning the impact of different mixing and kneading elements on the MWCNT dispersion. The extruder was stopped after reaching steady state extrusion conditions and the screws were pulled out from the processing unit within a few seconds. Several samples of approximately 1 gram were taken from the screws (using screw configurations SC2 and SC5, rotation speed 500 rpm and throughput 5 kg/h). The area ratio A_A of undispersed MWCNTs within the PCL masterbatches decreases exponentially along the extruder as illustrated in Fig. 4.30. The numbers 1 to 6 indicate some of the sampling positions, which will be referred to in Fig. 4.31.

The agglomerate size distributions as shown in Fig. 4.31 illustrate that their width was similar for all samples taken along the extruder. The maximum agglomerate size of 120 μm observed directly after the melting zone was also found in the material taken close to the extrusion die. This finding indicates, again, that the influence of extrusion length or residence time on the dispersion of large primary agglomerates is limited. However, it is the particle size distribution in the range between 10 and 60 μm , which changes significantly along the extruder. It has to be assumed that the breaking up of very big agglomerates into

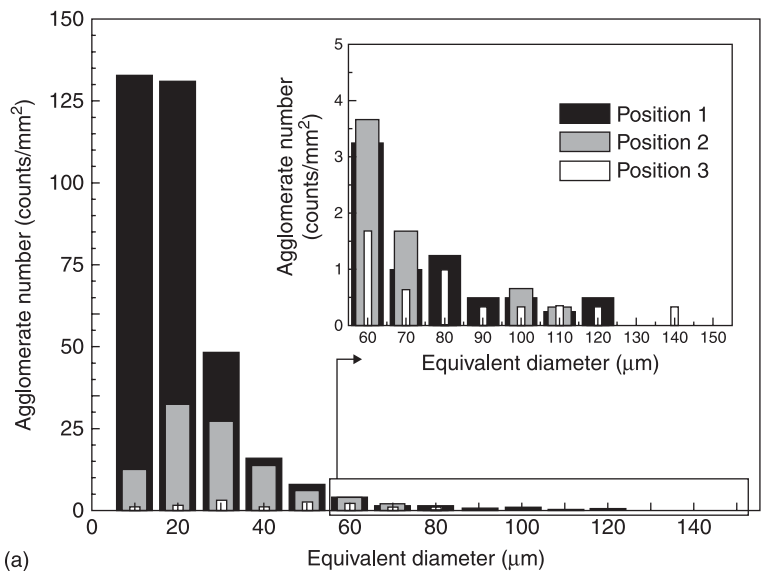


4.29 Influence of throughput on the macrodispersion (LM) and the agglomerate size distribution: (a) SC2; (b) SC5.

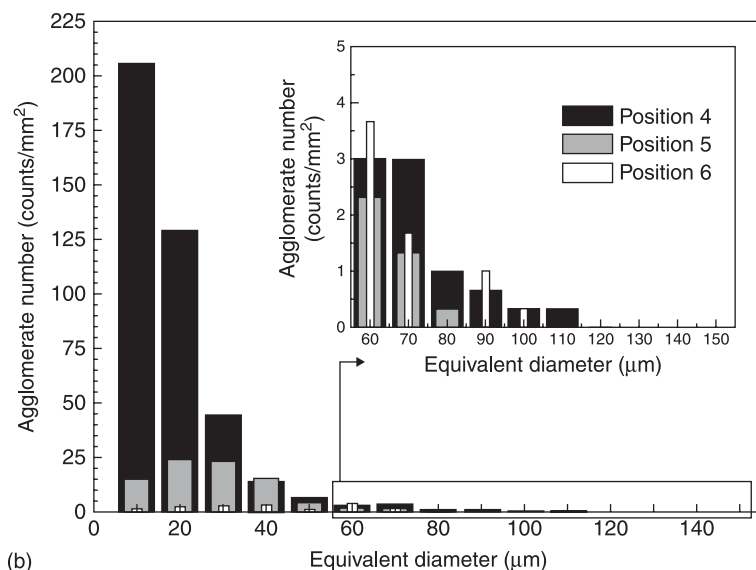
fragments of 100 µm or smaller happens in the melting zone of the twin-screw extruder at the very beginning of the mixing process and is thereby mainly influenced by the rotation speed, which controls the shear forces acting on the agglomerates.



4.30 Development of MWCNT macro dispersion along the extrusion length for screw profiles SC2 and SC5 (adapted from Villmow *et al.*, 2010).



4.31 Development of MWCNT agglomerate size distribution along the extrusion length for screw configurations SC2 (a) and SC5 (b) (adapted from Villmow *et al.*, 2010).



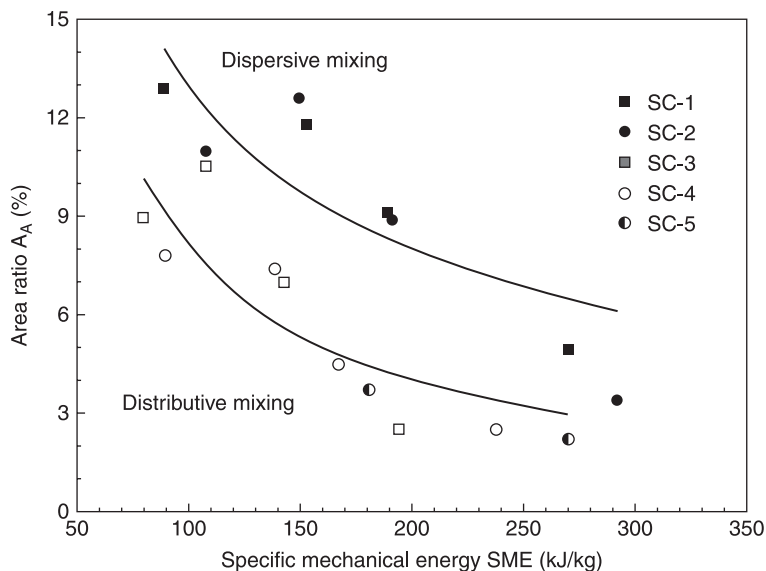
4.31 Continued.

The shear conditions during extrusion can be quantified using the specific mechanical energy input (SME), where the torque during extrusion is taken into account. Fig. 4.32 shows the area ratio A_A depending on SME and reveals a power law dependency for both types of mixing. Although the overall energy input is lower when using distributive screw configurations, they result in better MWCNT dispersion. This has to be attributed to the high mixing efficiency of mixing elements as compared to kneading elements. Generally, it can be concluded from these results that low throughputs and high rotation speeds could further improve the MWCNT's dispersion.

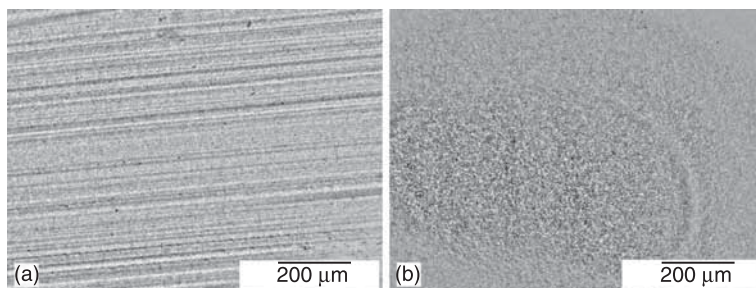
4.5.2 Masterbatch dilution

The final stage in the production of nanocomposites was done by dilution of the masterbatch exhibiting the best MWCNT macro dispersion, which was processed with an extended distributive screw under application of 500 rpm and 5 kg/h. The dilution process was done under the same conditions in order to get composites with MWCNT contents between 0.125 and 4.0 wt%.

Figure 4.33 shows light microscopic images of two different PCL composites with 0.5 and 1.0 wt% content and demonstrates that the primary MWCNT agglomerates were entirely dispersed within the matrix. The resulting composites showed a very low percolation threshold of 0.244 vol.%, as measured on compression moulded samples (Fig. 4.34).

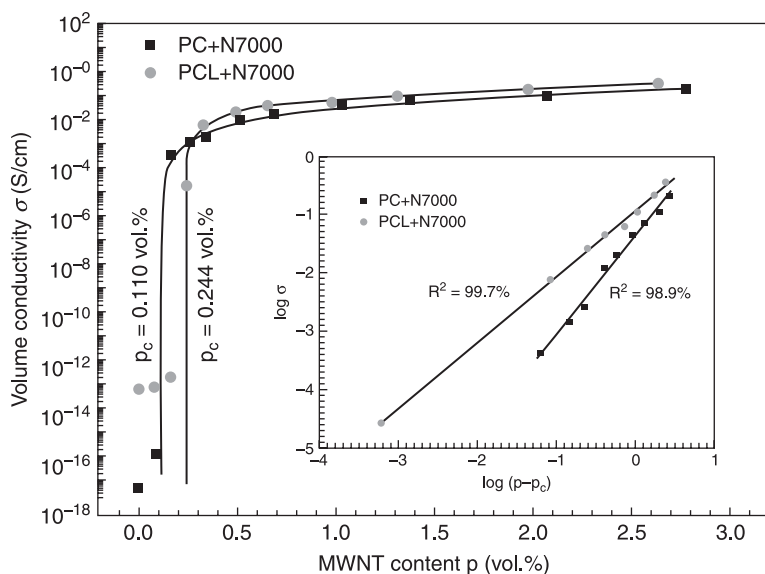


4.32 Correlation between macroscopic MWCNT dispersion and specific mechanical energy input SME for PCL-based masterbatches containing 7.5 wt% MWCNT, symbols follow the description in Fig. 4.28 (adapted from Villmow *et al.*, 2010).



4.33 Light microscopic images of PCL composites with different MWCNT contents: (a) 0.5 wt%; (b) 1.0 wt% (reproduced from Villmow *et al.*, 2010).

The mixing conditions found to be optimal for the preparation of the PCL-based masterbatches (7.5 wt% MWCNT, extended distributive screw (SC5), 500 rpm, 5 kg/h) were also applied to the production of masterbatches based on poly(carbonate) (Lexan 141R, from Sabic Innovative Plastics) with the same type of MWCNTs (NC7000, from Nanocyl S.A., Belgium). The mean barrel temperature was adapted to the poly(carbonate) and was in the range of 260 °C. The dilution of the masterbatch was repeated under the same conditions. The



4.34 Electrical volume conductivity σ vs. filler content p for composites of PC and PCL with MWCNT N7000 and fitted electrical percolation thresholds p_c .

MWCNT dispersion obtained was excellent, almost showing nearly no remaining primary agglomerates. Correspondingly, the percolation threshold as measured on compression-moulded plates was as low as 0.110 vol.% (Fig. 4.34). This outcome indicates that the results obtained for the optimization of extrusion processing for PCL/MWCNT composites can be transferred successfully to other polymer/CNT systems.

4.6 Conclusion and future trends

To make polymer–MWCNT composites a commercial success, the production of these composites free of undispersed primary MWCNT agglomerates is very important. Next to reducing the amount of nanotubes available for network formation, undispersed primary agglomerates above certain sizes act as crack initiators in mechanical tests and reduce surface appearance of parts made from such composites.

The factors influencing the dispersion of MWCNTs in a polymer matrix are numerous and can be divided into material and processing parameters. Different synthesis methods employed by CNT manufacturers result in MWCNT materials varying in certain characteristic features such as agglomerate structure, packing density, lengths and diameters, purity etc. These differences affect the dispersability of the as-produced primary MWCNT agglomerates. Thus, MWCNTs produced by different manufacturers disperse to different extents in a given polymer matrix.

Furthermore, polymer matrices differing in their chemical structure were found to influence the quality of MWCNT dispersion, whereby the exact reason behind these differences is still under discussion. The interfacial energy between MWCNTs and polymers is one of the factors that could influence the dispersion of MWCNTs, where lower interfacial energy was found to enhance dispersion. Other factors like chain stiffness and mobility could have determining effects. In addition, melt viscosity was shown to have counteracting effects on the step of melt infiltration of primary agglomerates and the generation of high shear stresses, which has to be balanced in order to get good nanotube dispersion. Interestingly, it could also be shown that next to melt viscosity, the molecular weight of the matrix polymer has an additional influence on dispersion, which can be attributed to the faster infiltration of lower molecular weight polymer chains, even if the polymer shows the same melt viscosity as higher molecular chains.

Concerning the processing parameters, the investigations of dispersion kinetics in small-scale mixing showed that two important parameters drive the size reduction of MWCNT agglomerates: polymer melt infiltration and applied shear stress. If the applied shear stresses are high enough, agglomerates can be broken up and quickly dispersed. When the agglomerates are well infiltrated, they can disperse by the application of relatively lower shear stresses. Thus, an optimum balance between melt infiltration and applied shear stresses is desirable for fast agglomerate dispersion. Such balanced optimized mixing conditions could be realized by using low melt viscosities, long mixing/residence time, and high mixing speeds.

Furthermore, masterbatch dilution technology is a promising route to produce composites with no or only small remaining agglomerates, as the materials undergo the mixing procedure twice, thus enhancing mixing energy input and residence time. However, the quality of the starting masterbatch is also important for the quality of the composites prepared from it by dilution.

In the case of continuous extruders, parameters such as screw configuration, mixing speeds, throughput, temperature profile, etc. have significant influences on the shear stresses and residence time and thereby on the quality of MWCNT dispersion. Based on investigations on PLA-based masterbatches, it was found that higher L/D ratios of screws with distributive screw configurations can yield better MWCNT dispersion.

Systematic studies on influencing factors on the dispersion of MWCNT in polymers by melt compounding have just started and are still in the state of development. So far, complete dispersion of MWCNT agglomerates via melt compounding has rarely been reported in the literature, let alone investigated seriously. To solve this problem, the application of additives and surfactant as dispersion aids could be promising. Such additives can tremendously influence the interfacial energy, thereby easing the agglomerate dispersion; however, further scientific studies are required on that topic, addressing other additive influences on other composite properties, like electrical and mechanical properties.

4.7 Acknowledgements

We thank Nanocyl S.A. (Sambreville, Belgium) for providing specially synthesized and prepared nanotubes as well as for supplying commercially available products. We also thank Dr Beate Krause for help in the analysis of MWCNT length based on TEM images generated by Regine Boldt (both IPF). Parts of the research were funded by the German Federal Ministry of Education and Research (BMBF) within the Framework Concept 'Research for Tomorrow's Production' (funding number 02PU2392), managed by the Project Management Agency Karlsruhe (PTKA). We also acknowledge financial support from the project INTELTEX (Intelligent multi-reactive textiles integrating nanofiller based CPC-fibres) – a European Integrated Project supported through the Sixth Framework Programme for Research and Technological Development.

4.8 References

- Alig I., Skipa, T., Lellinger, D., and Pötschke, P. (2008) Destruction and formation of a carbon nanotube network in polymer melts: rheology and conductivity spectroscopy, *Polymer*, 49, 3524–3532.
- Andrews, R., Jacques, D., Minot, M. and Rantell, T. (2002) Fabrication of carbon multiwall nanotube/polymer composites by shear mixing, *Macromolecular Materials and Engineering*, 287, 395–403.
- Baets, J., Godara, A., Devaux, J. and Verpoest, I. (2008) Toughening of polymerized cyclic butylene terephthalate with carbon nanotubes for use in composites. *Composites Part A-Applied Science and Manufacturing*, 39, 1756–1761.
- Barber, A., Cohen, S. and Wagner, H. (2004) Static and dynamic wetting measurements of single carbon nanotubes, *Physics Review Letters*, 92, 186103.
- Bolen, W. R. and Colwell, R. E. (1958) *Society of Plastics Engineering Journal*, 14, 24.
- Brühwiler, P.A., Barbezat, M., Necola, A., Kohls, D.J., Bunk, O., Schaefer, D.W. and Pötschke, P. (2010) Comparison of quasistatic to impact mechanical properties of multiwall carbon nanotube/polycarbonate composites, *Journal of Materials Research*, 25, 1118–1130.
- Chu, D., Nguyen, Q. and Baird, D.G. (2007) Effect of matrix molecular weight on the dispersion of nanoclay in unmodified high density polyethylene, *Polymer Composites*, 28, 499–511.
- Coran, A. Y. and Donnet, J. B. (1992) The dispersion of carbon-black in rubber: 2. The kinetics of dispersion in natural-rubber, *Rubber Chemistry and Technology*, 65, 998–1015.
- Du, F.M., Scogna, R.C., Zhou, W., Brand, S., Fischer, J.E. and Winey, K. I. (2004) Nanotube networks in polymer nanocomposites: rheology and electrical conductivity, *Macromolecules*, 37, 9048–9055.
- Fan, Z.H. and Advani, S.G. (2007) Rheology of multiwall carbon nanotube suspensions, *Journal of Rheology*, 51, 585–604.
- Fornes, T.D., Yoon, P. J., Keskkula, H. and Paul, D.R. (2001) Nylon 6 nanocomposites: the effect of matrix molecular weight, *Polymer*, 42, 9929–9940.
- Gianelli, W., Ferrara, G., Camino, G., Pellegatti, G., Rosenthal, J. and Trombini, R.C. (2005) Effect of matrix features on polypropylene layered silicate nanocomposites, *Polymer*, 46, 7037–7046.

- Hansen, S., Khakhar, D.V. and Ottino, J.M. (1998) Dispersion of solids in nonhomogeneous viscous flows, *Chemical Engineering Science*, 53, 1803–1817.
- Huang, Y.Y., Ahir, S.V. and Terentjev, E.M. (2006) Dispersion rheology of carbon nanotubes in a polymer matrix, *Physical Review B*, 73, 9.
- Jaycock, M.F. (1973) Properties of solid liquid interface of relevance to dispersion. In G.D. Parfitt, (ed.) *Dispersion of Powders in Liquids*, 2 edn, New York: Applied Science Publishers Ltd, pp. 44–80.
- Kao, S.V. and Mason, S.G. (1975) Dispersion of particles by shear, *Nature*, 253, 619–621.
- Kasaliwal, G., Göldel, A. and Pötschke, P. (2009) Influence of processing conditions in small-scale melt mixing and compression molding on the resistivity and morphology of polycarbonate-MWNT composites, *Journal of Applied Polymer Science*, 112, 3494–3509.
- Kasaliwal, G., Göldel, A., Pötschke, P., Pegel, S. and Heinrich, G. (2010a) Analysis of agglomerate dispersion mechanisms of multiwalled carbon nanotubes during melt mixing in polycarbonate, *Polymer*, 51, 2708–2720.
- Kasaliwal, G., Göldel, A., Pötschke, P. and Heinrich, G. (2010b) Influences of polymer matrix melt viscosity and molecular weight on MWNT agglomerate dispersion, submitted.
- Krause, B., Mende, M., Pötschke, P. and Petzold, G. (2010) Dispersability and particle size distribution of CNTs in an aqueous surfactant dispersion as a function of ultrasonic treatment time, *Carbon*, 48, 2746–2754.
- Krause, B., Pötschke, P. and Häussler, L. (2009) Influence of small scale melt mixing conditions on electrical resistivity of carbon nanotube-polyamide composites, *Composites Science and Technology*, 69, 1505–1515.
- Le, H.H., Ilisch, S., Prodanova, I. and Radusch, H.J. (2004) Online electrical conductivity as a measure to characterize the rheological and thermodynamic effects on the carbon black dispersion in rubber compounds, *Kautschuk Gummi Kunststoffe*, 57, 355–362.
- Le, H.H., Kasaliwal, G., Ilisch, S. and Radusch, H.J. (2009) Online measured electrical conductance in-process characterization of the dispersion behaviour of carbon nanotubes in rubber compounds, *Kautschuk Gummi Kunststoffe*, 62, 326–333.
- Leer, C., Carneiro, O.S., Covas, J. A., Maia, J.M., Van Hattum, F.W.J., Bernardo, C.A., Biro, L.P., Horvath, Z.E. and Kiricsi, I. (2006) Dispersion of carbon nanotubes in polycarbonate and its effect on the composite properties. In P.M. Vilarinho (ed.) *Advanced Materials Forum III, Pts 1 and 2*, Zurich-Uetikon: Trans Tech Publications Ltd, pp. 514–516, 1125–1130.
- Lellinger, D., Xu, D.H., Ohneiser, A., Skipa, T. and Alig, I. (2008) Influence of the injection moulding conditions on the in-line measured electrical conductivity of polymer-carbon nanotube composites, *Physica Status Solidi B: Basic Solid State Physics*, 245, 2268–2271.
- Levesse, P., Manas-Zloczower, I., Feke, D.L., Bomal, Y. and Bortzmeyer, D. (1999) Observation and analysis of the infiltration of liquid polymers into calcium carbonate agglomerates, *Powder Technology*, 106, 62–70.
- Lin, B., Sundararaj, U. and Pötschke, P. (2006) Melt mixing of polycarbonate with multi-walled carbon nanotubes in miniature mixers, *Macromolecular Materials and Engineering*, 291, 227–238.
- Lozano, T., Lafleur, P.G., Grmela, M. and Vergnes, B. (2003) Modelling filler dispersion along a twin-screw extruder, *International Polymer Processing*, 18, 12–19.
- Manas-Zloczower, I. (1994) Dispersive mixing of solid additives, in Z. Tadmor and I. Manas-Zloczower (eds) *Mixing and Compounding of Polymers: Theory and Practice*, Munich: Hanser Publishers, pp. 55–83.
- Manas-Zloczower, I. and Feke, D.L. (1989) Analysis of agglomerate rupture in linear flow-fields, *International Polymer Processing*, 4, 3–8.

- Manas-Zloczower, I., Nir, A. and Tadmor, Z. (1982) Dispersive mixing in internal mixers – a theoretical-model based on agglomerate rupture, *Rubber Chemistry and Technology*, 55, 1250–1285.
- Masuda, J. and Torkelson, J.M. (2008) Dispersion and major property enhancements in polymer/multiwall carbon nanotube nanocomposites via solid-state shear pulverization followed by melt mixing, *Macromolecules*, 41, 5974–5977.
- McNally, T., Pötschke, P., Halley, P., Murphy, M., Martin, D., Bell, S.E.J., Brennan, G.P., Bein, D., Lemoine, P. and Quinn, J.P. (2005) Polyethylene multiwalled carbon nanotube composites, *Polymer*, 46, 8222–8232.
- Mičušík, M., Omastova, M., Krupa, I., Prokes, J., Pissis, P., Logakis, E., Pandis, C., Pötschke, P. and Pionteck, J. (2009) A comparative study on the electrical and mechanical behaviour of multi-walled carbon nanotube composites prepared by diluting a masterbatch with various types of polypropylenes, *Journal of Applied Polymer Science*, 113, 2536–2551.
- Parfitt, G.D. (1973) Fundamental aspects of dispersion, In G.D. Parfitt (ed.) *Dispersion of Powders in Liquids*, 2nd edn, New York: Applied Science Publishers Ltd., pp. 1, 1–39.
- Pegel, S., Pötschke, P., Petzold, G., Alig, I., Dudkin, S.M. and Lellinger, D. (2008) Dispersion, agglomeration, and network formation of multiwalled carbon nanotubes in polycarbonate melts, *Polymer*, 49, 974–984.
- Potente, H., Kretschmer, K. and Flecke, J. (2002) A physical-mathematical model for the dispersion process in continuous mixers, *Polymer Engineering and Science*, 42, 19–32.
- Pötschke, P., Dudkin, S.M. and Alig, I. (2003) Dielectric spectroscopy on melt processed polycarbonate – multiwalled carbon nanotube composites, *Polymer*, 44, 5023–5030.
- Pötschke, P., Fornes, T.D. and Paul, D.R. (2002) Rheological behaviour of multiwalled carbon nanotube/polycarbonate composites, *Polymer*, 43, 3247–3255.
- Powell, R.L. and Mason, S.G. (1982) Dispersion by laminar-flow, *Aiche Journal*, 28, 286–293.
- Prashantha, K., Soulestin, J., Lacrampe, M.F., Krawczak, P., Dupin, G. and Claes, M. (2009) Masterbatch-based multi-walled carbon nanotube filled polypropylene nanocomposites: assessment of rheological and mechanical properties, *Composites Science and Technology*, 69, 1756–1763.
- Pujari, S., Ramanathan, T., Kasimatis, K., Masuda, J., Andrews, R., Torkelson, J.M., Brinson, L.C. and Burghardt, W.R. (2009) Preparation and characterization of multiwalled carbon nanotube dispersions in polypropylene: melt mixing versus solid-state shear pulverization, *Journal of Polymer Science Part B: Polymer Physics*, 47, 1426–1436.
- Roland, C.M., Robertson, C.G., Nikiel, L. and Puskas, J.E. (2004) Filler dispersion in hyperbranched polyisobutylene, *Rubber Chemistry and Technology*, 77, 372–379.
- Rumpf, H. (1970) Theory of tensile strength of agglomerates in which transfer of force takes place at points of contact of particles, *Chemie Ingenieur Technik*, 42, 538–540.
- Rwei, S.P., Manas-Zloczower, I. and Feke, D.L. (1990) Observation of carbon-black agglomerate dispersion in simple shear flows, *Polymer Engineering and Science*, 30, 701–706.
- Rwei, S.P., Manas-Zloczower, I. and Feke, D.L. (1991) Characterization of agglomerate dispersion by erosion in simple shear flows, *Polymer Engineering and Science*, 31, 558–562.
- Rwei, S.P., Manas-Zloczower, I. and Feke, D.L. (1992) Analysis of dispersion of carbon-black in polymeric melts and its effect on compound properties, *Polymer Engineering and Science*, 32, 130–135.
- Schubert, H. (1979) Principles of agglomeration, *Chemie Ingenieur Technik*, 51, 266–277.

- Seyvet, O. and Navard, P. (2001) In situ study of the dynamics of erosion of carbon black agglomerates, *Journal of Applied Polymer Science*, 80, 1627–1629.
- Shiga, S. and Furuta, M. (1985) Processability of electron-paramagnetic-res in an internal mixer. 2. Morphological-changes of carbon-black agglomerates during mixing, *Rubber Chemistry and Technology*, 58, 1–22.
- Skipa, T., Lellinger, D., Böhm, W. Saphiannikova, and M. Alig, I. (2010) Influence of shear deformation on carbon nanotube networks in polycarbonate melts: interplay between build-up and destruction of agglomerates, *Polymer*, 51, 201–210.
- Tadmor, Z. (1976) Forces in dispersive mixing, *Industrial and Engineering Chemistry Fundamentals*, 15, 346–348.
- Takase, H. (2007) Evaluation and applications of dispersing carbon nanotube in the polymers, in M. Hosokawa, K. Nogi, M. Naito, and T. Yokoyama (eds) *Nanoparticle Technology Handbook*, 1st edn, Oxford: Elsevier, pp. 588–593.
- Tomas, J. (2007) Adhesion of ultrafine particles: a micromechanical approach, *Chemical Engineering Science*, 62, 1997–2010.
- Tomas, J. and Kleinschmidt, S. (2009) Improvement of flowability of fine cohesive powders by flow additives, *Chemical Engineering and Technology*, 32, 1470–1483.
- Triebel, C., Katsikis, N., Stará, H. and Münstedt, H. (2010) Investigations on the quality of dispersion of nanofillers in poly(methyl methacrylate) composites by creep-recovery experiments, *Journal of Rheology*, 54, 407–420.
- Vaia, R.A., Jandt, K.D., Kramer, E.J. and Giannelis, E.P. (1995) Kinetics of polymer melt intercalation, *Macromolecules*, 28, 8080–8085.
- Villmow, T., Kretzschmar, B. and Pötschke, P. (2010) Influence of screw configuration, residence time, and specific mechanical energy in twin-screw extrusion of polycaprolactone/multi-walled carbon nanotube composites, *Composites Science and Technology*, 70, 2045–2055.
- Villmow, T., Pegel, S., Pötschke, P. and Wagenknecht, U. (2008a) Influence of injection molding parameters on the electrical resistivity of polycarbonate filled with multi-walled carbon nanotubes, *Composites Science and Technology*, 68, 777–789.
- Villmow, T., Pötschke, P., Pegel, S., Häußler, L. and Kretzschmar, B. (2008b) Influence of twin-screw extrusion conditions on the dispersion of multi-walled carbon nanotubes in a poly(lactic acid) matrix, *Polymer*, 49, 3500–3509.
- Wang, M. (2003) Developing bioactive composite materials for tissue replacement, *Biomaterials*, 24, 2133–2151.
- Yamada, H., Manas-Zloczower, I. and Feke, D.L. (1997) Influence of matrix infiltration on the dispersion kinetics of carbon black agglomerates, *Powder Technology*, 92, 163–169.
- Yamada, H., Manas-Zloczower, I. and Feke, D.L. (1998) The influence of matrix viscosity and interfacial properties on the dispersion kinetics of carbon black agglomerates, *Rubber Chemistry and Technology*, 71, 1–16.

High-shear melt processing of polymer–carbon nanotube composites

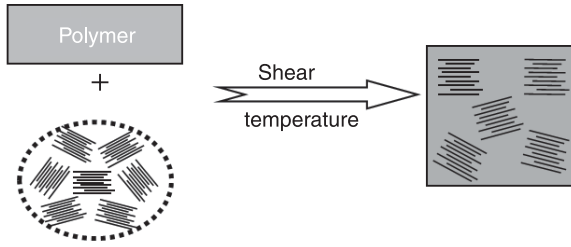
Y. LI and H. SHIMIZU, National Institute of Advanced
Industrial Science and Technology (AIST), Japan

Abstract: This chapter discusses the shear rate effects on the structure and properties of polymer–carbon nanotube (CNT) composites. The chapter first introduces the newly developed high-shear processing technique and its application for preparing polymer nanoblends. We then discuss the morphologies and properties of CNT nanocomposites based on homopolymers and polymer blends by the high-shear processing technique.

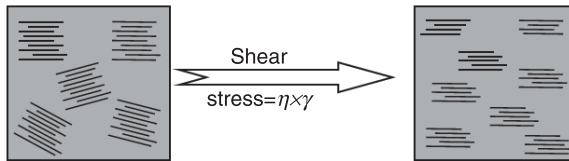
Key words: dispersion, double percolation, high-shear processing, nanocomposites.

5.1 Introduction

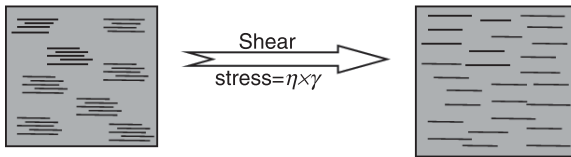
The nanoscale dimension, along with their large shape anisotropy, high mechanical strength, and very high thermal and electrical conductivities, makes carbon nanotubes (CNTs) excellent filler for preparing polymer-based nanocomposites (Xie *et al.*, 2005; Thostenson *et al.*, 2005; Moniruzzaman, 2006). Multifunctional polymer nanocomposites containing CNTs have become one of the hottest research topics in materials science. Dispersion of CNTs is an important first step toward many potential applications that harness the unique physical properties of the individual tube. Because of the substantial van der Waals attraction (-950eV/nm) and the insolubility of CNTs in polymer matrix, nanotubes tend to aggregate easily and are difficult to disperse in a polymer matrix. Therefore, the fabrication methods of polymer–CNT nanocomposites have overwhelmingly focused on improving nanotube dispersion. Although various fabrication methods, such as solution blending (Andrews *et al.*, 1999; Shaffer, 1999), melting blending (Pötschke *et al.*, 2003; Liu *et al.*, 2004), *in-situ* polymerization (Zhu *et al.*, 2003; Wu *et al.*, 2003; Gao *et al.*, 2005), surfactant-assisted processing (Vigolo *et al.*, 2002; Sundararajan *et al.*, 2004), have been applied to manufacture polymer–CNT nanocomposites, melt blending using high temperature and shear forces is the way most compatible with practical industrial applications. Whereas in Chapter 4 aspects of filler dispersion, such as melt infiltration into primary agglomerates, rupture and erosion are discussed based on a literature review and experiments, we simply assume in this chapter that the applied shear stress is the main influencing factor for CNTs' dispersion. Figure 5.1 shows a simplified schematic diagram of the CNTs' dispersion states depending on the applied shear



Step 1. Agglomerates of CNT break up into small stacks



Step 2. Shearing leads to smaller CNT bundles



Step 3. Tubes peel apart by combined polymer diffusion/shear process

5.1 Schematic illustration of the CNTs' dispersion states depending on the applied shear stress during melt compounding.

stress during melt compounding. First, the CNTs agglomerates break up into the small CNT stacks, upon the shear stress applied on the CNTs in the polymer melts. The shear stress helps break up the small stacks into CNT bundles upon increasing the applied shear rate. Finally, the individual tubes peel apart and disperse in the polymer matrix, if the applied shear stress is sufficiently high and can overwhelm the electrostatic and van der Waals interactions between the carbon nanotubes. Unfortunately, in many cases using conventional polymer melt processing equipment which is commercially available does not lead to the homogeneous dispersion of as-produced CNTs. Mixers using high shear stresses therefore may be very suitable for good dispersion due to very high shear stresses helping to individualize the nanotubes. However, high shear forces also may lead to nanotube breakage which may positively influence dispersion but negatively affect the electrical and mechanical properties of the nanocomposites. Another

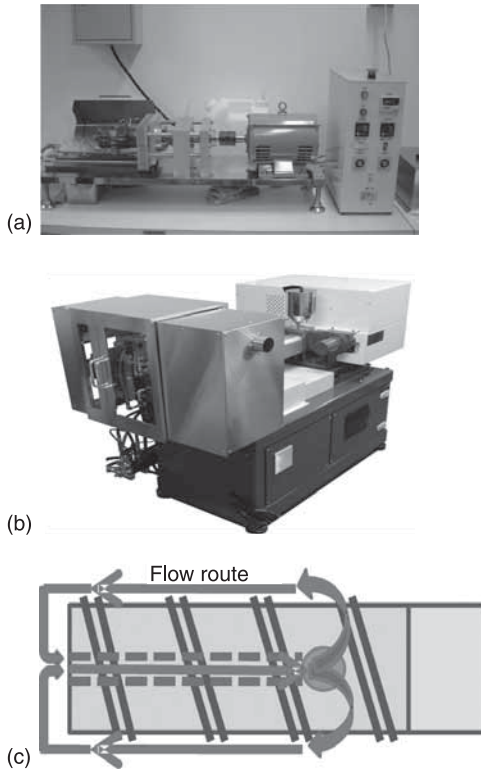
way to improve dispersion is CNT surface treatment, leading to improved compatibility between CNT and polymers. However, the treatment (especially if done by chemical means) can damage the structure and properties of CNTs, but also increase costs and may cause environmental problems.

In this chapter, we present a new melt blending technique, a high-shear melt processing technique, for fabricating polymer–CNT nanocomposites where no surface modification is needed for the CNTs to obtain excellent dispersion. In Section 5.2, we introduce the newly developed processing technique and its main characteristics. Section 5.3 illustrates briefly nanostructured blends from immiscible polymer components prepared using this technique in order to show the capability of that technique. In Section 5.4, the structure and properties of various polymer–CNT nanocomposites produced by high shear processing will be discussed. Finally, in Section 5.5, some conclusions and prospects for future work are presented.

5.2 High-shear processing technique

The high-shear processing technique was first developed to improve the compatibility between immiscible polymer blends. Although both the kinetics and the thermodynamic investigations indicate the possibility of decreasing the phase size of polymer blends by increasing the shear rate during processing (Wu, 1987; Uttandaraman, 1995; Shimizu *et al.*, 2004), fewer attempts have been made to develop polymer processing equipment that can exert high shear rate ($>1000 \text{ sec}^{-1}$) on polymer melt during processing. We have established a polymer processing technique that can exert extremely high shear rates on polymer melts during melt processing by incorporation with an extruder maker. We call this equipment a high shear extruder (HSE). The overviews of the first and second generation of HSE are shown in Figs 5.2 (a) and 5.2 (b), respectively. Now the HSE is commercially available with the trade name of NHSS2-28. The main characteristics of this high shear extruder include:

1. *Extremely high shear rate and adjustable shear rate:* The HSE can apply a maximum 4400 sec^{-1} shear rate on polymer melts and the screw rotation speeds are changeable.
2. *Combination of shear flow and extensional flow:* A special feed-back screw was used and this makes the shear flow and extensional flow simultaneous during melt compounding. The flow route of polymer melt during melt mixing is shown in Fig. 5.2 (c).
3. *Changeable mixing time:* The HSE includes a plastizing part and a high-shear mixing part. The high-shear mixing part is a batch-style mixer. The mixing time can be adjusted according to requirements. After the processing, the sample was extruded through a T-tie and cooled down using cooling water or air depending on the requirements.

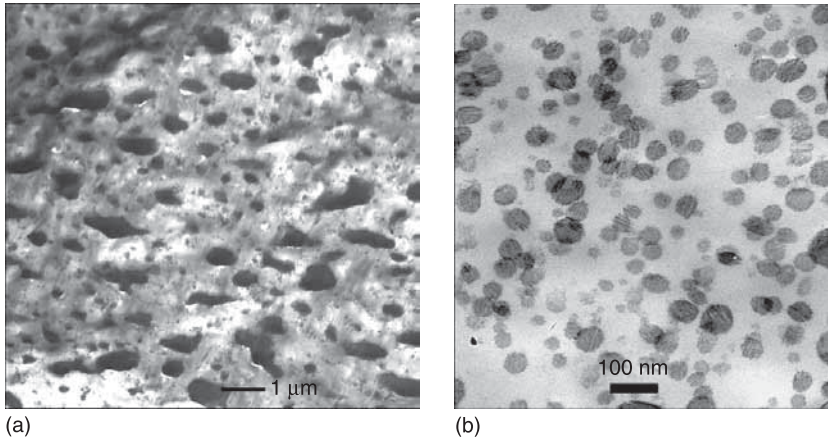


5.2 (a) Overview of HSE in first generation; (b) overview of HSE in second generation; (c) schematic diagram of polymer melt flow route in HSE.

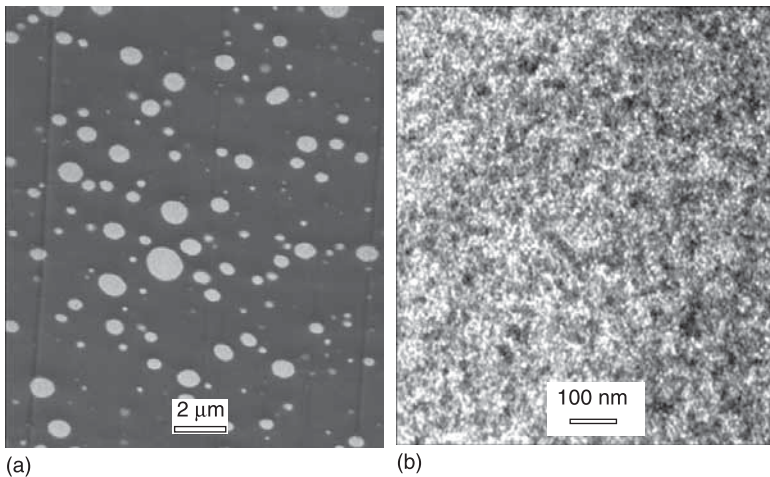
4. *Fully automatic and well-controlled processing parameters:* All the processing parameters, such as processing temperature, torque, pressure, are highly controlled and fully recorded.
5. *Production capacity:* Can reach 10–20 kg/day depending on the mixing time.

5.3 Polymer nanoblends by high-shear processing

A high-shear processing technique is effective to improve the compatibility of immiscible polymer blends. Figure 5.3 displays the TEM images for immiscible polyamide 11 (PA11)–poly(vinylidene fluoride) (PVDF) = 20/80 wt% blends processed at 230°C for 4 min. under the shear rates of 146 sec^{-1} and 1750 sec^{-1} . As expected for immiscible polymer blends, a coarse and heterogeneous macrophase separation is observed for the blend prepared at low shear rate. The domain size ranges from 0.2 to 1 μm . However, a totally different morphology was obtained for PA11–PVDF blends when processed at a high shear rate. PA11 domains are estimated to be only about 20 nm and they are dispersed homogeneously in the PVDF phase. The detailed structural investigation displayed a molecular chain



5.3 TEM images of PVDF–PA11 (= 80/20) prepared under shear rates of (a) 146 sec^{-1} and (b) 1460 sec^{-1} using the HSE.



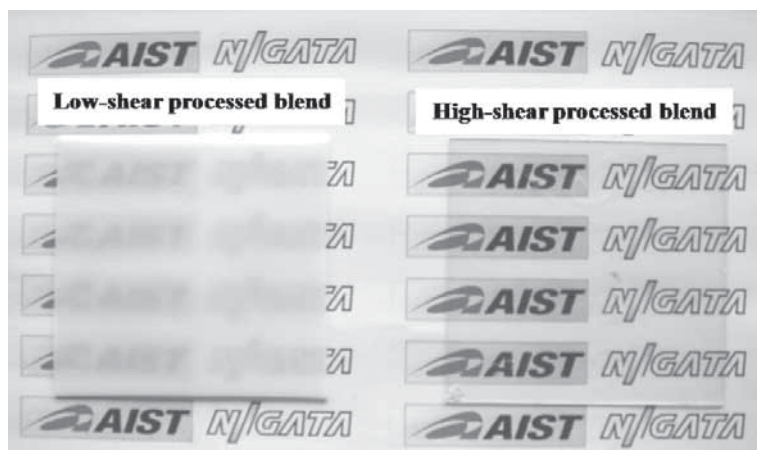
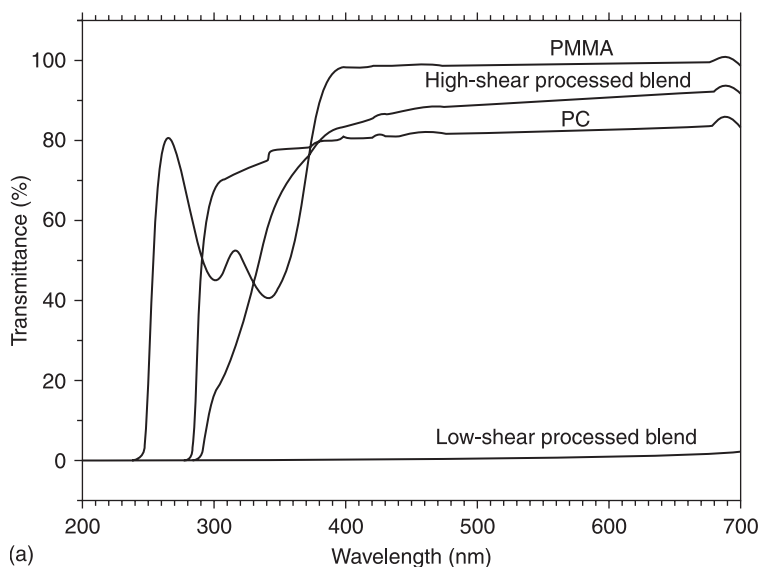
5.4 TEM images for (a) PC–PMMA (= 80/20) blend at 220 sec^{-1} and (b) PC–PMMA (= 80/20) blend at 1650 sec^{-1} .

interpenetration between PVDF and PA11 under high shear rate (Shimizu *et al.*, 2005; Shimizu *et al.*, 2006). Moreover, this nanostructure PVDF–PA11 blend exhibits improved mechanical and electrical performance (Li and Shimizu, 2006, 2007a, 2007b).

Polycarbonate and poly(methyl methacrylate) have also been blended in order to prepare transparent polymer blends with controllable mechanical and optical performance (Li and Shimizu, 2010). Figure 5.4 shows TEM images of PC–PMMA = 80/20 samples processed at 225°C for 30 sec. using shear rates of 220 sec^{-1} and 1650 sec^{-1} . The low-shear-processed sample has a coarse phase

morphology with the PMMA domain size ranging from 200 nm to 2 μm . In addition, a weak interface can also be discerned for this sample. On the other hand, all the PMMA domains are homogeneously dispersed in the PC matrix for the high-shear-processed sample. The domain size of PMMA is less than 50 nm, which is significantly smaller than that in the low-shear-processed sample.

Figure 5.5 (a) shows the quantitative UV-vis transmittance spectra of pure PC, pure PMMA, and PC-PMMA (= 80/20) blends prepared at the high and low



5.5 (a) UV-vis transmittance spectra of pure PC, pure PMMA, and PC-PMMA (= 80/20) blends prepared at the high and low shear rates; (b) the appearance of the PC-PMMA films processed at high and low shear rates (sample thickness: 0.5 mm).

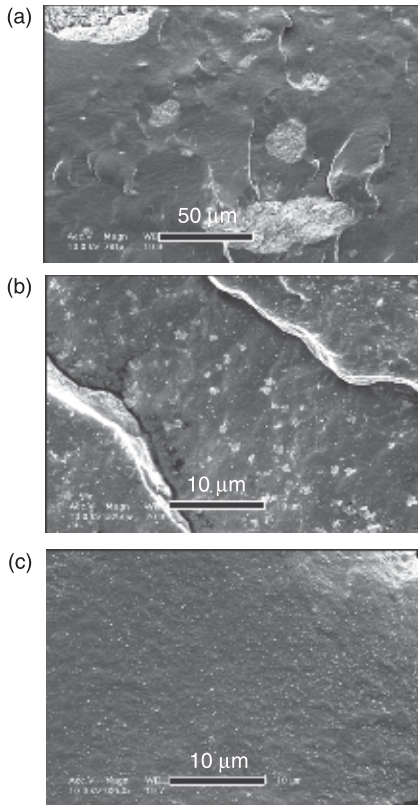
shear rates. All samples have a thickness of about 500 μm . PMMA exhibits a very high transmittance of about 93% above a wavelength of 450 nm, while pure PC has a transmittance of about 82% in the same wavelength region. The high-shear-processed blend exhibits a UV–vis spectrum between those of PC and PMMA. The transmittance in the visible region is 91%, indicating the high clearance of the high-shear-processed blend. In contrast, the sample processed under the low screw rotation speed, i.e. 220 sec^{-1} , has no transmittance in the entire wavelength region. Figure 5.5 (b) shows photographs of the hot-pressed film obtained from the PC–PMMA blends processed at the high and low screw rotation speeds. It is clear that the high-shear-processed blend exhibits excellent optical transparency due to the fine nanostructure, while the low-shear-processed sample is opaque.

5.4 Polymer–carbon nanotube (CNT) nanocomposites by high-shear processing

5.4.1 Homopolymer–CNT composites by high-shear processing

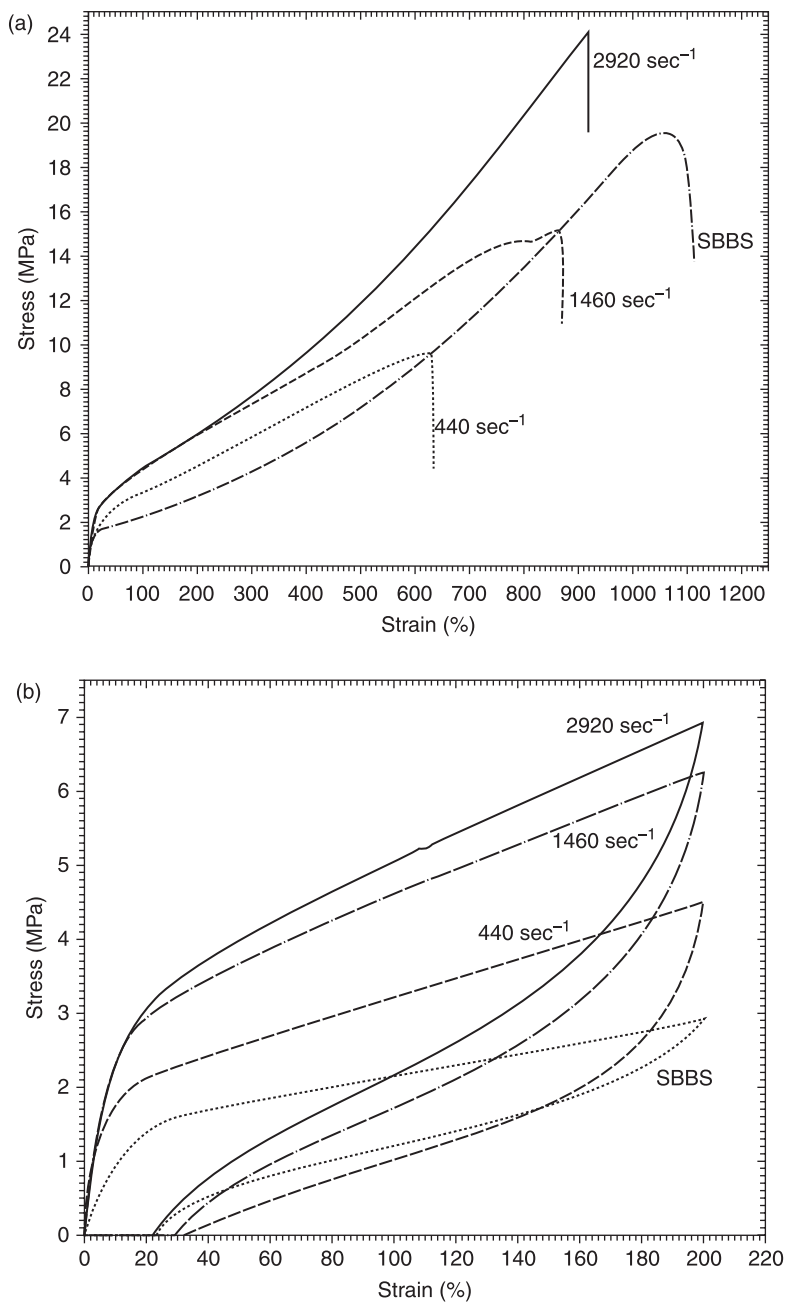
The pristine multi-walled carbon nanotubes (from CNT Co., Ltd of Korea) were mixed with poly(styrene-*b*-butadiene-*co*-butylene-*b*-styrene) (SBBS) using the high-shear processing technique (Li and Shimizu, 2007b). The dispersion of CNTs in the polymer matrix was highly dependent on the shear rates exerted, as shown in Fig. 5.6 for composites with 3 wt% CNTs. The fractured surface of the high-shear-processed sample after immersing in liquid nitrogen was observed. Many CNT aggregates with sizes ranging from 5 to 50 μm are clearly observed for the composites processed at 200°C for 4 min. under the shear rate of 440 sec^{-1} . This means that the CNTs are not well dispersed in the SBBS matrix and most of the CNTs still remain in agglomerates when processed at this shear rate. Note that the shear rate used is even higher than that of conventional extruders and injection molding machines. The size of the CNT agglomerates was significantly decreased to sub- μm scale upon increasing the shear rate to 1460 sec^{-1} , as seen in Fig. 5.6 (b). For the sample processed at the shear rate of 2920 sec^{-1} , the CNTs are homogeneously distributed in the SBBS matrix without any agglomerates. The typical diameter of the bright regions in the SEM image in Fig. 5.6 (c) ranges from 20 to 50 nm, which is consistent with the diameter of a single carbon nanotube, indicating that most of the CNTs are dispersed in the matrix as individual tubes. It is apparent that the dispersion of pristine CNTs is greatly improved upon increasing the exerted shear rate and a homogeneous dispersion is successfully achieved by using the shear rate of 2920 sec^{-1} . It is considered that high shear rate imparts high shear stresses on the CNTs agglomerates, which may skew the stacks of carbon nanotubes and finally separate them into individual tubes.

The physical properties are different for the composites prepared under different shear rates even with the same CNTs' loading content (as shown in Fig. 5.7 (a))



5.6 SEM images for the SBBS–CNTs nanocomposites with 3 wt% loading processed under the shear rate of: (a) 440 sec^{-1} ; (b) 1460 sec^{-1} ; (c) 2920 sec^{-1} .

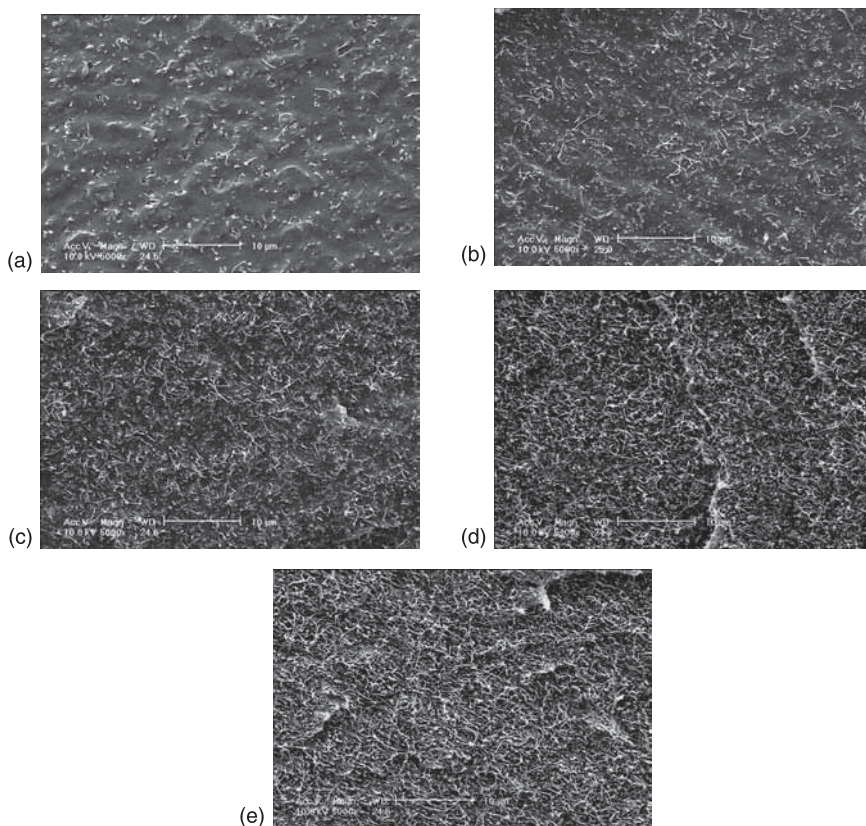
on tensile tests performed at a cross-head speed of 50 mm/min at 20°C and 50% relative humidity. The fact that better reinforcement effects of CNTs in the composites are found at 2920 sec^{-1} than those in the composites at 440 sec^{-1} is obviously due to the fine carbon nanotube dispersion. Moreover, the elongation at break of the composites at high shear rate is also much larger than the value for the composites processed at the low shear rate. The existence of CNT agglomerate may decrease the elongation of nanocomposites. Elasticity is very important for thermoplastic elastomer composites. Figure 5.7 (b) presents the stress–strain recovery behavior of the neat SBBS and the composites prepared at different shear rates. The neat SBBS as received by simple hot pressing shows excellent elastic recovery with a residual strain of about 20.3%. The best CNTs dispersion composites processed at a high shear rate yield a slightly higher residual strain of about 22.6%. However, the residual strain for the composites processed under low shear is 34.4%, indicating the deteriorated elasticity of the composites.



5.7 Stress–strain curves (a) and strain recovery curves (b) for the SBBS–CNTs composites under indicated shear rates (CNTs loading is 3 wt%).

It is clear that the mechanical properties of the composites greatly depend on the shear rate during processing. The difference in these properties can be attributed to the different dispersion states of CNTs in the SBBS matrix. In our example we found that a higher screw rotation speed at a constant mixing time of 4 min. resulted in better carbon nanotube dispersion in the matrix, leading to the improved physical properties.

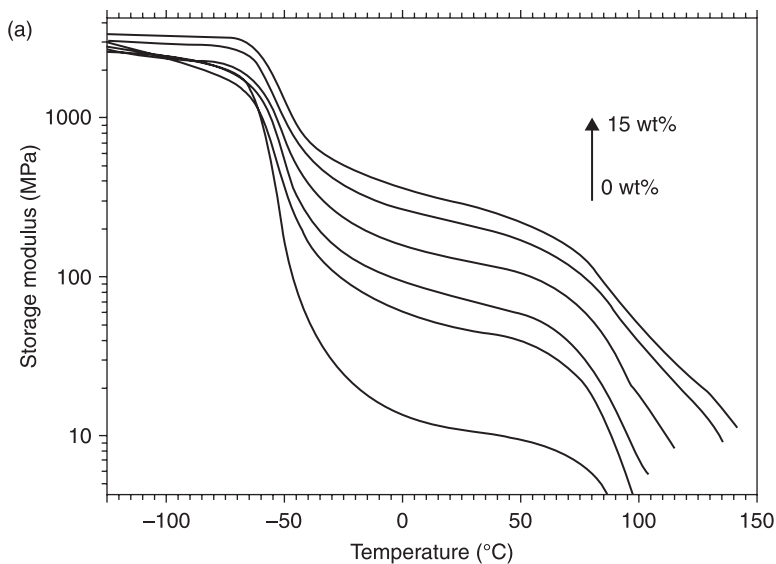
Similar results can also be obtained using another type of carbon nanotubes (from Nikkiso Co., Ltd. Japan), which have much higher electrical conductivity. We tried to disperse the CNTs in a poly[styrene-*b*-(ethylene-*co*-butylene)-*b*-styrene] triblock copolymer (SEBS) matrix aiming at fabricating an elastic conductive polymer nanocomposite (Li and Shimizu, 2009). The SEBS pellets and the CNTs as received were directly melt mixed using the HSE, and SEBS-CNT nanocomposite sheets were obtained through the T-tie after processing. The fracture surface was observed using SEM. Figure 5.8 shows the SEM images of



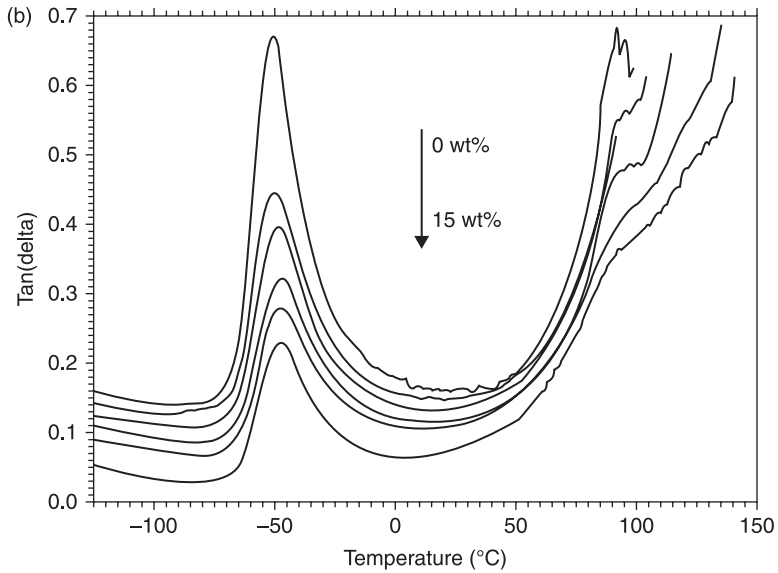
5.8 SEM images of SEBS-MWCNT nanocomposites with different nanotube loadings: (a) 1.25 wt%; (b) 2.5 wt%; (c) 5.0 wt%; (d) 10 wt%; (e) 15 wt%.

the SEBS–CNT nanocomposites with different CNT loadings at 200°C for 2 min. under the shear rate of 1460 sec⁻¹. The homogeneous dispersion of CNTs in the SEBS matrix can be obtained even at very high CNTs loading. No CNT agglomerates are observed in SEM at the CNT content as high as 15 wt%.

All the extruded nanocomposites sheets were hot-pressed again at 200°C to a film with a thickness of 500 µm, followed by cooling to room temperature. The rectangular sample with the size of 60mm × 8mm × 0.5mm was punched from the pressed film and used for the dynamic mechanical analysis in tensile mode. Figure 5.9 shows the variation of storage modulus and the loss tangent as a function of temperature for the various nanotube compositions. The storage modulus values for nanocomposites are higher than that for neat SEBS over the whole temperature range. Moreover, the nanocomposites with high CNT content (>2.5 wt%) exhibit greatly improved thermal resistance. Neat SEBS starts to flow (modulus tends to 0) when the temperature is higher than 75°C. However, for the nanocomposites with more than 2.5 wt% CNTs, all samples are self-supporting at the high temperatures due to the formed CNTs networks. The variation of loss tangent (Fig. 5.9 (b)) for neat SEBS and the nanocomposites with temperature shows an EB glass transition at a temperature of about -50°C. The glass transition temperature of the nanocomposites with more than 2.5 wt% CNTs is around -47°C, which is higher than -50.7°C for the neat SEBS and the nanocomposite with 1.25 wt% nanotubes. The increased glass transition of EB block can be attributed to the geometrically confined environments by the well-dispersed CNTs.

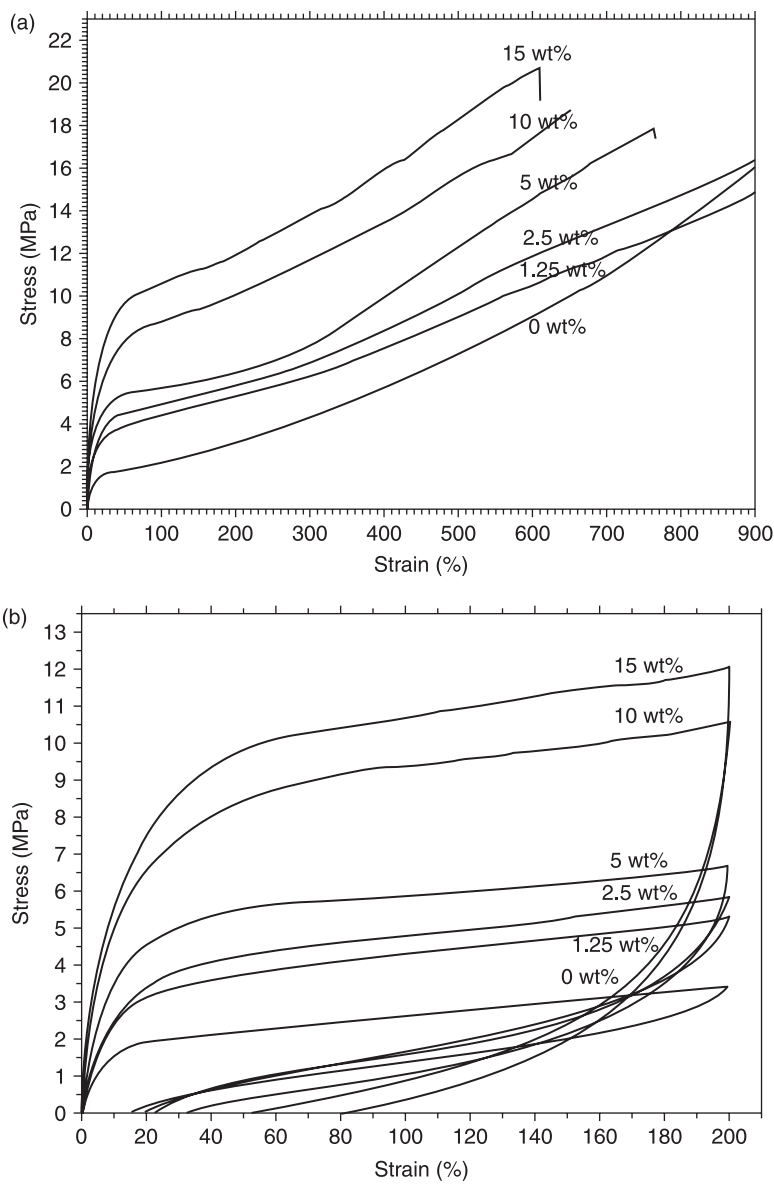


5.9 Temperature dependence of: (a) storage modulus; (b) $\tan\delta$ for the SEBS–MWCNT nanocomposites with indicated MWCNT loadings.
(Continued)



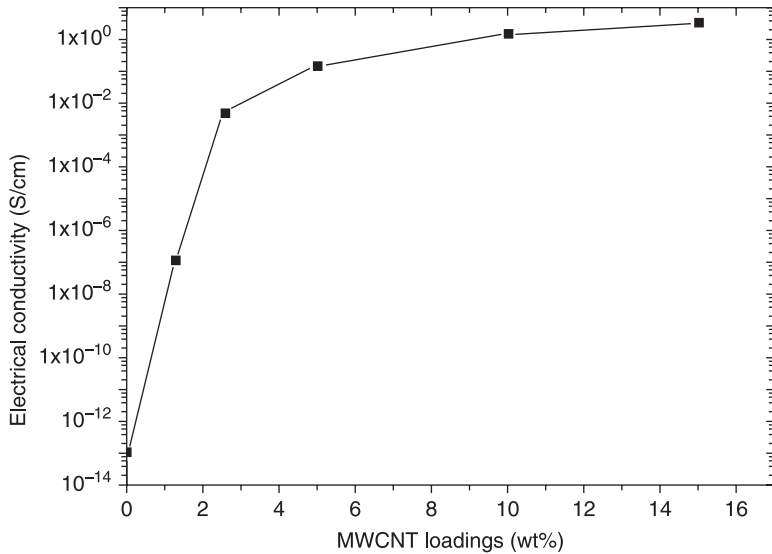
5.9 Continued.

Figure 5.10 (a) illustrates the strain–stress curves for neat SEBS and its nanocomposites. It is clear that the added CNTs show dramatic reinforcement effects for SEBS matrix because all the nanocomposites have a higher modulus and greater strength than neat SEBS. This strengthening effect increases with increasing CNT loading. Interestingly, all the nanocomposites show excellent stretchability as evidenced by the very high elongation at break. Moreover, the stretchability of the nanocomposites only slightly decreases upon increasing the CNT content, in contrast to most inorganic filler strengthened polymer systems. Figure 5.10 (b) shows the strain–recovery curves for neat SEBS and the nanocomposites. Neat SEBS exhibits excellent elasticity with a residual strain of about 15%. With the addition of CNTs, the residual strain increases gradually, indicating the decreased elasticity of the nanocomposites. Two factors may account for the decreasing elasticity of the nanocomposites. On the one hand, the elasticity of the SEBS originates from the physical cross-linking network with the rigid PS nanodomains as the cross-link points. Both small angle X-ray scattering and transmission electron microscopy indicate that the CNTs disturb the microphase separation behavior of SEBS (Li, 2008). Therefore, the cross-link density may decrease gradually upon the incorporation of CNTs. On the other hand, there is no covalent bonding connection between the CNT surface and SEBS even though strong interfacial adhesion has been observed. An irreversible slip is highly likely to occur between the CNT surface and SEBS upon mechanical



5.10 Strain–stress curves (a) and strain recovery (b) for the SEBS–CNT nanocomposites.

deformation. Although the CNTs deteriorate the elastic properties of SEBS, all the nanocomposites still show good strain-recovery properties. The residual strain of the nanocomposite with 15 wt% CNTs is 76% after 200% stretching, which means that about 62% of the deformation is recovered.



5.11 Electrical conductivity of SEBS–MWCNT nanocomposites as a function of CNT loadings.

Figure 5.11 shows the volume conductivities for SEBS–MWCNT nanocomposites as a function of the MWCNT loading content. As expected, the electrical conductivity of all the composites strongly depends on the nanotube loading content. A sudden increase in the conductivity was observed as the MWCNT loading content increased from 1.25 to 2.5 wt%, indicating the formation of a percolating network. This is consistent with the SEM observation that an MWCNT network forms at the nanotube loading of 2.5 wt%. The conductivity increases continuously with increasing CNT content above this percolation threshold. The maximum conductivity was 5.16 S/cm for the nanocomposites with 15 wt% MWCNTs.

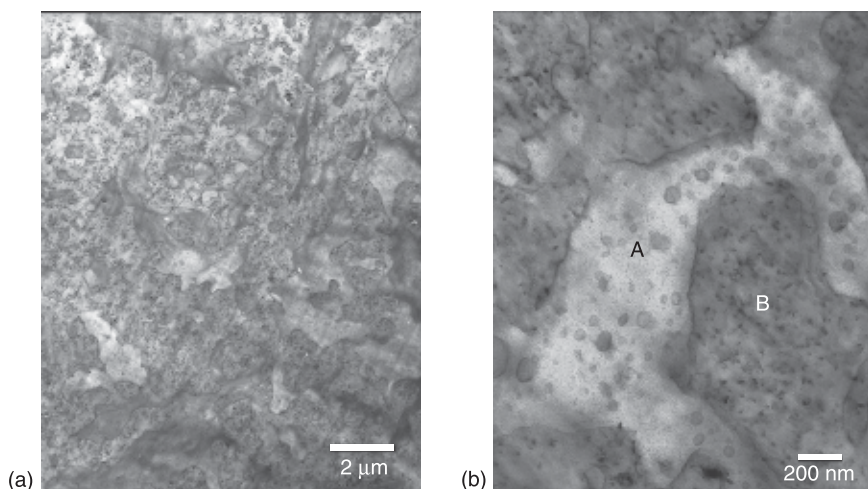
The high-shear processing technique has also been reported to be very effective for fabricating some other homopolymers–CNTs nanocomposites, like polylactide (PLA)–CNTs (Chen *et al.*, 2007) and poly(vinylidene fluoride) (PVDF)–CNTs nanocomposites (Chen and Shimizu, 2008). The high shear stress exerted on the polymer melt during processing helps the dispersion of carbon nanotubes.

5.4.2 Polymer blends–CNTs nanocomposites by high-shear processing

The investigations of conductive polymer composites have focused mainly on decreasing the percolation threshold to lower the cost, improve processability, and enhance the mechanical properties of composites. An important way of reducing the percolation threshold of composites is to induce selective localization of

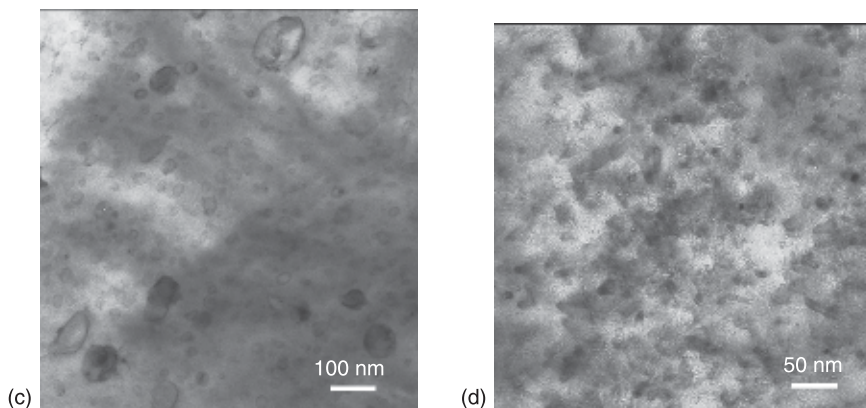
conductive fillers in the materials (Wignall *et al.*, 1990; Levon *et al.*, 1993; Luo *et al.*, 1998; Meincke *et al.*, 2004; Pötschke *et al.*, 2004; Gödel *et al.*, 2009). The most effective method is to make a double percolation structure, in which a two-phase (immiscible) polymer blend is used as the polymer matrix in composites (Gubbels *et al.*, 1994; Meincke *et al.*, 2004; Pötschke *et al.*, 2004; Gödel *et al.*, 2009). In this type of polymer blend composite, either one of the two polymer phases is continuous and a conducting filler is selectively localized in the continuous phase, or the two phases are co-continuous and the filler has preferably to be in one phase (Levon *et al.*, 1993; Meincke *et al.*, 2004; Pötschke *et al.*, 2004; Gödel *et al.*, 2009) or at the interface (Gubbels *et al.*, 1994; Gubbels *et al.*, 1995). However, the co-continuous type of conductive polymer composite without compatibilization usually exhibits poor mechanical properties due to incompatibilities between component polymers. Moreover, the formed morphologies are sometimes not stable upon thermal annealing at melting temperature. Therefore, the fabrication of a thermally stable co-continuous conductive polymer composite with further reduced filler loading content and improved mechanical properties still poses significant scientific and industrial challenges. The high-shear processing technique was used to fabricate the polymer blend nanocomposites for the purpose of making high performance polymer conductive composites.

The morphological investigations indicate that high-shear-processed PVDF–PA6–CNTs composites have unique hierarchical structures (Li and Shimizu, 2008). Note that the three components were added together to the HSE and the blend nanocomposites were then extruded after the melt mixing. Figure 5.12



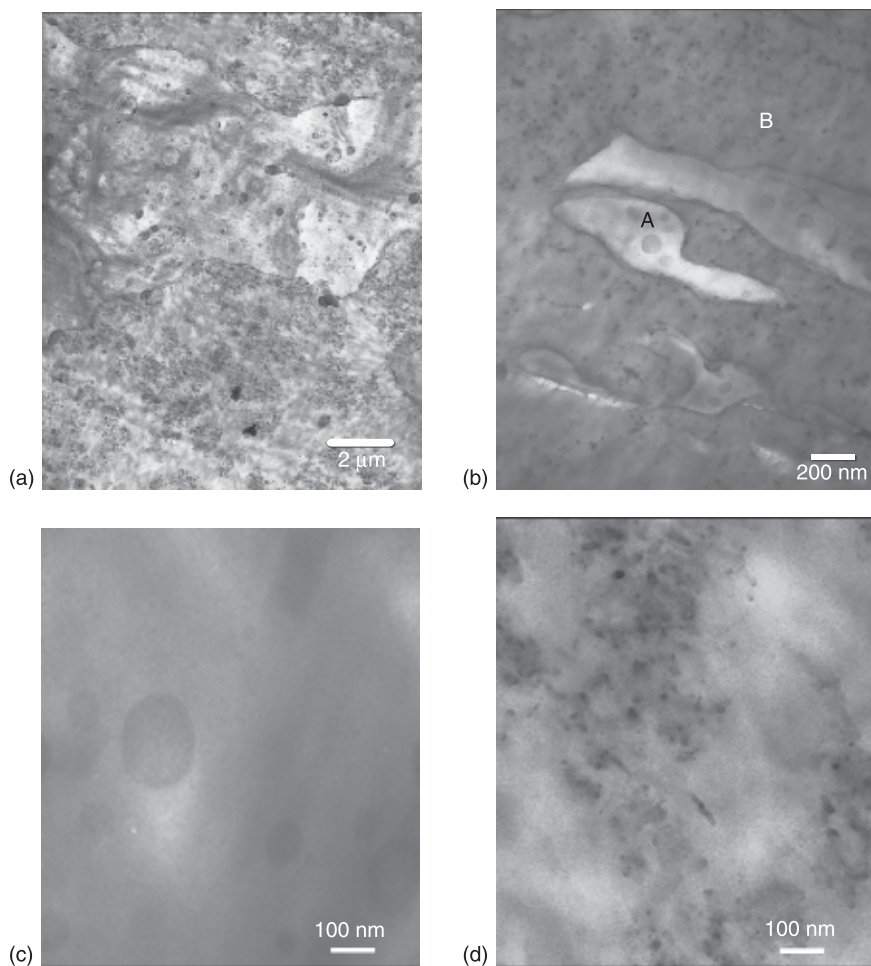
5.12 TEM image of high-shear-processed PVDF–PA6–CNTs composites (CNT loading content is 1.8 wt%): (a) at ×5000 magnification; (b) at ×50,000 magnification; (c) enlarged part of region A; (d) enlarged part of region B.

(Continued)



5.12 Continued.

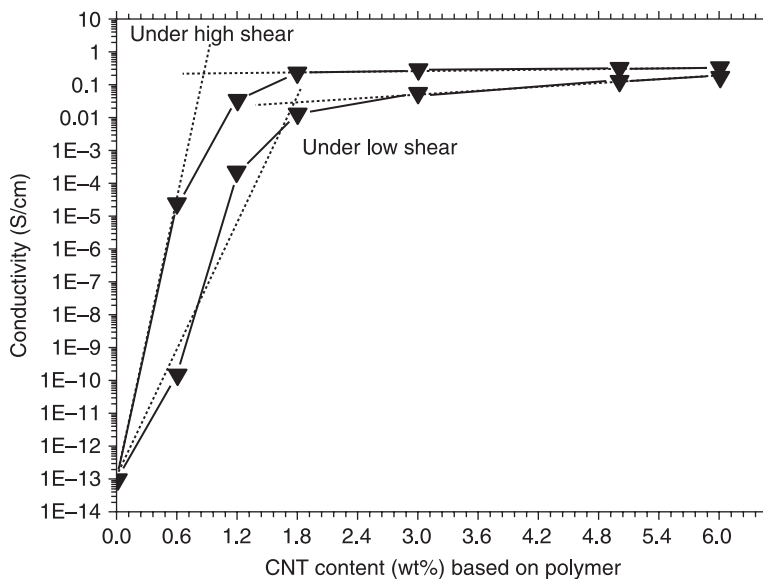
shows typical TEM images obtained by changing the magnifications of the PVDF–PA6–CNTs composites processed at 240 °C for 2 min. under a screw rotation speed of 1460 sec^{-1} (designated high-shear-processed sample). In this composite, a hierarchical structure was observed. PVDF and PA6 basically form the co-continuous structure on the micrometer scale. The substructure in both of the two phases can be discerned. CNTs have homogeneously and selectively located in the PA6 phase and many PA6 nanodomains with sizes of several tens of nanometers are dispersed in the PVDF phase. It was further found that this hierarchical structure is very stable when subjected to thermal annealing. The composite structure processed at a high shear showed no change when we remelt the sample at 240 °C for 2 hours using a hot-press machine with no shear. In contrast, a different morphological structure was obtained for the same composites prepared using the shear rate of 146 sec^{-1} (designated low-shear-processed sample) during melt processing, as shown in Fig. 5.13. Similar to the composite prepared under the high shear rate, the low-shear-processed sample shows a co-continuous structure with all CNTs located in the PA6 phase. However, two significant differences can be observed with the detailed observation in both PVDF and PA6 phases. First, few PA6 nanodomains can be found in the PVDF phase for the low-shear-processed sample. Second, the dispersion of the CNTs in the PA6 phase is not very homogeneous and clear CNTs agglomerates can be observed. The morphological difference between the two samples leads to the significant variation in electrical conductivity, as shown in Fig. 5.14. Near the percolation threshold of about 1 wt% the conductivities for the sample at low shear rate are much lower than those for the high-shear-processed sample at the same CNT loading content. At 0.6 wt% CNT loading, the conductivity of the high-shear-processed sample is about five decades higher than that of the low-shear-processed sample. The percolation threshold value can be determined as the intersection point of two lines which are where the conductivity increases



5.13 TEM image of the low-shear-processed PVDF–PA6–CNTs composites (CNT loading content is 1.8 wt%): (a) at $\times 5000$ magnification; (b) at $\times 50\,000$ magnification; (c) enlarged part of region A; (d) enlarged part of region B.

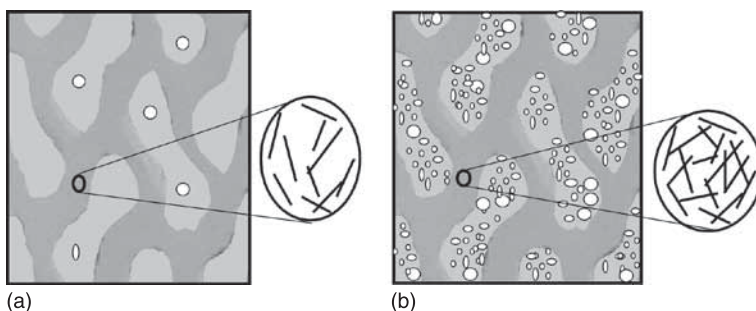
gradually with the CNT loading and the conductivity levels off with the CNT loading. It was therefore found that the percolation threshold value of the low-shear-processed sample is about 1.7 wt%, which is almost twice that of the high-shear-processed sample.

It is obvious that carbon nanotubes are well exfoliated and highly dispersed in the PA6 phase in the high-shear-processed sample, in comparison with those in the low-shear-processed sample. Therefore, an interconnecting CNT conducting network is readily formed at lower CNT concentrations for the high-shear-processed sample. On the other hand, numerous PA6 nanodomains are observed in the PVDF phase for

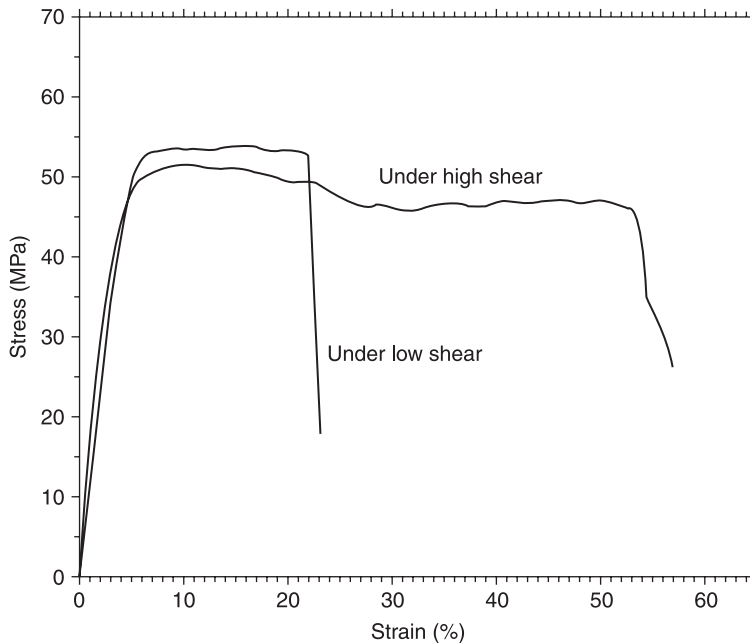


5.14 Electrical conductivity for the PVDF–PA6–CNTs composites fabricated under the different shear rates.

the high-shear-processed sample, which means that some parts of PA6 are trapped in the PVDF phase as induced by the high shear stress during the melt mixing. Although CNTs have a higher affinity with PA6 than with PVDF, they still cannot locate in PA6 nanodomains with sizes less than 200 nm in the PVDF phase, because the lengths of a single carbon nanotube range from 5 μm to 20 μm , which is much longer than the diameter of PA6 nanodomains. Therefore, the actual CNT concentration in the PA6 matrix in the high-shear-processed sample is higher than that in the low-shear-processed sample (Fig. 5.15). Although we did not estimate the PA6 ‘trapping’ content in PVDF phase, one can see that the CNT concentration in PA6 phase in the high-shear-processed sample is higher than that in the low-shear-processed sample



5.15 Morphological schematic representations of PVDF–PA6–CNTs composites processed under (a) low shear and (b) high shear.



5.16 Stress–strain curves for the PVDF–PA6–CNTs composites fabricated under the different shear rates.

owing to the formation of nanodomains in the PVDF phase. Therefore, the high-shear-processed composites have higher electrical conductivity than the low-shear-processed composites, even with the same composition ratio.

Generally, polymer blend composites with selectively located fillers show poor mechanical properties and low ductility because of the weak interface between the two phases. Figure 5.16 exhibits a comparison of the stress–strain curves for the high-shear- and low-shear-processed PVDF–PA6–CNTs composites using dumbbell-shaped specimens punched from the hot-pressed sample. The tensile tests were carried out at a rate of 10 mm/min. at 20°C and 50 % relative humidity. The blend composites fabricated using different screw rotation speeds have almost the same modulus, but different elongations at break. The elongation at break for the high-shear-processed composites is about 200% higher than that for the low-shear-processed composites. The marked improvement in the physical properties of the composites is also related to the improved compatibility between PVDF and PA6 induced by the high-shear processing.

5.5 Conclusion and future trends

The dispersion of carbon nanotubes in polymer matrix was found to be highly dependent on the applied shear rate during melt mixing. The higher the shear rate

exerted, the better CNTs dispersion was obtained. Therefore, the high shear processing technique is very effective for fabricating polymer–CNT nanocomposites, and improved physical properties of the nanocomposites can be achieved. The technique is simple and compatible with the industrial application and it does not cause any environmental problem. However, the critical shear rate for the homogeneous CNT dispersion depends not only on the polymer matrix used, but also on the nature of the carbon nanotubes. Moreover, the extremely high shear stress may lead to both the degradation of polymer matrix and the scission of CNTs, which has not yet been investigated in detail but could be the topic of the future work. It is believed that the balance for the CNT shortening and improved dispersion is the most important factor in fabricating useful CNT nanocomposites. Finally, it should be mentioned that the high-shear processing technique was also found to be effective for making other polymer nanocomposites based on various types of nanofillers such as TiO_2 , POSS, SiC, and SiO_2 .

5.6 References

- Andrews R, Jacques D, Rao A, Rantell T, Derbyshire F, Chen Y, Chen J, Haddon R C (1999) 'Nanotube composite carbon fibers', *Appl. Phys. Lett.*, 75, 1329–1331.
- Chen G X, Li Y, Shimizu H (2007) 'Ultrahigh-shear processing of polymer/carbon nanotube composites', *Carbon*, 45, 2334–2340.
- Chen G X, Shimizu H (2008) 'Multiwalled carbon nanotubes grafted with polyhedral oligomeric silsesquioxane and its dispersion in poly(L-lactide) matrix', *Polymer*, 49, 943–951.
- Gao J, Itkis M E, Yu A, Bekyarova E, Zhao B, Haddon R C (2005) 'Continuous spinning of a single-walled carbon nanotube-nylon composite fiber', *J. Am. Chem. Soc.*, 127, 3847–3854.
- Gödel A, Kasaliwal G, Pötschke P (2009) 'Selective localization and migration of multiwalled carbon nanotubes in blends of polycarbonate and poly(styrene-acrylonitrile)', *Macromol. Rapid Communications*, 30, 423–429.
- Gubbels F, Blacher S, Vanlathem E, Jérôme R, Deltour R, Brouers F, Teyssie Ph (1995) 'Design of electrical conductive composites – key role of the morphology on the electrical-properties of carbon black filler polymer blends', *Macromolecules*, 28, 1559–1566.
- Gubbels F, Jérôme R, Teyssie Ph, Vanlathem E, Deltour R, Calderone A, Parente V, Bredas J L (1994) 'Selective localization of carbon black in immiscible polymer blends- a useful tool to design electrical conductive composites', *Macromolecules*, 27, 1972–1974.
- Levon K, Margolina A, Pateshinsky A Z (1993) 'Multiple percolation in conducting polymer blends', *Macromolecules*, 26, 4061–4063.
- Li Y, Shimizu H (2006) 'Morphological investigations on the nanostructured poly(vinylidene fluoride)/polyamide 11 blends by high shear processing', *Eur. Polym. J.*, 42, 3202–3211.
- Li Y, Shimizu H (2007a) 'Crystal forms and ferroelectric properties of poly(vinylidene fluoride)/polyamide 11 blends prepared by high-shear processing', *J. Polym. Sc. Part B: Polym. Phys.*, 45, 2707–2714.
- Li Y, Shimizu H (2007b) 'High shear processing induced homogenous dispersion of pristine multiwalled carbon nanotubes in a thermoplastic elastomer' *Polymer*, 48, 2203–2207.

- Li Y, Shimizu H (2008) 'Conductive PVDF/PA6/CNT nanocomposites fabricated by dual formation of cocontinuous and nanodispersion structures', *Macromolecules*, 41, 5339–5344.
- Li Y, Shimizu H (2009) 'Towards a stretchable, elastic and electrically conductive nanocomposite: morphology and properties of poly[styrene-*b*-(ethylene-*co*-butylene)-*b*-styrene]/multiwalled carbon nanotube composites fabricated by high-shear processing', *Macromolecules*, 42, 2587–2593.
- Li Y, Shimizu H (2010) 'Achievement of nanostructured PC/PMMA blends with excellent transparency by high-shear processing', Submitted for publication.
- Liu T, Phang I Y, Shen L, Chow S Y, Zhang W D (2004) 'Morphology and mechanical properties of multiwalled carbon nanotubes reinforced nylon-6 composites', *Macromolecules*, 37, 7214–7222.
- Luo Y L, Wang G C, Zhang B Y, Zhang Z P (1998) 'The influence of crystalline and aggregate structure on PTC characteristic of conductive polyethylene carbon black composite', *Eur. Polym. J.*, 34, 1221–1227.
- Meinke O, Kaempfer D, Weickmann H, Friedrich C, Vathauer M, Warth H (2004) 'Mechanical properties and electrical conductivity of carbon-nanotube filled polyamide-6 and its blends with acrylonitrile/butadiene/styrene', *Polymer*, 45, 739–748.
- Moniruzzaman M, Winey K I (2006) 'Polymer nanocomposites containing carbon nanotubes', *Macromolecules*, 39, 5194–5205.
- Pötschke P, Bhattacharyya A R, Janke A (2004) 'Carbon nanotube-filled polycarbonate composites produced by melt mixing and their use in blends with polyethylene', *Carbon*, 42, 965–969.
- Pötschke P, Bhattacharyya A R, Janke A, Goering H (2003) 'Melt mixing of polycarbonate/multi-wall carbon nanotube composites', *Comp. Interfaces*, 1, 389–404.
- Shaffer M S P, Windle A H (1999) 'Fabrication and characterization of carbon nanotube/poly(vinyl alcohol) composites', *Adv. Mater.*, 11, 937–942.
- Shimizu H, Komori K, Inoue T (2004) 'The phase behavior of polymer blends under high shear flow/high pressure fields', *Trans. of Mater. Res. Soc. Jpn*, 29, 263–265.
- Shimizu H, Li Y, Kaito A, Sano H (2005) 'Formation of nanostructured PVDF/PA11 blends using high-shear processing', *Macromolecules*, 38, 7880–7883.
- Shimizu H, Li Y, Kaito A, Sano H (2006) 'High-shear effects on the nano-dispersed structure of the PVDF/PA11 blend', *J. Nanosci. Nanotech.*, 6, 3923–3928.
- Sundararajan P R, Singh S, Moniruzzaman M (2004) 'Surfactant-induced crystallization of polycarbonate', *Macromolecules*, 37, 10208–10211.
- Thostenson E T, Li C Y, Chou T W (2005) 'Nanocomposites in context', *Comp. Sci. Tech.*, 65, 491–516.
- Uttandaraman S, Macosko C W (1995) 'Drop breakup and coalescence in polymer blends: the effects of concentration and compatibilization', *Macromolecules*, 28, 2647–2657.
- Vigolo B, Poulin P, Lucas M, Lunois P, Bernier P (2002) 'Improved structure and properties of single-wall carbon nanotube spun fibers', *Appl. Phys. Lett.*, 81, 1210–1212.
- Wignall G D, Farrar N R, Morris S (1990) 'Characterization of carbon-filled polymers by small-angle scattering techniques', *J. Mat. Sci.*, 25, 69–75.
- Wu S (1987) 'Formation of dispersed phase in incompatible polymer blends: interfacial and rheological effects', *Polym. Eng. Sci.*, 27, 335–343.
- Wu W, Zhang S, Li Y, Li J, Liu L, Qin Y, Guo Z X, Dai L, Ye C, Zhu D (2003) 'PVK-modified single-walled carbon nanotubes with effective photoinduced electron transfer', *Macromolecules*, 36, 6286–6288.

- Xie X L, Mai Y W, Zhou X P (2005) ‘Dispersion and alignment of carbon nanotubes in polymer matrix: a review’, *Mater. Sc. Eng.*, R49, 89–112.
- Zhu J, Kim J, Peng H, Hargrave J L, Khabashesku V N, Barrera E V (2003) ‘Improving the dispersion and integration of single-walled carbon nanotubes in epoxy composites through functionalization’, *Nano. Lett.*, 3, 1107–1113.

Injection moulding of polymer–carbon nanotube composites

C. Y. LEW, C. DEWAGHE and M. CLAES, Nanocyl S.A., Belgium

Abstract: The electrical resistivity of a polymer–carbon nanotube (CNT) composite is sensitive to injection moulding parameters and, therefore, imparts flexible property design to meet different application requirements. In this chapter, the authors attempt to identify via a 2^I factorial design of experiment the interactions between injection parameters, volume resistivity, surface resistivity and surface finish, using a low viscosity polycarbonate (melt flow index, MFI, 38 g/10min) and then verify the interactions in more detail using a higher viscosity polycarbonate (MFI 20 g/10min). Results indicated that the volume resistivity was most sensitive to injection melt temperature, while injection speed has the greatest influence on surface conductivity. Surface resistivity was found to increase with injection speed while volume resistivity decreases with injection speed. The effect of polymer molecular weight (M_w) on electrical resistivity was also investigated. Volume resistivity decreases with increasing M_w , but the reverse trend was observed for surface resistivity.

Key words: carbon nanotube, electrical resistivity, injection moulding, polycarbonate, rheology.

6.1 Introduction

Collectively, the global market for electro-conductive polymer compounds is forecast to reach US\$2.78 billion by 2014 and the filler-based composites segment currently accounts for 84% of the segment, according to a recent analysis by Market and Markets Consulting.¹ This is driven by increasing application in electrostatic discharge (ESD), electro-conductive (EC), electromagnetic interference (EMI) and radio frequency interference (RFI) applications. By economy scale, both in dollar and volume, the fabrication of conductive compounds in manufactured products is dominated by injection moulding mobilised by fast growing demand for electronics goods and automotives components. In addition, given the ease of processing and improved heat dissipation properties, polymer–carbon nanotube (CNT) composites become attractive in the manufacture of automotive under-the-hood metals replacement in close proximity to a heat source such as an engine or in parts that would generate a high level of heat (e.g. the power transmission system and the fuel rails) or in power computing.

In the past few years, multi-walled CNTs have progressively captured wider industrial acceptance, as well as being a cleaner composite solution (i.e. lower

¹ Markets and Markets Consulting, 'Global electroactive polymers market 2009–2014', Report CH1055, February 2010.

out-gassing material) to carbon black, delivering new design opportunities inconceivable for other traditional conductive fillers, at least as measured by products' performance and cost efficiency. Out-gassing materials, when subjected to heat under low pressure, emit volatiles that would contaminate the application, therefore requiring a very high vacuum environment. Today, CNT composites have entered the mass production shop floor as, for example, polyoxymethylene–CNT and polyamide 12–CNT in fuel lines application for automobiles, as polycarbonate–CNT in integrated-circuit tray and hard-disk drive spindle and high density polyethylene–CNT in extrusion-blown moulded drums.

Because of its relatively low loading level, typically at a fraction of conventional conductive fillers (e.g. 2 wt% CNT versus 10 wt% conductive carbon black), the polymers can retain a higher degree of mechanical properties and an aesthetically more appealing surface finish. For an application requiring very high conductivity, the polymer–CNT composite could transform the design economy of connectors, switches, sensors, actuators, convertors, control modules, supercapacitors, batteries and transistors.

Electrically conductive plastics have been commercially used for many years already and the application of CNT has grown at an exponential rate, from US\$290 million in 2006 to an estimated US\$5 billion by 2012 (Barron and Khan, 2008). Despite the glitch of the current economic climate, CNT-based polymer products are well positioned to enter mainstream commercial production in this decade.

6.2 Background

Injection moulding is characterised by flow at high shear rate and the shear field is generally non-uniform. Predicting the physical properties of an injection-moulded polymer can be a formidable task because even a minor alteration of an injection parameter or mould design can influence the polymer crystallisation behaviour, chain orientation, skin layer formation and residual stress. Furthermore, the effect of an injection parameter can differ from one polymer to another and the variation is non-linear. For example, increasing the injection speed in general enhances the orientation of polymeric-chain lengthwise which, in turn, increases the tensile strength of polypropylene (PP) (Aarøe *et al.*, 2009). However, the reverse trend was found for acrylonitrile butadiene styrene (ABS), while the tensile strength of PC was less sensitive to injection speed (Aarøe *et al.*, 2009; Mekhilef *et al.*, 1991). In a polymer system filled with a conductive particle such as CNT, a higher injection speed can lead to more non-uniform shear across the flow direction and, as a result, the electrical conductivity may vary across the moulding dimension.

For a pressure-driven incompressible viscous flow through a channel, shear stress and shear rate are greatest at the boundary and lowest near the centreline. This difference in shear field gives rise to shear gradient across the flow stream. The gradient in shear rate causes a gradient in the elastic energy for a viscoelastic polymer melt and on the basis of shear-field fractionation, the larger and more

elastic chain (i.e. higher molecular weight, M_w) will diffuse away from the wall and towards the centreline to reduce their potential energy (Shelby and Caflish, 2004). Similarly, in a particle-concentrated flow, the larger and more elastic particles will migrate away from the wall. This phenomenon is termed shear-induced migration theory and is widely studied in the domain of physics of fluids (Leighton and Acrivos, 1987; Phillips *et al.*, 1992).

Not only can the change of injection moulding parameter affect the shear flow and in turn particle distribution of CNT in a polymer, the presence of CNT can also affect the shear flow and solidification behaviour of the polymer, both of which cause change in the final properties. For example, the increase in mould temperature will reduce the shear gradient and therefore more uniform properties across the moulding. Similarly, if CNT can act as a viscous thinning agent (Kharchenko *et al.*, 2004; Ma *et al.*, 2008; Lew *et al.*, 2009b), the shear gradient may also become narrower. Or if the presence of CNT causes the crystal size and size distribution to decrease (Zhang and Zhang, 2007), mechanical toughness could be improved.

To date, there are two general agreements on the effect of injection moulding parameters on the pattern of electrical conductivity of a polymer–CNT composite. First is that by increasing the injection melt temperature, the electrical conductivity increases (Lellinger *et al.*, 2008). For example, the electrical surface resistivity of an injection-moulded PP–CNT decreases from $5 \times 10^8 \text{ ohm.sq}^{-1}$ at 165°C to $1.8 \times 10^6 \text{ ohm.sq}^{-1}$ at 180°C and $6 \times 10^3 \text{ ohm.sq}^{-1}$ at 205°C (Lew *et al.*, 2009a). This is attributed to the fact that higher injection temperature (a) reduces the shear (and hence orientation of CNT), thus enhancing the build-up of conductive network; (b) decreases the orienting skin effect; and (c) possibly reduces the shear gradient, therefore reducing shear-induced migration of CNT away from the wall. Second, the electrical resistivity generally decreases at lower injection speed due to lesser degree of CNT orientation in the core and skin layer (Lellinger *et al.*, 2008; Villmow *et al.*, 2008). A short overview of recent data on the relationship between injection moulding parameters and electrical resistivity is given below.

Park *et al.* (2009) performed an injection moulding study of PC–CNT (2 wt%) using different injection pressure, hold pressure, injection speed and mould temperature and analysed the surface resistivity across the specimen length. Independent of injection parameter, surface resistivity was always higher at near-end region and lowest at near-gate region. They attributed the non-homogeneous distribution of surface resistivity to difference in flowability between CNT and melt, affected by injection parameters. When the relative velocity of the melt was greater than the CNT (higher injection speed), surface resistivity became higher and less uniform. This was corroborated via SEM that showed, for the specimen produced with a combination of a low mould temperature and a high injection speed ($60^\circ\text{C}/22 \text{ mm.s}^{-1}$), CNT distribution was non-homogeneous. In the near-gate region, the CNT concentration was higher as compared to the end region. When an experiment was performed using a high mould temperature and a low injection speed ($120^\circ\text{C}/13 \text{ mm.s}^{-1}$), distribution of CNT was more or less

uniform across the length. To test if difference in flowability was the main reason for non-homogeneity, measurement was conducted across the lateral thickness of the specimen and found the surface resistivity decreases when moving from the surface towards the core region. Difference in hold pressure, however, has no effect on the surface resistivity.

Chandra *et al.* (2007) studied the effect of injection moulding parameters on volume resistivity of PC-CNT (1.8 wt%). Volume resistivity was measured across the width and length of specimen by cutting the gauge section of the specimen. At a higher injection temperature, because of reduced melt viscosity and higher diffusivity which promoted polymer penetration into the CNT bundles, volume resistivity was lower. Non-homogeneous distribution of volume resistivity was observed across both the length and width of the specimen, independent of injection parameters. At a low injection temperature (255 °C), (a) across the width, volume resistivity was higher at the near-mid section and lower at the near-edge section when injection speed was high ($9 \text{ cm}^3 \cdot \text{s}^{-1}$), but the distribution was narrower when the injection speed was low ($5 \text{ cm}^3 \cdot \text{s}^{-1}$); (b) while across the length, volume resistivity was always higher at the near-gate section and lower at the near-end section, but the difference became greater at a high injection speed. At a high injection temperature (285 °C), the effect of injection speed on volume resistivity across the width was reversed, but the effect of injection speed on volume resistivity across the length was the same.

Hong *et al.* (2004) investigated the effect of shear flow on injection moulding of PP carbon black and found that the conductivity of the composite changed drastically due to non-homogeneous pressure/shear flow caused by the concentration gradient across the flow direction. Because the shear rate and the shear stress were maximal near the wall and minimum at the centre of flow, a shear gradient would develop and cause the filler to fractionalise away from the wall toward the centre. Consequently, the region near the surface became filler-depleted while the region near the centre became filler-enriched. A loss of surface and volume conductivity, however, does not automatically point to particle migration, given other factors such as annealing, crystallisation (quasi-static or shear-induced), and orientation of the skin and shear layer can have significant effect. To verify the shear-induced migration kinetics could be extended to the filler with a larger dimension, capillary flow experiments were performed with a PP compound containing 30 wt% of glass bead at shear rates of 7.2 and 4865 s^{-1} . Because the shear gradient increases proportional with the shear rate, the strand produced at the lower shear exhibited a rough spherical texture (less migration) while the strand produced at a higher shear exhibited a smoother surface (more migration). Additionally, surface conductivity measurements were performed across the lateral thickness of compression- and injection-moulded carbon black polypropylene and polystyrene specimens. For the compression-moulded specimen, surface conductivity was more or less constant across the lateral depth. For the injection-moulded specimen, conductivity increases with lateral depth. This would indicate that the spatial conductivity gradient increases with the

injection velocity. However, the volume conductivity measured across the total length was roughly the same for both the compression-moulded and the injection-moulded specimens. In this case, a compensation effect occurs where the depletion of filler near to the surface enriches the bulk.

Villmow *et al.* (2008) recently carried out one of the most thorough studies on the influence of injection moulding parameters on the electrical resistivity of PC–CNT composites using a design of experiment method. Correlation between electrical resistivity and morphology of the composites was examined via TEM analysis of the skin layer. Villmow found the uniformity of through-plane volume resistivity of the composites was sensitive to the concentration of CNT. The uniformity was poorer at the lower CNT concentration (up to five orders of magnitude at 2 wt% and two orders at 5 wt%). TEM analysis of the skin layer revealed a skin layer with highly oriented CNT in the case of a higher injection speed and a low melt temperature (measuring higher resistivity), but a network-like structure at a low injection speed and a high melt temperature (measuring lower resistivity).

The complexity of injection moulding behaviour on the CNT distribution and orientation in a polymer is so great that many features of its electrical resistivity response in the processing parameters regime have not yet been fully captured. Hence there is an urgent need for more comprehensive experimental data to further develop an understanding in a predictive relationship for polymer processors and injection moulders. The in-depth study by Villmow *et al.* (2008) has contributed significantly to the understanding of injection moulding parameters affecting the through-plane volume resistivity of PC–CNT and could be extended to other polymer CNT composites. The work carried out in this chapter was intended to understand more thoroughly the relationship between surface resistivity, in-plane volume resistivity and injection parameters.

6.3 Experiment design and materials

6.3.1 Materials and methods

Materials

The multi-walled carbon nanotube used in this study was a 90 % purity commercial grade CNT with the trade name NC7000, manufactured by Nanocyl S.A. Belgium. It has a mean diameter and length of 9.5 nm and 1.5 μm respectively, according to the manufacturer's technical datasheet. Five different grades of polycarbonates produced by Bayer Materials Science A.G., with different melt flow indices (MFI) and different molecular weights (M_w) were used in the study (see Table 6.1). M_w values were measured via gel permeation chromatography (GPC).

Makrolon 2205 (MFI 38) was used in the $2 \times$ factorial statistical process optimisation study. The subsequent individual parametric study was performed using Makrolon 2405 (MFI 20). For the study of the effect of M_w on the electrical resistivity of injection-moulded PC–CNT, three additional polycarbonates were

Table 6.1 List of polycarbonates used in the study

PC grade	MFI, g/10min at 1.2 kg/300°C	M _w , g/mol
Makrolon OD2015	63	13,000
Makrolon 2205	38	15,000
Makrolon 2405	20	17,500
Makrolon 2805	10	21,000
Makrolon 3105	6.5	23,500

compared, Makrolon OD2015 (MFI 63), Makrolon 2805 (MFI 10) and Makrolon 3105 (MFI 6.5).

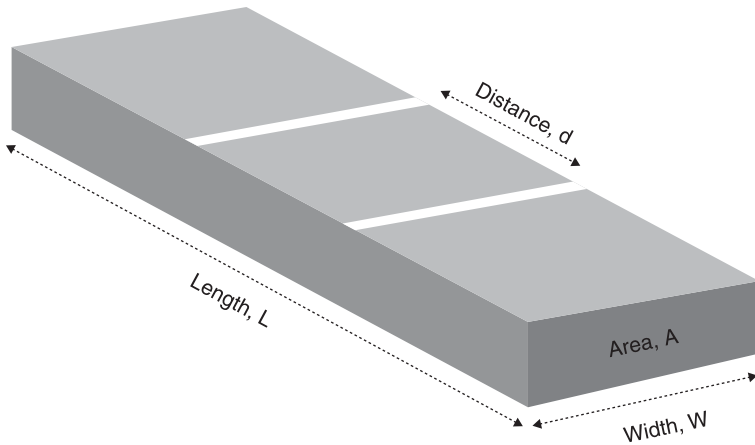
Processing

The PC–CNT compounds used in the study were manufactured via twin-screw extrusion processing using an industrial Leistritz ZSK-27 MAXX 48 L/D ratio co-rotating extruder, adapted with an automated CNT replenishment system. Extrusion was carried out at 300 rpm screw speed using proprietary screw configuration optimised for PC–CNT performance. The extruder consisted of 11 heated barrel zones where the temperature profile was ramped from: zone 1: 250°C, zone 2: 270°C, zones 3–10: 280°C, zone 11: 290°C and the melt temperature in the die was controlled at $300 \pm 1.5^\circ\text{C}$. CNT was gravimetrically fed via zone 4 by means of a twin-screw side feeder system. Vent ports were fitted at appropriate zones for effective moisture venting.

Injection moulding was performed using an Engel Victor 80 tons injection moulding machine. Specimens were ASTM D256 Izod bar (for resistivity, Izod impact and flexural testing) and ASTM D638 tensile bar (for tensile testing). The Makrolon 2205 PC used in the $2 \times$ factorial study contained 3.0 wt% CNT while the Makrolon 2405 PC used in the parametric study contained 2.5 wt% CNT. All compounds were dried at 120°C in an air circulating oven for 4 hours prior to injection moulding.

Characterisation

Resistivity measurement was carried out using a Keithley 2405 DC multimeter. Referring to Fig. 6.1, in-plane volume resistance was measured by means of electrodes contact at opposite edges of an Izod test bar. The edges were cryogenically fractured to preserve the original composite morphology, and painted lightly with silver paint to enhance electrode contact. Surface resistance measurement was performed by means of electrodes contact with two thin silver lines painted on an Izod bar. Volume resistivity, ρ_v and surface resistivity, ρ_s were calculated according to Equations 6.1 and 6.2. All resistivity results were an average of eight specimens' measurements.



6.1 Schema of injection-moulded Izod test bar used for electrical resistivity measurement.

$$\text{Volume resistivity, } \rho_v = \text{volume resistance} \times (A/L) \quad [6.1]$$

$$\text{Surface resistivity, } \rho_s = \text{surface resistance} \times (W/d) \quad [6.2]$$

The state of agglomerate dispersion was analysed using an Axio-Zeiss Imager-M1 light optical microscopy, equipped with an AxioCam MRc5 CCD camera in transmission mode. Specimens of about 100 micron thick were obtained from microtome. The specimens were pre-melted between two thin glass slides at 310°C using a Mettler-Toledo FP2HT hot-stage, then gently pressed and allowed to solidify. The surface finish (defects) of injection-moulded Izod test bars were analysed by means of the following procedure. Bright light of a suitable intensity was projected at the test specimen and a digital camera fixed vertically above the specimen and focused to obtain a photo of the specimen's surface. Digital grids were printed on the photos using graphical software. The indices representing the degree of surface defects were computed by calculating the numbers and size of defects per square grid.

Impact testing was carried out using a Tinius Olsen model IT 503 impact tester. The notch was prepared in accordance with ASTM D256 standard, using an automated Tinius Olsen model 899 notcher. Tensile and flexural testing was performed using a Tinius Olsen H25KS extensometer in accordance with ASTM D638 and D790 standards respectively.

6.3.2 Design of experiments

In this section, a 7 factor \times 2 level fractional design of experiment was carried out to evaluate the influence of injection parameters on volume resistivity, surface resistivity and surface finish of PC composites (see Table 6.2). The PC used here was a

Table 6.2 Parameters and setpoint values used in the 2^7 DOE study

Factors (parameters)	Unit	Code	Lower level value (+)	Upper level value (–)
Injection temperature	°C	<i>a</i>	285	300
Injection speed	cm ³ .s ^{–1}	<i>b</i>	8	30
Hold pressure	bar	<i>c</i>	250	450
Back pressure	bar	<i>d</i>	40	80
Mould temperature	°C	<i>e</i>	100	120
Plasticising speed	cm.s ^{–1}	<i>f</i>	40	60
Hold time	s	<i>g</i>	8	12

Makrolon 2205 compound containing 3 wt% CNT. Constant injection parameters were; 28 cm³ fill volume, 25 seconds mould cooling time, 3.7 cm³ volume decompression after plasticising, and 10 cm³.s^{–1} volume decompression speed.

The aim of a design of experiment (DOE) activity is to obtain the maximum information with the minimum number of tests to identify the main factors that affect the responses. In this case, the factors were injection parameters and responses were the volume resistivity, surface resistivity and surface finish. A full factorial experiment (which consists of varying one factor at a time and performs experiments for all levels of all factors) is most effective, but it runs up a very large number of trials and often untenable cost. Taking a simple example of an experiment consisting of 7 factors, k and 2 levels i , the total number of experiments, n , that need to be performed in a full factorial design before considering replication would already be, $n = i^k = 2^7 = 128$. Therefore, fractional factorial design was used to reduce the number of experiments and yet obtain adequate representation of the relationship between the experiment responses and variation of the factors.

The experiment was structured in form of 2^{7-h} fractional factorial treatment where h describes the fraction of the full factorial used or, formally, the number of generators assigned to which effects or interactions are confounded, (i.e. difficult to estimate independently of each other). Experiments were generated from the full factorial treatment by choosing an alias structure, where the alias structure determined the confounding effects. Referring to Table 6.3, e , f and g were chosen as confounding factors with interactions (thus, $k = 3$ and $n = 16$) generated by $e = a \cdot b \cdot c$, $f = a \cdot c \cdot d$ and $g = b \cdot c \cdot d$. The effect of factor e , therefore, was a combination of the main effect of factor e and three factors' interaction involving a , b and c . Another important feature of a fractional design is the defining relation, say, denoted by Z , which gave the set of interaction columns equal in the design matrix to a column of plus (+) sign. Since $e = a \cdot b \cdot c$, $f = a \cdot c \cdot d$ and $g = b \cdot c \cdot d$, then $a \cdot b \cdot c \cdot e$, $a \cdot c \cdot d \cdot f$, and $b \cdot c \cdot d \cdot g$ were three additional columns of (+) sign, and consequently so was $c \cdot e \cdot f \cdot g$. This defining relation allowed the combination of parameter set points of the DOE to be determined in Table 6.4.

Table 6.3 2^{7-k} fractional factorial DOE consisted of 16 runs, where e, f, g were generators

Run no.	Sample code	Injection temperature a	Injection speed b	Hold pressure c	Back pressure d	Mould temperature $e = a \cdot b \cdot c$	Plasticising speed $f = a \cdot c \cdot d$	Hold time $g = b \cdot c \cdot d$
01	A	+	-	+	-	-	-	+
02	B	-	-	-	-	-	-	-
03	C	-	-	+	+	+	-	-
04	D	+	-	-	+	+	+	+
05	E	+	-	+	+	-	-	-
06	F	+	-	-	-	+	+	-
07	G	-	-	-	+	-	+	+
08	H	-	-	+	-	+	+	+
09	I	-	+	-	-	+	-	+
10	J	+	+	-	+	-	-	-
11	K	-	+	+	+	-	-	+
12	L	+	+	+	-	+	-	-
13	M	-	+	-	+	+	+	-
14	N	+	+	-	-	-	+	+
15	O	+	+	+	+	+	+	+
16	P	-	+	+	-	-	+	-

Table 6.4 Lower and upper level values listing for the 2⁷⁻¹ fractional factorial DOE

Run no.	Sample code	Injection speed (cm ³ .s ⁻¹)	Plasticising speed (cm.s ⁻¹)	Injection temperature (°C)	Mould temperature (°C)	Back pressure (bar)	Hold pressure (bar)	Hold time (sec)
01	A	8	40	300	100	40	450	12
02	B	8	40	285	100	40	250	8
03	C	8	40	285	120	80	450	8
04	D	8	40	300	120	80	250	12
05	E	8	60	300	100	80	450	8
06	F	8	60	300	120	40	250	8
07	G	8	60	285	100	80	250	12
08	H	8	60	285	120	40	450	12
09	I	30	40	285	120	40	250	12
10	J	30	40	300	100	80	250	8
11	K	30	40	285	100	80	450	12
12	L	30	40	300	120	40	450	8
13	M	30	60	285	120	80	250	8
14	N	30	60	300	100	40	250	12
15	O	30	60	300	120	80	450	12
16	P	30	60	285	100	40	450	8

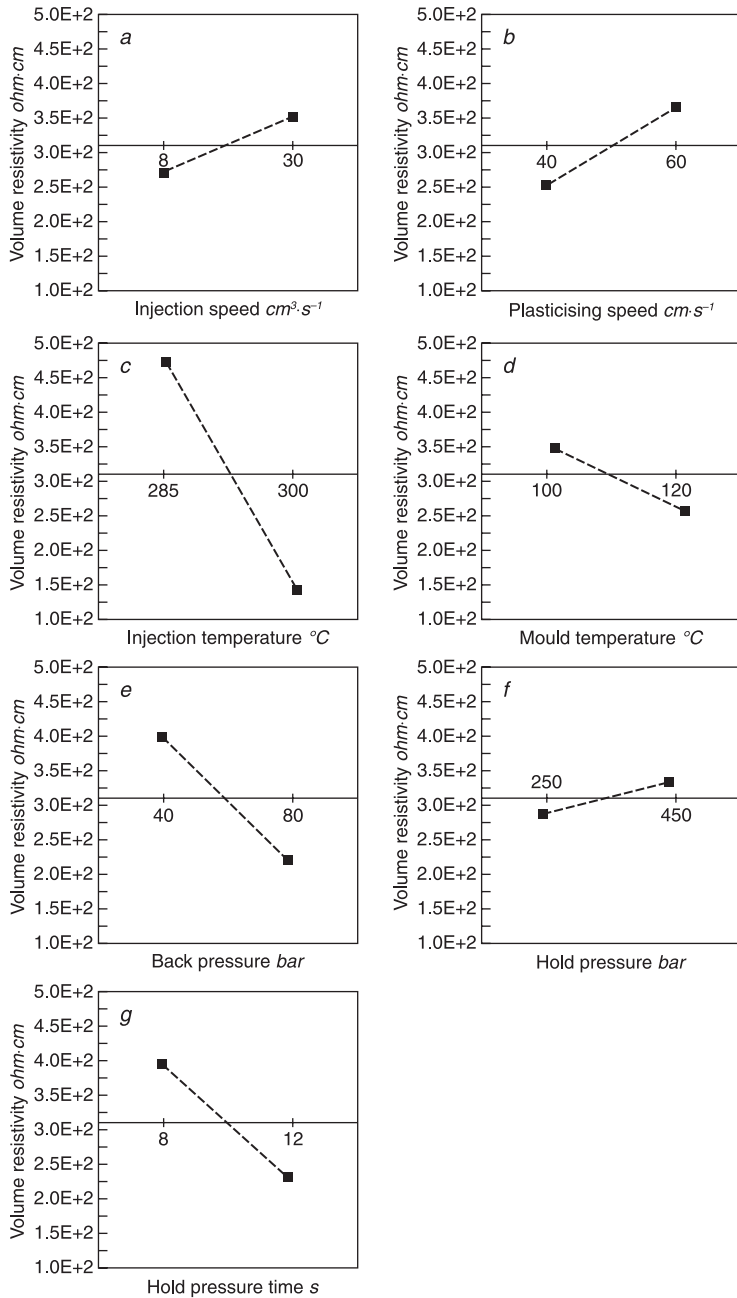
6.4 Analysis

6.4.1 Main effects of injection moulding parameters

The injection moulding process was carried out using the combination of DOE parameters listed in Table 6.4. Figure 6.2 compares the response of volume resistivity with respect to the various injection factors (parameters), termed as ‘main effects’ plots. The response’s values were average measurement from six injected specimens and given in Table 6.5. All specimens were conditioned at room temperature for at least 24 hours before measurement. In a main effect plot, a parameter is more influential if the absolute gradient of the slope between the lower and upper data point is greater, and vice versa. The data points in each of the plots were calculated by taking the sum average of the volume resistivity of the parameter, corresponding to its lower or upper level set point. For example, in Fig. 6.2 (a), the lower data point was the sum average of ρ_v for samples A–H in Table 6.5. Samples A–H correspond to the lower level set point of injection speed ($8 \text{ cm}^3\cdot\text{s}^{-1}$) listed in Table 6.4. As such, its upper data point was the sum average of ρ_v for samples I–P, with an upper level set point of ($30 \text{ cm}^3\cdot\text{s}^{-1}$).

By examining the gradient of slopes in the plots in Fig. 6.2, injection temperature, back pressure and hold pressure time first appeared to have greatest effect on the volume resistivity of the PC composites. However, this could be misleading since the slope’s gradient was affected by the chosen lower and upper level set points, for example, if the upper set point of injection speed in Fig. 6.2 (a) was chosen as $60 \text{ cm}^3\cdot\text{s}^{-1}$ instead of $30 \text{ cm}^3\cdot\text{s}^{-1}$, the gradient of its slope could become greater than that of the main effect plot for injection temperature in Fig. 6.2 (c). But this does not mean that the injection speed had a greater influence on the volume resistivity than the injection temperature. Therefore, the slope should first be normalised with respect to a coefficient of tolerance, r , where r is the magnitude (upper limit minus lower limit) of tolerance of a parameter (see Table 6.6). Outside the tolerance, a sample could not be suitably injection moulded, e.g. injecting at 250 bar back pressure would cause problematic specimen ejection from mould. The values of normalised slopes are given in Table 6.7. Injection temperature and back pressure appeared to have greatest influence on the volume resistivity and within the processing tolerance, the influence of hold pressure least significant.

Figure 6.3 shows the main effect plots of surface resistivity versus the various injection parameters. Within the set points studied, surface resistivity appeared to be sensitive to only two major parameters: injection speed and injection temperature. The increase of surface resistivity with injection speed was most likely to be attributed to the formation of an orienting skin layer which in turn disrupts the conductive network path of the CNT. This result is consistent with similar findings by Villmow on through-plane volume resistivity (Villmow *et al.*, 2008).



6.2 Main effect plots of volume resistivity versus injection moulding parameters.

Table 6.5 Volume and surface resistivity values of Makrolon 2205, 3 wt% PC–CNT

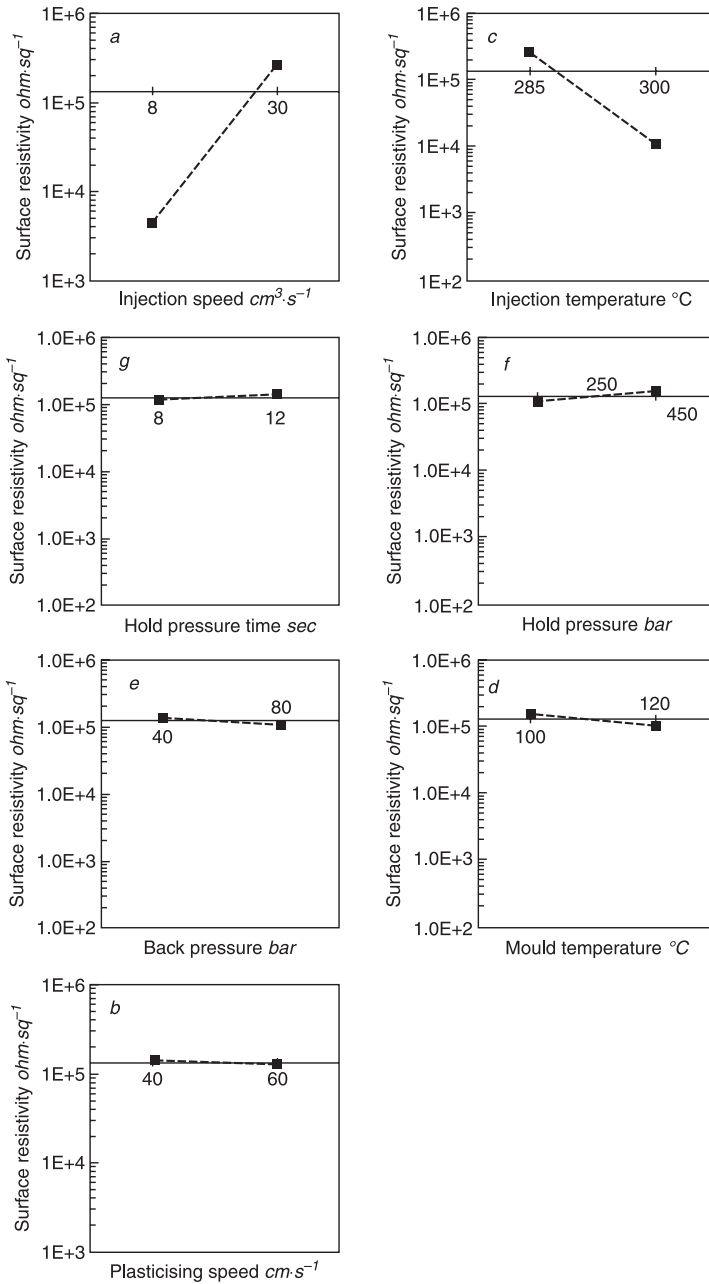
Samples code	Volume resistivity, ρ_v (ohm.cm)	Surface resistivity, ρ_s (ohm.sq ⁻¹)
A	1.2×10^2	1.8×10^3
B	5.6×10^2	5.1×10^3
C	4.9×10^2	8.3×10^3
D	6.9×10^1	1.4×10^3
E	1.3×10^2	1.6×10^3
F	6.6×10^1	1.6×10^3
G	3.1×10^2	9.8×10^3
H	4.3×10^2	5.8×10^3
I	4.5×10^2	5.0×10^5
J	2.4×10^2	2.1×10^4
K	1.1×10^1	5.6×10^5
L	8.6×10^1	6.7×10^3
M	3.5×10^2	3.1×10^5
N	2.6×10^2	3.0×10^4
O	1.8×10^2	2.0×10^4
P	1.2×10^3	6.3×10^5

Table 6.6 Injection moulding tolerance used for calculation of normalised main effect slopes

Injection parameters	Value range	Tolerance, r
Injection speed	10–100	90
Plasticising speed	20–60	40
Injection temperature	260–310	50
Mould temperature	80–130	50
Back pressure	20–200	180
Holding pressure	100–800	700
Hold time	5–20	15

Table 6.7 Effect of injection moulding parameters affecting the volume and surface resistivities by order of ranking. The greater the slope's value, the greater the effect

Rank	Parameters affecting volume resistivity	Normalised VR-slope	Parameters affecting surface resistivity	Normalised SR-slope
1	Injection temperature	1.1×10^3	Injection speed	1.2×10^6
2	Back pressure	1.1×10^3	Injection temperature	8.1×10^5
3	Hold pressure time	6.2×10^2	Hold pressure	1.5×10^5
4	Injection speed	3.3×10^2	Back pressure	1.3×10^5
5	Plasticising speed	2.3×10^2	Mould temperature	1.3×10^5
6	Mould temperature	2.3×10^2	Hold pressure time	7.1×10^4
7	Hold pressure	1.6×10^2	Plasticising speed	2.5×10^4



6.3 Main effect plots of surface resistivity versus injection moulding parameters.

Figures 6.4 and 6.5 show the main effect plots for two types of surface defects presented on the injection-moulded test specimens: pinholes and spots. Their corresponding intensity indices, p and q are given in Table 6.8, where 0 = lowest (no defect) and 1 = greatest. The p and q indices were obtained through methods described in the experimental section by calculating the numbers and size of pinholes and spots presented on the grids of the specimen photos. The normalised slopes for the main effect plots of surface defects were calculated in Table 6.9. Interpretation based on the slope's gradient showed pinholes defect and spots formation to be most sensitive to injection speed and mould temperature. Increasing injection speed or reducing mould temperature typically improves the surface finish of the PC composites.

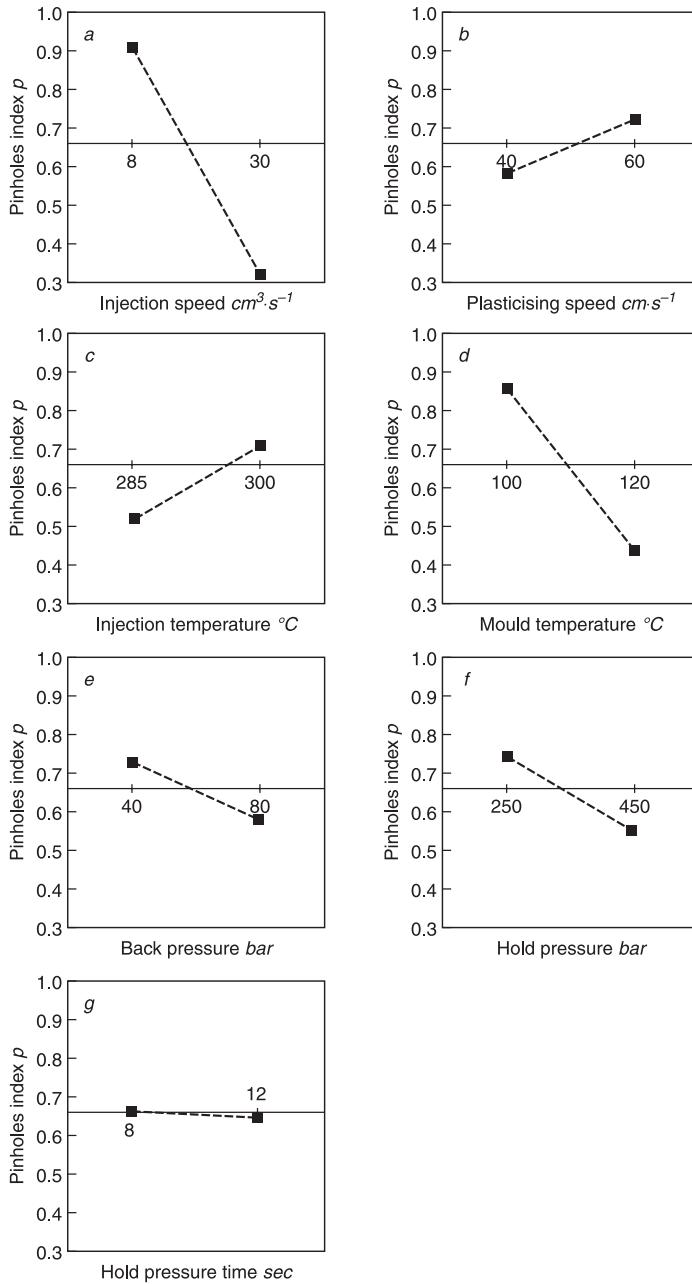
Based on the obtained main effect results of volume resistivity, surface resistivity, pinhole index and spots formation index, a regression model using statistical software analysis was applied and the equation optimisation was performed by means of partial derivations and solving the system of equations (the optimisation procedure can be found in Joiner *et al.*, 2004). The analytically optimised equation returned with parameters similar to run 12 (sample L) trial in Table 6.5, except $P_h = 390$ bar. The following results (within margin of errors) were compared, both parameters yielded the same resistivities but run 12 gave much better surface finish.

- (a) Optimised: $\rho_v = 8.2 \text{ ohm}\cdot\text{cm}$, $\rho_s = 9.2 \text{ ohm}\cdot\text{sq}^{-1}$, no pinholes, minor visible spots.
- (b) Run 12, L: $\rho_v = 6.7 \text{ ohm}\cdot\text{cm}$, $\rho_s = 8.6 \text{ ohm}\cdot\text{sq}^{-1}$, no pinholes, no visible spots.

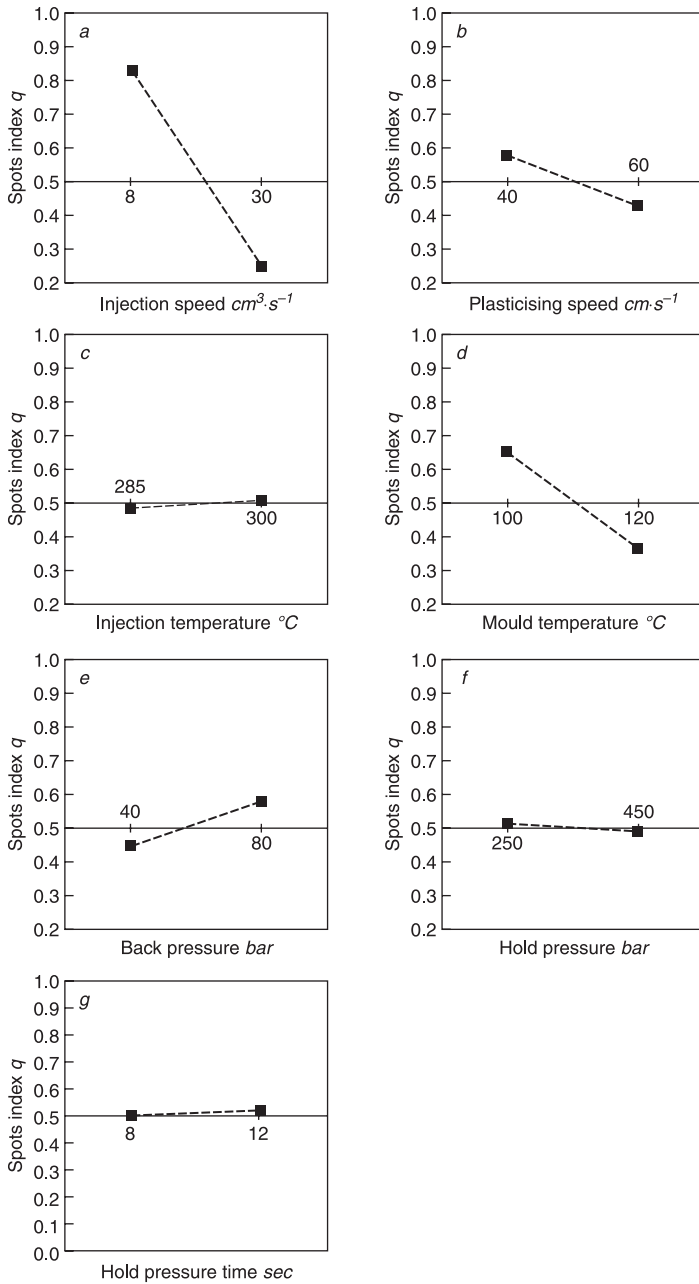
In conclusion, the DOE optimisation analysis gave a result very close to the ideal processing condition despite not being as satisfactory compared to run 12 trial. This could be attributed to the lack of data points for a more accurate regression model fitting and can be improved by either reducing the number of generator h from 3 to 2 or by running a central composite design augmented with centre points that allow estimation of curvature.

6.4.2 Steady-state rheological analysis

Capillary rheology is an experimental technique whereby a melt sample experiences die shear to mimic realistic viscosity and high shear rates (of up to $10,000 \text{ s}^{-1}$) relevant to most extrusions and injection moulding processes. By applying this rheological method in steady-state conditions, information with regard to the power-law regime of a composite melt that is not observed at lower shear rates ($<100 \text{ s}^{-1}$) can be studied. Figure 6.6 shows the plots of steady-state apparent shear viscosity, η versus shear rate of PC composites and their virgin melt based on Makrolon 2205. Experiments were performed using a dual capillary rheometer and



6.4 Main effect plots of surface defect, pinholes index, p versus injection moulding parameters.



6.5 Main effect plots of surface defect, spots index, p versus injection moulding parameters.

Table 6.8 Index of surface defects

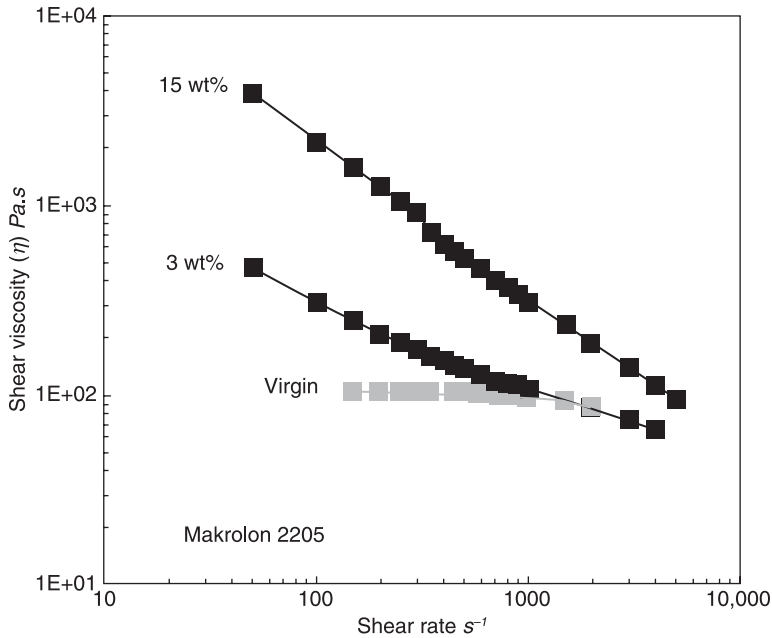
Samples code	Index, <i>p</i> pinholes	Index, <i>q</i> spots
A	1	1
B	1	1
C	0.5	0.5
D	1	1
E	1	1
F	1	1
G	0.9	1
H	0.4	1
I	0	0
J	0.3	1
K	1	0.1
L	0	0
M	0	0
N	0	1
O	0	0
P	0.2	0.8

Note: 0 = lowest intensity, 1 = greatest intensity.

Table 6.9 Effect of injection moulding parameters affecting the formation of pinholes and spots surface defects by order of ranking. The greater the slope's value, the greater the effect

Rank	Parameters affecting pinholes formation	Normalised <i>p</i> -slope for pinholes	Parameters affecting spots formation	Normalised <i>q</i> -slope for spots
1	Injection speed	2.42	Injection speed	2.37
2	Mould temperature	1.05	Mould temperature	0.73
3	Back pressure	0.68	Back pressure	0.59
4	Injection temperature	0.67	Plasticising speed	0.30
5	Hold pressure	0.67	Hold pressure time	0.08
6	Plasticising speed	0.28	Hold pressure	0.07
7	Hold pressure time	0.06	Injection temperature	0.07

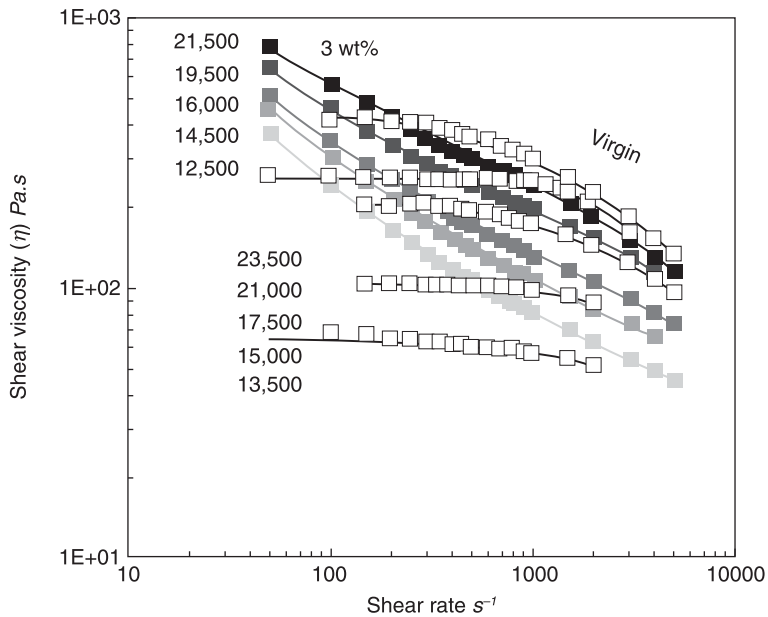
results were Bagley corrected for die effect. The virgin PC exhibited, at $\dot{\gamma} < 1000 \text{ s}^{-1}$, Newtonian-like flow behaviour (i.e. constant shear viscosity versus shear rate). In contrast, the PC composite exhibited intense shear thinning across the range of shear rate studied. The data plot demonstrated that η of the PC composite converged with η of the virgin PC at a shear rate $K \cdot \approx 1500 \text{ s}^{-1}$ and at $K \cdot \geq 2000 \text{ s}^{-1}$, η of the PC composite appeared to cross over below the η of the virgin PC.



6.6 Plots of shear viscosity versus shear rate of virgin PC and PC–CNT, 3 wt% and 15 wt%, based on Makrolon 2205.

Lew *et al.* (2009b) had investigated the steady-state rheological behaviour of PC composites (with 3wt% CNT) using five different molecular weight PCs (between 13,000 and 23,500 g/mol) and observed the same phenomenon for all PC composites. The viscosity of all the PC composites melt would converge and then cross over to below their virgin melt. The convergence shear rate was dependent on the molecular weight, lower for higher M_w PC composite. Lew attributed this behaviour to flow-induced orientation of CNT that in turn led to interface chain slippage. This is given by the anisotropy structure realignment of the CNT particles and when exfoliated, its semi-graphitic wall could further act as plasticising agent.

Figure 6.7 shows the shear viscosity versus shear rate plots of different M_w PC (as-supplied pellets) and their corresponding compounded PC composites with 3 wt% CNT loading. All composites shear thinned intensely irrespective of M_w and more remarkably, the PC composites exhibited unique flow modification where the melt exhibited power law flow behaviour. This could, in part, explain the reduced die swellability found previously: (a) shear thinnability of virgin PC melt increases with increasing M_w ; and (b) shear thinnability of PC composites roughly followed a power law described by $\eta = K \cdot \dot{\gamma}^{n-1}$ where the exponential n was almost independent of M_w .



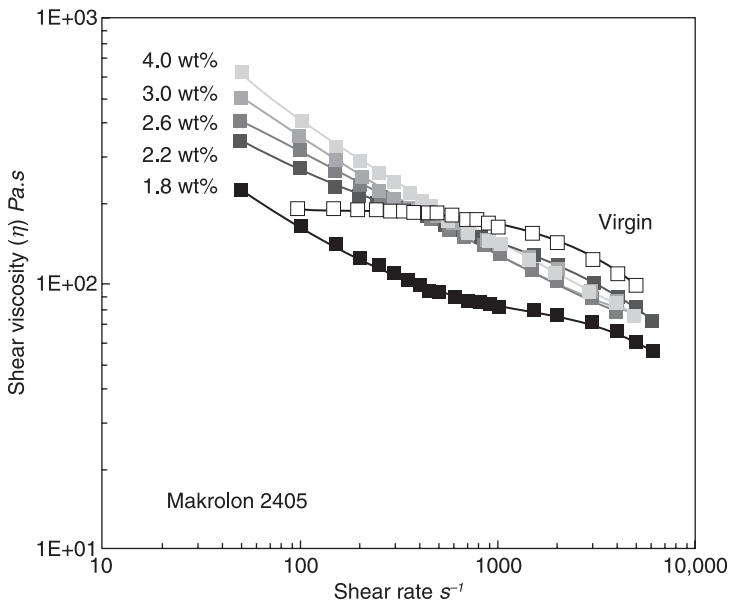
6.7 Plots of shear viscosity versus shear rate of various virgin PCs and their corresponding 3 wt% PC–CNTs. In the order from highest M_w to lowest M_w are Makrolon 3105, Makrolon 2805, Makrolon 2405, Makrolon 2205 and Makrolon OD2015.

As early as 2004, researchers from the National Institute of Standards and Technology (NIST) (Kharchenko *et al.*, 2004) had observed the shear thinning behaviour of PP melt imparted by CNT. They also found the presence of CNT would eliminate die swell in polymers, an effect crucial to processing. Vega *et al.* (2009) had compared the extrusion die swell ratio of a virgin HDPE and HDPE–CNT and they too observed that HDPE–CNT exhibited lower die swell compared to the virgin HDPE and the increase in die swell versus apparent shear rate was lower for the HDPE–CNT. Several authors ascribed the decrease in the polymer–CNTs viscosity relative to their respective virgin polymer to an increase in molecular mobility as a result of the increase in free volume (Jin *et al.*, 2008; Ma *et al.*, 2008; Rahmatpour and Aalaie, 2008).

The M_w data measured for all materials in Fig. 6.7, obtained via gel permeation chromatography (GPC) analysis, showed slightly lower M_w for the composites vis-à-vis their virgin polymers, which could be an indication of degradation. The M_w data for the virgin PCs were measured on the as-supplied pellets without processing history. Pötschke *et al.* (2002) reported a similar reduction in M_w of melt compounded PC–CNT which was discussed to be due to high shear forces during composite preparation. However, from the GPC data of virgin PCs (for example, Makrolon 2205) compounded under the same processing history as its

PC composites, it was shown that its M_w was slightly lower than that of the Makrolon 2205 PC composites (M_w of virgin as-supplied PC = 15,000 g/mol, M_w of PC composite = 14,500 g/mol, M_w of virgin PC undergone same processing history = 14,000 g/mol) (Lew *et al.*, 2009a). This would indicate the M_w degradation found in the composites was most likely attributed to degradation of the virgin PC alone and not caused by the presence of CNT.

Figure 6.8 shows the plots of virgin PC and PC composite melts at 1.8, 2.2, 2.6, 3.0 and 4.0 wt% CNT loading, based on Makrolon 2405 (MFI 20 g/10min). The entire composite melts demonstrated shear thinning effect within the range of shear rates investigated. The flow behaviour of the virgin PC was Newtonian-like at $K \cdot < 500$ whereas all composites had already exhibited intense shear thinning at $K \cdot = 50 \text{ s}^{-1}$. At lower CNT loading (1.8 wt%), three distinct melt flow regimes could be observed: (a) power law flow at $K \cdot < 500 \text{ s}^{-1}$; (b) Newtonian plateau between 900 and 2000 s^{-1} ; and then (c) power law flow at $K \cdot > 4000 \text{ s}^{-1}$. These three regimes appeared to conflate into a single power law regime as the CNT loading increases. In addition, the power law exponent n decreases (i.e. the slope's gradient increases) in proportion with CNT loading and this had concurred with study by Teng *et al.* (2008) on polypropylene–CNT composites. The same phenomenon was seen formerly in Fig. 6.6 where the curvature in the viscosity versus shear rate plot at 3 wt% CNT changed into a linear at 15 wt% of CNT loading.



6.8 Plots of shear viscosity versus shear rate of virgin PC and PC–CNT containing different CNT loading, based on Makrolon 2405.

The results showed that at 1.8 wt% CNT, the PC composite already exhibited lower viscosity than its virgin melt at $K = 100 \text{ s}^{-1}$ and electrical resistivity data for this composite (shown later in Section 6.4.4, Fig. 6.13) recorded favourably values of $\rho_v < 10^2 \text{ ohm}\cdot\text{cm}$ and $\rho_s < 10^3 \text{ ohm}\cdot\text{sq}^{-1}$. Another unique behaviour was observed in Fig. 6.8 where the rate of shear thinning decreases with increasing CNT percentage, or in terms of power law, the exponential n increases with increasing loading. This could be ascribed to an increase in the chain plasticising effect discussed previously. Furthermore, there appeared an inverse intersecting point at $K = 1000 \text{ s}^{-1}$ at which the proportional relationship between CNT loading and viscosity was reversed.

Most of the rheological experiments found in the literature for polymer CNT composite were conducted in dynamic oscillatory mode and typically the composite registered a higher shear viscosity compared to its virgin melt, although the difference became smaller as the rate of deformation increases (McNally *et al.*, 2005). Discrepancies in flow mechanics arise between steady-state shear and oscillatory experiments because: (a) in a steady-state flow the polymer experiences linear mode deformation vis-à-vis nonlinear deformation in dynamic mode; and (b) deformation strain and rate experienced in steady-state experiment ($K = 100\text{--}10,000 \text{ s}^{-1}$) exceed the critical elongational for the polymer chain to change from coil (entanglement) behaviour into stretched conformation (laminar) behaviour. Typical deformation rates in a dynamic oscillatory experiment are in the range of $0.001\text{--}100 \text{ s}^{-1}$ or $\text{rad}\cdot\text{s}^{-1}$. In addition, the shear viscosity in dynamic mode is more complex (η^*) because it is very sensitive to the elastic (G') and viscous (G'') components. Finally, it should be highlighted that flow behaviour in the majority of polymer processing is more closely related to steady state kinematics in both deformation mechanics and shear rate, $> 300 \text{ s}^{-1}$ for single-screw extrusion, $> 2000 \text{ s}^{-1}$ for twin-screw extrusion and $> 5000 \text{ s}^{-1}$ for injection moulding.

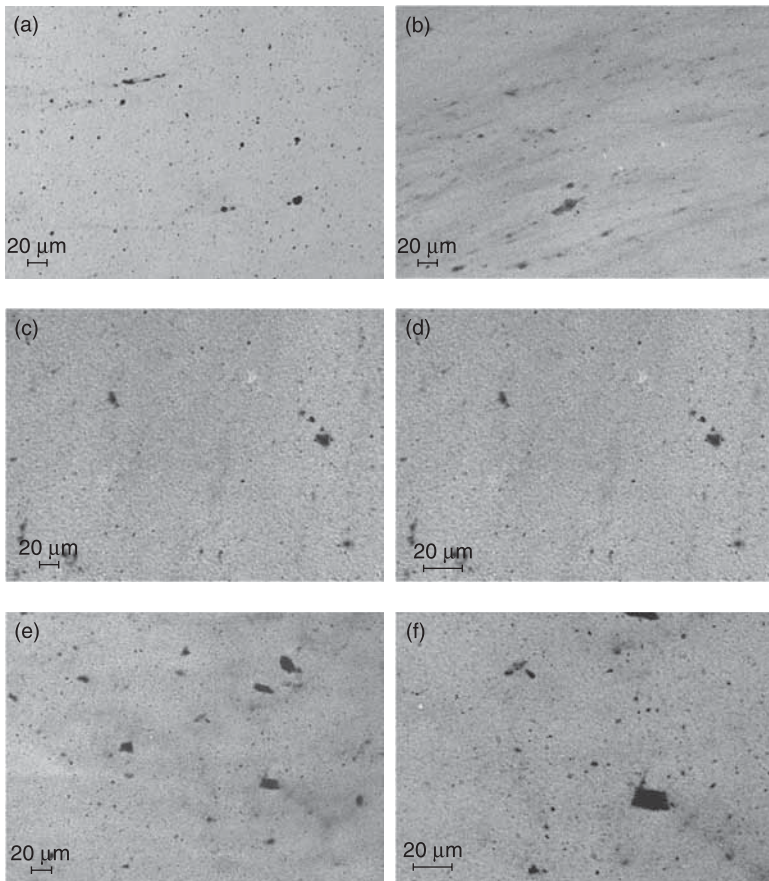
6.4.3 Analysis of nanotube agglomerates in composites

The structure of agglomerates derived from dispersion in a compounding process typically does not change during the injection moulding process, in the absence of mixing kinematics and because of short residence time. However, change in local distribution of CNT agglomerates can be induced during injection moulding, especially during the mould-filling process arising from the difference in flow behaviour and shear gradient experienced in different sections of the mould. Therefore, it needs to be pointed out that the section from which an injection-moulded specimen was obtained could have an effect on the outcome of the analysis. All specimens used for agglomerates inspection in this work were obtained from the mid-plane section of injection-moulded Izod test bars.

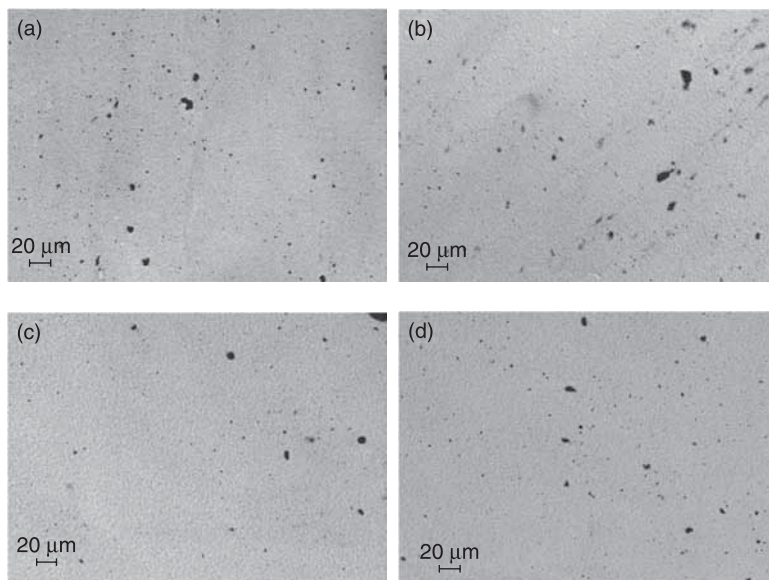
Figures 6.9–6.12 show the optical microscopy inspection of the patterns of CNT agglomerates presented in Makrolon 2405 PC composites. For composites containing different levels of CNT loading, from 1.4 to 4 wt%, the agglomerates

were visible at two levels of dimension: (a) well-distributed sub-5 micron particles; and (b) 10–20 micron particles. However, at a CNT loading of 3 wt% or higher, agglomerate domains of larger than 20 micron became visible.

The influence of injection fill speed on the patterns of agglomerates is illustrated in Fig. 6.10. No significant difference in the pattern of agglomerate distribution and size was observed within the range of injection speed applied. The influence of the injection moulding temperature (from 245 to 295°C) on the pattern of agglomerate distribution and size is shown in Fig. 6.11. Two patterns were found in the observation: (a) between 245 and 265°C, larger and poorly distributed agglomerates; and (b) between 275 and 295°C, smaller and better distributed

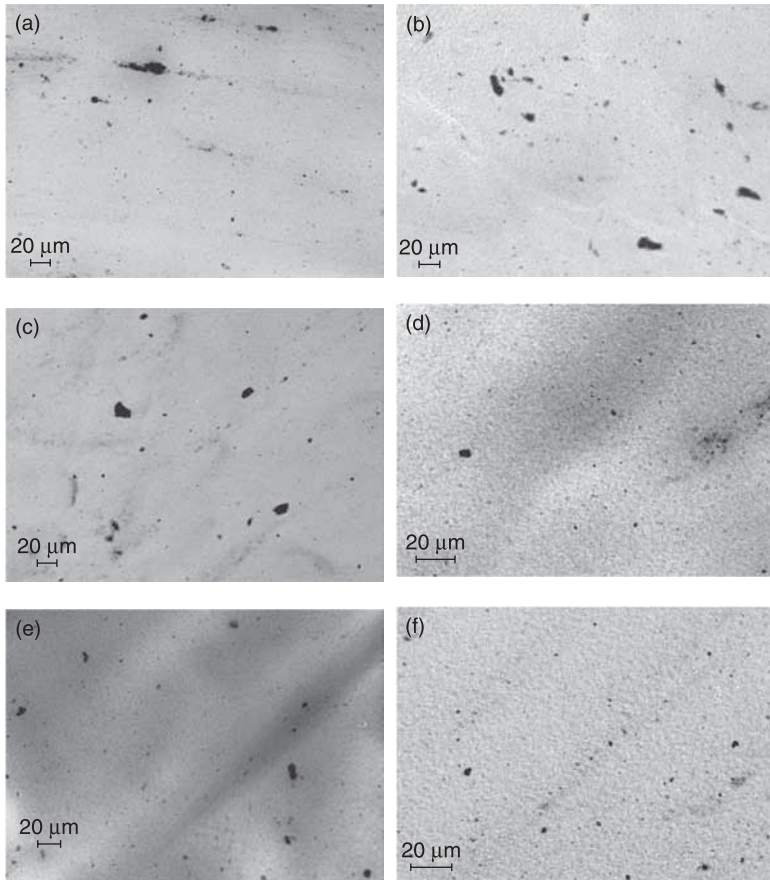


6.9 Optical microscopy inspection of agglomerates in Makrolon 2205 PC–CNT containing different CNT loading: (a) 1.4; (b) 1.8; (c) 2.2; (d) 2.6; (e) 3.0; (f) 4.0 wt%.



6.10 Optical microscopy inspection of agglomerates in Makrolon 2205, 3 wt% PC–CNT moulded at different injection speeds: (a) 10; (b) 20; (c) 60; (d) 100 cm³.s⁻¹.

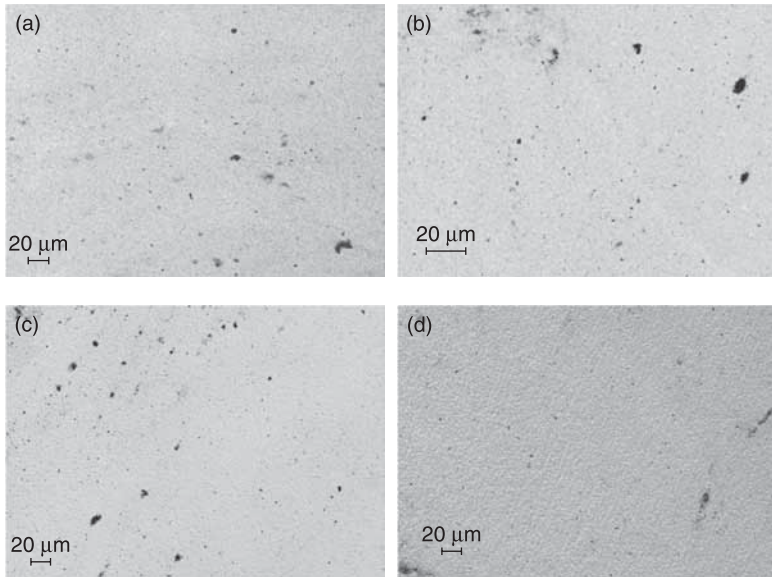
agglomerates. This could indicate the presence of a critical injection temperature between 265 and 275°C. More coincidentally, the same critical temperature between 265 and 275°C was observed later in the volume resistivity versus injection temperature plots in Fig. 6.15, at which point the resistivity began to level off. In the twin-screw extrusion investigation of PC–CNT by Lew *et al.* (2009a), he had shown, through scanning electron microscopy and transmission electron microscopy, the effect of the extrusion temperature (230–290°C) on the morphologies of CNT aggregates. Despite the fact that aggregates of PC–CNT extruded at higher temperature were slightly larger than aggregates extruded at lower temperature, they exhibited a looser structure due to more improved wetting with the polymer. The reduction in larger agglomerates size observed in this work could therefore be attributed to a critical decrease in surface tension occurring at between 265 and 275°C, which caused the agglomerates to rupture. However, more detailed transmission electron microscopy and scanning electron microscopy work are required to determine this phenomenon. Figure 6.12 shows the effect of injection back pressure on the size and distribution pattern of the CNT agglomerates. Generally, a more increase in back pressure will contribute to a more improved mixing in the nozzle section and increase in the plasticising time which might improve the rupturing of agglomerates. However, the photomicrographs in Fig. 6.12 did not detect significant change of the agglomerate size within the range of back pressure studied (25–200 bar).



6.11 Optical microscopy inspection of agglomerates in Makrolon 2205, 3 wt% PC–CNT moulded at different injection melt temperatures: (a) 245; (b) 255; (c) 265; (d) 275; (e) 285; (f) 295°C.

6.4.4 Analysis of electrical resistivity

This section presents the parametric correlation between injection moulding parameters and behavioural change in electrical resistivity. The wider range of injection moulding parameters and parameter values than available hitherto in the literature were investigated (see Table 6.10). The PC grade used in this study was Makrolon 2405 (MFI 20 g/10min) and contained 2.5 wt% CNT, unless stated otherwise. For each of the investigated parameters, values of all other parameters were maintained constant (see Table 6.11). The parameters investigated were: (a) injection temperature; (b) injection speed; (c) back pressure; (d) hold pressure; (e) hold pressure time; (f) mould temperature; (g) plasticising speed; and (h) volume decompression after plasticising.



6.12 Optical microscopy inspection of agglomerates in Makrolon 2205, 3 wt% PC–CNT moulded at different injection back pressures: (a) 25; (b) 50; (c) 100; (d) 200 bar.

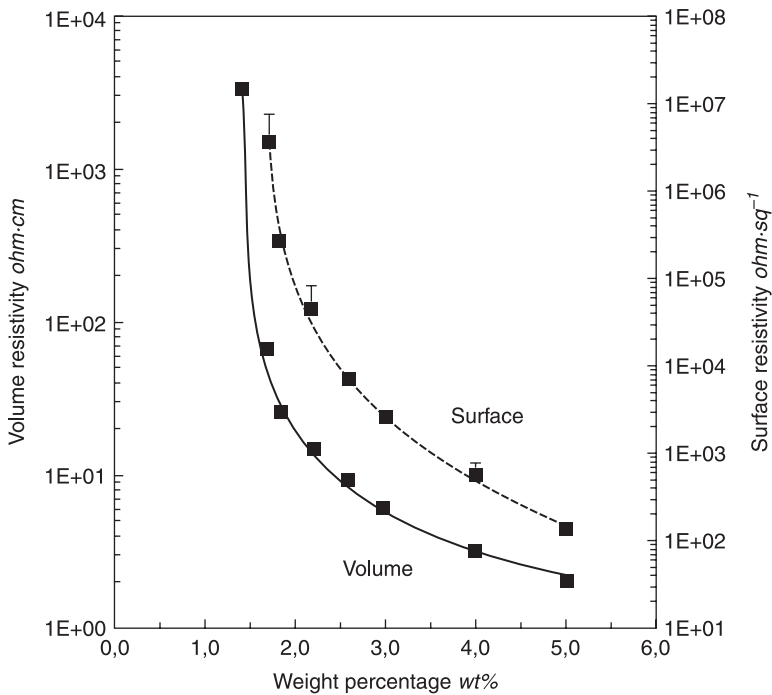
Table 6.10 List of injection moulding conditions used for parametric study in Section 6.4.4

Parameter	Unit	Values
Injection speed	$\text{cm}^3 \cdot \text{s}^{-1}$	10–20–30–40–50–60–80–100
Plasticising speed	$\text{cm} \cdot \text{s}^{-1}$	5–10–20–30–40–50–62
Injection temperature	$^{\circ}\text{C}$	235–245–255–265–275–285–295–305–315–325–335
Mould temperature	$^{\circ}\text{C}$	40–50–60–70–80–90–100–110–120–130–140–150
Back pressure	bar	25–50–100–150–200–300
Hold pressure	bar	50–100–200–300–400–500–600–750–900–1050
Hold pressure time	s	1.5–3.5–6.5–10–15–21–28
Decompression volume	%	0.37–11.9–22.2–44.4–59.3–74.1

Injection-moulded polymer is usually characterised by tri-layer morphology. The outer layer is a highly oriented skin, formed as a result of extensional flow that took place at the flow front. The mid-zone is a shear layer formed as a result of shear flow, where chains are highly oriented along the flow direction. The third layer is the core which was formed after cessation of flow. The thickness of the skin and shear layers decreases while the core increases with the increase of the mould temperature or injection speed.

Table 6.11 Standard injection moulding conditions for Makrolon 2405, 2.5 wt% PC–CNT ASTM D256 Izod test bar

Parameter	Unit	Values
Injection speed	$\text{cm}^3 \cdot \text{s}^{-1}$	30
Plasticising speed	$\text{cm} \cdot \text{s}^{-1}$	40
Injection temperature	$^{\circ}\text{C}$	295
Mould temperature	$^{\circ}\text{C}$	120
Back pressure	bar	50
Hold pressure	bar	450
Hold pressure time	s	10
Mould cycle time	s	24
Decompression volume	%	11.9



6.13 Plots of volume and surface resistivities of Makrolon 2405 PC–CNT versus wt% CNT loading.

Figure 6.13 shows the electrical percolation plots of volume resistivity and surface resistivity versus wt% CNT loading. The lowest and highest test points were 1.4 and 5.0 wt%. The corresponding volume and surface resistivity at the lowest test point were 3.4×10^3 ohm-cm and 1.0×10^{12} ohm-sq⁻¹.

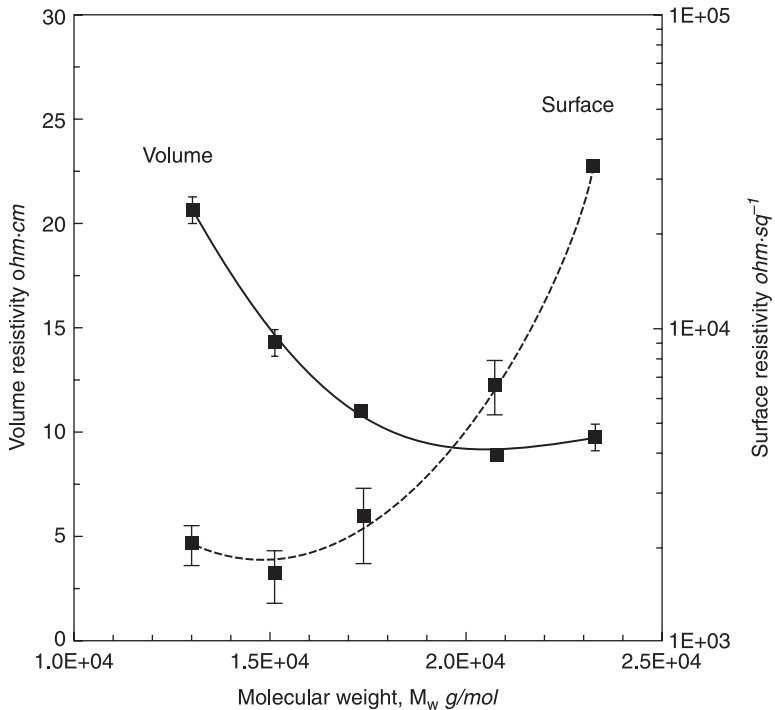
In order to estimate the percolation threshold, curve fitting analysis was performed according to Equations 6.3 and 6.4 for volume and surface resistivity respectively.

$$\ln y = a + b/x^{1.5} + ce^{-x} \quad [6.3]$$

$$\ln y = (a + cx)/(1 + bx) \quad [6.4]$$

where in Equation 6.3, $a = 8.574$, $b = 101.187$, $c = -179.926$, in Equation 6.4, $a = -1.737$, $b = -0.884$, $c = -3.45$ and $r^2=1$ for both equations. The estimated percolation threshold was remarkably low, ranging between 1.05–1.15 wt% ($6 \times 10^9 - 1.5 \times 10^7$ ohm-cm) for volume resistivity and 1.5 – 1.6 wt% ($1.6 \times 10^9 - 4.0 \times 10^7$ ohm-sq⁻¹) for surface resistivity. In addition to favourable injection moulding parameters, this was largely attributed to optimisation of twin-screw processing condition during the compounds production.

Figure 6.14 shows the relationship between electrical resistivity and polymer M_w . All compounds contained 3 wt% CNT and were produced under the same extrusion and injection moulding condition. The polycarbonates were Makrolon

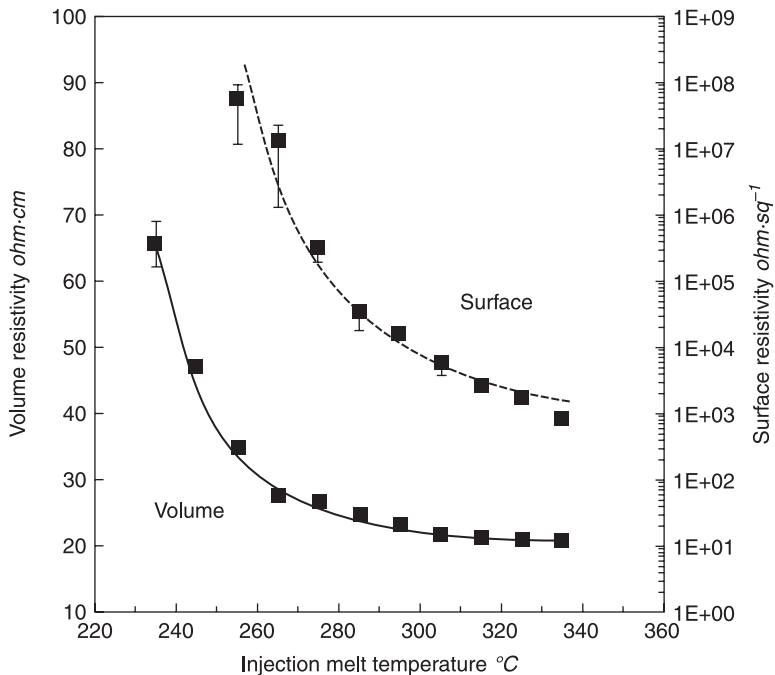


6.14 Plots of volume and surface resistivities of 3 wt% PC-CNT injection moulded from PCs with different molecular weights.

OD2015, 2205, 2405, 2805 and 3105. A unique trend was observed where $\rho_v \propto 1/M_w$, $\rho_s \propto M_w$ and at a critical M_w the resistivity levels off and then increases after critical M_w . In a steady state shear flow, shear gradient increases with M_w since a higher M_w species is more shear sensitive. This might possibly induce greater CNT migration towards the core and depletes CNT near to the wall which, in turn, increases surface resistivity. Another possible explanation was as M_w increases, the wall section experiences greater shear stress and, as a result, increases CNT orientation near to the surface.

Figure 6.15 shows the influence of injection temperature on electrical resistivity. Both surface and volume resistivity were observed to decrease with injection temperature. This was due to alteration of flow behaviour at higher temperature where:

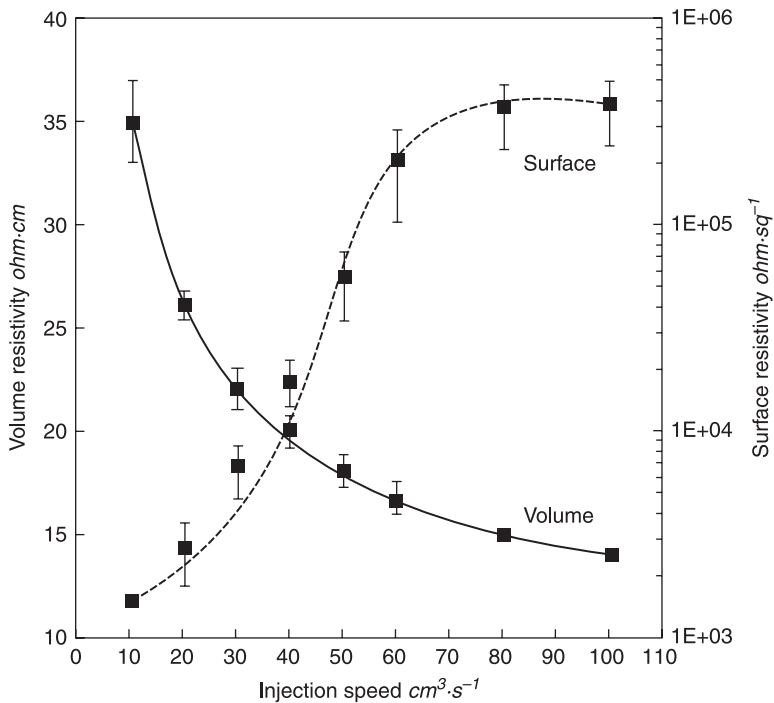
- polymer viscosity decreases (and hence shear stress), and as a result decreases CNT orientation which, in turn, increases network connectivity between the CNT particles, as reported by Villmow *et al.* (2008);
- relaxation of the polymer chain improves, causing short-range reflocculation of the CNT particles;



6.15 Plots of volume and surface resistivities of Makrolon 2405, 2.5 wt% PC–CNT versus injection melt temperature.

- reduced shear gradient which caused less migration away from the wall. As volume conductivity acts in parallel with surface conductivity, a decrease in surface resistivity also reduces the volume resistivity. However, because the effect has a greater influence on the surface, therefore the rate of conductivity decrease is greater for the surface compared to the volume.

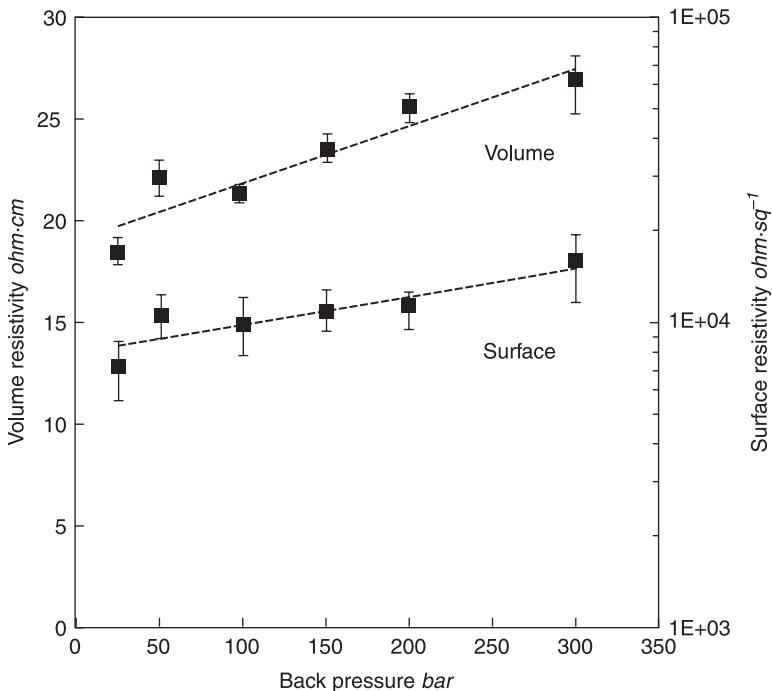
Figure 6.16 illustrates the relationship between injection speed and electrical resistivity. The opposing trend was observed for the volume resistivity (decreases with speed) and surface resistivity (increases with speed). The increase in volume resistivity with injection speed could be attributed to the migration of CNT from the wall towards the core because of increased shear gradient which, in turn, resulted in higher concentration of CNT in the sample's bulk. On the contrary, Villmow *et al.* (2008) had shown that the volume resistivity of PC-CNT composites rises with increasing injection speed, attributed to more formation of skin layer with more highly oriented CNT. Contradiction between results in this study and that of Villmow *et al.* was due to different types of volume resistivity measurement used; in-plane volume resistivity versus through-plane volume resistivity by Villmow. The through-plane volume resistivity measurement applied



6.16 Plots of volume and surface resistivities of Makrolon 2405, 2.5 wt% PC-CNT versus injection speed.

by Villmow was sensitive to the morphology of the skin layer as in surface resistivity measurement. Figure 6.16 shows that the surface resistivity (sensitive to skin layer) increases as the injection speed increases and is consistent with the through-plane volume resistivity results by Villmow *et al.* (2008). As the injection speed decreases, orientation of CNT was less intense in the skin layer and therefore gave rise to lower surface resistivity.

Figure 6.17 shows that both the volume and surface resistivity increase with the back pressure. The trend is subtle but clear. To explain the trend, it is important for the reader to understand the effect of back pressure on the flow kinematics. Back pressure is related to the amount of force (hydrostatic pressure) exerted on melt in the nozzle section during the plasticising stage. Increasing the back pressure will (a) increase the nozzle melt filling time, which means longer plasticising time; and (b) increase the flow pressure. Therefore, an increase in back pressure can be associated with an increase of mixing in the nozzle melt and injection speed. This would lead to increased orientation of CNT on the skin and hence higher resistivity. However, the flow behaviour derived from the increase of back pressure was different from that of the increase of injection speed, in which the flow experienced a surge when exiting the nozzle and therefore reducing the shear

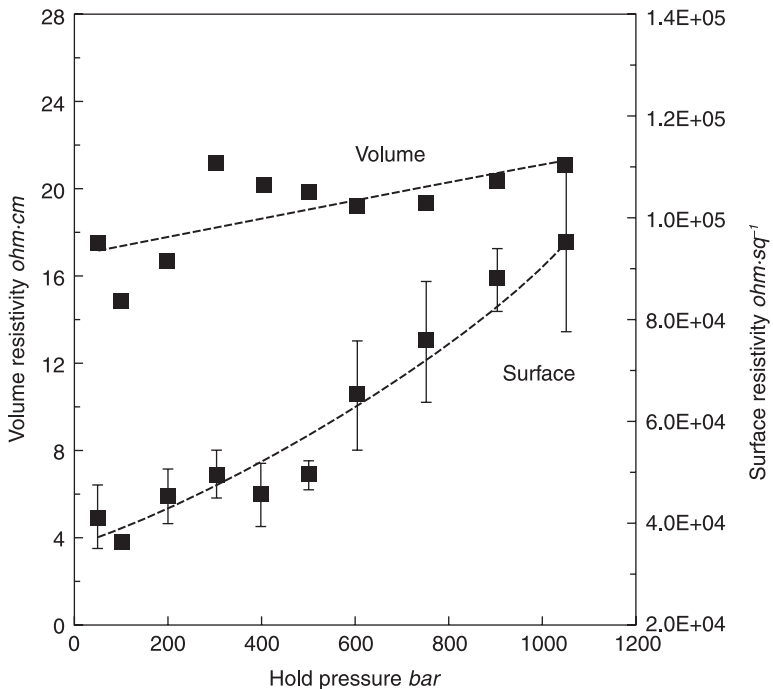


6.17 Plots of volume and surface resistivities of Makrolon 2405, 2.5 wt% PC-CNT versus injection back pressure.

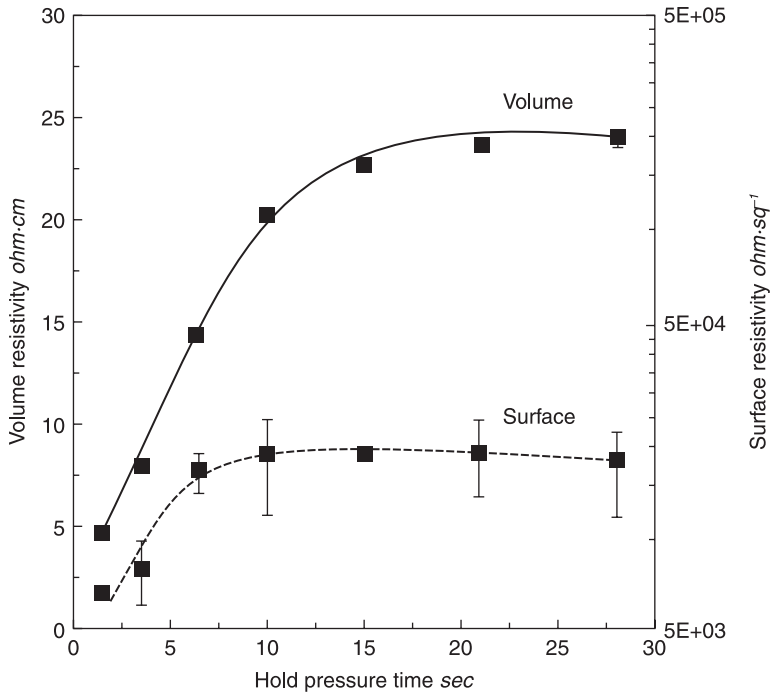
gradient. Because of the reduction in shear gradient but the increase in skin orientation, the volume resistivity also increases.

Figure 6.18 shows the relationship between electrical resistivity and injection hold pressure. No significant difference was observed for the volume resistivity on alteration of the injection hold pressure. This may be attributed to: (a) insensitivity of the CNT-enriched core (bulk) region to an increase in hold pressure or (b) insensitivity of the core to an increase in compaction force because the specimen's core, gates or sprue have already been solidified before the application of hold pressure. The increase in hold pressure (compaction force), however, led to an increase in the surface resistivity. Figure 6.19 shows the relationship between electrical resistivity and injection hold pressure time. Both the volume and surface resistivities appeared to increase with increasing hold pressure time up to a point and then level off (15 seconds for volume resistivity and 10 seconds for surface resistivity).

The effect of mould temperature on electrical resistivity is shown in Fig. 6.20. Surface resistivity increases proportionally with the mould temperature. This is an obvious effect of thicker skin layer formation and greater skin layer orientation,



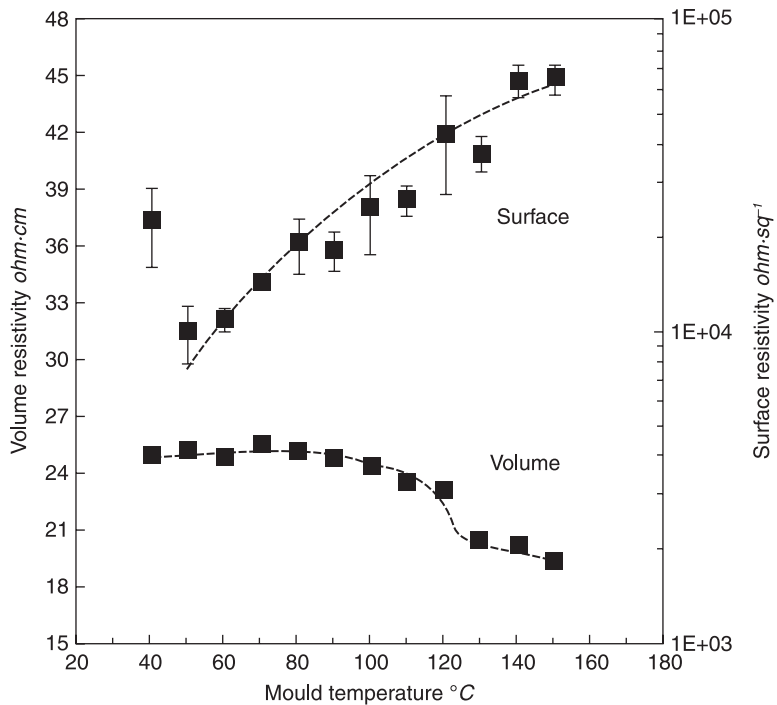
6.18 Plots of volume and surface resistivities of Makrolon 2405, 2.5 wt% PC-CNT versus injection hold pressure.



6.19 Plots of volume and surface resistivities of Makrolon 2405, 2.5 wt% PC–CNT versus injection hold pressure time.

as had been demonstrated by Villmow *et al.* (2008) through TEM analysis. No notable effect was detected on the volume resistivity for mould temperature between 40 and 100°C. This was consistent with work by Lellinger *et al.* (2008) that showed the volume resistivity was consistent across the mould temperature range from 70–100°C.

The effect of screw plasticising speed on the electrical resistivity is shown in Fig. 6.21. There was a clear increase in volume resistivity with increasing plasticising speed, but the magnitude was very small and almost negligible. Nonetheless, plasticising speed was found to have more effect on the surface resistivity. Surface resistivity was lowest at the very low plasticising speed of 5–10 cm·s⁻¹, followed by an abrupt rise at between 10–20 cm·s⁻¹ and, then, to decrease gradually with a further increase in speed. When the plasticising speed was too low, the time required for melting and nozzle filling increased and the flow pressure profile in the nozzle became more homogeneous. Because of increased residence time, melt temperature was also higher and, thus, contributed to a lower surface resistivity. When the plasticising speed was too high, not only the melt residence time in the nozzle was reduced, but the melt could be non-

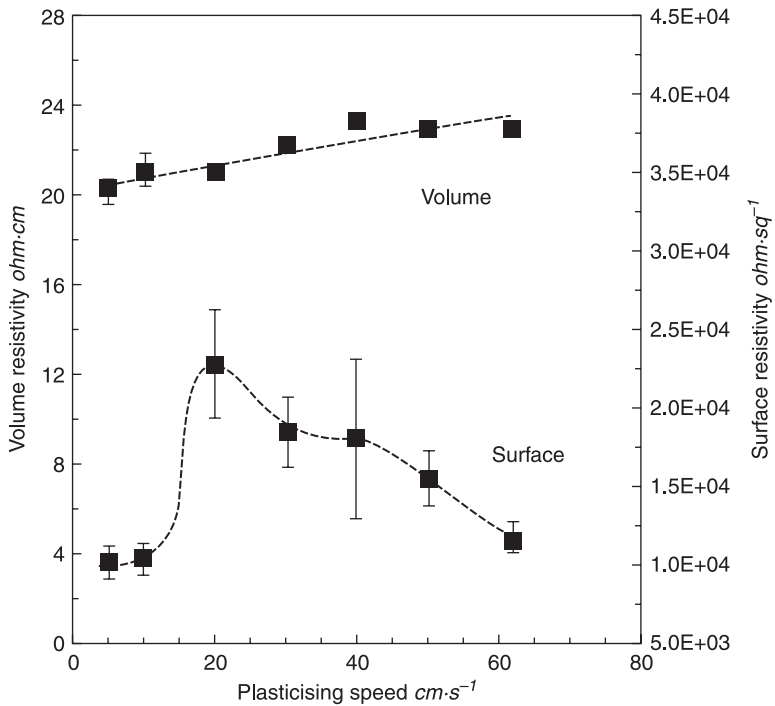


6.20 Plots of volume and surface resistivities of Makrolon 2405, 2.5 wt% PC–CNT versus injection mould temperature.

uniform (in this case, back pressure would play a more important role). Figure 6.22 shows the influence of volume decompression after plasticising on the electrical resistivity. The unique pattern was seen in which the volume resistivity was reciprocal to the surface resistivity. A reversal in the curve gradient was observed at a percentage decompression between 40 and 50%. The kinematics of influence was not clear but may be associated with the reduction in back pressure, increased melt relaxation and modification of flow behaviour at higher volume decompression.

6.5 Conclusion

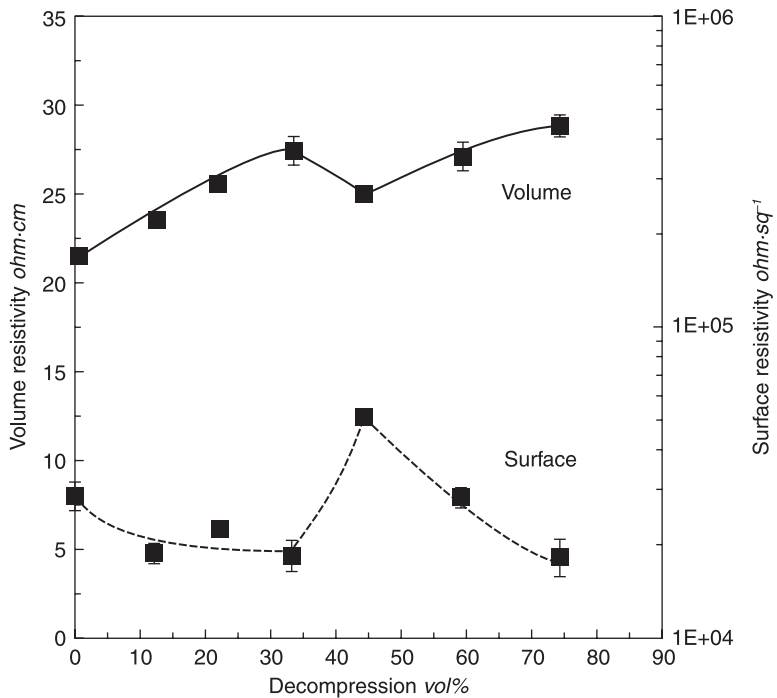
The work carried out in this chapter is intended to provide a clearer insight into the relationship between injection moulding parameters and the electrical resistivity of polymer CNT composites. Polycarbonates were used in this study, but the trend is expected to be applicable for larger families of polymers. To meet this objective, our work features more comprehensive experimental data points and sets of injection parameters than hitherto available in the literature. Resistivity



6.21 Plots of volume and surface resistivities of Makrolon 2405, 2.5 wt% PC–CNT versus injection plasticising speed.

in both volume (in-plane) and surface was tested and explained in parallel since their relationship is not always proportional and the mechanism governing their evolution is different. The relationship between injection parameters and surface finish was also investigated given its ramifications in industrial products development, where surface aesthetic value is an important issue. In the first section, an experiment design was conducted to find the optimum process–properties relationship between volume resistivity, surface resistivity, and surface finish. The optimum set of found parameters was adjusted for the parametric study in the subsequent sections on the effect of individual injection condition. The effect of molecular weight (viscosity) on modification of flow behaviour and, consequently, electrical resistivity was investigated using five different grades of polycarbonates.

Results indicated the two most influential parameters on the modification of electrical resistivity (both volume and surface) were the injection melt temperature and injection speed. On the other hand, the surface finish was most affected by the injection speed and mould temperature. In general, both the volume and surface resistivities followed a proportional increase relationship with the injection melt



6.22 Plots of volume and surface resistivities of Makrolon 2405, 2.5 wt% PC-CNT versus volume decomposition after plasticising.

temperature. Increasing injection speed decreases the volume resistivity but increases the surface resistivity. Higher mould temperature and greater injection speed improve the surface finish (reduce the formation of spots and pinholes).

In addition to the classical explanation relating the modification of electrical resistivity (in particular surface resistivity) to the alteration of the chain and nanotube orientation, a complementary explanation was given based on the influence of shear-induced migration. Shear-induced migration relates reciprocally to shear field fractionation of lower molecular weight or smaller species away from the point of lowest shear rate (centreline). Following the shear-induced migration kinetics, it may be possible to decrease the surface resistivity by means of blunting the flow profile or reducing the flow gradient of a shear stream during mould filling.

The steady-state rheological analysis showed that incorporation of CNT at a lower percentage (< 5 wt%) has not affected the melt viscosity in the region of processing windows corresponding to industrial plastic fabrication. On the contrary, the presence of CNT has demonstrated a shear thinning effect even at very low shear rate (< 100 s⁻¹), where the flow of the virgin polymer is governed by a Newtonian flow behaviour. The shear thinning effect imparted by CNT

would have significant implications in terms of melt processability. Shear thinning of a polymer–CNT composite decreases its melt viscosity to become comparable or lower than its virgin form, and therefore, improved processability.

6.6 References

- Aarøe E R, Blaimschein K S, Decker L, Stentoft-Christensen H C, 'Examining the influence of injection speed and mould temperature on the tensile strength of polypropylene and ABS', Report no. 71738, Experimental Plastic Technology, DTU Mekanik, Institut for Mekanisk Teknologi, June 2009.
- Barron A R and Khan M R, 'Carbon nanotubes: opportunities and challenges', *Adv. Mater. Processes*, 2008, **166**, 41–43.
- Chandra A, Kramschuster A J, Hu X, Turng L-S, 'Effect of injection molding parameters on the electrical conductivity of polycarbonate/carbon nanotube nanocomposites', in *Proc. Annual Technical Conference of the Society of Plastics Engineers, Cincinnati, US*, 2007, **3**, 2184–2188.
- Hong C-M, Kim J, Jana S C, 'Shear-induced migration of conductive fillers in injection molding', *Polym. Eng. Sci.*, 2004, **44**, 2101–2109.
- Jana S C and Doni S, 'On the effects of migration of filler particles on conductivity and mechanical properties', in *Proc. Annual Technical Conference of the Society of Plastics Engineers, Dallas, US*, 2001, **59**, 2022–2026.
- Jin S H, Choi D K, Lee D S, 'Electrical and rheological properties of polycarbonate/multiwalled carbon nanotube nanocomposites', *Coll. Surf. A: Physicochem. Eng. Asp.*, 2008, **313–314**, 242–245.
- Joiner B, Cryer J, Ryan B F (2004), *Minitab B, 5th edn.*, New York: Brooks/Cole.
- Kharchenko S B, Douglas J F, Obrzut J, Grulke E A, Migler K B, 'Flow-induced properties of nanotube-filled polymer materials', *Nature*, 2004, **3**, 564–568.
- Leighton D and Acrivos A, 'The shear-induced self-diffusion in concentrated suspension', *J. Fluid Mech.*, 1987, **181**, 415–439.
- Lellinger D, Xu D, Ohneiser A, Skipa T, Alig, I., 'Influence of the injection moulding conditions on the in-line measured electrical conductivity of polymer-carbon nanotube composites', *Phys. Stat. Sol. (B)*, 2008, **245**, 2268–2271.
- Lew C Y, Claes M, Luizi F, 'The influence of processing conditions on the electrical properties of polypropylene nanocomposites incorporating multiwall carbon nanotube', in *Proc. 6th European Conference on Additives and Colors, Antwerp, Belgium*, 2009a, 1–7.
- Lew C Y, Xia H, McNally T, Fei G, Vargas J, Millar B, Douglas P, Claes M, Luizi F, 'A unified strategy to incorporating nanotube in twin-screw extrusion processing', in *Proc. Polymer Processing Society Annual Regional Conference, Larnaca, Cyprus*, 2009b, 1–10.
- Ma A W K, Chinesta F, Mackley M R, Ammar A, 'The rheological modelling of carbon nanotube (CNT) suspensions in steady shear flows', *Int. J. Mater. Forming*, 2008, **1**, 83–88.
- McNally T, Pötschke P, Halley P, Murphy M, Martin D, Bell S E J, Brennan G P, Bein D, Lemoine P, Quinn J P, 'Polyethylene multiwalled carbon nanotube composites', *Polymer*, 2005, **46**, 8222–8232.
- Mekhilef N, Ait-Kadi A, Ajji A, 'Effect of processing conditions on mechanical properties of polycarbonate-polyethylene blends', in *Proc. Annual Technical Conference of the Society of Plastics Engineers, Montreal, Canada*, 1991, 1118–1121.

- Park D H, Yoon K H, Park Y-B, Lee Y S, Lee Y J, Kim S W, 'Electrical resistivity of polycarbonate/multiwalled carbon nanotube composites under varying injection molding conditions', *J. Appl. Polym. Sci.*, 2009, **113**, 450–455.
- Phillips R J, Armstrong R C, Brown R A, Graham A L, Abbott J R, 'A constitutive model for concentrated suspensions that accounts for shear-induced particle migration', *Phys. Fluids A*, 1992, **4**, 30–40.
- Pötschke P, Fornes T D, Paul D R, 'Rheological behaviour of multiwalled carbon nanotube/polycarbonate composites', *Polymer*, 2002, **43**, 3247–3255.
- Rahmatpour A and Aalaie J, 'Steady shear rheological behaviour, mechanical properties, and morphology of polypropylene/carbon nanotube nanocomposites', *J. Macromol. Sci., Part B*, 2008, **47**, 929–941.
- Shelby M D and Cafilisch G B, 'Shear field induced diffusion and molecular weight fractionation during polymer processing', *Polym. Eng. Sci.*, 2004, **44**, 1283–1294.
- Teng C C, Ma C C M, Huang T W, Yuen S M, Weng C C, Chen C H and Su S F, 'Effect of MWCNT content on rheological and dynamic mechanical properties of multiwalled carbon nanotube/polypropylene composites', *Composites: Part A*, 2008, **39**, 1869–1875.
- Vega J F, Martinez-Salazar J, Trujillo M, Arnal M L, Muller A J, Bredeau S and Dubois Ph, 'Rheology, processing, tensile properties, and crystallization of polyethylene/carbon nanotube nanocomposites', *Macromolecules*, 2009, **42**, 4719–4727.
- Villmow T, Pegel S, Pötschke P, Wagenknecht U, 'Influence of injection molding parameters on the electrical resistivity of polycarbonate filled with multi-walled carbon nanotubes', *Comp. Sci. Tech.*, 2008, **68**, 777–789.
- Zhang H and Zhang Z, 'Impact behaviour of polypropylene filled with multi-walled carbon nanotubes', *Eur. Polym. J.*, 2007, **43**, 3197–3207.

6.7 Appendix: list of units

	Nomenclature	Unit
ρ_V	Volume resistivity	$\Omega\cdot\text{cm}$
ρ_S	Surface resistivity	$\Omega\cdot\text{sq}^{-1}$
T_{inj}	Injection temperature*	$^{\circ}\text{C}$
T_{mo}	Mould temperature	$^{\circ}\text{C}$
P_{ba}	Back pressure	bar
P_{h}	Hold pressure	bar
V_{inj}	Injection speed	$\text{cm}^3\cdot\text{s}^{-1}$
V_{plas}	Plasticising speed	$\text{cm}\cdot\text{s}^{-1}$
V_{de}	Volume decompression	$\% \text{ cm}^3$
t_{h}	Hold pressure time	s

*Melt temperature measured at the injection nozzle.

Elastomer–carbon nanotube composites

J. FRITZSCHE, H. LORENZ and M. KLÜPPEL,
German Institute of Rubber Technology, Germany and A. DAS,
R. JURK, K. W. STÖCKELHUBER and G. HEINRICH,
Leibniz Institute of Polymer Research Dresden, Germany

Abstract: Different techniques to disperse multi-walled carbon nanotubes (MWCNT) in elastomers using an internal mixer are applied and the physical properties of the resulting composites are evaluated. It is demonstrated that the dispersion can be improved if the CNT are suspended in a liquid agent in a first step to break up the bonds. Here, ethanol proved to be a good dispersion agent without any additional surfactant and could be vaporized during the mixing process. These investigations are extended to technologically more relevant filler hybrid systems, where parts of the reinforcing filler are exchanged by CNT. Additionally, the use of ionic liquids for improved CNT–polymer interaction is discussed. The dielectric properties, electrical DC conductivity, thermal diffusivity, dynamic-mechanical as well as the stress–strain and fracture mechanical behavior of CNT-filled composites are investigated. The effect of nanoscopic gaps between adjacent CNT on the electrical and thermal conductivity of the composites and the missing percolation behavior of the thermal conductivity are discussed.

Key words: carbon nanotubes, elastomers, hybrid systems, ionic liquids, reinforcement.

7.1 Introduction

Carbon nanotubes have been shown to be attractive fillers in various applications due to their unique combination of outstanding mechanical properties, high electrical conductivity and reinforcement quality. Various reports can be found in the literature describing the properties of individual single-walled carbon nanotubes (SWCNT) and multi-walled carbon nanotubes (MWCNT) such as high flexibility (Cooper *et al.*, 2001), extremely high tensile strength (150–180 GPa) and high electrical and thermal conductivity (De Heer, 2004). Due to these excellent properties, a great enthusiasm to explore the potential as nanofillers exists around the world. Nevertheless, the number of commercial products based on CNT at the moment is very small (Moniruzzaman *et al.*, 2006). As a matter of fact, the dispersion of CNT in a polymer matrix is still a great challenge due to the attractive interaction between neighboring CNT and the very large specific surface area of the tube, leading to heavy agglomeration. Considerable effort has been made to disperse CNT in a polymer matrix by solution mixing (Du *et al.*, 2003; Islam *et al.*, 2003; Sundararajan *et al.*, 2004; Cho *et al.*, 2005; Koerner *et al.*, 2005;

Haggenmueller *et al.*, 2006) or *in-situ* polymerization (Ajayan *et al.*, 2000; Gong *et al.*, 2000; Zhu *et al.*, 2003; Jung *et al.*, 2006; Moniruzzaman *et al.*, 2006; Xia *et al.*, 2006) in the presence of nanotubes. In contrast, there are only a few examples of melt mixing, which is the most promising way from the viewpoint of the industrial compounding practice. Successful dispersion was reported for CNT-polycarbonate (Pötschke *et al.*, 2003), CNT-nylon (Liu *et al.*, 2004; Zhang *et al.*, 2004), SWCNT-polypropylene (Battacharyya *et al.*, 2003) and SWCNT-polyimide (Siochi *et al.*, 2004). Pötschke *et al.* (Pötschke *et al.*, 2007) reported on the successful dispersion of CNT in thermoplastic polyurethanes with promising properties. Similar good results were recently found for CNT-PDMS (polydimethylsiloxan) composites (Bokobza, 2008).

Nevertheless, the distribution of CNT in technical elastomers, which often is not comparable to thermoplastics, has not been well investigated. Considerable improvement of physical properties was reported when carbon nanotubes were incorporated in styrene-butadiene rubber (SBR) (Bokobza, 2007; Bokobza and Belin, 2007). In another work, the reinforcing effect of SWCNT in natural rubber was revealed by dynamic mechanical analysis and Raman spectroscopy (Lopez-Manchado *et al.*, 2004). Here, a noticeable decrease of the loss tangent ($\tan \delta$) peak height, as well as a marked shift of glass transition temperature (T_g) towards higher temperature was observed. Fakhru'l-Razi *et al.* (Fakhru'l-Razi *et al.*, 2006) showed that the initial modulus of a natural rubber (NR) composite was increased by a factor of up to 12 times in relation to pure NR, followed by Wang *et al.* (Wang *et al.*, 2006) who dispersed CNT in NR via latex mixing.

Kim *et al.* (Kim *et al.*, 2006) evaluated the mechanical, thermal and electromagnetic shielding properties of ethylene propylene diene monomer rubber (EPDM)-CNT composites. They concluded that the alignment of tubes in an EPDM rubber matrix, arising from the mill processing, resulted in significant improvements in mechanical, electrical and thermal properties. Frogley *et al.* (Frogley *et al.*, 2003) reported the improvement of the mechanical properties of CNT-filled silicone rubber. In their work, it was reported that with the increase in the number of carbon nanotubes, a remarkable enhancement of the initial modulus (Young's modulus) was observed, accompanied by a reduction of the ultimate tensile strength. However, at higher strains ($\approx 20\%$), the modulus was found not to change upon further increase of CNT concentration. Hydrogenated nitrile rubber was also used to prepare nanocomposites with CNT (Yue *et al.*, 2006). The authors reported a serious breakage of the CNT during the ultrasonic dispersion, which resulted in a poor electrical conductivity of such nanocomposites. Additionally, the dispersion behavior of CNT in epoxy materials has been investigated (Shaffer and Sandler, 2006).

In order to obtain thermoplastic elastomer-CNT composites for tribological applications, EPDM with a high ethylene content was spray-coated with an aqueous dispersion of the CNT, which was then dried and melt blended with the

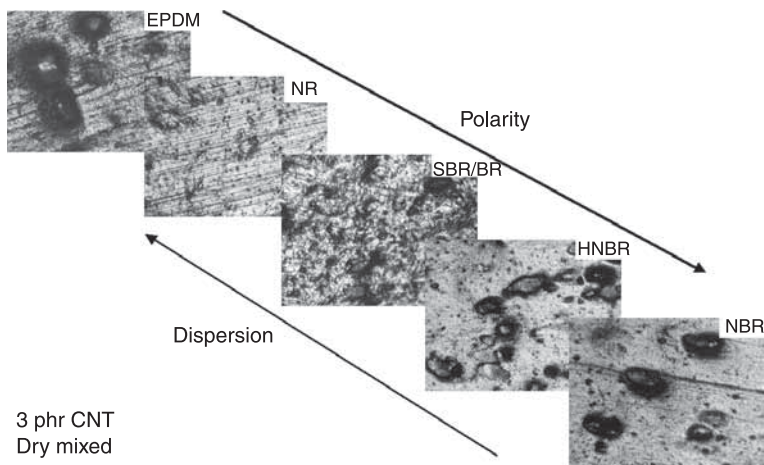
thermoplastic elastomer (Karger-Kocsis *et al.*, 2008). Synthetic polyisoprene–CNT composites were also prepared by a solution method and the effect of stretching on the electrical properties has been discussed (Knite *et al.*, 2007). Nevertheless, until now, the mechanism of reinforcement and the details of the polymer interaction of CNT with polymer matrices have not been well understood.

7.2 Processing

7.2.1 Variation of the polymer type

When mixed into rubber, normally a poor dispersion of the CNT results. This is due to attractive van der Waals bonds between the outer planes of neighboring nanotubes which result in agglomeration of the powder material. The quality of dispersion depends significantly on the polarity of the used rubber and, therefore, from its interaction with the CNT as well as the rheological properties and the mixing procedure.

To obtain a first impression of the rubber–CNT compatibility, a series of five rubbers varying in polarity and in rheological properties are mixed with 3 phr (parts per hundred rubber) of CNT (Nanocyl 7000, from Nanocyl S. A., Sambreville, Belgium, industrial grade, 90% purity). The macrodispersion was first evaluated analyzing the sample surface by light microscopic techniques in combination with the evaluation program DIAS (dispersion index analyzing system) resulting in a value for the amount of dispersed material. The results are shown in Fig. 7.1.



7.1 Dispersion characteristics of different elastomers as indicated with 3 phr CNT dry mixed, analyzed by light microscopic techniques.

The CNT consists of 90% carbon in graphite layers as well as a small amount of amorphous carbon and has, therefore, a more nonpolar behavior which is only slightly influenced by catalysator waste and undesired functional groups. As a matter of principle, therefore, the best dispersion is obtained by dispersing the CNT in nonpolar natural rubber (NR, SVR CV 50). Here, due to the high molecular weight, also high shear forces can be obtained during the mixing process which improves the dispersion additionally. Similar results can be found for styrene-butadiene/butadiene-rubber (SBR/BR) (SBR: S-SBR VSL 2525-0, Lanxess, BR: CB 24, Lanxess (50:50)). Here the polarity is similar but the shear forces obtained during mixing are lower due to the slightly lower viscosity of the used SBR. The polar rubbers hydrogenated nitrile rubber (HNBR, Therban A3406, Lanxess) and nitrile rubber (NBR, Perbunan NT 3470) show very bad dispersion characteristics as expected due to the weak interaction between the rubber and the CNT, although the shear forces for both types of rubber are high. Additionally, the nonpolar EPDM (Keltan 512, DSM) also shows large agglomerates; here probably the rheological properties are the crucial factor, since EPDM has the lowest viscosity and therefore only low shear forces can be obtained during the mixing process.

The dispersion characteristics are reflected in the mechanical as well as electrical properties which are displayed in Table 7.1. The mechanical properties were analyzed by measuring the tensile properties using a Zwick 1456 (model 1456, Z010) with a cross-head speed of 200 mm/min (ISO 527). In most tested materials, an increase of the tensile strength is obtained with 3 phr CNT. The highest improvements of 176% and 150% are obtained for the SBR/BR and the NR samples, respectively. In the elongation at break values for the SBR/BR blend a reduction of the elongation at break is always observed. Probably, the less than optimal dispersion of CNT results in agglomerates which act as stress concentrators and, therefore, reduce the failure strain. To analyze the electrical properties,

Table 7.1 Influence of 3 phr CNT (dry mixed) on the mechanical and electrical properties of different rubber types

	σ_{\max} [MPa]		ε_{\max} [%]		σ_0 [S/cm]
	Value	Improvement (%)	Value	Improvement (%)	
EPDM unfilled	2.7		310		3.5×10^{-7}
EPDM (3 phr CNT)	3.5	130	220	70	
NR unfilled	12		480		
NR (3 phr CNT)	17	142	420	87	5.2×10^{-6}
SBR/BR unfilled	1.7		150		
SBR/BR (3 phr CNT)	3.0	176	175	116	
HNBR unfilled	7		830		5.0×10^{-10}
HNBR (3 phr CNT)	10.5	150	780	94	
NBR unfilled	3		425		
NBR (3 phr CNT)	4	133	350	82	

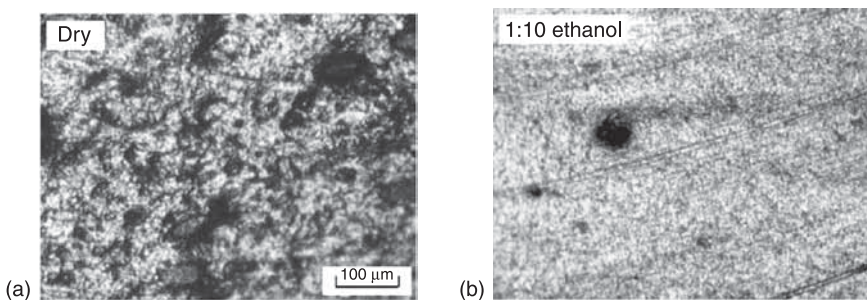
dielectric investigations were carried out at room temperature at frequencies from 0.1 Hz to 10 MHz using a broadband dielectric spectrometer BDS 40 (from Novocontrol GmbH, Germany). With the limit of 0.1 Hz, the measured real part of the conductivity σ' reaches a plateau value which corresponds directly to the DC conductivity σ_0 . In these measurements, for all materials, no high electrical conductivity is observed, the highest value here is obtained for NR with an AC conductivity of 5.2×10^{-6} S/cm in the limit of 0.1 Hz.

7.2.2 Influence of predispersing solvents

The literature shows that for epoxy and thermoplastic materials the application of additives has proved to be successful in dispersing CNT. Therefore, one approach is to transfer and adapt this method to rubber materials. The used solvents have to fulfill various requirements such as low vapor pressure, an evaporation temperature in the range of the mixing temperature, incompatibility with the rubber used, environmental friendliness and no interaction with the curing system. Therefore, the CNT (Nanocyl 7000, industrial grade) is first mixed with the solvents and dispersed in an ultrasonic bath. Afterwards the CNT-solvent mix was incorporated into the rubber by classical melt mixing in an internal mixer. The rubber used was an SBR/BR-blend (S-SBR 2525–0/CB 24 70:30), and the solvents ethanol and 2-propanol were applied in two weight ratios of solvent:CNT as 5:1 and 10:1. Further details about the sample preparation can be found in (Lorenz *et al.*, 2009).

The effect of the predispersing agent on the dispersion of the CNT can first be evaluated by microscopic techniques. As can be seen in the light microscopic images in Fig. 7.2, significant improved macro dispersion can be stated by use of ethanol with only a few and small agglomerates of CNT. The best results are obtained with an ethanol to CNT ratio of 10:1.

For this ethanol-containing sample, additionally TEM measurements were carried out to investigate the distribution on a microscale. Therefore thin sections of the



7.2 Dispersion characteristics of 3 phr CNT in SBR/BR (70:30) illustrated by light microscopic images: (a) dry mixed; (b) with CNT:ethanol in a weight ratio of 1:10.

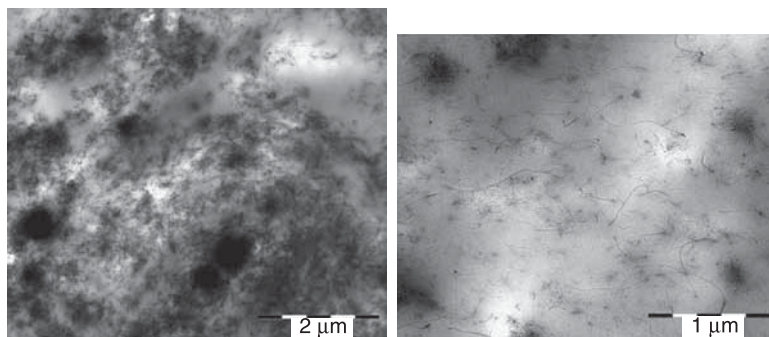
investigated sample were cut with a microtome. With magnification from Fig. 7.3, it is obvious that the distribution of the CNT is not completely homogeneous, regions of high CNT concentration can be seen that are surrounded by polymer containing only a few CNT. However, it is also revealed from the measure of electrical conductivity that the carbon nanotubes are forming a percolating network at 3 phr loading.

Due to the best dispersion, the SBR/BR-composite prepared using ethanol shows the largest gain in the AC electrical conductivity (Fig. 7.4 (a)) with up to $\sigma_0 = \sigma'_{0.1 \text{ Hz}} = 10^{-1} \text{ S/m}$. This value is similar to the values of elastomer composites filled with a highly active carbon black at 10 times higher loading (Kluppel, 2003; Meier *et al.*, 2007). The composite produced with the aid of 2-propanol delivers slightly lower conductivity values, probably due to the slightly lower dispersion. Fig. 7.4 (b) shows the mechanical strength of the different systems. With ethanol, a threefold amplification of stress can be achieved in relation to the unfilled rubber. It is observed that the stress–strain curves of the composites prepared using 2-propanol exhibit somewhat smaller stress values and mechanical strength than those mixed with ethanol.

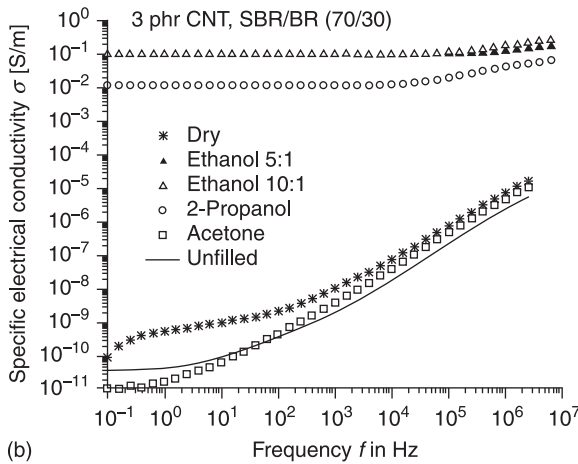
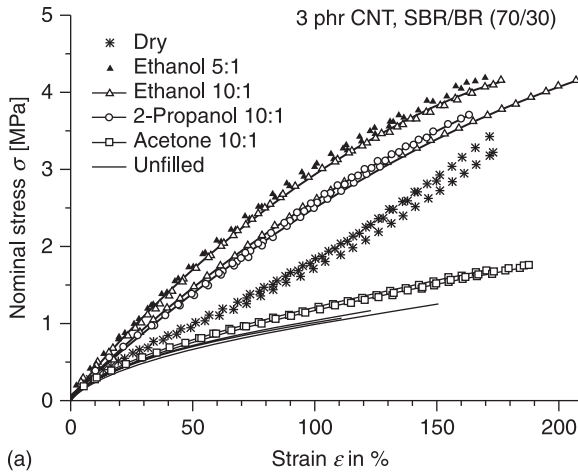
7.2.3 Variation of the carbon nanotube (CNT) concentration

To investigate the influence of the CNT concentration on the investigated properties, a variation of the CNT content between 1 and 4 phr of CNT was carried out for SBR/BR composites (S-SBR 2525–0/CB 24 = 70:30). In the preparation of these composites, ethanol was used as an additive in a weight ratio of 10:1 as described before, since in this case the best properties have been obtained.

As seen in Fig. 7.5, the mechanical reinforcement of these samples rises quite linearly with the CNT content. There is already a considerable reinforcement of 1.6 at 1 phr below the electrical percolation threshold without a continuous filler network. With only 4 phr, nearly five times higher tensile strength values can be



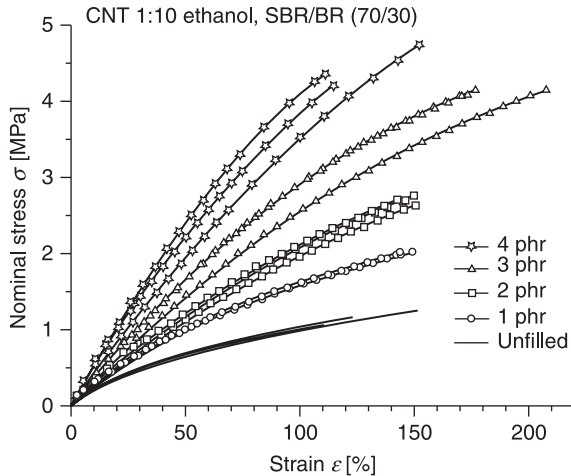
7.3 Dispersion characteristics of 3 phr CNT in SBR/BR (70:30) (CNT:ethanol = 1:10) illustrated by transmission electron microscopy (TEM) images.



7.4 Influence of the dispersion on (a) quasi-static mechanical properties and (b) frequency dependent conductivity.

achieved. The elongation at break stays nearly constant, with 4 phr, only a slight decrease is observed. Here the fracture surfaces show that cracks are initiated at small dots with diameters of some 100 μm . Therefore, it is supposed that for highly CNT-filled materials, the dispersion is more critical and cracks originate at CNT agglomerates which behave as stress concentrators.

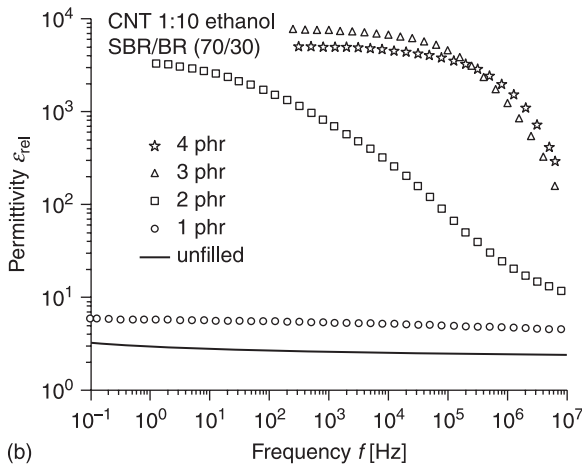
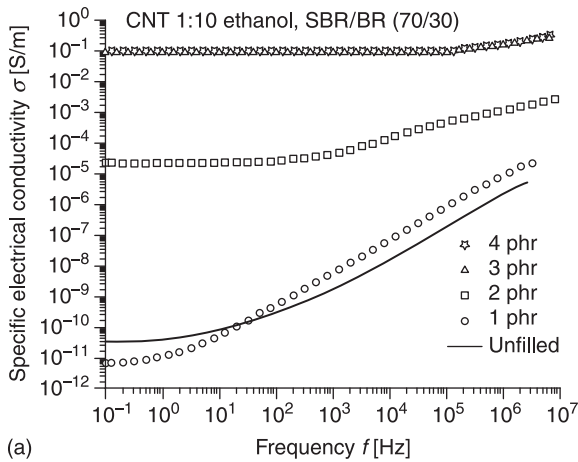
Figure 7.6 demonstrates a drastic change of the dielectric properties of the described composites. Above a critical volume fraction of carbon nanotubes ϕ_c , the percolation threshold, an interconnecting filler network is formed, which results in a sharp increase of the electrical conductivity of the nanocomposites. It



7.5 Quasi-static stress-strain curves of SBR/BR composites (SBR:BR = 70:30) mixed with ethanol (10:1) for different CNT concentrations as indicated.

is evident from Fig. 7.6 that the percolation threshold is reached when the filler concentration increases from 2 to 3 phr. The very high aspect ratio of the carbon nanotubes is mainly responsible for this percolation behavior at very low loadings of CNT. Supposing a mass density of the CNT of 1.7 g/cm^3 , which corresponds to the density of carbon black and 0.9 g/cm^3 for the matrix, which is typical for elastomers, this results in a volume-related percolation threshold of $\phi_c = 0.01$, which is quite low but about one order of magnitude higher than theoretical estimations $\phi_c = 0.001$. This indicates that there is still the potential for an improvement of the dispersion.

A closer look at the frequency dependent behavior of the dielectric properties results in a deeper understanding of the CNT networking. In the real part of the frequency dependent AC conductivity σ' (Fig. 7.6 (a)), a cross-over from a plateau at low frequencies to a power-law behavior at higher frequencies is observed for all samples, which is also well known for carbon black-filled samples (Jonscher, 1977). The characteristic cross-over frequency moves to higher values with increasing concentration of CNT. For the unfilled and the low filled sample (1 phr), the slope m of the high frequency part above the cross-over frequency is nearly $m = 1$, indicating an insulator-like behavior with an almost linear increase of the conductivity with frequency. For the filled samples with 2 phr CNT this slope decreases to a value around $m = 0.6$. This transition of the scaling behavior results from the formation of a conducting CNT network on mesoscopic length scales. In the case of carbon black composites a similar scaling behavior with $m = 0.6$ has been observed and related to anomalous diffusion on a fractal percolation network (Kluppel, 2003).



7.6 Influence of the CNT concentration in SBR/BR composites (SBR:BR = 70:30) mixed with (10:1) ethanol on (a) frequency dependent conductivity and (b) frequency dependent permittivity.

The conducting nature of the composites becomes very pronounced above the percolation threshold of filler particles. The composites containing 3–4 phr of CNT are definitely above the percolation threshold as the power law regime is particularly shifted to higher frequencies and thus the material behaves like an Ohmic conductor with the conductivity almost independent of frequency.

The frequency dependency of the real part of the permittivity ϵ' is shown in Fig. 7.6 (b) and characterizes the polarization of the sample in an alternating field. In the unfilled sample and the sample filled with 1 phr of CNT, the permittivity has

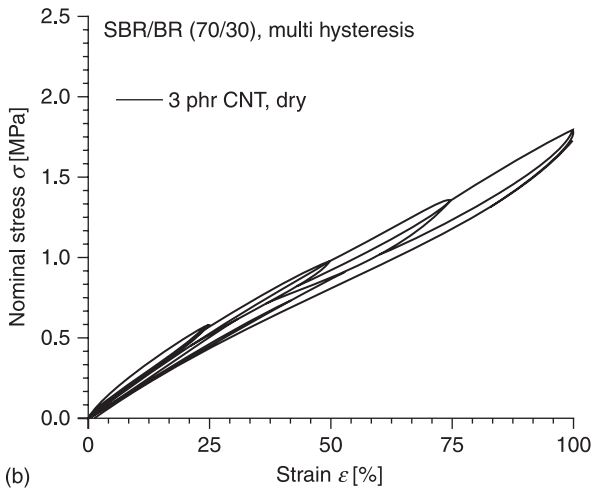
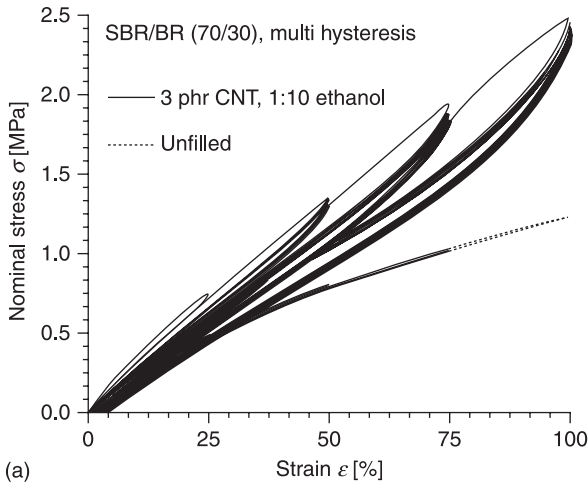
low values and behaves almost independent of frequency. With the increasing number of nanotubes, this behavior changes. At low frequencies the permittivity is significantly increasing with the amount of filler. Additionally, at a certain frequency, a relaxation process takes place, resulting in a drastic drop of the permittivity with increasing frequency. With increasing loading of CNT, the relaxation transition is shifted towards higher frequencies. We point out that the behavior of the dielectric response functions shown in Figs 7.6 (a) and 7.6 (b) is very similar to that of carbon black-filled elastomers above the percolation threshold (Jonscher, 1977; Klüppel, 2003; Meier and Klüppel, 2007).

7.3 Structure–property relationships

7.3.1 Mechanical properties

The observed amplification of stress is undoubtedly connected to the high specific surface area of CNT, but it is not typical of ‘hydrodynamic reinforcement’. This mechanism is caused by a ‘shielding’ and immobilization of polymer chains, e.g. by stiff clusters of carbon black. In CNT-filled elastomers, it can only play a role when larger network-like filler clusters are present. This seems to be the case for the ‘dry’ mixed compounds in Fig. 7.4(b). Here, also an upturn of the stress strain curves above 100% is found. The missing upturn for the samples containing ethanol may be caused by the geometry of dispersed nanotubes which hardly allows for a ‘shielding’ effect, but also by a lower CNT/polymer interface strength resulting in de-bonding. It is pointed out that hydrodynamic reinforcement is marked by a ‘shift’ of the upturn from high strains in unfilled rubber to lower strains in the filled rubber, since the local strain in the rubber matrix is essentially a product of the global strain multiplied by a strain amplification factor.

Considering a CNT content of 3 phr in SBR/BR (S-SBR 2525–0/CB 24 70:30) composites mixed with ethanol in a weight ratio of 1:10 CNT:EtOH, the so-called ‘discontinuous damage’ test depicted in Fig. 7.7 (a) reveals a strong stress softening and hysteresis behavior that increase with the applied maximum strain. This effect is well known from carbon black-reinforced elastomers and is typically not observed for the unfilled reference, also shown in Fig. 7.7 (a). It may be related to a breakdown of the CNT network or alternatively to a sliding between the CNT and the polymer, corresponding to an insufficient CNT/matrix coupling. For the dry mixed composite shown in Fig. 7.7 (b), a much less pronounced stress softening and hysteresis is observed. This indicates that no CNT network is formed, which is in agreement with the low electrical DC conductivity of $\sigma < 10^{-11}$ S/m. Furthermore, the marked stress relaxation and permanent set increasing with strain are observed for the samples mixed with ethanol, which may be caused by low filler/matrix interaction but may also be due to a softener effect of the remaining ethanol within the rubber matrix. Nevertheless, the insufficient filler/matrix interaction seems probable since CNTs have no structured, active surface like e.g. carbon black, consequently, there will be no tightly bound rubber.



7.7 Quasi-static stress–strain cycles of unfilled and CNT-filled SBR/BR samples mixed (a) with (1:10) ethanol and (b) dry mixing; five repeated cycles for various maximum strain values from 25% up to 100% are shown.

From stress–strain experiments, Young’s modulus can be evaluated and utilized to roughly estimate an apparent effective aspect ratio (length/width) of the tubes following the Guth–Gold–Smallwood equation (Guth and Gold, 1938; Smallwood, 1944; Guth, 1945):

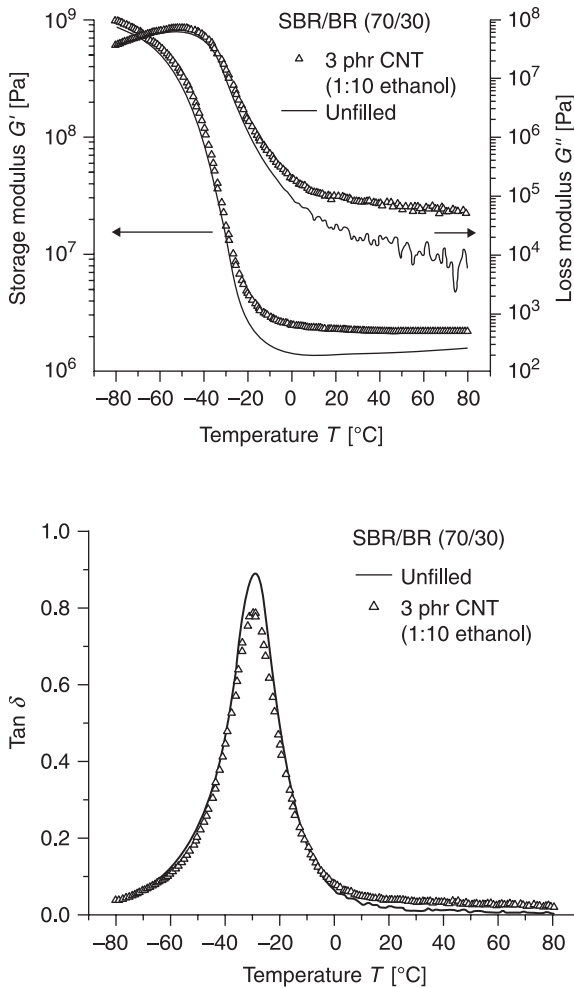
$$E_f/E_u = 1 + 0.67\phi + 1.62f^2\phi' \quad [7.1]$$

where E_f is Young's modulus of the filled elastomer, E_u is the value for the unfilled rubber and ϕ is the volume fraction of the filler. The shape factor f is defined as the aspect ratio of a non-spherical particle. The quadratic term of Equation 7.1 can be ignored at low filler concentrations and for low f -values. The aspect ratios were calculated according to Equation 7.1 and it was found that the f -values vary between 15–20 for dry mixed compounds and 50–60 for ethanolic dispersed compounds. The estimated values are far below the expected values for CNT with an aspect ratio for a typical single stretched nanotube of nearly 1000. The main factors hindering the utilization of the high aspect ratio for the reinforcement process probably are agglomerates of bundled nanotubes due to low dispersion and breakage of CNT during ultrasonication or processing.

Recently, it has been reported that the Guth model and the Halpin–Tsai model fit very well after considering the aspect ratio of 40–45 for multi-walled carbon nanotubes in styrene-butadiene rubber (Bokobza, 2007). The Halpin–Tsai model also describes the relation between the aspect ratio of a fiber and the modulus of a reinforced polymer. It must be noted that originally Equation 7.1 was derived and validated for anisotropic fillers with relatively low aspect ratio. These fillers were assumed to behave totally rigid. For the CNT, the rigid condition is probably not fulfilled if the aspect ratio is large. Accordingly, the longer CNT visible in the TEM micrographs of Fig. 7.3 (b) will bend in the stress field of the rubber matrix and the strain amplification factor estimated in Equation 7.1 can be considered only as an effective one. For that reason, the fitted values for the aspect ratio are expected to be smaller than the values obtained from morphological measurements. Nevertheless, the procedure presented for a rough estimation of an apparent f -value is considered to be useful.

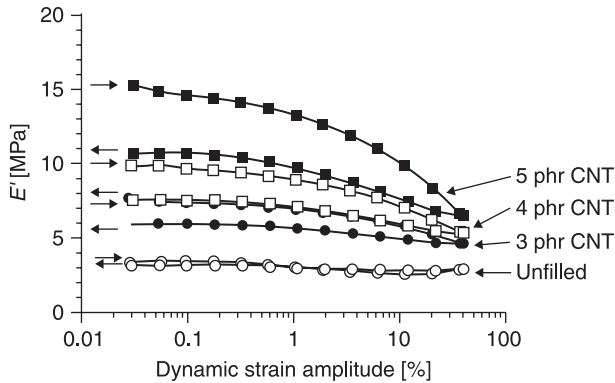
7.3.2 Dynamic-mechanical properties

The dynamic-mechanical properties are also influenced by the incorporation of CNT. Therefore, the properties were analyzed with a Rheomix ARES at a constant frequency of 1 Hz and dynamical strain amplitude of 0.5%, varying the temperature between -80°C and $+80^{\circ}\text{C}$. Figures 7.8 (a) and 7.8 (b) show the temperature-dependent behavior of the shear storage moduli G' , the shear loss moduli G'' , and the loss factor $\tan \delta$ of the unfilled sample and the nanocomposite filled with 3 phr CNT. Figure 7.8 (a) illustrates that with an increase in temperature the storage modulus of both samples decreases, which is associated with the glass transition phenomenon of the elastomer chains. Above room temperature, the values of G' and G'' increase significantly with CNT. As seen in Fig. 7.8 (b), the glass transition temperature at the maxima of the $\tan \delta$ plot does not change with the incorporation of CNT in the rubber matrix. However, the peak height is considerably reduced. This behavior also indicates the strong reinforcement efficiency with only a low content of CNT.



7.8 Dynamic-mechanical analysis of the unfilled and CNT-filled SBR/BR composite mixed with 10:1 ethanol: (a) temperature sweep of G' and G'' ; (b) loss tangent ($\tan \delta$).

The storage modulus of unfilled rubbers, E' , is independent of the deformation amplitude. In contrast, E' for the filled rubber shows a significant dependency on the dynamic deformation (Payne, 1965; Heinrich and Klüppel, 2002), i.e. E' considerably decreases with increasing strain amplitude. This non-linear behavior of filled rubbers is known as the 'Payne effect' (Payne, 1965) and has been explained by the existence of a filler network in the rubber matrix above the percolation threshold. With increasing strain amplitude, the filler network breaks down, which results in the lower E' values. In a SBR/BR-blend with various



7.9 Strain dependency of the elastic modulus E' for CNT filled S-SBR/BR blends (SBR/BR 50:50).

concentrations of CNT (dispersed with ethanol), no Payne effect is observed at small CNT loading (up to 2 phr) as seen in Fig. 7.9 (Das *et al.*, 2008). With the increase of the CNT content, an increase of E' at low deformation amplitudes is observed. So, even with 3 phr of CNT, the tubes obviously form a continuous filler network in the rubber matrix. The filler-filler network can be reformed again after a certain time interval. Payne revealed that the value of E' is largely recoverable upon return to smaller amplitudes in the linear regime. So, flexible rubber chains allow the filler particles to rearrange again to form a three-dimensional filler network in the rubber matrix (Payne, 1965). In order to investigate the ability to recover, the strain-sweep experiments were also carried out in the reverse direction from higher to lower strain amplitudes for the samples with unmodified CNT dispersed with an ethanol suspension. It is observed that the E' values do not reach their original value within the relaxation time of the experiment, but a recovery of the E' values in the limit of low strain has been attained (Fig. 7.9). This behavior of a rubber can be explained by the stress-softening effect during the dynamic strain. So at least it can be said that rather than damage or permanently break the tubes, the amplitude sweep disrupted the filler-filler network in the rubber matrix.

7.3.3 Electrical transport processes

The data in Fig. 7.6 (b) showed that the permittivity of the samples above the percolation threshold $\phi > \phi_c$ is very high and a relaxation transition appears, which shifts to higher frequencies with increasing CNT loading. This behavior is also observed for carbon black-filled elastomers (Kluppel, 2003; Meier *et al.*, 2007) and can be explained qualitatively by a combined effect of nanoscopic gaps between the adjacent CNT and the predictions of the percolation models, e.g. the

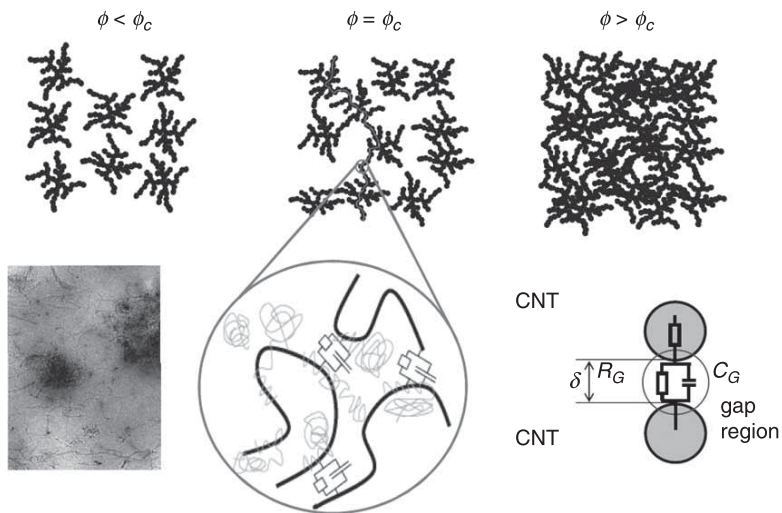
resistor-capacitor (RC) model (Kirkpatrick, 1973; Havlin and Bunde, 1991; Meier *et al.*, 2007). In such systems there is no perfect electrical contact between the carbon clusters, due to a layer of ‘bound rubber’ that fills the gap between contacting clusters (Kluppel, 2003; Meier *et al.*, 2007). Adopting an RC model of the percolation network, this small layer corresponds to a large contact resistance and a capacitance parallel to it (Fig. 7.10). This unit forms a micro capacitor with a capacity C_G and the bound rubber a resistor R_G . A detailed derivation can be found elsewhere (Sheng *et al.*, 1978; Sichel *et al.*, 1978; Kluppel, 2003; Meier *et al.*, 2007; Meier and Kluppel, 2008). In the case of nanometer-sized gaps between the conducting particles, free electrons can tunnel from one particle to another.

In this frame, the relaxation process can be referred to the movement of electrons by tunneling over these gaps. The characteristic frequency of the relaxation transition observed at high frequencies (~ 1 MHz) can be related to the distance between adjacent filler particles (Meier *et al.*, 2007).

In detail, the resistivity can be calculated as a quantum mechanical tunneling current and does follows an exponential function of the gap distance δ :

$$R_G = \frac{16\pi^2\hbar}{3e^2} \frac{\delta}{k_0 A} \exp(k_0\delta) \text{ with } k_0 = \frac{2\sqrt{2m_e}}{\hbar} \sqrt{V} \quad [7.2]$$

where A is the cross-section of the gap, k_0 describes the potential barrier with the potential height V , the Planck constant \hbar and the electron mass m_e . The characteristic frequency of a tunneling process over such a CNT–CNT connection can then be described by Equation 7.3:



7.10 Schematic representation of a percolation network based on CNT, description of the CNT–CNT connection as an RC-unit.

$$\omega_G = \frac{1}{R_G C_G} = \frac{3e^2}{16\pi^2 \hbar \epsilon_0} \frac{k_0}{\epsilon} e^{-k_0 \delta} \quad [7.3]$$

Therefore, with the knowledge of the characteristic frequency ω_G and the assumption of a typical potential barrier of $V = 0.3 \text{ eV}$ and a dielectric constant of the polymer in the gap of $\epsilon = 3$ the gap distance can be calculated. We point out, that in (Sheng *et al.*, 1978) and (Sichel *et al.*, 1978), the value of $V = 0.2 \text{ eV}$ was assumed to be characteristic for carbon black polymer composites. The present somewhat larger choice of $V = 0.3 \text{ eV}$ is based on recent TEM investigations of the gap distance in carbon black-SBR composites (Fritzsche and Klüppel, 2008). It delivers slightly smaller values for δ .

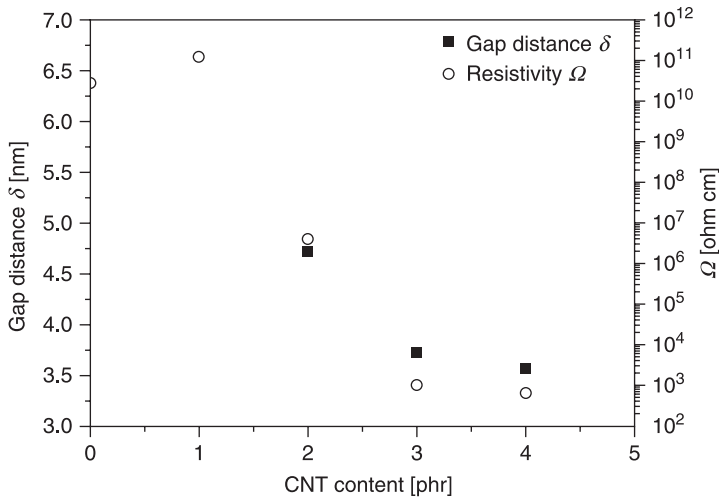
The characteristic frequency ω_G has been determined by a quantitative evaluation of the dielectric spectra by fitting Cole-Cole functions (Equation 7.4) simultaneously on the quantities ϵ' and ϵ'' :

$$\epsilon_{CC}^*(\omega) = \epsilon_\infty + \sum_j \frac{\Delta\epsilon_j}{1 + (i\omega\tau_j)^{\alpha_j}} + \frac{\sigma_{dc}}{i\epsilon_0\omega} \quad [7.4]$$

As fit parameters beside the relaxation frequency ω_G , the DC conductivity σ_{dc} , the relaxation strength $\Delta\epsilon = \epsilon_s - \epsilon_\infty$ as well as the broadening parameter α are obtained. For the fitting procedure, one fit function was sufficient, additionally, the term for the DC conductivity has been added. It was clearly shown that the relaxation time $\tau = 1/\omega$ decreased with the rising CNT concentration, which is in correlation to the shift of the relaxation process to higher frequencies.

The resulting gap distances δ calculated in Equation 7.3 are plotted against the filler volume fraction in Fig. 7.11. Additionally, the dependence of the DC resistivity plateau measured at 0.1 Hz on the filler content is included. An important result in this context is that the gap distance δ is exponentially decreasing with increasing CNT concentration and does reach a plateau value. This behavior is identical to carbon black composites (Kohjiya *et al.*, 2006; Fritzsche and Klüppel, 2008). Additionally, it can be stated that the decreasing gap distance is connected to a decreasing resistivity.

The amount of polymer bound to the filler particles is dependent not only on the specific surface area, but also on the surface activity. Due to the low activity of graphitic carbon, it is not clear if such a rubber layer also exists in CNT-polymer networks, but it is indicated by the dielectric data. However, it is clear that the charge transport through the tube network is strongly hindered by hopping or tunneling of charge carriers over small gaps, indicating that adjacent tubes do not touch but are separated by thin polymer layers. This is also confirmed by the obtained maximum conductivity values of 10^{-1} S/m for the percolated systems which lie several orders of magnitude below that found for bundles or single CNT. The percolation threshold indicated by the steep increase of the conductivity lies around 1 vol.% CNT. This indicates that the dispersion of the CNT is quite good though it may be further improved.



7.11 Percolation behavior of the plateau value of the AC resistivity for SBR/BR (70:30) and gap distances between nanotubes calculated by the RC model of the CNT network based on permittivity data.

7.3.4 Thermal transport processes

The thermal diffusivity of the CNT composites was evaluated by measuring the temperature development in SBR/BR samples (S-SBR 2525–0/CB24 70:30) filled with 3 phr CNT (Nanocyl 7000). Therefore two plates of one sample were placed in a heating press with a temperature of $T_u = 100^\circ\text{C}$. A temperature sensor was placed in between the two sample plates and the temperature increase $T(t)$ is measured in dependence on time t compared to the start temperature T_0 . To calculate the thermal diffusivity a , the resulting values can be described by Equation 7.5 with $\delta = 10$ cm the thickness of the sample plates:

$$T(t) = T_u - \frac{4}{\pi}(T_u - T_0)e^{-\left(\frac{2\pi}{\delta}\right)^2 at} \quad [7.5]$$

To evaluate, the measured values were plotted as $\ln\{(T(t) - T_u)/(T_0 - T_u)\}$ against time t . The slope in that plot is then directly connected to the thermal diffusivity a by using only that part of the temperature curve showing a linear dependence.

The regression statistical error of the calculated values was about 1%. For the unfilled rubber, one obtains a thermal diffusivity of $a = 0.83 \times 10^{-7} \text{ m}^2/\text{s}$, which increased to $1 \times 10^{-7} \text{ m}^2/\text{s}$ with 3 phr CNT mixed 1:10 with ethanol. A similar value of $a = 1.01 \times 10^{-7} \text{ m}^2/\text{s}$ is obtained with 3 phr CNT mixed 1:10 with 2-propanol. This results in a thermal conductivity of $\lambda = 0.19 \text{ W(m K)}^{-1}$ for the unfilled polymer and $\lambda = 0.21 \text{ W(m K)}^{-1}$ for the composite with 3 phr CNT, respectively. This means that λ increases by only 20%, while the electrical conductivity increased by about 10 orders of magnitude.

Since the charge transport through the tube network is controlled by hopping or tunneling over gaps, it is clear that the DC conductivity of the composite would be dominated by the gap, rather than the much higher conductivity of the CNT. This also affects the thermal conductivity induced by electron transport. In addition, the transport of heat in isolated CNTs is dominated by phonons showing a characteristic quadratic dependence on temperature in the range between 50 and 300 K. The thermal conductivity exhibits a maximum at about 320 K of more than 3000 W(m K)^{-1} , and for higher temperatures the thermal conductivity decreases due to phonon back-scattering effects. For CNT dispersed in a polymer matrix, further scattering effects, e.g. interfacial boundary and defect scattering, will appear, leading to a drastic reduction of thermal transport properties (Gojny *et al.*, 2006). In addition, the thermal transport through the CNT network by phonons will be strongly hindered by the gaps between adjacent tubes. From these arguments we conclude that the thermal conductivity of the CNT/rubber composites should lie several orders of magnitude below that of the isolated CNT (up to 3000 W(m K)^{-1} (Berber *et al.*, 2000; Kim *et al.*, 2001). Accordingly, the thermal conductivity of the CNT network in rubber composites should be not much larger or even smaller than that of the pure polymer (about 0.1 W(m K)^{-1}).

7.4 Systems with ionic liquids for increased coupling activity

Ionic liquids with imidazolium ions can be transformed into a ‘gel’ in the presence of a small amount of SWCNT (Fukushima *et al.*, 2003) due to the strong physical interaction of the π electrons of the nanotubes with the imidazolium ions. By assuming that some ionic liquids may behave like a coupling agent between rubber polymer and CNT, a series of ionic liquids were considered in order to find good rubber/nanotubes compatibility. Further details can be found in (Das *et al.*, 2009). The ionic liquids used are summarized in Table 7.2. As a basis polymer an SBR/BR blend (S-SBR 2525–0/CB 24 50:50) was used with a constant CNT concentration of 3 phr CNT. The composites were prepared by mixing the CNT with ethanol in a weight ratio of 1:10 and adding 3 m mol ionic liquid to this mixture as well in a weight ratio of 1:10 CNT to ionic liquid. This pre-batch was then remixed with the polymer in an internal mixer.

As previously described, the addition of 3 phr CNT without any ionic liquid increases the elongation at break value to a certain extent. However, the presence of ionic liquid enhances this property even further (Table 7.3). Here the ionic liquid AMIC (1-Allyl-3-methyl imidazolium chloride) along with 3 phr CNT shows an elongation at break value of 457% which is nearly three times higher than the value of the unfilled sample. For these particular composites, the tensile strength as well as the 100% modulus has the highest values among all other 3 phr filled composites. From these physical data, it is clear that AMIC with a double bond in the tail shows the best reinforcing activity. It is believed that the double bond is chemically

Table 7.2 Chemical structures of the ionic liquids

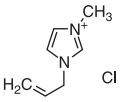
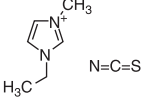
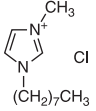
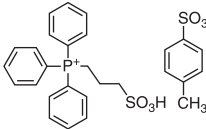
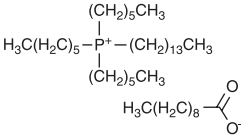
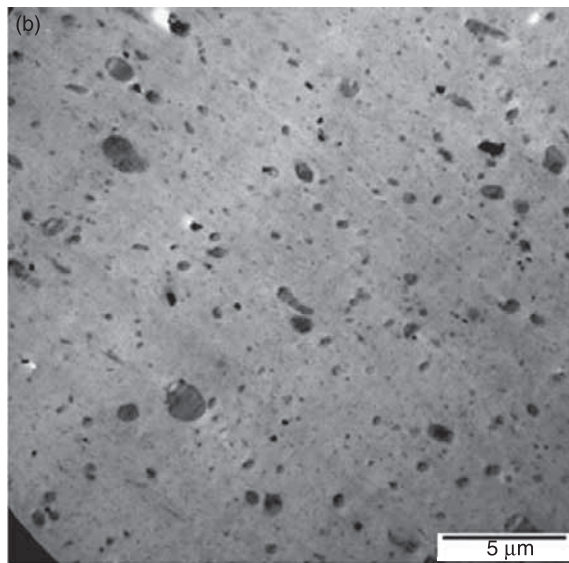
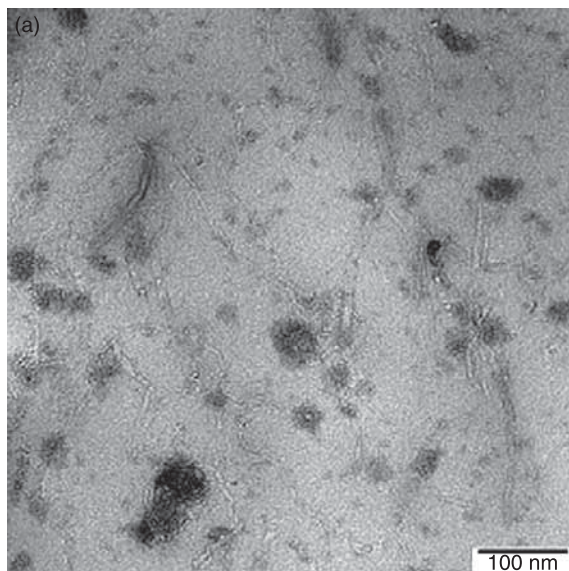
Chemical name	Given name	Structure
1-Allyl-3-methyl imidazolium chloride	AMIC	
1-Ethyl-3-methyl imidazolium thiocyanate	EMIT	
1-Methyl-3-octylimidazolium chloride	MOIC	
3-(Triphenylphosphonic)-1-sulfonic acid tosylate	TPST	
Trihexyl tetradecyl phosphonium decanoate	TTDPD	

Table 7.3 Mechanical and electrical properties of SBR/BR (50:50) filled with different concentrations of CNT with and without additional use of the ionic liquid AMIC

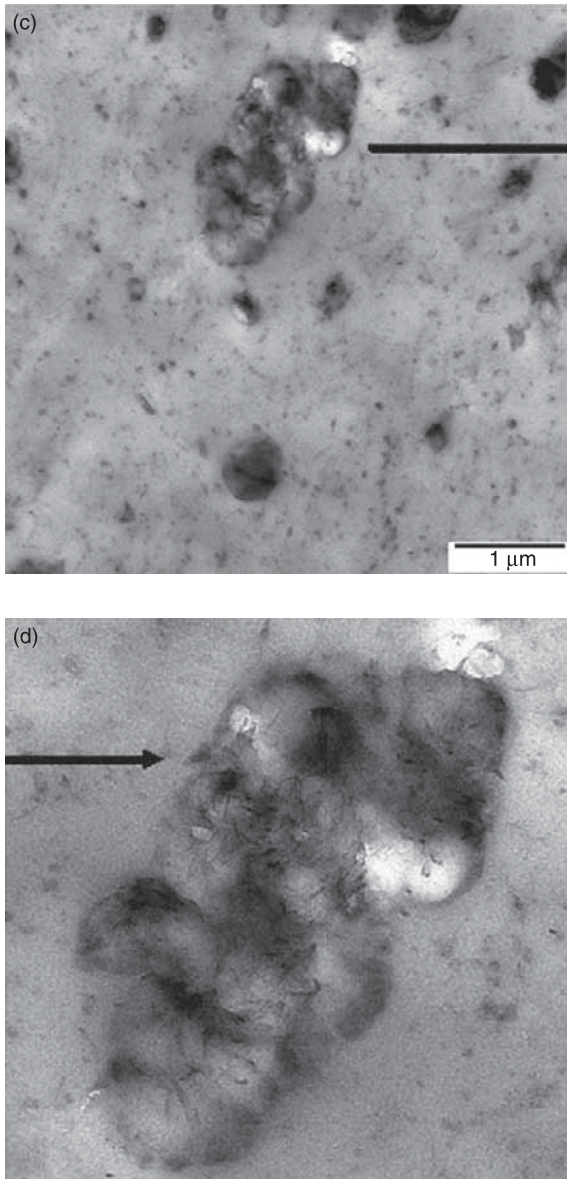
Sample	Modulus (100%) [MPa]	Tensile strength [MPa]	Elongation at break [%]	Conductivity [S/cm]
Unfilled	0.95	1.22	151	4.1×10^{-13}
1 phr CNT	1.16	1.57	179	1.1×10^{-12}
3 phr CNT	1.71	2.67	211	4.5×10^{-6}
5 phr CNT	2.47	4.07	238	3.3×10^{-5}
1 phr CNT/AMIC	1.28	1.97	233	1.8×10^{-13}
3 phr CNT/AMIC	2.18	4.12	457	7.7×10^{-4}
5 phr CNT/AMIC	2.71	4.05	410	9.5×10^{-3}

linked to the double bond of the diene rubber molecules by sulphur bridges and simultaneously has strong interactions with the π electron cloud of the CNT due to delocalization of the π electrons in the imidazolium carbocation.

In order to check the dispersion and the CNT network in the rubber matrix, TEM studies were done with the AMIC containing CNT composites shown in Fig. 7.12. In the evaluated pictures, no agglomeration of the CNT has been



7.12 TEM images of a SBR/BR (50:50) matrix loaded with 3 phr CNTs in the presence of 1-allyl-3-methylimidazolium chloride: (a) exhibiting the evenly distributed CNTs with an interconnecting network; (b) overall dispersion of the CNTs; (c) clusters of 'cellular structure' formed by CNTs; (d) a magnified image of the cellulation structure.



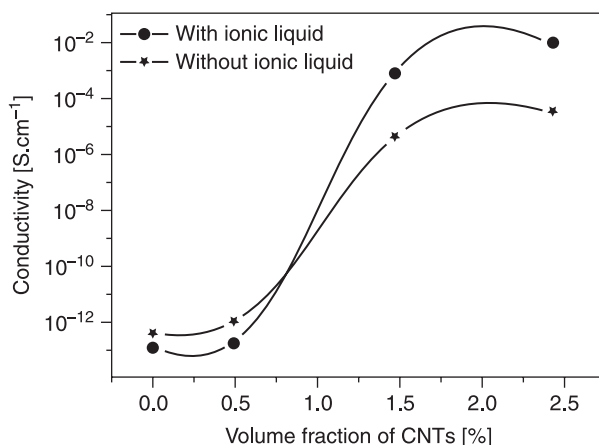
7.12 Continued.

observed and a continuous percolating network within 3 phr of CNT loading is assumed. However, at less magnification, some spheres with dark color were observed (Fig. 7.12 (b)). One of the dark phases was further focused upon and it was found that CNTs were forming a cluster of a spherical phase

along with the wrapping network of CNTs on the surface of the spherical phase (Fig. 7.12 (c)). These three-dimensional interconnected globular-like structures are defined as ‘cellular structures’ of the composites comprised of CNTs (Endo *et al.*, 2008). At 11 wt% loading, the formation of cellular structures was also reported in fluoro-rubber filled with CNTs. In the present case, at relatively low loading (3 wt% of CNT), cellular structures are formed, promoted by AMIC ionic liquid.

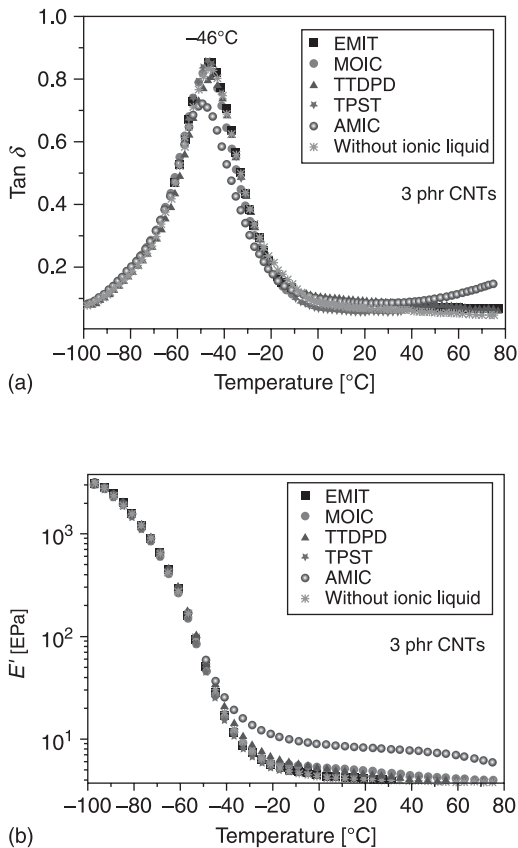
Since the use of AMIC as ionic liquid gave rise to the highest mechanical performance compared to other composites at same CNT loading, it is also interesting to determine the electrical properties of the composite containing AMIC. Figure 7.13 shows the dependence of the electrical conductivity on the volume fraction of CNT. Again, at least 10^2 times higher conductivities have been found with AMIC compared to other composites at 3 phr CNT. It was clear from the conductivity data of the unfilled rubber compounds with only 3 mmol phr ionic liquids that the significant increase of the conductivity is not related to the ionic liquid itself. Therefore, all effects can be traced back to the CNT percolation network.

Dynamic mechanical properties of the pure S-SBR/BR blend and its composites with 3 phr CNT and different ionic liquids were studied at 1 Hz and 0.5% strain amplitude over a wide temperature range (-80 to $+80^\circ\text{C}$) and in some cases from -80 to $+140^\circ\text{C}$. The dependency of the $\tan \delta$ on the temperature is illustrated in Fig. 7.14 (a). Here the addition of AMIC in the composite filled with 3 phr CNT clearly reduces the peak height. In the storage modulus (Fig. 7.14 (b)), it can be



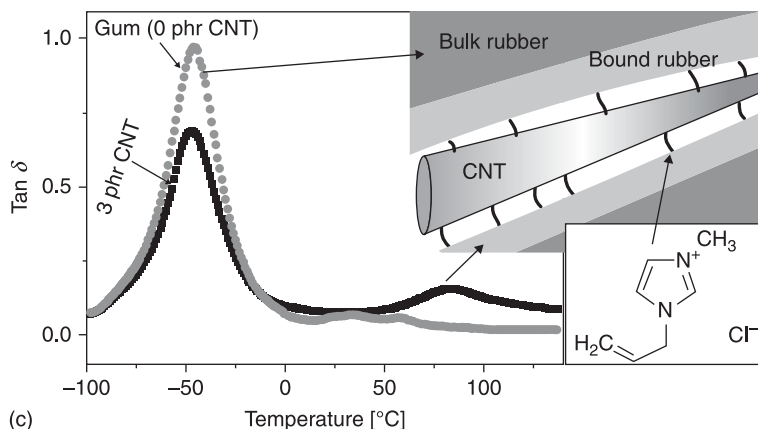
7.13 Dependence of the conductivity on the volume fraction of CNT in the presence and absence of 1-allyl-3-methylimidazolium chloride ionic chloride. The lines are a guide only.

seen that the storage modulus sensibly increases in the presence of AMIC which is attributed to the higher reinforcement effect. A distinguishable increment of the modulus at the same filler loading directly indicates a strong rubber–filler interaction. Additionally, from Figs 7.14 (a) and 7.14 (c), it can be seen that an extra relaxation process is taking place at high temperatures for AMIC containing composites with a peak position around 80°C. This observation indicates the presence of a relatively rigid rubber polymer in the whole rubber matrix. A schematic presentation of the dynamic mechanical behavior is illustrated in Fig. 7.14 (c).



7.14 Dynamic-mechanical properties of S-SBR/BR with 3 phr CNT in the presence of different ionic liquids: (a) dependence of $\tan \delta$ over temperature; (b) storage modulus over temperature; (c) dependence of $\tan \delta$ over temperature with and without 1-allyl-3-methylimidazolium chloride and schematic representation of the chemical interaction between polymer and carbon nanotubes.

(Continued)



7.14 Continued.

7.5 Hybrid systems based on silica filler

Conventional fillers like silica are widely used in the rubber industry especially for high performance rubber goods like tires (Wypych, 1999). The use of silica results in improved resistance to wear and tear, decreasing heat build-up (Berriott *et al.*, 2003), increased stiffness, modulus, rupture energy, tear strength, tensile strength, cracking resistance, fatigue resistance and abrasion resistance (Dannenberg, 1975). However, the dispersion of silica nano-particles in the polymer matrix is also problematic in the case of strong polar bonds between the filler particles, especially for non-polar rubbers. In particular, the application of precipitated silica in high performance tires could become a successful technology only after the dispersion problem was solved by coating the silica with a bifunctional silane in a complicated multi-step mixing procedure. However, in contrast to carbon black-filled samples, silica-filled materials always result in non-conducting samples. Here in several applications the tailor-made silica-based properties in combination with sufficient electrical conductivity, would be advantageous, for example, in antistatic materials.

Usually the low electrical conductivity of polymers is improved by the incorporation of conductive fillers like carbon black. For sufficient high conductivity depending on the structure and the size of the primary aggregates and the specific interaction with the used polymer, percolation thresholds in the range of 8 to 20 vol.% of carbon black are found (O'Farrell *et al.*, 2000). However, with such high amounts of carbon black necessary for a high electrical conductivity, the typical silica properties, such as low rolling resistance and high wet traction, are lost and therefore other techniques to obtain a sufficient conductivity are necessary. Due to the low percolation threshold of CNT, which can potentially be reduced to 0.1 vol.% in the case of optimal dispersion, the addition of a small

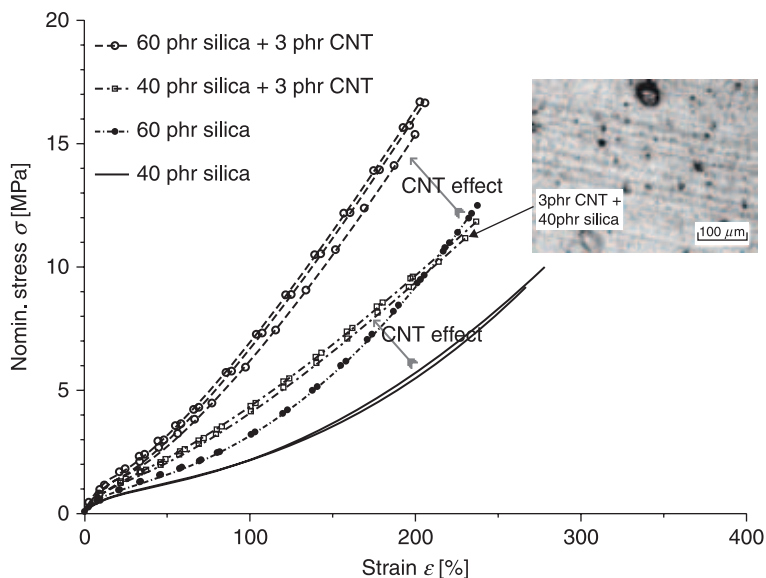
amount of CNT is one possibility to make silica-filled materials conductive. Additionally, the use of silica is expected to improve the dispersion of the CNT due to the higher shear forces experienced during the mixing process.

7.5.1 Styrene/butadiene (SBR/BR) with silica and addition of CNT

Figure 7.15 shows the quasi-static stress–strain behavior of SBR/BR composites (S-SBR 2525/CB 24 70:30) filled with CNT and silica (Ultrasil 7000 GR, from Evonik Industries). With 3 phr CNT and ethanol as the dispersion agent, the mechanical stress increases by a factor of about 3 related to the unfilled SBR/BR. A similar reinforcing effect can also be observed when 3 phr CNT are added to silica-filled systems. This is indicated in Fig. 7.15 by the two arrows, demonstrating a further increase of the stress for both systems with 40 phr and 60 phr silica. Obviously, CNTs cause an increase in tensile strength of the rubber when added to silica-filled SBR/BR. The ultimate properties of the samples are summarized in Table 7.4. The last column of Table 7.4 shows that the conductivity plateau $\sigma_{dc} = 0.10$ S/m of the system with CNT is quite high compared to $\sigma_{dc} = 10^{-11}$ S/m for unfilled SBR/BR. Adding 40 phr silica, σ_{dc} increases further to 0.15 S/m. It appears that silica helps to disperse the CNT and, accordingly, lowers the percolation threshold. This can be related to the higher shear forces in the highly filled rubber, causing the breakage of CNT agglomerates. In all cases, only some small agglomerates could be seen in the light microscopic image (inset of Fig. 7.15) confirming that the dispersion is good. Accordingly, the mechanical and electrical properties of the SBR/BR composites filled with CNT and silica appear promising.

7.5.2 Natural rubber with silica partially exchanges against CNT

Compounds with high silica content (up to 90 phr) are technologically widely used in passenger car tire treads, particularly in SBR/BR/NR blends. Therefore the incorporation of small amounts of CNT in such systems is of high technological interest. Since the dispersion and distribution of CNT by dry melt mixing have proved to be most successful in NR (Lorenz *et al.*, 2009), the first investigation was made with this material combination. This method offers the possibility of using such highly filled NR systems as the masterbatch as well as adapting this concept to other polymer types. It might also serve as a guideline for the development of highly conductive silica-filled truck tire treads with reduced rolling resistance, which meets the growing requirements of improved energy efficiency by reducing the high fuel consumption of trucks. Therefore composites based on NR (SVR-CV 50) with 90 phr silica (Ultrasil 7000 GR, from Evonik) were prepared. To allow adequate processing, 30 phr paraffinic processing oil (Sunpar 2280) was added to all samples. To distinguish between properties based



7.15 Stress–strain behavior of SBR/BR(70:30) composites with 3 phr CNT mixed with ethanol (10:1) and varied silica content; inset: light-microscopy image characterizing the filler dispersion.

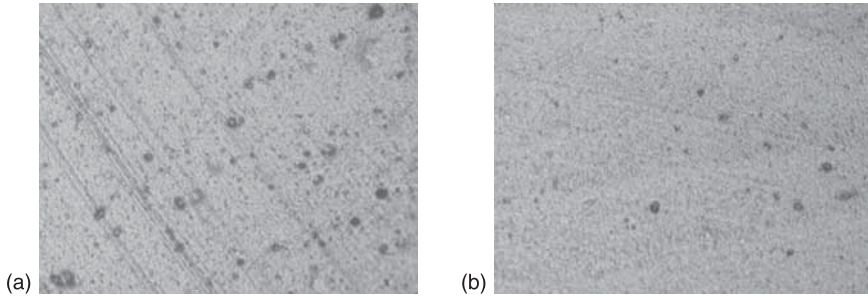
Table 7.4 Influence of CNT on mechanical and electrical properties in silica-filled SBR/BR (70:30) blends

Sample	Modulus (100%) [MPa]	Tensile strength [MPa]	Elongation at break [%]	Conductivity [S/m]
Unfilled	1.0	1.15	129	10–11
3 phr CNT	2.8	4.1	186	1.0×10^{-1}
40 phr silica	2.2	8.6	255	–
3 phr CNT/40 phr silica	4.2	10.8	221	1.53×10^{-1}
60 phr silica	3.1	12	232	–
3 phr CNT/60 phr silica	6.4	16.2	203	1.1×10^{-2}

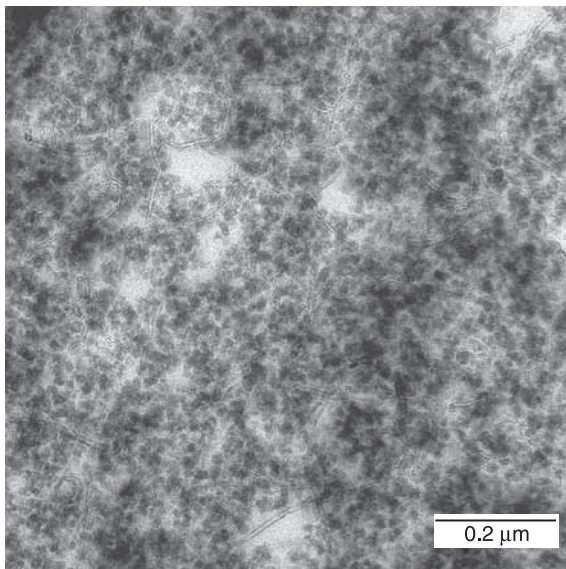
on silica and based on CNT, up to 10 phr of silica was successively replaced by the same amount of carbon nanotubes (Nanocyl 7000). Further details can be found in (Fritzsche *et al.*, 2009).

The dispersion of both types of filler determined by light microscopy is displayed in Fig. 7.16 (a) and 7.16 (b) for the only silica-filled sample and the sample filled with additionally 6 phr of CNT. In both cases, the dispersion is very

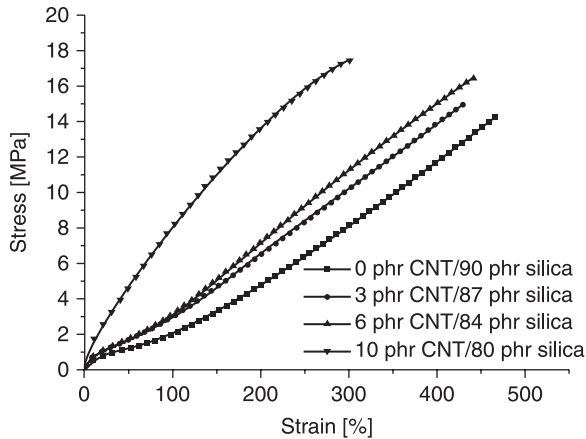
good with 92–98% indicating that only 2–8% of the filler is not macroscopically dispersed. In TEM measurements (Fig. 7.17), in a huge number of spherical silica particles, small and long nanotubes are visible in the background. These nanotubes are well dispersed in the rubber matrix and almost no agglomeration takes place. The aspect ratio for the tubes lies around 100, based on an average length of 1 μm and an average diameter of 10 nm. The orientation of the CNTs can be ignored.



7.16 Dispersion characteristics of natural rubber samples filled with: (a) 90 phr of silica; (b) 84 phr of silica and 6 phr of CNT illustrated by light-microscopic images.



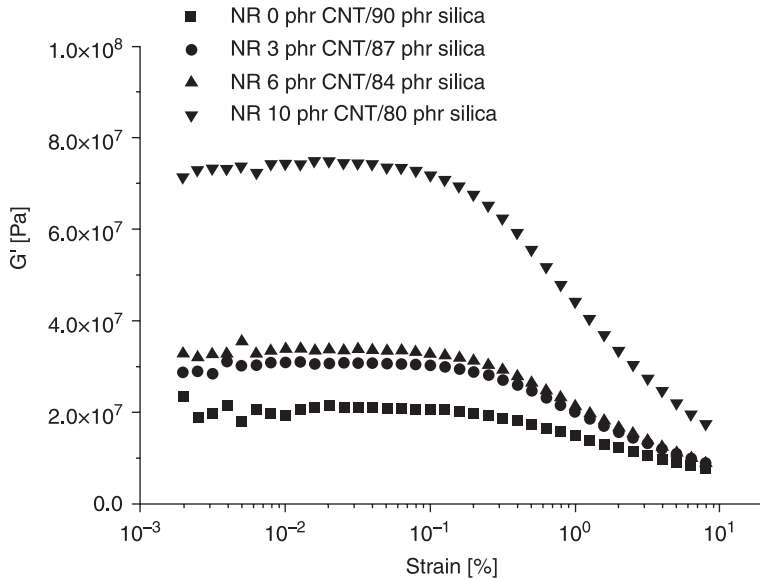
7.17 Dispersion characteristics of the sample filled with 84 phr of silica and 6 phr of CNT illustrated by TEM image.



7.18 Quasi-static stress–strain behavior of the investigated NR samples with varying concentrations of silica and CNT.

The mechanical properties are shown in Fig. 7.18. With increasing exchange of silica against CNT, a significant increase in the tensile strength from 14 to 17 MPa is observable. The elongation at break seems to be nearly constant up to an amount of 6 phr CNT. With an exchange of 10 phr CNT against 10 phr of silica, a complete change of the stress–strain behavior sets in, resulting in a significant increase of the stress at low strains (σ_{100}) from 3 MPa to 8 MPa at 100% elongation and a considerable drop of the elongation at break from over 400 to 300%. The characteristic shape of the stress–strain curve changes significantly to a more linear behavior. In the literature, the influence of nanoparticles on the strain-induced crystallization of natural rubber is discussed. For example, this has been investigated by Carretero-González *et al.* (Carretero-González *et al.*, 2008) concerning NR/nanoclay-composites. Here depending on the aspect ratio and the orientation of the single platelets, crystallization at smaller strains that does not appear for the unfilled samples has been observed. Similar effects could occur with CNT as the reinforcing filler, if during the stress–strain measurements an orientation of the tubes takes place. Such behavior could explain the increase of the stress, especially at low strain, compared to the silica-filled system, since with most filler systems, like silica or carbon black, the strain-induced crystallization is rather reduced.

The dynamic property measurements depending on the strain amplitude can deliver information about the filler–filler network as well as the rubber–filler interaction. In the present investigations at room temperature and at a frequency of 1 Hz, the plots of G' versus double strain amplitude are shown in Fig. 7.19. It can clearly be seen that up to 0.1% strain amplitude, the values of G' remain constant in all cases and thereafter a significant drop of the values is observed. The G' value at low strains does significantly increase with the increase of CNT

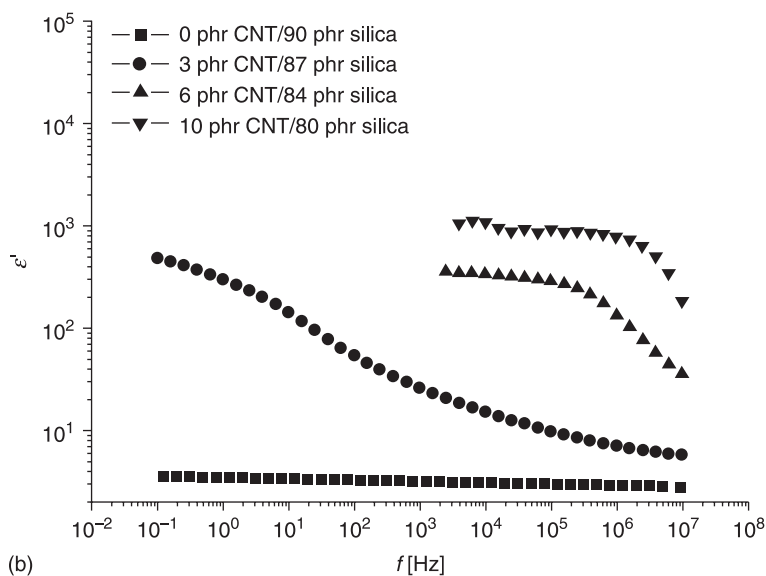
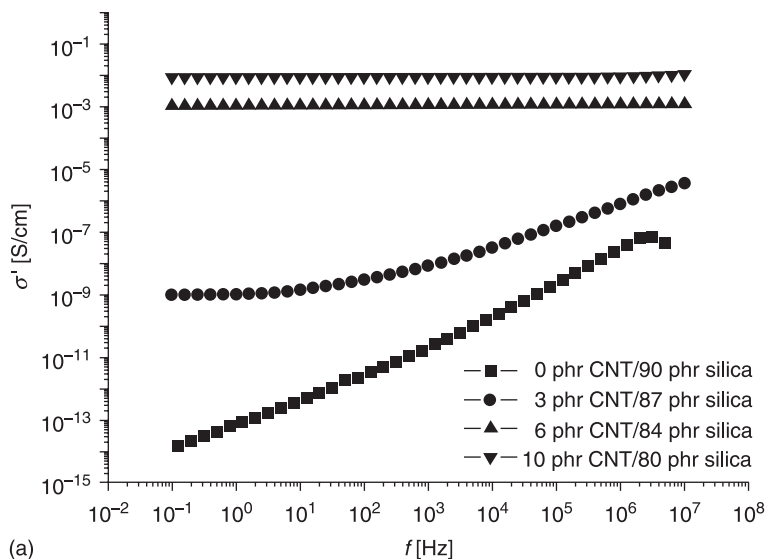


7.19 Strain-dependent storage modulus of the NR samples in varying concentrations of silica and CNT showing the characteristic non-linear behavior of filled rubbers (Payne effect).

loading. Especially with the sample with 10 phr of CNT, a significant increase of G' is observed. This behavior is attributed to hydrodynamic effects and an increase of the formation of bound or trapped rubber with the rising amount of CNT.

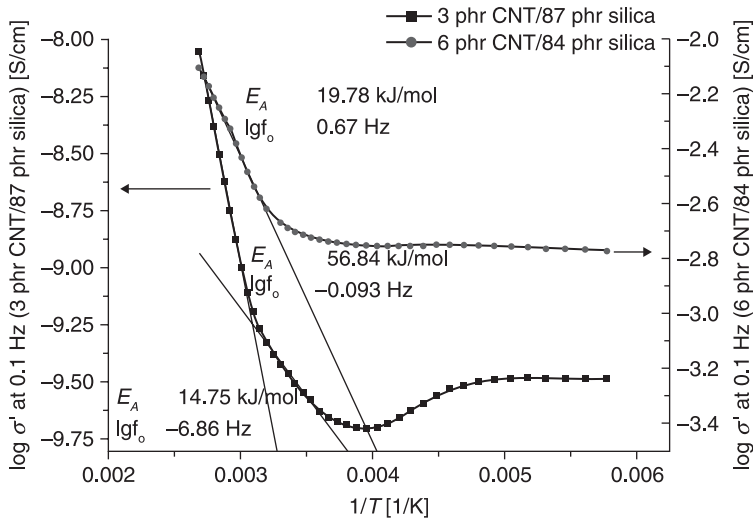
In the dielectric properties (Fig. 7.20), it is found that the plateau conductivity measured by dielectric spectroscopy in the limit of 0.1 Hz significantly increases with the amount of CNTs. With an amount of 6 phr of CNT, the percolation threshold is already passed. This indicates that for a non-conducting material with a high amount of silica, less than 6 phr CNT are necessary to obtain a conducting network. With 10 phr CNT, the conductivity even slightly increases, resulting in a maximum conductivity of about 10^{-2} S/cm. The relaxation process described in section 7.3.3 appears at relatively low frequencies for the sample containing 3 phr of CNT. With increasing amounts of CNTs, this relaxation process increases in strength and moves to higher frequencies as seen below. This behavior can be related to the decrease in the gap distance between adjacent tubes with rising CNT content.

Additionally, measurements depending on the temperature between -100°C and $+100^{\circ}\text{C}$ were performed. In Fig. 7.21 the temperature-dependent behavior at 0.1 Hz was investigated in detail. Here the conductivity is plotted against the reciprocal temperature for the sample with 3 phr and the sample with 6 phr of CNT. At low frequencies at around -60°C ($1/T = 0.0047\text{ K}^{-1}$), a relaxation process is visible for both samples. It is related to the thermal expansion of the polymer with increasing temperature. Since the glass transition temperature lies in that temperature region, a



7.20 Dielectric properties of NR samples filled with silica and CNT: (a) conductivity; (b) permittivity.

connection between the glass transition and the thermal expansion of the polymer is plausible. The thermal expansion of the polymer results in increasing gaps between adjacent filler particles and therefore in a slight decrease of the conductivity. Usually these effects are more pronounced in systems with unstable polymer networks



7.21 Arrhenius plot of the temperature-dependent conductivity at 0.1 Hz for the samples filled with 87 phr silica/3 phr CNT and 84 phr silica/6 phr CNT and evaluation of the hopping activation energy.

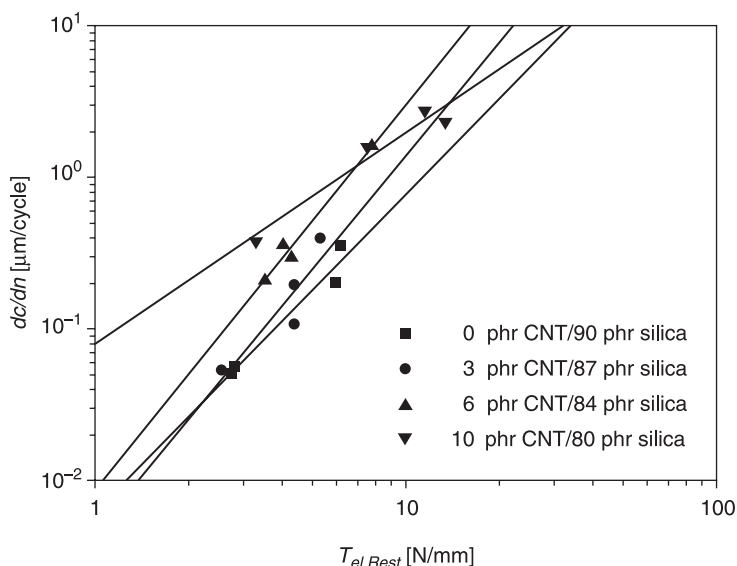
directly above the percolation point. In both samples at low temperatures, beside the mentioned relaxation process, the conductivity is more or less independent of temperature. At higher temperatures, a temperature-dependent behavior sets in, resulting in a pronounced increase of the conductivity with temperature. For the sample with 6 phr CNT, the transition starts around 60°C. This transition indicates a change in the conductivity mechanism from tunneling to a thermally activated hopping mechanism. In the higher filled sample, the transition to the hopping mechanism starts very sharply; this means for all transport processes the hopping mechanism is allowed at nearly the same temperature. Hence, the network is more homogeneous; the distance between the filler particles is similar in the whole sample. The activation energy can be estimated by describing the increase of the conductivity by a simple Arrhenius equation. The slope is then related to the activation energy of the hopping mechanism resulting in $E_A \approx 20$ kJ/mol for the higher filled sample. In the lower filled sample, the transition is in two steps. Therefore, different temperatures are necessary for the hopping transition, the network is more heterogeneous. The first hopping transport processes start at room temperature. Since the gaps between the clusters are small, the activation energy is quite low with $E_A \approx 15$ kJ/mol. At higher temperatures, the hopping processes for the clusters with larger gaps set in where higher activation energies of around $E_A \approx 57$ kJ/mol are necessary. The results are in agreement compared to those found for carbon black-filled samples. Hence the interpretation based on the percolation theory can also be applied to describe the qualitative properties of the conduction mechanism in CNT–polymer composites.

7.5.3 Fracture mechanical investigation of silica-based hybrid-CNT composites

The fracture mechanical properties of the CNT composites were investigated by analyzing the dynamic crack propagation rates under cyclical loading by a tear fatigue analyzer (TFA, from Coesfeld) at a frequency of 10 Hz. The determination of the tearing energy, T_{el} , is based on the following semi-empirical equation (Gent, 2001):

$$T_{el} = \frac{2\pi}{\sqrt{\lambda}} W_{el}(\lambda) c \quad [7.6]$$

Here, c is the crack length, λ is the strain ratio and W_{el} is the elastically stored energy density far away from the crack tip. The latter has been estimated approximately by numerical integration of the stress cycles measured on-line for every 1000th cycle during the test at the notched samples. Thereby the remaining cross-section of the sample after subtraction of the crack area was taken as the reference cross-section. Data points were only evaluated in the range where the crack length is small compared to the sample width. Figure 7.22 shows a double logarithmic plot of the fatigue crack propagation rate dc/dn against the tearing energy T_{el} at high severity under pulsed loading with n being the number of cycles. This type of power law behavior is known as Paris plot with α and β being polymer-specific constants.



7.22 Crack growth rate vs. tearing energy for NR-silica composites, with and without CNT.

$$\frac{dc}{dn} = \alpha T_{el}^{\beta} \quad [7.7]$$

This equation has been fitted to the experimental data which is shown as solid lines in Fig. 7.22. The tear fatigue measurements demonstrate that below $T_{el} = 3$ N/mm the crack growth rate of the NR-silica composites with 3 phr CNT is smaller compared to the composite without CNT. This indicates that, at small strains, the fatigue performance of the CNT samples is even better than for the silica-filled sample without CNT. Nevertheless, the power exponent β , corresponding to the steepness of the log–log plot, shows a slight increase for the systems with CNT, implying a cross-over of crack propagation rates at lower tearing energies. This behavior correlates with the already observed decrease in elongation at break (high tearing energy) by the addition of CNTs.

7.6 Conclusion

Huge progress in carbon nanotube applications based on elastomer composites can only be realized when a proper dispersion of the entangled agglomerates of as-prepared CNT products is achieved, without damaging their unique properties. Advancements in the use of carbon nanotubes as reinforcing filler in elastomers have been achieved by applying melt mixing techniques for the incorporation of the CNT in elastomers. The use of predispersing solvents like ethanol results in a good dispersion of the CNT as evinced by light microscopy (Fig. 7.2) and transmission electron microscopy (Fig. 7.3). It was observed that the mechanical properties of CNT-filled S-SBR/BR blends are improved considerably compared to the unfilled rubber.

High electrical conductivities of about 10^{-3} S/cm with the quite low amount of 2–3 phr of CNT are achieved, indicating a percolation threshold of 1 vol.% of CNT (Fig. 7.6). The conduction mechanism was proved to take place over nanoscopic gaps between adjacent tubes; hereby, the gap size decreased with increasing CNT concentration which is analogous to carbon black composites. An increase in thermal conductivity by 20% can be achieved in an SBR–BR blend by incorporation of 1.6 vol.% CNT with ethanol as dispersion agent. This relatively small effect has been explained by the presence of these gaps and the inability of phonons to overcome these distances.

In hybrid filler systems, based on conventional fillers, the best dispersion can be achieved related to the high shearing forces applied during the mixing process (Fig. 7.16). The resulting samples show an increased mechanical stiffness and tensile strength as well as a high electrical conductivity. Dynamic-mechanical measurements show a significant increase of the storage modulus at low strains with rising CNT content and a pronounced Payne effect (Fig. 7.19). The fracture mechanical measurements show lower crack propagation rates under cyclic loading at low severity conditions (Fig. 7.22). This study has shown that there is a high potential of

using CNT in technical rubber goods like tire treads, where a sufficient high electrical conductivity is necessary but the ideal properties of the silica-filled compounds, like low rolling resistance and high wet traction, should be retained.

7.7 References

- Ajayan P M, Schadler L S, Giannaris C and Rubio A (2000) 'Single-walled carbon nanotube-polymer composites: strength and weakness', *Adv. Mater.*, 12, 750–753.
- Battacharyya A R, Sreekumar T V, Liu T, Kumar S, Ericson L M, Hauge R H and Smalley R E (2003) 'Crystallization and orientation studies in polypropylene/single wall carbon nanotube composite', *Polymer*, 44, 2373–2377.
- Berber S, Kwon Y K and Tomanek D (2000) 'Unusually high thermal conductivity of carbon nanotubes', *Phys. Rev. Lett.*, 84(20), 4613–4616.
- Berriot J, Montes H, Lequeux F, Long D and Sotta P (2003) 'Gradient of glass transition temperature in filled elastomers', *Europhys. Lett.*, 64(1), 50–56.
- Bokobza L (2007) 'Multiwall carbon nanotube elastomeric composites: a review', *Polymer*, 48, 4907–4920.
- Bokobza L (2008) 'Multiwall carbon nanotube elastomeric composites', in *Conference Proceedings*, 8th Rubber Fall Colloquium, Hannover, Germany.
- Bokobza L and Belin C (2007) 'Effect of strain on the properties of a styrene-butadiene rubber filled with multiwall carbon nanotubes', *J. Appl. Polym. Sci.*, 105, 2054.
- Carretero-González J, Retsos H, Verdejo R, Toki S, Hsiao B S, Giannelis E P and Lopez-Manchado M A (2008) 'Effect of nanoclay on natural rubber microstructure', *Macromolecules*, 41(18), 6763–6772.
- Cho J W, Kim J W, Jung Y C and Goo N S (2005) 'Electroactive shape memory polyurethane composites incorporating carbon nanotubes', *Macrom. Rapid. Commun.*, 26, 412.
- Cooper C A, Young R J and Halsall M (2001) 'Investigation into the deformation of carbon nanotubes and their composites through the use of Raman spectroscopy', *Composites, Part A*, 32A, 401–411.
- Dannenberg, E M (1975) 'Rubber effects of surface chemical interactions on the properties of filler-reinforced rubbers', *Rubber Chem. Technol.*, 48, 410.
- Das A, Stöckelhuber K W, Jurk R, Fritzsche J, Klüppel M and Heinrich G (2009) 'Coupling activity of ionic liquids between diene elastomers and multi-walled carbon nanotubes', *Carbon*, 47, 3313–3321.
- Das A, Stöckelhuber K W, Jurk R, Saphiannikova M, Fritzsche J, Lorenz H, Klüppel M and Heinrich G (2008) 'Modified and unmodified multiwalled carbon nanotubes in high performance solution-styrene-butadiene and butadiene rubber blends', *Polymer*, 49, 5276–5283.
- De Heer W A (2004) 'Nanotubes and the pursuit of application', *MRS Bull.*, 29, 281–285.
- Du F, Fischer J E and Winey K I (2003) 'Coagulation method for preparing single-walled carbon nanotube/poly(methyl methacrylate) composites and their modulus, electrical conductivity, and thermal stability', *J. Polym. Sci., Part B, Polym. Phys.*, 41, 3333–3338.
- Endo M, Noguchi T, Ito M, Takeuchi K, Hayashi T and Kim Y A (2008) 'Extreme-performance rubber nanocomposites for probing and excavating deep oil resources using multi-walled carbon nanotubes', *Adv. Funct. Mater.*, 18, 3403–3409.
- Fakhru'l-Razi A, Atieh M A, Girun N, Chuah T G, El-Sadig M and Biak D R A (2006) 'Effect of multi-walled carbon nanotubes on the mechanical properties of natural rubber', *Compos. Struct.*, 75, 496.

- Fritzsche J and Klüppel M (2008) 'Filler networking and reinforcement of carbon black filled styrene-butadiene-rubber', *Conference Proceedings*, 8th Rubber Fall Colloquium, Hannover, Germany.
- Fritzsche J, Lorenz H and Klüppel M (2009) 'CNT based elastomer-hybrid-nanocomposites with promising mechanical and electrical properties', *Macromol. Mater. Eng.*, 294, 551–560.
- Frogley M D, Ravich D and Wagner H D (2003) 'Mechanical properties of carbon nanoparticle-reinforced elastomers', *Compos. Sci. Technol.*, 63, 1647.
- Fukushima T, Kosaka A, Ishimura Y, Yamamoto T, Takigawa T and Ishii N (2003) 'Molecular ordering of organic molten salts triggered by single-walled carbon nanotubes', *Science*, 300, 2072–2074.
- Gent A N (2001) *Engineering with Rubber*, 2nd edn, München: Hanser Publishers.
- Gojny F H, Wichmann M H G, Fiedler B, Kinloch I A, Bauhofer W, Windle A H and Schulte K (2006) 'Evaluation and identification of electrical and thermal conduction mechanisms in carbon nanotube/epoxy composites', *Polymer*, 47(6), 2036–2045.
- Gong X, Liu J, Baskaran S, Voise R D and Young J S (2000) 'Surfactant-assisted processing of carbon nanotube/polymer composites', *Chem. Mater.*, 12, 1049–1052.
- Guth E (1945) 'Theory of filler reinforcement', *Appl. Phys.*, 16, 20.
- Guth E and Gold O (1938) 'On the hydrodynamic theory of the viscosity of suspensions', *Phys. Rev.*, 53, 322.
- Haggenmueller R, Fischer J E and Winey K I (2006) 'Single wall carbon nanotubes/polyethylene nanocomposites: nucleating and templating polyethylene crystallites', *Macromolecules*, 39, 2964–2971.
- Havlin S and Bunde A (1991) 'Percolation II', in A Bunde and S Havlin (eds) *Fractals and Disordered Systems*, Berlin: Springer, pp. 137–143.
- Heinrich G and Klüppel M (2002) 'Recent advances in the theory of filler networking in elastomers', *Adv. Polym. Sci.*, 160, 1.
- Islam M F, Rojas E, Bergey D M, Johnson A T and Yodh A G (2003) 'High weight fraction surfactant solubilization of single-wall carbon nanotubes in water', *Nano. Lett.*, 3, 269–273.
- Jonscher A K (1977) 'The "universal" dielectric response', *Nature*, 267, 673.
- Jung Y C, Sahoo N G and Cho J W (2006) 'Polymeric nanocomposites of polyurethane block copolymers and functionalized multi-walled carbon nanotubes as crosslinkers', *Macrom. Rapid. Commun.*, 27, 126–131.
- Karger-Kocsis J, Felhoes D and Thomann R (2008) 'Tribological behavior of a carbon-nanofiber-modified santoprene thermoplastic elastomer under dry sliding and fretting conditions against steel', *J. Appl. Polym. Sci.*, 108(2), 724–730.
- Kim P, Shi L, Majumdar A and McEuen P L (2001) 'Thermal transport measurements of individual multiwalled nanotubes', *Phys. Rev. Lett.*, 87, 215502.
- Kim YA, Hayashi T, Endo M, Gotoh Y, Wada N and Seiyama (2006) 'Fabrication of aligned carbon nanotube-filled rubber composite', *J. Scr. Mater.*, 54, 31.
- Kirkpatrick S (1973) 'Percolation and conduction', *Rev. Mod. Phys.*, 45, 574–588.
- Klüppel M (2003) 'The role of disorder in filler reinforcement of elastomers on various length scales', *Adv. Polym. Sci.*, 164, 1–86.
- Knite M, Tupureina, Fuith A, Zavickis J and Teteris V (2007) 'Polyisoprene-multi-wall carbon nanotube composites for sensing strain', *Mater. Sci. Eng.*, 27, 1125–1128.
- Koerner H, Liu W, Alexander M, Mirau P, Dowty H and Vaia R A (2005) 'Deformation-morphology correlations in electrically conductive carbon nanotube-thermoplastic polyurethane nanocomposites', *Polymer*, 46, 4405.

- Kohjiya S., Katoh A., Suda T., Shimanuki J., and Ikeda Y. (2006) 'Visualization of carbon black networks in rubbery matrix by skeletonization of 3D TEM image', *Polymer*, 47, 3298–3301.
- Liu T, Phang L Y, Shen L, Chow S Y and Zhang W D (2004) 'Morphology and mechanical properties of multiwalled carbon nanotubes reinforced nylon-6 composites', *Macromolecules*, 37, 7214–7222.
- Lopez-Manchado M A, Biagiotti J, Valentini L and Kenny J M (2004) 'Dynamic mechanical and Raman spectroscopy studies on interaction between single-walled carbon nanotubes and natural rubber', *J. Appl. Polym. Sci.*, 92(5), 3394–3400.
- Lorenz H, Fritzsche J, Das A, Stöckelhuber K W, Jurk R, Heinrich G and Klüppel M (2009) 'Advanced elastomer nano-composites based on CNT-hybrid filler systems', *Comp. Sci. Technol.*, 69, 2135–2143.
- Meier J G and Klüppel M (2008) 'Carbon black networking in elastomers monitored by dynamic mechanical and dielectric spectroscopy', *Macromol. Mater. Eng.*, 293, 12.
- Meier J G, Mani J G and Klüppel M (2007) 'Analysis of carbon black networking in elastomers by dielectric spectroscopy', *Phys. Rev. B*, 75, 054202, 1–10.
- Moniruzzaman M, Du F, Romero N and Winey K I (2006) 'Increased flexural modulus and strength in SWNT/epoxy composites by a new fabrication method', *Polymer*, 47, 293–298.
- Moniruzzaman M and Winey K I (2006) 'Polymer nanocomposites containing carbon nanotubes', *Macromolecules*, 39(16), 5194–5205.
- O'Farrell C P, Gerspacher M and Nikiel L (2000) 'Carbon black dispersion by electrical measurements', *Kautschuk Gummi Kunstst.*, 53(12), 701–710.
- Payne A R. (1965) In Kraus G (ed.) *Reinforcement of Elastomers*, New York: Interscience Publisher, Chapter 3.
- Pötschke P, Battacharyya A R, Janke A and Goering H (2003) 'Melt mixing of polycarbonate/multi-wall carbon nanotube composites', *Compos. Interfaces*, 10, 389–404.
- Pötschke P, Häußler L, Pegel S, Steinberger R and Scholz G (2007) 'Thermoplastic polyurethane filled with carbon nanotubes for electrical dissipative and conductive applications', *Kautschuk Gummi Kunstst.*, 60, 432–437.
- Shaffer M and Sandler J (2006) 'Carbon nanotube/nanofibre polymer composites', in S. G. Advani (ed.) *Processing and Properties of Nanocomposites*, New York: World Scientific Publishing Company.
- Sheng P, Sichel E K and Gittleman J I (1978) 'Fluctuation-induced tunneling conduction in carbon-polyvinylchloride composites', *Phys. Rev. Lett.*, 40(18), 1197–1200.
- Sichel E K, Gittleman J I and Sheng P (1978) 'Transport properties of the composite material carbon-poly(vinyl chloride)', *Phys. Rev. B*, 18, 5712.
- Siochi E J, Working D C, Park C, Lillehei P T, Rouse J H, Topping C C, Battacharyya A R and Kumar S (2004) 'Melt processing of SWCNT-polyimide nanocomposite fibers', *Composites, Part B*, 35B, 439–446.
- Smallwood H M (1944) 'Limiting law of the reinforcement of rubber', *J. Appl. Phys.*, 15, 758.
- Sundararajan P R, Singh S and Moniruzzaman M (2004) 'Surfactant induced crystallization of polycarbonate', *Macromolecules*, 37, 10208–10211.
- Wang J D, Zhu Y F, Zhou X W, Sui G and Liang J (2006) 'Preparation and mechanical properties of natural rubber powder modified by carbon nanotubes', *J. Appl. Polym. Sci.*, 100, 4697–4702.
- Wypych G (1999) *Handbook of Fillers*, Toronto: ChemTec Publishing.

- Xia H and Song M (2006) 'Preparation and characterisation of polyurethane grafted single-walled carbon nanotubes and derived polyurethane nanocomposites', *J. Mater. Chem.*, 16, 1843.
- Yue D, Liu Y, Shen Z and Zhang L, (2006) 'Study on preparation and properties of carbon nanotubes/rubber composites', *J. Mater. Sci.*, 41, 2541.
- Zhang W D, Shen L, Phang I Y and Liu T (2004) 'Carbon nanotubes reinforced nylon-6 composite', *Macromolecules*, 37, 256–259.
- Zhu J, Kim J, Peng H, Margrave J L, Khabashesku V N and Barrera E V (2003) 'Improving the dispersion and integration of single-walled carbon nanotubes in epoxy composites through functionalization', *Nano. Lett.*, 3, 1107–1113.

Epoxy–carbon nanotube composites

J. M. KENNY, Institute of Polymer Science and Technology (ICTP-CSIC), Spain and L. VALENTINI, D. PUGLIA and A. TERENCE, University of Perugia, Italy

Abstract: The primary current objective is to develop knowledge-based technologies of carbon nanotubes (CNTs), understanding the surface chemistry and processing tools used in designing polymer-based composites. The chapter emphasizes the different functionalization processes and the parameters affecting the nanotube dispersability in polymeric matrices. We also describe different processing methods for incorporating such functional nanofillers into the polymer backbone. How functionalized carbon nanotubes can improve the thermal, mechanical and electrical properties of common epoxy matrices already used in advanced applications is also reported. Moreover, the chapter reviews the different chemorheological approaches adopted to describe the catalytic effects of pristine and functionalized CNTs on the curing of epoxy systems through the development and application of coupled kinetic and rheological models. Finally, the effects of functionalized CNTs on the thermal, electric and mechanical properties are reviewed and explained in terms of the interactions between the functionalized CNTs and typical epoxy resins used in advanced applications.

Key words: chemorheology, electrical properties, epoxy, functionalization, kinetic model, reaction kinetics, rheology, thermal properties.

8.1 Introduction

Due to their exceptional mechanical, thermal and electrical properties, in addition to low density with respect to the class of organic and inorganic tubes, carbon nanotubes (CNTs) are extremely promising for the development of high performance nanostructured materials.^{1,2} Single-walled carbon nanotubes (SWNTs) and multi-walled carbon nanotubes (MWNTs) consist of one or more graphitic sheet, which has been rolled up into a cylindrical shape, respectively. However, the incorporation of nanotubes is not a trivial task mainly if a good dispersion is needed together with a chemical grafting to the polymer matrix which is mandatory to maximize the advantage of nanotube reinforcement. The affinity to adhere to each other renders nanotubes intractable and indispersable in common solvents.³

For this reason, the incorporation of nanotubes is not a trivial task; they can be dispersed in some solvents by sonication, but precipitate after the treatment. To avoid this problem, it has been demonstrated that CNTs can interact with different classes of compounds.^{4–20} The formation of such supramolecular complexes allows a better dispersion of CNTs toward the processing of innovative composites. In

addition, surface-modified CNTs undergo chemical reactions making them soluble for their integration into organic systems. Two of the key challenges to realizing composites made out of carbon nanotubes are securing a reliable control over their surface chemistry through either covalent or non-covalent modification, and achieving dispersion.

In this section, we report some examples of nanocomposites with CNTs, highlighting a meshwork of interactions between the thermal, rheological, mechanical and electrical properties of CNTs dispersed into epoxy systems with the aim of offering an overview of the approaches of chemical functionalization of CNTs and to account for the advances that have been produced so far.

8.2 Experimental materials and methods

8.2.1 Carbon nanotubes (CNTs) and their interactions with epoxy systems

The development of CNT-based nanocomposites can only be achieved by solving two main problems: (a) the large contact area of CNT and the relatively strong inter-tube attraction via van der Waals forces that make the CNTs spontaneously bundle together, thus making their dispersion in polymeric matrices difficult; and (b) the poor interfacial adhesion between the raw CNT and the matrix. More recently the development of CNT-based nanocomposites has been achieved thanks to approaches that can exfoliate bundles of CNT through the wrapping of the tubular surface by various species of polymers, aromatic compounds²¹ and surfactants.²²

Different works have been dedicated to the effect of CNT on the cure kinetics of an epoxy resin. Puglia *et al.*²³ stated that single-walled carbon nanotubes accelerated the cure reaction of the diglycidyl ether of bisphenol A–diethylenetriamine (DGEBA–DETA) epoxy system studied by means of DSC analysis. The role played by the amine functional groups when they interact with the surface of the SWNT has been considered to be the origin of the modification of the cure behavior.²⁴ Similar results were reported by Xie *et al.*;²⁵ they reported an acceleration effect in the case of carbon nanotubes dispersed in the tetraglycidyl-4,4'-diaminodiphenylmethane (TGDDM) and 4,4'-diaminodiphenylsulfone (DDS) epoxy system. In this case, the presence of hydroxyl groups on the surface of the tubes has been considered the main factor which has a catalytic effect on the epoxy ring opening.

A decrease in the onset temperature was observed also by Tao *et al.*²⁶ in the SWNT–diglycidyl ether of bisphenol-F (DGEBF)–diethyl toluene diamine (DETD) system. In the above mentioned cases,^{23–26} the modification of the cure behaviour in its early stage can be attributed to surface functional groups on the CNT or catalyst particles. More generally, it was found that the acceleration of the curing time was related to the specific surface area of the filler considering the proportional relationship between the surface area and the peak temperature (the

higher the surface area, the higher the temperature drop).²⁷ Bae *et al.*²⁸ investigated the effect of CNT on the cure reaction of liquid crystalline epoxy. The authors reported a retardation effect of CNT, indicating that the presence of CNT did not have a significant effect on the total heat of reaction if compared to that of the unfilled system.

8.2.2 Epoxy resins and effects of CNTs on curing systems

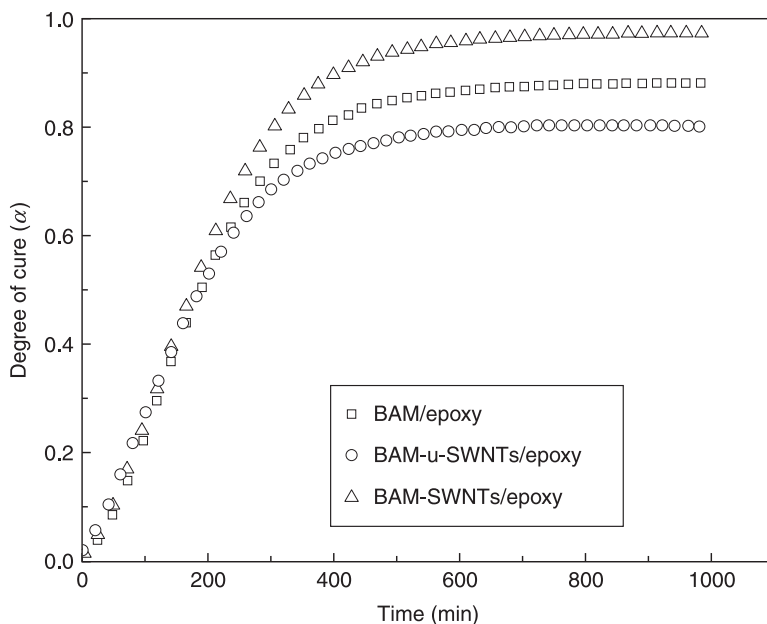
Studies on CNT–polymer nanocomposites have been reported for various kinds of organic polymers. In most cases, homogeneous dispersion of CNTs is hindered by ‘entangled’ and ‘agglomerate’ structures of CNTs. It has been suggested that oxidation or chemical functionalization of CNTs and covalent attachment of polymer chains to the CNTs make the dispersion better and improve the strength of the interfacial bonding between the CNTs and the polymer matrices, which is beneficial to the performance of CNT–polymer composites.

Among polymers, epoxy resins are especially interesting because of their high modulus, low shrinkage in cure, high adhesion, and their good chemical and corrosion resistance. In an attempt to make optimum use of CNT–epoxy resin nanocomposites, it is necessary to understand the nature of their curing process. The final properties of the nanocomposites depend significantly on the curing conditions. Some investigations on the cure behaviour of MWNT–epoxy resin nanocomposites and the effect of the functional groups on the surface of MWNTs on cure reaction have been done.^{23,28–30}

According to this approach, we investigated the cure reaction of diglycidyl ether of bisphenol A-based epoxy resin when it reacted with butylamine (BAM) molecules anchored onto the fluorinated SWNTs obtained by plasma treatment. The results confirmed that the higher extent of reaction observed for the composite obtained with the BAM-SWNTs is due to the large aspect ratio of nanotubes and the covalently attached amine surrounding F-SWNTs (Fig. 8.1).

8.2.3 Effects of CNT functionalization on epoxy–CNT composites

For most of those methods, functionalization implies formation of covalent bonds, made by additional reactions to CNT double bonds. The final result is the formation of a new single bond with simultaneous local destruction of conjugation on the nanotube wall. As an alternative method, non-covalent functionalization offers the possibility of attaching organic moieties without affecting the electronic network of the tubes. These interactions are of the same kind as those keeping the various graphite layers close to one another (π -stacking). In this regard, interactions



8.1 Degree of cure of the reaction as a function of the time at 30°C for BAM-SWNTs–epoxy, butylamine-unmodified SWNTs–epoxy (BAM-u-SWNTs–epoxy) nanocomposites.

between nanotubes and polynuclear species as well as pyrene-modified oxidized surfaces have been used for the assembly of single-walled carbon nanomaterials.³¹ Surfactants have generally been used for the purification and dispersing process of raw CNTs.²⁴ Then, surfactant-stabilized dispersions of individual CNTs were used for compatibility enhancement of the tubes in the preparation of composite materials.^{32–35}

CNTs are considered ideal materials for reinforcing fibres due to their exceptional mechanical properties. Functionalization of CNT seems to be the most effective way to incorporate these nanofibers into the polymer matrix. It is generally accepted that the fabrication of high performance nanotube–polymer composite depends on the efficient load transfer from the host matrix to the tubes. If the percentage of nanoreinforcements is very low or if it is well dispersed, there are more strong interfaces that slow down the progress of the crack.^{36,37}

Therefore, nanotube–polymer composites have potential applications in aerospace science, where lightweight robust materials are needed.³⁶ To address these issues, several strategies for the preparation of such composites have been reported. Here we report some of these strategies involving physical mixing in solution, infiltration of monomers in the presence of nanotube sheets, and chemical functionalization of CNTs by plasma treatment.

The direct fluorination of SWNTs and their subsequent derivatization provide a versatile tool for the preparation and manipulation of nanotubes with variable sidewall functionalities.^{38–43} Recent studies have shown that fluorine in SWNTs can be efficiently displaced by alkylamino functionalities.⁴³ The nucleophilic substitution offers an opportunity for SWNTs to be integrated into the structure of the epoxy systems through the sidewall amino functional groups.

The plasma treatment for the functionalization of carbon nanotubes represents a novel approach easy to scale up to industrial application. More recently there have been many attempts to fluorinate carbon nanotube sidewalls in such manner.^{44–47} The CF_4 plasma treatment of SWNT sidewall was demonstrated to enhance the reactivity with aliphatic amines.⁴⁶

Since fluorine groups covalently attached to the nanotubes offer the opportunity for chemical interactions with the amine systems, it was recently demonstrated that this reaction proceeds through the intermolecular elimination of HF and the formation of the C–N bond.^{43–45}

8.3 Chemorheological approach

In this section, the chemorheological behaviour of the epoxy–CNT system is reported. Chemorheology is a very important aspect because it is strongly connected with the processing of the materials, conditioning both manufacturing methods and parameters.

The presence of CNTs dispersed in the matrix has a significant influence on the overall chemorheological behaviour with an important effect on parameters such as gel time and induction time. However, in order to better understand the approach, a preliminary summary of the main theoretical aspects and some data on the analysis of the epoxy–CNT system are reported.

Chemorheology is defined as the study of viscoelastic behaviour of reacting systems. This study encompasses knowledge of the variations in viscosity due to chemical reactions and processing conditions (chemoviscosity) and characterization of the growth of the infinite molecular network and immobilized glassy state (gelation and vitrification). In particular, the standard procedure generally used in a chemorheological model is as follows.

8.3.1 Determination of the kinetic model

This model is necessary to know how the degree of cure varies with time. The differential scanning calorimeter (DSC) analysis is an ideal tool for monitoring these kinds of reactions. The DSC indeed provides the heat flow ($\partial H/\partial t$), or instantaneous heat, released or absorbed by the reactive system as a function of the absolute temperature or time. Dynamic and isothermal DSC analyses are widely used to obtain an indirect estimation of the degree of cure of thermosetting systems,

assuming that the heat released during polymerization is always proportional to the consumption rate of the reactive groups (which actually describes the extent of the reaction). Calorimetric data can therefore be used to both create and verify theoretical and empirical kinetic models and obviously to calculate kinetic parameters.

8.3.2 Determination of the relationship between glass transition temperature (T_g) and the degree of cure (α)

It is of interest to relate the degree of cure (α) to the glass transition temperature T_g for several reasons. It may be easier to determine the glass transition temperature than the degree of cure. Furthermore, it is very important to know the relationship between α and T_g when determining the chemorheological model.

8.3.3 Definition of the rheological model

The rheological model combined with the kinetic model creates the chemorheological model. The chemorheological model describes the dependence of viscosity on both the degree of cure (α) and temperature.

8.3.4 Kinetic model

Many studies have been conducted on the kinetics of the cure reactions, and a variety of kinetic models have been used to relate the rate of the chemical reactions to the time, temperature, and extent of cure.⁴⁸ In general, the kinetic models fall into two main categories:

- phenomenological models;
- mechanistic models.

A phenomenological model is generally expressed in a relatively simple rate equation, and is developed, ignoring the details of how reactive species take part in the reaction.

On the other hand, mechanistic models are obtained from balances of reactive species involved in the reaction. In spite of a better prediction and interpretation offered by mechanistic models, it is not always possible to derive such models due to the complexity of cure reactions. In addition, they generally require more kinetic parameters than phenomenological models do. So in most cases, phenomenological models are preferred when studying the cure processes. Mechanistic models have some advantages over empirical ones. For instance, without conducting laborious and time consuming cure experiments, one can treat separately the influence of the type, concentration or number of initiators on the overall reaction rate. For both kinds of models, different works have been

Table 8.1 Some examples of kinetic models typically used in different thermosetting systems

Model	Expression	System	Notes
First order	$d\alpha/dt = k(1 - \alpha)$ $k = A \exp(-Ea/RT)$	Epoxy resin	k = rate constant Ea = activation energy A = coefficient
Second order	$d\alpha/dt = k(1 - \alpha)^2$ $k = A \exp(-Ea/RT)$	Epoxy resin	
n^{th} order	$d\alpha/dt = k(1 - \alpha)^n$ $k = A \exp(-Ea/RT)$	Polyester Epoxy resin	n = reaction order
Series of n^{th} order reaction	$\frac{d\alpha}{dt} = \sum_i g_i \frac{A_i}{\beta} \exp\left(-\frac{E_i}{RT}\right) (1 - \alpha_i)^{n_i}$	Tri-epoxy system	g_i = factor A_i = coefficient β = heating rate n_i = reaction order
Polynomial	$d\alpha/dt = k \exp(-Ea/RT)$	Epoxy resin	
Autocatalytic-1	$d\alpha/dt = k_1 + k_2 \alpha^m (1 - \alpha)^n$ $k_1 = k_0 \exp(-\bar{E}_a/RT)$ $k_2 = k_0 \exp(-Ea/RT)$	Polyester Epoxy Novolac+filler Epoxy resin Thermosets	n, m = reaction order k_1, k_2 = rate constants E_1, E_2 = activation energies
Autocatalytic-2	$d\alpha/dt = (k_1 + k_2 \alpha)(1 - \alpha)(B - \alpha)$	Epoxy resin	B = stoichiometric factor
Mechanistic	$\alpha/\alpha_{gel} = f(\text{concentration})$	Unsat. polyester/ styrene Epoxy resin	α_{gel} = conversion at gelation
Self acceleration	$d\beta/dt = k(1 - \beta)(1 + C\beta)$	Thermosets	C = constant
Self inhibition	$d\beta/dt = k(1 - \beta)(1 - \varepsilon\beta)$	Thermosets diffusion limited	ε = constant
Combined	$d\beta/dt = k(1 - \beta)(1 + C\beta)(1 - \varepsilon\beta)$	Thermosets	

performed and several models are now available in the literature; in Table 8.1, some examples are reported.

The use of phenomenological models requires experimental data; in fact, the parameters of the models have to be found by fitting experimental curves. Also, in this case, two approaches can be followed for the determination of model parameters depending on the kinetic models applied:

- DSC isothermal tests;
- DSC dynamic tests.

8.3.5 Correlation between glass transition temperature and cure degree: Di Benedetto's equation

Understanding the glass transition temperature (T_g) of thermosetting polymers is very important for various reasons. First and most obvious is that T_g determines an upper bound for the use temperature of the polymer; other reasons include the intimate relationship between the onset of the so-called diffusion control regime during the isothermal cure of a thermoset and its glass transition,^{49–52} the influence of T_g on the chemorheology of a thermoset^{53,54} and the correlation between internal stresses and T_g .⁵⁵

The effect of cross-linking on T_g has been studied by using several experimental approaches, including modifying the amount of cross-linker, changing the molecular weight of the pre-polymer, altering the stoichiometry, and stopping the reaction at different degrees of conversion. This last case is of great practical importance because it follows the actual curing process; however, this is probably the most difficult case to study because there are many changes taking place simultaneously.

Several authors have reported T_g data as a function of conversion; most of this data is for epoxy systems.^{56–62} The experimental technique used to obtain the glass transition temperature at different degrees of conversion often consists of interrupting the reaction at different times, usually by quenching, and then scanning the sample to obtain the T_g . The extent of reaction is commonly determined by measuring the residual heat of reaction through differential scanning calorimetry (DSC) by spectroscopic analysis, typically infrared spectroscopy.

Though several equations to describe the T_g versus conversion data have been utilized in the literature, this can still be considered an unresolved problem, particularly for systems with high cross-link density. Riccardi and co-workers,⁶³ for example, have limited themselves to empirically fit a polynomial to their data. Other authors have tried to empirically fit Di Benedetto's equation (Equation 8.1)⁶⁴ to the experimental results, with a moderate degree of success:

$$\frac{T_g - T_{gu}}{T_{gu}} = \frac{(\epsilon_\infty/\epsilon_0 - c_\infty/c_0)x}{1 - (1 - c_\infty/c_0)x} \quad [8.1]$$

where x is the cross-link density defined as 'the fraction of all segments that are cross-linked', T_{gu} is the glass transition of the uncross-linked polymer, ϵ is the lattice energy, c is the segmental mobility, and the sub-indexes ∞ and 0 refer to the uncross-linked and the fully cross-linked polymers respectively, x has been regarded as the conversion and T_{gu} as the glass transition of the un-reacted system.

For a system exhibiting a unique one-to-one relationship between the glass transition temperature⁶⁵ and conversion, Di Benedetto's equation⁶⁶ is one of the easiest approaches for stoichiometric ratios to express this relationship using only a single parameter model as:

$$T_g = T_{g0} + \frac{(T_{g\infty} - T_{g0})\lambda c}{1 - (1 - \lambda)c} \quad [8.2]$$

where T_{g0} is the glass transition temperature of the monomer, $T_{g\infty}$ is the glass transition temperature of the fully reacted network, λ is a structure dependent parameter theoretically equated to $\Delta C_{p\infty}/\Delta C_{p0}$. The values of $\Delta C_{p\infty}$ and ΔC_{p0} are the differences in the heat capacity between the glassy and rubbery state for the fully cured network and monomer, respectively.

8.3.6 Rheological model

One of the most essential properties of a polymer, considering its importance in polymer processing, is viscosity. The variation of viscosity caused by chemical reactions is referred to as chemoviscosity. Chemorheology is the study of chemoviscosity.⁶⁷

The rheological characterization of reactive polymers is complicated since polymer rheology depends on a variety of variables, such as time, temperature, deformation rate, pressure, filler concentration, chemical formulation, etc.⁶⁸

Two different possibilities exist in modelling the chemoviscosity of a reactive polymer:

1. An expression can be developed to represent the time dependency of viscosity. Consequently, the temperature dependency of parameters belonging to this expression may be evaluated.
2. An expression can be developed to represent the temperature dependency of viscosity. Afterwards, the parameters of this expression can be related to an appropriate kinetic expression.

Some researchers, including White⁶⁹ and Tajima and Crozier,⁷⁰ have suggested semi-empirical models to predict the variation of viscosity during the cure process. The models representing the changes of viscosity with reaction time have the following form:

$$\eta(t) = \eta_0 \exp(kt) \quad [8.3]$$

where η_0 represents the isothermal melt viscosity and k is the reaction rate constant. Roller^{71,72} extended Equation 8.3 by assuming an Arrhenius temperature dependence for η_0 and k :

$$\ln \eta(t) = \ln \eta_{\infty} + \Delta E_{\eta}/RT + tk_{\infty} \exp(\Delta E_k/RT) \quad [8.4]$$

where $\eta(t)$ represents viscosity as a function of time at temperature T , η_{∞} stands for calculated viscosity at $T = \infty$, ΔE_{η} is the Arrhenius activation energy for viscosity, R is the universal gas constant, T denotes absolute temperature, t is time, k_{∞} represents the kinetic analogue of η_{∞} and ΔE_k is the kinetic analogue of ΔE_{η} . At the early stage of cure, it is generally assumed that the viscosity is Newtonian. As can be seen from Equation 8.4, in this model no form of kinetic model is assumed. Equation 8.4 was modified by introducing an integral form to predict the viscosity changes in non-isothermal systems:

$$\ln \eta(t, T) = \ln \eta_{\infty} + E_{\eta}/RT + \int_0^t k_{\infty} \exp(\Delta E_k/RT) dt \quad [8.5]$$

Since evaluation of the parameters in Equation 8.5 from multiple isothermal experiments is time-consuming, Eley⁷³ developed a technique to obtain these parameters from a single dynamic measurement. By comparing the values of steady shear viscosity, dynamic viscosity, and complex viscosity, it was found that they were virtually identical at short times and low viscosities.

Kamal and Ryan⁷⁴ stated that dynamic measurements had the drawback of being more dependent or sensitive to structural variations or resin chemistry; however, dynamic measurements in oscillatory shear were considered advantageous because they could be conducted even beyond the gelation point.

Tungare *et al.*⁷⁵ conducted a sensitivity analysis on parameters of Equation 8.5. It was indicated that the four parameters in this equation had different sensitivities, and the sensitivities changed with the cross-linking reactions. It is repeatedly indicated in the literature that the flow activation energy is independent of the shear rate but may increase with progress of the cure reactions. Thus, the application of Equation 8.5 is limited since the flow activation energy is considered to be independent of the extent of cure.

Ryan⁷⁶ expressed the viscosity of epoxy resin as a function of temperature, shear rate, and conversion using the following form:

$$\eta = f_1(T) f_2(\dot{\gamma}) f_3(\alpha) \quad [8.6]$$

By an empirical fit, the viscosity was expressed as:

$$\eta = \eta_0 \exp \left(C' \int_{\alpha_0}^{\alpha} \frac{d\alpha}{\alpha^m (1-\alpha)^n} \right) \quad [8.7]$$

where η_0 was represented by:

$$\eta_0 = \eta^* \dot{\gamma}^{n'-1} \exp(E_{\dot{\gamma}}/RT) \quad [8.8]$$

where m and n are kinetic exponents, α represents the critical extent of cure, η^* is a constant and n' is the power-law index.

Based on the second approach in modelling the chemoviscosity of a reactive system, the temperature dependence of viscosity may be expressed in the form of a Williams-Landel-Ferry (WLF) equation (see Equation 8.3):

$$\log \eta(T) = \log \eta(T_g) + \frac{a(T - T_g)}{b + (T - T_g)} \quad [8.9]$$

where η represents viscosity, T denotes temperature, T_g is a reference temperature and a and b are constants.

The parameters T_g and $\eta(T_g)$ vary with the progress of cure so they can be expressed as a function of conversion (α). Using this approach, Tajima and Crozier⁷⁷ demonstrated the variation of viscosity for epoxy resins in the course of

cure reactions by the WLF equation. The 'viscosity-temperature' shift factor was defined as: $a_t = \eta(T)/\eta(T_s)$.

By regression analysis, a relationship was established between T_s and the amount of hardener consumed to react with the epoxy resin. Moreover, $\log\eta(T_s)$ was found to be proportional to T_s .

According to Tajima and Crozier,⁷⁷ for epoxy resin T_s might be expressed as a linear function of α_2 and $\log q(TJ)$ as a linear function of a . Lee and Han applied the WLF equation to unsaturated polyester cure system. They expressed both activation energy of flow, E , and frequency factor, A , in terms of extent of cure, a . By establishing relationships between the reference temperature T , and the extent of cure, as well as between $\log\eta(T_2)$ and T_s , the following form was obtained:

$$\log\eta(T, \alpha) = (a_1 + b_1\alpha) - \frac{a_2(b_2 + T - c_2\alpha)}{a_3 + T - c_2\alpha} \quad [8.10]$$

where a_1 , b_1 , a_2 , b_2 , c_2 , and a_3 are parameters.

Lee and Han⁷⁸ applied a WLF equation to model

$$\log\eta(T) = \log\eta(T_g) - \frac{a(T - T_g)}{51.6 + T - T_g} \quad [8.11]$$

where a is a free volume parameter, and T_g is the glass transition temperature of the resin. The main difference between Equations 8.9 and 8.11 is that the former treats T_s as an unknown parameter, whereas the latter considers T_g as a physical property of the cured resin. On the basis of experimental data obtained from partially cured samples, T_g was related to the extent of cure, α .

$\log\eta(T_g)$ and the free volume parameter a were also expressed in terms of α , using least squares analysis. They claimed that the theoretical predictions showed a good agreement with experimental data at low extent of cure.

8.4 Chemorheological analysis of epoxy-CNTs systems

The systems analysed in this work are based on a diglycidyl ether of bisphenol A-based (DGEBA) epoxy resin cured with a solid N-methyldiethanolamine. Different types of CNTs have been used in order to analyse the influence of morphology and functionalization on the chemorheological behaviour of the system. The presence of functional groups bonded to CNTs implies a significant influence on the mathematical models applied to the chemorheological analysis; in particular, for the systems filled with CNTs functionalized with carboxyl group, the following kinetic model equations have been used:

$$\begin{cases} \frac{d\alpha}{dt} = K_1(T) \cdot \alpha^{m_1} \cdot (\alpha_{MAX} - \alpha)^{n_1} + K_2(T) \cdot \alpha^{m_2} \cdot (\alpha_{MAX} - \alpha)^{n_2} \\ K_i(T) = K_{0i} \exp\left(-\frac{Ea_i}{RT}\right) \\ \alpha_{MAX}(T) = \frac{1}{1 + \exp(\beta \cdot T_{0.5}) \cdot \exp(-\beta \cdot T)} \end{cases} \quad [8.12]$$

Whereas, for the systems with non-functionalized CNTs, the following kinetic model was used:

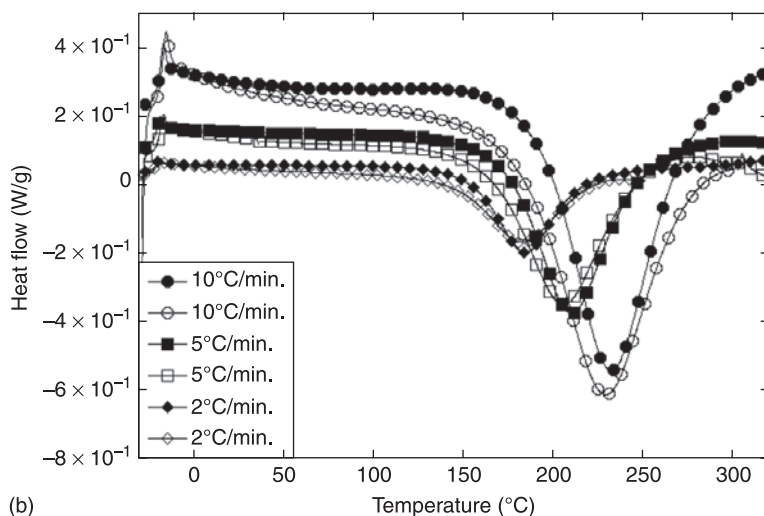
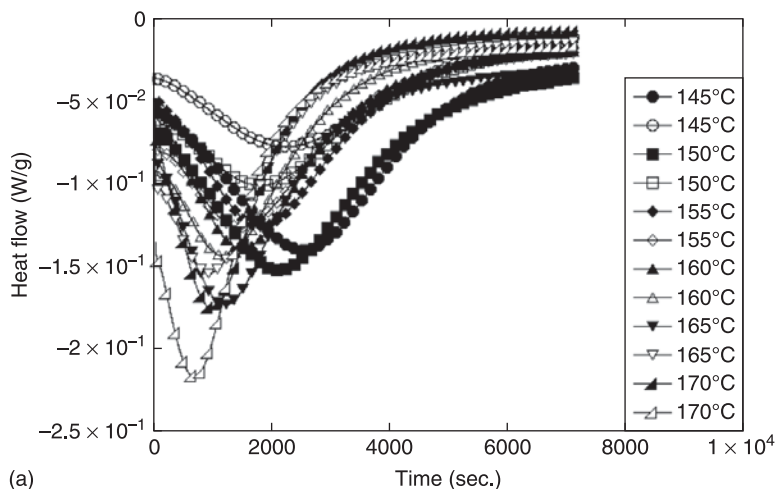
$$\begin{cases} \frac{d\alpha}{dt} = K_1(T) \cdot (\alpha_{MAX} - \alpha)^{n_1} + K_2(T) \cdot \alpha^{m_2} \cdot (\alpha_{MAX} - \alpha)^{n_2} \\ K_i(T) = K_{0i} \exp\left(-\frac{Ea_i}{RT}\right) \\ \alpha_{MAX}(T) = \frac{1}{1 + \exp(\beta \cdot T_{0.5}) \cdot \exp(-\beta \cdot T)} \end{cases} \quad [8.13]$$

Concerning the morphology, three types of CNTs have been used, in particular, SWNT, DWNT and MWNT. In the following sections, the results of the chemorheological study are reported for all analysed systems.

8.4.1 Study of the diglycidyl ether of bisphenol-A (DGEBA)–double-walled carbon nanotube (DWNT) mixture

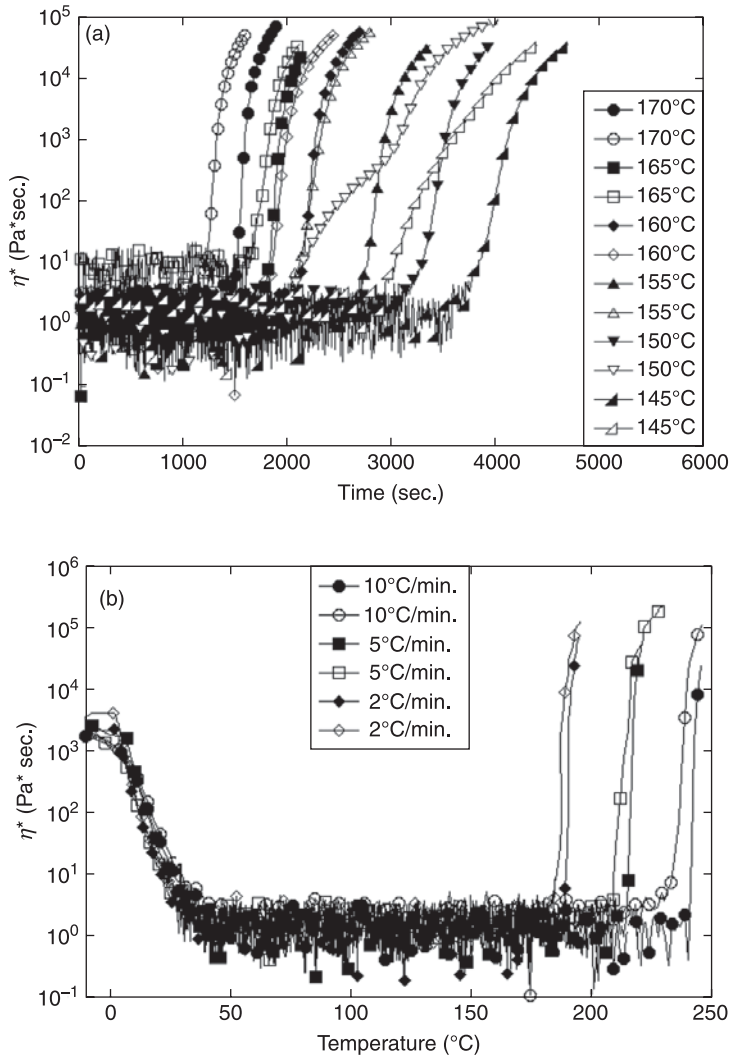
The results of the calorimetric test in isothermal and dynamic conditions⁷⁹ are reported in Figs 8.2 and 8.3 respectively. These results show an important catalytic effect of the carboxylic double-walled carbon nanotubes (C-DWNTs) on the cure reaction of the DGEBA–MDEA system with a shift of the cure reaction peak toward a lower time (in isothermal tests) and lower temperature (in dynamic test). Moreover, it is also possible to note that the cure rate (Fig. 8.3) for the system obtained with MDEA-modified C-DWNT is higher than the conversion speed of the neat epoxy system.

The rheological measurements (Figs 8.3 (a) and 8.3 (b)) confirm what was observed in the calorimetric tests. Also in this case, the onset of the cure reaction for the filled system is shifted to lower time and temperatures, respectively. The results obtained from the calorimetric and rheological tests are summarized in Table 8.2 and Table 8.3. The displacement of the gel point to a lower time and temperature is due to the fact that the functionalized nanotubes interact with the epoxy matrix via the amino groups immobilized on the tube sidewall, reducing the mobility of chains of the epoxy molecules.



8.2 Calorimetric tests on DGEBA-MDEA (filled symbols) and DGEBA-MDEA-C-DWNTs (open symbols) systems under (a) isothermal; (b) dynamic conditions.

The model shows a very good fit in both isothermal and dynamic conditions for all the materials tested. The comparisons between experimental data and model predictions in specific isothermal and dynamic conditions are reported in Figs 8.4 (a) and 8.4 (b). In Fig. 8.4 (a), it is important to note that at 160°C the pure DGEBA-MDEA system reaches a maximum degree of cure of approximately 0.65 and about 66 min. are necessary to get $\alpha = 0.5$. At the same temperature conditions, the nanocomposite obtained with MDEA modified C-DWNTs reaches



8.3 Complex viscosity (η^*) rheological measurements on DGEBA–MDEA (filled symbols) and DGEBA–MDEA–C-DWNTs (open symbols) systems under (a) isothermal; (b) dynamic conditions.

a maximum degree of cure of 0.99 and the time necessary to reach the degree of reaction of 0.5 is about 20 min. Moreover, it is possible to observe that a temperature of 210 °C is necessary to make the neat system reach an a max similar to that of the filled system. The kinetic parameters are reported in Table 8.4.

The comparisons among experimental data and chemorheological model (numerically integrated according to the fourth order Runge–Kutta method⁸⁰) for

Table 8.2 Time of maximum reaction rate and maximum reaction peak temperature for isothermal and dynamic tests of DGEBA–MDEA and DGEBA–MDEA–C-DWNTs systems

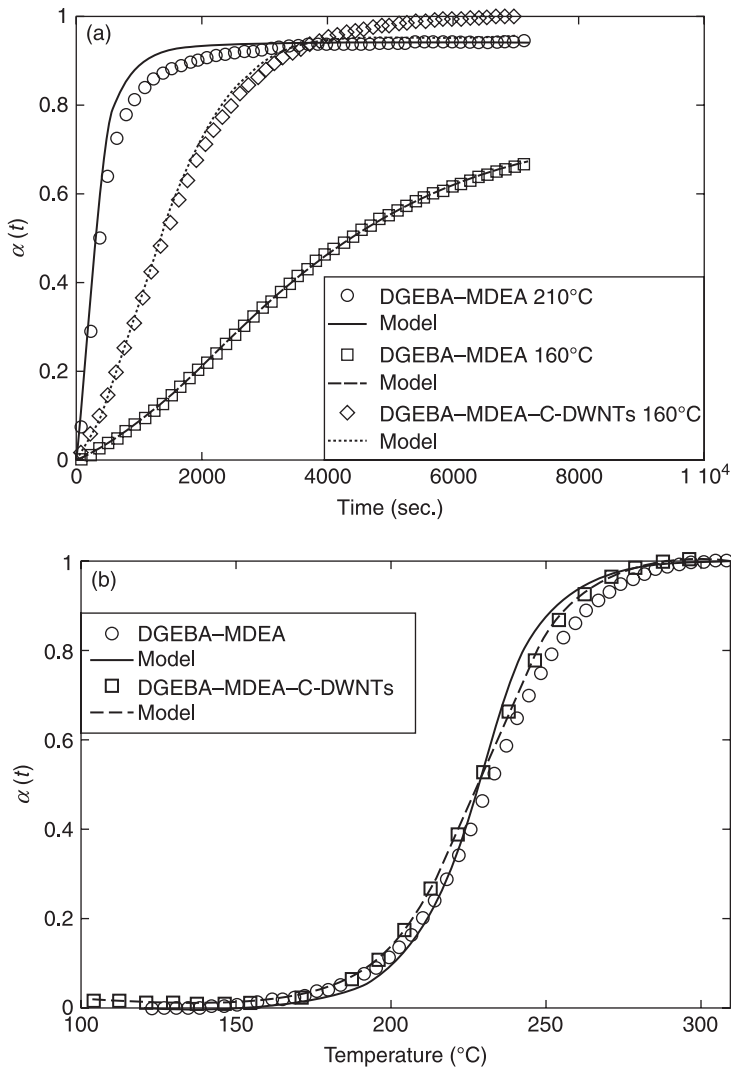
Test condition (°C)	DGEBA–MDEA	DGEBA–MDEA–C-DWNTs	Test condition (°C/min.)	DGEBA–MDEA	DGEBA–MDEA–C-DWNTs
	Peak time (s)	Peak time (s)		Peak temperature (°C)	Peak temperature (°C)
145	2613	2229	2	184	181
150	2126	1896	5	209	205
155	1806	1575	10	231	226
160	1537	1191			
165	1242	948			
170	948	653			

Table 8.3 Time onsets for isothermal rheological tests, and onset and gel temperatures for dynamic rheological tests of DGEBA–MDEA and DGEBA–MDEA–C-DWNTs systems

Test condition (°C)	DGEBA–MDEA	DGEBA–MDEA–C-DWNTs	DGEBA–MDEA	DGEBA–MDEA–C-DWNTs
	Onset time (s)	Gel time (s)	Onset time (s)	Gel time (s)
145	4030	4670	3523	4377
150	3443	3941	3085	3779
155	2882	3362	2274	2775
160	2241	2704	1953	2434
165	1895	2126	1793	2071
170	1583	1912	1313	1569
Test condition (°C/min.)	Onset temperature (°C)	Gel temperature (°C)	Onset temperature (°C)	Gel temperature (°C)
2	190	195	187	196
5	216	221	214	230
10	242	245	238	246

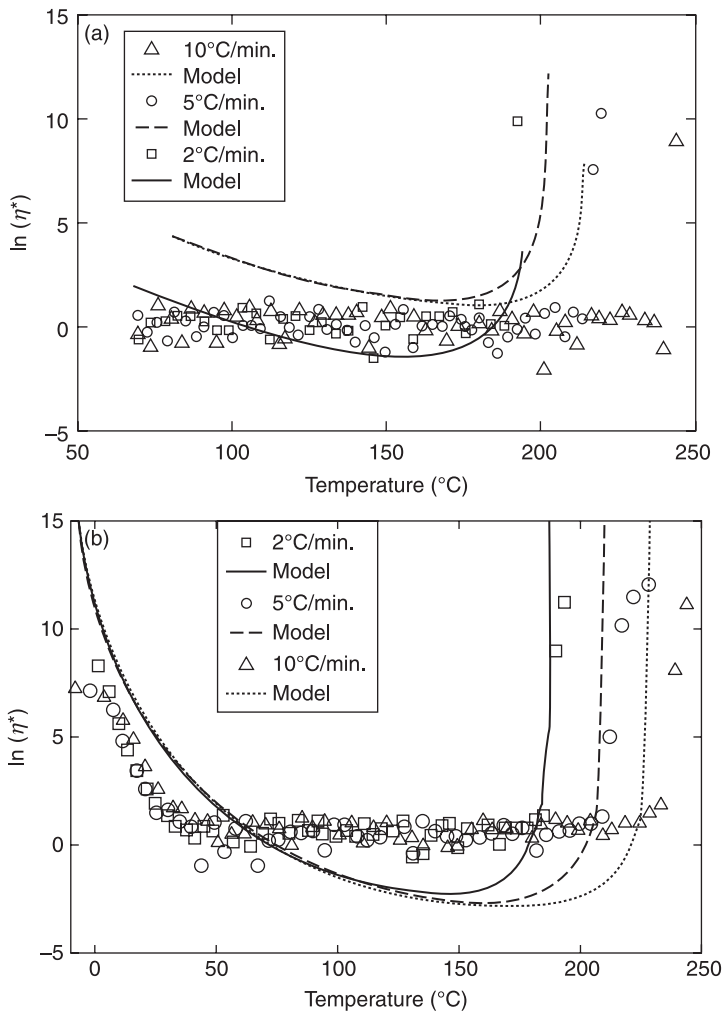
the DGEBA–MDEA and DGEBA–MDEA–C-DWNTs systems are reported in Figs 8.5 (a) and 8.5 (b), respectively. The parameters of the model are reported in Table 8.4.

From these figures, the accordance between the experimental data and the model is evident. Moreover, the higher reaction enthalpy, together with the $T_{0.5}$ and β parameters obtained for the nanocomposite, make the sigmoid function steeper than that calculated for the DGEBA–MDEA neat system. This could lead to the



8.4 Comparison between experimental data and kinetic model for the calorimetric measurements performed on DGEBA–MDEA and DGEBA–MDEA–C-DWNTs systems under (a) isothermal; (b) dynamic conditions.

conclusion that the C-DWNTs play a catalytic role in the networking process. On the other hand, all the remaining kinetic parameters are lower in the case of the nanocomposite (i.e. the reaction works more slowly), probably due to some kind of obstacle generated by the tubes against the mobility of polymer chains.



8.5 Comparison between experimental data and the chemorheological model for (a) DGEBA-MDEA; (b) DGEBA-MDEA-C-DWNTs systems.

Table 8.4 Parameters of the chemorheological model for the DGEBA-MDEA and DGEBA-1%DWNTs systems

	Neat resin	DGEBA-1%DWNTS
ΔH (J/g)	-326.6	-333.4
<i>Rheological model</i>		
C_1	-35.16	-34.01
C_2	15.38	21.86
n_{rheo}	1.65	1.85
α_g	0.76	0.71

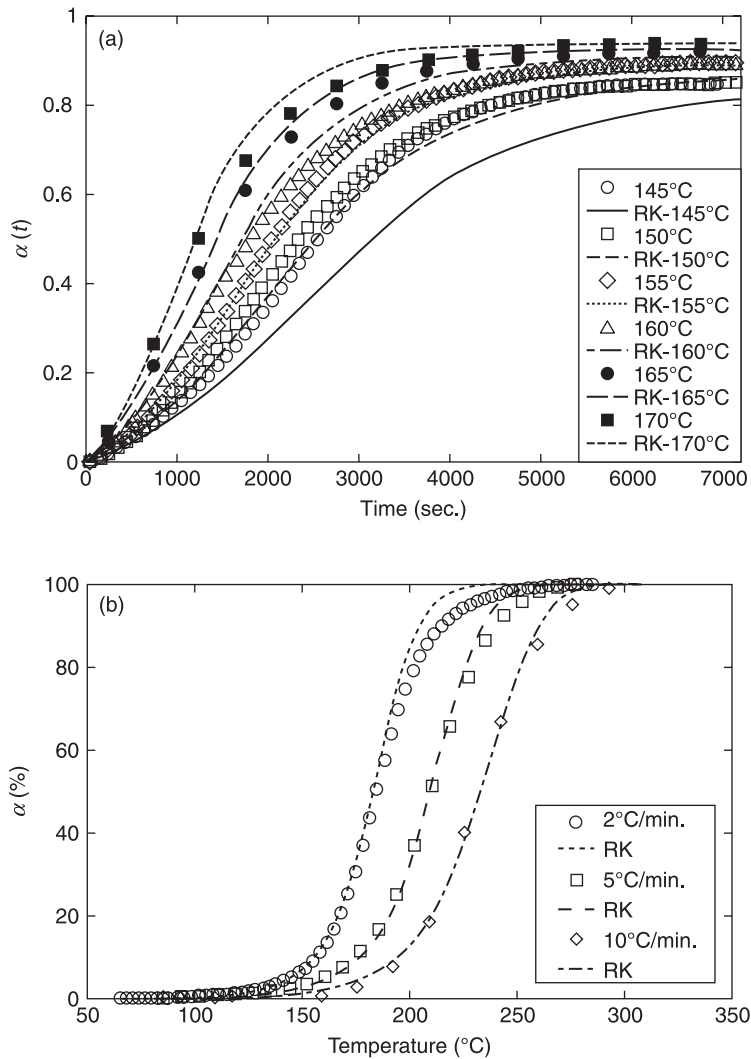
	Neat resin	DGEBA–1%DWNTs
<i>Kinetic model</i>		
Ea_1 (J)	10934	12406
$\ln(K_1)$	6.60	8.16
m_1	0.15	0.074
n_1	1.07	0.46
Ea_2 (J)	8916	9670
$\ln(K_2)$	4.53	6.12
m_2	1.63	1.50
n_2	2.34	1.84
<i>Degree of cure</i>		
145°C	0.29	0.81
150°C	0.43	0.93
155°C	0.56	0.99
160°C	0.67	0.99
165°C	0.75	1.00
170°C	0.80	1.00
175°C	0.84	1.00
180°C	0.88	1.00
190°C	0.91	1.00
200°C	0.92	1.00
210°C	0.95	1.00

8.4.2 Study of the DGEBA–MWNTs mixture

In this section is reported the chemorheological study of the epoxy–MWNT system and in this case the second kinetic model is used (Figs 8.6 and 8.7). The degree of cure reached at 160°C is lower than the DGEBA–DWNTs system and is probably due to the non-carboxylic group present on the carbon nanotubes. However, the different geometry can modify the system cure: as a matter of fact, it is possible to note that at 160°C, the degree of cure reached is very high. As it is possible to see, the model can fit the experimental results very well but more work can be done in analyzing the parameters reported in Table 8.5.

8.4.3 Study of epoxy–SWNTs functionalized and non-functionalized mixture

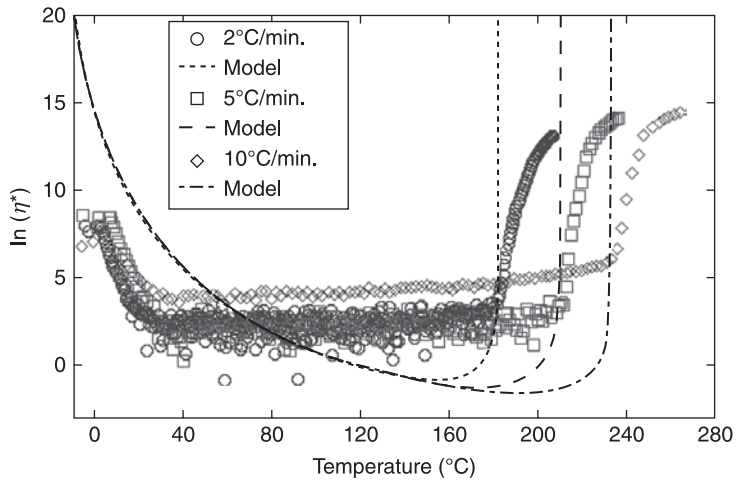
To confirm the effect of carboxylation on the kinetic and rheological study, it was necessary to study a system with the same geometry. The only difference is in functionalization. As we will see, not only are the models able to describe the kinetic and rheological results but also the catalytic effect produced from the nanotube modification is evident.



8.6 Kinetic model for DGEBA-1%MWNTs. Runge-Kutta (RK) integration of (a) isothermal fitting curves; (b) dynamic fitting curves.

The case study of functionalized SWNTs

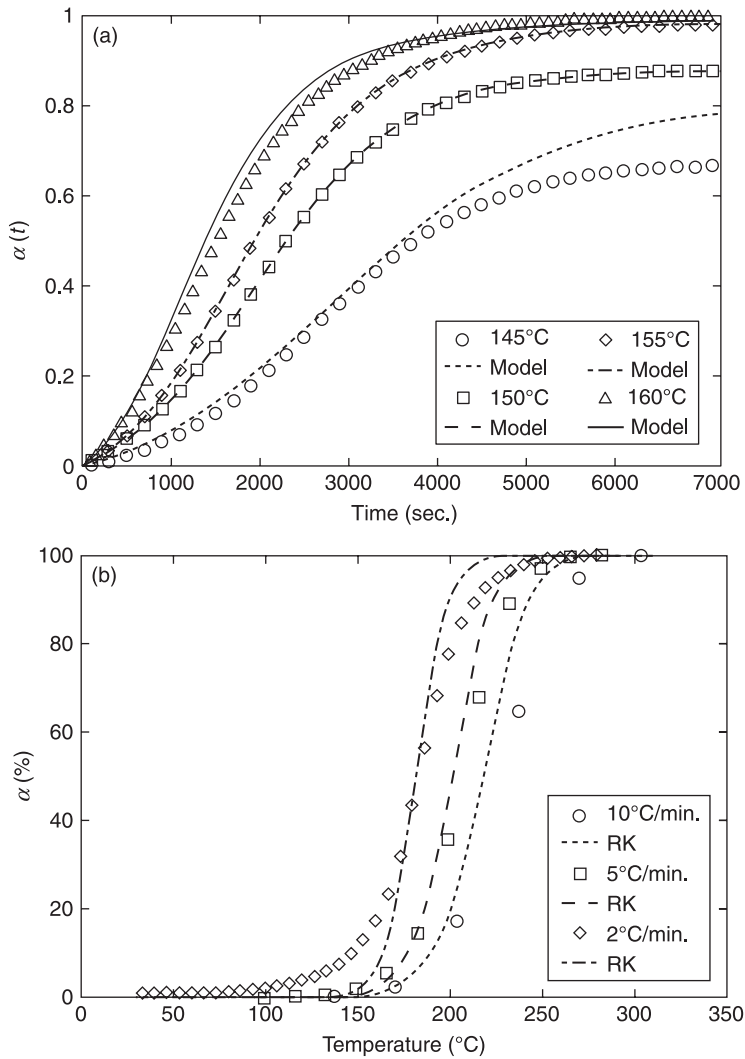
This section describes the chemorheological study of the 1%SWNTs (carboxylated)-epoxy system. Figure 8.8 presents the results of the kinetic study for isothermal and dynamic tests. It shows that a good agreement with the experimental test is obtained only for a high temperature and also for the dynamic



8.7 Chemorheological model for DGEBA–1% MWNTs.

Table 8.5 Parameters of the chemorheological model for the DGEBA–MDEA and DGEBA–1%MWNTs systems

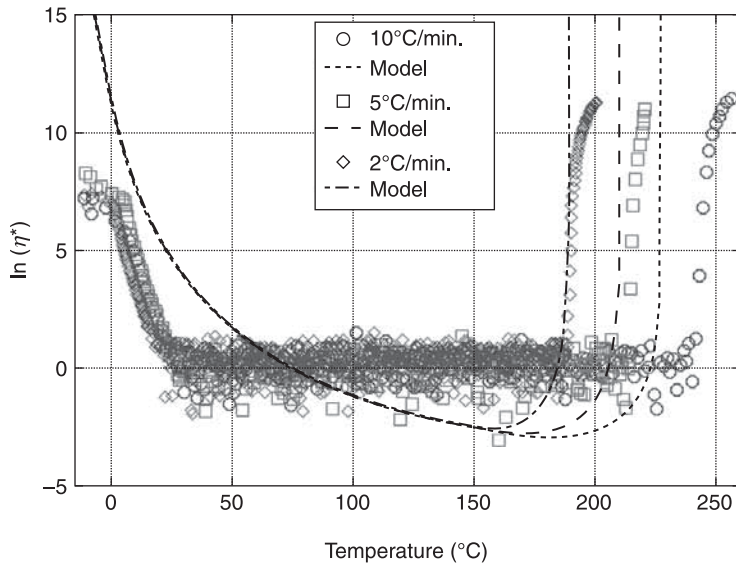
	Neat resin	DGEBA–1%MWNTs
ΔH (J/g)	–326.56	–352.2
<i>Rheological model</i>		
C_1	–35.16	–33.90
C_2	15.38	31.80
n_{rheo}	1.65	1.85
α_g	0.76	0.50
<i>Kinetic model</i>		
Ea_1 (J)	10934	6933
$\ln(K_1)$	6.60	7.19
m_1	0.15	–
n_1	1.07	0.56
Ea_2 (J)	8916	4998
$\ln(K_2)$	4.53	5.36
m_2	1.63	1.15
n_2	2.34	1.41
<i>Degree of cure</i>		
145°C	0.30	0.85
150°C	0.43	0.85
155°C	0.56	0.90
160°C	0.67	0.95
165°C	0.75	0.92
170°C	0.80	0.94
175°C	0.84	1.00
180°C	0.88	1.00
190°C	0.91	1.00
200°C	0.92	1.00
210°C	0.95	1.00



8.8 Kinetic model for DGEBA-1%SWNTs functionalized. Runge-Kutta (RK) integration of (a) isothermal fitting curves; (b) dynamic fitting curves.

test. The dynamic tests are also well described from the model. The rheological model is presented in Fig 8.9.

In Table 8.6, the parameters of the rheological and kinetic models are compared. As we can see, the degree of cure reached at 160°C for the DGEBA-SWNTs system is comparable to the degree reached for the DGEBA-DWNTs system. Anyway it is possible to argue that the CNTs' carboxylation affects the cure of the systems.



8.9 Chemorheological model for DGEBA–1% SWNTs functionalized.

The case study of neat SWNTs

As confirmation of the results obtained for the CNTs' carboxylated systems, a further test was conducted for the DGEBA–SWNTs non-functionalized system (Figs 8.10 and 8.11). As reported in the introduction to this chapter, the model used for the chemorheological characterization is different with respect to the other one used. However, this model can also describe very well the DGEBA–MWNTs system although the rheological curves are not as clearly represented (this due to a variation of the transducer sensibility). The results are summarized in Table 8.7. It is possible to see the degree of cure reached at 160°C is lower than the one reached for the DGEBA–SWNTs carboxylated system. However, the degree of cure reached is very high.

8.4.4 Conclusion

The carboxylation of the CNTs can affect the cure of the DGEBA systems; in particular, the presence of the carboxylation on CNTs has a catalytic effect. It has been observed how N-methyldiethanolamine modified carboxy-DWNTs are used to obtain a cross-linked epoxy nanocomposite. Calorimetric and rheological tests reveal how the presence of MDEA-modified CDWNTs has a strong influence on the maximum degree of cure and on the gel time of the epoxy system. The use of kinetic and chemorheological models shows excellent agreement with the experimental data, as the catalytic effect of the tubes was observed also in the

Table 8.6 Parameters of the chemorheological model for the DGEBA–MDEA and DGEBA–1%SWNTs functionalized systems

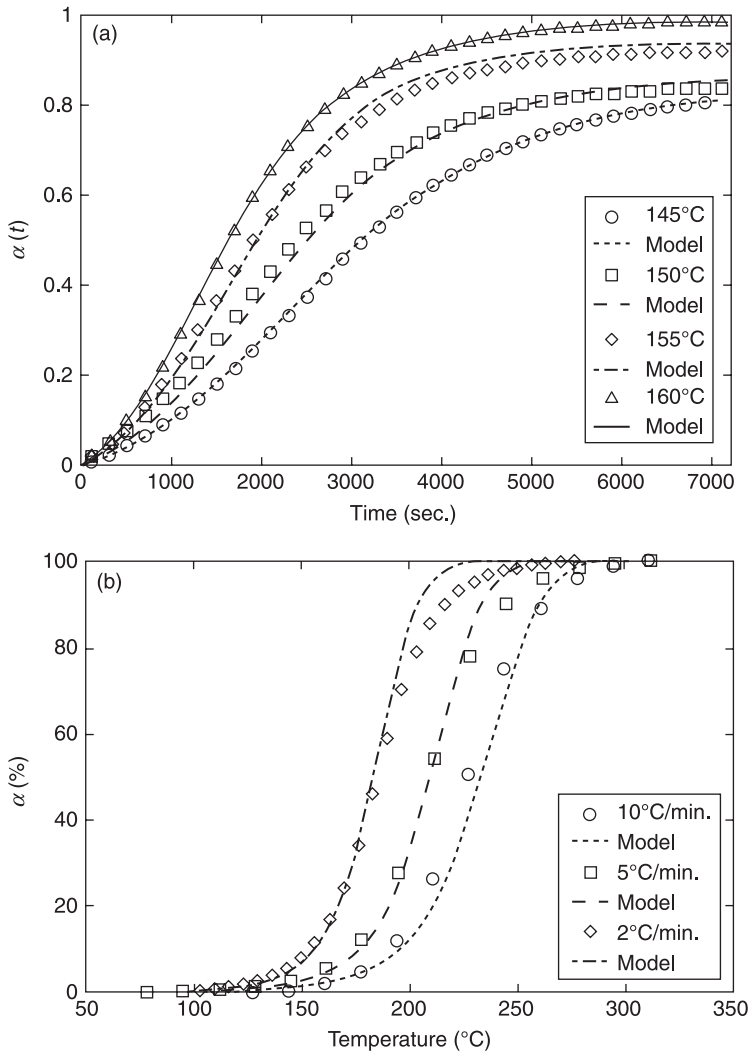
	Neat resin	DGEBA–1% SWNTs
ΔH (J/g)	–326.6	–376.0
<i>Rheological model</i>		
C_1	–35.16	–34.50
C_2	15.38	21.86
η_{rheo}	1.65	1.70
α_g	0.76	0.84
<i>Kinetic model</i>		
Ea_1 (J)	10934	10526
$\ln(K_1)$	6.60	15.820
m_1	0.15	0.04
n_1	1.07	1.24
Ea_2 (J)	8916	5977
$\ln(K_2)$	4.53	7.59
m_2	1.63	1.12
n_2	2.34	1.31
<i>Degree of cure</i>		
145°C	0.30	0.86
150°C	0.43	0.88
155°C	0.56	0.98
160°C	0.67	0.99
165°C	0.75	1.00
170°C	0.80	1.00
175°C	0.84	1.00
180°C	0.88	1.00
190°C	0.91	1.00
200°C	0.92	1.00
210°C	0.95	1.00

variation of specific parameters of these models. Following these indications, we claim that the presented synthesis strategy could have implications in building some novel architectures with nanotubes and polymers.

8.5 Properties of epoxy–CNT composites

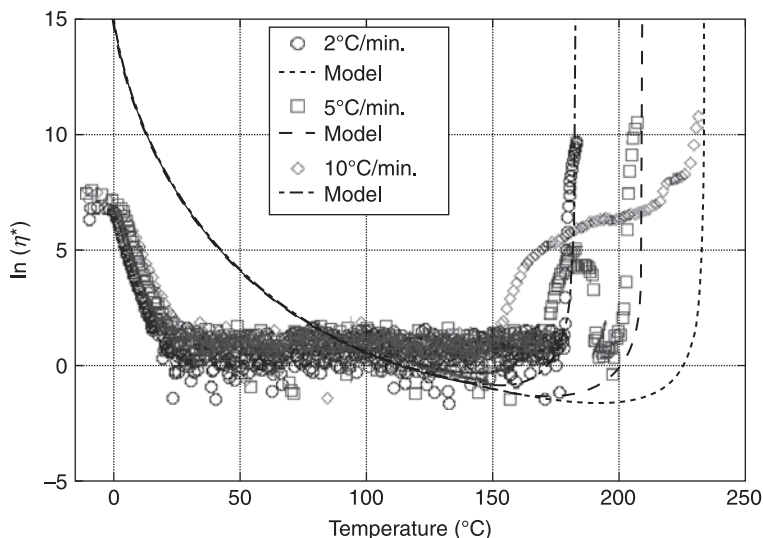
8.5.1 Thermal and mechanical properties

As reported in the previous sections, a homogeneous dispersion of carbon nanotubes in a polymer matrix is the first requirement to improve the thermal and mechanical properties. Xia *et al.*⁸¹ used a milling process to disperse their CNTs



8.10 Kinetic model for DGEBA–1%SWNTs non-functionalized. Runge–Kutta (RK) integration of (a) isothermal fitting curves; (b) dynamic fitting curves.

into a polyurethane–CNT composite with good dispersion and showed that the incorporation of well-dispersed nanotubes delayed the polymer degradation due to the thermo-oxidative stability of the polymer near the tube surface and an enhanced thermal conductivity of the composite rendering the heat transport easier, increasing the thermal stability through stabilized CNT-bonded macro-radicals.



8.11 Chemorheological model for DGEBA–1% SWNTs non-functionalized.

Other investigators have reported an improvement of the thermal stability by the interfacial bonding between the tubes and the polymer matrix due to covalent chemical linkages.^{82–84} Jung *et al.* reported multi-walled carbon nanotube–polyurethane nanocomposites via cross-linking of the polymer with carboxyl functionality of carbon nanotubes.⁸³ They prepared composites via an *in-situ* polymerization and showed that the modified carbon nanotubes induced better thermal stability in the composite. Kuan *et al.* prepared CNT-based composites and demonstrated that the covalent attachment improves the thermal stability with respect to the ionic one.⁸⁵ In the recent literature, it is also reported that the thermal conductivity of MWNT–epoxy composites can be enhanced (684%) with low MWNT loading (~5 vol%) using benzenetricarboxylic acids (BTC): the good dispersion and good compatibility of BTC–MWNTs in epoxy matrix provided higher efficiency than pristine-MWNTs and acid-treated MWNTs on the thermal conductivity enhancement of epoxy composites.⁸⁶

8.5.2 Electric and dielectric behaviour

The potential of nanotubes has been evidenced by the fact that an enhancement of several orders of magnitude was observed in the electrical conductivity at small loading (0.1 wt %), maintaining unaltered the optical transparency, the mechanical properties, viscosity, etc.⁸⁷ Several applications are being envisaged for these conductive systems: electrostatic dissipation, electromagnetic interference (EMI) shielding, printable circuit wiring, and transparent conductive coating.⁸⁸ Generally

Table 8.7 Parameters of the chemorheological model for the DGEBA–MDEA and DGEBA–1%SWNTs non-functionalized systems

	Neat resin	DGEBA–1% SWNTs
ΔH (J/g)	–326.56	–360.32
<i>Rheological model</i>		
C_1	–35.16	–34.07
C_2	15.38	31.08
η_{theo}	1.65	1.68
α_g	0.76	0.49
<i>Kinetic model</i>		
$Ea1$ (J)	10934	7001
$\ln(K1)$	6.60	7.23
$m1$	0.15	–
$n1$	1.07	0.62
$Ea2$ (J)	8916	5123
$\ln(K2)$	4.53	5.50
$m2$	1.63	1.17
$n2$	2.34	1.40
<i>Degree of cure</i>		
145°C	0.30	0.61
150°C	0.43	0.84
155°C	0.56	0.92
160°C	0.67	0.99
165°C	0.75	1.00
170°C	0.80	1.00
175°C	0.84	1.00
180°C	0.88	1.00
190°C	0.91	1.00
200°C	0.92	1.00
210°C	0.95	1.00

composites containing electrically conducting fillers become conductive when a three-dimensional conductive network of the fillers within the matrix has been created.

A CNT–epoxy system was reported by Kovacs *et al.*⁸⁹ In this case, percolation refers to randomly distributed filler particles that are free to move and can form a conducting network at lower particle concentrations. Particle movement can be caused by diffusion, shearing, or external fields.

The percolation threshold for the electrical conductivity in nanotube–polymer composites is influenced by several nanotube characteristics: aspect ratio,⁹⁰ dispersion⁹¹ and alignment.^{92,93} Bryning *et al.* prepared SWNT–epoxy composites and found a smaller percolation threshold with the higher aspect ratio nanotubes. Bai and Allaoui found that to improve the electrical conductivity, the length of

MWNTs had a dominant role. Regarding the mechanical properties, a good compromise of aggregate size and aspect ratio of MWNTs gave better results. Generally, since isolated well-dispersed nanotubes have a higher aspect ratio than entangled nanotube mats, the percolation threshold decreases with better dispersion. Bryning *et al.*,⁹⁴ on the contrary, demonstrated that slight aggregation induces a lower percolation threshold by increasing the 3D network. Alignment of the nanotubes in the polymer matrix has a strong effect on the electrical conductivity and on the percolation threshold. Aligned nanotubes in composites reduce the number of contacts between them, which results in an increase in the electrical resistivity as compared to those in a composite with entangled nanotubes. It is widely accepted that chemical functionalization disrupts the extended π -conjugation of nanotubes and thereby reduces the electrical conductivity of isolated nanotubes. However, it was found²⁴ how the functionalization can improve the electrical properties of the composites. For example, Valentini *et al.*²⁴ pointed out that the amine-functionalized SWNTs in an epoxy matrix allow migration of intrinsic charges, which contribute to the overall conductivity. It appears that the disadvantages of functionalization with respect to SWNT conductivity are balanced by the improved dispersion enabled by functionalization.

8.6 Conclusion and future trends

Polymers hold great promise for the widely applicable design and fabrication of structural and functional materials. A new paradigm of ordering polymeric materials at the mesoscale is required. Importantly, a novel approach must assist in bridging the gap between intrinsic properties of organic/inorganic materials and the final hybrid material.

Epoxy–CNT-based composites are one of the most versatile classes of materials today, considering their demand for industrial utilization. The application of such composites requires an understanding of the chemistry and processing as prerequisites to obtain tailor-made industrial products for high performance applications. The primary objective is to obtain a knowledge-based understanding of the raw carbon nanotubes, understanding the surface chemistry and processing tools used for designing polymer-based composites. This review emphasized the different functionalization processes and the parameters affecting the nanotube dispersability in polymeric matrices. We have also described different processing methods for incorporating such functional nanofillers into the polymer backbone. It was also reported how the use of functionalized carbon nanotubes can improve the thermal and mechanical properties, together with the electrical ones.

8.7 References

1. Kratschmer K, Lamb L D, Fostiropoulos K, Huffman R D, 'Solid C-60: a new form of carbon', *Nature*, 1990, 347, 354–358.

2. Iijima S, Ichihashi T, 'Single-shell carbon nanotubes of 1-nm diameter', *Nature*, 1993, 363, 603–605.
3. Baughman R H, Zakhidov A A, de Heer W A, 'Carbon nanotubes: the route toward applications', *Science*, 2002, 297, 787–792.
4. Thostenson E T, Ren Z, Chou T W, 'Advances in the science and technology of carbon nanotubes and their composites: a review', *Compos. Sci. Technol.*, 2001, 61, 1899–1912.
5. Dai L, Mau A W H, 'Controlled synthesis and modification of carbon nanotubes and C-60: carbon nanostructures for advanced polymer composite materials', *Adv. Mater.*, 2001, 13, 899–901.
6. Hirsch A, 'Functionalization of single-walled carbon nanotubes', *Angew. Chem., Int. Ed.*, 2002, 41, 1853–1859.
7. Bahr J L, Tour J M, 'Covalent chemistry of single-wall carbon nanotubes', *J. Mater. Chem.*, 2002, 12, 1952–1958.
8. Sinnott S B, 'Modification of carbon nanotube-polystyrene matrix composites through polyatomic-ion beam deposition: predictions from molecular dynamics simulations', *J. Nanosci. Nanotechnol.*, 2002, 2, 113–123.
9. Andrews R, Jacques D, Qian D, Rantell T, 'Multiwall carbon nanotubes: synthesis and application', *Acc. Chem. Res.*, 2002, 35, 1008–1017.
10. Fischer J E, 'Chemical doping of single-wall carbon nanotubes', *Acc. Chem. Res.*, 2002, 35, 1079–1086.
11. Rao C N R, Satishkumar B, Govindaraj A, Nath M, 'Nanotubes', *Chem.-Phys. Chem.*, 2001, 2, 78–105.
12. Sun Y-P, Fu K, Lin Y, Huang W, 'Functionalized carbon nanotubes: properties and applications', *Acc. Chem. Res.*, 2002, 35, 1096–1104.
13. Niyogi S, Hamon M A, Hu H, Zhao B, Bhowmik P, Sen R, Itkis M E, Haddon R C, 'Chemistry of single-walled carbon nanotubes', *Acc. Chem. Res.*, 2002, 35, 1105–1113.
14. Banerjee S, Hemraj-Benny T, Wong S S, 'Covalent surface chemistry of single-walled carbon nanotubes', *Adv. Mater.*, 2005, 17, 17–29.
15. De la Torre G, Blau W, Torres T, 'A survey on the functionalization of single-walled nanotubes: the chemical attachment of phthalocyanine moieties', *Nanotechnology*, 2003, 14, 765–771.
16. Davis J J, Coleman K S, Azamian B R, Bagshaw C B, Green M L H, 'Chemical and biochemical sensing with modified single walled carbon nanotubes', *Chem. Eur. J.*, 2003, 9, 3732–3739.
17. Tasis D, Tagmatarchis N, Georgakilas V, Prato M, 'Soluble carbon nanotubes', *Chem. Eur. J.*, 2003, 9, 4000.
18. Terrones M, 'Science and technology of the twenty-first century: synthesis, properties and applications of carbon nanotubes', *Annu. Rev. Mater. Res.*, 2003, 33, 419–501.
19. Katz E, Wilner I, 'Biomolecule-functionalized carbon nanotubes: applications in nanobioelectronics', *Chem. Phys. Chem.*, 2004, 5, 1084–1104.
20. Lu X, Chen Z, 'Curved Pi-conjugation, aromaticity, and the related chemistry of small fullerenes (< C-60) and single-walled carbon nanotubes', *Chem. Rev.*, 2005, 105, 3643–3696.
21. Nakashima N, Tomonari Y, Murakami H, 'Water-soluble single-walled carbon nanotubes via noncovalent sidewall-functionalization with a pyrene-carrying ammonium ion', *Chem. Lett.*, 2002, 31, 638–639.
22. Islam M F, Rojas E, Bergey D M, Johnson A T, Yodh A G, 'High weight fraction surfactant solubilization of single-wall carbon nanotubes in water', *Nano. Lett.*, 2003, 3, 269–273.

23. Puglia D, Valentini L, Armentano I, Kenny J M, 'Effects of single-walled carbon nanotube incorporation on the cure reaction of epoxy resin and its detection by Raman spectroscopy', *Diamond and Related Materials*, 2003, 12, 827–832.
24. Valentini L, Armentano I, Puglia D, Kenny J M, 'Dynamics of amine functionalized nanotubes/epoxy composites by dielectric relaxation spectroscopy', *Carbon*, 2003, 42, 323–329.
25. Xie H, Liu B, Yuan Z, Shen J, Cheng R, 'Cure kinetics of carbon nanotube/tetrafunctional epoxy nanocomposites by isothermal differential scanning calorimetry', *Journal of Polymer Science Part B: Polymer Physics*, 2004, 42, 3701–3712.
26. Tao K, Yang S, Grunlan J C, Kim Y-S, Dang B, Deng Y, Thomas R L, Wilson B L, Wei X, 'Effects of carbon nanotube fillers on the curing processes of epoxy resin-based composites', *Journal of Applied Polymer Science*, 2006, 102, 5248–5254.
27. Wu J, Chung D D L, 'Calorimetric study of the effect of carbon fillers on the curing of epoxy', *Carbon*, 2004, 42, 3039–3042.
28. Bae J, Jang J, Yoon S-H, 'Cure behavior of the liquid-crystalline epoxy/carbon nanotube system and the effect of surface treatment of carbon fillers on cure reaction', *Macromolecular Chemistry and Physics*, 2002, 203, 2196–2204.
29. Puglia D, Valentini L, Kenny J M, 'Analysis of the cure reaction of carbon nanotubes/epoxy resin composites through thermal analysis and Raman spectroscopy', *J. Appl. Polym. Sci.* 2003, 88, 452–458.
30. Valentini L, Puglia D, Frulloni E, Armentano I, Kenny J M, Santucci S, 'Dielectric behavior of epoxy matrix/single-walled carbon nanotube composites', *Compos. Sci. Technol.*, 2004, 64, 23–33.
31. Zhu, J, Yudasaka, M, Zhang, M, Kasuya, D, Iijima, S, 'Surface modification approach to the patterned assembly of single-walled carbon nanomaterials', *Nano. Lett.*, 2003, 3, 1239–1243.
32. Moore, V C, Strano, M S, Haroz, E H, Hauge, R H, Smalley, R E, Schmidt, J, Talmon, Y, 'Individually suspended single-walled carbon nanotubes in various surfactants', *Nano. Letters*, 2003, 3(10), 1379–1382.
33. O'Connell, M J, Bachilo, S M, Huffman, C B, Moore, V C, Strano, M S, Haroz, E H, Rialon, K L, Boul, P J, Noon, W H, Kittrell, C, Ma, J, Hauge, R H, Weisman, R B, Smalley, R E, 'Band gap fluorescence from individual single-walled carbon nanotubes', *Science*, 2002, 297, 593–596.
34. Yurekli, K, Mitchell, C A, Krishnamoorti, R, 'Small-angle neutron scattering from surfactant-assisted aqueous dispersions of carbon nanotubes', *J. Am. Chem. Soc.*, 2004, 126, 9902–9903.
35. Gong, X Y, Liu, J, Baskaran, S, Voise, R D, Young, J S, 'Surfactant-assisted processing of carbon nanotube/polymer composites', *Chem. Mater.*, 2000, 12, 1049–1052.
36. Calvert, P D, 'Nanotube composites – A recipe for strength', *Nature*, 1999, 399, 210–211.
37. Andrews, R, Weisenberger, M C, 'Carbon nanotube polymer composites', *Curr. Opin. Solid. State. Mater. Sci.*, 2004, 8, 31–37.
38. Plank, N O V, Forrest, G A, Cheung, R, Alexander, A J, 'Electronic properties of n-type carbon nanotubes prepared by cf₄ plasma fluorination and amino functionalization', *J. Phys. Chem. B*, 2005, 109, 22096–22101.
39. Wang, Y Q, Sherwood, P M A, 'Studies of carbon nanotubes and fluorinated nanotubes by X-ray and ultraviolet photoelectron spectroscopy', *Chem. Mater.*, 2004, 16, 5427–5436.
40. Zhang, L, Kiny, V U, Peng, H, Zhu, J, Lobo, R F M, Margrave, J L, Khabashesku, V N, 'Sidewall functionalization of single-walled carbon nanotubes with hydroxyl group-terminated moieties', *Chem. Mater.*, 2004, 16, 2055–2061.

41. Pehrsson, P E, Zhao, W, Baldwin, J W, Song, C, Liu, J, Kooi, S, Zheng, B, 'Thermal fluorination and annealing of single-wall carbon nanotubes', *J. Phys. Chem. B*, 2003, 107, 5690–5695.
42. Stevens, J L, Huang, A Y, Peng, H, Chiang, I W, Khabashesku, V N, Margrave, J L, 'Sidewall amino-functionalization of single-walled carbon nanotubes through fluorination and subsequent reactions with terminal diamines', *Nano. Lett.*, 2003, 3, 331–336.
43. Khabashesku, V N, Billups, W E, Margrave, J L, 'Fluorination of single-wall carbon nanotubes and subsequent derivatization reactions', *Acc. Chem. Res.*, 2002, 35, 1087–1095.
44. Khare, B N, Wilhite, P, Meyyappan, M, 'The fluorination of single wall carbon nanotubes using microwave plasma', *Nanotechnology*, 2004, 15, 1650–1654.
45. Felten, A, Bittencourt, C, Pireaux, J J, 'Radio-frequency plasma functionalization of carbon nanotubes surface O-2, NH3, and CF4 treatments', *J. Appl. Phys.*, 2005, 98.
46. Valentini, L, Puglia, D, Armentano, I, Kenny, J M, 'Sidewall functionalization of single-walled carbon nanotubes through CF4 plasma treatment and subsequent reaction with aliphatic amines', *Chem. Phys. Lett.*, 2005, 403, 385–388.
47. Valentini, L, Armentano, I, Mengoni, F, Puglia, D, Pennelli, G, Kenny, J M, 'Chemical gating and photoconductivity of CF4 plasma functionalized single-walled carbon nanotubes by butylamine', *J. Appl. Phys.*, 2005, 97, 114320–114325.
48. Yousefi A, Lajleur P G, Gauuin R, 'Kinetic studies of thermoset cure reactions: a review', *Polymer Composites*, 1997, 18, 157–168.
49. Lunak, S, Vladyka, J, Dusek, K, 'Effect of the diffusion control on the gel point conversion in curing of epoxy resins', *Polymer*, 1998, 19, 931–933.
50. Bair, H E, Ludwick, A G, *Am Phys 13th North American Thermal Analysis Society Annual Meeting*, 1984, 224; and Huguenin, F G T, Klein, M, 'Intrinsic and transport-limited epoxyamine cure kinetics', *Industrial & Engineering Chemistry Product Research and Development*, 1985, 24, 166–171.
51. Dusek K, Havlicek I, 'Diffusion controlled kinetics of crosslinking', *Progress in Organic Coatings*, 1993, 22, 145–159.
52. Matsuoka S, Quan X, Bair H E, Boyle D J, 'A model for the curing reaction of epoxy resins', *Macromolecules*, 1989, 22, 4093–4098.
53. Bidstrup S A, Macosko CW, 'Chemorheology relations for epoxy-amine crosslinking', *J. Polym. Sci., Part B Polym. Phys.*, 1990, 28, 691–709.
54. Scott, Chris E, Macosko, CW, 'Characterization of reactive blending kinetics', *Polymeric Materials Science and Engineering, Proceedings of the ACS Division of Polymeric Materials Science and Engineering*, 1988, 58, pp. 104.
55. Shimbo M, Ochi M, Arai K, 'Internal stress of cured epoxide resin coatings having different network chains', *J. Coat. Technol.*, 1984, 56 (713), 45–51.
56. Stutz H, Illers K H, Mertes J, 'A generalized theory for the glass transition temperature of crosslinked and uncrosslinked polymers', *J. Polym. Sci. Part B: Polym. Phys.*, 1990, 28, 1483–1498.
57. Barton, J. M, 'Kinetics of cure of epoxy resin system bisphenol-A diglycidyletherdi(4-aminophenyl)sulphone', *Polymer*, 1980, 21, 603–606.
58. Adabbo H E, Williams R J J, 'The evolution of thermosetting polymers in a conversion-temperature phase diagram', *J. Appl. Polym. Sci.*, 1982, 27, 1327.
59. Barrau S, Demont P, Maraval C, Bernes A, Lacabanne C, 'Glass transition temperature depression at the percolation threshold in carbon nanotube-epoxy resin and polypyrrole-epoxy resin composites', *Macromolecular Rapid Communications*, 2005, 26, 390–394.

60. Enns J, Gillham B, 'Time-temperature-transformation (TTT) cure diagram: modeling the cure behavior of thermosets', *J. Appl. Polym. Sci.*, 1983, 28, 2567–2591.
61. Bair, H. E., *Polym. Prepr. Am. Chem.* 1985, 26, 10.
62. Pang K P, Gillham J K, 'Anomalous behavior of cured epoxy resins: density at room temperature versus time and temperature of cure', *J. Appl. Polym. Sci.*, 1989, 37, 1969–1991.
63. Riccardi C C, Adabbo H E, Williams R J J, 'Curing reaction of epoxy resins with diamines', *J. Appl. Polym. Sci.*, 1984, 29, 2481–2492.
64. Nielsen L E, 'Cross-linking-effect on physical properties of polymers', *Polymer Reviews*, 1969, 3, 69–103.
65. Theriault R P, Osswald T A, Castro J M, 'Processing induced residual stress in asymmetric laminate panels', *Polymer Composites*, 1999, 20, 493–509.
66. Di Benedetto, A T, 'Prediction of the glass transition temperature of polymers: a model based on the principle of corresponding states', *Journal of Polymer Science, Part B: Polymer Physics*, 1987, 25, 1949–1969.
67. Tajima Y A, Crozier D G, 'Thermokinetic modeling of an epoxy resin I. Chemoviscosity', *Polym. Eng. Sci.*, 1983, 23, 186–190.
68. Ryan M E, 'Rheological and heat-transfer considerations for the processing of reactive systems', *Polym. Eng. Sci.*, 1984, 24, 698–706.
69. White R P, 'Time-temperature superpositioning of viscosity-time profiles of three high temperature epoxy resins', *Journal Polym. Eng. Sci.*, 1974, 14, 50–57.
70. Tajima Y A, Crozier D G, 'Chemorheology of an amine-cured epoxy resin', *Polym. Eng. Sci.*, 1986, 28, 427–431.
71. Roller M B, 'Rheology of curing thermosets: a review', *Polym. Eng. Sci.*, 1986, 28, 432–440.
72. Roller M B, 'Characterization of the time-temperature-viscosity behavior of curing B-staged epoxy resin', *Polym. Eng. Sci.*, 1975, 15, 406–414.
73. Eley, R. R., *ACS Symposium Series*, Washington, DC, 1983.
74. Kamal M R, Ryan M E, 'Models of material behavior', in C L Tucker (ed.) *Fundamentals of Computer Modeling for Polymer Processing*, Munich: Hanser Publishers, 1989.
75. Tungare A V, Martin G C, Gotro J T, 'Chemorheological characterization of thermoset cure', *Polym. Eng. Sci.*, 1988, 28, 1071–1077.
76. Ryan M E, *The Injection Molding of Thermosets*, Montreal: McGill University, 1978.
77. Tajima Y A, Crozier D G, 'Thermokinetic modeling of an epoxy resin I. Chemoviscosity', *Polym. Eng. Sci.*, 1988, 23, 186–190.
78. Lee, D S, Han, C D, 'A chemorheological model for the cure of unsaturated polyester resin', *Polym. Eng. Sci.*, 1987, 27, 955–963.
79. Terenzi A, Vedova C, Lelli G, Mijovic J, Torre L, Valentini L, Kenny J M, 'Chemorheological behaviour of double-walled carbon nanotube-epoxy nanocomposites', *Comp. Sci. Technol.*, 2008, 68, 1862–1868.
80. Janezic D, Orel B, 'Implicit Runge-Kutta method for molecular dynamics integration', *J. Chem. Inf. Comput. Sci.*, 1993, 33, 252–257.
81. Xia H, Song M, 'Preparation and characterization of polyurethane-carbon nanotube composites', *Soft Matter*, 2005, 1, 386–394.
82. Sahoo N G, Jung Y C, Yoo H J, Cho J W, 'Effect of functionalized carbon nanotubes on molecular interaction and properties of polyurethane composites', *Macromol. Chem. Phys.*, 2006, 207, 1773–1780.

83. Jung Y C, Sahoo N G, Cho J W, 'Polymeric nanocomposites of polyurethane block copolymers and functionalized multi-walled carbon nanotubes as crosslinkers', *Macromol. Rapid. Commun.*, 2006, 27, 126–131.
84. Gojny F H, Nastalczyk J, Roslaniec Z, Schelte K, 'Surface modified multi-walled carbon nanotubes in CNT/epoxy-composites', *Chem. Phys. Lett.*, 2003, 370, 820–824.
85. Kuan H C, Ma C H M, Chang W P, Yuen S M, Wu H H, Lee T M, 'Synthesis, thermal, mechanical and rheological properties of multiwall carbon nanotube/waterborne polyurethane nanocomposite', *Compos. Sci. Technol.*, 2005, 65, 1703–1710.
86. Yang S Y, Ma C C M, Teng C C, Huang Y W, Liao S H, Huang Y L, Tien H W, Lee T M, Chiou K C., 'Effect of functionalized carbon nanotubes on the thermal conductivity of epoxy composites', *Carbon*, 2010, 48, 592–603.
87. Bryning M B, Islam M F, Kikkawa J M, Yodh A G, 'Very low conductivity threshold in bulk isotropic single-walled carbon nanotube-epoxy composites', *Adv. Mater.*, 2005, 17, 1186–1191.
88. Baughman R H, Zakhidov A A, de Heer W A, 'Carbon nanotubes: the route toward applications', *Science*, 2002, 297, 787–792.
89. Kovacs J Z, Velagala B S, Schulte K, Bauhofer W, 'Two percolation thresholds in carbon nanotube epoxy composites', *Compos. Sci. Technol.*, 2007, 67, 922–928.
90. Bai J B, Allaoui A, 'Effect of the length and the aggregate size of MWNTs on the improvement efficiency of the mechanical and electrical properties of nanocomposites: experimental investigation', *Composites, Part A*, 2003, 34, 689–694.
91. Barrau S, Demont P, Perez E, Peigney A, Laurent C, Lacabanne C, 'Effect of palmitic acid on the electrical conductivity of carbon nanotubes-epoxy resin composites', *Macromolecules*, 2003, 36, 9678–9680.
92. Du F, Fischer J E, Winey K I, 'Coagulation method for preparing single-walled carbon nanotube/poly(methyl methacrylate) composites and their modulus, electrical conductivity, and thermal stability', *J. Polym. Sci., Part B: Polym. Phys.*, 2003, 41, 3333–3338.
93. Haggenueller R, Gommans H H, Rinzier A G, Fischer J E, 'Aligned single-wall carbon nanotubes in composites by melt processing methods', *Chem. Phys. Lett.*, 2000, 330, 219–225.
94. Bryning M B, Islam M F, Kikkawa J M, Yodh A G, 'Very low conductivity threshold in bulk isotropic single-walled carbon nanotube-epoxy composites' *Adv. Mater.*, 2005, 17, 1186–1191.

Quantification of dispersion and distribution of carbon nanotubes in polymer composites using microscopy techniques

S. PEGEL, T. VILLMOW and P. PÖTSCHKE,
Leibniz Institute of Polymer Research Dresden, Germany

Abstract: Different stereological approaches have been applied to micrographs of light microscopy and transmission electron microscopy to estimate the degree of carbon nanotube dispersion in polymer composites at different length scales. Quantitative information about the spatial relationships between individual carbon nanotubes has been obtained by means of the spherical contact distribution function and a Boolean fibre model. The correlation function has been used to gain an orientation factor as a measure of carbon nanotube alignment. The corresponding theoretical foundations and suitable digital image processing techniques are introduced and illustrated with some specific examples.

Key words: carbon nanotube composites, dispersion analysis, image processing.

9.1 Introduction

The quantification of carbon nanotube (CNT) dispersion, distribution, and alignment within polymeric matrices can help gain a better understanding of structure–property relationships, to perform quality controls, or to optimize processing conditions. The aim of this chapter is to introduce some basic microscopy-based techniques to gain such morphological information.

Regarding polymer–CNT composites, the dispersion process refers to the individualization or spreading of the CNTs within the polymer matrix. Thus, the state of dispersion is commonly understood to describe the relationship between dispersed and not dispersed CNTs. For the purpose of dispersion quantification, the general degree of dispersion D can be defined straightforwardly as the ratio between the volume fraction of dispersed nanotubes V_{VD} and the total volume fraction V_{VT} of CNTs:

$$D = \frac{V_{VD}}{V_{VT}}. \quad [9.1]$$

The quantity V_{VT} is given by the composition of the mixture and can be estimated from the mass fraction $w = (m_{CNT}/(m_{CNT} + m_M))$ and the density ratio of matrix $v = \rho_M/\rho_{CNT}$ of matrix and carbon nanotube material, respectively, using Equation 9.2.

$$V_{VT} = \frac{v \cdot w}{1 + v \cdot w - w} \quad [9.2]$$

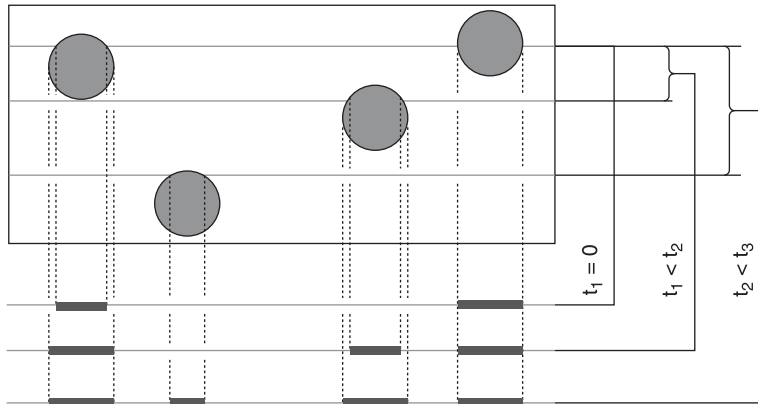
In contrast to V_{VT} , the estimation of V_{VD} is more difficult. Since only isolated CNTs (not in touch with other CNTs) can be considered as dispersed, the connectivity of every single CNT to its next neighbour has to be investigated. This can be managed practically only by using very elaborate techniques such as TEM tomography which offers nanometre resolution. However, in order to gain meaningful information about the composite morphology using simpler and more accessible methods, the definition of the term dispersion has to be reduced or differentiated.

In the case of light microscopy (LM), agglomerates larger than 1 μm can be detected. The corresponding agglomerate area fraction A_A is the ratio of the cumulative area fraction of all agglomerates within a micrograph and the total area of the micrograph, and therefore is sometimes referred to as the area ratio. This quantity is related to the amount of non-dispersed CNT and has been used as a simple measure for dispersion (the higher the A_A , the worse the dispersion, Kasaliwal *et al.*, 2010; Krause *et al.*, 2010). Additionally, the agglomerate size distribution, number density (Villmow *et al.*, 2008b; Kasaliwal *et al.*, 2010) as well as spatial relationships between the agglomerates have been evaluated to gain information about processing–structure–property relationships (Kashiwagi *et al.*, 2007; Li *et al.*, 2007).

Next to scanning electron microscopy (SEM) and atomic force microscopy (AFM), transmission electron microscopy (TEM) is used to gain information about CNT dispersion in the submicrometre range (Pötschke *et al.*, 2004; Pötschke *et al.*, 2008). In all cases it is commonly understood that the quality of dispersion increases with increasing spatial separation between neighbouring CNTs. Nevertheless, quantitative investigations concerning spatial relationships between individual CNTs are rarely performed. Bellayer *et al.* (2005), for instance, evaluated the nearest neighbour distance distribution of the nanotube centres within TEM micrographs to access a quantity for CNT dispersion. However, it has to be considered that the 2D micrographs only partially reflect the 3D structure of the material, i.e. the 3D nearest neighbour distance distribution cannot be evaluated by means of 2D micrographs. Thus the ‘true’ dispersion situation cannot be resolved.

Generally, quantitative morphological investigations based on classical microscopic techniques have to be carried out carefully. Next to the corresponding 3D morphology, the content of nanotubes or agglomerates observed in a micrograph depends on the section thickness t as schematically shown in Fig. 9.1. It can easily be seen that the number of objects involved in the projection increases with t . In the case of opaque spheres embedded in a transparent medium this means an increase of the A_A with increasing t . Additionally, the 2D, particle size distribution (PSD) is dependent on t . This is also known as the Wicksell corpuscle problem (Wicksell, 1925).

The former considerations show that morphological quantities of the 3D structures, e.g. the volume content of a certain phase, can only be estimated by

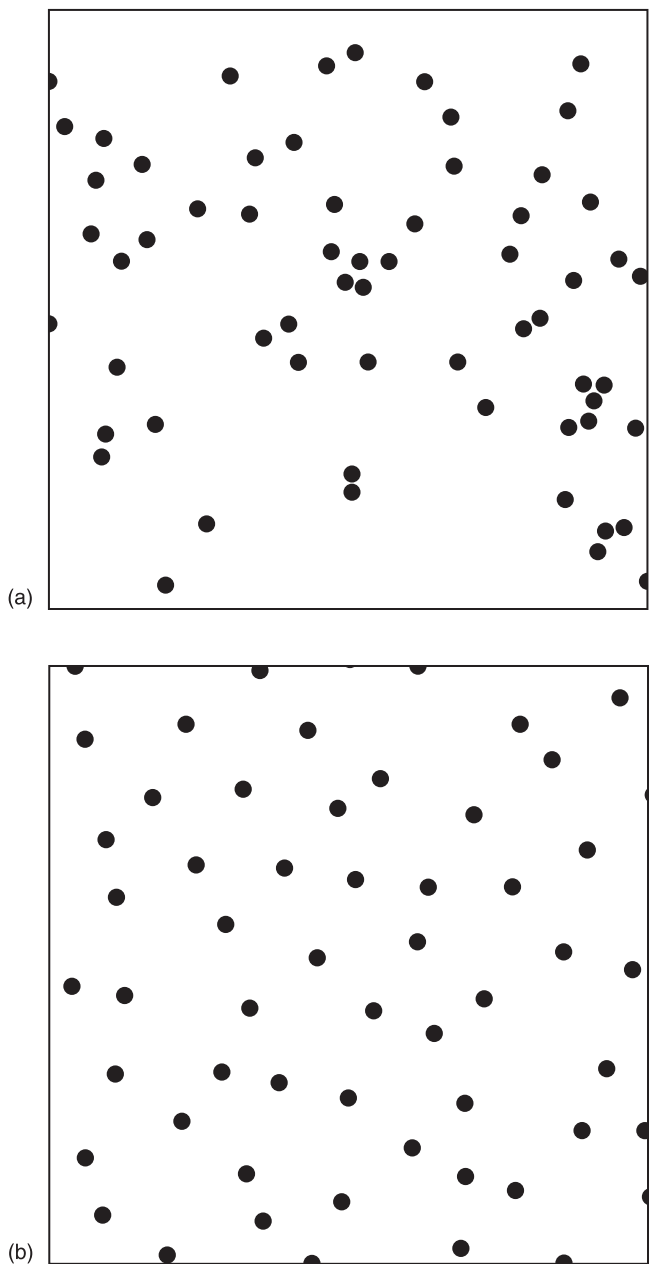


9.1 Schematic of the relationship between section thickness and features appearing in projections or micrographs.

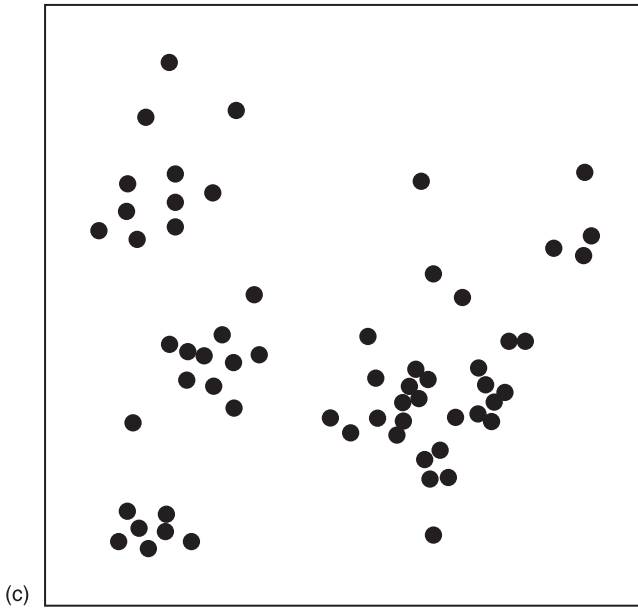
means of suitable stereological approaches. In Section 9.2.1, a germ grain model will be applied to LM micrographs to get an unbiased estimate of the CNT agglomerate volume fraction in polymer CNT composites. It can be used to estimate the light microscopy degree of dispersion D_{LM} . In Section 9.3.1, a stereological approach for fibre processes will be used to get an unbiased estimate of V_{VD} directly from TEM micrographs. Accordingly, the TEM degree of dispersion D_{TEM} will be derived.

Next to the dispersion, it can be important to obtain more detailed information about the spatial distribution of individual CNTs within polymer matrices. Principally, morphologies with ‘correlated’ and ‘uncorrelated’ covering probabilities can be distinguished. In the case of ‘uncorrelated’ covering probability, the CNTs are randomly distributed in space (Poisson distribution) as shown exemplarily by means of the 2D point pattern of Fig. 9.2 (a). In contrast, Figs 9.2 (b) and 9.2 (c) show examples with ‘correlated’ probabilities. For ‘hard core’ processes, the covering probability near an object is smaller as compared to the left space (Fig. 9.2 (b)). For ‘cluster’ processes the covering probability near an object is larger, compared to the left space (Fig. 9.2 (c)). In Section 9.3.2, the distribution coefficient Q_p is introduced as a measure for the tendency of CNT cluster formation.

CNT alignment is another important aspect of CNT microstructure. Principally, it can be quantified by means of X-ray (Jin *et al.*, 1998; Fischer *et al.*, 2003; Sandler *et al.*, 2004; Du *et al.*, 2005; Fornes *et al.*, 2006) or Raman (Wood *et al.*, 2001; Bhattacharyya *et al.*, 2003; Fischer *et al.*, 2003; Pötschke *et al.*, 2005; Fornes *et al.*, 2006) scattering experiments. However, due to the limitations in focusing the X-ray or laser beam, the spatial resolution is limited for these methods. Furthermore, low filler contents cause high signal-to-noise ratios. The statistical analysis of suitable micrographs can provide information about CNT alignment at high resolutions and low filler contents. Shaffer *et al.* (1998) have already demonstrated



9.2 Different spatial distributions of random point pattern: (a) Poisson distribution; (b) hard core; (c) cluster process.



9.2 Continued.

the use of the power spectrum to evaluate local order parameters for different CNT films by means of scanning electron micrographs. In Sections 9.3.3 and 9.3.4, the similar covariance (Stoyan *et al.*, 1987) or two point probability function (Torquato, 2006) is used to derive an orientation factor for CNTs.

9.2 Light microscopy

It is recommended to always start morphological investigations on polymer CNT composites with light microscopy, as the existence of remaining primary agglomerates can easily be seen. LM is a fast and comparatively simple method capable of investigating relatively large sample volumes.

9.2.1 Degree of dispersion

Due to the resolution limit of light microscopy, agglomerates in the micrometre range and below (typically $< 1\mu\text{m}$ diameter) are considered to belong to the fraction of dispersed fillers. The volume fraction of non-dispersed CNTs is given by the product: $f \cdot V_{VA}$, where V_{VA} is the volume fraction of agglomerates and f the packing density or volume fraction of CNT within the agglomerates. Thus, the volume fraction of dispersed nanotubes is given by: $V_{VD} = V_{VT} - f \cdot V_{VA}$. Together with Equation 9.1, this leads to the light microscopic degree of dispersion:

$$D_{LM} = 1 - \frac{f \cdot V_{VA}}{V_{VT}}. \quad [9.3]$$

This calculation is similar to the macroscopic dispersion index used for rubber carbon black compounds (ASTM, 2008) and has been successfully applied also to rubber CNT composites by Le *et al.* (2009). For the packing density f , Le used a value of 0.25 without further explanation. The investigations were performed on planar sections ($t = 0$) and thus D_{LM} could be estimated quite easily by means of the stereological formula $V_{VA} = A_A$.

However, sometimes it is not possible to obtain suitable planar micrographs which can be analysed properly, for instance, due to bad contrast between matrix and agglomerates or artefacts resulting from sample preparation (e.g. scratches on the sample surface). In such cases, the slightly more elaborated evaluation of thin sections can be helpful. If the sections are thin enough, the agglomerates do not overlap in the projection and A_A depends linearly on t (Stoyan *et al.*, 1987):

$$A_A(t) = \frac{S_{VA}}{4} t + V_{VA}. \quad [9.4]$$

The constant of proportionality is given by a quarter of the volume specific surface of the agglomerates S_{VA} . The agglomerate volume fraction can be obtained by analysing series of sections with different thicknesses and extrapolation of A_A towards $t = 0$.

Next to V_{VA} , an estimate of f is needed to evaluate D_{LM} . Usually, the infiltration method can be used to get a rough estimate of pure CNT materials. For this purpose the nanotube material is infiltrated with a low viscosity epoxy resin. After curing of the resin, V_{VA} is estimated for the infiltrated material by means of LM and the stereological approach as described before. If no swelling takes place, the infiltrated material can be considered as a composite with $D_{LM} = 0$ and together with V_{VA} and the known value of V_{VT} , Equation 9.3 can be solved for f . Thus, f is basically given by the ratio of V_{VT} and V_{VA} ($f = V_{VT}/V_{VA}$). If it is not possible to estimate the packing density of a CNT material with the infiltration method, it is appropriate to obtain a lower bound f_{min} using the nanotube powder density ρ_P . Due to the empty spaces between the agglomerates, the packing density must be larger than $f_{min} = \rho_P/\rho_{CNT}$. An upper bound of the packing density f_{max} can be estimated by uniaxial compression tests of the crude CNT material up to pressures expected in the processing equipment, for instance.

Since the three quantities V_{VA} , V_{VT} and f are experimentally determined, they contain uncertainties. The propagation of uncertainty leads to:

$$u_{DLM} = \sqrt{\left(\frac{V_{VA}}{V_{VT}} u_f\right)^2 + \left(\frac{f}{V_{VT}} u_{VA}\right)^2 + \left(\frac{f \cdot V_{VA}}{V_{VT}^2} u_{VT}\right)^2}, \quad [9.5]$$

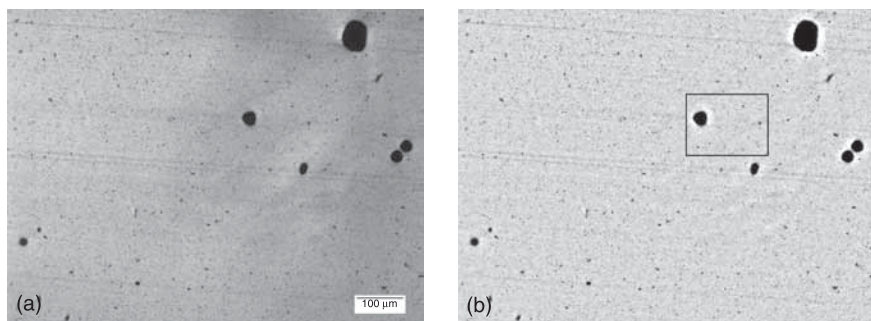
with the uncertainties u_{DLM} , u_f , u_{VA} and u_{VT} of the degree of dispersion, based on light microscopy packing density, agglomerate volume fraction and total volume fraction of incorporated nanotubes.

9.2.2 Digital image processing and specific examples

For the evaluation of the agglomerate area fraction A_A , the light microscopic micrographs have to be segmented adequately. This means that the content of the digital image has to be assigned either to the matrix or the agglomerates. Usually, the pixels are simply reassigned to black and white (binarization). In the present case, the binarization can be carried out by application of a global threshold to the intensity of background corrected grey scaled images.

The background correction is applied to obtain an even background illumination and to improve the contrast of the agglomerates. Most of the commercially and freely available image processing systems, e.g. ImageJ (Abramoff *et al.*, 2004; Rasband, 2008) provide more or less suitable functions for this purpose. Comparatively good results can be obtained with the following procedure: A mean filter is applied to a copy of the original image. To avoid artefacts, the filter size has to be in the range of the largest agglomerates. A new image is created whereby the filtered image is compared with the original and the brighter pixels have been taken over. The mean filter is applied to the result again. Finally, each pixel is divided by the corresponding value of the original. In Figs 9.3 (a) and 9.3 (b) this is demonstrated for a sample with 1 wt% multi-walled CNTs (MWCNTs) in polycarbonate (PC).

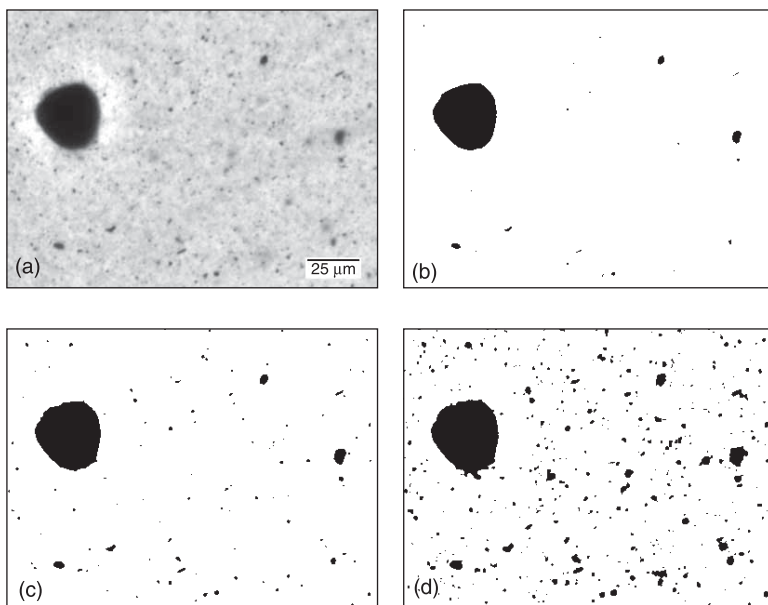
To determine adequate threshold values, some automated algorithms are available (Sahoo *et al.*, 1988; Russ and Woods, 1995; Sezgin and Sankur, 2004). Most of these techniques evaluate the distribution of grey values (Otsu, 1975; Kapur *et al.*, 1985). However, in the case of the presence of many small agglomerates with weak contrasts to the background, the corresponding histograms do not provide sufficient information and such algorithms are not applicable (Figs 9.4 (a)–(e)). Comparatively good results can be obtained with the feature-based algorithm described as follows: The correlation between the threshold and number of individual objects with roundness less than 0.5 is determined (Fig. 9.4 (e)). Generally, the number of detected objects increases with the threshold until a strong maximum is reached. This can be attributed to the inclusion of more and more background pixels which form objects with very irregular



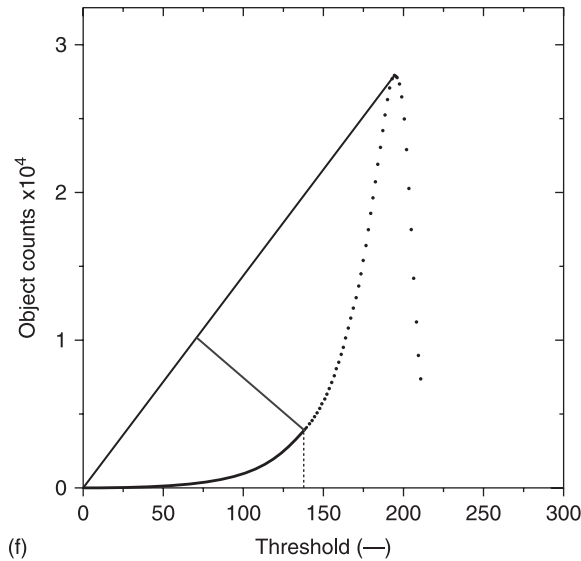
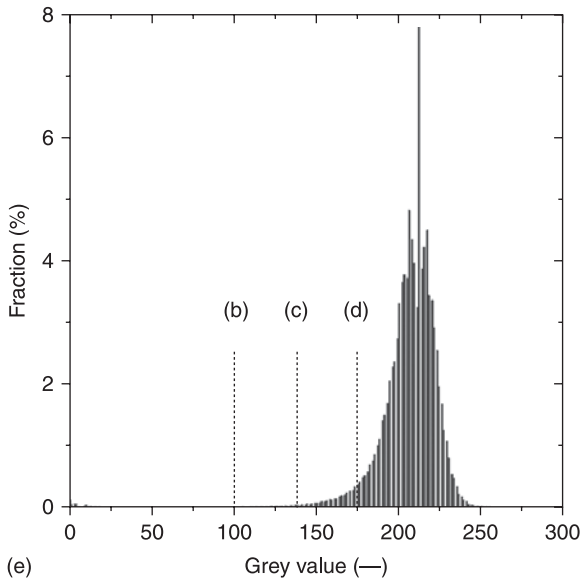
9.3 Application of a background correction procedure to an LM micrograph: (a) original; (b) filtered image.

shapes. On exceeding the maximum, the individual objects aggregate and thus the total amount decreases. The binarization threshold is given by the longest distance between the curve and a straight line between the maximum and the origin of the diagram. To the binarized image, the morphological filter 'open' is applied to remove smaller objects (Fig. 9.4 (f)). The area fraction of agglomerates is given simply by the ratio of the black and total amount of pixels, which can be accessed by the histogram of the binary image.

As an example, two composites with 1 wt% MWCNT (Nanocyl 7000, from Nanocyl S.A., Belgium) in PC processed under different melt mixing conditions are considered. The samples were processed with a small-scale batch compounder (such as described in Chapter 4) at 240°C and 50 rpm. Sample 1 was mixed for 30 min and sample 2 for 5 min. Light microscopy ($t = 25\ \mu\text{m}$) reveals a better filler dispersion for sample 1 as compared to sample 2 as indicated by the lower amount of visible agglomerates (Figs 9.5 (a) and 9.5 (b)). The evaluation of several digital micrographs as previously described leads to the relationship between the section thickness and the agglomerate area fraction $A_A(t)$, as shown in Figs 9.6 (a) and 9.6 (b). Linear fits with instrumental weighting result in agglomerate volume fractions

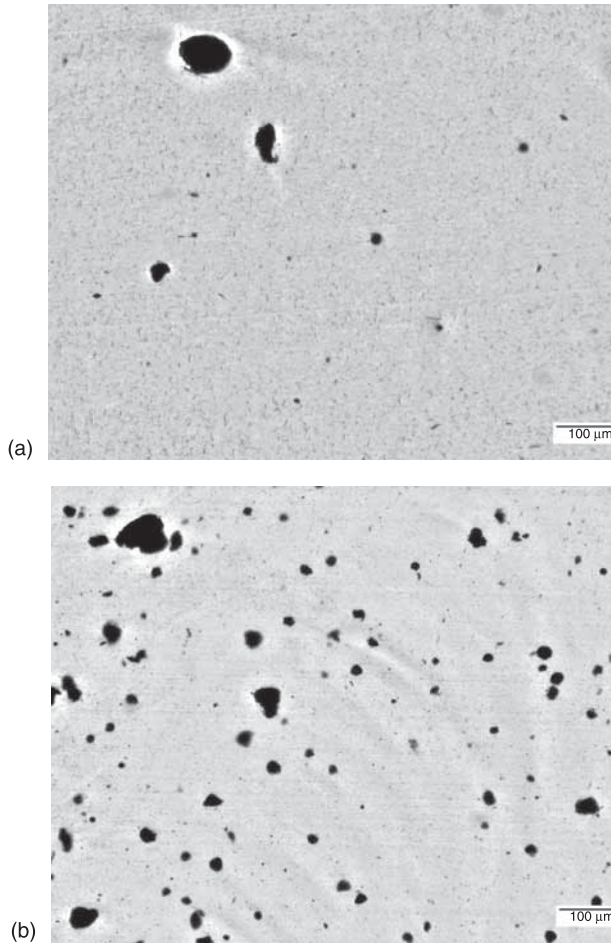


9.4 Feature-based algorithm for segmentation of grey scaled light microscopy micrographs with carbon nanotube agglomerates: (a) detail of Fig. 9.5, this is binarized with grey scale thresholds of (b) 100, (c) 138, and (d) 175. With the increasing threshold value, the number of agglomerates and thus A_A increases. The corresponding grey scale histogram (e) cannot be used to determine an accurate threshold value. In contrast, the object count method (f) delivers a reliable threshold value of 138 with the corresponding binary image (c).



9.4 Continued.

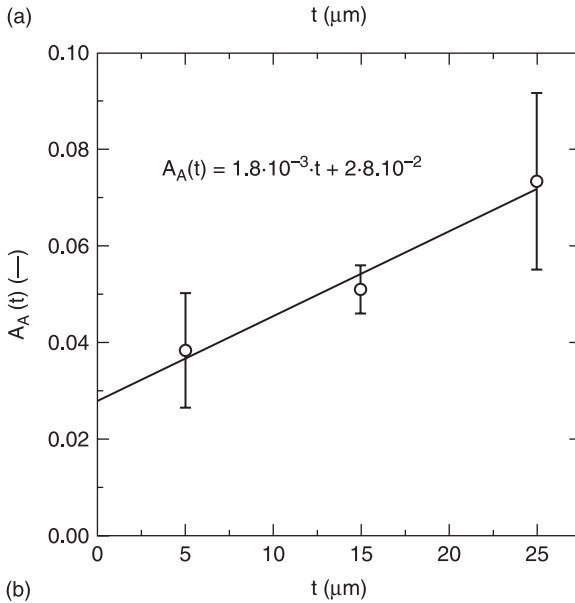
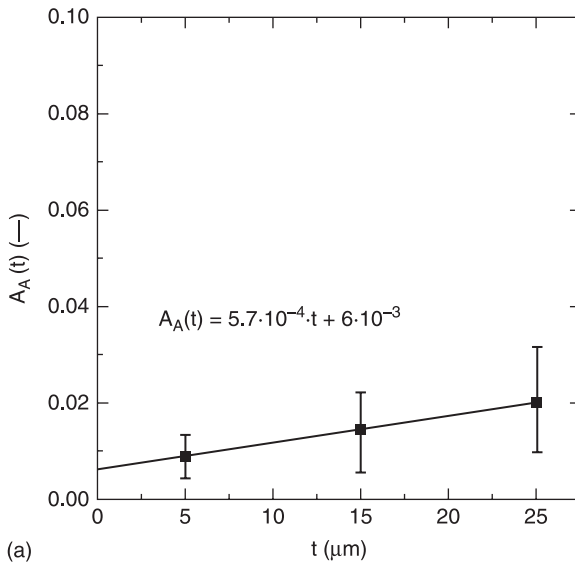
of 0.6 ± 0.1 and 2.80 ± 0.05 vol.% for sample 1 and 2, respectively. The infiltration method yields an estimation of the packing density for the pure nanotube material of approximately 0.07. This is a comparatively low value and it cannot be ruled out that the CNT material is further compressed during processing. Therefore, uniaxial



9.5 Micrographs of differently melt processed composites (small-scale batch compounder such as used in Chapter 4) with 1 wt% MWCNT in PC obtained by light microscopy ($t = 25\ \mu\text{m}$): (a) sample 1 mixed at 240°C and 50 rpm for 30 min, $D_{\text{LM}} = 0.87 \pm 0.08$; (b) sample 2 mixed at 240°C and 50 rpm for 5 min, $D_{\text{LM}} = 0.33 \pm 0.40$.

compression tests have been carried out to obtain an upper bound of approximately 0.25. Thus, the mean packing density is given by 0.16 with an uncertainty of 0.09.

Accordingly, the degree of dispersion is $D_{\text{LM}} = 0.87 \pm 0.08$ for sample 1 and $D_{\text{LM}} = 0.33 \pm 0.40$ for sample 2. The comparatively large uncertainty of D_{LM} of sample 2 is caused by the large uncertainty of packing density and the large agglomerate volume fraction. For low agglomerate volume fractions, the uncertainty of packing density is insignificant (sample 1). Generally, the light microscopic degree of dispersion exhibits a good dispersion measure, especially for small agglomerate volume fractions.



9.6 Evaluation of A_A for different section thickness: (a) sample 1 and (b) sample 2. The extrapolation $t \rightarrow 0$ yields agglomerate volume fractions of 0.6 ± 0.1 and 2.80 ± 0.05 vol.%, respectively.

9.2.3 Further remarks

The specific examples illustrate that an unbiased estimate of the agglomerate volume fraction can be obtained with a series of thin sections. However, the determination of D_{LM} can be inaccurate for samples with high agglomerate

volume fractions and CNT materials with low packing densities f . Due to the possible densification of CNT agglomerates during processing, the estimate for f is afflicted with a comparatively high uncertainty. If highly packed CNT materials (see also Chapter 4) are used, the uncertainty of f and thus D_{LM} is comparatively small since the agglomerates cannot be further compressed during processing.

9.3 Transmission electron microscopy

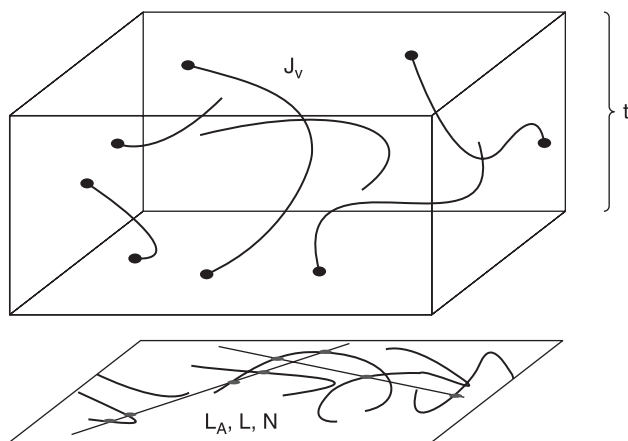
In contrast to LM, micrographs with nanometre resolution can be obtained by means of transmission electron microscopy and thus individual CNTs can be recognized. This leads to the possibility of estimating the volume fraction of dispersed CNTs directly and of evaluating spatial relationships between individual CNTs. However, to ensure a sufficient confidence level, a reasonable number of micrographs have to be evaluated.

9.3.1 Degree of dispersion

To estimate the volume fraction of dispersed CNTs, they are treated as a 3D fibre system. In 3D, this can be characterized by the total fibre length per unit volume J_V . Accordingly, a 2D fibre system can be characterized by the total fibre length per unit area L_A . For a projection of an isotropic 3D fibre system on a plane, the intensities J_V and L_A are connected to the section thickness t by:

$$J_V = \frac{4 \cdot L_A}{\pi \cdot t} \quad [9.6]$$

L_A can be obtained with a system of test lines as schematically shown in Fig. 9.7. With a sufficient total length of the test system L , an unbiased estimate for L_A can



9.7 Schematic for the determination of the volume specific fibre length by means of planar projection and a system of test lines.

be evaluated by means of the number of intersections with the fibre system N and Equation 9.7.

$$L_A = \frac{\pi \cdot N}{2 \cdot L} \quad [9.7]$$

The volume content of dispersed CNTs is simply given by: $V_{VD} = J_V \cdot A_0$, where A_0 denotes the mean cross-sectional area of the nanotubes (Pegel *et al.*, 2009). Thus, the degree of dispersion D_{TEM} is given by Equation 9.8.

$$D_{TEM} = \frac{J_V \cdot A_0}{V_{VT}} \quad [9.8]$$

Finally, the Equations 9.7 and 9.8 as well as the law of the propagation of uncertainty lead to:

$$u_{D_{TEM}} = \frac{4}{\pi} \sqrt{\left(\frac{A_0}{V_{VT} \cdot t} u_{LA} \right)^2 + \left(\frac{A_0 \cdot L_A}{V_{VT} \cdot t^2} u_t \right)^2 + \left(\frac{A_0 \cdot L_A}{V_{VT}^2 \cdot t} u_{VT} \right)^2 + \left(\frac{L_A}{V_{VT} \cdot t} u_{A0} \right)^2} \quad [9.9]$$

where $u_{D_{TEM}}$, u_{LA} , u_t , u_{VT} and u_{A0} are the uncertainties of D_{TEM} , L_A , t , V_{VT} and A_0 , respectively.

9.3.2 Distribution coefficient

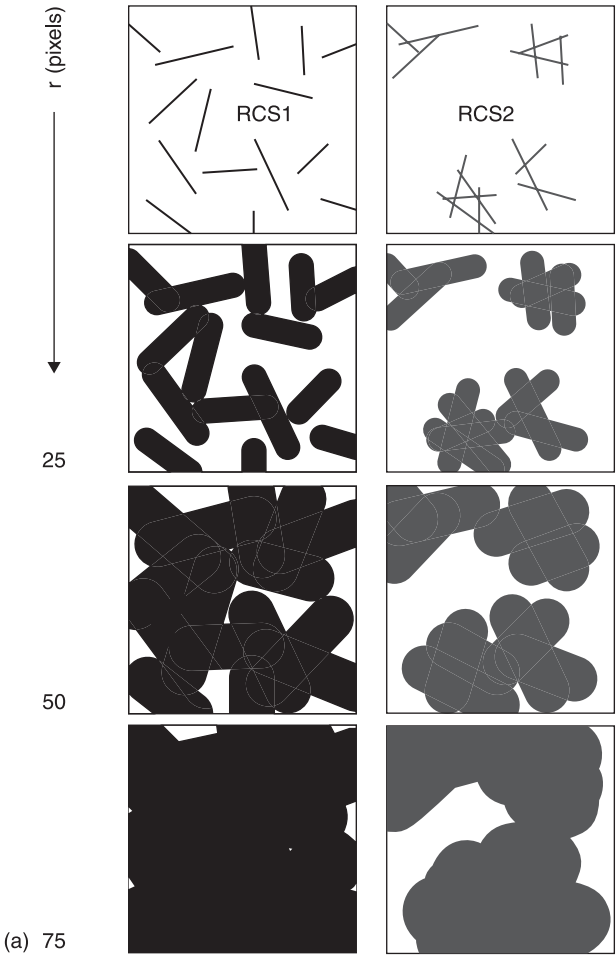
To investigate the distribution characteristics of individual nanotubes, the spherical contact distribution function (SCDF) can be employed. Mathematically, the SCDF $H_S(r)$ basically describes the distribution of the shortest distance between a random closed set (RCS) Ξ and a random point which is located outside Ξ . For the evaluation of a binarized TEM micrograph the pixels which are assigned to carbon nanotubes are treated as realization of a RCS. The corresponding empirical SCDF $\hat{H}_S(r)$ can be derived by dilation with spherical structure elements of different radii as demonstrated in Fig. 9.8. With increasing radius r of the structure element the area fraction of a dilated set $T_{\Xi}(r)$ increases as well. For $r \rightarrow \infty$ the function $T_{\Xi}(r)$ approaches the limit one. $\hat{H}_S(r)$ can be estimated from $T_{\Xi}(r)$ by means of Equation 9.10.

$$\hat{H}_S(r) = 1 - \frac{1 - T_{\Xi}(r)}{1 - A_A} \quad [9.10]$$

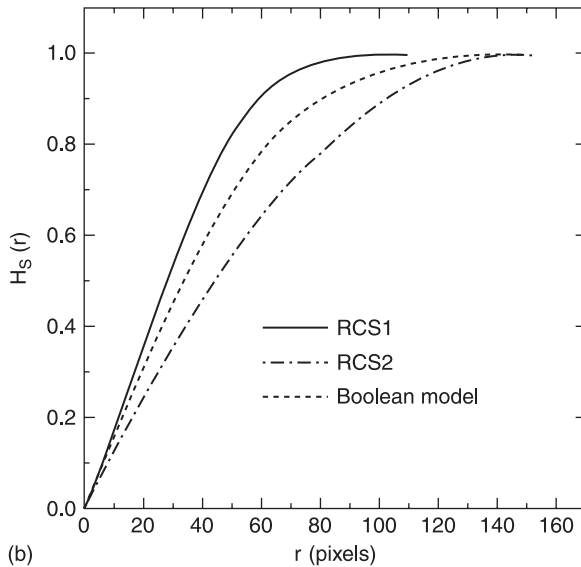
For planar fibre processes with randomly distributed straight line segments, i.e. the covering probability for the line segments is uniformly distributed in space, the SCDF can be estimated with Equation 9.11 (Boolean model). Hereby, the number of fibre segments per unit area is denoted by λ (intensity of the fibre process) and the mean fibre length by m_1 .

$$H_S(r) = 1 - \exp\{-\lambda \cdot r (2 \cdot m_1 + \pi \cdot r)\} \quad [9.11]$$

A deviation of the SCDF of a RCS with line segments of length m_l and intensity λ from the corresponding Boolean model can be attributed either to attractive (cluster process) or repulsive (hard core process) interactions between the fibre segments. Fibre processes with the tendency to maximize the distance between the individual fibres are characterized by comparatively fast convergence of $T_{\Xi}(r)$ and thus $\hat{H}_S(r)$ against the limit of one. For cluster processes, this function approaches the limit of one comparatively slowly due to the larger spacing between the fibre segments. Figure 9.8 shows a schematic to illustrate the differences.



9.8 Two realizations of an RCS with differently distributed line segments (similar mean fibre length and intensity, image size 500×500 pixels) dilated with circles of 25, 50 and 75 pixels radius (a). In the diagram the SCDF of those sets as well as the corresponding Boolean model is shown (b).



9.8 Continued.

To obtain a metric for the deviation of the empirical data from the corresponding Boolean model the distribution coefficient Q_p is introduced:

$$Q_p = \frac{\int_0^{\infty} 1 - \hat{H}_S(r) dr}{\int_0^{\infty} \exp\{-\lambda \cdot r(2 \cdot m_1 + \pi \cdot r)\} dr} \quad [9.12]$$

Since the integral $\int_0^{\infty} 1 - F(X)$ results in the mean value of random variable X with the cumulative distribution function $F(X)$, the intensity Q_p can be considered the ratio of the mean values of the empirical SCDF and the corresponding Boolean model. Due to the larger gaps between fibre clusters, Q_p is larger than 1 for this kind of processes. Values of Q_p smaller than 1 indicate a hard core process.

The uncertainty of Q_p depends mainly on the uncertainties of m_1 and λ . Especially for systems with strongly clustered filler particles, it can be problematic to get an unbiased estimate due to the overlap of neighbouring CNTs. Additionally, it has to be considered that only the distribution of the projected CNT system is analysed. Thus, it has to be assumed that the distribution state of the 3D system is somehow connected to the distribution of the projected 2D system. Furthermore, only a limited section of the entire CNT system can be evaluated due to the limits in resolution and data processing capability, i.e. a holistic investigation on several length scales is not possible.

9.3.3 Orientation factor

The evaluation of the covariance (Stoyan *et al.*, 1987) or the two-point probability function (Torquato, 2006) is a comparatively convenient way to gain information about the state of CNT orientation. The covariance $C(\mathbf{r})$ of a RCS Ξ is defined by the probability P that a randomly chosen point \mathbf{x} and a second point $\mathbf{x} + \mathbf{r}$ both belong to Ξ . If $\Xi \in \mathbb{R}^2$ holds, this can also be expressed as the area fraction of the intersection between Ξ and Ξ shifted by the vector \mathbf{r} (Equation 9.13).

$$C(\mathbf{r}) = P(\mathbf{x} \in \Xi, \mathbf{x} + \mathbf{r} \in \Xi) = A_A(\Xi \cap (\Xi + \mathbf{r})) \quad [9.13]$$

To elucidate some important properties of $C(\mathbf{r})$ in Fig. 9.9(a) an example with four parallel bars is considered. For small \mathbf{r} ($\|\mathbf{r}\|$ in the range of the bar width), it can easily be seen that the intersection area of the original and shifted set of bars is strongly related to the orientation of the vector \mathbf{r} (Fig. 9.9 (b)). The corresponding 2D covariance (Fig. 9.9 (c)) exhibits a kind of averaged structure whereby the alignment of the bars is reflected by the distortion of the central pattern. Furthermore, the uniform lateral distance between the bars results in periodic pattern of $C(\mathbf{r})$ in the x -direction.

The normalization of the covariance leads to the correlation function $\kappa(\mathbf{r})$ where the influence of area fraction A_A of the RCS is eliminated:

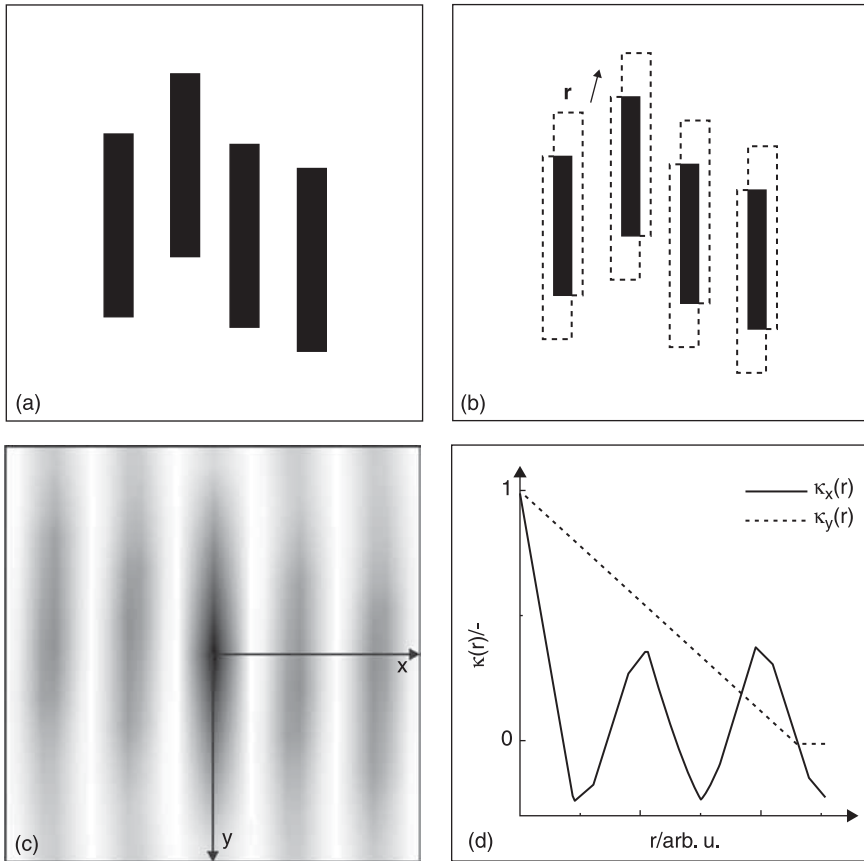
$$\kappa(\mathbf{r}) = \frac{C(\mathbf{r}) - A_A^2}{A_A(1 - A_A)}. \quad [9.14]$$

For stationary (invariance of translation) and isotropic (invariance of rotation) RCS, the correlation function as well as the covariance depends only on the distance $r = \|\mathbf{r}\|$. In this case, the correlation function holds the properties: $\kappa(0) = 1$ and $\kappa(\infty) = 0$. As in the case of the covariance, for anisotropic RCS, the curve shape of the correlation function is direction-dependent.

The example with the four oriented bars reveals that the drop of the correlation function in the direction coinciding with the main bar orientation $\kappa_y(r)$ is much less pronounced as compared to the direction perpendicular to the main bar orientation $\kappa_x(r)$ (Fig. 9.9 (d)). To obtain a measure for orientation, different features of $\kappa_x(r)$ and $\kappa_y(r)$ can be compared. The orientation factor O_r is a relatively simple measure (Equation 9.15), whereby the ratio $\kappa_x(r)/\kappa_y(r)$ is considered at a given distance r (practically r has to be in the range of the width of the elongated objects).

$$O_r = 1 - \frac{\kappa_x(r)}{\kappa_y(r)} \quad [9.15]$$

With increasing anisotropy of the investigated system the orientation factor approaches one. For isotropic systems, the orientation factor equals zero, since $\kappa_x(r)$ and $\kappa_y(r)$ overlap.

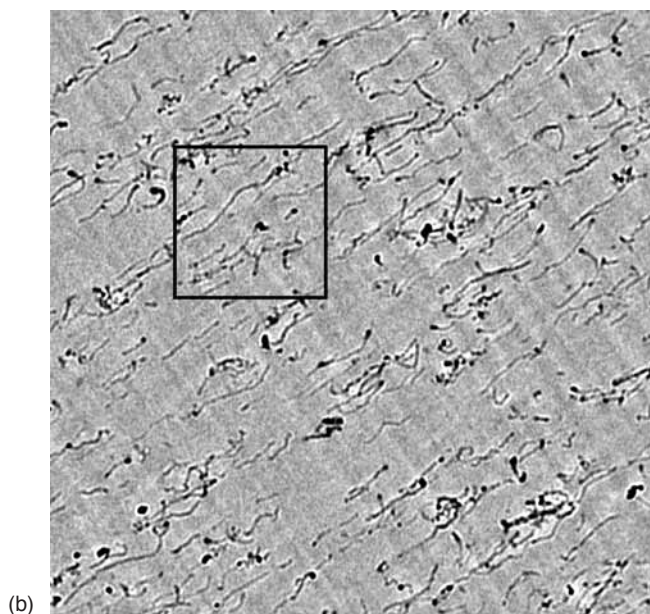
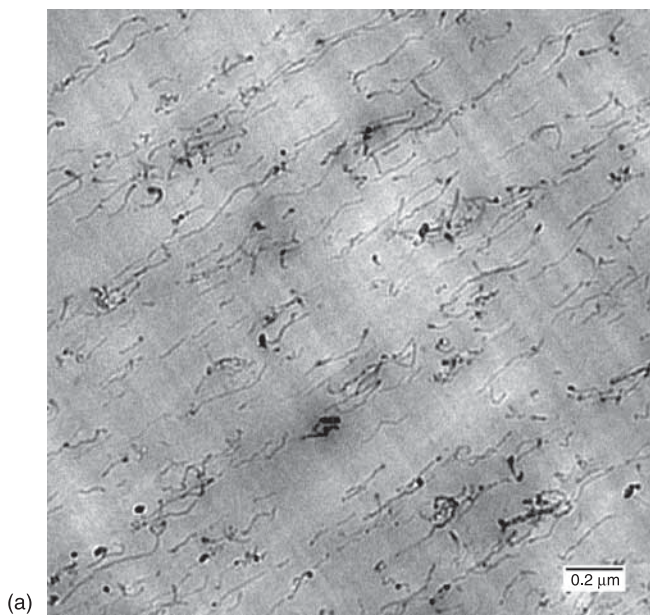


9.9 Adapted from (Pegel *et al.*, 2009): (a) a 2D realization of a RCS Ξ with the shape of four parallel bars; (b) the intersection of Ξ and Ξ shifted by the vector \mathbf{r} depends on the modulus and the orientation of \mathbf{r} ; (c) 2D covariance as grey scaled image; (d) 1D correlation function derived from the covariance along the x- and y-direction.

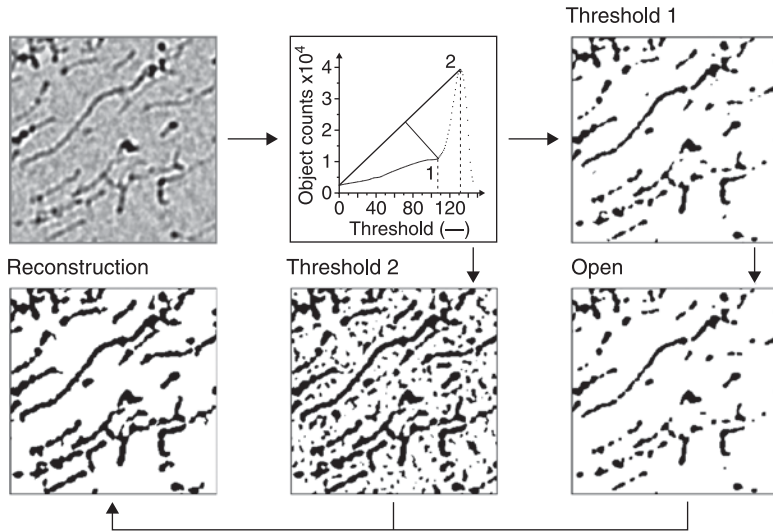
9.3.4 Digital image processing and specific examples

As in the case of LM analysis, the TEM micrographs have to be segmented at first. A Fourier band pass filter can be used to provide an even background illumination and to increase the contrast of nanotubes (Fig. 9.10). If necessary, further improvements can be achieved with the background correction used for the LM micrographs.

For the binarization of the background-corrected TEM micrographs, an algorithm based on the scheme shown in Fig. 9.11 gives reasonable results. At first, the total number of objects depending on the threshold value is determined. In the next steps two binary images with two thresholds are created. The first



9.10 TEM micrograph of an injection-moulded PC sample with 2 wt% MWCNT near the mould wall: (a) original; (b) after filtering with a Fourier band pass filter.

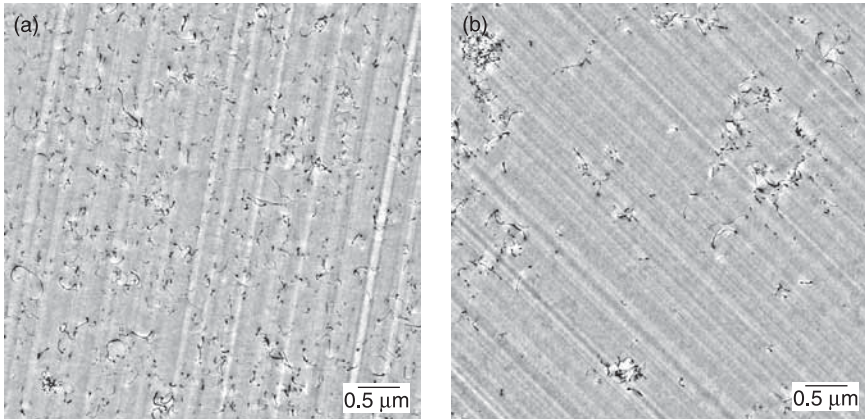


9.11 Scheme for the binarization of TEM micrographs.

threshold is chosen at the point when some background pixels are involved by the selection. This point 1 is determined by the longest distance between the particle threshold curve and the straight line between the maximum and the origin of the diagram. To remove the few background pixels or artefacts, the morphological filter 'open' is applied. The second binary image is created with the threshold corresponding to the maximum of detected particles (point 2 in Fig. 9.11). The two binary images serve as seed and mask for the final binary reconstruction. This means basically that disconnected regions of the second image are removed if they are not marked by the first one.

As examples, TEM micrographs of sample 2 (Fig. 9.12 (a), see section 9.2.2) and another composite with 1 wt% MWCNTs in PC (sample 3, Fig. 9.12 (b)) are considered. As mentioned before, sample 2 was mixed with a small-scale batch compounder at 240°C and 50 rpm for 5 min. In contrast, sample 3 (same composition) was mixed at 300°C and 50 rpm for 5 min. The thin sections shown in Figs 9.12 (a) and 9.12 (b) have been prepared from the extruded strands ($t \approx 120$ nm, estimated from interference colours). In sample 2, the amount of dispersed MWCNTs is obviously larger compared to sample 3. The non-dispersed MWCNTs of sample 3 remain in larger agglomerates which are not considered here. Furthermore, the MWCNTs seem to be more clustered in sample 3.

For the quantitative morphological analysis five TEM micrographs of each sample were binarized as described before. To obtain an estimate of L_A , a set of horizontal and vertical test lines (line distance 10 pixels) was created. The number of intersections with the projected MWCNT system has been counted by evaluating the intensity profiles along each test line (number of peaks counted).

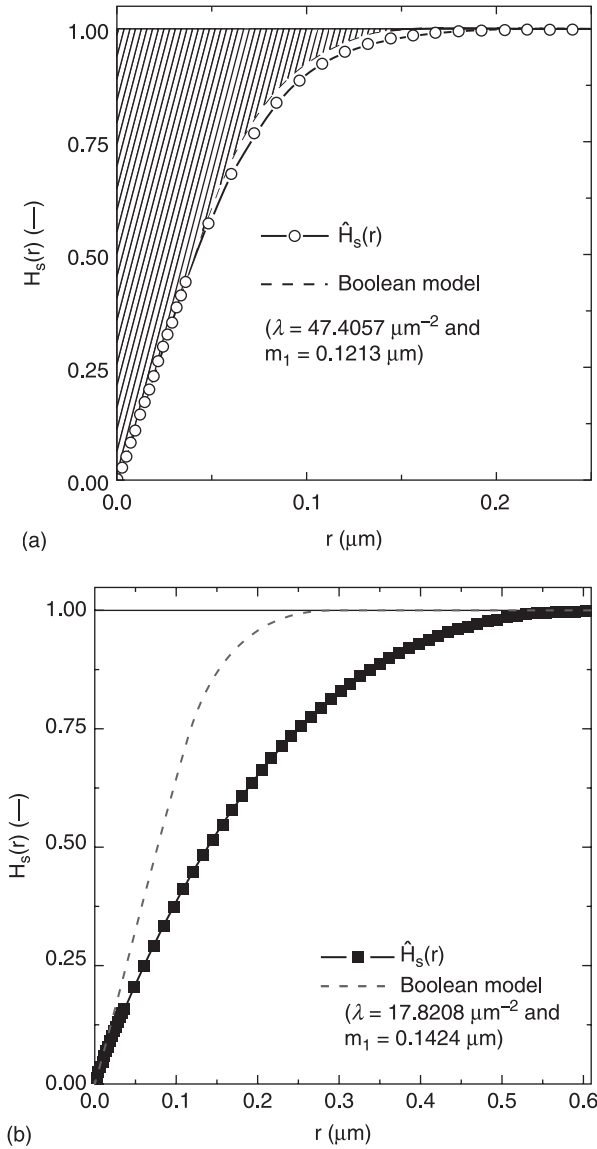


9.12 TEM micrographs of two composites with 1 wt% MWCNT in PC prepared by means of a small-scale batch compounder and different melt mixing conditions: (a) sample 2 mixed at 240°C and 50 rpm for 5 min, $D_{\text{TEM}} = 0.77 \pm 0.13$; (b) sample 3 mixed at 300°C and 50 rpm for 5 min and $D_{\text{TEM}} = 0.28 \pm 0.06$.

The mean cross-sectional area $A_0 \approx 81 \pm 25 \text{ nm}^2$ of the MWCNTs (Nanocyl 7000) was determined by means of higher magnified micrographs of the composite and an algorithm based on that reported by Gommès *et al.* (2003). Considering the uncertainty of the section thickness $u_t \approx 10 \text{ nm}$ (Sakai, 1980; Michler *et al.*, 2004), the results obtained are $D_{\text{TEM}} = 0.77 \pm 0.13$ for sample 2 and $D_{\text{TEM}} = 0.28 \pm 0.06$ for sample 3. In contrast to light microscopy, the TEM investigations result in a comparative large degree of dispersion for sample 2. With regard to the statistical significance of D_{TEM} (many TEM micrographs have been taken at different positions), the difference to D_{LM} can be explained by the high uncertainty of the CNT packing density within the agglomerates.

To investigate the distribution state of the individual MWCNTs, the empirical SCDF was determined for both micrographs by dilating the binary images with disc-like structuring elements and evaluation of the area fraction. To obtain the SCDF of the corresponding Boolean model, the fibre ends were counted and the values for λ and m_1 determined. The ends can be counted simply by performing the morphological operation of skeletization and determining the number of pixels with a connectivity number (connected pixels in the neighbourhood) of one. The mean fibre length m_1 is given by L_A/λ .

The empirical SCDF of the TEM micrographs of Figs 9.12 (a) and 9.12 (b), as well as the SCDF of the corresponding Boolean models, are shown in Figs 9.13 (a) and 9.13 (b), respectively. Evidently, the MWCNTs of sample 2 are arranged with an uncorrelated covering probability. The curves of the SCDF of the empirical data and the Boolean fibre model with the same intensity and mean fibre length ($\lambda \approx 47.41 \text{ } \mu\text{m}^{-2}$ and $m_1 \approx 0.12 \text{ } \mu\text{m}$) are very similar. Thus, the improper



9.13 SCDF of the binarized TEM micrographs shown in Fig. 9.12: (a) sample 2, $Q_p = 1.04 \pm 0.01$; (b) sample 3, $Q_p = 2.07 \pm 0.12$.

integrals and $\int_0^\infty 1 - \hat{H}_s(r) dr$ and $\int_0^\infty \exp\{-47.41\mu\text{m}^{-2} \cdot r(2 \cdot 0.12\mu\text{m} \pi r)\} dr$ (this basically corresponds to the shaded area in Fig. 9.13 (a)) yield very similar values. The evaluation of five micrographs leads to a distribution coefficient of 1.04 ± 0.01 for sample 2. Considering the TEM micrograph of sample 3 shown in Fig. 9.12 (b), a totally different behaviour of the SCDF of empirical data and the

Table 9.1 Injection moulding parameters of samples 4 and 5 (2 wt% MWCNT in PC)

	Injection velocity	Melt temperature	Holding pressure	Mould Temperature
Sample 4	150 mm/s	280 °C	400 bars	60 °C
Sample 5	10 mm/s	320 °C	400 bars	100 °C

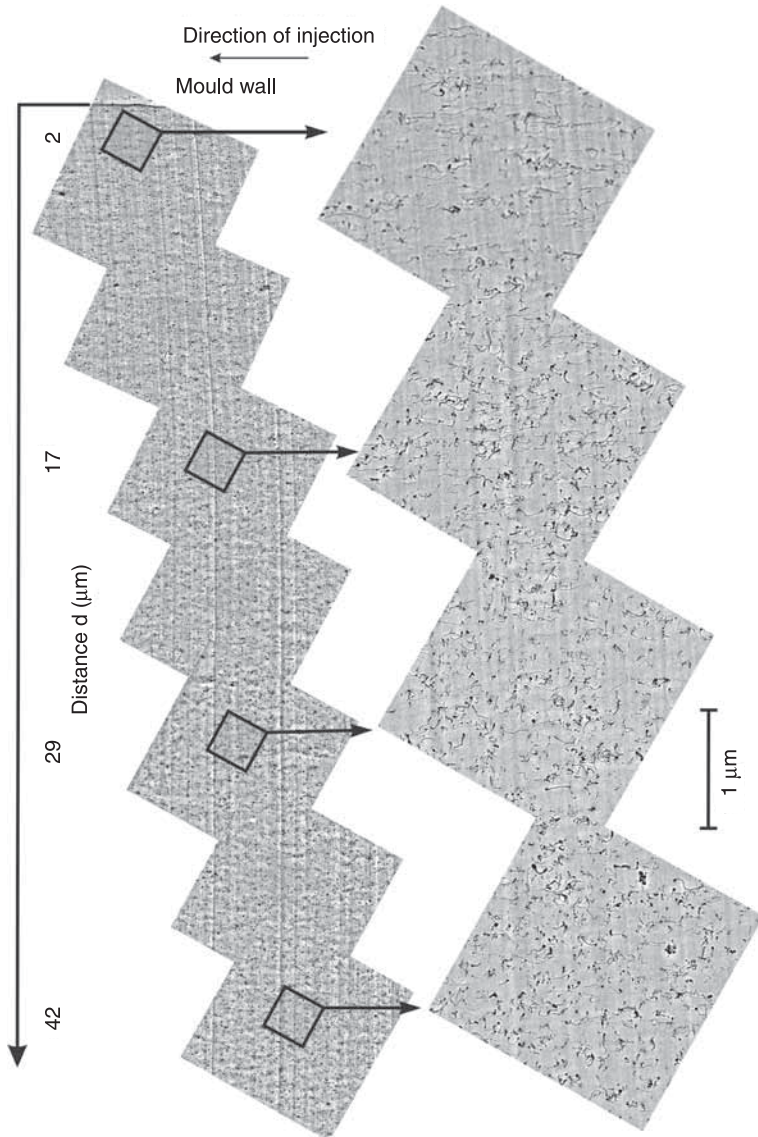
corresponding Boolean fibre model ($\lambda \approx 17.82 \mu\text{m}^{-2}$ and $m_1 \approx 0.14 \mu\text{m}$) can be observed. Due to the tendency of MWCNT cluster formation, the empirical SCDF approaches the limit $\lim_{r \rightarrow \infty} \hat{H}_S(r) = 1$ only at comparatively large values of r (Fig. 9.13 (b)). The evaluation of five micrographs of sample 3 results in $Q_p = 2.07 \pm 0.12$.

In a second example, the morphology of two different injection-moulded plates here referred to as samples 4 and 5 are discussed. Both samples consist of a composite with 2 wt% MWCNTs in PC which was produced by means of masterbatch dilution using a co-rotating twin screw extruder (for details, see Villmow *et al.*, 2008a). The samples have dimensions of $80 \times 80 \times 2 \text{ mm}^3$ and were processed under the injection moulding conditions as listed in Table 9.1. The different injection moulding conditions resulted in electrical volume conductivities measured through the sample thickness of approximately 10^{-13} and 10^{-8} S/cm for samples 4 and 5, respectively.

TEM investigations near the mould wall resulted in the micrographs shown in Figs 9.14 and 9.15. In this case, the low resolution micrographs have been used to obtain an overview and to determine the distance to the mould wall for the high resolution micrographs. The high resolution images have been used for the detailed morphological studies as shown below.

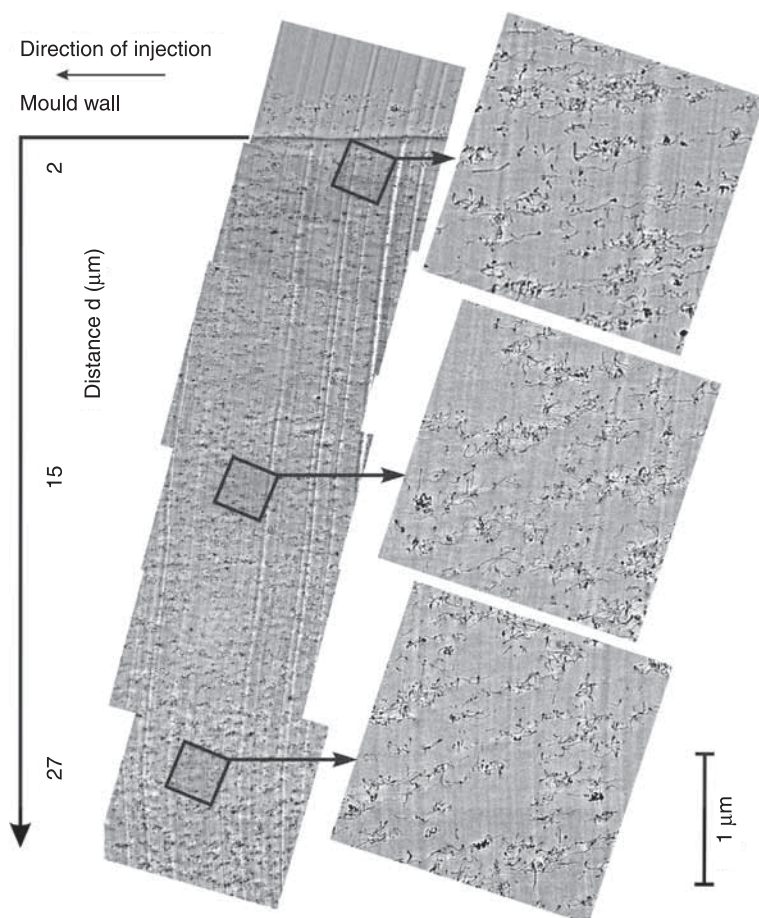
To gain information about the state of MWCNT orientation, the orientation factor O_r was evaluated as demonstrated by means of the two examples shown in Figs 9.16 (a) and 9.16 (b). These are two binarized micrographs of sample 4 taken at 2 and $42 \mu\text{m}$ distance to the mould wall. The grey scaled images shown in Figs 9.16 (c) and 9.16 (d) represent enlarged sections of the corresponding 2D correlation functions, which can easily be obtained by application of the fast Fourier transform (Wiener-Khinchin theorem) as well as normalization (see Equation 9.14). It can be seen that the distinct orientation of MWCNT at a distance of $2 \mu\text{m}$ to the mould wall (Fig. 9.16 (a)) leads to a strong elliptical distortion of the corresponding 2D correlation function (Fig. 9.16(c)). In contrast, the 2D correlation function of the micrograph taken at $42 \mu\text{m}$ distance to the mould wall (Figs 9.16 (b) and 9.16 (d)) exhibits a comparatively regular angular intensity distribution originating from the image centre.

To evaluate the mean direction of the MWCNT orientation, different thresholds were applied to the 2D correlation function to filter regions which correspond to



9.14 TEM micrographs of the injection-moulded sample 4 at different positions to the mould wall (adapted from Villmow *et al.*, 2008a).

small $\|r\|$ (centre of image). By means of an elliptical fit to the selected set of pixels, the major and minor directions (respectively the y and x directions) were determined for the different thresholds. The major and minor directions were calculated and the corresponding radial intensity profiles extracted from the 2D

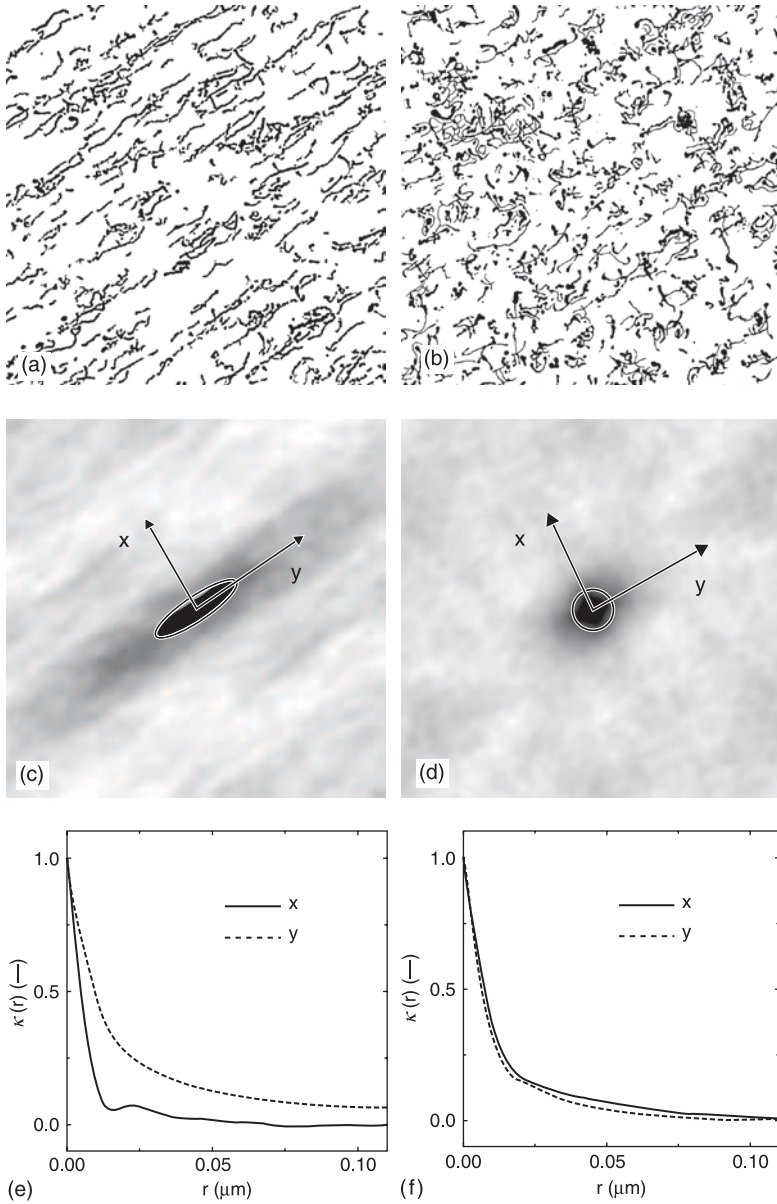


9.15 TEM micrographs of the injection-moulded sample 5 at different positions to the mould wall (adapted from Villmow *et al.*, 2008a).

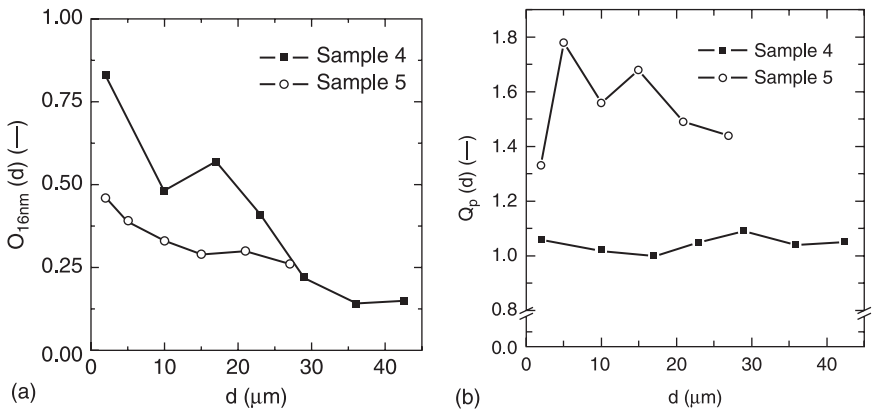
correlation function (Figs 9.16 (e) and 9.16 (f)). To obtain a meaningful measure for the state of MWCNT alignment, the orientation factor O_r was determined at $l|l| = 16$ nm (correlations to neighbouring CNTs are not considered).

In Fig. 9.17, the dependency of O_{16nm} from the distance d to the mould wall is shown for samples 4 and 5. It can be seen that both samples exhibit a significant MWCNT alignment in the proximity of the mould wall. In comparison to sample 5, the MWCNT alignment is more pronounced in sample 4. However, already at distances from the mould wall greater than 25 μm , no significant differences can be seen.

To gain more information about the morphology, for these samples the distribution coefficient has also been evaluated (Fig. 9.17 (b)). It can be seen that



9.16 Binarized TEM images of sample 4 at (a) 2 μm and (b) 42 μm distance to the mould wall, enlarged 2D correlation function of the binary images with elliptical fits (c) $d = 2 \mu\text{m}$ and (d) $d = 42 \mu\text{m}$, 1D correlation function in the major (y-) and minor (x-) directions of MWCNT orientation; (e) $d = 2 \mu\text{m}$; (f) $d = 42 \mu\text{m}$. Panels (e) and (f) are adapted from Pegel *et al.* (2009).



9.17 Morphological quantities of the injection moulded samples 4 and 5 with regard to mould wall distance (adapted from Pegel *et al.*, 2009): (a) orientation factor; (b) distribution coefficient.

the MWCNTs are almost randomly distributed within sample 4 ($Q_p \approx 1$). In contrast, $Q_p > 1.3$ indicates a significant MWCNT cluster formation in sample 5. For both samples no clear correlation between d and Q_p can be seen.

The results illustrate that the higher electrical volume conductivity of sample 5 as compared to sample 4 can be attributed to the less pronounced MWCNT alignment within a surface zone of approximately $25 \mu\text{m}$, combined with cluster formation through the whole sample.

9.3.5 Further remarks

Principally, the concepts of dispersion degree and distribution coefficient can be adapted to other microscopic methods such as SEM or AFM. In that case, a stereological approach for planar sections through isotropic fibre systems and the SCDF of point patterns has to be used.

The number of cross-section points per unit area P_A of an isotropic 3D fibre system with random plane section is given by the simple Equation 9.16. With the cross-sectional area A_0 of the CNT the volume fraction of dispersed CNT V_{VD} and thus the degree of dispersion can be estimated as shown before.

$$J_V = 2P_A \quad [9.16]$$

The SCDF of a point pattern with Poisson distribution is given by Equation 9.17. To obtain a distribution coefficient according to Equation 9.12, the empirical contact distribution function $\hat{H}_S(r)$ has to be determined by dilation of the point pattern with spherical structure elements of different radii as described before.

$$H_S(r) = 1 - \exp(-P_A \pi r^2) \quad [9.17]$$

9.4 Conclusion and future trends

LM and TEM can be used to gain a measure of the state of CNT dispersion in polymer CNT composites at different length scales. In the case of LM, the volume fraction of CNT agglomerates is used to estimate the fraction of dispersed CNT. However, for this purpose, the packing density of CNT within the agglomerates has to be known as closely as possible. At high agglomerate volume fractions, a high uncertainty of the packing density can cause significant uncertainties about D_{LM} . In such cases, TEM investigations can provide further information since the uncertainty of D_{TEM} is small for poorly dispersed CNT. Additionally, the TEM micrographs can be used to evaluate Q_p which serves as measure for CNT clustering.

The basic image processing algorithms which have been applied to some selected examples are usually available in every common image processing software. The single processing steps can easily be automated by means of macro programming. Thus, very large sample series can be evaluated in short time periods. In practice, the algorithms proved to be very reliable.

For the future it could be interesting to develop algorithms for statistical evaluation of 3D data with nanometre resolution. In this way for instance, percolation or agglomerate structures can be characterized in more detail.

9.5 References

- Abramoff MD, Magelhaes PJ & Ram SJ (2004) Image processing with ImageJ, *Biophoton. Intern.*, 11, 36–42.
- ASTM (2008) D 2663 Standard Test Methods for Carbon Black—Dispersion in Rubber.
- Bellayer S, Gilman JW, Eidelman N, Bourbigot S, Flambard X, Fox DM, De Long HC & Trulove PC (2005) Preparation of homogeneously dispersed multiwalled carbon nanotube/polystyrene nanocomposites via melt extrusion using trialkyl imidazolium compatibilizer, *Advanced Functional Materials*, 15, 910–916.
- Bhattacharyya AR, Sreekumar TV, Liu T, Kumar S, Ericson LM, Hauge RH & Smalley RE (2003) Crystallization and orientation studies in polypropylene/single wall carbon nanotube composite, *Polymer*, 44, 2373–2377.
- Du F, Fischer JE & Winey KI (2005) Effect of nanotube alignment on percolation conductivity in carbon nanotube/polymer composites, *Physical Review B (Condensed Matter and Materials Physics)*, 72, 121404-1–121404-4.
- Fischer JE, Zhou W, Vavro J, Llaguno MC, Guthy C, Haggemueller R, Casavant MJ, Walters DE & Smalley RE (2003) Magnetically aligned single wall carbon nanotube films: Preferred orientation and anisotropic transport properties, *Journal of Applied Physics*, 93, 2157–2163.
- Fornes TD, Baur JW, Sabba Y & Thomas EL (2006) Morphology and properties of melt-spun polycarbonate fibers containing single- and multi-wall carbon nanotubes, *Polymer*, 47, 1704–1714.
- Gommes C, Blacher S, Masenelli-Varlot K, Bossuot C, McRae E, Fonseca A, Nagy JB & Pirard JP, (2003) Image analysis characterization of multi-walled carbon nanotubes, *Carbon*, 41, 2561–2572.

- Jin L, Bower C & Zhou O (1998) Alignment of carbon nanotubes in a polymer matrix by mechanical stretching, *Applied Physics Letters*, 73, 1197–1199.
- Kapur JN, Sahoo PK & Wong AKC (1985) A new method for gray-level picture thresholding using the entropy of the histogram, *Computer Vision, Graphics, and Image Processing* 29, 273–285.
- Kasaliwal GR, Pegel S, Gödel A, Pötschke P & Heinrich G (2010) Analysis of agglomerate dispersion mechanisms of multiwalled carbon nanotubes during melt mixing in polycarbonate, *Polymer*, 51, 2708–2720.
- Kashiwagi T, Fagan J, Douglas JF, Yamamoto K, Heckert AN, Leigh SD, Obrzut J, Du F, Lin-Gibson S & Mu M (2007) Relationship between dispersion metric and properties of PMMA/SWNT nanocomposites, *Polymer*, 48, 4855–4866.
- Krause B, Ritschel M, Täschner C, Oswald S, Gruner W, Leonhardt A & Pötschke P (2010) Comparison of nanotubes produced by fixed bed and aerosol-CVD methods and their electrical percolation behaviour in melt mixed polyamide 6.6 composites, *Composites Science and Technology*, 70, 151–160.
- Le HH, Kasaliwal G & Ilisch S. (2009) Online measured electrical conductance: in-process characterization of the dispersion behavior of carbon nanotubes in rubber compounds, *KGK. Kautschuk, Gummi, Kunststoffe*, 06, 326–333.
- Li J, Ma PC, Chow WS, To CK, Tang BZ & Kim JK (2007) Correlations between percolation threshold, dispersion state, and aspect ratio of carbon nanotubes, *Advanced Functional Materials*, 17, 3207–3215.
- Michler GH, Lebek W, Godehardt R, Gnägi H & Vastenhout B (2004) *Ultramikrotomie in der Materialforschung*, Munich: Hanser Fachbuchverlag.
- Otsu N (1975) A threshold selection method from gray-level histograms, *Automatica*, 11, 285–296.
- Pegel S, Pötschke P, Villmow T, Stoyan D & Heinrich G (2009) Spatial statistics of carbon nanotube polymer composites, *Polymer*, 50, 2123–2132.
- Pötschke P, Bhattacharyya AR & Janke A (2004) Melt mixing of polycarbonate with multiwalled carbon nanotubes: microscopic studies on the state of dispersion, *European Polymer Journal*, 40, 137–148.
- Pötschke P, Brüning H, Janke A, Fischer D & Jehnichen D (2005) Orientation of multiwalled carbon nanotubes in composites with polycarbonate by melt spinning, *Polymer*, 46, 10355–10363.
- Pötschke P, Pegel S, Claes M & Bonduel D (2008) A novel strategy to incorporate carbon nanotubes into thermoplastic matrices, *Macromolecular Rapid Communications*, 29, 244–251.
- Rasband WS. (2008) *ImageJ*. 1.41 edn. Bethesda, MD, USA: U.S. National Institutes of Health. Available at: <http://rsb.info.nih.gov/ij/>, 1997–2009.
- Russ JC & Woods RP (1995) *The Image Processing Handbook*, Boca Raton, FL: CRC Press.
- Sahoo PK, Soltani S, Wong AKC & Chen YC (1988) A survey of thresholding techniques, *Computer Vision, Graphics, and Image Processing*, 41, 233–260.
- Sakai T (1980) Relation between thickness and interference colors of biological ultrathin section, *Journal of Electron Microscopy*, 29, 369–375.
- Sandler JKW, Pegel S, Cadek M, Gojny F, VanEs M, Lohmar J, Blau WJ, Schulte K, Windle AH & Shaffer MSP (2004) A comparative study of melt spun polyamide-12 fibres reinforced with carbon nanotubes and nanofibres, *Polymer*, 45, 2001–2015.
- Sezgin M & Sankur B (2004) Survey over image thresholding techniques and quantitative performance evaluation, *Journal of Electronic Imaging*, 13, 146–165.

- Shaffer MSP, Fan X & Windle AH (1998) Dispersion and packing of carbon nanotubes, *Carbon*, 36, 1603–1612.
- Stoyan D, Kendall WS & Mecke J (1987) *Stochastic Geometry and its Applications*, Chichester: John Wiley & Sons, Ltd.
- Torquato S (2006) *Random Heterogeneous Materials: Microstructure and Macroscopic Properties*, Berlin: Springer.
- Villmow T, Pegel S, Pötschke P & Wagenknecht U (2008a) Influence of injection molding parameters on the electrical resistivity of polycarbonate filled with multi-walled carbon nanotubes, *Composites Science and Technology*, 68, 777–789.
- Villmow T, Pötschke P, Pegel S, Häussler L & Kretschmar B (2008b) Influence of twin-screw extrusion conditions on the dispersion of multi-walled carbon nanotubes in a poly (lactic acid) matrix, *Polymer*, 49, 3500–3509.
- Wicksell SD (1925) The corpuscle problem, *Biometrika*, 17, 84–99.
- Wood JR, Zhao Q & Wagner HD (2001) Orientation of carbon nanotubes in polymers and its detection by Raman spectroscopy, *Composites Part A: Applied Science and Manufacturing*, 32, 391–399.

9.6 Appendix: list of abbreviations

AFM	Atomic force microscopy
CNT	Carbon nanotube
LM	Light microscopy
MWCNT	Multi-walled carbon nanotube
PC	Polycarbonate
PSD	Particle size distribution
RCS	Random closed set
SCDF	Spherical contact distribution function
SEM	Scanning electron microscopy
TEM	Transmission electron microscopy
A_0	Cross-sectional area of the CNT
A_A	Area fraction of agglomerates or RCS
$C(r)$	Covariance
D	Degree of dispersion (general case)
d	Distance to the mould wall (injection-moulded samples)
D_{LM}	Light microscopic degree of dispersion
D_{TEM}	Transmission electron microscopic degree of dispersion
f	Packing density of CNT within the agglomerates
f_{max}	Maximum packing density of CNT within agglomerates (estimated by means of pressed tablets)
f_{min}	Minimum packing density of CNT within agglomerates (estimated by means of the powder density)
$H_S(r)$	Spherical contact distribution function
J_V	Volume specific fibre length
$\kappa(r)$	Correlation function

λ	Intensity (number of fibres per unit area)
L_A	Area specific fibre length (cumulative fibre length per unit area)
m_l	Mean length of line segments
m_{CNT}	CNT mass within a composite
m_M	Matrix mass within a composite
N	Number of intersections with a system of test lines
O_r	Orientation factor
P_A	Points per unit area
Q_P	Distribution coefficient
r	Radius, distance
ρ_{CNT}	CNT density
ρ_M	Matrix density
S_{VA}	Volume specific surface of agglomerates (agglomerate surface area per unit volume)
t	Section thickness
T_{Ξ}	Area fraction of an RCS Ξ dilated with a disc-like structure element of radius r (capacity functional)
u_{A0}	Uncertainty of CNT cross-sectional area
u_{DLM}	Uncertainty of D_{LM}
u_{DTEM}	Uncertainty of D_{TEM}
u_f	Uncertainty of f
u_{LA}	Uncertainty of L_A
u_t	Uncertainty of t
u_{VA}	Uncertainty of V_{VA}
u_{VT}	Uncertainty of V_{VT}
v	Ratio of CNT and matrix density
V_{VA}	Agglomerate volume fraction (agglomerate volume per unit volume)
V_{VD}	Volume fraction of dispersed CNT
V_{VT}	Total volume fraction of CNT (dispersed and non-dispersed)
w	CNT mass fraction
Ξ	Identifier for a realization of an RCS

Influence of thermo-rheological history on electrical and rheological properties of polymer–carbon nanotube composites

I. ALIG, D. LELLINGER and T. SKIPA,
German Polymer Institute, Germany

Abstract: Electrical conductivity and mechanical properties of carbon nanotube (CNT)–polymer composites depend greatly on the structure of the filler network. Therefore, knowledge of the relation between thermo-rheological history and the structure of the filler network in the polymer matrix is of great scientific and industrial interest. This chapter reviews the knowledge on the relation between filler history created by the processing conditions, the structure of the nanotube network and the resulting composite properties. An overview of model approaches for the description of the electrical conductivity in composites filled with interacting fillers is given. Rheo-electrical laboratory experiments with well-defined shear flow conditions as well as in-line conductivity measurements during processing of composite melts are presented and discussed.

Key words: carbon nanotube–polymer composites, electrical conductivity, filler network, rheology, thermo-rheological history.

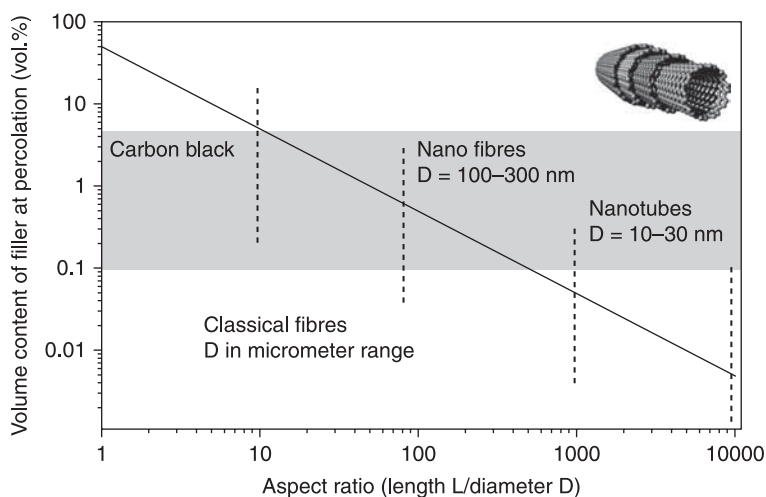
10.1 Introduction

Adding small amounts of carbon nanotube (CNT) additive turns an electrically insulating polymer into a conductive composite and can lead to reinforcement of its mechanical properties, which is usually not possible with small amounts of conventional conductive fillers (Szeleifer and Yerushalmi-Rozen, 2005). Apart from the traditional application of conductive or reinforced plastics, new specific applications of nanotube-filled polymers have been proposed in the past few years, e.g. for gas-sensing (An *et al.*, 2004), liquid crystal displays (Russell *et al.*, 2006), optical transparent films (Carroll *et al.*, 2005), or smart materials or actuators (Kang *et al.*, 2006; Li *et al.*, 2008). Electrical conductivity and reinforcement in such composite materials are usually explained by the formation of a percolating network of interconnected filler particles, which transfer the electrical current and/or the mechanical stress (Kluppel, 2003). In this picture, the high aspect ratio (length to diameter ratio) of CNT is considered to be one of the main advantages of carbon nanotubes with respect to other fillers. The high aspect ratio of CNT of up to 1000 theoretically enables the formation of a nanotube network at extremely low critical volume fractions $\sim 1/(\text{aspect ratio})$ (Balberg *et al.*, 1984). However, in reality, the CNT are bent objects, which tend

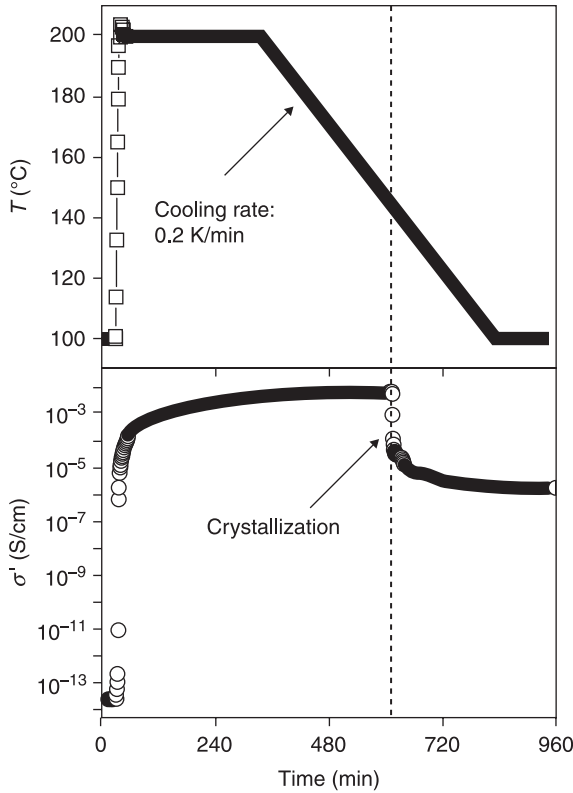
to form agglomerates, so that the experimental percolation concentrations usually exceed the theoretical expected values for fully elongated objects.

In Fig. 10.1 the theoretically predicted (Balberg *et al.*, 1984) dependence of the critical volume concentration of fillers at percolation threshold is plotted versus the aspect ratio of the fillers. The grey area indicates the typical range of experimentally determined percolation concentrations for melt mixed thermoplastics containing CNT, which has been found between about 0.1 to 5 vol.% (Alig *et al.*, 2008b). These values are one to two orders of magnitude above the theoretically expected values. At first glance, this difference can be explained by the worm-like structure of the CNT and/or by remaining (primary) CNT agglomerates. However, the nanotube fraction for the insulator-conductor transition in thermoplastic polymers is still low, so that – in contrast to classical conductive fillers – the desired properties of the polymer matrix (for example, its elongation to break) are almost unchanged.

Although different types of multi-walled carbon nanotubes (MWNTs) are commercially available, the industrial acceptance of the nanotube-polymer composites is still limited. Apart from other reasons, this is due to the broad variation of their physical properties depending on the processing conditions. During compounding, extrusion and injection moulding of the composites, polymer melts undergo moderate to very strong mechanical deformations which affect the state of filler network. It was shown previously (Alig *et al.*, 2007a; Alig *et al.*, 2008a; Pegel *et al.*, 2008; Lellinger *et al.*, 2008 Villmow *et al.*, 2008a; Villmow *et al.*, 2008b), that the state of the nanotube network – which is induced by processing of the polymer melt and frozen ('frustrated') in the short period



10.1 Critical volume fractions of fillers at percolation threshold versus aspect ratio (after Balberg *et al.*, 1984).



10.2 Influence of thermo-rheological history on the electrical conductivity σ' of a CNT–polypropylene composite. The upper graph shows the temperature program applied to a pressed sample (after squeeze flow).

prior to vitrification or crystallization – mainly defines the physical properties of the final plastic part. An example of conductivity changes during isothermal annealing and crystallization during cooling is shown in Fig. 10.2 for a pressed plate of polypropylene with 2 wt% CNT (Alig *et al.*, 2008b). The temperature program is shown in the upper part of Fig. 10.2: after very fast heating from 100 °C up to 200 °C (which is above the melting temperature of $T_m \approx 145^\circ\text{C}$), the sample was annealed for 5 hours at 200 °C. The annealed sample was then cooled below the crystallization temperature with a cooling rate of 0.2 K/min. The initial conductivity at 100 °C represents a situation below the electrical percolation threshold, since the conductive CNT network was at least partially destroyed by the ‘squeeze flow’ during pressing. During fast melting and isothermal annealing, the composite undergoes a thermally induced insulator–conductor transition and tends to approach an equilibrium value of the conductivity for long annealing times. During cooling, the polypropylene crystallizes and the decrease of the

conductivity is associated with a reduction of the matrix conductivity due to immobilization of the charge carriers in the crystalline (stepwise decrease) and in the amorphous phase (continuous decrease). The conductive filler network formed during annealing becomes frustrated in the semicrystalline structure.

As will be shown below (see Sections 10.3.1 and 10.4), rheo-electrical experiments combining measurements of electrical conductivity and rheological properties under well-defined shear conditions (Kharchenko *et al.*, 2004; Alig *et al.*, 2007b; Alig *et al.*, 2008d; Obrzut *et al.*, 2007; Lellinger *et al.*, 2009; Skipa *et al.*, 2009; Skipa *et al.*, 2010) can provide a deeper understanding of the underlying physical mechanisms of the CNT network formation and destruction. The first indication of destruction of electrical and rheological nanotube networks under steady shear flow was given by Kharchenko *et al.* (Kharchenko *et al.*, 2004) for polypropylene (PP) composites filled with MWNT. The breakdown of the conductive nanotube network for a wide variation of shear rates and MWNT concentrations was somewhat later observed by Obrzut *et al.* (Obrzut *et al.*, 2007) for PP–MWNT. A tremendous decrease in electrical conductivity during transient shear deformation was monitored in similar laboratory experiments for polycarbonate (PC)–MWNT composite melts (Alig *et al.*, 2007b; Alig *et al.*, 2008d). The time-dependent recovery of the conductivity in the quiescent state (following the transient shear) was attributed to the reformation of the conductive network in the melt.

Parallel to the laboratory experiments, the influence of shear and elongation flow on the electrical conductivity of CNT polymer composites has also been found in processing-related studies (Alig *et al.*, 2007a; Alig *et al.*, 2008a; Pegel *et al.*, 2008; Lellinger *et al.*, 2008; Villmow *et al.*, 2008a; Villmow *et al.*, 2008b) during extrusion, pressing and injection moulding. The destruction of the conductive filler network by mechanical deformation (nanotube de-agglomeration and/or orientation) was observed for the first time in in-line conductivity experiments during extrusion of polypropylene (Alig *et al.*, 2007a), PC and polyamide 6 (PA6) (Alig *et al.*, 2008a) containing different amounts of MWNT. (Pegel *et al.*, 2008) showed examples of deformation-induced agglomeration and de-agglomeration of CNT in PC composites in the squeeze flow during pressing. Villmow *et al.* (Villmow *et al.*, 2008a; Villmow *et al.*, 2008b) demonstrated the destructive effect of mechanical deformation on the electrical conductivity of injection-moulded plastic parts. In (Villmow *et al.*, 2008a), a conductivity variation up to 5 orders of magnitude within the same injection-moulded PC–MWNT plastic part was found, which they attributed to different flow conditions. Similar results were obtained by in-line and off-line conductivity measurements during and after injection moulding for the plastic parts of PC–MWNT, polyamide–MWNT and an acrylonitrile-butadiene-styrene–polycarbonate blend (Bayblend™) with MWNT for a wide variation of the processing parameters (Lellinger *et al.*, 2008). The strong dependence of the conductivity on injection velocity, melt temperature and viscosity was explained by the competition between deformation-induced formation and destruction of the conductive CNT network.

In addition to nanotube-filled (highly viscous) thermoplastic polymers, there are several works on low viscous colloidal suspensions (Lin-Gibson *et al.*, 2004; Hobbie and Fry, 2006, 2007) and epoxy resins filled with MWNT (Martin *et al.*, 2004; Sandler *et al.*, 2004; Kovacs *et al.*, 2007; Ma *et al.*, 2007). In those systems, shear can also induce agglomeration of nanotubes. The process of nanotube agglomeration can be considered similar to flow-induced flocculation of particles in colloidal suspensions (Switzer and Klingenberg, 2004; Vermant and Solomon, 2005; Guery *et al.*, 2006) or shear-induced phase separation in polymer blends (see e.g. Hobbie *et al.*, 2002; Han *et al.*, 2006). The structures of the filler network which appear under shear can also lead to a notable change in the composites' viscosity and conductivity (Lin-Gibson *et al.*, 2004; Martin *et al.*, 2004; Sandler *et al.*, 2004; Switzer and Klingenberg, 2004; Vermant and Solomon, 2005; Guery *et al.*, 2006; Hobbie and Fry, 2007; Kovacs *et al.*, 2007; Ma *et al.*, 2007). These findings correspond to earlier experiments by Schueler *et al.* (Schueler *et al.*, 1996; Schueler *et al.*, 1997) on epoxy systems containing carbon black (CB). The authors attributed the increase of electric conductivity to the agglomeration of CB induced by external shear forces. The agglomeration of particles in sheared carbon black-filled epoxies was explained analogically to colloidal dispersions by the interplay between attractive London–van der Waals forces and repulsive Coulomb forces causing a potential energy barrier between filler particles. Since it is difficult to overcome such barrier by thermal energy alone, shear deformation can accelerate the agglomeration process. Furthermore, it was theoretically shown (Switzer and Klingenberg, 2004) that rigid elongated objects like carbon nanotubes in the presence of shear will always aggregate due to friction forces (even without attraction between them).

In order to demonstrate the influence of thermo-rheological history on the electrical and rheological properties on CNT–polymer composites, the results of rheo-electrical laboratory experiments, which allow simultaneous measurements of the electrical conductivity and the complex dynamic shear modulus ($G^* = G' + i G''$) under well-defined shear conditions will be shown in Section 10.4 (Lellinger *et al.*, 2009; Skipa *et al.*, 2010; Skipa *et al.*, 2009). The results of rheo-electrical experiments are discussed together with in-line conductivity measurements during extrusion (Section 10.4) and injection moulding (Section 10.5).

10.2 Background

10.2.1 Percolation and insulator–conductor transition

In the framework of the percolation theory, a mixture of two materials with different conductivities (here: CNT in a polymer matrix) can be modelled by the lattice built up by bonds chosen randomly to be a conductor or an insulator (Clerc *et al.*, 1990; Sahimi, 1994; Stauffer and Aharony, 1994; Bunde and Havlin, 1996). The percolation threshold p_c is defined as a critical value of volume fraction p of

the conductive component, separating the states, where only finite clusters of the conductor exist $p < p_c$ and, where conduction paths between opposite edges of the lattice (infinite cluster) appear $p > p_c$. The macroscopic frequency dependent complex conductivity $\sigma^* = \sigma' + i\sigma''$ and complex permittivity $\varepsilon^* = \varepsilon' - i\varepsilon''$ of percolating systems have been described by two different physical models: the equivalent circuit (or intercluster polarization) model (Kirkpatrick, 1973; De Gennes, 1976b; Efros and Shklovskii, 1976; Straley, 1976; Bergman and Imry, 1977; Webman *et al.*, 1977; Stephen, 1978; Stroud and Bergman, 1982; Wilkinson *et al.*, 1983) and the anomalous diffusion model (Scher and Lax, 1973; De Gennes, 1976a; Stauffer, 1979; Straley, 1980; Gefen *et al.*, 1981; Gefen *et al.*, 1983; Laibowitz and Gefen, 1984; Weiss and Rubin, 1983; Hong *et al.*, 1986).

It has been established theoretically and experimentally (Kirkpatrick, 1973; De Gennes, 1976b; Efros and Shklovskii, 1976; Straley, 1976; Bergman and Imry, 1977; Webman *et al.*, 1977), that near the critical concentration p_c the DC conductivity and the static permittivity follow power laws:

$$\sigma_{DC} \equiv \sigma'(p, \omega=0) \propto (p_c - p)^{-s}, \quad p < p_c \quad [10.1]$$

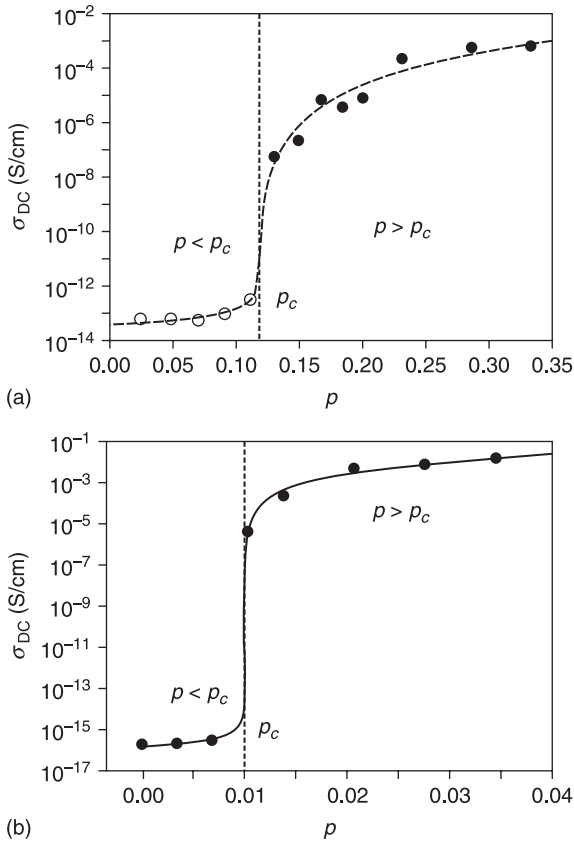
$$\sigma_{DC} \equiv \sigma'(p, \omega=0) \propto (p - p_c)^t, \quad p > p_c \quad [10.2]$$

$$\varepsilon_s \equiv \varepsilon'(p, \omega=0) \propto |p - p_c|^{-s'}, \quad p < p_c, \quad p > p_c \quad [10.3]$$

where $\omega = 2\pi f$ is the angular frequency. The critical exponents s and t are assumed to be universal and depend only on the dimension of the percolation system and not on the details of cluster geometry (Kirkpatrick, 1973; De Gennes, 1976b; Efros and Shklovskii, 1976; Straley, 1976; Bergman and Imry, 1977; Stephen, 1978; Webman *et al.*, 1977; Clerc *et al.*, 1990). The currently accepted values of these exponents (Clerc *et al.*, 1990; Sahimi, 1994; Stauffer and Aharony, 1994; Bunde and Havlin, 1996) are $s = t \approx 1.3$ for two dimensions and $s \approx 0.73$, $t \approx 2.0$ for three dimensions.

For example, in Fig. 10.3, the concentration dependencies of the DC conductivity at room temperature for carbon black (CB) in natural rubber (left graph) and MWNT in a PC matrix (right graph) are compared. For the MWNT-PC composite the percolation threshold (p_c) is observed at a concentration between 1 and 1.5 wt% (Pötschke *et al.*, 2003). In the case of CB, between 8 and 20 wt% are needed to reach percolation threshold. The solid lines fit with Equations 10.1 and 10.2 with exponents $s = 0.73$, $t = 3.5$ (CB) and $t = 2.1$ (MWCNT). The values for p_c were 11.9 wt% and 1.44 wt% for CB and MWNT, respectively. The power law behaviour for the DC conductivity values above p_c is visualized in a log-log plot of conductivity versus reduced filler content ($p - p_c$) in Fig. 10.4. Further details are given in (Pötschke *et al.*, 2003; Alig *et al.*, 2007a).

The frequency dependencies of the real part $\sigma'(\omega)$ of the conductivity and the real part of the permittivity $\varepsilon'(\omega)$ at the percolation threshold also show a power-law behaviour (Straley, 1976; Bergman and Imry, 1977; Webman *et al.*, 1977; Laibowitz and Gefen, 1984):



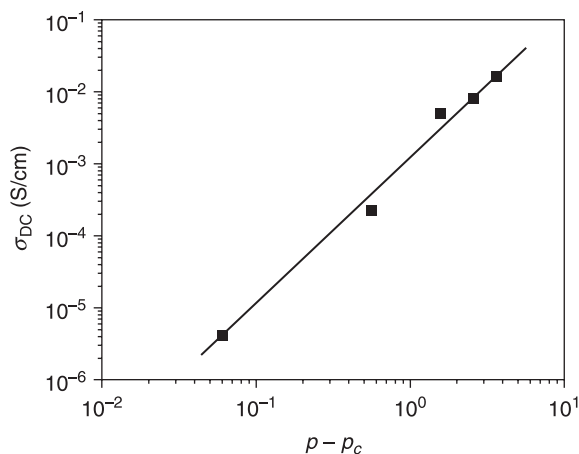
10.3 DC conductivity versus volume content of carbon black in natural rubber (a) and for MWNT in PC (b). The percolation thresholds (p_c) are indicated by a dotted line. The solid lines are fits with Equations 10.1 and 10.2.

$$\sigma'(\omega) \propto \omega^x \quad [10.4]$$

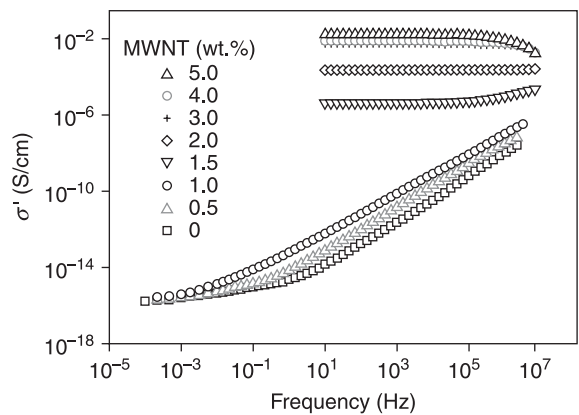
$$\varepsilon'(\omega) \propto \omega^{-y} \quad [10.5]$$

where critical indices x and y should satisfy the relation $x + y = 1$ (Bergman and Imry, 1977; Webman *et al.*, 1977; Laibowitz and Gefen, 1984).

In the anomalous diffusion model the transport properties of the percolation system are formulated terms of diffusion (random walk) within the clusters. The correlation time τ_ξ , which a charge carrier needs to traverse a cluster of correlation length ξ is inversely proportional to a critical frequency ω_ξ . This frequency shows a critical slowing down at percolation concentration: $\omega_\xi \propto 1/\tau_\xi \propto |p - p_c|^{v d_w}$, where d_w is the effective fractal dimensionality of the random walk ('diffusion exponent') and v is the critical exponent of the correlation length. For frequencies



10.4 DC conductivities above the percolation threshold versus reduced MWNT content in PC. The solid line represents a fit with Equation 10.2.



10.5 AC conductivity as a function of frequency for PC with different MWNT content.

$\omega < \omega_\xi$, the charge carriers can explore different clusters within one period (normal diffusion), whereas for frequencies above ω_ξ , the charge carriers visit only parts of the percolation cluster within one period and anomalous charge carrier diffusion in the fractal percolation clusters takes place. The case $\omega < \omega_\xi$ is expressed by a frequency independent plateau in $\sigma' = \sigma'(\omega)$.

As an example, in Fig. 10.5, the frequency dependences of the AC conductivity at room temperature are shown for MWNT-PC composites with different CNT content below and above the percolation threshold. The frequency dependence of the conductivity can be described in the frame of charge carrier diffusion in

percolation structures or alternatively by resistor–capacitor composites (for details, see references in Pötschke *et al.*, 2003; Alig *et al.*, 2007a). Below the percolation threshold, the expected slowing down of the critical frequency with increasing MWNT content can be seen. The critical frequency is indicated in the experimental $\sigma'(\omega)$ curves for $p < p_c$ by the cross-over from DC plateau to power law behaviour.

An alternative description of the insulator–conductor transition is the generalized effective medium (GEM) theory (Equation 10.6) (see McLachlan *et al.*, 1990; Andrews *et al.*, 2001; Almond and Bowen, 2004):

$$(1-p) \frac{\sigma_{matrix}^{1/s} - \sigma_{DC}^{1/s}}{\sigma_{matrix}^{1/s} + A\sigma_{DC}^{1/s}} + p_A \frac{\sigma_{filler}^{1/t} - \sigma_{DC}^{1/t}}{\sigma_{filler}^{1/t} + A\sigma_{DC}^{1/t}} = 0, \quad [10.6]$$

where $A = \frac{1-p_c}{p_c}$. σ_{DC} , σ_{matrix} and σ_{filler} are the electrical conductivities of the composite, the polymer matrix and the filler. It will be shown in the next section, that the ‘fillers’ are not necessarily the individual nanotubes. The assumption that conductive (sphere-like) agglomerates form the conductive filler network has been shown to be rather successful to describe the time-evolution of the electrical conductivity under shear and in the quiescent melt (Alig *et al.*, 2007b; Alig *et al.*, 2008a; Alig *et al.*, 2008c; Lellinger *et al.*, 2009; Skipa *et al.*, 2009; Skipa *et al.*, 2010). In this model, the filler content p has to be replaced by a time-dependent agglomerate concentration $p_A(t)$ and σ_{filler} becomes the conductivity of agglomerates $\sigma_{0,A}$.

An empirical equation to describe the insulator–conductor transition has been proposed by (Fournier *et al.*, 1997) and was successfully applied to polymers containing CNT by Coleman *et al.* (Coleman *et al.*, 1998), Curran *et al.* (Curran *et al.*, 2006) and McCullen *et al.* (McCullen *et al.*, 2007). A modified Fournier equation has been proposed more recently (Alig *et al.*, 2008c):

$$\log \sigma_{DC} = \log \sigma_{matrix} + \left(\log \sigma_{filler} - \log \sigma_{matrix} \right) \frac{f(p) - f(0)}{f(1) - f(0)}, \quad [10.7]$$

where $f(p) = 1/(1 + \exp[b(p - p_c)])$ and b is an empirical parameter. This equation was also extended to the assumption of time-dependent agglomerate concentration $p_A(t)$ (Alig *et al.*, 2008c; Deng *et al.*, 2009; Skipa *et al.*, 2009).

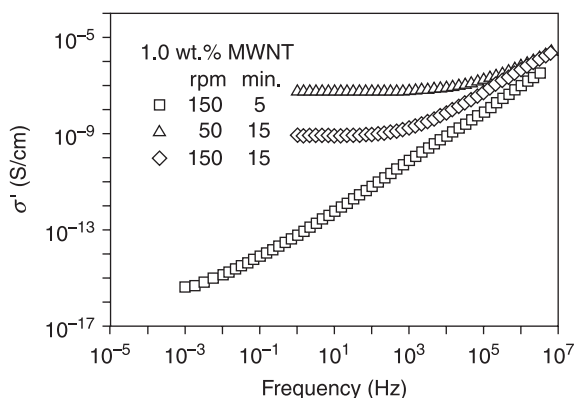
All three approaches (percolation, GEM theory and empirical Fournier equation) were compared for the same set of MWNT concentrations in PC (Alig *et al.*, 2008c) and in polypropylene (Deng *et al.*, 2009). It turns out that all three equations can fit the conductivity data with similar accuracy. Since the classical percolation theory assumes a random distribution of conductive fillers, it does not describe the distribution of fillers with (attractive) interactions. In order to keep the advantages of the percolation approach, we had to assume that the agglomerates (forming the percolation network) are randomly distributed (Alig *et al.*, 2007b).

10.2.2 Primary and secondary agglomeration

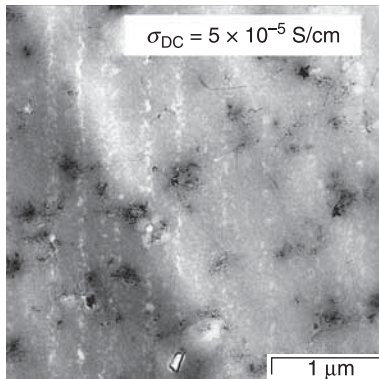
Primary agglomeration

A first indication of the influence of melt mixing on electrical conductivity was found by measurements of the frequency dependent conductivity on samples prepared by a twin-screw microcompounder (DACA) at different mixing conditions (Pötschke *et al.*, 2003). For a MWNT concentration close to the percolation threshold (1.0 wt% in PC), the mixing time and the screw speed of the microcompounder were varied at a constant processing temperature of 260 °C.

The measurements of AC conductivity (Fig. 10.6) were performed at room temperature on pressed plates prepared under controlled (identical) conditions from extruded strands. The differences in dispersion of the MWNT in the PC matrix are reflected in the AC conductivity spectra. The increase of the low frequency plateau values of the conductivity and in the cross-over frequencies in Fig. 10.6 indicate a transition from an insulator (150 rpm for 5 min.) to a conducting filler network with increasing mixing time or screw speed. These changes cannot be explained in the frame of classical percolation theory alone. One has to assume an increase in the effective amount of nanotubes contributing to the conductive network by destruction of the *primary agglomerates* during melt mixing. An example of remaining primary agglomerates is shown in Fig. 10.7 for a PC-MWNT composite (0.6 vol.% MWNT) after insufficient melt mixing (for 5 min. with a screw speed of 50 rpm at 300 °C) and gently pressing at 300 °C. The conductivity of this sample is 5×10^{-5} S/cm and below the value of 5×10^{-4} S/cm for the same material mixed for 15 min. with the same parameters and pressed under identical conditions (see Fig. 10.8(b)).



10.6 Influence of melt mixing: AC conductivity as a function of frequency for different mixing conditions (screw speed of the microcompounder and mixing time) for PC with 1.0 wt.% MWNT (measurements on pressed plates at room temperature).

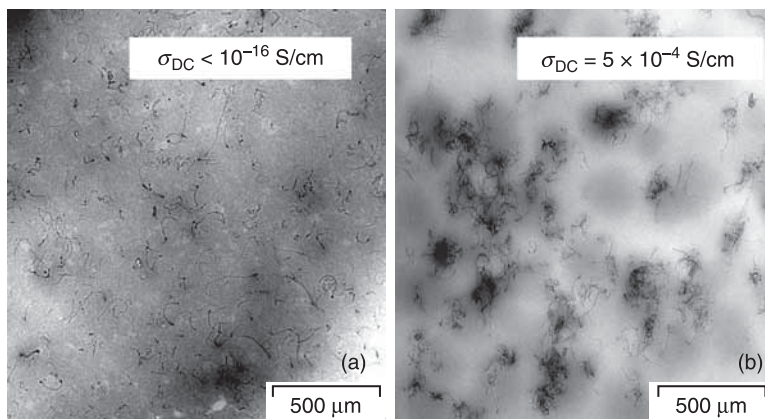


10.7 Example of remaining primary agglomerates: transmission electron micrograph of PC with 0.6 vol.% MWNT (mixing time: 5 min., screw speed: 50 rpm, mixing temperature: 300°C and pressing at $T = 300^\circ\text{C}$).

Secondary agglomeration

It is usually assumed that nanofillers have to be well dispersed in the polymer matrix to achieve the desired properties. Therefore, a lot of effort is spent during sample preparation or polymer melt processing (especially during compounding) to avoid agglomeration of nanofillers. The left transmission electron microscope (TEM) image in Fig. 10.8 shows a sample with well-dispersed nanotubes, where the primary agglomerates are assumed to be almost destroyed by the pre-treatment: melt mixing for 15 min. with 50 rpm at 250°C and pressing at 250°C with 0.5 mm/min. However, for this sample, the DC conductivity is below 10^{-16} S/cm, which is in the order of magnitude of the conductivity of the net polymer.

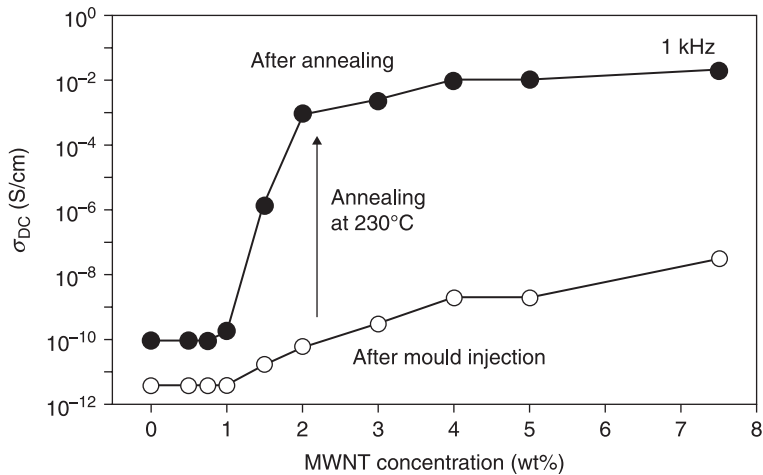
A sample prepared by mixing for 15 min. with 15 rpm at 300°C and pressed at $T = 300^\circ\text{C}$ shows a considerable nanotube agglomeration (see Fig. 10.8 (b)). Surprisingly, the electrical conductivity of this sample is about twelve orders of magnitude higher (5×10^{-4} S/cm) than that for the sample pressed at lower temperature and showing well-dispersed nanotubes. It has been assumed that the higher viscosity at 250°C leads to a higher shear stress during compounding and in the squeeze flow during pressing, which destroys the conductive agglomerates. On the other hand, the lower viscosity of the polymer matrix at 300°C may accelerate nanotube agglomeration during pressing. The considerably higher conductivity of the sample with secondary agglomerates (Fig. 10.8 (b)), which are assumed to be formed by attractive interactions between nanotubes, compared to the sample (Fig. 10.8 (a)) with well-dispersed CNT is remarkable. A more detailed study of the influence of extrusion and pressing conditions on the secondary agglomeration (TEM and conductivity) can be found in (Pegel *et al.*, 2008).



10.8 Transmission electron micrographs from PC–MWNT plates with 0.6 vol.% MWNT: (a) non-conductive state ($\sigma_{DC} < 10^{-16}$ S/cm) with well-dispersed nanotubes (mixing time of 15 min. at 250°C and pressed at 265°C); (b) conductive state ($\sigma_{DC} = 5 \times 10^{-4}$ S/cm) with nanotube agglomerates mixed for 15 min. at 300°C and pressed at 300°C.

A similar increase in conductivity was found for PC–MWNT melts during isothermal annealing in the quiescent melt (absence of shear) and has also been attributed to secondary agglomeration of nanotubes and formation of a conductive network of interconnected agglomerates (Alig *et al.*, 2007b; Alig *et al.*, 2008a; Alig *et al.*, 2008c; Alig *et al.*, 2008d). Fig. 10.9 shows the DC conductivities for a series of injection-moulded samples before and after annealing for one hour at 230°C. The samples after injection moulding represent a state with almost well-dispersed nanotubes (Alig *et al.*, 2008c). The increase of conductivity with annealing time is discussed in terms of a time-dependent insulator–conductor transition due to nanotube agglomeration or by ‘dynamic percolation’ (Alig *et al.*, 2008c).

Based on these results, secondary agglomeration is considered to be a key process in understanding the dependence of electrical conductivity on thermal and rheological prehistory. Therefore, it was discussed for PC–MWNT that the dispersed state of nanotubes leads to a low conductivity due to the insulating polymer chains in the contact regions between the nanotubes (Pötschke *et al.*, 2004; Alig *et al.*, 2007b; Alig *et al.*, 2008d). In this picture, the nanotube agglomeration is assumed to result in a denser packing of nanotubes inside the agglomerates and correspondingly in a smaller distance between MWNT. Very small inter-particle distances (\sim few nm, almost physical contacts) are necessary for low contact resistance (Ruschau *et al.*, 1992; Gojny *et al.*, 2005; Gojny *et al.*, 2006; Meier and Klüppel, 2008) and efficient electron transport through the conductive filler network. For the electron transport between CB, tunnelling of electrons was proposed (Meier and Klüppel, 2008). This explanation can be



10.9 Insulator–conductor transition for injection-moulded PC plates with MWNT. The open circles represent conductivity after injection moulding (dispersed nanotubes) and the closed circles represent the conductivity after annealing for about 5 hours at 230°C.

extended to CNT contact regions. We assume that sufficiently small MWNT distances can only be achieved inside the densely packed filler agglomerates.

10.2.3 Modelling of build-up and destruction of agglomerates

The growth of the conductive network in a polymer melt can be considered in the simplest case as a clustering process in which two non-conductive particles (e.g. well-dispersed nanotubes) interact and create a conductive agglomerate A . For attractive particles in a quiescent melt, this leads to a time-dependent increase of the volume concentration of agglomerates $p_A(t)$. These agglomerates are assumed to form the conductive filler network. For a description of the agglomeration of nanotubes, a kinetic equation of n -th order can be written.

In the presence of steady shear, the kinetic equation has to be extended by two additional shear-dependent terms for shear-induced destruction and agglomeration (Alig *et al.*, 2007b; Alig *et al.*, 2008a; Alig *et al.*, 2008c; Alig *et al.*, 2008d). For the assumption of additivity and first order kinetics one can write:

$$\frac{dp_A}{dt} = k_0(p_{A\infty} - p_A) + k_1(\dot{\gamma})(p_{A\infty} - p_A) - k_2(\dot{\gamma})p_A, \quad [10.8]$$

where p_A is the volume concentration of conductive agglomerates, p_{A0} is the starting agglomerate concentration, $p_{A\infty}$ is the value for $\dot{\gamma} = 0$ and $t \rightarrow \infty$, k_0 is the

kinetic coefficient for quiescent agglomeration, $k_1(\dot{\gamma})$ for shear-stimulated agglomeration and $k_2(\dot{\gamma})$ for the shear-stimulated destruction process. The coefficients k_1 and k_2 are assumed to depend on shear rate. Equation 10.8 can be rewritten as:

$$\frac{dp_A}{dt} = k(p_{A\infty} - p_A) - k_2(\dot{\gamma})p_A, \quad [10.9]$$

with $k = (k_0 + k_1)$.

For steady shear conditions, the concentration of agglomerates approaches a steady state value, which is determined by the interplay of destruction and build-up effects on filler network in flowing matrices (Skipa *et al.*, 2009, 2010).

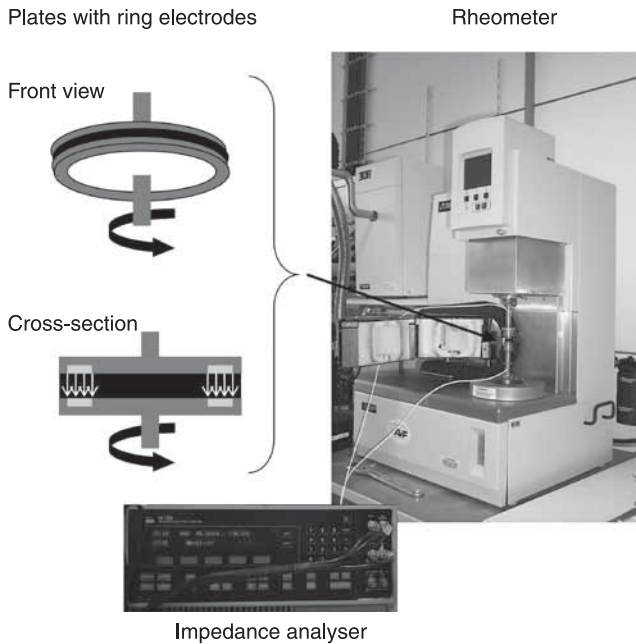
The solution of Equation 10.9 $p_A(t)$ can be set alternatively into the percolation equations (Equations 10.1 and 10.2), the effective medium approach (Equation 10.6) or the modified Fournier expression (Equation 10.7) to describe the conductivity in the quiescent melts or melts under shear (Alig *et al.*, 2007b; Alig *et al.*, 2008a; Alig *et al.*, 2008c; Alig *et al.*, 2008d). The filler content p_{filler} in Equations 10.1 and 10.2, 10.6 and 10.7 has to be replaced by the time-dependent content of conductive agglomerates $p_A(t)$. For σ_{filler} and σ_{matrix} the conductivity values of the nanotube agglomerates σ_A and polymer matrix have to be taken. The value p_c is now the percolation threshold of the percolating conductive agglomerates. In the following sections, example fits to the time-dependent conductivity data during quiescent agglomeration and shear-stimulated insulator-conductor transition will be shown. For a more detailed description, the shape and size distribution of conductive agglomerates/clusters has to be considered. A first attempt to consider different sizes of agglomerates has been discussed by Skipa *et al.* (2010).

10.3 Measuring techniques and materials

10.3.1 Rheo-electrical experiments

The time-dependent conductivity measurements were performed using a Novocontrol impedance analyser coupled with a laboratory rheometer (Ares, from Rheometric Scientific) in which the rheometer tools (plate-plate geometry) act as electrodes (Alig *et al.*, 2007b; Alig *et al.*, 2008c; Alig *et al.*, 2008d). The set-up is schematically shown in Fig. 10.10.

For most of the experiments, the plates were equipped with ring electrodes (inner diameter 19 mm, outer diameter 25 mm). By using ring electrodes, it is possible to ensure a relatively narrow distribution of the shear rates in the relevant region of electrical field during rotation. Tangential shear is applied to the melt by rotating the lower rheometer plate, and the electrical conductivity is measured perpendicular to the direction of applied shear. This monitors the electrical conductivity in the volume between the two ring electrodes. The set-up covers a broad frequency range from 10^{-3} to 10^7 Hz for the dielectric measurements



10.10 Schematic representation of the rheometer combined with conductivity (dielectric) spectroscopy.

(Alig *et al.*, 2008d; Lellinger, 2009). Since recording of a conductivity (or permittivity) spectrum over a wide range of frequencies needs at least several minutes, the measured (properties) can change during the measurement. Thus, for the monitoring of fast (time-dependent) processes, the conductivity measurements were performed at a single frequency. In most cases the frequency of $f = 1$ kHz could be taken as representative of the DC conductivity as discussed in (Alig *et al.*, 2008d).

For simultaneous electrical and rheological measurements during steady shear, the rheometer was connected to a data acquisition system (NI PXI-10042) with an analogue output for the motor control (Lellinger *et al.*, 2009; Skipa *et al.*, 2009; Skipa *et al.*, 2010). Using the analogue outputs of the rheometer and the electrometer, it is possible to measure strain, torque and conductivity with high acquisition rate, and this is perfectly synchronized with the motor control signal. With the modified rheometer it became possible to apply a combined deformation program overlaying steady and oscillatory motions. The motor thus can simultaneously perform steady rotation γ_{steady} (shear flow) and short oscillations. $\dot{\gamma}(t) = \dot{\gamma}_0 \sin 2\pi f t$. From the torque data of the oscillations the complex shear modulus of the composite melt can be deduced. The oscillation frequency and the strain rate amplitude were typically taken to be $f = 1$ Hz and $\dot{\gamma}_0 = 0.0628$ rad/s (corresponding to $\gamma_0 = 1\%$ of sample strain amplitude). For calculation of the transient shear viscosity $\eta^+ = \langle \tau(t) \rangle / \dot{\gamma}_{steady}$ the torque averaged over one period of

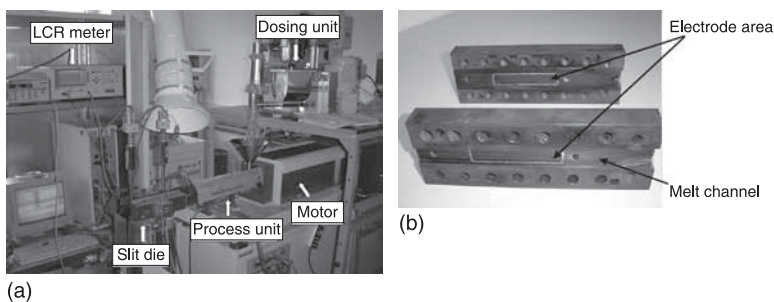
the overlaid oscillation $\langle \tau(t) \rangle$ was divided by the averaged shear rate $\dot{\gamma}_{steady}$. The set-up allowed simultaneous (time-resolved) monitoring of the DC conductivity (σ_{DC}), the components of the complex shear modulus (G' and G'') and the transient viscosity (η^+) under quasi-stationary shear conditions. To measure G' and G'' in quiescent melts, a small oscillatory shear of 1% strain was applied. The influence of such small oscillations on the electrical conductivity can almost be ignored in the 'quasi-quiescent' experiment (Skipa *et al.*, 2010).

10.3.2 In-line monitoring during extrusion

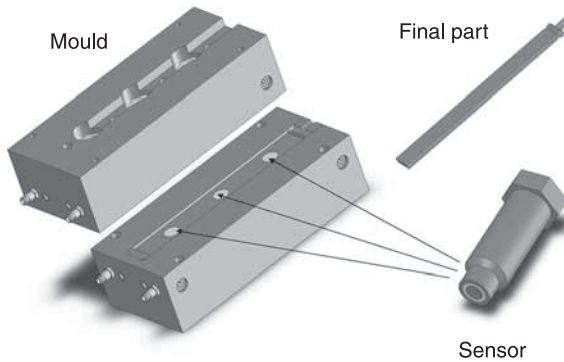
For in-line measurements during extrusion a measurement slit die is flanged to the outlet of a twin-screw extruder. A typical set-up for laboratory-scale experiments is shown in Fig. 10.11. Figure 10.11 (b) shows the two half-shells of a slit die with two rectangular electrodes in capacitor geometry (Alig *et al.*, 2008a). For insulation, the electrodes are embedded in a ceramic inlay. After mounting, the two electrode areas are face to face and the assembly was attached to the extruder. An LCR meter (HP4284A, from Agilent) was used to measure parallel capacitance C_p and $\tan \delta$ in a frequency range from 21.5 Hz to 1 MHz. For experimental details, see (Alig *et al.*, 2007a; Alig *et al.*, 2008a; Alig *et al.*, 2008b). The real parts of the complex conductivity σ' and permittivity ϵ' spectra were calculated from the air capacitance and the measured values of C_p and $\tan \delta$, respectively. For measurements of the DC conductivity another electrode was connected to an electrometer. In order to investigate the time-dependent changes of AC or DC conductivity under quiescent melt conditions, the extruder was stopped for a few minutes.

10.3.3 In-line measurements during injection moulding

For time-resolved in-line measurements of the DC conductivity an injection moulding machine (Klöckner Ferromatik Desma FX75-2F, Germany) was equipped with a mould (Fig. 10.12) containing three borings on every side to



10.11 Measurement slit die for in-line conductivity measurements flanged to the outlet of a twin-screw laboratory extruder (a) and opened slit die in capacitor geometry (b).



10.12 Scheme of the mould, the plastic part and the conductivity sensor used for in-line conductivity measurements during injection moulding.

accommodate conductivity and/or pressure sensors in different arrangements (Lellinger *et al.*, 2008). The dimensions of the produced model parts were $220 \times 30 \times 6 \text{ mm}^3$. The electrical conductivity sensor (Fig. 10.12) consists of an inner electrode (diameter 9 mm) electrically insulated by 2 mm thick ceramic material from the ground electrode (outer shell of the sensor and the whole mould). In this study the conductivity sensor was mounted in the central position between two pressure sensors. An electrometer (Keithley 6514) was used to measure the resistance R at constant current. By FEM simulations of the electrode configuration, the geometrical factor A/d was estimated to determine the specific electrical conductivity $\sigma = (R A/d)^{-1}$ (Lellinger *et al.*, 2008).

The corresponding off-line measurements of the conductivities at the same location of the final parts were conducted using two opposing electrodes with 17 mm diameter. The geometrical factor to calculate the specific electrical conductivities for this electrode configuration was calculated by FEM as well.

10.3.4 Materials and samples

The nanotubes used in this study were MWNTs supplied as PC masterbatches from Hyperion Catalysis International, Inc. (Cambridge, MA, USA) or as masterbatches and premixed compounds from Bayer Technology Services (Leverkusen, Germany). According to the supplier, the diameter of Hyperion nanotubes is approximately 10 nm and its length is above 10 μm . The Baytubes[®] are high purity multi-walled carbon nanotubes with an outer diameter of 5 to 20 nm, a length of 1 to 10 μm and an electrical conductivity of above 10^4 S/cm (specification, Baytubes[®]).

Using a DACA microcompounder or a Haake PTW 16/25 twin screw laboratory extruder, the masterbatches from Hyperion Catalysis International, Inc. were melt

mixed into PC of the same type as used for the masterbatches. Details of the mixing conditions are given in (Pötschke *et al.*, 2003; Alig *et al.*, 2007a; Alig *et al.*, 2008a). Injection-moulded plates were prepared by Bayer Technology Services from PC (Makrolon 2600, Bayer MaterialScience AG) containing different amounts of high purity Baytubes®. The process parameters for injection moulding are given in (Alig *et al.*, 2008c; Skipa *et al.*, 2009; Skipa *et al.*, 2010). For the rheo-electrical measurements, round samples of 25 mm and 2 mm thickness diameter were cut from injection-moulded plates. Transmission electron microscopy (TEM) investigations showed that the injection-moulded samples contain dispersed MWNT with only a small amount of agglomerates (Alig *et al.*, 2008c; Skipa *et al.*, 2009). It was also shown by X-ray experiments that these composites do not contain significant amounts of oriented MWNT (Richter *et al.*, 2009). The electrical conductivity of the injection-moulded plates at room temperature was found to be quite low, having a percolation threshold well above 5 wt% MWNT (Alig *et al.*, 2008c; Skipa *et al.*, 2009).

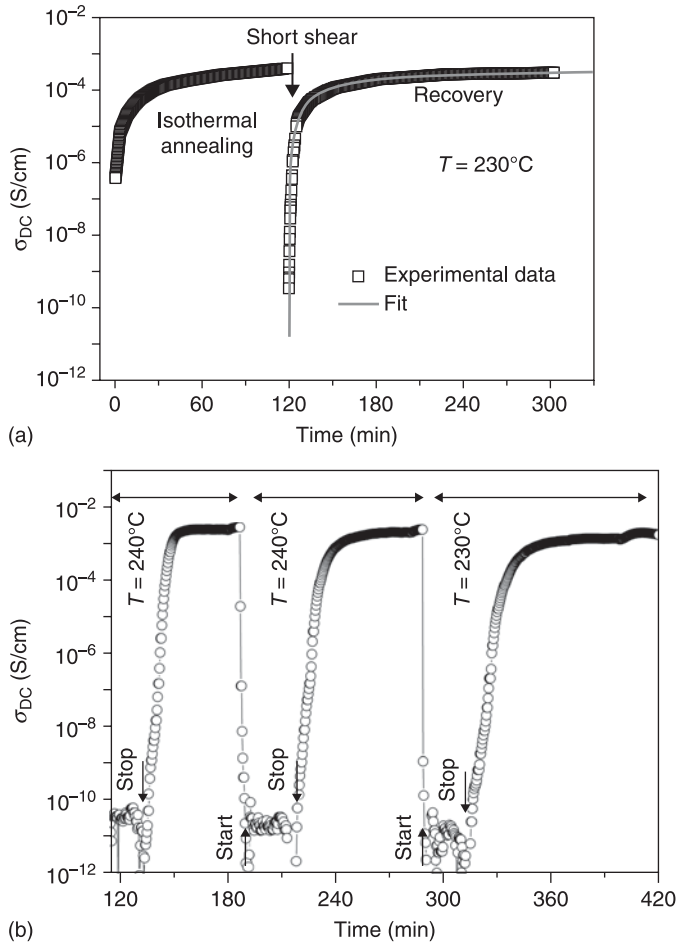
The in-line investigations during injection moulding (Lellinger *et al.*, 2008) were performed for a wide variety of the processing parameters on PC, an acrylonitrile-butadiene-styrene/polycarbonate blend (Bayblend™) and polyamide-12 (PA12) containing different amounts of high purity multi Baytubes®. The PC and Bayblend™ compounds were provided by Bayer Technology Services and the polyamide-12/MWNT compounds were provided by Evonik Industries AG (Marl, Germany).

10.4 Destruction and formation of electrical and rheological networks

10.4.1 Conductive filler network

Shear induced destruction and conductivity recovery

In Fig. 10.13 time-dependent conductivity measurements for the same PC-MWNT composite with 0.6 vol.% MWNT using the rheo-electrical set-up (Fig. 10.13 (a)) and the in-line set-up (Fig. 10.13 (b)) are arranged together to illustrate the effect of shear-induced destruction of the conductive filler network and conductivity recovery in the quiescent melt. The first time interval in Fig. 10.13 (a) shows a conductivity increase by about three orders of magnitude during isothermal annealing of the as-prepared sample measured in the rheo-electrical set-up at 230 °C for 2 hours. This increase can be explained by secondary agglomeration after the sample is heated above its glass transition temperature (Alig *et al.*, 2007b; Alig *et al.*, 2008b). During the short transient shear ($t_s = 10$ s, $d\gamma/dt = 1\text{ s}^{-1}$), the electrical conductivity decreases tremendously, which can be explained by the (at least partial) destruction of the conductive filler network in the shear field. Due to the reformation of the conductive filler network in the quiescent melt ($t > 120$ min), the conductivity increases again ('conductivity

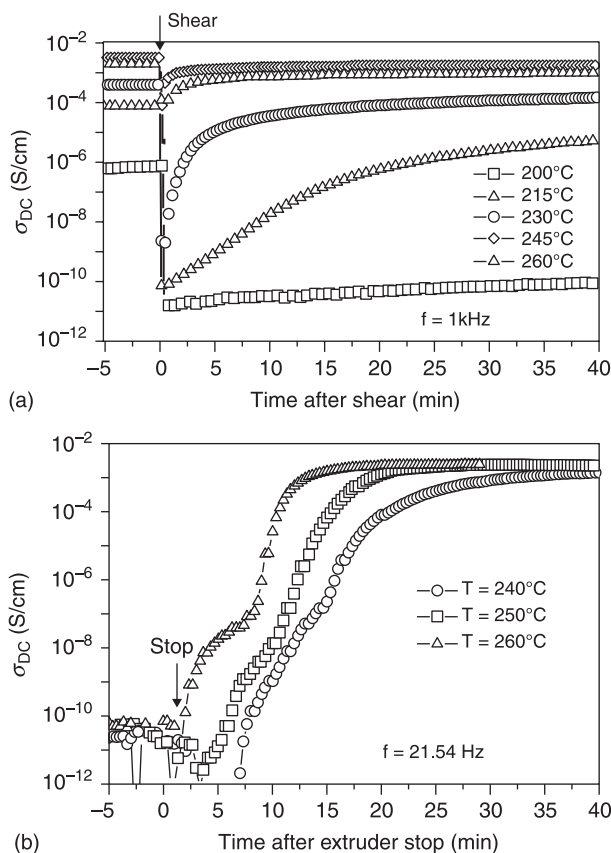


10.13 Indication of shear-induced destruction of the conductive filler network and conductivity recovery in the quiescent melt. Time-dependent conductivity measurements of a PC–CNT composite with 0.6 vol.% MWNT: (a) in a rheometer during isothermal annealing after short transient shear ($t_s = 10$ s, $d\gamma/dt = 1$ s $^{-1}$); (b) in a measurement slit die during melt extrusion at different melt temperatures (screw speed: 175 rpm) and after the extruder has stopped.

recovery'). Parallel measurements of the real part of the shear modulus G' in the quiescent melt (not shown) also exhibit an increase of G' in this time interval. However, the shear modulus increases only from about 60 Pa to about 1000 Pa, whereas the conductivity increases by about 6 orders of magnitude in the same time interval. This 'modulus recovery' indicates that the 'healing' of the viscoelastic filler network after mechanical deformation is somehow related to the reformation of the conductive filler network, although the stress transfer and the charge transport mechanisms are different (see below).

In Fig. 10.13 (b), an example (Alig *et al.*, 2008a) of in-line conductivity measurements during extrusion is shown for the same material. The dependence of the conductivity on processing time was studied using the slit die shown in Fig. 10.11. During extrusion of the PC-MWNT melt (screw speed: 175 rpm), the conductivity is very low, since the conductive filler network is almost destroyed by the shear and elongation flow in the extruder and/or the slit die. The conductivity recovers by reformation of the conductive filler network in the quiescent melt (after stopping the extruder).

In Fig. 10.14, the temperature dependence of the conductivity recovery is shown for the same PC-MWNT as in Fig. 10.13 in the quiescent melt after a short shear deformation (shear rate $d\gamma/dt = 1 \text{ s}^{-1}$ for 10 s) in the rheometer (a) and after the extruder was stopped (b) (Alig *et al.*, 2008a). The data in Fig. 10.14 (b)



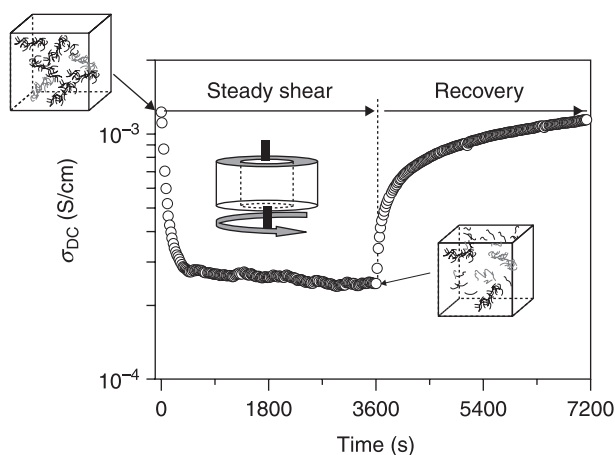
10.14 Temperature dependence of the conductivity recovery in PC containing 0.6 vol.% MWNT in a rheometer with ring electrodes after a short shear deformation (1 rad/s for 10 s) (a) and in a measurement slit die after the extruder was stopped (b). The data after stopping the extruder are taken from Fig. 10.13 (b).

are taken from Fig. 10.13 (b). As expected, the conductivity recovery becomes faster with increasing melt temperature. This temperature dependence is typical of a thermal activated process and can be related to the lower melt viscosity and the faster nanotube agglomeration.

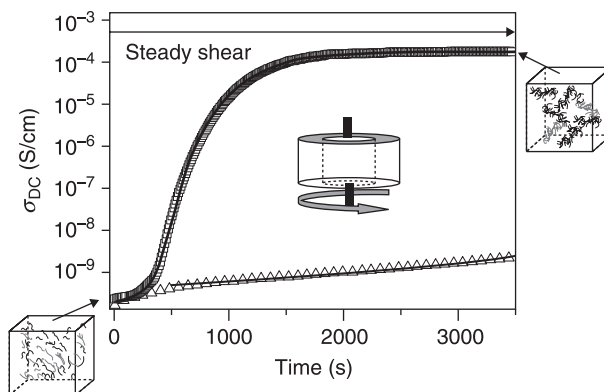
Steady shear conditions

To study the shear-induced destruction of a conductive filler network in more detail, time-dependent conductivity measurements were performed in the rheo-electrical set-up for a PC–MWNT composite with initially well-agglomerated MWNT (Fig. 10.15). The initial state was prepared by one hour of isothermal annealing (not shown). First, a steady shear deformation (shear rate of 0.02 rad/s) was applied for one hour, followed by isothermal annealing without shear. During one hour of steady shear the conductivity tends to approach an equilibrium value which indicates a dynamic equilibrium state of the conductive filler network. In the quiescent melt (after shear deformation), the conductivity increases due to the reformation of the conductive CNT network (Skipa *et al.*, 2009; Skipa *et al.*, 2010). Interestingly, the kinetic constant for destruction (assuming first order kinetics) is faster than the kinetic constant for quiescent melt recovery.

In Fig. 10.16, the formation of a conductive nanotube network by agglomeration during quiescent annealing (triangles) and by shear-stimulated coalescence of nanotubes under steady shear (squares) are compared for an MWNT–PC melt with 1 wt% MWNT at 230°C. Both samples represent initially well-dispersed nanotubes (Skipa *et al.*, 2009). It is obvious that a small shear deformation



10.15 Time-dependent conductivity for an initially agglomerated PC–CNT composite with 0.6 vol.% MWNT in a rheometer under steady shear ($d\gamma/dt = 0.02$ rad/s for 1 hour) and during isothermal annealing after shear at 230°C.



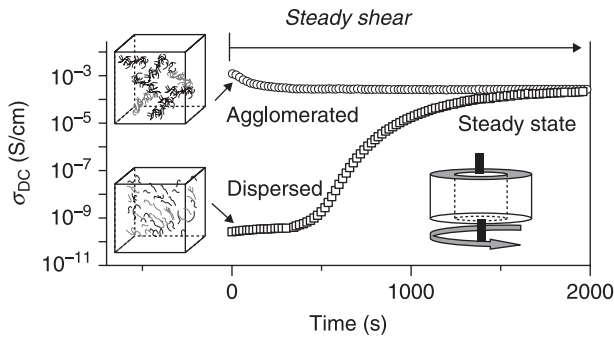
10.16 Conductivity of MWNT–PC melts measured during steady shear (upper curve) and quiescent annealing (lower curve). The solid lines represent fits. The inset schematically shows the measuring cell with the sample. The direction of the applied shear is perpendicular to the electrical field for conductivity measurement.

(0.02 rad/s) can already induce an insulator–conductor transition with a conductivity increase by about 6 orders of magnitude. In contrast, the composite melt annealed in the quiescent melt without shear shows a much slower increase of the DC conductivity, which can be attributed to a diffusion controlled agglomeration of attractively interacting nanotubes. Details of the fits are given by (Skipa *et al.*, 2010).

In contrast to quiescent polymer melts where the nanotube network formation is driven by Brownian diffusion of attractively interacting nanofillers, the formation of the network in external shear fields can be explained by a ‘picking-up’ mechanism under steady shear (Skipa *et al.*, 2009, 2010), where the nanotubes in a shear gradient are collecting other nanotubes on their way and sticking to each other.

Steady state network

In Fig. 10.17, the time development of the DC conductivity under steady shear (shear rate: 0.02 rad/s) is compared for two samples (same material with 1 wt% MWNT in PC), one with initially ‘dispersed’ (squares) and the other with ‘agglomerated’ nanotubes (circles). Interestingly, both samples approach for sufficient duration of steady shear flow the same value of the electrical conductivity. This steady conductivity value is assumed to represent a dynamic equilibrium state of the conductive filler network. This supports the assumption of a stationary equilibrium between destruction and build-up of the filler network under steady shear (Skipa *et al.*, 2009, 2010).



10.17 Time dependence of the DC conductivity during 1 hour of steady shear (shear rate: 0.02 rad/s) for two samples (1 wt.% MWNT) with initially 'dispersed' (squares) and 'agglomerated' nanotubes (circles).

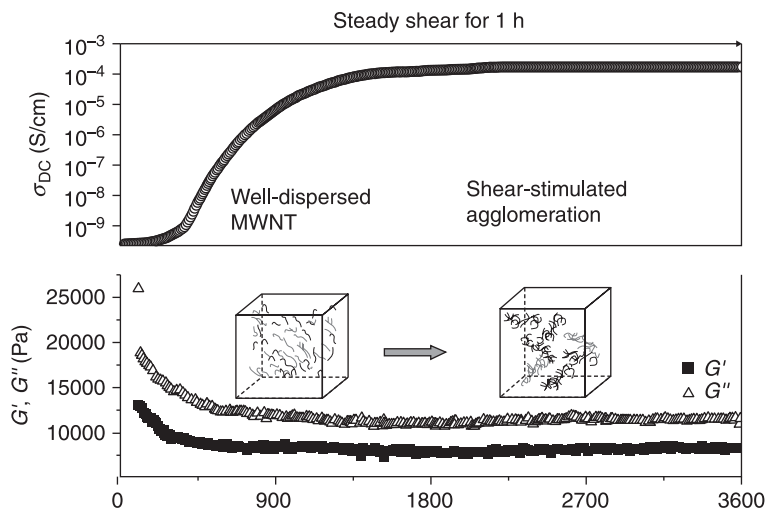
10.4.2 Conductive and viscoelastic filler network

Relation between electrical and rheological properties

In Fig. 10.18, the conductivity (upper part) and the components of the complex shear modulus, G' (squares) and G'' (triangles), for a MWNT–PC melt with 1 wt% MWNT measured during steady shear (0.02 rad/s) at 230°C are plotted versus time. The initial sample ($t = 0$), prepared by injection moulding (Skipa *et al.*, 2009, 2010), represents a state with almost well-dispersed nanotubes.

Both conductivity and rheological measurements were performed in parallel and reflect the same phenomenon which takes place in the shear flow. The initial melt had a very low conductivity of about 10^{-10} S/cm. This value is similar to that of the pure PC melt. At the same time, the initial sample possesses a quite high storage modulus of $G' = 13$ kPa and a loss modulus of $G'' = 25$ kPa, measured with a frequency of 1 Hz and 6.28% strain amplitude. For comparison, the pure PC has $G' = 4$ kPa and $G'' = 25$ kPa.

When steady shear is applied, a tremendous increase of the DC-conductivity (as shown previously in Figs 10.16 and 10.17) and a simultaneous decrease of G' and G'' are observed. As discussed in Section 10.4.1, both processes can be related to the formation of a filler network formed by agglomerates (Skipa *et al.*, 2009, 2010). The nanotube agglomeration and network formation are schematically shown in Fig. 10.18 as insets. However, for the electrical conductivity, the network of agglomerated CNT is preferred, whereas it is not optimal for the mechanical reinforcement. In general, the mechanisms for charge transport and mechanical reinforcement in composite materials are expected to be different (Rothon, 2003). In order to obtain a conducting pathway in the matrix, an electrical percolation network of *interconnected* filler conductive particles is necessary. Very small inter-particle distances (~ 1 nm, almost physical contact) are needed for low contact resistance and efficient electron transport through the conductive network.

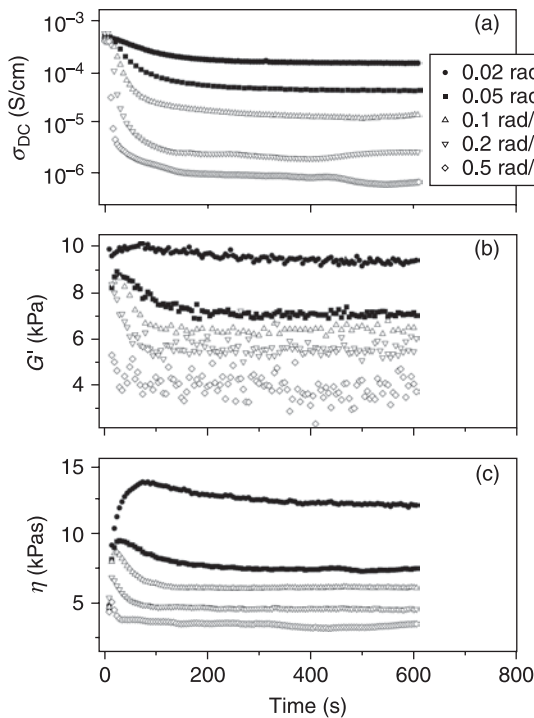


10.18 Shear-induced insulator-conductor (upper graph) transition in a PC-MWNT melt (230°C, 1 wt.% MWNT) during steady shear (shear rate: 0.02 rad/s) and simultaneously measured storage (G') and loss modulus (G'') (lower graph).

Since the nanotubes in thermoplastic composites are considered to be surrounded or bridged by polymer chains (Pötschke *et al.*, 2004), very small intertube distances are assumed to be achieved only by dense packing of nanotubes inside the agglomerates. In contrast, for efficient reinforcement, a strong interfacial interaction of nanotubes with the matrix and a homogeneous space distribution is needed. The optimal mechanical reinforcement is thus expected for well-mixed MWNTs which strongly interact with the polymer chains. Direct contact between the nanotubes is not necessary in this case. During agglomeration of the nanotubes, a new distribution of the nanotubes is created which results in a new (less efficient) type of the reinforcement: macro-fillers with a low aspect ratio (spherical-like agglomerates) replace nanofillers with high aspect ratio (individual MWNTs).

Shear rate dependence and dynamic filler network

In order to investigate the shear-rate dependence of the electrical and mechanical properties under steady flow condition, six similar samples (PC-MWNT, 1 wt.% MWNT) were cut out of one injection-moulded plate (Alig *et al.*, 2008c) and thermo-rheologically pre-treated in order to obtain samples with 'well-agglomerated' nanotubes and a high level of electrical conductivity. For details of the pre-treatment, see (Skipa *et al.*, 2010). Different shear rates varying from 0.02 rad/s to 0.5 rad/s were applied to the thus prepared samples. In Fig. 10.19, the



10.19 Time evolution of electrical conductivity (a); real part of the storage modulus G' (b); and the transient shear viscosity $\eta^+ = \langle \tau(t) \rangle / \dot{\gamma}_{steady}$ (c) of a PC–MWNT melt (230°C, 1 wt.% MWNT) with initially well-agglomerated nanotubes during 1 hour of steady shear for different shear rates.

electrical conductivity (a), the storage modulus G' (b), and the transient shear viscosity $\eta^+ = \langle \tau(t) \rangle / \dot{\gamma}_{steady}$ (c) are shown as a function of time after the shear deformation started. The transient viscosity shown in Fig. 10.19 (c) shows a viscosity overshoot, which shifts toward shorter times with increase of the shear rate. The pure PC does not show shear-thinning for the shear rates and temperatures used in this experiment and does not exhibit such a shear overshoot. Furthermore, no indication of (re)-orientation of MWNTs has been found for this system by X-ray measurements (Richter, 2009). Therefore, the appearance of maxima in the transient viscosity curves and the shear thinning can be ascribed to the shear-induced destruction of the MWNT network. For a more detailed discussion and further references, see (Skipa *et al.*, 2010).

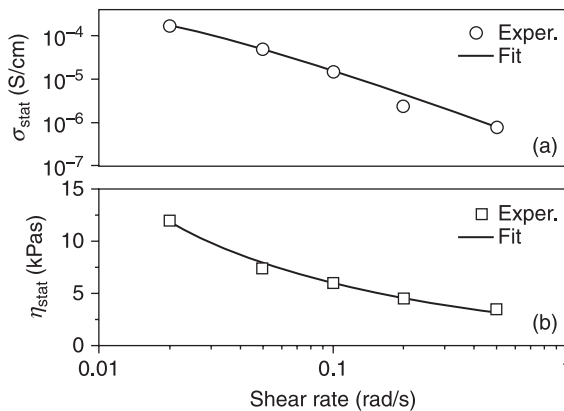
After 1 hour of shear, all three quantities achieved for every shear rate almost constant values representing a stationary state of the dynamic filler network. Correspondingly, the values of, σ_{DC} , G' , G'' and η^+ at $t = 600$ s can be taken for the stationary (subscript: *stat*) values for $t \rightarrow \infty$. In Fig. 10.19 $\sigma_{stat} = \sigma_{DC}(t \rightarrow \infty)$

and $\eta_{stat} = \eta^+(t \rightarrow \infty)$ are plotted versus shear rate. The decrease of σ_{stat} and η_{stat} with the increase of the shear rate is due to the dominance of destruction of the ‘conducting’ and ‘viscoelastic’ networks, respectively. However, the steady state values of the conductivity, the shear modulus G' and G'' (not shown) and the viscosity represent a dynamic equilibrium between destruction and build-up of the filler network in the steady shear flow. The assumption of a steady state of the ‘dynamic filler network’ seems to be of general importance to attractive interacting fillers in a liquid matrix. A similar shear rate dependence of electrical conductivity and viscosity was reported by Kharchenko *et al.* (2004) and Obrzut *et al.* (2007). In these papers, the time-evolution of the conductivity and the rheological properties are not investigated. Kharchenko *et al.* (2004) described the shear thinning of a PP-MWNT composite by the empirical Carreau equation (Tanner, 2000), $\eta(\dot{\gamma}) = \eta_0 [1 + (\dot{\gamma}\tau_\eta)^2]^{-n} \propto \dot{\gamma}^{-m}\eta$, where τ_η and $\dot{\gamma}\tau_\eta$ are the characteristic time and the reduced shear rate, respectively. The decrease of the electrical conductivity was described by an analogous empirical function $\sigma(\dot{\gamma}) = \sigma_0[1 + (\dot{\gamma}\tau_\sigma)^2]^{-n'} \propto \dot{\gamma}^{-m}\sigma$. The decrease of both quantities $\dot{\gamma}$ with was explained by the reduction in the number of nanotube contacts by orientation or by disruption in the flow.

The steady state conductivity data extracted from Fig. 10.19, we assumed as a simple semi-empirical equation (Skipa *et al.*, 2010):

$$\sigma_{stat} = \frac{\sigma_0}{(1 + t_1 \dot{\gamma})^t} \quad [10.10]$$

The solid line in Fig. 10.20 (a) represents a fit with Equation 10.10. The fit parameters are: $t_1 = 64.5$ s and $\sigma_0 = 8.9 \times 10^{-4}$ S/cm. The exponent t was taken to



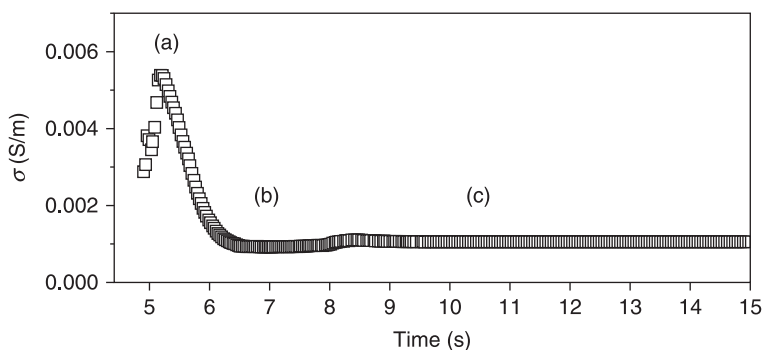
10.20 Stationary values for the DC conductivity (a) and viscosity (b) after 600 s of steady shear vs. shear rate (data extracted from Fig. 10.19). The lines indicate fits as discussed in the text.

be 2. For the fit of the shear-dependent viscosity, the empirical Carreau equation (see above) has been assumed. Further details are discussed in (Skipa *et al.*, 2010).

10.5 Influence of processing history

Examples of the influence of pressing conditions, thermal annealing and extrusion conditions have already been shown in Sections 10.2 and 10.4. These examples are representative of the melt stage and concentrated on the influence of processing conditions on the CNT dispersion: destruction of primary agglomerates and the formation and destruction conductive (or viscoelastic) network by secondary agglomeration. However, the last step of melt processing is the ‘frustration’ of the filler network by solidification of the plastic part (crystallization or passing the glass transition). Here, we will consider the influence of processing conditions on the electrical conductivity during injection moulding, which is the final process step for most plastic parts. Using the in-line set-up for conductivity measurements shown in Fig. 10.12, different polymer–CNT compounds (MWNT in PC, polyamide and blends) were therefore investigated under different injection moulding conditions (Lellinger *et al.*, 2008).

The electric conductivity during a typical injection cycle is shown in Fig. 10.21 for a polycarbonate–styrene-co-acrylonitrile blend (Bayblend®) containing 4 wt% MWNTs. At the start of the cycle, the mould is empty and the measured conductivity is below the instrument limit. When the melt approaches the conductivity sensor (a), the measured conductivity value increases with the degree of covering of the sensor until it reflects the specific electric conductivity of the part. After the sensor is fully covered by melt, the conductivity immediately decreases, which can be related to the cooling-down and vitrification of the melt at the sensor/mould surface. A few seconds later, the mould is completely filled,

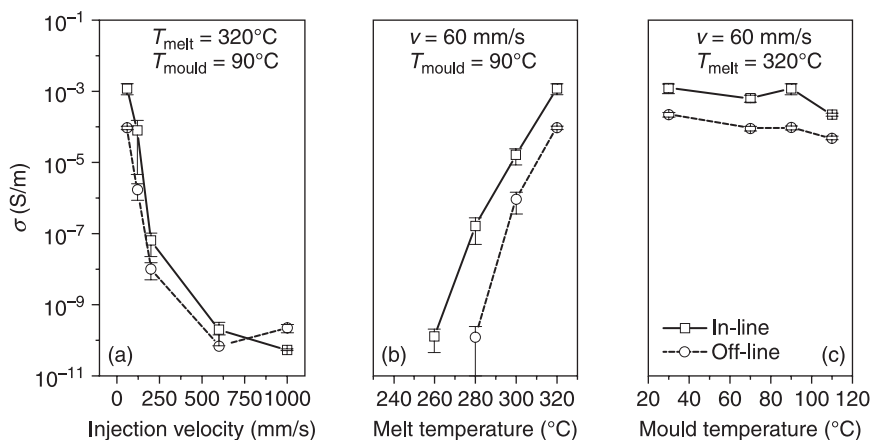


10.21 Electric conductivity in the first few seconds of an injection cycle for a polycarbonate–styrene-co-acrylonitrile blend (Bayblend®) containing 4 wt.% MWNT (melt temperature 320°C, mould temperature 90°C, injection velocity 60 mm/s). For explanations, see text.

which induces a pressure increase up to the holding pressure (here: 400 bar). The pressure increases the density of the sample and thus reduces the distances between the nanotubes, which causes an increase of the conductivity (b). The conductivity in the following time period (c) is nearly constant, until the part breaks off the sensor (not shown).

In Fig. 10.22, the in-line conductivity data of injection moulding of Bayblend® with 4 wt% MWNT are shown together with off-line measured values for different injection velocity, melt and mould temperature. For the in-line conductivity data, the values recorded 9 secs after the start of injection were taken. The offline data are measured at the same position on the vitrified sample. The good correlation between in-line and off-line data supports the assumption that the in-line values after 9 secs already represent a vitrified (glassy frozen) sample. The same was found for semicrystalline polyamide (Lellinger *et al.*, 2008) where the measured values after about 10 secs represent a semicrystalline state. The tremendous decrease in the conductivity with increasing injection speed and decreasing temperature can be explained by the dominance of destruction of the conductive filler network due to increasing shear stress either because of an increasing shear rate (with injection velocity) or because of increasing viscosity (with temperature decrease). The relative high conductivity values at low injection velocities and high melt temperatures cannot be explained by the destructive effect of shear deformation alone.

Therefore, we assume that the measured conductivity values in the solidified state represent the ‘frustrated’ conductivity values resulting from the competition of deformation-induced build-up and destruction along the injection track. No



10.22 Influence of injection speed v (a), melt temperature (b) and mould temperature T_{mould} (c) on the in-line and off-line measured electrical conductivity of a polycarbonate-styrene-co-acrylonitrile blend (Bayblend®) containing 4 wt.% MWNT.

significant effect of the mould temperature is seen. Since the mould temperature mainly determines the average cooling rate for the ‘frustration’ of the filler network by vitrification or crystallization, this finding supports our assumption that the conductivity values are mainly determined by the flow conditions and that the time for conductivity recovery is too short for typical injection cycles.

10.6 Conclusion

The influence of thermo-rheological prehistory on the electrical conductivity and the viscoelastic properties of polymer melts filled with carbon nanotubes is reviewed. For an illustration of shear-induced destruction and the build-up of the filler network and its reformation in the quiescent melt, time-resolved rheo-electrical laboratory experiments and in-line measurements during extrusion and injection moulding are presented and discussed. The experimental set-ups for simultaneous (time-resolved) measurements of the electrical conductivity and the storage (G') and loss components (G'') of the complex shear modulus and for in-line conductivity measurements during extrusion and injection moulding are described.

The main results can be summarized as follows:

1. To achieve a polymer–carbon nanotube composite with high electrical conductivity, the primary agglomerates have first to be ‘dissolved’ in the polymer matrix to get well-separated nanotubes, which can then rearrange into secondary agglomerates forming the conductive filler network. For well-dispersed nanotubes, a high contact resistance between the nanotubes is expected due to the surrounding polymer chains, whereas nanotube agglomeration is assumed to result in denser packing, small inter-particle distances (which possibly allow tunnelling of electrons) and a low contact resistance. The latter allows efficient charge carrier transport through the conductive filler network.
2. Secondary agglomeration of attractive filler particles is assumed to be thermally activated (Brownian filler diffusion in the melt) and can be accelerated by external mechanical energy (shear-induced agglomeration).
3. Steady state values of electrical conductivity, storage (G') and loss modulus (G'') for steady shear conditions indicate an equilibrium between build-up and destruction of the filler network (‘dynamic equilibrium’). The competition between formation and destruction of agglomerates under shear can be described by kinetic models.
4. A model combining agglomeration kinetics and an equation for the insulator–conductor transition was developed to describe the electrical conductivity in composites containing conductive fillers. Different approaches to the insulator–conductor transition have been tested: the classical percolation model, the modified Fournier equation, and the generalized effective medium (GEM) theory.

5. The mechanisms of charge carrier transport in a nanotube network and the effect of mechanical reinforcement are found to be different. From simultaneous measurements of electrical conductivities and shear modulus (G' and G''), it became evident that a network formed by nanotube agglomerates increases the electrical conductivity, whereas the shear modulus is reduced. The optimal mechanical reinforcement is expected for randomly distributed nanotubes forming a combined (viscoelastic) nanotube–polymer network.

The results found for carbon nanotubes in a polymer matrix seem to have general importance for filler networks in viscoelastic or viscous matrices. Apart from its scientific interest, the results can help optimize industrial production of polymer–nanotube composites.

10.7 Acknowledgements

Part of the results was funded by the German Federal Ministry of Education and Research (BMBF) in the WING Program ‘Virtual Material Development’ (CarboNet, funding No. 03X0504E) and in the Framework Concept ‘Research for Tomorrow’s Production’ (CompoMel, funding No. 02PU2394). Furthermore, we thank the Bundesministerium für Wirtschaft (German Federal Ministry for Economic Affairs) via the Arbeitsgemeinschaft Industrieller Forschungsgesellschaften (AiF) for financial support of the AiF projects No. 122Z and 14454N. We would like to acknowledge W. Böhm (DKI) and Dr. M. Engel (DKI, TU Darmstadt) for their help with dielectric and rheological measurements and Dr. M. Bierdel (Bayer Technology Services), Dr. H. Meyer (Bayer MaterialScience AG) and Dr. S. Hermasch (Evonik Industries AG, Marl, Germany) for providing part of the samples. Furthermore, we would like to thank Hyperion Catalysis International, Inc. (Cambridge, MA, USA) for providing MWNT masterbatches. Dr. M. Engel (DKI, TU Darmstadt), Dr. D. Xu (DKI), A. Ohneiser (DKI), H. Dörr (DKI), F. Pflieger (DKI) and G. Vulpius (DKI), we would like to acknowledge for their contribution to the in-line experiments. Prof. G. Heinrich and Dr. M. Grenzer (IPF, Dresden) we thank for helpful discussions. Last but not least, we would like to thank Dr. P. Pötschke (IPF, Dresden) for the very fruitful cooperation over the past few years.

10.8 References

- Alig, I., Lellinger, D., Dudkin, S. M. & Pötschke, P. (2007a) Conductivity spectroscopy on melt processed polypropylene-multiwalled carbon nanotube composites: recovery after shear and crystallization, *Polymer*, 48, 1020–1029.
- Alig, I., Skipa, T., Engel, M., Lellinger, D., Pegel, S. & Pötschke, P. (2007b) Electrical conductivity recovery in carbon nanotube polymer composites after transient shear, *Physica Status Solidi B: Basic Solid State Physics*, 244, 4223–4226.
- Alig, I., Lellinger, D., Engel, M., Skipa, T. & Pötschke, P. (2008a) Destruction and formation of a conductive carbon nanotube network in polymer melts: in-line experiments, *Polymer*, 49, 1902–1909.

- Alig, I., Pötschke, P., Pegel, S., Dudkin, S. & Lellinger, D. (2008b) Plastic composites containing carbon nanotubes: optimisation of processing conditions and properties, *Rubber Fibre Plastics*, 3(2), 92–95.
- Alig, I., Skipa, T., Lellinger, D., Bierdel, M. & Meyer, H. (2008c) Dynamic percolation of carbon nanotube agglomerates in a polymer matrix: comparison of different model approaches, *Physica Status Solidi B: Basic Solid State Physics*, 245, 2264–2267.
- Alig, I., Skipa, T., Lellinger, D. & Pötschke, P. (2008d) Destruction and formation of a carbon nanotube network in polymer melts: rheology and conductivity spectroscopy, *Polymer*, 49, 3524–3532.
- Almond, D. P. & Bowen, C. R. (2004) Anomalous power law dispersions in AC conductivity and permittivity shown to be characteristics of microstructural electrical networks, *Physical Review Letters*, 92, 157601.1–4.
- An, K. H., Jeong, S. Y., Hwang, H. R. & Lee, Y. H. (2004) Enhanced sensitivity of a gas sensor incorporating single-walled carbon nanotube-polypyrrole nanocomposites, *Advanced Materials*, 16, 1005–1009.
- Andrews, R., Jacques, D., Qian, D. & Dickey, E. C. (2001) Purification and structural annealing of multiwalled carbon nanotubes at graphitization temperatures, *Carbon*, 39, 1681–1687.
- Balberg, I., Binenbaum, N. & Wagner, N. (1984) Percolation thresholds in the 3-dimensional sticks system, *Physical Review Letters*, 52, 1465–1468.
- Bergman, D. J. & Imry, Y. (1977) Critical behavior of complex dielectric-constant near percolation threshold of a heterogeneous material, *Physical Review Letters*, 39, 1222–1225.
- Bunde, A. & Havlin, S. (1996) *Fractals and Disordered Systems*, Berlin: Springer.
- Carroll, D. L., Czerw, R. & Webster, S. (2005) Polymer-nanotube composites for transparent conductive thin films, *Synthetic Metals*, 155, 694–697.
- Clerc, J. P., Giraud, G., Laugier, J. M. & Luck, J. M. (1990) The AC electrical-conductivity of binary disordered-systems, percolation clusters, fractals and related models, *Advances in Physics*, 39, 191–308.
- Coleman, J. N., Curran, S., Dalton, A. B., Davey, A. P., McCarthy, B., Blau, W. & Barklie, R. C. (1998) Percolation-dominated conductivity in a conjugated-polymer-carbon-nanotube composite, *Physical Review B*, 58, R7492–R7495.
- Curran, S. A., Zhang, D. H., Wondmagegn, W. T., Ellis, A. V., Cech, J., Roth, S. & Carroll, D. L. (2006) Dynamic electrical properties of polymer-carbon nanotube composites: Enhancement through covalent bonding, *Journal of Materials Research*, 21, 1071–1077.
- De Gennes, P. G. (1976a) La percolation: un concept unificateur, *La Recherche*, 7.
- De Gennes, P. G. (1976b) One has relation between percolation theory and the elasticity of gels, *Journal de Physique Letters (Paris)*, 37.
- Deng, H., Skipa, T., Zhang, R., Lellinger, D., Bilotti, E., Alig, I. & Peijs, T. (2009) Effect of melting and crystallization on the conductive network in conductive polymer composites, *Polymer*, 50, 3747–3754.
- Efros, A. L. & Shklovskii, B. I. (1976) Critical behavior of conductivity and dielectric-constant near metal-non-metal transition threshold, *Physica Status Solidi B: Basic Research*, 76, 475–485.
- Fournier, J., Boiteux, G., Seytre, G. & Marichy, G. (1997) Percolation network of polypyrrole in conducting polymer composites, *Synthetic Metals*, 84, 839–840.
- Gefen, Y., Aharony, A. & Alexander, S. (1983) Anomalous diffusion on percolating clusters, *Physical Review Letters*, 50, 77–80.

- Gefen, Y., Aharony, A., Mandelbrot, B. B. & Kirkpatrick, S. (1981) Solvable fractal family, and its possible relation to the backbone at percolation, *Physical Review Letters*, 47, 1771–1774.
- Gojny, F. H., Wichmann, M. H. G., Fiedler, B., Kinloch, I. A., Bauhofer, W., Windle, A. H. & Schulte, K. (2006) Evaluation and identification of electrical and thermal conduction mechanisms in carbon nanotube/epoxy composites, *Polymer*, 47, 2036–2045.
- Gojny, F. H., Wichmann, M. H. G., Fiedler, B. & Schulte, K. (2005) Influence of different carbon nanotubes on the mechanical properties of epoxy matrix composites: a comparative study, *Composites Science and Technology*, 65, 2300–2313.
- Guery, J., Bertrand, E., Rouzeau, C., Levitz, P., Weitz, D. A. & Bibette, J. (2006) Irreversible shear-activated aggregation in non-Brownian suspensions, *Physical Review Letters*, 96, 198301.1–4.
- Han, C. C., Yao, Y. H., Zhang, R. Y. & Hobbie, E. K. (2006) Effect of shear flow on multi-component polymer mixtures, *Polymer*, 47, 3271–3286.
- Hobbie, E. K. & Fry, D. J. (2006) Nonequilibrium phase diagram of sticky nanotube suspensions, *Physical Review Letters*, 97, 3–6, 036101.
- Hobbie, E. K. & Fry, D. J. (2007) Rheology of concentrated carbon nanotube suspensions, *Journal of Chemical Physics*, 126, 124907.
- Hobbie, E. K., Jeon, H. S., Wang, H., Kim, H., Stout, D. J. & Han, C. C. (2002) Shear-induced structure in polymer blends with viscoelastic asymmetry, *Journal of Chemical Physics*, 117, 6350–6359.
- Hong, D. C., Stanley, H. E., Coniglio, A. & Bunde, A. (1986) Random-walk approach to the 2-component random-conductor mixture – perturbing away from the perfect random resistor network and random superconducting-network limits, *Physical Review B*, 33, 4564–4573.
- Kang, I. P., Heung, Y. Y., Kim, J. H., Lee, J. W., Gollapudi, R., Subramaniam, S., Narasimhadevara, S., Hurd, D., Kirikera, G. R., Shanov, V., Schulz, M. J., Shi, D. L., Boerio, J., Mall, S. & Ruggles-Wren, M. (2006) Introduction to carbon nanotube and nanofiber smart materials, *Composites Part B: Engineering*, 37, 382–394.
- Kharchenko, S. B., Douglas, J. F., Obrzut, J., Grulke, E. A. & Migler, K. B. (2004) Flow-induced properties of nanotube-filled polymer materials, *Nature Materials*, 3, 564–568.
- Kirkpatrick, S. (1973) Percolation and conduction, *Reviews of Modern Physics*, 45, 574–588.
- Klüppel, M. (2003) The role of disorder in filler reinforcement of elastomers on various length scales, *Advances in Polymer Science*, 164, 1–86.
- Kovacs, J. Z., Velagala, B. S., Schulte, K. & Bauhofer, W. (2007) Two percolation thresholds in carbon nanotube epoxy composites, *Composites Science and Technology*, 67, 922–928.
- Laibowitz, R. B. & Gefen, Y. (1984) Dynamic scaling near the percolation-threshold in thin au films, *Physical Review Letters*, 53, 380–383.
- Lellinger, D., Skipa, T., Böhm, W. & Alig, I. (2009) Spatial decorrelation of the conductive nanotube network in a polymer melt, *Physica Status Solidi B: Basic Solid State Physics*, 246, 2667–2670.
- Lellinger, D., Xu, D. H., Ohneiser, A., Skipa, T. & Alig, I. (2008) Influence of the injection moulding conditions on the in-line measured electrical conductivity of polymer-carbon nanotube composites, *Physica Status Solidi B: Basic Solid State Physics*, 245, 2268–2271.
- Li, C., Thostenson, E. T. & Chou, T. W. (2008) Sensors and actuators based on carbon nanotubes and their composites: a review, *Composites Science and Technology*, 68, 1227–1249.

- Lin-Gibson, S., Pathak, J. A., Grulke, E. A., Wang, H. & Hobbie, E. K. (2004) Elastic flow instability in nanotube suspensions, *Physical Review Letters*, 92, 048302.1–4.
- Ma, A. W. K., Mackley, M. R. & Rahatekar, S. S. (2007) Experimental observation on the flow-induced assembly of carbon nanotube suspensions to form helical bands, *Rheologica Acta*, 46, 979–987.
- Martin, C. A., Sandler, J. K. W., Shaffer, M. S. P., Schwarz, M. K., Bauhofer, W., Schulte, K. & Windle, A. H. (2004) Formation of percolating networks in multi-wall carbon-nanotube-epoxy composites, *Composites Science and Technology*, 64, 2309–2316.
- McCullen, S. D., Stevens, D. R., Roberts, W. A., Ojha, S. S., Clarke, L. I. & Gorga, R. E. (2007) Morphological, electrical, and mechanical characterization of electrospun nanofiber mats containing multiwalled carbon nanotubes, *Macromolecules*, 40, 997–1003.
- McLachlan, D. S., Blaszkiewicz, M. & Newnham, R. E. (1990) Electrical resistivity of composites, *Journal of the American Ceramic Society*, 73, 2187–2203.
- Meier, J. G. & Klüppel, M. (2008) Carbon black networking in elastomers monitored by dynamic mechanical and dielectric spectroscopy, *Macromolecular Materials and Engineering*, 293, 12–38.
- Obraztsov, J., Douglas, J. F., Kharchenko, S. B. & Migler, K. B. (2007) Shear-induced conductor-insulator transition in melt-mixed polypropylene-carbon nanotube dispersions, *Physical Review B*, 76, 195420–9.
- Pegel, S., Pötschke, P., Petzold, G., Alig, I., Dudkin, S. M. & Lellinger, D. (2008) Dispersion, agglomeration, and network formation of multiwalled carbon nanotubes in polycarbonate melts, *Polymer*, 49, 974–984.
- Pötschke, P., Abdel-Goad, M., Alig, I., Dudkin, S. & Lellinger, D. (2004) Rheological and dielectrical characterization of melt mixed polycarbonate-multiwalled carbon nanotube composites, *Polymer*, 45, 8863–8870.
- Pötschke, P., Dudkin, S. M. & Alig, I. (2003) Dielectric spectroscopy on melt processed polycarbonate – multiwalled carbon nanotube composites, *Polymer*, 44, 5023–5030.
- Richter, S., Saphiannikova, M., Jehnichen, D., Biedel, M. & Heinrich, G. (2009) Experimental and theoretical studies of agglomeration effects in multi-walled carbon nanotube-polycarbonate melts, *Express Polymer Letters*, 3, 753–768.
- Rothon, R. N. (2003) *Particulate-filled Polymers*, Rapra Technology Limited, Shawbury, Shropshire, SY4 4NR, UK.
- Ruschau, G. R., Yoshikawa, S. & Newnham, R. E. (1992) Resistivities of conductive composites, *Journal of Applied Physics*, 72, 953–959.
- Russell, J. M., Oh, S. J., Larue, I., Zhou, O. & Samulski, E. T. (2006) Alignment of nematic liquid crystals using carbon nanotube films, *Thin Solid Films*, 509, 53–57.
- Sahimi, M. (1994) *Applications of Percolation Theory*, London: Taylor & Francis Ltd.
- Sandler, J. K. W., Windle, A. H., Martin, C. A., Schwarz, M. L., Bauhofer, W., Schulte, K. & Shaffer, M. S. P. (2004) Percolation in multi-wall carbon nanotube-epoxy composites: influence of processing parameters, nanotube aspect ratio and electric fields on the bulk conductivity, *Continuous Nanophase and Nanostructured Materials*, 788, 221–226.
- Scher, H. & Lax, M. (1973) Stochastic transport in a disordered solid .1. Theory, *Physical Review B*, 7, 4491–4502.
- Schueler, R., Petermann, J., Schulte, K. & Wentzel, H. P. (1996) Percolation in carbon black filled epoxy resin, *Macromolecular Symposia*, 104, 261–268.
- Schueler, R., Petermann, J., Schulte, K. & Wentzel, H. P. (1997) Agglomeration and electrical percolation behavior of carbon black dispersed in epoxy resin, *Journal of Applied Polymer Science*, 63, 1741–1746.

- Skipa, T., Lellinger, D., Saphiannikova, M. & Alig, I. (2009) Shear-stimulated formation of carbon nanotube networks in polymer melts, *Physica Status Solidi B: Basic Solid State Physics*, 246, 2453–2456.
- Skipa, T., Lellinger, D., Böhm, W., Saphiannikova, M. & Alig, I. (2010) Influence of shear deformation on carbon nanotube networks in polycarbonate melts: interplay between build-up and destruction of agglomerates, *Polymer*, 51, 201–210.
- Specification. Baytubes. Available: <http://www.baytubes.com>.
- Stauffer, D. (1979) Scaling theory of percolation clusters, *Physics Reports*, 54, 1–74.
- Stauffer, D. & Aharony, A. (1994) *Introduction to Percolation Theory*, London: Taylor & Francis Ltd.
- Stephen, M. J. (1978) Mean-field theory and critical exponents for a random resistor network, *Physical Review B*, 17, 4444–4453.
- Straley, J. P. (1976) Critical phenomena in resistor networks, *Journal of Physics C: Solid State Physics*, 9, 783–795.
- Straley, J. P. (1980) The ant in the labyrinth – diffusion in random networks near the percolation-threshold, *Journal of Physics C: Solid State Physics*, 13, 2991–3002.
- Stroud, D. & Bergman, D. J. (1982) Frequency-dependence of the polarization catastrophe at a metal-insulator-transition and related problems, *Physical Review B*, 25, 2061–2064.
- Switzer, L. H. & Klingenberg, D. J. (2004) Flocculation in simulations of sheared fiber suspensions, *International Journal of Multiphase Flow*, 30, 67–87.
- Szleifer, I. & Yerushalmi-Rozen, R. (2005) Polymers and carbon nanotubes – dimensionality, interactions and nanotechnology, *Polymer*, 46, 7803–7818.
- Tanner R. I. (2000) *Engineering Rheology*, New York: Oxford University Press.
- Vermant, J. & Solomon, M. J. (2005) Flow-induced structure in colloidal suspensions, *Journal of Physics-Condensed Matter*, 17, R187–R216.
- Villmow, T., Pegel, S., Pötschke, P. & Wagenknecht, U. (2008a) Influence of injection molding parameters on the electrical resistivity of polycarbonate filled with multi-walled carbon nanotubes, *Composites Science and Technology*, 68, 777–789.
- Villmow, T., Pötschke, P., Pegel, S., Haussler, L. & Kretzschmar, B. (2008b) Influence of twin-screw extrusion conditions on the dispersion of multi-walled carbon nanotubes in a poly(lactic acid) matrix, *Polymer*, 49, 3500–3509.
- Webman, I., Jortner, J. & Cohen, M. H. (1977) Critical exponents for percolation conductivity in resistor networks, *Physical Review B*, 16, 2593–2596.
- Weiss, G. H. & Rubin, R. J. (1983) Random-walks – theory and selected applications, *Advances in Chemical Physics*, 52, 363–505.
- Wilkinson, D., Langer, J. S. & Sen, P. N. (1983) Enhancement of the dielectric-constant near a percolation-threshold, *Physical Review B*, 28, 1081–1087.

Electromagnetic properties of polymer–carbon nanotube composites

F. NANNI and M. VALENTINI, INSTM–University of Rome
‘Tor Vergata’, Italy

Abstract: The use of plastic materials as shielding enclosures, electromagnetic (EM) absorbing materials, and radio frequency (RF) components has greatly increased in the past few years. Shielding deals with the protection of workspaces from external radiation, usually achieved by conductive materials by means of wave reflection. In absorbing media, the incident wave energy is dissipated within lossy medium. Such EM properties can be modulated by adding conductive fillers (such as carbon nanotubes, CNTs) to an insulating matrix. In this chapter, the shielding and absorbing performance of CNT-loaded polymers is described and their intrinsic electromagnetic properties (complex permittivity and conductivity) are correlated to material composition and microstructure.

Key words: electromagnetic properties, electromagnetic wave absorbing materials, shielding materials.

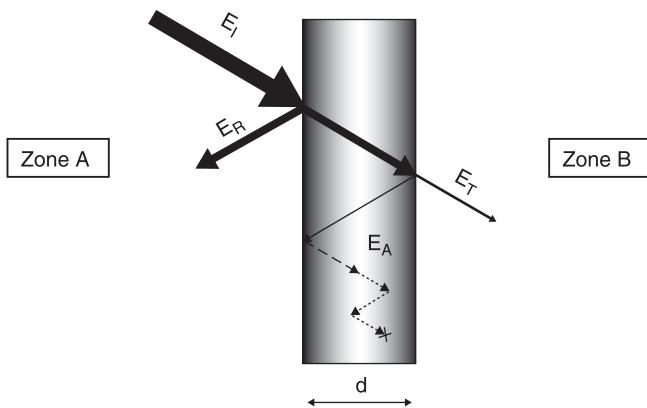
11.1 Introduction

Full comprehension of, as well as possible modeling and simulation of the electromagnetic behavior of materials in waves is extremely interesting in view of the many possible engineering applications such as antennas, circuits, RFID devices, absorbing or shielding media, etc. Historically, the electromagnetic behavior of materials in waves was widely studied during the Second World War for military purposes with the introduction of radar and stealth technologies, nevertheless very little data was divulged in the scientific literature due to strategic needs. More recently, the advent of computers and the spread of electronic devices have brought to light new concerns regarding electromagnetic interference (EMI) phenomena that are at least harmful, if not seriously dangerous, when occurring in particular instances such as airplane electronic systems and radar air traffic control communications. Moreover, unlike the past century, today tremendous progress in material science has been made (up to the advent of nanomaterials and nanotechnology), so that new phenomena must be considered and, possibly, explained when dealing with materials in waves.

Generally the topic of EM waves’ interaction with materials can be dealt with by starting either from a macroscopic approach (Maxwell’s equations and constitutive relations¹), or a microscopic point of view, that considers the interaction between waves and material microstructure. The former is the prerogative of electromagnetic engineering, while the latter is more pertinent to material science engineers.

It is well known that an incident electromagnetic wave (E_I) passing through a material undergoes three main processes: reflection (E_R), transmission (E_T) and absorption ($E_A = E_I - E_R - E_T$) (Fig. 11.1). All these phenomena are strictly related to the medium's intrinsic properties, namely, electric conductivity (σ), complex permittivity ($\epsilon^* = \epsilon' - j\epsilon''$), and complex permeability ($\mu^* = \mu' - j\mu''$), as well as to its geometrical characteristics, in particular, thickness.² From time to time, depending on the application, any one of the aforesaid mechanisms can be promoted by performing an appropriate component design, that involves both the right choice of material, in relation to its intrinsic properties (i.e. σ , ϵ^* and μ^*), as well as geometrical considerations.³ When shielding is required, in fact, the material has to be mostly conductive to reflect the incident wave and preserve the environment behind the shield (zone B in Fig. 11.1).⁴ In the case of absorbing, instead, both reflection of the incident wave and transmission through the medium are unwanted (both zones A and B in Fig. 11.1 have to be preserved) and therefore the energy associated with the material has to be somehow dissipated.⁵ It can be noted that an absorbing structure implies the function of shielding, while the contrary is not true.

As previously mentioned, the prospect of designing and realizing materials with specific EM properties is of great interest, nevertheless this need translates into the feasibility to tailor material composition and microstructure to achieve the required electromagnetic specifications. This is why the research in this field usually involves composite materials (more often polymer matrix composites, PMCs), due to their natural versatility and potential to mix and incorporate fillers, with different intrinsic electromagnetic properties, to gain specific EM characteristics. Moreover, PMCs are low density materials, a property which makes them attractive in many applications where weight is a big concern.



11.1 Reflection (E_R), transmission (E_T) and absorption (E_A) of an EM wave through a medium.

Generally, in both shielding and absorbing applications, lossy materials with a different degree of conductivity are involved. This is because in the case of shielding reflectivity has to be assured, while in the case of absorbing, one of the main mechanisms of energy dissipation (the predominant one when dealing with conductive elements in an insulating medium as in the case of carbon nanotube (CNT) in polymer matrix) is its conversion into heat, by means of the joule effect.

Understanding material behavior in waves when involving composite materials is, however, particularly challenging, since the effect of mixing two or more distinct materials is not always easily predictable, due to the rise of interaction effects. Many attempts at numerical modeling are reported in the literature,^{6,7} even if a complete dissertation that includes all the different aspects and that is valid under all conditions is still lacking, due to the complexity of the involved phenomena. Usually the proposed models either make too stringent a hypothesis, or are confined to the case of well-dispersed non-interacting geometrical perfect particles, or follow an experimental approach, whose validity is confirmed only under specific conditions.^{8,9} Therefore, the current state of the art concerning EM properties of PMC reports mainly experimental results. In this situation, modeling the electromagnetic behavior of composites containing nanofillers is even more challenging, due to the lack of knowledge in understanding phenomena at the nanoscale level, that can be very different from their corresponding micrometric analogs.

Many studies have been carried out in past years regarding the electromagnetic properties of PMC,^{10,11} many of which involve the use of carbon as a conductive filler in the form of either long and/or short fibers, or particles.^{12,13} In this regard, though, the advent of nano-sized carbon fillers (as carbon nanofibers and nanotubes) was a remarkable innovation. In fact, recently many papers have been published on EM properties and performance achievable when involving nanofillers and, in particular, CNTs, and trying to explain why such fillers seem to be tremendously more efficient than the more traditional carbon black or graphite. Distinctive features of CNTs are the high aspect ratio and electrical conductivity, that achieve composites with electric properties comparable and even superior to those shown by today's more used carbon black (CB) loaded polymers, with much lower nanofiller content, allowing avoidance of, or at least minimizing, the degradation of other composite performance such as mechanical properties, aesthetic aspect, processability, etc. Moreover, the cost of nanofillers and CNTs, that nowadays is still a big concern, is thought to become absolutely comparable to those of today's more common fillers in view of the introduction of mass production.

The following paragraphs are devoted to the description of the main mechanisms that achieve an absorbing and shielding performance in CNT-loaded polymers, considering the latest available scientific researches. Particular attention has been paid to link materials' microstructure and CNT intrinsic properties to the final macroscopic EM performance.

11.2 Electromagnetic wave absorbing CNT composites

The main aim of an electromagnetic wave absorbing material is to dissipate the energy associated with the incident wave, by transforming it in to other forms to avoid any reflection and/or transmission. Reflection can be controlled by achieving good impedance matching between free space and the material surface,¹⁴ while transmission is hindered by means of energy dissipation, enhancing magnetic and/or dielectric loss.

For an EM wave incident normal to a slab, the coefficients of reflection (ρ) and transmission (τ) are respectively:⁵

$$\rho = \frac{Z_2 - Z_1}{Z_2 + Z_1} \quad [11.1a]$$

$$\tau = \frac{2Z_2}{Z_2 + Z_1} \quad [11.1b]$$

where Z_1 and Z_2 are the impedance of the media, one of which can be equal to Z_0 (impedance of free space, 377 Ω) in the case of propagation in air. Impedance matching to avoid reflection can be achieved by tailoring material electromagnetic characteristics (complex permeability and permittivity, respectively μ^* and ϵ^* in Equation 11.2) so that its characteristic impedance (Z_m in Equation 11.2) becomes as close as possible to that of free space:

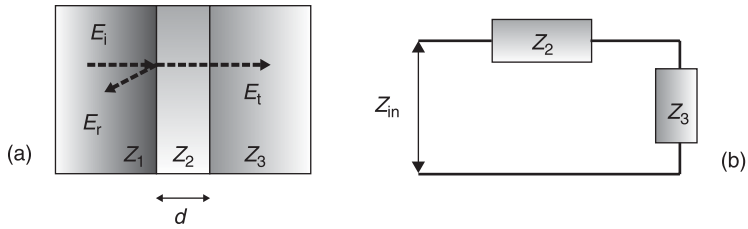
$$Z_m \sqrt{\frac{\mu^*}{\epsilon^*}} \quad [11.2]$$

Often, to increase the bandwidth of the operation, multilayer absorbing structures are designed^{15,16} where, for example, a thin slab is sandwiched between two media. In this case, the analysis is made tractable by drawing upon an analog in the transmission line theory, that gives, for the case depicted in Fig. 11.2, the following equation:⁵

$$Z_{in} = Z_2 \frac{Z_3 \cosh(\gamma d) + Z_2 \sinh(\gamma d)}{Z_2 \cosh(\gamma d) + Z_3 \sinh(\gamma d)} \quad [11.3]$$

where Z_{in} is the input impedance at the surface of the absorber, γ is the propagation constant ($\gamma = j\omega\sqrt{\epsilon\mu}$) and d the thickness of the absorber. The reported equations (that present different forms depending on the propagation condition, presence of metal backing, oblique incidence, etc.) highlight how and by how much electromagnetic and material designs overlap.

As previously reported, the ability shown by some materials to absorb the electromagnetic energy associated with incident waves passing through them, is due to the presence of loss mechanisms that allow energy dissipation. Such dissipation, at the material microscopic level, occurs by means of different



11.2 EM wave propagation through a thin slab between two semi-infinite media: (a) schematic sketch; (b) transmission line equivalent.

mechanisms such as power loss during domain rotation in magnetic materials, transformation of power into heat (with mechanisms analogous to the way energy is consumed by a resistor) in not-perfect conductors, and power loss due to dipole rotation in pure dielectric materials.

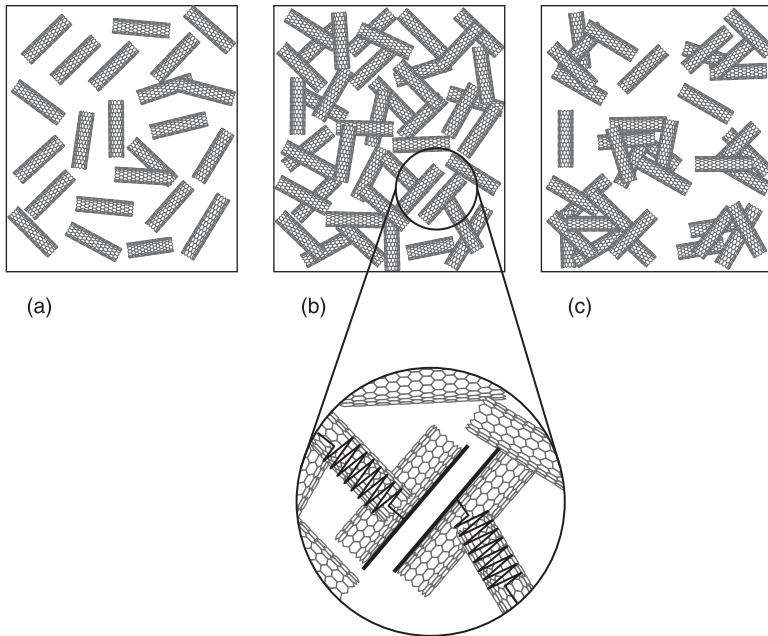
Generally speaking, CNTs can be considered to be non-magnetic fillers, being the only possible magnetism associated with the residual presence of catalysts (usually consisting of magnetic metals as Co or Ni),¹⁷ therefore, all contributions to energy dissipation deriving from magnetic loss can usually be ignored. It is advisable, though, to check CNT purity or to perform preliminary EM measurements to ascertain the assumption of absence of any magnetism.

Mechanisms of energy dissipation in CNT-loaded polymers have therefore to be searched in dielectric loss, since the system is a lossy material made of conductive elements within a dielectric medium. It is customary (engineers are usually interested in the cumulative effect) to group the effects of dielectric loss under one term, named permittivity, that is a material intrinsic property. The effective permittivity for linear, isotropic materials, that includes DC conductivity, is defined as¹⁸

$$\epsilon^* = \epsilon'_r \epsilon_0 - j(\epsilon''_r \epsilon_0 + \frac{\sigma}{\omega}) \quad [11.4]$$

where ϵ_0 is the permittivity of vacuum, ϵ' is real part of permittivity, ϵ'' is the imaginary part of permittivity (i.e. the polarization loss, an entropic term owed to all intrinsic losses arising from the delay of the material in changing polarization in frequency) and σ is the electric conductivity. Thus ϵ' is an enthalpic term, which accounts for the energy stored in the material. The term in brackets in Equation 11.4 embodies all dielectric losses for the system under consideration, that are due to electric conductivity and polarization effects.

It is well known that materials can show many possible polarization mechanisms such as ionic polarization, dipole rotation polarization, electronic displacement polarization, interface polarization, etc., any of which can be ignored or become the main absorbing mechanism, depending on operation frequency and material intrinsic properties. Electronic and ionic polarizations, for instance, produce loss at very high frequency (time to rotate the dipoles 10^{14} – 10^{15} s), while dipole



11.3 System of CNT forming a resistance-capacitance network:
 (a) well-dispersed few CNTs; (b) well-dispersed numerous CNTs;
 (c) numerous aggregated CNTs.

polarization occurs at lower frequencies (time to rotate the dipoles 10^8 – 10^2 s).^{19,20} Interface polarization at the CNT–polymer interface is very important in CNT-loaded polymers, due to the large surface area of CNT.²¹

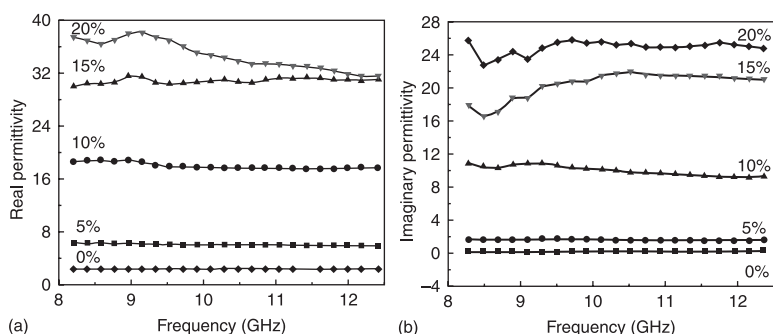
As reported, in order to achieve good absorbing performance, good impedance, matching and high losses (usually encountered by means of a high tangent loss $\text{tg} \delta = \epsilon''/\epsilon'$) are required. The latter involves material design and composition. But, how can this target be reached in CNT composite materials? This question can be answered when understanding the origin of dielectric losses in such systems. In CNT composites many factors strictly related to filler type, amount and characteristics (such as intrinsic permittivity, permeability and conductivity, size, morphology, etc.) as well as its distribution within the matrix, affect the resulting electromagnetic behavior. Generally, a system of CNTs dispersed in an insulating resin can be regarded as a system of resistors in a theoretical resistance-capacitance (RC) network^{22,23} (Fig. 11.3).

In such a system, the losses are introduced by means of electrically conductive fillers, the amount of which is the first parameter affecting ϵ'' (Fig. 11.4b). In particular, it was proved^{23,24} that an increase of CNT results in an increase of ϵ'' , due in part to the mere increase of conducting elements (σ in Equation 11.3) and in part to the formation of more numerous and more closely spaced microcapacitors, thus promoting either the formation of conductive paths and/or

electrons flow by means of tunneling effects (Figs 11.3 (a and b)). Often the increase in imaginary permittivity becomes steeper above a certain CNT concentration. Such an event has been attributed to the onset of percolation,²⁵ when the system shifts from insulator to conductive. It is important not to make the mistake of thinking that the larger the complex permittivity, the better is EM absorption. This is because materials that exhibit too large permittivities tend to reflect a large part of the incident wave,²⁶ and therefore this parameter has to be properly chosen each time according to practical need. Increasing CNT content leads to an increase of ϵ' too (Fig. 11.4a), and this, recalling the RC model, is due to the enlarged contribution of the increased number of microcapacitors to the capacitive term.

Once the RC network scheme has been accepted, then it follows that CNT distribution in the matrix is another important parameter affecting dielectric losses. On equal CNT content, in fact, well-disentangled and well-dispersed nanotubes increase the number of microcapacitors and decrease the distance between them.²⁷ When, instead, highly entangled CNTs are dispersed within the matrix, then the RC scheme is still valid if considering the microcapacitors formed by CNT agglomerates²⁷ (Figs 11.3 (b and c)). In this case, though, the efficiency of the CNT loading is somehow limited and the advantage deriving from their use that is linked to their high aspect ratio is not fully exploited. CNT distribution in the matrix is in turn affected by their amount: if CNT concentration is small, then intramolecular van der Waals interactions between tubes are weaker, so that it is easier to disentangle them, so that CNTs result randomly oriented and well dispersed in the matrix.²²

Since CNT dispersion in resin is a crucial parameter, it follows that the composite manufacturing process plays a role. In ref. 28, wave attenuations of SWCNT–PC composites manufactured by either lamination, coagulation or melt-extrusion were compared, indicating that the higher attenuation performance, shown



11.4 Real and imaginary permittivity vs frequency of MWCNT loaded epoxy samples (%) at different CNT loading (wt%) measured in the x-band frequency range by means of wave guide technique.¹

Note: 1EM measurements carried out at CEMIn s.r.l., Via della Farnesina 363, 00135 Rome, Italy.

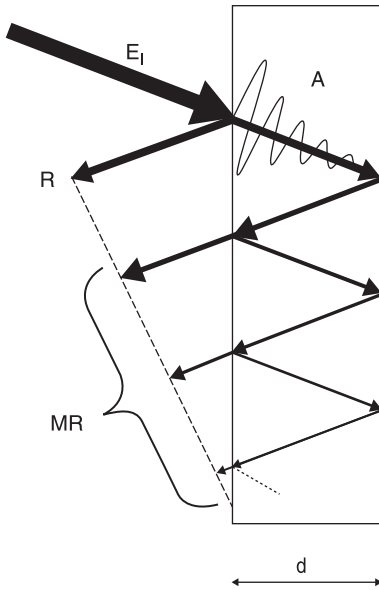
by samples prepared by coagulation, has to be referred to the resulting different microstructure made of more finely spread SWCNT. In ref. 29, the co-precipitation method and melt-blending were compared when preparing MWCNTs in poly ϵ -caprolactone (PCL) composites. It was found that in composites prepared by melt blending, MWCNTs show an extended breakdown, thus hindering percolation and reducing electromagnetic absorbing. Such an effect was proved to be more evident in thick (average outer diameter ≈ 25 nm) than in thin (average outer diameter ≈ 10 nm) MWCNTs, that are more fragile, due to the presence of more numerous structural defects.

As previously seen, conductivity is an important parameter in CNT-loaded polymers, since it affects energy dissipation. Therefore, CNTs' intrinsic conductivity and purity are very important features. SWCNTs are small-diameter structures (diameter < 5 nm) with a wide range of electrical conductivity changing from metallic behavior (even showing ballistic transport at low temperature³⁰) to semiconductors depending on their structure and chirality.³¹ On the other hand, MWCNTs, made of concentric SWCNTs of larger diameter (> 5 nm), present a weak semi-metallic behavior. The accurate choice of CNT is therefore an important start to build a material that can fulfill the required final properties.

Purity of CNT is another important aspect affecting conductivity. As a matter of fact, it was proved³² that the same MWCNTs exhibit different electric conductivity in the as-fabricated or graphitized state. In fact, thermal treatment eliminates microstructural defects and promotes the graphitic structure, both features that result in an increase of conductivity. Contemporarily, for the same reason, the permittivity spectra up to 2 GHz is reduced in magnitude. For modeling purposes, moreover, it has to be remembered that the conductivity of graphite is highly anisotropic, with the c-axes conductivity over 10^3 less than the in-plane value.³³

11.3 Electromagnetic shielding CNT composites

There is an increasing demand for electromagnetic interference (EMI) shielding materials, mainly due to the increase in radio-frequency radiation sources. Electromagnetic shielding (SE) is needed to protect the environment and workspaces from radiation coming from computers and telecommunication equipment, as well as to protect sensitive circuits. Historically metals were used as EMI shields due to their high conductivity, consequently reflection was the main active mechanism. Nevertheless, metals present some shortcomings due to their heavy weight (particularly relevant in aeronautic and aerospace applications), physical rigidity and corrosion. Therefore metal-coated polymers first,^{34,35} and conductive composites later,³⁶ were proposed as an alternative. Conductive composites, made of electrically conductive fillers (as metal fibers³⁷ or carbon fibers or particles³⁸) in an insulating matrix, offer very interesting shielding performance (commercial applications require SE above 20 db, i.e. less than 1% transmission of the EM wave), nevertheless usually a high amount of common



11.5 Absorption (A), reflection (R) and multiple reflections (MR) within a thin slab.

filler (such as carbon black) is required to achieve an adequate level of conductivity. Even more recently, carbon nanofibers and nanotubes polymer composites have been shown to be very effective, reaching a higher shielding performance than that of micro-sized carbon filler composites, at a lower filler content.³⁹ This is because CNTs are very proficient, high aspect ratio conductive nanofillers.

Shielding in CNT-loaded polymers cannot be ascribed to pure reflection (as in homogeneous conductive media) but to the concurrent presence of three mechanisms (Fig. 11.5): reflection (R), absorption (A) and multiple reflections (MR) occurring within the shield.⁴⁰

$$SE = R + A + MR \text{ (in db)} \quad [11.5]$$

Multiple reflections decrease the shielding performance if the shield is thinner than the skin depth,⁴¹ which is defined as the depth at which the electric field drops to $(1/e)$ ⁴² and is given by:

$$\delta = \frac{1}{\sqrt{\mu\sigma\pi f}} \quad [11.6]$$

with δ skin depth, f frequency, μ magnetic permeability and σ electrical conductivity. According to ref. 43, multiple reflections can be ignored if the distance between reflecting surfaces (i.e. shield thickness) is larger than the skin depth. If the thickness is equal to skin depth, instead, shielding has to be considered primary due to reflection.⁴⁰ It follows that the mechanism of multiple reflections

has to be taken into account when dealing with films and coatings. As a rule of thumb, MR have practically no influence when SE is over 15 dB.^{44, 45}

The power absorbed (P_{ab}) in EMI shields is an inverse function of conductivity⁴⁶ (symbols as above).

$$P_{ab} = \frac{1}{2\sigma\delta} = \sqrt{\frac{\pi\mu f}{2\sigma}} \quad [11.7]$$

It results from Equation 11.5 that, on equal frequency and if multiple reflection can be ignored, the larger the conductivity the lower is the power absorbed, and reflection becomes the predominant occurring phenomenon.

Actually the influence of the three cited mechanisms (i.e. A, R and MR) on the overall shielding performance of respectively MWCNT/polypropylene (PP) and SWCNT/polyurethane (PU) composites is very well described and discussed.^{44,45} In particular, it can be deduced⁴⁵ that the predominant effect in SE depends on material tangent loss (i.e. $\tan\delta = \epsilon''/\epsilon'$), that indicates the ability of a material to convert stored energy into heat (therefore dissipating energy), as well as pointing out how well a material can be penetrated by an electrical field. If $\tan\delta \gg 1$ the material is a good conductor and SE is mainly decided by σ , not ϵ , while if $\tan\delta \ll 1$, then the material is a weak conductor and dissipation has to be mainly referred to ϵ . In relative conductive CNT-loaded polymers, however, although reflection remains an important mechanism, absorption is likewise important, being the low amount of power blocked by absorption due to the lower power transmitted into the sample.⁴⁰ If, finally, $\tan\delta \approx 1$ then both σ and ϵ combine to bring out shielding. In such cases the increase of CNT content as well as, on equal filler content, the increase of frequency, shifts the predominant shielding mechanism from reflection to absorption.⁴⁵ An explanation of this trend has been attempted considering that absorption is linked to $\tan\delta$, that increases fast with frequency. As reported, $\tan\delta$ is the ratio between imaginary and real permittivity, therefore it is clear that when dealing with SE or absorbing systems (particularly in the case of CNT-loaded polymers), the knowledge of both entities is just as important as well as the knowledge of conductivity.

Generally speaking, conductivity in CNT-loaded polymer is a function of nanotubes content. In particular, it is well known that, above a definite CNT content, the nanotubes become sufficiently contiguous to form a conductive network, so that electrical conductivity, and hence SE, increase sharply. Many papers, in fact, report a clear correlation between the increase of CNT content and SE enhancement, both when using SWCNTs⁴⁶ and MWCNTs.⁴⁷ Moreover, although this behavior has always been verified, it is important to note that EMI shielding was found to increase much faster at low CNT loading than it does at high CNT content.⁴⁶

Practically, conductivity of the medium, frequency of operation and thickness of the shield are concurrent factors determining the overall SE performance and predominant mechanism. This is why, depending on the specific system, SE and

the investigated frequency spectrum, SE can be found to remain constant,^{39,47} increase⁴⁸ or decrease³¹ with increasing frequency.

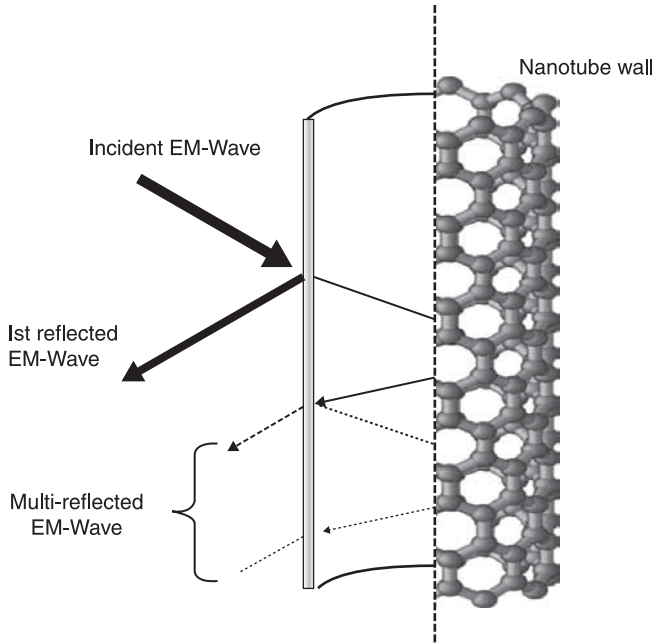
In SE performance, CNT morphology plays a role as well.³¹ On equal filler content, high aspect ratio CNTs show higher SE than low aspect ratio nanotubes. This is most probably due to the fact that ‘long’ (i.e. high aspect ratio) SWCNTs reach percolation at a lower filler content than ‘short’ SWCNTs, since they more easily form a conductive network. In ref. 49, it was shown that the SE of CNF-loaded polyvinylidene fluoride (PVDF) coatings containing short CNF, obtained with 1 hour of ball-milling, was half that obtained with longer not-milled nanofibres.

Even ‘annealing’, i.e. thermal treatment of SWCNT, has an effect on SE. In fact, it is hypothesized that the removal of wall defects and functional groups by means of thermal treatment results, *ceteris paribus*, in an increase in SE,³¹ since it improves conductivity. In the same work, though, it is shown that aspect ratio is an effective parameter influencing SE more than annealing does.

The importance of CNT dispersion in the resin has already been highlighted when discussing the absorbing properties, nevertheless it affects SE too. In particular, SE can be reached at lower filler content if a sufficiently good and homogeneous distribution of CNT in the matrix is insured. This is because, with equal filler content, a more efficient system of conductive pathways is formed, that behaves like a conductive mesh, intercepting the electromagnetic wave. The importance of the formation of an efficient conductive net in view of EMI shielding applications is pointed out,⁵⁰ where it is reported that a slight addition of 1 wt% nanotubes to a larger amount of carbon nanofibers (CNF, 5 or 10 wt%, respectively around or above percolation) in polystyrene (PS) results in a dramatic improvement of SE, even if, in samples with CNF content above percolation, the same improvement was not registered for electrical conductivity.

Some researchers⁵¹ investigated the SE performance of metal-coated (nickel or silver) CNT in siloxane/poly(urea urethane) (PDMS-based PUU) between 400 and 1300 MHz, suggesting this methodology to increase SE at low filler content. The results, though, showed that there is not a clear improvement of SE when involving metal coating, nevertheless it was undoubtedly proved that, when using this method, coating thickness is the key parameter that influences the final SE performance. In particular, too thick coatings lead to aggregation of CNT, reducing the network structure and, hence SE. Moreover, the use of Ni-coated CNT showed better SE than that obtained when employing Ag-coated ones. The authors attribute this result to the magnetic properties of Ni, so that some degree of magnetic loss arises. This hypothesis is supported by the fact that it was seen⁵² that poly(methylmethacrylate) (PMMA) loaded with raw MWCNTs, synthesized by chemical vapor deposition using Fe as the main catalyst, possesses higher SE than purified CNT-loaded PMMA, again referring this result to the magnetic nature of iron.

Coming back to the concept of multiple reflections, previously introduced when dealing with EM wave propagation within a slab, it is important to point out



11.6 Multiple reflection occurring between a CNT wall.

that such phenomena can occur even between CNT walls (Fig. 11.6). The skin depth of a single carbon nanotube, with negligible permeability and a conductivity of 1×10^5 S/m, has been calculated, in the x-band, in the range of 14–18 μm ,⁴⁰ which is far higher than the CNT diameter, implying that in such a system multiple reflections cannot be ignored. Moreover, the MR occurring between the CNT internal surfaces are expected, *per se*, to produce a negative effect on EMI SE. Instead, if a system of CNTs dispersed in the resin is considered (as previously depicted in Fig. 11.3 (a)) and if the model proposed in⁵³ is assumed valid, then a possible positive contribution to SE can be taken into account. Such a positive increase in SE derives from the presence of additional surfaces that combine to bring out wave reflection, and is expected to arise when the surface area/diameter ratio and spacing among CNT are optimized.

11.4 Other CNT composites' electromagnetic applications

The advent of CNT with their terrific properties and potential has aroused great attention for many electronic and electromagnetic applications as plastic transceiver modules,⁵⁴ RFID⁵⁵ and antennas (it is reported that an array of aligned carbon nanotubes can behave like an electromagnetic antenna).⁵⁶ Antennas can

receive different wavelengths depending on their dimensions⁵⁷ and therefore, due to their nanoscale dimensions, CNT can be naturally employed to develop nanoantennas for terahertz, IR and optical ranges.⁵⁸ As happens when dealing with other properties or applications, nanoantennas require that both theoretical and experimental investigations will be done in a qualitatively new context, since, for instance, the capabilities of the frequency, spatial and polarization filtration and noise characteristic of nanoscale objects are basically different from those of the corresponding macroscopic analogs.⁵⁹ The working principle of CNT-based antennas is to some extent analogous to that of macroscopic vibrator antennas, the main difference being the slowing modes of the vibrator that are strongly slowed down surface plasmons in contrast to weakly slowed down quasi-TEM modes in single wire line.⁵⁹ In metallic achiral CNT antennas, the radiation field is formed by the successive reflections of CNT edges that are fundamental to form the antenna pattern.

At the Department of Physics at the University of Berkeley (research team K. Jensen and others⁶⁰) the first ‘nanoradio’ (i.e. a functioning, fully integrated radio receiver) from a single carbon nanotube has been constructed. The single nanotube serves, at once, as all the major components of a radio: antenna, tuner, amplifier, and demodulator. Moreover, the antenna and tuner are implemented in a radically different manner than traditional radios, receiving signals via high frequency mechanical vibrations of the nanotube rather than through traditional electrical means.

Up to now, one of the big concerns in nanotechnology has been to connect nanoelectronic devices with the macroscopic world, i.e. to microscopic electronic devices. Therefore, topics like electric field analysis, and other important parameters like field distribution, gain, radiation patterns and radiation efficiency of CNT antennas, are of great interest.⁵⁹ As is widely known, a CNT is a sheet of graphite rolled up into a tube, and, from an electromagnetic point of view, it can be seen as an electric dipole with a cylindrical shape. Array patterns, instead, can be considered as an assortment of single dipoles made up of identical elements, that, in the case under examination, can be an assortment of CNTs. Numerical simulations⁵⁹ of both single dipole and array patterns showed that, while a single dipole exhibits low gain and efficiency, these parameters can be changed by introducing an appropriate pattern. Particularly, in the cited work, it was demonstrated that the antenna’s gain can be significantly enhanced by working on CNT length, quantity (i.e. number of dipoles) and intertube distance, which means strict control on material processing and, particularly, CNT manipulation. Intertube distance, for instance, relates again to the degree of CNT disentanglement, that is confirmed as a very important parameter when dealing with EM properties. CNT antenna design and simulations are based on the hypothesis of well-separated individual nanotubes with specific lengths, while, in practice, although CNTs are easy to find commercially, they are usually available in entangled bundles. This explains why, in recent years, many attempts have been made, for what concerns this field of

research, to improve and focus CNT synthesis methodologies on these parameters. Control of CNT length is particularly crucial with regard to enlarging the potential applications of nanomaterials to lower frequency applications, such as microwaves. Nanoelectronic devices made up of nanotubes, nanoparticles and nanowires, in fact, offer negligible coupling to microwaves, due to the fact that microwave wavelength (centimeters) is much larger than device scale. Fortunately, many successful improvements have been made^{61,62,63} to control and optimize CNT synthesis so that CNTs with a length in the range of millimeters to centimeters, to suit microwave and RF applications, have been fabricated. In ref. 64, for example, it is reported that SWCNTs were grown under controlled conditions so that the fabrication of a dipole antenna was attempted. In particular, an electrode pattern for an antenna probing made up of 5 micron square islands separated by 100 μ m was realized. On these islands, made of catalyst deposited by standard lithography, single long (5mm) metallic CNTs were grown and their orientation controlled by gas flow.

11.5 Conclusion

In this chapter, the most recent literature in the field of electromagnetic materials based on CNT-loaded polymers was reported. It was highlighted that the overall electromagnetic performance (either when shielding or absorbing is required) is strongly linked to material composition and microstructure; both features that can modify electromagnetic intrinsic parameters such as conductivity and complex permittivity. In particular, the following can be noted:

- Conductivity increases with increasing CNT content, and this is why SE usually follows the same trend.
- Real and imaginary permittivity increase with increasing CNT content: the former because a large number of microcapacitors are formed, the latter because conductivity (and hence losses) are enhanced.
- Real and imaginary permittivity increase with increasing efficiency of CNT dispersion.
- It is not possible to give the 'perfect recipe' to obtain efficient absorbing or shielding materials, because material composition and microstructure have to be tailored from time to time to suit the electromagnetic design that actually takes into account many other features such as frequency of operation, thickness, geometrical shape, etc.

It is important to note that, when dealing with this type of application, strict control on CNT manipulation is fundamental to reach the desired material properties and microstructure (either when making shielding, absorbing materials or nanoscale antennas), nevertheless, even more important is to insure a confident degree of repeatability, that is essential in view of wide industrial productions. It is, in fact, without a doubt that these innovative materials will occupy an

outstanding position in the field of electromagnetic materials, due to their very interesting EM performance, as soon as the costs of CNT become comparable to those of today's more common fillers.

11.6 References

- 1 Ramo S. Whinnery J.R., Van Dutzer T. (1994) *Fields and Waves in Communication Electronics*, New York: John Wiley & Sons, Ltd., p. 132.
- 2 Knott E.F., Shaeffer J.F., Tuley M.T. (2004) *Radar Cross Section*, Singapore: SciTech Publishing, p. 300.
- 3 Neelakanta P.S. (1995) *Handbook of Electromagnetic Materials*, Boca Raton, FL: CRC Press, p. 13.
- 4 Chung D.D.L. (1991) *Applied Materials Science*, Boca Raton, FL: CRC Press, p. 53.
- 5 Vinoy K.J., Jha R.M. (1996) *Radar Absorbing Materials*, Dordrecht: Kluwer Academic Publisher, p. 3.
- 6 Sareni B., Krahenbuhl L., Beroual A., Brosseau C. (1996) Effective dielectric constant of periodic composite materials, *J. Appl. Phys.*, 80(3), 1688–1696.
- 7 Lagarkov A.N., Sarychev A.K. (1996) Electromagnetic properties of composites containing elongated conducting inclusions, *Phys. Rev. B*, 53(10), 6318–6336.
- 8 Prasad A., Prasad K. (2007) Effective permittivity of random composite media: a comparative study, *Physica B*, 396, 132–137.
- 9 Serdyuk Y.V., Podoltsev A.D., Gubanski S.M. (2004) Numerical simulations and experimental study of frequency-dependent dielectric properties of composite material with stochastic structure, *IEEE Trans. on Dielect. and Electr. Insul.*, 11(3), 379–392.
- 10 Brosseau C., Queffelec P., Talbot P. (2001) Microwave characterization of filled polymers *J. of Appl. Phys.*, 89(8), 4532–4540.
- 11 Barba A.A., Lamberti G., D'Amore M., Acierno D. (2003) Carbon black silicon rubber blends as absorbing materials to reduce electromagnetic interference (EMI), *Polym. Bull.*, 57, 587–593.
- 12 Annadurai P., Mallick A.K., Tripathy D.K. (2002) Studies on microwave shielding materials based on ferrite and carbon black-filled EPDM rubber in the X-band frequency, *J. Appl. Polym. Sci.*, 83(1), 145–150.
- 13 Won S.K., Ahn J.M., Kim G. H., C.W. Chun C.W., Wang J.S., Lee E.W. (2002) Microwave absorbing properties of CB-silicon rubber blends, *Polym. Eng. Sci.*, 42(11), 2165–2171.
- 14 Grimes C. A., Grimes D.M. (1993) *Proc. Aerospace Application Conference, Digest*, IEEE, pp. 217–226.
- 15 Park K.Y., Lee S.E., Kim C.G., Han J.H. (2006) Fabrication and electromagnetic characteristics of electromagnetic wave absorbing sandwich structure, *Com. Sci. and Tech.*, 66, 576–584.
- 16 Lee S.E., Kang J.H., Kim C.G. (2006) Fabrication and design of multi-layered radar absorbing structures of MWNT-filled glass/epoxy plain weave composites, *Composite Structure*, 76, 397–405.
- 17 Zhao D.L., Chi W.D., Shen Z.M. (2007) Preparation of carbon nanotube reinforced epoxy resin coating and its microwave characteristics, *Key Engineering Materials*, 334–335, 677–680.
- 18 D.K. Ghodgaonkar, V.V. Varadan, V.K. Varadan, (1990) Free-space measurement of complex permittivity and complex permeability of magnetic materials at microwave frequencies, *IEEE Trans Instrum Meas.*, 39, 387–394.

- 19 Qiu J.X., Wang Y., Gu M.Y. (2007) Microwave absorption properties of substituted $\text{BaFe}_{12}\text{O}_{19}/\text{TiO}_2$ nanocomposite multilayer film, *J. Mater. Sci.*, 42, 166–169.
- 20 Huo J., Wang L., Yu H. (2009) Polymeric nanocomposites for electromagnetic wave absorption, *J. Mater. Sci.*, 44, 3971–3973.
- 21 Fan Z., Luo G., Zhang Z., Zhou L., Wei F. (2006) Electromagnetic and microwave absorbing properties of multi-walled carbon nanotubes/polymer composites, *Mat. Sci and Eng. B*, 132, 85–89.
- 22 Zhihua P., Jingcui P., Yanfeng P., Yangyu O., Yantao N. (2008) Complex permittivity and microwave absorption properties of carbon nanotubes/polymer composite: a numerical study, *Physics Letters A*, 372, 3714–3718.
- 23 Saib A., Bednarz L., Dausi R., Bailly C., Lou X., Thomassin J.M. *et al.* (2006) Carbon nanotube composites for broadband microwave absorbing materials, *IEEE Trans. on Microw. Theory and Tech.*, 54(6), 2745–2754.
- 24 Wu J., Kong L. (2004) High microwave permittivity of multiwalled carbon nanotube composites, *Appl. Phys. Lett.*, 84(24), 4956–4958.
- 25 Pötschke P., Dudkin S.M., Alig I. (2003) Dielectric spectroscopy on melt processed polycarbonate—multiwalled carbon nanotube composites, *Polymer*, 44, 5023–5030.
- 26 Zhang X. F., Dong X.L., Huang H., Lu H., Lei B., Choi C.J. (2007) Microstructure and microwave absorption properties of carbon-coated iron nanocapsules, *J. Phys. D: Appl. Phys.*, 40, 5383–5387.
- 27 Nanni F., Travaglia P., Valentini M. (2009) Effect of carbon nanofibres' dispersion on the microwave absorbing properties of CNF/epoxy composites, *Comp. Sci. and Tech.*, 69, 485–490.
- 28 Hornbostel B., Leute U., Potschke P., Kotz J., Kornfeld D., Chiu P.W. *et al.* (2008) Attenuation of electromagnetic waves by carbon nanotube composites, *Physica E*, 40, 2425–2429.
- 29 Thomassin J.M., Lou X., Pagnouille C., Saib A., Bednarz L., Huyen I. *et al.* (2007) Multiwalled carbon nanotube/poly(ϵ -caprolactone) nanocomposites with exceptional electromagnetic interference shielding properties, *J. Phys. Chem.*, 111, 11186–11192.
- 30 Javey A., Guo J., Wang Q., Ludstrom M., Dai H.J. (2003) Ballistic carbon nanotube transistors, *Nature*, 424, 654–657.
- 31 Li N., Huang Y., Du F., He X., Lin X., Gao H. *et al.* (2006) Electromagnetic interference (EMI) shielding of single-walled carbon nanotube epoxy composites, *Nanoletters*, 6(6), 1141–1145.
- 32 Grimes C.A., Dickey E.C., Mungle C., Ong K.G., Qian D. (2003) Effect of purification of the electrical conductivity and complex permittivity of multiwall carbon nanotubes, *J. Appl. Phys.*, 90(8), 4134–4137.
- 33 Zeller C., Foley G.M., ER Falardeau, Vogel F.L. (1997) Measurement of electrical conductivity under condition of high anisotropy of graphite intercalation compounds, *J. Mater. Sci.*, 31, 255–259.
- 34 Jiang G., Gilbert M., Hitt D.J., Wilconx G.D., Balasubramanian K. (2002) Preparation of nickel coated mica as conductive filler, *Composite Part A*, 33(5), 745–751.
- 35 Murthy M. (1994) Permanent EMI shielding of plastics using copper fibres, paper presented at Annual Technical Conference ANTEC, San Francisco, CA, USA.
- 36 Wu J., Chung D.D.L. (2002) Increasing the electromagnetic shielding effectiveness of carbon fibre-polymer-matrix composite by using activating carbon fibres, *Carbon*, 40, 445–467.

- 37 Amarasekera J. (2005) Conductive plastics for electrical and electronic applications, *Reinf. Plast.*, 49(8), 2645–2661.
- 38 Chung D.D.L. (2001) Electromagnetic materials shielding effectiveness of carbon materials, *Carbon*, 39, 279–285.
- 39 Yang S.Y., Lozano K., Lomeli A. Foltz H.D., Jones R. (2005) Electromagnetic interference shielding effectiveness of carbon nanofibres/LCP composites, *Compos Part A*, 36(5), 691–697.
- 40 Al Saleh M.H., Sundararaj U. (2009a) Electromagnetic interference shielding mechanisms of CNT/polymer composites *Carbon*, 47: 1738–1746.
- 41 Al Saleh M.H., Sundararaj U. (2009b) Review of vapor grown carbon nanofibre/polymer conductive composites *Carbon*, 47: 2–22.
- 42 Chung D.D.L. (2000) Materials for electromagnetic interference shielding, *J. Mater. Eng. Perform.*, 69(1): 62–69.
- 43 Chung D.D.L. (2001) Electromagnetic interference shielding effectiveness of carbon materials, *Carbon*, 39(2), 279–285.
- 44 Joo J., Epstein A.J. (1994) Electromagnetic radiation shielding by intrinsically conducting polymers, *Appl. Phys. Lett.*, 65(18), 2278–2280.
- 45 Liu Z., Bai G., Huang Y., Ma Y., Du F., Li F., Guo T., Chen Y. (2007) Reflection and absorption contributions to the electromagnetic interference shielding of single-walled carbon nanotube/polyurethane composites, *Carbon*, 45, 821–827.
- 46 Grimes C.A., Grimes D.M. (1993) A brief discussion of EMI shielding materials, in *Proc. Aerospace Application Conference, Digest 1993, IEEE*, pp. 217–226.
- 47 Li Y., Chen C., Zhang S., Ni Y., Huang Y. (2008) Electrical conductivity and electromagnetic interference shielding characteristics of multiwalled carbon nanotube filled polyacrylate composite films, *Appl. Surf. Sci.*, 254, 5766–5771.
- 48 Ma C.M., Huang Y.L., Kuan H.C., Chiu Y.S. Preparation and electromagnetic interference shielding characteristics of novel carbon-nanotube siloxane, *J. Polym. Sci. B*, 43, 345.
- 49 Lee B.O., Woo W.J., Park H.S., Hahm H.S., Wu J.P., Kim M.S. (2002) Influence of aspect ratio and skin effect on EMI shielding of coating materials fabricated with carbon nanofibre/PVDF, *J. Mater. Sci.*, 37, 1839–1843.
- 50 Yang Y., Gupta M.C., Dudley K.L. (2007) Towards cost-efficient EMI shielding materials using carbon nanostructure-based nanocomposites, *Nanotechnology*, 18, 345701.
- 51 Ma C.M., Huang Y.L., Kuan H.C., Chiu Y.S. (2004) Preparation and electromagnetic shielding characteristics of novel carbon nanotube/siloxane/poly(urea erethane) nanocomposites, *J. of Polym. Sci.*, 43, 345–358.
- 52 Kim H.M., Kim K., Lee Y., Joo J., Cho S.J., Yoon H.S., *et al.* (2004) Electrical conductivity and electromagnetic interference shielding of multiwalled carbon nanotube composites containing Fe Catalyst, *App. Phys. Lett.*, 84, 589–591.
- 53 Kaiser K.L. (2006) *Electromagnetic Shielding*, Boca Raton, FL: CRC Press.
- 54 Chang C.M., Lin M.C., Chiu J.C., Shiarng W., Cheng W.H. (2006) High performance electromagnetic susceptibility of plastic transceiver modules using carbon nanotubes, *IEEE J. of Selected Topics in Quantum Electr.*, 12(6), 1091–1096.
- 55 Yang, L., Zhang R., Staiculescu D., Wong C.P., Tentzeris M. (2009) A novel conformal RFID-enabled module utilizing inkjet-printed antennas and carbon nanotubes for gas-detection, *IEEE Antennas and Wireless Propagation Letters*, 8, 653–656.
- 56 Wang Y., Kempa K., Kimball B., Carlson J.B., Benham G., Li W., *et al.* (2004) Receiving and transmitting light-like radio waves: antenna effect in arrays of aligned carbon nanotubes, *Appl. Phys. Lett.*, 85(13), 2607–2609.
- 57 Dresselhaus M.S. (2004) Nanotube antennas, *Nature*, 432, 959.

- 58 Wang Y., Wu Q., Shi W., He X., Sun X., Gui T. (2008) Radiation properties of carbon nanotubes antenna at terahertz/infrared range, *Int. J. Infrared Milli Waves*, 29, 35–42.
- 59 Maksimenko S.A., Slepian G.Y., Nemilentsau A.M., Shuba M.V. (2008) Carbon nanotube antenna: far field, near field and thermal noise properties, *Physica E*, 40, 2360–2364.
- 60 Available at: www.nanoradio.com.
- 61 Li S., Yu Z., Burke P.J. (2004) Electrical properties of 0.4 cm single walled carbon nanotubes, *Nano. Letters*, 4, 2003–2007.
- 62 Yu Z., Li S., Burke P.J. (2004) Synthesis of aligned arrays of millimeter long, straight, single walled carbon nanotubes, *Chemistry of Materials*, 16, 3414–3416.
- 63 Zheng L.X., O'Connell M.J., Doom S.K., Liao X.Z., Zhao Y.H., Akhadow E.A. *et al.* (2004) Ultralong single walled carbon nanotubes, *Nature Materials*, 3, 673–676.
- 64 Chen M.Y., Yuan D., Liu J., Han X. (2007) Nanoscale dipole antennas based on long carbon nanotubes, in *Proc. 7th IEEE Int. Conf. on Nanotechnology, Hong Kong*, pp. 846–849.

Mechanical properties of polymer–polymer-grafted carbon nanotube composites

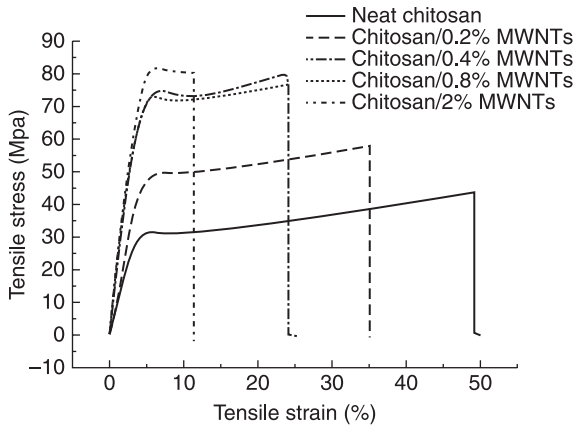
S. H. GOH, National University of Singapore, Singapore

Abstract: This chapter reviews the use of polymer-grafted carbon nanotubes (CNTs) to enhance the mechanical properties of various polymers. Pristine CNTs generally improve the stiffness and strength of a polymer, at the expense of ductility and toughness. Grafting of polymers onto CNTs reduces the tendency of the nanotubes to aggregate and improves the efficiency of stress transfer from the matrix to the nanotubes. As a result, the mechanical properties of polymers are significantly enhanced by the incorporation of polymer-grafted CNTs.

Key words: carbon nanotube, mechanical properties, polymer composites.

12.1 Introduction

Both single-walled and multi-walled carbon nanotubes (SWCNTs and MWCNTs, respectively) are noted for their outstanding mechanical properties. Based on *in-situ* pulling and bending tests on individual MWCNTs in a transmission electron microscope, the tensile strength and Young's modulus of MWCNTs were found to be 0.15 TPa and 0.9 TPa, respectively (Demczyk *et al.*, 2002). Moreover, MWCNTs were also found to exhibit a remarkable flexural robustness, making them exceedingly resilient materials (Demczyk *et al.*, 2002). The use of carbon nanotubes (CNTs) as reinforcing fillers for polymers has received increasing attention in recent years (Coleman *et al.*, 2006a, 2006b; Moniruzzaman and Winey, 2006; Bose *et al.*, 2010; Martinez-Hernández *et al.*, 2010; Spitalsky *et al.*, 2010). In general, the addition of pristine CNTs increases the stiffness and the strength of a polymer, but not the ductility. Figure 12.1 shows the stress–strain curves of chitosan and its composites (Wang S. F. *et al.*, 2005). The addition of pristine MWCNTs progressively increased Young's modulus and the tensile strength of chitosan. On the other hand, the ultimate strain of chitosan progressively decreased with increasing MWCNTs content. As such, the area under the stress–strain curve, which represents the energy required to break the sample, is reduced substantially by increasing the MWCNTs content. In some cases, the reduction in ductility is so severe that a flexible polymer becomes very brittle upon the incorporation of CNTs. For example, the ultimate strain of isotactic polypropylene (PP) was reduced from 450% to just about 10% upon the incorporation of 2.1 wt% of MWCNTs (Koval'chuk *et al.*, 2008a). Therefore, it is a challenge to develop polymer–CNT composites with enhanced stiffness and strength, but without sacrificing the ductility and toughness.



12.1 Stress-strain curves of chitosan and its composites. (Reprinted with permission from Wang S. F. *et al.* (2005). Copyright American Chemical Society.)

There are four main requirements for CNTs to achieve effective reinforcement: large aspect ratio, alignment, homogeneous dispersion in polymer matrix, and efficient stress transfer from the matrix to CNTs, with the latter two being the most important. CNTs tend to aggregate to form bundles held by strong van der Waals forces, and hence they are difficult to disperse in the polymer matrix. When CNTs are not homogeneously dispersed in the polymer matrix, the applied stress cannot be distributed evenly throughout the composite. Furthermore, the CNTs' aggregates act as stress concentration centers and thus weaken the polymer. The dispersion of CNTs in a polymer matrix is commonly examined using scanning electron microscopy (SEM) and transmission electron microscopy (TEM). The existence of bundles of CNTs indicates poor dispersion. Weak polymer-CNT interfacial adhesion prevents efficient stress transfer from the matrix to CNTs. As such, a SEM micrograph of a fracture surface reveals a large number of unbroken CNTs. On the other hand, strong polymer-CNT interfacial adhesion is evidenced by the appearance of broken CNTs on the fracture surface.

Several approaches have been used to overcome the two problems. Chemical functionalization of CNTs is able to improve the dispersion of CNTs and to increase the interfacial adhesion. The functional groups attached to CNTs can interact with suitable functional groups of polymers through hydrogen-bonding or ionic interactions to achieve stronger interfacial adhesion. For example, the storage modulus of poly(methyl methacrylate) (PMMA) at room temperature was increased by 86% by the addition of 1 wt% of amide-functionalized SWCNTs, whereas the increase was only 48% using 1 wt% pristine SWCNTs (Ramanathan *et al.*, 2005). Recent studies have shown that polymer-grafted CNTs are highly effective in enhancing the mechanical properties of polymers. The polymer chains

grafted onto CNTs reduce the tendency of nanotubes to aggregate and hence the nanotubes can be dispersed homogeneously in the polymer matrix. Stress can be more efficiently transferred from the matrix to CNTs through the polymer chains grafted onto CNTs. The matrix polymer and the polymer grafted onto CNTs do not have to be the same. As long as the two dissimilar polymers are miscible with each other, the intimate mixing of the polymer chains will allow an efficient stress transfer. This chapter reviews the mechanical reinforcement of various polymers using polymer-grafted CNTs.

12.2 Grafting of polymers onto CNTs

Grafting of polymers onto CNTs is usually achieved by ‘grafting-to’ and ‘grafting-from’ methods (Liu, 2005; Tasis *et al.*, 2006; Homenick *et al.*, 2007; Lin *et al.*, 2007). For the ‘grafting-to’ method, polymers containing functional groups are grafted onto functionalized CNTs through chemical reactions. This method allows the attachment of polymers with known molecular weights and structures. However, the grafting density is usually low because of the steric hindrance associated with the long polymer chains. For the ‘grafting-from’ method, monomers or initiators are first attached to CNTs, followed by polymerization of the monomers. This method allows higher grafting densities, and also control of polymer molecular weights and structures.

12.2.1 ‘Grafting-to’ method

Polymers containing functional groups at their chain ends or along the main chains react with functionalized CNTs to achieve grafting. CNTs are treated with HNO_3/HCl to introduce carboxylic acid groups on the surface. The carboxylic acid groups are sometime transformed to acid chloride groups by treatment with thionyl chloride. Polymers such as poly(vinyl alcohol) (Lin *et al.*, 2003), poly(ethylene glycol) (Zhao *et al.*, 2005), poly(propylene glycol) (Xiong *et al.*, 2006), polycaprolactone (PCL) (Guojian *et al.*, 2009), poly(L-lactic acid) (Chen *et al.*, 2005), poly(hydroxyl ether of bisphenol-A) (Yang *et al.*, 2007b), poly(aminobenzene sulfonic acid) (Zhao *et al.*, 2005), and chitosan (Shieh and Yang, 2006; Wu *et al.*, 2007) have been grafted onto CNTs using this method.

For polymers which do not possess interacting functional groups, special synthetic methodologies have been used to incorporate functional groups. For example, poly(methyl methacrylate) (PMMA) was grafted onto MWCNTs through the reaction of hydroxyl-terminated PMMA and acid chloride-functionalized MWCNTs (Baskaran *et al.*, 2005). Polystyrene (PS) prepared by atom transfer radical polymerization (ATRP) contains terminal bromine groups, which can then be converted to azide groups. The azide groups undergo cycloaddition reaction with SWCNTs to achieve grafting (Qin *et al.*, 2004c). Azide-functionalized PS was

grafted onto alkyne-decorated SWCNTs through ‘click coupling’ (Li *et al.*, 2005). PS was grafted onto MWCNTs through the reaction between bromine-terminated PS and MWCNTs functionalized with 2,2,6,6-tetramethylpiperidiny-1-oxy (TEMPO) (Sui *et al.*, 2009). PS, PCL and poly(2-vinylpyridine) (P2VPy) containing terminal TEMPO groups reacted with MWCNTs surface (Lou *et al.*, 2004a, 2004b). Poly(N-vinyl carbazole) copolymer containing a small amount of styrene units bearing pendant hydroxyl groups reacted with acid chloride-functionalized MWCNTs to achieve grafting (Wang W. *et al.*, 2005). A thiol-coupling reaction was used to graft thiol-terminated poly[N-(2-hydroxypropyl)methacrylamide] onto thiol-reactive-functionality MWCNTs (You *et al.*, 2006a). Poly(styrene-co-acrylonitrile) (SAN) was grafted onto MWCNTs using a reactive blending method (Shi *et al.*, 2009). A small amount of cyano groups in SAN was converted to oxazoline groups through reaction with 2-aminoethanol. The melt blending of oxazoline-containing SAN and acidified MWCNTs led to the grafting of SAN onto MWCNTs arising from reactions between oxazoline and carboxylic acid groups. This method can be used to graft other acrylonitrile-containing polymers onto MWCNTs. Polyethylene (PE) was grafted onto fluorinated SWCNTs by a shear mixing process as evidenced by the partial defluorination after the process (Shofner *et al.*, 2006). PE and polypropylene (PP) were grafted onto MWCNTs using the reactive blending method (Yang *et al.*, 2007a; Yang *et al.*, 2008). PE or PP containing a small amount of reactive maleic anhydride groups was grafted onto MWCNTs. Acidified MWCNTs were allowed to react with ethylenediamine. The amine groups of functionalized MWCNTs then reacted with maleic anhydride groups, enabling PE or PP chains to be grafted onto MWCNTs. Grafting of MWCNTs with chlorinated polypropylene (CPP) was achieved using a generic organometallic approach (Blake *et al.*, 2004). MWCNTs were treated with n-butyllithium. The n-butyllithium-functionalized MWCNTs then reacted with CPP. Grafting was achieved via the elimination of LiCl.

12.2.2 ‘Grafting-from’ method

Various approaches have been used to allow the growth of polymer chains from the CNTs’ surface. In general, monomer units or suitable initiating species are first anchored on CNTs, followed by *in-situ* surface-initiated polymerization. Examples of various methods are given below.

ϵ -Caprolactam was attached to SWCNTs by heating with acid chloride-functionalized SWCNTs (Qu *et al.*, 2005). A different synthetic route was used to attach ϵ -caprolactam onto SWCNTs (Yang M. *et al.*, 2007). Anionic ring-opening polymerization of ϵ -caprolactam using ϵ -caprolactam-functionalized SWCNTs led to the grafting of polyamide-6 onto SWCNTs. 2-Hydroxyethyl methacrylate (HEMA) was attached to MWCNTs by reacting with acid-chloride functionalized MWCNTs (Kumar *et al.*, 2008). Free radical polymerization of HEMA was then initiated by 2,2’-azobis(isobutyronitrile).

There are reports that polymerization can take place from CNTs without anchoring monomer or initiating fragment on CNTs' surface. For example, poly(sodium 4-styrenesulfonate) and poly(4-vinylpyridine) were grafted onto SWCNTs by free-radical polymerization (Qin *et al.*, 2004a, 2004c). Another example is the grafting of PMMA by *in-situ* emulsion polymerization (Hwang *et al.*, 2004). Direct melt polycondensation of L-lactic acid with carboxylated MWCNTs enabled the attachment of polymer chains onto MWCNTs (Song *et al.*, 2007; Yoon *et al.*, 2009). *In-situ* polycondensation of sebacoyl chloride and 1,6-hexamethylene diamine in the presence of acid chloride-functionalized SWCNTs led to the attachment of polyamide-6,10 onto nanotubes (Moniruzzaman *et al.*, 2007).

As mentioned in Section 12.2.1, TEMPO-terminated PS, PCL and P2VPy were prepared by nitroxide-mediated radical polymerization (NMRP), and subsequently grafted onto CNTs. Conversely, CNTs can be functionalized with TEMPO groups and then undergo NMRP with monomers such as styrene and 4-vinylpyridine (Zhao X *et al.*, 2006). The living nature of NMRP enabled the synthesis of block copolymer-grafted CNTs (Zhao X D *et al.*, 2006).

ATRP makes use of carbon–carbon formation by an atom transfer radical addition commonly used in organic synthesis. ATRP is very versatile and can be carried out in bulk or in solution for various monomers such as styrenic monomers, acrylates, methacrylates, methacrylamides, and acrylonitrile, etc. The living nature of ATRP also enables the growth of block copolymers from CNTs. A large number of polymers have been grown from CNTs using ATRP, including PMMA (Yao *et al.*, 2003; Baskaran *et al.*, 2004; Kong *et al.*, 2004a), poly(*t*-butyl acrylate) (Yao *et al.*, 2003), poly(*n*-butyl methacrylate) (Qin *et al.*, 2004d), poly(acrylic acid) (Yao *et al.*, 2003), PS (Baskaran *et al.*, 2004; Kong *et al.*, 2004b; Qin *et al.*, 2004b), polyacrylonitrile (Shanmugaraj *et al.*, 2007), poly(styrene-co-acrylonitrile) (Shanmugaraj *et al.*, 2007), hyperbranched polymer (Hong *et al.*, 2005b), V-shaped poly(styrene-*b*-*N*-isopropylacrylamide) (Liu and Chen, 2007), poly(styrene-*b*-methyl methacrylate) (Baskaran *et al.*, 2004), and poly(methyl methacrylate-*b*-styrene) (Baskaran *et al.*, 2004). Recently, Priftis *et al.* (2009) reported a novel method to allow the simultaneous growth of two different polymers from MWCNTs. A [4 + 2] Diels-Alder cycloaddition was used to functionalize MWCNTs with two different precursor initiators, one for ATRP and one for ring-opening polymerization. The binary functionalized MWCNTs were then used to initiate the polymerizations of two different monomers simultaneously, for example, styrene and ϵ -caprolactone.

Another widely used method to allow the growth of polymer chains from CNTs is based on reversible addition fragmentation chain-transfer (RAFT) polymerization. RAFT polymerization needs a reversible chain-transfer agent, usually a dithio compound ZSC(S)R where Z = aryl, alkyl, SR', OR' and R is a good homolytic leaving group with radical R• capable to initiate polymerization. Cui *et al.* (2004) first used RAFT polymerization to achieve the growth of PS

from MWCNTs. RAFT polymerization has been used to achieve the grafting of a number of polymers such as PMMA (Xu *et al.*, 2007), polyacrylamide (Wang G. J. *et al.*, 2007), poly(N-(2-hydroxypropyl)methacrylamide) (Hong *et al.*, 2006b), poly(N-isopropylacrylamide) (Hong *et al.*, 2005a), PMMA-*b*-PS (Xu *et al.*, 2006b), and ionic polymers (You *et al.*, 2006b). RAFT polymerization was used to attach poly(styrene-co-maleic anhydride) on MWCNTs, which could then be used to attach other polymer chains containing hydroxyl or amino groups by the ‘growing-on’ method (Hong *et al.*, 2006a).

Other approaches have also been used to graft polymers onto CNTs by the ‘grafting-from’ method. The lithium salt of SWCNTs was used to initiate the polymerization of methyl methacrylate (Liang *et al.*, 2006). SWCNTs functionalized with 4-hydroxymethylaniline were used to initiate the polymerization of ϵ -caprolactone (Buffa *et al.*, 2005). The growth of polyacrylonitrile from MWCNTs was achieved by a cathodic electrochemical process (Petrov *et al.*, 2004). Several studies have shown that metallocene catalysts anchored on the CNTs’ surface allowed the growth of PE (Trujillo *et al.*, 2007; Park *et al.*, 2008; Vega *et al.*, 2009), PP (Funck and Kaminsky, 2007; Koval’chuk *et al.*, 2008a, 2008b), and PMMA (Cui *et al.* 2009) from CNTs. Li *et al.* (2007) functionalized SWCNTs with α -alkene groups, which were then used to polymerize ethylene using a metallocene catalyst.

12.3 Fabrication of composites

Solution mixing and melt blending are commonly used to fabricate polymer–polymer-grafted CNTs composites. CNTs grafted with polymers are soluble in a variety of solvents. As such, polymer-grafted CNTs and matrix polymer are dissolved in a solvent, and the solvent is subsequently removed by evaporation or precipitation in a non-solvent. The need to remove the solvent makes this method unsuitable for large-scale production of composites. Polymers such as PE and PP require the use of high-boiling solvents, making this method unattractive. Furthermore, the choice of solvent can also affect the mechanical properties of composites (Khan *et al.*, 2007). Melt blending offers a simple and convenient means to fabricate composites using common processing equipment such as an extruder, internal mixer and injection molding machine. This method is suitable for large-scale production of composites. One main concern of melt blending is the possible damage and breakage of nanotubes during blending at high temperatures. Jin *et al.* (2001) used a laboratory mixing molder to fabricate PMMA–MWCNTs composites at 200°C for 20 minutes. The nanotubes were found to be well dispersed in the matrix with no apparent damage or breakage. Some melt blending processes such as the dynamic packing injection molding process can produce highly oriented polymer–CNTs composites with enhanced mechanical properties (Zhao *et al.*, 2007).

12.4 Mechanical properties of polymer composites containing polymer-grafted CNTs

The basic tensile properties of a material such as Young's modulus, tensile strength and ultimate strain are determined by tensile testing in which the material is pulled at a constant strain rate. The area under the stress–strain curve is usually taken to be a measure of toughness of the material. The tensile properties are sensitive to temperature and strain rate. Most tensile tests are conducted at ambient temperature, but different strain rates may be used. The dynamic mechanical properties of a material are determined by dynamic mechanical analysis (DMA) which measures the response of the material to an oscillating force as a function of temperature, time or oscillating frequency. From DMA tests, the ability of the material to store energy (E' , the storage modulus), to lose energy (E'' , the loss modulus) and the E''/E' ratio (the loss tangent) are obtained. Most works deal with the storage modulus as a function of temperature.

In general, the mechanical properties of composites improve with increasing the CNTs content up to a certain content, beyond which the mechanical properties deteriorate. The downturn in the mechanical properties at higher CNTs contents is attributed to increasing difficulty in dispersing CNTs homogeneously in the polymer matrix and/or the hindering of stress–strain behavior of polymer chains by the overlapping nanotube percolated networks.

12.4.1 Polyolefin polymer composites

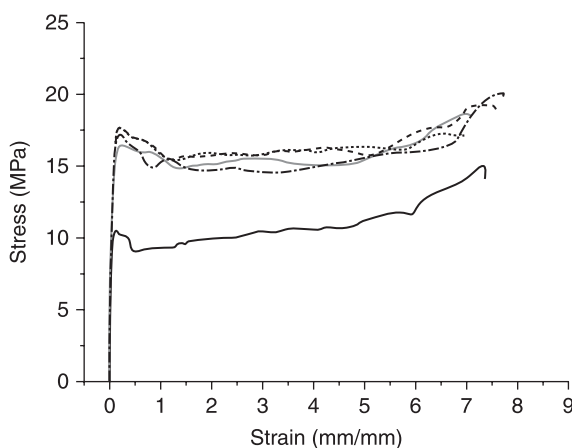
Polyethylene (PE) composites

The incorporation of pristine CNTs increases Young's modulus and the tensile strength of PE, but not the ultimate strain. The incorporation of 2 wt% of MWCNTs to linear low-density PE improved Young's modulus and the tensile strength by 38 and 34%, respectively, but the ultimate strain was reduced by 75% (Mahfuz *et al.*, 2005). McNally *et al.* (2005) found that the yield stress of medium-density PE was improved marginally by the addition of MWCNTs, but the tensile strength and ultimate strain continuously decreased with increasing MWCNTs content. The storage modulus of medium-density PE at 15°C was not improved by the addition of 5 wt% SWCNTs (Shofner *et al.*, 2006). However, the addition of 5 wt% fluorinated SWCNTs led to an improvement in storage modulus by 44% (Shofner *et al.*, 2006). It was proposed that PE chains were grafted onto fluorinated SWCNTs through the elimination of HF.

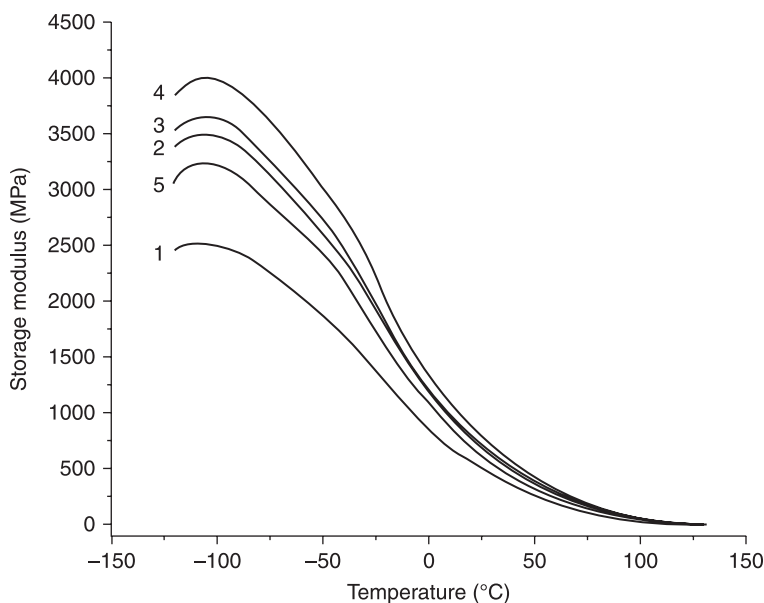
B. X. Yang *et al.* (2007a) studied the reinforcement of linear low-density PE (LLDPE) using PE-grafted MWCNTs. As compared to LLPDE, the incorporation of 1 wt% of pristine MWCNTs led to improvements in Young's modulus and yield stress by 17 and 14%, respectively, and decreases in tensile strength, ultimate strain and toughness by 23, 69 and 68%, respectively. Scanning electron microscopy (SEM) micrographs of a fractured surface showed the presence of

large bundles of unbroken carbon nanotubes, indicating that the nanotubes were not well dispersed and the interfacial adhesion was weak. In contrast, PE-grafted MWCNTs are more effective in reinforcing LLDPE as evidenced by the stress–strain curves as shown in Fig. 12.2 Most importantly, the ultimate strains of the composites were about the same as that of the matrix polymer. At an effective MWCNTs content of 1 wt%, Young's modulus, the yield stress, tensile strength, and toughness of LLDPE were improved by 74, 56, 15 and 36%, respectively, whereas the ultimate strain was reduced by only 5%. SEM micrographs showed that PE-grafted MWCNTs were dispersed individually in the matrix. Moreover, the nanotubes were broken rather than being pulled out, suggesting a strong polymer–nanotube interfacial adhesion. B. X. Yang *et al.* (2007a) also found that the storage modulus of LLDPE was improved by PE-grafted MWCNTs but not by pristine MWCNTs. As shown in Fig. 12.3, the storage modulus of LLDPE progressively increased when the effective MWCNTs content increased from 0.5 to 1.5 wt%. At -100°C , the storage modulus was improved by about 60%. However, there was a decrease in the storage modulus when the effective MWCNTs content was increased to 2.0 wt%.

PE–MWCNTs composites prepared by *in-situ* polymerization using metallocene catalysts were also found to possess good mechanical properties. Park *et al.* (2008) found that high-density PE (HDPE) containing 1.25 wt% pristine MWCNTs showed improvements in Young's modulus by 18%, and a significant reduction in ultimate strain by 89%. However, for a composite fabricated by *in-situ* polymerization, Young's modulus was improved by 214%, and the ultimate strain was reduced by 55%. Similarly, Vega *et al.* (2009) found



12.2 Stress–strain curves of PE (bottom curve) and four composites containing varying amounts of PE-grafted MWCNTs (upper curves). (Reprinted with permission from Yang *et al.* (2007a). Copyright WILEY-VCH Verlag GmbH & Co.)

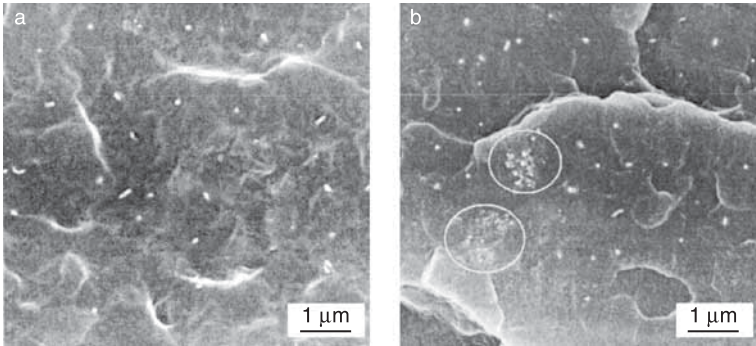


12.3 Storage moduli of PE/PE-grafted MWCNTs composites. Effective MWCNTs content: (1) 0%; (2) 0.5%; (3) 1.0%; (4) 1.5%; (5) 2.0%. (Reprinted with permission from Yang *et al.* (2007a). Copyright WILEY-VCH Verlag GmbH & Co.)

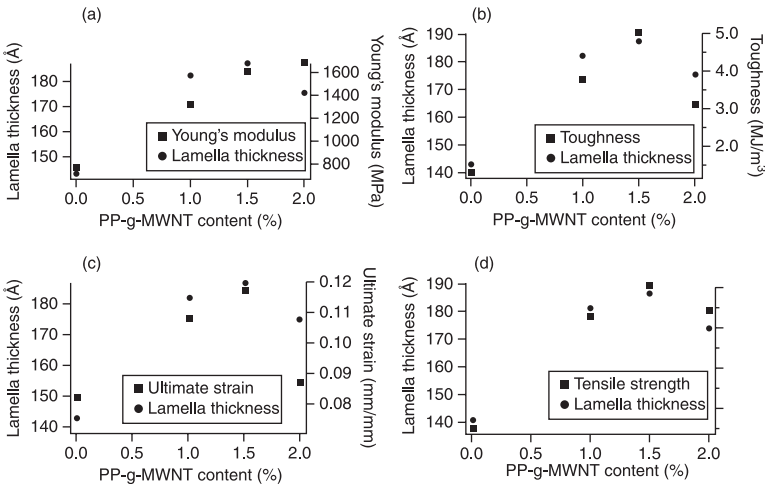
that a HDPE composite containing 0.54 wt% MWCNTs showed improvements in Young's modulus, yield stress and tensile strength of 83, 5 and 5%, respectively, whereas the ultimate strain was reduced by only 10%. Li *et al.* (2007) reported marginal increases in Young's modulus (2%) and tensile strength (13%) of PE–PE-grafted SWCNTs (2.5 wt% SWCNTs), but a substantial increase (56%) in ultimate strain.

Polypropylene (PP) composites

B. X. Yang *et al.* (2008) studied the reinforcement of PP using PP-grafted MWCNTs. The addition of pristine MWCNTs increased Young's modulus and the tensile strength of PP, but the ultimate strain was significantly reduced. On the other hand, at an effective MWCNTs content of 1.5 wt%, PP-grafted MWCNTs improved Young's modulus, tensile strength, ultimate strain and toughness by 108, 141, 49 and 287%, respectively, as compared to PP. However, the mechanical properties decreased when the effective MWCNTs content was further increased to 2.0 wt%. The downturn in mechanical properties was attributed to increasing difficulty in dispersing a larger amount of PP-grafted MWCNTs in the PP matrix as shown by SEM. As shown in Fig. 12.4, PP-grafted MWCNTs were dispersed

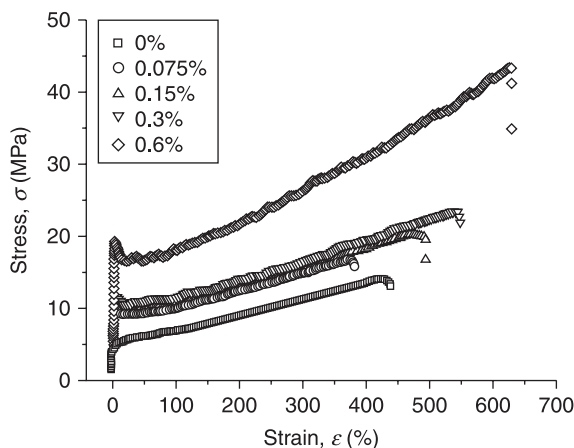


12.4 SEM micrographs of fracture surfaces of PP/PP-grafted MWCNTs composites. (a) Effective MWCNTs content of 1.5 wt %; (b) effective MWCNTs content of 2.0 wt %. Bright spots are broken nanotubes, and bundles of nanotubes are circled in (b). (From Yang B. X. *et al.* (2008). Copyright Elsevier Ltd.)



12.5 Variation of lamellar thickness and mechanical property as a function of PP-g-MWCNTs content. (Reprinted with permission from Causin *et al.* (2009). Copyright Elsevier Ltd.)

individually in the PP composite with an effective MWCNTs content of 1.5 wt%. For the PP–PP-grafted MWCNTs composite with an effective MWCNTs content of 2.0 wt%, in addition to individually dispersed nanotubes, small bundles of nanotubes could also be seen. Causin *et al.* (2009) recently found that the changes in mechanical properties of PP–PP-grafted MWCNTs composites were closely related to the lamellar thickness of PP spherulites as shown in Fig. 12.5. Therefore, in addition to dispersion and interfacial adhesion, lamellar morphology can also play an important role in determining the mechanical properties of semicrystalline polymer–CNTs composites.



12.6 Stress–strain curves of CPP and CPP/CPP-grafted MWCNTs composites containing varying vol% of nanotubes. (Reprinted with permission from Coleman *et al.* (2004). Copyright WILEY-VCH Verlag GmbH & Co.)

Another recent study also showed that significant improvements in mechanical properties of PP were achieved using PP-grafted MWCNTs (Li *et al.*, 2009). The tensile strength and Young's modulus of PP were improved by 18 and 50%, respectively, by the addition of 3 wt% of pristine MWCNTs. In comparison, the addition of 3 wt% of PP-grafted MWCNTs led to increases in Young's modulus and tensile strength by 113 and 110%, respectively.

Chlorinated polypropylene (CPP) composites

CPP-grafted MWCNTs are highly effective in reinforcing CPP. At a nanotube content of 1 wt% (0.6 vol.%), Young's modulus, the tensile strength and toughness of CPP were increased by 3.1, 3.9 and 4.4 times, respectively (Blake *et al.*, 2004; Coleman *et al.*, 2004). The stress–strain curves of CPP and various composites are shown in Fig. 12.6. The findings represent the first report that the stiffness, strength, ductility and toughness of a polymer can be simultaneously improved by the addition of polymer-grafted CNTs.

Poly(1-butene) (PB) composites

Unlike PE and PP, PB–CNTs composites have received scant attention. The only study on the mechanical properties of PB–CNTs composites was reported by Yang *et al.* (2009). They compared the reinforcing effects of pristine MWCNTs and PP-grafted MWCNTs. PB and PP are miscible with each other, particularly when the blend contains only a small amount of either polymer (less than 20 wt%). Pristine MWCNTs provided marginal improvements in Young's modulus

and yield stress. However, the tensile strength, ultimate strain and toughness of PB were substantially decreased. In contrast, PP-grafted MWCNTs improved the stiffness, strength, and toughness significantly, with only a marginal reduction in the ductility of PB. At an effective MWCNTs content of 1.5 wt%, the addition of PP-grafted MWCNTs improved Young's modulus, the yield stress, tensile strength, ultimate strain and toughness of PB by 91, 83, 61, and 67%, respectively, and reduced the ultimate strain by only 3%. PP-grafted MWCNTs are more effective than organoclay in enhancing the mechanical properties of PB.

12.4.2 Vinyl polymer composites

Poly(vinyl alcohol) (PVA) composites

Paiva *et al.* (2004, 2005) studied the reinforcement of PVA using PVA-grafted SWCNTs. Two batches of SWCNTs were used, one grafted with PVA having the same molecular weight as the matrix polymer (70,000–100,000) and the other grafted with PVA having a lower molecular weight of 22,000. The addition of pristine SWCNTs improved the stiffness, but decreased the strength and ductility. The incorporation of 5 wt% of SWCNTs grafted with high molecular weight PVA improved both Young's modulus and the yield stress by 55%. While there was no change in the yield strain, the ultimate strain was reduced markedly from > 0.60 to 0.06. At the same content of functionalized SWCNTs of 1 wt%, nanotubes grafted with high-molecular weight PVA were better than those grafted with low-molecular weight PVA in improving the yield stress and yield strain. The two types of nanotubes improved Young's modulus of PVA by the same amount. It should be noted that Coleman *et al.* (2004) reported significant improvements in mechanical properties of PVA using pristine MWCNTs. Increases in Young's modulus, tensile strength and toughness by 3.7, 4.3 and 1.7 times, respectively, were observed using less than 1 wt% of pristine MWCNTs. They also observed the formation of a crystalline coating around the nanotubes which maximized interfacial stress transfer.

Poly(vinyl chloride) (PVC) composites

PVC has been reinforced with CPP-grafted MWCNTs (Blake *et al.*, 2006), poly(n-butyl methacrylate) (PnBMA)-grafted MWCNTs (Shi *et al.*, 2007), styrene-maleic anhydride copolymer (SMA)-grafted MWCNTs (Guojian *et al.*, 2008), or polycaprolactone (PCL)-grafted MWCNTs (Guojian *et al.*, 2009).

Both Blake *et al.* (2006) and Shi *et al.* (2007) found that pristine MWCNTs produced no reinforcing effects on PVC at all. However, the stiffness, strength, ductility and toughness of PVC were improved significantly by CPP-grafted and PnBMA-grafted MWCNTs. Close to twofold increases in Young's modulus and tensile strength, and a tenfold increase in toughness of PVC were achieved in a CPP-grafted MWCNTs content of less than 1 vol.%. Shi *et al.* (2007) also

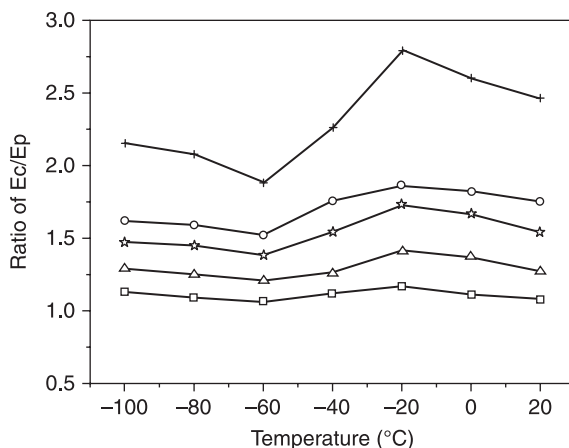
reported that Young's modulus, the yield stress, tensile strength, ultimate strain, and toughness of PVC were increased by 40, 74, 84, 38 and 140%, respectively, by the addition of 0.2 wt% of PnBMA-grafted MWCNTs. The unusually large improvement in toughness observed by Blake *et al.* could be due to the residual tetrahydrofuran (THF) in the composites as they were dried at room temperature for 12 hours. The residual solvent could serve as a plasticizer to increase the ductility and toughness. On the other hand, the THF-cast composites prepared by Shi *et al.* (2007) were thoroughly dried under vacuum at 80°C for one week. In terms of the rate of increase of a particular tensile property with volume fraction of MWCNTs, PnBMA-grafted MWCNTs appeared to be more effective than CPP-grafted MWCNTs in improving the mechanical properties of PVC. Both research groups observed that a further increase in the amount of polymer-grafted MWCNTs did not further improve the mechanical properties.

Guojian *et al.* (2008, 2009) reported remarkable improvements in the ductility and un-notched Charpy impact strength of PVC using polymer-grafted MWCNTs. The composites contained other ingredients such as calcium carbonate, titanium dioxide, a plasticizer and a stabilizer. Even composites reinforced by pristine MWCNTs showed unusually good ductility and toughness. At a pristine MWCNTs content of 0.72 vol.%, the ultimate strain and impact strength of PVC were improved by 173 and 359%, respectively (Guojian *et al.*, 2009). Since polymer composites containing pristine CNTs usually possess poor ductility and toughness, the plasticizer must have contributed to the remarkably improved ductility and toughness of PVC. The addition of PCL-grafted MWCNTs (0.72 vol.%) improved the ultimate strain and impact strength by 280 and 418%, respectively.

Poly(vinylidene fluoride) (PVDF) composites

In view of the miscibility of PVDF and PMMA, Wang M. *et al.* (2007) used PMMA-grafted MWCNTs to enhance the storage modulus of PVDF. The incorporation of PMMA-grafted MWCNTs (effective MWCNT content of 1.93 wt%) led to an improvement of the storage modulus by 100–150% over a wide temperature range (Fig. 12.7). PMMA has been used to improve the storage modulus of PVDF. Since the composite with an effective MWCNTs content of 1.93 wt% contained 17.4 wt% of PMMA, the storage modulus of a PVDF–PMMA blend containing 17.4 wt% of PMMA was also evaluated. As shown in Fig. 12.7, the storage modulus of PVDF was improved by about 50% by the addition of PMMA. For a composite containing 1.6 wt% of pristine MWCNTs, the improvement of storage modulus was around 25% over the same temperature range. In other words, PMMA-grafted MWCNTs are more effective than pristine MWCNTs or PMMA in enhancing the storage modulus of PVDF.

Chang and Liu (2010) recently used an ozone-mediated process to graft PVDF and polysulfone (PSF) onto MWCNTs. Ozone generated peroxides and hydroperoxides in polymer chains. These groups decomposed to radicals which

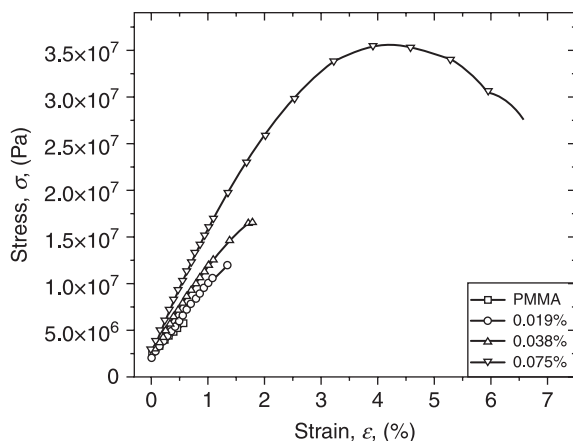


12.7 E_c/E_p ratios of PVDF composites: effective MWCNTs content of 0.42 wt% (☆); effective MWCNTs content of 1.66 wt% (○); effective MWCNTs content of 1.93 wt% (+); PVDF/pristine MWCNTs composite containing 1.60 wt% of MWCNTs (□); PVDF/PMMA (82.6/17.4) blend (△). (Reprinted with permission from Wang M. *et al.* (2007). Copyright Institute of Physics Publishing Ltd.)

reacted with the sp^2 carbons of MWCNTs to achieve grafting. The addition of 0.3 wt% pristine MWCNTs led to increases in Young's modulus and ultimate strain by only 3 and 14%, respectively, and a reduction in tensile strength by 14%. For a composite containing PVDF-grafted MWCNTs with an effective MWCNTs content of 0.3 wt%, the tensile strength, Young's modulus and ultimate strain were improved by 90, 58 and 110%, respectively (Chang and Liu, 2010). Similar to other studies mentioned in the earlier sections, further increase in PVDF-grafted MWCNTs led to decreases in mechanical properties. In comparison, PSF-grafted MWCNTs were not as effective as PVDF-grafted MWCNTs in enhancing the mechanical properties of PVDF. At the same effective MWCNTs content of 0.3 wt%, the addition of PSF-grafted MWCNTs led to increases in tensile strength, Young's modulus and ultimate strain by 58, 26 and 42%, respectively. The miscibility between PVDF and PSF has not been established. If PVDF and PSF were immiscible with each other, the stress transfer would not be that efficient, leading to the poorer reinforcing ability of PSF-grafted MWCNTs.

Poly(methyl methacrylate) (PMMA) composites

Hwang *et al.* (2004) reported a significant increase in the storage modulus of PMMA by PMMA-grafted MWCNTs. The storage modulus of PMMA at 20°C was improved from 2.5 to 31 GPa (1100% increase) by the addition of 20 wt% of



12.8 Stress–strain curves of PMMA and PMMA/PMMA-grafted MWCNTs composites. (Reprinted with permission from Blond *et al.* (2006). Copyright WILEY-VCH Verlag GmbH & Co.)

PMMA-grafted MWCNTs. Microscopic studies showed that the nanotubes were broken rather than an adhesive failure between the nanotubes and the polymer. Cui *et al.* (2009) recently found that the storage moduli of PMMA–MWCNTs composites prepared by *in-situ* polymerization were significantly larger than those of PMMA–clay composites with the same filler contents.

Blond *et al.* (2006) showed that the tensile properties of PMMA were similarly improved significantly by PMMA-grafted MWCNTs. Young's modulus, the tensile strength and toughness were improved by 1.9, 4.6 and 13.7 times, respectively, upon the addition of less than 0.5 wt% of nanotubes. The stress–strain curves of PMMA and composites are shown in Fig. 12.8. They also observed that effective reinforcement was observed up to a nanotube content of around 0.1 vol.%, above which the mechanical properties deteriorated probably due to nanotube aggregation.

Polystyrene (PS) composites

The reinforcement of PS using CPP-grafted MWCNTs was reported by Blake *et al.* (2006). Young's modulus, the tensile strength and toughness of PS were increased by 58, 49 and 63%, respectively, upon the addition of a small amount of CPP-grafted MWCNTs (0.26 vol.%). However, the mechanical properties deteriorated at higher loadings of CPP-grafted MWCNTs. The composite containing 1.0 vol.% of CPP-grafted MWCNTs was mechanically weaker than PS. Furthermore, SEM micrographs of fractured composite films showed that a significant number of nanotubes had been pulled out. The pulling out of nanotubes

was considered to indicate that the nanotubes used were shorter than the critical length. In this author's view, the pulling out of nanotubes also indicates weak interfacial adhesion arising from a possible immiscibility between PS and CPP. Since PS is immiscible with either PVC or PP, it is very likely to be immiscible with CPP as well. An immiscible blend usually possesses mechanical properties lower than those predicted by the linear additivity rule, and its mechanical properties can even be poorer than the component polymers. It is then possible that the weak PS–CPP interface may have contributed to the inefficient reinforcement at higher CPP-grafted MWCNT loadings.

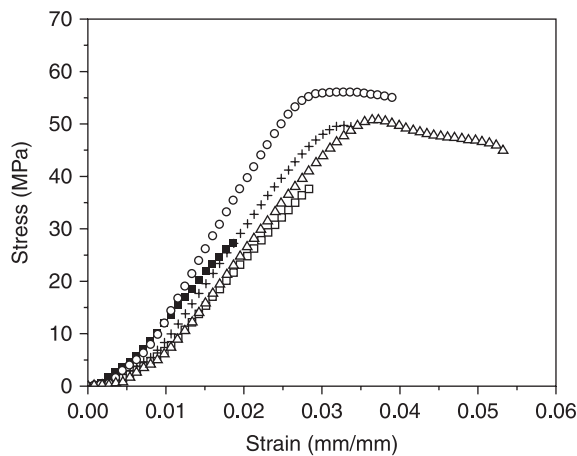
Xie *et al.* (2007) observed a pronounced reinforcement of the mechanical properties of PS using PS-grafted SWCNTs. At a low nanotube content of 0.06 wt%, the tensile strength and Young's modulus of PS were improved by 82 and 78%, respectively. The ultimate strain also improved from 1.3 to about 3.5%. The remarkable reinforcing effect was attributed to high grafting density and high molecular weight of PS grafted onto SWCNTs.

Kwon *et al.* (2008) prepared cross-linked PS-grafted MWCNT balls by *in-situ* suspension polymerization of styrene with MWCNTs and divinyl benzene as a cross-linking agent. They found that Young's modulus, the tensile strength, ultimate strain and un-notched Izod impact strength of PS were decreased by 5.2, 2.3, 13.6 and 21.6%, respectively, by the addition of 1.0 wt% pristine MWCNTs. In comparison, 1.0 wt% of PS-grafted MWCNT balls led to increases in Young's modulus, tensile strength, ultimate strain and impact strength by 19.7, 24, 63.6 and 16.2%, respectively.

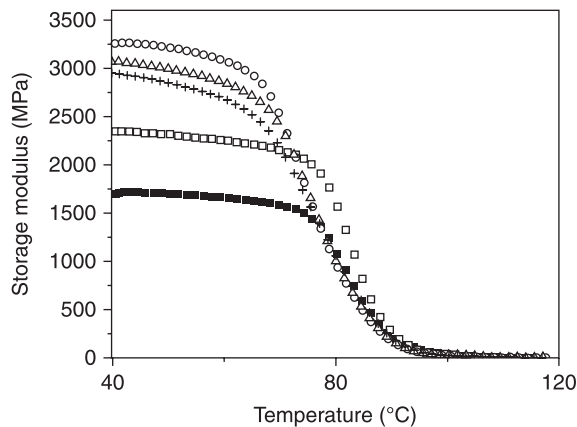
In a related study, Dai *et al.* (2009) fabricated composite films based on sulfonated polystyrene (SPS) and sulfonated SWCNTs, with glycerin added as a cross-linking agent. The resulting materials are essentially SPS–SPS-grafted SWCNTs composites. For a composite containing 5 wt% SWCNTs, the tensile strength was better than those of PS and SPS by 84 and 67%, respectively. However, the other mechanical properties of the composites were not determined.

Poly(styrene-co-acrylonitrile) (SAN) composite

SAN with an acrylonitrile content of 25 wt% was reinforced using PMMA-grafted MWCNTs (Wang M. *et al.*, 2005). The miscibility between PMMA and SAN allowed the efficient stress transfer from the matrix to the nanotubes, leading to significant improvements in various mechanical properties. Figure 12.9 shows the stress–strain curves of SAN and several composites. The addition of PMMA-grafted MWCNTs increased the stiffness, strength, ductility and toughness simultaneously. At an effective MWCNTs content of 1.0 wt%, PMMA-grafted MWCNTs led to increases in Young's modulus, tensile strength, ultimate strain and toughness by 51, 99, 105 and 464%, respectively. In comparison, the addition of 1.0 wt% of pristine MWCNTs led to increases in tensile strength, ultimate



12.9 Stress–strain curves of SAN (■), SAN/pristine MWCNTs composite (1.0 wt %) (□), and SAN/PMMA-grafted MWCNTs composites with effective MWCNTs content of 0.5 wt % (△), 1.0 wt % (○), and 2.0 wt % (+). (Reprinted with permission from Wang M. *et al.* (2005). Copyright Elsevier Ltd.)



12.10 Storage moduli of SAN (■), SAN/pristine MWCNTs composite (1.0 wt %) (□), and SAN/PMMA-grafted MWCNTs composites with effective MWCNTs content of 0.5 wt % (△), 1.0 wt % (○), and 2.0 wt % (+). (Reprinted with permission from Wang M. *et al.* (2005). Copyright Elsevier Ltd.)

strain and toughness by 36, 47, and 89%, respectively, and a decrease in Young’s modulus by a marginal 2%. Similarly, PMMA-grafted MWCNTs are better than pristine MWCNTs in enhancing the storage modulus of SAN as shown in Fig. 12.10. It is also noted from Figs 12.9 and 12.10 that further increase in the

amount of PMMA-grafted MWCNTs to 2.0 wt% led to reductions in the mechanical properties.

12.4.3 Other polymer composites

Chitosan composites

Chitosan is a natural polymer which has applications in biomedical, agricultural and food industries. However, its mechanical properties are not sufficiently good to meet industrial requirements. CNTs have been used to enhance the mechanical properties of chitosan. The stress–strain curves of chitosan–pristine MWCNTs composites were shown earlier in Fig. 12.1. Shieh and Yang (2006) examined the dynamic mechanical properties of chitosan–chitosan-grafted MWCNTs composites. The storage modulus of chitosan at -75°C was increased by 134% from 6.4 GPa to 15 GPa for a composite containing 40 wt% chitosan-grafted MWCNTs.

Recently, Cao *et al.* (2009) reported the tensile properties of chitosan reinforced by chitosan-grafted MWCNTs. Grafting of chitosan was achieved through the use of two coupling agents. The addition of chitosan-grafted MWCNTs progressively improved the stiffness and strength of chitosan. At a nanotube content of 1 wt%, Young's modulus and the tensile strength of chitosan were increased by 93 and 148%, respectively, although the ultimate strain was reduced by 26%. They also found that the water contact angle decreased from 90° to 53° for a composite containing 3 wt% chitosan-grafted MWCNTs.

Polyamide composites

Gao *et al.* (2005) fabricated SWCNTs–polyamide-6 fibers by *in-situ* ring-opening polymerization. Condensation between the carboxylic acid groups of acidified SWCNTs and the amino end groups of polyamide-6 led to grafting. Young's modulus and the tensile strength of the fibers improved progressively with increasing nanotube contents, but the ultimate strain decreased progressively. At a SWCNTs content of 1.5 wt%, Young's modulus and the tensile strength were improved significantly by 173 and 84%, respectively.

Moniruzzaman *et al.* (2007) grafted polyamide-6,10 from SWCNTs using an *in-situ* polycondensation method. The sidewalls of SWCNTs were linked to polyamide-6,10 via alkyl (C4 or C9) segments. Functionalized SWCNTs improved the stiffness and strength of nylon fibers without compromising the ductility and toughness. At a CNT content of 1 wt%, pristine SWCNTs increased Young's modulus and the tensile strength and by 38 and 17%, respectively, but reduced the ultimate strain and toughness by 40 and 14%, respectively. For fibers containing functionalized SWCNTs with C9 spacer segments, Young's modulus, the tensile strength and toughness were increased by 132, 163 and 136%, respectively, with only a slight reduction in ultimate strain of 16%.

Polybenzimidazole (PBI) composites

Shao *et al.* (2009) grafted PBI onto MWCNTs using a one-pot synthesis which combined *in-situ* modification of nanotubes and *in-situ* polymerization of 2,2'-(p-oxydiphenylene)-5,5'-bibenzimidazole in one reaction pot. The incorporation of 1 wt% pristine MWCNTs increased Young's modulus and the yield stress of PBI by 27 and 39%, respectively, and decreased the tensile strength and ultimate strain by 12 and 46 %, respectively. The use of 1 wt% PBI-grafted MWCNTs improved Young's modulus, yield stress and tensile strength by 37, 60 and 19%, respectively, with a 19% reduction in ultimate strain.

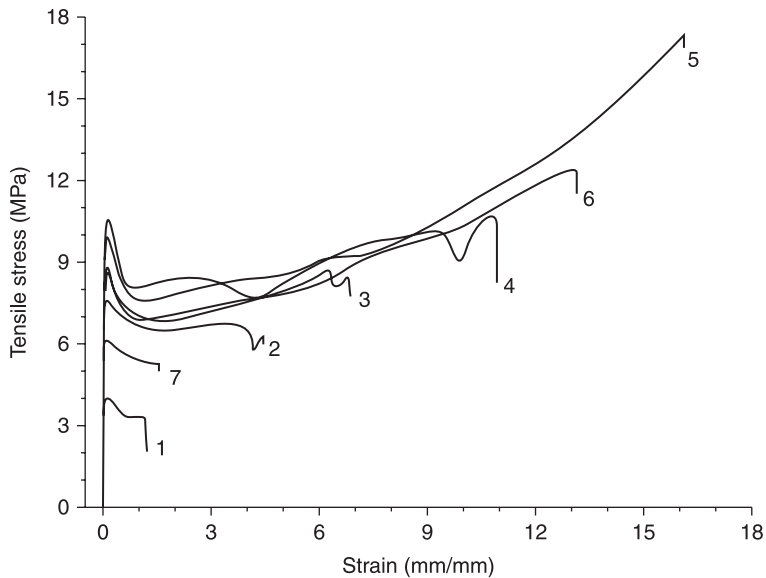
Poly(2,6-dimethyl-1,4-phenylene oxide) (PPO) composites

Liu *et al.* (2008) grafted PPO onto MWCNTs using brominated PPO under ATRP condition. The successful grafting made use of the ability of brominated PPO to serve as a macro-initiator for ATRP using the benzylbromide groups as initiating sites. The benzylbromide groups were reactive towards MWCNTs surface through atom transfer radical addition. The mechanical properties of PPO were substantially improved by PPO-grafted MWCNTs without compromising the ductility. At a PPO-grafted MWCNTs content of 2 wt%, the maximum stress attained was doubled and the ultimate strain was improved by about 30%.

Poly(ethylene oxide) (PEO) composites

Shieh *et al.* (2005) studied the enhancement of the storage modulus of PEO using PMMA-grafted MWCNTs. PEO and PMMA are miscible with each other. The storage modulus of PEO at -100°C increased from 3.2 GPa to 4.4 GPa upon the addition of 20 wt% PMMA-grafted MWCNTs.

Awasthi *et al.* (2006) found that the maximum stress attained by PEO was increased from 0.5 to 50 MPa upon the addition of 50 wt% of MWCNTs, and the ultimate strain was improved from 2.5 to 5.0%. However, the use of such a large amount of MWCNTs is not cost effective. B. X. Yang *et al.* (2007b) showed that spectacular improvements in stiffness, strength, ductility and toughness of PEO were achieved using phenoxy-grafted MWCNTs as shown by the stress–strain curves in Fig. 12.11. The miscibility between PEO and phenoxy allowed efficient stress transfer from matrix to nanotubes. At a phenoxy-grafted MWCNTs content of 1.5 wt%, Young's modulus, the yield stress, tensile strength, ultimate strain and toughness of PEO were increased by 228, 166, 442, 1240, and 4080%, respectively. At a higher phenoxy-grafted MWCNTs content of 2.0 wt%, the mechanical properties showed a downturn trend due to the difficulty in dispersing the nanotubes homogeneously as evidenced from polarized light microscopy. It is of interest to note that PEO end-capped with C_{60} also showed unusually good ductility and toughness (Song *et al.*, 2003). B. X. Yang *et al.* (2007b) also found



12.11 Stress–strain curves of PEO and composites: (1) PEO; (2) PEO/0.1%PG; (3) PEO/0.5%PG; (4) PEO/1.0%PG; (5) PEO/1.5%PG; (6) PEO/2.0%PG; (7) PEO/1.0%AR. PG denotes phenoxyl-g-MWCNTs and AR denotes pristine MWCNTs. (Reprinted with permission from Yang *et al.* (2007b). Copyright Institute of Physics Publishing Ltd.)

that the storage modulus of PEO at -110°C was improved from 3.09 to 3.46 GPa (12% increase) by the addition of 1.0 wt% of pristine MWCNTs. In comparison, the composite containing 1.5 wt% phenoxyl-grafted MWCNTs possessed a storage modulus of 6.58 GPa (113% increase) at the same temperature.

Polyimide (PI) composites

The grafting of PI onto SWCNTs and MWCNTs was reported by Qu *et al.* (2004) and Hill *et al.* (2005). PI-grafted CNTs were homogeneously dispersed in PI matrix to produce high quality and optically transparent films.

Yuen *et al.* (2007) grafted PI onto MWCNTs. Precursor polyamic acid was first prepared. Acidified MWCNTs were grafted with soluble polyimide, which were then added to the polyamic acid and heated to 300°C to form composites. PI-grafted MWCNTs were more effective than acidified MWCNTs in enhancing the mechanical properties of PI, particularly at nanotube contents less than 2.5 phr. At a nanotube content of 1 phr, Young's modulus and the tensile strength of PI were improved by 62 and 17%, respectively, using PI-grafted MWCNTs. In comparison, the increases in Young's modulus and the tensile strength by acidified MWCNTs were 37 and 8%, respectively.

Poly(L-lactide) (PLLA) composites

In view of the biodegradability and biocompatibility of PLLA, its composites with CNTs have been fabricated. Chen *et al.* (2007) synthesized PLLA-grafted MWCNTs by surface-initiated ring-opening polymerization. Upon the addition of 1 wt% PLLA-grafted MWCNTs, Young's modulus of PLLA was improved from 2463 to 4710 MPa (91% increase) and the tensile strength was increased from 56.4 to 85.6 MPa (52% increase), and a reduction of ultimate strain from 7.5 to 6.8% (9% decrease). On the other hand, when 1 wt% of hydroxyl-functionalized MWCNTs was added, Young's modulus and tensile strength of PLLA were improved by 20% and 14 %, respectively, whereas the reduction in ultimate strain was 39%.

Yoon *et al.* (2009) showed that Young's modulus and the yield strength of PLLA were improved by 32% and 47%, respectively, by the addition of 1 wt% PLLA-grafted MWCNTs, and the ultimate strain was reduced by 22%. Yoon *et al.* (2010) recently reported the effect of PLLA chain length grafted onto MWCNTs on the mechanical properties of the composites. The molecular weights PLLA grafted onto MWCNTs ranged from 122 to 530 g/mol. Longer PLLA chain length led to better dispersion, resulting in increased Young's modulus and tensile strength.

Polyurethane (PU) composites

Kuan *et al.* (2005) grafted waterborne PU onto MWCNTs by covalent bonding or ionic bonding. At the same carbon nanotube loading of 5 phr, PU-grafted MWCNTs prepared by covalent bonding increased Young's modulus and the tensile strength by 171 and 370%, respectively. In comparison, PU-grafted MWCNTs prepared by ionic bonding increased Young's modulus and the tensile strength by 56% and 170%, respectively. Wang *et al.* (2008) found that the addition of 1 wt% of PU-grafted MWCNTs improved Young's modulus and the tensile strength of PU by 61% and 6%, respectively, without affecting the ultimate strain. A recent study showed that the tensile strength and ultimate strain of PU were remarkably improved by 900% and 741%, respectively, by PU-grafted MWCNTs at a nanotube content of 1 wt% (Chen X. *et al.*, 2009).

Wang and Tseng (2007) grafted segmented PU to MWCNTs by esterification reaction. Similar to the parent PU, the PU-grafted MWCNTs were soluble in a number of highly polar solvents. The storage modulus of PU and the glass transition temperature of the soft segment increased with increasing PU-grafted MWCNTs content from 1 to 10 wt%. The tensile strength increased from 377 kPa to 1167 kPa (210% increase) for PU containing 10 wt% PU-grafted MWCNTs, but the ultimate strain decreased from 190% to 115% (39% decrease).

Blighe *et al.* (2008) used a dispersion technology to incorporate a large quantity of SWCNTs or poly(ethylene glycol) (PEG)-grafted SWCNTs to PU

(up to 80 wt%). PEG was considered to be miscible with PU in view of their closely matched solubility parameters. The tensile strength of PU did not vary significantly with nanotube content. Young's modulus increased dramatically by 825 times for a composite containing 75 wt% PEG-grafted SWCNTs. Meanwhile, the ultimate strain dropped from 1140% for PU to 3% for the composite. As a result, the toughness also experienced an unusually large drop by more than 99%. Therefore, PEG-grafted SWCNTs-PU composite films exhibited tunable stiffness and toughness, without sacrificing strength. The composite films are stiff and brittle at high nanotube loadings, and compliant and ductile at low nanotube loadings.

Polyurethane-urea (PUU) was grafted onto MWCNTs using a coupling agent (Xu M. *et al.* 2006). A small amount of PUU-grafted MWCNTs (0.1–0.5 wt%) led to significant improvements in the mechanical properties of PUU. At a nanotube content of 0.5 wt%, Young's modulus and the tensile strength were increased by 275% and 59%, respectively, and the ultimate strain was reduced by only 11%.

12.5 Conclusion

The use of polymer-grafted CNTs enables the nanotubes to be well dispersed in polymer matrices and allows a more efficient stress transfer from the matrix to CNTs. As a result, polymer-grafted CNTs can simultaneously improve the stiffness, strength, ductility and toughness of polymers. However, there is an optimal amount of polymer-grafted CNTs to achieve maximum enhancement, beyond which the composites show downturns in mechanical properties. In comparison, pristine CNTs usually improve only the stiffness and strength of polymers, but not the ductility and toughness. In other words, polymer-grafted CNTs are superior to pristine CNTs in enhancing the mechanical properties of polymers.

For industrial applications, the cost of producing polymer-grafted CNTs is the main issue. Simple and less laborious grafting/fabrication methods are therefore highly desirable. Several methods are worthy of mention. Y. Chen *et al.* (2009) reported a microwave-assisted solid-state grafting of polyurethane onto MWCNTs, and this one-step method needs only 10 minutes to complete. The reactive blending method is another promising method. Take, for example PE, as discussed on p.350. Grafting was achieved by melt blending PE-g-MA and amine-functionalized MWCNTs. The PE-grafted MWCNTs were separated and characterized, and then melt blended with PE (Yang B. X. *et al.*, 2007a). To reduce the production cost, composites may be prepared using a one-pot grafting/fabrication process by melt blending PE, PE-g-MA and amine-functionalized MWCNTs. The one-pot grafting/fabrication of composites by reactive blending can be similarly applied to PP (Yang *et al.*, 2008) and PB (Yang *et al.*, 2009) composites.

12.6 References

- Awasthi K, Awasthi S, Srivastava A, Kamalakaran R, Talapatra S, Ajayan P M and Srivastava O N (2006) 'Synthesis and characterization of carbon nanotube-polyethylene oxide composites', *Nanotechnology*, 17, 5417–5422.
- Baskaran D, Dunlap J R, Mays J M and Bratcher M S (2005) 'Grafting efficiency of hydroxy-terminated poly(methyl methacrylate) with multiwalled carbon nanotubes', *Macromol. Rapid. Commun.*, 26, 481–486.
- Baskaran D, Mays J M and Bratcher M S (2004) 'Polymer-grafted multiwalled carbon nanotubes through surface-initiated polymerization', *Angew. Chem. Int. Ed.*, 43, 2138–2142.
- Blake R, Coleman J N, Bryne M T, McCarthy J E, Perova T S, Blau W J, Fonseca A, Nagy J B and Gun'ko Y K (2006) 'Reinforcement of poly(vinyl chloride) and polystyrene using chlorinated polypropylene grafted carbon nanotubes', *J. Mater. Chem.*, 16, 4206–4213.
- Blake R, Gun'ko Y K, Coleman J, Cadek M, Fonseca A, Nagy J B and Blau W J (2004) 'A generic organometallic approach toward ultra-strong carbon nanotube polymer composites', *J. Am. Chem. Soc.*, 126, 10226–10227.
- Blighe F M, Blau W J and Coleman J N (2008) 'Towards tough, yet stiff, composites by filling an elastomer with single-walled nanotubes at very high loading levels', *Nanotechnology*, 29, article 415709.
- Blond D, Barron V, Reuther M, Ryan KP, Nicolosi V, Blau WJ, and Coleman J N (2006) 'Enhancement of modulus, strength and toughness in poly(methyl methacrylate)-based composites by the incorporation of poly(methyl methacrylate)-functionalized nanotubes', *Adv. Funct. Mater.*, 16, 1608–1614.
- Bose S, Khare R A and Moldenaers P (2010) 'Assessing the strengths and weaknesses of various types of pre-treatments of carbon nanotubes on the properties of polymer/carbon nanotubes composites: a critical review', *Polymer*, 51, 975–993.
- Buffa F, Hu H and Resasco D E (2005) 'Side-wall functionalization of single-walled carbon nanotubes with 4-hydroxymethylaniline followed by polymerization of ϵ -caprolactone', *Macromolecules*, 38, 8258–8263.
- Cao X, Dong H, Li C M and Lucia L A (2009) 'The enhanced mechanical properties of a covalently bound chitosan-multiwalled carbon nanotube nanocomposite', *J. Appl. Polym. Sci.*, 113, 466–472.
- Causin V, Yang B X, Marega C, Goh S H and Marigo A (2009) 'Nucleation, structure and lamellar morphology of isotactic polypropylene filled with polypropylene-grafted multiwalled carbon nanotubes', *Eur. Polym. J.*, 45, 2155–2163.
- Chang C M and Liu Y L (2010) 'Functionalization of multi-walled carbon nanotubes with non-reactive polymers through an ozone-mediated process for the preparation of a wide range of high performance/carbon nanotube composites', *Carbon*, 48, 1289–1297.
- Chen G X, Kim H S, Park B H and Yoon J S (2005) 'Controlled functionalization of multiwalled carbon nanotubes with various molecular weight poly(L-lactic acid)', *J. Phys. Chem. B.*, 109, 22237–22243.
- Chen G X, Kim H S, Park B H and Yoon J S (2007) 'Synthesis of poly(L-lactide)-functionalized multiwalled carbon nanotubes by ring-opening polymerization', *Macromol. Chem. Phys.*, 208, 389–398.
- Chen X, Wang J, Zou J, Wu X, Chen X and Xue F (2009) 'Mechanical and thermal properties of functionalized multiwalled carbon nanotubes and multiwalled carbon nanotube-polyurethane composites', *J. Appl. Polym. Sci.*, 114, 3407–3413.

- Chen Y, Muthukumar S, Wang Y, Li C, Krishnan S K, Sai S S S, Venkataramaniah K and Mitra S (2009) 'Microwave-assisted solid-state grafting of multi-walled carbon nanotubes on polyurethane for the synthesis of a composite with optical limiting properties', *J. Mater. Chem.*, 19, 6568–6572.
- Coleman J N, Cadek M, Blake R, Nicolosi V, Ryan K P, Belton C, Fonseca A, Nagy J B, Gun'ko Y K and Blau W J (2004) 'High performance nanotube-reinforced plastics: understanding the mechanism of strength increase', *Adv. Funct. Mater.*, 14, 791–798.
- Coleman J N, Khan U, Blau W J and Gun'ko Y K (2006a) 'Small but strong: a review of the mechanical properties of carbon nanotube-polymer composites', *Carbon*, 44, 1624–1652.
- Coleman J N, Khan U and Gun'ko Y K (2006b) 'Mechanical reinforcement of polymers using carbon nanotubes', *Adv. Mater.*, 18, 689–706.
- Cui J, Wang W P, You Y Z, Liu C and Wang P (2004) 'Functionalization of multiwalled carbon nanotubes by reversible addition fragmentation chain-transfer polymerization', *Polymer*, 45, 8717–8721.
- Cui L, Tarte N H and Woo S I (2009) 'Synthesis and characterization of PMMA/MWNT composites prepared by *in situ* polymerization with Ni(acac)₂ catalyst', *Macromolecules*, 42, 8649–8654.
- Dai Y, Hong H, Guiver M and Welsh J S (2009) 'Reinforced films based on cross-linked water-soluble sulfonated carbon nanotubes with sulfonated polystyrene', *J. Nanosci. Nanotechnol.*, 9, 5150–5156.
- Demczyk B G, Wang Y M, Cumings J, Hetman M, Han W, Zettl A and Ritchie R O (2002) 'Direct mechanical measurement of the tensile strength and elastic modulus of multiwalled carbon nanotubes', *Mater. Sci. Eng. A.*, 334, 173–178.
- Funck A and Kaminsky W (2007) 'Polypropylene carbon nanotube composites by *in situ* polymerization', *Compos. Sci. Technol.*, 67, 906–915.
- Gao J, Itkis M E, Yu A, Bekyarova E, Zhao B and Haddon R C (2005) 'Continuous spinning of a single-walled carbon nanotube-nylon composite fiber', *J. Am. Chem. Soc.*, 127, 3847–3854.
- Guojian W, Lijuan W, Mei Z and Zhengmian C (2009) 'Reinforcement and toughening of poly(vinyl chloride) with poly(caprolactone) grafted carbon nanotubes', *Composites Part A*, 40, 1476–1481.
- Guojian W, Zehua Q, Lin L, Quan S and Jianlong G (2008) 'Study of SMA graft modified MWNT/PVC composite materials', *Mater. Sci. Eng. A.*, 473, 136–139.
- Hill D, Lin Y, Qu L, Kitagorodskiy A, Connell J W, Allard L F and Sun Y P (2005) 'Functionalization of carbon nanotubes with derivatized polyimides', *Macromolecules*, 38, 7670–7675.
- Homenick C M, Lawson G and Adronov A (2007) 'Polymer grafting of carbon nanotubes using living free-radical polymerization', *J. Macromol. Sci. Part. C. Polym. Rev.*, 47, 265–290.
- Hong C Y, You Y Z and Pan C Y (2005a) 'Synthesis of water-soluble multiwalled carbon nanotubes with grafted temperature-responsive shells by surface RAFT polymerization', *Chem. Mater.*, 17, 2247–2254.
- Hong C Y, You Y Z and Pan C Y (2006a) 'A new approach to functionalize multi-walled carbon nanotubes by the use of functional polymers', *Polymer*, 47, 4300–4309.
- Hong C Y, You Y Z and Pan C Y (2006b) 'Functionalized multi-walled carbon nanotubes with poly(N-(2-hydroxypropyl)methacrylamide) by RAFT polymerization', *J. Polym. Sci. Part A: Polym. Chem.*, 44, 2419–2427.

- Hong C Y, You Y Z, Wu D, Liu Y and Pan C Y (2005b) ‘Multiwalled carbon nanotubes grafted with hyperbranched polymer shell via SCVP’, *Macromolecules*, 38, 2606–2611.
- Hwang G L, Shieh Y T and Hwang K C (2004) ‘Efficient load transfer to polymer-grafted multiwalled carbon nanotubes in polymer composites’, *Adv. Funct. Mater.*, 14, 487–491.
- Jin Z X, Pramoda K P, Xu G Q and Goh S H (2001) ‘Dynamic mechanical behavior of melt-processed multi-walled carbon nanotubes/poly(methyl methacrylate) composites’, *Chem. Phys. Lett.*, 337, 43–47.
- Khan U, Ryan K, Blau W J and Coleman J N (2007) ‘The effect of solvent choice on the mechanical properties of carbon nanotube-polymer composites’, *Compos. Sci. Technol.*, 67, 3158–3167.
- Kong H, Gao C and Yan D (2004a) ‘Controlled functionalization of multiwalled carbon nanotubes by atom transfer radical polymerization’, *J. Am. Chem. Soc.*, 126, 412–413.
- Kong H, Gao C and Yan D (2004b) ‘Functionalization of multiwalled carbon nanotubes by atom transfer radical polymerization and defunctionalization of the products’, *Macromolecules*, 37, 4022–4030.
- Koval’chuk A A., Shchegolikhin A N, Shevchenko V G, Nedorezova P M, Klyamkina A N and Aladyshev A M (2008a) ‘Synthesis and properties of polypropylene/multiwalled carbon nanotube composites’, *Macromolecules*, 41, 3149–3156.
- Koval’chuk A A, Shevchenko V G, Shchegolikhin A N, Nedorezova P M, Klyamkina A N and Aladyshev A M (2008b) ‘Effect of carbon nanotube functionalization on the structural and mechanical properties of polypropylene/MWCNT composites’, *Macromolecules*, 41, 7536–7542.
- Kuan H C, Ma C C M, Chang W P, Yuen S M, Wu H H and Lee T M (2005) ‘Synthesis, thermal, mechanical and rheological properties of multiwall carbon nanotube/waterborne polyurethane nanocomposites’, *Compos. Sci. Technol.*, 65, 1703–1710.
- Kumar N A, Ganapathy H S, Kim J S, Jeong Y S and Jeong Y T (2008) ‘Preparation of poly 2-hydroxyethyl methacrylate functionalized carbon nanotubes as novel biomaterial nanocomposites’, *Eur. Polym. J.*, 44, 579–586.
- Kwon S M, Kim H S, Kim D Y, Yun Y S and Jin H J (2008) ‘Polystyrene composites containing crosslinked polystyrene-multiwalled carbon nanotube balls’, *J. Appl. Polym. Sci.*, 110, 3737–3744.
- Li H, Cheng F, Duft A M and Adronov A (2005) ‘Functionalization of single-walled carbon nanotubes with well-defined polystyrene by “click” coupling’, *J. Am. Chem. Soc.*, 127, 14518–14524.
- Li S, Chen H, Bi W, Zhou J, Wang Y, Li J, Cheng W, Li M, Li L and Tang T (2007) ‘Synthesis and characterization of polyethylene chains grafted onto the sidewalls of single-walled carbon nanotubes via copolymerization’, *J. Polym. Sci. Part A: Polym. Chem.*, 45, 5459–5469.
- Li W H, Chen X H, Yang Z and Xu L S (2009) ‘Structure and properties of polypropylene-wrapped carbon nanotubes composites’, *J. Appl. Polym. Sci.*, 113, 3809–3814.
- Liang F, Beach J M, Kobashi K, Sadana A K, Vega-Cantu Y I, Tour J M and Billup W E (2006) ‘In situ polymerization initiated by single-walled carbon nanotube salts’, *Chem. Mater.*, 18, 4764–4767.
- Lin Y, Meziani M J and Sun Y P (2007) ‘Functionalized carbon nanotubes for polymeric nanocomposites’. *J. Mater. Chem.*, 17, 1143–1148.
- Lin Y, Zhou B, Fernando K A S, Liu P, Allard L F and Sun Y P (2003) ‘Polymeric carbon nanocomposites from carbon nanotubes functionalized with matrix polymer’, *Macromolecules*, 36, 7199–7204.

- Liu P (2005) 'Modifications of carbon nanotubes with polymers', *Eur. Polym. J.*, 41, 2693–2703.
- Liu Y L, Chang Y H and Liang M (2008) 'Poly(2,6-dimethyl-1,4-phenylene oxide) (PPO) multi-bonded carbon nanotube (CNT): Preparation and formation of PPO/CNT nanocomposites', *Polymer*, 49, 5405–5409.
- Liu Y L and Chen W H (2007) 'Modification of multiwalled carbon nanotubes with initiators and macroinitiators of atom transfer radical polymerization', *Macromolecules*, 40, 8881–8886.
- Lou X, Detrembleur C, Pagnoulle C, Jérôme R, Bocharova V, Kiri A and Stamm M (2004a) 'Surface modification of multiwalled carbon nanotubes by poly(2-vinylpyridine): dispersion, selective deposition, and decoration of the nanotubes', *Adv. Mater.*, 16, 2123–2127.
- Lou X, Detrembleur C, Sciannamea V, Pagnoulle C and Jérôme R (2004b) 'Grafting of alkoxyamine end-capped (co)polymers onto multi-walled carbon nanotubes', *Polymer*, 45, 6097–6102.
- Mahfuz H, Adnan A, Rangari V K and Jeelani S (2005) 'Manufacturing and characterization of carbon nanotube/polyethylene composites', *Int. J. Nanosci.*, 4, 55–72.
- Martínez-Hernández A L, Velasco-Santos C and Castaño V M (2010) 'Carbon nanotubes composites: processing, grafting and mechanical and thermal properties', *Curr. Nanosci.*, 6, 12–39.
- McNally T, Pötschke P, Halley P, Murphy M, Martin D, Bell S E J, Brennan G P, Bein D, Lemoine P and Quinn J P (2005) 'Polyethylene multiwalled carbon nanotube composites', *Polymer*, 46, 8222–8232.
- Moniruzzaman M, Chattopadhyay J, Billups E W and Winey K I (2007) 'Tuning the mechanical properties of SWNT/nylon 6,10 composites with flexible spacers at the interface', *Nano. Lett.*, 7, 1178–1185.
- Moniruzzaman M and Winey K I (2006) 'Polymer nanocomposites containing carbon nanotubes', *Macromolecules*, 39, 5194–5205.
- Paiva M C, Zhou B, Fernando K A S, Lin Y, Kennedy J M and Sun Y P (2004) 'Mechanical and morphological characterization of polymer-carbon nanocomposites from functionalized carbon nanotubes', *Carbon*, 42, 2849–2854.
- Paiva M C, Zhou B, Fernando K A S, Lin Y, Lopes P E, Pennington W T, Kennedy J M and Sun Y P (2005) 'Physical and mechanical characterization of nanocomposites with carbon nanotubes functionalized with the matrix polymer', *Compos Interf.*, 12, 757–68.
- Park S, Yoon S W, Choi H, Lee J S, Cho W K, Kim J, Park H J, Yun W S, Choi C H, Do Y and Choi I S (2008) 'Pristine multiwalled carbon nanotube/polyethylene nanocomposites by immobilized catalysts', *Chem. Mater.*, 20, 4588–4594.
- Petrov P, Lou X, Pagnoulle C, Jérôme C, Calberg C and Jérôme R (2004) 'Functionalization of multi-walled carbon nanotubes by electrografting of polyacrylonitrile', *Macromol. Rapid. Commun.*, 25, 987–990.
- Priftis D, Sakellariou G, Baskaran D, Mays J W and Hadjichristidis N (2009) 'Polymer grafted Janus multi-walled carbon nanotubes', *Soft Matter*, 5, 4272–4278.
- Qin S, Qin D, Ford W T, Herrera J E and Resasco D E (2004a) 'Grafting of poly(4-vinylpyridine) to single-walled carbon nanotubes and assembly of multilayer films', *Macromolecules*, 37, 9963–9967.
- Qin S, Qin D, Ford W T, Herrera J E, Resasco D E, Bachilo S M and Weisman R B (2004b) 'Solubilization and purification of single-wall carbon nanotubes in water by in situ radical polymerization of sodium 4-styrenesulfonate', *Macromolecules*, 37, 3965–3967.

- Qin S, Qin D, Ford W T, Resasco D E and Herrera J E (2004c) 'Functionalization of single-walled carbon nanotubes with polystyrene via grafting to and grafting from methods', *Macromolecules*, 37, 752–757.
- Qin S, Qin D, Ford W T, Resasco D E and Herrera J E (2004d) 'Polymer brushes on single-walled carbon nanotubes by atom transfer radical polymerization of n-butyl methacrylate', *J. Am. Chem. Soc.*, 126, 170–176.
- Qu L, Lin Y, Hill D E, Zhou B, Wang W, Sun X, Kitaygorodskiy A, Suarez M, Connell J W, Allard L F and Sun Y P (2004) 'Polyimide-functionalized carbon nanotubes: synthesis and dispersion in nanocomposite films', *Macromolecules*, 37, 6055–6060.
- Qu L, Veca L M, Lin Y, Kitaygorodskiy A, Chen B, McCall A M, Connell J W and Sun Y P (2005) 'Soluble nylon-functionalized nanotubes from anionic ring-opening polymerization from nanotube surface', *Macromolecules*, 38, 10328–10331.
- Ramanathan T, Liu H and Brinson L C (2005) 'Functionalized SWNT/polymer nanocomposites for dramatic property improvement', *J. Polym. Sci. Part B: Polym. Phys.*, 43, 2269–2279.
- Shanmugharaj A M, Bae J H, Nayak R R and Ryu S H (2007) 'Preparation of poly(styrene-co-acrylonitrile)-grafted multiwalled carbon nanotubes via surface-initiated atom transfer radical polymerization', *J. Polym. Sci. Part A: Polym. Chem.*, 45, 460–470.
- Shao H, Shi Z, Fang J and Yin J (2009) 'One pot synthesis of multiwalled carbon nanotubes reinforced polybenzimidazole hybrids: preparation, characterization and properties', *Polymer*, 50, 5987–5995.
- Shi J H, Yang B X and Goh S H (2009) 'Covalent functionalization of multiwalled carbon nanotubes with poly(styrene-co-acrylonitrile) by reactive melt blending', *Eur. Polym. J.*, 45, 1002–1008.
- Shi J H, Yang B X, Pramoda K P and Goh S H (2007) 'Enhancement of the mechanical performance of poly(vinyl chloride) using poly(n-butyl methacrylate)-grafted multiwalled carbon nanotubes', *Nanotechnology*, 18, article 375704.
- Shieh Y T, Liu G L, Hwang K C and Chen C C (2005) 'Crystallization, melting and morphology of PEO in PEO/MWNT-g-PMMA blends', *Polymer*, 46, 10945–10951.
- Shieh Y T and Yang Y F (2006) 'Significant improvements in mechanical property and water stability of chitosan by carbon nanotubes', *Eur. Polym. J.*, 42, 3162–3170.
- Shofner M L, Khabashesku V N and Barrera E V (2006) 'Processing and mechanical properties of fluorinated single-walled carbon nanotube-polyethylene composites', *Chem. Mater.*, 18, 906–913.
- Song T, Goh S H and Lee S Y (2003) 'Mechanical behavior of double-C₆₀-end-capped poly(ethylene oxide)', *Polymer*, 44, 2563–2567.
- Song W, Zheng Z, Tang W and Wang X (2007) 'A facile approach to covalently functionalized carbon nanotubes with biocompatible polymer', *Polymer*, 48, 3658–3663.
- Spitalsky Z, Tasis D, Papagelis K and Galiotis C (2010) 'Carbon nanotube-polymer composites: chemistry, processing, mechanical and electrical properties', *Prog. Polym. Sci.*, 35, 357–401.
- Sui K, Yang C, Gao S, Shan X, Xia Y and Zheng Q (2009) 'A novel route for well-defined polystyrene-grafted multiwalled carbon nanotubes via the radical coupling reaction', *J. Appl. Polym. Sci.*, 114, 1914–1920.
- Tasis D, Tagmatarchis N, Bianco A and Prato M (2006) 'Chemistry of carbon nanotubes', *Chem. Rev.*, 106, 1105–1136.
- Trujillo M, Arnal M L, Muller A J, Laredo E, Bredeau St, Bonduel and Dubois Ph (2007) 'Thermal and morphological characterization of nanocomposites prepared by in-situ polymerization of high-density polyethylene on carbon nanotubes', *Macromolecules*, 40, 6268–6276.

- Vega J F, Martinez-Salazar J, Trujillo M, Arnal M L, Muller A J, Bredeau S and Dubois Ph (2009) 'Rheology, processing, tensile properties, and crystallization of polyethylene/carbon nanotube nanocomposites', *Macromolecules*, 42, 4719–4727.
- Wang G J, Huang S Z, Wang Y, Liu L, Qiu J and Li Y (2007) 'Synthesis of water-soluble single-walled carbon nanotubes by RAFT polymerization', *Polymer*, 48, 728–733.
- Wang M, Pramoda K P and Goh S H (2005) 'Enhancement of the mechanical properties of poly(styrene-co-acrylonitrile) with poly(methyl methacrylate)-grafted multiwalled carbon nanotubes', *Polymer*, 46, 11510–11516.
- Wang M, Shi J H, Pramoda K P and Goh S H (2007) 'Microstructure, crystallization and dynamic behaviour of poly(vinylidene fluoride) composites containing poly(methyl methacrylate)-grafted multiwalled carbon nanotubes', *Nanotechnology*, 18, article 235701.
- Wang S F, Shen L, Zhang W D and Tong Y J (2005) 'Preparation and properties of chitosan/carbon nanotubes composites', *Biomacromolecules*, 6, 3067–3072.
- Wang T L and Tseng C G (2007) 'Polymeric carbon nanocomposites from multiwalled carbon nanotubes functionalized with segmented polyurethane', *J. Appl. Polym. Sci.*, 105, 1642–1650.
- Wang W, Lin Y and Sun Y P (2005) 'Poly(N-vinyl carbazole)-functionalized single-walled carbon nanotubes: synthesis, characterization, and nanocomposite thin films', *Polymer*, 46, 8634–8640.
- Wang X, Du Z, Zhang C, Li C, Yang X and Li H (2008) 'Multi-walled carbon nanotubes encapsulated with polyurethane and its nanocomposites', *J. Polym. Sci. Part A: Polym. Chem.*, 46, 4857–4865.
- Wu Z, Feng W, Feng Y, Liu Q, Xu X, Sekino T, Fujii A and Ozaki M (2007) 'Preparation and characterization of chitosan-grafted multiwalled carbon nanotubes and their electrochemical properties', *Carbon*, 45, 1212–1218.
- Xie L, Xu F, Qiu F, Lu H and Yang Y (2007) 'Single-walled carbon nanotubes functionalized with high bonding density of polymer layers and enhanced mechanical properties of composites', *Macromolecules*, 40, 3296–3305.
- Xiong J, Zhou D, Zheng Z, Yang X and Wang X (2006) 'Fabrication and distribution characteristics of polyurethane/single-walled carbon nanotube composite with anisotropic structure', *Polymer*, 47, 1763–1766.
- Xu G, Wang Y, Pang W, Wu W T, Zhu Q and Wang P (2007) 'Fabrication of multiwalled carbon nanotubes with polymer shells through surface RAFT polymerization', *Polym. Int.*, 56, 847–852.
- Xu G, Wu W T, Wang Y, Pang W, Zhu Q, Wang P and You Y (2006a) 'Constructing polymer brushes on multiwalled carbon nanotubes by in situ reversible addition fragmentation chain transfer polymerization', *Polymer*, 47, 5909–5918.
- Xu M, Zhang T, Gu B, Wu J and Chen Q (2006b) 'Synthesis and properties of novel polyurethane-urea/multiwalled carbon nanotube composites', *Macromolecules*, 39, 3540–3545.
- Yang B X, Pramoda K P, Xu G Q and Goh S H (2007a) 'Mechanical reinforcement of polyethylene using polyethylene-grafted multiwalled carbon nanotubes', *Adv. Funct. Mater.*, 17, 2062–2069.
- Yang B X, Shi J H, Pramoda K P and Goh S H (2007b) 'Enhancement of stiffness, strength, ductility and toughness of poly(ethylene oxide) using phenoxy-grafted multiwalled carbon nanotubes', *Nanotechnology*, 18, article 125606.
- Yang B X, Shi J H, Pramoda K P and Goh S H (2008) 'Enhancement of the mechanical properties of polypropylene using polypropylene-grafted multiwalled carbon nanotubes', *Compos. Sci. Technol.*, 68, 2490–2497.

- Yang B X, Shi J H, Pramoda K P and Goh S H (2009) ‘Mechanical reinforcement of poly(1-butene) using polypropylene-grafted multiwalled carbon nanotubes’, *J. Appl. Polym. Sci.*, 113, 1165–1172.
- Yang M, Gao Y, Li H and Adronov A (2007) ‘Functionalization of multiwalled carbon nanotubes with polyamide 6 by anionic ring-opening polymerization’, *Carbon*, 45, 2327–2333.
- Yao Z, Braidy N, Botton G A and Adronov A (2003) ‘Polymerization from the surface of single-walled carbon nanotubes – preparation and characterization of nanocomposites’, *J. Am. Chem. Soc.*, 125, 16015–16024.
- Yoon J T, Jeong Y G, Lee S C and Min B G (2009) ‘Influences of poly(lactic acid)-grafted carbon nanotube on thermal, mechanical, and electrical properties of poly(lactic acid)’, *Polym. Adv. Technol.*, 20, 631–638.
- Yoon J T, Lee S C and Jeong Y G (2010) ‘Effects of grafted chain length on mechanical and electrical properties of nanocomposites containing polylactide-grafted carbon nanotubes’, *Compos. Sci. Technol.*, 70, 776–782.
- You Y Z, Hong C Y and Pan C Y (2006a) ‘Functionalization of carbon nanotubes with well-defined functional polymers via thiol-coupling reaction’, *Macromol. Rapid. Commun.*, 27, 2001–2006.
- You Y Z, Hong C Y and Pan C Y (2006b) ‘Directly growing ionic polymers on multi-walled carbon nanotubes via surface RAFT polymerization’, *Nanotechnology*, 17, 2350–2354.
- Yuen S M, Ma C C M, Chiang C L, Lin Y Y and Teng C C (2007) ‘Preparation and morphological, electrical, and mechanical properties of polyimide-grafted MWCNT/polyimide composite’, *J. Polym. Sci. Part A: Polym. Chem.*, 45, 3349–3358.
- Zhao B, Hu H, Yu A, Perea D and Haddon R C (2005) ‘Synthesis and characterization of a water-soluble single-walled carbon nanotube graft copolymer’, *J. Am. Chem. Soc.*, 127, 8197–8203.
- Zhao P, Wang K, Yang H, Zhang Q, Du R and Fu Q (2007) ‘Excellent tensile ductility in highly oriented injection-molded bars of polypropylene/carbon nanotubes composites’, *Polymer*, 48, 5688–5695.
- Zhao X, Lin W, Song N, Chen X, Fan X and Zhou Q (2006) ‘Water soluble multi-walled carbon nanotubes prepared via nitroxide-mediated radical polymerization’, *J. Mater. Chem.*, 16, 4619–4625.
- Zhao X D, Fan X H, Chen X F, Chai C P and Zhou Q F (2006) ‘Surface modification of multiwalled carbon nanotubes via nitroxide-mediated radical polymerization’, *J. Polym. Sci. Part A: Polym. Chem.*, 44, 4656–4667.

Multiscale modeling of polymer–carbon nanotube composites

G. M. ODEGARD, Michigan Technological University, USA

Abstract: Carbon nanotube (CNT) composite materials have the potential to provide significant increases in specific stiffness and specific strength relative to materials used for many engineering structural applications. To facilitate the design and development of CNT composites, structure–property relationships must be established that predict the bulk thermo-mechanical response of these materials as a function of the molecular and micro-structure. The objective of this chapter is to describe a general framework for multiscale modeling of CNT composites. First, the fundamental aspects of efficient and accurate modeling techniques are discussed. This is followed by a review of current state-of-the-art modeling approaches. Finally, a specific example is presented that describes the application of the approach to a specific CNT composite system.

Key words: continuum mechanics, micromechanics, molecular dynamics, representative volume element, structure–property relationships.

13.1 Introduction

While many experimental-based methods for characterizing the mechanical behavior of composite materials have proven to be robust and accurate, they incur high costs due to expensive testing equipment, specimen fabrication, and labor. Fortunately, computational modeling can be used to facilitate the development, characterization, and testing of composite materials by providing reliable and efficient structure–property relationships that are determined via inexpensive computational simulations.

In the past two decades, computational molecular modeling approaches (Leach, 2001) have emerged as important tools that can be used to predict atomic structure, vibrational frequencies, binding energies, heats of reaction, electrical properties, and mechanical properties of organic and inorganic materials. These methods are ideal for studying the behavior of atoms on the scale of nanometers or below. While the very largest of these simulations can include up to a billion (1×10^9) atoms, most engineering structures contain atoms numbering on the order of at least Avagadro's number (1×10^{23} atoms). Clearly, many orders of magnitude exist between the number of atoms that computational chemistry methods can model and which engineering structures contain.

Since the 17th century, mathematicians, scientists, and engineers have continually worked to establish models for the understanding of behavior of bulk

quantities of homogeneous and composite materials (Truesdell and Toupin, 1960; Herakovich, 1998; Truesdell and Noll, 2004). These models are important for understanding the motion, deformation, failure, buckling, and vibration of engineering structures and components. Because models that are established for these purposes cannot realistically contain all of the details used in computational chemistry simulations, approximations to the behavior of material must be made for which the number of atoms is minimally on the order of 1×10^{23} atoms. The assumption in continuum mechanics is that matter is modeled in a three-dimensional Euclidean point space for which points in a body in motion do not represent individual atoms. Instead, a body in motion contains an infinite number of points which form a continuum.

For the development of carbon nanotube (CNT) nanocomposite materials for engineering applications, it is often necessary to establish structure–property relationships, for which the molecular structure must be related to engineering-scale behavior. This clearly requires tools to relate the predicted molecular structure and behavior from computational chemistry techniques to the engineering structural level. These tools must span the length scale difference between Angstroms and meters. Many studies have focused on the modeling of CNT composites at more than one length-scale, including molecular and continuum-based scales (Frankland *et al.*, 2003; Odegard *et al.*, 2003; Odegard *et al.*, 2004; Odegard *et al.*, 2005b; Shi *et al.*, 2005; Jiang *et al.*, 2006; Grujicic *et al.*, 2007; Karakasidis and Charitidis, 2007; Mokashi *et al.*, 2007; Liu *et al.*, 2008; Lu *et al.*, 2008; Tserpes *et al.*, 2008; Zeng *et al.*, 2008; Shen, 2009; Takeda *et al.*, 2009). These studies employ a wide range of philosophical approaches. A generalized framework needs to be established that provides a common structure to these different approaches.

This chapter presents generalized methods for multi-scale modeling of CNT composites. Basic descriptions of the computational chemistry and continuum mechanics modeling tools are described first. Following this, methods for linking the different length-scale models are presented. This chapter is not intended to present an exhaustive review of the modeling techniques of CNT composites that numerous researchers have reported in the past few years. Instead, this chapter focuses on establishing a mathematical framework that presents a general approach to modeling CNT/polymer composite materials.

13.2 Computational modeling tools

Molecular dynamics (MD) (Leach, 2001) is a computational technique in which a time evolution of a set of interacting atoms is followed by integrating their equations of motion. The forces between atoms are due to the interactions with the other atoms. A trajectory is calculated in a $6-N$ dimensional phase space (three position and three momentum components for each of the N atoms). Typical MD simulations of CNT composites are performed on molecular systems containing up to tens of thousands of atoms and for simulation times up to nanoseconds.

The physical quantities of the system are represented by averages over configurations distributed according to the chosen statistical ensemble. A trajectory obtained with MD provides such a set of configurations. Therefore the computation of a physical quantity is obtained as an arithmetic average of the instantaneous values. Statistical mechanics is the link between the nanometer behavior and thermodynamics. Thus the atomic system is expected to behave differently for different pressures and temperatures.

The interactions of the particular atom types are described by the total potential energy of the system, U , as a function of the positions of the individual atoms at a particular instant in time

$$U = U(\mathbf{X}_1, \dots, \mathbf{X}_N) \quad [13.1]$$

where \mathbf{X}_i represents the coordinates of atom i in a system of N atoms. The potential equation is invariant to the coordinate transformations, and is expressed in terms of the relative positions of the atoms with respect to each other, rather than from absolute coordinates.

Continuum mechanics (Truesdell and Toupin, 1960; Truesdell and Noll, 2004) describes the motion and interaction of a set of 0-dimensional particles that form a mathematical continuum. For a given set of initial and boundary conditions of a particular volume of a continuous medium, the motion and interaction of the particles are governed by a series of fundamental laws. The balance of mass governs the change in mass that occurs for a control volume. The balance of linear momentum and angular momentum for a continuum ultimately leads to equations of motion. The balance of energy forces the continuous system to follow the first law of thermodynamics and includes changes in energy due to damage or other physical phenomena. The Clausius-Duhem inequality ensures that the continuous system obeys the second law of thermodynamics. Finally, the constitutive equations govern the behavior between thermodynamic forces (e.g. temperature, applied deformation, applied electric and magnetic fields) and thermodynamics fluxes (e.g. stress, entropy, electric polarization).

Perhaps the most important aspect of continuum mechanics is its absolute flexibility for any type of material system. By appropriately modifying the balance laws and constitutive equations, complex material systems such as biological tissue, cellular materials, piezoelectric materials, and composites can be modeled on any length-scale level. Although this flexibility allows the behavior of any material to be modeled on the bulk-level, it also renders continuum models to be dependent on empirical data obtained through testing for accurate material characterization. This is in contrast to the MD approach in which the atomic behavior is established from basic physical principles of atomic theory.

Often, structures must be analyzed that are assumed to be composed of a continuous material that behaves according to a predefined continuum theory. For many complex structure geometries and loading conditions, closed-form solutions to the governing laws of continuum mechanics are not available. In this case, the

finite element analysis (FEA) method (Bathe, 1996) is particularly useful in predicting the behavior for a wide range of structural geometries and load conditions. Using FEA, the stress and strain fields in an engineering structure are determined by discretizing the continuum into *elements* of primitive shapes (e.g. bricks, tetrahedrons). The *nodes* are at the corners, and sometimes, on the mid-sides of the element boundaries. As long as the geometry of the elements (mesh) is not too coarse, the overall predicted properties of FEA models can be accurately estimated by solving for the stress and strain fields of all of the elements in the model using standard numerical approaches.

Micromechanical methods are used to predict the bulk properties of continuous yet heterogeneous solids. While the assumption of continuity is maintained, it is assumed that different phases of the material exist that interact with each other by transferring load. A large number of micromechanical approaches have been developed (Herakovich, 1998) with a wide range of assumptions. While many approaches are efficient with less accuracy, others are mathematically complex with tremendous accuracy. It is important to note that FEA can be used as a micromechanical tool.

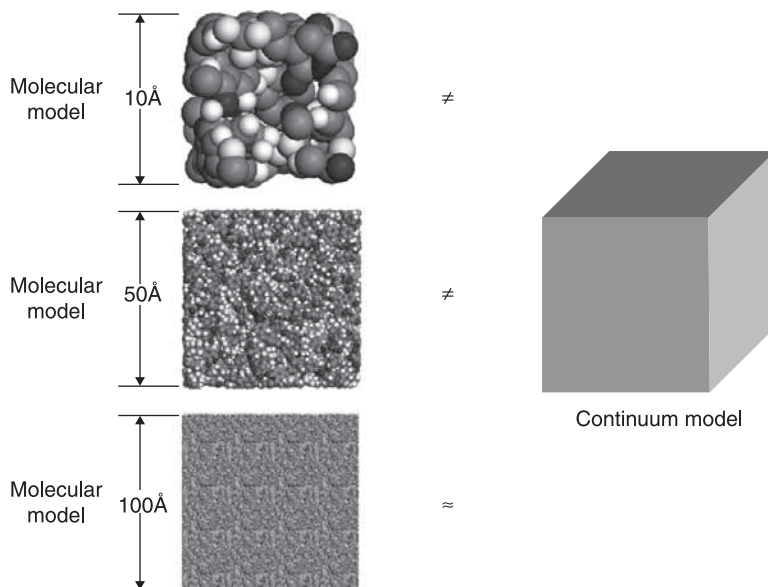
The analysis tools described in this section will be placed in the context of multiscale modeling throughout the rest of this chapter.

13.3 Equivalent-continuum modeling concepts

Many material properties are used to describe the behavior of continuum-based systems, such as Young's modulus, and ultimate strength. While these types of parameters are indispensable to design engineers, they are defined for a mathematical continuum. Therefore, these quantities cannot be used to describe the properties of a discrete structure. For example, a lattice structure (truss, frame, or molecular structure) as a whole cannot have a corresponding value of Young's modulus associated with it directly. However, the lattice structure can be modeled as an equivalent-continuum structure in which the overall behavior is similar to that of the lattice structure for the same loading conditions. The equivalent continuum must have equivalent material properties such as Young's modulus associated with it in order to describe the mechanical behavior. This raises the question: How are the properties of an equivalent-continuum of a discrete structure determined? This is the topic of this section.

13.3.1 Representative volume element

Consider Fig. 13.1, which shows three different molecular models with different length-scale levels. The structure of these three molecular models is compared with the structure of an element of a mathematical continuum. When comparing the molecular model with a side length of 10 \AA to the continuum model, it is clear that the points in the continuum do not have a one-to-one correspondence with the atoms

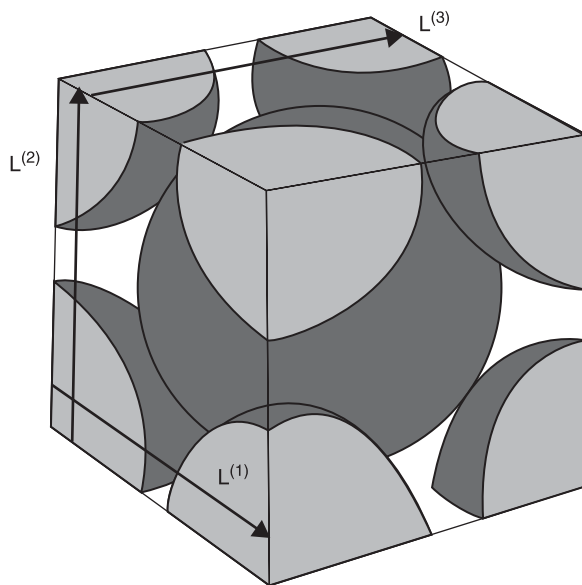


13.1 Different length scales of molecular models (Odegard, 2009).
(Reproduced with kind permission of Springer Science and Business Media.)

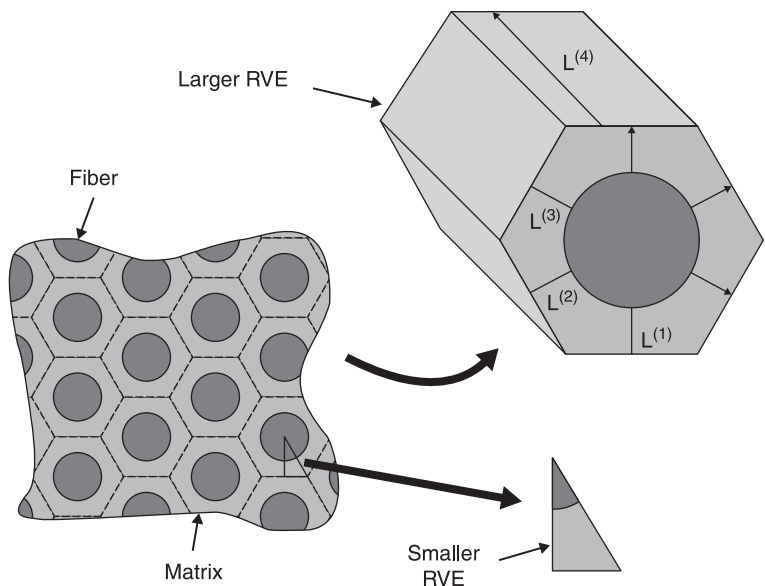
in the molecular model. Even if the centroid of each atom in the molecular model were mapped to the corresponding points in the continuum model, there are points in the continuum model that do not correspond to atoms in the molecular model, thus eliminating a one-to-one correspondence of points and atoms. As the length scale of the molecular model increases from 10 \AA to 50 \AA , it is clear that there are more points in the continuum model that correspond to centroids of atoms in the molecular model, although there is still not a one-to-one correspondence between the two. As the length scale continues to grow to 200 \AA , it becomes difficult to discern individual atoms in the image, as the atom sizes become very small compared to the molecular model size. In fact, the cubes of the molecular models with side lengths of 10 \AA and 200 \AA contain approximately 80 and 640,000 atoms, respectively. Therefore, comparison of the 200 \AA molecular model with the continuum model clearly shows the nearly continuous nature of the 200 \AA molecular model, as the significance of the behavior of individual atoms significantly decreases with increased molecular model size. In fact, it is generally assumed that molecular models of about the size of the 200 \AA model behave like the continuous, mathematical continuum model with clearly defined elastic constants and smooth fields. However, large molecular models are computationally difficult to work with, so methods are necessary to model smaller molecular models as continuum-based entities.

A *representative volume element* (RVE) is such a model. The morphological structural features of the RVE do not necessarily behave like points on a homogeneous continuum when a motion or deformation is applied. Instead, the RVE is defined as the volume element that efficiently and effectively describes the structure of the material in a statistical sense. That is, if a solid is built up of identical RVEs that are placed side-by-side with a perfect packing, then the resulting macrostructure will effectively describe the structure of the material. In some cases, RVEs can perfectly describe the minimum building block necessary to describe the continuum, such as the unit cell of a single crystal metal (Fig. 13.2) or the fiber composite material with hexagonal packing (Fig. 13.3). These materials are referred to as periodic materials. In other cases, the RVE can only approximately describe the minimum-sized building block of a material, such the RVE of bulk metallic glass (Fig. 13.4). Such amorphous materials have no long-range order, so that an RVE of an amorphous material can never exactly model the structure of the material at any spatial point. Rather, the RVE of an amorphous material only models the structure in a statistically accurate manner.

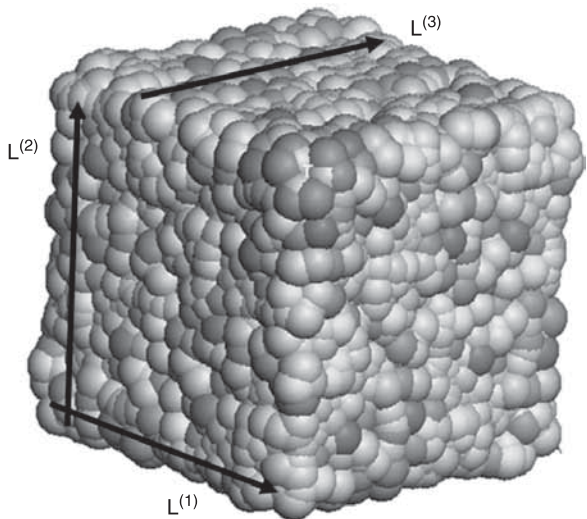
In Figs 13.2, 13.3, and 13.4, the periodicity vectors are indicated by $\mathbf{L}^{(1)}, \dots, \mathbf{L}^{(4)}$. The periodicity vector components describe the length between opposite sides of a RVE. For the cubic RVEs shown in Figs 13.2 and 13.4, there are three vectors, $\mathbf{L}^{(1)}$, $\mathbf{L}^{(2)}$ and $\mathbf{L}^{(3)}$, each corresponding to a pair of sides of the RVE. For the more complex RVE shown in Fig. 13.3, there are four vectors $\mathbf{L}^{(1)}, \dots, \mathbf{L}^{(4)}$.



13.2 Crystal unit cell.



13.3 Fiber composite microstructure (Odegard, 2009). (Reproduced with kind permission of Springer Science and Business Media.)



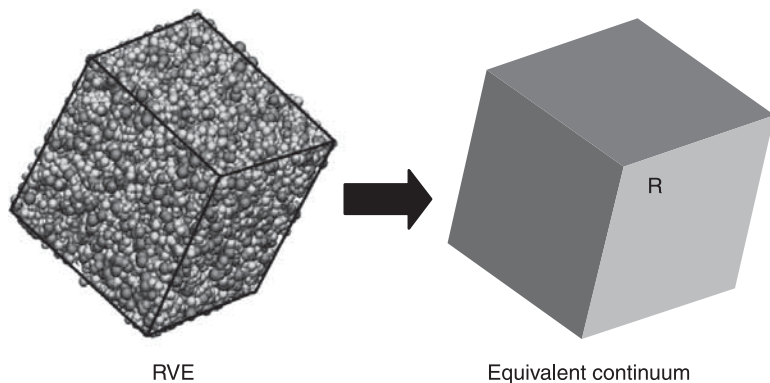
13.4 Bulk metallic glass molecular model (Odegard, 2009). (Reproduced with kind permission of Springer Science and Business Media.)

The question remains: How is the RVE of a heterogeneous non-continuous structure used to establish the continuum-based balance laws and constitutive equations? As we have seen, the balance laws and constitutive equations of continuum mechanics assume the presence of a mathematical continuum, which

clearly does not exist in the RVEs shown in Figs 13.2, 13.3, and 13.4. The answer to this question will be addressed in the next section.

13.3.2 Equivalent continuum

At some level, no material is truly described by a mathematical continuum. All materials contain a heterogeneous or discrete structure on some length-scale level. Some materials contain a definite structure at the micrometer length scale, such as wood and fiber-reinforced composites. Some materials exhibit a nearly homogeneous texture except on the atomic level, such as single-crystal metals. Therefore, it can be argued that any material that is described by a constitutive equation is an equivalent continuum. However, the concept of the equivalent continuum is applied to the modeling of materials at length scales in which the characteristic size of the inhomogeneity exists. For example, the modeling of the mechanical behavior of a fiber-reinforced composite material at length scales that are orders of magnitude larger than the fiber diameters does not require an effective continuum, as the material on that level closely approximates a continuum (recall the large molecular model of Fig. 13.1). That is, the fibers are so small with respect to the modeled continuum that they behave similar to a material point in the field equations described above. If the behavior is modeled at length scales that are about the same size of the fiber, then the material will no longer behave in the smooth manner associated with the field equations of a classical continuum. In this case, the equivalent-continuum properties are determined by studying the effective mechanical response of the RVE. Consider the molecular RVE shown in Fig. 13.5. Suppose that an equivalent volume and shape of a mathematically continuous solid is used to represent the RVE, denoted as region \mathcal{R} (with boundary $\partial\mathcal{R}$). The equivalent-continuum solid should mimic the behavior of the molecular model as closely as possible under all mechanical loadings. It is important to note



13.5 Equivalent-continuum model of a molecular RVE.

that an equivalent-continuum model will ideally represent the behavior of an arbitrary volume of the actual material, not just the shape defined by the RVE. The definition of \mathcal{R} is only necessary to relate the mechanical response of the RVE to that of the equivalent material points in the equivalent continuum.

The mechanical response of the RVE can only be studied by applying boundary conditions to the RVE. This is usually performed computationally. For example, displacements can be applied to the surface of a RVE to calculate the resulting loads, and hence mechanical properties, of a solid material. Although electric and magnetic fields can also be applied as boundary conditions, the following discussion will focus on mechanical properties. There are four types of boundary conditions for RVEs in static equilibrium: (1) *displacement-controlled* boundary conditions (also called kinematic or Dirichlet boundary conditions); (2) *traction-controlled* boundary conditions (also called static or Neumann boundary conditions); (3) *periodic* boundary conditions; or (4) a mixture of these three. The boundary conditions are applied at locations in the RVE (such as the centroids of atoms) that have the same locations as material points in the equivalent continuum \mathcal{R} .

For displacement-controlled boundary conditions, the components of the prescribed displacement vector $\bar{\mathbf{u}}$ (boldface indicates a vector quantity) are specified everywhere on $\partial\mathcal{R}$

$$\bar{u}_i = u_i \quad \forall \mathbf{X} \in \partial\mathcal{R} \quad [13.2]$$

where \mathbf{u} is the displacement vector. For traction-controlled boundary conditions, the components of the prescribed traction vector $\bar{\mathbf{s}}$ are specified everywhere on $\partial\mathcal{R}$ as

$$\bar{s}_i = S_{ij}N_j \quad \forall \mathbf{X} \in \partial\mathcal{R} \quad [13.3]$$

where S_{ij} are the stress tensor components and N_j are the surface unit normal vector components. For periodic boundary conditions, the prescribed displacements and tractions are given by

$$\bar{u}_i(\mathbf{X} + \mathbf{L}) = u_i(\mathbf{X}) + u_i^{ave} \quad \bar{s}_i(\mathbf{X} + \mathbf{L}) = -s_i(\mathbf{X}) \quad \forall \mathbf{X} \in \partial\mathcal{R} \quad [13.4]$$

where \mathbf{u}^{ave} is the average displacement vector associated with the bulk deformation of the solid material, and \mathbf{L} is the periodicity vector of the RVE (shown in Figs 13.2, 13.3, and 13.4). For the case of mixed boundary conditions, the boundary of region \mathcal{R} can be divided into three sub-boundaries $\partial\mathcal{R}_d$, $\partial\mathcal{R}_t$, and $\partial\mathcal{R}_p$, such that

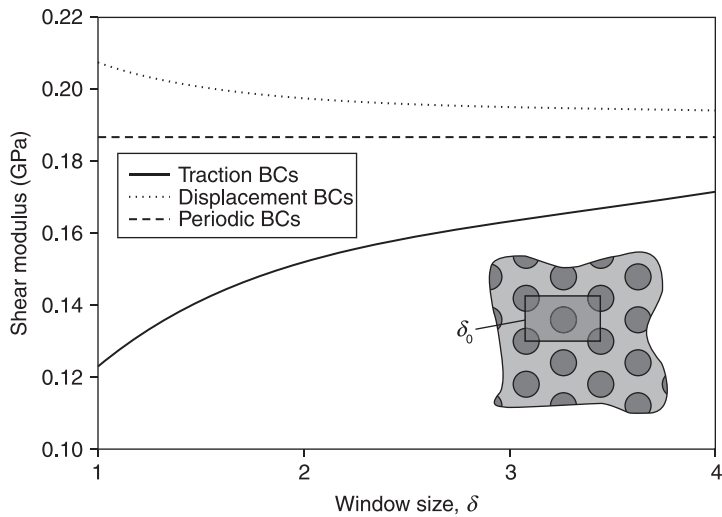
$$\partial\mathcal{R} = \partial\mathcal{R}_d \cup \partial\mathcal{R}_t \cup \partial\mathcal{R}_p \quad \partial\mathcal{R}_d^\circ \cap \partial\mathcal{R}_t^\circ \cap \partial\mathcal{R}_p^\circ = \emptyset \quad [13.5]$$

where \emptyset is the null set and the superscript $^\circ$ denotes the relative interior. The corresponding boundary conditions are

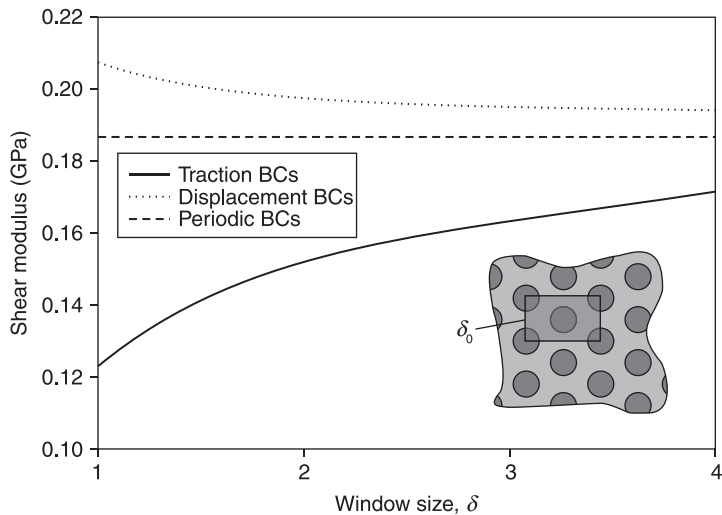
$$\begin{aligned}
 \bar{u}_i &= u_i & \forall \mathbf{X} \in \partial \mathcal{R}_d \\
 \bar{s}_i &= S_{ij} N_j & \forall \mathbf{X} \in \partial \mathcal{R}_t \\
 \bar{u}_i(\mathbf{X} + \mathbf{L}) &= u_i(\mathbf{X}) + u_i^{ave}; \bar{\mathbf{s}}(\mathbf{X} + \mathbf{L}) = -\mathbf{s}(\mathbf{X}) & \forall \mathbf{X} \in \partial \mathcal{R}_p
 \end{aligned} \quad [13.6]$$

Although the simplest approach to applying boundary conditions to a RVE (either computationally or analytically) is to use the displacement- or traction-controlled boundary conditions, it has been shown (Jiang *et al.*, 2001; Jiang *et al.*, 2002) that the application of periodic or mixed boundary conditions to the RVE results in a more realistic material response.

When determining effective-continuum properties of a material by computationally simulating the deformation of a RVE, the natural question arises: What size do the edges of a RVE need to be? The answer to this question depends mostly on two issues: The periodicity of the specific material and the boundary conditions that will be used to compute the material structure and properties. Specifically, the minimum size of an RVE for a periodic material is the minimum size of a possible repeatable structure, as shown in Fig. 13.3 for the smaller RVE of the fiber-composite material. However, if periodic boundary conditions are applied to the edges of the RVE, then the minimal size of the RVE is the minimum size necessary to construct the material structure without rigid rotations of the RVE, such as the larger RVE in Fig. 13.3 and the RVE in Fig. 13.2. If periodic boundary conditions are not used, then the computational results will depend on the RVE size. This dependence will depend on the morphology and properties of the material. Generally, the larger the RVE, the more accuracy is obtained with the results. For example, consider the elastic properties of aligned-fiber composites established by Jiang *et al.* (Jiang *et al.*, 2002). Traction-controlled, displacement-controlled, and periodic boundary conditions were applied for bulk-level transverse shear (shear in the plane transverse to the fiber direction). Two cases were simulated, one which contained inclusions that were stiffer than the matrix by an order of magnitude and one in which the matrix was stiffer than the inclusions by an order of magnitude. Young's modulus of the matrix was assumed to be 1 GPa. The corresponding transverse shear modulus was determined using all three boundary conditions for the two composite systems for RVE sizes of $\delta = \delta_0, 2\delta_0, 3\delta_0$ and $4\delta_0$, where δ_0 is the RVE size shown in the inset of Figs 13.6 and 13.7. Figures 13.6 and 13.7 show the calculated shear modulus for the stiff inclusions and matrix, respectively, for the different RVE lengths. The data has been plotted with smooth lines to emphasize the overall trend. Clearly, for the case of stiff inclusions shown in Fig. 13.6, the discrepancy between the predicted modulus from the periodic and displacement boundary conditions is larger than that between the periodic and traction boundary conditions. Both discrepancies decrease as the RVE size increases. For the case of the stiff matrix shown in Fig. 13.7, the predicted shear modulus from the displacement boundary conditions has better agreement with the periodic boundary conditions than does the modulus predicted with the traction boundary conditions. Again, as the RVE size increases, the different sets of boundary conditions predict a more similar shear modulus.



13.6 Transverse shear modulus of fiber composite with stiff inclusions (Odegard, 2009). BC, boundary condition. (Reproduced with kind permission of Springer Science and Business Media.)



13.7 Transverse shear modulus of fiber composite with stiff matrix (Odegard, 2009). (Reproduced with kind permission of Springer Science and Business Media.)

For amorphous materials, such as that shown in Fig. 13.4, the minimum size of the RVE is the size that statistically represents the structure of the material. This is a fairly ambiguous statement; however, there is no general agreement of a minimum necessary size of an RVE that produces more accurately predicted

bulk-level properties. Of course, as the RVE size increases, the more likely the predicted properties will agree with those measured at the bulk-length scale level.

Once an RVE of a molecular structure is established, then it must be used to establish equivalent-continuum constitutive properties. This process is described in the next section.

13.3.3 Equivalence of averaged scalar fields

So far, the necessity of constructing an RVE to mimic the bulk-scale mechanical response (equivalent continuum) of a material has been discussed. However, the determination of the properties of the equivalent continuum based upon the response of the RVE to applied boundary conditions has not been detailed. The establishment of an equivalent continuum model that behaves the same as the RVE under identical boundary conditions is important when attempting to understand molecular structure/bulk-level property relationships.

In general, an equivalent continuum must meet two requirements in order to accurately predict the behavior of a particular material:

1. Under identical applied far-field deformations (or loads), the RVE and the equivalent continuum must have identical (or nearly identical) values of one or more scalar fields that are averaged over the volume of the RVE and volume \mathcal{R} .
2. The material points of the equivalent continuum volume \mathcal{R} must have the same kinematic motion as material points (atoms in some cases) of the heterogeneous RVE at the same locations relative to some defined basis set and origin.

This subsection describes Requirement 1, the Equivalence of averaged scalar fields, in detail.

Requirement 1 expresses the need to have one or more scalar parameters; such as the scalar strain-energy density or the six scalar components of the stress tensor averaged over the RVE; to have equal values under identical loads applied to the RVE and equivalent-continuum models. For example, if periodic boundary conditions are applied to the RVE via Equation 13.4 such that the total potential energy, as calculated with an atomic potential, is equal to the strain energy of the effective continuum if a homogeneous deformation field, which matches the deformations averaged over the RVE, is applied to the effective continuum. In other words, if identical deformations are applied to a very large RVE and the equivalent continuum, the total energies should be the same. Moreover, the material parameters of the equivalent continuum can be adjusted such that the energies of the two models match. It is important to note that many researchers choose to match components of virial and continuum stress tensors (from the RVE and effective continuum models, respectively) under identical conditions. Although this approach makes intuitive sense, matching a single scalar parameter, such as strain energy, is a much more efficient approach than matching six independent components of a symmetric stress

tensor. Further details on this requirement can be found elsewhere (Odegard *et al.*, 2002). Once Requirement 1 is satisfied, then Requirement 2 must be considered.

13.3.4 Kinematic equivalence

Requirement 2 is often referred to as the *Cauchy-Born Rule*, which requires the kinematic motions of the RVE and the equivalent continuum to match for each atom (in the case of a molecular RVE) or each material point (for a heterogeneous micro-scale model) of the RVE. For example, in the case of the RVE shown in Fig. 13.2, the equivalent continuum should deform in the same identical manner on both the edges and in the interior as the center of the atoms in the RVE. This requirement often requires higher-order elasticity theories (Aifantis, 1984; Eringen, 1999, 2002) to be used to accurately match RVE and effective continuum deformations.

Although this requirement can be easily satisfied for the deformations of simple RVEs such as that shown in Fig 13.2, this rule is usually ignored for more complex RVEs, such as those shown in Figs 13.3 and 13.4, for one of the following reasons. Either (a) this requirement is over-restrictive and unnecessary given the required predictive accuracy of the effective continuum, or (b) this requirement is extremely difficult to impose on very complex RVEs. An example of point (a) is captured with the heterogeneous RVE of Fig. 13.3. In the composites community, it is often unnecessary to have predictive effective continuum models to predict the point-to-point kinematic mechanical behavior of the microstructure. The relaxation of this requirement has presented few difficulties in the successful design and implementation of most fiber-reinforced composite materials in the past several decades. An example of item (b) for the amorphous RVE is shown in Fig. 13.4. Given the complex atomic interactions that occur on this length scale for a set of atoms that have no local geometric order, the kinematic motion of the atoms is not expected to be uniform. Establishing a higher-order effective continuum model to match a highly non-uniform deformation field would be an exhausting and unnecessary task. Therefore, although Requirement 2 is rigorously followed for simple crystalline (or highly ordered) material systems, it is rarely followed for amorphous or structurally complex materials. The following section describes how these requirements are met for specific material systems.

13.4 Specific equivalent-continuum modeling methods

This section addresses specific approaches to establishing an equivalent-continuum representation of a molecular representation of a material.

13.4.1 Fluctuation methods

A broad class of methods has been developed to predict effective mechanical properties of materials based on the thermal fluctuation behavior of a RVE when

no loads or deformations are applied. The resulting *fluctuation methods* are based on the work of Parrinello and Rahman (Parrinello and Rahman, 1982). As the RVE is simulated using MD, the geometric fluctuations of the RVE are correlated with the corresponding potential energy of the system. Because the average stress components in the RVE can be related to the derivative of free energy with respect to deformation, a series of stress–strain behaviors are observed computationally as the molecular system evolves over time. The thermal fluctuations of the RVE include axial deformation and shear deformation modes. Therefore, for a given sampling of simulation time, the six independent components of stress can be correlated with the six independent components of strain, and the corresponding elastic constants are subsequently established via the constitutive equation. A wide range of specific techniques have been utilized for specific materials and simulation ensembles (Ray and Rahman, 1984; Gusev *et al.*, 1996; Zhou, 2001; Van Workum and de Pablo, 2003; Meyers *et al.*, 2005; Yoshimoto *et al.*, 2005; Miranda *et al.*, 2006).

Although the fluctuation methods offer an efficient approach to establishing elastic constants of a wide range of materials, the obvious drawback is the inability of this approach to predict the mechanical response of materials to large deformations. To achieve this, the RVE must be subjected to applied loads or deformations of the appropriate magnitude. This process is described in the next two sub-sections for static and dynamic problems.

13.4.2 Static deformation methods

Perhaps the most common approach to determining the elastic properties of an effective continuum is with the *static deformation method* (Theodorou and Suter, 1986; Fan and Hsu, 1992; Hutnik *et al.*, 1993; Fan *et al.*, 1994; Raaska *et al.*, 1994; Aleman and Munoz-Guerra, 1996; Kang *et al.*, 1998; Jang and Jo, 1999a; Jang and Jo, 1999b; Yang and Jo, 2001; Odegard *et al.*, 2003; Saether *et al.*, 2003; Wang *et al.*, 2003; Odegard *et al.*, 2004; Odegard *et al.*, 2005a; Odegard *et al.*, 2005b; Li and Chou, 2006; Raffaini *et al.*, 2006; Wang *et al.*, 2006; Wu and Xu, 2006; Papakonstantopoulos *et al.*, 2007; Valavala *et al.*, 2007). Although many variations exist, this technique involves the application of homogeneous axial, volumetric and shear deformations/loads to the boundaries of an RVE. Consistent with requirement #1 of an effective continuum, the corresponding strain energy, stress, or strain is calculated. Constitutive equations are used to determine the elastic properties based on the response of the RVE to applied loads. This approach is applicable to amorphous material systems.

A reference configuration of the molecular structure of the RVE is determined by subjecting an equilibrated molecular structure to an energy minimization. The reference configuration of the RVE is subsequently exposed to the applied deformations. Initially, the boundaries and the atoms are displaced uniformly and the molecular structure is again subjected to an energy minimization to establish

the deformed configuration. The potential energy or the stresses are calculated and compared to the corresponding values in the reference configuration, and elastic properties are determined based on the constitutive equations. Alternatively, loads can be applied to the reference configuration, and the resulting deformations can be determined for an equilibrated deformed state. This method has been extended into a hyperelastic framework to allow for large deformations of materials (Valavala *et al.*, 2007).

The entire static molecular deformation process is usually performed using molecular mechanics or FEA. Therefore, the effects of the thermal motion of atoms on the mechanical behavior of the material are disregarded with this method. However, the efficiency and accuracy of this method have made it a popular choice for predicting bulk mechanical properties of finite-sized molecular systems. For modeling time-dependent effects, such as thermal motion, many researchers use the dynamic methods described in the next sub-section.

13.4.3 Dynamic deformation methods

Similar to the static deformation method, the *dynamic deformation method* involves deformation of the RVE to determine effective continuum properties (Raaska *et al.*, 1994; Frankland *et al.*, 2002; Brown *et al.*, 2003; Frankland *et al.*, 2003; Jin and Yuan, 2003; Griebel and Hamaekers, 2004; Sheng *et al.*, 2004; Qi *et al.*, 2005; Valavala *et al.*, 2007). However, in the dynamic approach, the motion of the atoms in response to a deformation is determined with MD. Therefore, the time-dependent response of the atoms to applied deformations is computed with the integrated equations of motion, not energy minimizations. This allows the effect of the thermal motion of the atoms on the predicted properties to be determined.

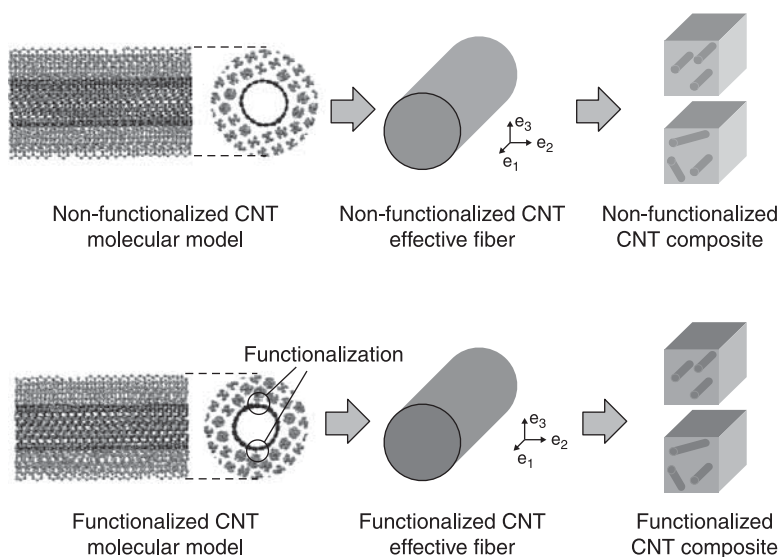
Associated with the deformation of the RVE with this approach is a strain rate (or loading rate). The applied deformation is incrementally prescribed onto the RVE to simulate an applied bulk strain rate. However, because such simulated strain rates are orders of magnitude larger than those experienced in the laboratory and in most engineering applications, the resulting calculated effective continuum properties may not match experimentally-determined values and they may not be practical for the design of engineering materials. Furthermore, determination of effective continuum properties with the dynamic approach generally requires significantly more computational time than with the static approach. The selection of one of the methods described in this sub-section strongly depends on the material and behavior type that need to be modeled. Every particular problem has a different approach, as demonstrated in the following section.

13.5 Example: polymer–carbon nanotube composite

In 2005, Odegard *et al.* (Odegard *et al.*, 2005b) reported on the constitutive modeling of CNT–polyethylene composites for the two cases in which the CNT

reinforcement was functionalized and was not functionalized with the surrounding polyethylene molecules. The purpose of the investigation was to determine if the chemical bonds between the CNTs and surround polymer matrix transferred more load than the van der Waals forces alone in a non-functionalized composite. A SWNT (10,10) of radius 6.78 \AA was modeled as being surrounded by polyethylene polymer chains. Both functionalized and non-functionalized systems were modeled. Figure 13.8 shows the modeled RVE for the two systems. In the composite with CNT functionalization, two polymer chains were attached to six carbons on the CNT by chemical linkages of 2 CH_2 groups.

The geometry of the equivalent continuum was assumed to be cylindrical for ease in use in subsequent micromechanical analyses. Thus, the equivalent continuum for these materials is henceforth referred to as the *effective fiber*. It was assumed that the polymer molecules that were near the polymer–CNT interface were included in the effective fiber. The effective fiber radius and length were 1.1 and 4.3 nm, respectively. The material composing the effective fiber was assumed to exhibit orthotropic symmetry. The elastic properties of the effective fiber were determined by equating the total strain energies of the effective fiber and molecular model RVE under identical boundary conditions. Further details on this portion of the analysis can be found elsewhere (Odegard *et al.*, 2005b). Once the effective fiber properties were determined, a micromechanics analysis was performed to model the reinforcement of a polyethylene matrix reinforced with effective fibers (Fig. 13.8). It was assumed that the matrix polymer surrounding the effective fiber

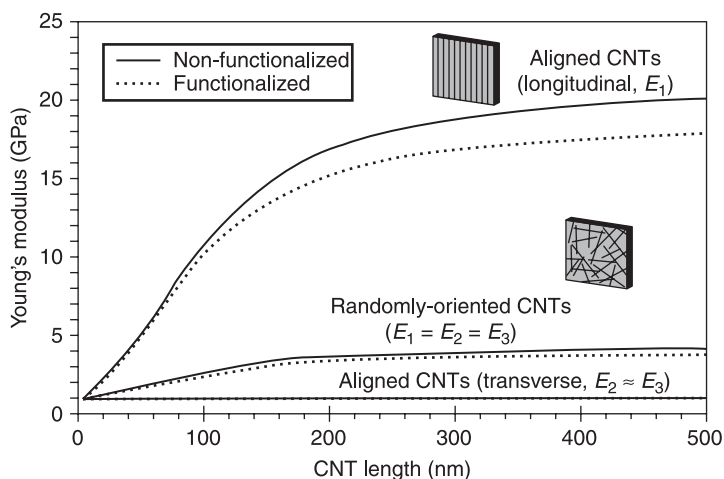


13.8 RVEs of non-functionalized and functionalized CNT composite materials (Odegard, 2009). e_1, e_2, e_3 = basis set reactors. (Reproduced with kind permission of Springer Science and Business Media.)

had mechanical properties equal to those of bulk amorphous polyethylene. All relative movement and interaction of the polymer chains with respect to each other were modeled at the molecular level. This motion and interactions were therefore indirectly considered in the subsequent determination of the properties for the effective fibers, and it is therefore assumed that perfect bonding existed between the CNT-polymer effective fibers and the surrounding polymer matrix in the micromechanical analysis.

The elastic stiffness components, volume fraction, length, and orientation of the effective fiber were used for the fiber properties in the micromechanical analysis. Although the CNT and effective-fiber lengths were equivalent, the CNT volume fraction was determined to be 52.9% of the effective-fiber volume fraction. The overall composite stiffness was calculated for effective fiber lengths up to 500 nm and effective fiber volume fractions up to 90%, which corresponds to the maximum volume fraction for hexagonally packed fibers. The calculations were performed assuming both perfectly aligned and three-dimensional randomly oriented effective fibers in an amorphous polyethylene matrix.

The calculated Young's moduli of the CNT composites are plotted in Fig. 13.9 as a function of CNT length, for a 2% CNT volume fraction. The longitudinal Young's modulus of the aligned composite, E_1 , and Young's modulus of the random composite, E ($E = E_1 = E_2 = E_3$), had a nonlinear dependence on the CNT length. An increase in Young's modulus with respect to an increase in CNT length is expected to correspond to a relative increase in load transfer efficiency between the CNT and surrounding polymer. The data in Fig. 13.9 indicate that at a CNT length of about 250 nm, the efficiency of load transfer is nearly maximized, as evidenced by the nearly zero slope in the data curve. Further increases in CNT length beyond



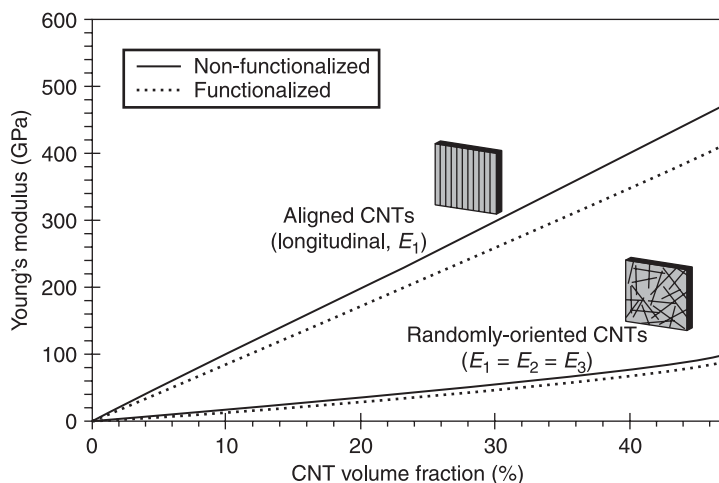
13.9 Young's moduli of the composite systems for a 2% CNT volume fraction.

250 nm resulted in relatively small increases in Young's modulus for a given CNT volume fraction. As the CNT length became greater than approximately 100 nm, Young's modulus for the composite without CNT functionalization became larger than that of the composite with CNT functionalization for the random composite and longitudinal deformation of the aligned composite. At 500 nm, the functionalization reduced the longitudinal Young's modulus of the aligned composite and Young's modulus of the random composite by 11 and 9%, respectively. In contrast, the transverse Young's modulus of the aligned composite, $E_2 \approx E_3$, had no dependence on CNT length. Also, there was no effect of functionalization on the transverse deformation of the aligned composite.

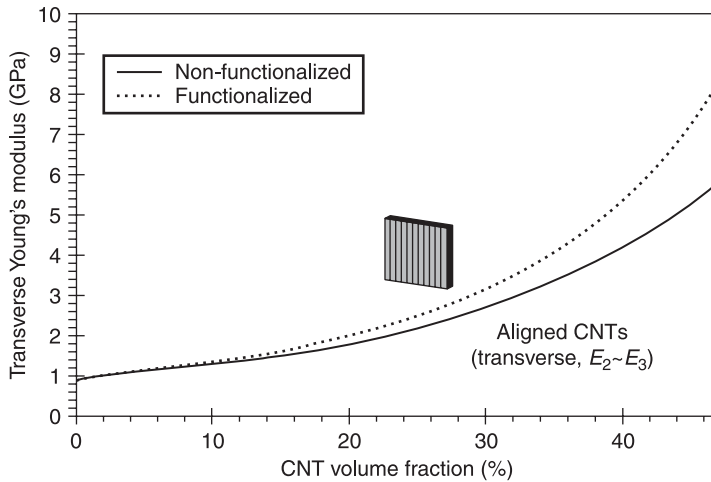
The longitudinal Young's moduli of the random and aligned composites are plotted in Fig. 13.10 as a function of CNT volume fraction, for a constant CNT length of 500 nm. At this CNT length, the change in the longitudinal Young's modulus with respect to CNT volume fraction of the aligned composite was nearly linear. Over the complete range of CNT volume fractions, the functionalization of the CNT reduced the longitudinal Young's modulus of the two composites.

The transverse Young's moduli of the aligned composite systems with a range of volume fractions and a CNT length of 500 nm are shown in Fig. 13.11. In contrast to the Young's moduli in Fig. 13.10, the transverse Young's moduli improved when the CNTs were functionalized. The enhancement is evident for CNT volume fractions greater than 10%.

The primary implication of these results is that although chemical functionalization of single-walled carbon CNTs has been considered as a means to



13.10 Young's moduli of the composite systems for CNT lengths of 500 nm.



13.11 Transverse Young's moduli of composite systems for CNT lengths of 500 nm.

increase load-transfer efficiency in CNT–polymer composites, this functionalization has, in fact, degraded most of the macroscopic elastic stiffness components of the composite materials considered in this study. This is possibly due to the change in chemistry at the functionalization site. The carbon atom on the CNTs that is functionalized goes from an aromatic state to an aliphatic state upon functionalization. As a result, it is possible that the stiffness of the C–C bonds in the CNT is reduced at the functionalization site, thus reducing the overall composite stiffness in the direction parallel to the CNTs. However, the increase in C–C bond stiffness perpendicular to the surface of the CNT after functionalization naturally increases the overall transverse stiffness of the composite. It is important to note that these results are highly dependent on the specific materials that are considered. Different combinations of reinforcement and matrix materials would likely yield different results.

13.6 Conclusion and future trends

This chapter has discussed some of the very fundamental aspects of multiscale modeling of CNT composite materials. Although many different approaches have been taken in the literature to predict bulk properties as a function of molecular/micro-structure, all multiscale modeling approaches should follow some basic guidelines to ensure consistency with the physical assumptions of the continuum-based and non-continuum-based modeling tools. This consistency will lead to more reliable predictions and, ultimately, more efficient material development efforts.

Multiscale modeling approaches that incorporate both molecular- and continuum-level simulations are relatively new. This is mostly due to the rapid rise in computational power in the past two decades that has enabled more efficient simulations, and due to the large-scale world-wide investment in nanoscale research that was initiated around the year 2000. As a consequence, these multiscale modeling efforts are still in their infancy. There are still many aspects of multiscale modeling that will likely experience advancement in the coming years.

Many of the modeling approaches referenced herein have very limited experimental validation. This is partially due to the complicated nature of testing small-scale materials and structures, and due to the relative difficulty of fabricating test specimens of CNT composites. As multiscale modeling approaches become more sophisticated, powerful, and efficient, more reliance will be placed on their predictions for the design of engineering structures. Therefore, it is important that a greater degree of confidence must be established with the models. This will need to be achieved with more rigorous experimental validation attempts. Properly validated and benchmarked multiscale modeling tools will greatly facilitate the overall material design and development process.

Another important future direction for multiscale modeling of CNT composites is the direct modeling of time-dependent behavior. While the continuum-based tools work well for viscoelastic polymer composites whose relaxation times are on the order of seconds, minutes, hours, or days; molecular dynamics simulations of polymers typically can efficiently simulate the molecular behavior only over a span of a nanoseconds, or less. This discrepancy between time scales between tools in multiscale modeling is a fundamental road block that must be eventually cleared to truly model the time-dependent response of CNT–polymer composites.

13.7 Sources of further information

Although there have been countless journal articles in the past decade that describe multiscale modeling of nanostructured materials, the vast majority of them have focused on crystalline and other highly-ordered materials, such as metals and stand-alone carbon CNTs. By comparison, amorphous materials (e.g. polymers) are much more difficult to model and have thus received significantly less attention by multiscale modelers. Because the molecular structure of amorphous polymers lacks symmetry, simulations are restricted to much smaller systems, and the atomic potentials (force fields) are not generally as accurate as those used for crystalline systems. As a result, there are few publications outside of journal articles that address the multiscale modeling of CNT composites. Those that do address the multiscale modeling of polymer composites only do so briefly. Researchers who are interested in learning more about this field are encouraged to consult some of the journal articles referenced herein as a starting point (Frankland *et al.*, 2003; Odegard *et al.*, 2003; Odegard *et al.*, 2004; Odegard *et al.*, 2005b; Shi *et al.*, 2005; Jiang *et al.*, 2006; Grujicic *et al.*, 2007; Karakasidis and Charitidis,

2007; Mokashi *et al.*, 2007; Liu *et al.*, 2008; Lu *et al.*, 2008; Tserpes *et al.*, 2008; Zeng *et al.*, 2008; Shen, 2009; Takeda *et al.*, 2009).

13.8 References

- Aifantis E C (1984) 'On the microstructural origin of certain inelastic models', *Journal of Engineering Materials and Technology-Transactions of the ASME*, 106, 326–330.
- Aleman C & Munoz-Guerra S (1996) 'On the mechanical properties of poly(ethylene terephthalate): force-field parametrization and conformational analysis for the prediction of the crystal moduli', *Journal of Polymer Science Part B: Polymer Physics*, 34, 963–973.
- Bathe K J (1996) *Finite Element Procedures*, Englewood Cliffs, NJ: Prentice-Hall, Inc.
- Brown D, Mele P, Marceau S & Alberola N D (2003) 'A molecular dynamics study of a model nanoparticle embedded in a polymer matrix', *Macromolecules*, 36, 1395–1406.
- Eringen A C (1999) *Microcontinuum Field Theories*, New York: Springer-Verlag.
- Eringen A C (2002) *Nonlocal Continuum Field Theories*, New York: Springer-Verlag.
- Fan C F, Cagin T, Chen Z M & Smith K A (1994) 'Molecular modeling of polycarbonate. 1. force field, static structure, and mechanical properties', *Macromolecules*, 27, 2383–2391.
- Fan C F & Hsu S L (1992) 'Application of the molecular simulation technique to characterize the structure and properties of an aromatic polysulfone system. 2. Mechanical and thermal properties', *Macromolecules*, 25, 266–270.
- Frankland S J V, Caglar A, Brenner D W & Griebel M (2002) 'Molecular simulation of the influence of chemical cross-links on the shear strength of carbon nanotube-polymer interfaces', *Journal of Physical Chemistry B*, 106, 3046–3048.
- Frankland S J V, Harik V M, Odegard G M, Brenner D W & Gates T S (2003) 'The stress-strain behavior of polymer-nanotube composites from molecular dynamics simulation', *Composites Science and Technology*, 63, 1655–1661.
- Griebel M & Hamaekers J (2004) 'Molecular dynamics simulations of the elastic moduli of polymer-carbon nanotube composites', *Computer Methods in Applied Mechanics and Engineering*, 193, 1773–1788.
- Grujicic M, Angstadt D C, Sun Y P & Koudela K L (2007) 'Micro-mechanics based derivation of the materials constitutive relations for carbon-nanotube reinforced poly-vinyl-ester-epoxy based composites', *Journal of Materials Science*, 42, 4609–4623.
- Gusev A A, Zehnder M M & Suter U W (1996) 'Fluctuation formula for elastic constants', *Physical Review B*, 54, 1–4.
- Herakovich C T (1998) *Mechanics of Fibrous Composites*, New York: John Wiley & Sons, Inc.
- Hutnik M, Argon A S & Suter U W (1993) 'Simulation of elastic and plastic response in the glassy polycarbonate of 4,4'-isopropylidenediphenol', *Macromolecules*, 26, 1097–1108.
- Jang S S & Jo W H (1999a) 'Analysis of the mechanical behavior of amorphous atactic poly(oxypropylene) by atomistic modeling', *Macromolecular Theory and Simulations*, 8, 1–9.
- Jang S S & Jo W H (1999b) 'Analysis of the mechanical behavior of poly(trimethylene terephthalate) in an amorphous state under uniaxial extension-compression condition through atomistic modeling', *Journal of Chemical Physics*, 110, 7524–7532.
- Jiang L Y, Huang Y, Jiang H, Ravichandran G, Gao H, Hwang K C & Liu B (2006) 'A cohesive law for carbon nanotube/polymer interfaces based on the Van der Waals force', *Journal of the Mechanics and Physics of Solids*, 54, 2436–2452.

- Jiang M, Alzebedeh K, Jasiuk I & Ostoj-Starzewski M (2001) ‘Scale and boundary conditions effects in elastic properties of random composites’, *Acta Mechanical*, 148, 63–78.
- Jiang M, Jasiuk I & Ostoj-Starzewski M (2002) ‘Apparent elastic and elastoplastic behavior of periodic composites’, *International Journal of Solids and Structures*, 39, 199–212.
- Jin Y & Yuan F G (2003) ‘Simulation of elastic properties of single-walled carbon nanotubes’, *Composites Science and Technology*, 63, 1507–1515.
- Kang J W, Choi K, Jo W H & Hsu S L (1998) ‘Structure-property relationships of polyimides: a molecular simulation approach’, *Polymer*, 39, 7079–7078.
- Karakasidis T E & Charitidis C A (2007) *Multiscale Modeling in Nanomaterials Science*, Oxford: Elsevier Science Bv.
- Leach A R (2001) *Molecular Modelling: Principles and Applications*, New York: Prentice Hall.
- Li C Y & Chou T W (2006) ‘Multiscale modeling of compressive behavior of carbon nanotube/polymer composites’, *Composites Science and Technology*, 66, 2409–2414.
- Liu Y J, Nishimura N, Qian D, Adachi N, Otani Y & Mokashi V (2008) ‘A boundary element method for the analysis of CNT/polymer composites with a cohesive interface model based on molecular dynamics’, *Engineering Analysis with Boundary Elements*, 32, 299–308.
- Lu W B, Wu J, Song J, Hwang K C, Jiang L Y & Huang Y (2008) ‘A cohesive law for interfaces between multi-wall carbon nanotubes and polymers due to the Van der Waals interactions’, *Computer Methods in Applied Mechanics and Engineering*, 197, 3261–3267.
- Meyers M T, Rickman J M & Delph T J (2005) ‘The calculation of elastic constants from displacement fluctuations’, *Journal of Applied Physics*, 98, 1–3.
- Miranda C R, Tretiakov K V & Scandolo S (2006) ‘A computational study of elastic properties of disordered systems with voids’, *Journal of Non-Crystalline Solids*, 352, 4283–4286.
- Mokashi V V, Qian D & Liu Y J (2007) ‘A study on the tensile response and fracture in carbon nanotube-based composites using molecular mechanics’, *Composites Science and Technology*, 67, 530–540.
- Odegard G M (2009) ‘Multiscale modeling of nanocomposite materials’, in B Farahmand (ed.) *Virtual Testing and Predictive Modeling: For Fatigue and Fracture Mechanics Allowables*, New York: Springer.
- Odegard G M, Clancy T C & Gates T S (2005a) ‘Modeling of the mechanical properties of nanoparticle/polymer composites’, *Polymer*, 46, 533–562.
- Odegard G M, Frankland S J V & Gates T S (2005b) ‘Effect of nanotube functionalization on the elastic properties of polyethylene nanotube composites’, *AIAA Journal*, 43, 1828–1835.
- Odegard G M, Gates T S, Nicholson L M & Wise K E (2002) ‘Equivalent-continuum modeling of nano-structured materials’, *Composites Science and Technology*, 62, 1869–1880.
- Odegard G M, Gates T S, Wise K E, Park C & Siochi E (2003) ‘Constitutive modeling of nanotube-reinforced polymer composites’, *Composites Science and Technology*, 63, 1671–1687.
- Odegard G M, Pipes R B & Hubert P (2004) ‘Comparison of two models of SWCN polymer composites’, *Composites Science and Technology*, 64, 1011–1020.

- Papakonstantopoulos G J, Doxastakis M, Nealey P F, Barrat J L & De Pablo J J (2007) 'Calculation of local mechanical properties of filled polymers', *Physical Review E*, 75, 1–13.
- Parrinello M & Rahman A (1982) 'Strain fluctuations and elastic constants', *Journal of Chemical Physics*, 76, 2662–2666.
- Qi D, Hinkley J & He G (2005) 'Molecular dynamics simulation of thermal and mechanical properties of polyimide-carbon nanotube composites', *Modeling and Simulation in Materials Science and Engineering*, 13, 493–507.
- Raaska T, Niemela S & Sundholm F (1994) 'Atom-based modeling of elastic constants in amorphous polystyrene', *Macromolecules*, 27, 5751–5757.
- Raffaini G, Elli S & Ganazzoli F (2006) 'Computer simulation of bulk mechanical properties and surface hydration of biomaterials', *Journal of Biomedical Materials Research A*, 77, 618–626.
- Ray J R & Rahman A (1984) 'Statistical ensembles and molecular dynamics studies of anisotropic solids', *Journal of Chemical Physics*, 80, 4423–4428.
- Saether E, Frankland S J V & Pipes R B (2003) 'Transverse mechanical properties of single-walled carbon nanotube crystals. Part I: Determination of elastic moduli', *Composites Science and Technology*, 63, 1543–1550.
- Shen H S (2009) 'Nonlinear bending of functionally graded carbon nanotube-reinforced composite plates in thermal environments', *Composite Structures*, 91, 9–19.
- Sheng N, Boyce M C, Parks D M, Rutledge G C, Abes J I & Cohen R E (2004) 'Multiscale micromechanical modeling of polymer/clay nanocomposites and the effective clay particle', *Polymer*, 45, 487–506.
- Shi D L, Feng X Q, Jiang H Q, Huang Y Y & Hwang K C (2005) 'Multiscale analysis of fracture of carbon nanotubes embedded in composites', *International Journal of Fracture*, 134, 369–386.
- Takeda T, Shindo Y, Narita F & Mito Y (2009) 'Tensile characterization of carbon nanotube-reinforced polymer composites at cryogenic temperatures: experiments and multiscale simulations', *Materials Transactions*, 50, 436–445.
- Theodorou D N & Suter U W (1986) 'Atomistic modeling of mechanical properties of polymeric glasses', *Macromolecules*, 19, 139–154.
- Truesdell C & Noll W (2004) *The Non-Linear Field Theories of Mechanics*, New York: Springer-Verlag.
- Truesdell C A & Toupin R A (1960) 'The classical field theories', in S Flugge (ed.) *Encyclopedia of Physics, Volume III/1: Principles of Classical Mechanics and Field Theory*, Berlin: Springer-Verlag.
- Tserpes K I, Papanikos P, Labeas G & Pantelakis S G (2008) 'Multi-scale modeling of tensile behavior of carbon nanotube-reinforced composites', *Theoretical and Applied Fracture Mechanics*, 49, 51–60.
- Valavala P K, Clancy T C, Odegard G M & Gates T S (2007) 'Nonlinear multiscale modeling of polymer materials', *International Journal of Solids and Structures*, 44, 1161–1179.
- Van Workum K & de Pablo J J (2003) 'Computer simulation of the mechanical properties of amorphous polymer nanostructures', *Nano. Letters*, 3, 1405–1410.
- Wang Y, Sun C, Sun X, Hinkley J, Odegard G M & Gates T S (2003) '2-D nano-scale finite element analysis of a polymer field', *Composites Science and Technology*, 63, 1581–1590.
- Wang Y, Zhang C, Zhou E, Sun C, Hinkley J, Gates T S & Su J (2006) 'Atomistic finite elements applicable to solid polymers', *Computational Materials Science*, 36, 292–302.

- Wu C & Xu W (2006) 'Atomistic molecular modelling of crosslinked epoxy resin', *Polymer*, 47, 6004–6009.
- Yang J S & Jo W H (2001) 'Analysis of the elastic deformation of semicrystalline poly(trimethylene terephthalate) by the atomistic-continuum model', *Journal of Chemical Physics*, 114, 8159–8164.
- Yoshimoto K, Papakonstantopoulos G J, Lutsko J F & De Pablo J J (2005) 'Statistical calculation of elastic moduli for atomistic models', *Physical Review B*, 71, 1–6.
- Zeng Q H, Yu A B & Lu G Q (2008) 'Multiscale modeling and simulation of polymer nanocomposites', *Progress in Polymer Science*, 33, 191–269.
- Zhou Z (2001) 'Fluctuations and thermodynamics properties of the constant shear strain ensemble', *Journal of Chemical Physics*, 114, 8769–8774.

Raman spectroscopy of polymer–carbon nanotube composites

H. D. WAGNER, Weizmann Institute of Science, Israel

Abstract: Over the past 30 years Raman spectroscopy has transformed the field of composite micromechanics and is being successfully applied to the field of nanotube-reinforced polymers. Under the effects of stress, careful study of the Raman spectrum of carbon nanotubes provides a unique insight into various physical phenomena in nanocomposites. This chapter demonstrates the power of the Raman signature of carbon nanotubes as a detector of bulk matrix defects, the occurrence of polymer phase transitions, and the nanotubes' own orientation change with respect to applied stress, stress profiles from Raman-insensitive fibers, and dual information about improvements in the stress transfer ability and about nanotube wall structure degradation due to the surface treatment itself. Remaining challenges are described.

Key words: carbon nanotube sensors, interfacial stress profiles, nanotube wall structure degradation, Raman spectroscopy, stress transfer ability.

14.1 Introduction

The interesting history of the discovery of carbon nanotube (CNT) structures, which is not well known, has recently been documented by Monthieux and Kuznetsov (2006). These remarkable materials were experimentally observed for the first time by Radushkevich and Lukyanovich (1952), whose work remains largely unknown to the scientific community. It was only much later, following the discovery of fullerenes by Kroto *et al.* (1985) that CNTs became an active and fascinating field of research, thanks to a celebrated report by Iijima (1991) on the synthesis of multi-walled carbon nanotubes (MWCNTs). The formation of single-walled carbon nanotubes (SWCNTs) was later reported almost simultaneously by Iijima and Ichihashi (1993) and by Bethune *et al.* (1993).

The structure, topology and size of carbon nanotubes are the source of their outstanding mechanical and electronic properties, and of a whole range of promising applications (Hu *et al.*, 2006; Chou *et al.*, 2010). The latter include their use as electron field emitters for vacuum microelectronic devices, nanoprobe at the tip of an Atomic Force Microscope (AFM), efficient supports in heterogeneous catalysis, a medium for lithium and hydrogen storage, and much more. Nanotubes have been embedded into various materials to produce composites with modified electrical conductivity, magnetic properties and optical properties. Nanotubes are also promising candidates as a mechanical reinforcement phase in composite materials. Compared to micron scale reinforcing fibers,

however, nanotube reinforcement involves a number of important differences, which have consequences on the performance of the corresponding nanocomposites, as well as on the behavior and use of the nanotube itself. For example, distinctive mechanical effects arise, such as large increases in Young's modulus and strength below a certain tube diameter (Arinstein *et al.*, 2007; Sui and Wagner, 2009), resulting from molecular confinement: such effects are genuine nano-effects. CNTs can be spread in polymers and used either as reinforcement, or as molecular sensors, or both. Unlike micron-size reinforcement, nanotubes possess geometrical chirality, which has special significance regarding their physical (and possibly mechanical) properties. Raman spectroscopy, which beyond doubt has transformed the field of composite micromechanics since the late 1970s, has a special role to play in CNT-reinforced polymers, in many ways. This is the main focus of the present chapter.

14.2 The Raman effect: basic principles

Light scattering is the result of the relaxation of the dipole induced in a molecule by the application of the electric field that is part of an incident light beam. The scattering of light by matter is either elastic when the scattered light has the same frequency as the incident light, or inelastic when the frequency changes. In the former case the phenomenon is termed Rayleigh or Mie-Tyndall ('classical') scattering, and in the latter case it is termed Raman or Brillouin scattering. The intensity of classical scattering is proportional to the 4th power of the frequency of the incident light, thus, if white light is used, the blue end of the spectrum is scattered more strongly than the red end (which explains the blue color of the clear sky which arises from the Rayleigh scattering of white sunlight by the molecules in the atmosphere). It can easily be shown that the induced polarizability P of a molecule (the ease with which the electron cloud can be distorted by an applied electric field E) is the sum of three terms (Woodward, 1967; Turrell, 1996):

$$P = f_1(\cos(2\pi\nu_0 t)) + f_2(\cos(2\pi(\nu_0 - \nu)t)) + f_3(\cos(2\pi(\nu_0 + \nu)t)) \quad [14.1]$$

where ν_0 is the frequency of the exciting light wave, t is time, and ν is the frequency of the vibrating molecule. The first term on the right-hand side of Equation 14.1 predicts that a dipole is induced (and thus scattering will occur) at the same frequency as the exciting radiation (ν_0), which constitutes elastic (Rayleigh) scatter. The second and third terms indicate that elastic scattering will also be accompanied by inelastic scatter, namely radiation at decreased frequencies $\nu_0 - \nu$ (known as Stokes Raman scatter) and at increased frequencies $\nu_0 + \nu$ (anti-Stokes Raman scatter). Rayleigh scatter is weak (about 10^{-3} of the intensity of the incident exciting radiation), Raman scattering is much weaker (10^{-2} to 10^{-3} of the intensity of Rayleigh scattering), and the intensity of the Stokes scatter is always greater than the anti-Stokes equivalent bands. Thus, intense monochromatic light

sources and sensitive detectors are required. Details of the history of the inelastic scattering effect, observed for the first time by Raman and Krishnan (1928), can be found in articles by Turrell (1996) and Woodward (1967).

14.3 Molecules and fibers under strain: how the Raman spectrum is affected

A remarkable phenomenon generated a flurry of activity in the early 1980s in the area of composite micromechanics: It was observed that the frequencies of specific Raman bands of polymers possessing high structural perfection decrease upon application of a tensile stress. This stress- (or strain-) induced frequency shift was first reported by Mitra *et al.* (1976) for monocrystalline polydiacetylene fibers and subsequently by others (Batchelder and Bloor, 1979; Galiotis *et al.*, 1983; Wu *et al.*, 1989; Young, 1993, 1997). The reason why this discovery was so significant is that it became possible to obtain exceptional insight into the effect of macroscopic deformation on the molecules in the probed polymer under a variety of conditions and, in the field of composites, to monitor and quantify with so far unequalled precision the local values and variations of key mechanical parameters. Prominent among these was the mapping of the stress profile $\sigma(x)$ along the length (x) of fibers such as aromatic poly(aramid) (Kevlar) or graphite and, most importantly (for composites technology), the interfacial adhesion (or shear) strength $\tau(x) = (r/2)(d\sigma/dx)$ (where r is the fiber radius) between the fibers and polymer matrices, as well as the fiber-fiber interactions due to increasing far-field stresses resulting in isolated but progressively interacting fiber breaks. As an example of the latter issue, micro-Raman spectroscopy was employed to map the strain along accurately positioned, individual fibers in a polymeric matrix (Grubb *et al.*, 1995; Wagner *et al.*, 1996; Van Den Heuvel *et al.*, 1996). The objective was to detect possible load redistribution and sharing effects from a broken fiber onto its (still intact) near neighbors, and thereby to estimate the stress concentration factors (SCF) in these. The effect of variable inter-fiber distance upon the SCF was also examined by means of carefully prepared microcomposites, or model composites (Wagner and Steenbakkers, 1989; Jones and DiBenedetto, 1994). See also the more recent work of Kim *et al.* (2009). Quantitative examples of the amount of frequency shift per unit amount of strain may be found in Young (1993, 1997) for a number of rigid-rod polymer fibers and non-polymeric micron-scale fibers such as carbon, silicon carbide and alumina. The magnitude of the observed decrease in frequency varies between 5 and 20 cm^{-1} per percent of strain (see Table 1 in Young, 1993). The reader is also referred to Young and Eichhorn (2009) for an interesting discussion of the use of two alternative models, based on uniform stress or uniform strain, regarding the change in Raman wavenumber with applied stress or strain in polymeric fibers. The same effect and method were also applied to the study of some typical carbon and ceramic fibers, in ceramic- or metal-matrix composites (Colomban, 1999; Gouadec *et al.*, 2001).

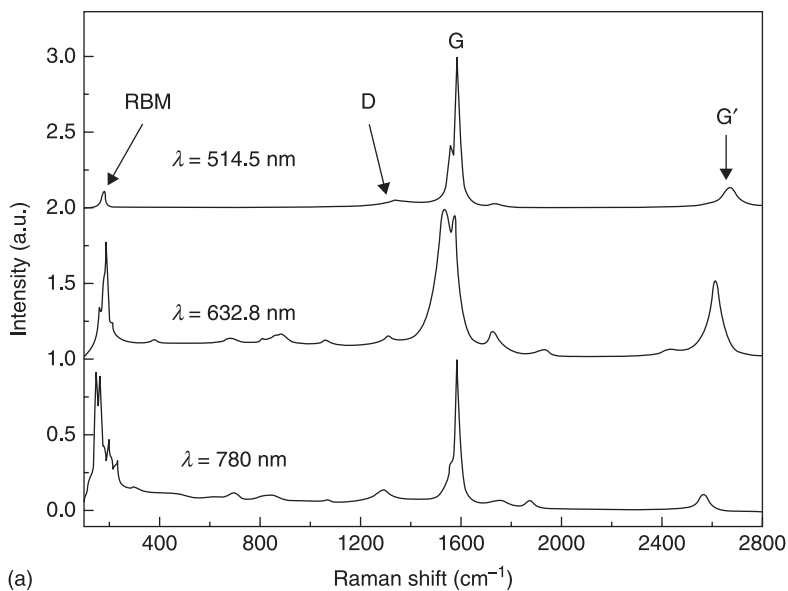
Once CNTs were discovered, it was natural, and only a matter of time, until the strain-induced Raman band shift just described for micron size fibers possessing high structural perfection would be investigated for CNTs.

14.4 Raman signature of carbon nanotubes

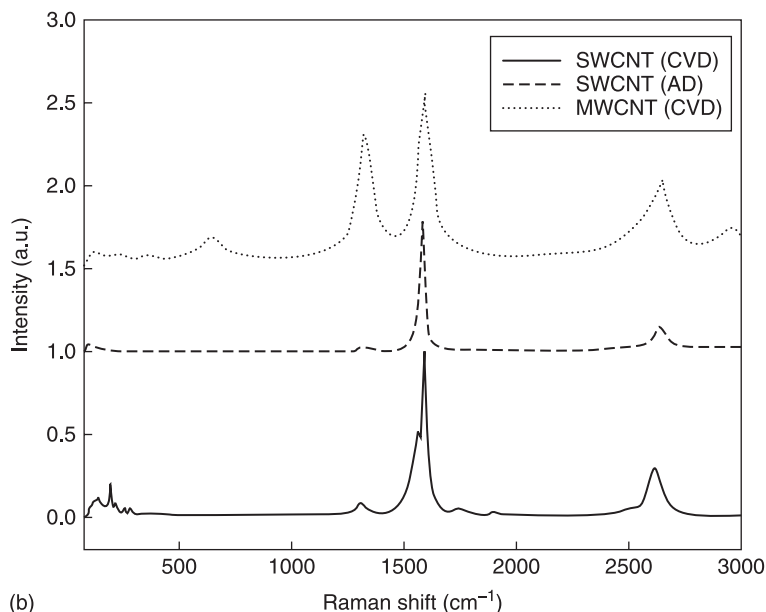
The Raman spectra of carbon nanotubes are shown in Figs 14.1 (a) and 14.1 (b). They are not greatly different from that of a high modulus graphite fiber. However, a key Raman feature of SWNTs is the radial breathing mode (RBM) cluster in the 160 to 300 cm^{-1} region, associated with a symmetric movement of all carbon atoms in the radial direction. Both theoretical and experimental investigations, mainly by Young and colleagues (Lucas and Young, 2004a, 2004b, 2007a, 2007b), have shown that the frequency of the RBM is inversely proportional to the diameter of an individual nanotube. However, low-frequency Raman modes have also been observed in MWNTs samples, although their origin has not been clearly identified. Calculations suggested that van der Waals interactions between concentric tubes of different diameters could lead to such low frequency breathing modes, the effect of the interactions being to upshift the Raman modes compared to those of individual tubes (Stephan *et al.*, 2002).

The D Raman band of carbon nanotubes observed between 1250 and 1450 cm^{-1} has a linear dependence on the laser excitation energy (Lourie *et al.*, 1999). This band is activated in the first order scattering process of sp^2 carbons by the presence of in-plane substitutional hetero-atoms, vacancies, grain boundaries or other defects (D stands for ‘defects’) and by finite size effects, all of which lower the crystalline symmetry of the quasi-infinite lattice. The G' (or D^*) band is the second order overtone of the D band. The locations of D and G' Raman bands of carbon nanotubes depend linearly on the laser excitation energy and this dispersion relation of the D and G' band of nanotubes is similar to that in other sp^2 carbons, though with some distinct characteristic behavior that is specific to nanotubes. A shift of the D and G' bands of carbon nanotubes has been observed in different cases. As seen in Fig. 14.1 (b), the presence of a strong D band in the spectrum of MWNTs reflects the much greater density of defects in these tubes, compared to SWNTs. Also, SWNTs prepared by the arc discharge (AD) method are of better quality (less defects) than those prepared by chemical vapor deposition (CVD).

Raman spectroscopy can provide unique information about vibrational and electronic properties of CNTs. It can also be used to identify materials through the characteristic vibrations of certain structures. Because the Raman intensity of a vibration or phonon in a crystal depends on the relative directions of the crystal axis and the electric wave polarization of the incident and scattered light, it may also be used to determine the orientation of CNTs in polymer matrices or within CNT bundles. Reviews of Raman spectroscopy as a sensitive probe of SWNT properties are given in Zhao and Wagner (2004) and Dresselhaus *et al.* (2005). Raman spectroscopy has been used to determine the diameter of SWNTs, the



(a)



(b)

14.1 (a) Raman spectra of SWNTs in air at $T = 295$ K using three excitation wavelengths. The changes in intensity, shape, and position of the spectra features are due to diameter-selective Raman scattering. From Lourie *et al.* (1999). (b) Comparison of Raman spectra of SWNTs prepared by the CVD and AD methods, and of MWNTs prepared by the CVD method, in air at $T = 295$ K.

diameter distribution of SWNT bundles and the structural properties of nanotubes (Dresselhaus *et al.*, 2002a). The unique 1D molecular nature of SWNTs makes the resonance Raman technique an extremely useful and accurate method for the identification of the diameter and chirality of an individual SWNT. If the (n, m) vector is known, the dependence of all the features of the spectra on the diameter, chiral angle, laser excitation energy and other parameters can be worked out in detail. Therefore, the spectrum of SWNT bundles can be interpreted and the effect of nanotube–nanotube interactions can be deduced (Dresselhaus *et al.*, 2002b). Raman spectroscopy has been used to identify the structure of individual SWNTs (Souza Filho *et al.*, 2001), to investigate the diameter distributions of bulk samples (Rao *et al.*, 1997), to study the transfer of stress to nanotubes during the deformation of nanocomposites (Cooper *et al.*, 2001), and to follow the effect of stress upon the electronic structure of SWNTs (Lucas and Young, 2007b). Raman spectroscopy was also used to non-invasively determine the ratio of metallic SWNTs to semiconducting SWNTs (Jorio *et al.*, 2005). Selected applications of the Raman technique specifically dealing with CNT-based nanocomposites will be described in the next section.

14.5 Usefulness of Raman spectroscopy in nanotube-based composites

There is wide-ranging conviction that carbon nanotubes are promising reinforcement materials for a new class of nanocomposites with much higher stiffness, strength and toughness, owing to the great strength of the sp^2 bonds in the graphite structure of CNTs, since all basal planes run approximately parallel to the CNT axis. In comparison, however, commercial graphite fibers contain various types of structural defects and misaligned planes, and by contrast, the quasi-perfect structure of CNTs opens a new route to super-strong nanofibers. Nonetheless, the potentially outstanding mechanical properties of CNTs will be of little engineering value unless nanotubes can either form macroscopic cables (Atkinson *et al.*, 2007; Koziol *et al.*, 2007), or can be incorporated into a matrix to form a (preferably unidirectional) composite. A large amount of research has appeared in the literature over the past decade, dealing with possible significant improvements in the mechanical and electrical properties of CNT-reinforced polymers. In the present chapter we only focus on those works which include a significant contribution of Raman spectroscopy. We show that when CNTs are embedded in polymers, Raman spectroscopy may achieve a number of unique functions, including as a detector of CNT orientation, as a molecular sensor of structural defects and of second phase materials (such as micron-size fiber reinforcement), as a sensor of the CNTs' own chirality and diameter, or as a quantitative probe of CNT–polymer adhesion strength, and more. This is now reviewed in sequence.

14.5.1 Nanotube–liquid and nanotube–polymer interactions

G' Raman wavenumber shifts (as mentioned earlier, the G' band is sometimes termed D*) are observed when SWNTs are dispersed in liquids, the extent of shifting compared with the initial G' wavenumber in air being dependent on the nature of the liquid. A correlation is found between the cohesive energy density (CED, or, more loosely, the surface tension) of a medium and the G' wavenumber of the dispersed CNT (Wood *et al.*, 2000). To corroborate this, further research was done by using a diamond anvil cell (DAC) to apply hydrostatic stress while the Raman response of both the G and G' peaks was monitored *in situ*. A striking similarity was indeed observed between the hydrostatic pressure experiments, on the one hand, and the molecular pressure experiments with different media, on the other, regarding the degree of Raman wavenumber shift (Wood *et al.* 1999, 2000). The fact that both sets of data agree with each other demonstrates the sensitivity of nanotubes to molecular pressure from the surrounding medium, as measured either by CED or by mechanical pressure using a DAC. A similar study was performed by Cooper *et al.* (2001), where SWNT material was pressurized in a diamond anvil cell and it was found that the G' Raman band shifts to a higher wavenumber with increasing pressure, with initial Raman shift of 23 cm⁻¹/GPa.

Furthermore, Raman spectroscopy has been used to probe the interaction between polymers and nanotubes in CNT-based composites. Generally, such interaction is reflected by a peak shift or a peak width change. In the field of fiber composite materials, it has been known for more than two decades that the application of a mechanical strain to fibers (in air, thus without any polymer matrix) such as carbon or Kevlar results in shifted frequencies of the Raman bands (usually the G' band), which are directly related to the interatomic force constants. A similar effect is observed when carbon nanotubes are embedded in polymers. Correlating such shifts with the applied strain, through a calibration procedure, leads to the determination of local stress profiles in the embedded fibers. In particular, a tensile strain transferred from the polymer matrix to SWNTs results in a downward shift of the G' Raman wavenumber of the nanotubes (Cooper *et al.*, 2001). The stress transfer issue is further discussed in Section 14.5.6.

An empirical linear relationship exists between the SWNT G' wavenumber shift and the applied elastic strain (Wood *et al.*, 2001). If the nanotube G' wavenumber difference between zero strain and the applied strain (ϵ) is defined as the Raman wavenumber shift Δw_n , then the empirical slope m of the wavenumber–strain relation is

$$\Delta w_n = m\epsilon \text{ or } m = \Delta w_n / \epsilon \quad [14.2]$$

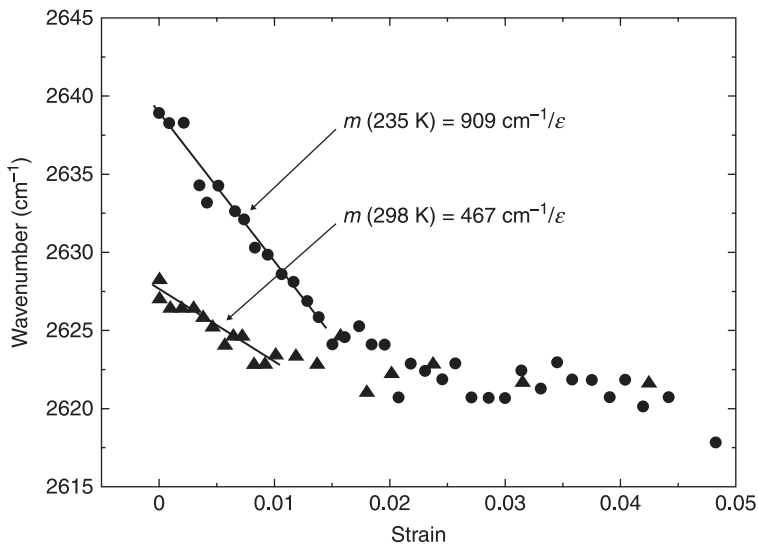
A mechanical stress–strain curve can be recorded simultaneously with the Raman measurement. In the elastic regime of a tensile test, Hooke's law of linear elasticity states that the stress σ and the strain ϵ in the polymer are related by

$$\sigma = \epsilon E \quad [14.3]$$

where E is Young's modulus of the polymer. Therefore, the matrix stress may be deduced from the Raman measurement by combining Equations 14.2 and 14.3:

$$\sigma = \varepsilon E = \left(\frac{\Delta \omega n}{m} \right) E \quad [14.4]$$

Thus, in parallel to the standard mechanical stress–strain curve for the matrix material, the Raman signal captured from the embedded SWNT under strain permits the construction of a spectroscopic stress–strain curve, using the stress calculated by Equation 14.4. Experiments show that m varies when nanotubes are embedded in different polymer matrices (Wood *et al.*, 2001; Zhao *et al.*, 2001b; Frogley *et al.*, 2002), and that, for a given matrix, m is temperature dependent. Figure 14.2 shows the Raman wavenumber–strain response of SWNTs embedded in polyurethane acrylate (PUA) at 298 K (room temperature) and at 235 K. The initial part of both data sets is approximately linear within the elastic strain region (up to $\sim 1.5\%$). The values of m at both temperatures are $467 \text{ cm}^{-1}/\varepsilon$ and $909 \text{ cm}^{-1}/\varepsilon$, respectively (Wood *et al.*, 2001). As the tensile strain increases, the wavenumber stabilizes at a plateau value of about 2622 cm^{-1} where it becomes insensitive to increasing strain, for both temperatures. The temperature dependence of the m values of the SWNTs in PUA can be attributed to the fact that Young's modulus (E) of the polymer is a temperature-dependent parameter, $E(T)$, in other words, Equation 14.4 becomes:



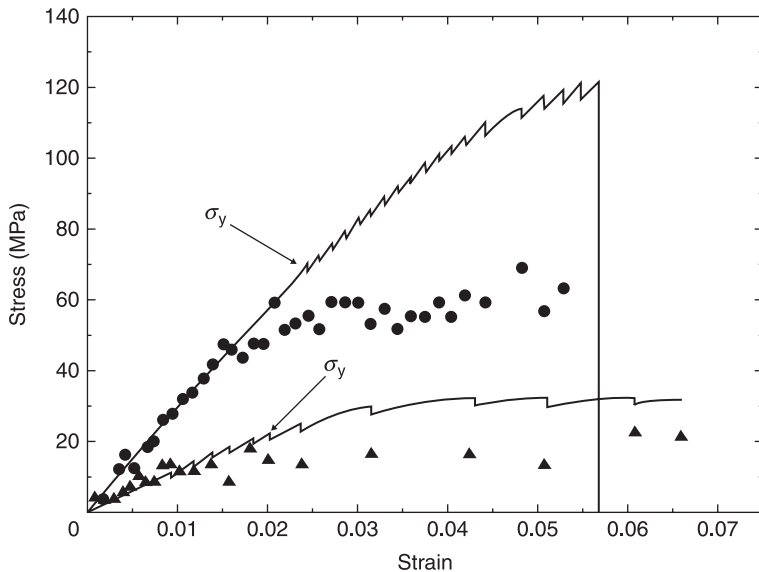
14.2 The wavenumber–strain response of SWNTs embedded in PUA. Symbols: \blacktriangle data at 298 K (room temperature) and \bullet data at 235 K. From Zhao and Wagner (2004).

$$\sigma = \varepsilon E(T) = \left(\frac{\Delta w n}{m(T)} \right) E(T) \quad [14.5]$$

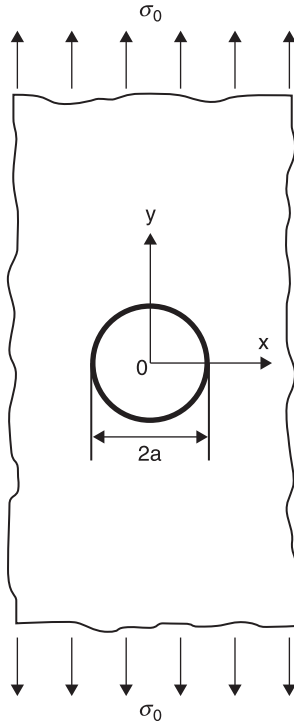
In Figure 14.3, the solid lines represent the mechanical stress–strain curves of PUA at 235 K and 298 K, and the symbols are the spectroscopic stress–strain signatures obtained from the Raman data in Fig. 14.2, using the values of $m(T)$, $E(T)$ at the corresponding temperatures. Within the linear region, the mechanical and spectroscopic curves are in perfect agreement, and beyond about 1.5%, they deviate from each other, likely because of local matrix yielding beyond which the CNT strain does not follow the matrix strain anymore. The yield stress σ_y at which the mechanical stress–strain curve becomes non-linear is also indicated in Fig. 14.3.

14.5.2 Nanotubes as sensors of material discontinuities and local stress concentrations

To demonstrate that embedded nanotubes can accurately map stress fields, a simple classical elasticity problem with a known analytical solution is first selected, namely, that of a circular hole in a plate under uniaxial tension (Dally and Riley, 1985). Referring to Fig. 14.4 and Equation 14.6, the solution shows that the maximum value of the σ_{yy} stress component occurs at the boundary of the



14.3 Independently obtained mechanical and spectroscopic stress–strain curves. The latter was determined from the Raman shift data presented in Fig. 14.2. Symbols: ▲ data at 298 K (room temperature) and ● data at 235 K. σ_y is the yield stress of the polymer according to the mechanical stress–strain curve. From Zhao and Wagner (2004).

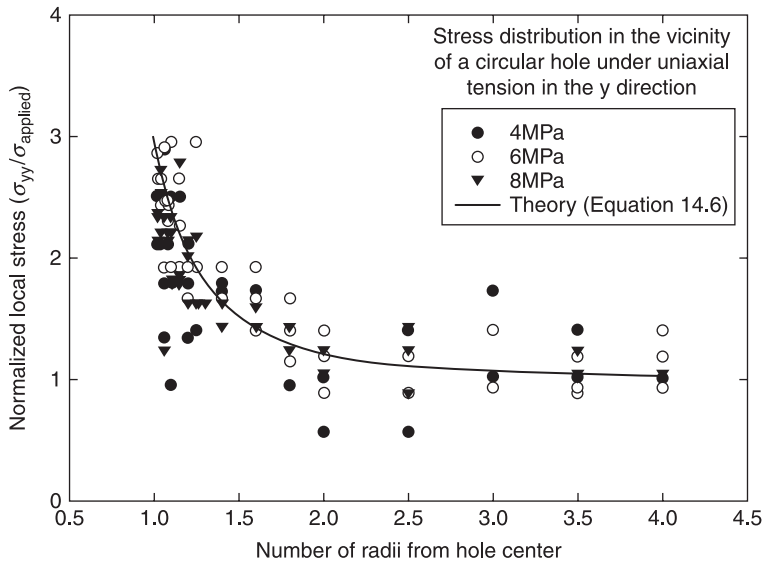


14.4 Circular hole of radius a , in a thin, infinite plate under unidirectional tensile stress σ_0 .

hole (along the x axis, at the ends of the diameter perpendicular to the direction of applied tensile stress) and that, at that point, it is three times larger than the applied stress:

$$\sigma_{yy} = \frac{\sigma_0}{2} \left(2 + \frac{a^2}{x^2} + \frac{3a^4}{x^4} \right) \quad [14.6]$$

where a is the hole radius and σ_0 is the applied stress. From an experimental viewpoint, the first issue that needs to be addressed concerns the orientation of the nanotubes within the (polymer) plate. When the tubes are randomly oriented in the plate, in the case of a uniaxial stress, as in simple mechanical tension, Poisson contraction occurs in the transverse direction. Thus, some nanotubes will be under compression while others will be under tension, resulting in a mixed signal. Aligning the nanotubes is thus preferable – although generally more complicated in practice – to measure the specific components of the complex strain or stress distributions. A simple shear flow method can be developed to orient nanotubes in a polymer such as polyurethane acrylate (PUA). The elastic strain dependence of the G' wavenumber shift was indeed measured with the loading parallel and



14.5 Normalized stress along the x axis (refer to Fig. 14.4) from the edge of a circular hole, based on the G' peak shift of SWNTs in a UV cured urethane-acrylate polymer. Applied loads (σ_0) of 4, 6, and 8 MPa were employed. The solid line is the linear elastic solution given by Equation 14.6. Adapted from Figure 2 in Zhao *et al.* (2001b), with permission from the American Institute of Physics.

perpendicular to the flow direction. A significant difference between the two cases was found, indicating that this orientation method is effective (Wood *et al.*, 2001). However, regardless of whether SWNTs are or are not oriented in PUA, the stress distribution in the plate around the circular hole under uniaxial tension can be mapped, as shown by Zhao *et al.* (2002). Figure 14.5 shows the normalized matrix stress data (calculated from the experimental Raman shift) along the x axis, starting at the edge of a circular hole, under three increasingly higher levels of applied stress. The experimental results fit the linear elastic solution (Equation 14.6) very well, showing that SWNT sensors indeed provide accurate quantitative stress field distribution information at a stress discontinuity (Zhao *et al.*, 2001c).

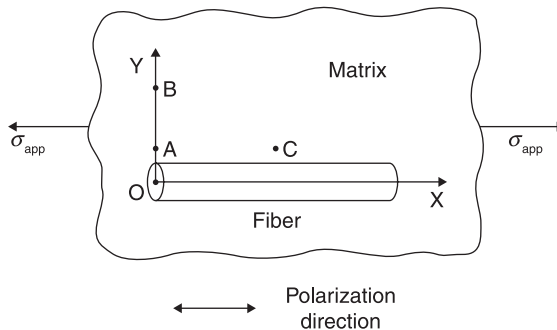
However, it is not always straightforward to induce shear flow and orient nanotubes in a polymer. An alternative is to use plane polarized Raman measurements. In this case, the measured G' Raman peak intensity from a single nanotube is high when the polarization direction is parallel to the nanotube axis, and low when the polarization direction is perpendicular to it (Saito *et al.*, 1998; Duesberg *et al.*, 2000; Gommans *et al.*, 2000; Wood *et al.*, 2001; Zhao *et al.*, 2002). This implies that randomly oriented SWNTs in a polymer can perform as strain sensors if polarized Raman spectroscopy is used – as an alternative to using unpolarized Raman spectroscopy with oriented SWNTs – provided that a

sufficiently high density of nanotubes are present in the polarization direction. The advantage of this technique is that, when nanotubes are used as strain sensors, randomly oriented nanotubes combined with polarized Raman may be used to detect the stress or strain distribution in any direction in the polymer matrix. The G' peak position of SWNTs embedded in PUA was measured as a function of tensile strain, for both uniaxial and random tube orientations (Frogley *et al.*, 2002). The results showed that the polarized Raman can indeed 'select' those nanotubes that are lying in one direction.

Further convincing evidence for the exploitation of nanotubes as mechanical sensors, again using polarized Raman, was demonstrated for complex stress state systems by monitoring the stress in the matrix in the vicinity of a fiber end (Zhao *et al.*, 2001a, 2001c) and of a single fiber break (Zhao and Wagner, 2003).

The discussion thus far shows that SWNTs indeed perform as sensors to detect the elastic stress or strain in a polymer matrix. Such a microscale Raman sensing technique has important practical importance, for example, to measure the matrix stress distribution in the vicinity of fibers to detect or predict the onset of failure in composite materials. As already mentioned, Raman spectroscopy has been successfully used since the early 1980s to monitor the deformation of specific fibers such as aramid, SiC and carbon, since specific Raman bands of these fibers are indeed sensitive to the applied strain (Mitra *et al.*, 1976; Batchelder and Bloor, 1979; Galiotis *et al.*, 1983; Robinson *et al.*, 1987). Correlating these Raman shifts with the applied strain leads to an evaluation of the stress distributions in the fibers at a micron scale, and provides a mean to deduce the interfacial shear stress (Galiotis and Batchelder, 1988; Galiotis *et al.*, 1984; Nielsen and Pyrz, 1999; Wagner *et al.*, 2000). In reality, the micro-Raman technique cannot be universally applied, since some fibers do not have strain-sensitive Raman peaks, glass fibers being the best-known example. In other words, it is impossible to perform *in-situ* measurements of the stress (or strain) distribution in glass fibers. Moreover, since most polymers do not have strain sensitive Raman bands, it is practically impossible to use the Raman spectra of those materials to detect stress (or strain) distributions around discontinuities in polymers. Such measurements become possible, however, by dispersing SWNT sensors in Raman insensitive polymer matrices, or in the sizing layer of Raman insensitive glass fibers. These two cases are now discussed.

The stress field in a polymer matrix in the vicinity of a single glass fiber was mapped on the micron scale by using the strain response of the Raman spectrum of SWNTs embedded in the matrix (Zhao *et al.*, 2001a). A stress concentration zone was observed around the fiber end. Referring to Fig. 14.6, the applied stress value is recovered at a radial distance of 5 or 6 fiber radii from the fiber end (along A–B), whereas axially the stress returns back to the applied value only after about 2 fiber radii (along C–A). Moreover, again for a single glass fiber embedded in a polymer, the tangential thermal residual stress in the vicinity of the fiber was found by Raman spectroscopy to be in satisfactory agreement with a standard



14.6 Strain mapping around a glass fiber: all the measurements were performed with the Raman polarization direction parallel to the fiber axis. From Zhao *et al.* (2001c).

two-phase concentric cylinder model (Wagner, 1996; Wagner and Nairn, 1997; Zhao *et al.*, 2001c).

As an alternative to spreading SWNTs in the matrix around a (Raman-insensitive) glass fiber, Sureeyatanapas and Young (2009) adopted a different approach by preparing a model glass-fiber/epoxy composite with SWNTs incorporated as a strain sensor on the fiber surface. The SWNTs were distributed along the fiber surface either by dispersing them in an amino-silane coupling agent or coating with an epoxy resin solution containing the SWNTs. Point-by-point mapping of the fiber strain in single fiber fragmentation tests was then performed and the interfacial shear stress distribution along the fiber length could be determined. The behavior was found to be consistent with the classical shear-lag model. The effects of SWNT type and preparation procedure on the sensitivity of the technique were evaluated and optimized from single fiber deformation tests. Such SWNT-containing coatings can be used in composites to follow fiber deformation and stress transfer between the matrix and reinforcing glass fibers. This technology has considerable potential for a number of composite systems for which it is not possible to use Raman spectroscopy to follow fiber deformation.

14.5.3 Thermal stress sensing

Significant G' Raman shifts are measured when a nanotube polymer composite is probed at different temperatures under no mechanical tension. Lourie and Wagner (1998a) found that the Raman bands of SWNT shift to a higher wavenumber ($\sim 15 \text{ cm}^{-1}/\%$ strain) when embedded in a thermally cured epoxy resin and cooled to room temperature, due to thermal contraction of the resin. Zhao *et al.* (2001c) have observed irregularities (or discontinuities) in the wavenumber–temperature plot for both amorphous bisphenol A polycarbonate (PC) and polyurethane acrylate (PUA), in which SWNTs had been embedded. The Raman results were

compared with dynamic mechanical thermal analysis (DMTA) data for both polymers, and the sources of the discontinuities were investigated. The concordance found between the DMTA data and the Raman spectral response shows that these irregularities reflect basic polymer phase transitions, namely, glass-transition temperatures and secondary transitions, which may thus be sensed by nanotubes. In other words, this confirms that the Raman spectral response of carbon nanotubes embedded in polymers is sensitive to polymer transitions. In a recent study, De la Vega *et al.* (2009) used SWNTs to monitor internal stresses developing during the curing process of thermoset materials. *In-situ* Raman spectroscopy was used to identify chemical and thermal-induced stresses by following the changes in the G' band versus time and temperature.

14.5.4 Nanotube orientation in polymers

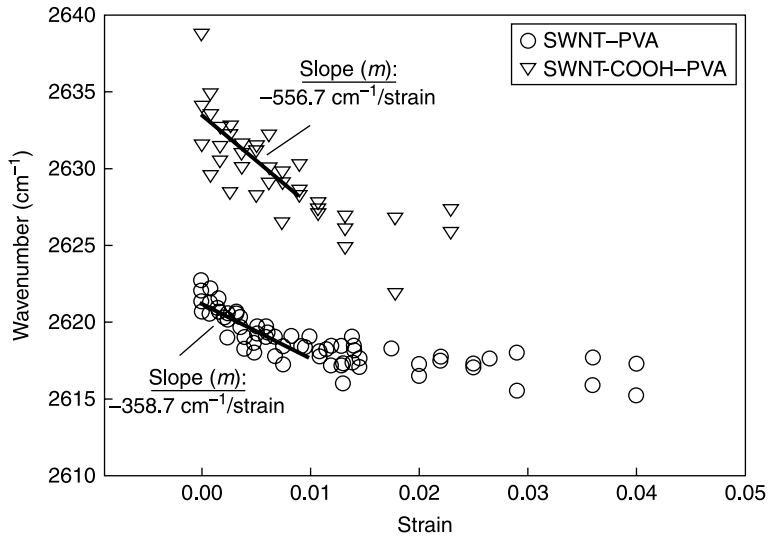
Raman spectroscopy combined with mechanical testing provides a way to probe the alignment of SWNTs in composites. Zhao *et al.* (2001c) prepared specimens using a flow orientation method designed to align SWNTs in the matrix. The matrix was a UV curable urethane acrylate. Raman spectra obtained for specimens cut both parallel and perpendicular to the (average) tube direction were found to be significantly different, as a function of mechanical strain. The Raman shift–strain response for samples loaded perpendicular to the flow direction suggested that nanotube reorientation was achieved upon straining the polymer beyond its yield point. Frogley *et al.* (2002, 2003) and Frogley and Wagner (2002) then performed a thorough study of nanotube alignment in polymers using polarized Raman spectroscopy, and compared a large amount of experimental results with existing models such as those by Saito *et al.* (1998), Gommans *et al.* (2000), and Hwang *et al.* (2000). Specimens with a good degree of nanotube alignment could be prepared by a simple shear-flow technique. For single-walled carbon nanotubes excited with polarized light of wavelength 632.8 nm, the Raman scattering is resonant so that for a single nanotube, or for tubes oriented perfectly along one direction, the total intensity of the Raman modes is found to vary as $\cos^4(\theta)$ (Frogley *et al.*, 2002, 2003), where θ is the angle between the nanotube and the loading directions. Kao and Young (2005) and Cooper *et al.* (2001) performed similar studies with randomly oriented SWNTs. Polarized Raman spectroscopy has also been used by other authors to probe the orientation of CNT bundles prepared by an electrophoretic method (Poulin *et al.*, 2002). In another case, nanotubes were oriented into bundles by applying an electric field between a carbon fiber and an ultrasonicated SWNT/N, N-dimethylformamide (DMF) suspension, and polarized Raman spectroscopy was then used to quantify the alignment of nanotubes as a function of the angle θ between the fiber and the polarizer (Gommans *et al.* 2000). The crystallite orientation and the SWNT alignment in melt-blended SWNT–PP composites fibers have been studied using X-ray diffraction and polarized Raman spectroscopy, which showed that there is

an orientation effect in the drawn SWNT–PP fiber (Bhattacharyya *et al.* 2003). A combination of solvent casting and melt mixing was used to disperse SWNTs in poly(methyl methacrylate) (PMMA), and polarized Raman spectroscopy was again used to demonstrate the alignment of nanotubes in the PMMA (Haggenmueller *et al.* 2000).

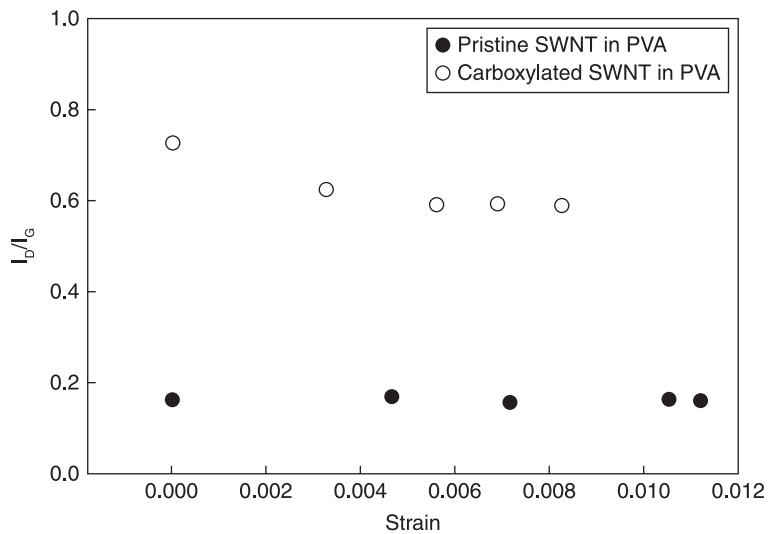
14.5.5 Nanotube molecular surface defects

The previous sections clearly demonstrate that carbon nanotubes embedded in composite fibers allow these to be used as strain or stress sensors by measuring the shift of the G' Raman band under mechanical load. Surface functionalization of the nanotubes with carboxylic groups, which provides better tube–polymer adhesion and thus stress transfer, leads to substantial improvements of the fiber as a Raman strain sensor. This opens the way for the inclusion of such fibers in structural composites, to probe their sensing ability in practical applications.

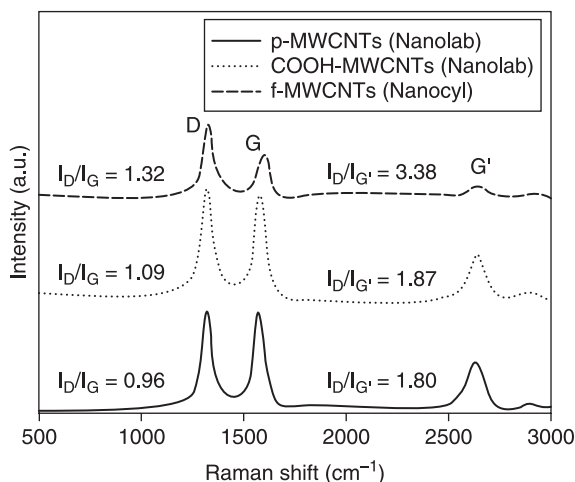
However, the following examples show that surface functionalization is unfortunately also a double-edged sword, which at the same time brings about improved tube dispersion in the polymer mass but also degrades the structural integrity of the tube walls, the consequence of which is a decrease in mechanical properties of the nanotubes. Indeed, carboxylation by acid nitric treatments can degrade the wall structure of single-walled carbon nanotubes (Liu *et al.*, 1998; Monthieux *et al.*, 2001; Hu *et al.*, 2003) and thus reduce their Young's modulus and tensile strength. The defect density can be quantified by Raman spectroscopy, as in our recent investigation (Lachman *et al.*, 2009) of the strain-induced shift of the G' Raman band of single-walled carbon nanotubes in polyvinyl alcohol (PVA)–nanotube composite fibers (Fig. 14.7). The Raman D band (D = disorder) located at 1320 cm^{-1} (Fig. 14.1) originates from amorphous carbon and structural defects; the G band (G = graphite) at 1570 cm^{-1} is related to graphite structures, and stems from tangential shearing mode of the carbon atoms (Coleman *et al.*, 2004). The G' band at 2640 cm^{-1} is an overtone of the D band. The ratio of integrated intensities of the D and G bands, I_D/I_G , can be used to estimate the density of defects in the CNT structure: the larger the value of the I_D/I_G ratio, the higher the defect density (Lachman *et al.*, 2009, and references therein). Indeed, the integrated peak intensity ratio, I_D/I_G (based on the area under the peaks), of pristine SWNT–PVA was found to be 0.16, whereas that of COOH–SWNT–PVA is 0.73 (Lachman *et al.*, 2009). Such a large difference confirms that COOH–SWNTs contain significantly more defects than pristine SWNTs. In other words, carboxylation by nitric acid treatment has significantly degraded the wall structure of single-wall carbon nanotubes. Moreover, referring to Fig. 14.8, upon straining, the I_D/I_G ratio of the COOH-based specimen is seen to progressively decrease down to a constant value, whereas this ratio remains constant for the pristine tube-based specimen. This leads to a lower but constant, large difference between the I_D/I_G ratio at higher strains. This CNT wall structure degradation effect is most



14.7 Strain-induced shifts of the G' band for carboxylated and pristine single-walled nanotubes in PVA. At low strain ($\varepsilon < \sim 0.01$), in the elastic regime, the data can be approximately fitted by linear relationships. At larger strain, in the plastic regime, the Raman response becomes insensitive to strain, likely due to weakening of the interfacial adhesion as the polymer chains possibly slide at the nanotube interface. (From Lachman *et al.* (2009).)



14.8 Effect of applied strain on the integrated peak intensity ratio, I_D/I_G , for pristine SWNT–PVA and COOH–SWNT–PVA fibers. The intensity ratio calculation is based on the measurement of the areas under the D and G peaks. (From Lachman *et al.* (2009).)



14.9 Raman spectra of pristine and functionalized MWCNTs. The ratio I_D/I_G of integrated intensities of the D and G peaks reflects the amount of defects in the CNT structure, with larger ratio values corresponding to higher defect densities. (From Sui *et al.* (2009), with permission from the American Institute of Physics.)

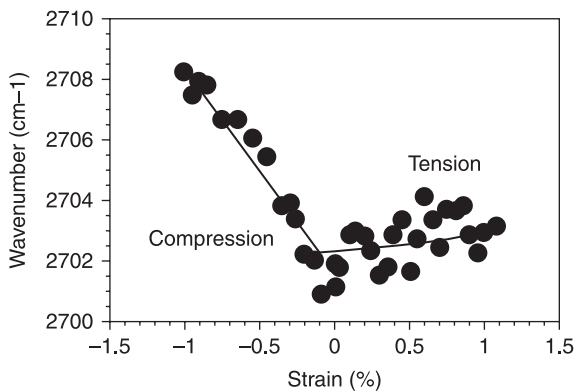
likely the main cause of the lack of improvement in the mechanical properties of the PVA fibers. In such conditions, it is possible that, in spite of a better chemical adhesion to the matrix, the weakening or shortening of carboxylated nanotubes produces no improvement in the mechanical properties of the nanocomposites.

As a second example, taken from Sui *et al.* (2009), the mechanical properties of electrospun fibers made of PMMA containing surface modified nanotubes generally fall below those of fibers with pristine nanotubes, sometimes below those of pure polymer fibers. We show that covalent functionalization produces defects in the graphene structure, leading to mechanical weakening of the nanotube and, therefore, of the nanocomposite. To demonstrate the presence of defects in the functionalized MWCNTs, Raman and transmission electron microscopy (TEM) characterization were performed. As indicated in Fig. 14.9, the values of I_D/I_G for the functionalized MWCNTs are found to be larger than for pristine MWCNTs, the largest ratio being observed for f-MWCNTs. The same trend is observed by using the ratio of intensities of the D and G' bands, $I_D/I_{G'}$. Thus, chemical surface modification indeed again causes defects in the CNT structure.

14.5.6 Nanotube–polymer stress transfer and interface adhesion

So far, it has not been possible to calibrate the shift of a Raman peak position with an applied strain in CNTs, as is done with individual graphite fibers in air. In

composites it is clear, however, that the larger the Raman peak shift, the larger is the strain carried by the nanotubes. Schadler *et al.* (1998) measured the peak shift for the sensitive G' band of nanotubes (2700 cm^{-1}), a strong peak for MWNT, with no epoxy peak overlap in this region. Figure 14.10 shows the G' Raman peak shift in tension and compression. Under a 1% compressive strain the peak is observed to shift upwards by 7 cm^{-1} , whereas only a slightly positive shift appears when the composites are under tension. The shifts are thought to arise from the strain transferred from the matrix to nanotubes. The different Raman responses in tension and compression are most likely due to the structure of MWNTs. Indeed, Schadler *et al.* (1998) believe that, under tension, the outer layer of the MWNT is loaded, but load is not effectively transferred to the inner layers due to the relatively weak bonding between the nanotube layers. Instead, the inner tubes may slip with respect to the outer tubes. Since the Raman signal is averaged over the whole MWNT, the result is only an insignificant Raman peak shift. Under compression, however, the load transfer to the inner layers of the MWNT occurs through buckling and the bent sections of the nanotubes. Slippage of nanotubes layers in compression is prevented because of the seamless structure of the tubes and of the geometrical constraint the outer layer imposes on the inner layers (Schadler *et al.* 1998). Similar experiments have been performed by Ajayan *et al.* (2000) with SWNTs, but the G' Raman results showed that under compression there is almost no shift and only a small downward shift under tension. Ajayan *et al.* (2000) observed that the applied compressive stress is transferred into buckling, bending or twisting of the nanotube network without introducing important local deformations that can be monitored by Raman. Since SWNTs tend to form ropes, the small Raman shift under tension is due to the fact that the individual SWNTs are slipping within the ropes and decrease the load required to

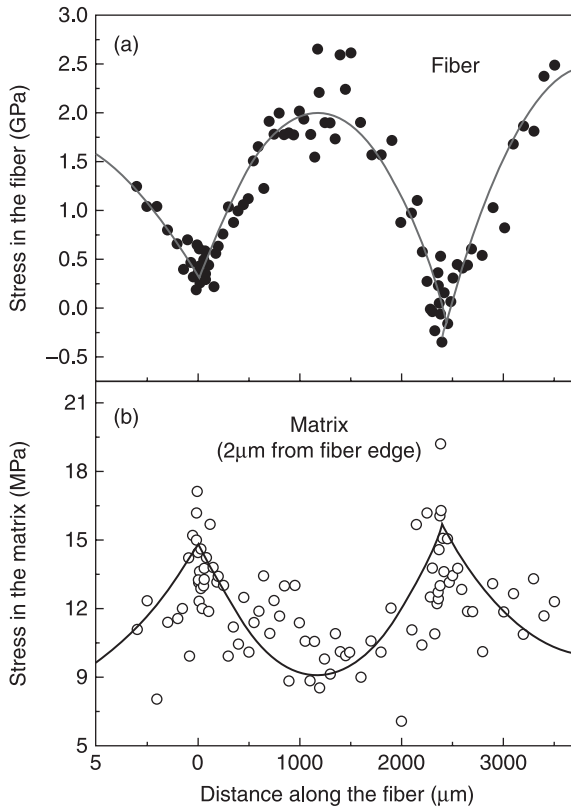


14.10 Nanotube Raman peak shift as a function of applied strain showing the large shift in the Raman peak (second order peak at 2700 cm^{-1}) in compression compared to tensile loading. (From Schadler *et al.* (1998), with permission from the American Institute of Physics.)

deform the ropes (Ajayan *et al.*, 2000). In both cases, the tensile and compressive strains are applied uniaxially on the samples, though the nanotubes are dispersed randomly in the polymer matrix (Schadler *et al.*, 1998; Ajayan *et al.*, 2000). When the nanotube composite samples are under tension, nanotubes lying along the tensile direction are under tension, but those in the perpendicular direction are under compression because of Poisson's contraction. The reverse is true when the sample is under compression. Since the Raman laser spot size is ca. 1–5 μm thick, and nanotube diameters are several nanometres in size, the Raman signal is averaged over nanotubes in all directions, but Ajayan *et al.* (2000) and Schadler *et al.* (1998) do not consider this in detail.

The mechanical properties of a composite depend not only on the properties of the fiber and the matrix, but also on the quality of the interface between these. In composite material research a single fiber composite test is often used to quantify the level of interfacial adhesion. The single fiber fragmentation technique is a known, practically convenient and reproducible method often used to characterize the fiber-matrix adhesion or interfacial properties. However, it also is a complex test which involves shear yielding of the matrix, interfacial debonding and transverse matrix cracking (Kelly and Tyson, 1965; Wagner and Eitan, 1990, 1993; Eitan and Wagner, 1991; Detassis *et al.*, 1996). The occurrence of these additional damage events during the fragmentation test makes the conventional data reduction technique (based on the constant shear model) problematic. Thus, a determination of the stress distribution around the fiber break in the matrix is necessary. This is illustrated in an experiment in which two-dimensional stress profiles around a glass fiber break were mapped using SWNT sensors randomly dispersed in a PUA matrix, by means of polarized Raman spectroscopy. A contour map showing the distribution of the stress concentration factor around a fiber break could be produced (Zhao and Wagner, 2003). The stress concentration (defined as $K_c = \text{local stress}/\text{applied stress}$) reached a maximum value just near the glass fiber break ($K_c = 1.42$) and decreased radially and longitudinally away from the break point, as expected (Eitan and Wagner, 1991; Wagner and Eitan, 1993).

A further experiment demonstrating the sensing power of Raman microscopy was performed by combining the Raman sensitivity of both a carbon fiber and carbon nanotubes, the latter being dispersed in the polymer around the former. The basic idea of this experiment was to simultaneously detect the stress distributions in the fiber and in the matrix using Raman spectroscopy, and to compare the results with existing stress transfer models. A continuous high modulus carbon fiber (HMCF)-PUA composite with nanotubes dispersed in the matrix was chosen. The G' Raman band of HMCF shifts linearly under an applied strain. The strains in the fiber and the matrix were measured simultaneously under several applied stress levels, parallel to the fiber direction. Figure 14.11 presents the distributions of stress in the carbon fiber and in the matrix, between two break locations measured at an applied stress of 10 MPa. Polynomial curves were fitted through the experimental data points. As seen, the stress profiles in the matrix and



14.11 Stress distributions in the HMCF (a) and the PUA matrix along the fiber edge (b), measured simultaneously by microRaman spectroscopy. The distributions are mirror images of each other. The applied stress level was 10 MPa. The solid line in (a) is a polynomial fit to the data. In (b), the line is the mirror image of the fit in (a), scaled accordingly. (From Zhao and Wagner (2003).)

the fiber, measured simultaneously for the first time, complement each other well (Zhao and Wagner, 2003).

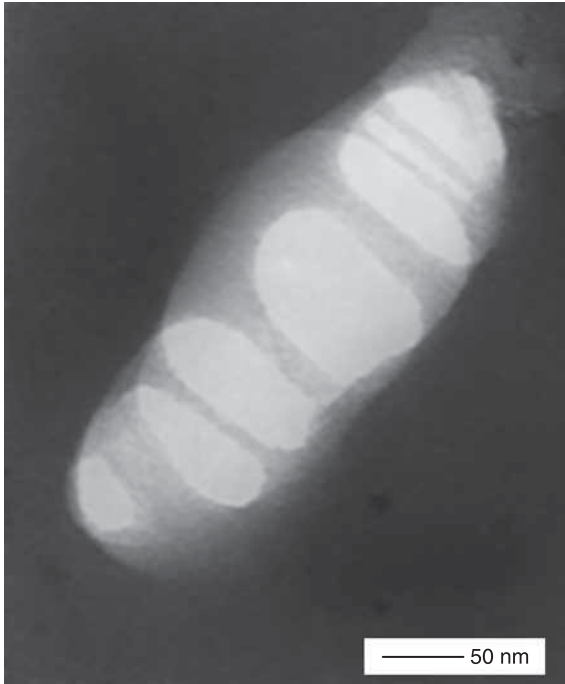
Most recently, the deformation micromechanics of SWNTs embedded in a polymeric matrix was investigated (Kao and Young, 2010) through the use of Raman spectroscopy. The degree of interfacial adhesion in nanotube–epoxy composites was evaluated through cyclic deformation of the specimens and was found to be dependent on the maximum loading strain and the numbers of deformation cycles. A hysteresis loop was observed from the mismatch between the loading and unloading results and the loop area was estimated to evaluate the energy dissipated in the composites. This was employed in an approximate model to quantify the extent of interface damage, using assumptions about the nanotube distribution in the composite. In other words, in this case, the Raman technique

did not lead to a measurement of the stress but an energy-based approach was used to monitor stress transfer.

The use of Raman spectroscopy to produce the full interface shear strength profile along a tube in a single nanotube pull-out or a fragmentation test, similar to the one produced in a micromechanical test using a micron-size carbon or Kevlar fiber, remains an elusive challenge. If the interfacial shear strength in CNT-based nanocomposites is to be evaluated by a combination of, say, Raman measurement and a model for the interfacial strength based on a force balance – in traditional micron-size fibers this is done using the Kelly–Tyson model (Kelly and Tyson, 1965) – the fact that tubes are hollow becomes crucial. This was examined and discussed by Wagner (2002). The interrelation between the tube–matrix interfacial (adhesion) shear strength τ_{NT} , the tensile strength $\sigma_{NT}(l_c)$ of a tube fragment (of length l_c), the (empirically measured) critical length l_c , and the inner and outer diameters d_{NT} and D_{NT} , is given by

$$\tau_{NT} = \sigma_{NT}(l_c) \left[0.5 \left(\frac{l_c}{D_{NT}} \right)^{-1} \left(1 - \frac{d_{NT}^2}{D_{NT}^2} \right) \right] \quad [14.7]$$

and the nanotube wall thickness is $h = (D_{NT} - d_{NT})/2$. It is easily seen that high values of the interfacial shear strength (compared to those in current advanced fiber-based polymer composites) are in principle attainable. Defects in the hexagonal structure of a nanotube, which technically is a ‘perfect’ material, are expected to strongly reduce its strength and the model predicts that, as a consequence, large variability should be experimentally observed in either the interfacial strength or the critical length of apparently identical nanotubes. The presence or absence of such defects in the structure of the CNT could in principle be detectable by Raman spectroscopy through the I_D/I_G ratio, and an experimental correlation with the interfacial shear strength be found via Equation 14.7. However, at the present time, such a correlative experiment seems beyond reach. The CNT critical length and interfacial strength could be measured by either nanofragmentation or nanopull-out testing. However, the occurrence of the CNT fragmentation phenomenon has been observed only occasionally, with great difficulty (Wagner *et al.*, 1998; Lourie *et al.*, 1998; Lourie and Wagner, 1999). In addition, Lourie and Wagner (1998b) provide evidence of significant polymer–nanotube wetting and interfacial adhesion, see Fig. 14.12. Unique single nanotube pull-out experiments were conducted by Barber *et al.* (2003, 2004, 2006), following a preliminary attempt to experimentally ‘drag out’ a nanotube from a polymer matrix by means of an AFM tip (Cooper *et al.*, 2002). The pull-out model of Gou *et al.* (2005) predicts the effects of temperature and of the number of walls on the interfacial shear strength. See also an interesting paper by Lau (2003). Interestingly, very high values (hundreds of MPa) of the CNT–matrix interface strength are attainable in principle, based on the models by Wagner (2002) and Zhang and Wang (2005), as well as on numerical simulations (Liao and Li, 2001).



14.12 TEM image of aligned single-walled carbon nanotube ropes bridging an elliptical hole in a polymer film. The ropes tend to orient parallel to each other and to the short axis of the elliptical hole. The image provides strong evidence of significant polymer–nanotube wetting and interfacial adhesion. (From Lourie and Wagner (1998b), with permission from the American Institute of Physics.)

The effect of chirality on the interfacial strength is also of interest (Zheng *et al.*, 2008) but a challenging correlation with Raman spectroscopy has not been attempted.

14.6 Conclusion

Recent developments in the application of Raman spectroscopy to carbon nanotube-based composite materials have been reviewed. This technique may be used to distinguish carbon nanotubes from other carbon materials or polymers, as well as to sort nanotubes by diameter or length (Zhao and Wagner, 2004). Raman spectroscopy has also been used to check the dispersion of nanotube in polymers, evaluate nanotube–matrix interactions, and detect polymer phase transitions. The Raman spectra of nanotubes can also be utilized to quantify the strain or stress transferred to nanotubes from the surrounding environment. Since the small amounts of embedded nanotubes required to make the polymer Raman sensitive

to strain do not affect the mechanical properties of the embedding matrix, these nanoscale tubes may be used to investigate local stresses and strains in polymer materials, a result that is so far inaccessible by other methods. Polarized Raman can be used to detect the orientation of nanotubes in polymer matrices. Oriented SWNT sensors can be used to detect stress fields around a circular hole in a plate, demonstrating the applicability of the technique for the mapping of the stress distribution in the vicinity of discontinuities.

A polarized Raman technique may be used to detect the stress or strain in a matrix using randomly dispersed SWNTs, based on the fact that the intensity of the signal arising from SWNTs is a function of the polarization direction. This method is more convenient than the tube orientation technique since it is not always possible to orient SWNTs inside a polymer.

Finally, the sensing capability of nanotubes clearly makes it possible to investigate and settle various fracture mechanics problems, including so far unsolved ones. For example, current studies of stress transfer and fiber–fiber interactions in fiber reinforced composites are all based on theoretical models (such as shear-lag models) which involve a ‘characteristic distance’ in the matrix, radially from the fiber–matrix interface (one version of this is the so-called inverse Cox parameter, β^{-1}). This fundamental parameter, which represents a ‘zone of influence’ around a fiber break or end, is currently difficult to measure directly. The relatively simple measurement of such characteristic distance would be an immediate outcome of the mapping of the stress or strain field using nanotubes as Raman sensors in composites.

14.7 Acknowledgements

This author wishes to acknowledge support from the Israel Ministry of Industry, Trade and Labor, through the Nanotubes Empowerment Solutions (NES) Magnet research consortium, and from the G. M. J. Schmidt Minerva Centre of Supramolecular Architectures. This research was also made possible in part by the generosity of the Harold Perlman family. Thanks are due to Dr Shigeo Maruyama (The University of Tokyo) and Dr Hagai Cohen (Weizmann Institute of Science) for providing the SWNT sample prepared by CVD, the Raman spectrum of which is shown in Fig. 14.1 (b). Thanks are gratefully extended to my postdoctoral fellow Dr XiaoMeng Sui for producing the Raman spectra shown in that figure. H. D. Wagner is the recipient of the Livio Norzi Professorial Chair in Materials Science.

14.8 References

- Ajayan P M, Schadler L S, Giannaris C, Rubio A (2000) ‘Single-walled carbon nanotube-polymer composites: strength and weakness’, *Adv. Mater.*, 12(10), 750–753.
- Arinstein A, Burman M, Gendelman O, Zussman E (2007) ‘Effect of supramolecular structure on polymer nanofibre elasticity’, *Nat. Nanotech.*, 2, 59–62.

- Atkinson K R, Hawkins S C, Huynh C, Skourtis C, Dai J, Zhang M, Fang S, Zakhidov A A, Lee S B, Aliev A E, Williams C D, Baughman R H (2007) 'Multifunctional carbon nanotube yarns and transparent sheets: fabrication properties and applications', *Phys. B: Cond. Matter.*, 394(2), 339–343.
- Barber A H, Cohen S R, Eitan A, Schadler L S, Wagner H D (2006) 'Fracture transitions at carbon nanotube-polymer interfaces' *Adv. Mater.*, 18, 83–87.
- Barber A H, Cohen S R, Kenig S, Wagner H D (2004) 'Interfacial fracture energy measurements for multi-walled carbon nanotubes pulled from a polymer matrix', *Compos. Sci. Tech.*, 64, 2283–2289.
- Barber A H, Cohen S R, Wagner H D (2003) 'Measurement of carbon nanotube-polymer interfacial strength', *Appl. Phys. Lett.*, 82(23), 4140–4142.
- Batchelder D N, Bloor D (1979) 'Strain dependence of the vibrational modes of a diacetylene crystal', *J. Polym. Sci. Polym. Phys.*, 17, 569–581.
- Bethune DS, Kiang CH, De Vries MS, Gorman G, Savoy R, Vazquez J, Beyers R (1993) 'Cobalt catalysed growth of carbon nanotubes with single-atomic-layer walls', *Nature*, 363, 605–607.
- Bhattacharyya A R, Sreekumar T V, Liu T, Kumar S, Ericson L M, Hauge R H, Smalley R E (2003) 'Crystallization and orientation studies in polypropylene/single wall carbon nanotube composite', *Polymer*, 44, 2373–2377.
- Chou T-W, Gao L, Thostenson E T, Zhang Z, Byun J-H (2010) 'An assessment of the science and technology of carbon nanotube-based fibers and composites', *Compos. Sci. Technol.*, 70, 1–19.
- Coleman J N, Cadek M, Blake R, Nicolosi V, Ryan K P, Belton C, Fonseca A, Nagy J B, Gun'ko Y K, Blau W J (2004) 'High performance nanotube-reinforced plastics: understanding the mechanism of strength increase', *Adv. Funct. Mater.*, 14(8), 791–798.
- Colomban Ph (1999) 'Tailoring and control of the micro (nano) structure of functional CMCs and MMCs', *Korean. J. Ceram.*, 5(1), 55–72.
- Cooper C A, Cohen S R, Barber A H, Wagner H D (2002) 'Detachment of nanotubes from a polymer matrix', *Appl. Phys. Lett.*, 80(20), 3873–3875.
- Cooper C A, Young R J, Halsall M (2001) 'Investigation into the deformation of carbon nanotubes and their composites through the use of Raman spectroscopy', *Compos. A.*, 32, 401–411.
- Dally J W, Riley W F (1985) *Experimental Stress Analysis*, New York: McGraw-Hill Book Company.
- De la Vega A, Prado L A S de A, Kovacs J Z, Bauhofer W, Schulte K (2009) 'SWCNT as cure-induced stress sensors in epoxy nanocomposites', *Sol. State. Phen.*, 151, 48–53.
- Detassis M, Pegoretti A, Migliaresi C, Wagner H D (1996) 'Experimental evaluation of residual stresses in single fiber composites by means of the fragmentation test', *J. Mater. Sci.*, 31, 2385–2392.
- Dresselhaus M S, Dresselhaus G, Jorio A, Souza Filho A G, Saito R (2002b) 'Raman spectroscopy on isolated single wall carbon nanotubes', *Carbon*, 40, 2043–2061.
- Dresselhaus M S, Dresselhaus G, Saito R, Jorio A (2005) 'Raman spectroscopy of carbon nanotubes', *Phys. Rep.*, 409, 47–99.
- Dresselhaus M S, Jorio A, Souza Filho A G, Dresselhaus G, Saito R (2002a) 'Raman spectroscopy on one isolated carbon nanotube', *Physica B*, 323, 15–20.
- Duesberg G S, Loa I, Burghard M, Syassen K, Roth S (2000) 'Polarized Raman spectroscopy on isolated single-wall carbon nanotubes', *Phys. Rev. Lett.*, 85, 5436–5439.
- Eitan A, Wagner H D (1991) 'Fiber interactions in two-dimensional composites', *Appl. Phys. Lett.*, 58(10), 1033–1035.

- Frogley M D, Ravich D, Wagner H D (2003) 'Mechanical properties of carbon nanoparticle-reinforced elastomers', *Compos. Sci. Tech.*, 63, 1647–1654.
- Frogley M D, Wagner H D (2002) 'Mechanical alignment of quasi-one-dimensional nanoparticles', *J. Nanosci. Nanotech.*, 2(5), 517–521.
- Frogley M D, Zhao Q, Wagner H D (2002) 'Polarized resonance-Raman spectroscopy of single-wall carbon nanotubes within a polymer under strain', *Phys. Rev. B*, 65, 113413–(1–4).
- Galiotis C, Batchelder D N (1988) 'Strain dependences of the 1st-order and 2nd-order Raman spectra of carbon fibers', *J. Mater. Sci. Lett.*, 7, 545–547.
- Galiotis C, Young R J, Batchelder D N (1983) 'A resonance Raman-spectroscopic study of the strength of the bonding between an epoxy-resin and a polydiacetylene fiber', *J. Mater. Sci. Lett.*, 2, 263–266.
- Galiotis C, Young R J, Yeung P H J, Batchelder D N (1984) 'The study of model polydiacetylene epoxy composites. 1. The axial strain in the fiber', *J. Mater. Sci.*, 19, 3640–3648.
- Gommans H H, Alldredge J W, Tashiro H, Park J, Magnuson J, Rinzler A G (2000) 'Fibres of aligned single-walled carbon nanotubes: polarized Raman spectroscopy', *J. Appl. Phys.*, 88, 2509–2514.
- Gou J, Liang Z Y, Zhang C, Wang B (2005) 'Computational analysis of effect of single-walled carbon nanotube rope on molecular interaction and load transfer of nanocomposites', *Composites B: Engineering*, 36, 524–533.
- Gouadec G, Karlin S, Wua J, Parlier M, Colomban Ph (2001) 'Physical chemistry and mechanical imaging of ceramic-fibre-reinforced ceramic- or metal-matrix composites', *Compos. Sci. Tech.*, 61, 383–388.
- Grubb D T, Li Z-F, Phoenix S L (1995) 'Measurement of stress concentration in a fiber adjacent to a fiber break in a model composite', *Compos. Sci. Tech.*, 54, 237–249.
- Haggenmueller R, Gommans H H, Rinzler A G, Fischer J E, Winey K I (2000) 'Aligned single-wall carbon nanotubes in composites by melt processing methods', *Chem. Phys. Lett.*, 330, 219–225.
- Hu H, Zhao B, Itkis M E, Haddon R C (2003) 'Nitric acid purification of single-walled carbon nanotubes', *J. Phys. Chem. B*, 107, 13838–13842.
- Hu Y, Shenderova O A, Hu Z, Padgett C W, Brenner D W (2006) 'Carbon nanostructures for advanced composites', *Rep. Prog. Phys.*, 69, 1847–1895.
- Hwang J, Gommans H H, Ugawa A, Tashiro H, Haggenmueller R, Winey K I, Fischer J E, Tanner D B, Rinzler A G (2000) 'Polarized spectroscopy of aligned single-wall carbon nanotubes', *Phys. Rev. B*, 62(20), R13310.
- Iijima S (1991) 'Helical microtubules of graphitic carbon', *Nature*, 354, 56–58.
- Iijima S, Ichihashi T (1993) 'Single-shell carbon nanotubes of 1-nm diameter', *Nature*, 363, 603–605.
- Jones K D, DiBenedetto A T (1994) 'Fiber fracture in hybrid composite systems', *Compos. Sci. Tech.*, 51, 53–62.
- Jorio A, Santos A P, Ribeiro H B, Fantini C, Souza M, Vieira J P M, Furtado C A, Jiang J, Saito R, Balzano L, Resasco D E, Pimenta M A (2005) 'Quantifying carbon-nanotube species with resonance Raman scattering', *Phys. Rev. B*, 72, 075207.
- Kao C C, Young R J (2005) 'Angular dependence upon deformation of SWNT/epoxy composites using polarized Raman spectroscopy (2005)', *CNT-Polymer Composites International Conference*, Hamburg, Germany.
- Kao C C, Young R J (2010) 'Assessment of interface damage during the deformation of carbon nanotube composites', *J. Mater. Sci.*, 45, 1425–1431.

- Kelly A, Tyson W R (1965) 'Tensile properties of fibre-reinforced metals: copper/tungsten and copper/molybdenum', *J. Mech. Phys. Sol.*, 13, 329–350.
- Kim J H, Hettenhouser J W, Moon C K, Holmes G A (2009) 'A fiber placement device and methodology for preparing 2-D and 3-D combinatorial microcomposites', *J. Mater. Sci.*, 44, 3626–3632.
- Koziol K, Vilatela J, Moissala A, Motta M, Cunniff P, Sennett M, Windle A (2007) 'High-performance carbon nanotube fiber', *Science*, 318, 1892–1895.
- Kroto H W, Heath J R, O'Brien S C, Curl S C, Smalley R E (1985) 'C₆₀: Buckminsterfullerene', *Nature*, 318, 162–163.
- Lachman N, Bartholome C., Miaudet P, Maugey M, Poulin P, Wagner H D (2009) 'Raman response of carbon nanotube/PVA fibers under strain', *J. Phys. Chem. C*, 113(12), 4751–4754.
- Lau K-T (2003) 'Interfacial bonding characteristics of nanotube/polymer composites', *Chem. Phys. Lett.*, 370, 399–405.
- Liao K, Li S (2001) 'Interfacial characteristics of a carbon nanotube–polystyrene composite system', *Appl. Phys. Lett.*, 79, 4225–4227.
- Liu J, Rinzler A G, Dai H, Hafner J H, Bradley, R K, Boul P J, Lu A, Iverson T, Shelimov K, Huffman C B, Rodriguez-Macias F, Shon Y-S, Lee T R, Colbert D T, Smalley R E (1998) 'Fullerene pipes', *Science*, 280, 1253–1256.
- Lourie O, Cox D M, Wagner H D (1998) 'Buckling and collapse of embedded carbon nanotubes', *Phys. Rev. Lett.*, 81(8), 1638–1641.
- Lourie O, Wagner H D (1998a) 'Evaluation of Young's modulus of carbon nanotubes by micro-Raman spectroscopy', *J. Mater. Res.*, 13, 2418–2422.
- Lourie O, Wagner H D (1998b) 'Transmission electron microscopy observations of fracture of single-wall carbon nanotubes under axial tension', *Appl. Phys. Lett.*, 73(24), 3527–3529.
- Lourie O, Wagner H D (1999) 'Evidence of stress transfer and formation of fracture clusters in carbon nanotube-based composites', *Compos. Sci. Tech.*, 59, 975–977.
- Lourie O, Wagner H D, Zhang Y, Iijima S (1999) 'Dependence of elastic properties on morphology in single-wall carbon nanotubes', *Adv. Mater.*, 11, 931–934.
- Lucas M, Young R J (2004a) 'Effect of uniaxial strain deformation upon the Raman radial breathing modes of single-wall carbon nanotubes in composites', *Phys. Rev. B*, 69, 085405.
- Lucas M, Young R J (2004b) 'Raman spectroscopic study of the effect of strain on the radial breathing modes of carbon nanotubes in epoxy/SWNT composites', *Compos. Sci. Tech.*, 64, 2297–2302.
- Lucas M, Young R J (2007a) 'Effect of residual stresses upon the Raman radial breathing modes of nanotubes in epoxy composites', *Compos. Sci. Tech.*, 67, 840–843.
- Lucas M, Young R J (2007b) 'Unique identification of single-walled carbon nanotubes in composites', *Compos. Sci. Technol.*, 67, 2135–2149.
- Mitra V K, Risen M R, Baughman R H (1976) 'A laser Raman study of the stress dependence of vibrational frequencies of a monocrystalline polydiacetylene', *J. Chem. Phys.*, 66(6), 2731–2736.
- Monthieux M, Kuznetsov V L (2006) 'Who should be given the credit for the discovery of carbon nanotubes?', *Carbon*, 44, 1621–1623.
- Monthieux M, Smith B W, Berteaux B, Claye A, Fischer J E, Luzzi D E (2001) 'Sensitivity of single-wall carbon nanotubes to chemical processing: an electron microscopy investigation', *Carbon*, 39, 1251–1272.
- Nielsen A S, Pyrz R (1999) 'Study of the influence of thermal history on the load transfer efficiency and fibre failure in carbon/polypropylene microcomposites using Raman spectroscopy', *Compos. Interf.*, 6, 467–482.

- Poulin P, Vigolo B, Launois P (2002) 'Films and fibers of oriented single wall nanotubes', *Carbon*, 40, 1741–1749.
- Radushkevich L V, Lukyanovich V M O (1952) 'Strukture ugleroda obrazujucesja pri termiceskom razlozenii okisi ugleroda na zeleznom kontakte', *Zurn Fisic. Chim.*, 26, 88–95.
- Raman C V, Krishnan K S (1928) 'A new type of secondary radiation', *Nature*, 121, 501–502.
- Rao A M, Richter E, Bandow S, Chase B, Eklund P C, Williams K A, Fang S, Subbaswamy K R, Menon M, Thess A, Smalley R E, Dresselhaus G, Dresselhaus M S (1997) 'Diameter-selective Raman scattering from vibrational modes in carbon nanotubes', *Science*, 275, 187–191.
- Robinson I M, Zakikhani M, Day R J, Young R J, Galiotis C (1987) 'Strain dependence of the Raman frequencies for different types of carbon fibres', *J. Mater. Sci. Lett.*, 6, 1212–1214.
- Saito R, Takeya T, Kimura T, Dresselhaus G, Dresselhaus M S (1998) 'Raman intensity of single-wall carbon nanotubes', *Phys. Rev. B*, 57, 4145–4153.
- Schadler L S, Giannaris S C, Ajayan P M (1998) 'Load transfer in carbon nanotubes epoxy composites', *Appl. Phys. Lett.*, 73, 3842–44.
- Souza Filho A G, Jorio A, Hafner J H, Lieber C M, Saito R, Pimenta M A, Dresselhaus G, Dresselhaus M S (2001) 'Electronic transition energy E_{ii} for an isolated single-wall carbon nanotube obtained by anti-Stokes/Stokes resonant Raman intensity ratio', *Phys. Rev. B*, 63, 241404.
- Stephan C, Nguyen T P, Lahr B, Blau W, Lefrant S, Chauvet O (2002) 'Raman spectroscopy and conductivity measurements on polymer-multiwalled carbon nanotubes composites', *J. Mater. Res.*, 17, 396–400.
- Sui X M, Giordani S, Prato M, Wagner H D (2009) 'Effect of carbon nanotube surface modification on dispersion and structural properties of electrospun fibers', *Appl. Phys. Lett.*, 95, 233113.
- Sui X M, Wagner H D (2009) 'Tough nanocomposites: the role of carbon nanotube type', *Nano. Lett.*, 9(4), 1423–1426.
- Sureeyatanapas P, Young R J (2009) 'SWNT composite coatings as a strain sensor on glass fibres in model epoxy composites', *Compos. Sci. Tech.*, 69, 1547–1552.
- Turrell G (1996) 'The Raman effect', in G Turrell and J Corset, *Raman Microscopy: Developments and Applications*, London: Academic Press Ltd, pp. 1–23.
- Van Den Heuvel P W J, Peijs T, Young R J (1996) 'Analysis of stress concentrations in multi-fibre microcomposites by means of Raman spectroscopy', *J. Mater. Sci. Lett.*, 15, 1908–1911.
- Wagner H D (1996) 'Thermal residual stress in composites with anisotropic interphases', *Phys. Rev. B*, 53(9), 5055–5058.
- Wagner H D (2002) 'Nanotube-polymer adhesion: a mechanics approach', *Chem. Phys. Lett.*, 361, 57–61.
- Wagner H D, Amer M S, Schadler L S (1996) 'Fibre interactions in two-dimensional composites by micro-Raman spectroscopy' *J. Mater. Sci.*, 31 1165–1173.
- Wagner H D, Amer M S, Schadler L S (2000) 'Residual compression stress profile in high modulus carbon fiber embedded in isotactic polypropylene by micro-Raman spectroscopy', *Appl. Compos. Mater.*, 7, 209–217.
- Wagner H D, Eitan A (1990) 'Interpretation of the fragmentation phenomenon in single-filament composite experiments', *Appl. Phys. Lett.*, 56(20), 1965–1967.
- Wagner H D, Eitan A (1993) 'Stress concentration factors in two-dimensional composites: effects of material and geometrical parameters', *Compos. Sci. Tech.*, 46(4), 353–362.

- Wagner H D, Lourie O, Feldman Y, Tenne R (1998) 'Stress-induced fragmentation of multiwall carbon nanotubes in a polymer matrix', *Appl. Phys. Lett.*, 72(2), 188–190.
- Wagner H D, Nairn J A (1997) 'Residual thermal stresses in three concentric transversely isotropic cylinders: application to thermoplastic matrix composites containing a transcrystalline interphase', *Compos. Sci. Technol.*, 57, 1289–1302.
- Wagner H D, Steenbakkers W (1989) 'Microdamage analysis of fibrous composite monolayers under tensile stress', *J. Mater. Sci.*, 24, 3956–3975.
- Wood J R, Frogley M D, Meurs E R, Prins A D, Peijs T, Dunstan D J, Wagner H D (1999) 'Mechanical response of carbon nanotubes under molecular and macroscopic pressures', *J. Phys. Chem. B*, 103, 10388–10392.
- Wood J R, Zhao Q, Frogley M D, Meurs E R, Prins A D, Peijs T, Dunstan D J, Wagner H D (2000) 'Carbon nanotubes: from molecular to macroscopic sensors', *Phys. Rev. B*, 62, 7571–7575.
- Wood J R, Zhao Q, Wagner H D (2001) 'Orientation of carbon nanotubes in polymers and its detection by Raman spectroscopy', *Compos. A*, 32, 391–399.
- Woodward L A (1967), Chapter 1, in H A Szymanski, *Raman Spectroscopy*, New York: Plenum Press.
- Wu G, Tashiro K, Kobayashi M (1989) 'Vibrational spectroscopic study on molecular deformation of polydiacetylene single crystals: stress and temperature dependences of Young's modulus', *Macromol.*, 22, 188–196.
- Young R J (1993) 'Characterization of interfaces in polymers and composites using Raman spectroscopy', in W J Feast *et al.*, *Polymer Surfaces and Interfaces, II*, New York: John Wiley & Sons Ltd.
- Young R J (1997) 'Analysis of composites using Raman and fluorescence microscopy: a review', *J. Microscopy*, 185(2), 199–205.
- Young R J, Eichhorn S J (2009) 'Raman applications in synthetic and natural polymer fibres and their composites', in M S Amer, *Raman Spectroscopy for Soft Matter Applications*, New York: John Wiley & Sons Inc, pp. 63–94.
- Zhao Q, Frogley M D, Wagner H D (2001a) 'The use of carbon nanotubes to sense matrix stresses around a single glass fiber', *Compos. Sci. Technol.*, 61, 2139–2143.
- Zhao Q, Frogley M D, Wagner H D (2002) 'Direction-sensitive strain-mapping with carbon nanotube sensors', *Compos. Sci. Technol.*, 62, 147–150.
- Zhao Q, Wagner H D (2003) 'Two-dimensional strain mapping in model fiber-polymer composites using nanotube Raman sensing', *Compos. A*, 34, 1219–1225.
- Zhao Q, Wagner H D (2004) 'Raman spectroscopy of carbon-nanotube-based composites', *Phil. Trans. R. Soc. Lond. A*, 362, 2407–2424.
- Zhao Q, Wood J R, Wagner H D (2001b) 'Using carbon nanotubes to detect polymer transitions', *J. Polym. Sci. B: Polym. Phys.*, 39, 1492–1495.
- Zhao Q, Wood J R, Wagner H D (2001c) 'Stress fields around defects and fibres in a polymer using carbon nanotubes as sensors', *Appl. Phys. Lett.*, 78, 1748–1750.
- Zheng Q, Xue Q, Yan K, Gao X, Li Q, Hao L (2008) 'Influence of chirality on the interfacial bonding characteristics of carbon nanotube polymer composites', *J. Appl. Phys.*, 103, 044302.

Rheology of polymer–carbon nanotube composites melts

M. R. NOBILE, University of Salerno, Italy

Abstract: The knowledge of the rheological properties of molten polymer–carbon nanotubes (CNT) composites is fundamental to the comprehension of their dynamics and microstructure. The linear viscoelastic behaviour of polymer–CNT composites has been found to be extremely sensitive to the interaction between nanotubes and polymer chains in the melt, dispersion state, aspect ratio and alignment of nanotubes in the nanocomposites. The rheological behaviour of polymer–CNT composites melts was also examined in steady-shear and uniaxial elongational flows, to investigate their processing conditions. Finally, the role of CNTs in the flow-induced crystallization of polymer nanocomposites has been analyzed.

Key words: carbon nanotubes, multi-walled carbon nanotubes, polymer composites, rheology, viscoelasticity.

15.1 Introduction

The knowledge of the rheological properties of molten polymer carbon nanotubes (CNT) composites is fundamental to both their processing and the comprehension of their microstructure and dynamics. Processing of polymer–CNT composites requires, thus, information on the rheological properties which depend on the interactions between nanotubes and polymer chains.

The linear viscoelastic behaviour of polymer–CNT composites has recently been investigated in the literature since it was found to be extremely sensitive to the CNT–polymer composites microstructure. Carbon nanotubes, due to their extremely high aspect ratio (length-to-diameter ratio) up to 1000, have the ability to affect the rheological properties at very low loadings, with a dramatic increase in the storage and complex viscosity and the detection of an apparent yield stress at low frequencies. The increase in the carbon nanotube content, in fact, produces a change from a viscous fluid to a solid-like behaviour in the polymer nanocomposites, due to the presence of a percolated network structure that creates additional contributions to nanocomposite viscoelasticity. The linear viscoelastic behaviour is also related to the dispersion state, the aspect ratio and the alignment of nanotubes in the nanocomposites.

Processing conditions, however, are characterized by non-linear viscoelastic behaviour. The rheological behaviour of polymer–CNT composites melts was, then, examined in shear and uniaxial elongational flows. The steady-state shear viscosity flow curves have been investigated in the literature to verify the possibility of processing the polymer–CNT composites melts at high shear rates using

conventional equipment. On the other hand, the first normal stress difference was studied for polymer–CNT composites to gain a measure of the stored elastic energy during flow, that is related to the die swell phenomenon which usually is a problem in polymer melts processing. The elongational viscosity measurements gave indications of the flow behaviour of the polymer–CNT composites in melt spinning, film blowing, and blow molding processing. The main rheological features shown by polymer–CNT composites melts are reported in the literature also for carbon nanotube suspensions, as well as for carbon nanofibre composites.

The role of multi-walled carbon nanotubes in the flow-induced crystallization of nanocomposites has recently been studied by means of rheology and the literature results showed that the rheological measurements are particularly suitable when determining the effects of shear and MWNT on the crystallization behaviour of polymer–CNT composites.

15.2 Linear rheological properties of polymer–carbon nanotube (CNT) composites

The viscoelastic behaviour in the linear regime is specified if the relaxation modulus, $G(t)$, is known as a function of time for times from zero to infinity (Ferry, 1980; Dealy and Larson, 2006). However, due to instrument limitations, it is difficult to track the very rapid initial decay of the stress upon the classical step–strain experiment (i.e. a practically instantaneous deformation) and to obtain the completely relaxed behaviour. In order to characterize the viscoelastic behaviour of polymer melts, oscillatory shear experiments are often used. In these experiments the sample is subjected to a homogeneous deformation at a varying shear strain or shear stress. The response is linear if the strain amplitude is sufficiently small, and the resulting stress is also sinusoidal. The dynamic tests results are usually reported in terms of the storage, $G'(\omega)$, and loss moduli, $G''(\omega)$, as a function of frequency.

Oscillatory shear mode tests within the linear viscoelastic range have recently been used by different authors to study the melt rheological properties of polymer–CNT composites since these tests have been found to be extremely sensitive to the CNT–polymer composites structure. Recent works showed that the addition of small amounts of CNTs in a polymer matrix can produce significant changes in their viscoelastic properties. The storage and the loss moduli are, indeed, strongly influenced by the nanotube content, interactions between nanotubes and polymer chains in the melt state, dispersion, alignment, and percolation state of CNTs within the composite.

15.2.1 Oscillatory shear measurements

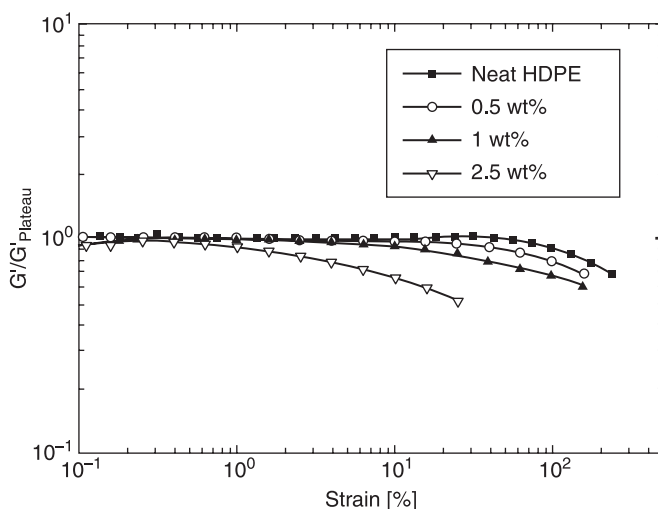
In order to gain accurate knowledge of the relaxation behaviour of polymer–CNT composites, it is necessary to have oscillatory shear data over the broadest possible

frequency range. The melt viscoelastic properties of different polymer–CNT composites were determined in the literature, using strain-controlled and/or stress-controlled rotational rheometers where the strain or stress amplitude was selected to be within the linear viscoelastic range. Care must be taken to verify that the measured moduli represent linear behaviour. To determine the maximum strain for linear behaviour, it is, therefore, necessary to carry out an oscillatory amplitude sweep test. The moduli will start to decrease at the strain when the behaviour becomes nonlinear. This amplitude represents the critical deformation, γ_c , characterizing the limit of the linear viscoelastic regime.

The upper limit of the linear viscoelastic range was found to be strongly dependent on the nanotube content in polymer–CNT composites (Mitchell *et al.*, 2002; Pötschke *et al.*, 2002, 2003, 2004; Du *et al.*, 2004; Abdel-Goad and Pötschke, 2005; Handge and Pötschke, 2007; Nobile *et al.*, 2007; Wu *et al.*, 2007a).

In Fig. 15.1, strain-sweep results obtained by Nobile *et al.* (2007) for multi-walled carbon nanotubes (MWNT) in high density polyethylene (HDPE) composites with several CNTs concentrations are reported at the frequency $\omega = 0.1$ rad/s. The MWNTs were synthesized by chemical vapour deposition (CVD) at CSIRO (Commonwealth Scientific and Industrial Research Organization, Australia) with an average diameter of 50 nm and a length up to 100 μm .

The high density polyethylene (HDPE0790) was supplied by Qenos, with the average molecular weight, M_w of 52 570 g/mol. The nanocomposites were



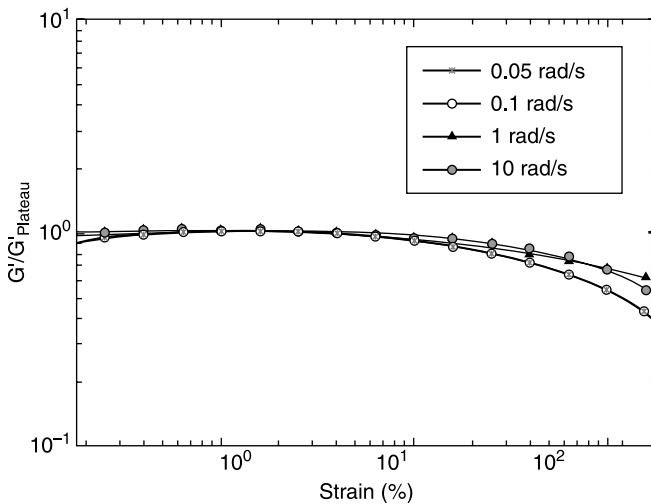
15.1 Storage modulus (G') normalized to plateau value vs. strain (γ) at $\omega = 0.1$ rad/s for MWNT/HDPE0790 composites and pure HDPE0790 at $T = 200$ °C (Nobile *et al.*, 2007. Reproduced by permission of WILEY-VCH, Copyright© 2007, WILEY-VCH Verlag GmbH & Co.).

prepared by melt mixing in a micro-twin screw extruder (Haake Minilab Rheomex CTW5), provided with a re-circulating channel. After the melt blending process, an average length of 7 μm for the MWNT nanotubes was determined by SEM measurements of MWNTs emerging from the dissolved composite; then, the aspect ratio of the MWNTs after melt compounding was estimated to be about 140 (Morcom, 2008).

The data reported in Fig. 15.1 show that the linear viscoelastic limit is 40% for the neat HDPE, while it dramatically reduces to 5% with the inclusion of 1 wt% MWNT, and it further reduces to 1% when 2.5 wt% MWNT is added into the composite.

In order to verify if a frequency effect on the linear viscoelastic limit occurs over the frequency range of interest, the strain sweep measurements were carried out at different frequencies on the 1 wt% MWNT–HDPE0790 nanocomposite. The results, reported in Fig. 15.2, show that the upper limit of the linear viscoelastic behaviour is independent of the applied frequency, since the storage modulus starts to decrease at a strain of $\sim 5\%$ for all the tested frequencies.

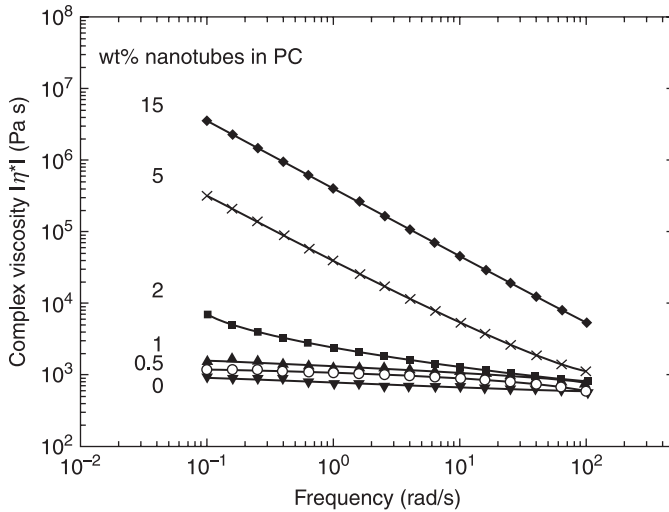
The oscillatory shear measurements in the frequency domain, reported in the literature for different polymer–CNT composites, have been, therefore, carried out at low strains within the linear viscoelastic range. Pötschke *et al.* (2002) first reported the melt oscillatory shear behaviour of MWNT nanocomposites. In their paper, the viscoelastic rheological properties of polycarbonate (PC)



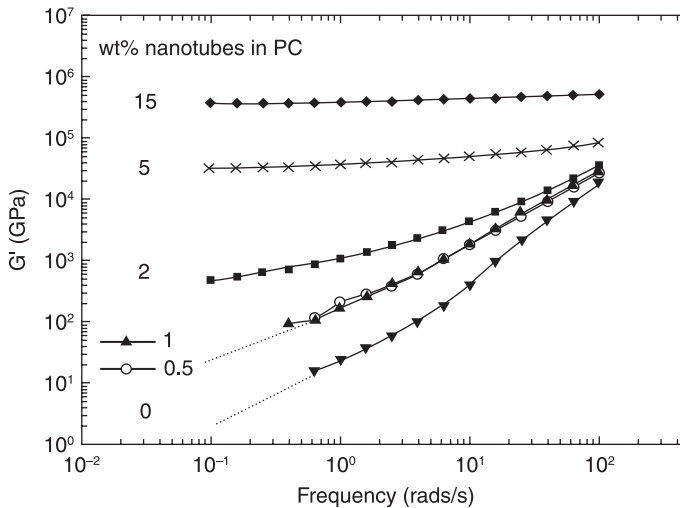
15.2 Storage modulus (G') normalized to plateau value vs. strain (γ) at different frequencies for the 1 wt % MWNT/HDPE0790 composite at $T = 200\text{ }^{\circ}\text{C}$ (Nobile *et al.*, 2007. Reproduced by permission of WILEY-VCH, Copyright© 2007, WILEY-VCH Verlag GmbH & Co.).

nanocomposites with MWNTs (diameter of about 10–15 nm and lengths 1–10 μm), obtained by melt extrusion, were investigated and their results are reported in Figs 15.3, 15.4 and 15.5. The results reported in Fig. 15.3 show that the complex viscosity increases with the nanotube content. The authors pointed out that this event is most pronounced at low frequencies, with the relative effect diminishing with increasing frequency due to the strong shear thinning behaviour of the high CNT content composites. The rheological features of the polymer–CNT composites were found to be in agreement with literature results for fibre-reinforced composites (Kataoka *et al.*, 1978; Kitano *et al.*, 1980, 1981, 1984; Utracki, 1987; Dealy and Wissbrun, 1999). Differently from the common polymer filled systems, however, Pötschke *et al.* revealed that the flow behaviour of the pure PC is dramatically modified with the inclusion of only 2 wt% CNT, a filler content much lower than that of traditional fibre-reinforced composites. The rheological results showed, therefore, that the carbon nanotubes, once dispersed into polymer matrices, can affect the rheology of the nanocomposite at relatively small concentrations, analogously to other physical properties, such as electrical, thermal, and mechanical properties. Indeed, the viscosity curves shown in Fig. 15.3 for the nanocomposites with 0.5 and 1 wt% nanotubes in polycarbonate are characterized by a Newtonian plateau at low frequencies, similar to the pure PC, while at 2 wt% CNT content the viscosity curve shows a much steeper slope at low frequencies. Compared to results reported in literature by Lozano *et al.* (2001a, 2004) for vapour-grown carbon nanofibres, VGFCs (diameter in the range 50–200 nm), the increase in viscosity with CNT composition shown by Pötschke *et al.* (2002) is much higher. The enhancement in complex viscosity, at a given filler content, was attributed by the authors to the much higher aspect ratio, L/D , of the carbon nanotubes ($L/D \sim 100\text{--}1000$) versus the aspect ratio of the carbon fibres used by Lozano *et al.* ($L/D \sim 10\text{--}100$). The viscosity increase, therefore, is higher, the larger the aspect ratio of the filler is.

The increase in complex viscosity with CNT content was mostly caused by a dramatic increase in the storage modulus, G' , as shown in Fig. 15.4. Again, the effect of the CNT inclusion was much higher at the low frequencies than at high frequencies. Starting at about 2 wt% nanotubes, G' became nearly independent of frequency at low frequency. The presence of a plateau modulus at low frequencies was interpreted by the authors in terms of an interconnected structure of anisometric fillers that provides an apparent yield stress, reported in the literature also for conventionally filled polymers. The authors regarded the critical composition of 2 wt% nanotubes as a rheological percolation composition. At higher MWNT concentrations, an enhanced elasticity was detected due to more pronounced connectivity. A modified Cole–Cole plot (Han and Kim 1987; Nakayama and Harrel 1987) was used to explore structure differences in the nanocomposite. In this kind of plot the storage modulus, G' , is reported versus the loss modulus, G'' , with frequency as a parameter. Curves of $\log G'$ versus $\log G''$ should superimpose if the microstructure does not change. In the PC–MWNT

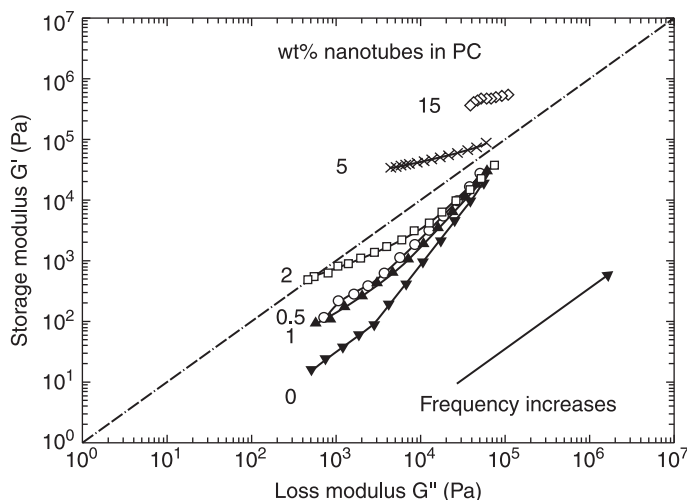


15.3 Complex viscosity of nanotube-filled polycarbonate at 260 °C (Pötschke *et al.*, 2002. Reproduced by permission of Elsevier, Copyright© 2002, Elsevier Ltd. All rights reserved.).



15.4 Storage modulus G' of nanotube-filled polycarbonate at 260 °C (Pötschke *et al.*, 2002. Reproduced by permission of Elsevier, Copyright© 2002, Elsevier Ltd. All rights reserved.).

composites, it was found that G' , for a given G'' , increases with increasing CNT content (Fig. 15.5); Pötschke *et al.* (2002) suggested that the shift and the change in slope of the storage modulus versus the loss modulus curves were indicative of significant changes in the microstructure with the inclusion of nanotubes. The



15.5 Storage modulus G' as function of loss modulus G'' of nanotube-filled polycarbonate at 260 °C (Pötschke *et al.*, 2002. Reproduced by permission of Elsevier, Copyright© 2002, Elsevier Ltd. All rights reserved.).

rheological response was found, then, to be very sensitive to the interconnectivity of the nanotubes.

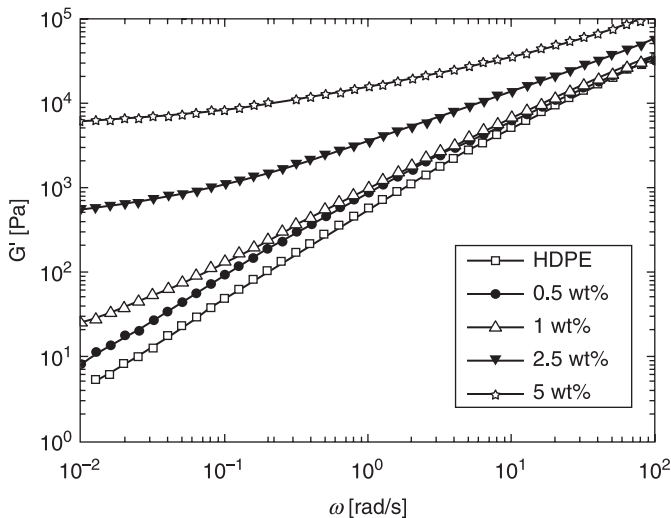
Similar rheological results have been reported in various polymer–CNT composites, in matrices as polystyrene (Mitchell *et al.*, 2002; Kota *et al.*, 2007), polypropylene (Kharchenko *et al.*, 2004; Seo and Park, 2004; Xu *et al.*, 2008; Wu *et al.*, 2008), polycarbonate (Pötschke *et al.*, 2004; Abdel-Goad and Pötschke, 2005; Sung *et al.*, 2006; Satapathy *et al.*, 2007), poly(methyl methacrylate) (Du *et al.*, 2004), polyethylene (Zhang *et al.*, 2006b; Nobile *et al.*, 2007; Valentino *et al.*, 2008), poly(ethylene oxide) (Song, 2006a), poly(ethylene terephthalate) (Hu *et al.*, 2006), poly(butylene terephthalate) (Wu *et al.*, 2007a), polyamide (Bhattacharyya *et al.*, 2004; Meincke *et al.*, 2004; Schartel *et al.*, 2005; Bhattacharyya and Pötschke, 2006), poly(ethylene 2,6-naphthalate) (Kim and Kim, 2006), blends of polyamide-6 and acrylonitrile-butadiene-styrene (PA6–ABS) (Bose *et al.*, 2007, 2008), polycaprolactone (Mitchell and Krishnamoorti, 2007; Wu *et al.*, 2007b), epoxy resins (Huang *et al.*, 2006; Song and Youn, 2005; Rahatekar *et al.*, 2006).

15.2.2 The rheological percolation threshold

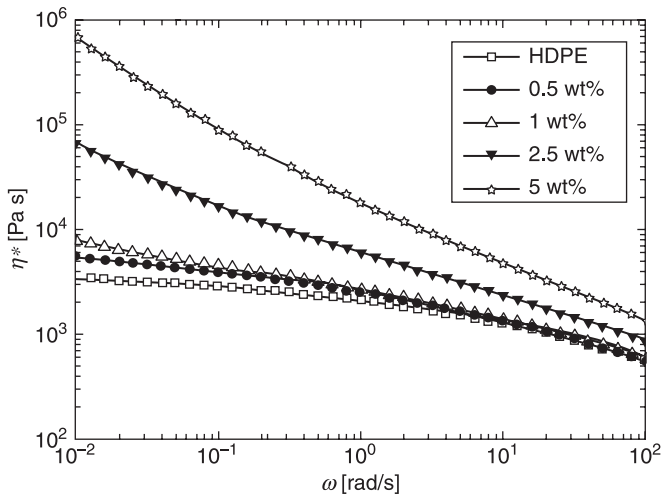
The dependence of low frequency viscoelastic parameters on CNT loading has largely been studied and discussed in the literature for different polymer–CNT composites, since the rheological experiments are very sensitive to the percolation phenomenon.

In Figs 15.6 and 15.7, the frequency response, in terms of the storage modulus and complex viscosity, is reported for the MWNT–HDPE0390 nanocomposite and the neat HDPE0390 (M_w of $\sim 60\,000$ g/mol) investigated by Nobile and co-workers (Nobile *et al.*, 2007; Valentino, 2008; Valentino *et al.*, 2008) in the range 0.01–100 rad/s at $T = 200^\circ\text{C}$. The strain of 0.2 % for the 2.5 wt% MWNT–HDPE0390 composite, and of 1% for the other nanocomposites and the neat matrix were chosen to guarantee the linear viscoelastic behaviour.

In Fig. 15.6, it is shown that the HDPE neat matrix is fully relaxed at low frequencies and exhibits typical terminal behaviour with G' scaling about as ω^2 . However, this terminal behaviour is gradually modified with the inclusion of the MWNTs; the dependence of G' on the frequency first weakens at 0.5 and 1 wt% nanotube content, and then a plateau in G' at 2.5 wt% nanotube content is clearly detected. Moreover, at this MWNT percentage, the storage modulus value is increased more than two orders of magnitude compared to the corresponding G' values of the neat HDPE. The presence at low frequencies of a plateau in G' at 2.5 wt% MWNT content can be attributed to the formation of a percolation network in the nanocomposite. An evident change in the viscoelastic behaviour is then recorded between 1 and 2.5 wt% nanotube content, where large-scale polymer relaxations in the nanocomposites are restrained by the presence of the nanotubes and the rheological percolation threshold can be identified, in agreement with the literature (Mitchell *et al.*, 2002; Pötschke *et al.*, 2002, 2004; Du *et al.*, 2004; Kharchenko *et al.*, 2004; Seo and Park, 2004; Song and Youn, 2005;



15.6 Storage modulus (G') vs. frequency (ω) for MWNT–HDPE0390 composites and pure HDPE0390 at $T = 200^\circ\text{C}$ (Valentino *et al.*, 2008. Reproduced by permission of Elsevier, Copyright© 2008, Elsevier B.V.).



15.7 Complex viscosity (η^*) vs. frequency (ω) for the MWNT–HDPE0390 composites and the pure HDPE0390 at $T = 200\text{ }^\circ\text{C}$ (Valentino *et al.*, 2008. Reproduced by permission of Elsevier, Copyright© 2008, Elsevier B.V.).

Hu *et al.*, 2006; Huang *et al.*, 2006; Rahatekar *et al.*, 2006; Song, 2006a; Zhang *et al.*, 2006b; Kota *et al.*, 2007; Wu *et al.*, 2007a, 2007 b; Xu *et al.*, 2008).

Non-terminal rheological response at low-frequencies, related to interconnected structures of anisometric fillers (Utracki, 1987; Dealy and Wissbrun, 1999; Shenoy, 1999), has already been reported on composites containing carbon nanofibres (Xu *et al.*, 2005; Wang *et al.*, 2006), layered silicates (Krishnamoorti and Giannelis, 1997; Giannelis *et al.*, 1999; Ren *et al.*, 2000; Krishnamoorti and Yurekli, 2001; Solomon *et al.*, 2001; Zhang and Archer, 2002; Wu *et al.*, 2005) and thermotropic liquid crystalline polymers (Guskey and Winter, 1991; Langelan and Gotsis, 1996; Romo-Uribe *et al.*, 1997; Somma and Nobile, 2004).

The complex viscosity versus the frequency curve for the nanocomposites and the pure HDPE are reported in Fig. 15.7. The Newtonian plateau, detectable in the viscosity curve of the pure HDPE, gradually disappears, increasing the MWNT content. The composite with 2.5 wt% nanotube content clearly shows a shear thinning behaviour with η^* values more than one order of magnitude higher than those of the pure HDPE at low frequencies. On the contrary, at high frequencies, typical of processing operations, the complex viscosity of the percolated nanocomposite is only slightly higher than that of HDPE, showing that the presence of MWNT, whether percolated or not, does not significantly influence the short-range relaxation of the HDPE chains. In agreement with literature findings (Pötschke *et al.*, 2002, 2004; Du *et al.*, 2004; Wu *et al.*, 2007a, 2007 b), our results suggested that the polymer–CNT composites have a similar processability to the pure matrix.

The van Gorp–Palmen plot (van Gorp and Palmen, 1998; Trinkle *et al.*, 2002) has been used in the literature to identify the rheological percolation threshold of polymer–CNT composites (Meincke *et al.*, 2004; Pötschke *et al.*, 2004; Kim and Kim, 2006; Lin *et al.*, 2006; Wu *et al.*, 2007a; Bose *et al.*, 2008; Valentino *et al.*, 2008). In this plot, the phase angle, δ , is plotted versus the absolute value of the complex modulus, G^* . In Fig. 15.8, the van Gorp–Palmen plot obtained by Nobile and co-workers for the MWNT–HDPE0390 nanocomposite is reported (Valentino *et al.*, 2008). At low complex moduli, the HDPE matrix shows the flow behaviour of a viscous fluid since the curve approaches a phase angle of 90° . A similar trend is also observed in the case of the 0.5 wt% MWNT inclusion in the HDPE matrix. On the other hand, increasing the MWNT content, a significant decrease of the phase angle at low complex modulus can be detected. The sample with 2.5 wt% resembles the behaviour of an elastic solid, whose corresponding equilibrium modulus can be determined extrapolating the curves to a phase angle of 0° . The rheological percolation threshold can, therefore, be determined between 1 and 2.5 wt% MWNT content, and the equilibrium moduli increase with increasing MWNT content. These results are in good agreement with the literature findings (Meincke *et al.*, 2004; Pötschke *et al.*, 2004; Lin *et al.*, 2006; Kim and Kim, 2006; Wu *et al.*, 2007a; Bose *et al.*, 2008).

Pötschke *et al.* (2004) found that the rheological percolation threshold is strongly dependent on the measurement temperature. A series of composites of polycarbonate (PC) with 23 different concentrations of MWNTs were tested by dynamic melt rheology at different temperatures between 170 and 280 °C. A clear change in the frequency dependence of dynamic moduli on MWNT content at low frequency was detected, and the van Gorp–Palmen plots revealed a change of the rheological percolation threshold from about 5 to 0.5 wt% MWNT by increasing the temperature from 170 to 280 °C. Recently Nobile and co-workers (Somma *et al.*, 2009; Iervolino, 2009) found a similar behaviour for nanocomposites based on high density polyethylene (MWNT–HDPE), as well as for nanocomposites based on isotactic poly(1-butene) (MWNT–PB).

The use of the van Gorp–Palmen plot assumes that a fluid–solid transition at the percolation of CNT within the composite occurred. In the literature it has been suggested that the CNT–polymer composites could reveal a new kind of physical gel (Liu *et al.*, 2003; Meincke *et al.*, 2004; Valentino, 2008; Valentino *et al.*, 2009) that can be described by the Winter–Chambon method developed for polymer gel systems (Winter and Chambon, 1986; Chambon and Winter, 1987; Winter and Mours, 1997). In cross-linking polymers Winter and Chambon hypothesized that at the gel point, the loss and storage modulus were congruent and proportional to ω^n over the whole range $0 < \omega < \infty$ of frequency, where n is the relaxation exponent ($0 < n < 1$). The rheological properties at the gel point can be described by the constitutive equation:

$$G(t) = S t^{-n} \quad [15.1]$$

The only material parameter in the constitutive equation is the strength S of the network at the gel point. The determination of the gelation can be obtained with a plot of the loss tangent, $\tan(\delta)$ versus the angular frequency (ω), the frequency independence of the loss tangent characterizes the gel point:

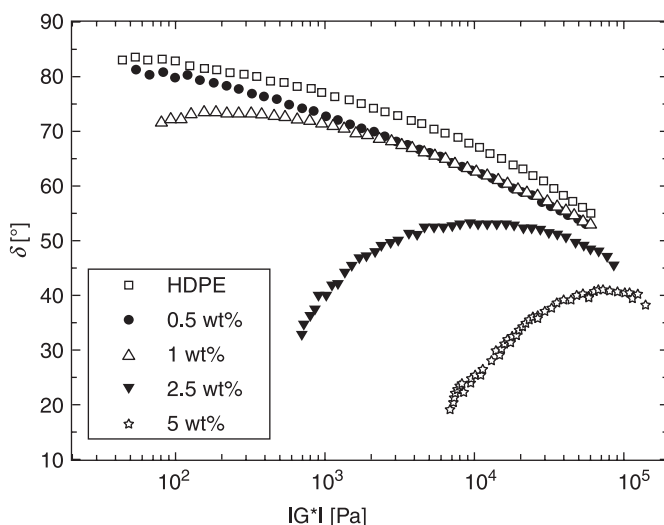
$$G''(\omega)/G'(\omega) = \tan(\delta) = \tan(n\pi/2) \quad [15.2]$$

Moreover, at the gel point, it is:

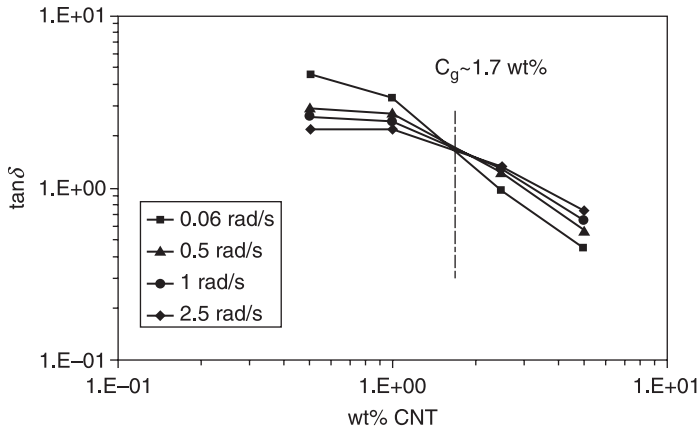
$$G'(\omega) = G''(\omega)/\tan(n\pi/2) = S \omega^n \Gamma(1 - n) \cos(n\pi/2) \quad [15.3]$$

where Γ is the gamma function.

The phase angle data, δ , for the MWNT–HDPE0390 nanocomposite obtained by Nobile and co-workers (Valentino *et al.*, 2008), and reported in Fig. 15.8, are shown in terms of $\tan(\delta)$ versus nanotube wt% content in Fig. 15.9. The multifrequency plot data show a decrease in the loss tangent with increasing MWNT concentration; this decrease is most pronounced at the lowest frequencies. The frequency independence of the loss tangent can be clearly observed at the cross-point that defines the gelation concentration for our MWNT–HDPE0390 nanocomposite, $c_g \sim 1.7$ wt%. The value $n = 0.67$ has also been calculated from Equation 15.2. The MWNT concentration of 1.7 wt%, represents, therefore, the rheological percolation threshold for the MWNT–HDPE0390 nanocomposite at 200 °C.



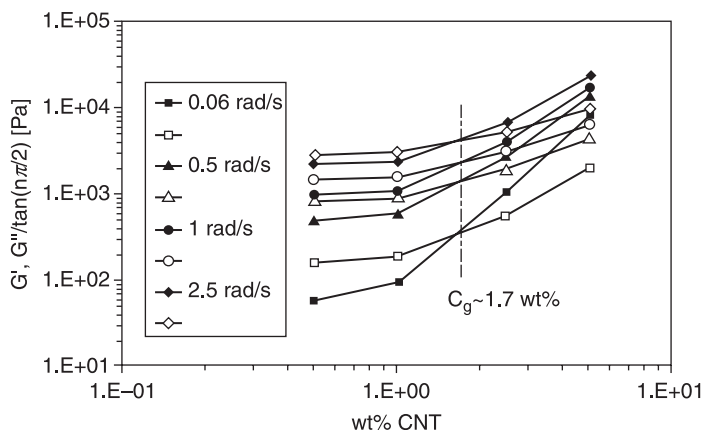
15.8 Phase angle (δ) vs. the absolute value of the complex modulus $|G^*|$ (van Gurp–Palmen plot) for the MWNT–HDPE0390 composites and pure HDPE at $T = 200$ °C (Valentino *et al.*, 2008. Reproduced by permission of Elsevier, Copyright© 2008, Elsevier B.V.).



15.9 Loss tangent ($\tan\delta$) vs. nanotube concentration for MWNT–HDPE0390 composites at $T = 200\text{ }^{\circ}\text{C}$.

The plot of G' and $G''/(\tan(n\pi/2))$ versus nanotube concentration at different frequencies, Fig. 15.10, can be used to determine the gel strength S as defined by Equation 15.1. The existence of a cross-over of G' and $G''/(\tan(n\pi/2))$ at the gel point, as suggested by Equation 15.3, identifies the value of G' at the gel point. Then, the strength $S = 1576\text{ Pa s}^n$ was calculated. The cross-over appears, as expected, at $c_g \sim 1.7\text{ wt}\%$. The S and n values obtained for the MWNT–HDPE0390 nanocomposite compare well with previous results obtained for gels by Winter and Mours (1997).

The electrical and rheological percolation thresholds have been discussed in the literature in terms of different types of network structures. At the electrical percolation threshold a sharp drop of orders of magnitude in the volume resistivity of the polymer composite occurs. Electrical conductivity depends on size, shape, content, dispersion and surface treatment of the fillers. The electrical percolation has been considered as an approximation for the geometrical percolation. In the work by Garboczi *et al.* (1995), the geometrical percolation threshold has been numerically computed by the percolation data for ellipsoids of revolution whose aspect ratio varied in a range of six orders of magnitude (1/2000–500). In particular, the percolation threshold for overlapping ellipsoids with aspect ratios ranging between 100 and 500 (i.e. the usual aspect ratio of carbon nanotubes dispersed in polymer nanocomposites) is approximately in the range 1.2–0.7 volume %. Indeed, the nanotubes do not always geometrically overlap when the electrical percolation is reached because at distances between the nanotubes between 5 and 10 nm the electron hopping/tunnelling mechanism can already occur. Compared to traditional fillers as well as to the carbon nanofibres, carbon nanotubes reach the electrical percolation threshold at much lower concentrations of carbon nanotube, due to their high aspect ratio.



15.10 Storage modulus (solid symbols) and loss modulus/ $\tan(n\pi/2)$ (open symbols) vs. nanotube concentration for MWNT–HDPE0390 composites at $T = 200\text{ }^{\circ}\text{C}$.

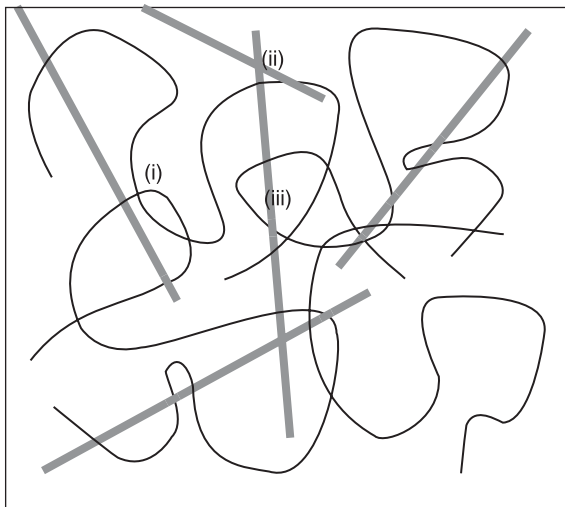
To obtain electrical percolation in PP, a carbon black content of 10–20 wt% was necessary (Yui *et al.*, 2006), and a similar percolation content of 9–18 wt% for the vapour-grown carbon nanofibres (with aspect ratio 10–100) always in PP has been reported by Lozano *et al.* (2001; Lozano and Barrera, 2001). On the other hand, Seo and Park (2004) and Lee *et al.* (2007, 2008) showed that the electrical percolation threshold was formed at the lower content of 1–2 wt% when multi-walled carbon nanotubes are added to the PP matrix. The lowest electrical percolation threshold of 0.04 wt% of CNT was measured by Sandler *et al.* (1999) for catalytically-grown carbon nanotubes dispersed in an epoxy matrix and by Krause *et al.* (2010) for melt mixed PA6.6–MWNT composites with MWNT produced by an aerosol-CVD method. The formation of electrical percolating networks in MWNT epoxy composites at very low MWNT contents was also detected by Martin *et al.* (2004). A detailed discussion of the influence of thermorheological history on electrical properties of polymer–CNT composites can be found in Chapter 10 of the present volume.

On the other hand, polymer chain immobility determines the rheological percolation threshold. Pötschke *et al.* (2004) and Du *et al.* (2004) independently reported that different tube–tube distances are required for rheological or electrical percolation. In Fig. 15.11, the illustration of the network types suggested by Pötschke *et al.* (2004) is shown. The authors indicate that three networks are expected: (i) the temporary polymer network due to polymer entanglements; (ii) the carbon nanotube network; and (iii) a combined carbon nanotube–polymer network. The last one is assumed to be formed by ‘entanglements’ between the polymer chains and the nanotubes when two nanotubes meet each other within the distance smaller than the radius of gyration of the polymer chain. At low frequencies, the

superposition of the entangled polymer network and the combined carbon nanotube–polymer network is assumed to dominate the rheological percolation rather than the carbon nanotube network. The contribution of the geometrical CNT network to the rheological properties can, then, be almost ignored. The low frequency plateau in G' was thus explained by the authors with the hypothesis that the disentanglement time for the combined carbon nanotube–polymer network is longer than the characteristic time for polymer–polymer entanglements. Pötschke *et al.* also suggested that the temperature dependence for the rheological percolation threshold, found in the MWNT–PC composite, cannot be explained by a classical liquid–solid transition but may be justified in terms of the combined carbon nanotube–polymer network.

In general, therefore, differences in electrical and rheological percolation threshold would be expected due to the smaller nanotube–nanotube distance required for electrical conductivity as compared to that required to impede chain mobility (i.e. a rheological threshold lower than the electrical threshold would be expected). Moreover, the rheological threshold has been proven to depend on temperature.

The rheological percolation thresholds, evaluated for different polymer–CNT composites, have been compared in the literature with the corresponding electrical percolation thresholds and some examples from the literature results are reported in Table 15.1. The results show that, depending on measurement conditions, the rheological percolation threshold is found to be lower, higher or at the same composition as compared to the electrical percolation threshold.



15.11 Illustration of the different network types: (i) temporary polymer–polymer network; (ii) nanotube–nanotube network; (iii) combined polymer–nanotube network (Pötschke *et al.*, 2004. Reproduced by permission of Elsevier, Copyright© 2004, Elsevier Ltd. All rights reserved.).

Table 15.1 Summary of the rheological and electrical percolation thresholds results of the reviewed publications

Matrix	Carbon nanotube	Rheological percolation threshold (nanotube content)	Electrical percolation threshold (nanotube content)	References	Nanocomposite preparation and remarks
PP	MWNT	In the range 1–2 wt%	In the range 1–2 wt%	Seo and Park (2004)	• Composite prepared by melt-blending
PP	MWNT	In the range 1–2 wt%	In the range 1–2 wt%	Lee <i>et al.</i> (2007, 2008)	<ul style="list-style-type: none"> • MWNT chemically functionalized through heat treatments • Composites were prepared by melt compounding with a twin-screw extruder • Homogeneous dispersion of nanotubes in i-PP • Strong interaction created by heat treatment of MWNTs because oxygen and carboxyl group generated by the heat treatment reacted with hydrogen atoms of PP matrix
PP	MWNT	In the range 0.25–1 vol%	In the range 0.25–1 vol%	Kharchenko <i>et al.</i> (2004)	• Simultaneous measurements of the electrical and rheological percolation threshold at $T = 200\text{ }^{\circ}\text{C}$
PMMA	SWNT	~0.12 wt%	~0.39 wt%	Du <i>et al.</i> (2003, 2004)	<ul style="list-style-type: none"> • Composites prepared via coagulation method • Wet purified SWNT • Uniform dispersion of the nanotubes bundles in the matrix

PET	MWNT	~0.6 wt% (T = 265 °C)	~0.9 wt% at room temperature	Hu <i>et al.</i> (2006)	<ul style="list-style-type: none"> Composites prepared via coagulation method Encapsulation of MWNT by PET Good interfacial interaction between MWNT and PET chains
PA6	MWNT	In the range 2–4 wt% (T = 260 °C)	In the range 4–6 wt% at room temperature	Meinke <i>et al.</i> (2004)	<ul style="list-style-type: none"> Composites prepared via coagulation method Co-rotating twin-screw extruder
PA6	SMA* encapsulated SWNT	~1 wt%	~1 wt%	Pötschke and co-workers (Bhattacharyya and Pötschke, 2006)	<ul style="list-style-type: none"> Melt mixed composites in a conical twin-screw extruder Reactive compatibilization Improved dispersion of encapsulated nanotubes in the matrix compared to untreated SWNT Enhanced interfacial adhesion SMA surface layer was thin enough to allow electron hopping among the SWNT bundles.
PA 12	SMA* encapsulated SWNT	~3%		Pötschke and co-workers (Bhattacharyya <i>et al.</i> , 2004)	<ul style="list-style-type: none"> Melt mixed composites in a conical twin-screw extruder The SMA made the composites insulating
PA6-ABS blends	MWNT	(a) In the range 1–2 wt% (b) In the range 2–3 wt%	(a) In the range 3–4 wt% (b) In the range 3–4 wt%	Bose <i>et al.</i> (2008)	<ul style="list-style-type: none"> Melt mixed composites in a conical twin-screw microcompounder (a) Purified MWNTs (p-MWNTs) (b) ~NH₂ functionalized MWNTs (f-MWNTs)
PS	MWNT	~2 vol%	~8 vol%	Kota <i>et al.</i> (2007)	<ul style="list-style-type: none"> Composites prepared by a solvent evaporation method

Table 15.1 Continued.

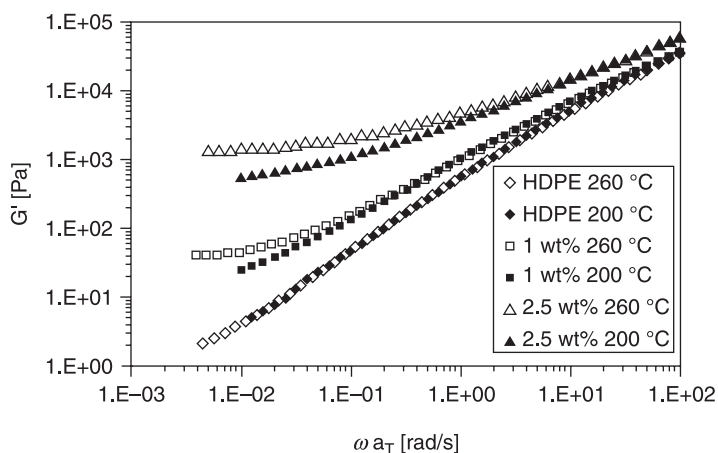
Matrix	Carbon nanotube	Rheological percolation threshold (nanotube content)	Electrical percolation threshold (nanotube content)	References	Nanocomposite preparation and remarks
PC	MWNT	5–0.5 wt% in the range 170–280 °C	1 wt% at room temperature	Pötschke and co-workers (2002, 2004)	<ul style="list-style-type: none"> Composites prepared by melt mixing dilution of a masterbatch of 15 wt% MWNT in PC
UHMWPE	SWNT	~1.5 wt%	~4 wt%	Zhang <i>et al.</i> (2006b)	<ul style="list-style-type: none"> The dispersion is obtained by spraying an aqueous solution of SWNT onto a fine UHMWPE powder and then composites were prepared by melt processing the powder with a co-rotating twin-screw extruder
UHMWPE	SWNT	~0.6 wt%	~0.6 wt%	Zhang <i>et al.</i> (2006a)	<ul style="list-style-type: none"> The dispersion is obtained by spraying an aqueous solution of SWNT onto a fine UHMWPE powder and then dissolving in xylene. Solution-crystallized films were obtained
HDPE	MWNT	~5 wt%	~5 wt%	Han <i>et al.</i> (2009)	<ul style="list-style-type: none"> Composites prepared by melt mixing with twin screw extruder
III generation linear MDPE (metallocene catalysed)	MWNT	~7.5 wt%	~7.5 wt%	McNally <i>et al.</i> (2005)	<ul style="list-style-type: none"> Composites prepared by melt-blending with mini twin screw extruder Good dispersion of CNT in the matrix Alignment of CNT in the flow direction Enhanced interfacial adhesion 16 orders of magnitude increasing of the electrical conductivity at the percolation threshold

HDPE	MWNT	In the range 1–2.5 wt%	In the range 1–2.5 wt%	Nobile and co-workers (Neitzert <i>et al.</i> , 2008; Valentino <i>et al.</i> 2008)	<ul style="list-style-type: none"> Composites prepared by melt mixing with a mini twin screw extruder Good dispersion of CNT in the matrix
LDPE	MWNT	~2.5 wt%	In the range 1–2.5 wt%	Nobile and co-workers (Neitzert <i>et al.</i> , 2008; Valentino <i>et al.</i> 2008)	<ul style="list-style-type: none"> Composites prepared by melt mixing with a mini twin screw extruder
PPS	MWNT	~3 wt%	~3 wt%	Han <i>et al.</i> (2009)	<ul style="list-style-type: none"> Composites melt mixed with a twin screw extruder Homogeneous dispersion of CNT in the matrix

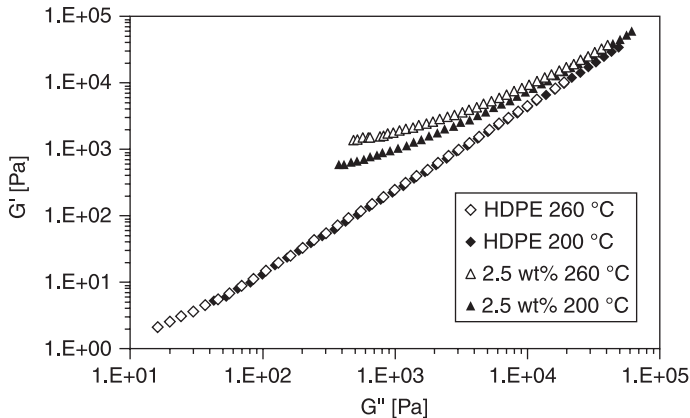
Note: Styrene maleic anhydride copolymer (SMA).

Due to the presence of the combined carbon nanotube–polymer network, the time–temperature superposition (TTS) may be invalid for the polymer–CNT composites. The G' data for the MWNT–HDPE0390 composites obtained by Nobile and co-workers (Valentino, 2008; Valentino *et al.*, 2008) at the temperatures of 200 and 260 °C are here shifted to the reference temperature of 200 °C to verify the validity of the TTS principle with the inclusion of CNT (Fig. 15.12). As expected, in the case of the neat HDPE, the master curve was obtained. On the contrary, the data for the nanocomposites, although showing a good superposition at high frequency due to the dominant polymer chain dynamics, could not be superimposed at low frequencies. This event was already evident at 1 wt% of MWNT, a composition lower than the rheological thresholds of 1.7 and 1.2 wt% detected at $T = 200$ and 260 °C, respectively (Valentino, 2008; Somma *et al.*, 2009). Finally, this result is verified by plotting the G' vs. the G'' data in a modified Cole–Cole plot (Fig. 15.13). The viscoelastic G' and G'' are quantities not containing units of time, this implies that a plot of G' vs. G'' will be temperature independent and the isothermal curves merge into a common line if the TTS holds. The results show that the curves do not merge for compositions near and beyond the percolation threshold, confirming the previous results for TTS. Such behaviour was also detected in MWNT–PB composites (Iervolino, 2009), in MWNT–PC (Pötschke *et al.*, 2004; Handge and Pötschke, 2007), as well as in MWNT–Poly(butylenes terephthalate) and MWNT–PCL composites (Wu *et al.*, 2007a, 2007 b).

The invalidity of the TTS principle and of the modified Cole–Cole plot at low frequencies confirms that the carbon nanotube network interpenetrating the polymer matrix creates additional contributions to nanocomposite viscoelasticity.



15.12 Storage modulus (G') vs. frequency (ω) for MWNT–HDPE0390 composites and pure HDPE0390 at 200 °C and 260 °C shifted at $T_{\text{ref}} = 200$ °C.



15.13 Storage modulus (G') vs. loss modulus (G'') for 2.5 wt% MWNT–HDPE0390 composites and pure HDPE0390 at 200 °C and 260 °C.

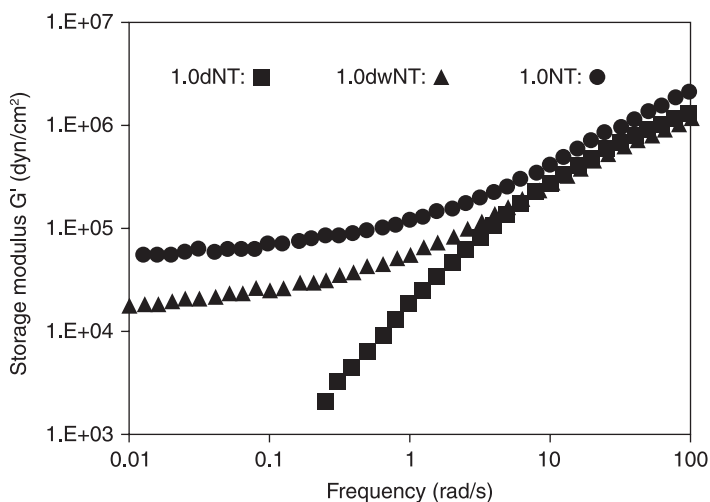
15.2.3 The effect of CNT dispersion, aspect ratio and alignment in the polymer matrix on the rheology of polymer–CNT composites

The issues of a stable homogeneous dispersion of the carbon nanotubes in the host polymer matrix and of an adequate interfacial adhesion between the phases are fundamental to obtain the transfer of the superior properties of the CNTs to the nanocomposites, allowing significant improvements in the electrical conductivity and in the mechanical properties of the resulting composites. The synthesis procedures often result in highly entangled carbon nanotubes that form big primary agglomerates. The presence of strong inter-tube van der Waals forces hinders the uniform dispersion of CNTs through the polymer matrix, also due to the lack of chemical compatibility between the polymers and the carbon nanotubes. To characterize the nanotube dispersion in nanocomposites, microscopy (i.e. optical, scanning and transmission electron microscopy, atomic force microscopy), Raman spectroscopy and small angle neutron scattering techniques are commonly used. Melt state rheology has also proved to be a useful tool to obtain indications about the state of dispersion of CNTs in polymer composites. The rheological properties of CNT–polymer composites, indeed, strongly depend on the interactions between nanotubes and polymer chains in the melt that can be changed by modifying nanotube surfaces chemically or physically and/or modifying the polymer matrix by functional reactive groups. Functionalization of CNTs, covalent or non-covalent, may help the homogeneity of dispersion, interfacial compatibility with the matrix and the exfoliation of SWNTs bundles (Mitchell *et al.*, 2002; Bhattacharyya *et al.*, 2004; Du *et al.*, 2004, Bhattacharyya and Pötschke, 2006; Moniruzzaman and Winey, 2006; Mitchell and Krishnamoorti, 2007; Bose *et al.*, 2008, 2010). On the

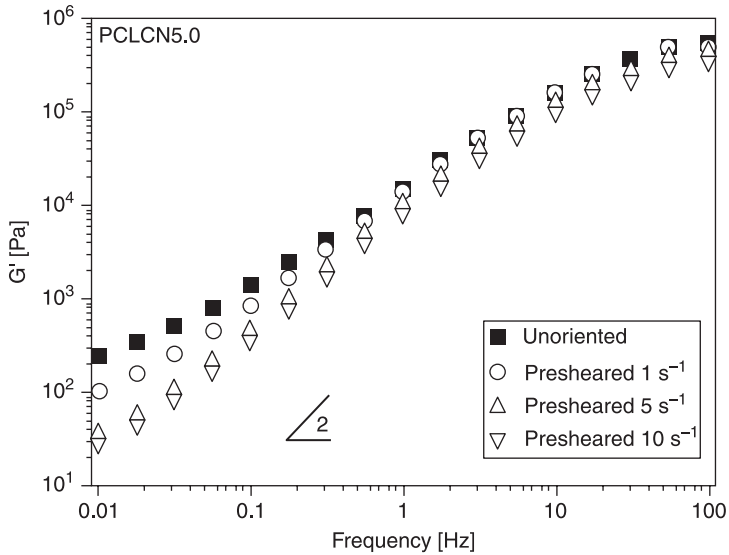
other hand, the length of the covalent functionalized MWNT can be shortened, due to the functionalization, compared to that of the untreated MWNTs, consequently, a decrease in properties of the composite can occur. Moreover, nanotube orientation in the composites and the aspect ratio of MWNTs also affect the rheological behaviour of polymer–CNT composites. Table 15.2 (where Fig. 15.14, Fig. 15.15 and Fig. 15.16 are mentioned) summarizes a comprehensive literature survey concerning the use of melt state rheology as a method to investigate the state of CNT dispersion and alignment in the host polymer matrix.

15.3 Non-linear rheological properties of polymer–carbon nanotube (CNT) composites

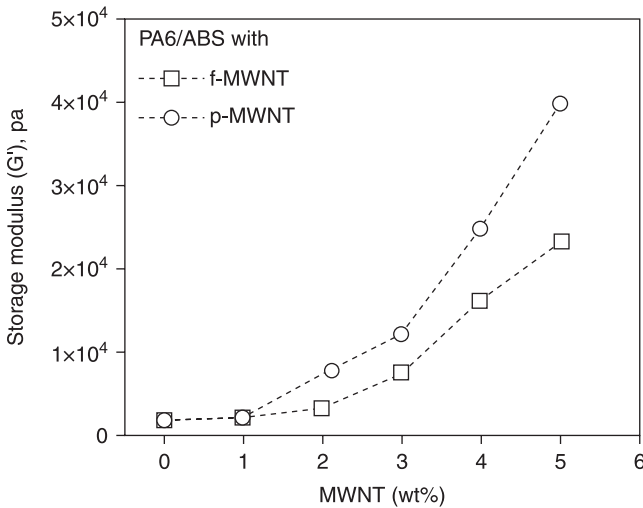
The linear oscillatory rheological analysis has suggested that the presence of a nanotube network interpenetrating the polymer matrix creates additional and significant contributions to nanocomposites' viscoelasticity. However, the polymer processing technologies are usually characterized by steady shear and elongational flows. Non-linear rheological measurements in terms of transient, steady shear, and elongational rheological investigations have been reported in the literature for different types of CNTs and suspending medium to gain further insight into the modifications of their internal structure during flows typical of processing condition.



15.14 Frequency response of the storage modulus for SWNT–PMMA nanocomposites with 1 wt% SWNT with improving nanotube dispersion from 1.0dNT (poor dispersion) to 1.0NT (good dispersion) (Du *et al.*, 2004. Reproduced by permission of American Chemical Society, Copyright© 2004, American Chemical Society.).



15.15 Dynamic storage modulus (G') for the PCLCN5.0 sample presheared at various shear rates (Wu *et al.*, 2007b. Reproduced by permission of Wiley Periodicals, Inc., Copyright© 2007, Wiley Periodicals, Inc.).



15.16 Comparison of storage modulus (at 15.7 rad/s) for blends with f-MWNT and p-MWNT (Bose *et al.*, 2008. Reproduced by permission of Wiley Periodicals, Inc., Copyright© 2008, Wiley Periodicals, Inc.).

Table 15.2 Summary of literature investigations on the rheological results related to the state of CNT dispersion and alignment in the host polymer matrix

Authors/ references	Materials	Dispersion/orientation change strategies	Main rheological results/remarks	Figures
Mitchell <i>et al.</i> (2002)	PS-SWNT	Pristine SWNTs and functionalized SWNTs	Functionalized SWNTs: – Improved state of dispersion of CNTs in the matrix – Rheological percolation threshold at ~1.5 wt% Pristine SWNTs: – Poor state of dispersion – Rheological percolation threshold >3 wt%	
Du <i>et al.</i> (2004)	PMMA-SWNT	Dried and wet purified SWNTs	<ul style="list-style-type: none"> • 1 wt% dried SWNT composites show poor nanotube dispersion and a terminal flow behaviour similar to the neat PPMA (nanotube-rich domains rather than a nanotube network) • Good dispersion of wet purified SWNTs in the matrix • 1 wt% wet SWNT composites are above the rheological percolation threshold 	Figure 15.14 (see also Table 15.1)
Pötschke and co-workers (Bhattacharyya <i>et al.</i> , 2004; Bhattacharyya and Pötschke, 2006)	PA12-SWNT and PA6-SWNT	Pristine SWNTs and SMA encapsulated SWNTs	<ul style="list-style-type: none"> • The wrapping of SWNT by SMA enhances the dispersion of the CNT in the matrix • The composites with SMA wrapping show higher G' moduli as compared to those without modifier 	(See also Table 15.1)
Song and Youn (2005)	Epoxy resins-MWNT	The dispersion states were altered depending upon the use of a solvent	<ul style="list-style-type: none"> • The CNT were first dispersed in ethanol • The CNT-ethanol solution was mixed with the epoxy resin and then the hardener was added • The composites with the solvent showed better dispersion and higher G' moduli as compared to those without solvent 	

Huang <i>et al.</i> (2006)	PDMS-MWNT	Study of the effect of mixing time on the nanotube dispersion	<ul style="list-style-type: none"> • The viscosity of the mixture had a direct correlation with the distribution of CNT in the matrix • The rheological results showed that a critical mixing time needs to be achieved to obtain satisfactory dispersion • Elastic gel of entangled nanotubes above the rheological percolation threshold (about 2–3 wt%) • A divergence of the MWNT–epoxy system viscosity versus temperature curve from the expected pattern was recorded • The use of a compatibilizer made the viscosity–temperature profile normal, indicating improved interactions between MWNTs and the epoxy matrix 	(See also Table 15.1)
Moldenaers and co-workers (Godara <i>et al.</i> , 2009)	Epoxy resin–CNT	The nanocomposites were heated from room temperature to about 140°C in order to mix the hardener and then to follow the curing cycle. Use of a compatibilizer	<ul style="list-style-type: none"> • Rheological data were indicative of a strong improvement in the dispersion of the SWNTs in the polymer when the surfactant was used 	
Mitchell and Krishnamoorti (2007)	PCL–SWNT	A surfactant capable of interacting with both the SWNTs and the polymer was used		
Sung <i>et al.</i> (2006)	PC–MWNT	The MWNTs were functionalized by treating with hydrogen peroxide	<ul style="list-style-type: none"> • The rheological properties of the PC–MWNT (H_2O_2 treated) composites increased compared to those of the PC–MWNT (untreated) composites 	
Lee <i>et al.</i> (2007)	PP–MWNT	Chemically functionalized MWNTs and two types of compatibilizers were investigated	<ul style="list-style-type: none"> • Rheological properties of PP–MWNT heat treated composites increased significantly compared with those of the PP–MWNT untreated composites 	
Song (2006b)	Poly(ethylene oxide)–CNT	Different surface-treated CNTs are prepared and investigated	<ul style="list-style-type: none"> • Acid-treated CNT nanocomposites possess the highest shear viscosities and storage moduli • These findings indicate that the acid-treated CNTs are well dispersed in the polyethylene oxide (PEO) 	

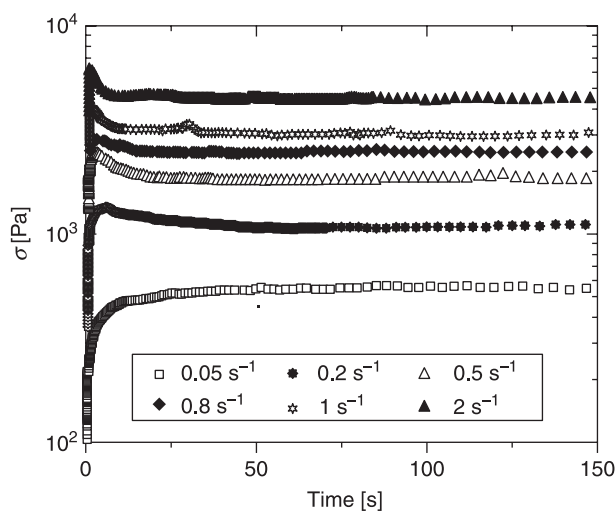
Table 15.2 Continued

Authors/ references	Materials	Dispersion/orientation change strategies	Main rheological results/remarks	Figures
Wu <i>et al.</i> (2007a)	PBT-MWNT	Functionalized carboxylic MWNTs and purified MWNTs	<ul style="list-style-type: none"> • A higher rheological percolation threshold for functionalized MWNTs is detected from dynamic modulus data • The rheological data indicate that the extent of reinforcement and state of dispersion are considerably improved for the functionalized MWNTs in PBT as compared to the purified MWNTs in PBT 	
Zhang <i>et al.</i> (2008)	PS-MWNT	Functionalized MWNTs, using strong acids and purified MWNTs	<ul style="list-style-type: none"> • The rheological data indicate higher viscosities and storage moduli for the surface-functionalized MWNT composites as compared to the crude MWNT composites • This event indicates that the functionalized MWNTs with strong acids are better dispersed in the matrix as compared to the crude MWNTs 	
Du <i>et al.</i> (2004)	PMMA-SWNT	Nanotube orientation by melt fibre spinning	<ul style="list-style-type: none"> • The authors found a decrease in G' with nanotube alignment, even though non-terminal behaviour was still detected 	(See also Table 15.1)
Wu <i>et al.</i> (2007b)	Poly (ϵ -caprolactone)-MWNT	Nanotube orientation by preshearing the composites	<ul style="list-style-type: none"> • The dynamic moduli significantly decrease with increasing the pre-shear rate • The percolation network was very sensitive to steady shear flow, in fact the MWNT oriented along the shear direction and no percolation was observed for the samples pre-sheared at the higher shear rates 	Figure 15.15

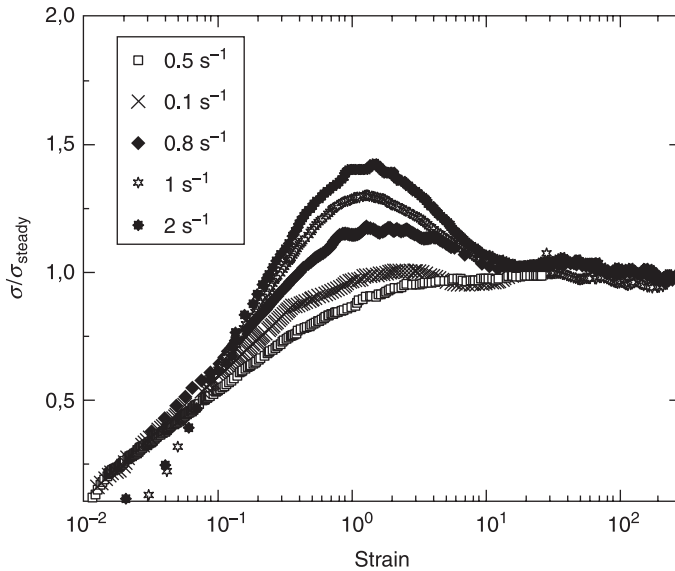
McNally <i>et al.</i> (2005)	PE-MWNT	Nanotube orientation by the extruder die geometry during the composite preparation	<ul style="list-style-type: none"> The extruder die may produce alignment of MWNT and reduce the number of entanglements so that a high rheological percolation threshold of 7.5 wt% MWNT content is measured. The authors pointed out that the alignment of MWNTs during melt flow may, in part, explain the lower percolation thresholds obtained for polymer-CNT composites prepared by solution mixing or <i>in situ</i> polymerization compared to the nanocomposites obtained by melt blending 	(See also Table 15.1)
Pötschke and co-workers (Bose <i>et al.</i> 2008)	MWNT-PA6-ABS	<p>(a) Purified MWNT (p-MWNT) L=1.5 μm; D=9.5 nm</p> <p>(b) $\sim\text{NH}_2$ functionalized MWNT (f-MWNT) L<1 μm; D=9.5 nm</p>	<ul style="list-style-type: none"> The functionalization process established a strong interfacial bonding between CNT and the matrix polymer at the expense of defects on the walls and shortening of MWNTs Higher G' values were measured for blends with p-MWNT as compared to blends with f-MWNT The rheological percolation threshold was 1–2 wt% in the case of p-MWNT and 2–3 wt% in the case of f-MWNT The authors pointed out that both the aspect ratio, L/D, and defects (due to functionalization) are responsible for the electrical percolation threshold, while the aspect ratio of the tubes plays a major role in controlling the flow behaviour. Therefore, the higher L/D of the purified p-MWNT determines the lower rheological percolation threshold of the corresponding composites. 	Figure 15.16 (see also Table 15.1)

15.3.1 The transient and the steady-shear viscosity

The transient shear stress (σ) response for the neat HDPE0790 (with $M_w = 52\,570$ g/mol, $M_w/M_n = 5.3$) and for MWNT–HDPE0790 nanocomposites with different CNT contents and at different shear rates is currently being investigated by Nobile and co-workers in start-up shear flow experiments using a strain-controlled ARES (TA) rheometer with a cone and plate geometry. The transient shear stress for the neat HDPE0790 at low shear rates gradually approached the steady state, while at higher shear rates an overshoot in σ appeared before it approached the steady state value. This overshoot is a typical non-linear response of the polymer related to the entanglement resistance to flow. In the case of the 2.5 wt% MWNT–HDPE0790 nanocomposite, that is in a percolated state, the overshoot already appears at the shear rate of 0.2 s^{-1} (Fig. 15.17), indicating that the CNT–polymer interaction contributes to the viscoelasticity of the HDPE matrix itself. Moreover, the transient shear stress is found to scale with strain, see Fig. 15.18, in agreement with results reported for the PBT–CNT composite by Wu *et al.* (2007a). Such scaling behaviour has been previously observed in the case of polymer–clay nanocomposites (Krishnamoorti and Giannelis, 1997; Solomon *et al.*, 2001; Wu *et al.*, 2005) as well as in the case of lyotropic (Doppert and Picken, 1987; Mewis and Moldenaers, 1987; Sigillo and Grizzuti, 1994) and thermotropic liquid crystalline polymers (Cocchini *et al.*, 1991; Guskey and Winter, 1991; Giles and Denn, 1994).

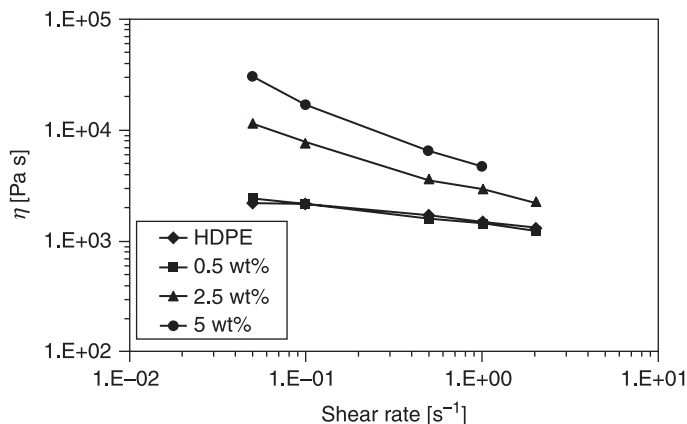


15.17 Transient shear stress (σ) for the 2.5 wt% MWNT–HDPE0790 composite at $T = 200\text{ °C}$.



15.18 Transient shear stress (σ) normalized to steady value vs. strain for the 2.5 wt% MWNT–HDPE0790 composite at $T = 200\text{ }^{\circ}\text{C}$.

The steady shear viscosity behaviour has been already reported for the MWNT–HDPE0390 nanocomposites (Somma *et al.*, 2008a, 2008b). Analogous results on the steady shear viscosity flow curves for the neat HDPE0790 and the MWNT–HDPE0790 are shown in Fig. 15.19. The data indicate that the inclusion of 0.5 wt% MWNT, below the percolation threshold, does not influence the flow behaviour of the neat HDPE. On the contrary, in the case of the 2.5 and 5 wt% MWNT–HDPE0790 composites (with a content of MWNT higher than the percolation threshold), at low shear rates, the steady shear viscosity shows values about one order of magnitude higher than those of the neat HDPE. On increasing the shear rates, this effect remarkably decreases, due to a shear thinning behaviour, and the viscosity values approach those of the neat HDPE. Indeed, this rheological result can be explained by taking into account that, at MWNTs' loadings equal or higher than the rheological percolation threshold, the interconnected CNT–polymer network is strong enough to offer resistance to the flow. Consequently, a strong increase in viscosity is recorded above this critical concentration at low shear rates, whereas by increasing the applied shear rate, the level of interconnection decreases and the nanotubes begin to orient in the flow direction. Owing to the high aspect ratio of the nanotubes, the shear thinning behaviour becomes evident in polymer–CNT composites at much lower concentrations than in traditional fibres-filled polymers. Indeed, such a strong influence of the aspect ratio on the steady shear flow behaviour is clearly demonstrated by Wang *et al.* (2006) in the

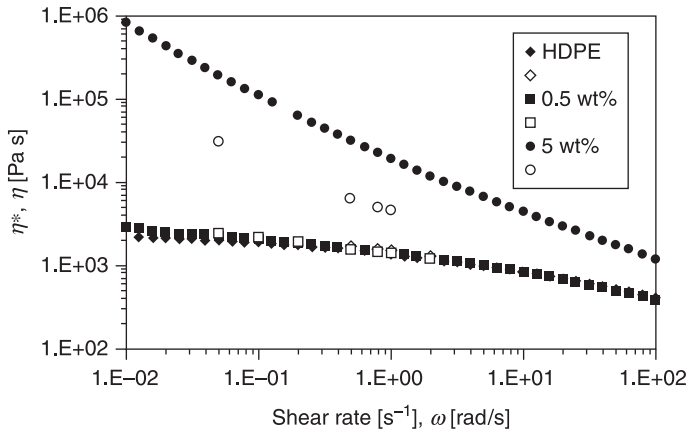


15.19 Steady shear viscosity (η) vs. shear rate for MWNT–HDPE790 composites and pure HDPE790 at $T = 200\text{ }^{\circ}\text{C}$.

case of carbon nanofibres–polystyrene composites. For CNF composites obtained by solvent-casting process, the length of the as-received fibres was retained ($L/D = 20\text{--}500$) and an evident shear thinning in the viscosity flow curve was detected for composites with CNF content between 5 and 10 wt%. On the contrary, in the melt blended composites, the CNF were damaged, becoming shorter ($L/D = 10\text{--}100$) and no shear thinning behaviour was recorded for concentrations of CNF up to 10 wt%.

Steady shear viscosity flow curves indicating a strong shear thinning trend have been reported in the literature for MWNT–PP composites by Kharchenko *et al.* (2004) and by Song (2006a, 2006 b) for CNT–poly(ethylene oxide) composites; capillary data for MWNT–PP are measured by Teng *et al.* (2008). In the case of SWNT–UHMWPE composites, made with a broad molecular weight distribution UHMWPE, a peculiar behaviour with a considerable decrease in viscosity of the composites compared to the neat matrix has been reported by Zhang *et al.* (2006a), in the range of compositions 0.1–1 wt%. Vega *et al.* (2009) reported a similar decrease in viscosity for MWNT–HDPE systems when a bimodal MWD high density polyethylene was used. In both cases this event was explained by the authors as a consequence of the selective adsorption of the longest molecules onto the CNT surface, the apparent molar mass of the polymer decreased and, consequently, the entanglement density and the viscosity are decreased.

The phenomenological Cox–Merz (1958) rule states that the steady state shear viscosity is numerically equal to the complex viscosity obtained from small-amplitude oscillatory measurements, and it has been successfully used to describe the behaviour of isotropic polymer melts and polymeric solutions. In our case, Fig. 15.20 shows that the Cox–Merz (1958) rule holds with a satisfactory approximation for the neat HDPE and the 0.5 wt% MWNT–HDPE composite,



15.20 Complex viscosity (η^*) vs. frequency (ω) (solid symbols) and steady shear viscosity (η) vs. shear rate (open symbols) for MWNT–HDPE0790 composites and pure HDPE0790 at $T = 200\text{ }^\circ\text{C}$.

but it clearly fails in the case of the 5 wt% MWNT–composite, that is characterized by a MWNT content higher than the corresponding rheological percolation threshold. In this latter case the steady-state viscosity of the MWNT–HDPE composites is one order of magnitude lower than the corresponding complex viscosity, showing that the imposed shear flow significantly modifies the CNT–polymer percolation network with the MWNT orienting along the shear direction. This result is in agreement with literature data on concentrated aqueous MWNT dispersions (Kinloch *et al.*, 2002), CNF composites (Wang *et al.*, 2006) as well as polymer–layered silicate composites (Ren and Krishnamoorti, 2003).

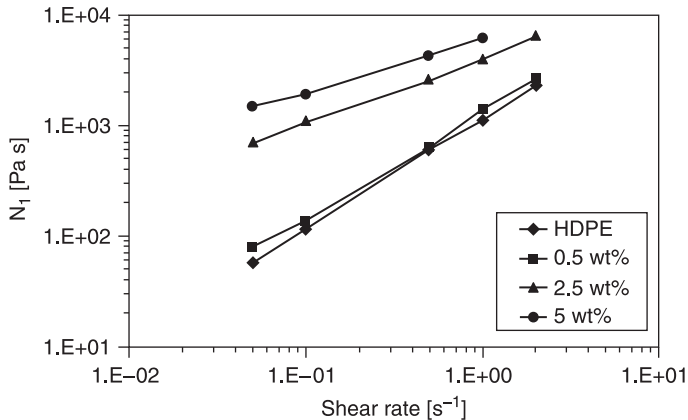
In the case of uncured epoxy resins, Rahatekar *et al.* (2006) showed that the shear thinning behaviour of their untreated nanotube suspensions was related to the size and the state of interconnection of the nanotube aggregates, whereas Fan and Advani (2005) related the flow curve trend to the CNTs aspect ratio. Unusual helical bands, formed perpendicular to the shear flow, were observed by Mackley and co-workers in CNT epoxy suspensions (Ma *et al.*, 2007, 2008). Detailed studies of CNT orientation in a variety of solvents have been reported in the works by Hobbie *et al.* (2003), Fry *et al.* (2006) and Pujari *et al.* (2009).

The experimental behaviour of the CNT suspensions has recently been modelled by Mackley and co-workers both for aggregating and non-aggregating CNT suspensions in Newtonian epoxy matrix (Ma *et al.*, 2008, 2009a, 2009 b), whereas Hobbie and Fry (2007), based on their rheological measurements on non-Brownian MWNT suspended in a low-molecular mass polyisobutylene (PIB), suggested a universal scaling of both the linear viscoelastic and steady-shear viscometric responses.

The study of the kinetics of destruction and reformation of a CNT network in a polymer melt was performed by Alig *et al.* (2008) by simultaneous time resolved measurements of electrical conductivity and dynamic shear modulus during thermal annealing well above glass transition and after short shear deformations of a 0.6 vol.% MWNT–PC conductive composite. The dramatic decrease of the DC conductivity as well as of the shear storage modulus, G' , down to the values of the polymer matrix recorded during the applied shear flow, was explained by the authors in terms of the destruction of the filler network. After the shear deformation, a complete recovery of the electrical conductivity and G' was obtained that was attributed by the authors to the re-formation of the network of interconnected nanotube agglomerates. The idea of cluster aggregation was used to describe the recovery of the shear modulus using different mechanical mixing rules in which the agglomerates were assumed to act as a 'solid-like' filler in the polymer, representing first attempts to describe the time dependence of the rheological properties. In a recent paper, Alig and co-workers (Skipa *et al.*, 2010) observed a shear-induced insulator-conductor transition, explained by the agglomeration of nanotubes under steady shear and the formation of an electrical conductive network of interconnected agglomerates. Simultaneously, a drastic decrease of the shear modulus during steady shear was recorded. These findings suggested a substantial difference in the nature of 'electrical' and 'mechanical' networks, showing that the steady shear is not always destructive to the conductive filler network in polymer–CNT composites.

15.3.2 The first normal stress difference

The first normal stress difference, N_1 , for the neat and for MWNT–HDPE0390 nanocomposites with different CNT contents and at different shear rates has been measured by Nobile and co-workers (Somma *et al.*, 2008a, 2008b). Analogous results on the first normal stress difference curves for the neat HDPE0790 and the MWNT–HDPE0790 are shown in Fig. 15.21. The data at $T = 200^\circ\text{C}$ indicate that positive N_1 values are detected for our MWNT–HDPE0790 composites at all the shear rates investigated. The measured N_1 for the nanocomposites increased about 30% compared to those of neat HDPE polymer, when the MWNT is added with a 0.5 wt% content that is below the rheological percolation threshold. On the contrary, a dramatic increase in the N_1 values is recorded for the 2.5 and 5 wt% MWNT inclusion. Analogously to the case of the steady shear viscosity flow curves, this remarkable increase is much more evident at the lower shear rates, with N_1 values one order of magnitude higher than those of the neat HDPE, while the effects of MWNTs on N_1 diminish, increasing the shear rates. The modification of the level of the interconnected CNT–polymer network with the applied shear flow can explain the N_1 behaviour, similar to the shear thinning observed in the flow curves. These results have been confirmed for MWNT–PB nanocomposites studied in our group (Iervolino, 2009) and they also agree with the literature



15.21 First normal stress difference (N_1) vs. shear rate for MWNT–HDPE0790 composites and pure HDPE0790 at $T = 200^\circ\text{C}$.

findings for nanofibre–PS composites (Wang *et al.*, 2006) as well as for MWNT–PP composites obtained by Xu *et al.* (2008) with nanotubes characterized by aspect ratio in the range 22–45.

The first normal stress difference provides a measure of stored elastic energy during flow, so that positive N_1 are associated with a die swell phenomenon which usually represents a difficulty in polymer melts processing. Kharchenko *et al.* (2004) used very high aspect ratio MWNTs (L/D about 300–400) in MWNT–PP composites and they report negative first normal stress differences values in percolated composites. This event was shown to have a dramatic impact on processing of these materials, indeed, their extruded MWNT–PP composites showed a suppression of die swell observed in the extruded neat PP polymer. Recently, negative first normal stress differences have been also reported for CNT suspensions by Davis *et al.* (2004) and Lin-Gibson *et al.* (2004).

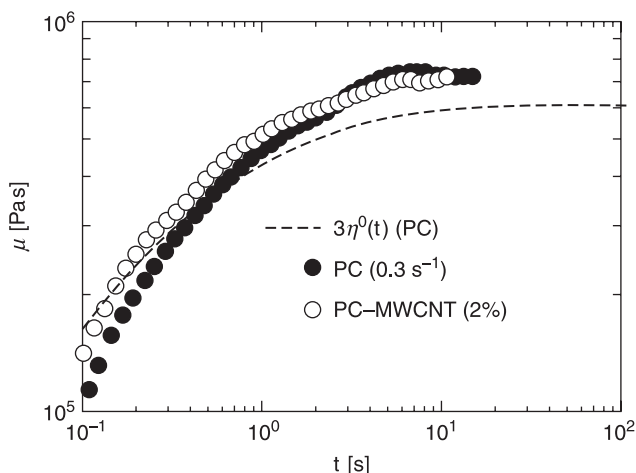
It has been suggested in the literature that, at high CNT concentration levels in CNT suspensions, the formation of a lyotropic nematic phase, where the carbon nanotubes are characterized by long-range orientational order and only short-range positional order, can occur (Somoza *et al.*, 2001; Song W. *et al.*, 2003; Davis *et al.*, 2004). In lyotropics liquid crystalline polymers (LCPs), negative N_1 values have been definitely observed with the two sign changes in N_1 as a function of the shear rate (Kiss and Porter, 1978; Moldenaers and Mewis, 1986; Grizzuti *et al.*, 1990), while in thermotropic LCPs, generally positive N_1 have been measured first by Nobile and co-workers (Cocchini *et al.*, 1991, 1992) as well as by other authors (Meissner, 1992; Han *et al.*, 1994; Langelaan and Gotsis, 1996; Zhou *et al.*, 1999). The negative N_1 values are associated with director tumbling in the wagging regime (Marrucci and Maffettone, 1989) that occurs in

lyotropics LCPs. The appearance of negative N_1 values in CNT composites can, then, be correlated to the analogy of CNT suspension with lyotropic LCPs.

15.3.3 The elongational viscosity

Elongational flow occurs in various polymer processing operations such as melt spinning, film blowing, and blow moulding; however, only a few studies in the literature have reported rheological investigations on the elongational flow behaviour of polymer–CNT composites melts and suspensions, as well as on carbon nanofibre suspensions (Xu *et al.*, 2005; Handge and Pötschke, 2006, 2007; Lee *et al.*, 2007; Pötschke *et al.*, 2007; Ma *et al.*, 2008, Tiwari *et al.*, 2009).

The transient elongational behaviour of polymer–CNT composite melts was first studied by Handge and Pötschke (2006, 2007) who had previously also investigated the orientation of MWNT–PC composites by melt spinning (Pötschke *et al.*, 2005). In their study, Handge and Pötschke (2007) compared the transient elongational viscosity of pure PC with that of 2 wt% MWNT–PC composites at $T = 190^\circ\text{C}$, measured by the uniaxial elongational rheometer RME. The comparison revealed that the addition of 2 wt% MWNT only moderately modified the time dependence and the value of the elongational viscosity, as shown in Fig. 15.22. The authors pointed out that the stress of the PC matrix was much higher than the stress caused by the carbon nanotubes, so that small stresses are necessary to deform the carbon nanotube network arrangement. They also



15.22 Transient elongational viscosity μ as a function of time t of pure PC and the PC–MWCNT (2 wt%) composite at $T = 190^\circ\text{C}$. The linear viscoelastic elongational viscosity $\mu^0(t) = 3\eta^0(t)$ for pure PC has also been plotted. The Hencky strain rate is 0.3 s^{-1} (Handge and Pötschke, 2007. Reproduced by permission of Springer-Verlag, Copyright© 2007, Springer-Verlag.).

discussed that this result in elongational flow compares well with the high frequency behaviour of polymer–CNT composites where the complex modulus was mostly determined by the viscoelasticity of the polymer matrix. The morphological investigation, performed by transmission electron microscopy (TEM), revealed that, after elongation to the maximum Hencky strain of 2.4, the isolated carbon nanotubes were oriented parallel to the flow direction and were partially straightened. The clusters with higher density of intertwined CNTs were also oriented, while the random arrangement within them was still preserved.

In the study of foaming behaviour of PP, Pötschke *et al.* (2007) measured an enhanced elongational viscosity for a 5 wt% MWNT–PP composite compared to that of the neat PP at different strain rates. The higher viscosity level led to an enhanced melt strength and to an improved foamability of the PP polymer matrix with the inclusion of nanotubes.

Lee *et al.* (2007) studied the effect of compatibilizers and chemical functionalization on the uniaxial elongational flow of MWNT–PP composites. They found that the transient elongational viscosity curves of the acid-treated or heat-treated MWNT composites showed strain-hardening because the chemically functionalized MWNT behaved as reinforcing fillers due to oxidation and enhanced interfacial interaction between PP matrix and nanotubes.

The transient recovered stretch λ_r of the MWNT–PC composites was studied in Handge and Pötschke's papers (2006, 2007). The transient recovered stretch is composed of two contributions: the molecular-driven recovery to an isotropic coiled state and, at larger time scales, the surface tension-driven recovery. The authors reported that the average retardation times of the macromolecules were not significantly modified by the presence of carbon nanotubes. Their results also proved that at low Hencky strain rates the recovered stretch values for pure PC was not modified much by the inclusion of the carbon nanotubes, whereas at Hencky strain rates equal and higher than 0.3 s^{-1} , the recovered stretch values for the PC–MWNT are dramatically reduced (at the same recovery time) compared to the λ_r values of the pure PC. The authors pointed out that their recovery data indicate that the arrangement of carbon nanotubes produced a yield stress and prohibited large extensions of the macromolecules during elongation.

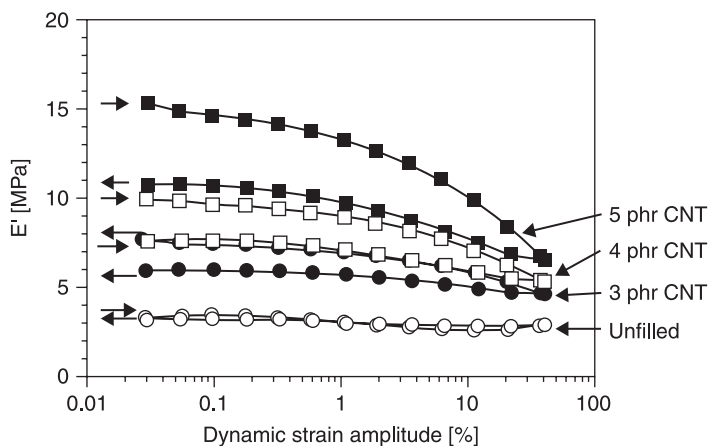
15.3.4 Non-linear oscillatory measurements

Non-linear viscoelastic measurements of dynamic moduli data performed on large amplitude oscillatory shear (LAOS) have been used in the literature to classify different non-linear responses of complex fluids.

Wu *et al.* (2007b) measured the dynamic moduli for a MWNT–PBT composite with an MWNT content higher than the rheological percolation threshold, in non-linear regime at strains up to 50%, for comparison with small amplitude oscillatory shear data (SAOS). Analogously to dynamic data obtained after shear flow, the storage modulus was found to decrease gradually with the increase of amplitude,

suggesting that the interactions among nanotubes decrease under the large deformation. The loss tangent increased with increasing amplitude, indicating that the nanocomposite becomes more viscous at high strain level; however, despite this dominant viscous response, the modulus is nearly not dependent on frequency at low frequencies. The use of a Cole–Cole plot suggested the long-term relaxation behaviour of nanotubes under LAOS.

The dynamic mechanical behaviour of nanocomposites of MWNTs in high performance solution-styrene-butadiene and butadiene rubber blends (S-SBR-BR) with increasing strain amplitude has recently been investigated by Das *et al.* (2008) in the tension mode. The unfilled rubbers are characterized by storage modulus values, E' , dependent on frequency and temperature, but independent of the deformation amplitude. On the contrary, filled rubbers show non-linear behaviour, known as the ‘Payne effect’ (Payne, 1965). In filled rubbers, indeed, a significant dependence of E' , on the strain amplitude is recorded that is explained by Payne in terms of the presence of a filler network in the rubber matrix which breaks down with increasing strain amplitude. The experimental results reported by Das *et al.* showed that the ‘Payne effect’ is observed with content equal and higher than 3 phr of MWNT in the S-SBR-BR rubber blend, indicating that the nanotubes form a continuous filler network in the rubber matrix at the low 3 phr content of MWNT. The ‘Payne effect’ is also observed in the case of silica and OH- functionalized MWNTs, even though the E' values were lower than those of the untreated MWNTs. The authors also tested the ability to recover the initial E' value for their untreated MWNT composites to confirm previous findings by Payne, showing that E' is largely recoverable at smaller amplitudes in the linear regime. Das *et al.*’s (2008) results, shown in Fig. 15.23, revealed that a partial



15.23 Strain dependencies of dynamic properties for CNT filled S-SBR-BR blends (Das *et al.*, 2008. Reproduced by permission of Elsevier, Copyright© 2008, Elsevier Ltd. All rights reserved.).

recovery of the E' values has been attained, even if the initial E' values are not reached within the relaxation time of the experiment. The high extent of recovery demonstrates that a good filler–filler network (previously disrupted by the large amplitude sweep) has been re-established in the reverse amplitude sweep, as pointed out by the authors. The recovery results also indicated that damage or permanent break of the nanotubes on increasing the strain amplitude to the high 40% value did not occur.

15.4 Flow-induced crystallization in polymer–carbon nanotube (CNT) composites

The crystallization behaviour of semicrystalline polymer–CNT composites incorporating multi-walled or single-walled CNTs has also recently been explored in the literature. Typical polymer nanocomposites processing operations involve solidification from a molten state by crystallization, consequently, the physical semicrystalline nanocomposites properties are strictly related to their crystalline morphology, crystalline fraction and crystallization kinetics. Hence, the investigation of the crystallization behaviour of polymer–CNT composites is necessary to establish the structure–property relationships.

Upon quiescent crystallization conditions, uniformly dispersed CNTs can act as a heterogeneous nucleating agent producing a higher crystallization temperature during the nonisothermal crystallization process, a dramatic increase in the number of nuclei and an associated decrease in the average size of crystallites (Grady *et al.*, 2002; Bhattacharyya *et al.*, 2003, 2005, 2007; Probst *et al.*, 2004; Valentini *et al.*, 2003, 2004; Mitchell and Krishnamoorti, 2005; Seo *et al.*, 2005; Leelapornpisit *et al.*, 2005; Anand *et al.*, 2006; Kim *et al.*, 2006; Nobile *et al.*, 2007, Wu *et al.*, 2007b; Valentino, 2008; Logakis *et al.*, 2009). Recently it has been also shown that carbon nanotubes can be very efficient in templating oriented polymer crystal growth perpendicular to the nanotube axis with the polymer chain aligned parallel to the nanotube longitudinal axis (Li *et al.*, 2005; Haggemueller *et al.*, 2006; Minus *et al.*, 2006; Garcia-Gutierrez *et al.*, 2006, 2008; Hernandez *et al.*, 2009).

The isothermal crystallization process of semi-crystalline polymers has been monitored by means of dynamic rheological experiments by different authors (Khanna, 1993; Bove *et al.*, 2001; Bove and Nobile, 2002a, 2002 b; Kelarakis *et al.*, 2005), but only recently has this technique been used to investigate the isothermal crystallization of polymer–CNT composites (Zhang *et al.*, 2006a; Wang *et al.*, 2007; Somma *et al.*, 2008a, 2008b; Iervolino *et al.*, 2008, 2009b; Ciambelli *et al.*, 2009; Valentino *et al.*, 2009). It was found that the presence of the nanotubes dramatically shortens the rheological induction times as well as the ‘rheological half-time’ of crystallization, $t_{0.5}^Q$, consequently, the overall crystallization rate becomes dramatically faster. Processing conditions involve a combination of shear and elongational flow fields, and the flow-induced crystallization behaviour has long been considered relevant in controlling the final properties of semi-crystalline

polymers in industrial processing because it can affect the overall kinetics and morphology of the resulting product. The applied flow fields, indeed, may strongly affect the nucleation density of the polymer matrix, the orientation of the nanoadditive and the orientation of the polymer matrix. Viscoelastic rheological measurements have proved to be a reliable technique to study the crystallization kinetics of semi-crystalline polymers after the application of a shear flow, i.e. in the flow-induced crystallization case. In the following, recent findings of the rheological investigations for the isothermal shear-enhanced crystallization of polymer–CNT composites will be presented and discussed.

15.4.1 The shear-enhanced crystallization of polymer–CNT composites

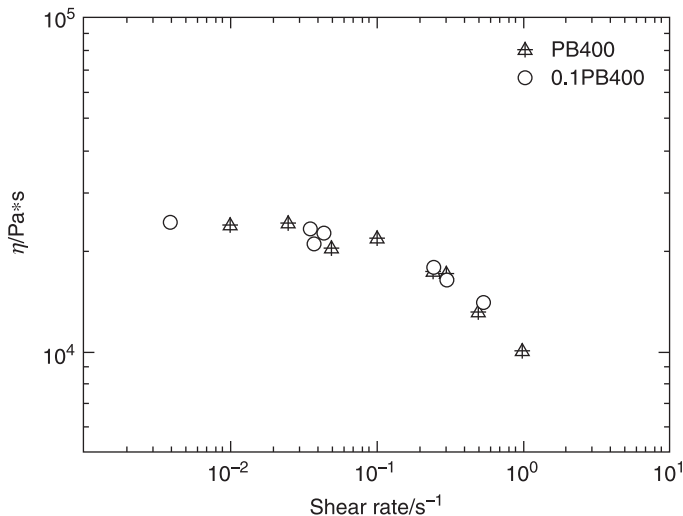
This section intends dealing with the combined role of shear flow and carbon nanotubes inclusion on the isothermal crystallization kinetics of polymer–CNT nanocomposites. Recently, several studies have become available in the literature that deal with the effects of processing parameters (e.g. shear rate and shear strain) and molecular properties of the polymer (e.g. molecular weight, molecular weight distribution, and traditional fibre fillers) on flow-induced crystallization (Lagasse and Maxwell, 1976; Vleeshouwers and Meijers, 1996; Eder and Janeschitz-Kriegl, 1997; Jay *et al.*, 1999; Somani *et al.*, 2000, 2005; Bove and Nobile, 2002a, 2002b; Seki *et al.*, 2002; Acierno *et al.*, 2003; Elmoumni *et al.*, 2003; Hsiao *et al.*, 2005; Larin *et al.*, 2005, 2008; Baert and Van Puyvelde, 2006; Dai *et al.*, 2006; Elmoumni and Winter, 2006). On the other hand, only a few papers have investigated the effect of the inclusion of carbon nanotubes on the flow-induced crystallization of semi-crystalline polymers (Garcia-Gutierrez *et al.*, 2006, 2008; Haggemueller *et al.*, 2006; Wang *et al.*, 2007; Kelarakis *et al.*, 2006; Mago *et al.*, 2008; Iervolino *et al.*, 2008, 2009a, 2009 b; Hernandez *et al.*, 2009; Valentino *et al.*, 2009).

One key factor governing the orientation-induced crystallization is the relaxation behaviour of polymer chains. When the flow is applied to the polymer, a conformational change with respect to the equilibrium, isotropic state can take place which depends on the coupling between the intensity of the flow field and the relaxation behaviour of the polymer chain. The relaxation behaviour of the polymer melt can be described in terms of the reptation or disengagement time of the macromolecules (τ_d) (Doi and Edwards, 1986), and the Rouse relaxation time, τ_R . Chain segments' orientation takes place when the flow time, $\dot{\gamma}^{-1}$, is shorter than the reptation or disengagement time. On the other hand, possible stretching of the chains can occur only if $\dot{\gamma}^{-1}$ is less than both the Rouse relaxation time, τ_R , and the reptation time, τ_d (i.e. $\dot{\gamma}^{-1} < \tau_R < \tau_d$). Shear rate, then, must be high enough to orient, and eventually stretch, polymer chains in the melt to form stable nuclei. The stability of the resulting orientation-induced nuclei also depends on the level of deformation (strain) on the sample (at low strains, the orientation and alignment of polymer chains may not be sufficient to form stable oriented nuclei). It is

necessary to overcome the critical shear strain (at constant shear rate) or a critical shear rate (at a constant shear strain) in order to enhance the nucleation and thus shorten the crystallization time after flow. To analyze the flow-induced crystallization behaviour, it is, therefore, necessary to investigate the relaxation behaviour of the polymer at the crystallization temperature.

Nobile and co-workers analyzed the shear-enhanced crystallization of MWNT composites based on HDPE (Valentino, 2008; Valentino *et al.*, 2009) and isotactic poly(1-butene) (PB) (Iervolino, 2009; Iervolino *et al.*, 2009a, 2009 b). Here we will discuss in detail the results for the MWNT–PB nanocomposites.

The flow curves for the pure PB400 and 0.1PB400 nanocomposite samples are reported in Fig. 15.24 at the isothermal crystallization temperature $T_c = 95^\circ\text{C}$, after cooling from the annealing treatment at $T_A = 180^\circ\text{C}$. Before the crystallization process sets in, the samples remain essentially in the state of an undercooled melt, where the corresponding viscosity values can be measured. The flow curves for the PB400 matrix and the 0.1PB400 nanocomposite nearly overlap, with the Newtonian and shear thinning regions occurring at similar shear rates. Thus, the coupling effects between the flow intensity and the relaxation behaviour of polymer chains seem to produce a similar degree of orientation during flow in the melt, for both pure PB400 and 0.1PB400 nanocomposite samples, where the latter contained a very low percentage of nanotube (0.1 wt% of MWNT), well below the percolation threshold.



15.24 Flow curve (η vs. shear rate) of the pure PB400 and the 0.1PB400 nanocomposite at $T_c = 95^\circ\text{C}$ (Iervolino *et al.*, 2009b. Reproduced by permission of Springer-Verlag, Copyright© 2009, Springer-Verlag.).

The longest relaxation time, i.e. the disengagement time of the macromolecules (τ_d), can be clearly defined and used to characterize a narrow distribution of molecular weight. With the broadening of the molecular weight distribution, such a relaxation time cannot be well defined but the longest relaxation time can be estimated as the inverse of the critical shear rate at the onset of shear thinning in the flow curve (τ_η). In particular, Fig. 15.24 shows that the viscosity of the pure PB400 starts to decrease at the shear rate $\dot{\gamma} \sim 0.1 \text{ s}^{-1}$, which corresponds to $\tau_\eta \sim 10 \text{ s}$. To confirm this estimate for the longest relaxation time, we have also fitted dynamic data previously published (Bove and Nobile, 2002a) with the BSW-GEX model described in a recent paper (Nobile and Cocchini, 2008) and the calculated average τ_η yields a value of 5.7 s, which is in good agreement with the estimated value based on the flow curve.

The analysis of the crystallization kinetic parameters in different step-shear flow experiments determines the individual *versus* the combined role(s) of the molecular orientation during flow and of the inclusion of CNTs in enhanced crystallization kinetics. The flow-induced crystallization tests at $T_c = 95^\circ\text{C}$ under short-time simple shear conditions (with parallel superposition of steady flow and dynamic conditions) have been performed on the 0.1PB400 nanocomposite at different shear rates, which belong both to the Newtonian and shear thinning region of the flow curve. The results showed that the flow does not significantly perturb the quiescent state and no significant enhancement in the crystallization kinetics in the nanocomposite melt is recorded, when the applied flow time, $\dot{\gamma}^{-1}$, is longer than the characteristic relaxation time. The crystallization ‘rheological half-time’ for the 0.1PB400 after step-shear flow at $\dot{\gamma} = 0.004 \text{ s}^{-1}$ (referred as $t_{0.5}^{\text{SS}}$ and reported in Table 15.4) is similar to the corresponding value evaluated for the quiescent state (indicated as $t_{0.5}^{\text{Q}}$ and reported in Table 15.3). Similar results have been also obtained for the neat PB400 matrix (see Tables 15.3 and 15.4).

On the other hand, the crystallization ‘rheological half-time’ for the 0.1PB400 nanocomposite after shear flow at $\dot{\gamma} = 0.3 \text{ s}^{-1}$, which is a shear rate that belongs to the shear thinning region of the flow curve, dramatically decreased with respect to the corresponding nanocomposite quiescent case (see Tables 15.3 and 15.4). Always at the shear rate of 0.3 s^{-1} , the neat PB matrix shows a modest decrease in $t_{0.5}^{\text{SS}}$ compared to its quiescent case. The flow-induced crystallization results for

Table 15.3 Kinetic parameters for the isothermal quiescent crystallization of the PB400–MWNT nanocomposites and the pure PB400 at $T_c = 95^\circ\text{C}$

Sample	$t_{\text{onset}}^{\text{Q}}$ (s)	$t_{0.5}^{\text{Q}}$ (s)
PB400	984±98	4950
0.1PB400	750±75	3600
1PB400	555±55	2800

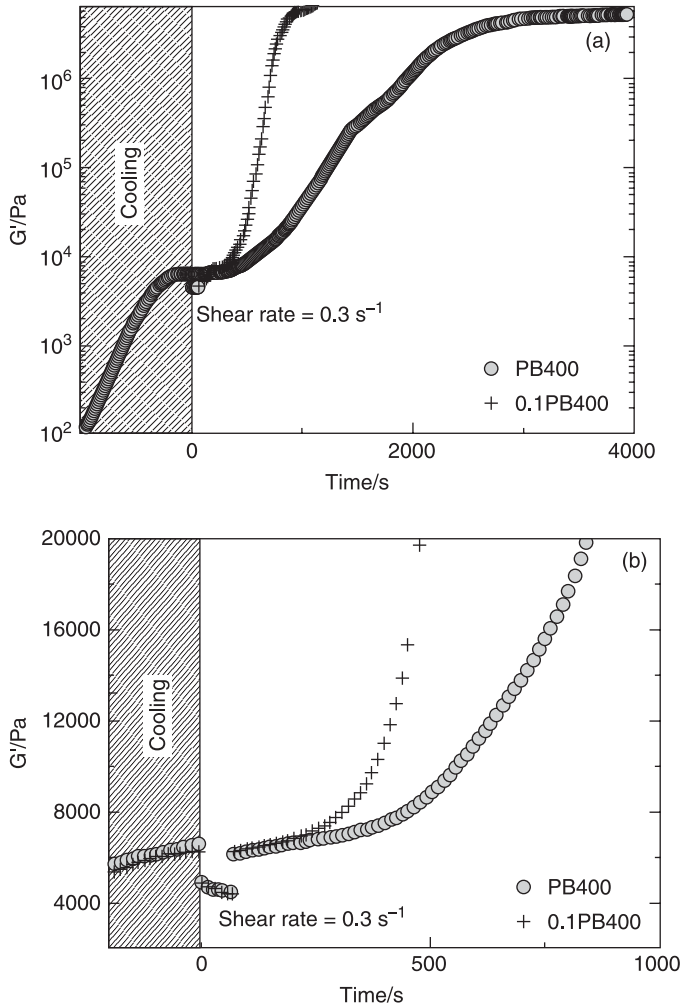
Table 15.4 Kinetic parameters for the isothermal flow-induced crystallization of the pure PB400 and 0.1PB400 nanocomposite calculated from the step-shear flow tests at $T_c = 95^\circ\text{C}$

	Shear rate (s^{-1})	$t_{0.5}^{\text{SS}}$ (s)	k_{SS} (s^{-1})	k_{SS}/k_0
Pure PB400	2.30×10^{-2}	4800	2.08×10^{-4}	1.03
	3.00×10^{-1}	3520	2.84×10^{-4}	1.41
	5.10×10^{-1}	2400	4.17×10^{-4}	2.06
0.1PB400 nanocomposite	4.00×10^{-3}	3400	2.94×10^{-4}	1.06
	3.00×10^{-1}	770	1.30×10^{-3}	4.68
	5.20×10^{-1}	650	1.54×10^{-3}	5.54

the 0.1PB400 nanocomposite and the pure PB400 samples in different step-shear flow experiments at the crystallization temperature of 95°C are summarized in Table 15.4, in terms of the crystallization ‘rheological half-time’ after step-shear flow, $t_{0.5}^{\text{SS}}$, and of the overall crystallization constant (k_{SS}).

A direct comparison of G' profiles for the PB400 and 0.1PB400 samples during both the step-shear at the shear rate of 0.3 s^{-1} (i.e. in the shear thinning region, with a shearing time of 70 s), and the subsequent crystallization process, is shown in Figs 15.25 (a) and (b). In agreement with the flow curve results, a similar decrease in G' during the application of the shear flow is detected in both samples (Fig. 15.25 (b)), suggesting a similar degree of molecular anisotropy. Nonetheless, Fig. 15.25 (a) clearly shows that the presence of carbon nanotubes produces a much faster crystallization kinetics after flow in the nanocomposite compared to the flow-induced kinetics recorded for the neat PB.

In the case of the neat PB400, the moderate increase in the step-shear crystallization kinetics recorded at the shear rate of 0.3 s^{-1} versus its quiescent case (discussed above and shown in Tables 15.3 and 15.4) can be well explained in terms of the Weissenberg number, $We = \dot{\gamma} \tau_\eta$. Indeed, if the We number is higher than 1, the flow time ($1/\dot{\gamma}$) becomes smaller than the disengagement time and chain segment orientation can take place during flow. In the literature it has been shown that shearing at We higher than 1 can result in an increase of nucleation density, and thus in the enhancement in the crystallization rate, while the anisotropic growth of crystal structures can be obtained only at $We \gg 1$, where stretching of the chain can occur. For this latter case, in flexible polymer melts without fillers, the initially formed precursor structure can consist of shish-kebab entities with multiple short shish that can incorporate the entanglement points as defects in the shish assembly (Hsiao *et al.*, 2005). Nevertheless, as pointed out by Winter and co-workers (Elmoumni *et al.*, 2003), the Weissenberg number does not capture the relaxation process after the cessation of flow, so that he suggested that the good correlation with We is due to the fact that the shear influence is crucial at the beginning of the crystallization process, probably



15.25 (a) Storage modulus (G') vs. time for the pure PB400 and the 0.1PB400 nanocomposite during the step-shear crystallization experiment with shear rate = $0.3 \text{ s}^{-1} \times 70 \text{ s}$ at $T_c = 95^\circ \text{C}$. (b) Storage modulus vs. time, during the application of the shear flow and the early stages of the step-shear crystallization experiment (Iervolino *et al.*, 2009b. Reproduced by permission of Springer-Verlag, Copyright© 2009, Springer-Verlag.).

mainly through enhanced nucleation. Moreover, only when the strain is kept constant, can the We criterion be used to determine the flow-induced crystallization kinetics.

In the case of the neat PB400 at $\dot{\gamma} = 0.3 \text{ s}^{-1}$ (and strain of 21) with $\tau_{\eta} \sim 10 \text{ s}$, We is between 1.71 and 3.0, i.e. a value that is only slightly higher than 1,

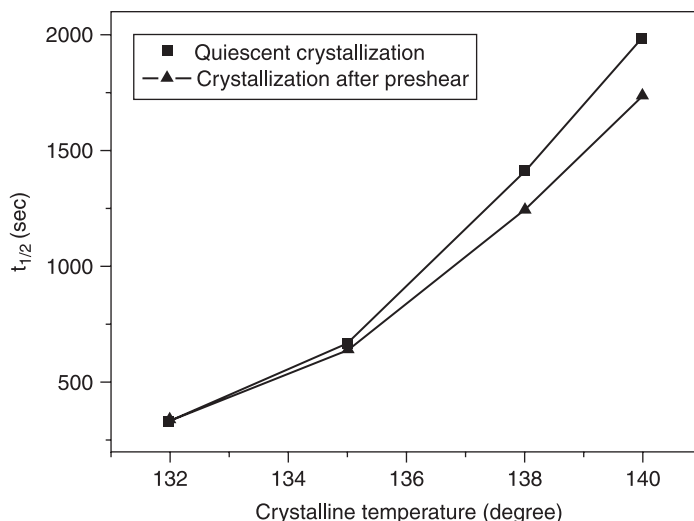
and that well correlates with the moderate increase in its crystallization kinetics. On the other hand, the strong enhancement in the flow-induced crystallization kinetics observed for the 0.1PB400 nanocomposite at the same shear rate of 0.3 s^{-1} can be interpreted in the framework of recent literature findings that clearly shows how the carbon nanotubes can hinder the motion of polymer chains and delay their relaxation process (Haggenmueller *et al.*, 2006; Kelarakis *et al.*, 2006; Garcia-Gutierrez *et al.*, 2008). The carbon nanotubes, therefore, may increase the relaxation time of the surrounding polymer chains which would retain their molecular orientation after flow. Winey and co-workers (Haggenmueller *et al.*, 2006) and Garcia-Gutierrez *et al.* (2008) showed that the nucleation and crystallization predominately occur at the SWNTs, with the polymer molecules preferentially aligned parallel to the nanotube axis in the melt state (Wei *et al.*, 2004). In the flow-induced crystallization process, the carbon nanotubes, indeed, provide surfaces that stabilize nuclei, enhancing oriented crystallization with crystalline lamellae growing perpendicular to the carbon nanotube surface, in addition to the usual quiescent nucleation effect of carbon nanotubes.

Optical microscopic measurements have also been carried out after flow by Nobile and co-workers (Iervolino *et al.*, 2009b). It was found that the PB400 only exhibits an isotropic spherulitic structure, consistent with the expectation of the structure formed at a moderate We value between 1.7 and 3.0. In the case of the 0.1PB400 sample, a much higher density of crystallites is seen and a thread-like structure, aligned in the direction of flow, was detected.

Hsiao and co-workers (Iervolino *et al.*, 2009a) performed the investigation of the shear-induced behaviour for the same neat PB and the nanocomposite 0.1PB400 samples by rheo-SAXS and rheo-WAXD techniques. The results confirmed the enhancement in the crystallization kinetics, and they also showed an increase in the amount of oriented crystals.

In the work by Fu and co-workers (Wang *et al.*, 2007), the crystallization process of PP–MWNT composites after step-shear flow was followed by dynamic melt rheometry. The steady shear deformation was imposed at the temperature $T = 180 \text{ }^{\circ}\text{C}$ on the melt; after cessation of flow, the melt was cooled rapidly to the crystallization temperature ($132\text{--}140 \text{ }^{\circ}\text{C}$) at a cooling rate of $-30 \text{ }^{\circ}\text{C min}^{-1}$, finally, the crystallization process was followed under small oscillatory shear state.

In this study, the shear flow was applied on the melt (prior to cooling the polymer at the crystallization temperature), unlike in our case where the shear-step flow was imposed on the undercooled melt, as discussed earlier. Fu and co-workers investigated the effectiveness of melt-shearing on the enhancement of the crystallization kinetics at different T_c values in the range $132\text{--}140 \text{ }^{\circ}\text{C}$. Their crystallization ‘rheological half-time’ results, summarized in Fig. 15.26, suggested two different mechanisms of shear-enhanced crystallization for i-PP–MWNT depending on the crystallization temperature. At low T_c values, strong heterogeneous nucleation plays a dominant



15.26 Crystallization temperature dependence of the half-crystallization time ($t_{0.5}$) for i-PP-PPgMA-MWCNT (90:10:0.3 wt-%) composite (Wang *et al.*, 2007. Reproduced by permission of WILEY-VCH, Copyright© 2007, WILEY-VCH Verlag GmbH & Co.).

role and the effect of melt-shear on the crystallization kinetics was weak; at high T_c values, the effect of heterogeneous nucleation was depressed and the crystallization kinetics was enhanced by the shear on the melt. In this latter case, thread-like crystallites appeared earlier than the spherulites. The authors attributed their results to the fact that nanotubes act as a crystalline template for oriented PP chains that are adjacent to nanotubes, inducing a low activation energy for nucleation and growth and the formation of thread-like crystallites at higher crystallization temperatures.

In conclusion, the rheological investigations have shown that the presence of carbon nanotubes under flow may hinder the motion of polymer chains and delay their relaxation process, resulting in a dramatic increase in the crystallization kinetics associated with the transition from isotropic spherulites to an oriented crystallization.

15.5 Conclusion

In this chapter, the rheology of polymer–CNT composites melts has been reviewed both in linear and non-linear regimes. The linear viscoelasticity of polymer–CNT composites melts at low frequencies showed that the viscoelastic properties of the nanocomposites at low MWNTs contents are still dominated by the polymer matrix while, by increasing the CNT loading, the nanocomposite experiences a transition from liquid to solid-like behaviour. The dynamic melt rheological

results in polymer–CNT nanocomposites can be interpreted in terms of a nanotube network interpenetrating the polymer matrix that creates additional and significant contributions to the nanocomposite viscoelasticity. Rheological measurements can, then, readily provide evaluation of the ‘rheological percolation threshold’, determined by polymer chain immobility in a combined carbon nanotube–polymer network. The percolation threshold was found to depend on the dispersion state of the carbon nanotubes; indeed, the goal of a good dispersion without reducing nanotube length remains a challenging issue in the preparation of the nanocomposites.

In the high frequency results, on the other hand, the complex modulus was mostly determined by the viscoelasticity of the matrix.

In non-linear rheology, the steady shear viscosity flow curves indicated a strong shear thinning trend, with the effect of the nanotubes on the rheological behaviour of the polymer matrix becoming relatively weak at the high shear rates. The imposed shear flow, then, significantly modifies the CNT–polymer percolation network, and the network structure is easily broken with the MWNT orienting along the shear direction. After the shear deformation, a re-formation of the network of interconnected nanotube agglomerates can occur under quiescent annealing conditions. The elongational flows results compared well with the high shear rates behaviour of the polymer–CNT composites.

Moreover, the presence of carbon nanotubes under flow may hinder the motion of polymer chains and delay their relaxation process, resulting in a dramatic increase in the crystallization kinetics.

In conclusion, the experimental rheological results clearly indicate that short-range polymer dynamics are not influenced by the nanotubes, while the CNTs influence the polymer relaxation dynamics at a length scale longer than the entanglement distance. The ability to predict the rheological behaviour in polymer–CNT composites, on the other hand, still represents a great challenge in the rheology of these composites. Microstructural models have been developed so far only for CNT suspension rheology. Their absolute validity, however, remains uncertain since all the models depend on the states of aggregation and CNT ordering which are still not well defined.

15.6 References

- Abdel-Goad M and Pötschke P (2005) ‘Rheological characterization of melt processed polycarbonate-multiwalled carbon nanotube composites’, *Journal of Non-Newtonian Fluid Mechanics*, 128, 2–6.
- Acierno S, Palomba B, Winter H H and Grizzuti N (2003) ‘Effect of molecular weight on the flow-induced crystallization of isotactic poly(1-butene)’, *Rheol. Acta.*, 42, 243–250.
- Alig I, Skipa T, Lellinger D and Pötschke P (2008) ‘Destruction and formation of a carbon nanotube network in polymer melts: Rheology and conductivity spectroscopy’, *Polymer*, 49, 3524–3532.
- Anand K A, Agarwal U S and Joseph R (2006) ‘Carbon nanotubes induced crystallization of poly(ethylene terephthalate)’, *Polymer*, 47, 3976–3980.

- Azzurri F and Alfonso G C (2005) 'Lifetime of shear-induced crystal nucleation precursors', *Macromolecules*, 38, 1723–1728.
- Baert J and Van Puyvelde P (2006) 'Effect of molecular and processing parameters on the flow-induced crystallization of poly-1-butene. Part 1: Kinetics and morphology', *Polymer*, 47, 5871–5879.
- Bhattacharyya A R, Bose S, Kulkarni A R, Pötschke P, Häußler L, Fisher D and Jehnichen D (2007) 'Styrene maleic anhydride copolymer mediated dispersion of single wall carbon nanotubes in polyamide 12: crystallization behavior and morphology', *J. Appl. Polym. Sci.*, 106, 345–353.
- Bhattacharyya A R and Pötschke P (2006), 'Mechanical properties and morphology of melt-mixed PA6/SWNT composites: effect of reactive coupling', *Macromol. Symp.*, 233, 161–169.
- Bhattacharyya A R, Pötschke P, Abdel-Goad M and Fischer D (2004) 'Effect of encapsulated SWNT on the mechanical properties of melt mixed PA12/SWNT composites', *Chemical Physics Letters*, 392, 28–33.
- Bhattacharyya A R, Pötschke P, Häußler L and Fisher D (2005) 'Reactive compatibilization of melt mixed PA6/SWNT composites: mechanical properties and morphology', *Macromol. Chem. Phys.*, 206, 2084–2095.
- Bhattacharyya A R, Sreekumar T V, Liu T, Kumar S, Ericson L M, Hauge R H and Smalley R E (2003) 'Crystallization and orientation studies in polypropylene/single wall carbon nanotube composite', *Polymer*, 44, 2373–2377.
- Bose S, Bhattacharyya A R, Bondre A P, Kulkarni A R and Pötschke P (2008) 'Rheology, electrical conductivity, and the phase behavior of cocontinuous PA6/ABS blends with MWNT: correlating the aspect ratio of MWNT with the percolation threshold', *J. Polym. Sci.: B Polym. Phys.*, 46, 1619–1631.
- Bose S, Bhattacharyya A R, Kodgire P V, Misra A and Pötschke P (2007) 'Rheology, morphology, and crystallization behavior of melt-mixed blends of polyamide6 and acrylonitrile-butadiene-styrene: influence of reactive compatibilizer premixed with multiwall carbon nanotubes', *J. Appl. Polym. Sci.*, 106, 3394–3408.
- Bose S, Khare R A, Moldenaers P (2010) 'Assessing the strengths and weaknesses of various types of pre-treatments of carbon nanotubes on the properties of polymer/carbon nanotubes composites: a critical review', *Polymer*, 51, 975–993.
- Bove L and Nobile M R (2002a) 'Shear flow effects on polymer melts crystallization: kinetic features', *Macromol. Symp.*, 180, 169–180.
- Bove L and Nobile M R (2002b) 'Shear-induced crystallization of isotactic poly(1-butene)', *Macromol. Symp.*, 185, 135–147.
- Bove L, Nobile M R, Azzurri F and Alfonso G C (2001) 'Shear-induced crystallization of isotactic polyolefins', *The 17th Annual Meeting of the Polymer Processing Society (PPS-17)*, Montreal, Canada, 21–24 May.
- Chambon F and Winter H H (1987) 'Linear viscoelasticity at the gel point of a crosslinking PDMS with imbalanced stoichiometry', *J. Rheol.*, 31, 683–697.
- Ciambelli P, Sarno M, Neitzert H C, Nobile M R, Somma E and Valentino O (2009) 'Influence of MWNT on the physical properties of polyethylene nanocomposites', *Nanotech Conference & Expo 2009: An Interdisciplinary Integrative Forum on Nanotechnology, Biotechnology and Microtechnology*, Houston, TX, United States, 473–476.
- Cocchini F, Nobile M R and Acierio D (1991) 'Transient and steady rheological behaviour of the thermotropic liquid crystal copolymer 73/27 HBA/HNA', *J. Rheol.*, 35, 1171–1189.

- Cocchini F, Nobile M R and Acierno D (1992) 'Letter: About negative first normal stress differences in a thermotropic liquid crystalline polymer', *J. Rheol.*, 36, 1307–1311.
- Cox W P and Merz E H (1958) 'Correlation of dynamic and steady flow viscosities', *J. Polym. Sci.*, 28, 619–622.
- Dai S C, Qi F and Tanner R I (2006) 'Strain and strain-rate formulation for flow-induced crystallization', *Polym. Eng. Sci.*, 46, 659–669.
- Das A, Stockelhuber K W, Jurk R, Saphiannikova M, Fritzsche J, Lorenz H, Kluppel M and Heinrich G (2008) 'Modified and unmodified multiwalled carbon nanotubes in high performance solution-styrene–butadiene and butadiene rubber blends', *Polymer*, 49, 5276–5283.
- Davis V A, Ericson L M, Parra-Vasquez A N G, Fan H, Wang Y, Prieto V, Longoria J A, Ramesh S, Saini R K, Kittrell C, Billups W E, Wade Adams W, Hauge R H, Smalley R E and Pasquali M (2004) 'Phase behavior and rheology of SWNTs in superacids', *Macromolecules*, 37, 154–160.
- Dealy J M and Larson R G (2006) *Structure and Rheology of Molten Polymers*, Munich: Hanser.
- Dealy J M and Wissbrun K F (1999) *Melt Rheology and its Role in Plastics Processing: Theory and Applications*, Dordrecht: Kluwer Academic Publisher.
- Doi M and Edwards S F (1986) *The Theory of Polymer Dynamics*, Oxford: Oxford University Press.
- Doppert H L and Picken S J (1987) 'Rheological properties of aramidic solutions: transient flow and rheo-optical measurements', *Mol. Cryst. Liq. Cryst.*, 153, 109–116.
- Du F, Fischer J E and Winey K I (2003) 'Coagulation method for preparing single-walled carbon/nanotube/Poly(methyl methacrylate) composites and their modulus, electrical conductivity, and thermal stability', *J. Polym. Sci.: B Polym. Phys.*, 41, 3333–3338.
- Du F, Scogna R C, Zhou W, Brand S, Fischer J E and Winey K I (2004) 'Nanotube networks in polymer nanocomposites: rheology and electrical conductivity', *Macromolecules*, 37, 9048–9055.
- Eder G and Janeschitz-Kriegl H (1997) 'Crystallization', in HEH Meijer (ed.), *Materials Science and Technology: A Comprehensive Treatment*. Vol. 18: *Processing of Polymers*. New York: Wiley-VCH, pp. 269–342.
- Elmoumni A and Winter H H (2006) 'Large strain requirements for shear-induced crystallization of isotactic polypropylene', *Rheol. Acta.*, 45, 793–801.
- Elmoumni A, Winter H H, Waddon A J and Fruitwala H (2003) 'Correlation of material and processing time scales with structure development in isotactic polypropylene crystallization', *Macromolecules*, 36, 6453–6461.
- Fan Z and Advani S G (2005) 'Characterization of orientation state of carbon nanotubes in shear flow', *Polymer*, 46, 5232–5240.
- Ferry J D (1980) *Viscoelastic Properties of Polymers*, New York: Wiley & Sons.
- Fry D, Langhorst B, Wang H, Becker M L, Bauer B J, Grulke E A and Hobbie E K (2006) 'Rheo-optical studies of carbon nanotubes suspensions', *J. Chem. Phys.*, 124, 054703 (1–9).
- Garboczi E J, Snyder K A, Douglas M F and Thorpe M F (1995) 'Geometrical percolation threshold of overlapping ellipsoids', *Phys. Rev. E*, 52, 819–828.
- Garcia-Gutierrez M C, Hernandez J J, Nogales A, Panine P, Rueda D R and Ezquerro T A (2008) 'Influence of shear on the templated crystallization of poly(butylene terephthalate)/single wall carbon nanotube nanocomposites', *Macromolecules*, 41, 844–851.
- Garcia-Gutierrez M C, Nogales A, Rueda D R, Domingo C, Garcia-Ramos J V, Broza G, Roslaniec Z, Schulte K, Davies R J and Ezquerro T A (2006) 'Templating of

- crystallization and shear-induced self-assembly of single-wall carbon nanotubes in a polymer-nanocomposite', *Polymer*, 47, 341–345.
- Giannelis E P, Krishnamoorti R and Manias E (1999) 'Polymer-silicate nanocomposites: model systems for confined polymers and polymer brushes', *Adv. in Polym. Sci.*, 138, 107–147.
- Giles D W and Denn M M (1994) 'The effect of suppression of offgassing on the rheometry of thermotropic liquid crystalline polymers', *J. Rheol.*, 38, 617–637.
- Godara A, Mezzo L, Luizi F, Warriar A, Lomov S V, van Vuure A W, Gorbatikh L, Moldenaers P, Verpoest I (2009) 'Influence of carbon nanotube reinforcement on the processing and the mechanical behaviour of carbon fiber/epoxy composites', *Carbon*, 47, 2914–2923.
- Grady B P, Pompeo F, Shambaugh R L and Resasco E D (2002) 'Nucleation of polypropylene crystallization by single-walled carbon nanotubes', *J. Phys. Chem. B*, 106, 5852–5858.
- Grizzuti N, Cavella S and Cicarelli P (1990) 'Transient and steady state rheology of a liquid crystalline hydroxypropylcellulose solution', *J. Rheol.*, 34, 1293–1310.
- Guskey S M and Winter H H (1991) 'Transient shear behaviour of a thermotropic liquid crystalline polymer in the nematic state', *J. Rheol.*, 35, 1191–1207.
- Haggenmueller R, Fischer J E and Winey K I (2006) 'Single wall carbon nanotube/polyethylene nanocomposites: nucleating and templating polyethylene crystallites', *Macromolecules*, 39, 2964–2971.
- Han C D, Chang S and Kim S S (1994) 'Rheological behavior of thermotropic liquid crystalline polymers: effects of thermal and deformation histories', *Mol. Cryst. Liq. Cryst.*, 254, 335–368.
- Han C D and Kim J (1987) 'Rheological technique for determining the order-disorder transition of block copolymers', *J. Polym. Sci. B Polym. Phys.*, 25, 1741–1764.
- Han M S, Lee Y K, Lee H S, Yun C H and Kim W N (2009) 'Electrical, morphological and rheological properties of carbon nanotube composites with polyethylene and poly(phenylene sulfide) by melt mixing' *Chem. Eng. Sci.*, 64, 4649–4656.
- Handge U A and Pötschke P (2006) 'Melt elongation and recovery of polycarbonate/carbon nanotube composites', *Macromol. Bioscience*, 6, F20–F21.
- Handge U A and Pötschke P (2007) 'Deformation and orientation during shear and elongation of a polycarbonate/carbon nanotubes composite in the melt', *Rheol. Acta.*, 46, 889–898.
- Hernandez J J, Garcia-Gutierrez M C, Nogales A, Rueda D R and Ezquerro T A (2009) 'Shear effect on crystallizing single wall carbon nanotube/poly(butylene terephthalate) nanocomposites', *Macromolecules*, 42, 4374–4376.
- Hobbie E K and Fry D J (2007) 'Rheology of concentrated carbon nanotube suspensions', *J. Chem. Phys.*, 126, 124907.
- Hobbie E K, Wang H, Kim H, Gibson S L and Grulke E A (2003) 'Orientation of carbon nanotubes in a sheared polymer melt', *Physics of Fluids*, 15, 1196–1202.
- Hsiao B S, Yang L, Somani R H, Avila-Orta C A and Zhu L (2005) 'Unexpected shish-kebab structure in a sheared polyethylene melt', *Phys. Rev. Lett.*, 94, 117802–117806.
- Hu G, Zhao C, Zhang S, Yang M and Wang Z (2006) 'Low percolation threshold of electrical conductivity and rheology in poly(ethylene terephthalate) through the networks of multi-walled carbon nanotubes', *Polymer*, 47, 480–488.
- Huang Y Y, Ahir S V and Terentjev E M (2006) 'Dispersion rheology of carbon nanotubes in a polymer matrix', *Phys. Rev. B*, 73, 125422.
- Iervolino O (2009) 'Rheology and morphology of the flow induced crystallization in polymers', PhD thesis, Salerno, University of Salerno.

- Iervolino R, Somma E, Nobile M R and Hsiao B S (2008) 'Cristallizzazione del poli(1-butene) isotattico: effetto combinato di un flusso di shear e di nanotubi al carbonio a parete multipla', *Panta Rei*, 9, 10–15.
- Iervolino R, Somma E, Nobile M R and Hsiao B S (2009a) 'The combined effect of multi-walled carbon nanotubes and shear flow on the crystallization of isotactic poly(1-butene)', *Proceedings of the 5th Annual European Rheology Conference*, Cardiff, United Kingdom.
- Iervolino R, Somma E, Nobile M R, Chen X and Hsiao B S (2009b) 'The role of multi-walled carbon nanotubes in shear enhanced crystallization of isotactic poly(1-butene)', *J. Therm. Anal. Calorim.*, 98, 611–622.
- Jay F, Haudin J M and Monasse B (1999) 'Shear-induced crystallization of polypropylenes: effect of molecular weight', *J. Mater. Sci.*, 34, 2089–2102.
- Kataoka T, Kitano T, Sasahara M and Nishijima K (1978) 'Viscosity of particle filled polymer melts' *Rheol. Acta.*, 17, 149–155.
- Kelarakis A, Mai S M, Booth C and Ryan A J (2005) 'Can rheometry measure crystallization kinetics? A comparative study using block copolymers', *Polymer*, 46, 2739–2747.
- Kelarakis A, Yoon K, Sics I, Somani R H, Chen X, Hsiao B S and Chu B (2006) 'Shear-induced orientation and structure development in isotactic polypropylene melt containing modified carbon nanofibers', *J. Macromol. Sci. Phys.*, 45, 247–261.
- Khanna Y P (1993) 'Rheological mechanism and overview of nucleated crystallization kinetics', *Macromolecules*, 26, 3639–3643.
- Kharchenko S B, Douglas J F, Obrzut J, Grulke E A and Migler K B (2004) 'Flow-induced properties of nanotube-filled polymer materials', *Nature Materials*, 3, 564–568.
- Kim J Y and Kim S H (2006) 'Influence of multiwall carbon nanotube on physical properties of poly(ethylene 2,6-naphthalate) nanocomposites', *J. Polym. Sci. B Polym. Phys.*, 44, 1062–1071.
- Kim J Y, Park H S and Kim S H (2006) 'Unique nucleation of multi-walled carbon nanotube and poly(ethylene 2,6-naphthalate) nanocomposites during non-isothermal crystallization', *Polymer*, 47, 1379–1389.
- Kinloch I A, Roberts S A and Windle A H (2002) 'A rheological study of concentrated aqueous nanotube dispersions', *Polymer*, 43, 7483–7491.
- Kiss G and Porter R S (1978) 'Rheology of concentrated solutions of Poly(- γ -benzylglutamate)', *J. Polym. Sci.: Polym. Symp.*, 65, 193–211.
- Kitano T and Kataoka T (1980) 'The effect of the mixing methods on viscous properties of polyethylene melts filled with fibers', *Rheol. Acta*, 19, 753–763.
- Kitano T, Kataoka T and Nagatsuka Y (1984) 'Shear flow rheological properties of vinylon- and glass-fiber reinforced polyethylene melts', *Rheol. Acta*, 23, 20–30.
- Kitano T, Kataoka T and Shirota T (1981) 'An empirical equation of the relative viscosity of polymer melts filled with various inorganic fillers', *Rheol. Acta*, 20, 207–209.
- Kota A K, Cipriano B H, Duesterberg M K, Gershon A L, Powell D, Raghavan S R and Bruck H (2007) 'Electrical and rheological percolation in polystyrene/MWCNT nanocomposites', *Macromolecules*, 40, 7400–7406.
- Krause B, Ritschel M, Taschner Ch, Oswald S, Gruner W, Leonhardt A and Pötschke P (2010) 'Comparison of nanotubes produced by fixed bed and aerosol-CVD methods and their electrical percolation behaviour in melt mixed polyamide 6.6 composites', *Composites Science and Technology*, 70, 151–160.
- Krishnamoorti R and Giannelis E P (1997) 'Rheology of end-tethered polymer layered silicate nanocomposites', *Macromolecules*, 30, 4097–4102.

- Krishnamoorti R and Yurekli K (2001) 'Rheology of polymer layered silicate nanocomposites', *Current Opinion in Colloid & Interface Science*, 6, 464–470.
- Lagasse R R and Maxwell B (1976) 'An experimental study of the kinetics of polymer crystallization during shear flow', *Polym. Eng Sci*, 16, 189–199.
- Langelaan H C and Gotsis A D (1996) 'The relaxation of shear and normal stresses of nematic liquid crystalline polymers in squeezing and shear flows', *J. Rheol.*, 40, 107–129.
- Larin B, Avila-Orta C A, Somani R H, Hsiao B S and Maron G (2008) 'Combined effect of shear and fibrous fillers on orientation-induced crystallization in discontinuous aramidic fiber/isotactic polypropylene composites', *Polymer*, 49, 295–302.
- Larin B, Maron G, Avila-Orta C A, Somani R H and Hsiao B S (2005) 'Orientated crystallization in discontinuous aramidic fiber/isotactic polypropylene composites under shear flow conditions', *J. Appl. Polym. Sci.*, 98, 1113–1118.
- Lee S H, Cho E, Jeon S H and Youn J R (2007) 'Rheological and electrical properties of polypropylene composites containing functionalized multi-walled carbon nanotubes and compatibilizers', *Carbon*, 45, 2810–2822.
- Lee S H, Kim M W, Kim S H and Youn J R (2008) 'Rheological and electrical properties of polypropylene/MWCNT composites prepared with MWCNT masterbatch chips', *Eur. Polym. J.*, 44, 1620–1630.
- Leelapornpisit W, Ton-That M T, Perrin-Sarazin F, Cole K C, Denault J and Simard B (2005) 'Effect of carbon nanotubes on the crystallization and properties of polypropylene', *J. Polym. Sci.: B Polym. Phys.*, 43, 2445–2453.
- Li C Y, Li L, Cai W, Kodjie S L and Tenneti K K (2005) 'Nanohybrid shish-kebabs: periodically functionalized carbon nanotubes', *Advanced Materials*, 17, 1198–1202.
- Lin B, Sundararaj U and Pötschke P (2006) 'Melt mixing of polycarbonate with multi-walled carbon nanotubes in miniature mixers', *Macromol. Mater. Eng.*, 291, 227–238.
- Lin-Gibson S, Pathak J A, Grulke E A, Wang H and Hobbie E K (2004) 'Elastic flow instability in nanotube suspensions', *Phys. Rev. Letters*, 92, 048302.
- Liu C, Zhang J, He J, Hu G (2003) 'Gelation in carbon nanotube/polymer composites', *Polymer*, 44, 7529–7535.
- Logakis E, Pandis C, Peoglos V, Pissis P, Stergiou C, Pionteck J, Pötschke P, Micusik M and Omastova M (2009) 'Structure-properties relationships in polyamide6/multi-walled carbon nanotubes nanocomposites', *J. Polym. Sci.: B Polym. Phys.*, 47, 764–774.
- Lozano K and Barrera E V (2001) 'Nanofiber-reinforced thermoplastic composites. I. Thermoanalytical and mechanical analysis', *J. Appl. Polym. Sci.*, 79, 125–133.
- Lozano K, Bonilla-Rios J and Barrera E V (2001) 'A study on nanofiber -reinforced thermoplastic composites (II): investigation of the mixing rheology and conduction properties', *J. Appl. Polym. Sci.*, 80, 1162–1172.
- Lozano K, Yang S and Zeng Q (2004) 'Rheological analysis of vapour-grown carbon nanofiber-reinforced polyethylene composites', *J. Appl. Polym. Sci.*, 93, 155–162.
- Ma A W K, Chinesta F and Mackley M R (2009a) 'The rheology and modelling of chemically treated carbon nanotubes suspensions', *J. Rheol.*, 53, 547–573.
- Ma A W K, Mackley M R and Chinesta F (2008) 'The microstructure and rheology of carbon nanotube suspensions', *Int. J. Mater. Form.*, 1, 75–81.
- Ma A W K, Mackley M R and Rahatekar S S (2007) 'Experimental observation on the flow-induced assembly of carbon nanotube suspensions to form helical bands', *Rheol. Acta*, 46, 979–987.
- Ma A W K, Yearsley K M, Chinesta F and Mackley M R (2009b) 'A review of the microstructure and rheology of carbon nanotubes suspensions', *J. Nanoengineering and Nanosystems*, 222, 71–94.

- Mago G, Fisher F T and Kalyon D M (2008) 'Effects of multiwalled carbon nanotubes on the shear-induced crystallization behavior of poly(butylene terephthalate)', *Macromolecules*, 41, 8103–8113.
- Marrucci G and Maffettone P L (1989) 'A description of the liquid crystalline phase of rod-like polymers at high shear rates', *Macromolecules*, 22, 4076–4082.
- Martin C A, Sandler J K W, Shaffer M S P, Schwarz, Bauhofer W, Schulte K and Windle A H (2004) 'Formation of percolating networks in multi-wall carbon-epoxy composites', *Composites Sci. and Technol.*, 64, 2309–2316.
- McNally T, Pötschke P, Halley P, Murphy M, Martin D, Bell S E J, Brennan G P, Bein D, Lemoine P and Quinn J P (2005) 'Polyethylene multiwalled carbon nanotube composites', *Polymer*, 46, 8222–8232.
- Meincke O, Kaempfer D, Weickmann H, Friedrich C, Vathauer M and Warth H (2004) 'Mechanical properties and electrical conductivity of carbon-nanotube filled polyamide-6 and its blends with acrylonitrile/butadiene/styrene', *Polymer*, 45, 739–748.
- Meissner J (1992) 'Experimental problems and recent results in polymer melt rheometry', *Makromol. Chem. Macromol. Symp.*, 56, 25–42.
- Mewis J and Moldenaers P (1987) 'Transient rheological behaviour of a lyotropic polymeric liquid crystal', *Mol. Cryst. Liq. Cryst.*, 153, 291–300.
- Minus M L, Chae H G and Kumar S (2006) 'Single wall carbon nanotube templated oriented crystallization of poly(vinyl alcohol)', *Polymer*, 47, 3705–3710.
- Mitchell C A, Bahr J L, Arepalli S, Tour J M and Krishnamoorti R (2002) 'Dispersion of functionalized carbon nanotubes in polystyrene', *Macromolecules*, 35, 8825–8830.
- Mitchell C A and Krishnamoorti R (2005) 'Non-isothermal crystallization of in situ polymerized poly(ϵ -caprolactone) functionalized-SWNT nanocomposites', *Polymer*, 46, 8796–8804.
- Mitchell C A and Krishnamoorti R (2007) 'Dispersion of single-walled carbon nanotubes in poly(ϵ -caprolactone)', *Macromolecules*, 40, 1538–1545.
- Moldenaers P and Mewis J (1986) 'Transient behaviour of liquid crystalline solutions of Poly(benzylglutamate)', *J. Rheol.*, 30, 567–584.
- Moniruzzaman M and Winey K I (2006) 'Polymer nanocomposites containing carbon nanotubes', *Macromolecules*, 39, 5194–5205.
- Morcom M (2008) 'Carbon nanotube polymer composites: the effect of the interface', PhD thesis, Monash University, Australia.
- Nakayama N and Harrel ER (1987) 'Modified Cole-Cole plot as a tool for rheological analysis of polymers', in RM Ottenbrite, LA Utracki, and S Inoue (eds) *Current Topics in Polymer Science, Rheology and Polymer Processing/Multiphase Systems*, vol. II, Munich: Carl Hanser, pp. 149–165.
- Neitzert H C, Rainone N C, Valentino O, Nobile M R, Sarno M and Ciambelli P (2008) 'Monitoring of the sample electrical conductivity during temperature cycling of polyethylene/CNT composites', paper presented at PPS-24, 24th Annual Meeting Polymer Processing Society, Salerno, Italy.
- Nobile M R and Cocchini F (2008) 'A generalized relation between MWD and relaxation time spectrum', *Rheol. Acta*, 47, 509–519.
- Nobile M R, Simon G P, Valentino O and Morcom M (2007) 'Rheological and structure investigation of melt mixed multi-walled carbon nanotube/PE composites', *Macromol. Symp.*, 247, 78–87.
- Payne A R (1965) in Kraus G, *Reinforcement of Elastomers*, New York: Interscience Publisher.

- Pötschke P, Abdel-Goad M, Alig I, Dudkin S and Lellinger D (2004) 'Rheological and dielectrical characterization of melt mixed polycarbonate-multiwalled carbon nanotube composites', *Polymer* 24, 8863–8870.
- Pötschke P, Bhattacharyya A R, Janke A and Goering H (2003) 'Melt mixing of polycarbonate/multi wall carbon nanotubes composites', *Composite Interfaces* 10, 389–404.
- Pötschke P, Brünig H, Janke A, Fischer D and Jehnichen D (2005) 'Orientation of multiwalled carbon nanotubes in composites with polycarbonate by melt spinning', *Polymer*, 46, 10355–10363.
- Pötschke P, Fornes T D and Paul D R (2002) 'Rheological behavior of multiwalled carbon nanotube/polycarbonate composites', *Polymer* 43, 3247–3255.
- Pötschke P, Krause, Stange B J and Münstedt H (2007) 'Elongational viscosity and foaming behavior of PP modified by electron irradiation or nanotube addition', *Macromol. Symp.* 254, 400–408.
- Probst O, Moore E M, Resasco D E and Grady B P (2004) 'Nucleation of polyvinyl alcohol crystallization by single-walled carbon nanotubes', *Polymer*, 45, 4437–4443.
- Pujari S, Rahatekar S S, Gilman J W, Koziol K K, Windle A H and Burghardt W R (2009) 'Orientation dynamics in multiwalled carbon nanotube dispersions under shear flow', *J. Chem. Phys.*, 130, 214903 (1–9).
- Rahatekar S S, Koziol K K K, Butler S A, Elliot J A, Shaffer M S P, Mackley M R and Windle A H (2006) 'Optical microstructure and viscosity enhancement for an epoxy resin matrix containing multi wall carbon nanotubes', *J. Rheol.*, 50, 599–610.
- Ren J and Krishnamoorti R (2003) 'Nonlinear viscoelastic properties of layered-silicate-based intercalated nanocomposites', *Macromolecules*, 36, 4443–4451.
- Ren J, Silva A S and Krishnamoorti R (2000) 'Linear viscoelasticity of disordered polystyrene-polyisoprene block copolymer based layered-silicate nanocomposites', *Macromolecules*, 33, 3739–3746.
- Romo-Urbe A, Lemmon T J and Windle A H (1997) 'Structure and linear viscoelastic behaviour of main-chain thermotropic liquid crystalline polymers', *J. Rheol.*, 41, 1117–1145.
- Sandler J, Shaffer M S P, Prasse T, Bauhofer W, Schulte K and Windle A H (1999) 'Development of a dispersion process for carbon nanotubes in an epoxy matrix and the resulting electric properties', *Polymer*, 40, 5967–5971.
- Satapathy B K, Weidisch R, Pötschke P and Janke A (2007) 'Tough-to-brittle transition in multiwalled carbon nanotube (MWNT)/polycarbonate nanocomposites', *Composites Science and Technology*, 67, 867–879.
- Schartel B, Pötschke P, Knoll U and Abdel-Goad M (2005) 'Fire behaviour of polyamide 6/multiwall carbon nanotube nanocomposites', *European Polymer Journal*, 41, 1061–1070.
- Seki M, Thurman D W, Oberhauser J P and Kornfield J A (2002) 'Shear-mediated crystallization of isotactic polypropylene: the role of long chain-long chain overlap', *Macromolecules*, 35, 2583–2594.
- Seo M K, Lee J R and Park S J (2005) 'Crystallization kinetics and interfacial behaviors of polypropylene composites reinforced with multi-walled carbon nanotubes', *Mat. Sci. Eng. A*, 404, 79–84.
- Seo M K and Park S J (2004) 'Electrical resistivity and rheological behaviors of carbon nanotubes-filled polypropylene composites', *Chem. Phys. Lett.*, 395, 44–48.
- Shenoy A V (1999) *Rheology of Filled Polymer Systems*, Dordrecht: Kluwer Academic Publishers.

- Sigillo I and Grizzuti N (1994) 'The effect of molecular weight on the steady shear rheology of lyotropic solutions: a phenomenological study', *J. Rheol.*, 38, 589–599.
- Skipa T, Lellinger D, Böhm W, Saphiannikova M and Alig I (2010) 'Influence of shear deformation on carbon nanotube networks in polycarbonate melts: interplay between build-up and destruction of agglomerates', *Polymer*, 51, 201–210.
- Solomon M J, Almusallam A S, Seefeldt K F, Somwangthanaroj A and Varadan P (2001) 'Rheology of polypropylene/clay hybrid materials', *Macromolecules*, 34, 1864–1872.
- Somani R H, Hsiao B S, Nogales A, Srinivas S, Tsou A H, Sics I, Balta-Calleja F J and Ezquerro T A (2000) 'Structure development during shear flow induced crystallization of i-PP: in-situ small angle X-ray scattering study', *Macromolecules*, 33, 9385–9394.
- Somani R H, Yang L, Zhu L and Hsiao B S (2005) 'Flow-induced shish-kebab precursor structures in entangled polymer melts', *Polymer*, 46, 8587–8623.
- Somma E and Nobile M R (2004) 'The linear viscoelastic behavior of a series of molecular weights of the thermotropic main-chain liquid crystal polymers HBA/HNA 73/27', *J. Rheol.*, 48, 1407–1423.
- Somma E, Valentino O, Iervolino R, Simon G P, Hsiao B S and Nobile M R (2009) 'Temperature effect on the percolation network of multi-walled carbon nanotubes polymer nanocomposites', in *Proceedings of the 5th Annual European Rheology Conference*, Cardiff, United Kingdom.
- Somma E, Valentino O and Nobile M R (2008a) 'Reologia e cristallizzazione di nanocompositi di polietilene e nanotubi in carbonio a parete multipla', in *Proceedings of X Convegno Nazionale della Società Italiana Reologia*, Ravenna, Italy, pp. 259–264.
- Somma E, Valentino O, Nobile M R and Simon G P (2008b) 'Rheology and crystallization of multi-walled carbon nanotubes polymer composites', in *Proceedings of PPS-24, 24th Annual Meeting Polymer Processing Society*, Salerno, Italy.
- Somoza A M, Sagui C and Roland C (2001) 'Liquid-crystal phases of capped carbon nanotubes', *Physical Review B*, 63, 081403.
- Song W, Kinloch I A and Windle A H (2003) 'Nematic liquid crystallinity of multiwall carbon nanotubes', *Science*, 302, 1363.
- Song Y S (2006a) 'Rheological characterization of carbon nanotubes/poly(ethylene oxide) composites', *Rheol. Acta*, 46, 231–238.
- Song Y S (2006b) 'Effect of surface treatment for carbon nanotubes on morphological and rheological properties of poly(ethylene oxide) nanocomposites', *Polym. Eng. Sci.*, 46, 1350–1357.
- Song Y S and Youn J R (2005) 'Influence of dispersion states of carbon nanotubes on physical properties of epoxy nanocomposites', *Carbon*, 43, 1378–1385.
- Sung Y T, Han M S, Song K H, Jung J W, Lee H S, Kum C K, Joo J and Kim W N (2006) 'Rheological and electrical properties of polycarbonate/multi-walled carbon nanotube composites', *Polymer*, 47, 4434–4439.
- Teng C C, Ma C C M, Huang Y W, Yuen S M, Weng C C, Chen C H and Su S F (2008) 'Effect of MWCNT content on rheological and dynamic mechanical properties of multiwalled carbon nanotube/polypropylene composites', *Composites: Part A*, 39, 1869–1875.
- Tiwari M K, Bazilevsky A V, Yarin A L and Megaridis C M (2009) 'Elongational and shear rheology of carbon nanotube suspensions', *Rheol. Acta*, 48, 597–609.
- Trinkle S, Walter P and Friedrich C (2002) 'Van Gurp-Palmen Plot II-classification of long chain branched polymers by their topology', *Rheol. Acta*, 41, 103–113.
- Utracki L A (1987) 'Rheology and processing of multiphase systems', in R M Ottenbrite, L A Utracki and S Inoue (eds) *Current Topics in Polymer Science*:

- Rheology and Polymer Processing/Multiphase Systems*, vol. II, Munich: Carl Hanser, pp. 7–59.
- Valentini L, Biagiotti J, Kenny J M and Santucci S (2003) 'Morphological characterization of single-walled carbon nanotubes-PP composites', *Compos. Sci. Technol.*, 63, 1149–1153.
- Valentini L, Biagiotti J, Lopez-Manchado M A, Santucci S and Kenny J M (2004) 'Effects of carbon nanotubes on the crystallization behavior of polypropylene', *Polym. Eng. Sci.*, 44, 303–311.
- Valentino O (2008) 'The effect of surface treatment and matrix properties on CNT/Polymer composites', PhD thesis, University of Salerno.
- Valentino O, Sarno M, Rainone N G, Nobile M R, Ciambelli P, Neitzert H C and Simon G P (2008) 'Influence of the polymer structure and nanotube concentration on the conductivity and rheological properties of polyethylene/CNT composites', *Physica E*, 40, 2440–2445.
- Valentino O, Somma E, Nobile M R and Simon G P (2009) 'Reologia e cristallizzazione di nanocompositi HDPE e nanotubi in carbonio', *Panta Rei*, 10, 3–9.
- Van Gurp M, and Palmen J (1998) 'Time-temperature superposition for polymeric blends', *Rheol. Bull.*, 67, 5–8.
- Vega J F, Martinez-Salazar J, Trujillo M, Arnal M L, Muller A J, Bredeau S and Dubois P (2009) 'Rheology, processing, tensile properties, and crystallization of polyethylene/carbon nanotubes nanocomposites', *Macromolecules*, 42, 4719–4727.
- Vleeshouwers S and Meijer H E H (1996) 'A rheological study of shear induced crystallization', *Rheol. Acta*, 35, 391–399.
- Wang K, Tang C, Zhao P, Yang H, Zhang Q, Du R and Fu Q (2007) 'Rheological investigations in understanding shear-enhanced crystallization of isotactic poly(propylene)/multi-walled carbon nanotube composites', *Macromol. Rapid Commun.*, 28, 1257–1264.
- Wang Y, Xu J, Bechtel S E and Koelling K W (2006) 'Melt shear rheology of carbon nanofiber/polystyrene composites', *Rheol. Acta*, 45, 919–941.
- Wei C and Srivastava D (2004) 'Structural ordering in nanotube polymer composites', *Nano. Lett.*, 4, 1949–1952.
- Winter H H and Chambon F (1986) 'Analysis of linear viscoelasticity of a crosslinking polymer at the gel point', *J. Rheol.*, 30, 367–382.
- Winter H H and Mours M (1997) 'Rheology of polymers near liquid-solid transitions', *Adv. Polym. Sci.*, 134, 165–234.
- Wu D, Sun Y, Wu L and Zhang M (2008) 'Linear viscoelastic properties and crystallization behaviour of multi-walled carbon nanotube/polypropylene composites', *J. Appl. Polym. Sci.*, 108, 1506–1513.
- Wu D, Wu L, Sun Y and Zhang M (2007b) 'Rheological properties and crystallization behaviour of multi-walled carbon nanotube/poly(ϵ -caprolactone) composites', *J. Polym. Sci. B Polym. Phys.*, 45, 3137–3147.
- Wu D, Wu L and Zhang M (2007a) 'Rheology of multi-walled carbon nanotube/poly(butylene terephthalate) composites', *J. Polym. Sci. B Polym. Phys.*, 45, 2239–2251.
- Wu D, Zhou C, Hong Z, Mao D and Bian Z (2005) 'Study on rheological behaviour of poly(butylenes terephthalate)/montmorillonite nanocomposites', *Europ. Polym. J.*, 41, 2199–2207.
- Xu D H, Wang Z G and Douglas J F (2008) 'Influence of carbon nanotube aspect ratio on normal stress differences in isotactic polypropylene nanocomposite melts', *Macromolecules*, 41, 815–825.
- Xu J, Chatterjee S, Koelling K W, Wang Y and Bechtel S E (2005) 'Shear and extensional rheology of carbon nanofiber suspensions', *Rheol. Acta*, 44, 537–562.

- Yui H, Wu G, Sano H, Sumita M and Kino K (2006) 'Morphology and electrical conductivity of injection-molded polypropylene/carbon black composites with addition of high density polyethylene', *Polymer*, 47, 3599–3608.
- Zhang Q and Archer L A (2002) 'Poly(ethylene oxide)/silica nanocomposites: structure and rheology', *Langmuir*, 18, 10435–10442.
- Zhang Q, Fang F, Zhao X, Li Y, Zhu M and Chen D (2008) 'Use of dynamic rheological behavior to estimate the dispersion of carbon nanotubes in carbon nanotube/polymer composites', *J. Phys. Chem. B*, 112, 12606–12611.
- Zhang Q, Lippits D and Rastogi S (2006a) 'Dispersion and rheological aspects of SWNTs in ultrahigh molecular weight polyethylene', *Macromolecules*, 39, 658–666.
- Zhang Q, Rastogi S, Chen D, Lippits D and Lemstra P J (2006b) 'Low percolation threshold in single-walled carbon nanotube/high density polyethylene composites prepared by melt processing technique', *Carbon*, 45, 778–785.
- Zhou W J, Kornfield J A, Ugaz V M, Burghardt W R, Link D R and Clark N A (1999) 'Dynamics and shear orientation behaviour of a main-chain thermotropic liquid crystalline polymer', *Macromolecules*, 32, 5581–5593.

Thermal degradation of polymer–carbon nanotube composites

S. P. SU and Y. H. XU, Hunan Normal University, P. R. China and
C. A. WILKIE, Marquette University, USA

Abstract: This chapter discusses the thermal degradation of polymer–carbon nanotube (CNT) composites which plays a crucial role in determining their processing and applications. The chapter first reviews the mechanisms of thermal degradation/stability improvement by carbon nanotubes, which is affected by the barrier effect, thermal conductivity of CNT, physical or chemical adsorption, radical scavenging action, and polymer–nanotube interaction. It then describes the thermal degradation/stability of polymer–CNT composites and their development trends. It is necessary and meaningful to further investigate the thermal degradation of polymer–CNTs.

Key words: carbon nanotube, composites, thermal degradation, thermal stability.

16.1 Introduction

Since the work of Iijima in 1991, many polymer–carbon nanotubes (CNT) composites (Chen *et al.*, 2006; Yuen *et al.*, 2007; Chen and Wu, 2007; Kanagaraj *et al.*, 2007; Kim *et al.*, 2009a) have been studied with promising applications due to the unique combination of electronic, thermal, optical, and mechanical properties of CNT (Schadler *et al.*, 1998; Stephan *et al.*, 2002; Dalton *et al.*, 2003; Barrau *et al.*, 2003; Thostenson and Chou, 2003; Coleman *et al.*, 2006), as summarized in recent review articles (Lau and Hui, 2002; Breuer and Uttandaraman, 2004; Moniruzzaman and Winey, 2006; Chen *et al.*, 2009a; Mohammed and Uttandaraman, 2009). However, there are only a few studies on the thermal properties, especially thermal degradation or thermal stability, which is very important in the application of polymer–CNT composites.

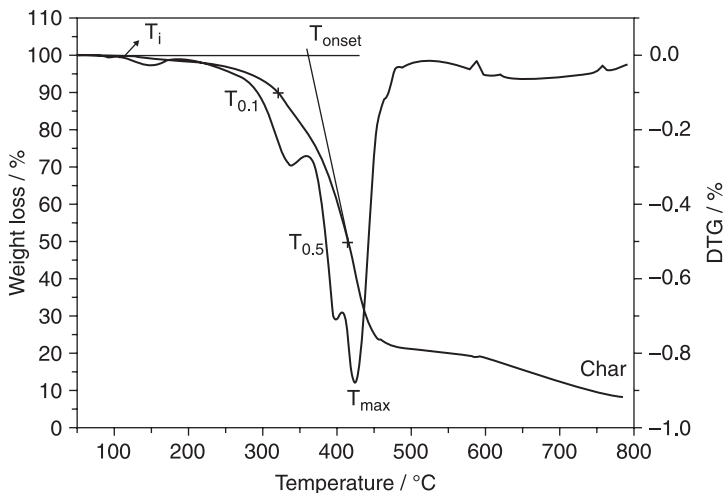
The thermal stability of polymer–CNT composites plays a crucial role in determining their processing and applications because it affects the final properties of polymer–CNT composites, such as the upper limit use temperature and dimensional stability. For the fabrication of polymer–CNT composites with better balance in processing and performance, it is necessary to characterize the thermal stability and decomposition kinetics of polymer composites. Thus, an understanding of the thermal decomposition behavior of polymer–CNT composites makes it possible to develop commercial applications in a broad range of industries. At the same time, the thermal stability, in turn, is closely connected to fire retardancy. The thermal degradation/stability improvement also facilitates enlarging the applications

in the field of fire retardancy. So, in this chapter, the thermal degradation of polymer–CNT composites is reviewed.

In general, the thermal degradation of materials is assessed by thermogravimetry analysis (TGA). However, there is no uniform standard on the characteristic temperature of materials from TGA curves. The characteristic values in the TGA curve that are commonly used include the temperature of the initial weight loss (T_i), the temperature of maximum weight loss rate (T_{\max}), the onset temperature obtained from the intersection between the baseline and the tangent at maximum weight loss rate (T_{onset}); the temperature at which 10% degradation occurs ($T_{0.1}$), the temperature at which 50% degradation occurs, the mid-point of the degradation process ($T_{0.5}$); and the amount of residue, denoted as char. Sometimes, it is considered that $T_{0.1}$ is consistent with T_{onset} . A typical TGA curve for a polyurea containing 0.2% MWNT is shown in Fig. 16.1.

16.2 Mechanisms of thermal degradation/stability improvement by CNTs

It is now well accepted that the improved thermal stability of polymer–CNT composites is due to the following: barrier effect, thermal conductivity of CNTs, physical or chemical adsorption, radical scavenging action, and polymer–nanotube interaction. For each polymer–CNT composite, thermal stability may be due to one mechanism or the combined action of several processes, which depend on the different components, microstructures and exterior conditions.



16.1 A typical TGA curve for a polyurea containing 0.2% MWNT.

Barrier effect: The nanotube barrier effect of polymer-CNT composite degradation processes is mainly a mass transport barrier, which slows the escape of the volatile products during the process of degradation and the permeation of O₂ or air. It is related to the network structure and dispersion of nanotube in the composites and the compact char formation. The well-dispersed nanotubes could hinder the transport of polymer degradation products from the condensed phase to the gas phase compared to composites with poorly-dispersed nanotubes (Marosfoi *et al.*, 2006). The accumulation of CNT with a network structure in the composites also tends to increase the mechanical integrity of a protective layer or barrier to prevent the evolution of degradation products to the gas phase. This protective layer or barrier will also limit air or oxygen diffusion into or within the polymer composite, and this is extremely efficient at low temperatures. However, on increasing the temperature up to a limiting value, the superficial protecting nanotube network will be destroyed and the large mass loss starts until degradation is complete. In addition, the formation of a compact char of CNT and polymer matrix during the thermal degradation is beneficial to the barrier labyrinth effect of CNT so that the diffusion of degradation products from the bulk of the polymer to the gas phase is slowed (Kashiwagi *et al.*, 2002).

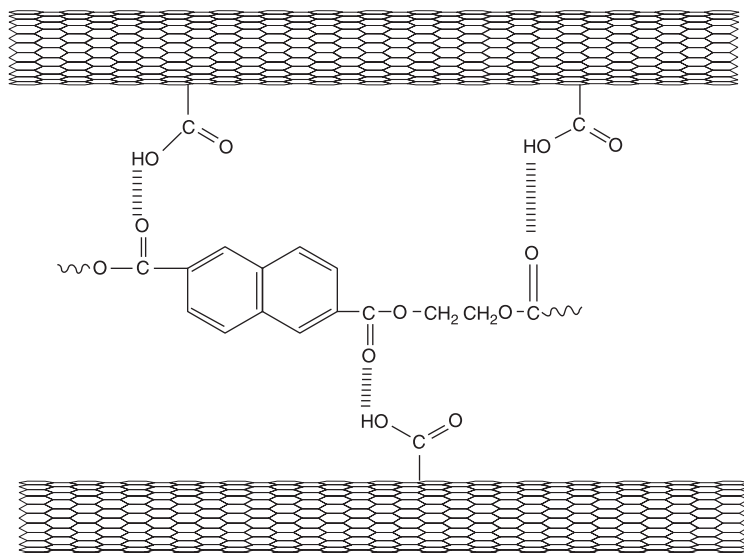
Thermal conductivity of CNTs: It is well known that CNTs, as compared to the polymers, show higher thermal conductivity in the axial direction. The addition of CNTs will assist in conducting heat from the surface and facilitate heat dissipation within the composites, resulting in slow degradation of the composites (Yu *et al.*, 2000). CNTs in the composites form a network by connecting with each other in a random way. This special morphology can effectively promote the thermal conductivity of the CNT network in the entire composite to improve the thermal stability (Fujii *et al.*, 2005). On the other hand, CNTs are sometimes functionalized or modified to obtain good dispersion, which may impair thermal conductivity due to separation of the CNTs (Stevens *et al.*, 2003; Sakellariou *et al.*, 2008; Bartholome *et al.*, 2008; Gao *et al.*, 2009).

Physical or chemical adsorption: CNTs have typical diameters in the range of ~1–50 nm, lengths of many microns and a large aspect ratio which can physically or chemically adsorb the decomposition products; in addition, polymers near the nanotubes might degrade more slowly due to decreasing activity, which would move degradation to higher temperatures. It has been reported that bundle exfoliation could remarkably increase the aspect ratio of the CNT in the composites, and result in a more effective absorption of the degradation products during the degradation processes (Zanetti *et al.*, 2001; Yang *et al.*, 2005).

Polymer-nanotube interaction: The interfacial interaction of the polymer-nanotube is significantly affected by the surface characteristics of the CNTs. The pure CNT is easy to agglomerate and the interface is poor. Surface functionalization could significantly modify the surface characteristics of CNTs and strengthen the interfacial bonding between CNTs and the polymer matrix (Markovic *et al.*, 2006; Lee *et al.*, 2007; Kim *et al.*, 2008a). Good interfacial interaction will increase the

activation energy of degradation. The higher the activation energy of degradation, the more stable the composite. It also reduces the interfacial thermal resistance (Yang *et al.*, 2008). However, the functionalization of CNTs will also have a negative effect on the thermal stability of the CNT due to the degradation of polymers grafted onto the surface of the CNT. Therefore, the optimum degree of functionalization for the CNT must be considered (Wang, 2009). Figure 16.2 shows an example of the interfacial interaction between m-CNT and poly(ethylene 2,6-naphthalate) (PEN) matrix.

Radical scavenging action: Generally, it is known that the thermal degradation of most polymers occurs by random chain scission to form radicals that are susceptible to reagents capable of trapping the radicals. Fang *et al.* (2008) proposed the free radical-trapping mechanism of C_{60} to explain the enhanced thermal properties. At the initial degradation stage of polymers, C_{60} simultaneously traps macromolecular free radicals and other small free radicals, like $H\cdot$ and $\cdot OH$, to form cross-link gel networks. On the other hand, the radical trapping effect of C_{60} also allows the macromolecular radicals more time to recombine, which also contributes to the formation of a gel network. Furthermore, at some elevated temperatures, the degradation of polymers will produce macromolecular radicals with several active sites. These active sites are easily attacked by the C_{60} particles and subsequently form a branching or 3D gel network structure. The CNTs have high electron affinities, similar to C_{60} , and have been proposed to act as scavengers of free radicals (Watts *et al.*, 2003). In fact, CNTs are usually purified, by using



16.2 Possible interaction of hydrogen bonding between m-CNT and poly(ethylene 2,6-naphthalate) matrix.

concentrated $\text{HNO}_3/\text{H}_2\text{SO}_4$ mixtures before use. The surface of the oxidized CNT is covered to some extent with carboxylic ($-\text{COOH}$), carbonyl ($\text{C}=\text{O}$) and hydroxyl ($-\text{OH}$) groups. These groups can trap active free radicals to form more stable species during the degradation process of polymers such as PE, PP, and PMMA. Investigations also indicate that the iron oxides in CNTs could also act as a radical trapping component during the process of degradation (Zhu *et al.*, 2001; Kashiwagi *et al.*, 2002; Du *et al.*, 2006; Sahoo *et al.*, 2009). The entangled network structure of the CNT also helps the radical trapping through restricting the thermal motion of the polymer chains, and keeps the degrading polymer radicals together to present radical recombination reactions during the degradation process, which has been called nano-confinement (Gorrasí *et al.*, 2007; Costache *et al.*, 2007; Chen *et al.*, 2007). When the radicals produced are relatively unstable, there is no time for them to participate in radical recombination reactions (Costache *et al.*, 2006).

16.3 The thermal degradation of polymer–CNT composites

16.3.1 The thermal degradation of CNTs

Amount and type of impurities in the nanotubes

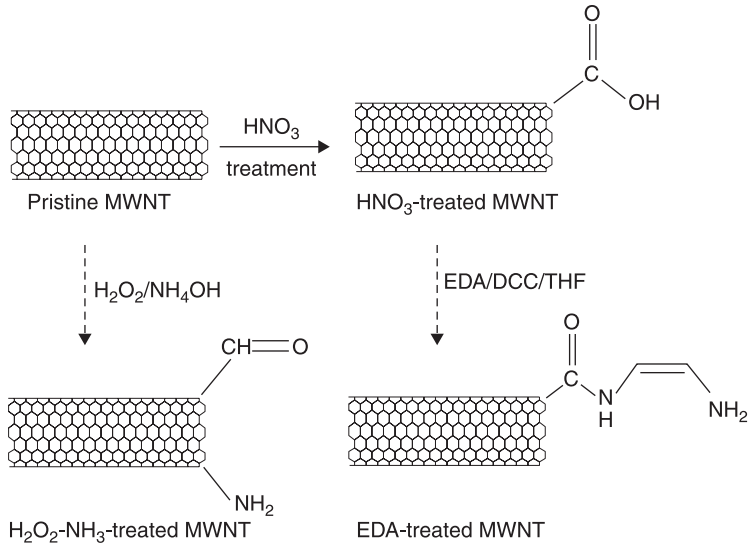
The intrinsic thermal stability of CNTs is important for the thermal properties of polymer–CNT composites. In general, pristine CNTs are thermally stable up to 3073 K in a vacuum, 1023 K in air and there is no significant mass loss in N_2 below 1073 K (Wang, 2009). But CNTs always contain amorphous carbon, carbon nanoparticles, hemifullerenes and residues from the metal catalysts. These have an effect on the thermal stability of the CNT. The thermal stability of amorphous carbon, carbon nanoparticles, and hemifullerenes is comparatively lower than that of CNT itself. Therefore, the lower the purity of the CNT, the easier is the degradation. For residues from the metal catalysts, such as Fe^{3+} , Ni^{2+} or Co^{2+} , although the thermal degradation of the CNT is not affected, there are important influences on the thermal stability of polymers such as PMMA (Xi *et al.*, 2005), EVA (Marosfoi *et al.*, 2006) and PC (Schartel *et al.*, 2008); these metal ions are Lewis acids which can bond with the carbonyl oxygen in PMMA and form an intermediate complex. Due to conjugation, free radicals are weakened, the activity of free radicals increases and the PMMA thermal degradation reaction occurs more easily. However, Kashiwagi *et al.* (2002) proposed that iron did not affect the thermal stability of PP in PP–iron-containing MWNTs. Since the iron particles are inside and at ends of the MWNTs, the chances of contact with PP chains during the TGA experiments would be low and would not occur until the walls of the nanotube were destroyed. Bocchini *et al.* (2007) also reported that impurities in MWNTs (e.g. metal oxides from the MWNT synthesis catalyst) do not influence the thermal stability of LLDPE in nitrogen.

The thermal stability of CNTs also depends on the structure of the CNT. Marosfoi *et al.* (2006) reported that DWNTs undergo a two-step degradation and start to lose mass at 723 K; the majority of the mass loss occurred in the second step with a degradation temperature of 798 K in air. In the case of MWNTs, the mass loss starts at 877 K and large mass loss occurs at 1003 K. One could even observe the mass loss at temperatures up to 1073 K. The differences in degradation behavior between DWNTs and MWNTs could be explained by the higher number of defects in DWNTs formed in the synthetic process, and these defects make DWNTs more subject to the degradative action of air compared to MWNTs. Liew *et al.* (2005) have studied the thermal stability of single-walled and multi-walled carbon nanotubes and found that SWNTs are thermally more stable than MWNTs, due to the presence of more than one layer in the MWNT. When a MWNT is subjected to thermal load, the atoms from different layers start to vibrate. At high temperatures, the vibrations become stronger and the atoms from one layer collide with the atoms from the neighboring layers, making it easier for the MWNT to degrade.

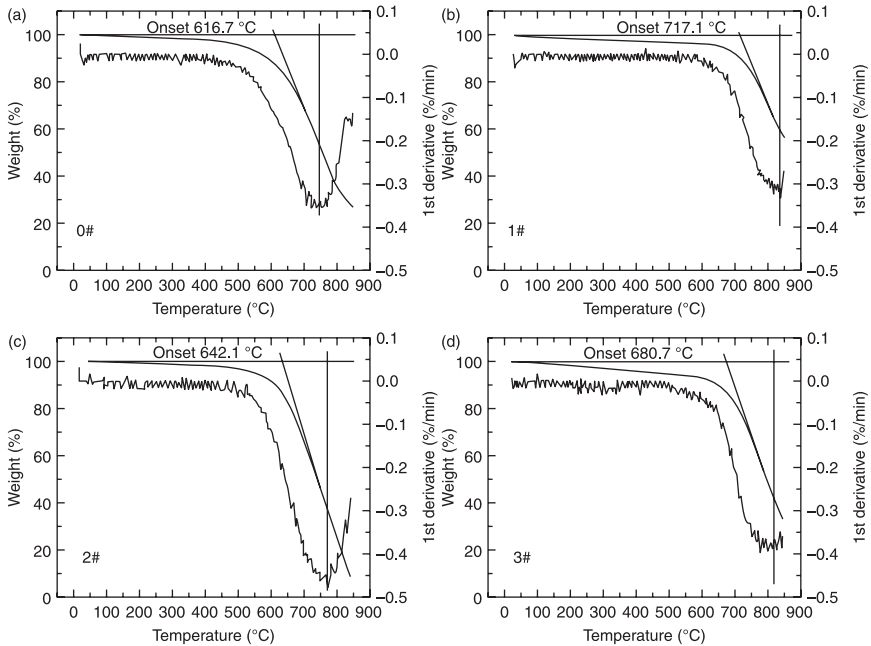
Chemically treated CNTs

CNTs are highly polarizable carbon compounds with an attractive interaction of 0.5 eV per nanometer of inter-tube contact. The cohesive force makes it difficult to disperse CNTs into individual nanotubes, and limits the potential applications of CNTs (Wang, 2009). Chemical treatment of CNTs becomes an attractive strategy to overcome these barriers. One of the most common chemical techniques is the oxidative treatment in solution. While good dispersion of CNT could be achieved through modification, the thermal stability of the CNT is affected, depending on the modification methods. The enhanced thermal stability of functionalized MWNTs by different chemical treatments was reported by Yang *et al.* (2008). Figure 16.3 shows the synthesis and structure of functionalized MWNTs. Their TGA traces are shown in Fig. 16.4. It has been observed that the T_{onset} of pristine MWNT (0#), HNO_3 -treated MWNT(1#), H_2O_2 - NH_3 -treated MWNT(2#), and EDA-treated MWNT(3#) appears at 890 K, 991 K, 916 K, and 954 K, respectively. The degradation temperature of MWNTs treated by nitric acid is higher than that oxidized by $\text{H}_2\text{O}_2/\text{NH}_3$ or EDA. The onset degradation temperature difference between EDA-treated MWNT and nitric acid-treated MWNT is attributed to the amine-functionalization which may have weakened the interfacial bonding between graphite sheets of the MWNT. Impurities have been removed by chemical treatment in the preparation of peroxide-ammonia-treated-MWNTs, resulting in better intrinsic thermal stability than in the pristine material. Similar experimental results have been reported in other papers (Andrews *et al.*, 2004; Ovejero *et al.*, 2006).

Defect functionalization is another effective chemical treatment. An obvious decrease in thermal stability of MWNT obtained by defect functionalization and

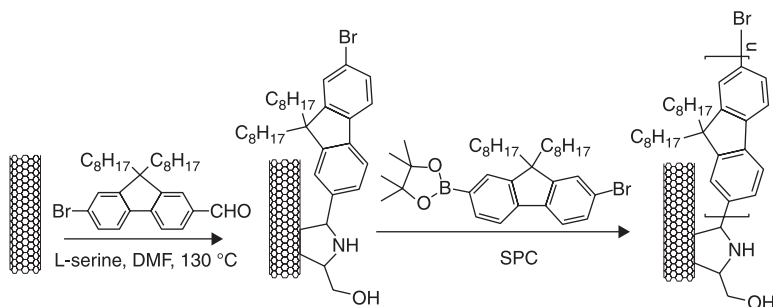


16.3 The synthesis and structure of functionalized MWNTs.



16.4 The TGA traces of functionalized MWNTs by different chemical treatments. Reprinted with permission from Yang *et al.* (2008).

'grafting to' technique was observed by Xu *et al.* (2007). The structures are presented in Fig. 16.5. The acid-treated MWNT exhibited very good thermal stability which showed 8% mass loss at 873 K in N_2 . The mono-fluorene-functionalized MWNT displayed 15% mass loss at 873 K. Furthermore, the polyfluorene (PF)-functionalized MWNT started to decompose at about 423 K and lost about 50% of the mass at 873 K. The decreased decomposition temperature of the PF-functionalized MWNT is due to the bromo-end groups of the grafted polyfluorenes which dramatically promote the decomposition of conjugated polymers. Similar observations were presented for PLA-g-MWNT (poly(L-lactic acid) (Chen *et al.*, 2005). Lower thermal stability was observed for PLA-g-MWNT systems compared to that of the acid-treated MWNT (MWNT-COOH). Moreover, the extent of the decrease depends on the different molecular weight of PLA. The molecule chain length of PLA grafted onto the MWNT used in this study is presented in Fig. 16.6. The thermal degradation of PLA-g-MWNT gradually increased with the increase of molecule weight. Jana and Cho (2008) also reported that T_i of poly(ϵ -caprolactone)diol-g-MWNT (PCL-g-MWNT) decreased regularly with the increase in wt% of PCL due to the increased proportion of the carbonyl groups coming from the f-MWNT. The carbon atoms of the f-MWNT attached to the carboxylic group are sp^3 hybridized, which causes high inherent strain, making them more susceptible to thermal degradation. The T_{onset} of various modified carbon nanotubes are summarized in Table 16.1.

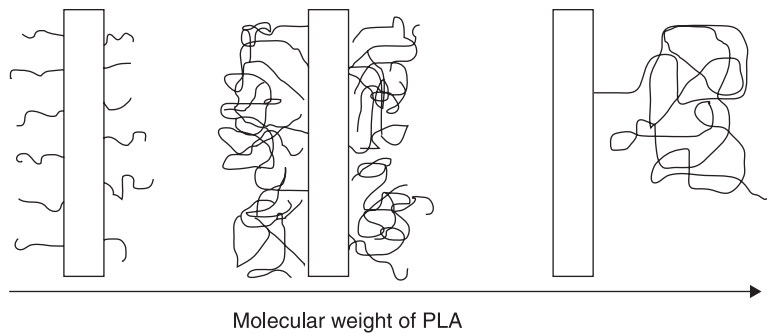


16.5 Synthesis of the PF-functionalized MWNT.

16.3.2 The thermal degradation of polymer–CNT composites

Polyolefins

In most cases, CNTs incorporated into the polyolefins can lead to a stabilization of the polymeric matrix. Gorrasi *et al.* (2007) revealed that the thermal degradation of LLDPE–MWNT composites in the air was significantly delayed with 1–10wt% of MWNT. T_{onset} of LLDPE was enhanced by about 40 K for a 10 wt%



16.6 Illustration of the molecule chain length of the PLA grafted onto the MWNT.

Table 16.1 T_{onset} of the various functionalized carbon nanotubes

Functionalized carbon nanotubes	T_{onset} (°C)	Ref.
MWNT-COOH	717	Yang <i>et al.</i> (2008)
NH ₂ -MWNT-C=O	642	Yang <i>et al.</i> (2008)
MWNT-CONHCH=CHNH ₂	680	Yang <i>et al.</i> (2008)
MWNT-g-PLLA	250	Chen <i>et al.</i> (2005)
MWNT-g-PCL	280	Jana and Cho (2008)
MWNT-PA	200	Zhang <i>et al.</i> (2008b)
MWNT-g-PS	310	Wang <i>et al.</i> (2006b)
SWNT-g-PS	337	Wang <i>et al.</i> (2006b)

loading of MWNT. In the Costache *et al.* (2007) study, two different CNTs were used in the preparation of PE–CNT composites. $T_{0.1}$ and $T_{0.5}$ of PE–MWNT were respectively increased by about 16 K and 5 K, respectively, while for PE–SWNT, the increases are 13 K and 3 K, compared to PE. No significant difference has been observed between MWNT and SWNT. For PP–MWNT a slight increase of T_{max} was reported by Wiemann *et al.* (2005). These findings were related to the high thermal stability, good thermal conductivity, and network structure of CNTs. Meanwhile, impurities in the CNTs will be inevitably brought into the composites. These impurities can promote the degradation of polyolefins. Kanagaraj *et al.* (2007) observed that T_{onset} of HDPE–MWNT composites rapidly decreased with the addition of MWNTs (range of diameter 60–100 nm, length of the tubes 5–15 μm , and purity >95%). T_{onset} are 668 K, 628 K, 600 K and 589 K for pure HDPE, 0.11%, 0.22% and 0.44% MWNT in PE, respectively. However, this could be avoided by purifying MWNT. McNally *et al.* (2005) reported that T_{onset} of PE–MWNT composites, where MWNTs were treated with acid and distilled water, was enhanced by about 20 K at a 10 wt% loading of MWNTs.

Experimental results indicated that chemically-modified CNTs could improve the mechanical properties, but this does not always enhance the thermal stability of polyolefin composites. The Kovalchuk *et al.* (2008) study showed that the addition of 0.1 wt% modified MWNTs obtained from methylaluminumoxane reacting with –COOH groups on the MWNT increases T_{\max} of the iPP/modified MWNT by about 30 K in comparison with pristine iPP, and this parameter rises with a further increase in the filler content. By introducing just 3.5 wt% of modified MWNT, T_{\max} surpasses the characteristic value of the neat polymer by about 60 K. This thermal stabilization effect is mostly connected with the nanotube barrier effect. The thermal degradation temperature will be improved if the interfacial interaction between polyolefin and CNT is enhanced. Shofner *et al.* (2006) provided an improved thermal stable effect for PE–CNT composites through comparative experiments among PE, PE–pure SWNTs and PE–fluorinated SWNTs systems. Although the interfacial interaction of PE–fluorinated SWNTs was modified, PE–fluorinated SWNTs show smaller differences in the thermal behavior than PE–pure-SWNTs compared to the pure PE. The difference would be accounted for by a lower carbon loading in the fluorinated SWNTs because of fluorine mass included in the fluorinated SWNTs.

The formation of a protective char is another reason for the delayed thermal and oxidative degradation of polyolefin/CNT. Bocchini *et al.* (2007) did research on the thermal degradation of LLDPE–MWNT. SEM and ATR–FTIR experimental data indicated the presence of a thin protective film of MWNT–carbon char composite on the surface of the nanocomposites, and this has been used to explain the delayed thermal degradation temperature of LLDPE–MWNT in N_2 or in air. This protective char was formed by the catalyzed oxidative dehydrogenation of LLDPE in the presence of MWNTs, which prevents oxygen diffusion towards the underlying polymer matrix and the loss of volatile products from the polymer. Kashiwagi *et al.* (2002) and Kashiwagi *et al.* (2004) also observed that a nanotube network layer is formed which insulates PP from the external radiant flux during burning of the PP–MWNT nanocomposites. Their research indicates that this nanotube layer could physically reduce the external heat flux up to one-half. The formation of nanotube layer also was confirmed by Zhao *et al.* (2006) and Seo and Park (2004).

Most research on the degradation of polyolefin/CNT indicated that free radical trapping plays an important role in the enhancement of thermal stability of the composites. The C–C bond in the main chains of polyolefin breaks at a high temperature to form carbon-based radicals, or the C–H bond is attacked by oxygen to generate $HO\bullet$ and alkoxy free radicals in the presence of O_2 , and subsequently leads to a series of polymer chain degradations through random scission. The addition of CNTs can delay the degradation of polyolefins by trapping free radicals. Watts *et al.* (2003) revealed that the thermal-oxidative stability of PE, PP and poly(vinylidene fluoride) (PVDF) is retarded by MWNT. The oxidation induction temperatures (OIT) for pure PP, CNT-PP (1:5) and CNT-PP(1:10) are

431 K, 443 K and 448 K, respectively. In the case of PVDF, it is also evident that the OIT shifts from 398 K for pure PVDF to >433 K for CNT-PVDF. CNT contain localized trapping sites due to lattice defects (e.g. vacancies, dangling bonds, OH and C=O attachments). These localized states are acceptor-like, which can terminate radicals during polymer degradation. In Kodjie *et al.*'s (2006) work, the thermal stability of HDPE-CNT also showed dramatic enhancement based on the radical scavenging action, as high as 70 K/115 K improvement of T_{\max} in N_2 /air atmosphere, respectively.

In another study carried out by Wang *et al.* (2006a), it was demonstrated that physical or chemical adsorption of the MWNT (diameter 10–30 nm, length 0.5–40 μm) for the PP molecules could significantly increase the thermal degradation temperature. The improvements in the T_{\max} for PP at the 1% and 5% loading of unmodified MWNT are about 40 K and 70 K, respectively. TGA and DTG data suggest a two-step degradation in the PP-MWNT composites, which indicates that the incorporation of MWNT induces PP molecular to form two different aggregation structures; this has been explained by physical adsorption of MWNT. Nanotubes were covered with a layer of PP molecules through physical adsorption in the PP-MWNT composites prepared by the melt mixing method. The adsorbed PP molecules are much less active than those far from the nanotube surface, and their degradation is delayed. Similar physical or chemical adsorption of the MWNTs takes place in the investigation by Yang *et al.* (2005). In their work, MWNTs were added to the aPP, weight-averaged molecular weight and number averaged molecular weight are 41,402 and 1481, respectively, by melt blending at 353 K in a Barabender mixer. TGA results indicate that thermal stability of the aPP-MWNT composite in nitrogen is enhanced significantly by the addition of nanotubes. The peak temperature of the DTG curve for the nanocomposites with 5 wt% nanotube loading is about 70 K higher than that of pure aPP.

The defects and acid sites such as $-\text{COOH}$ and $-\text{OH}$ on the MWNTs caused by acid treatment can impair the thermal or thermo-oxidative stability of polyolefin. Bikiaris *et al.* (2008) pointed out that a decreasing trend is seen in the iPP-MWNT nanocomposites with an increase in the acid-treatment time of the MWNT. Thermal or thermo-oxidative decomposition data of the iPP-MWNT nanocomposites are presented in Table 16.2. These can be explained by more defects and acid sites on the MWNT which degrade at low temperature to induce the degradation of iPP.

Polyamides (PA)

Polyamides belong to the group of polar polymers. Li *et al.* (2006) investigated the thermal degradation difference between PA6-p-MWNT and PA6-f-MWNT, where f-MWNT was prepared by grafting 1, 6-hexamethylenediamine onto the MWNT. T_i in air of PA6 was improved by 5 K for PA6-p-MWNT and 14 K for

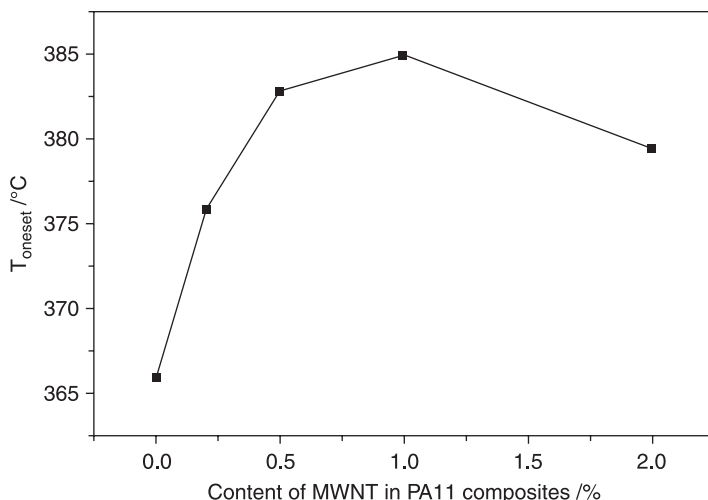
Table 16.2 Characteristic thermal degradation temperatures of the iPP–MWNT nanocomposites in different carrier gases. Reprinted with permission from (Bikiaris *et al.*, 2008)

Sample ^a	T _{onset} (°C)	T _{2%} (°C)	T _{15%} (°C)	T _{max} (°C)	T _{endset} (°C)
Carrier gas: N ₂					
iPP	265	331	379	437	486
iPP–MWNT	263	355	410	454	493
iPP–MWNT 15	273	339	399	453	499
iPP–MWNT 30	275	355	409	458	502
iPP–MWNT 60	276	329	376	436	485
Carrier gas: O ₂					
iPP	204	240	258	281	354
iPP–MWNT	201	235	272	358	373
iPP–MWNT 15	199	231	261	337	359
iPP–MWNT 30	197	229	261	330	354
iPP–MWNT 60	193	224	241	254	338
Carrier gas: air					
iPP	229	272	306	365	410
iPP–MWNT	225	276	325	394	417
iPP–MWNT 15	217	261	302	378	405
iPP–MWNT 30	216	261	301	389	407
iPP–MWNT 60	215	256	292	356	401

^a The numbers following the sample names indicate acid treatment time.

PA6–f–MWNT at 0.5 wt% MWNT loading. The higher thermal stability of PA6–f–MWNT is due to the stronger interfacial interactions, which were evidenced by the degradation activation energy of composites in air obtained by the Kissinger method. The degradation activation energy of PA6–f–MWNT is 169 kJ/mol while that of PA6–p–MWNT composites is 165 kJ/mol. The effect of different functionalized MWNT on the thermal stability of PA6–MWNT composites was also investigated (Chen *et al.*, 2006). TGA data suggested that the PA6–MWNT–NH₂ composites exhibited greater thermal stability than PA6–MWNT–COOH composites at the same MWNT loading. This difference could be due to the strong interfacial interaction between MWNT–NH₂ and PA6 and the PA6–MWNT–NH₂ composite showed higher degradation activation energy compared to PA6–MWNT–COOH composite.

The thermal degradation of PA–CNT composites was also affected by the amount of CNT used in the composites. According to Huang *et al.* (2009), the thermal stability of polyamide 11 (PA11)–MWNT composites is highly dependent on the concentration of MWNTs; in this study, CNT was prepared by catalytic chemical vapor deposition of methane on Co–Mo/MgO catalysts and then further treated in 2.6 M nitric acid. TGA data show that T_{onset} of the composite increases with an increase of the MWNT content, and the composites containing 1 wt%



16.7 Relationship between T_{onset} and MWNT concentration in the PA11–MWNT composites.

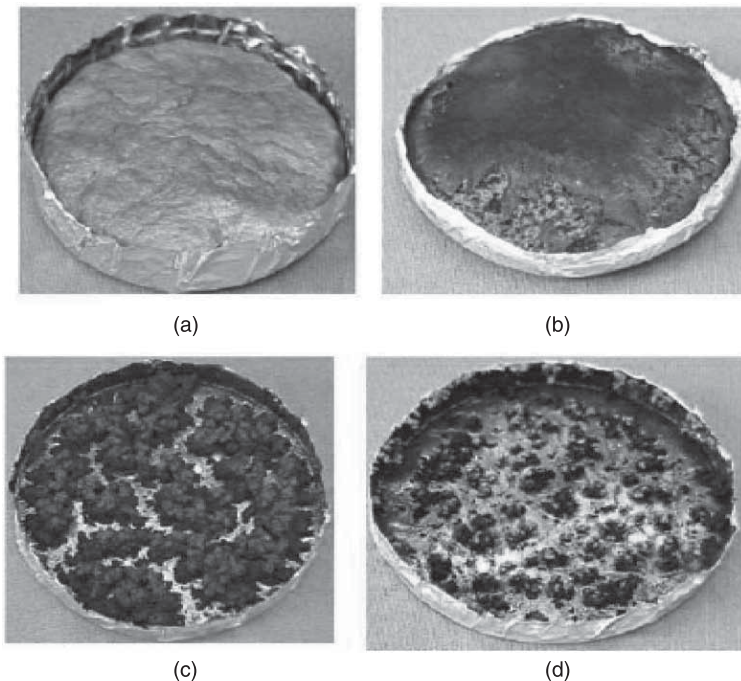
MWNT have the best thermal stability, and the decomposition temperature is improved about 20 K compared to PA11. The relationship between T_{onset} and MWNT concentration in the PA11–MWNT composites is shown in Fig. 16.7. This trend was confirmed in PA6 (Gao *et al.*, 2005b; Shen *et al.*, 2009).

A study by Sahoo *et al.* (2009) indicated that processing methods have an influence on the improvement of the thermal properties of the PA6–MWNT composites. The composite containing 10 wt% MWNT prepared in a Haake internal mixer (method I) showed delayed degradation compared to the same MWNT composition prepared by an extrusion process and subsequently injection molding (method II). The 10% and 50% decomposition temperatures of PA6–MWNT obtained from method I are higher by 10 K and 5 K compared to the composite from method II. Such an improvement can be associated with the better dispersion of MWNT in the Haake internal mixer. This investigation reveals that thermal stability of MWNT-filled polymer composites is highly dependent on the state of dispersion, mixing and processing conditions.

The thermal degradation of PA6–MWNT showed no obvious changes, but the flame retardancy of PA6–MWNT is significantly influenced by the incorporation of MWNTs (Schartel *et al.*, 2005). The cone calorimeter results indicate that during the burning of PA6–MWNT, the MWNT interconnected network structure remained in the materials, since it was thermally stable and had strong mechanical properties. The rheological measurements suggested that the melt viscosity increased which not only prevented dripping and flowing, but also hindered the decomposition of volatiles feeding the flame.

Poly(methyl methacrylate) (PMMA)

The addition of CNTs does not change the thermal degradation mechanism of PMMA composites. However, the dispersion and concentration of SWNTs were found to significantly influence the thermal degradation of PMMA–SWNT in the work of Kashiwagi *et al.* (2005). Evidence from the cone calorimeter and optical microscopy experiments indicated that a nanotube-containing network layer without any cracks or openings was formed during the burning tests, and the entire surface of the sample with good dispersion was covered by this protective layer (Fig. 16.8), while the composites with poor dispersion or a low content of the nanotubes (0.2% by mass or less) formed numerous black discrete islands and vigorous bubbling was observed between the islands. The peak heat release rate of the composites forming the network layer is about one-half that of those which formed the islands. More experimental data from TGA, TGA-FTIR, GC-MS, and cone calorimetry (Costache *et al.*, 2006) revealed that MWNTs served as a barrier in the degradation of PMMA–MWNT.



16.8 Effect of nanotubes' dispersion on residues of PMMA–SWNT (0.5%): (a) nitrogen gasification residue, good dispersion sample; (b) burned residue, good dispersion sample; (c) nitrogen gasification residue, poor dispersion sample; (d) burned residue, poor dispersion sample. (Reprinted with permission from Kashiwagi *et al.*, 2005.)

In the case of PMMA–CNT composites prepared by *in-situ* dispersion polymerization, many researchers (Dai *et al.*, 2007; Kashiwagi *et al.*, 2007; Kovalchuk *et al.*, 2008; Zhang *et al.*, 2008a; Choi *et al.*, 2008) have found that TGA data of the thermal degradation temperature of PMMA–CNT composites could be improved by about 10–60 K. This improved thermal stability of PMMA–CNT composites was attributed to strong interfacial interaction and outstanding thermal conductivity, determined by the method of preparation. SWNTs or MWNTs can react with the initiator to open the π -bond, participate in PMMA polymerization and form strong interfacial interaction between CNT and PMMA (Jia *et al.*, 1999; Park *et al.*, 2003), and the heat dissipation rate of the interface between CNT and matrix can be improved. In addition, it is also related to the enhanced thermal conductivity of composites due to the addition of SWNTs or MWNTs compared to the pure PMMA (Bagchi and Nomura, 2006).

Yuen *et al.* (2007) reported that the presence of silane-modified MWNT increased the thermal stability of the PMMA–VTES polymer matrix both in N₂ and in air. The thermal degradation data for the Si-MWNT–PMMA–VTES composites are summarized in Table 16.3. The authors stated that the increased thermal degradation characteristic temperature is caused by the interposition of Si. However, thermal conductivity data provided in the research suggested that this increased thermal degradation characteristic temperature should be related to the improved thermal conductivity between the MWNT and polymer matrix. The thermal conductivity of Si-MWNT–PMMA–VTES increased with the addition of Si-MWNT compared to neat PMMA–VTES, since Si-MWNT was bonded to PMMA–VTES via SiO_x, improving the interfacial interaction between the MWNTs and the polymer matrix and facilitating heat dissipation.

Styrenic polymers

The addition of CNTs will change the degradation pathway of styrenic polymers. Kong and Zhang's (2008) work revealed that the thermal stability of HIPS–CNT

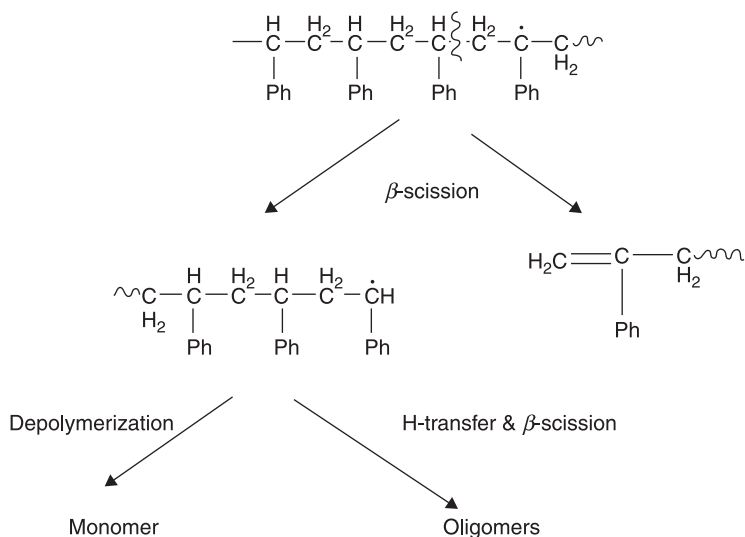
Table 16.3 Characteristic thermal degradation temperature of Si-MWNT–PMMA–VTES composites. Reprinted with permission from Yuen *et al.* (2007)

Si-MWNT content (wt%)	T ₅ (°C)		T ₁₀ (°C)		T _{max} (°C)	
	In N ₂	In air	In N ₂	In air	In N ₂	In air
0	292.2	297.9	303.9	311.0	384.3	368.3
0.5	311.7	301.3	340.5	344.6	384.2	388.5
0.99	314.2	304.0	348.7	352.9	393.6	392.9
1.96	317.0	302.8	354.8	352.9	393.8	401.0
2.91	315.5	299.1	356.9	351.7	404.2	401.7
3.85	313.1	306.5	357.5	355.2	401.9	379.5

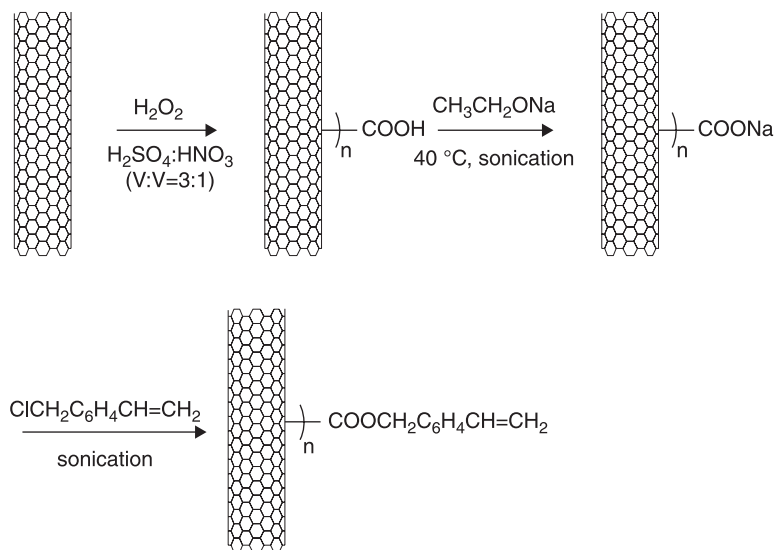
composites is better than that of HIPS in N_2 , in which the CNT was prepared by the method using the catalytic decomposition of ethanol with $LaNiO_3$ as catalyst in an autoclave at 973 K.

T_{onset} and $T_{0.5}$ of HIPS–CNT are 21 K and 10 K, respectively, higher than that of HIPS. Py-GC-MS was used to determine the reason for the high thermal stability of the HIPS–CNT composites. The routine degradation mechanism of pure HIPS starts by β -scission of a chain-end radical; the dimer and trimer are produced by an intermolecular transfer (backbiting) reaction. The abundant product is styrene, and a small amount of α -methylstyrene is also seen. However, GC-MS experiments suggested that in the process of degradation of HIPS–CNT, there is a high yield of α -methylstyrene. It is explained that the primary radical is willing to transform into the tertiary radical because of its increased stability after the formation of primary and secondary radicals by β -scission, which leads to the higher yield of α -methylstyrene (Jang and Wilkie, 2009). Schematics of β -cracking are shown in Fig. 16.9. The degradation follows this pathway when CNT is mixed with HIPS. This degradation model was also observed in HIPS–Fe–MMT nanocomposites (Kong *et al.*, 2008).

Chemical modification of CNT is also an efficient way to affect the thermal stability of styrenic polymers–CNT composites. Chen *et al.* (2009c) reported a specific process of styryl-modified MWNT, as shown in Fig. 16.10, and proved that the degradation temperature of styryl-modified MWNT–PS has been improved compared to MWNT–COOH–PS. This improvement of PS-g-MWNT was also reported in other studies (Kong *et al.*, 2004). All research indicated that



16.9 Schematic of β -cracking.



16.10 Preparation scheme of styryl-modified MWNT by esterification.

this improved thermal stability was associated with the imposed restrictions due to the interaction between the styryl groups on the MWNT surface and the polymer chains which was enhanced by the chemical modification.

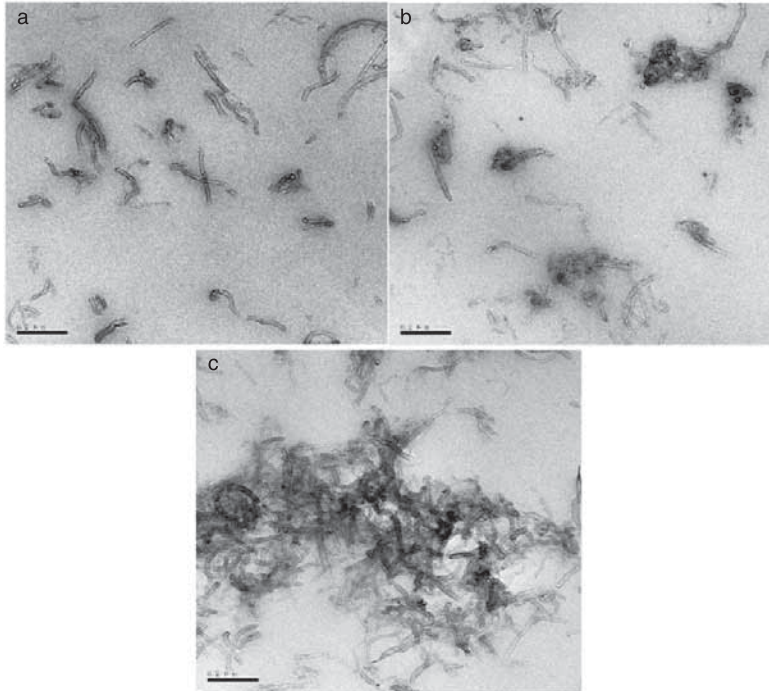
Polyaniline (PANI) is one of the most important hydrophilic-conducting polymers; the thermal stability of PANI-MWNT composites was studied in some research (Ma, *et al.*, 2006; Markovic *et al.*, 2006; Qi *et al.*, 2008). Qi *et al.* (2008) reported that the incorporation of MWNTs (diameter: <10 nm and length range: $5\text{--}15$ μm , purity: 95%) achieved improved thermal stability for PANI-MWNT composites prepared by *in-situ* polymerization. T_i and the peak temperature of PANI-MWNTs were delayed about 40 K and 100 K, respectively. Another study on the thermal degradation of PANI-MWNT (8–20 nm in diameter and 2–20 μm in length) composites prepared by ultrasonically initiated, *in-situ* emulsion polymerization was reported by Markovic *et al.* (2006). T_i of PANI-MWNT composites increased by ~ 35 K. The phenomenon is related to the interactions between the aromatic ring π -bonds of PANI and graphitic structures of MWNT.

The incorporation of CNT into styrenic polymers does not always improve the thermal stability of composites. In the case of acrylonitrile-butadiene-styrene (ABS)-SWNT composite, one could see a two-step degradation process, however, the initial degradation temperature is decreased, and the second degradation temperature is increased, compared to those of pure ABS. A catalytic effect of SWNT was proposed although the full understanding of the role of SWNT in the radical degradation initiation is still needed (Yang *et al.*, 2004). For

the decreased initial degradation temperature of styrene-butadiene-styrene tri-block copolymer (SBS)–MWNT composites (Lu *et al.*, 2009), a different mechanism was proposed. The presence of low molecular weight materials produced in the melt mixing process was taken as the source which led to the decrease of initial degradation temperature.

Polyesters

The thermal degradation of polyesters could be affected because of the barrier effect of CNTs. Research indicates that the thermal stability of CNT–polyesters composites including poly(ethylene 2,6-naphthalate)(PEN)–CNT composites (Kim and Kim, 2006; Hu *et al.*, 2008; Kim *et al.*, 2008b; Kim *et al.*, 2009b), poly(butylene terephthalate)(PBT)–MWNT composites (Mathew *et al.*, 2005; Wu *et al.*, 2008a; Kim, 2009), poly(ethylene terephthalate)(PET)–MWNT composites (Lee *et al.*, 2005; Anand *et al.*, 2007; Vassiliou *et al.*, 2009), poly(ϵ -caprolactone)diol (PCL)–MWNT composites (Sivalingam *et al.*, 2003; Wu *et al.*, 2007) and PC–MWNT composites (Schartel *et al.*, 2008) was significantly affected compared to the pure polyesters. There is no doubt that the enhancement of thermal stability was due to the barrier effect of CNTs which was proved by the high char yield on TGA analysis. However, the improved thermal stability of polyester composites is sensitive to the purity and chemical modification of CNT. In the case of poly(L-lactic acid) (PLA)–CNT, one can see the difference in the thermal degradation of PLA–CNT caused by the purity of CNT (Moon *et al.*, 2005; Kim *et al.*, 2007; Kim *et al.*, 2008a). The decomposition temperature of PLA–purified CNT composites is about 10 K higher than that of PLA–non-purified CNT composites (Chiu *et al.*, 2008). The $T_{0.1}$ of PC–MWNT composites shifted with increasing MWNT content up to 95 K towards lower temperatures which is also related to additional components or impurities incorporated during processing, such as remaining catalysts from nanotube synthesis (Schartel *et al.*, 2008). To understand how the difference in the chemical modification affects the thermal stability of PLA–CNT composites, Wu *et al.* (2008b) prepared PLA–CNT composites using various functionalized CNT including carboxylic and hydroxy MWNT. The thermal stability order of composites is: PLA–hydroxy CNT < PLA < PLA–carboxylic CNT. After the initial stage of degradation, the PLA–hydroxy CNT sample has a higher degradation rate, even in contrast to that of neat PLA, since the hydroxy groups produce Lewis or Bronsted acid sites on the surface of the CNT at a high temperature and the relative poor dispersion state of the MWNT reduces thermal conductivity efficiency. Although the carboxylic groups can also produce Lewis acid sites on the surface of a MWNT, the good dispersion shown by SEM (Fig. 16.11) enhances the barrier effect of the carboxylic MWNT. The functionalized MWNT affected the thermal stability of PLA composites by changing the dispersion state of CNT in polymer matrix.



16.11 TEM images of (a) PLA–carboxylic (CNT); (b) PLA–hydroxy (CNT); and (c) PLA–pure (CNT) samples at a magnification of 596,000. Reprinted with permission from Wu *et al.* (2008b).

Others

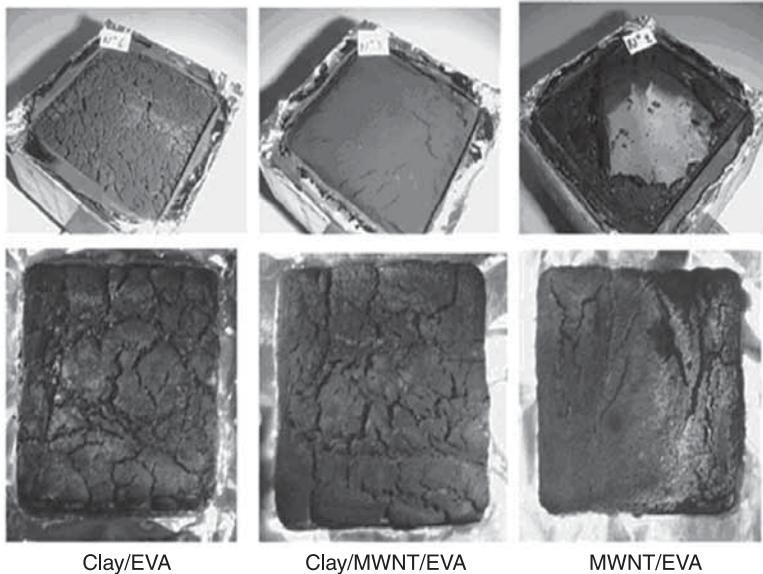
Lai *et al.* (2004) reported that the degradation temperature of poly(hydroxybutyrate-co-hydroxyvalerate)(PHBV)–MWNT composites was 16 K higher than that of pure PHBV due to the nanodispersion of CNT. In the case of polyacrylonitrile (PAN)–surface-oxidized MWNT composites, T_{onset} shifts from 541 K for pure PAN to 565 K for the PAN–MWNT (95/5) composites in N_2 . This change is attributed to the enhanced interfacial interaction due to the chemical binding of negatively charged $-C\equiv N$ groups on the MWNT (Ge *et al.*, 2004). In Probst *et al.*'s (2004) work on poly(vinyl alcohol) (PVA)–SWNT, SWNT were found to promote the thermal degradation of PVA due to the impurities and defects on the SWNT. Similar decreased thermal stability was also reported in the cross-linked composites of PVA–MWNT prepared by the addition of glutaraldehyde to PVA–CNT dispersions to form cross-link PVA chains via an acetalization reaction (Basiuk *et al.*, 2009) and PVDF–SWNT composites fabricated by dispersion of SWNT in an aqueous surfactant solution, followed by mixing with PVDF powder, filtration and hot pressing (Xu *et al.*, 2006).

Recently, Chen *et al.* (2009b) studied the effect of the combined action of clay and carboxylated MWNT with 3 wt% carboxyl content and where 10–20 nm outer diameter on the thermal degradation of hydrogenated nitrile-butadiene rubber (HNBR) and the Kissinger, Flynn-Wall-Ozawa, and Friedman methods were used to evaluate the activation energy sequence of HNBR and its nanocomposites. Both the initial degradation temperature and activation energy sequence of HNBR and its nanocomposites are in the order: HNBR–clay–MWNT > HNBR–clay > HNBR. HNBR–clay–MWNT composites had higher char yield at 873 K than HNBR–clay, which was attributed to the interaction between clay and MWNT. The activation energies of HNBR and HNBR composites showed a sharp increase in the low conversion area and a slow increase in the high conversion region. A reduction in the diffusion speed of the degradation products gives the lower thermal degradation rate observed for HNBR–clay–CNT nanocomposites. The coexistence of clay and CNT could form compact char layers with better barrier properties than clay alone. Similar experimental results were found in the clay-supported CNT–poly (vinyl alcohol) (PVA) nanocomposites reported by Zhao *et al.* (2009).

Accelerated char formation due to presence of clay and MWNT was again indicated as a mechanism of thermal stability improvement by Gao *et al.* (2005a) in the ethylene vinyl acetate copolymer (EVA) composites with MWNT and clays. In the morphology of the chars in the composites (presented in Fig. 16.12) produced after cone calorimetry and the natural burning experiment, it was found that nanotubes act as the site of nucleation of graphitization leading to the formation of turbostratic and graphitic carbons. Perfect crystallites of graphite are shown by a broad peak at 0.3354 nm, exactly the interlayer distance of pure graphite, in the XRD pattern of the char of the composite containing both nanotube and clay. In addition, there is remarkable difference in the number of cracks in the char, shown in Fig. 16.12. The char is the barrier to the evolution of flammable volatiles to the vapor phase and oxygen ingress to the condensed phase while the cracks permit evolution and ingress. A similar thermal stability improvement of MWNT with magnesium hydroxide in EVA was also reported by Ye *et al.* (2009) and Beyer (2002).

16.4 Future trends

Considering the literature available on polymer–CNT composites, both degradability and stability for several composites have not yet been studied completely and the mechanisms of degradation have also not been clearly explained (Kashiwagi *et al.* 2002; Breuer and Uttandaraman, 2004; Bocchini *et al.* 2007; Kumara *et al.* 2009). For instance, how does one prove the thermal stability improvement or interactions at the molecular level between CNT and polymers? In particular, the combination of excellent properties and the gradually decreasing cost of CNT make them an ideal candidate as an advanced filler



16.12 The morphology of the chars produced from clay–EVA, clay–MWNT–EVA and MWNT–EVA nanocomposites following the cone calorimeter test (top row) and the natural burning (bottom row). (Reprinted with permission from Gao *et al.*, 2005a.)

material for the next generation of high performance structural and multifunctional composites (Njuguna *et al.* 2008, Chen *et al.*, 2009a), which will play an important role in a wide range of material applications and fundamental science in the future. It is therefore necessary and important to further investigate the thermal degradation of polymer–carbon nanotubes.

In conclusion, the thermal degradation of nanotube–polymer composites offers both great potential and great challenges, making it a vibrant area of work for years to come. The improvement and application of these composites at high temperature and their utility in fire retardancy will depend on how effectively we can handle the challenges. The significant progress in the understanding of these composite systems within the past few years points toward a bright future (Gelves *et al.* 2005; Moniruzzaman and Winey, 2006).

16.5 Conclusion

In this review, we provide an overview of research in the past decade on the thermal degradation of polymer–CNT composites and give insights into the factors that will ultimately control this. However, there are no universal conclusions that can be drawn because of the complexity of thermal degradation

and the variety of composites. The following points are evident for the thermal degradation of polymer–CNT composites:

First, the particular structure and excellent thermal properties of CNT are particularly important in the thermal stability of polymer–CNT composites so that the incorporation of CNTs into polymers can significantly influence the thermal degradation of polymer–CNT composites, particularly the thermal stability improvement of composites.

Second, the thermal degradation behavior of polymer–CNT composites is affected by many factors, such as component, structure, interfacial interaction, exterior conditions and so on. The changes in the thermal stability of polymer–CNT composites may be ascribed to one dominant factor or a combination of factors.

Third, the mechanisms of thermal degradation of composites mainly include good matrix–nanotube interactions, good thermal conductivity of the nanotubes, barrier effect, the network character and dispersion of carbon nanotubes, and radical scavenger action and physical-chemical adsorption by carbon nanotubes.

16.6 References

- Anand K.A., Agarwal U.S., Joseph R. (2007) 'Carbon nanotubes-reinforced PET nanocomposite by melt-compounding', *J. Appl. Polym. Sci.*, 104, 3090–3095.
- Andrews R., Weisenberger M.C., Opin C. (2004) 'Carbon nanotube polymer composites', *Current Opinion in Solid State Mater. Sci.*, 8, 31–37.
- Bagchi A. and Nomura S. (2006) 'On the effective thermal conductivity of carbon nanotube reinforced polymer composites', *Comp. Sci. Technol.*, 66, 1703–1712.
- Barrau S., Demont P., Peigney A., *et al.* (2003) 'DC and AC conductivity of carbon nanotubes-epoxy composites', *Macromolecules*, 36, 5187–5194.
- Bartholome C., Miaudet P., Derré A., *et al.* (2008) 'Influence of surface functionalization on the thermal and electrical properties of nanotube-PVA composites', *Comp. Sci. Technol.*, 68, 2568–2573.
- Basiuk E.V., Anis A., Bandyopadhyaya S., *et al.* (2009) 'Poly(vinyl alcohol)/CNT composites: an effect of cross-linking with glutaraldehyde', *Superlattices and Microstructures*, 46, 379–383.
- Beyer G. (2002) 'Short communication: carbon nanotubes as flame retardants for polymers', *Fire Mater.*, 26, 291–293.
- Bikiaris D., Vassiliou A., Chrissafis K., *et al.* (2008) 'Effect of acid treated multi-walled carbon nanotubes on the mechanical, permeability, thermal properties and thermo-oxidative stability of isotactic polypropylene', *Polym. Degrad. Stab.*, 93, 952–967.
- Bocchini S., Frache A., Camino G., *et al.* (2007) 'Polyethylene thermal oxidative stabilisation in carbon nanotubes based nanocomposites', *Europ. Polym. J.*, 43, 3222–3235.
- Breuer O., Uttandaraman S. (2004) 'Big returns from small fibers: a review of polymer/carbon nanotube composites', *Polym. Comp.*, 25, 630–645.
- Chen E.C., Wu T.M. (2007) 'Isothermal crystallization kinetics and thermal behavior of poly(3-caprolactone)/multi-walled carbon nanotube composites', *Polym. Degrad. Stab.*, 92, 1009–1015.

- Chen G.X., Kim H.S., Park B.H., Yoon, J.S. *et al.* (2005) 'Controlled functionalization of multiwalled carbon nanotubes with various molecular-weight poly(l-lactic acid)', *J. Phys. Chem. B*, 109, 22237–22243.
- Chen G.X., Kim H.S., Park B.H., Yoon, J.S. *et al.* (2006) 'Multi-walled carbon nanotubes reinforced nylon 6 composites', *Polymer*, 47, 4760–4767.
- Chen K., Wilkie C.A., Vyazovkin S. (2007) 'Nanoconfinement revealed in degradation and relaxation studies of two structurally different polystyrene-clay systems', *J. Phys. Chem. B*, 111, 12685–12692.
- Chen P., Kim H.S., Jin H.J. (2009a) 'Preparation, properties and application of polyamide/carbon nanotube nanocomposites', *Macromolecules Research*, 17, 207–217.
- Chen S.G., Yu H.Y., Ren W.T., *et al.* (2009b) 'Thermal degradation behavior of hydrogenated nitrile-butadiene rubber (HNBR)/clay nanocomposite and HNBR/clay/carbon nanotubes nanocomposites', *Thermochim. Acta*, doi 10.1016/j.tca.03.010.
- Chen X.H., Tao F., Wang J. F., *et al.* (2009c) 'Concise route to styryl-modified multi-walled carbon nanotubes for polystyrene matrix and enhanced mechanical properties and thermal stability of composite', *Mater. Sci. Eng. A*, 499, 469–475.
- Chiu W.M., Chang Y.A., Kuo H.Y., *et al.* (2008) 'A study of carbon nanotubes/biodegradable plastic polylactic acid composites', *J. Appl. Polym. Sci.*, 108, 3024–3030.
- Choi H.J., Lim J.Y., Zhang K., *et al.* (2008) 'Poly(methyl methacrylate)/multi-walled carbon nanotube microbead composites via dispersion polymerization under ultrasonication', *Diamond & Related Materials*, 17, 1498–1501.
- Coleman J.N., Khan U., Gun'ko Y.K. (2006) 'Mechanical reinforcement of polymers using carbon nanotubes', *Adv. Mater.*, 18, 689–706.
- Costache M.C., Heidecker M.J., Wilkie C.A., *et al.* (2007) 'The influence of carbon nanotubes, organically modified montmorillonites and layered double hydroxides on the thermal degradation and fire retardancy of polyethylene, ethylenevinyl acetate copolymer and polystyrene', *Polymer*, 48, 6532–6545.
- Costache M.C., Wang D.Y., Wilkie C.A., *et al.* (2006) 'The thermal degradation of poly(methyl methacrylate) nanocomposites with montmorillonite, layered double hydroxides and carbon nanotubes', *Polym. Adv. Technol.*, 17, 272–280.
- Dai J. F., Wang Q., Li W. X., *et al.* (2007) 'Properties of well aligned SWNT modified poly (methyl methacrylate) nanocomposites', *Mater. Lett.*, 61, 27–29.
- Dalton A.B., Collins S., Munoz E., *et al.* (2003) 'Super-tough carbon-nanotube fibres', *Nature*, 423, 703.
- Du M.L., Guo B.C., Jia D.M. (2006) 'Thermal stability and flame retardant effects of halloysite nanotubes on poly(propylene)', *Europ. Polym. J.*, 42, 1362–1369.
- Fang Z.P., Song P.G., Tong L.F., *et al.* (2008) 'Thermal degradation and flame retardancy of polypropylene/C60 nanocomposites', *Thermochim. Acta*, 473, 106–108.
- Fujii M., Zhang X., Xie H.Q. (2005) 'Measuring the thermal conductivity of a single carbon nanotube', *Phys. Rev. Lett.*, 95, 065502.
- Gao C., He H.K., Zhou L., *et al.* (2009) 'Scalable functional group engineering of carbon nanotubes by improved one-step nitrene chemistry', *Chem. Mater.*, 21, 360–370.
- Gao F.G., Beyer G., Yuan Q.C. (2005a) 'A mechanistic study of fire retardancy of carbon nanotube/ethylene vinyl acetate copolymers and their clay composites', *Polym. Degrad. Stab.*, 89, 559–564.
- Gao J.B., Itkis M.E., Yu A.P., *et al.* (2005b) 'Continuous spinning of a single-walled carbon nanotube-nylon composite fiber', *J. Am. Chem. Soc.*, 127, 3847–3854.

- Ge J.J., Hou H.Q., Li Q., *et al.* (2004) 'Assembly of well-aligned multiwalled carbon nanotubes in confined polyacrylonitrile environments: electrospun composite nanofiber sheets', *J. Am. Chem. Soc.*, 126, 15754–15761.
- Gelves G.A., Sundararaj U., Haber J. A. (2005) 'Electrostatically dissipative polystyrene nanocomposites containing copper nanowires', *Macromol. Rapid Commun.*, 26, 1677–1681.
- Gorrasi G., Sarno M., Bartolomeo A.D., *et al.* (2007) 'Incorporation of carbon nanotubes into polyethylene by high energy ball milling: morphology and physical properties', *J. Polym. Sci. Part B: Polym. Phys.*, 45, 597–606.
- Hu N.T., Zhou H.W., Dang G.D., *et al.* (2008) 'Preparation and characterization of multi-walled carbon nanotubes/polymer gradient composite films', *Polym. Int.*, 57, 927–931.
- Huang S., Wang M., Liu T.X., *et al.* (2009) 'Morphology, thermal, and rheological behavior of nylon 11/multi-walled carbon nanotube nanocomposites prepared by melt compounding', *Polym. Eng. Sci.*, 49, 1063–1068.
- Iijima S. (1991) 'Helical microtubes of graphitic carbon', *Nature*, 354, 56–58.
- Jana R.N., Cho J.W. (2008) 'Thermal stability, crystallization behavior, and phase morphology of poly(ϵ -caprolactone)diol-grafted-multiwalled carbon nanotubes', *J. Appl. Polym. Sci.*, 110, 1550–1558.
- Jang B.N., Wilkie C.A., (2005) 'The thermal degradation of polystyrene nanocomposite', *Polymer*, 46, 2933–2942.
- Jia Z., Wang Z., Xu C., *et al.* (1999) 'Study on poly(methyl methacrylate)/carbon nanotube composites', *Mater. Sci. Eng., A*, 271, 395–400.
- Kanagaraj S., Varanda F.R., Zhiltsova T.V., *et al.* (2007) 'Mechanical properties of high density polyethylene/carbon nanotube composites', *Comp. Sci. Technol.*, 67, 3071–3077.
- Kashiwagi T., Du F., Winey K.I., *et al.* (2005) 'Flammability properties of polymer nanocomposites with single-walled carbon nanotubes: effects of nanotube dispersion and concentration', *Polymer*, 46, 471–481.
- Kashiwagi T., Fagan J., Douglas J.F., *et al.* (2007) 'Relationship between dispersion metric and properties of PMMA/SWNT nanocomposites', *Polymer*, 48, 4855–4866.
- Kashiwagi T., Grulke E., Hilding J., *et al.* (2002) 'Thermal degradation and flammability properties of poly(propylene)/carbon nanotube composites', *Macromol. Rapid Commun.*, 23, 761–765.
- Kashiwagi T., Grulke E., Hilding J., *et al.* (2004) 'Thermal and flammability properties of polypropylene/carbon nanotube nanocomposites', *Polymer*, 45, 4227–4239.
- Kim H.S., Chae Y.S., Park B.H., *et al.* (2008a) 'Thermal and electrical conductivity of poly(L-lactide)/multiwalled carbon nanotube nanocomposites', *Current Applied Physics*, 8, 803–806.
- Kim H.S., Park B.H., Yoon J.S., *et al.* (2007) 'Thermal and electrical properties of poly(L-lactide)-graft-multiwalled carbon nanotube composites', *Europ. Polym. J.*, 43, 1729–1735.
- Kim J.Y. (2009) 'The effect of carbon nanotube on the physical properties of poly(butylene terephthalate) nanocomposite by simple melt blending', *J. Appl. Polym. Sci.*, 112, 2589–2600.
- Kim J.Y., Han S. Il., Hong S. (2008b) 'Effect of modified carbon nanotube on the properties of aromatic polyester nanocomposites', *Polymer*, 49, 3335–3345.
- Kim J.Y., Han S., Kim D.K., *et al.* (2009a) 'Mechanical reinforcement and crystallization behavior of poly(ethylene 2,6-naphthalate) nanocomposites induced by modified carbon nanotube', *Composites, Part A*, 40, 45–53.

- Kim J.Y., Kim S.H. (2006) 'Influence of multiwall carbon nanotube on physical properties of poly(ethylene 2,6-naphthalate) nanocomposites', *J. Polym. Sci. Part B: Polym. Phys.*, 44, 1062–1071.
- Kim J.Y., Park H.S., Kim S.H. (2009b) 'Thermal decomposition behavior of carbon-nanotube-reinforced poly(ethylene 2,6-naphthalate) nanocomposites', *J. Appl. Polym. Sci.*, 113, 2008–2017.
- Kodjie S.L., Li L.Y., Li B., *et al.* (2006) 'Morphology and crystallization behavior of HDPE/CNT nanocomposite', *J. Macromol. Sci., Part B: Phys.*, 45, 231–245.
- Kong H., Gao C., Yan D.Y. (2004) 'Functionalization of multiwalled carbon nanotubes by atom transfer radical polymerization and defunctionalization of the products', *Macromolecules*, 37, 4022–4030.
- Kong Q. H., Lu R. B., Zhang S. J. (2008) 'Flame retardant and the degradation mechanism of high impact polystyrene/Fe-montmorillonite nanocomposites', *J. Polym. Res.*, 15, 453–458.
- Kong Q.H., Zhang J.H. (2008) 'Synthesis of carbon nanotubes, and the effect on thermal stability in high-impact polystyrene', *Aust. J. Chem.*, 61, 72–76.
- Kovalchuk A.A., Shchegolikhin A.N., Shevchenko V.G., *et al.* (2008) 'Synthesis and properties of polypropylene/multiwall carbon nanotube composites', *Macromolecules*, 41, 3149–3156.
- Kumara A.P., Depana D., Tomerb N.S., *et al.* (2009) 'Nanoscale particles for polymer degradation and stabilization—trends and future perspectives', *Progress in Polymer Science*, 34, 479–515.
- Lai M.F., Li J., Yang J., *et al.* (2004) 'The morphology and thermal properties of multi-walled carbon nanotube and poly(hydroxybutyrate-co-hydroxyvalerate) composite', *Polym. Int.*, 53, 1479–1484.
- Lau K.T., Hui D. (2002) 'The revolutionary creation of new advanced materials-carbon nanotube composites', *Composites, Part B*, 33, 263–277.
- Lee H.J., Oh S.J., Choi J.Y., *et al.* (2005) 'In situ synthesis of poly(ethylene terephthalate) (PET) in ethylene glycol containing terephthalic acid and functionalized multiwalled carbon nanotubes (MWNTs) as an approach to MWNT/PET nanocomposites', *Chem. Mater.*, 17, 5057–5064.
- Lee H.K., Pejanovic S., Mondragon I., *et al.* (2007) 'Dynamics of single-walled carbon nanotube (SWNT)/polyisoprene (PI) nanocomposites in electric and mechanical fields', *Polymer*, 48, 7345–7355.
- Li J., Tong L.F., Fang Z.P. *et al.* (2006) 'Thermal degradation behavior of multi-walled carbon nanotubes/polyamide 6 composites', *Polym. Degrad. Stab.*, 91, 2046–2052.
- Liew K. M., Wong C. H., He X. Q., *et al.* (2005) 'Thermal stability of single and multi-walled carbon nanotubes', *Physical Review B*, 71, 075424, pp. 6.
- Lu L., Yu H.Y., Wang S.F. *et al.* (2009) 'Thermal degradation behavior of styrene-butadiene-styrene tri-block copolymer/multiwalled carbon nanotubes composites', *J. Appl. Polym. Sci.*, 112, 524–531.
- Ma X.F., Zhang X.B., Li Y., *et al.* (2006) 'Preparation of nano-structured polyaniline composite film via carbon nanotubes seeding approach and its gas-response studies', *Macromol. Mater. Eng.*, 291, 75–82.
- Markovic M.G., Matison J.G., Cervini R., *et al.* (2006) 'Synthesis of new polyaniline/nanotube composites using ultrasonically initiated emulsion polymerization', *Chem. Mater.*, 18, 6258–6265.

- Marosfoi B.B., Marosi G.J., Szep A., *et al.* (2006) 'Complex activity of clay and CNT particles in flame retarded EVA copolymer', *Polym. Adv. Technol.*, 17, 255–262.
- Marosfoi B.B., Szabo A., Marosi G., *et al.* (2006) 'Thermal and spectroscopic characterization of polypropylene-carbon nanotube composites', *J. Therm. Anal. Cal.*, 86, 669–673.
- Mathew G., Hong J.P., Rhee J.M., *et al.* (2005) 'Preparation and characterization of properties of electrospun poly(butylene terephthalate) nanofibers filled with carbon nanotubes', *Polymer Testing*, 24, 712–717.
- McNally T., Pötschke P., Halley P., *et al.* (2005) 'Polyethylene multiwalled carbon nanotube composites', *Polymer*, 46, 8222–8232.
- Mohammed H.A.S., Uttandaraman S. (2009) 'A review of vapor grown carbon nanofiber/polymer conductive composites', *Carbon*, 47, 2–22.
- Moniruzzaman M., Winey K.I. (2006) 'Polymer nanocomposites containing carbon nanotubes', *Macromolecules*, 39, 5194–5205.
- Moon S., Jin F.Z., Lee C.J., *et al.* (2005) 'Novel carbon nanotube/poly(L-Lactic acid) nanocomposites; their modulus, thermal stability, and electrical conductivity', *Macromol. Symp.*, 224, 287–295.
- Njuguna J., Pielichowski K. and Desai S. (2008) 'Nanofiller-reinforced polymer nanocomposites', *Polym. Adv. Technol.*, 19, 947–959.
- Ovejero G., Sotelo J.L., Romero M.D., *et al.* (2006) 'Multiwalled carbon nanotubes for liquid-phase oxidation. functionalization, characterization, and catalytic activity', *Ind. Eng. Chem. Res.*, 45, 2206–2212.
- Park S.J., Cho M.S., Lim S.T., *et al.* (2003) 'Synthesis and dispersion characteristics of multi-walled carbon nanotube composites with poly(methyl methacrylate) prepared by in situ bulk polymerization macromol', *Rapid Commun.*, 24, 1070–1073.
- Probst O., Moore E.M., Resasco D.E., *et al.* (2004) 'Nucleation of polyvinyl alcohol crystallization by single-walled carbon nanotubes', *Polymer*, 45, 4437–4443.
- Qi Y.N., Xu F., Sun L.X. (2008) 'Thermal stability and glass transition behavior of PANI/MWNT composites', *J. Therm. Anal. Cal.*, 94, 137–141.
- Sahoo N.G., Cheng H.K.F., Cai J.W., *et al.* (2009) 'Improvement of mechanical and thermal properties of carbon nanotube composites through nanotube functionalization and processing methods', *Comp. Sci. Technol.*, 69, 313–320.
- Sakellariou G., Ji H.N., Mays J.W., *et al.* (2008) 'Enhanced polymer grafting from multiwalled carbon nanotubes through living anionic surface-initiated', *Polymerization. Chem. Mater.*, 20, 6217–6230.
- Schadler L.S., Giannaris S.C., Ajayan P.M. (1998) 'Load transfer in carbon nanotube epoxy composites', *Appl. Phys. Lett.*, 73, 3842–3843.
- Schartel B., Braun U., Knoll U. *et al.* (2008) 'Mechanical, thermal, and fire behavior of bisphenol A polycarbonate/multiwall carbon nanotube nanocomposites', *Polym. Eng. Sci.*, 48, 149–158.
- Schartel B., Pötschke P., Knoll U., *et al.* (2005) 'Fire behaviour of polyamide 6/multiwall carbon nanotube nanocomposites', *Europ. Polym. J.*, 41, 1061–1070.
- Seo M.K., Park S.J. (2004) 'A kinetic study on the thermal degradation of multi-walled carbon nanotubes-reinforced poly(propylene) composites', *Macromol. Mater. Eng.*, 289, 368–374.
- Shen Z.Q., Bateman S., Wu D.Y., *et al.* (2009) 'The effects of carbon nanotubes on mechanical and thermal properties of woven glass fiber reinforced polyamide-6 nanocomposites', *Comp. Sci. Tech.*, 69, 239–244.
- Shofner M.L., Khabashesku V.N., Barrera E.V. (2006) 'Processing and mechanical properties of fluorinated single-wall carbon nanotube-polyethylene composites', *Chem. Mater.*, 18, 906–913.

- Sivalingam G., Karthik R., Madras G. (2003) 'Kinetics of thermal degradation of poly(ϵ -caprolactone)', *J. Anal. Appl. Pyrolysis*, 70, 631–647.
- Stephan C., Nguyen T.P., Lahr B., *et al.* (2002) 'Raman spectroscopy and conductivity measurements on polymer-multiwalled carbon nanotubes composites', *Mater. Res.*, 17, 396–400.
- Stevens J.L., Huang A.Y., Peng H.Q., *et al.* (2003) 'Sidewall amino-functionalization of single-walled carbon nanotubes through fluorination and subsequent reactions with terminal diamines', *Nano. Lett.*, 3, 331–336.
- Thostenson E.T., Chou T.W. (2003) 'On the elastic properties of carbon nanotube-based composites: modelling and characterization', *J. Phys. D: Appl. Phys.*, 36, 573–582.
- Vassiliou A.A., Chrissafis K., Bikiaris D.N. *et al.* (2009) 'Thermal degradation kinetics of in situ prepared PET nanocomposites with acid-treated multi-walled carbon nanotubes', *J. Therm. Anal. Calorim.* Published on line, DOI: 10.1007/s10973-009-0426-4.
- Wang B., Sun G.P., Sun G.E., *et al.* (2006a) 'The thermal characterization and rheology behavior of PP/MWNTs nanocomposites', *Acta Polymeric Sinica*, 3, 408–413.
- Wang G.J., Dong Y., Qiu J., *et al.* (2006b) 'Studies on carbon nanotube surface modified with polystyrene', *Chem. J. Chinese Universities*, 27, 1157–1161.
- Wang S. (2009) 'Optimum degree of functionalization for carbon nanotubes', *Current Applied Physics*, 9, 1146–1150.
- Watts P.C.P., Fearon P.K., Hsu W.K., *et al.* (2003) 'Carbon nanotubes as polymer antioxidants', *J. Mater. Chem.*, 13, 491–495.
- Wiemann, K., Kaminsky, W., Gojny F.H., *et al.* (2005) 'Synthesis and properties of syndiotactic poly(propylene)/carbon nanofiber and nanotube composites prepared by in situ polymerization with metallocene/MAO catalysts', *Macromol. Chem. Phys.*, 206, 1472–1478.
- Wu D.F., Wu L., Sun Y.R. (2007) 'Rheological properties and crystallization behavior of multi-walled carbon nanotube/poly(ϵ -caprolactone) composites', *J. Polym. Sci. Part B: Polym. Phys.*, 45, 3137–3147.
- Wu D.F., Wu L., Yu G.C., *et al.* (2008a) 'Crystallization and thermal behavior of multiwalled carbon nanotube/poly(butylene terephthalate) composites', *Polym. Eng. Sci.*, 48, 1057–1067.
- Wu D.F., Wu L., Zhang M., *et al.* (2008b) 'Viscoelasticity and thermal stability of polylactide composites with various functionalized carbon nanotubes', *Polym. Degrad. Stab.*, 93, 1577–1584.
- Xi G.X., Song S.L., Liu Q. (2005) 'Kinetics of thermal degradation of waste poly(methylmethacrylate) on metal oxide catalysts', *Petrochemical Technology*, 34, 250–253.
- Xu G.D., Zhu B., Han Y., *et al.* (2007) 'Covalent functionalization of multi-walled carbon nanotube surfaces by conjugated polyfluorenes', *Polymer*, 48, 7510–7515.
- Xu Y.S., Ray G., Magid B.A., *et al.* (2006) 'Thermal behavior of single-walled carbon nanotube polymer-matrix composites', *Composites, Part A*, 37, 114–121.
- Yang J., Lin Y.H., Wang J.F., *et al.* (2005) 'Morphology, thermal stability, and dynamic mechanical properties of atactic polypropylene/carbon nanotube composites', *J. Appl. Polym. Sci.*, 98, 1087–1091.
- Yang K., Gu M.Y., Han H.B., *et al.* (2008) 'Influence of chemical processing on the morphology, crystalline content and thermal stability of multi-walled carbon nanotubes', *Mater. Chem. Phys.*, 112, 387–392.
- Yang S.Y., Castilleja J. R., Barrerab E.V., *et al.* (2004) 'Thermal analysis of an acrylonitrile-butadiene-styrene/SWNT composite', *Polym. Degrad. Stab.*, 83, 383–388.

- Ye L., Wu Q.H., Qu B.J. (2009) ‘Synergistic effects and mechanism of multiwalled carbon nanotubes with magnesium hydroxide in halogen-free flame retardant EVA/MH/MWNT nanocomposites’, *Polym. Degrad. Stab.*, 94, 751–756.
- Yu M.F., Files B.S., Arepalli S., *et al.* (2000) ‘Tensile loading of ropes of single wall carbon nanotubes and their mechanical properties’, *Phys. Rev. Lett.*, 84, 5552–5555.
- Yuen S.M., Ma C.C.M., Chiang C.L., *et al.* (2007) ‘Silane-modified MWCNT/PMMA composites—preparation, electrical resistivity, thermal conductivity and thermal stability’, *Composites, Part A: Applied Science and Manufacturing*, 38, 2527–2535.
- Zanetti M., Camino G., Reichert P., *et al.* (2001) ‘Thermal behaviour of poly(propylene) layered silicate nanocomposites’, *Macr. Rapid. Commun.*, 22, 176–180.
- Zhang K., Lim J.Y., Choi H.J., *et al.* (2008a) ‘Core-shell structured carbon nanotube/poly (methyl methacrylate) composite and its electrorheological characteristics’, *Diamond & Related Materials*, 17, 1604–1607.
- Zhang Y.C., Broekhuis A.A., Stuart M.C.A., *et al.* (2008b) ‘Cross-linking of multiwalled carbon nanotubes with polymeric amines’, *Macromol.*, 41, 6141–6146.
- Zhao Y., Ding X.J., Jiao Q.Z., *et al.* (2006) ‘Thermal stability of polypropylene/carbon naotube composites’, *China Plastics*, 20, 43–46.
- Zhao Y.Q., Lau K.T., Wang Z., *et al.* (2009) ‘Fabrication and properties of clay-supported carbon nanotube/poly (vinyl alcohol) nanocomposites’, *Polym. Compos.*, 30, 702–707.
- Zhu J., Uhl F.M., Morgan A.B., Wilkie C.A. (2001) ‘Studies on the mechanism by which the formation of nanocomposites enhances thermal stability’, *Chem. Mater.*, 13, 4649–4654.

16.7 Appendix: symbols and abbreviations

ABS	acrylonitrile-butadiene-styrene
aPP	atactic PP
ATR-FTIR	attenuated total reflectance-Fourier transform infrared spectroscopy
CNT	carbon nanotubes
DCC	dicyclohexylcarbodiimide
DMF	dimethylformamide
DTG	derivative thermogravimetry
DWNT	double-walled carbon nanotube
E _a	activation energy
EDA	ethylenediamine
EVA	ethylene vinyl acetate copolymers
Fe-MMT	Fe-montmorillonite
f-MWNT	functionalized multi-walled carbon nanotubes
FTIR	Fourier transform infrared spectroscopy
GC-MS	gas chromatography-mass spectrometry
HDPE	high density polyethylene
HEBM	high energy ball milling
HIPS	high-impact polystyrene
HNBR	hydrogenated nitrile-butadiene rubber
iPP	isotactic polypropylene

IPTES	isocyanato-propyltriethoxysilane
LDH	layered double hydroxides
LLDPE	linear low density polyethylene
m-CNT	modified carbon nanotubes
MMT	montmorillonite
MWNT	multi-walled carbon nanotubes
MWNT-COOH	multi-walled carbon nanotubes with carboxyl groups
MWNT-NH ₂	multi-walled carbon nanotubes with amine groups
OIT	oxidation induction temperature
PA	polyamide
PAN	polyacrylonitrile
PANI	polyaniline
PBT	poly(butylene terephthalate)
PCL	poly(ϵ -caprolactone)diol
PEN	poly(ethylene 2,6-naphthalate)
PET	poly(ethylene terephthalate)
PF	polyfluorene
PHBV	poly(hydroxybutyrate-co-hydroxyvalerate)
PLA	poly(L-lactic acid)
PMDETA	N,N,N',N'',N''-pentamethyldiethylenetriamine
p-MWNT	pure multi-walled carbon nanotubes
PP	polypropylene
PS	polystyrene
PVA	poly (vinyl alcohol)
PVDF	poly (vinylidene fluoride)
Py-GC-MS	pyrolysis-gas chromatography-mass spectrometry
SBS	styrene-butadiene-styrene tri-block copolymer
SEM	scanning electron microscope
SPC	Suzuki polycondensation
SWNT	single-walled carbon nanotubes
TGA	thermogravimetry analysis
THF	tetrahydrofuran
T _i	the temperature of initial degradation
T _{max}	the temperature of maximum weight loss rate
T _{onset}	the onset of degradation temperature
T _{0.1}	the temperature of degradation at 10% weight loss
T _{0.5}	the temperature of degradation at 50% weight loss
VTES	vinyltriethoxysilane
WAXD	wide-angle X-ray diffraction
XRD	X-ray diffraction

Polyolefin–carbon nanotube composites

M. MORCOM and G. SIMON, Monash University, Australia

Abstract: There is increasing interest in the incorporation of carbon nanotubes in commodity matrices such as polyolefins, in order to produce materials with increased performance and functionality, while also taking advantage of properties that these plastics offer, such as low moisture absorption. The review focuses on polyethylene and polypropylene carbon nanotube nanocomposites in particular, with an emphasis on the processing methods used to produce these materials, along with the effect of the incorporation of carbon nanotubes on their crystallinity, mechanical, rheological, electrical and thermal properties. Aspects of carbon nanotube modification in order to produce optimal dispersion and better interfacial adhesion are also discussed.

Key words: carbon nanotubes, nanocomposites, polyethylene, polyolefin, polypropylene.

17.1 Introduction

Polyolefins are the result of polymerization of olefin or alkene monomers, which usually have the monomeric equation, C_nH_{2n} and include two of the most widely used plastics, polyethylene and polypropylene. The quantity of research published on blends of carbon nanotubes (CNTs) with this class of material has lagged behind other CNT blends, but is currently accelerating for a number of reasons. One relates to the fact that CNT nanocomposites have focused more on the reinforcement of ‘higher value’ polymers, not surprising given the relative cost of nanotubes. However, after years of promise, it appears that with more companies on the market producing larger volumes of nanotubes, the price is dropping, opening up the possibility of using them to reinforce or provide functionality to more commodity polymers such as the polyolefins.

For many applications, the ease of processing of polyolefins, and their resistance to moisture can make them good matrices in which to disperse nanotubes. Given the carbon-ring structure of (particularly unmodified) nanotubes, it could be assumed that the dispersion of nanotubes in a matrix which also lacks polar functional groups might be quite good. Another advantage of polyolefins is their relatively low surface free energies in the melt (compared to polymers such as nylon and polycarbonate) (Brandrup *et al.*, 1999), resulting in a larger driving force for the wetting of carbon nanotubes, wetting being favoured by high solid surface free energy and low liquid surface free energy (Comyn, 1997). Polyolefins also provide an interesting family of materials in which to study the effect of nanotube addition (and hopefully make use of it) since they range from semi-crystalline to elastomeric to (if one includes cyclic olefinic copolymers) glassy

and amorphous. The relatively low modulus and strength of a number of these classes of material mean that significant property enhancement (not to mention conductivity and fire retardance) can likely be achieved.

In this review of the literature in the area of olefinic nanotube nanocomposites, we have divided the sections not into *types* of polyolefins, but really into *thematic aspects* that we believe are important such as: methods of blending, types of property behaviour (rheological, mechanical, electrical, thermal), as well as aspects of CNT modification to produce optimal dispersion and better interfacial adhesion.

17.2 Processing methods used in CNT–polyolefin nanocomposites

There are three commonly used processing methods for producing thermoplastic nanocomposites: solution mixing, *in-situ* polymerization and melt processing.

17.2.1 Solvent processing

Solution processing is a common method used to disperse nanotubes in polymers in the research environment given its relative ease and capacity for small-scale production. In general, it consists of dissolving the polymer in a suitable solvent, followed by mixing in the nanotubes and eventual evaporation of the solvent. This process may first involve dispersing the nanotubes in solvent, and then adding them to a dissolved polymer solution (Grady *et al.*, 2002), or the nanotubes may be added directly straight to the polymer solution (Assouline *et al.*, 2003; Esawi *et al.*, 2009), or polymer pellets may be added to the nanotube dispersion (Kearns and Shambaugh, 2002; Moore *et al.*, 2004). It should be emphasized that the nanotubes are not, of course, dissolved but rather act as a ‘colloidal dispersion’ (Grady *et al.*, 2002) in these processes. While the nanotubes may be suspended in the solution by methods such as mechanical or ultrasonic agitation, unless they are functionalized, they will often fall out of the suspension at cessation of the mixing process.

Solvent mixing is more difficult for polyolefins than for many other polymers, due to limited solubility of these polymers in organic liquids. For polypropylene, Decalin (decahydronaphthalene) is a common solvent (Grady *et al.*, 2002; Kearns and Shambaugh, 2002; Moore *et al.*, 2004), with temperatures of between 70 °C and 140 °C required in order to enable the polypropylene to be dissolved. Other solvents that have been used in the production of polypropylene–nanotube composites include toluene (at 80 °C) (Assouline *et al.*, 2003) and m-Xylene (Esawi *et al.*, 2009) (at 80 °C). In the production of ultra-high molecular weight polyethylene (UHMWPE)–nanotube composites, Decalin (at 140 °C) has also been used successfully (Bin *et al.*, 2003), while non-polar paraffin was found to be less effective in providing good dispersion (Xi *et al.*, 2007).

The mixing/agitation has generally been provided by either shear mixing (Xi *et al.*, 2007) (often simply involving manual stirring with a spatula or stirrer rod) or sonication (Moore *et al.*, 2004; Esawi *et al.*, 2009) (either mild sonication using an ultrasonic bath or more high-powered sonication using a tip/horn (Coleman *et al.*, 2006)). However care must be taken when using sonication as the process has been shown to damage nanotubes by increasing defect concentration and causing damage to the walls of the nanotubes, similar to that caused by oxidation. It also can remove graphite layers, and even cause tube breakage (Lu *et al.*, 1996).

Solvent is usually removed from the mixture by placing the mixture in a vacuum oven for 2 to 7 days (Grady *et al.*, 2002; Kearns and Shambaugh, 2002; Moore *et al.*, 2004), however, in certain cases it may be removed using a different solvent, for example Xi *et al.* (2007) used benzene to remove paraffin, with the resultant product generally a powder (Grady *et al.*, 2002) which was subsequently either processed by melt spinning to form fibres (Kearns and Shambaugh, 2002), extruded (Esawi *et al.*, 2009) or compressed into a solid sheet using hot platens (Grady *et al.*, 2002).

The main advantages of solution mixing are that composites can be made from small quantities of raw materials and thermal processing equipment is not required (especially for small-scale mixing). However, there are major disadvantages of solution mixing. The solvent must be removed and may be hard to recover, the composites may also contain residual solvents which lower the glass transition temperatures and mechanical strengths of the polymers, and the method is not conducive to industrial scale-up. Recently, Esawi *et al.* (2009) highlighted the differences in a study which compared the effect of solvent versus dry mixing on the mechanical properties of polypropylene–MWNT composites. Although higher degrees of dispersion were achieved via the solution mixing, this method was found to degrade the polymer, with significant reductions in yield stress, hardness and modulus in the control (unfilled) solvent mixed sample relative to the control dry mixed sample.

17.2.2 *In-situ* polymerization

In-situ polymerization is a promising method to produce CNT–polymer composites, and involves polymerization of the monomer in the presence of carbon nanotubes. The advantages of this process include being able to graft polymer macromolecules onto the carbon nanotube walls, and the ability to prepare composites with high nanotube loadings. It has good compatibility with a wider range of polymers, including those that are insoluble or thermally unstable and thus unsuitable for solution or melt processing (Coleman *et al.*, 2006). For polyolefin–CNT composites, *in-situ* polymerization has also been undertaken where the catalyst is anchored to the surface of the nanotubes, followed by polymerization.

Metallocene–methylaluminoxane (MAO) catalyst systems are commonly used in this context, due to their solubility in hydrocarbons like toluene, and their ability

to produce tailored microstructures and tacticities in polypropylene (Funck and Kaminsky, 2007; Kaminsky and Funck, 2007). When using these systems, functionalized MWNTs are reacted with MAO (prior functionalization of the nanotubes allowing the nanotubes to react with the MAO without deactivating the catalyst), the MAO anchoring to the walls of the nanotubes due to the formation of covalent oxygen aluminum bonds (Kaminsky and Funck, 2007). Excess MAO is removed through washing, followed by the addition of a transition metal compound (such as Cp_2ZrCl_2 (Li *et al.*, 2009a)) to produce catalytically active sites on the surface of the nanotubes (Kaminsky and Funck, 2007). These MWNT-supported catalysts are then dispersed in a solvent such as toluene, followed by the addition of monomer (ethylene or propylene) to produce polyethylene-coated (Li *et al.*, 2009a) or polypropylene-coated (Funck and Kaminsky, 2007) nanotubes. As the polymer is grown directly onto the nanotubes, they are covalently attached. Monomer can continue to be added to produce composites at the desired concentration (Li *et al.*, 2009a), or additional MAO can be added to increase the activity of the process (Kaminsky and Funck, 2007).

Work by Bonduel (Bonduel *et al.*, 2005) also used MAO as a catalyst for the *in-situ* polymerization of ethylene onto the surface of carbon nanotubes. In this work, however, the nanotubes were not functionalized, the polymer being formed close to the carbon nanotube surface rather than being covalently bonded onto the nanotubes. As the molecular weight of the polymer chains increased, the polymer was found to precipitate onto the surface of the nanotubes, coating them and ultimately separating them.

Other catalyst systems have also been used in the preparation of *in-situ* polymerized polyolefin carbon nanotube composites. For example, Tong *et al.* (2004) attached a $\text{MgCl}_2/\text{TiCl}_4$ catalyst to the surface of SWNTs and used *in-situ* Ziegler-Natta polymerization to coat the surface of the nanotubes with PE. These coated nanotubes were then melt-blended with PE and the resulting composites were found to have better levels of dispersion and improved mechanical properties when compared with those made with uncoated SWNTs. Li *et al.* (2009b) further treated functionalized CNTs with maleic anhydride, and grafted this on to PP using benzoylperoxide when the CNTs-MAH were mixed with molten PP.

17.2.3 Shear mixing (melt processing)

Melt processing is a method that is widely used in the production of CNT thermoplastic composites. Also referred to as melt blending or melt mixing, this method involves heating the polymer into the melt and using shear mixing to break nanotube aggregates and disperse them throughout the polymer melt. Bulk samples can then be produced utilizing techniques such as extrusion, injection moulding or compression moulding. The advantages of this technique are its speed and simplicity, as well as its wide use in industry (Coleman *et al.*, 2006). Early studies tended not to use this method due to the relatively large volumes of nanotubes

required. However, with production of nanotubes increasing and the subsequent reduction in their cost (especially for MWNTs), melt processing is becoming the preferred method, especially when looking towards commercialization.

Various mixers have been used for shear melt mixing of polyolefin nanocomposites, including rheometers (Tong *et al.*, 2004; Zhou *et al.*, 2008), simple cup and cone mixers such as an Atlas Minimax mixer (Yang *et al.*, 2009), Banbury mixers (Zhao *et al.*, 2006), internal mixers such as the Haake Rheomix (Bikiaris *et al.*, 2008; Manchado *et al.*, 2005), single screw extruders (Esawi *et al.*, 2009) and twin screw extruders (Morcom, 2008; Prashantha *et al.*, 2009). In general, a higher degree of mixing can be achieved using a twin screw extruder or internal mixer such as a Haake Rheomix, while simple cup and cone type mixers provide poorer mixing (Holmstrm and Srvik, 1974). Likewise lower levels of dispersion can be expected from experiments performed within shear rheometers.

When selecting a mixing method, it is important to ensure that it will enable a high level of dispersion, while also limiting degradation of the polymer. The three main risk factors for degradation are exposure to air while in the melt, high shear stresses and high temperatures. While degradation of polypropylene occurs via chain scission resulting in lower molecular weight, lower viscosity and poorer mechanical properties (Arostegui *et al.*, 2008), polyethylene suffers from a combination of chain scission and cross-linking, the degree of each being dependent on processing conditions (Holmstrm and Srvik, 1974).

A disadvantage that is often cited when comparing melt mixing to methods such as solution mixing and *in-situ* polymerization, is that the energy input required to disperse the CNTs in melt processing tends to break them into shorter segments, decreasing their aspect ratio (Andrews *et al.*, 2002a; Andrews *et al.*, 2002b).

17.2.4 Melt spinning

There has been significant interest in the production of carbon nanotube-containing polymer fibres for a number of reasons. First, the small diameters of carbon nanotubes make them highly suitable to reinforce polymer fibres which are typically only 10–100 µm in diameter (Kearns and Shambaugh, 2002). Secondly, the fibre production method promotes the alignment of the carbon nanotubes, maximizing the effect of their mechanical properties. Three main methods are used in the production of CNT–polymer composite fibres: melt spinning, electrospinning and solution/coagulation spinning.

Melt spinning is the most common method used for the production of CNT–polyolefin fibres. This method involves extruding the composite melt through a fine die, forming a polymer fibre, air cooling and drawing the fibre under tension onto a wind-up spool/take-up roll (Kearns and Shambaugh, 2002). This method has been successfully used by a number of groups with both SWNTs (Bhattacharyya *et al.*, 2003) and MWNTs (Dondero and Gorga, 2006; Jose *et al.*, 2007). Fibres can

then be melt drawn, passing from one roller to another, which if set at a higher speed can produce the desired draw ratio (Dondero and Gorga, 2006).

Fibres can also be post-drawn, where the fibre is stretched in a controlled manner in a separate step after initial fibre production (Moore *et al.*, 2004). For polymer fibres, this can lead to an increase in orientation and crystallization, with a concomitant increase in strength and modulus (Moore *et al.*, 2004). This process can be achieved using two rolls with independent speed controls, the fibre passing from one roll through an oven onto the other roll, the latter set at a higher speed than the first to enable the desired draw ratio (Kearns and Shambaugh, 2002; Moore *et al.*, 2004). The addition of nanotubes has been found to decrease the maximum achievable post-draw ratio (Moore *et al.*, 2004).

A variation on this method was reported by Yeh *et al.* (2008), who dispersed MWNTs in a gel solution of UHMWPE, and then spun fibres from the composite, removing the solvent after spinning, enabling higher draw ratios and improved tensile properties.

17.2.5 Other methods used to process CNT–polyolefin nanocomposites

A variety of other methods have also been used in the production of CNT–polyolefin nanocomposites, including:

- electrostatic spraying, followed by sintering (Bakshi *et al.*, 2007);
- dispersing nanotubes in solution, using this to coat polymer granules, followed by sintering (Mierczynska *et al.*, 2007);
- using a CNT–polymer masterbatch to melt blend (Prashantha *et al.*, 2009);
- high energy ball milling (Gorrasi *et al.*, 2007b);
- combinations of methods such as solution mixing, followed by melt mixing (Zhao *et al.*, 2006);
- solution crystallization (He *et al.*, 2009);
- solid shear state pulverization (Pujari *et al.*, 2009).

Sintering of nanotube-coated polymer pellets/granules has been used by a variety of researchers in an effort to locate nanotubes on the granule boundaries, in order to produce electrically conductive networks at low concentrations (reduce percolation threshold) (Bakshi *et al.*, 2007) on the basis that the high viscosity of the melt will ensure that the particles remain broadly dispersed in a similar fashion as in the dry powder blend, thus resisting reagglomeration.

17.2.6 Use of compatibilizers to process polyolefin–CNT composites

Compatibilizing agents have been used by various researchers in order to assist with enabling high degrees of dispersion in polyolefinic systems. Surfactants can

aid dispersion and nanotube wetting by coating the nanotubes and introducing steric repulsions which counteract the van der Waals attractions between the nanotubes, hence preventing agglomeration (Maser *et al.*, 2003). However, surfactants must be used with care as they can act as plasticizers within the matrix proper, decreasing the elastic modulus and strength of the polymer matrix into which they are dispersed. For example, Wu *et al.* (2009) and Jin *et al.* (2009) both used maleic anhydride-grafted polypropylene (mPP) as a compatibilizer when melt blending MWNT–PP composites, with Wu *et al.* (2009) finding that the addition of mPP enabled the nanotubes to be dispersed on the nanoscale, reducing the rheological percolation threshold while Jin *et al.* (2009) reported that MA-g-PP had a strong compatibilizing effect on diamine-functionalized MWNT–PP composites, resulting in composites with higher thermal stability and complex viscosity. Lee *et al.* (2007) also found that addition of the combatabilizers MA-g-PP and MA-g-SEBS (maleic anhydride grafted styrene-ethylene/butylene-styrene) both increased the electrical conductivity of PP–MWNT composites, by enhancing the dispersion of MWNTs.

17.2.7 Functionalization of CNT to manipulate dispersion and properties

The application of CNTs as structural reinforcement in polyolefins is dependent on achieving good nanotube dispersion, along with effective interfacial stress transfer. With many researchers citing insufficient dispersion as a process limitation, nanotube functionalization or grafting of polymer molecules to the walls of the nanotubes has been investigated by numerous teams in an effort to increase dispersion and increase stress transfer across the CNT–polymer interface.

Nanotube functionalization treatments, such as heating in acid, can produce functional groups which can assist in nanotube dispersion (particularly in polar matrices), however, this is often at the expense of the nanotube structure as it introduces defects into the graphene wall of the nanotube, reducing its electrical and mechanical properties (Lordi and Nan, 2000; Shieh *et al.*, 2007). The most common functionalization procedure involves treating the nanotube with acids, often by refluxing the CNTs in a nitric acid solution or a mixture of nitric and sulfuric acid, usually while concurrently applying a high power sonication treatment. This treatment usually results in shortening (cutting) of the CNTs and the formation of surface groups such as hydroxyl, carbonyl and carboxylic acid groups. (Bikiaris *et al.*, 2008).

Acid functionalization of nanotubes has had mixed effects on the properties of CNT–polyolefin composites. Tabuani *et al.* (2008) found that carboxylic acid functionality of CNTs decreased the compatibility of the CNTs with polypropylene, resulting in the nanotubes being less effective at improving the thermal and thermo-oxidative behaviour of polypropylene. In comparison, Bikiaris *et al.* (2008) found that acid treatment of MWNTs led to finer dispersion in

polypropylene, with increased treatment time yielding increased Young's modulus, tensile strength and storage modulus of the MWNT–PP nanocomposites. Nanotube functionalization was also effective in experiments performed by Lee *et al.* (2007) who functionalized nanotubes using three different methods: (1) acid treating in a 3:1 mixture of H_2SO_4 and HNO_3 ; (2) amine treating by heating the acid-treated MWNTs with octadecylamine; and (3) heat treating of pristine MWNTs at 500°C in air for 1 hour. They found that chemical functionalization decreased the amount of MWNT aggregates in the PP composites, with heat and acid-treated MWNT–PP composites having increased storage modulus and complex viscosity (due to a more homogeneous dispersion of nanotubes and stronger interactions between the nanotubes and polymer), while amine treatment led to a reduced storage modulus and complex viscosity (relative to that of the untreated MWNT–PP composites) assigned to excessive hydrogen bonding between the functional groups of the nanotubes, leading to nanotube aggregation and possibly imperfect penetration of the polymer into nanotube clusters.

Improved interaction between polymer and nanotubes can also be brought about by grafting the matrix polymer onto the walls of the nanotubes. Yang *et al.* (2007) grafted polyethylene onto MWNTs by a reactive blending process, where polyethylene containing 0.85 wt% of maleic anhydride was melt blended with amine-functionalized MWNTs. The grafting of the polyethylene onto the MWNTs improved the dispersion of nanotubes in the PE matrix and improved MWNT–PE interfacial adhesion, leading to improved stiffness, strength, ductility and toughness of the polyethylene. Similar results were reported by Li *et al.* (2007) who grafted polyethylene chains to the sidewalls of SWNTs via ethylene copolymerization, the grafting process improving the thermal stability and mechanical properties of these nanocomposites.

17.3 Mechanical properties of CNT–polyolefin nanocomposites

Nanotubes have been shown to increase the elastic modulus, yield strength and tensile strength of polyolefins, while generally decreasing polymer ductility. A summary of results reported in the literature, presented in Table 17.1, however, indicates that the effectiveness of nanotubes as a mechanical reinforcement varies with nanotube quality and mixing method. Some researchers have found poor dispersion an issue, with improvements at low loading levels disappearing as the concentration increases (Esawi *et al.*, 2009; Zhou *et al.*, 2008), while others have found that strength and elastic modulus keep increasing as concentrations were raised above 5 wt% (Xiao *et al.*, 2007; Zhao *et al.*, 2006).

The addition of even low concentrations of nanotubes can lead to significant improvement of elastic modulus, with increases larger than 100% recorded at concentrations less than 5 wt% in LDPE (Morcom, 2008), UHMWPE (Mierczynska *et al.*, 2007) and polypropylene (Chang *et al.*, 2005). While

Table 17.1 Mechanical properties of polyolefin-CNT composites

Nanotubes-polymer system	Nanotube treatment	Processing	Wt %	Elastic modulus (MPa)	Yield strength (MPa)	Tensile strength (MPa)	Strain at break (%)	Reference
LDPE-MWNT	-	Solution mixing (using ultrasonication), followed by melt mixing using a Banbury mixer and compression moulding	0			9.3	275	(Zhao <i>et al.</i> , 2006)
			5			10.8	130	
			10			11.5	120	
			30			15.5	30	
LDPE-MWNT	-	Mechanically mixed at 140 °C, compressed into a mould, cut into small pieces and process repeated ten times.	0	235		10.7	380	(Xiao <i>et al.</i> , 2007)
			5	386		14.5	160	
			10	444		15.6	12	
LDPE-MWNT	-	Melt blending (twin screw extruder), followed by injection moulding	0	160		15.9	88	(Morcom, 2008)
			5	340		18	43	
			5	320		17.6	44	
PE-MWNT	Washed with HCl	Melt blending (twin screw extruder), mini tensile specimens punched from sheets	0		11.2	21	20	(McNally <i>et al.</i> , 2005)
			5		13	16	12	
			10		13	12	5	
PE-MWNT	PE grafted MWNTs Untreated	SWNT suspension sprayed onto PE power, which was dried and processed using twin-screw extruder	0	210	11.0	15.2	7.24	(Yang <i>et al.</i> , 2007)
			2	405	16.7	18.7	7.0	
			2	253	12.7	11.7	1.02	
LLDPE-MWNT	Purified in concentrated HCl solution, and HC/HNO ₃ solution	High energy ball milling, followed by hot pressing and rapid quenching	0	460	8	8	690	(Gorrasí <i>et al.</i> , 2007b)
			5	650	13	17	680	
			10	660	13.5	15	800	

Continued

Table 17.1 Continued

Nanotubes-polymer system	Nanotube treatment	Processing	Wt %	Elastic modulus (MPa)	Yield strength (MPa)	Tensile strength (MPa)	Strain at break (%)	Reference
PE-SWNT	Functionalized by grafting α -alkene groups to the side walls of the SWNTs	Solution mixing (using functionalized SWNTs)	0	643		32	923	(Li <i>et al.</i> , 2007)
		<i>In-situ</i> polymer (using purified SWNTs)	2	558		33	922	
			2	651		27	1302	
		<i>In-situ</i> polymerization (using functionalized SWNTs)	2	656		36	1438	
PE-SWNT	Functionalized by refluxing in concentrated nitric acid	<i>In-situ</i> polymerization	0	700		25	900	(Li <i>et al.</i> , 2009)
			2.4	450		33	1200	
PE-SWNT	Raw SWNTs	SWNTs were covered in a layer of PE by <i>in-situ</i> polymerization,	0	808	27	34	801	(Tong <i>et al.</i> , 2004)
	Modified SWNTs (<i>in-situ</i> polymerization)	these were mixed with PE pellets in a mortar and melt blend using a torque rheometer (with comparison to unmodified SWNTs)	0.5	638	22	29	769	
			0.5	800	27.5	33	931	
HDPE-MWNT		MWNTs were mixed with an ethanol solution containing polyethylene glycol, a coupling agent and SiO ₂ with the aim of wrapping the MWNTs with polymer chains. This solution was dried and mixed with HDPE in a twin screw extruder and injection moulded	0	520		23	49	(Zou <i>et al.</i> , 2004)
			1	920		28.2	27	
			3	840		26.3	53	

HDPE-MWNT	Refluxed in a concentrated solution of nitric acid and sulphuric acid	Treated CNTs were sonicated with deionized water and then mixed with HDPE pellets to provide a CNT coating. Once dried the coated pellets were injection moulded to form tensile specimens	0 0.44 (vol%)	1095 1338	105.8 109.9	863 1069	(Kanagaraj <i>et al.</i> , 2007)
HDPE-SWNT	SWNTs were purified with undisclosed method	SWNTs suspended in solution and sprayed onto polymer powder. This powder was dried and mixed using a twin-screw extruder, followed by compression moulding	0 5	460 725	14 24		(Zhang <i>et al.</i> , 2006)
HDPE-MWNT	<i>In-situ</i> polymerization	MWNT-HDPE masterbatch produced by <i>in-situ</i> polymerization which was then melt blended with HDPE using an Atlas mini-extruder	0 0.52	334 610	22 23	500 450	(Vega <i>et al.</i> , 2009)
HDPE-MWNT	–	Melt blending using Haake-Buchler Reomixer, followed by compression moulding and stamping of tensile specimens	0 2.5	609 796	19.7 19.5	770 54	(Chrissafis <i>et al.</i> , 2009)
HDPE-MWNT	–	Melt blending (twin screw extruder), followed by injection moulding	0 1 5 5	877 947 1335 1180	21.2 23.4 32.8 30.8	1110 1030 34 40	(Morcom, 2008)
UHMWPE-MWNT	Oxidation (1 hr, 500 °C, 95% N ₂ , 5% O ₂) Refluxed in a solution of nitric acid and sulphuric acid	Solution mixed, followed by solution casting and hot drawing	0 1	977 1352	8.3 12.4		(Ruan <i>et al.</i> , 2003)

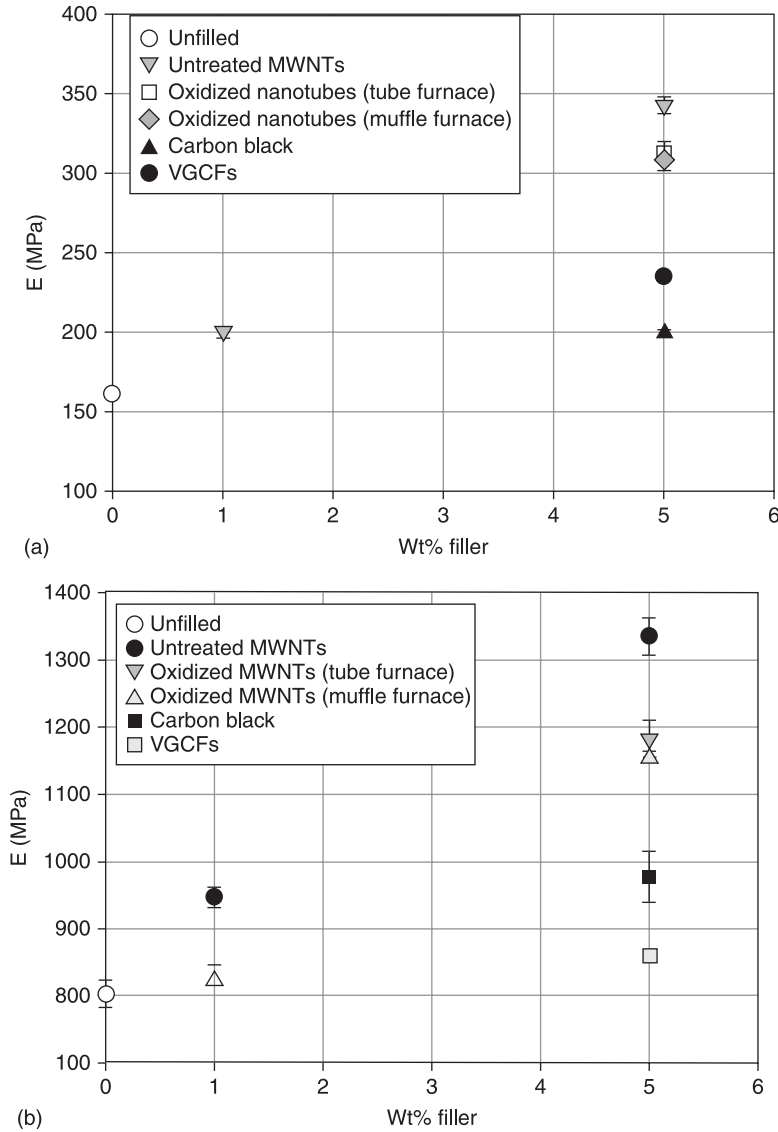
Continued

Table 17.1 Continued

Nanotubes– polymer system	Nanotube treatment	Processing	Wt %	Elastic modulus (MPa)	Yield strength (MPa)	Tensile strength (MPa)	Strain at break (%)	Reference
UHMWPE– MWNT	–	Powders mixed (polymer and MWNTs), electrostatic spray and then heat to melt	0	682		14.3	3.9	(Bakshi <i>et al.</i> , 2007)
			5	1240		12.4	1.4	
UHMWPE– MWNT	–	Dispersed nanotubes in a liquid (using ultrasound and a surfactant to stabilize the solution), mixed the polymer granules into solution (nonsolvent for PE), followed by drying and sintering	0	430	17	55	1800	(Mierczynska <i>et al.</i> , 2007)
			3.5	1200	40	38	1000	
UHMWPE– SWNT	–		3.5	740	27	34	600	
Polypropylene– MWNTs	–	Melt mixed using a Haake PolyLab Reomix shear mixer, followed by compression moulding to form films from which tensile specimens were cut	0	1000	30			(Andrews <i>et al.</i> , 2002a)
			12.5 (vol%)	2400	18			
Polypropylene– SWNTs	–	Melt mixed using a Haake Reomix internal mixer, followed by compression moulding and cutting of tensile specimens	0	850		30.8		(Manchado <i>et al.</i> , 2005)
			0.75	1190		35.5		
			1	1090		33.8		
Polypropylene– SWNT	–	Solution mixing followed by fibre spinning	0	400				(Chang <i>et al.</i> , 2005)
			1	1000				
			5	1400				

Polypropylene-MWNT	- Acid treated with nitric acid sulphuric acid	Melt mixing in a Haake-Buchler Reomixer, followed by compression moulding and stamping of tensile specimens	0 2.5 2.5	600 1300 1400	27.9	28.7 31.0 34.5	640 4.9 6.6	(Bikiaris <i>et al.</i> , 2008)
Polypropylene-MWNT	PP grafted MWNTs	Melt blending using an Atlas Minimax mixer, followed by the pressing of thin films	0 2	900 1700		25.2 54.6	7.2 7.7	(Yang <i>et al.</i> , 2008)
Polypropylene-MWNT	-	Melt mixed using a twin screw extruder, followed by injection moulding	0 5	1250 1800	31.5 38			(Ganß <i>et al.</i> , 2008)
Polypropylene-MWNT	-	Melt blended using a Haake RC90 Rheometer, followed by compression moulding	0 1 5 1 5			36 38 37 39.5 37.5		(Zhou <i>et al.</i> , 2008)
Polypropylene-MWNT	-	Melt mixed samples in a twin screw extruder using a masterbatch (produced by nanocyl using an extrusion process). Tensile samples formed by injection moulding	0 5	1280 2150	28.2 35.3		620 12	(Prashantha <i>et al.</i> , 2009)
Polypropylene-MWNT	-	Dry mixing of pellets and nanotubes, followed by extrusion using a single screw extruder. Tensile testing of extruded strands	0 1 5 0 1 5		17 21 18 13 25 16			(Esawi <i>et al.</i> , 2009)
Polybutene-MWNT	PP-g-MWNTs pristine MWNTs	Polypropylene grafted MWNTs compared with pristine MWNTs. Melt blending using an Atlas Minimax mixer	0 2 2	380 777 431	15.4 25.2 18.7	31.1 43.1 19.5	270 244 119	(Yang <i>et al.</i> , 2009)

Morcom (2008) observed a linear relationship between elastic modulus and MWNT weight fraction in LDPE and HDPE at loading levels up to 5 wt% (see Fig. 17.1) (as predicted by composite theories such as the Halpin-Tsai equations and the modified rule of mixtures), this is not consistent across all studies, with



17.1 The elastic modulus of: (a) LDPE nanocomposites; and (b) HDPE nanocomposites as a function of filler concentration. Untreated MWNTs providing a significantly larger reinforcing effect than carbon black, vapour grown carbon fibres (VGCFs) or functionalized MWNTs (oxidized in a 95% nitrogen, 5% oxygen atmosphere at 500 °C) (Morcom, 2008).

researchers such as Gorrasi *et al.* (2007b) finding that while small concentrations can provide significant increases at low nanotube concentrations, further increasing the nanotube content provides more modest additional increases, most likely due to limited degrees of dispersion.

Nanotubes have also been shown to substantially increase the yield and tensile strengths of polyolefins, however, since failures initiate at the weakest point in a material (such as within a nanotube agglomerate) (Bert and Kline, 1985; Coleman *et al.*, 2004), smaller increases or even decreases in these properties have also been observed when nanotubes are poorly dispersed. Significant increases have been observed when processing methods are used which aim to reduce these agglomerates, with over 50% increases in yield strength being reported in LDPE (Morcom, 2008), polyethylene (Yang *et al.*, 2007), HDPE (Vega *et al.*, 2009), UHWMPE (Mierczynska *et al.*, 2007) and polypropylene (Andrews *et al.*, 2002a; Chang *et al.*, 2005; Bikiaris *et al.*, 2008; Prashantha *et al.*, 2009) using various mixing methods including *in-situ* polymerization, solution blending and various melt mixing techniques. Although many studies such as that by Chrissafis *et al.* (2009) have found that the addition of nanotubes decreases the tensile strength of polyolefins, a small number have reported significant increases, with Yang *et al.* (2008) reporting over a 100% increase in tensile strength using polypropylene grafted MWNTs while over 50% increases have been measured by Zhao *et al.* (2006) and Gorrasi *et al.* (2007b).

With regard to the effect of nanotubes on the toughness of polymers, there are mixed results, with toughness being highly dependent on polymer and processing methods. While most researchers have found that the incorporation of nanotubes decreases the strain to failure in most rigid polymers, reducing both ductility and toughness (see Table 17.1), Kanagaraj *et al.* (2007) found that the addition of MWNTs to HDPE provided up to a 30% increase in toughness. Ruan *et al.* (2003) measured even larger improvements in ultra high molecular weight polyethylene (UHMWPE), with 1 wt% MWNTs increasing the ductility (strain at break) by 150% while the yield strength increased from 8.3 MPa to 12.4 MPa. However, while Ruan stated that these increases were due to the MWNTs providing an increase in the mobility of the polymer, findings by others do not support this suggestion. Since UHMWPE usually has a yield strength of 12–28 MPa and undergoes 350–525% elongation before break (Callister, 1990), compared to the 4% elongation (Ruan *et al.*, 2003) observed for their unfilled UHMWPE, it is possible that the solution processing method used by Ruan to produce these composite films may not be ideal.

Some researchers have found that functionalization of nanotubes leads to significant increases in the mechanical properties of polyolefins, with Zhou *et al.* (2008) finding that MWNTs functionalized with a silane coupling agent were more effective than untreated MWNTs, while Bikiaris *et al.* (2008) recorded similar improvements from acid treatment. In comparison, Morcom (2008) found that oxidation of nanotubes reduced the effectiveness of MWNTs as a

reinforcement. Grafting of α -alkene groups to the side walls of the SWNTs can also lead to improvements (Li *et al.*, 2007), while PE-grafted MWNTs (Yang *et al.*, 2007) and PP-grafted MWNTs (Yang *et al.*, 2009) were more effective than untreated MWNTs in polyethylene and polypropylene respectively. However, it should be noted that many of these researchers have used mixing methods such as the Atlas Mini-Max mixer (a cup-and-rotor melt mixer) (Yang *et al.*, 2008; Yang *et al.*, 2009) which are prone to poor dispersion, and this effect may not be as significant when using more effective mixing methods.

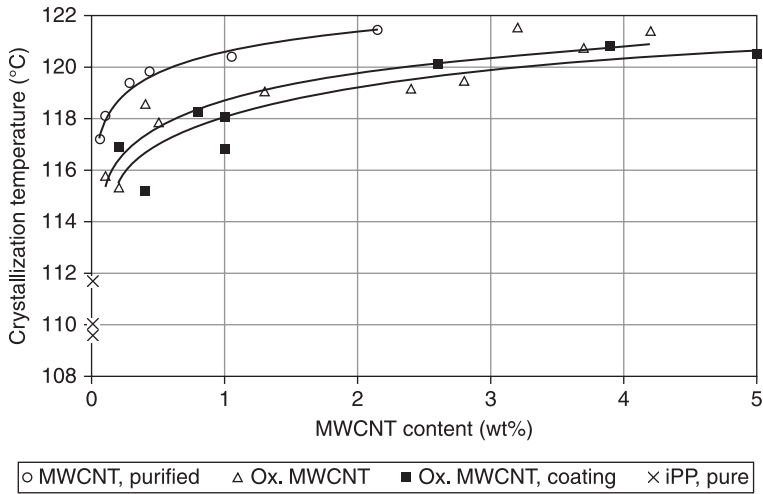
In general, MWNTs have been found to have a larger effect than SWNTs (Mierczynska *et al.*, 2007), with many researchers such as Tong *et al.* (2004) and Li *et al.* (2007) recording significant decreases in mechanical properties of polymers with the addition of SWNTs. This is usually attributed to poor levels of dispersion, with SWNTs being significantly more difficult to disperse than MWNTs (Mierczynska *et al.*, 2007) due to self-association.

17.4 Crystallinity of polyolefin-CNT blends

A large number of studies have been undertaken to investigate the effect of carbon nanotubes on the morphology and crystallization behaviour of polyolefins, with the universal consensus that nanotubes act as good nucleating agents.

The addition of nanotubes to polyolefins can result in relatively large increases in crystallization temperature. In polyethylene, McNally *et al.* (2005) found that the addition of 10 wt% MWNTs resulted in an 8 °C increase in crystallization temperature, while the addition of SWNTs to HDPE led to a 4 to 5 °C increase (Jeon *et al.*, 2007). In the case of polypropylene, Funck and Kaminsky (2007) reported that the addition of 0.1 wt% MWNTs could lead to the crystallization temperature increasing from 111 °C by 4 to 5 °C, while raising the concentration to 2 wt% could lead to a 9 °C increase, oxidized and coated nanotubes were found to have a much smaller effect (Fig. 17.2). Bhattacharyya *et al.* (2003) found that the large surface area of SWNTs could also lead to significant effects, with 11 °C increase in the crystallization temperature of polypropylene reported, while Valentini *et al.* (2003) reported similarly large effects with the addition of 20 wt% SWNTs increasing the crystallization temperature of polypropylene from 101 °C to 119 °C. Similar results have also been reported for syndiotactic polypropylene (Gorrasi *et al.*, 2007a).

Nanotubes have also been found to increase the rate of crystallization, with the increase being strongly dependent on the degree of nanotube dispersion. Isothermal measurements of the crystallization half-times have been used to assess the degree of dispersion, with Pujari *et al.* (2009) finding that an increased mixing time leads to a reduction in the crystallization half-time, the more well-dispersed composites providing a greater area of contact between the CNT and polymer and therefore providing a higher number of heterogeneous nucleation sites for PP crystallization and correspondingly accelerated nucleation kinetics.



17.2 Crystallization temperatures of pure isotactic polypropylene (iPP) and the dependence of various MWNT–iPP nanocomposites on the MWNT content (Funck and Kaminsky, 2007).

Likewise, Xie *et al.* (2003) found that the addition of a compatibilizer increased the crystallization rate of CNT–UHMWPE composites, due to the increased dispersion of CNTs.

However, with increasing nanotube concentration, it is found that a maximum crystallization rate is reached, with further nanotube addition providing negligible change or even decreasing the crystallization rate. Causin *et al.* (2009) found that the nucleation effect of polypropylene-grafted MWNTs in polypropylene was saturated beyond 1.5 wt% filler, addition of further filler did not bring about significant increases in the crystallization rate, because at that point the rate-determining step became crystal growth, rather than nucleation. Likewise, Xu and Wang (2008) found that crystallization rates did not significantly change with increasing nanotube concentration once the critical gelation CNT concentration was reached (7.4 wt% for their MWNT–iPP composites), further addition of nanotubes reducing the mobility and diffusion of iPP chains for crystallization, reflected in an observed reduction of the radial growth rates of the iPP spherulites.

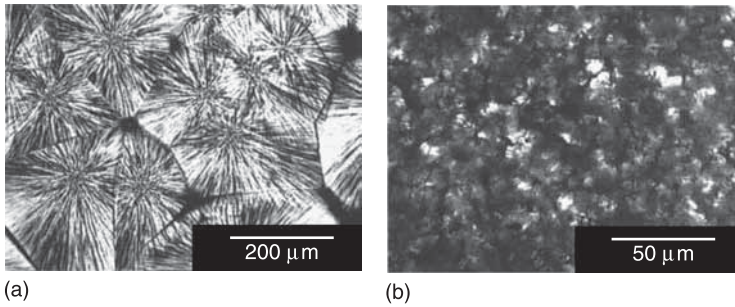
There are conflicting reports regarding the effects of carbon nanotubes on the degree of crystallinity of polyolefins. While most authors find that they have minimal effect (Manchado *et al.*, 2005), a few exceptions have recorded increases or decreases. While most describe only small effects, Aalaie *et al.* (2007) found a large increase in crystalline fraction, from 22.1% (neat LLDPE) to 30.32% with the addition of 5 wt% MWNTs, while Vega *et al.* (2009) found that the addition of 0.52 wt% MWNTs to HDPE resulted in a small increase in crystallinity (59 to 62%).

This is in contrast with other studies which have measured a reduction in the degree of crystallinity, explained by the CNTs inhibiting the formation of large uniform lamellae, increasing the number of grain boundaries and other defects which leads to crystallinity reduction (Kodjie *et al.*, 2006; Jose *et al.*, 2007). Both McNally *et al.* (2005) and Bakshi *et al.* (2007) measured slight reductions in the degree of crystallinity of medium density polyethylene and UHMWPE respectively, while a detailed study by Causin *et al.* (2009) using polypropylene-grafted MWNTs (PP-g-MWNTs) found that the degree of crystallinity of polypropylene decreased from 66% to 61% with the addition of 2 wt% PP-g-MWNTs, while the addition of the same quantity of ungrafted MWNTs resulted in a larger decrease, down to 59%. Causin *et al.* (2009) postulated that the reductions in crystallinity were due to the nanotubes causing rapid crystallization of the polypropylene which prevented the polymer from reaching a highly regular, semicrystalline framework. It was thought that the effect was smaller for the PP-g-MWNTs, as these grafted MWNTs allowed more efficient and unhindered crystallization at a lamellar level. The tendency of the ungrafted MWNTs to aggregate may have disrupted the ordering of the lamellar stacks.

The effect of high concentrations of nanotubes on crystallinity has been found to particularly inhibit crystallization, with significant CNT contents being shown to result in significant reductions. For example, McNally *et al.* (2005) found that the addition of 10 wt% MWNTs to polyethylene decreased the crystallinity from 32.5% to 27.6% while Haggemueller *et al.* (2007) found that 25 wt% MWNTs resulted in a 5% reduction in the crystallinity of HDPE, thought to be due to the increased confinement experienced by the HDPE chains at the interfaces. Bao and Tjong (2007) reported minimal change in the degree of crystallinity of polypropylene with the addition of 0.1 wt% MWNTs, however, a 5.5% decrease was reported when the concentration was increased to 1 wt%.

The nucleating effect of carbon nanotubes also leads to a reduction in crystallite size (Razavi-Nouri *et al.*, 2009), with work by Jeon *et al.* (2007) using polarized optical microscopy showing that the addition of SWNTs changed the spherulitic morphology of HDPE from banded spherulites of ~30–50 μm diameter to smaller aggregates of 1–2 μm . Likewise, Valentini *et al.* (2004) found that the addition of 5 wt% SWNTs to polypropylene reduced the polymer's grain size from 100 μm , to 10 μm (Fig. 17.3), while Lee *et al.* (2008) observed that the addition of 1 wt% nanotubes to polypropylene decreased spherulite diameter from about 400 μm to 20 μm . Lee *et al.* (2008) also proposed that the narrowing of crystallization and melting peaks of PP indicated that the addition of SWNT to crystallization resulted in a narrower crystal size distribution.

In some polyolefin systems, particularly in polypropylene, different forms of crystals can result. While DSC studies by Grady *et al.* (2002) indicated that nanotubes promoted growth of the less-preferred β -form of crystalline polypropylene, this finding is contradicted by numerous other DSC and XRD studies by groups such as Leelapornpisit *et al.* (2005), Manchado *et al.* (2005),



17.3 Micrographs of (a) neat PP; and (b) 5 wt% SWNT/PP composite illustrating nucleating effect of nanotubes SWNTS (Valentini *et al.*, 2004).

Seo *et al.* (2005), Bao and Tjong (2007), Avila-Orta *et al.* (2007), Tabuani *et al.* (2008), where only the more commonly observed monoclinic α -crystalline form has been observed in CNT–polypropylene composites. Likewise, XRD studies have shown that incorporation of MWNTs results in no change in the crystalline structure of the HDPE (Chrissafis *et al.*, 2009).

A number of studies have used the Avrami model to study the crystallization behaviour of polyolefin CNT composites. This model can be used ‘to describe the development of the relative degree of crystallization in isothermal processes accordingly with the following equation’ (Valentini *et al.*, 2004).

$$X_r(t) = 1 - \exp(-K(t - t_i)^n) \quad [17.1]$$

where X_r is the relative degree of crystallization in isothermal processes, n the Avrami exponent, K is the kinetic constant, t_i is the induction time for the crystallization and t is the crystallization time. The parameters n and K can be used to qualitatively interpret the nucleation mechanism, morphology and overall crystallization (Valentini *et al.*, 2004).

Jeon *et al.* (2007) used the above equation to model the kinetics of crystallization in a SWNT–HDPE composite, finding that although nucleation density increased exponentially with the presence of nanotubes, the growth mechanism was unchanged (for concentrations below 2 wt% SWNTs, after which the nucleation rates were too fast to get reliable data). They measured an Avrami exponent of 3, consistent with nucleation arising from pre-existing centres in the melt and three-dimensional growth. Similar results have been found in a number of other studies (Bhattacharyya *et al.*, 2003; Valentini *et al.*, 2004; Xu and Wang, 2008) with Avrami exponent values between 2 and 3, consistent with nucleation from pre-existing centres in the melt and three-dimensional growth, traditionally attributed to heterogeneous nucleation followed by spherulitic crystalline growth.

Other studies, such as those by Funck and Kaminsky (2007), for example, found that the Avrami parameter showed a slight enhancement in the dimensionality of the crystallite growth for *in-situ* polymerized MWNT–polypropylene composites.

Causin *et al.* (2009) also reported an increase, from an n value of about 2 for the pure matrix (indicative of two-dimensional growth with simultaneous nucleation), to a value in the interval between 2 and 3.

In contrast, significant reductions in indices have also been reported by researchers such as Haggemueller *et al.* (2007) who found that the addition of SWNTs to HDPE resulted in a reduction in index value from 2 to 1.5, while He *et al.* (2009) found that the addition of MWNTs to HDPE reduced the n value to approximately 2, suggesting that addition of MWNTs influences the mechanism of nucleation and growth, the density of the nuclei becoming too high for spherulites to develop, and the morphology resembling something closer to 2D lamellae sticks. Likewise, Assouline *et al.* (2003) used a different model and calculated the Ozawa exponent, finding that n changed from 3 to 1 with the addition of nanotubes to polypropylene, suggesting that the crystals grow as fibrils. SEM micrographs by Avila-Orta *et al.* (2007) also showed that MWNTs can induce a fibril-like structure in polypropylene (instead of spherulitic).

Zhang *et al.* (2008) used isothermal crystallization to form polypropylene transcrystallinity on incorporated nanotubes (an oriented crystalline layer that grows normal to the axis of the nanotube), with the hope that this microstructure would increase the effective adhesion and stress transfer across the nanotube–polymer interface. Polarized optical micrographs clearly show that nucleation occurred at the surface of the carbon nanotubes and grew into trans-crystals, perpendicular to the nanotube fibre axis.

Most studies have found that the addition of carbon nanotubes generally does not cause a change in polymer melting temperature for polypropylene (Funck and Kaminsky, 2007; Valentini *et al.*, 2004; Manchado *et al.*, 2005) and HDPE (Chrissafis *et al.*, 2009). However, Aalaie *et al.* (2007) did report that MWNTs melt-blended into LDPE resulted in a slight increase in melting temperature, while Trujillo *et al.* (2008) found that the addition of CNTs to *in-situ* polymerized HDPE composites led to the formation of a population of thicker lamellar crystals that melted at higher temperatures compared to crystals formed in neat HDPE (a finding that was not replicated in their physically blended MWNT–HDPE composites). Likewise, Causin *et al.* (2009) found that functionalized nanotubes resulted in composites with higher equilibrium melting temperatures than those with pristine MWNTs, indicating a more ordered crystal structure.

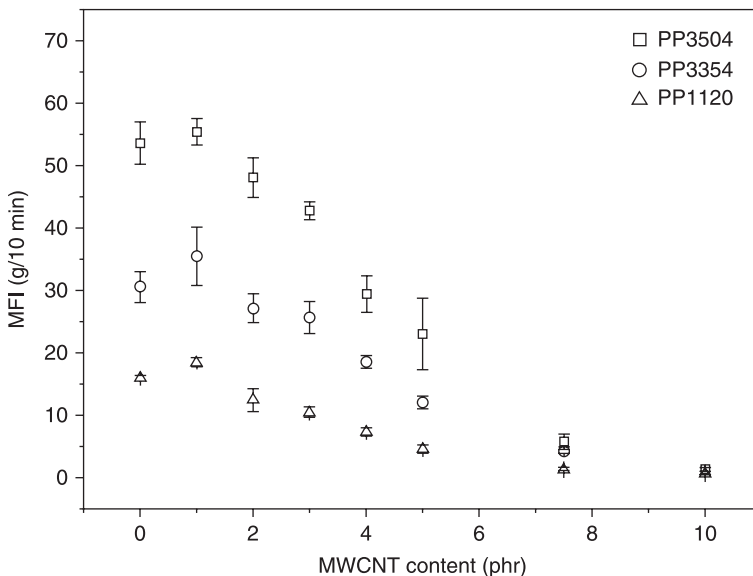
17.5 Rheological properties of CNT–polyolefin blends

For industrial processing it is critical that the rheological properties of CNT–polyolefin composites are well understood. In general, carbon nanotubes lead to dramatic increases in melt viscosity of polyolefins, with Seo and Park (2004) showing that polypropylene composites containing 5 wt% nanotubes are orders of magnitude more viscous than neat polypropylene, while McDaniel *et al.* (2009) found that carbon nanotubes had a stronger effect on the viscosity of polyethylene

than other fillers, with even small amounts of nanotubes greatly increasing the viscosity at all shear rates. It should be noted, however, that the effect of nanotubes is most pronounced at low frequencies, with the relative effect decreasing with increasing frequencies, the composite materials exhibiting a strong shear thinning effect, while neat polypropylene shows only a small frequency dependence (Seo and Park, 2004; McDaniel *et al.*, 2009).

However, some studies have shown that the addition of low concentrations of nanotubes can lead to a decrease in viscosity. For example, Teng *et al.* (2008) found that the addition of 1 wt% MWNTs to a number of polypropylene matrices resulted in an increase of melt flow index (MFI) and decrease of melt viscosity, however, with increasing MWNT content the melt flow index decreased while the melt viscosity increased (Fig.17.4). Similar decreases in melt viscosity at low nanotube concentrations have been reported by Vega *et al.* (2009) and Zhang *et al.* (2005) in HDPE and UHMWPE, respectively, with both postulating that this was due to the use of either bimodal/broad distributions in the molecular weights of the matrix polymers, with the selective adsorption of the high molar mass fraction onto the nanotubes' surface, leading to the polymer which formed the remaining matrix effectively having a lower average relaxation time and reduced entanglement density.

Many researchers have also reported that CNT–polyolefin nanocomposites display rheological percolation thresholds, with a clear transition to non-Newtonian behaviour when the nanotube loading is increased above a critical concentration.



17.4 Effect of MWNT content on melt flow index of three types of polypropylene (Teng *et al.*, 2008).

This transition is attributed to the high aspect ratio nanotubes forming a network, restraining the mobility of the polymer chains, resulting in a solid-like response at low frequencies (Prashantha *et al.*, 2009). For example, Nobile *et al.* (2007) and Valentino *et al.* (2008) reported a clear change to non-Newtonian behaviour at a concentration of 2.5 wt%, the storage modulus showing a plateau indicating the formation of a CNT–polymer network. Fluid–solid transitions have also been observed in LDPE by Xiao *et al.* (2007), with a continuous MWNT network forming at 4.8 wt%, while Prashantha *et al.* (2009) recorded a fluid to solid transition at 2 wt% in MWNT–polypropylene nanocomposites.

17.6 Electrical properties of CNT–polyolefin blends

The high electrical conductivity and large aspect ratio of carbon nanotubes make them an attractive filler material to enhance the conductivity of polymers for applications where static electrical dissipation or electromagnetic interference (EMI) shielding is required (Han *et al.*, 2009). The large aspect ratio of carbon nanotubes has been shown to result in lower percolation thresholds than using fillers such as carbon fibres or carbon black, with percolation threshold found to decrease with increasing nanotube length (Bai and Allaoui, 2003) (the percolation threshold being the filler loading required to produce an interconnected network through the volume of the sample, thus providing a conductive pathway for charge to flow).

Orders of magnitude increases in electrical conductivity have been reported at very low loadings levels, with the conductivities and percolation thresholds of CNT–polyolefin nanocomposites being highly dependent on method used to make the composites (see Table 17.1). Percolation thresholds as low as 0.035 vol.% have been observed in composites produced using a sintering method (Lisunova *et al.*, 2007). This method, sometimes known as the ‘filler prelocalization method’ or ‘segregated network concept’ has also been successfully used by (Mierczynska *et al.*, 2007) and involves coating polymer particles with carbon nanotubes, followed by hot pressing, resulting in the conductive nanotubes lying on the boundaries between the polymer particles, thereby forming a continuous conductive network at low concentrations.

CNT–polyolefin composites produced by melt blending or solution blending tend to exhibit higher percolation thresholds, generally between 1 and 5 wt% (Table 17.1), the conductivity of these composites being highly dependent on the degree and state of nanotube dispersion. The conductivity of CNT–polymer composites is sometimes used to characterize the state of dispersion, Pujari *et al.* (2009) finding that the conductivity of melt mixed MWNT–PP composites increased linearly as a function of mixing time, indicating a progressive increase in quality of dispersion and network formation. However, Bauhofer and Kovacs (2009) note that a good dispersion implies the formation of a polymer layer around each nanotube, which would likely insulate the nanotubes, suggesting that solvent

processing techniques can improve the electrical performance of composites by preventing polymer sheathing, or at least reducing sheath thickness.

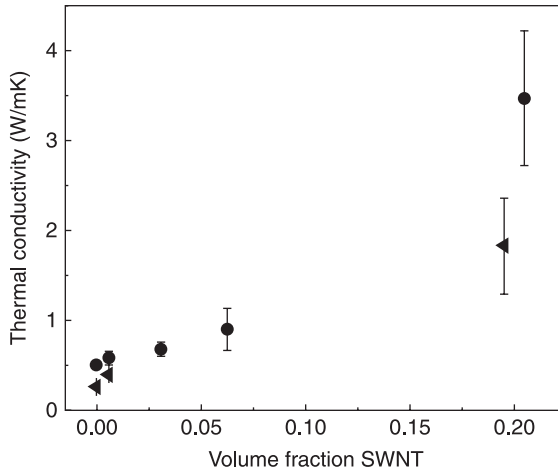
Interestingly, the conductivity of CNT–polyolefin composites has been found to be sensitive to thermal cycling under an applied electric fields, with Ferrara *et al.* (2007) finding that this can cause the conductivity to increase, thought to be due to rearrangement, clustering and/or orientation of CNTs in the polymer melt

17.7 Wear behaviour of polyolefin–CNT composites

Nanotubes have been shown to increase the wear resistance of polyolefins. In an effort to develop a wear-resistant material for artificial joints, MWNTs have been added to HDPE, with Johnson *et al.* (2009) finding that the wear resistance of HDPE increased with increasing MWNT content, 5 wt% MWNTs decreasing the overall wear rate by up to 50% and the friction coefficient by at least 12%, bringing the wear rates of HDPE down to the level seen in UHMWPE. MWNTs have also been found to improve the wear behaviour of HDPE–UHMWPE blends (Jacobs *et al.*, 2008), the wear rate of the blend reducing sharply with the addition of MWNTs, passing through a minimum at 0.5 wt% MWNTs and increasing slightly with further addition of nanotubes, while pretreatment of the CNTs (boiling them in nitric acid) was found not to improve the wear performance of the composites. MWNTs have also been found to increase the wear resistance of neat UHMWPE, with Wei *et al.* (2006) using scratch tests to show that MWNTs increased the wear resistance and decreased the friction coefficient compared to the pure UHMWPE.

17.8 Thermal conductivity of polyolefin–CNT composites

The thermal conductivity of individual MWNTs has been measured to be more than 600 W/mK at room temperature (Berber *et al.*, 2000), with some reported values of up to 3000 W/mK (Kim *et al.*, 2002), while mats/films of MWNTs have been recorded to have thermal conductivities of around 15 W/mK (Da Jiang *et al.*, 2002). Only a few studies have looked at the effect of nanotubes on the thermal conductivities of polyolefins in blends, with those reporting a limited effect at low volume fractions (Kashiwagi *et al.*, 2004; Haggenmueller *et al.*, 2007). Significant increases have been observed at high volume fractions, with Haggenmueller *et al.* (2007) observing an increase from 0.26 W/mK (for neat LDPE) to 1.8 W/mK with the addition of 20 vol.% SWNTs, while observing a larger 700% increase from 0.5 W/mK (neat) to 3.5 W/mK (20 vol.% SWNTs) in HDPE (Fig. 17.5). It was postulated that the larger increases seen in HDPE were due to the PE crystallites (which have higher thermal conductivity than amorphous PE, and which have been found to nucleate on SWNTs) being more likely to span between SWNTs at high nanotube concentrations in the HDPE than the LDPE, these bridging lamellae reducing interfacial thermal resistance.



17.5 Thermal conductivity for isotropic (tilted ▲) SWNT–LDPE and (●) SWNT–HDPE composites at various SWNT loadings, measured perpendicular to pressing direction (Haggenmueller *et al.*, 2007).

(Kashiwagi *et al.*, 2004) measured the thermal conductivity of PP–MWNT blends as a function of temperature, finding that at 40 °C the addition of up to 15 wt% nanotubes provided less than a 0.1 W/mK increase to the thermal conductivity of PP. However, as the temperature increased above 150 °C, while the thermal conductivity of the unfilled PP was found to decrease (due to the melting of the polymer crystals), the presence of nanotubes lessened this effect, the thermal conductivity of composites containing 15 wt% or greater actually increasing monotonically with temperature.

17.9 Thermal degradation and flame-retardant properties

MWNTs have been shown to act as antioxidants in both polyethylene and polypropylene, with thermal gravimetric analysis (TGA) and chemiluminescence showing that they provide significant retardation to polymer oxidation (Watts *et al.*, 2003). While their effectiveness is weak compared to conventional phenolic antioxidants (Zou *et al.*, 2004), at low concentrations, they are more effective than carbon black.

Polypropylene thermally degrades in nitrogen to volatile products in a single step radical chain process with $T_{5\%}$ (the temperature at which 5% degradation has occurred) at 396 °C and T_{\max} (the temperature at which maximum degradation rate is observed) at 448 °C (Tabuani *et al.*, 2008). The addition of nanotubes has been found to increase these temperatures, with Marosfoi *et al.* (2006) finding that 3 wt% MWNTs led to a 32 °C increase in $T_{5\%}$ and 18 °C increase in T_{\max} , while

Tabuani *et al.* (2008) showed a linear relationship between increases in these temperatures and nanotube concentration, with similar increases of 30 °C for $T_{5\%}$ and of 10 °C for T_{\max} at the same 3 wt% loading. At a higher concentration the effect can be more pronounced, with Jin *et al.* (2009) recording a 50 °C increase in the decomposition temperature with the addition of 10 wt% MWNTs. Kashiwagi *et al.* (2004) also showed that the polypropylene behaves quite differently to polypropylene–MWNT nanocomposites when burnt under nitrogen in a gasification test, polypropylene behaving like liquid, the sample surface covered by a fine froth due to the bursting of small bubbles at the sample's surface, while PP–MWNT samples behaved like solids without visible melting and no significant shape/size changes occurring during the test.

More significant protective effects have been observed when CNT–polyolefin composites are heated in the presence of oxygen, with Marosfoi *et al.* (2006) reporting a T_{\max} increase of 101 °C with the addition of 3 wt% pristine MWNTs to polypropylene, the effect being less significant for DWNTs. Watts *et al.* (2003) also showed that the addition of 10 wt% MWNTs can increase the oxidation induction temperature (OIT) of polypropylene from 158 °C to 170 °C while 20 wt% MWNTs can increase it even further up to 175 °C. A study into the flammability of polypropylene by Kashiwagi *et al.* (2004) using a cone calorimeter in air found that the addition of MWNTs to polypropylene also significantly reduced the peak heat release rate, with the greatest reduction at 1 wt% MWNTs. Increased nanotube concentration was shown to lead to a longer ignition delay time and higher peak heat release rates, thought to be due to an increase in the thermal conductivity of the PP–MWNT composites.

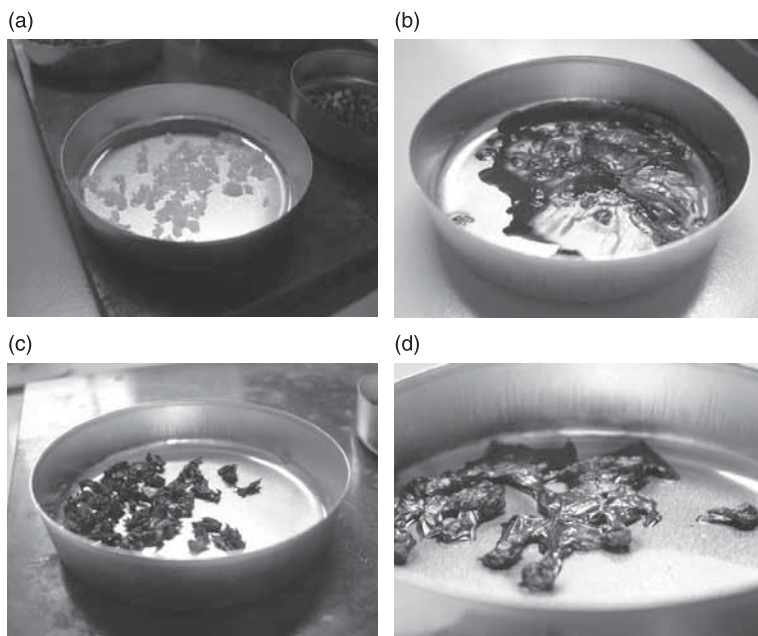
Similar increases to the thermal stability of polyethylene–CNT nanocomposites have also been reported (Chrissafis *et al.*, 2009), with McNally *et al.* (2005) observing that MWNTs led to a 10 °C increase in the onset degradation temperature of polyethylene in nitrogen, while also decreasing the peak heat release rates. Li *et al.* (2009a) reported even larger effects with up to 50 °C increases in onset temperatures for degradation and 18 °C increase in peak mass loss temperature (in a nitrogen atmosphere). In air, Gorrasi *et al.* (2007b) showed that MWNTs significantly delayed the thermal degradation of polyethylene, with Watts *et al.* (2003) reporting a 20 °C increase in the OIT while Beyer (2004) used cone calorimetry to show that MWNTs are more effective in heat reduction of polyethylene than organoclays.

Work by Bocchini *et al.* (2007) found that while MWNT–LLDPE composites show a small stabilization in nitrogen which is independent of nanotube concentration, the effect is much larger in an oxidizing atmosphere. In air, degradation began at 250 °C for both LLDPE and LLDPE–MWNT nanocomposites, however, after an initial weight loss (4–8%), the nanocomposites become stable until decomposing extensively at temperatures above 400 °C. The addition of MWNTs thus increasing the temperature of maximum rate of weight loss by between 85 and 105 °C. Bocchini *et al.* (2007) propose that after the initial weight

loss, the nanotubes prevent further oxidation due to the nanotubes forming a film over the surface of the composite which protects the composite from oxygen, this film being thermally stable to about 400 °C. At a higher temperature, the second degradation step begins as the film starts to degrade. This theory would explain why when Bocchini *et al.* (2007) heated LLDPE in air from 25 °C to 400 °C, there is an approximate 50% weight loss, while MWNT–LLDPE nanocomposites exhibit no decrease in weight, the samples being covered by a black thin film which SEM reveals is a network of entangled MWNTs, forming a mat-like structure (Fig. 17.6).

Other mechanisms of the fire retardance of CNTs have also been proposed, with Gorrasi *et al.* (2007b) suggesting that MWNTs could also increase the oxidative stability of the composites by trapping polymer peroxy radicals, while Kashiwagi *et al.* (2004) postulated that the flame-retardant properties of MWNTs are due to the nanotubes forming a structural, floccular network layer (during burning, the nanotubes stay almost in place in the nanocomposite as the upper layer of polymer recedes), this layer re-emitting much of the incident radiation back into the gas phase, thus protecting the polymer and slowing the rate of pyrolysis.

However, not all nanotubes have the same effect on the thermal degradation of polyolefins. Acid treatment can decrease the protective effect of nanotubes, with



17.6 Oxidative degradation test specimens were heated in an oven under air from 25 °C to 400 °C at the rate of 10 °C min⁻¹. LLDPE before (a) and after (b) the test. 5 wt% MWNT/LLDPE nanocomposite before (c) and after (d) the test (Bocchini *et al.*, 2007).

Bikiaris *et al.* (2008) finding that acid-treated MWNT accelerated the oxidation of polypropylene at low temperatures (up to 230 °C), while at temperatures higher than 300 °C, the trend was reversed. Bikiaris *et al.* (2008) used incubation studies to show that the first stages of oxidation were due to random chain scission of polypropylene and oxygen uptake, the carboxylic groups on the surface of the MWNTs accelerating this process. Alternately, at high temperatures, the MWNTs acted to shield the polypropylene and hinder removal of the gases produced during decomposition. SWNTs have also generally been found to have a limited effect as antioxidants, with Beyer (2004) finding that SWNTs had no effect on the peak heat release rate of polyethylene. Meanwhile, Li *et al.* (2007) found that SWNT-grafted-PE samples provided a 10–15 °C increase in peak mass loss temperature, compared to functionalized SWNTs and *in-situ* polymerized PE–SWNT composites, which only provided 3–5 °C increases.

17.10 Conclusion and future trends

This chapter has reviewed much of the recent work reported with regard to the dispersion of various carbon nanotubes in polyolefin matrices of various types. Despite such nanomaterials involving the combination of a relatively cheap commodity matrix with a high value additive, significant work has been done across a range of areas. Indeed, the nature of the work covers most of the processing techniques found in other nanocomposite systems – melt, solution and *in-situ* processing – perhaps surprising given the greater complexities of polyolefin synthesis and dissolution. Clearly, as well as adding functionality to such materials, particularly improved mechanical properties, fire retardance, electrical and thermal conductivity, the moisture/solvent resistant polyolefin matrix can offer a convenient, readily processable (in particular for melt techniques) method of encapsulating these materials, and it represents a non-polar matrix not unlike the intrinsic low polarity of the nanotubes–graphene additives. The fact that most polyolefins can be so readily spun into fibres is also advantageous, giving the usefulness of objects (i.e. fibres) which can take good advantage of the high nanotube anisotropy. Any such systems make for an interesting study, not least because of the relatively high crystalline nature of most olefins, and their ability to be influenced by small particles both in the nature and rate of crystallization. This range of properties, and the ability of carbon nanotubes to influence other properties such as wear and surface properties, mean that there is likely to be considerable continuing interest in polyolefin–carbon nanotube blends, and this is well borne out by the rate of publications currently appearing in this area.

17.11 References

- Aalaie, J., Rahmatpour, A. & Maghami, S. (2007) Preparation and characterization of linear low density polyethylene/carbon nanotube nanocomposites, *Journal of Macromolecular Science, Part B*, 46, 877–889.

- Andrews, R., Jacques, D., Minot, M. & Rantell, T. (2002a) Fabrication of carbon multiwall nanotube/polymer composites by shear mixing, *Macromolecular Materials and Engineering*, 287, 395–403.
- Andrews, R., Jacques, D., Qian, D. & Rantell, T. (2002b) Multiwall carbon nanotubes: synthesis and application, *Accounts of Chemical Research*, 35, 1008–1017.
- Arostegui, A., Aurrekoetxea, J., Sarrionandia, M. A., Urrutibeascoa, I. & Maspocho, M. L. (2008) Characterization of recycling induced degradation based on fracture mechanics approach, in H. W. Moeller (ed.) *Polymer Degradation and Stability Research*, New York: Nova Science Publishers.
- Assouline, E., Lustiger, A., Barber, A., Cooper, C. A., Klein, E., Wachtel, E. & Wagner, H. D. (2003) Nucleation ability of multiwall carbon nanotubes in polypropylene composites, *Journal of Polymer Science, Part B: Polymer Physics*, 41, 520–527.
- Avila-Orta, C. A., Medellín-Rodríguez, F. J., Dávila-Rodríguez, M. V., Aguirre-Figueroa, Y. A., Yoon, K. & Hsiao, B. S. (2007) Morphological features and melting behavior of nanocomposites based on isotactic polypropylene and multiwalled carbon nanotubes, *Journal of Applied Polymer Science*, 106, 2640–2647.
- Bai, J. B. & Allaoui, A. (2003) Effect of the length and the aggregate size of MWNTs on the improvement efficiency of the mechanical and electrical properties of nanocomposites: experimental investigation, *Composites Part A: Applied Science and Manufacturing*, 34, 689–694.
- Bakshi, S. R., Tercero, J. E. & Agarwal, A. (2007) Synthesis and characterization of multiwalled carbon nanotube reinforced ultra high molecular weight polyethylene composite by electrostatic spraying technique, *Composites Part A: Applied Science and Manufacturing*, 38, 2493–2499.
- Bao, S. P. & Tjong, S. C. (2007) Mechanical behaviors of polypropylene/carbon nanotube nanocomposites: the effects of loading rate and temperature, *Materials Science and Engineering: A*, 485, 508–516.
- Bauhofer, W. & Kovacs, J. Z. (2009) A review and analysis of electrical percolation in carbon nanotube polymer composites, *Composites Science and Technology*, 69, 1486–1498.
- Berber, S., Kwon, Y.-K. & Tománek, D. (2000) Unusually high thermal conductivity of carbon nanotubes, *Physical Review Letters*, 84, 4613–4616.
- Bert, C. W. & Kline, R. A. (1985) Composite-material mechanics: properties of planar-random fiber composites, *Polymer Composites*, 6, 133–141.
- Beyer, G. (2004) Filler blend of carbon nanotubes and organoclays with improved char as a new flame retardant system for polymers and cable applications, *Fire and Materials*, 29, 61–69.
- Bhattacharyya, A. R., Sreekumar, T. V., Liu, T., Kumar, S., Ericson, L. M., Hauge, R. H. & Smalley, R. E. (2003) Crystallization and orientation studies in polypropylene/single wall carbon nanotube composite, *Polymer*, 44, 2373–2377.
- Bikiaris, D., Vassiliou, A., Chrissafis, K., Paraskevopoulos, K. M., Jannakoudakis, A. & Docolis, A. (2008) Effect of acid treated multi-walled carbon nanotubes on the mechanical, permeability, thermal properties and thermo-oxidative stability of isotactic polypropylene, *Polymer Degradation and Stability*, 93, 952–967.
- Bin, Y., Kitanaka, M., Zhu, D. & Matsuo, M. (2003) Development of highly oriented polyethylene filled with aligned carbon nanotubes by gelation/crystallization from solutions, *Macromolecules*, 36, 6213–6219.
- Bocchini, S., Frache, A., Camino, G. & Claes, M. (2007) Polyethylene thermal oxidative stabilisation in carbon nanotubes based nanocomposites, *European Polymer Journal*, 43, 3222–3235.

- Bonduel, D., Mainil, M., Alexandre, M., Monteverde, F. & Dubois, P. (2005) Supported coordination polymerization: a unique way to potent polyolefin carbon nanotube nanocomposite, *Chem. Commun.*, 781–783.
- Brandrup, J., Immergut, E. H. & Grulke, E. A. (1999) Surface and interfacial tensions of polymers, oligomers, plasticizers, and organic pigments, in S. Wu (ed.) *Polymer Handbook*, 4th edn, New York: John Wiley & Sons.
- Callister, W. D. J. (1990) *Materials Science and Engineering: An Introduction*, New York: John Wiley & Sons, Inc.
- Causin, V., Yang, B.-X., Marega, C., Goh, S. H. & Marigo, A. (2009) Nucleation, structure and lamellar morphology of isotactic polypropylene filled with polypropylene-grafted multiwalled carbon nanotubes, *European Polymer Journal*, 45, 2155–2163.
- Chang, T. E., Jensen, L. R., Kisliuk, A., Pipes, R. B., Pyrz, R. & Sokolov, A. P. (2005) Microscopic mechanism of reinforcement in single-wall carbon nanotube/polypropylene nanocomposite, *Polymer*, 46, 439–444.
- Chrissafis, K., Paraskevopoulos, K. M., Tsiaoussis, I. & Bikiaris, D. (2009) Comparative study of the effect of different nanoparticles on the mechanical properties, permeability, and thermal degradation mechanism of HDPE, *Journal of Applied Polymer Science*, 114, 1606–1618.
- Coleman, J. N., Cadek, M., Blake, R., Nicolosi, V., Ryan, K. P., Belton, C., Fonseca, A., Nagy, J. B., Gun'ko, Y. K. & Blau, W. J. (2004) High performance nanotube-reinforced plastics: understanding the mechanism of strength increase, *Advanced Functional Materials*, 14, 791–798.
- Coleman, J. N., Khan, U., Blau, W. J. & Gun'ko, Y. K. (2006) Small but strong: a review of the mechanical properties of carbon nanotube-polymer composites, *Carbon*, 44, 1624–1652.
- Comyn, J. (1997) *Adhesion Science*, London: The Royal Society for Chemistry.
- Da Jiang, Y., Qing, Z., Chen, G., Yoon, S. F., Ahn, J., Wang, S. G., Zhou, Q., Wang, Q. & Li, J. Q. (2002) Thermal conductivity of multiwalled carbon nanotubes, *Physical Review B (Condensed Matter and Materials Physics)*, 66, 165440–165446.
- Dondero, W. E. & Gorga, R. E. (2006) Morphological and mechanical properties of carbon nanotube/polymer composites via melt compounding, *Journal of Polymer Science Part B: Polymer Physics*, 44, 864–878.
- Esawi, A. M. K., Salem, H. G., Hussein, H. M. & Ramadan, A. R. (2009) Effect of processing technique on the dispersion of carbon nanotubes within polypropylene carbon nanotube-composites and its effect on their mechanical properties, *Polymer Composites*, 2009, DOI 10.1002/pc.20859.
- Ferrara, M., Neitzert, H.-C., Sarno, M., Gorrasi, G., Sannino, D., Vittoria, V. & Ciambelli, P. (2007) Influence of the electrical field applied during thermal cycling on the conductivity of LLDPE/CNT composites, *Physica E: Low-Dimensional Systems and Nanostructures*, 37, 66–71.
- Funck, A. & Kaminsky, W. (2007) Polypropylene carbon nanotube composites by in situ polymerization, *Composites Science and Technology*, 67, 906–915.
- Ganß, M., Satapathy, B. K., Thunga, M., Weidisch, R., Pötschke, P. & Jehnichen, D. (2008) Structural interpretations of deformation and fracture behavior of polypropylene/multi-walled carbon nanotube composites, *Acta Materialia*, 56, 2247–2261.
- Gorrasi, G., Romeo, V., Sannino, D., Sarno, M., Ciambelli, P., Vittoria, V., Vivo, B. D. & Tucci, V. (2007a) Carbon nanotube induced structural and physical property transitions of syndiotactic polypropylene, *Nanotechnology*, 18, 275703.

- Gorrasi, G., Sarno, M., Bartolomeo, A. D., Sannino, D., Ciambelli, P. & Vittoria, V. (2007b) Incorporation of carbon nanotubes into polyethylene by high energy ball milling: Morphology and physical properties, *Journal of Polymer Science Part B: Polymer Physics*, 45, 597–606.
- Grady, B., Pompeo, F., Shambaugh, R. & Resasco, D. (2002) Nucleation of polypropylene crystallization by single-walled carbon nanotubes, *Journal of Physical Chemistry B*, 106, 5852–5858.
- Haggenmueller, R., Guthy, C., Lukes, J. R., Fischer, J. E. & Winey, K. I. (2007) Single wall carbon nanotube/polyethylene nanocomposites: thermal and electrical conductivity, *Macromolecules*, 40, 2417–2421.
- Han, M. S., Lee, Y. K., Lee, H. S., Yun, C. H. & Kim, W. N. (2009) Electrical, morphological and rheological properties of carbon nanotube composites with polyethylene and poly(phenylene sulfide) by melt mixing, *Chemical Engineering Science*, 64, 4649–4656.
- He, L., Xu, Q., Song, R. & Hua, C. (2009) Thermal and morphological characterization of composites prepared by solution crystallization method of high-density polyethylene on carbon nanotubes. *Polymer Composites*, 2009, DOI 10.1002/pc.20875.
- Holmström, A. & Sörvik, E. (1974) Thermal degradation of polyethylene in a nitrogen atmosphere of low oxygen content. III: structural changes occurring in low-density polyethylene at oxygen contents below 1.2%, *Journal of Applied Polymer Science*, 18, 3153–3178.
- Jacobs, O., Schädel, B. & Klaus Friedrich & Alois, K. S. (2008) *Wear Behavior of Carbon Nanotube-Reinforced Polyethylene and Epoxy Composites*, Oxford: Elsevier.
- Jeon, K., Lumata, L., Tokumoto, T., Steven, E., Brooks, J. & Alamo, R. G. (2007) Low electrical conductivity threshold and crystalline morphology of single-walled carbon nanotubes: high density polyethylene nanocomposites characterized by SEM, Raman spectroscopy and AFM, *Polymer*, 48, 4751–4764.
- Jin, S. H., Kang, C. H., Yoon, K. H., Bang, D. S. & Park, Y.-B. (2009) Effect of compatibilizer on morphology, thermal, and rheological properties of polypropylene/functionalized multi-walled carbon nanotubes composite, *Journal of Applied Polymer Science*, 111, 1028–1033.
- Johnson, B. B., Santare, M. H., Novotny, J. E. & Advani, S. G. (2009) Wear behavior of carbon nanotube/high density polyethylene composites, *Mechanics of Materials*, 41, 1108–1115.
- Jose, M. V., Dean, D., Tyner, J., Price, G. & Nyairo, E. (2007) Polypropylene/carbon nanotube nanocomposite fibers: process-morphology-property relationships, *Journal of Applied Polymer Science*, 103, 3844–3850.
- Kaminsky, W. & Funck, A. (2007) In situ polymerization of olefins with nanoparticles by metallocene-catalysis, *Macromolecular Symposia*, 260, 1–8.
- Kanagaraj, S., Varanda, F. R., Zhil'tsova, T. V., Oliveira, M. S. A. & Simoes, J. A. O. (2007) Mechanical properties of high density polyethylene/carbon nanotube composites, *Composites Science and Technology*, 67, 3071–3077.
- Kashiwagi, T., Grulke, E., Hilding, J., Groth, K., Harris, R., Butler, K., Shields, J., Kharchenko, S. & Douglas, J. (2004) Thermal and flammability properties of polypropylene/carbon nanotube nanocomposites, *Polymer*, 45, 4227–4239.
- Kearns, J. C. & Shambaugh, R. L. (2002) Polypropylene fibers reinforced with carbon nanotubes, *Journal of Applied Polymer Science*, 86, 2079–2084.
- Kim, P., Shi, L., Majumdar, A. & McEuen, P. L. (2002) Mesoscopic thermal transport and energy dissipation in carbon nanotubes, *Physica B: Condensed Matter*, 323, 67–70.

- Kodjie, S. L., Li, L., Li, B., Cai, W., Li, C. Y. & Keating, M. (2006) Morphology and crystallization behaviour of HDPE/CNT nanocomposite, *Journal of Macromolecular Science, Part B: Physics*, 45, 231–245.
- Lee, G.-W., Jagannathan, S., Chae, H. G., Minus, M. L. & Kumar, S. (2008) Carbon nanotube dispersion and exfoliation in polypropylene and structure and properties of the resulting composites, *Polymer*, 49, 1831–1840.
- Lee, S. H., Cho, E., Jeon, S. H. & Youn, J. R. (2007) Rheological and electrical properties of polypropylene composites containing functionalized multi-walled carbon nanotubes and compatibilizers, *Carbon*, 45, 2810–2822.
- Leelapornpisit, W., Ton-That, M.-T., Perrin-Sarazin, F., Cole, K. C., Denault, J. & Simard, B. (2005) Effect of carbon nanotubes on the crystallization and properties of polypropylene, *Journal of Polymer Science Part B: Polymer Physics*, 43, 2445–2453.
- Li, S., Chen, H., Bi, W., Zhou, J., Wang, Y., Li, J., Cheng, W., Li, M., Li, L. & Tang, T. (2007) Synthesis and characterization of polyethylene chains grafted onto the sidewalls of single-walled carbon nanotubes via copolymerization, *Journal of Polymer Science Part A: Polymer Chemistry*, 45, 5459–5469.
- Li, S., Chen, H., Cui, D., Li, J., Zhang, Z., Wang, Y. & Tang, T. (2009a) Structure and properties of multi-walled carbon nanotubes/polyethylene nanocomposites synthesized by in situ polymerization with supported catalyst, *Polymer Composites*, 31, 507–515.
- Li, W.-H., Chen, X.-H., Yang, Z. & Xu, L.-S. (2009b) Structure and properties of polypropylene-wrapped carbon nanotubes composite, *Journal of Applied Polymer Science*, 113, 3809–3814.
- Lisunova, M. O., Mamunya, Y. P., Lebovka, N. I. & Melezhyk, A. V. (2007) Percolation behaviour of ultrahigh molecular weight polyethylene/multi-walled carbon nanotubes composites, *European Polymer Journal*, 43, 949–958.
- Lordi, V. & Nan, Y. (2000) Molecular mechanics of binding in carbon-nanotube-polymer composites, *Journal of Materials Research*, 15, 2770–2779.
- Lu, K. L., Lago, R. M., Chen, Y. K., Green, M. L. H., Harris, P. J. F. & Tsang, S. C. (1996) Mechanical damage of carbon nanotubes by ultrasound, *Carbon*, 34, 814–816.
- Manchado, M. A. L., Valentini, L., Biagiotti, J. & Kenny, J. M. (2005) Thermal and mechanical properties of single-walled carbon nanotubes-polypropylene composites prepared by melt processing, *Carbon*, 43, 1499–1505.
- Marosfoi, B., Szabó, A., Marosi, G., Tabuani, D., Camino, G. & Pagliari, S. (2006) Thermal and spectroscopic characterization of polypropylene-carbon nanotube composites, *Journal of Thermal Analysis and Calorimetry*, 86, 669–673.
- Maser, W., Benito, A. M., Callejas, M., Seeger, T., Martinez, M., Schreiber, J., Muszynski, J., Chauvet, O., Osvath, Z., Koos, A. & Biro, L. (2003) Synthesis and characterization of new polyaniline/nanotube composites, *Materials Science and Engineering, C: Biomimetic and Supramolecular Systems*, 23, 87–91.
- Mcdaniel, N. D., Mcdaniel, M. P., Balzano, L. & Resasco, D. E. (2009) Silica supported single-walled carbon nanotubes as a modifier in polyethylene composites, *Journal of Applied Polymer Science*, 111, 589–601.
- McNally, T., Potschke, P., Halley, P., Murphy, M., Martin, D., Bell, S. E. J., Brennan, G. P., Bein, D., Lemoine, P. & Quinn, J. P. (2005) Polyethylene multiwalled carbon nanotube composites, *Polymer*, 46, 8222–8232.
- Mierczynska, A., Mayne-L'hermite, M., Boiteux, G. & Jeszka, J. K. (2007) Electrical and mechanical properties of carbon nanotube/ultrahigh-molecular-weight polyethylene

- composites prepared by a filler prelocalization method, *Journal of Applied Polymer Science*, 105, 158–168.
- Moore, E. M., Ortiz, D. L., Marla, V. T., Shambaugh, R. L. & Grady, B. P. (2004) Enhancing the strength of polypropylene fibers with carbon nanotubes, *Journal of Applied Polymer Science*, 93, 2926–2933.
- Morcom, M. (2008) Carbon nanotube polymer composites, PhD, Monash University, Australia.
- Nobile, M. R., Simon, G. P., Valentino, O. & Morcom, M. (2007) Rheological and structure investigation of melt mixed multi-walled carbon nanotube/PE composites, *Macromolecular Symposia*, 247, 78–87.
- Prashantha, K., Soulestin, J., Lacrampe, M. F., Krawczak, P., Dupin, G. & Claes, M. (2009) Masterbatch-based multi-walled carbon nanotube filled polypropylene nanocomposites: assessment of rheological and mechanical properties, *Composites Science and Technology*, 69, 1756–1763.
- Pujari, S., Ramanathan, T., Kasimatis, K., Masuda, J. I., Andrews, R., Torkelson, J. M., Brinson, L. C. & Burghardt, W. R. (2009) Preparation and characterization of multiwalled carbon nanotube dispersions in polypropylene: melt mixing versus solid-state shear pulverization., *Journal of Polymer Science Part B: Polymer Physics*, 47, 1426–1436.
- Razavi-Nouri, M., Ghorbanzadeh-Ahangari, M., Fereidoon, A. & Jahanshahi, M. (2009) Effect of carbon nanotubes content on crystallization kinetics and morphology of polypropylene, *Polymer Testing*, 28, 46–52.
- Ruan, S. L., Gao, P., Yang, X. G. & Yu, T. X. (2003) Toughening high performance ultrahigh molecular weight polyethylene using multiwalled carbon nanotubes, *Polymer*, 44, 5643–5654.
- Seo, M.-K., Lee, J.-R. & Park, S.-J. (2005) Crystallization kinetics and interfacial behaviors of polypropylene composites reinforced with multi-walled carbon nanotubes, *Materials Science and Engineering: A*, 404, 79–84.
- Seo, M.-K. & Park, S.-J. (2004) Electrical resistivity and rheological behaviors of carbon nanotubes-filled polypropylene composites, *Chemical Physics Letters*, 395, 44–48.
- Shieh, Y. T., Liu, G. L., Wu, H. H. & Lee, C. C. (2007) Effects of polarity and pH on the solubility of acid-treated carbon nanotubes in different media, *Carbon*, 45, 1880–1890.
- Tabuani, D., Gianelli, W., Camino, G. & Claes, M. (2008) Polypropylene based carbon nanotubes composites: structure and properties, *E-Polymers*, 103, 12 pp.
- Teng, C.-C., Ma, C.-C. M., Huang, Y.-W., Yuen, S.-M., Weng, C.-C., Chen, C.-H. & Su, S.-F. (2008) Effect of MWCNT content on rheological and dynamic mechanical properties of multiwalled carbon nanotube/polypropylene composites, *Composites Part A: Applied Science and Manufacturing*, 39, 1869–1875.
- Tong, X., Liu, C., Cheng, H.-M., Zhao, H., Yang, F. & Zhang, X. (2004) Surface modification of single-walled carbon nanotubes with polyethylene via in situ Ziegler-Natta polymerization, *Journal of Applied Polymer Science*, 92, 3697–3700.
- Trujillo, M., Arnal, M. L., Muller, A. J., Bredeau, S., Bonduel, D., Dubois, P., Hamley, I. W. & Castelletto, V. (2008) Thermal fractionation and isothermal crystallization of polyethylene nanocomposites prepared by in situ polymerization, *Macromolecules*, 41, 2087–2095.
- Valentini, L., Biagiotti, J., Kenny, J. M. & Santucci, S. (2003) Morphological characterization of single-walled carbon nanotubes-PP composites, *Composites Science and Technology*, 63, 1149–1153.

- Valentini, L., Biagiotti, J., López-Manchado, M. A. & Kenny, S. S. J. M. (2004) Effects of carbon nanotubes on the crystallization behavior of polypropylene, *Polymer Engineering and Science*, 44, 303–311.
- Valentino, O., Sarno, M., Rainone, N. G., Nobile, M. R., Ciambelli, P., Neitzert, H. C. & Simon, G. P. (2008) Influence of the polymer structure and nanotube concentration on the conductivity and rheological properties of polyethylene/CNT composites, *Physica E: Low-dimensional Systems and Nanostructures*, 40, 2440–2445.
- Vega, J. F., Martiñ Nez-Salazar, J., Trujillo, M., Arnal, M. L., Muller, A. J., Bredeau, S. & Dubois, P. (2009) Rheology, processing, tensile properties, and crystallization of polyethylene/carbon nanotube nanocomposites, *Macromolecules*, 42, 4719–4727.
- Watts, P. C. P. P., Fearon, K., Hsu, W. K., Billingham, N. C., Kroto, H. W. & Walton, D. R. M. (2003) Carbon nanotubes as polymer antioxidants, *J. Mater. Chem.*, 13, 491–495.
- Wei, Z., Ya-Pu, Z., Ruan, S. L., Gao, P. & Yu, T. X. (2006) A study of the tribological behavior of carbon-nanotube-reinforced ultrahigh molecular weight polyethylene composites, *Surface and Interface Analysis*, 38, 883–886.
- Wu, D., Sun, Y. & Zhang, M. (2009) Kinetics study on melt compounding of carbon nanotube/polypropylene nanocomposites, *Journal of Polymer Science Part B: Polymer Physics*, 47, 608–618.
- Xi, Y., Yamanaka, A., Bin, Y. & Matsuo, M. (2007) Electrical properties of segregated ultrahigh molecular weight polyethylene/multiwalled carbon nanotube composites, *Journal of Applied Polymer Science*, 105, 2868–2876.
- Xiao, K. Q., Zhang, L. C. & Zarudi, I. (2007) Mechanical and rheological properties of carbon nanotube-reinforced polyethylene composites, *Composites Science and Technology*, 67, 177–182.
- Xie, X., Aloys, K., Zhou, X. & Zeng, F. (2003) Ultrahigh molecular mass polyethylene/carbon nanotube composites: crystallization and melting properties, *Journal of Thermal Analysis and Calorimetry*, 74, 317–323.
- Xu, D. & Wang, Z. (2008) Role of multi-wall carbon nanotube network in composites to crystallization of isotactic polypropylene matrix, *Polymer*, 49, 330–338.
- Yang, B.-X., Shi, J.-H., Li, X., Pramoda, K. P. & Goh, S. H. (2009) Mechanical reinforcement of poly(1-butene) using polypropylene-grafted multiwalled carbon nanotubes, *Journal of Applied Polymer Science*, 113, 1165–1172.
- Yang, B.-X., Shi, J.-H., Pramoda, K. P. & Goh, S. H. (2008) Enhancement of the mechanical properties of polypropylene using polypropylene-grafted multiwalled carbon nanotubes, *Composites Science and Technology*, 68, 2490–2497.
- Yang, B. X., Pramoda, K. P., Xu, G. Q. & Goh, S. H. (2007) Mechanical reinforcement of polyethylene using polyethylene-grafted multiwalled carbon nanotubes, *Advanced Functional Materials*, 17, 2062–2069.
- Yeh, J.-T., Lin, S.-C., Chen, K.-N. & Huang, K.-S. (2008) Investigation of the ultradrawing properties of gel spun fibers of ultra-high molecular weight polyethylene/carbon nanotube blends, *Journal of Applied Polymer Science*, 110, 2538–2548.
- Zhang, Q., Lippits, D. R. & Rastogi, S. (2005) Dispersion and rheological aspects of SWNTs in ultrahigh molecular weight polyethylene, *Macromolecules*, 39, 658–666.
- Zhang, S., Minus, M. L., Zhu, L., Wong, C.-P. & Kumar, S. (2008) Polymer transcrystallinity induced by carbon nanotubes, *Polymer*, 49, 1356–1364.
- Zhao, D., Lei, Q., Qin, C. & Bai, X. (2006) Melt process and performance of multi-walled carbon nanotubes reinforced LDPE composites, *Pigment & Resin Technology*, 35, 341–345.

- Zhou, Z., Wang, S., Lu, L., Zhang, Y. & Zhang, Y. (2008) Functionalization of multi-wall carbon nanotubes with silane and its reinforcement on polypropylene composites, *Composites Science and Technology*, 68, 1727–1733.
- Zou, Y., Feng, Y., Wang, L. & Liu, X. (2004) Processing and properties of MWNT/HDPE composites, *Carbon*, 42, 271–277.

Composites of poly(ethylene terephthalate) and multi-walled carbon nanotubes

K. McCROSSAN, C. McCLORY, B. MAYORAL,
D. THOMPSON, D. McCONNELL and T. McNALLY, Queen's
University Belfast, UK and M. MURPHY, T. NICHOLSON,
D. MARTIN and P. HALLEY, The University of Queensland, Australia

Abstract: The unique and extraordinary mechanical, electrical and thermal conductivity properties of multi-walled carbon nanotubes (MWCNTs) make them ideal candidates as functional fillers for polymeric materials. Poly(ethylene terephthalate) (PET) is an important engineering plastic finding widespread application in automotive, electronic and packaging technologies. The key challenge to achieving enhanced polymer properties is efficient dispersion and distribution of MWCNTs in the polymer matrix. In this chapter, we describe the preparation of composites of a PET with MWCNTs via melt mixing and, employing many of the characterisation techniques described elsewhere in this book, we investigate the extent of MWCNT dispersion by correlating microscopic observations with electrical and rheological percolation measurements. We also report the effect of MWCNT addition on PET thermal stability using thermal gravimetry analysis, and on PET crystallisation behaviour using a combination of Fourier transform infrared and Raman spectroscopy, differential scanning calorimetry and wide angle X-ray diffraction.

Key words: multi-walled carbon nanotubes, nanocomposites, poly(ethylene terephthalate).

18.1 Introduction

Iijima reported the synthesis of MWCNTs in 1991 with the preparation of coaxial tubes of graphitic sheets (Iijima, 1991), and clearly identified the concentric arrangement of multi-walled carbon nanotubes using high resolution transmission electron microscopy. However, it is generally accepted that such structures had existed prior to this, but had not been characterised fully (see McClory *et al.*, 2009 and references therein). Subsequently, the unique and extraordinary mechanical properties of carbon nanotubes (CNTs) were first demonstrated by Ajayan *et al.* during the cutting of thin slices of an epoxy–CNT composite (Ajayan *et al.*, 1994). The CNTs retained structural integrity and were aligned normal to the cutting surface, and thus established the prospective use of CNTs as a mechanism of mechanical reinforcement for polymeric materials. Since this account by Ajayan *et al.* in 1994, there has been an exponential growth in research into polymer–CNT composites for a multitude of applications, including, but not

limited to, aerospace, automotive, electronic, biomedical and technical textiles. The high aspect ratio and exceptional mechanical (tensile strength 63 GPa (Yu *et al.*, 2000)), Young's modulus 1TPa (Treacy *et al.*, 1996), electrical (current density $>10^7$ A/cm² (Frank *et al.*, 1998)) and thermal (thermal conductivity >2000 W/mK Φ 9.8 nm (Fujii *et al.*, 2005)) properties of MWCNTs have fuelled the desire to design and characterise a new class of advanced polymeric materials with tailored physical properties. A homogeneous composite nano- and/or microstructure achievable through excellent CNT dispersion and distribution, coupled with the efficient transfer of applied load across this large interfacial region are critical factors for the successful translation of CNT mechanical and other properties to a polymer matrix. Interfacial shear strength (ISS), a measure of polymer–CNT interactions, is dependent on the topography of the nanotube surface and chemical (e.g. hydrogen bonding) or van der Waals interactions between CNTs and polymer matrix (Schadler *et al.*, 1998). Many indirect experimental measurements of polymer–CNT interfacial adhesion have been attempted but have employed other mechanical test methods incorporating mathematical models (Wagner *et al.*, 1998) or computer simulations (Liao and Li, 2001) to generate relevant results. The first direct measurement of the ISS between a MWCNT and a polymer (polyethylene-butene) was performed using atomic force microscopy (AFM) (Barber *et al.*, 2003). An individual MWCNT attached to an AFM tip was pulled out of the polymer and using the measured pull-out force, an average ISS was determined. This study determined an average ISS of 47 MPa, associated with covalent bonding existing between defect sites on the MWCNT and the polyethylene–butene matrix. Ideally, the addition of small quantities of CNTs will provide the plastics industries with solutions for material enhancement by utilising existing conventional polymer processing technologies, at a relatively low cost.

This chapter provides a comprehensive account of the preparation and characterisation of composites of an important engineering plastic, poly(ethylene terephthalate) (PET) with pristine MWCNTs, using many of the characterisation techniques described elsewhere in this book. The structure of the composites is examined using a combination of microscopic methods: polarised optical microscopy (POM), field emission scanning electron microscopy (FESEM) and high resolution transmission electron microscopy (HRTEM) across the length scales. The extent of CNT dispersion and distribution throughout the PET matrix is correlated with composite properties. In particular, the effect of MWCNT addition on PET crystallisation behaviour and kinetics is studied using a range of techniques, including Fourier transform infrared spectroscopy (FTIR), Raman spectroscopy and differential scanning calorimetry (DSC). The thermal stability of PET after MWCNT addition is assessed using thermo-gravimetric analysis. In the final section, the formation of both electrical and rheological percolated networks of CNTs in the PET matrix is investigated using volume resistivity and oscillatory rheology measurements, respectively.

18.2 Poly(ethylene terephthalate)–MWCNT composites: a literature survey

Poly(ethylene terephthalate) (PET) is a thermoplastic polyester resin which can be synthesised by the condensation reaction between terephthalic acid (TPA) and ethylene glycol or ethanediol. It is an important industrial engineering polymer as a result of its relatively low cost/high performance comparison. Due to the polarity of the ester groups located in the polymer main chain, PET is a semi-crystalline polymer which exists as an imperfect two-phase system of interconnected crystalline and amorphous domains (Vaia, 2000). It is an important engineering plastic used widely in the automotive, electronic, packaging and textile fibre industries due to its high strength, high chemical and dimensional stability and dielectric properties. Closely monitoring processing parameters, such as temperature, screw speed, residence time, and in particular cooling profiles can effectively control PET morphology, chain orientation and subsequently the physical properties of PET. Despite significant research effort, the successful incorporation of CNTs into polymer matrices for property enhancement and reinforcement has been limited predominantly by inadequate CNT dispersion and distribution and poor polymer–CNT interfacial adhesion. The problems arise from the tendency of neighbouring CNTs to agglomerate due to the π – π stacking effect of the hexagonal carbon arrangement of the tube structure. PET–MWCNT composite production methodologies have been studied extensively to overcome these problems using various approaches involving solution mixing (Chen *et al.*, 2009), *in-situ* polymerisation (Lee *et al.*, 2005), and melt-mixing techniques (Kim *et al.*, 2007). Numerous CNT pre-treatments are currently under investigation with the goal of achieving enhanced CNT dispersion and increased interfacial interaction.

18.2.1 CNT pre-treatment, solution mixing and *in-situ* polymerisation methods

Modification or treatment of the CNT surface prior to PET–CNT composite preparation has included nanotube purification by acid (Jin *et al.*, 2008), inert argon plasma treatments (Ahn *et al.*, 2003), chemical functionalisation by acid (Tzavalas *et al.*, 2006), organic molecules (Yoo *et al.*, 2008), and fluorine and hydrogen plasma treatments (Yu *et al.*, 2003; Luo *et al.*, 2009). A coagulation method described by Hu *et al.* involved the initial purification of MWCNTs by oxidation in air, followed by acid treatment in HCL, prior to ultrasonication in ODCB–phenol, followed by PET addition (Hu *et al.*, 2006). The dispersion of MWCNTs in ODCB–phenol remained stable for up to several weeks. Pre-treatment of the tubes did not affect their mean length (5–15 μm) although opening of tube end-caps was observed (from TEM images) and the addition of carboxyl groups ($-\text{COOH}$) was confirmed by FTIR analysis. The low electrical and

rheological percolation thresholds, 0.9 wt% and 0.6 wt% respectively, were attributed to the homogeneous dispersion of high aspect ratio COOH–MWCNTs and augmentation of tube–matrix interactions achieved by the design of the solution process and nanotube pre-treatment. In particular, the formation of a uniformly dispersed and distributed network of COOH–MWCNTs in PET in this study was due to the already stable dispersion of CNTs in ODCB–phenol. The CNTs resisted re-agglomerating on addition of PET during solution mixing, due to the enhanced interaction between PET and COOH–MWCNTs by the π – π conjugation of common aromatic groups and esterification of hydroxyl (PET) and carboxyl (MWCNT) groups. Evidence supporting improved interfacial interaction between PET and pre-treated MWCNTs was provided by Jin *et al.*, by the preparation of acid and diamine functionalised MWCNTs prior to *in-situ* polymerisation (Jin *et al.*, 2007). The improved dispersion of carboxyl and diamine functionalised CNTs in PET compared with PET–pristine MWCNTs could be explained both by the presence of functional groups and the ease of processing of shorter tubes, the latter present due to tube scission during acid pre-treatment. The promotion of interfacial interactions between PET and carboxyl and diamine groups on the MWCNT surface was evident from the absence of nanotube pull-out and increased tube surface wetting with PET. Raman spectroscopy, an effective tool for interfacial analysis of polymer–CNT composites, recorded an up-shift of the G-band position of diamine functionalised MWCNTs to a higher frequency ($+10\text{ cm}^{-1}$) which was interpreted as the insertion of PET polymer chains between tubes, separated and dispersed to a greater extent than the pristine or acid-functionalised tubes. The diamine-functionalised MWCNTs yielded the largest improvement in mechanical properties ($+350\%$, $+290\%$), in strength (for a 0.5 wt% CNT loading) and modulus (for a 2 wt% CNT loading), respectively. In contrast, the mechanical properties of the untreated CNTs dropped drastically, mainly due to large CNT agglomerates acting as stress concentration points within the bulk material. In a similar study by the same authors, MWCNTs first treated with nitric acid, then acetic anhydride, before the same *in-situ* polymerisation process achieved mechanical reinforcement similar to that obtained for diamine-functionalised tubes despite the reduction in CNT aspect ratio and associated tube damage due to the functionalisation process (Jin *et al.*, 2008). Extensive damage to the structure of MWCNTs after treatment with concentrated nitric and sulphuric acid was evident from SEM imaging, although addition of 0.05 wt% COOH–MWCNTs to PET resulted in a 23% increase in storage modulus and accelerated the rate of crystallisation by acting as an efficient nucleating agent at very low loadings (Wang *et al.*, 2007). During *in-situ* polymerisation of PET–MWCNT composites, ethylene-glycol (EG) is usually ultrasonicated with either pristine or pre-treated tubes before polymerisation. In order to produce homogeneous dispersions of functionalised CNTs in EG, it is important to select and attach structurally similar chemical moieties to the surface of CNTs that will form stable dispersions in EG prior to polymerisation. Wang

et al. showed digital photographs of treated and pristine MWCNTs ultrasonicated in a range of solvents for 10 mins and allowed to stand for 15 days. Pristine and nitric acid pre-treated MWCNTs had completely or partially formed a precipitate after the 15 days had passed. Only COOH–MWCNTs added to H₂O and EG formed stable dispersions and remained in solution, due to hydrogen bonding (Wang *et al.*, 2007). These stable dispersions promoted the formation of nanotube networks and interfacial interactions of CNTs in PET matrices after esterification and polycondensation following TPA addition. Similarly, Lee *et al.* formed stable dispersions of EG and modified MWCNTs by grafting 4-methoxybenzoic acid and 4-ethoxybenzoic acid to pristine MWCNTs via a Friedel-Crafts acylation reaction in polyphosphoric acid, yielding MWCNTs with methoxybenzoyl (–MeO) and ethoxybenzoyl (–EtO) functional groups attached (Lee *et al.*, 2005). Dispersions of EtO–MWCNTs in EG were significantly more homogeneous than pristine MWCNTs or MeO–MWCNTs in EG due to the chemical similarity of ethoxy groups on EtO–MWCNTs and EG molecules (OCH₂CH₂O) (Lee *et al.*, 2005). SEM images indicated the alkoxybenzoyl functional groups uniformly coated the MWCNT surface, the tube diameter increased from 18 nm to 40 nm and 45 nm after the grafting of MeO and EtO groups, respectively. After nanocomposite formation, the fractured surface of the PET–EtO–MWCNT nanocomposite revealed a highly adhered layer of polymer to the surface of the EtO–MWCNTs, to the extent that the boundary between the matrix and CNT was indiscernible. Compared with pristine and MeO-functionalised MWCNTs, the compatibility of EtO–MWCNTs in EG prior to polymerisation is the governing factor in the production of homogeneously dispersed MWCNT in PET by *in-situ* polymerisation. However, from an industrial scale perspective, both solution and *in-situ* polymerisation processes are limited due to environmental issues regarding the extensive use of harmful organic solvents and also the high cost and low yield of materials. In contrast, melt-mixing of polymer–CNT composites is favoured by industry due to the convenient adaptation of conventional polymer processing technologies to the nanocomposite production process. Ideally, the addition of small quantities of CNTs could provide the plastics industry with advanced materials by utilising already existing manufacturing equipment and technologies at a relatively low cost.

18.2.2 Melt processing of PET–MWCNT composites

Previous studies on PET–MWCNT composites prepared by melt mixing have focussed mainly on the effect of the extrusion process and CNT addition on PET chain conformations, crystallinity and crystallisation behaviour of PET (Tzavalas *et al.*, 2006; Kim *et al.*, 2007; Tzavalas *et al.*, 2008). It is generally accepted there are three known PET chain conformations: a crystalline phase involving only *trans* crystalline segments (TC); an intermediate phase involving *trans* noncrystalline segments, i.e. not belonging to the crystalline phase (TX);

and finally a phase lacking in general order consisting of *gauche* conformations (G) (Tzavalas and Gregoriou, 2008). Tzavalas *et al.* studied the *trans* and *gauche* conformations of PET chains in the presence of COOH–MWCNTs produced using a batch melt-mixing process, and reported the change in the relative distribution of these units throughout the PET matrix, thus altering its final crystalline content (Tzavalas *et al.*, 2006). DSC analysis indicated the crystallisation temperature (T_c) increased and the full width at half maximum (FWHM) decreased, demonstrating the addition of CNTs' increased PET crystallinity by acting as a nucleating agent and promoting the growth of more perfect crystallites. This effect was observed up to 2 wt% CNT loading, however, higher CNT loadings were difficult to disperse and resulted in reduced PET crystalline content. The addition of modified MWCNTs up to 2 wt% increased the proportion of *trans* conformers in the crystalline region which would originally have resided in non-crystalline regions. The newly promoted crystals formed were of a higher order and hence more perfect with a narrower size distribution (Tzavalas *et al.*, 2006). FT-IR, Raman spectroscopy and DSC can readily monitor crystal transformations due to thermal treatment and changes in crystallinity due to the presence of CNTs. In other studies, Tzavalas *et al.* uniaxially stretched PET and PET–MWCNT composites to investigate the effect of MWCNTs on the chain conformation of PET using FTIR spectroscopy (Tzavalas and Gregoriou, 2008). After uniaxial stretching, low (1.5 wt%) CNT content had a minor effect on the crystallisation of PET as a small transition of *gauche* to *trans* crystalline conformations occurred. At higher CNT concentrations, increased PET crystal conformation transitions from G to TX and TX to TC occurred with a sharp increase at 3 wt% MWCNT loading. This behaviour was not observed in unstretched PET–MWCNT composites in a similar study by the same authors (Tzavalas *et al.*, 2008). In contrast, a sharp decrease in crystalline content was observed for a 1 wt% CNT loading, before crystallinity increased again with increased CNT concentration. CNT reagglomeration and poor dispersion, observed by TEM imaging, at 1 wt% CNT are thought to account for the drop in crystallinity.

Chain orientation and crystallisation effects as a consequence of melt processing PET are of extreme importance, and of particular interest due to the dependence of material properties on these factors. The majority of studies on melt-processed PET–MWCNT composites to date have focussed on PET crystallinity and crystal structure (Tzavalas *et al.*, 2008; Tzavalas and Gregoriou, 2008), chain conformations (Chen *et al.*, 2009), effect of CNT addition and nucleation effects (Tzavalas *et al.*, 2006), matrix–CNT interfacial interactions (Gao *et al.*, 2008), and mechanical properties (Kobayashi *et al.*, 2007). A small number of studies on melt mixed PET–CNT composites have focused on bulk material properties such as electrical conductivity, viscoelastic properties, thermal and dynamic mechanical properties. These properties are altered as a result of the melt processing regime employed and the extent of formation of continuous CNT networks throughout

the PET matrix (Anand *et al.*, 2007; Kim *et al.*, 2007). Anand *et al.* melt processed PET and pristine SWCNTs in a lab-scale Haake Kneader at 270 °C. Improvements in modulus (50%) and strength (25%) were achieved on addition of 1 wt% SWCNTs, although the composites were embrittled due to the lack of interfacial interactions, evident from a 30% reduction in strain at break. The electrical conductivity of PET increased from 10^{17} S/cm to 10^7 S/cm and an electrical percolation threshold of just above 2 wt% SWCNTs was recorded. In a further study by Kim *et al.*, PET–pristine-MWCNT composites were melt mixed using a Haake rheometer equipped with a twin-screw. Improvements in modulus (9%) and tensile strength (10%) were recorded on addition of 1 wt% MWCNTs. At higher CNT loadings, the formation of interconnected or network-like structures of MWCNT in the PET–MWCNT composites was detected, from rheological measurements (Kim *et al.*, 2007).

Research into the melt-processing of PET–pristine-MWCNT composites by twin screw extrusion has not been widely explored. This chapter gives a comprehensive account of the characterisation of PET–pristine-MWCNT composites, focusing on composite morphology, CNT dispersion and orientation, crystal structure, crystallinity, non-isothermal crystallisation kinetics, viscoelastic and electrical properties and thermal degradation.

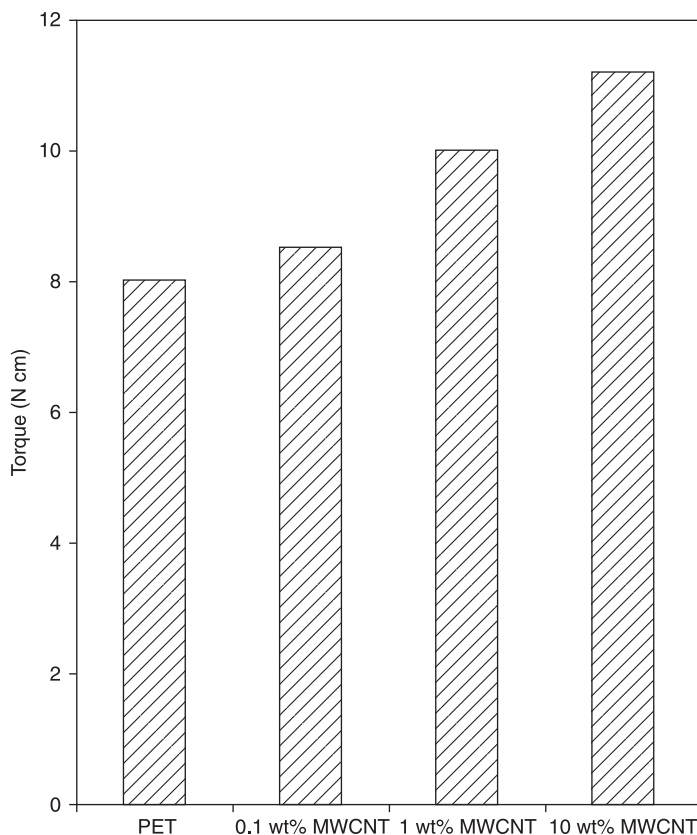
18.3 Poly(ethylene terephthalate)–MWCNT melt processing and bulk material properties

The PET used in this study was TS5 Laser+ Melinar, IV = 0.82–0.84 dl/g, melt viscosity of 655 Pa.s at 295 °C, $T_m = 250$ °C, supplied by DuPont Ltd. The MWCNTs used in this study were produced using chemical vapour deposition (>90% purity) and supplied by Sun Nanotech Co Ltd, from People's Republic of China. These tubes had diameters between 10 nm and 30 nm and varied in length from 1 µm to 10 µm, giving an average aspect ratio of approximately 500.

18.3.1 Composite preparation by melt mixing

All materials were dried for 12 hours at 80 °C prior to processing. The PET–MWCNT composites (4.5 g) were melt mixed using a Haake twin screw microcompounder for MWCNT loadings of 0, 0.1, 0.5, 1.0, 3.0, 7.0 and 10% by weight. The extruder barrel temperature was set at 255 °C and a constant screw speed of 25 rev/min and recycle time of 2 minutes was employed. Under constant screw speed, the torque measured at the motor increased from 8 N/cm for neat PET to 11.2 N/cm on addition of 10 wt% MWCNTs, see Fig. 18.1.

The viscosity of the composites increased with increasing MWCNT concentration due to the high aspect ratio of the CNTs. A similar increase in melt viscosity has also been reported by Pötschke *et al.* on addition of 15 wt% CNTs to polycarbonate (Pötschke *et al.*, 2002).

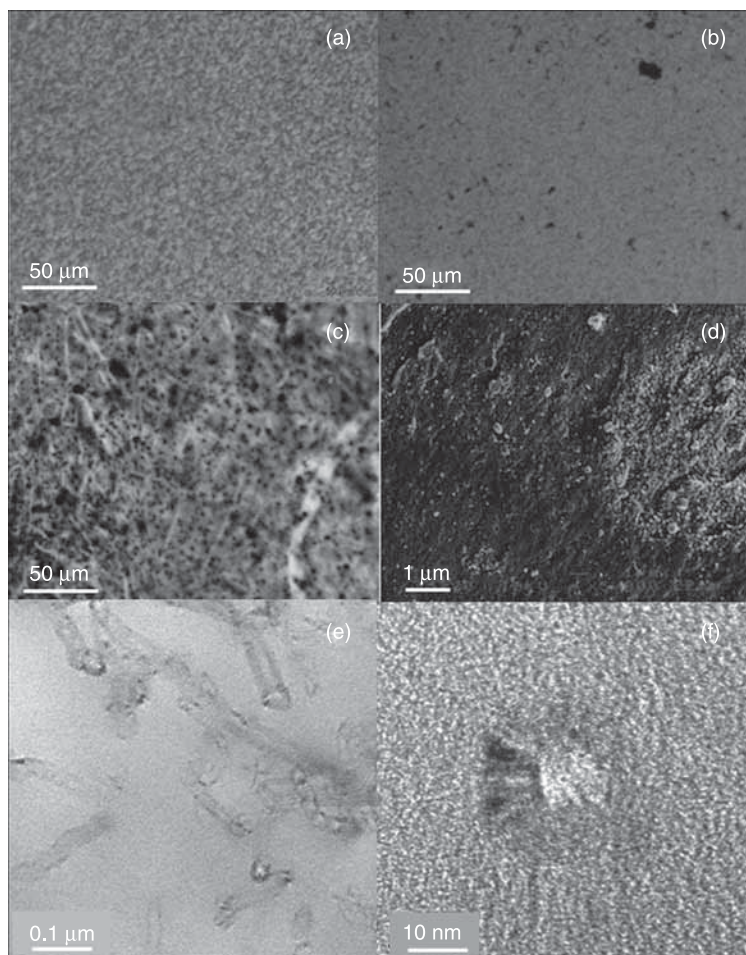


18.1 Variation in extruder torque as a function of CNT loading.

18.3.2 Composite morphology

Figures 18.2 (a) and 18.2 (b) show polarised optical photographs of virgin PET and the PET–1 wt% MWCNT composite. The samples were heated on a hot stage accessory operating between 250 and 270 °C and cooled at 4 K/min to room temperature. The images shown in Fig. 18.2 (a) and 18.2 (b) were captured immediately after crystallisation and spherulite impingement was complete. As can be observed, the addition of CNTs to PET significantly altered the crystalline texture of the polymer when compared to the neat polymer. The CNTs provide a nucleating site for PET crystal growth and initiate heterogeneous nucleation, resulting in the formation of smaller crystallites. The extent of CNT dispersion and distribution throughout the PET matrix was studied across the length scales using a combination of optical microscopy, FESEM (Joel 6400) and HRTEM (FEI Tecnai F20). For low MWCNT loadings (<1 wt%), few large MWCNT agglomerates were observed, see Fig. 18.2 (b). However, at higher loadings,

agglomerates of MWCNTs were readily seen in the PET matrix, particularly when the MWCNT loading was 10 wt%, see Fig. 18.2 (c). Typically, agglomerates having diameters between 1 μm and 5 μm were distributed in the PET matrix, although larger agglomerates up to 10 μm were also evident. Examination of the composites by SEM also revealed the CNTs, for lower loadings only, were highly dispersed in the PET matrix. By way of example, Fig. 18.2 (d) shows a representative SEM image of the PET–10 wt% MWCNT composite. At higher magnification ($\times 400\text{k}$), images were obtained using HRTEM, and individual MWCNTs were



18.2 Polarised optical micrograph (POM) of: (a) neat PET; (b) POM image of PET–1 wt% MWCNT composite; (c) POM image of PET–10 wt% MWCNT composite; (d) SEM micrograph of PET–10 wt% MWCNT composite; and (e) and (f) HRTEM images of the 10 wt% PET–MWCNT composite at different magnifications.

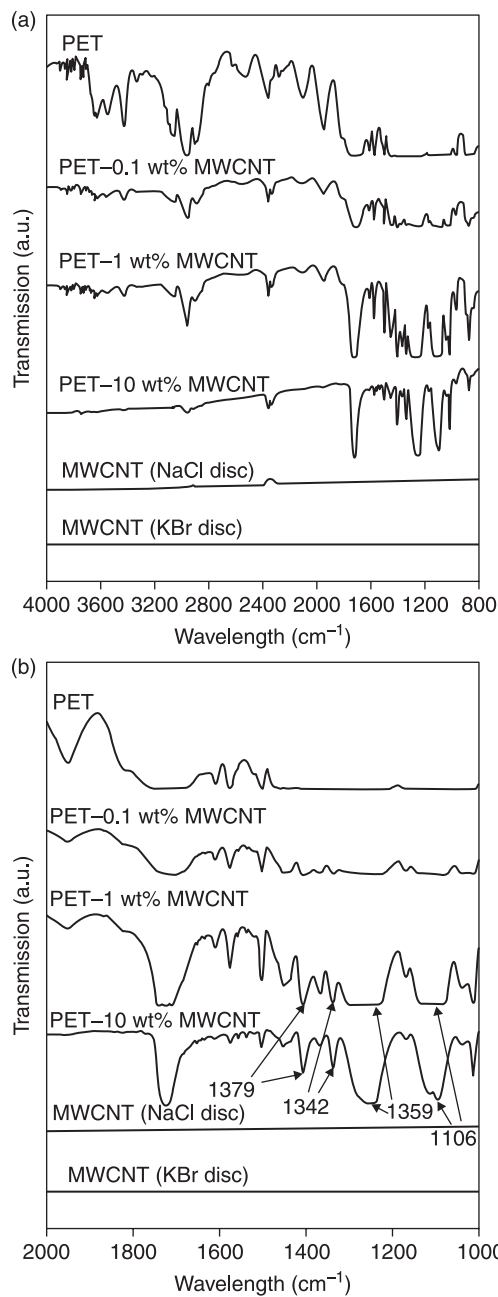
observed dispersed in the polymer matrix, see Fig. 18.2 (e). In Fig. 18.2 (f), a cross-sectional view of a MWCNT embedded in the PET matrix was obtained, where the concentric arrangement of CNT walls is identifiable. The CNT wall thickness was estimated to be up to 20 layers thick, giving a CNT outer diameter of 30 nm.

18.4 Changes in crystalline structure and crystal conformation

18.4.1 Fourier transform infrared spectroscopy (FTIR)

Fourier transform infrared spectroscopy (FTIR) has been employed to characterise and confirm chemically modified surfaces of CNTs' post-organic treatment (Jin *et al.*, 2007; Ahn *et al.*, 2008). Normally, treatment with concentrated acids such as sulphuric or nitric, carboxyl groups attach to the CNT surface and new peaks evolve in the FTIR spectra of the acid-treated CNTs associated with carboxyl groups. Peaks appearing at $1721\text{--}1730\text{ cm}^{-1}$ are indicative of C-O stretching, at 1176 cm^{-1} C-O stretching and a peak at 1400 cm^{-1} indicates O-H bending, all attributed to the addition of carboxyl functionality to CNTs (Jin *et al.*, 2007; Ahn *et al.*, 2008). In an FTIR study of acid and acetic anhydride functionalised CNTs, peaks attributed to carboxyl groups described in (Jin *et al.*, 2007) and (Ahn *et al.*, 2008) were obtained, but with an additional peak at $3000\text{--}2800\text{ cm}^{-1}$ corresponding to sp^3 C-H stretching, indicating the presence of $-\text{CH}_3$ groups on the surface of the MWCNTs used (Jin *et al.*, 2008). Figures 18.3 (a) and 18.3 (b) show infrared spectra for neat PET, pristine MWCNTs and PET-MWCNT composites prepared in this study between 800 cm^{-1} and 4000 cm^{-1} and an expanded view of the region between 1000 cm^{-1} and 2000 cm^{-1} , respectively (Perkin Elmer Spectrum 1000).

The peaks observed between 2800 cm^{-1} and 4000 cm^{-1} associated with inter- and intra-molecular hydrogen bonding decrease in intensity on addition of MWCNTs to PET, suggesting that the MWCNTs readily infiltrate between PET chains, see Table 18.1. Peaks displayed between wavelengths of 1900 cm^{-1} and 2200 cm^{-1} associated with carbon stretching vibrations and aromatic summation bands were also less intense for the composites. Studies on the correlation of PET chain conformations with the addition of MWCNTs has been investigated by Tzavalas *et al.* (Tzavalas *et al.*, 2008), *trans* segments (1340 cm^{-1}), *gauche* segments (1370 cm^{-1}) and in-plane vibration (G structure 1018 cm^{-1}) of ethylene glycol (EG) were also identified in previous work by Cole *et al.* (Cole *et al.*, 2002a, 2002b). These assignments were used by Tzavalas to map the relative population of *gauche* and *trans* crystal conformations as CNT content was increased (Tzavalas *et al.*, 2008). Other peaks assigned to *trans* segments of PET occur at 1098 cm^{-1} (carbonyl stretching) and 1259 cm^{-1} (in plane ester bond vibration). Figure 18.3 (b) shows the evolution of 2 peaks, one at 1342 cm^{-1} assigned to *trans* segments of EG and another at 1379 cm^{-1} assigned to *gauche* segments.

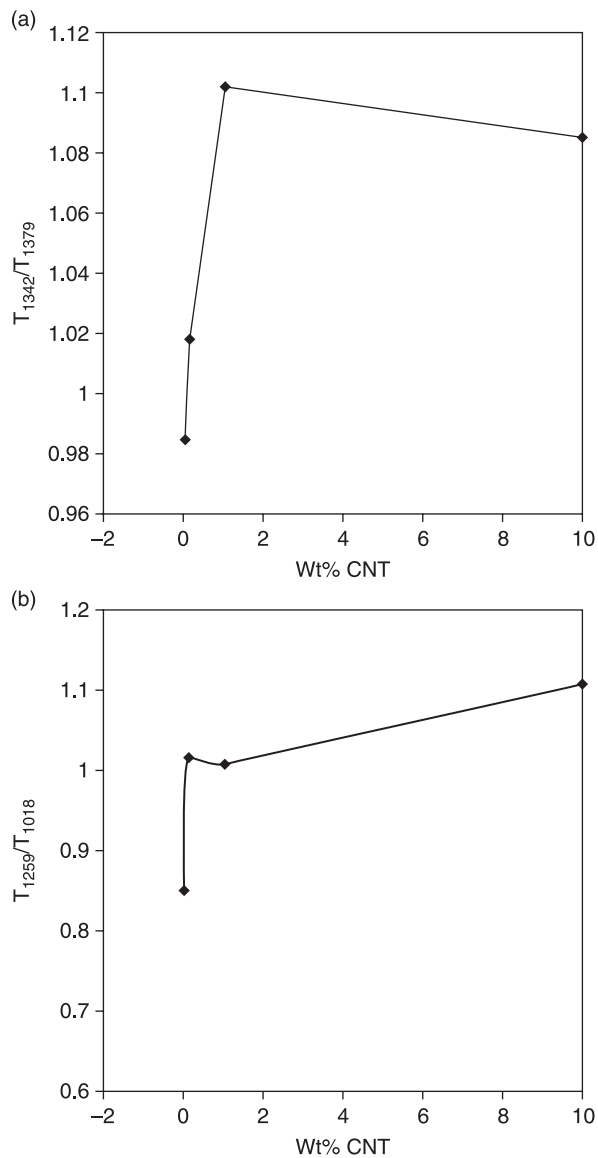


18.3 FTIR spectra of PET, pristine MWCNTs and PET-MWCNT composites in the spectral region: (a) 800–4000 cm⁻¹ and (b) 1000–2000 cm⁻¹.

Table 18.1 Band assignment for the infrared spectrum of PET and PET-10 wt% MWCNT composite

Possible band assignments for neat PET		Possible band assignments for PET-10 wt% MWCNT composite	
Wavenumber (cm ⁻¹)	Assignment	Wavenumber (cm ⁻¹)	Assignment
3690-4000	Absorbed moisture	3697-3644	Absorbed moisture
3644,3625,3616	Free OH	3624,3614	Free OH
3583,3562,3548,3472	Intra-molecular H bonds	3590-3499	Intra-molecular H bonds
3225	Inter-molecular H bonds	3430	Inter-molecular H bonds
3332,3295	=C-H	3330	=C-H
3329,3180	O-H stretching	3329,3180	O-H stretching
1948	Aromatic summation band	1951	Aromatic summation band
3122,3098,3075	H bonded NH	3123	H bonded NH
3050,3064	=C-H	3077	=C-H
2903,2961	C-CH ₃	2849,2959,2914	C-CH ₃
2887	CH		
2802	N-CH ₃ (aliphatic)		
2253	C-C=C-C		
2099	C=CH (terminal)		
1752	C=O stretching vibrations (non conjugated)	1866-1721	C=O stretching vibrations (non conjugated)
1742,1723,1708	C=O stretching vibrations (conjugated)	1683-1621	C=C stretching vibrations (non conjugated)
1689,1676	C=C stretching vibrations (non conjugated)	1613,1575	C=C stretching vibrations (conjugated)
1611,1576	C=C stretching vibrations (conjugated)		
1459,1380,1364	CH bending vibrations CH ₃		
1411,1439	CH ₂	1454,1407	CH ₂
1370, 1340	CH ₂ wagging vibration		
1364	CH ₃	1369,1470	CH ₃
1354	O-H deformation	1354	O-H deformation
1431	CH bending vibrations CH ₂		
1173	C-O-C vibration in esters (formates)	1172	C-O-C vibration in esters (formates)
1037	C-O-C vibration in esters (acetates)	1260,1041,1016	C-O-C vibration in esters (acetates)
929	-CH=CH ₂		
897	C=CH ₂	896	C=CH ₂

In work similar to that of Tzavalas *et al.* (Tzavalas *et al.*, 2008), a study on the change in the proportion of PET chains from amorphous to crystalline regions was performed. In Figs 18.4 (a) and 18.4 (b) the ratio of normalised transmission intensities of a range of *trans* to *gauche* segments demonstrated a clear change in crystalline structure.



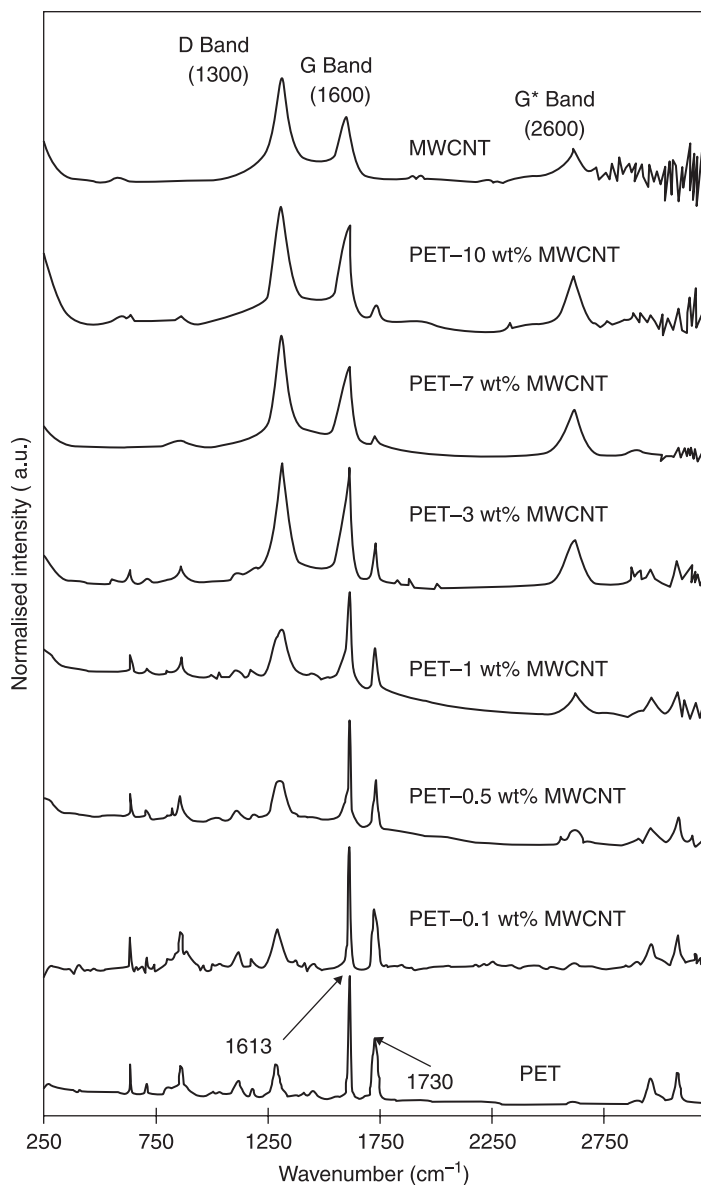
18.4 Plot of normalised intensities of the FTIR peaks at (a) 1342 cm^{-1} (*trans* segments) and 1379 cm^{-1} (*gauche* segments), and (b) 1259 cm^{-1} and 1018 cm^{-1} (G structure), versus MWCNT loading.

As CNT content was increased, the proportion of polymer chains residing in the *trans* crystalline phase increased relative to those residing in the *gauche* phase which indicated a clear transition to a more crystalline structure with the addition of MWCNTs. The CNTs initiate heterogeneous nucleation, inducing ordered crystal growth and alter composite morphology.

18.4.2 Raman spectroscopy

Raman spectroscopy has been widely used in the analyses of carbon nanotube materials (Han *et al.*, 1989) and polymers, including PET (Du *et al.*, 2004). This technique was used to evaluate the dispersion of MWCNTs in PET and the changes in the crystallinity of PET on addition of the CNTs. An Avalon Instruments Raman Station spectrometer was used to obtain Raman spectra of the PET-MWCNT composites using an excitation wavelength of 785 nm (1.58 eV) and a maximum power of 100 mW. However, in order to avoid laser damage to the samples, this power was reduced. A very long working distance (18 mm) lens was used to provide a laser spot size of over 200 μm as it was believed that a large spot size would give a more representative indication of the bulk material than a surface confocal spot. The spectral range collected was 250–3200 cm^{-1} in all cases as the advanced Echelle spectrograph employed in this system provided the ability to give this large spectral range in a single scan. The detector system used in this instrument was an Andor CCD camera, air-cooled to a temperature of -50 K . The laser system used was unpolarised, polarisation optics were not used in the excitation or collection optical paths, avoiding possible complications due to directional effects along the axis of the thin cylindrical specimen (an extruded rod) used to collect spectra. Samples were held vertically in a standard cuvette holder accessory, placed in the electro-mechanical 3-axis stage and user-positioned using an on-board alignment camera. Care was taken to avoid laser-induced thermal damage of the samples. Samples were assumed to be photo-chemically stable and therefore any change in a spectrum with respect to time was attributed to thermal modification of the sample. Laser power was decreased until the form of the spectrum did not change with a change in integration/scan time. Furthermore, samples were examined (after the Raman spectrum had been obtained) under an optical microscope to examine for visible evidence of laser-induced changes. Figure 18.5 shows the Raman spectra for PET, MWCNTs and composites of PET loaded with 0.1, 0.5, 1, 3, 7 and 10 % MWCNTs by weight.

The evolution of the characteristic carbon nanotube D, G and D* bands around 1300, 1600 and 2600 cm^{-1} are clearly evident (Han *et al.*, 1989; Du *et al.*, 2004). It is also apparent that the spectra of the composites is a summation of the PET and MWCNT spectra, as may be expected. The optical limiting properties of MWCNTs and polymer-MWCNT composites has been previously documented (Fakirov *et al.*, 1975; Tongyin *et al.*, 1983). The Raman spectra from the composites will be relatively under-represented in the polymer spectrum due to the nanotube absorption



18.5 Raman spectra of neat PET, pristine MWCNTs and PET-MWCNT composites.

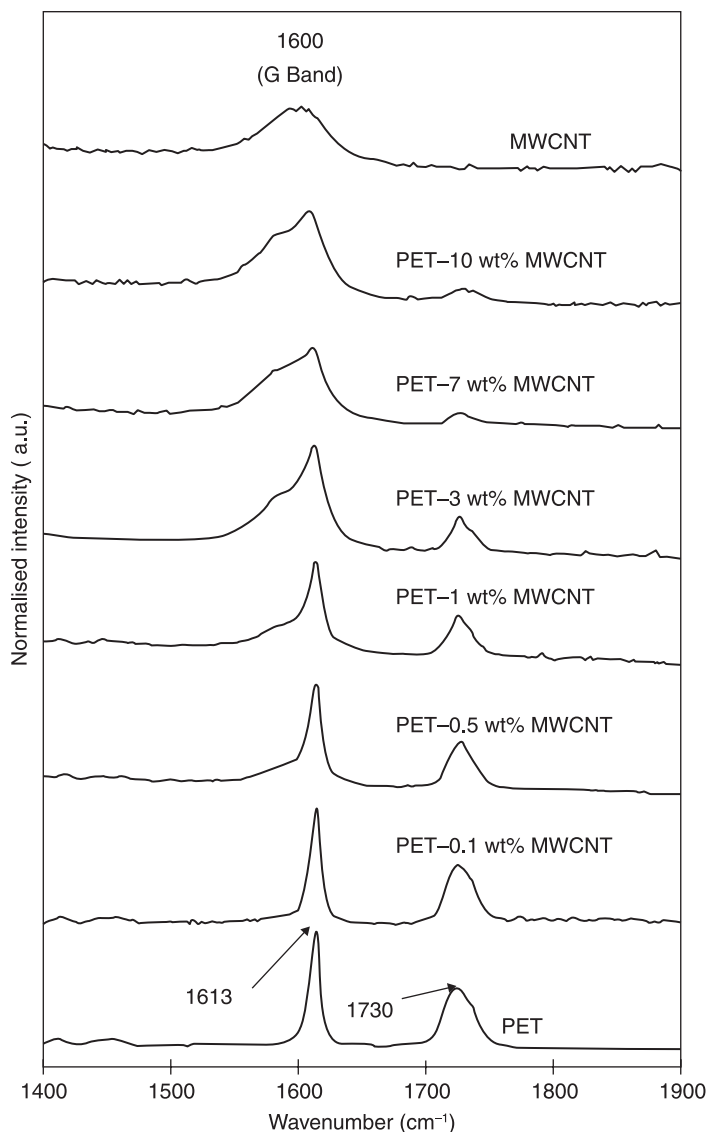
of both the excitation and scattered radiation, hence the weak contribution from the PET in the composite samples having in excess of 3 wt% MWCNT. Two dominant peaks exist in the PET spectrum, one at 1613 cm^{-1} , which is reported as varying little with change in crystallinity (Kiflie *et al.*, 2002), and the other at around

1730 cm^{-1} . From Fig. 18. 5, it is clear that the peak at 1613 cm^{-1} is in the same locality as the G band of the MWCNTs and so, although the two peaks may be independent, they overlap. The proximity of these peaks is not surprising since the 1613 cm^{-1} band in PET is attributed to C-C ring stretch, and the nanotube structure is composed of graphene-like rings. The nanotube peaks neither interfere nor overlap with the peak near 1730 cm^{-1} and this peak is definable in all spectra, although it is very weak, and therefore noisy, in the 7 and 10 wt% MWCNT traces. The peak at the nominal relative wavenumber of 1730 cm^{-1} is associated with a carbonyl stretching mode within the PET macromolecule (Kiflie *et al.*, 2002). In this study, the position of this peak was found to be at 1727 cm^{-1} for the amorphous PET sample with no MWCNTs added. Previously Yeh *et al.* had correlated the full width of this peak at half height (FWHH) with the degree of crystallinity in a stressed PET fiber sample (Yeh *et al.*, 1998). This width decreased by almost 50% between amorphous and semi-crystalline fibers indicating the narrower the band width, the greater the crystalline content. Considering the spectra of Fig. 18.6, which have been normalised for peak height, it is evident that the shape of this peak changes to a more triangular form with increasing MWCNT content.

This type of change of peak shape results in a decrease in the FWHH. In order to measure the FWHH, the standard method in the post-processor used (Thermogalactic-GramsTM) is to fit a Gaussian, Lorentzian or mixed Gaussian/Lorentzian and then take the FWHH of the mathematical curve. It was apparent that for many of the spectral lines under consideration a single fitted curve (even a mixed Gaussian/Lorentzian) did not give an adequate fit. The inadequacy of single mathematic curves to fit to PET peaks has been reported previously (Kiflie *et al.*, 2002; Antoniadis *et al.*, 2009). Although it would be possible to fit multiple mathematical curves to the spectral peaks, this would result in a complication when comparing peaks between spectra as a single FWHH figure would not exist. It was decided that a more accurate way to proceed was to measure the FWHH without presuming anything about the nature of the peak. Therefore, a FORTRAN program was written to calculate the peak FWHH numerically from the data points acquired in the spectrum. The results from the numerical analyses are given in Table 18.2 and

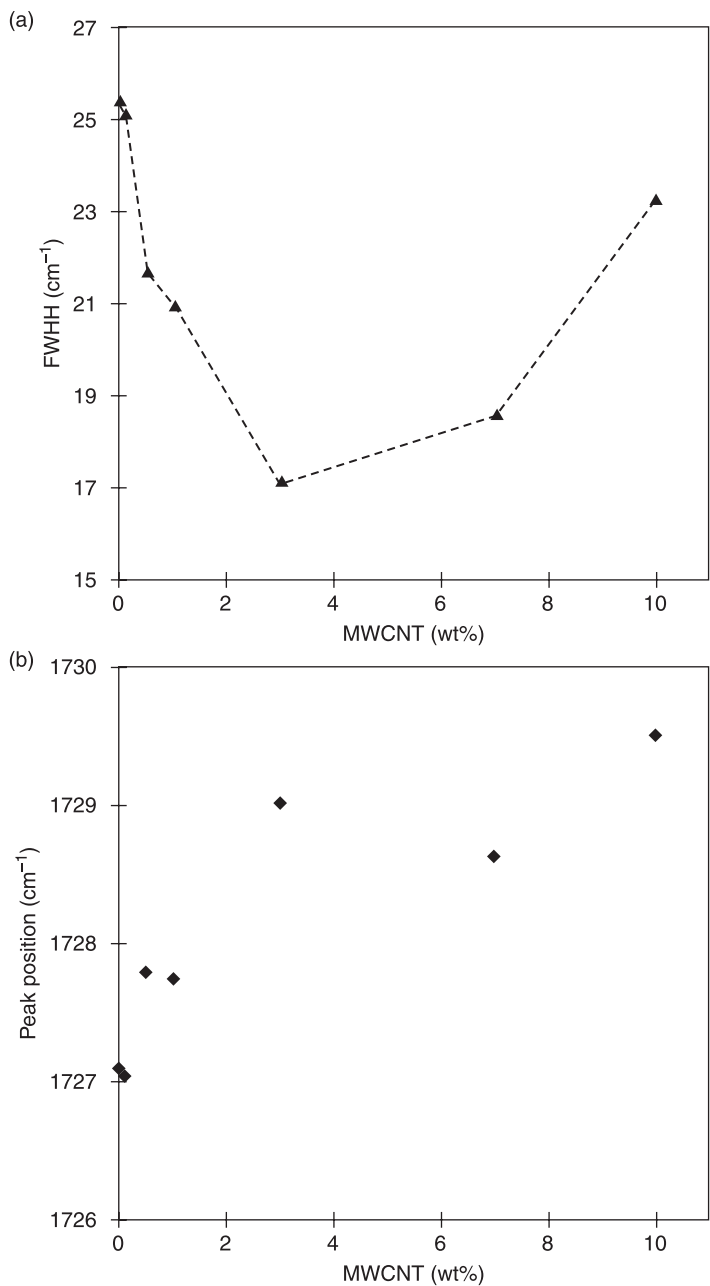
Table 18.2 Values for FWHH and weighted peak position determined from numerical analysis

Wt% CNT	FWHH (cm^{-1}) (calculated)	Weighted peak position (cm^{-1})
0	25.41	1727.1
0.1	25.15	1727.1
0.5	21.69	1727.8
1	20.93	1727.8
3	17.11	1729.0
7	18.61	1728.7
10	23.26	1729.5



18.6 Normalised Raman spectra for neat PET, pristine MWCNTs and PET-MWCNT composites.

plotted graphically in Figs 18.7 (a) and 18.7 (b). Both the peak FWHH and the weighted peak position change with nanotube content. Initially, the FWHH decreased with increasing MWCNT content to 3 wt% MWCNTs and thereafter appears to rise. The narrowest FWHH peak measured showed a 25.7% reduction over the amorphous which is significant, and is likely to be caused by the formation of a more crystalline phase in PET. The position of the weighted peak centre also

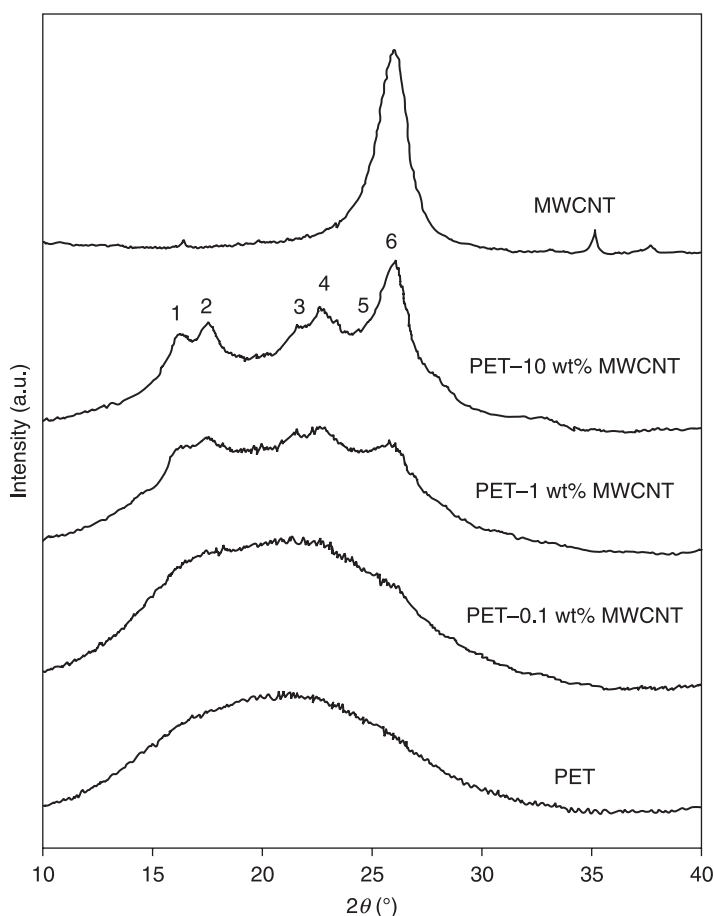


18.7 Change in (a) FWHH and (b) peak weighted position as a function of MWCNT loading, determined from numerical analysis.

upshifts with increasing MWCNT content to 3 wt% MWCNT, and thereafter appears to level off. It should be noted that the accuracy of the results for the 7 and 10 wt% MWCNT may be compromised due to the very weak nature of the signal of these peaks.

18.4.3 X-ray diffraction

The XRD traces for neat PET, pristine MWCNTs and PET–MWCNT composites are shown in Fig. 18.8 (PANalytical X'Pert PRO diffractometer with Cu- K_{α} radiation ($\lambda = 1.5406 \text{ \AA}$) at a scanning rate of $0.2^{\circ}/\text{min}$ over the range $1\text{--}50^{\circ}(2\theta)$). As expected, the diffractogram for neat PET showed a broad amorphous peak, however, as the proportion of MWCNTs added was increased the evolution of



18.8 X-ray diffractograms for neat PET, pristine MWCNTs and PET–MWCNT composites. For explanation of numbers, see text.

four clearly defined peaks for the PET-MWCNT composites, particularly at higher MWCNT loading, was obvious. These peaks were at $2\theta = 16^\circ$, 17.5° , 21.5° and 22.7° , confirmation that addition of MWCNTs to PET initiated polymer crystallisation.

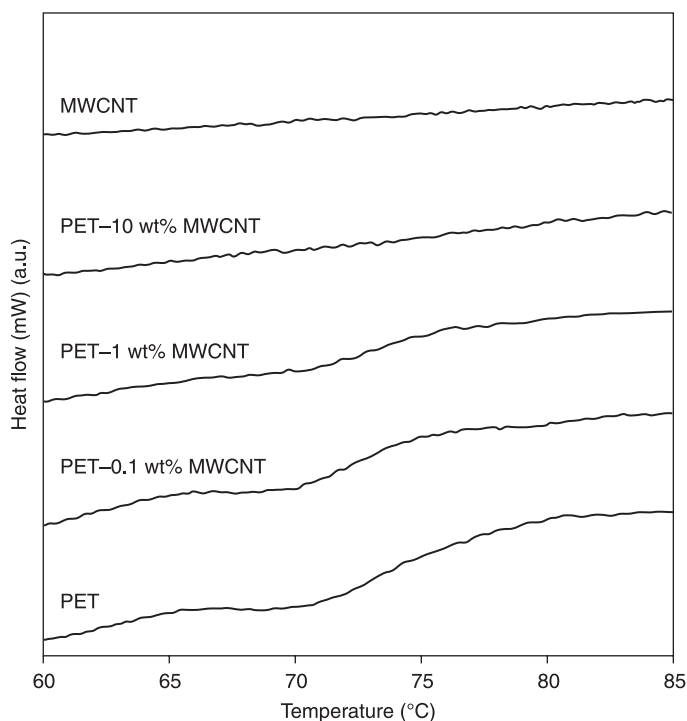
The diffractogram for neat MWCNTs showed two reflections at $2\theta = 26^\circ$ and 43° corresponding to the 002 and 100 crystal planes, respectively. The main 002 reflection is associated with the concentric arrangement of the CNTs and corresponds to a d -spacing of 3.41 \AA . This peak was absent from the composite materials, suggesting the tearing and shearing forces applied during melt extrusion were effective at disentangling the MWCNTs, although there may be some overlap between 100 reflection for PET and the 002 MWCNT reflection. The PET crystal faces have been assigned to the following diffraction peaks at 2θ angles: $(0\bar{1}1) = 16.3^\circ$; $(010) = 17.5^\circ$; $(\bar{1}11) = 21.5^\circ$; $(\bar{1}10) = 22.7^\circ$; $(100) = 26.1^\circ$; $(1\bar{1}1) = 27.65^\circ$ (Fakirov *et al.*, 1975). They are labelled in Fig.18.8 as: 1 = $(0\bar{1}1)$; 2 = (010) ; 3 = $(\bar{1}11)$; 4 = $(\bar{1}10)$; 5 = (100) ; 6 = $(1\bar{1}1)$. The diffraction peaks obtained for the PET-MWCNT composites appear at the same 2θ angles assigned to crystalline PET crystal faces, but appear narrower and more distinct with increasing MWCNT loading. This may be due in part to the gradual perfection of the crystallite although this rapid crystallization did not allow the polymer to reach a highly regular semicrystalline framework (Tongyin *et al.*, 1983). By way of example, the d -spacings for the composites of PET with 1 wt% and 10 wt% MWCNT are listed in Table 18.3. For each peak, the d -spacing decreased with increasing MWCNT loading, again supporting the hypothesis that MWCNTs act as nucleating agents for PET.

Table 18.3 The d -spacings calculated for composites of PET with 1 wt% and 10 wt% MWCNT

Sample	$2\theta^\circ$	d -spacing (\AA)
MWCNT	26.07	3.41
	43.4	2.08
PET-1 wt% MWCNT	16.47	5.38
	17.47	5.07
	21.61	4.11
	22.25	3.99
	25.77	3.45
PET-10 wt% MWCNT	16.22	5.46
	21.55	4.12
	22.68	3.92
	26.06	3.42
	43.33	2.09

18.4.4 Isothermal crystallisation behaviour

The physical and mechanical properties of PET post processing are governed by the associated crystallisation processes (Kiflie *et al.*, 2002). For this reason, the crystallisation and melt behaviour of semi-crystalline polymers such as PET are of extreme interest to researchers and industrialists alike. The introduction of MWCNTs to PET can both enhance the original properties of the PET while simultaneously altering the intended morphology of the polymer significantly. Previous studies have shown the addition of only small amounts of MWCNTs, typically 0.01 wt% can induce heterogeneous nucleation of crystallite growth and increase the temperature at which crystallisation begins (Wang *et al.*, 2007). The nucleating effect of MWCNTs is largely dependent on the initial state of dispersion of the nanotubes and the interaction between CNTs and polymer chains. In this study, the iso-thermal crystallisation behaviour of PET–MWCNT composites was investigated. Samples ranging in mass from ~5–10 mg were sealed in an aluminium pan, heated, then cooled and reheated at a constant rate of 10 K/min. The glass transition (T_g) regions of the DSC curves obtained are shown in Fig. 18.9. On addition of MWCNTs to PET a slight reduction in T_g from about

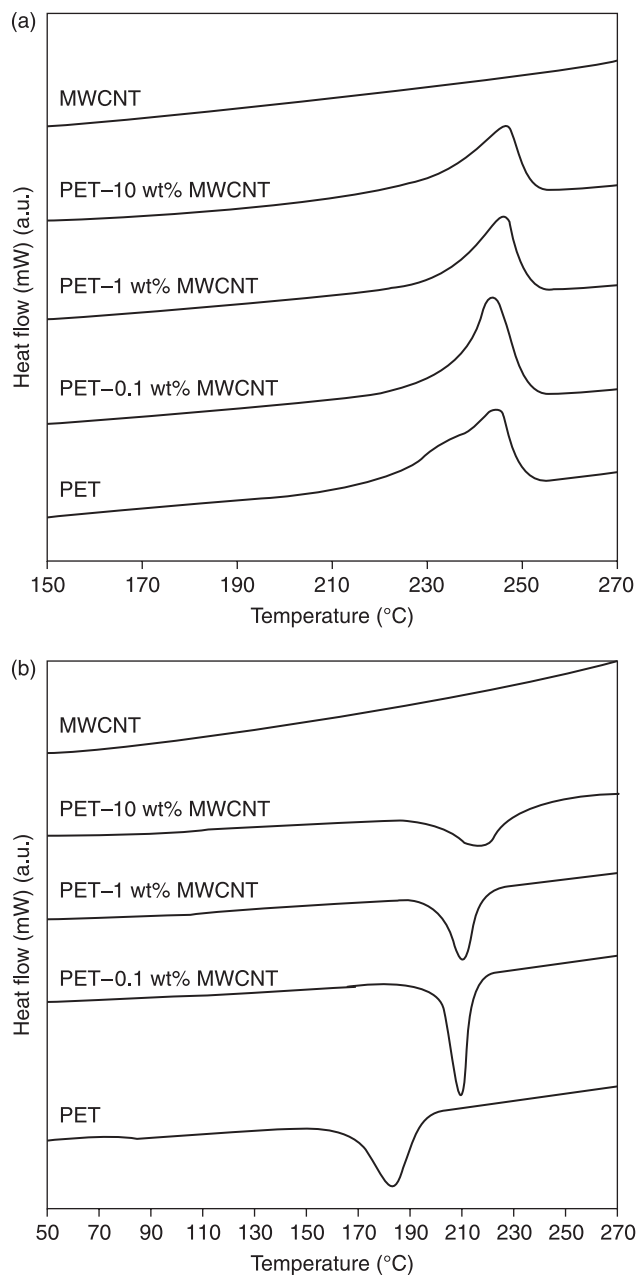


18.9 Change in glass transition temperature of PET as a function of MWCNT loading.

75 °C for virgin PET to 72 °C for the composite with 1 wt% MWCNT loading. However, this minor reduction in T_g was concomitant with a significant decrease in specific heat capacity (ΔC_p) such that no T_g was detected for the composites with higher CNT content. At higher MWCNT loading, PET chain dynamics is hindered and the degree of hydrogen bonding is reduced, in agreement with our FTIR observations.

The thermograms obtained for the reheat and cooling cycles are shown in Figs 18.10 (a) and 18.10 (b), and the corresponding calorimetric data; temperature of melting (T_m), crystallisation temperature (T_c), enthalpy of fusion (ΔH_m), enthalpy of crystallisation (ΔH_c), percentage crystallinity (X_c) and degree of supercooling (ΔT) in Table 18.4. X_c was calculated using, $X_c = \Delta H_m / \Delta H_f$, where ΔH_m is the enthalpy of melting for the sample of interest and ΔH_f is the enthalpy of melting for a theoretically 100% crystalline PET, taken as 117.6 J/g (Quintanilla *et al.*, 1996).

There was little change, possibly 2 K, in T_m of PET on addition of up to 10 wt% MWCNTs, although this may be within instrument error. Similarly, the PET crystalline content changed little when the MWCNTs were added. However, the shape of the PET melting peak obtained on addition of MWCNTs implies a change in crystallite size and order. This observation was probed further by examining the crystallisation exotherms, see Fig. 18.10 (b). T_c of neat PET was 183 °C which increased to 209 °C, 211 °C and 218 °C on the addition of 0.1 wt%, 1 wt% and 10 wt% MWCNTs, respectively. Consequently, the degree of supercooling (ΔT) decreased from 61 °C for PET alone to 28 °C for the composite with 10 wt% MWCNTs added. The 35 °C increase in T_c and 33 °C decrease in ΔT is further confirmation that the MWCNTs act as nucleating agents in PET, accelerating the rate of crystallisation and initiate crystal growth at the CNT surface. The crystallisation curve narrowed on MWCNT addition, the full width at half height (FWHH) decreased from 16 °C to 7 °C on the addition of only 0.1 wt% MWCNTs. This behaviour is typical of the growth of uniform, discrete crystalline regions and a reduction in crystal size distribution, as a consequence of the good dispersion of MWCNTs throughout the PET matrix, particularly at MWCNT loadings below 1 wt%. As CNT loading increased, the curves became gradually broader again as the variation in size and number of PET crystal growth regions increased, due to the increase in the number and size of CNT agglomerates. This effect on crystallisation behaviour was clearly evident from polarised optical microscopy experiments (see Figs 18.2 (a) and 18.2 (b)), where the addition of MWCNTs to PET induced the growth of smaller, more imperfect crystals by accelerating crystal growth due to the presence and abundance of random points for crystal nucleation, i.e. on the CNT surface. The average crystal size decreased due to the nucleating effect of the CNTs, resulting in an increase in T_c and a change in shape of the crystallisation curves. Similar crystallisation behaviour was observed in separate studies by Wang (Wang *et al.*, 2007) and Tzavalas (Tzavalas *et al.*, 2008) where 0.01 wt% and 1 wt% MWCNTs induced a decrease



18.10 DSC (a) crystallisation and (b) melting isotherms for neat and PET-MWCNT composites.

Table 18.4 DSC characteristics of PET and PET–MWCNT composites

Sample	T _m (°C)	T _c (°C)	ΔH _m (J/kg)	ΔH _c (J/kg)	X _c (%)	ΔT (°C)
PET	244	183	32	37	27	61
0.1 wt%	246	209	31	29	26	37
1.0 wt%	244	211	31	32	26	33
10 wt%	246	218	30	30	23	28

in T_c by 6 °C and 16 °C, respectively. Wang *et al.* also observed a double melting peak, where the lower temperature peak became more intense as CNT loading increased. This is due to the presence of less perfect crystallites forced to initiate by the presence of high CNT loading (Wang *et al.*, 2007). Multiple melting endotherms are common in polyesters, such as PET, due to the formation of crystals with different imperfections and a range of melt histories (Tzavalas *et al.*, 2008).

18.4.5 Non-isothermal crystallisation kinetics

Numerous mathematical models can be used to describe the iso-thermal and non-isothermal crystallisation kinetics of polymeric materials. A method commonly used to describe the complex processes involved in non-isothermal crystallisation kinetics was suggested by Ozawa (Ozawa, 1971) and was based on the same theory as predicted by Avrami (Avrami, 1939, 1941) and Evans (Evans, 1945). The Ozawa approach, described later in the text, has been applied in previous studies for the description of the non-isothermal crystallisation of PET (Ozawa, 1971; Sajkiewicz *et al.*, 2001) and indeed many other semi-crystalline polymers, including Nylon 12 (McFerran *et al.*, 2008), poly(propylene) (Mubarak *et al.*, 2001), and poly(p-phenylene sulphide) (López and Wilkes, 1989).

Non-isothermal crystallisation behaviour of unfilled PET and the PET 10 wt% MWCNT composite was investigated using a range of cooling rates. The samples were heated from 40 °C to 280 °C at a rate of 10 K/min, held at 280 °C for 10 minutes, to ensure complete crystallite melting, then cooled to room temperature at cooling rates of 5 K, 10 K, 20 K, 30 K and 40 K/min and heat flow as a function of time and temperature recorded. The relative degree of crystallinity (X_t) can be determined by integrating the area under the peak during the non-isothermal scan as a function of time and temperature:

$$X_t = \frac{A(T)}{A(\text{Total})} \quad [18.1]$$

where A(T) is the partial area of the peak at temperature (T) and A(Total) is the total peak area. The Ozawa model was applied to describe the crystallisation kinetics of unfilled PET and the PET–10 wt% MWCNT composite under non-

isothermal conditions. The activation energies were also obtained using the Kissinger method (Boswell, 1980). The non-isothermal crystallisation curves for neat PET and the PET–10 wt% MWCNT composite for the various cooling rates are shown in Figs 18.11 (a) and 18.11 (b) respectively and the values of T_c obtained as a function of cooling rate listed in Table 18.5. It is clear from Figs 18.11 (a) and 18.11 (b) that as the cooling rate increased, the crystallisation onset temperature (T_{con}), peak crystallisation temperature (T_c) and crystallisation offset temperature (T_{coff}) shifted to lower temperatures.

Moreover, as cooling rate decreased, the crystallisation peaks became more intense. This occurred as a slower cooling rate resulted in the formation of more perfect crystallites and as such crystal packing and density was improved. From Table 18.5, it can be seen that T_c increased from 182 °C to 209 °C and from 212 °C to 229 °C with decreasing cooling rate for neat PET and the PET–10 wt% MWCNT composite, respectively, again confirming the ability of MWCNTs to nucleate PET crystallisation.

For non-isothermal experiments, the recorded temperature of the sample must be corrected to account for the thermal lag between a point in the sample and the calorimeter furnace at any given time. The recorded temperatures were corrected using Equation 18.2 (Mubarak *et al.*, 2001):

$$T_{actual} = T_{disp} + 0.089 \Phi \quad [18.2]$$

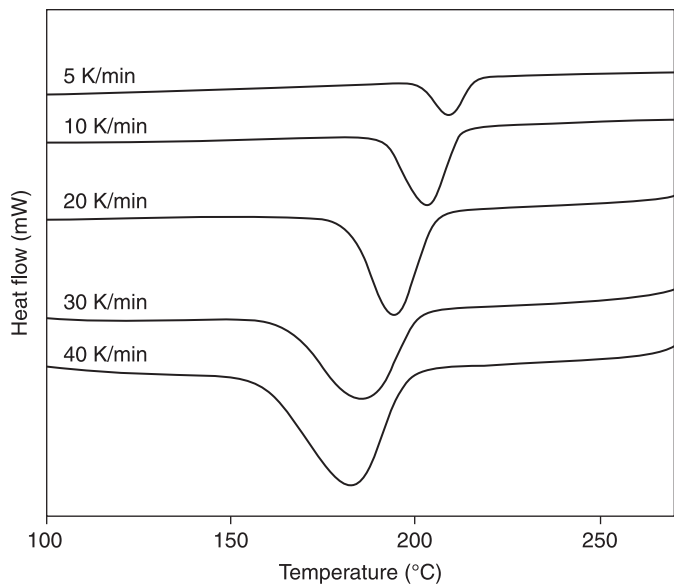
where, T_{disp} is the display temperature and Φ (K/min) is the cooling rate. Then, the degree of relative crystallinity can be plotted against temperature or time by converting temperature into time using Equation 18.3:

$$t = \frac{T_0 - T}{\Phi} \quad [18.3]$$

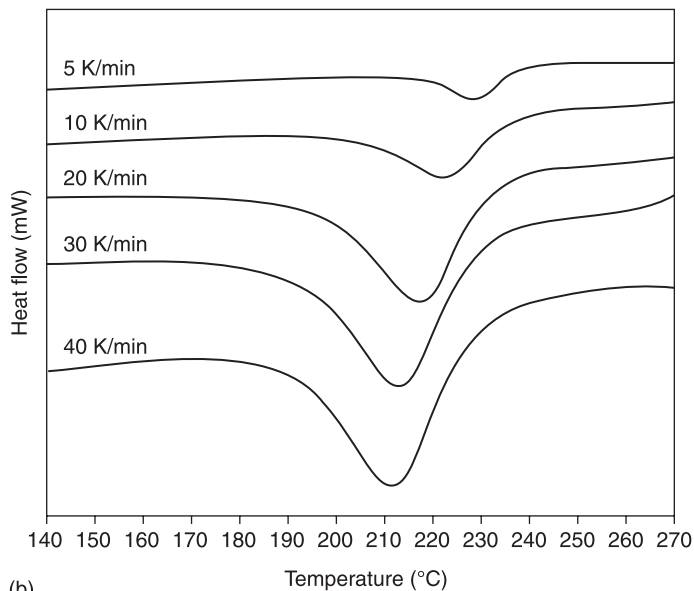
where, t is the crystallisation time, T is the crystallisation temperature, T_0 is initial temperature when crystallisation begins ($t = 0$) and (Φ) is the cooling rate. Figures 18.12 (a) and 18.12 (b) show plots of X_t against temperature for neat PET and the PET–10 wt% MWCNT composite, respectively.

A series of S-shaped curves are obtained which show that as cooling rate increased crystallisation occurred more rapidly. Both neat PET and the PET–MWCNT composites crystallise at lower temperatures with increasing cooling rate. The temperature range in which crystallisation occurred increased with increased cooling rate, e.g. for neat PET at cooling rate of 5 K/min the crystallisation range is 36 K whereas at 40 K/min the range is 60 K. Furthermore, the gradients of the curves are steeper for neat PET compared to those obtained for the PET–10 wt% MWCNT composite as addition of MWCNTs to PET has extended the crystallisation process but yields the growth of more perfect crystals.

A series of sigmoidal shaped curves were also obtained for a plot of X_t versus time, see Figs 18.13 (a) and 18.13 (b). Again, it was evident that as cooling rate decreases the time required for complete crystallisation was longer, therefore the



(a)



(b)

18.11 Non-isothermal crystallisation exotherms for (a) PET and (b) PET-10 wt% MWCNT composite.

Table 18.5 Change in T_c of PET, as a function of MWCNT loading

Cooling rate (K/min)	T_c (°C)	
	PET	PET–10 wt% MWCNT
40	182	212
30	186	213
20	194	217
10	203	222
5	209	229

crystallites have more time to form. Addition of MWCNTs to PET retards polymer crystallisation and extends the time for PET crystallisation to complete. For example, for a cooling rate of 5 K/min it took neat PET 7.2 mins to crystallise fully, whereas it took the PET–10 wt% MWCNT composite 11.2 mins to crystallise. In the primary crystallisation region, i.e. below $X_t = 0.8$, the rate of crystallisation is high, as shown by the steepness of the gradient of the curve in this region. Above $X_t = 0.8$, the rate of crystallisation slows and the curve plateaus, perhaps indicative of the onset of secondary crystallisation. For neat PET, the rate of crystallisation slows with decreasing cooling rate which can be attributed to spherulite impingement. The rate of crystallisation also slows on addition of MWCNTs to PET, particularly at slower cooling rates.

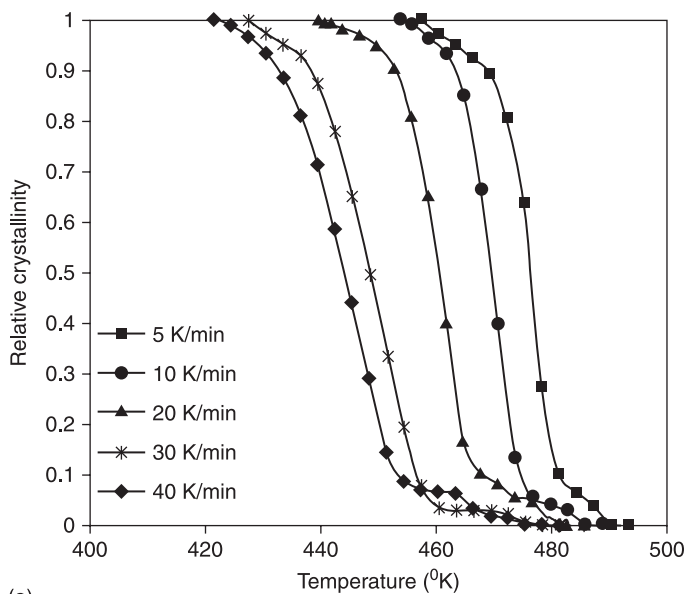
Several methods have been employed to describe the non-isothermal crystallisation kinetics of semi-crystalline polymers (Mubarak *et al.*, 2001). Ozawa derived a non-isothermal kinetic model to describe the process of nucleation and crystallite growth by modifying the Avrami model to allow for all non-isothermal processes (Ozawa, 1971). This method is used when crystallisation occurs at a constant cooling rate:

$$X(t) = 1 - \exp \left(\frac{-K^*(T)}{\phi^m} \right) \quad [18.4]$$

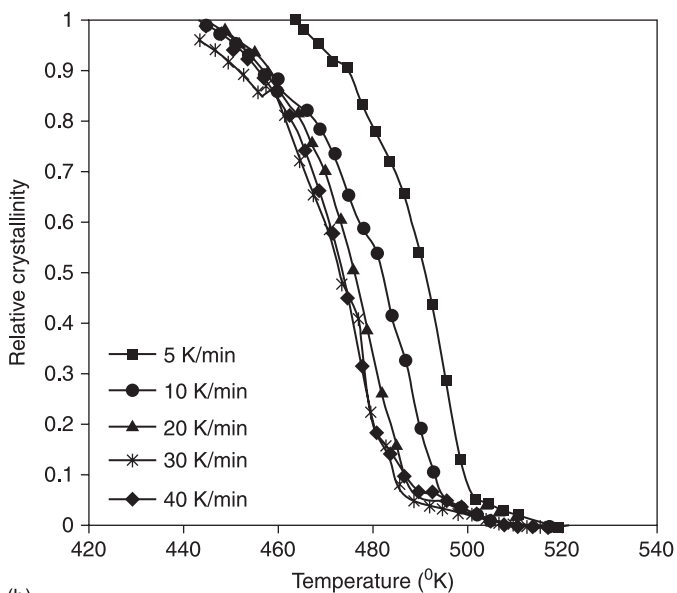
where $X(t)$ is the relative degree of crystallisation at a temperature (T), $K^*(T)$, is the cooling function which is related to the crystallisation rate and indicates how fast crystallisation proceeds, (ϕ) is the cooling rate and (m) is the Ozawa exponent which is dependant on the dimension of crystal growth. By transforming Equation 18.4 into a double-logarithmic form:

$$\ln[-\ln(1 - X(t))] = \ln[K^*(T)] - m \ln \phi \quad [18.5]$$

a plot of $\ln[-\ln(1 - X(t))]$ versus $\ln(\phi)$ at a given temperature will produce a straight line and the kinetic parameters (m) and ($K^*(T)$) can be derived from the slope and the intercept, respectively. Such graphs were constructed for neat PET and the PET–10 wt% MWCNT composite from data points taken at different temperatures in the range 440 K to 510 K, see Figs 18.14 (a) and 18.14 (b), respectively. Ozawa

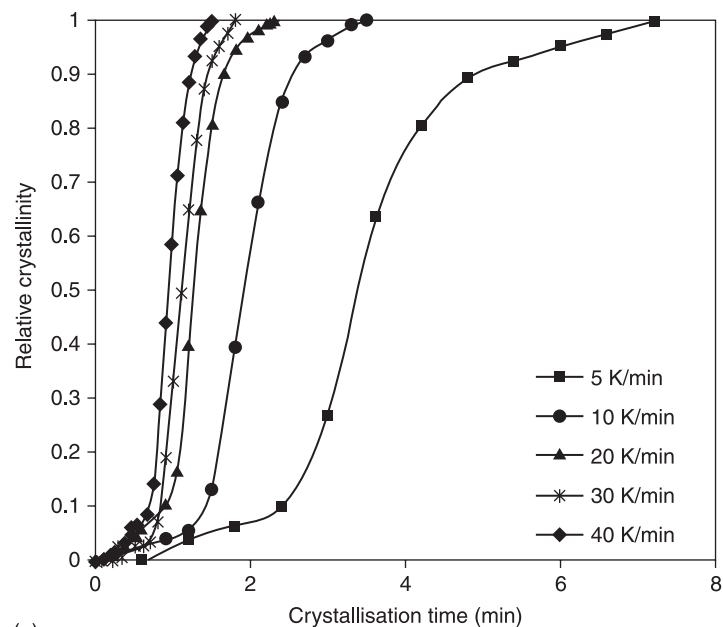


(a)

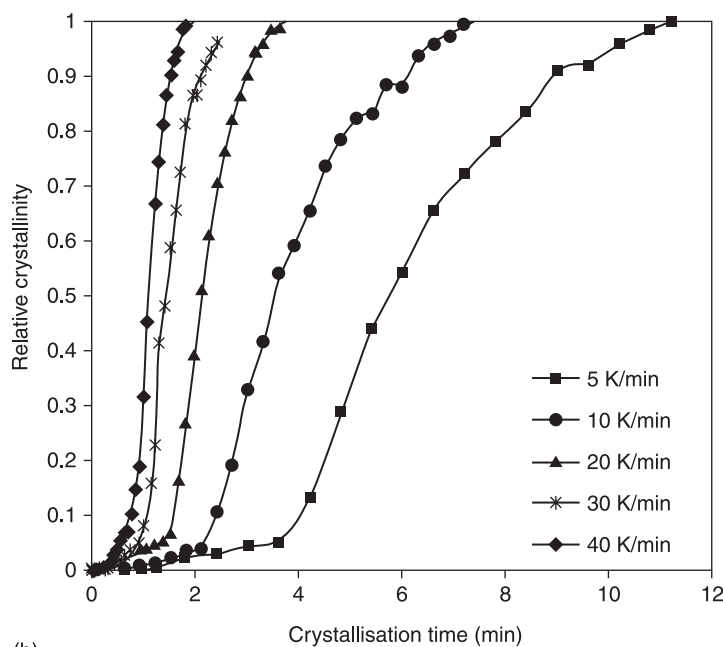


(b)

18.12 Change in relative crystallinity (X_t) as a function of temperature for: (a) PET and (b) PET-10 wt% MWCNT composite.

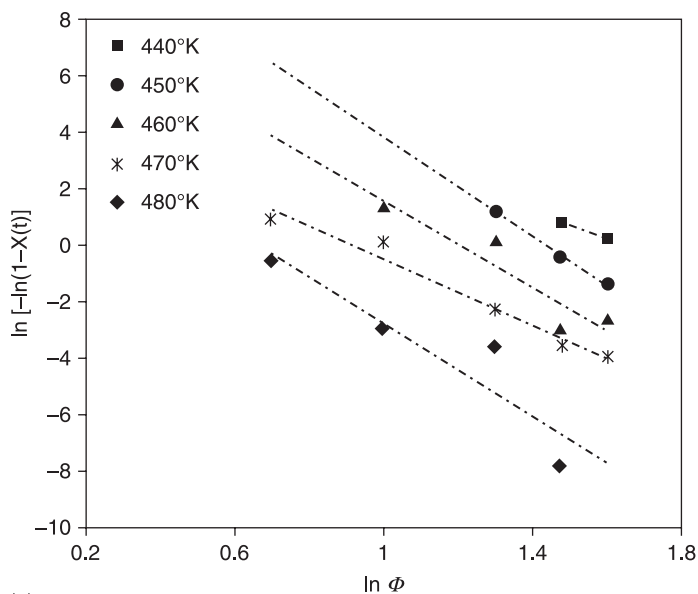


(a)

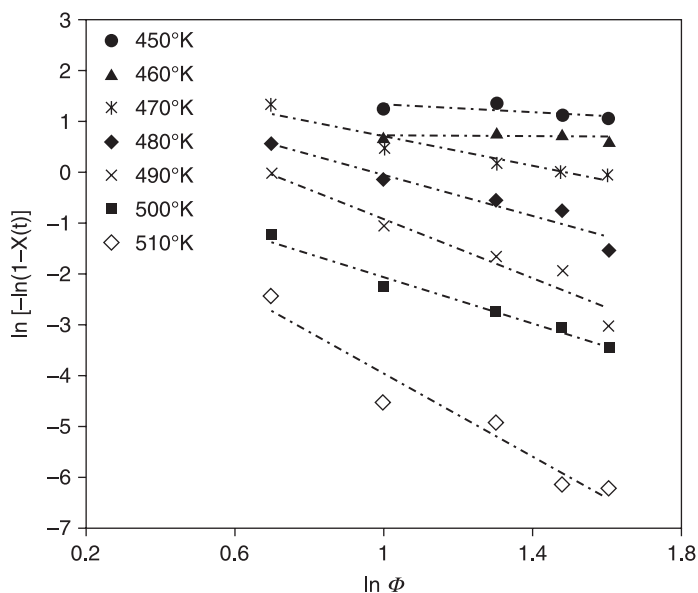


(b)

18.13 Change in relative crystallinity (X_t) as a function of time for (a) PET and (b) PET-10 wt% MWCNT composite.



(a)



(b)

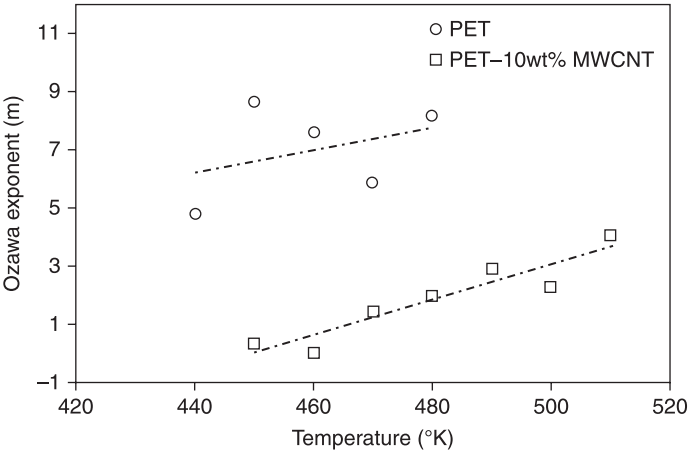
18.14 Plot of $\ln [-\ln(1-X(t))]$ versus $\ln \Phi$ for (a) PET and (b) PET-10 wt% MWCNT composite.

reported previously that this treatment was suitable for modeling the crystallisation behaviour of PET, although he ignored secondary crystallisation (Ozawa, 1971).

The data presented in Figs 18.14 (a) and 18.14 (b) could be fitted with straight lines with reasonable correlation coefficients (>0.9) for all the crystallisation temperatures examined, confirming that Equation 18.5 could be used to describe the non-isothermal crystallisation kinetics of PET and PET–MWCNT composites. The Ozawa exponents (m) were calculated from the slope of each trendline, and the values obtained for m are listed in Table 18.6 and the variation in m with temperature for neat PET and the PET–10 wt% MWCNT composites is shown in Fig. 18.15.

Table 18.6 Ozawa exponents for crystallisation process

Sample	Temperature (°K)	Ozawa exponent (m)
PET	480	8.19
	470	5.90
	460	7.62
	450	8.68
	440	4.80
PET–10 wt% MWCNT	510	4.09
	490	2.93
	480	2.04
	470	1.44
	460	0.05
	450	0.35



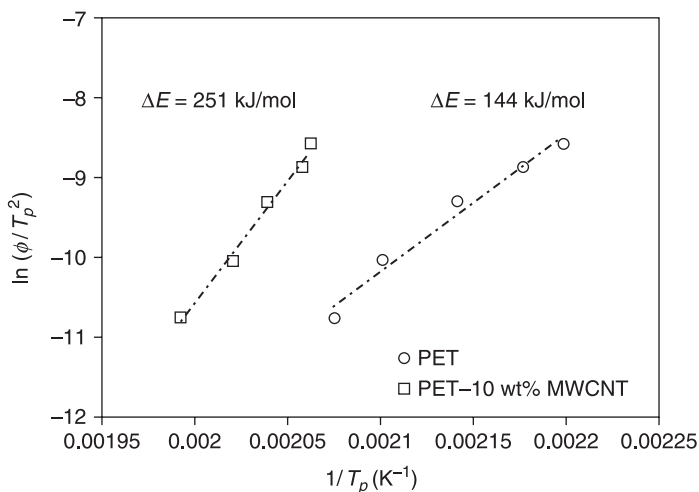
18.15 Plot of Ozawa exponent (m) as a function of temperature for neat PET and PET–10 wt% MWCNT composite.

There was some scatter in m for neat PET, understandable as non-isothermal crystallisation is a dynamic process and a function of time and cooling rate. For any given crystallisation temperature, the PET–10 wt% MWCNT composite had a lower Ozawa exponent compared to PET alone, see Table 18.6. This suggested that the addition of MWCNTs to PET significantly affected the crystal growth mechanisms and again demonstrated crystallite nucleation of PET by MWCNTs. The influence of MWCNTs and varying cooling rates on the activation energy (ΔE) required for crystallisation under non-isothermal conditions has been described by Kissinger using Equation 18.6 (Kissinger 1956):

$$\frac{d[\ln(\phi / T_p^2)]}{d(1/T_p)} = -\frac{\Delta E}{R} \quad [18.6]$$

where T_p is the peak temperature of crystallisation, ϕ is the cooling rate and R is the gas constant. A plot of $\ln(\phi/T_p^2)$ against $1/T_p$ yields a straight line with slope $= \Delta E/R$ (Liu *et al.*, 1998), see Fig. 18.16.

Activation energies of 144 kJ/mol and 251 kJ/mol were determined for PET and the PET–10 wt% MWCNT composite, respectively. An increase in activation energy on the addition of MWCNTs suggests that more energy is required for PET crystallisation to take place. Presumably, addition of MWCNTs to PET reduces polymer chain conformation and hinders chain dynamics. This corroborates the results shown in Figs 18.11 (a) and 18.11 (b). A combination of higher activation energy, together with a shift of the crystallisation curves to higher temperatures, confirmed that MWCNTs act as nucleating agents for PET.

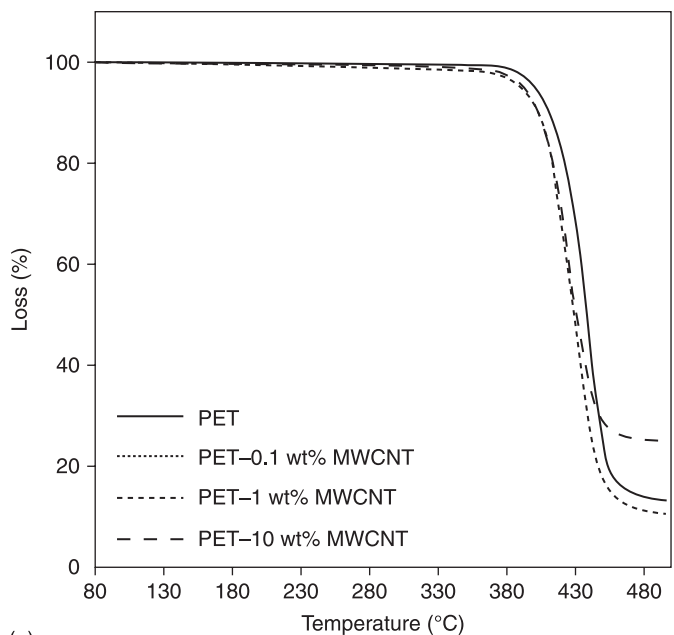


18.16 Plot of $\ln(\phi/T_p^2)$ versus $1/T_p$ (activation energy from the Kissinger method for PET and PET–10 wt% MWCNT composite).

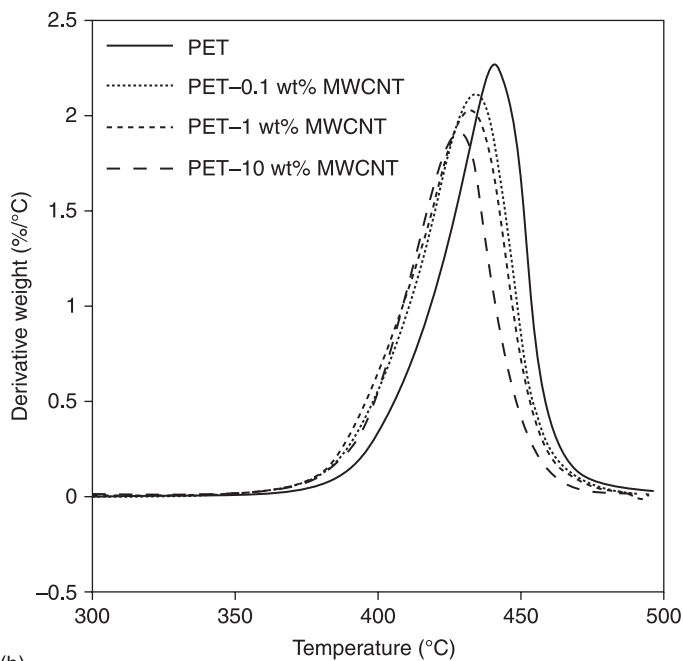
18.5 Thermal stability of PET–MWCNT composites

The thermal stability of PET on addition of MWCNTs was investigated using thermo-gravimetric analysis (Hi-Res TGA 2950, 10 K/min from RT to 500 °C). Figure 18.17 (a) shows the percentage mass loss for neat PET and PET–MWCNT composites with increasing temperature. From the weight loss plots, the onset of thermal degradation (T_{ond}) for neat PET was at 441 °C. T_{ond} decreased by about 10 to 12 K on addition of up to 10 wt% MWCNTs. The residual yield for neat PET was 13.5%, this decreased slightly to 11% for the composites with 0.1 wt% and 1 wt% MWCNTs, before increasing significantly to 25% on addition of 10 wt% MWCNTs to this PET.

This behaviour would suggest that at low MWCNT loadings (<1 wt%), the CNTs accelerate the thermal degradation of PET. However, for a loading of 10 wt% MWCNTs, the onset of thermal degradation decreased by 13 °C relative to unfilled PET, yet the residual yield for this composite was 25%. This behaviour may be associated with the high thermal conductivity of MWCNTs and more effective dissipation of thermal energy for the 10% mass fraction. As the MWCNT content was only 10 wt% for this composite, the composition of the residue must contain not only MWCNTs which are known to be thermally stable well above 500 °C (714 °C for the MWCNTs used in this study), residual metal catalysts, metal oxides, amorphous carbon, but also un- or partially degraded PET. It has been proposed that CNTs create a ‘barrier effect’ by preventing the release of volatiles and decomposed products from the composite material, resulting in the retardation of the thermal decomposition of the composites (Kim *et al.*, 2007). A critical concentration of MWCNTs is required to enhance the thermal stability of PET. The thermal stability of PET is better demonstrated by examining the derivative weight as a function of temperature, Fig. 18.17 (b). Here, the peak maxima (T_{max}) is clearly seen to decrease with increasing MWCNT content, suggesting the onset of thermal degradation of PET is shifted to lower temperatures. Some variability in the thermal stability of melt-processed PET–MWCNT composites has been reported previously. Kim *et al.* obtained an increase of 4 K in the thermal degradation temperature of PET on addition of 2 wt% MWCNTs (Kim *et al.*, 2007). Ahn *et al.* also achieved an increase in the degradation temperature of PET by 10 K on addition of 3 wt% MWCNTs (Ahn *et al.*, 2008). The authors proposed that the introduction of van der Waals or hydrogen bonding between carboxyl functionalised MWCNTs and PET retarded the onset of thermal degradation (Ahn *et al.*, 2008). In another study, well-dispersed SWCNTs had no appreciable effect on the thermal stability of PET (Anand *et al.*, 2007). The unpredictability of the thermal stability of PET–CNT composites implies that this property is controlled by a combination of factors, including CNT dispersion and distribution, CNT orientation – hence barrier properties, thermal conductivity of CNTs, polymer–CNT interactions and polymer crystallinity.



(a)



(b)

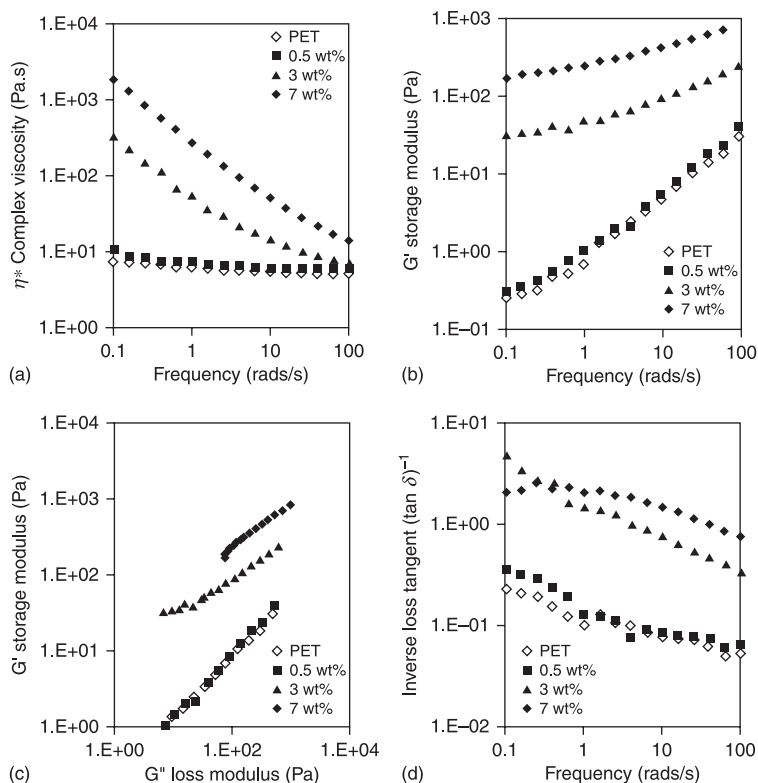
18.17 TGA thermograms: (a) weight loss and (b) derivative weight for neat PET and PET-MWCNT composites.

18.6 Formation of CNT networks in PET: rheological and electrical percolation

Oscillatory or dynamic shear rheology is a sensitive method for detecting the formation of possible CNT networks and in qualifying the distribution of CNTs within a polymeric material without the need for laborious microscopy and imaging techniques. By way of example, the rheological properties of virgin PET and composites of PET with 0.5 wt%, 3 wt% and 7 wt% MWCNTs were measured using an Advanced Rheometric Expansion System (ARES, TA) strain controlled rheometer with 25 mm parallel plate geometry. Samples of ~1 mm thick were equilibrated at 270 °C for 2 minutes using N₂ as the gas source for the oven to prevent any oxidative degradation. A strain sweep at 10 rad/s was first performed to establish the linear viscoelastic region and appropriate strains selected for frequency sweeps. The rheological properties, including tan delta, storage modulus (G'), loss modulus (G'') and complex viscosity (η^*) of neat PET and PET–MWCNT composites were measured at a constant temperature of 270 °C within the viscoelastic limit of each material. Unfilled PET and the PET–MWCNT 0.5 wt% composite exhibited near-Newtonian behaviour while the composites with 3 wt% and 7 wt% MWCNTs exhibited a clear transition to shear-thinning behaviour. The viscoelastic properties of neat PET were largely unchanged on addition of 0.5 wt% MWCNTs. However, addition of 3 wt% MWCNTs and above to PET resulted in an increase in η^* and G' , especially at low frequencies where the instrument is most sensitive in the detection of pseudo-solid like behaviour, see Figs 18.18 (a) and 18.18 (b). For example, at 0.3 rad/s, the η^* increased from 6 Pa.s for (0.5 wt% MWCNT) to 148 Pa.s (3 wt%), then to 856 Pa.s (7 wt%). G' for neat PET increased by 2 orders of magnitude from about 0.31 to 35 Pa with addition of 3 wt% MWCNTs, and by 3 orders of magnitude from 0.31 to 200 Pa on addition of 7 wt% MWCNTs.

The addition of the high modulus CNTs, as expected, increased the storage modulus of the polymer. A rheological percolation threshold is evident between 0.5 and 3 wt% manifest by a large step increases in η^* and G' at low frequencies. Kim *et al.* observed similar behaviour for melt processed PET–MWCNT composites, although a rheological percolation effect was noticeable on addition of 0.5 wt% MWCNTs (Kim *et al.*, 2007). This behaviour is indicative of the influence of polymer–CNT–polymer interactions and the onset of formation of an interconnected network of CNTs and CNT agglomerates which restrict long-range polymer chain motion.

Further evidence for the formation of a rheological percolated network can be extracted by constructing a Cole–Cole plot, i.e. $\log G'$ versus $\log G''$, see Fig. 18.18 (c). This is analogous to the Cole–Cole plots used in dielectric spectroscopy and described by Han *et al.* to probe temperature induced changes in the microstructure of homo-polymers, block copolymers and blends (Han *et al.*, 1989). Any positive deviation from a linear relationship between G' and G'' is evidence for the

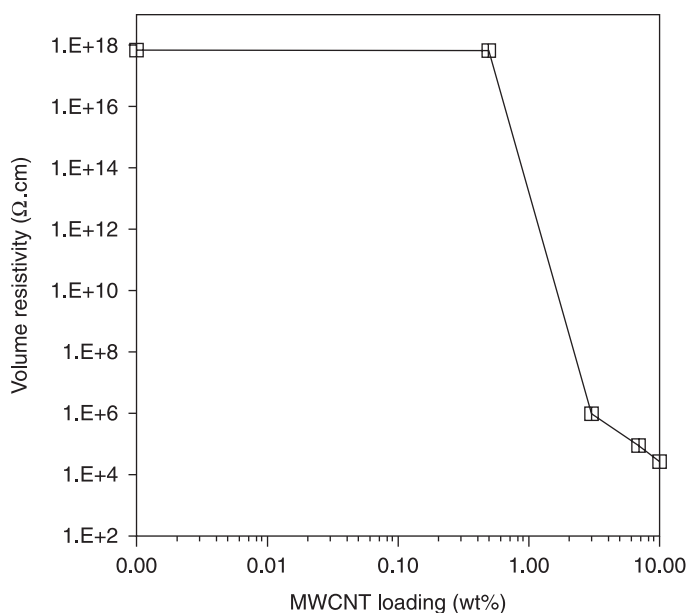


18.18 Variation in: (a) complex viscosity (η^*) as a function of ω ; (b) storage modulus (G') as a function of ω ; (c) Cole–Cole plots (G' versus G''); and (d) inverse loss tangent ($\tan \delta$) $^{-1}$ as a function of ω , for neat PET and PET–MWCNT composites.

formation of a percolated network. From Fig. 18.18 (c), it is obvious that the curves obtained for the 3 wt% and 7 wt% MWCNT composites have noticeably deviated from that for neat PET. The slopes of the Cole–Cole plots decreased with increasing MWCNT content, again indicative of the transition from liquid-like to solid-like behaviour as a consequence of well-dispersed, homogeneous network of high aspect ratio MWCNTs restricting polymer flow. Further evidence for network formation was apparent from a plot of inverse $\tan \delta$ (i.e. $(\tan \delta)^{-1} = G'/G''$) versus frequency, as an increase in $(\tan \delta)^{-1}$ is a measure of the increase in ‘solidity’ of the composite. It can be seen, across the frequency range studied, there is a significant increase in $\tan \delta^{-1}$, and clearly a percolated network is formed below 3 wt% MWCNTs. The formation of a rheological percolated network is governed by a combination of factors including the state of CNT dispersion, CNT alignment and polymer–CNT interactions (chemical and physical).

The formation of an electrically conducting percolated network can be studied by investigating the effect of MWCNT loading on the volume resistivity of a polymer. Volume resistivity is defined as the ratio of the potential gradient parallel to the current in the material to the current density (Shah, 1998). Volume resistivity measurements were made using high accuracy meters, a Keithley 6517A electrometer and a shielded test enclosure (Keithley 8009 resistivity test fixture). High resistivity testing was performed in accordance with ASTM-D257. For samples of low resistivity, two-point probe measurements were used using a Keithley 6517A electrometer in combination with two-point probes and the assistance of silver epoxy contact paint in order to minimise contact resistance effects. Volume resistivity measurements are made by using a strip of composite film of known thickness and geometry from point to point and measurements were made on multiple samples. The change in volume resistivity of neat PET and the PET–MWCNT composites is shown in Fig. 18.19.

The volume resistivity of neat PET was reduced by 12 orders of magnitude (i.e. electrical conductivity increased by 10^{12} S/cm), from 10^{17} to 10^5 $\Omega\cdot\text{cm}$ on the addition of 3 wt% MWCNTs. An electrical percolation threshold (ρ_c) was estimated at approximately 2 wt% MWCNTs. This value is comparable to that reported by Anand *et al.* for PET–SWCNT composites, although a more simple lab-scale kneading process was used to prepare these composites. However, these values are larger than those previously reported for Logakis *et al.* who recorded a $\rho_c = 0.1\text{--}0.2$ wt% for PET–MWCNT composites prepared using a combination



18.19 Variation in volume resistivity as a function of MWCNT loading.

of dry-mixing and twin-screw extrusion (Logakis *et al.*, 2010). In the study by Logakis *et al.*, the authors compared network formation and subsequent electrical conductivity of PET–MWCNT composites prepared by 3 methods, *in-situ* polymerisation, masterbatch dilution by melt mixing and dry blending prior to melt mixing. Electrical percolation values/ranges of 0.06 wt% (0.05–0.1 wt%) and (0.1–0.2 wt%) MWCNTs were achieved for each of the three preparation methodologies, respectively. In contrast, for composites of PET with SWCNTs, a lower electrical percolation of 0.024 wt% was obtained for composites prepared by direct mixing. Interestingly, *in-situ* polymerisation of a PET with the same SWCNTs yielded a higher electrical percolation, $\rho_c = 0.048$ wt%. The authors suggested that SWCNTs must retain some degree of agglomeration to form an electrically conducting network (Hernández *et al.*, 2009). There should be no expectation that an electrical and rheological percolation can be achieved for the same CNT loading. For example, for composites of PET with MWCNTs prepared by solution mixing, rheological and electrical percolation thresholds of 0.6 wt% and 0.9 wt% were obtained, respectively (Hu *et al.*, 2006). The discrepancy arises as the distance required to bridge polymer chains by CNTs and thus constrain polymer chain dynamics is different to the CNT loading required to form an electrically conducting pathway throughout the PET matrix to allow electrons to flow.

18.7 Conclusion and future trends

Composites of MWCNTs and PET were readily prepared using conventional twin-screw extrusion. Examination of these composite materials across the length scales using a combination of POM, FESEM and HRTEM revealed the CNTs were well-dispersed and distributed throughout the PET matrix. However, the number of MWCNT agglomerates increased with increasing MWCNT loading. MWCNTs act as nucleating agents for PET, initiating heterogeneous nucleation and alter PET crystallisation kinetics. From a FTIR study of PET chain conformations, the proportion of polymer chains residing in the *trans* crystalline phase increased relative to those residing in the *gauche* phase, indicating that addition of MWCNTs induced a more crystalline PET structure. Further evidence for increased PET crystalline content on MWCNT addition was also confirmed by Raman spectroscopy. The isothermal and non-isothermal crystallisation kinetics of these composites was investigated using DSC. Both the rate of crystallisation and temperature of crystallisation (T_c) of PET increased significantly on addition of MWCNTs. A critical concentration of MWCNTs (>1 wt%) was required to enhance the thermal stability of PET. MWCNTs provide a barrier to the release of volatiles and decomposed products, retarding the thermal degradation process. An electrical and rheological percolation of the MWCNTs used in this study was achieved at approximately < 2 wt% and < 3 wt%, respectively.

It is conclusive that MWCNTs alter the crystalline structure and electrical, thermal and viscoelastic properties of PET. Exploitation of such composite materials will only be fully realised if they can be prepared using conventional polymer processing methods, such as extrusion and injection moulding. However, there is little published literature which attempts to correlate the relationships between melt processing parameters (e.g. screw speed, screw profile, residence time, temperature) and polymer–CNT composite morphology and properties. Although there has been some focus on this topic recently, see Chapter 4 and (Villmow *et al.*, 2008), more systematic and detailed studies are required in the future. Furthermore, for engineering polymers, such as PET, these materials in most instances undergo secondary processing which typically includes uniaxial and/or biaxial deformation, e.g. stretch blow moulding of a PET bottle. Therefore, the final properties of the composite are only partly governed by the polymer–CNT morphology achieved post melt mixing. Again, future work must focus on the effect of quasi-solid and solid state deformation on polymer–CNT composite micro- and nano-structure.

18.8 Acknowledgements

The authors acknowledge the support of The Royal Society (574006/G503/24135) and The Nuffield Foundation (NAL/00696/G). We thank Dr Andrew Dennis (Avalon Instruments) for helpful discussions and BM thanks DEL and QUB for funding a studentship. The authors also acknowledge the formal exchange agreement between UQ and QUB that facilitates ongoing collaborations.

18.9 References

- Ahn, B.W., Chi, Y.S., Kang, T.J. (2008) 'Preparation and characterisation of multi-walled carbon nanotube/poly(ethylene terephthalate) nanoweb', *Journal of Applied Polymer Science*, 110(6), 4055–4063.
- Ahn, K. S., Kim, J.S., Kim, C.O., Hong, J.P. (2003) 'Non-reactive RF treatment of multiwall carbon nanotube with inert argon plasma for enhanced field emission', *Carbon*, 41, 2481–2485.
- Ajayan, P.M., Stephan, O., Colliex, C., Trauth, D. (1994) 'Aligned carbon nanotube arrays formed by cutting a polymer resin-nanotube composite', *Science*, 265(5176), 1212–1214.
- Anand K, A., Agarwal, U.S., Joseph, R. (2007) 'Carbon nanotubes-reinforced PET nanocomposite by melt-compounding', *Journal of Applied Polymer Science*, 104(5), 3090–3095.
- Antoniadis, G., Paraskevopoulos, K.M., Bikiaris, D., Chrissafis, K. (2009) 'Melt crystallisation mechanism of poly(ethylene terephthalate)/multi-walled carbon nanotubes prepared by *in situ* polymerisation', *Journal of Polymer Science:Part B: Polymer Physics*, 47(15), 1452–1466.
- Avrami, M. (1939) 'Kinetics of phase change. I General theory', *Journal of Chemical Physics*, 7, 12, 1103–1112.

- Avrami, M. (1941) 'Granulation, phase change and microstructure kinetics of phase change III', *Journal of Chemical Physics*, 9(2), 177–184.
- Barber, A.H., Cohen S.R., Wagner, H.D. (2003) 'Measurement of carbon-nanotube-polymer interfacial strength', *Applied Physics Letters*, 82(23), 4140–4142.
- Boswell, P.G. (1980) 'On the calculation of activation energies using a modified Kissinger method', *Journal of Thermal Analysis*, 18, 353–358.
- Chen, H., Liu, Z., Cebe, P. (2009) 'Chain confinement in electrospun nanofibers of PET with carbon nanotubes', *Polymer*, 50(3), 872–880.
- Cole, K.C., Aiji, A., Pellerin, E. (2002a) 'New insights into the development of ordered structure in poly(ethylene terephthalate). 1. Results from external reflection infrared spectroscopy', *Macromolecules*, 35(3), 770–784.
- Cole, K.C., Aiji, A., Pellerin, E. (2002b) 'New insights into the development of ordered structure in poly(ethylene terephthalate). 2. Results from transmission infrared spectroscopy of thin films', *Macromolecular Symposia*, 184, 1–18.
- Du, F., Scogna, R.C., Zhou, W., Brand, S., Fischer, J.E., Winey, K. (2004) 'Nanotube networks in polymer nanocomposites: rheology and electrical conductivity', *Macromolecules*, 37(24), 9048–9055.
- Evans, U.R. (1945) 'The laws of expanding circles and spheres in relation to the lateral growth of surface films and the grain size of metals', *Transactions of the Faraday Society*, 41, 365–374.
- Fakirov, S., Fischer, E.W., Schmidt, G.F. (1975) 'Unit cell dimensions of poly(ethylene terephthalate)', *Die Makromolekulare Chemie*, 176(8), 2459–2465.
- Frank, S., Poncharal, P., Wang, Z. L., de Heer, W.A. (1998) 'Carbon nanotube quantum resistors', *Science*, 280(5370), 1744–1746.
- Fujii, M., Zhang, X., Xie, H., Ago, H., Takahashi, K., Ikuta, T., Abe H., Shimizu, T. (2005) 'Measuring the thermal conductivity of a single carbon nanotube', *Phys. Rev. Lett.*, 95(6), 065502(4).
- Gao, Y., Wang, Y., Shi, J., Bai, H., Song, B. (2008) 'Functionalised multi-walled carbon nanotubes improve non-isothermal crystallisation of poly(ethylene terephthalate)', *Polymer Testing*, 27, 179–188.
- Han, C.D., Kim, J., Kim, J.K. (1989) 'Determination of the order-disorder transition temperature of block copolymers', *Macromolecules*, 22(1), 383–394.
- Hernández, J.J., García-Gutiérrez, M.C., Nogales, A. Rueda, D.R., Kwiatkowska, M., Szymczyk, A., Roslaniec, Z., Concheso, A., Guinea, I., Ezquerra, T.A. (2009) 'Influence of preparation procedure on the conductivity and transparency of SWCNT-polymer nanocomposites', *Composites Science and Technology*, 69(11–12), 1867–1872.
- Hu, G., Zhao, C., Zhang, S., Yang, M., Wang, Z. (2006) 'Low percolation thresholds of electrical conductivity and rheology in poly(ethylene terephthalate) through the networks of multi-walled carbon nanotubes', *Polymer*, 47, 480–488.
- Iijima, S. (1991) 'Helical microtubules of graphitic carbon', *Nature*, 354, 56–58.
- Jin, S.H., Park, Y-B., Yoon, K.H. (2007) 'Rheological and mechanical properties of surface modified multi-walled carbon nanotube-filled PET composite', *Composites Science and Technology*, 67, 3434–3441.
- Jin, S.H., Yoon, K.H., Park, Y-B., Bang, D.S., (2008) 'Properties of surface-modified multiwalled carbon nanotube filled poly(ethylene terephthalate) composite films', *Journal of Applied Polymer Science*, 107(2), 1163–1168.
- Kiflie, Z., Piccarolo, S., Brucato, V., Balta-Calleja, F.J. (2002) 'Role of thermal history on quiescent cold crystallisation of PET', *Polymer*, 43(16), 4487–4493.

- Kim, J.Y., Park, H.S., Kim, S.H. (2007) 'Multiwall carbon nanotube-reinforced poly(ethylene terephthalate) nanocomposites by melt compounding', *Journal of Applied Polymer Science*, 103(3), 1450–1457.
- Kissinger, H.E. (1956) 'Variation of peak temperature with heating rate in differential thermal analysis', *Journal of Research National Bureau of Standards (USA)*, 57, 217–221.
- Kobayashi, H., Shioya, M., Tanaka, T., Irisawa, T., Sakurai, S., Yamamoto, K. (2007) 'A comparative study of fracture behaviour between carbon black/poly(ethylene terephthalate) and multiwalled carbon nanotube/poly(ethylene terephthalate) composite films', *Journal of Applied Polymer Science*, 106(1), 152–160.
- Lee, H-J., Oh, S-J., Choi, J-Y., Kim, J.W., Han, J., Tan, L-S., Baek, J-B. (2005) 'In situ synthesis of poly(ethylene terephthalate) (PET) in ethylene glycol containing terephthalic acid and functionalised multiwalled carbon nanotubes (MWNTs) as an approach to MWNT/PET nanocomposites', *Chem. Mater.*, 17(20), 5057–5064.
- Li, Y., Zhou, C., Wang, G., Tao, Y., Liu Q., Li, Y. (2002) 'Isothermal and non-isothermal crystallisation kinetics of elastomeric polypropylene', *Polymer Testing*, 21(5), 583–589.
- Liao, K., Li, S. (2001) 'Interfacial characteristics of a carbon nanotube-polystyrene composite system', *Applied Physics Letters*, 79(25), 4225–4227.
- Liu, S., Yu, Y., Cui, Y., Zhang H., Mo, Z. (1998) 'Isothermal and non-isothermal crystallisation kinetics of nylon-11', *Journal of Applied Polymer Science*, 70(12), 2371–2380.
- Logakis, E., Pissis, P., Pospiech, D., Korwitz, A., Krause, B., Reuter, U., Pötschke, P. (2010) 'Low electrical percolation threshold in poly(ethylene terephthalate)/multi-walled carbon nanotube nanocomposites', *European Polymer Journal*, 46(5), 928–936.
- López, L.C., Wilkes, G.L. (1989) 'Nonisothermal crystallisation kinetics of poly (p-phenylene sulphide)', *Polymer*, 30(5), 882–887.
- Luo, P., Jiang, K., Wang, K., Yang, J., Xu, T., Chen, L., Fu, Q. (2009) 'Plasma treatment-induced fluorine-functionalised multi-walled carbon nanotubes to modify poly(ethylene terephthalate) obtained via *in situ* polymerisation', *Polymer International*, 59(2), 198–203.
- McClory, C., Chin, S.J., McNally, T. (2009) 'Polymer carbon nanotube composites', *Australian Journal of Chemistry*, 62(8), 762–785.
- McFerran, N.L.A., Armstrong, C.G., McNally, T. (2008) 'Non-isothermal and isothermal crystallisation kinetics of Nylon-12', *Journal of Applied Polymer Science*, 110(2), 1043–1058.
- Mubarak, Y., Harkin-Jones, E.M.A., Martin, P.J., Ahmad, M. (2001) 'Modelling of non-isothermal crystallisation kinetics of isotactic polypropylene', *Polymer*, 42(7), 3171–3182.
- Ozawa, T. (1971) 'Kinetics of non-isothermal crystallisation', *Polymer*, 12, 150–158.
- Pötschke, P., Fornes T.D., Paul, D.R. (2002) 'Rheological behaviour of multiwalled carbon nanotube polycarbonate composites', *Polymer*, 43(11), 3247–3255.
- Quintanilla, L., Alonso, M., Rodríguez-Cabello, J.C., Pastor, J.M. (1996) 'Structural analysis of poly(ethylene terephthalate) reinforced with glass fiber: thermal behaviour and correlation between PA-FTIR and DSC measurements', *Journal of Applied Polymer Science*, 59(5), 769–774.
- Sajkiewicz, P., Carpaneto, L., Wasiak, A. (2001) 'Application of the Ozawa model to nonisothermal crystallisation of poly(ethylene terephthalate)' *Polymer*, 42(12), 5365–5370.
- Schadler, L.S., Giannaris, S.C., Ajayan, P.M. (1998) 'Load transfer in carbon nanotube epoxy composites', *Applied Physics Letters*, 73(26), 3842–3844.

- Shah, V. (1998) *Handbook of Plastics Testing Technology*, Pomona, CA: Performance Engineered Products, Inc.
- Tongyin, Y.U., Haishan, B.U., Jiacong, H.U., Wei, Z., Qiaoying, G. (1983) 'The double melting peaks of poly(ethylene terephthalate)', *Chinese Journal of Polymer Science*, 1(1), 83–91.
- Treacy, M., Ebbesen, T., Gibson, J. (1996) 'Exceptionally high Young's modulus observed for individual carbon nanotubes', *Nature*, 381, 678–680.
- Tzavalas, S., Drakonakis, V., Mouzakis, D.E., Fischer, D., Gregoriou, V.G. (2006) 'Effect of carboxy-functionalised multiwall nanotubes (MWNT-COOH) on the crystallisation and chain conformations of poly(ethylene terephthalate) PET in PET-MWNT nanocomposites', *Macromolecules*, 39, 9150–9156.
- Tzavalas, S., Gregoriou, V.G. (2008) 'Uniaxially stretched PET/PET-MWNT nanocomposites: effect of the MWNTs on the chain conformations of PET', *Vibrational Spectroscopy*, 46(2), 135–140.
- Tzavalas, S., Mouzakis, D.E., Drakonakis, V., Gregoriou, V.G. (2008) 'Poly(ethylene terephthalate)-multiwall nanotube nanocomposites: effect of nanotubes on the conformations, crystallinity and crystallisation behaviour of PET', *Journal Polymer Science: Pt. B: Polymer Physics*, 46(7), 668–676.
- Vaia, R.A. (2000) 'Structural characterisation of polymer-layered silicate nanocomposites', in T.J. Pinnavaia, and G.W. Beall (eds) *Polymer-Clay Nanocomposites*, Chichester: John Wiley & Sons, Ltd.
- Villmow, T., Pegel, S., Pötschke, P., Wagenknecht, U. (2008) 'Influence of injection molding parameters on the electrical resistivity of polycarbonate filled with multi-walled carbon nanotubes', *Composites Science & Technology*, 68(3–4), 777–789.
- Wagner, H.D., Lourie, O., Feldman Y., Tenne, R. (1998) 'Stress-induced fragmentation of multiwall carbon nanotubes in a polymer matrix', *Applied Physics Letters*, 72(2), 188–190.
- Wang, Y., Deng, J., Wang, K., Zhang, Q., Fu, Q. (2007) 'Morphology, crystallisation and mechanical properties of poly(ethylene terephthalate)/multiwall carbon nanotube nanocomposites via *in situ* polymerisation with very low content of multiwall carbon nanotubes', *Journal of Applied Polymer Science*, 104, 3695–3701.
- Yeh, W.Y. and Young, R.J. (1998) 'Deformation processes in poly(ethylene terephthalate) fibers', *J. Macromol. Sci. Phys., B*, 37(1), 83–118.
- Yoo, H.J., Jung, Y.C., Cho, J.W. (2008) 'Effect of interaction between poly(ethylene terephthalate) and carbon nanotubes on the morphology and properties of their nanocomposites', *Journal of Polymer Science: Part B: Polymer Physics*, 46, 900–910.
- Yu, K., Zhu, Z., Xu, M., Li, Q., Lu, W. (2003) 'Electron field emission from soluble carbon nanotube films treated by hydrogen plasma', *Chemical Physics Letters*, 373, 109–114.
- Yu, M-F., Lourie, O., Dyer, M.J., Moloni, K., Kelly, T.F., Ruoff, R.S. (2000) 'Strength and breaking mechanism of multi-walled carbon nanotubes under tensile load', *Science*, 287(5453), 637–640.

Carbon nanotubes in multiphase polymer blends

A. GÖLDEL and P. PÖTSCHKE, Leibniz Institute of Polymer Research Dresden, Germany

Abstract: Nowadays, melt blending of two or more polymers in a conventional extruder is one of the cheapest and fastest ways to tailor the material's properties according to the requirements of novel applications. By combining the various blend phase structures and property profiles with a conductive, high aspect ratio nanofiller such as carbon nanotubes (CNTs), specific morphological structures can be achieved that offer a much higher potential for the development of new functional materials than single-polymer composites. Thus, understanding and control of CNT localization inside the developing phase morphology during melt mixing are the keys to the desired structures and thus to new high performance materials.

Key words: aspect ratio, blend morphology, CNT dispersion, CNT migration, CNT transfer, double percolation, electrical conductivity, filler geometry, interface, melt mixing, morphology development, polymer blend, rheology, selective localization.

19.1 Introduction

Around the turn of the millennium, polymer blends constituted 36% of the total polymer production and are still growing far above average (Utracki, 2002). The combination of conductive, high aspect ratio nanofillers such as carbon nanotubes (CNTs) with the various phase structures and property profiles of polymer blends offers, compared to single-polymer composites, a much higher potential for the development of CNT-based functional materials for commercial applications.

This chapter introduces the most important phenomena regarding melt processing of thermoplastic polymer blends with CNTs and the connected morphological structures and thus the general properties of the resulting blends. The discussion is focused on melt processing as it is by far the most common and easiest production method for polymer blends and thermoplastics.

Generally, the field of CNT-filled polymer blends is closely connected to the other topics of CNT research. CNT production processes and the related surface characteristics, but also the aspect ratios, determine the localization behaviour in multiphase mixtures. The preference of CNTs for specific blend phases provides information about the interactions and interfacial energies of CNTs and polymers in the blend. These are, in turn, crucial factors for the strength of the polymer–CNT interface and the dispersability of primary CNT agglomerates (see Chapter 4).

Understanding and control of CNT localization inside the phase structure of molten polymers during melt blending are the keys to adjusting the macroscopic properties according to the requirements and thus achieve new commercial applications. Therefore, this topic is most comprehensively covered in this chapter, including the state of the art (Section 19.2). The present state of the discussion about the determination and importance of thermodynamic driving forces during melt blending is discussed next (Section 19.3.1). The explicit and fast selective localization of CNTs in one specific blend phase that is a peculiarity of CNTs and can include the CNT transfer from one phase to the other during a typical extrusion process is subsequently described with the help of an example (Section 19.3.2). Subsequently, the impact of the CNT aspect ratio on the peculiarities of the transfer and the localization within the blend morphology is discussed (Section 19.3.3).

Implications of the effect of selectively CNT-filled phases, that are typically obtained during and after melt blending on the final blend morphologies and the melt rheology are addressed in Section 19.3.4. Moreover, the present knowledge about the dynamics and the peculiarities of the CNT transfer from one thermodynamically unfavourable phase to another that can occur in extruders, kneaders or microcompounders is discussed (Section 19.3.5). The peculiarities of melt mixed CNT-filled blends are summarized in Section 19.3.6. A brief look at the possibilities of tailoring the localization of CNTs by utilizing chemically modified CNTs and reactive blend components is also presented (Section 19.4).

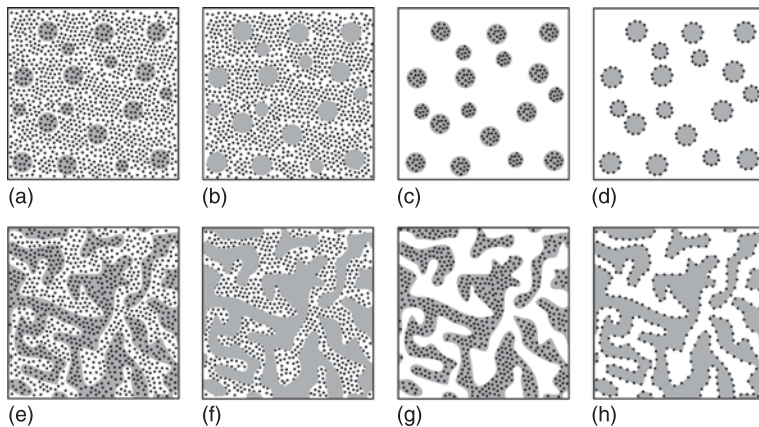
Finally, as an example of PC–ABS–CNT blends, the possibility of exploiting the discussed features of blends with CNTs in the manufacture of new functional materials is shown (Section 19.5). At the end of the chapter, a brief future outlook for the further potential of CNT blend nanocomposites is sketched, concerning the properties and the potential of so far unrealized morphologies of blends with carbon nanotubes (Section 19.6).

19.2 Current state of melt mixing polymer blends with nanotubes

The focus of this chapter is to summarize the experiences and approaches regarding the morphological features and the localization behaviour of CNTs in the blend phases during melt blending. The arrangement of morphological structures directly determines the macroscopic properties, and therefore understanding and control of CNT localization in typical melt mixing processes such as twin-screw extrusion opens the door to new commercial applications of functional polymer blends. Figure 19.1 shows possible combinations of phase morphologies and nanofiller localizations in a dual-phase polymer blend. These morphologies can also be adjusted with fillers that are not nanoscaled if those are sufficiently small, compared to the blend morphology. For commercial blends with a balanced property profile and sufficient compatibility, the phase size is

below the micro-level and thus only nanofillers will fulfil the precondition. For CNTs, due to the greatly differing diameters and lengths that result from the various production processes, a differentiated view is needed in this context. Typical diameters are from 1–50 nm and from 1 to more than 1000 μm length. Therefore, long tubes can be inhibited from penetrating in one blend phase or from positioning at the interface, whereas the diameters are always sufficiently small. In order to utilize combined approaches like those displayed in Fig. 19.1, the sizes of the blend system and the CNTs have to be appropriately selected. Furthermore, sufficient dispersion of the CNT primary agglomerates is also an essential precondition. If these major requirements are met, the combination of nanofillers with new or existing combinations of polymers will enable the rapid design and manufacture of new materials with properties that can be tailored according to the needs of the application.

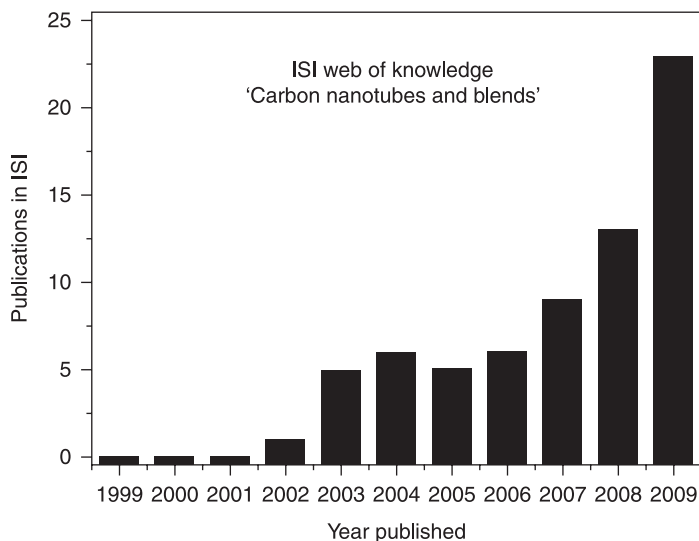
Thus, due to the greatly increasing production capacities and decreasing costs of multi-walled carbon nanotubes (MWCNTs), the melt processing of polymer



19.1 Possible combinations of phase morphologies in a dual-phase polymer blend with one nanoscaled filler. Even though the displayed schemes describe the most simple case, as only two phases and one filler are present, the combination of different blend morphologies and filler localizations results in a high variety of possible morphological structures. Sea-island morphologies with different nanofiller localizations might have interesting mechanical properties (a–d) but the potential is limited in terms of electrical conductivity. Co-continuous blends with unique filler distribution in both blend phases (e) can combine the advantages of both blend phases, while the filler provides certain properties or functionality. Double percolated blend structures (f, g) and co-continuous blends with filler-saturated interface (h) are presently the structures with the highest potential for commercial applications, as they can provide maximum blend functionality for minimum filler contents.

blends with different grades of MWCNTs has attracted significant interest in recent years. The promising experimental results of already published studies that indicate the possibility of manufacturing conductive blends with very low contents of CNTs are one of the reasons that motivate increasing research activity in the field of CNTs in polymer blends (Fig. 19.2). High economic potential can be expected when research leads to understanding and finally enables control of the CNT localization during extrusion. Presently, it is too early for generally valid conclusions and the research is focused on describing the phenomenology of blends with CNTs.

It is important to note that of the various possible combined morphological arrangements (Fig. 19.1), each has unique properties, but only a very few have desirable material properties. Superior properties can be expected specifically from two scenarios, both of them requiring co-continuous blend morphologies: on the one hand, the localization of fillers directly at the interface (Fig. 19.1 (h)), on the other, the selective filling of only one of the blend phases (Fig. 19.1 (g)). Whereas the former is believed to be the ideal scenario to achieve the lowest possible percolation concentrations, it is difficult to undertake and stabilize for high-aspect fillers such as carbon nanotubes. The reasons for this will be discussed in Section 19.3.3. In contrast, the implementation of blends with selective CNT-filled phases is feasible for different blend systems. In this context, the term of double percolation (Fig. 19.1 (g)) was initially introduced by (Sumita *et al.*, 1991) for immiscible blends where the percolation of a selective carbon-black filled blend phase (first percolation) in combination with the formation of a network of



19.2 Development of scientific research on CNTs in polymer blends between 1999 and 2009 (ISI, 2009).

carbon black particles within the percolated blend phase (second percolation) enabled the formation of conductive pathways with significantly reduced contents of conductive filler. Since then, the occurrence of double percolation has been described for several blend systems.

Among these, co-continuous, compatible blends of PC and SAN are so far closest to the model scenario due to the almost ideal selectivity and continuity of the structures (Gödel *et al.*, 2009a). Therefore, and as they are unaffected by crystallization phenomena, they are very suitable to discuss as examples of the peculiarities of MWCNTs in polymer blends. Thus, these blends will be addressed and described in different contexts in the following, completing the available contributions from the literature for the specific topics. Other examples of selective localization of MWCNTs in polymer blends with commercially important thermoplastics after melt mixing can be found for HDPE–PC, HDPE–PA6, PET–PVDF, PC–PE; PC–PP, PPS–PA66, PCL–PLA, PVDF–PA6, and PA6–ABS (Meincke *et al.*, 2004; Wu and Shaw, 2004; Pötschke *et al.*, 2005; Pötschke *et al.*, 2007; Pötschke *et al.*, 2008; Zou *et al.*, 2006; Li and Shimizu, 2008; Wu D, 2009) and are summarized in Table 19.1. For SWCNT, presently no related literature is available, most probably as melt blending requires relatively high quantities of CNTs, thus making melt mixing experiments presently extremely expensive.

In the listed literature, commonly MWCNTs are melt-blended with two immiscible polymers, and some specific material properties are discussed and correlated with the observed morphological structures. Versatile proceedings are described and the topic is approached from many different viewpoints, therefore a direct comparison of the different trends that have been observed so far is very difficult. Thus, it is too early to derive general correlations for many important issues. Representatively, and as an issue of central importance, the calculation or measurement of thermodynamic driving forces that determine the CNT transfer during melt mixing is still subject to serious uncertainties and inexplicable exceptions, where existing concepts like the wetting coefficient fail. The possibility of being misguided by the predictions of this equation increases with the decreasing differences in surface tensions and related polar contributions between the two polymer partners involved. As those differences are large for most of the listed examples, specifically for polyolefins with polar polymers, relatively good consistencies of predictions and localization behaviour are obtained. It appears that MWCNTs strictly avoid e.g. the polyolefin phases if another, more polar phase is present during blending. This localization behaviour strongly indicates that most MWCNTs reveal surface polarities that are significantly above those of the neat and ideal graphitic structures. One reason for this is the fact that, due to the specific multi-walled feature of MWCNTs, a small mass percentage of oxygen or nitrogen within the overall carbon content results specifically for a high number of walls in a relatively high density of these elements on the outer tube surface and an increased surface polarity. Consequently, SWCNTs with identical mass fractions of these

Table 19.1 Selected studies related to the localization of CNTs in melt mixed polymer blends

Blend system	Source	CNT grade	Method	Peculiarities in mixing regime	Wetting coeff.*	Localization of CNTs
<i>Non-reactive blend composites</i>						
PC-SAN	(Gödel <i>et al.</i> , 2009)	MWCNT	Melt mixing	Compatible blend/co-continuous morphology	Y/Y	PC
HDPE-PC HDPE-PA6	(Pötschke <i>et al.</i> , 2008)	MWCNT	Melt mixing	CNT-transfer/masterbatches	Y/Y	PC PA6
PET-PVDF	(Wu and Shaw, 2004)	MWCNT	Extrusion/ injection moulding	Double percolation in injection moulded parts/ improved conductivity	Y/Y	PET
PC-PE	(Pötschke <i>et al.</i> , 2005)	MWCNT	Melt mixing	Masterbatch technology/double percolation at low contents of CNT-filled phase	No	PC
PP-PC	(Pötschke <i>et al.</i> , 2007)	MWCNT	Melt mixing	Exfoliated and intercalated MMT at the interface, MWCNT in PC	No	PC
PPS-PA66	(Zou <i>et al.</i> , 2006)	MWCNT	Dry mixing + melt mixing	Change of blend continuity with CNT content + change of domain size	No	PA 66
PCL-PLA	(Wu, 2009)	Functionalized MWCNT	Melt mixing	Phase morphology change compatibilization improvement of mechanical properties	No	PCL and interface
PA6-(P)EA PA12-(P)EA	(Baudouin, 2010b)	MWCNT	Melt mixing	Stable localization of unmodified tubes at the interface of a non-reactive polymer blend	Y/~	Polymer+ interface
Copolymers (PA6-12-copo)- (EMA-copo)	(Baudouin <i>et al.</i> , 2010a)	MWCNT	Melt mixing	Copolymer of ethylene and methyl acrylate (EMA) and PA6/12 copolymer	Y/~	Polymer+ interface

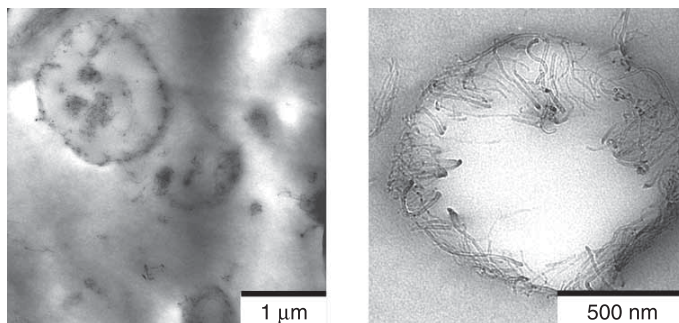
PVDF-PA6	(Li and Shimizu, 2008)	MWCNT	High shear processing	Phase morphology change-increase of melt viscosity of selectively MWCNT filled blend phase-change of phase-inversion concentration	No	PA 6
PA6-ABS	(Meincke <i>et al.</i> , 2004)	MWCNT	Melt mixing	Mechanical properties	No	PA 6
<i>Reactive blend composites</i>						
PA6-PP+MPP	(Zhang <i>et al.</i> , 2009)	MWCNT	Melt mixing	Reactive component maleated polypropylene (MPP) decrease in the size of the dispersed particles	Y/N	Most in PA 6, some at interface

Note: * The wetting coefficient column denotes whether the wetting coefficient was discussed/whether the prediction of the wetting coefficient is consistent with the observed CNT localization (Y/Y, Y/N).

elements reveal much lower densities on the tube surface and therefore can behave significantly differently. Furthermore, lower tube diameters are supposed to result in more extreme wetting angles, thus reinforcing either the repulsive or the attractive forces towards the respective polymer for SWCNTs.

Actual research reveals two new viewpoints beyond the traditional concepts to describe the localization behaviour of nanofillers. First, the impact of the particle aspect ratio on the speed of the CNT transfer and the stability at the blend interface (Section 19.3.3), and, second, the irreversible absorption of specific polymers on the CNT surface. This phenomenon accounts for so far the only example in literature, where the localization of a significant amount of MWCNTs at the interface of a polymer blend is stable during mixing (Fig. 19.3) and occurs in the absence of any chemical reaction (Baudouin *et al.*, 2010a; Baudouin *et al.*, 2010b). Irreversible absorption of polymers on fillers is found to occur only for a few specific polymers and is a field of science that is not directly connected to the discussion of filler localizations during blending. Nevertheless, if present, it can have a strong impact, as the sections of the tube where the polymer chains are adsorbed are efficiently anchored at the respective blend phase. Attempts are made to decouple the CNT localization from the thermodynamical driving forces by using modified CNTs and a chemically active additive in the blend (Section 19.4).

Summarizing the present state of the art, a dynamic development is presently observable in the field of polymer blends with CNTs. At the moment, the possibilities of designing new desirable structures have not been fully exploited. Several phenomena that determine the morphological features have not been



19.3 MWCNTs in a blend of copolyamide 6/12 (PA6/12) with a copolymer of ethylene and methyl acrylate (EMA). For these polymers, the MWCNTs show a strong deviation from their regular localization in one of the blend phases and a significant amount of MWCNTs can be found at the interface of the polymer blend during melt mixing. Reprinted with permission from Elsevier (Baudouin *et al.*, 2010a).

completely understood so far. Furthermore, experimental skill and labour will be needed to characterize, e.g. the mechanical properties of CNT blend structures independent of the CNT dispersion and the CNT-induced changes of the polymer phases such as crystallization or compatibilization. The literature provides the first indications of structure–property relationships of these special nanocomposite blends, whereas it is too early to derive generally valid conclusions in this field.

Nevertheless, it is now already possible to significantly reduce electrical percolation thresholds by employing the selective localization of CNTs during blending. In the medium term, by understanding and tailoring the morphology development, antistatic materials with ultralow percolation thresholds seem to be feasible. Thus, functional multiphase systems could be developed, that by far exceed the properties of the presently available materials and those of other CNT-filled bulk materials.

19.3 Localization of CNTs in polymer blends during melt mixing

19.3.1 Thermodynamic driving forces – a controversial discussion

In the literature, localization of fillers in thermoplastic polymer blends most commonly is explained by the general tendency of interfacial energy minimization, which results in a more or less pronounced driving force to arrange the fillers in that particular blend phase that is energetically preferred. This means that fillers that are incorporated in the thermodynamically unfavourable phase will be transferred to the most favourable phase of the blend during mixing. The transfer is a process that is dependent on time and mixing intensity, therefore non-equilibrium transition states can be obtained that are stabilized during solidification of the polymer blend after mixing. Preferential localization of fillers in one of the blend phases is most commonly correlated with the differences in interfacial energies of filler and the respective polymers that originate in the differing polarities and surface energies. To quantify the driving forces (Sumita *et al.*, 1991) introduced the wetting coefficient ω from Young's equation that describes the adjustment of wetting angles on ideally plane surfaces (Equation 19.1) This is presently the most common approach to predict the filler localization after melt blending:

$$\omega = \frac{\gamma_{\text{filler-polymer 1}} - \gamma_{\text{filler-polymer 2}}}{\gamma_{\text{polymer 1,2}}} \quad [19.1]$$

Based on the different interfacial energies γ between the liquid phases and fillers, the equilibrium filler localization can be calculated. The wetting coefficient most commonly is interpreted in a way that for $\omega < -1$, the filler is predicted to be in polymer 1 and for $\omega > -1$ in polymer 2. In the interval between 1 and -1 , fillers

are predicted to be at the interface. In Section 19.3.3, the influence of the filler geometry on the range of this interval and the consequences for melt blending of nanoscaled fillers are described.

The fact that a reliable prediction requires the exact calculation of the wetting coefficient and thus the exact measurement of the interfacial tensions between the blend polymers and the filler, can be considered the main drawback of the concept, which is designed for ideally plane surfaces. Unfortunately, typical nanoscaled fillers reveal macro-, micro-, and nanostructured surfaces that, according to the Lotus Effect, have a strong impact on the apparent wetting angle. Therefore, the standard measurement methods that are based on the measurement of the contact angle between nanofiller and polymer fail. These measurement problems can be avoided by calculating the interfacial energies from the individual surface energies of the polymers and the nanofillers. Thus, the thermodynamic preferences can be obtained for combinations of CNTs and polymers that so far have not yet been investigated. Nevertheless, reliable surface energy values are required. For CNTs, and despite the enormous experimental efforts by different research groups, the suitability of methods and the obtained surface energies are still the topic of controversial discussion. The main challenge is, as mentioned above, to avoid any measurement disturbance by the surface geometries. One example of how to overcome this problem is the studies of (Nuriel *et al.*, 2005) and (Barber *et al.*, 2004) that determined the interactions of isolated carbon nanotubes with well-known liquids and polymers. It is obvious that these procedures that include the operation of individual MWCNTs need enormous experimental skills and labour. Very recently, attempts were made to access the surface properties of CNTs by studying their gas adsorption behaviour using inverse gas chromatography (Menzel *et al.*, 2009). This method results in surface energies that are much higher than the above-mentioned values from the group of H. D. Wagner.

Another very recent approach is to access the interfacial energies between polymers and CNTs by implementing modulated differential scanning calorimetry. Thus, the influence of carbon nanotubes on the change of the heat capacity at the glass transition temperatures can be evaluated (Miltner *et al.*, 2007). As well as these measuring concepts, there are attempts to access the interactions of different polymers and carbon nanotubes by molecular dynamics simulation (Yang *et al.*, 2005). It is the task of future studies to evaluate which concepts will produce the most reliable predictions.

The results of the different methods show a very broad spectrum of CNT surface energies and polarities which might be due to the method itself or to the different characteristics and treatment histories of the investigated CNTs. Therefore, there is an urgent need for comparative investigations and standardization, and the literature sources for the calculation of interfacial tensions have to be carefully selected. Generally, predictions of filler localizations can be performed based on different concepts; for polymer blends with conductive fillers, most commonly the wetting coefficient is calculated.

The wetting coefficient (Equation 19.1) requires the interfacial energies in the three-component system, which, when applying the concept of polar and dispersive shares of surface energies, can be obtained by the utilization of the harmonic-mean (Equation 19.2) or the geometric-mean equation (Equation 19.3). The geometric-mean equation is described in the literature as more suitable for high surface energies (Wu, 1982):

$$\text{Harmonic-mean equation} \quad \gamma_{12} = \gamma_1 + \gamma_2 - 4 \left[\frac{\gamma_1^d \gamma_2^d}{\gamma_1^d + \gamma_2^d} + \frac{\gamma_1^p \gamma_2^p}{\gamma_1^p + \gamma_2^p} \right] \quad [19.2]$$

$$\text{Geometric-mean equation} \quad \gamma_{12} = \gamma_1 + \gamma_2 - 2 \left(\sqrt{\gamma_1^d \gamma_2^d} + \sqrt{\gamma_1^p \gamma_2^p} \right) \quad [19.3]$$

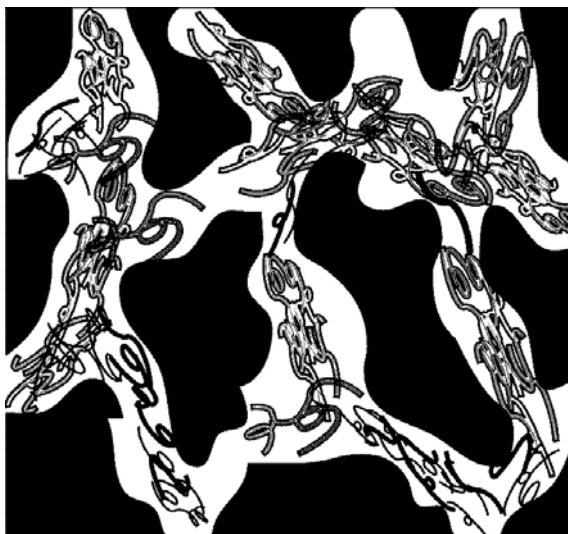
where: γ_1 , γ_2 are the surface energies of components 1 and 2; γ_1^d , γ_2^d are the disperse part of the surface energy of components 1 and 2; γ_1^p , γ_2^p are the polar part of the surface energy of components 1 and 2. Surface energies, disperse and polar contributions of different thermoplastic polymers can be found in online databases (e.g. Holz, 20 Nov. 2007). Some of the studies in Table 19.1 compared the predication of the wetting coefficient or related equations with the localization of carbon nanotubes in an immiscible two-phase blend with their experimental observations (Wu and Shaw, 2004; Pötschke *et al.*, 2008; Gödel *et al.*, 2009a; Baudouin, 2010a; Baudouin, 2010b; Zhang *et al.*, 2009). Generally, it appears that the reliability of the predictions is higher, the more the surface properties of the polymers differ from each other. The prediction is determined by the calculation procedure itself and the literature values for CNTs and polymers. Also for the latter, the insecurities concerning the respective surface energies should not be underestimated. Commercial polymers can exhibit differing polymerization procedures and structural differences while they are still assigned to the same polymer group. Furthermore, different measuring procedures can also result in deviating values. Thus, for the calculation of the wetting coefficient, only consistent literature values should be employed. If not available, the surface characteristics of the respective blend partners should be measured with one measuring method and ideally by the same operator. For CNTs, it appears that the more reliable predictions are obtained, when the selected values reflect to some degree the influence of the polar surface groups on the outer tube surface.

19.3.2 Selective localization of CNTs in double percolated polymer blends

The selective localization of CNTs in one phase of an immiscible polymer blend due to thermodynamic driving forces can occur for various blend systems during melt processing. The speed of CNT transfer and the selectivity of CNT localization presently appear to be superior compared to more traditional fillers such as carbon black or MMT. Whereas these peculiarities will be explained in Section 19.3.3, this chapter describes their exploitation in the manufacture of double percolated

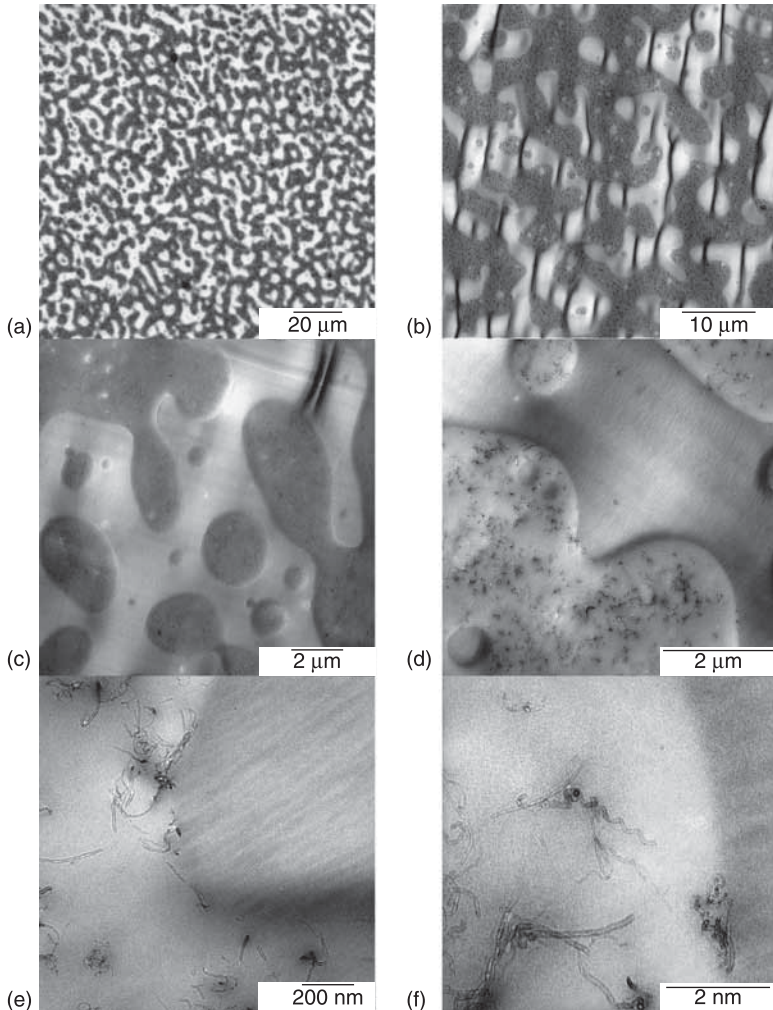
blend structures. Ideally, distinct co-continuous morphologies are combined with the highly selective filling of one of the phases with a percolated CNT network like the structure displayed schematically in Fig. 19.4. There, the continuous, selectively filled phase ensures the electrical conductivity, whereas the other continuous phase is completely free of tubes, but also contributes to thermo-mechanical, mechanical and physical properties and the solvent resistance of the blend. To give an example, the concept can be exploited for PC–SAN blends that are frequently studied to understand processes within the more complex commercial PC–ABS blends.

Whereas PC–SAN blends in principle can show LCST behaviour depending on the molecular structure of PC, the molecular weights and the AN content of the SAN phase, the literature as well as the transfer kinetics and the thermal analyses strongly indicate that both phases of the PC–SAN–MWCNT example blend are completely phase-separated during and after melt mixing. In these blends, PC is the thermodynamically preferred phase and contains almost all CNTs after 5 minutes melt mixing, independent of the mixing regime (Gödel *et al.*, 2009a) (Fig. 19.5). Once in the PC phase, the inverse transfer from PC to SAN is inhibited by the interface (Fig. 19.5 (e) and (f)). Besides the displayed morphologies of PC–SAN, selective localization during and after melt mixing can occur in many blend systems. Double percolation in some cases can be achieved for blends that are adjusted at the very edge of the co-continuous interval as shown, e.g. for blends of PC with only 25 wt% PA6 (Fig. 19.6). Even though the number of electrical pathways in these blends is significantly lower as in those in Fig. 19.5, they are sufficient to manufacture

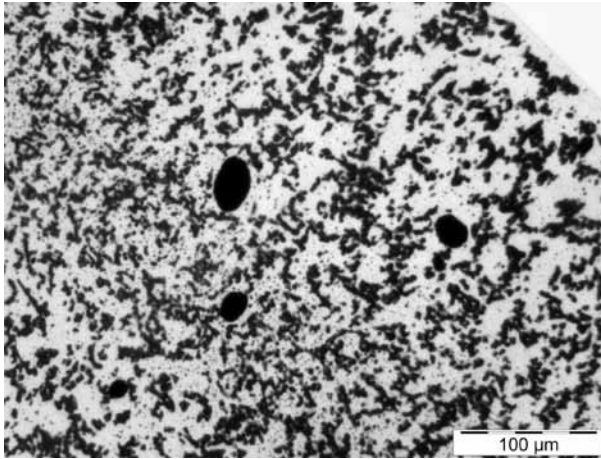


19.4 Double percolated blend with CNTs in one phase and this phase forming a percolated structure in a co-continuous blend.

antistatic composites. The CNT contents can be reduced to one-third or even one-quarter of that of the homopolymers. Also in this blend, the localization behaviour is consistent with the combined concept of wetting coefficient and the particle stability, according to the aspect ratio that is explained in Chapters 15 and 20.



19.5 Morphology of a co-continuous PC-SAN blend with MWCNT Baytubes® C150HP exclusively localized in the PC-phase after 5 minutes melt mixing at 100 rpm in a co-rotating microcompounder. Cutting direction was perpendicular to the die flow. The overall structure of PC-MWCNT (dark) and SAN (bright) can be seen in the transmission-light micrograph (a) and TEM images (b–f). The black lines in (b) and (c) are not a part of the morphology but artefacts from ultrathin cutting.



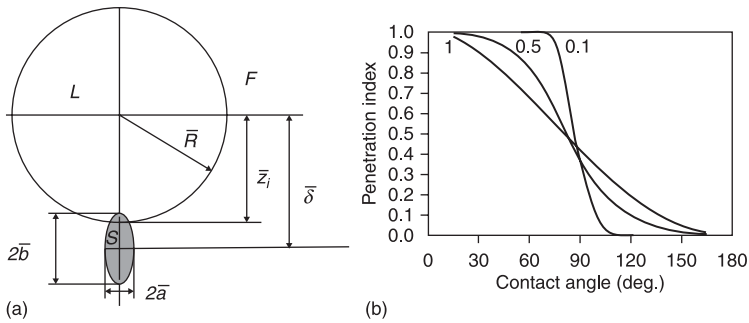
19.6 Another example of selective localization during melt mixing: MWCNTs (Baytubes® C150HP) selectively localized in the PA6 phase of a PA₆₂₅-PC₇₅ blend. Electrical percolation can be achieved for relatively low contents of the selectively filled phase (here 25 wt% PA6). In transmission light microscopy, the PA6 phase content appears to be beyond 25 wt% due to the cut thickness of 5 μm and the small domain size.

19.3.3 Aspect ratio dependence of nanofiller localization and the peculiar migration behaviour of CNTs

In contrast to low-aspect ratio fillers like carbon black, it seems that after melt mixing processes with an average mixing intensity, carbon nanotubes are commonly not, or only to a small extent, located at the interface of a polymer blend. Of that portion, only a small percentage is found to be orientated perpendicular to the interface while bridging both blend phases.

In contrast, the apparently higher stability of carbon black at the interface results, depending on the mixing regime and the thermodynamical driving forces, in less defined localization behaviour. Thus, scenarios where CB is at the interface of a non-reactive immiscible blend (Sumita *et al.*, 1991; Gubbels *et al.*, 1995; Calberg *et al.*, 1999) and/or distributed within one or both of the blend phases after melt mixing (Sumita *et al.*, 1991; Gubbels *et al.*, 1995; Tchoudakov *et al.*, 1996; Thongruang *et al.*, 2002; Feng *et al.*, 2003) are typically observed.

Whereas the surface tensions and polarities of CNTs and CBs can be in a related range and thus should be the interactions with the respective blend phases, their geometrical shapes exhibit a fundamental difference, namely the aspect ratio. The strong impact of this parameter on the equilibrium position of a solid, ellipsoidal particle at the interface of a liquid drop and a surrounding fluid (Fig. 19.7 (a)) was derived mathematically by (Krasovitski and Marmur, 2005).



19.7 Influence of different particle aspect ratios (1, 0.5, 0.1) on the equilibrium position at the interface of a liquid drop and a surrounding liquid. Reprinted with permission from Taylor & Francis (Krasovitski and Marmur, 2005). (a) Solid particle at the interface of a liquid drop and a surrounding liquid. (b) Correlation of penetration index and the contact angle for the attachment of an ellipsoidal particle to a spherical drop, assuming negligible line tension. The penetration index is defined as the share of the particle (0–1) that is penetrating one of the liquids. A penetration index of 0.5 therefore corresponds to equal penetration in both, whereas one or zero is equivalent to a complete penetration into either the liquid drop or the surrounding fluid.

An increase in the particle aspect ratio results in a sharper dependence of the penetration index on the contact angle (Fig. 19.7 (b)). Thus, for very high aspect ratios, the particles are almost completely located within the better wetting phase (for which the contact angle at the intersection of the three interfaces is less than 90°), almost independent of the actual value of the contact angle. Although describing an equilibrium phenomenon, consequences can be derived for the speed of the particle transfer as well as the prediction of the most stable localization during typical melt blending processes in kneaders or extruders (Gödel *et al.*, 2009b). First, the transfer of CB from one phase to the other is slower and the interfacial stability is higher than those of high aspect ratios CNTs. Second, the probability of reaching its lowest possible state of free energy by localizing the filler at the blend interface is relatively high for CB and very low for CNTs. Thus, the interval of wetting coefficient values, where the localization at the interface should occur is broad for CB (–1 and 1) and strictly narrows with increasing effective aspect ratios. This can explain why melt blending of two or more immiscible thermoplastic polymers with CNTs commonly results in morphological structures, where the CNTs are almost completely located in the thermodynamically preferred phase even for low mixing intensities and short mixing times (Gödel *et al.*, 2009b).

To transfer the CNTs from one phase to the other, direct contact with the blend interface is required. Generally, contact can be achieved by a flow field or by the motion of MWCNTs by diffusion, but the latter is very slow due to the MWCNT

diameters that are much larger compared to other macromolecules, even though temperatures during melt blending can exceed 300 °C and thus support Brownian motion in the polymer melt. Therefore, during blending, the contact and thus the transfer will be mainly ensured by the flow field that is characteristic of the mixing process and typically ensures several shear-induced contact locations of any random segment with the interface.

In the absence of supporting parameters like e.g. flow fields, CNTs that are not located at the interface will only be transferred on very long time scales. For the much lighter and more mobile SWCNTs, diffusion could significantly contribute, as their molecular dimensions are comparable to that of typical aromatic thermoplastics and their behaviour is presently discussed and correlated with that of macromolecules (Green *et al.*, 2009).

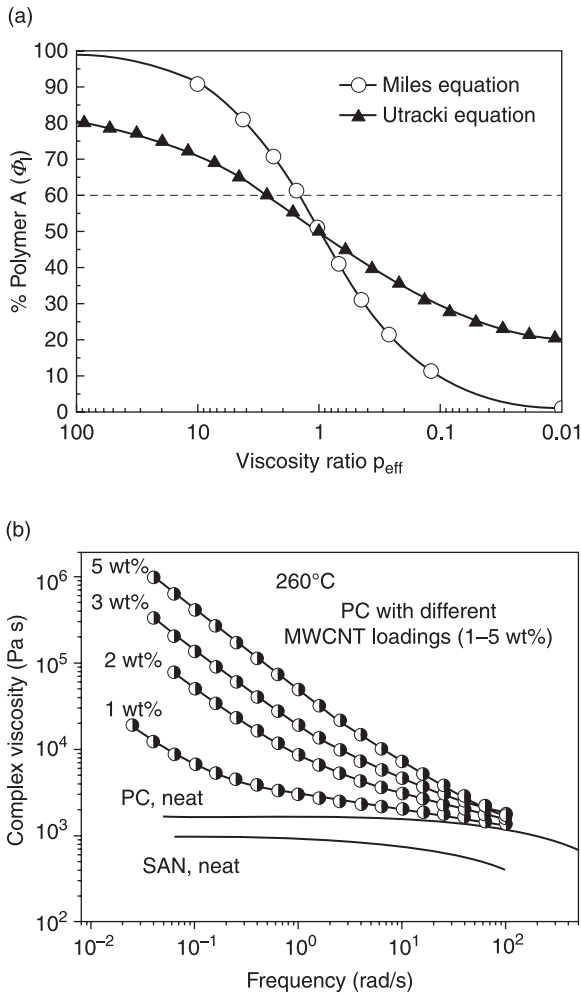
19.3.4 The impact of selective localization on rheological properties and the blend morphology

It is well known that carbon nanotubes strongly interact with the matrix polymer due to their enormous surface area. In the literature, examples can be found of the strong influence of even small concentrations of CNTs on the melt viscosity and the viscoelastic properties of the matrix polymer in the low frequency range, as described first by (Pötschke *et al.*, 2003). In the previous chapters it has been shown that MWCNTs tend to localize very selectively in one of the phases of an immiscible polymer blend. Thus, the rheological properties of this particular blend phase such as storage modulus and complex viscosity can be significantly changed, whereas those of the other blend phase(s) remain unaffected. The blend morphology development inside a kneader, compounder or extruder is again strongly dependent on the rheological interactions of the blend partners and thus can be affected by the incorporation of CNTs. Generally, the literature covers several correlations that have been used to discuss and predict the phase inversion composition and thus the centre of the co-continuous region based on rheological properties. Of those, the Utracki equation (Utracki, 1991) that predicts the phase inversion concentration employing the viscosity ratio of the two blend phases can be considered the most advanced model (Pötschke and Paul, 2003). The generally observable tendency of the higher viscous phase to be less continuous as the phase with the lower viscosity is combined in this advanced empirical model with an adaptation of the percolation theory. Figure 19.8 (a) shows the general interdependence of viscosity ratio and predicted phase inversion concentrations according to one of the first and simplest models (Miles and Zurek, 1988) and the more recent and complex Utracki model (Utracki, 1991). Especially for high viscosity ratios, the Miles equation is not suitable to describe the blend morphology, whereas good agreements can be achieved with the Utracki equation (see e.g. Göldel *et al.*, 2008). According to these findings, any modification of the blend that specifically changes the viscosity of only one of the blend phases will

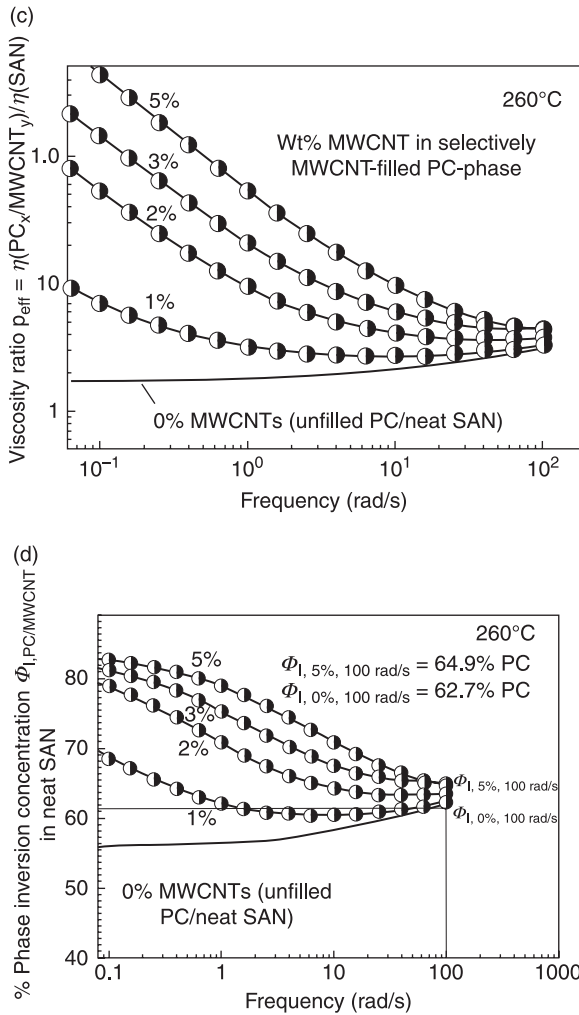
consequently affect the phase inversion concentration (PI). If the CNTs increase the melt viscosity of the selectively filled phase, it can be expected that the unfilled phase will gain some continuity at the cost of the other. So far, no investigations dealing with this specific phenomenology have been described in the literature. Therefore, the influence of a selectively filled blend phase is studied for co-continuous (PC–MWCNT)–SAN blends. These are well described and suitable model systems, as the morphological features and the explicit localization of MWCNTs in the PC phase after short mixing times have been comprehensively approved by several independent methods (Gödel *et al.*, 2009a). Therefore, the impact of MWCNTs on the viscoelastic properties of the blend during mixing and thus on the morphology development can be investigated by studying the shear-rate/frequency dependent properties of PC–MWCNT composites and of neat SAN, reflecting the situation in the blend. Addressing the broad spectrum of flows inside a microcompounder or extruder, the shear rate dependence of melt viscosity is considered, as can be seen in Fig. 19.8 (b) for different PC–MWCNT compounds. At low frequencies, the melt viscosity of PC is increased dramatically, even for low concentrations of MWCNTs. This means, that e.g. at 0.1 rad/s, the addition of 1% MWCNTs to PC results in viscosities that are a factor of 4 higher than those of the unfilled polymer, for 2% MWCNTs even a factor of 30 is obtained. This increase at very low frequencies is due to the long-range combined CNT–polymer networks and is a typical phenomenon of CNT-filled thermoplastics (Pötschke *et al.*, 2002; Pötschke *et al.*, 2004). Whereas this can result in strongly inhibited dripping of the polymer melt which might improve the flame resistance, for the formation of phase morphologies during melt blending much shorter excitation times and higher frequencies have to be considered. To correlate the angular speeds from the oscillatory measurements in the rheometer with the shear rates within microcompounders or extruders, for neat polymers the Cox–Merz rule can be applied (Cox and Merz, 1958):

$$\eta(\dot{\gamma}) = |\eta^*(\omega)| \quad \text{at} \quad \dot{\gamma} = \omega \quad [19.4]$$

This empirical relation allows comparison of the complex viscosities in oscillatory $|\eta^*(\omega)|$ and steady shear $\eta(\dot{\gamma})$ by equalizing the frequencies ω in rad/s and the rates of steady shear $\dot{\gamma}$ in s^{-1} . If was proved to be valid for almost all homopolymers. Although not accurate for filled polymer systems, the data at high frequencies are nevertheless suitable to estimate the change of rheological behaviour inside the microcompounder due to the selective filling of the PC phase. As the shear rate regime typically observed during twin-screw extrusion ranges from 1 to 1000 s^{-1} (Schramm, 1994), the rheological data presented here can cover three of the four relevant decades. Due to the impossibility of measuring shear rates in an extruder and to the strong local variation of shear according to the actual position of the screw elements, a medium shear rate has to be assumed. A possible change of blend morphology by the addition of MWCNTs is discussed in the following for the melt



19.8 Rheological properties, viscosity ratios p_{eff} and prediction of phase inversion concentration $\phi_{\text{I,PC-MWCNT}}$ for the immiscible phases in (PC-MWCNT)-SAN blends. (a) General prediction of the phase inversion concentration ϕ_{I} based on the blend phase viscosity ratio according to Utracki (1991) and Miles and Zurek (1988). (b) Complex viscosity of the immiscible blend phases for the example of selective localization of MWCNT within the PC phase as a function of the oscillatory frequency. (c) Respective viscosity ratio according to Equation 19.5. (d) Phase inversion concentration according to Equation 19.6.



19.8 Continued.

blending process, where the (PC–MWCNT)–SAN blends revealed morphologies like those displayed in Fig. 19.5 by applying rather low rotational speeds of 100 rpm in a microcompounder. For this process, a medium shear rate of 100 rad/s is assumed, which corresponds to the upper limit of the oscillatory experiment’s measuring range.

Due to the characteristic features of such filler networks, the dependence of melt viscosity and CNT content strongly decreases for increasing frequencies (Figure 19.8 (b), see also Chapter 15). The same holds for the viscosity ratio p_{eff} (Equation 19.5) that is defined as the ratio between the melt viscosities of the

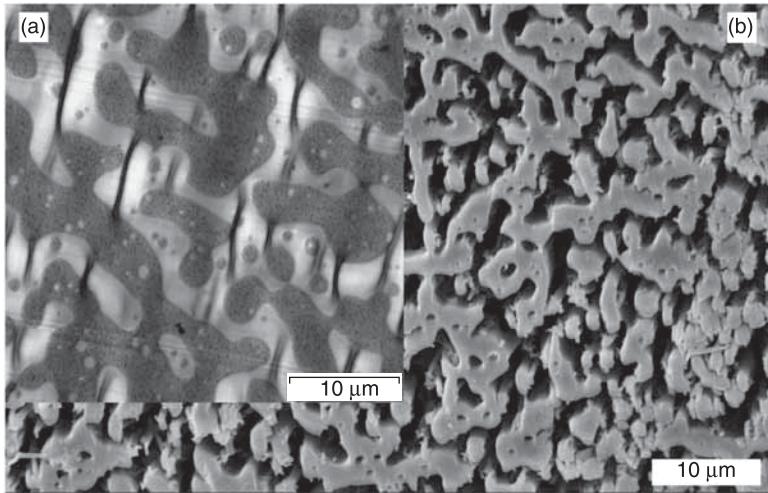
dispersed phase and the matrix phase. The strong and the negligible impact of the MWCNT concentration within the PC phase on p_{eff} at low and high shear rates, respectively, can be seen in Fig. 19.8 (c) for the example of (PC–MWCNT)–SAN blends.

$$p_{\text{eff}}(\dot{\gamma}) = \frac{\eta_d(\dot{\gamma})}{\eta_m(\dot{\gamma})}; \quad p_{\text{eff,example}}(\dot{\gamma}) = \frac{\eta_{\text{PC-MWCNT}}(\dot{\gamma})}{\eta_{\text{SAN}}(\dot{\gamma})} \quad [19.5]$$

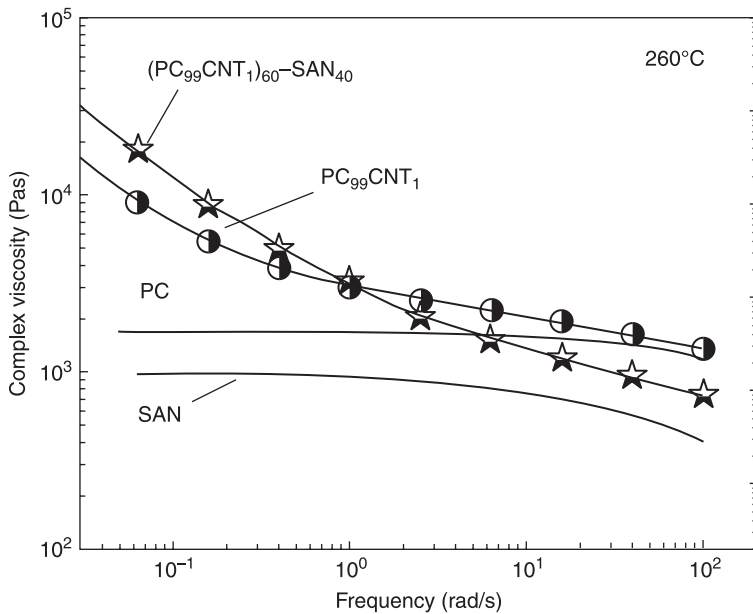
Consequently, a blend with 2wt% MWCNT within the PC phase reveals a viscosity ratio that is almost 30 times higher than that of the neat blend at very low frequencies (0.1 rad/s) whereas this effect almost disappears at elevated frequencies where the viscosity ratios are almost independent of the MWCNT content in the PC phase (3.1 for the unfilled and 3.8 for the PC_{2wt% CNT}–SAN blend, respectively). Finally, this characteristic feature is also reflected in the theoretical prediction of the phase-inversion concentration based on the Utracki equation (Utracki, 1991; Pötschke and Paul, 2003):

$$\Phi_I = \Phi_{I, \text{PC-MWCNT}} = \frac{\phi_m + (1 - \phi_m) \cdot p_{\text{eff}}^{\frac{1}{[\eta]\phi_m}}}{p_{\text{eff}}^{\frac{1}{[\eta]\phi_m}} + 1} \quad [19.6]$$

where Φ_I denotes the volume content of the higher viscous phase, where phase inversion (PI) occurs, which is PC in our example. The required constants, in particular, the maximum packing density of spheres ϕ_m and the intrinsic viscosity $[\eta]$ were selected according to (Utracki, 1991). The results of the calculation are displayed in Fig. 19.8 (d). It shows the shear rate-dependent respective contents of the PC–MWCNT phase ($\Phi_{I, \text{PC-MWCNT}}$) that are theoretically required to adjust the blend in the centre of the interval of co-continuous morphology by a melt blending process. Whereas significant shifts of the phase inversion concentration can be expected for blends processed at very low shear rates, in typical extrusion processes with assumed shear rates of 100 s^{-1} , no or only very minor shifts are expected even for high MWCNT contents. The validity of this correlation and thus the similarity of morphology and continuity of a PC₆₀–SAN₄₀ blend with (2 wt%) and without MWCNTs in PC are demonstrated in Fig. 19.9. Nevertheless, for mixing or kneading processes with very low rotational speeds or shear rates, the influence of the selective MWCNT loading can be much higher. One can deduce that the selective localization of MWCNTs in PC will most probably enable the manufacturing of PC–SAN blends with phase continuities and thus properties, which have not so far been described. There, co-continuity could be achieved for increased contents of the PC phase that would result in PC droplet–SAN matrix structures without carbon nanotubes. The rheological behaviour of co-continuous PC₆₀–SAN₄₀ blend with 1 wt% Baytubes® C150HP selectively localized in the PC phase is shown in Fig. 19.10. Due to the double percolated blend structure, the increase of viscosity at low frequencies can be attributed to



19.9 Comparison of the phase continuity in PC_{60} - SAN_{40} with (a) selectively MWCNT filled PC phase, TEM micrograph) and (b) the neat blend without CNTs (SEM picture PC phase was selectively hydrolysed (DSM 15 Microcompounder, 100 rpm, 5 min, Baytubes® C150HP).

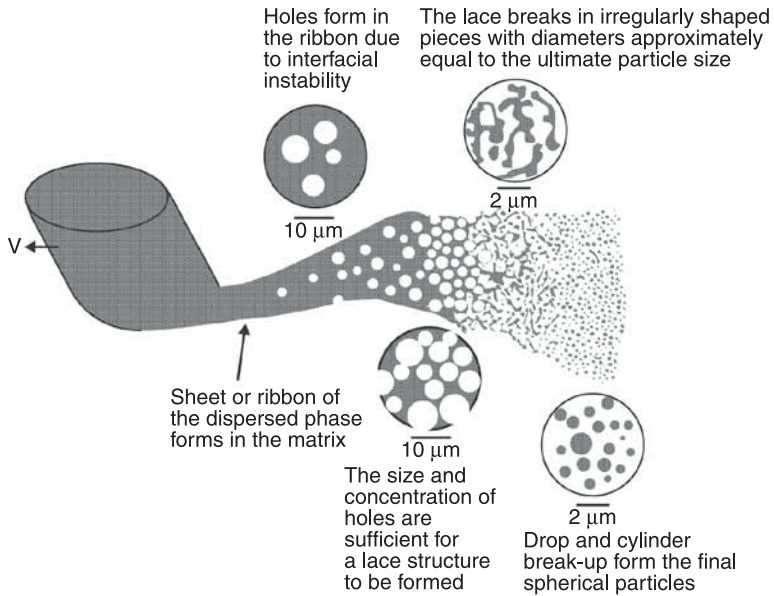


19.10 Complex melt viscosity of PC, SAN, PC with 1 wt% and of a co-continuous PC_{60} - SAN_{40} blend that reveals a PC phase that is selectively filled with 1 wt% Baytubes® C150HP (Ares plate-plate rheometer, 25 mm plate diameter, low strain, 260°C, oscillatory shear).

both the percolation of the CNT network inside PC and that of the PC phase within the co-continuous blend. For other blend systems, the influence of a selectively filled blend phase on the viscosity ratio and thus on the phase inversion concentration can be more pronounced. The impact is specifically high for blends where the selectively filled polymer reveals, in contrast to polycarbonate, a low melt viscosity. This holds for most of the semi-crystalline thermoplastics, as their melt and processing temperatures by far exceed the region of glass transition. Blends of PVDF–PA6 are good examples of this and of the inverse dependency of the phase viscosity and the continuity that is the base of the above-mentioned equations. In detail, a strong increase in the initially low melt viscosity of the PA6 phase can be observed by the selective localization of MWCNTs within this phase (Li and Shimizu, 2008). Therefore, the continuity of PA6 is decreased, whereas in return, that of the previously dispersed PVDF phase is increased in the final blend morphology. By the addition of a certain minimum amount (1.2wt% MWCNTs), the sea island morphology of the unfilled blend can be converted into a co-continuous type of morphology. Furthermore, the electrical properties are improved compared to the bulk materials with the same MWCNT content. Thus, the addition of CNTs offers the possibility of tailoring morphological structures and simultaneously improving the electrical performance of the blend. Beyond the change of phase continuity, CNTs can significantly reduce the domain sizes in polymer blends (Wu *et al.*, 2009), and thus affect the blend morphology like a compatibilizer. Unlike classical additives that compatibilize the phases mainly thermodynamically, for CNTs, the kinetic suppression of the selectively filled blend phase's coalescence is of higher importance (Vermant *et al.*, 2008; Bose *et al.* 2010). This mechanism would be most effective for the localization of CNTs at the blend interface according to the theory of solid particles in the emulsions, which is well described by Pickering (Pickering, 1907). The difficulties in achieving such a thermodynamic and mechanical compatibilization of polymer blends by selective localization of CNTs at the blend interface have been described in previous chapters in this volume.

19.3.5 The dynamics of CNT transfer

Generally, the time-dependent morphology development in a phase-separated polymer blend includes an endless number of transition states and morphological shapes. It has been shown that carbon nanotubes can be transferred from one of the blend phases to the other during this process. In parallel, the dispersion of primary CNT agglomerates will occur in one or in both phases. Beyond that, agglomerates will also be transferred from a thermodynamically unfavourable phase into the other by passing the interface, according to dependence on the transfer speed on the aspect ratio (Section 19.3.3), significantly slower than separated CNTs. Independent of shape, the transfer requires contact with the interface as explained above and thus the transfer speed will be strongly dependent on the developing

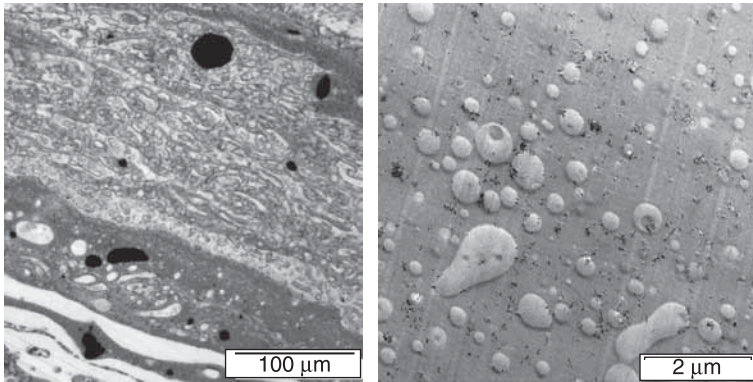


19.11 Morphology development mechanism of an immiscible polymer blend as proposed by Scott and Macosko (1995). Reprinted with permission from Elsevier.

amount of interfacial area. The parallel evolution of macroscopic and microscopic structures (Fig. 19.11) also results in a broad range of CNT transfer states. This can be nicely seen when blending a SAN–CNT pre-compound with neat PC (Fig. 19.12). Whereas the macroscopic domains of neat PC do not contain any CNTs after 10 seconds kneading (Fig. 19.12 (a), lower left corner), the transfer is quite advanced in directly neighbouring regions to the right. Intensive transfer is occurring in the regions where the interface of droplets and structures is visible, but where the phases themselves exhibit no contrast (grey). Therefore, the transfer can be highly advanced or almost completed in microstructured domains, whereas the macroscopic phases can still be in the initial state. In the very early mixing stages it is possible to observe even the thermodynamical highly unstable localization of separated CNTs at the blend interface (Section 19.3.5, Fig. 19.12 (b)).

19.3.6 Summary: factors influencing transfer and localization of carbon nanotubes and other nanoscaled fillers

Nowadays, carbon nanotubes are received from the manufacturers in the shape of more or less compact agglomerates, which is due to the available production processes and the strong van der Waals interactions between the individual tubes.



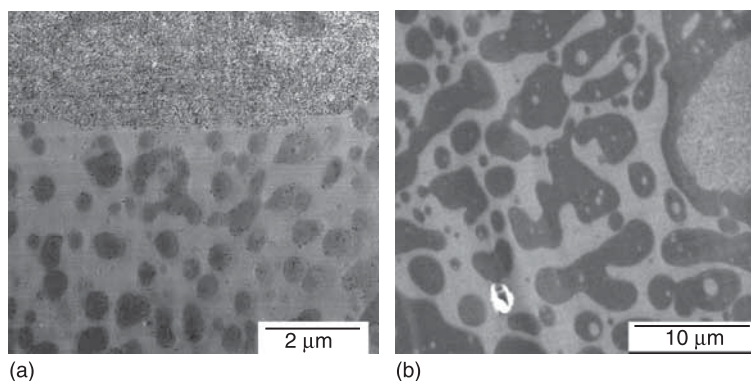
19.12 CNT and agglomerate transfer from a SAN-MWCNT precompound-phase to a unfilled PC-phase in a very early mixing stage (SAN-MWCNT)₄₀-PC₆₀. (a) 10 seconds kneading (transmission light microscopy). Black: MWCNT-agglomerate; different grey levels correspond to different MWCNT loadings. Unfilled polymer is transparent (both PC and SAN) and appears bright white. The macroscopic transparent (white) phase in the lower left corner is PC. (b) 30 seconds kneading (TEM). In this early stage, MWCNTs can frequently be observed during the transfer process, including even the highly unstable transition state of perpendicular orientation to the blend interface. From the visible characteristic features, the bright minority phase most likely corresponds to PC.

Earlier chapters of this book (Chapters 4–8) describe how the outstanding individual properties of CNTs can only be exploited in a polymer composite when it is possible to separate them from the agglomerates. Therefore, during melt blending of CNTs with polymer blends, usually a broad spectrum of different CNT shapes, sizes and aspect ratios is present inside the compounder, which is dependent on the intensity and state of the dispersion process. Furthermore, the transfer rate (e.g. CNTs/second) of CNTs through the interface is strongly coupled with the available interfacial area of the blend phases, and thus with morphology development from macroscopic granules to microscopic phase structures. Thus, if the carbon nanotubes are predispersed in a polymer that reveals high interfacial tensions towards the CNTs, during blending with an unfilled polymer of higher affinity, several processes will be present at the same time, specifically in the beginning of the blending process:

1. The development of blend morphology from macroscopic to microscopic structures and the creation of the interface.
2. The dispersion of CNT agglomerates in the unfavourable blend phase.
3. The transfer of CNTs that already were dispersed in the unfavourable blend phase to the favourable blend phase.

4. The transfer of agglomerates from the unfavourable blend phase into:
 - (a) unfilled domains of the favourable blend phase;
 - (b) CNT-filled domains of the favourable blend phase.
5. The wetting of large agglomerates in the better wetting blend phase.
6. Dispersion of transferred CNT agglomerates in the favourable blend phase.

Therefore, the peculiarities of CNTs such as the fast interfacial transfer and the subsequent selective localization that have been described in earlier chapters are only significant for separated CNTs or small bundles that still exhibit high aspect ratios. For coiled CNTs or agglomerates, different transfer mechanisms are present that depend on the geometrical shape and size of the CNT object. Extrusion processes with medium to long residence times will, for most blend–CNT composites, result in highly advanced dispersion and almost complete transfer of well-dispersed CNTs. The remaining agglomerates can, depending on wetting and phase viscosities, be either coated by the preferred phase or remain in the initial carrier polymer (Fig. 19.13).



19.13 Peculiarities of CNT agglomerates that are big compared to the blend morphology. Depending on mixing conditions and characteristic features of the blend partners, the interaction with the blend can follow different mechanisms. Here: PC–SAN with MWCNTs (Baytubes® C150HP). (a) Large agglomerate still covered by worse wetting (and less viscous) phase. Once dispersed in the surrounding SAN-melt, CNTs are immediately transferred into PC (grey). Thus even in the regions directly neighbouring the agglomerate, most of the CNTs are within the PC phase. (b) The better wetting phase (here PC) completely covers the CNT agglomerates in the upper right corner. For the displayed example the dispersion of MWCNTs will be dominated by the PC–MWCNT dispersion mechanisms (Chapter 4).

19.4 Tailoring the localization of CNTs

In the earlier chapters it was shown that during melt mixing of thermoplastic polymer blends the selective localization in the better wetting blend phases occurs

specifically for nanotubes or related nanofillers. Whereas those systems revealed in almost all cases particularly interesting electrical properties, the CNTs will always be in the thermodynamically preferred phase, in most cases, even independent of the processing parameters and mixing regime. For future applications, the possibility of tailoring those morphologies and the CNT localization is highly desirable, as this would enable the instant manufacture of new ‘tailor-made’ materials with superior properties. Presently, several manufacturers provide chemically modified carbon nanotubes, such as Nanocyl[®] with its 315× series. This enables the reaction with suitable reactive groups, such as, e.g. maleic anhydride (MA), which is also commonly employed for reactive extrusion and compatibilization of polymer blends. There have been recent studies on PA–ABS blends with MWCNTs and a reactive blend component (Bose *et al.*, 2007a, 2007b, 2009), but the impact of the potential reactions on blend morphology and CNT localization is still not completely clear. The common understanding is that those reactions or strong interactions will irreversibly couple the CNT versus their corresponding functional groups to the polymer. Considering the enormous length of typical CNTs it appears reasonable to imagine that some part of the CNT is thus coupled and covered by e.g. the thermodynamically unfavourable but reactive phase, while those areas that are not occupied are wetted by an energetically preferred polymer. This could result in the localization of the CNT at a blend interface. When large amounts of the surface are covered by the coupled polymer, the CNT will tend to be surrounded by more molecules of the reactive polymer or a compatible blend phase. This can be seen in a set of very recent experiments (Gültner *et al.*, 2009; Gültner *et al.*, 2011) that demonstrate the possibility of even inverting the phase selectivity by introducing groups of MA into the thermodynamically unfavourable phase (SAN). It was found that NH₂-modified MWCNTs (Nanocyl[®] 3152) localize, equal to Baytubes[®] C150HP (Section 19.3.2), entirely within the PC phase of unmodified and compatible PC–SAN blends, whereas they are completely located within SAN when this phase is composed of SAN and a related miscible copolymer that contains a sufficient number of MA groups.

Surprisingly, nominally unmodified MWCNTs (such as Nanocyl[®] 7000, Baytubes[®] C150P and Baytubes[®] C150HP) are found as well within the SAN–MA phase of PC–SAN–MA blends, although they are not expected to develop chemical bonds or strong irreversible interactions with MA. This behaviour that is similar to that of specifically surface-modified CNTs is an example of the present difficulties in characterizing and defining CNTs’ functionality and the chemical reactions within the melt. The direct quantification of the formation of chemical bonds between CNTs and polymers during melt mixing is, due to the low concentration of CNTs in the composite and that of reactive groups on the tube surface, very difficult to access analytically. One has to be aware that a typical composite with 3 wt% CNTs that are modified with e.g. 1% of reactive groups contains only 0.03 total wt% of surface active groups that will interact with the polymer. Even the characterization of reactive groups on the tube surface is delicate. The state of the art is to access the elements that can form potentially

reactive groups (mainly from main group V and VI) via XPS. In the example, for both CNTs, modified and unmodified, sufficient amounts of nitrogen (Nanocyl® 3152) and oxygen (Nanocyl® 3150) for the formation of reactive groups could be detected using XPS. The presence and quantity of these elements and the respective groups that can determine the CNT localization within polymer blends are strongly coupled to the proceedings during the CNT production process, specifically to acid treatment and purification. In this context, it is important to note that the amount of nitrogen that is detected via XPS is most probably covalently attached to the CNT surface and thus forms possible reactions, whereas a certain amount of the detected oxygen can also be non-covalently adsorbed from the surrounding atmosphere and thus cannot covalently couple the CNT to any reactive component. Furthermore, defect sites on the CNT surface, e.g. introduced by ball milling, also correspond to local maxima of free energy and thus possibly develop specific interactions with different polymers. Thus, any impurity on the CNT surface can affect the CNT localization behaviour in a polymer blend. This correlation is highlighted when CNTs with high surface purities such as HiPCO–SWCNTs (the surface of these specific CNTs is not disturbed by the included impurities of 5% that are caused by remaining catalyst particles) are incorporated in the blends with the above-mentioned MA-modified SAN phase. These SWCNTs locate within the PC phase despite the behaviour of the investigated MWCNTs. Therefore, before denoting CNTs as ‘unfunctionalized/functionalized’ or ‘unmodified/modified’, their surface characteristics should be characterized very carefully to prevent misinterpretation.

Besides these difficulties, and counteracting the high expectations that go hand in hand with CNTs covalently or physically coupled at e.g. blend interfaces, some mechanism related to the formation of these bonds between polymer and CNT seems to significantly worsen the electrical conductivity. One possible explanation for this behaviour could be the encapsulation of CNTs by specific polymers or reactive components (Bose *et al.*, 2007b).

Summarizing, highly sophisticated analytical methods will be needed to reliably describe the chemistry and surface interactions of CNTs in a melt blending process. The understanding of surface chemistry, reactions, localization behaviour and the resulting electrical properties could open up a new field of commercial applications for polymer blends manufactured by utilization of *in-situ* coupling during melt blending.

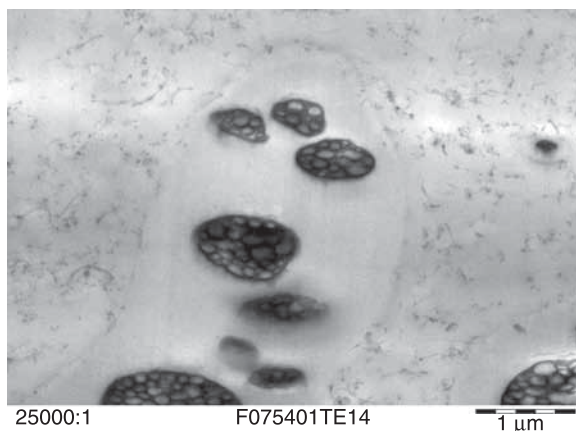
19.5 Utilization of selective localization: double percolated polycarbonate–acrylonitrile butadiene styrene (PC–ABS)-CNT blends

19.5.1 Nano- and micro-scaled morphological structures

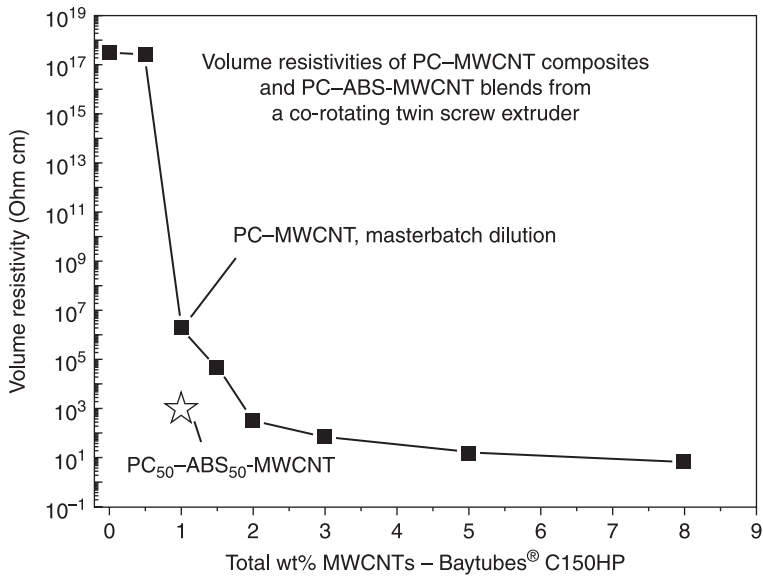
The peculiarities of CNTs such as the fast transfer to a thermodynamically preferred blend phase can be employed in various immiscible blends. The

possibility of manufacturing conductive or antistatic composites with very low content of the still expensive CNTs, e.g. by the application of the double percolation concept, opens the door to several potential commercial applications. Specifically for automotive and electronic applications, e.g. for electrostatic painted parts, there is a strong market for antistatic composites. In these sectors, PC–ABS blends exhibit a very strong market position, specifically due to their outstanding impact toughness that is combined with high stiffness and surface quality.

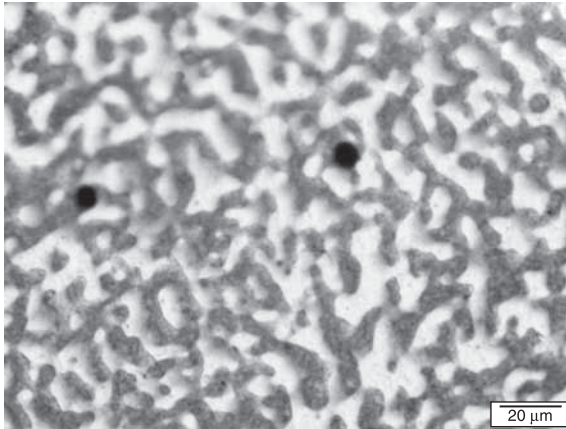
Figure 19.14 shows the morphology of a PC–ABS–CNT blend with Baytubes® C150HP, in which the characteristics of the CNT transfer during melt blending were utilized. The MWCNTs are selectively localized in the continuous PC phase and not within the complex structured ABS, which is composed of two immiscible components, SAN and butadiene rubber (BR). Adjusted mixing conditions and regimes enable the manufacturing of PC–ABS blends that reveal electrical conductivities that almost directly follow the theoretical predictions of the ideal double percolation concept. This implies that, e.g. for a phase composition of 50 wt% PC and 50 wt% ABS, such a blend is electrically percolated at roughly half the CNT content as in bulk PC. Thus the blend reveals electrical conductivities that can be factors or decades higher than those of a PC–CNT composite with the same CNT content. Aiming at the implementation of this concept for commercial application, a suitable twin-screw extrusion process can be developed, that results in significantly improved electrical conductivities (Fig. 19.15) and well-developed double percolated blend structures (Fig. 19.16). For identical MWCNT mass fractions, the resistivity of the displayed PC₅₀–ABS₅₀ blend is a factor of 2000 lower than that of the masterbatch dilution of MWCNTs in neat PC.



19.14 TEM micrograph of a PC₅₀–ABS₅₀ blend with MWCNTs after 5 minutes of melt mixing in a microcompounder. The blend was stained with OsO₄ in order to blacken the BR-phase inside ABS.



19.15 Resistivity of an extruded PC₅₀-ABS₅₀ blend as compared to that from masterbatch dilution of neat PC with Baytubes® C150HP.



19.16 Unstained transmission light microscopy of the extruded PC₅₀-ABS₅₀ blend from Fig. 19.15 (star symbol in Fig. 19.15). The selectively MWCNT filled PC phase appears dark. Primary MWCNT agglomerates appear black.

19.6 Conclusion and future trends

In contrast to conventional reinforced composites with e.g. glass or carbon fibres, most grades of carbon nanotubes can freely localize within the typical morphologies of polymer blends, as they are small enough. The fast interfacial transfer and

highly selective localization in the thermodynamically preferred blend phase of binary polymer blends are a peculiarity of such high-aspect ratio nanoscaled fillers, and are also expected to occur in ternary or quaternary polymer blends. Multiple morphologies are conceivable that can be tailored according to the requirements of the application of interest. Use will probably be found for both the fast CNT transfer as such and the selectively filled multiphase morphologies, respectively. The specific behaviour of CNTs in a molten multiphase blend structure already results now in material properties very close to application, such as the possibility of reducing the electrical percolation threshold by a factor of two and more by the application of the double percolation concept. These concepts work hand in hand with the advances in CNT production and the progress in dispersion and processing. This implies that, independently from what can be achieved e.g. in reducing the percolation thresholds of homopolymer CNT composites, they can subsequently be improved even more by a sophisticated blending step. The potential is also reflected in the strong increase in research activity during the last few years. Further research is needed on the investigation of CNT–polymer interactions and interfacial properties. Also the correlation of morphological features and mechanical properties is an issue of high importance for most technical applications and has to be evaluated independently of the influence of CNTs on the polymer itself and of CNT dispersion. In general, the properties of multiphase blends with CNTs are linked to the advances in CNT dispersion in homopolymers, and already now can push any progress in this field even one step further, in spite of the fact that the morphological potential so far has been only partially exploited. Commercial applications based on the reported technological achievements can be expected in the near future. Nevertheless, and although control of structural features in mixing processes is very difficult, the potentially possible ultra-low percolation thresholds of tailored blends promise a real breakthrough in the market of conductive thermoplastic nanocomposites with carbon nanotubes.

19.7 Acknowledgements

Part of this work was performed within the Framework Concept ‘Research for Tomorrow’s Production’ (fund number 02PU2392) managed by the Project Management Agency Karlsruhe (PTKA) that was funded by the German Federal Ministry of Education and Research (BMBF).

The authors thank Prof. Abraham Marmur from Technion Israel Institute of Technology (Haifa, Israel) for finding the key to correlate the localization behaviour of CNTs and other nanoscaled fillers to their aspect ratio.

The contribution of Maren Gültner to Section 19.4 concerning the use of functionalized CNTs in blends of PC–SAN is acknowledged.

The authors thank Bayer MaterialScience AG, Leverkusen (Germany) for support in TEM investigations of PC–ABS blends.

19.8 References

- Barber, A. H., Cohen, S. R. & Wagner, H. D. (2004) Static and dynamic wetting measurements of single carbon nanotubes, *Physical Review Letters*, 92, 18, Article Number: 186103.
- Baudouin, A.-C., Bailly, C. & Devaux, J. (2010a) Interface localization of carbon nanotubes in blends of two copolymers, *Polymer Degradation and Stability*, 95, 389–398.
- Baudouin, A.-C., Devaux, J. & Bailly, C. (2010b) Localization of carbon nanotubes at the interface in blends of polyamide and ethylene-acrylate copolymer, *Polymer*, 51, 1341–1354.
- Bose, S., Bhattacharyya, A. R., Kodgire, P. V. & Misra, A. (2007a) Fractionated crystallization in PA6/ABS blends: influence of a reactive compatibilizer and multi-wall carbon nanotubes, *Polymer*, 48, 356–362.
- Bose, S., Bhattacharyya, A. R., Kodgire, P. V., Misra, A. & Pötschke, P. (2007b) Rheology, morphology, and crystallization behavior of melt-mixed blends of polyamide6 and acrylonitrile-butadiene-styrene: influence of reactive compatibilizer premixed with multi-wall carbon nanotubes, *Journal of Applied Polymer Science*, 106, 3394–3408.
- Bose, S., Bhattacharyya, A. R., Kulkarni, A. R. & Pötschke, P. (2009) Electrical, rheological and morphological studies in co-continuous blends of polyamide 6 and acrylonitrile-butadiene-styrene with multiwall carbon nanotubes prepared by melt blending, *Composites Science and Technology*, 69, 365–372.
- Bose, S., Ozdilek, C., Leys, J., Seo, J. W., Wubbenhorst, M., Vermant, J. & Moldenaers, P. (2010) Phase separation as a tool to control dispersion of multiwall carbon nanotubes in polymeric blends, *ACS Applied Materials & Interfaces*, 2, 800–807.
- Calberg, C., Blacher, S., Gubbels, F., Brouers, F., Deltour, R. & Jérôme, R. (1999) Electrical and dielectric properties of carbon black filled co-continuous two-phase polymer blends, *Journal of Physics D: Applied Physics*, 32, 1517–1525.
- Cox, W. P. & Merz, E. H. (1958) Correlation of dynamic and steady flow viscosities, *Journal of Polymer Science*, 28, 619–622.
- Feng, J. Y., Chan, C. M. & Li, J. X. (2003) A method to control the dispersion of carbon black in an immiscible polymer blend, *Polymer Engineering and Science*, 43, 1058–1063.
- Gödel, A., Kasaliwal, G. & Pötschke, P. (2009a) Selective localization and migration of multiwalled carbon nanotubes in blends of polycarbonate and poly(styrene-acrylonitrile), *Macromolecular Rapid Communications*, 30, 423–429.
- Gödel, A., Kasaliwal, G. & Pötschke, P. (2009b) Selective localization and migration of multiwalled carbon nanotubes in blends of polycarbonate and styreneacrylonitrile, *ANTEC 2009*, Proceedings of the 67th Annual Technical Conference & Exhibition, Chicago.
- Gödel, A., Ruckdäschel, H., Müller, A. H. E., Pötschke, P. & Altstädt, V. (2008) Controlling the phase morphology of immiscible poly(2,6-dimethyl-1,4-phenylene ether)/poly(styrene-co-acrylonitrile) blends via addition of polystyrene, *E-Polymers*, 17, Article Number 151.
- Green, M. J., Behabtu, N., Pasquali, M. & Adams, W. W. (2009) Nanotubes as polymers, *Polymer*, 50, 4979–4997.
- Gubbels, F., Blacher, S., Vanlathem, E., Jérôme, R., Deltour, R., Brouers, F. & Teyssie, P. (1995) Design of electrical conductive composites: key role of the morphology on the electrical-properties of carbon-black filled polymer blends, *Macromolecules*, 28, 1559–1566.
- Gültner, M., Gödel, A. & Pötschke, P. (2009) Functionalized MWCNT in reactive PC/SAN blends. *4th International Conference on Carbon Based Nanocomposites*, Hamburg, TuTech Innovation GmbH, ISBN 978–3–941492–08–0.

- Gültner, M., Gödel, A. & Pötschke, P. (2011) *Macromolecular Rapid Communications*, in preparation.
- Holz, T. (2007) Solid surface energy. <http://www.surface-tension.de/solid-surface-energy.htm>. (accessed 20 Nov. 2007).
- Krasovitski, B. & Marmur, A. (2005) Particle adhesion to drops, *Journal of Adhesion*, 81, 869–880.
- Li, Y. & Shimizu, H. (2008) Conductive PVDF/PA6/CNTs nanocomposites fabricated by dual formation of cocontinuous and nanodispersion structures, *Macromolecules*, 41, 5339–5344.
- Meincke, O., Kaempfer, D., Weickmann, H., Friedrich, C., Vathauer, M. & Warth, H. (2004) Mechanical properties and electrical conductivity of carbon-nanotube filled polyamide-6 and its blends with acrylonitrile/butadiene/styrene, *Polymer*, 45, 739–748.
- Menzel, R., Lee, A., Bismarck, A. & Shaffer, M. S. P. (2009) Inverse gas chromatography of as-received and modified carbon nanotubes, *Langmuir*, 25, 8340–8348.
- Miles, I. S. & Zurek, A. (1988) Preparation, structure, and properties of 2-phase co-continuous polymer blends, *Polymer Engineering and Science*, 28, 796–805.
- Miltner, H. E., Peeterbroeck, S., Viville, P., Du Bois, P. & Van Mele, B. (2007) Interfacial interaction in EVA-carbon nanotube and EVA-clay nanocomposites, *Journal of Polymer Science Part B: Polymer Physics*, 45, 1291–1302.
- Nuriel, S., Liu, L., Barber, A. H. & Wagner, H. D. (2005) Direct measurement of multiwall nanotube surface tension, *Chemical Physics Letters*, 404, 263–266.
- Pickering, S. U. (1907) Emulsions, *Journal of the Chemical Society*, 91, 2001–2021.
- Pötschke, P., Abdel-Goad, M., Alig, I., Dudkin, S. & Lellinger, D. (2004) Rheological and dielectrical characterization of melt mixed polycarbonate-multiwalled carbon nanotube composites, *Polymer*, 45, 8863–8870.
- Pötschke, P., Bhattacharyya, A. R., Abdel-Goad, M., Janke, A. & Goering, H. (2005) Melt-mixed blends of carbon nanotube-filled polycarbonate with polyethylene, *Advances in Polycarbonates*, 898, 164–177.
- Pötschke, P., Bhattacharyya, A. R., Janke, A. & Goering, H. (2003) Melt mixing of polycarbonate/multi-wall carbon nanotube composites, *Composite Interfaces*, 10, 389–404.
- Pötschke, P., Fornes, T. D. & Paul, D. R. (2002) Rheological behavior of multiwalled carbon nanotube/polycarbonate composites, *Polymer*, 43, 3247–3255.
- Pötschke, P., Kretschmar, B. & Janke, A. (2007) Use of carbon nanotube filled polycarbonate in blends with montmorillonite filled polypropylene, *Composites Science and Technology*, 67, 855–860.
- Pötschke, P. & Paul, D. R. (2003) Formation of co-continuous structures in melt-mixed immiscible polymer blends, *Journal of Macromolecular Science-Polymer Reviews*, C43, 87–141.
- Pötschke, P., Pegel, S., Claes, M. & Bonduel, D. (2008) A novel strategy to incorporate carbon nanotubes into thermoplastic matrices, *Macromolecular Rapid Communications*, 29, 244–251.
- Schramm, G. (1994) *A Practical Approach to Rheology and Rheometry*, Karlsruhe: Gebrueder HAAKE GmbH.
- Scott, C. E. & Macosko, C. W. (1995) Morphology development during the initial stages of polymer-polymer blending, *Polymer*, 36, 461–470.
- Sumita, M., Sakata, K., Asai, S., Miyasaka, K. & Nakagawa, H. (1991) Dispersion of fillers and the electrical-conductivity of polymer blends filled with carbon-black, *Polymer Bulletin*, 25, 265–271.

- Tchoudakov, R., Breuer, O., Narkis, M. & Siegmann, A. (1996) Conductive polymer blends with low carbon black loading: polypropylene/polyamide, *Polymer Engineering and Science*, 36, 1336–1346.
- Thongruang, W., Balik, C. M. & Spontak, R. J. (2002) Volume-exclusion effects in polyethylene blends filled with carbon black, graphite, or carbon fiber, *Journal of Polymer Science Part B: Polymer Physics*, 40, 1013–1025.
- Utracki, L. A. (1991) On the viscosity-concentration dependence of immiscible polymer blends, *Journal of Rheology*, 35, 1615–1637.
- Utracki, L. A. (2002) *Polymer Blends Handbook*, Dordrecht: Kluwer Academic Publishers.
- Vermant, J., Vandebriel, S., Dewitte, C. & Moldenaers, P. (2008) Particle-stabilized polymer blends, *Rheologica Acta*, 47, 835–839.
- Wu, D. F., Zhang, Y. S., Zhang, M. & Yu, W. (2009) Selective localization of multiwalled carbon nanotubes in poly(epsilon-caprolactone)/polylactide blend, *Biomacromolecules*, 10, 417–424.
- Wu, M. & Shaw, L. L. (2004) On the improved properties of injection-molded, carbon nanotube-filled PET/PVDF blends, *Journal of Power Sources*, 136, 37–44.
- Wu, S. (1982) *Polymer Interface and Adhesion*, New York: Marcel Dekker Inc.
- Yang, M. J., Koutsos, V. & Zaiser, M. (2005) Interactions between polymers and carbon nanotubes: a molecular dynamics study, *Journal of Physical Chemistry B*, 109, 10009–10014.
- Zhang, L. Y., Wan, C. Y. & Zhang, Y. (2009) Investigation on the multiwalled carbon nanotubes reinforced polyamide 6/polypropylene composites, *Polymer Engineering and Science*, 49, 1909–1917.
- Zou, H., Wang, K., Zhang, Q. & Fu, Q. (2006) A change of phase morphology in poly(p-phenylene sulfide)/polyamide 66 blends induced by adding multi-walled carbon nanotubes. *Polymer*, 47, 7821–7826.

19.9 Appendix: list of abbreviations

ABS	acryl-butadiene-styrene
BR	butadiene rubber
CB	carbon black
CNT	carbon nanotube
DSC	differential scanning calorimetry
HDPE	high density polyethylene
MMT	montmorillonite
MWCNT	multi-walled carbon nanotube
PA6	polyamide 6
PA66	polyamide 6,6
PC	polycarbonate
PCL	polycaprolactone
PE	polyethylene
PEA	(poly)ethylene acrylate (EA) copolymer
PET	polyethylene terephthalate
PLA	polylactide

PP	polypropylene
PPS	poly(p-phenylene) sulfide
PVDF	polyvinylidene fluoride
SEM	scanning electron microscope
SWCNT	single-walled carbon nanotube
TEM	transmission electron microscope
XPS	X-ray photoelectron spectroscopy

Toxicity and regulatory perspectives of carbon nanotubes

D. MARTIN and R. F. MINCHIN, The University of Queensland,
Australia and M. BELKINA, A. MILEV and G. S. KAMALI
KANNANGARA, University of Western Sydney, Australia

Abstract: In 2010, the global capacity for production of carbon nanotubes was conservatively estimated at 350 tonnes/year.¹ With a substantial increase in manufacture, handling, use and disposal forecast, increasing human and environmental exposure is inevitable, and, as a result, carbon nanotubes (CNTs) in their many forms are beginning to increasingly come under toxicological scrutiny. The enormous number of permutations and combinations of CNTs being handled in the materials' discovery, production and biomedical or industrial application phases has led to a daunting bottleneck in relation to ensuring human and environmental safety. After a brief discussion of public perceptions and risk, this chapter summarizes many of the current CNT toxicity studies and provides a breakdown of the various CNT parameters thought to influence their toxicological properties. Subsequent sections give perspectives on potential future biological applications of CNTs, and on the shifting trends in regulatory frameworks and knowledge gaps which need to be addressed in order to ensure the safe and sustainable utility of CNTs in a range of important applications.

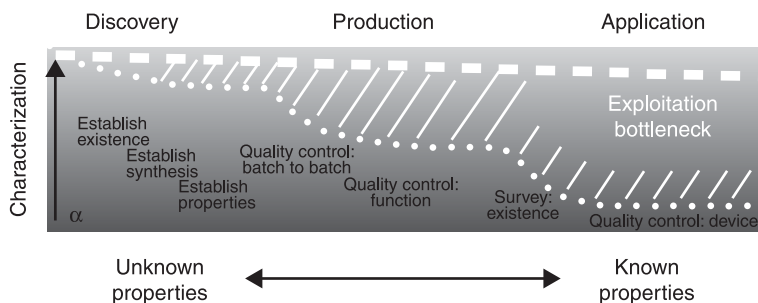
Key words: carbon nanotube, regulatory, toxicity.

20.1 Toxic effects of nanomaterials and nanoparticles: public perception and the necessary 'risk-versus-reward' debate

Current public commentary and debate on the risk governance of nanotechnology and nanomaterials have drawn polarized opinions, with some bodies calling for a ban or moratorium on the research, development and sale of nanomaterials and nanoscale products. Carbon nanotubes (CNTs) feature most prominently in this debate, both in the scientific literature and in the media. Due to their fibrous morphology, coupled with insolubility in the lungs, they have drawn natural comparisons with asbestos. Recent high impact findings provide evidence to support the hypothesis that an asbestos-like biological response is possible, and have strongly urged that inhalation during handling should be strictly minimized until further studies establish quantitative workplace exposure limits.²⁻⁴ These cautionary studies are balanced by many promising examples and applications where CNTs have already engendered considerable improvements to health, information technology, energy, environment and aerospace sectors. As is the case

with many rapidly evolving new technologies, our understanding of human health and environmental effects is incomplete. There are several excellent articles which articulate this dilemma,⁵⁻⁷ and while the *in-vitro* and *in-vivo* toxicology and epidemiological studies steadily accumulate and serve to inform regulatory legislation, it appears that one of the biggest hurdles to be overcome is in occupational medicine, where, for each specific nano-object of interest, new and robust methodologies for measuring, detecting and tracking nanomaterials need to be developed. Only then can the complex relationship between long-term cumulative workplace and environmental exposure and acute/chronic molecular, cellular and pathogenic toxicological mechanisms be understood. Thankfully, based on our current awareness of issues such as air pollution and asbestos, those researchers and industries working with nanomaterials have largely taken a conservative approach to handling these materials, thereby inherently minimizing the risks.

From a manufacturing perspective, a dilemma of a different kind faces manufacturers of nano-enabled products. In an excellent article, Richman⁸ explained that in order for nanotechnology discoveries to progress fully to mature applications, more efficient high throughput characterization tools with multiple capabilities are required in order to assure customers of quality, performance and safety. This relationship between the required level of characterization and stage of commercialization is shown in Fig. 20.1 for a new technology introduced in a mature field (e.g. semiconductor industry) contrasted with new nanotechnology implementation, showing a much slower rate of decrease in metrology required



20.1 Characterization level α as a function of known properties. Heavy characterization is necessary to establish existence, synthesis and properties. Production characterization is mostly concerned with batch-to-batch variation and maintaining advertised functions or properties. Ideally, characterization of developed materials for application is limited to quality control of the applied device. In a mature field (dotted line), this function drops off rapidly between stages of development. Generally, nanotechnology (dashed line) is not achieving the drop-off necessary for profitable deployment. The value of addressing this bottleneck is the impact that faster, facile and standardized characterization can make in developing nanotechnology.

for the nanomaterial-enabled product assurance. This relationship goes some way towards explaining the tremendous lag between early stage nanotechnologies and workable regulatory frameworks. This is particularly pertinent for CNTs, which are arguably the most inherently variable nanomaterials available.

For CNT-reinforced composites, studies also need to be done to ascertain downstream end-user exposure. For example, several manufacturers of composite golf shafts now incorporate small percentages of CNTs in the resin to improve the toughness, 'feel' and playability of these golf shafts. Rather than buy clubs off the shelf, it is commonplace in the industry for players to employ a club professional or club fitter to trim the tip of a graphite golf shaft in order to adjust its 'flex profile' and 'kickpoint' to match the player's particular swing speed, tempo, etc. Are free CNTs released in the dust during this cutting process, or are the dust particles essentially the same as when CNTs are not incorporated? Should the club fitter be wearing more suitable personal protective equipment or be using a dust extraction unit? There are many of these questions of a pragmatic nature that still remain unanswered.

20.2 Toxicology of carbon nanotubes in comparison to other particulate materials

For a better understanding of CNTs' toxicological response, a number of studies^{9–27} have explored CNT toxicology properties in comparison with other carbon-based and mineral materials. These studies found that single-walled carbon nanotubes (SWCNTs)^{9,10} and multi-walled carbon nanotubes (MWCNTs)^{11–14} interact with cells, and reduce cell activity in a dose-dependent and size-dependent manner. In comparison with silver (Ag) nano-sized particles, Shin *et al.*¹¹ found that nano Ag materials increased apoptosis and cytokine expression (IL-6 and IL-8) of human bronchial epithelial cells (BEAS-2B) when applied over 100 µg/ml concentration, while MWCNTs (diameters: 4–6 and 10–15 nm) weakly increased apoptosis and did not significantly increase cytokine expression in concentration less than 200 µg/ml.

Carbon nanomaterials are most commonly used as control materials.^{10,12,13,15,21,28–30} These nanomaterials are all made of carbon atoms but with distinct geometries. They provide an opportunity to explore the comparative toxicity particularly associated with geometrical structure and physical properties.²⁹ Thus, Walker *et al.*¹⁰ examined the effects of purified single-walled (BET average 56 m²/g; Fe content 0.27% by weight) and multi-walled (a specific surface area (BET) average 641 m²/g; Fe content 8.8% by weight) carbon nanotubes on human aortic endothelial cells by evaluating actin filament integrity and VE-cadherin distribution by fluorescence microscopy, membrane permeability by measuring the lactate dehydrogenase (LDH) release, proliferation/viability by WST-1 assay, and overall functionality by tubule formation assay. It was observed that marked actin filament and VE-cadherin disruption, cytotoxicity, and reduced

tubule formation occurred consistently at 24 hrs post-exposure to the highest concentrations [50–150 $\mu\text{g}/10^6$ cells (1.5–4.5 $\mu\text{g}/\text{ml}$)] for both SWCNTs and MWCNTs tested in their studies. Researchers did not observe these effects with carbon black exposure and CNT exposure in lower concentrations [1–10 $\mu\text{g}/10^6$ cells (0.04–0.4 $\mu\text{g}/\text{ml}$)] or in any tested concentrations at 3 hrs post-exposure.

The cytotoxicity of highly-purified MWCNTs obtained from catalytic chemical vapour deposition (average diameter, 67 nm; surface area, 26 m^2/g ; carbon purity, 99.79 wt%; iron impurity, ca. 2000 ppm; fibre length not specified)^{22,23} was found to be higher than that of crocidolite (also known as blue asbestos, the most hazardous of the amphibole asbestos family). Thus, mouse macrophages were exposed to MWCNTs or to Union Internationale Contre le Cancer (UICC) crocidolite in order to evaluate the toxicity of these nano-size fibres. The cytotoxicity of MWCNTs was found to be higher than that of crocidolite. Several proteins were found to adsorb onto MWCNTs when MWCNT-exposed macrophages were gently analysed. One of these proteins was macrophage receptor with collagenous structure (MARCO). MARCO-transfected CHO-K1 cells associated with MWCNTs more rapidly than mock-transfected cells. These results indicate that MWCNTs probably trigger cytotoxic effects in phagocytotic cells by reacting with MARCO on the plasma membrane and rupturing the plasma membrane. Studies using SWCNTs (High Pressure CO derived (HiPco), 10% iron catalyst residue, diameter 0.8–1.2 nm, average length 800 nm and bundle size of $2.6 \times 10^{14} \text{ m}^2$) evaluated the inflammatory response of immortalized and primary human lung epithelial cells (A549 and NHBE) with a special focus on the mediating role of dipalmitoylphosphatidylcholine (DPPC, the main component of lung lining fluid) on particle toxicity. It was revealed that DPPC helped improve the degree of SWCNT dispersion in A549 medium and in turn, increased particle toxicity. It was concluded that effective dispersion of the CNTs in biologically relevant media are important for the accuracy of the toxicological data.^{22,23}

Other studies have shown that with respect to certain metal oxide nanoparticles (TiO_2 , Al_2O_3), MWCNTs were more toxic to A549 human pneumocytes,²⁴ while CuO and $\text{CuZnFe}_2\text{O}_4$ nanoparticles were found to cause far greater cytotoxicity and DNA damage than carbon nanoparticles and MWCNTs.²⁵ Both CNTs and metal oxide nanoparticles were able to rapidly enter A549 cells, distributes in the cytoplasm and intracellular vesicles.

20.3 Comparisons between carbon nanotubes and asbestos: a summary of respiratory studies

Because it is generally agreed that CNT respiratory exposure is the route of highest concern, rodent studies looking at lung injury, inflammation and early signs of tumour formation are perhaps the best indicators of CNT-induced health risks.

There are various *in vivo* studies focused on assessing the potential impact of both unrefined and pristine CNTs on the lungs.^{15,21,30–33} Despite the first study

showing no initial indication of lung toxicity,³¹ subsequent studies have found histological evidence of lung inflammation and granuloma formation.^{15,21,32,33} The initial study in 2001 of Huczko *et al.*³¹ investigated the effects of unrefined CNT on the pulmonary function of guinea pigs. The authors did not indicate whether the CNTs used were SWCNTs or MWCNTs. Guinea pigs were given a single intratracheal instillation (IT) with 25 mg of unrefined CNT in 0.5 mL of saline solution, while control animals received 25 mg of CNT-free soot. Small amounts of surfactant were used to help disperse the nanotubes. Pulmonary function was investigated via non-invasive procedures 4 weeks after instillation. The animals were sacrificed at this time for further study. Neither the non-invasive procedures, nor the final bronchoalveolar lavage examination (BAL) showed any difference between the exposed or control groups, and it was concluded that 'working with soot containing CNT is unlikely to be associated with any health risk'.³¹ Subsequent detailed studies into CNT lung toxicity^{15,21} in 2004 were the first to present data raising concerns over potential CNT health hazards. Lam *et al.*²¹ investigated the pulmonary toxicity of three batches of SWCNTs (unrefined and purified samples from iron catalyzed HiPco synthesis and unrefined SWCNTs, containing nickel (25.99% by Wt) and yttrium (5.01% by Wt) synthesized *via* electrical arc discharge, dimensions not reported) and compared them to carbon black and quartz particles. Mice were again exposed via IT and then observed for either 7 or 90 days at which point they were sacrificed for histological examination. All three SWCNT products induced dose-dependent lung lesions, characterized by interstitial granulomas, regardless of the levels of metal impurities, although it was noted that the SWCNTs containing Ni produced a higher mortality rate. The purified CNTs were prepared by rigorous treatment (45-h reflux) with concentrated acids (2 M to 3 M nitric acid) to remove metal impurities. Although the procedure reduced the metal impurity content to 2% by weight, these harsh conditions can also modify the surface of the CNTs and introduce defects, which have not been investigated. Significantly, this study concluded that SWCNT were more toxic than carbon black, and CNT containing Ni was more toxic than quartz, the recognized positive inducer of lung toxicity.

Warheit *et al.*¹⁵ investigated the lung toxicity of SWCNTs in rats intratracheally instilled. The study exposed rats to unrefined SWCNTs (made by laser ablation, and containing 30–40% amorphous carbon and ~5% Co and ~5% Ni catalyst. The nominal size of these SWCNTs was 1.4 nm in diameter and more than 1 μm in length), quartz (as a positive control), carbonyl iron particles (as a negative control), graphite particles (with the same percentage Ni/Co as the SWCNT sample) and phosphate buffered saline solution. The rats were studied using BAL fluid markers, cell proliferation assays and histopathological examination at 24 h, 1 week, 1 month and 3 months after instillation. Initially, a mortality rate of approximately 15% was observed in rats exposed to 5 mg/kg SWCNT. However, this was later attributed to mechanical blockage of the upper airways causing asphyxiation, rather than toxicity of the SWCNT. Researchers found that exposure

to SWCNT produced only transient inflammation, as assessed by cell proliferation and cytotoxicity indices. Histological examination of exposed animals identified a series of non-dose-dependent multifocal granulomas. The granulomas were non-uniform in distribution and not progressive after 1 month. The presence of the granulomas was considered inconsistent with the lack of lung toxicity as determined by other parameters and the authors concluded that more research was needed.

Following their preliminary study in 2001,³¹ Huczko *et al.*³² published a follow-up study in 2005. In this investigation, five different samples of MWCNT (unrefined MWCNTs produced by both CVD and arc-discharge, and commercially available CNTs from a number of suppliers) were intratracheally instilled into guinea pigs. The animals were studied using BAL markers, lung resistance tests and histopathological examination at 90 days. Unlike the preliminary study, significant evidence of pulmonary toxicity was observed. These researchers found alveolar macrophage infiltration in the BAL of most of the non-control animals. Abnormal lung resistance was observed in all animals exposed to CNT samples, while lung histology reported multiple lesions in all CNT-exposed animals. The authors concluded that the exposure time was critical for induction of lung pathology.

Muller *et al.*³³ investigated the effect of intratracheally instilled MWCNTs on the pulmonary function of rats. Exposure to purified and milled (via oscillatory agate ball milling to reduce aggregation) MWCNTs (see Table 20.1) (CVD synthesis from ethylene over alumina support with Co and Fe catalyst, purified in NaOH) and monitored for up to 60 days. Asbestos and carbon black were used as controls. Rats were studied using BAL, inflammatory and fibrotic markers, biopersistence tests, and histopathological examination. Dose-dependent inflammation and granuloma formation was observed, but unlike previous studies,¹⁵ the inflammation persisted for the full 60 days. In all cases, both MWCNTs and milled MWCNTs were considered more inflammatory than carbon black, but less inflammatory than the asbestos fibers. In addition, the shorter milled MWCNTs were cleared faster than non-ground MWCNTs. The

Table 20.1 Characteristics of carbon nanotube (CNT) samples before and after agate milling³³

	CNT	Ground CNT
Length (μm)	5.9 ± 0.05	0.7 ± 0.07
Average inner diameter (nm)	5.2 ± 1.5	5.1 ± 2.1
Average outer diameter (nm)	9.7 ± 2.1	11.3 ± 3.9
Specific surface area (m^2/g)	378 ± 20	307 ± 15
Oxidized forms (atomic %)	13.7 ± 0.7	13.1 ± 0.7
Carbon content (%)	97.8 ± 0.2	98.0 ± 0.2

authors urged the introduction of appropriate safety measures for handling CNTs, while calling for more studies to accurately establish the toxicology of CNTs.

In the only study of its kind to date, Shvedova *et al.*³⁴ investigated the pharyngeal aspiration of SWCNTs (synthesized via the HiPco process and purified to >99%, Fe(CO)₅ catalyst, purified by acid treatment, diameter 1–4nm) in mice. The study found that SWCNT exposure (10, 20, 40 µg/animal) led to a dose-dependent increase in inflammatory markers at 1–3 days post exposure, granuloma formation and progressive interstitial fibrosis and alveolar wall thickening up to 60 days post exposure. Contrary studies utilizing intratracheal instillation for delivery,^{15,21,31–33} pharyngeal aspiration resulted in two distinct particle morphologies. The first particle morphology observed, compact SWCNT aggregates (>500 nm in diameter), was associated with acute inflammation and granuloma formation at the particle deposition sites. In contrast, the second particle morphology, dispersed SWCNT structures, was associated with diffuse interstitial fibrosis and alveolar wall thickening in areas further away from SWCNT aggregate. The researchers again concluded that more extensive inhalation studies were required to confirm these initial observations.

All studies that have utilized intratracheal instillation have reported major difficulties dealing with the agglomerative nature of CNTs in aqueous solutions.^{15,21,32,33} Although this method carries the advantage of being able to deliver a specific dose to the lung epithelium, it does not resemble exposure by natural respiration. There is also evidence that it takes significant energy and agitation to release fine CNT particles into the air.³⁵

In somewhat of a landmark study in 2008, Poland *et al.*² used a well-respected peritoneal cavity model (often used as a surrogate assay for lung toxicity) to demonstrate length-dependent MWCNT pathogenicity, reporting the existence of granulomas on the surface of the diaphragm in cases where mice were exposed to high aspect ratio MWCNTs ('NT_{long1}' from Mitsui, 85nm diameter, 24% of bundles longer than 15µm, residual Cu, Ni and Co catalyst (all <6%), and, 'NT_{long2}' from University of Manchester, 165nm diameter, 84% of bundles longer than 15µm, residual Fe (37%), Cu, Ni and Co catalyst (Cu, Ni and Co all < 6%)). These were compared to results where mice were exposed to low aspect ratio MWCNTs ('NT_{tang1}' and 'NT_{tang2}') consisting of CNTs arranged in low-aspect-ratio tangled aggregates (see Table 20.2). Motivated by this study, in the first published study to employ 'the gold standard'³ of inhalation exposure, Ryman-Rasmussen *et al.*⁴ reported results from a study where mice were allowed to inhale (30 mg/m³) MWCNT for 6 hours, after which their lung tissues were harvested and studied. MWCNTs were found throughout the lungs and within macrophages, and most importantly, they were seen deposited in the sub-pleural wall close to the very sensitive mesothelial tissue. Also significant was the lack of fibrosis observed when a lower inhalation exposure (1 mg/m) was employed; suggesting again that the minimization of inhalation during handling is very wise until further long-term inhalation exposure data comes to hand.

Table 20.2 Characterization of multi-walled carbon nanotubes (reproduced from ref. [2])

Parameters	NT _{tang1}	NT _{tang2}	NT _{long1}	NT _{long2}
Diameter as supplied by manufacture (nm)	15 ± 5	15 ± 5	40–50	20–100
Diameter as supplied by authors (nm)	14.84 ± 0.5	10.40 ± 0.32	84.89 ± 1.9	165.02 ± 4.68
Length as supplied by manufacture (μm)	1–5	5–20	Mean 13	Max 56
Soluble metals (μg g ⁻¹)				
Fe	7.9	13.4	ND*	37.3
Cu	5.1	1	1.2	1.2
V	ND*	ND*	0.8	ND*
Ni	9.7	5	6.2	6.2
Zn	5.5	7.5	0.7	ND*
Co	3.7	ND*	1.9	3.4

Note: *ND – not detectable.

20.4 Toxicity of carbon nanotubes

To date, several studies have compared toxicology properties of different CNT types: SWCNTs and MWCNTs. Most researchers^{36–40} concluded that the size (diameter) of carbon nanotubes is a key factor governing their antibacterial effects and that it is likely the main CNT-cytotoxicity mechanism is cell membrane damage by direct contact with CNTs.

Kang *et al.*^{36,37} studied the microbial cytotoxicity of four carbon-based nanomaterials [SWCNT ((Stanford Materials), purified (95% (w/w)), MWCNT ‘as-prepared’, CVD synthesized using iron catalyst (NanoTechLabs)], dry oxidized MWCNTs in air at 350°C to remove amorphous carbon and ‘acid-treated’ MWCNTs [10M HCl at 70 °C for 18hrs, and finally, ‘functionalized’, via sonication in H₂SO₄/HNO₃ (3:1 v/v)], aqueous phase of fullerene (C₆₀) nanoparticles, and colloidal graphite in Gram negative and Gram positive bacteria. Thus, SWCNTs inactivated the highest percentage of cells in monocultures of *Escherichia coli*, *Pseudomonas aeruginosa*, *Bacillus subtilis*, and *Staphylococcus epidermis*, as well as in the diverse microbial communities of river water and wastewater effluent.³⁷

Other results^{38,40} supported the finding that SWCNTs are more toxic than MWCNTs. De Nicola *et al.*³⁸ explored the toxicity of different types of carbon nanotubes (see Table 20.3), differing in preparation (arc discharge versus catalysed chemical vapour deposition); size (10–50 versus 100–150 nm wide × 1–10 μm long); contaminants (amorphous C, graphite, fullerenes or iron) and morphological type (multi-walled, MW, or single-walled, SW) on human U937 cells and Cheng *et al.*³⁹ studied nanoparticle effects on the cytoplasm, lysosomes, and nucleus of human monocyte-derived macrophage cells, and found that the most pronounced

Table 20.3 Description of the three types of carbon nanotube used in the present study³⁸

Material	Synthesis	Dimensions	Contaminants
MWCNTs	Synthesized by an electric arc discharge in deionized water	The diameter is in the range 10–50 nm and the length is up to 10 μ m	Graphite
50% MWCNTs + 30% SWCNTs	Synthesized by an electric arc discharge in helium	The diameter of the MWNTs is in the range 10–40 nm and the length is 1–5 μ m	20% fullerene and amorphous C
MWCNTs	Produced by CVD	The diameter is in the range 110–170 nm and the length is between 5 and 9 μ m	0.1% of Fe

effects on nuclear and plasma membrane potential were slightly more pronounced with SWCNT cell exposure than MWCNT.

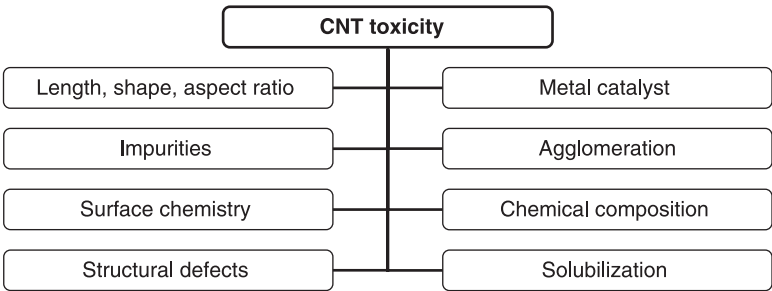
Jia *et al.*²⁹ tested cytotoxicity parameters of purified SWCNT (synthesized by arc discharge, ~90% purity (mainly amorphous C impurities, with traces of Fe, Y and Ni catalyst)), MWCNT (synthesized by CVD with diameters ranging from 10 to 20 nm, purity >95% (<3% amorphous C, ~0.6% Ni catalyst)), and fullerene (C_{60}). The cytotoxicity increased by as high as 35% when the dosage of SWCNTs was increased by 11.30 μ g/cm². No significant toxicity was observed for C_{60} up to a dose of 226 μ g/cm². The cytotoxicity apparently follows a sequence order on a mass basis: SWCNT > MWCNT > quartz > C_{60} . SWCNTs significantly impaired phagocytosis of AM at the low dose of 0.38 μ g/cm², whereas MWCNT and C_{60} induced injury only at the high dose of 3.06 μ g/cm².

Schrand *et al.*⁴¹ results confirmed a previous study indicating that carbon nanomaterials (nanodiamonds (ND), SWCNTs, MWCNTs and carbon black (CB)) displayed differential biocompatibility in neuronal and lung cell lines. The greatest biocompatibility was found after incubation with NDs and both cell types followed the trend: ND > CB > MWCNT > SWCNT.

As shown above, the major studies concluded that SWNTs have higher toxicity in comparison to MWCNTs. But most of studies did not provide details of CNT structure, physio-chemical properties, synthesis and purification methods. For example, it is well documented that nickel, which in combination with yttrium is used as a catalyst in the production of arc-discharged SWCNT nanotubes, is cytotoxic.⁴² Common SWCNT purification methods based on oxidation have the potential disadvantage of modifying the CNTs by introducing functional groups and defects which also can lead to CNT toxicity.^{43–46} These data confirm the necessity for reliable controlled synthetic methods and well-characterized carbon nanotubes, complex analyses of carbon nanotubes' properties in relation to their toxicity.

20.5 Influence of the parameters of carbon nanotubes on their toxicity

Carbon nanotubes can vary in length and shape, consist of different metal catalysts, may have some defects or functional groups (covalent and non-covalent) on the walls. Also, the extent and location of the functionalization can vary from sample to sample. All these key parameters, which are summarized in Fig. 20.2, can contribute to CNT toxicity.



20.2 Basic parameters contributing to CNT toxicity.

20.5.1 Length, morphology and aspect ratio

The length, shape and aspect ratio are some of the most important parameters determining CNT toxicity. However, it is difficult to properly correlate the impact of size dependency on CNT toxicity studies due to the lack of systematic investigation employing CNTs of known dimensions.

Takagi⁴⁷ and co-workers reported that MWCNTs induced mesothelioma along with a positive control, crocidolite (blue asbestos), when administered intraperitoneally to p53 heterozygous mice that have been reported to be sensitive to asbestos. The average diameter of MWCNTs employed was about 100 nm, and 27.5% of the particles were longer than 5 micrometers (5–20µm). The authors concluded that the genotoxic effect of MWCNTs is unclear, and current results suggested that intraperitoneal administration of MWCNTs possesses carcinogenic potential in p53 mice presumably depending on their size/shape and persistency in the organism.

Poland *et al.*² show that exposing the mesothelial lining of the body cavity of mice, as a surrogate for the mesothelial lining of the chest cavity, to long MWCNTs resulted in asbestos-like, length-dependent, pathogenic behaviour. They explored MWCNTs in a different length (short MWCNTs forming tightly packed spherical agglomerates, a large proportion of which are in the respirable size range <5 µm; bundles of intermediate-length MWCNTs, size range <5 µm;

dispersed bundles and singlets of long and intermediate-length MWCNTs, many in the range 10–20 μm and longer; regular bundles and ropes of MWCNTs with a fairly constant length and diameter in more than 20 μm in length). The accumulation of MWCNTs in the diaphragmatic mesothelium and the subsequent degree of granuloma lesion formation were significantly higher after injection of rigid MWCNTs longer than 20 μm compared with low-aspect ratio, tangled nanotube aggregates or a negative control carbon-containing compound that is not needle-shaped. This suggests increased risk associated with lung exposure to long and rigid CNTs. However, the differences in the source, preparation and purification of different commercial CNTs and therefore potential differences in physicochemical properties and contaminations were not properly taken into toxicological consideration.⁴⁸ For example, the two short tangled samples were acid-treated and this may have resulted in modifications to the CNTs, such as the removal of impurities (amorphous carbon and metal catalyst). Also the long nanotubes contained a higher amount of Fe (37.3 $\mu\text{g g}^{-1}$) in comparison to SWCNTs with total Fe content of 7.9 $\mu\text{g g}^{-1}$.⁴⁸

Sato *et al.*⁴⁵ used 220 nm and 825 nm-long MWCNTs (purity is about 80 wt% with impurities such as amorphous carbon, Fe, Mo, Cr and Al) samples for testing. The results indicated that the degree of inflammation around 825-CNTs was stronger than that around 220-CNTs since macrophages could envelop 220-CNTs more readily than 825-CNTs. However, no severe inflammatory response such as necrosis, degeneration or neutrophil infiltration *in vivo* was observed around both CNTs examined throughout the experimental period.⁴⁹

Agharkar with co-workers⁵⁰ hypothesized that short MWCNT treatment induces cytotoxicity in different cell phenotypes and functionalization of MWCNTs impacts the cytotoxic profile. The results demonstrated dose-dependent cytotoxicity of three different MWCNT types (carboxylated MWCNT, hydroxylated MWCNT and non-functionalized MWCNT) and it was found⁴³ that the reason CNT toxicity increases may be due to the presence of carboxyl and hydroxyl functional groups – not the increase in nanotubes' length by functionalization.

In another investigation,⁵¹ protein-binding mechanisms of pristine and functionalized MWCNTs (f-MWCNTs) were investigated by varying f-MWCNTs diameter, nanotube surface chemistry, and proteins using steady-state and time-resolved fluorescence, and circular dichroism spectroscopic techniques. The f-MWCNTs with a larger diameter (40nm) generally exhibited stronger protein binding compared to those with a smaller diameter (10nm), demonstrating that the curvature of nanoparticles plays a key role in determining the protein binding affinity.

The results reported by Becker *et al.*⁵² measured the length-dependence of DNA-wrapped SWCNTs. An assay was used to look for reductions in metabolic activity of the cell population upon exposure to the DNA-wrapped SWCNTs. Their results suggested that shorter tubes [shorter than (189 \pm 17) nm] may be more toxic to cells than longer SWCNTs.

On the other hand, Simon-Deckers *et al.*²⁴ studied the response of A549 human pneumocytes to carbon nanotubes and found that neither the CNT length nor the presence of metal catalysts impurities influenced cytotoxicity.

Journeay with co-workers⁵³ demonstrated that water-soluble rosette nanotube structures represent low pulmonary toxicity, likely due to their biologically inspired design, and their self-assembled architecture. The researches suggested that the novel nanostructures with biological design may negate toxicity concerns for biomedical applications of nanotubes. But this class of self-assembling rosette nanotubes was found to be naturally water-soluble and free of metal content upon synthesis. All these factors may have an influence on CNT toxicity.

20.5.2 Level of aggregation

MWCNTs range from 10 to 100 nm in diameter, they have a strong tendency to bundle together in 'ropes' due to van der Waals and electrostatic forces.⁵⁴ Bundles typically contain many tens of nanotubes and can be considerably longer and wider than the nanotubes from which they are formed. This is a very important factor modifying CNT toxicity.⁵⁵

Aggregates might have a much larger aerodynamic diameter (diameter of a particle of unit density) than singlet CNTs and so could be less respirable and could be large enough to deposit with a different anatomic pattern in the lungs compared to the singlet CNT.⁵⁵

The *in-vitro* cytotoxic experimentation was carried out with MSTO-211H cells using four samples of SWCNTs.⁵⁶ Non-cytotoxic polyoxyethylene sorbitan monooleate was found to well disperse CNTs. In the present study, the cytotoxic effects of well-dispersed SWCNTs were compared with that of conventionally purified rope-like agglomerated SWCNTs and asbestos as a reference. While suspended CNT-bundles were less cytotoxic than asbestos, rope-like agglomerates induced more pronounced cytotoxic effects than asbestos fibres at the same concentrations.

On the other hand, Soto *et al.*⁵⁷ explored cytotoxic effect of different aggregated nanomaterials, including Ag, TiO₂, Fe₂O₃, Al₂O₃, ZrO₂, Si₃N₄, naturally occurring mineral chrysotile asbestos and carbonaceous nanoparticulate materials such as multiwall carbon nanotube aggregates and black carbon aggregates. Cytotoxicological assays of these nanomaterials were performed utilizing a murine alveolar macrophage cell line and human macrophage and epithelial lung cell lines as comparators. The nanoparticulate materials exhibited varying degrees of cytotoxicity for all cell lines and the general trends were similar for both the murine and human macrophage cell lines. Authors concluded that the particle morphology or aggregate morphology is not correlated with the cytotoxicity response for either the murine or the human cell line exposure since a variety of morphologies within the nanorange exhibit equivalent or similar cytotoxicities.

The non-dependence of CNT toxicity on aggregation level was found by Muller and co-workers.³³ In their study, MWCNTs and ground CNTs were administered intratracheally (0.5, 2 or 5 mg) to Sprague Dawley rat's lung. CNTs and ground CNTs were still present in the lung after 60 days (80% and 40% of the lowest dose) and both induced inflammatory and fibrotic reactions. At 2 months, pulmonary lesions induced by CNTs were characterized by the formation of collagen-rich granulomas protruding in the bronchial lumen, in association with alveolitis in the surrounding tissues. These lesions were caused by the accumulation of large CNT agglomerates in the airways. Milled CNTs were better dispersed in the lung parenchyma and also induced inflammatory and fibrotic responses.

20.5.3 Solubilization

As-produced CNTs are insoluble in all organic solvents and aqueous solutions.⁵⁸ Since many applications of CNTs (biomedical or otherwise) require their dispersion in a variety of solvents (for example, organic solvents for polymer interactions and aqueous solvents for drug delivery), there have been many investigations into improving CNT solubility. This section discusses some of the successful and popular methods, namely: sonication, stabilization with surfactant and covalent functionalization.⁵⁹

Carbon nanotubes can be solubilized by a series of methods,⁶⁰ including their functionalization by the aryl diazonium process, use of elemental metals, simple inorganics, acids, esters, aldehydes, amines, aromatics, macrocycles, thiols, biomolecules, polymers, and using such techniques as pulsed streamer discharge, microwave treatment, cryogenic crushing and γ -irradiation.

Lacerda *et al.*⁶¹ show the importance of ensuring sufficient chemical functionalization to achieve a stable dispersion of individual f-MWCNTs in physiological media and conditions and revealed that urinary excretion rates are higher when f-MWCNTs are individualized rather than aggregated in the bloodstream. The study addresses the short-term impact (first 24 h) of intravenous administration of various types of multi-walled nanotubes on the physiology of healthy mice. Non-functionalized, purified MWCNTs and different types of water-dispersible, functionalized MWCNTs were tail-vein injected. Histological examination of tissues (kidney, liver, spleen and lung) harvested 24 h post-administration indicated that organ accumulation depended on the degree of ammonium ($-\text{NH}_3^+$) functionalization at the f-MWCNT surface. The results concluded that the higher the degree of functionalization of MWCNT- NH_3^+ , the less their accumulation in biological tissues.

A novel biomimetic amphiphilic polymer,⁶² cholesterol-end-capped poly(2-methacryloyloxyethyl phosphorylcholine) (CPMPC), was used as surfactant to achieve water soluble and biocompatible carbon nanotubes. Crude CNTs were facilely dispersed in aqueous media by ultrasonication with the help of CPMPC, with cholesterol-end-capped PEG and lecithin as controls. While CPEG-coated

CNTs showed obviously detrimental effects on the growth of HUVEC304 cells, CPMPC-coated CNTs did not exhibit obvious toxicity. The biocompatible CPMPC-coated CNTs represent an excellent nano-object for potential biomedical applications.

Deng *et al.*⁶³ used water soluble multi-walled carbon nanotubes functionalized by taurine (S-MWCNTs) as a model to investigate the possible toxicity of CNT to mouse spleen. The toxicity of various doses of S-MWCNTs was examined by carbon clearance measurement, oxidative stress assay, histopathologic and electron-microscopic examination. Compared with the control group, phagocytic activity of RES, activity of reduced glutathione, superoxide dismutase and malondialdehyde in splenic homogenate did not change significantly in 2 months. The histopathologic examination showed no observable sign of damage in spleen; however, the accumulated S-MWCNTs gradually transferred from the red pulp to the white pulp over the exposure time and it is possible to initiate the adaptive immune response of spleen.

The importance of solubilization was confirmed by Dumortier *et al.*⁶⁴ The authors address the impact of functionalized carbon nanotubes (f-CNTs) on cells of the immune system. Two types of f-CNTs were prepared, following the 1,3-dipolar cycloaddition reaction (f-CNT 1) and the oxidation/amidation treatment (f-CNT 3), respectively. It was found that both types of f-CNTs are taken up by B and T lymphocytes as well as macrophages *in vitro*, without affecting cell viability. It was discovered that f-CNT 1, which is highly water soluble, did not influence the functional activity of immunoregulatory cells. f-CNT 3, which instead possesses reduced solubility and forms mainly stable water suspensions, preserved lymphocytes' functionality while provoking secretion of proinflammatory cytokines by macrophages.

20.5.4 Surface chemistry

New potential applications are being investigated by introducing defects and modifying the surface chemistry of CNTs.⁶⁵ Nevertheless, since CNTs are considered as almost inert substrates, they are previously subjected to oxidizing treatments and, depending on the conditions and the oxidizing agents used, is possible to obtain modifications on the surface chemistry and in the structural integrity at distinct levels.

Acid functionalization is a technique used to increase the solubility, dispersion and purification of many different types of materials including nanotubes.⁴⁴ The previous investigations^{43–45,66,67} show that acid functionalization can significantly increase CNTs' toxic effects, particularly if they have been modified to express functionally reactive chemical groups on their surface.

To explore the effect of CNTs' surface chemistry on their toxicity, Magrez *et al.*⁴³ decorated the surface of MWCNTs (produced by chemical vapour deposition, with an average diameter of 20 nm and aspect ratios ranging from 80 to

90) by a chemical modification of the outer layer after acid treatment. This procedure resulted in adding carbonyl (C=O), carboxyl (COOH), and/or hydroxyl (OH) groups onto the nanotube surfaces. The toxicities of the functionalized MWCNTs were tested *in vitro* on lung tumour cells. The results show that toxicity increases significantly when carbonyl, carboxyl, and/or hydroxyl groups are present on their surface. In the same study, a comparison of the toxicities of carbon filaments revealed that MWCNTs exhibited less toxicity. However, the exact mechanisms that lead to cell death are still unclear, and can induce cell death either after contact with cell membranes or cellular internalization, which highlights the need to carry out further studies on carcinogenicity and on the handling of MWCNTs.

This hypothesis was confirmed by Tong *et al.*,⁴⁴ where acid functionalization (AF) enhanced the cardiopulmonary toxicity of SWCNTs. Mice were exposed by oropharyngeal aspiration to 10 or 40 µg of saline-suspended SWCNTs, and acid-functionalized SWCNTs (AF-SWCNTs, synthesized using 1:1 HNO₃:H₂SO₄, 20 psi, ~150 °C, 3 min in a microwave digester). The pulmonary inflammatory responses and cardiac effects were assessed by bronchoalveolar lavage and isolated cardiac perfusion respectively, and compared to saline or LPS-instilled animals. Additional mice were assessed for histological changes in lung and heart. Instillation of 40 µg of AF-SWCNTs increased the percentage of pulmonary neutrophils. Isolated perfused hearts from mice exposed to 40 µg of AF-SWCNTs had significantly lower cardiac functional recovery, greater infarct size, and higher coronary flow rate than other particle-exposed animals and controls, and also exhibited signs of focal cardiac myofiber degeneration. Therefore, it was concluded that the intrapulmonary instillation of AF-SWCNTs enhanced cardiac ischemia/reperfusion injury and caused myocardial degeneration in mice. There was no significant ischemia/reperfusion injury in mice exposed to non-functionalized SWCNTs. However, correlation of the results between the toxicity and the functionalization of SWCNTs may not be straightforward. For example, it is possible that not only a chemical modification of the surface is taking place, but also a combination of the chemical and structural changes (especially in a microwave digester), leading to more defects in the SWCNTs. In addition to the cytotoxicity of SWCNTs, the studies by Sato *et al.*⁶⁷ revealed that surface-modified carbon nanofibres prepared by sonication using a sulfuric acid–nitric acid mixture exhibited a significant cytotoxic factor that affected cell activation. Therefore, toxicological data related to the nature of the surface modification on SWCNTs needs further investigation.

On the other hand, functionalization or coating of carbon nanotubes with biomolecules^{68–76} such as nucleotide acids, proteins, and artificial polymers has emerged showing these agents improving the biocompatibility of carbon nanotubes. Thus, Dutta and co-workers⁷⁰ have investigated whether re-suspension methods that alter protein adsorption profiles would modulate nanomaterial toxicity and the characterization of proteins adsorbed to the surface of two distinct classes of nanomaterials (SWCNTs (the measured BET was 274.1 m²/g; the

contaminations of silica, yttrium and nickel were 0.12, 2.9 and 17.29 % by weight respectively); and 10-nm amorphous silica) provides insight into pathway-specific effects. Pre-coating SWCNTs with a nonionic surfactant (Pluronic F127) inhibited albumin adsorption and anti-inflammatory properties. Albumin-coated SWCNTs reduced LPS-mediated Cox-2 induction under serum-free conditions. The profile of proteins adsorbed onto amorphous silica particles (50–1000 nm) was qualitatively different, relative to SWCNTs, and pre-coating amorphous silica with Pluronic F127 dramatically reduced the adsorption of serum proteins and toxicity. The importance of using Pluronic F127 in the CNTs' coating has been confirmed by Bardi *et al.*⁷² They also show that MWCNTs coated with Pluronic F127 surfactant can be injected in the mouse's cerebral cortex without causing degeneration of the neurons surrounding the site of injection. This means that the use of a surfactant to disperse SWCNTs affects protein binding affinities and toxicity. Therefore, while surfactants may increase dispersion and prevent any clumping of materials, they can also prevent formation of desirable protein-CNT complexes that would govern the uptake and disposition, which in turn could be responsible for CNT toxicity. In addition, some surfactants treated CNT would provide platform to be physisorbed by lipids and proteins in the surrounding environment. Therefore, it needs to be understood that these surface modifications will play a key role in governing uptake and disposition, which in turn can be important determinants of toxicity.

Two-photon confocal microscopy studies,⁷¹ Raman microscopy and lactate dehydrogenase (LDH) assay, were employed to study the effect of CNTs on rat glioma cell line (C6 cells) and rat alveolar macrophage continuous cell line (AM 11). Two-photon confocal microscopy reveals that unmodified CNT is toxic to the C6 cell line but, when modified by DNA, it becomes relatively non-toxic. Both LDH assay and Raman microscopy show that CNTs dispersed in serum are not toxic to the AM11 and C6 cell lines. They have illustrated that the controversy in CNT toxicity will continue, even within the same laboratory, if the changes in the surface properties of CNTs are not considered and well understood before these materials are tested for toxicological properties.

Sayes *et al.*⁷³ performed *in vitro* cytotoxicity screens on cultured human dermal fibroblasts (HDF). The SWCNTs (synthesized using the HiPCo method, about 400 nm long) were subjected to functionalization techniques to synthesize SWCNT-phenyl-SO₃H and SWCNT-phenyl-SO₃Na (six samples with carbon/phenyl-SO₃X ratios of 18, 41, and 80), SWCNT-phenyl-(COOH)₂ (one sample with carbon/phenyl-(COOH)₂ ratio of 23), and underivatized SWCNT stabilized in 1% Pluronic F108. Authors have found that as the degree of side-walled functionalization increases, the SWCNTs sample becomes less cytotoxic. Further, side-walled functionalized SWCNT samples are substantially less cytotoxic than surfactant stabilized SWCNTs and direct contact between cellular membranes and water-dispersible SWCNTs has been observed by atomic absorption micrographs.

Bianco *et al.*⁷⁴ reported that functionalized CNTs are able to cross the cell membrane. This assay confirmed the results of the WST-1 test⁷⁵ in that almost no decrease in viability was observed after 24 hr exposure of NR8383 cells to CNTs at a concentration of 100 µg/ml. This is in accordance with other published results that demonstrate no cytotoxic effect of intact CNTs on cell membrane integrity by assessing the LDH levels of the supernatants of macrophage cultures.³³

Carrero-Sánchez *et al.*⁶⁹ compared the toxicological effects between pure MWCNTs and N-doped multiwalled carbon (CN_x) nanotubes. They found that when MWCNTs were injected into the mice's trachea, the mice could die by dyspnea depending on the MWCNTs' doses. However, CN_x nanotubes did not cause the death of any mouse. Extremely high concentrations of CN_x nanotubes administrated directly into the mice's trachea only induced granulomatous inflammatory responses. Therefore CN_x nanotubes are less harmful than MWCNTs or SWCNTs and may have the potential to be used in bioapplications.

Polymer-functionalized carbon nanotubes⁷⁶ hold great promise for their use in environmental and biomedical applications. In this work, polyethyleneimine (PEI) was covalently bonded to acid-treated MWCNTs through amide bond formation. Neutral and negatively charged MWCNTs are nontoxic to both cell lines at a concentration up to 100 µg/mL, whereas positively charged MWCNTs are toxic to FRO cells at 10 µg/mL. The results of this study demonstrate that PEI-modified MWCNTs can be chemically modified to alter their surface charges and cytotoxicity, thereby significantly improving the biocompatibility of the materials for a variety of biomedical applications.

20.5.5 Structural defects

Ideal CNTs are made of one (SWCNT) or more (MWCNT) graphene sheets with hexagonal display of sp² hybridized carbon atoms. However, CNTs are not the perfect structures they once were thought to be.⁶⁵ Several properties, which were studied for ideal CNTs, depending mainly on their diameter and chirality, are also strongly affected by the presence of defects such as pentagons, heptagons, vacancies or dopant species.⁷⁷

For most carbon materials, including carbon nanotubes, carbon atoms are arranged in aromatic rings which build up lamellae (graphene sheets) of various sizes and stacking heights. These aromatic layers are usually not structurally perfect and several types of defects may be present.⁷⁸ Carbon atoms in these defects as well as those present on the edges of the graphene sheets are much more reactive than the atoms in the interior of the graphene sheets. The common structural defects existing in CNTs are atomic vacancies and topologic defects, of which the former corresponds to the deficiency of carbon atoms in a CNT, and the latter is associated with the network topology deviated from the hexagon rings.⁷⁹

High-resolution transmission electron microscopy (TEM) images indicate⁸⁰ that acid treatment induce defects on the sidewalls of the nanotubes. The inner

walls can be damaged without affecting the outer walls, while the inner walls are opened along with the outer ones by heating in air. Also amorphous carbon was found inside the nanotubes after oxidation.⁸⁰

To examine how structural properties may modulate the toxicity of CNTs, Fenoglio *et al.*^{46,81} and Muller *et al.*⁸¹ explored the physicochemical determinants of these toxic responses with progressively and selectively modified CNTs: ground multi-walled CNTs modified by heating at 600 °C (loss of oxygenated carbon functionalities and reduction of oxidized metals) or at 2400 °C (annealing of structural defects and elimination of metals) and by grinding the material that had been heated at 2400 °C before (introduction of structural defects in a metal-deprived framework). The CNTs were administered intratracheally (2 mg/rat) to Wistar rats to evaluate the short-term response (3 days) in bronchoalveolar lavage fluid (LDH, proteins, cellular infiltration, IL-1 β , and TNF- α). The long-term (60 days) lung response was assessed biochemically by measuring the lung hydroxyproline content and histologically. *In vitro* experiments were also performed on rat lung epithelial cells to assess the genotoxic potential of the modified CNTs with the cytokinesis block micronucleus assay. The results show that the acute pulmonary toxicity and the genotoxicity of these CNTs were reduced upon heating but restored upon grinding, indicating that the intrinsic toxicity of CNTs is mainly mediated by the presence of defective sites in their carbon framework. Thus, defects may be one of the major factors governing the toxic potential of CNTs. The exact method of formation of defects is not well understood. However, there are certain spectroscopic evidence which confirms the creation of defects in CNTs under strong acid treatment, microwave digestion and sonication. This again highlights the fact that experimental procedures and characterization techniques for toxicological studies are highly necessary and such studies are probably ongoing in many laboratories in the world.

20.5.6 Metal catalyst residues and impurities

It is clear that the catalytically synthesized carbon nanotubes typically contain 3–30 wt% metal as produced, whereas most commercially ‘purified’ products contain lower but significant amounts of metal residue.⁸² These metal impurities can be from the catalyst used and/or those introduced inadvertently during the purification and functionalization steps. At present, thermal gravimetric analysis (TGA) and X-ray fluorescence (XRF) analysis are used for quantitative and qualitative analysis of multiple elements in CNTs respectively. However, each technique has its own limitations. Although inductively coupled plasma mass spectrometry (ICP-MS) is widely used for geological, environmental and biological samples to be digested and prepared into solutions, the chemical inertness of CNTs does not help the solubilization of CNTs. It is evident that in order to understand the toxicological investigations, such analytical techniques capable of effectively quantifying metallic impurities in CNTs are needed. For example, iron has been hypothesized to contribute to the toxicity of Fe-containing

carbon nanotubes.^{13,16,82–86} Recently, Ge and co-workers reported a practically useful neutron activation analysis (NAA) technique and inductively coupled plasma mass spectrometry (ICPMS) analytical method for quantitative determination of metallic impurities in CNTs.⁸⁶ Guo *et al.*⁸² confirmed the hypothesis that iron-catalyzed free-radical generation can contribute to oxidative stress and toxicity upon exposure to ambient particulate, amphibole asbestos fibres and SWCNTs. Generally, the iron phase both in the hollow cores and/or at the tips of as-synthesized carbon nanotubes consist of γ -iron, β -iron, Fe_3C and Fe_{1-x}S .⁸⁷ The Fe_{1-x}S phase decomposes completely around 1500 °C while the iron carbide phase decomposes in the temperature range of 1500–2400 °C. Thus, a thermal treatment method was developed to reduce metal impurities from carbon nanotubes. But, on the other hand, authors⁸² concluded that iron bioavailability varies greatly from sample to sample and cannot be predicted from total iron content as only the small amount of total Fe (1–7% wt) is responsible for CNT toxicity. Iron bioavailability is not fully suppressed by vendor ‘purification’ and is sensitive to partial oxidation, mechanical stress, sample age, and intentional chelation.

The hypothesis that SWCNT toxicity may be dependent upon the metal (particularly iron) content has been confirmed by Murray *et al.*⁸⁵ The toxic effect of SWCNTs may be explained via the metal’s ability to interact with the skin, initiate oxidative stress, and induce redox-sensitive transcription factors thereby affecting/leading to inflammation. To test this hypothesis, the effects of SWCNTs were assessed both *in vitro* and *in vivo* using EpiDerm FT engineered skin, murine epidermal cells (JB6 P+), and immune-competent hairless SKH-1 mice. No significant changes in AP-1 activation were detected when partially purified SWCNTs (0.23% iron) were introduced to the cells. The results indicated that topical exposure to unpurified SWCNTs induced free radical generation, oxidative stress, and inflammation, thus causing dermal toxicity.

In another work,⁷⁵ NR8383 and human A549 lung cells were incubated with commercial SWCNTs and MWCNTs, carbon black and quartz as reference particles as well as an acid-treated SWCNT preparation (SWCNT a.t.) with reduced metal catalyst content. The authors did not observe any acute toxicity on cell viability (WST-1, PI-staining) upon incubation with all CNT products. None of the CNTs induced the inflammatory mediators NO, TNF- α and IL-8. A rising tendency of TNF- α release from LPS-primed cells due to CNT treatment could be observed. However, they detected a dose- and time-dependent increase of intracellular reactive oxygen species and a decrease of the mitochondrial membrane potential with the commercial CNTs in both cell types after particle treatment whereas incubation with the purified CNTs (SWCNT a.t.) had no effect. Thus, the authors concluded that metal traces associated with the commercial nanotubes may be responsible for the toxicological effects.

On the other hand, contradictory results were shown by Lam *et al.*²¹ in the toxicological study of nanotubes produced under different conditions containing different heavy metals (see Table 20.4). Samples of ‘raw’ and ‘purified’ nanotubes

Table 20.4 Metal content of test samples and experimental design of the intratracheal instillation study in mice²¹

Test materials	Metal contents (% by wt.)*			Dust dose (mg/mouse)	Number of mice	
	Fe	Ni	Y	Others	7 days	90 days
Raw nanotubes (RNT), rice product	26.9	0.78	0.00	Cu: 0.36; Mo: 0.95; Zn: 0.01	LD 0.1 HD 0.5	4 5
Purified nanotubes (PNT), rice product	2.14	0.00	0.00	None	LD 0.1 HD 0.5	4 5
CarboLex nanotubes (CNT)	0.53	25.99	5.01	Al: 0.15; Zn: 0.15; Co: 0.02	LD 0.1 HD 0.5	4 5
Carbon black (Printex-90)	0.00	0.00	0.00	None	LD 0.1 HD 0.5	4 5
Quartz (Min-U-Sil-5)	ND	ND	ND	ND	LD 0.1 HD 0.5	4 5
Vehicle control (mouse serum)	ND	ND	ND	ND	– 0.0	4 5

Notes: mice (4 or 5 per group) were each intratracheally instilled once with 0, 0.1, or 0.5 mg dust in mouse serum and euthanized after 7 or 90 days for histopathology study.
ND: not determined. LD, low dose. HD, high dose.
* Metals with concentrations < 0.01% by weight are not shown.

both contained iron, while a third nanotube product contained nickel and yttrium. All animals treated with 0.1mg per mouse of nickel-yttrium containing nanotubes showed no overt clinical signs. But 5 of 9 mice treated with 0.5mg died: 2/4 within the 7-day group and 3/5 in the 90-day group. The iron-containing nanotubes (both raw and purified) did not cause deaths in the mice.

The Panessa-Warren *et al.*⁸⁸ investigation examined 'as-prepared' and acid-cleaned carbon nanoparticle physicochemical characteristics and whether these characteristics changed following 2.5–7 yr exposure to pH neutral saline or fresh water. To determine if these aqueous aged nanotubes were cytotoxic, these nanotubes were incubated with human epithelial monolayers and analyzed for cell viability (vital staining) and ultrastructural nanoparticle binding/localization. The presence of Ni and Y catalyst was less damaging to cells than CNT lattice surface oxidation. Extended fresh water storage of oxidized CNTs did not reduce surface reactive groups, nor lessen cell membrane destruction or cell death. However, storing oxidized CNTs in saline or natural organic matter (NOM) significantly reduced CNT-induced cell membrane damage and increased cell survival to control levels.

20.5.7 Type and level of impurities

Impurity atoms are always introduced during any growth method of a solid⁸⁹ and/or during the purification step of CNTs. For a reproducible growth method, it is necessary to know the source of impurities and to be able to control the type, concentration and depth distribution of impurities.

One very important point regarding toxicity is the variation of impurities of the different CNT preparations.⁹⁰ Most used fractions contain high amounts of metals. Another very important contamination is amorphous carbon, which exhibits comparable biological effects as carbon black. Impurities such as O, Si, P, S, Cl, Ar, Ti, Cr and Fe also were found.⁸⁹ Also, the presence of these amorphous carbon impurities may favour the covalent functionalization much more readily than the stable CNTs.

Different purification methods yield different CNT characteristics and may be suitable for the production of different types of CNTs.⁹¹ The purification methods can be categorized into two main groups, namely chemical and physical purifications. The chemical methods, such as oxidation by heating, acids and oxidizing agents, alkali treatment and annealing in inert gases separate the synthesis products based on their reactivity which normally introduce unavoidable defects along the tubes and the pentagonal structure at the tube ends, causing remarkable damages to the structure and morphology of the CNTs. However, with proper control of the reaction conditions, purification of CNTs through the removal of metal catalyst particles may result in higher purity as well as the tips opening.⁹¹

On the other hand, the physical methods, such as ultrasonication, filtration, centrifugation, and size-exclusive chromatography, separate the impurities based

on their size. These processes are relatively mild and do not cause severe damage to the tubes, but they are normally more complex and less effective.⁹²

Koyama *et al.*⁹³ clarified the effect of impurities within such tubes through systemic studies of immunological responses in mice by monitoring and examining changes in peripheral T-cell subset and peripheral cytokine levels and histology. Contaminated and thermally treated at 1800 °C and 2800 °C MWNTs (see Table 20.5) were subcutaneously implanted in mice. The implanted tubes with impurities clearly induced immunological toxicity and localized alopecia, whereas extremely pure implanted tubes showed good biocompatibility. Those studies suggest that such high-temperature thermal treatment is an effective way to improve the biocompatibility of carbon nanotubes.

Other studies^{21,39} demonstrated that nanotubes themselves have a toxic effect on the cells, but not the impurities. Thus, Cheng *et al.*³⁹ exposed human macrophage cells to unpurified MWCNTs and found that a decrease in cell viability due to mainly necrosis was correlated with uptake of MWCNTs. Cells treated with purified MWCNTs and the main contaminant Fe₂O₃ itself yielded toxicity only from the nanotubes and not from the Fe₂O₃. Researchers observed that unpurified MWCNTs entered the cell both actively and passively, frequently inserting through the plasma membrane into the cytoplasm and the nucleus. These suggest that MWCNTs may cause incomplete phagocytosis or mechanically

Table 20.5 Basic characteristic of as-grown and thermally treated multi-walled carbon nanotubes at 1800 and 2800 °C, respectively⁹²

Item	As-grown	HTT = 1800°C	HTT = 2800°C	Testing method
Diameter (nm)	100–150	100–150	100–150	FE-SEM
Length (μm)	10–20	10–20	10–20	FE-SEM
d_{002}	–	–	0.339	X-ray diffraction
$R(I_D/I_G)^a$	1.041	0.855	0.051	Raman spectroscopy
Specific surface area (m ² /g)	–	26	13	N ₂ adsorption
Real density (g/cm ³)	–	–	2.09	Pycnometer
Fe content (ppm)	12,000	80	<20	ICP-MS
Soluble iron content (%) ^b	0	91	100	ICP-MS
Polycyclic aromatic hydrocarbons (wt%) ^c	0.19	None	None	GC-MS spectroscopy
Oxidation temperature (°C) ^d	630	720	820	TGA

^a R refers to the intensity of D band over the intensity of G band.

^b We have determined the dissolved amount of iron by refluxing 5 g of nanotubes in hydrochloric acid (0.6 N) for 25 h.

^c We have measured acetone-soluble components.

^d We have determined the oxidation temperatures via the derivation of TGA curve.

pierce through the plasma membrane and result in oxidative stress and cell death.

On the other hand, Miyawaki *et al.*⁹⁴ investigated *in vitro* and *in vivo* toxicities of as-grown single-walled carbon nanohorns (SWNHs), a tubular nanocarbon containing no metal impurity. The SWNHs were found to be a non-irritant and a nondermal sensitizer through skin primary and conjunctival irritation tests and skin sensitization test. Negative mutagenic and clastogenic potentials suggest that SWNHs are not carcinogenic. The acute peroral toxicity of SWNHs was found to be quite low – the lethal dosage for rats was more than 2000 mg/kg of body weight. Intratracheal instillation tests revealed that SWNHs rarely damaged rat lung tissue for a 90-day test period, although black pigmentation due to accumulated nanohorns was observed. While further toxicological assessments, including chronic (repeated dose), reproductive, and developmental toxicity studies are still required, the present results strongly suggest that as-grown SWNHs have low acute toxicities.

20.6 Future biological applications of carbon nanotubes

Carbon-based biomaterials have been employed with great success for decades. Most notably, pyrolytic carbon has been used in biomedical implants and coatings, particularly in mechanical heart valve prostheses.⁹⁵ Pyrolytic carbons have excellent biocompatibility properties,^{96,97} with good adherence of endothelial cells and minimal adherence and activation of platelets demonstrated.⁹⁸ A more recent development in carbon biomaterials is diamond-like carbon (DLC). This dense metastable form of amorphous carbon has several properties which makes it desirable for biomedical applications. Most notable are its high hardness, low coefficient of friction, chemical inertness and good corrosion and wear resistance.^{99–101} DLC coatings for orthopedic and cardiovascular applications have also performed very well in terms of biocompatibility.^{99,102–105}

The potential biomedical utility of CNTs appears to carry momentum in three key areas: medical imaging and therapeutic delivery;^{106,107} regenerative medicine;¹⁰⁸ and nanocomposite biomaterials with improved mechanical and/or biological performance.^{109–114} Many of these applications are described in more detail in Chapter 22 of this book, and so will only be discussed briefly here.

CNTs and many other nanoscale objects are attractive as delivery vehicles and imaging agents due to their inherent chemical stability, ability to be internalized by cells, tunable surface functionality and unique electrical and spectroscopic properties.^{106,107,115} The many challenges of engendering physiological solubility and therapeutic activity via surface modification,^{58,106,107,116} and imaging via labeling with various radionuclides^{61,117–120} are being addressed, but still yet-to-come are studies which unequivocally demonstrate better therapeutic efficacy and safety of CNT-based technologies over established alternatives.¹⁰⁶

With the ageing population placing considerable pressure on the future need for therapies and devices based on regenerative rather than replacement modalities, CNTs are also finding their way into polymeric or ceramic composite scaffolds being developed for tissue engineering.¹⁰⁸ Clever incorporation of CNTs into scaffolds for bone regeneration can have multiple advantages. Porous 3-D structures are required to induce and accommodate the integration of new, properly organized and vascularized tissue, ideally by mimicking the native bone extracellular matrix. The mechanical properties of grafting materials are important factors in determining their suitability for use in orthopaedic therapies. When a graft is placed on injured bone site, it should be able to withstand both compressive and bending loads without failing, and should do so for the time required for complete growth of the new bone tissue. Most porous scaffold materials do not have adequate stiffness, strength or impact properties, therefore CNTs are being investigated as efficient high aspect ratio particulate reinforcement.^{109,110} Moreover, the surface of CNTs can be modified to enhance calcium phosphate biomineralization,¹¹¹ and the volume fraction and organization of CNTs can be altered to perturb the scaffold surface energy and texture,^{112,113,121} which have also been shown to lead to enhanced tissue regeneration. In a similar manner, the fatigue life acrylic bone cement (used essentially as a grout for metallic hip and knee implants and bone), has been improved through the reinforcement of MWCNTs.¹¹⁴ Naturally, one critical question which still needs answering is; when a biodegradable scaffold incorporating CNTs slowly breaks down, what happens to the CNTs over time, and do the risks of having remnant CNTs outweigh the advantages? Composite scaffold studies involving tracking of radio-labelled CNTs need to be performed in order to establish a better understanding of chronic biodistribution and biological interactions.

The unique electrical properties of CNTs have naturally attracted the attention of neural tissue engineers. Since the first reports of neuronal cell attachment and growth on MWCNTs in 2000,¹²² many other workers have reported improved neural generation activity when grown on polymer–SWCNT composites¹²³ and MWCNT substrates prepared with or without attachment of growth factors such as neurotrophin.^{124,125} CNT coatings on traditional metal wire electrodes have been shown to promote both enhanced recoding and stimulating characteristics.¹²⁶ Elegant layer-by-layer assembly of alternating SWCNT–polyelectrolyte layers has yielded exceptionally strong membranes which also demonstrated enhanced guided neurite outgrowth, with or without electrical stimulation.^{127–129} Another layer-by-layer CNT composite was shown to successfully enhance the differentiation of stem cells to neuronal cells when compared to a conducting polymer culture substrate.¹³⁰

20.7 Future trends

As nanotechnology discovery and innovation march rapidly ahead, there is a critical nexus which exists today, where a very difficult balancing act is taking

place. Generation of new toxicological scientific data and methodologies, rate-limited by finite R&D funding for 'risk-related' nanomaterials research, is balanced and influenced more by political agenda. For example, the inertia of retrospectively adapting inadequate regulatory frameworks for nanomaterials, and also the influence of the media, public perceptions and recent memories of 'unintended consequences' are inherited from previous rapid technological advances.¹³¹

Regulators and policy decision-makers are trying hard to arrive at more workable frameworks. In a collaborative paper summarizing conclusions from a 2008 NATO workshop on nanomaterial regulation, a multidisciplinary working group reviewed the documents listed in Table 20.6 and compared and contrasted their content under the categories of: (1) science and research aspects; (2) legal and regulatory aspects; (3) social engagements and partnerships; and (4) leadership and governance.¹³² Clearly, such in-depth international information sharing is going to be required to more efficiently address the existing bottleneck.

Choi *et al.*¹³³ estimated that if all nanomaterials required long-term *in vivo* testing (comprehensive precautionary approach), in the US alone it would cost \$1.18bn and take up to 53 years if all existing nanomaterials were to be thoroughly tested. They strongly supported a more tiered risk assessment strategy, similar to the EU's new REACH legislation¹³⁴ for regulating chemicals. In such a system, initial screening comprising simple and inexpensive tests is used to prioritize substances for further more complex and expensive tests, with increasing degrees of selectivity for adverse effect.^{133,134} Implicit here for suppliers of nanomaterials will be the need to provide more specific information and recommendation of risk management measures (not just classification and labelling) in the way of materials safety data sheets (MSDS). Information including physicochemical information, handling and storage, exposure controls/personal protection and toxicological/ecotoxicological information will be required. Clearly for this to happen most effectively, risk assessors need to be engaged in the nanomaterial research, development and manufacturing processes, so that lowest risk options or formulations can be selected without compromising ultimate product performance,¹³² and so that researchers and workers handling the nanomaterials can be properly protected from the outset.

The following key areas are seen as critical gaps in knowledge required to safely progress and mature nanomaterials technologies, including carbon nanotubes:

1. Attain reliable measurements of human and environmental exposure levels¹³⁵ to inform realistic and meaningful dosing and threshold bands for other toxicology studies. Development of associated metrology.
2. Assess genotoxic potential and improve methods for predicting potential long-term effects.¹³⁶
3. Improve or develop robust, chemically stable and sensitive fluorescent or radionuclide labelling methodologies which do not affect nanoparticle

Table 20.6 Elements of nanomaterial regulation frameworks discussed in each document at NATO workshop on nanomaterial regulation in 2008¹³²

	Science and research aspects				Legal and regulatory aspects				Social engagement and partnerships				Leadership and governance			
	1	2	3	4	1	2	3	4	1	2	3	4	1	2	3	4
USEPA 2007	■	■	■	■	■	■	■	■	■	■	■	■	■	■	■	■
US FDA 2007	■	■	■	■	■	■	■	■	■	■	■	■	■	■	■	■
Davies 2006	■	■	■	■	■	■	■	■	■	■	■	■	■	■	■	■
ED-DuPont 2007	■	■	■	■	■	■	■	■	■	■	■	■	■	■	■	■
Québec Commission 2006	■	■	■	■	■	■	■	■	■	■	■	■	■	■	■	■
UK Royal Society 2004	■	■	■	■	■	■	■	■	■	■	■	■	■	■	■	■
UK DEFRA 2006	■	■	■	■	■	■	■	■	■	■	■	■	■	■	■	■
Responsible NanoCode 2006	■	■	■	■	■	■	■	■	■	■	■	■	■	■	■	■
EC SCENIHR 2007	■	■	■	■	■	■	■	■	■	■	■	■	■	■	■	■
EC Action Plan 2005	■	■	■	■	■	■	■	■	■	■	■	■	■	■	■	■
IRGC 2005, 2006, 2007	■	■	■	■	■	■	■	■	■	■	■	■	■	■	■	■
US NNI 2008	■	■	■	■	■	■	■	■	■	■	■	■	■	■	■	■
REACH 2006	■	■	■	■	■	■	■	■	■	■	■	■	■	■	■	■

Sub-criteria for the table are as follows

Science and research aspects

1. Development of methods of detection/characterization/data collection
2. Assessment of environmental fate and transport/impacts
3. Assessment of toxicology/human health impacts
4. Assessment of health and environmental exposure

Legal and regulatory aspects

1. Voluntary regulatory and best-practices measures
2. Information-based regulatory tools (e.g. labeling)
3. Economic-based regulatory tools (e.g. tax or fee for safety testing)
4. Liability-based regulatory tools (e.g. penalty for pollution)

Social engagement and partnerships

1. Promotion of education and distribution of information/use of risk communication tools
2. Use of stakeholder engagement tools
3. Development of partnerships with academia, industry, public organizations, provinces, and international regulators
4. Emphasis of ethical conduct

Leadership and governance

1. Transparency in nanotechnology-related decisions
2. Consideration of benefits of nanotechnology
3. Adaptive modification of existing or development of new legislation
4. Consideration of precautionary principle

Criteria are numbered 1 to 4 under each category; for each document and criterion, ■ = document discussed the criterion, ■ = document mentioned the criterion, blank = document did not address the criterion; adapted from Linkov and Satterstrom 2008.

physicochemical or biological properties,^{117,137} thereby giving true biodistribution and toxicokinetic data.

4. Improved fundamental understanding of nanoparticle–biomolecule interactions (e.g. single and competitive protein interactions) and nanoparticle–cell interactions (e.g. nanoparticle interactions with cell-signalling pathways).

20.8 Conclusion

With the predicted increase in manufacture, use and disposal of CNTs in coming years, increased exposure of humans and the environment is inevitable. Currently, manufacturers and regulators face a dilemma due to rate-limiting finite R&D funding for ‘risk-related’ nanomaterials research, and also by the very high levels of metrology required to deliver CNT-related product assurance. These hurdles are balanced by the many very promising existing and potential future industrial and biomedical applications of CNTs and CNT composites.

Early results from toxicity studies comparing various forms of CNTs to other nanomaterials and asbestos do suggest that, for now, an extra conservative approach should be taken when handling CNTs of all forms to minimize exposure. There are also early indications that SWCNTs can display a higher level of toxicity than MWCNTs and that, in general, CNTs of higher aspect ratio are associated with increased health risks after lung exposure. However, differences in the source, preparation and purification of different commercial CNTs, and therefore potential differences in physicochemistry and contamination, are typically not fully taken into toxicological consideration. Improved CNT controls are required where at all possible, so that the number of variables known to affect CNT toxicity (aspect ratio, metal catalyst or other impurities, surface chemistry and defects, level of aggregation and hierarchical morphology and solubilization in physiological media) are minimized. As more long-term inhalation data linking measured exposure and chronic biological interactions comes to hand, a clearer picture will emerge. In order to do this successfully, more robust, chemically-stable and sensitive fluorescent or radionuclide-based labelling methodologies (which do not affect CNTs’ physicochemical or biological properties) will be required. New methods are also required to assess genotoxic potential and to be able to predict long-term biological effects. Understanding specific molecular interactions between nanomaterials and biomolecules and cells will be fundamentally critical.

Finally, large scale and multi-level cooperation between academia, industry and government sectors, media, NPOs and the community will be essential to avoid repeating past mistakes and ensuring that the tremendous utility of these materials is conservatively, responsibly and sustainably developed. The composites industry is one of the highest volume adopters of CNTs and therefore business and technical leaders in this sector will need to ensure they play their role in this evidence-based process.

20.9 References

- 1 Mueller, N. C., Som, C., Nowack, B. In *Nanotechnology 2009: Fabrication, Particles, Characterization, MEMS, Electronics and Photonics – Technical Proceedings of the 2009 NSTI Nanotechnology Conference and Expo, NSTI-Nanotech 2009* Houston, TX, 2009, Vol. 1, p 159–162.
- 2 Poland, C. A., Duffin, R., Kinloch, I., Maynard, A., Wallace, W. A. H., Seaton, A., Stone, V., Brown, S., MacNee, W., Donaldson, K. *Nature Nanotechnology*, 2008, 3, 423–428.
- 3 Donaldson, K., Poland, C. A. *Nature Nanotechnology*, 2009, 4, 708–710.
- 4 Ryman-Rasmussen, J. P., Cesta, M. F., Brody, A. R., Shipley-Phillips, J. K., Everitt, J. I., Tewksbury, E. W., Moss, O. R., Wong, B. A., Dodd, D. E., Andersen, M. E., Bonner, J. C. *Nature Nanotechnology*, 2009, 4, 747–751.
- 5 Sylvester, D. J., Abbott, K. W., Marchant, G. E. *Regulation and Governance*, 2009, 3, 165–185.
- 6 Handy, R. D., Shaw, B. J. *Health, Risk and Society*, 2007, 9, 125–144.
- 7 Chouard, C. H., Cabanis, E. A., Chambron, J., Milgrom, E. *Nanosciences et médecine*, 2008, 192, 1253–1259.
- 8 Richman, E. K., Hutchison, J. E. *ACS Nano*, 2009, 3, 2441–2446.
- 9 Cui, D., Tian, F., Ozkan, C. S., Wang, M., Gao, H. *Toxicology Letters*, 2005, 155, 73–85.
- 10 Walker, V. G., Li, Z., Hulderman, T., Schwegler-Berry, D., Kashon, M. L., Simeonova, P. P. *Toxicology and Applied Pharmacology*, 2009, 236, 319–328.
- 11 Shin, D. C., Jang, J. Y., Yang, J. Y., Kim, S. H., Choi, I. H., Lim, Y. W., Kim, C. S., Lee, G. T. In *Technical Proceedings of the 2008 NSTI Nanotechnology Conference and Trade Show, NSTI-Nanotech, Nanotechnology 2008*, Quebec City, QC, 2008, Vol. 2, pp. 142–145.
- 12 Liu, A., Sun, K., Yang, J., Zhao, D. *Journal of Nanoparticle Research*, 2008, 10, 1303–1307.
- 13 Liu, X., Guo, L., Morris, D., Kane, A. B., Hurt, R. H. *Carbon*, 2008, 46, 489–500.
- 14 Monteiro-Riviere, N. A., Nemanich, R. J., Inman, A. O., Wang, Y. Y., Riviere, J. E. *Toxicology Letters*, 2005, 155, 377–384.
- 15 Warheit, D. B., Laurence, B. R., Reed, K. L., Roach, D. H., Reynolds, G. A. M., Webb, T. R. *Toxicological Sciences*, 2004, 77, 117–125.
- 16 Shvedova, A. A., Castranova, V., Kisin, E. R., Schwegler-Berry, D., Murray, A. R., Gandelsman, V. Z., Maynard, A., Baron, P. *Journal of Toxicology and Environmental Health – Part A*, 2003, 66, 1909–1926.
- 17 Manna, S. K., Sarkar, S., Barr, J., Wise, K., Barrera, E. V., Jejelowo, O., Rice-Ficht, A. C., Ramesh, G. T. *Nano Letters*, 2005, 5, 1676–1684.
- 18 Pacurari, M., Yin, X. J., Zhao, J., Ding, M., Leonard, S. S., Schwegler-Berry, D., Ducatman, B. S., Sbarra, D., Hoover, M. D., Castranova, V., Vallyathan, V. *Environmental Health Perspectives*, 2008, 116, 1211–1217.
- 19 Ye, S. F., Zhong, L. M., Wu, Y. H., Zhang, Q. Q. *Gaodeng Xuexiao Huaxue Xuebao/ Chemical Journal of Chinese Universities*, 2009, 30, 497–501.
- 20 Park, E. J., Cho, W. S., Jeong, J., Yi, J., Choi, K., Park, K. *Toxicology*, 2009, 259, 113–121.
- 21 Lam, C. W., James, J. T., McCluskey, R., Hunter, R. L. *Toxicological Sciences*, 2004, 77, 126–134.
- 22 Hirano, S., Kanno, S., Furuyama, A. *Toxicology and Applied Pharmacology*, 2008, 232, 244–251.

- 23 Herzog, E., Byrne, H. J., Casey, A., Davoren, M., Lenz, A. G., Maier, K. L., Duschl, A., Oostingh, G. J. *Toxicology and Applied Pharmacology*, 2009, 234, 378–390.
- 24 Simon-Deckers, A., Gouget, B., Mayne-L’Hermite, M., Herlin-Boime, N., Reynaud, C., Carrière, M. *Toxicology*, 2008, 253, 137–146.
- 25 Karlsson, H. L., Cronholm, P., Gustafsson, J., Mällér, L. *Chemical Research in Toxicology*, 2008, 21, 1726–1732.
- 26 Li, J. G., Li, Q. N., Xu, J. Y., Cal, X. O., Liu, R. L., Li, Y. J., Ma, J. F., Li, W. X. *Journal of Nanoscience and Nanotechnology*, 2009, 9, 1384–1387.
- 27 Yang, S. T., Wang, X., Jia, G., Gu, Y., Wang, T., Nie, H., Ge, C., Wang, H., Liu, Y. *Toxicology Letters*, 2008, 181, 182–189.
- 28 Bello, D., Hsieh, S. F., Schmidt, D., Rogers, E. *Nanotoxicology*, 2009, 3, 249–261.
- 29 Jia, G., Wang, H., Yan, L., Wang, X., Pei, R., Yan, T., Zhao, Y., Guo, X. *Environmental Science and Technology*, 2005, 39, 1378–1383.
- 30 Bellucci, S., Bergamaschi, A., Bottini, M., Magrini, A., Mustelin, T. *Journal of Physics: Conference Series*, 2007, 95–98.
- 31 Huczko, A., Lange, H., Calko, E., Grubek-Jaworska, H., Droszcz, P. *Fullerene Science and Technology*, 2001, 9, 251–254.
- 32 Huczko, A., Lange, H., Bystrzejewski, M., Baranowski, P., Grubek-Jaworska, H., Nejman, P., Przybyłowski, T., Czumińska, K., Glapiński, J., Walton, D. R. M., Kroto, H. W. *Fullerenes Nanotubes and Carbon Nanostructures*, 2005, 13, 141–145.
- 33 Muller, J., Huaux, F., Moreau, N., Misson, P., Heilier, J. F., Delos, M., Arras, M., Fonseca, A., Nagy, J. B., Lison, D. *Toxicology and Applied Pharmacology*, 2005, 207, 221–231.
- 34 Shvedova, A. A., Kisin, E. R., Mercer, R., Murray, A. R., Johnson, V. J., Potapovich, A. I., Tyurina, Y. Y., Gorelik, O., Arepalli, S., Schwegler-Berry, D., Hubbs, A. F., Antonini, J., Evans, D. E., Ku, B. K., Ramsey, D., Maynard, A., Kagan, V. E., Castranova, V., Baron, P. *American Journal of Physiology – Lung Cellular and Molecular Physiology*, 2005, 289, L698–L708.
- 35 Maynard, A. D., Baron, P. A., Foley, M., Shvedova, A. A., Kisin, E. R., Castranova, V. *Journal of Toxicology and Environmental Health – Part A*, 2004, 67, 87–107.
- 36 Kang, S., Mauter, M. S., Elimelech, M. *Environmental Science and Technology*, 2008, 42, 7528–7534.
- 37 Kang, S., Mauter, M. S., Elimelech, M. *Environmental Science and Technology*, 2009, 43, 2648–2653.
- 38 De Nicola, M., Gattia, D. M., Bellucci, S., De Bellis, G., Micciulla, F., Pastore, R., Tiberia, A., Cerella, C., D’Alessio, M., Antisari, M. V., Marazzi, R., Traversa, E., Magrini, A., Bergamaschi, A., Ghibelli, L. *Journal of Physics Condensed Matter*, 2007, 19, 1–7.
- 39 Cheng, C., Muller, K. H., Koziol, K. K., Skepper, J. N., Midgley, P. A., Welland, M. E., Porter, A. E. *Biomaterials*, 2009, 30, 4152–4160.
- 40 Cheng, C., Porter, A. E., Muller, K., Koziol, K., Skepper, J. N., Midgley, P., Welland, M. *Journal of Physics: Conference Series*, 2009, 151, 1–15.
- 41 Schrand, A. M., Dai, L., Schlager, J. J., Hussain, S. M., Osawa, E. *Diamond and Related Materials*, 2007, 16, 2118–2123.
- 42 Pulido, M. D., Parrish, A. R. *Mutation Research – Fundamental and Molecular Mechanisms of Mutagenesis*, 2003, 533, 227–241.
- 43 Magrez, A., Kasas, S., Salicio, V., Pasquier, N., Seo, J. W., Celio, M., Catsicas, S., Schwaller, B., Forrè, L. *Nano Letters*, 2006, 6, 1121–1125.
- 44 Tong, H., McGee, J. K., Saxena, R. K., Kodavanti, U. P., Devlin, R. B., Gilmour, M. I. *Toxicology and Applied Pharmacology*, 2009, 239, 224–232.

- 45 Sato, Y., Yokoyama, A., Shibata, K. I., Akimoto, Y., Ogino, S. I., Nodasaka, Y., Kohgo, T., Tamura, K., Akasaka, T., Uo, M., Motomiya, K., Jeyadevan, B., Ishiguro, M., Hatakeyama, R., Watari, F., Tohji, K. *Molecular BioSystems*, 2005, *1*, 176–182.
- 46 Fenoglio, I., Greco, G., Tomatis, M., Muller, J., Raymundo-Piàtero, E., Bàcguin, F., Fonseca, A., Nagy, J. B., Lison, D., Fubini, B. *Chemical Research in Toxicology*, 2008, *21*, 1690–1697.
- 47 Takagi, A., Hirose, A., Nishimura, T., Fukumori, N., Ogata, A., Ohashi, N., Kitajima, S., Kanno, J. *Journal of Toxicological Sciences*, 2008, *33*, 105–116.
- 48 Kostarelos, K. *Nature Biotechnology*, 2008, *26*, 774–776.
- 49 Yu, Y., Zhang, Q., Mu, Q., Zhang, B., Yan, B. *Nanoscale Research Letters*, 2008, *3*, 271–277.
- 50 Agharkar, V. A., Bhushan, A., Lai, J. C. K., Daniels, C. K. In *Technical Proceedings of the 2008 NSTI Nanotechnology Conference and Trade Show, NSTI-Nanotech, Nanotechnology 2008* Quebec City, QC, 2008, Vol. 2, p 122–125.
- 51 Mu, Q., Liu, W., Xing, Y., Zhou, H., Li, Z., Zhang, Y., Ji, L., Wang, F., Si, Z., Zhang, B., Yan, B. *Journal of Physical Chemistry C*, 2008, *112*, 3300–3307.
- 52 Becker, M. L., Fagan, J. A., Gallant, N. D., Bauer, B. J., Bajpai, V., Hobbie, E. K., Lacerda, S. H., Migler, K. B., Jakupciak, J. P. *Advanced Materials*, 2007, *19*, 939–945.
- 53 Journeay, W. S., Suri, S. S., Moralez, J. G., Fenniri, H., Singh, B. *International Journal of Nanomedicine*, 2008, *3*, 373–383.
- 54 Tagmatarchis, N., Prato, M. *Journal of Materials Chemistry*, 2004, *14*, 437–439.
- 55 Donaldson, K., Aitken, R., Tran, L., Stone, V., Duffin, R., Forrest, G., Alexander, A. *Toxicological Sciences*, 2006, *92*, 5–22.
- 56 Wick, P., Manser, P., Limbach, L. K., Dettlaff-Weglikowska, U., Krumeich, F., Roth, S., Stark, W. J., Bruinink, A. *Toxicology Letters*, 2007, *168*, 121–131.
- 57 Soto, K., Garza, K. M., Murr, L. E. *Acta Biomaterialia*, 2007, *3*, 351–358.
- 58 Tasis, D., Tagmatarchis, N., Bianco, A., Prato, M. *Chemical Reviews*, 2006, *106*, 1105–1136.
- 59 Smart, S. K., Cassady, A. I., Lu, G. Q., Martin, D. J. *Carbon*, 2006, *44*, 1034–1047.
- 60 Kharisov, B. I., Kharissova, O. V., Gutierrez, H. L., Mández, U. O. *Industrial and Engineering Chemistry Research*, 2009, *48*, 572–590.
- 61 Lacerda, L., Soundararajan, A., Singh, R., Pastorin, G., Al-Jamal, K. T., Turton, J., Frederik, P., Herrero, M. A., Li, S., Bao, A., Emfietzoglou, D., Mather, S., Phillips, W. T., Prato, M., Bianco, A., Goins, B., Kostarelos, K. *Advanced Materials*, 2008, *20*, 225–230.
- 62 Xu, F., Xu, J., Ji, J., Shen, J. *Acta Polymerica Sinica*, 2008, 1006–1009.
- 63 Deng, X., Wu, F., Liu, Z., Luo, M., Li, L., Ni, Q., Jiao, Z., Wu, M., Liu, Y. *Carbon*, 2009, *47*, 1421–1428.
- 64 Dumortier, H., Lacotte, S., Pastorin, G., Marega, R., Wu, W., Bonifazi, D., Briand, J. P., Prato, M., Muller, S., Bianco, A. *Nano Letters*, 2006, *6*, 1522–1528.
- 65 Marques, R. R. N., Machado, B. F., Faria, J. L., Silva, A. M. T. *Carbon*, 2008, *46*, 1515–1523.
- 66 Saxena, R. K., Williams, W., McGee, J. K., Daniels, M. J., Boykin, E., Gilmour, M. I. *Nanotoxicology*, 2007, *1*, 291–300.
- 67 Sato, Y., Shibata, K. I., Kataoka, H., Ogino, S. I., Bunshi, F., Yokoyama, A., Tamura, K., Akasaka, T., Uo, M., Motomiya, K., Jeyadevan, B., Hatakeyama, R., Watari, F., Tohji, K. *Molecular BioSystems*, 2005, *1*, 142–145.
- 68 Guo, J., Zhang, X., Zhang, S., Zhu, Y., Li, W. *Current Nanoscience*, 2008, *4*, 240–245.
- 69 Carrero-Sánchez, J. C., Elàmas, A. L., Mancilla, R., Arrellàn, G., Terrones, H., Laclette, J. P., Terrones, M. *Nano Letters*, 2006, *6*, 1609–1616.

- 70 Dutta, D., Sundaram, S. K., Teeguarden, J. G., Riley, B. J., Fifield, L. S., Jacobs, J. M., Addleman, S. R., Kaysen, G. A., Moudgil, B. M., Weber, T. J. *Toxicological Sciences*, 2007, 100, 303–315.
- 71 Senanayake, V., Juurlink, B. H., Zhang, C., Zhan, E., Wilson, L. D., Kwon, J., Yang, J., Lim, Z. L., Brunet, S. M. K., Schatte, G., Maley, J. M., Hoffmeyer, R. E., Sammynaiken, R. *Journal of Biomedical Nanotechnology*, 2008, 4, 515–523.
- 72 Bardi, G., Tognini, P., Ciofani, G., Raffa, V., Costa, M., Pizzorusso, T. *Nanomedicine: Nanotechnology, Biology, and Medicine*, 2009, 5, 96–104.
- 73 Sayes, C. M., Liang, F., Hudson, J. L., Mendez, J., Guo, W., Beach, J. M., Moore, V. C., Doyle, C. D., West, J. L., Billups, W. E., Ausman, K. D., Colvin, V. L. *Toxicology Letters*, 2006, 161, 135–142.
- 74 Bianco, A., Kostarelos, K., Prato, M. *Current Opinion in Chemical Biology*, 2005, 9, 674–679.
- 75 Pulskamp, K., Diabatà, S., Krug, H. F. *Toxicology Letters*, 2007, 168, 58–74.
- 76 Shen, M., Wang, S. H., Shi, X., Chen, X., Huang, Q., Petersen, E. J., Pinto, R. A., Baker, J. R., Weber, W. J. *The Journal of Physical Chemistry C*, 2009, 113, 3150–3156.
- 77 Charlier, J. C. *Accounts of Chemical Research*, 2002, 35, 1063–1069.
- 78 Bâguin, F., Flahaut, E., Linares-Solano, A., Pinson, J. In *Lecture Notes in Physics*, Loiseau, A., Launois, P., Petit, P., Roche, S., Salvétat, J. P., Eds. 2006, 677, p 495–549.
- 79 He, H. Y., Pan, B. C. *Frontiers of Physics in China*, 2009, 4, 297–306.
- 80 Meyer, C., Spudat, C., Houben, L., Schneider, C. M. *Nanotechnology*, 2009, 20.
- 81 Muller, J., Huaux, F., Fonseca, A., Nagy, J. B., Moreau, N., Delos, M., Raymundo-Piàtero, E., Bâguin, F., Kirsch-Volders, M., Fenoglio, I., Fubini, B., Lison, D. *Chemical Research in Toxicology*, 2008, 21, 1698–1705.
- 82 Guo, L., Morris, D. G., Liu, X., Vaslet, C., Hurt, R. H., Kane, A. B. *Chemistry of Materials*, 2007, 19, 3472–3478.
- 83 Liu, X., Gurel, V., Morris, D., Murray, D. W., Zhitkovich, A., Kane, A. B., Hurt, R. H. *Advanced Materials*, 2007, 19, 2790–2796.
- 84 Kagan, V. E., Tyurina, Y. Y., Tyurin, V. A., Konduru, N. V., Potapovich, A. I., Osipov, A. N., Kisin, E. R., Schwegler-Berry, D., Mercer, R., Castranova, V., Shvedova, A. A. *Toxicology Letters*, 2006, 165, 88–100.
- 85 Murray, A. R., Kisin, E., Leonard, S. S., Young, S. H., Kommineni, C., Kagan, V. E., Castranova, V., Shvedova, A. A. *Toxicology*, 2009, 257, 161–171.
- 86 Ge, C., Lao, F., Li, W., Li, Y., Chen, C., Qiu, Y., Mao, X., Li, B., Chai, Z., Zhao, Y. *Analytical Chemistry*, 2008, 80, 9426–9434.
- 87 Chen, J., Kuno, A., Matsuo, M., Tsukada, T., Tamura, T., Osato, K., Shan, J. Y., Munekane, F., Kim, Y. A., Hayashi, T., Endo, M. *Carbon*, 2008, 46, 391–396.
- 88 Panessa-Warren, B. J., Maye, M. M., Warren, J. B., Crosson, K. M. *Environmental Pollution*, 2009, 157, 1140–1151.
- 89 Usov, I. O., Wang, Y. Q., Li, Q., Zhu, Y. T., DePaula, R. F., Arendt, P. N. *Nuclear Instruments and Methods in Physics Research Section B: Beam Interactions with Materials and Atoms*, 2007, 261, 574–577.
- 90 Wolrle-Knirsch, J. M., Pulskamp, K., Krug, H. F. *Nano Letters*, 2006, 6, 1261–1268.
- 91 Ismail, A. F., Goh, P. S., Tee, J. C., Sanip, S. M., Aziz, M. *Nano*, 2008, 3, 127–143.
- 92 Salernitano, E., Giorgi, L., Dikonimos Makris, T., Giorgi, R., Lisi, N., Contini, V., Falconieri, M. *Diamond and Related Materials*, 2007, 16, 1565–1570.
- 93 Koyama, S., Kim, Y. A., Hayashi, T., Takeuchi, K., Fujii, C., Kuroiwa, N., Koyama, H., Tsukahara, T., Endo, M. *Carbon*, 2009, 47, 1365–1372.

- 94 Miyawaki, J., Yudasaka, M., Azami, T., Kubo, Y., Iijima, S. *ACS Nano*, 2008, 2, 213–226.
- 95 Haubold, A. D., Shim, H. S., Bokros, J. C. *Biomaterials Medical Devices and Artificial Organs* 1979, 7, 263–269.
- 96 Cenni, E., Granchi, D., Arciola, C. R., Ciapetti, G., Savarino, L., Stea, S., Cavedagna, D., Di Leo, A., Pizzoferrato, A. *Biomaterials* 1995, 16, 1223–1227.
- 97 Ma, L., Sines, G. *Journal of Biomedical Materials Research*, 2000, 51, 61–68.
- 98 Haubold, A. D. *ASAIO Journal* 1983, 6, 88–93.
- 99 Cui, F. Z., Li, D. J. *Surface and Coatings Technology*, 2000, 131, 481–487.
- 100 Grill, A. *Diamond and Related Materials*, 2003, 12, 166–170.
- 101 Sheeja, D., Tay, B. K., Nung, L. N. *Diamond and Related Materials*, 2004, 13, 184–190.
- 102 Thomson, L. A., Law, F. C., Rushton, N., Franks, J. *Biomaterials* 1991, 12, 37–40.
- 103 Allen, M., Law, F., Rushton, N. *Clinical Materials* 1994, 17, 1–10.
- 104 Linder, S., Pinkowski, W., Aepfelbacher, M. *Biomaterials*, 2002, 23, 767–773.
- 105 Allen, M., Myer, B., Rushton, N. *Journal of Biomedical Materials Research*, 2001, 58, 319–328.
- 106 Kostarelos, K., Bianco, A., Prato, M. *Nat Nano*, 2009, 4, 627–633.
- 107 Liu, Z., Cai, W., He, L., Nakayama, N., Chen, K., Sun, X., Chen, X., Dai, H. *Nature Nanotechnology*, 2007, 2, 47–52.
- 108 Tran, P. A., Zhang, L., Webster, T. J. *Advanced Drug Delivery Reviews*, 2009, 61, 1097–1114.
- 109 Shi, X., Hudson, J. L., Spicer, P. P., Tour, J. M., Krishnamoorti, R., Mikos, A. G. *Nanotechnology*, 2005, 16, S531–S538.
- 110 Balani, K., Anderson, R., Laha, T., Andara, M., Tercero, J., Crumpler, E., Agarwal, A. *Biomaterials*, 2007, 28, 618–624.
- 111 Zhao, B., Hu, H., Mandal, S. K., Haddon, R. C. *Chemistry of Materials*, 2005, 17, 3235–3241.
- 112 Khang, D., Kim, S. Y., Liu-Snyder, P., Palmore, G. T. R., Durbin, S. M., Webster, T. J. *Biomaterials*, 2007, 28, 4756–4768.
- 113 Elias, K. L., Price, R. L., Webster, T. J. *Biomaterials*, 2002, 23, 3279–3287.
- 114 Marrs, B., Andrews, R., Rantell, T., Pienkowski, D. *Journal of Biomedical Materials Research – Part A*, 2006, 77, 269–276.
- 115 Kostarelos, K., Lacerda, L., Pastorin, G., Wu, W., Wieckowski, S., Luangsivilay, J., Godefroy, S., Pantarotto, D., Briand, J. P., Muller, S., Prato, M., Bianco, A. *Nature Nanotechnology*, 2007, 2, 108–113.
- 116 Ali-Boucetta, H., Al-Jamal, K. T., McCarthy, D., Prato, M., Bianco, A., Kostarelos, K. *Chemical communications*, 2008, 459–461.
- 117 McDevitt, M. R., Chattopadhyay, D., Jaggi, J. S., Finn, R. D., Zanzonico, P. B., Villa, C., Rey, D., Mendenhall, J., Batt, C. A., Njardarson, J. T., Scheinberg, D. A. *PLoS ONE*, 2007, 2, 1–10.
- 118 Singh, R., Pantarotto, D., Lacerda, L., Pastorin, G., Klumpp, C., Prato, M., Bianco, A., Kostarelos, K. *Proceedings of the National Academy of Sciences of the United States of America*, 2006, 103, 3357–3362.
- 119 Deng, X., Jia, G., Wang, H., Sun, H., Wang, X., Yang, S., Wang, T., Liu, Y. *Carbon*, 2007, 45, 1419–1424.
- 120 Wang, H., Wang, J., Deng, X., Sun, H., Shi, Z., Gu, Z., Liu, Y., Zhao, Y. *Journal of Nanoscience and Nanotechnology*, 2004, 4, 1019–1024.
- 121 Khang, D., Lu, J., Yao, C., Haberstroh, K. M., Webster, T. J. *Biomaterials*, 2008, 29, 970–983.

- 122 Mattson, M. P., Haddon, R. C., Rao, A. M. *Journal of Molecular Neuroscience*, 2000, 14, 175–182.
- 123 Hu, H., Ni, Y., Mandal, S. K., Montana, V., Zhao, B., Haddon, R. C., Parpura, V. *Journal of Physical Chemistry B*, 2005, 109, 4285–4289.
- 124 Lovat, V., Pantarotto, D., Lagostena, L., Cacciari, B., Grandolfo, M., Righi, M., Spalluto, G., Prato, M., Ballerini, L. *Nano Letters*, 2005, 5, 1107–1110.
- 125 Matsumoto, K., Sato, C., Naka, Y., Kitazawa, A., Whitby, R. L. D., Shimizu, N. *Journal of Bioscience and Bioengineering*, 2007, 103, 216–220.
- 126 Keefer, E. W., Botterman, B. R., Romero, M. I., Rossi, A. F., Gross, G. W. *Nature Nanotechnology*, 2008, 3, 434–439.
- 127 Mamedov, A. A., Kotov, N. A., Prato, M., Guldi, D. M., Wicksted, J. P., Hirsch, A. *Nature Materials*, 2002, 1, 190–194.
- 128 Gheith, M. K., Pappas, T. C., Liopo, A. V., Sinani, V. A., Shim, B. S., Motamedi, M., Wicksted, J. P., Kotov, N. A. *Advanced Materials*, 2006, 18, 2975–2979.
- 129 Gheith, M. K., Sinani, V. A., Wicksted, J. P., Matts, R. L., Kotov, N. A. *Advanced Materials*, 2005, 17, 2663–2670.
- 130 Jan, E., Kotov, N. A. *Nano Letters*, 2007, 7, 1123–1128.
- 131 Balbus, J. M., Florini, K., Denison, R. A., Walsh, S. A. *Journal of Nanoparticle Research*, 2007, 9, 11–22.
- 132 Linkov, I., Steevens, J., Adlakha-Hutcheon, G., Bennett, E., Chappell, M., Colvin, V., Davis, J. M., Davis, T., Elder, A., Foss Hansen, S., Hakkinen, P. B., Hussain, S. M., Karkan, D., Korenstein, R., Lynch, I., Metcalfe, C., Ramadan, A. B., Satterstrom, F. K. *Journal of Nanoparticle Research*, 2009, 11, 513–527.
- 133 Choi, J. Y., Ramachandran, G., Kandlikar, M. *Environmental Science and Technology*, 2009, 43, 3030–3034.
- 134 European Union, Brussels, Belgium, 15–16 Dec. 2008, 1907/2006.
- 135 Wilson, R. F. *Journal of Law, Medicine and Ethics*, 2006, 34, 704–713.
- 136 Singh, N., Manshian, B., Jenkins, G. J. S., Griffiths, S. M., Williams, P. M., Maffei, T. G. G., Wright, C. J., Doak, S. H. *Biomaterials*, 2009, 30, 3891–3914.
- 137 Jia, F., Wu, L., Meng, J., Yang, M., Kong, H., Liu, T., Xu, H. *Journal of Materials Chemistry*, 2009, 19, 8950–8957.

The use of polymer–carbon nanotube composites in fibres

H. DENG and Q. FU, Sichuan University, P. R. China and E. BILOTTI and T. PEIJS, Queen Mary University of London, UK

Abstract: A general review of carbon nanotube (CNT)–polymer fibres is undertaken in this chapter with main efforts focusing on the mechanical, electrical and sensing properties of CNT–polymer fibres. The review introduces issues related to the preparation of CNT–polymer fibres and orientation of CNTs, necessary to fully exploit the mechanical and electrical properties of CNT–polymer fibres. It is demonstrated that CNTs have great potential for a wide range of applications. Their large aspect ratio, excellent electrical conductivity and ultra-high mechanical properties make them outstanding candidates to be multi-functional nanofillers for polymer fibres.

Key words: carbon nanotube, conductive polymer composites, mechanical reinforcement, multi-function, polymer fibre, sensing ability.

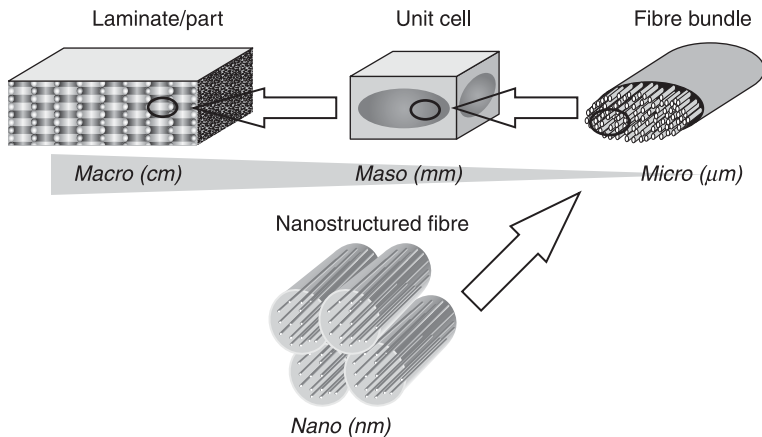
21.1 Introduction

The discovery of ways to produce highly orientated polymers has given tremendous stimulus to both basic polymer science and industrial developments since the 1970s.^{1,2} The first successful methodology to produce ultra-stiff and strong fibre with the molecules aligned in the direction of the fibre axis was by Kwolek *et al.*³ Here, a solution-based method was used to spin fibres from rigid rod *p*-aramid molecules with outstanding stiffness and strength, which was eventually developed into a commercial product known as Kevlar®.

It has been known since the 1930s¹ that a fully extended flexible polymer chain such as polyethylene (PE) would also be extremely stiff in the direction of the chain axis. Fully aligned chains have been achieved by two different methods: solution (gel) spinning or solid state deformation. The first successes were achieved by Capaccio and Ward,⁴ where an oriented polymer network was achieved by solid state drawing between T_g (glass transition temperature) and T_m (melting temperature). A number of subsequent studies on solid state drawing were then carried out on PE, but the real commercial breakthrough study was carried out by Smith and Lemstra⁵ using gel spinning. Here, ultra-high molecular weight polyethylene (UHMWPE) was spun from a disentangled semi-diluted solution, which, after drawing, resulted in fibres of 90 GPa stiffness and 3 GPa strength. These fibres were developed into commercial products by DSM and its alliance Honeywell, under the trade name of Dyneema® and Spectra®, respectively. Major applications are in ropes, cables, protective clothes and helmets.⁶

Under the pressure of environmental and recycling issues, recent development in orientated polymers has concentrated on single polymer composites, where the same polymer is used as both the matrix and fibre in the composites. Two remarkable achievements from Ward *et al.*⁷ and Peijs and co-workers,^{8–11} based on all-PP composites, were developed into commercialized products under the trade names of Curv® and PURE®, respectively.

Due to the one-dimensional structure of carbon nanotubes (CNTs), oriented polymer–CNT composites fibres or tapes attracted much attention, as such an oriented system could result in a high mechanical reinforcing efficiency.^{12,13} Furthermore, the introduction of such nanofibres into oriented polymer systems can mimic the structure of natural materials such as bone and tooth, creating ‘designed’ composite materials with additional levels of hierarchy (see Fig. 21.1). Therefore, CNT–polymer fibres as a research topic have recently been widely investigated. Researchers are mainly focusing on the mechanical,^{13–17} electrical^{18–22} and sensing properties.^{23,24}



21.1 Schematic of micro-nanohybrid composite with added level of hierarchy through nanostructured fibres. Reprinted with permission from reference 12.

21.2 Preparation of polymer–CNT fibres

There are two main categories of polymer–CNT fibres: one consists of polymer, where the CNT content is typically below 10 wt%; another type mainly contains CNTs. For the first category, to obtain a certain degree of orientation for the polymer matrix and CNTs, as-prepared CNT–polymer composites are often spun into fibres by different means, including gel spinning,²⁵ electro-spinning,^{26–28} melt spinning,^{29–32} and solid state drawing.^{20–22,33,34} As expected, fibre spinning

conditions play an important role on the final properties especially the speed, temperature and post-treatment.

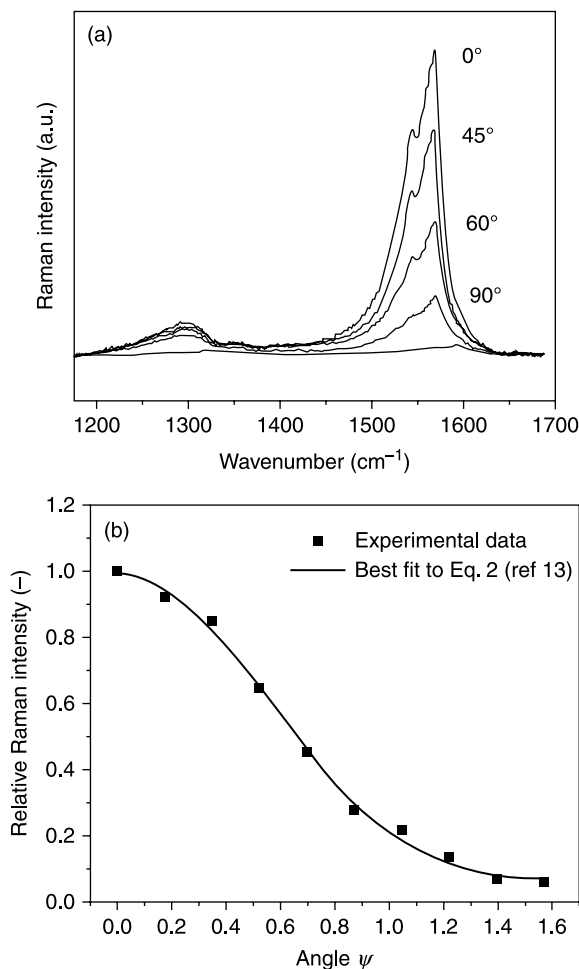
For the second category, methods including wet spinning,³⁵ dry spinning from CNT forests,^{36,37} and direct spinning from chemical vapour deposition (CVD) synthesis,^{38,39} have been used to produce neat CNT fibres (ribbons or yarns) in micrometre or millimetre size. These methods have the potential to be used to produce neat continuous CNT fibres or yarns on an industrial scale. Especially the method reported by Li *et al.*,³⁹ where CNT fibres are directly collected from CVD reaction are of interest for future high-strength fibre development. The fairly simple procedure and high mechanical property expectation of CNTs open up the possibility of ultimately producing neat CNT fibres with comparable or even higher mechanical properties than widely used carbon fibres. Nevertheless, so far the mechanical properties of most neat CNT fibres are still well below those of carbon fibres and further study is still needed to optimize such a process.

21.3 Orientation of CNTs and polymer

Due to the one-dimensional structure of CNTs, oriented polymer–CNT composite fibres or tapes generate intense interest as such oriented systems could result in high mechanical reinforcing efficiency. Ajayan *et al.*⁴⁰ were the first to consider drawing as a method to align CNTs in a polymer matrix. Since then, oriented polymer fibres or tapes containing CNTs have been extensively investigated. It is observed that CNTs could be aligned by process-induced shear, which could be caused by spinning or drawing.^{20,29} The orientation of CNTs in polymer fibres has been studied extensively by different methods, including Raman (see Fig. 21.2), SEM (see Fig. 21.3), and TEM,²⁹ etc.

Figure 21.2 presents a Raman study of the alignment of SWNTs. It has been observed that the Raman spectra intensity of the tangential mode G band ($1500\text{--}1700\text{ cm}^{-1}$) monotonically decreases with increasing the angle between the drawing direction and the polarization direction of the polarizer for SWNTs, and this phenomenon can be used to demonstrate the orientation effect of CNTs.¹³

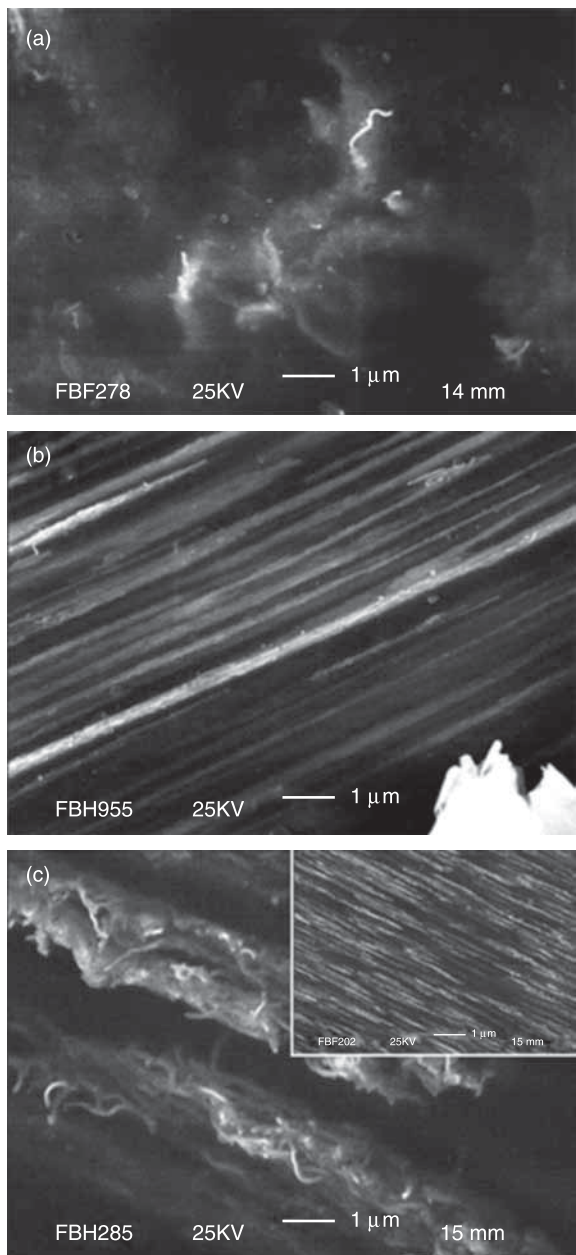
As shown in Fig. 21.3, MWNT networks can be observed by SEM at high accelerating voltage as previously reported by Loos *et al.*⁴¹ It is shown that MWNTs can be highly aligned after solid state drawing. This could be caused by the high shear rate during solid state drawing. Furthermore, interesting ‘relaxed hairy’ MWNT bundles have been observed after thermal annealing. The process is explained as following: after the solid-state drawing process, MWNT bundles are highly oriented and constrained in the surrounding polymer matrix. MWNTs in these bundles are entangled and under tension due to the deformation induced by the solid-state drawing process. Upon annealing above or close to the melting temperature of the polymer, these MWNT bundles, together with the polymer chains, have the ability to relax to a more isotropic state. Similar to the entropy-driven relaxation process in oriented polymers, the increase in polymer mobility



21.2 (a) Typical Raman spectra of an oriented CNT-polymer composite; each curve is the spectrum for the indicated tape orientation with respect to the incident polarization; (b) relative Raman intensity as a function of the angle ψ ($0 - \pi/2$) between the polarization direction and the sample axis for PVA-SWNT nanocomposite tapes at draw ratio 5, indicating a high degree of alignment of the nanotubes. Reprinted with permission from reference 13.

allows the relaxation of the nanotube bundles, bringing more disorder into the system. As a result, local lateral contacts between MWNT bundles are created.²¹

Kumar *et al.*¹⁶ reported an interesting approach based on a rigid rod polymer poly-p-phenylenebenzobisoxazole (PBO). Here PBO was synthesized in the presence of SWNTs to produce lyotropic liquid crystalline solutions which were spun into composite fibres using dry jet wet spinning. The tensile strength of these



21.3 SEM of MWNT-co-PP composite surface for: (a) isotropic film; (b) solid-state drawn tape; (c) solid-state drawn plus annealed tape. Please note the relaxed anisotropic nanotube bundle structure in the latter. Reprinted with permission from reference 22.

PBO–SWNT fibres containing 10 wt% SWNTs was around 50% higher than that of control PBO fibres containing no SWNTs. However, it should be noted that the tensile strength of commercial PBO fibre (Zylon HM) is 5.8 GPa compared to 2.5 GPa as found in their control study.

Another interesting method used to align CNTs in polymer composite fibres is electrospinning. This technique has been used to produce man-made fibres since the 1930s and involves electrostatically driving a jet of polymer solution out of a nozzle onto a metallic counter electrode. In 2005, Zhou *et al.*⁴² described electrospinning as a method to fabricate PEO and poly(vinyl alcohol) (PVA) nanofibres containing MWNTs. Recently, Wang *et al.*²⁶ and Kannan *et al.*⁴³ showed good reinforcement efficiency of CNTs in such electrospun PVA fibres.

21.4 Mechanical properties of polymer–CNT fibres

Due to their one-dimensional and outstanding mechanical properties, CNTs have become very interesting for reinforcing polymer fibres.^{12–14,16,18,19,25,27,29,33,34,44–53} However, it is difficult to compare the mechanical reinforcement results from the literature as there are many differences in these systems. It is shown that some basic models, such as the simple rule of mixture can be used to calculate and compare the effective mechanical properties of CNT in polymer matrix.^{13,15,26,48} Table 21.1 lists the calculated effective CNT modulus and strength from data reported in the literature. Again there are two categories of highly oriented CNTs fibres: one are fibres that mainly or solely consist of CNTs (such as work from Dalton *et al.*,⁴⁹ Zhang *et al.*⁵⁴ and Koziol *et al.*³⁸); another type are polymer fibres containing small amounts of CNTs (typically < 10 wt%).

The highest mechanical properties of neat CNT spun fibre that have been reported are by Koziol *et al.*,³⁸ where a modulus of 350 GPa and strength of 9 GPa are obtained. Its modulus is approaching the value of carbon fibre, while its best reported tensile strength value is indeed higher than any other man-made fibre. However, it needs to be noted that there is a large amount of scatter in their experimental data (see Table 21.1), while a 1 mm gage length is used in their tensile text experiments to minimize the influence of defects by CNT ends in the yarns. Nevertheless, the properties have yet to approach the theoretical values of CNTs of 1000 GPa for modulus and 50–150 GPa for tensile strength. The discontinuous nature of these CNT yarns is believed to be responsible for this as the strength is not determined by the intrinsic strength of the CNTs but by the nanotube–nanotube interactions and overlap length. Considering the variety of applications and importance of carbon fibre in a wide range of fields, such a spinning method reported by Koziol *et al.* to produce neat CNT fibre, the possibility of replacing carbon fibre is indeed exciting. However, more attention needs to be paid to the realistic potential and advantages of such CNT yarns compared to carbon fibres, rather than a one-to-one replacement.

Table 21.1 Calculated effective mechanical contribution of CNTs using rule of mixture for oriented polymer fibres or tapes reported in the literature

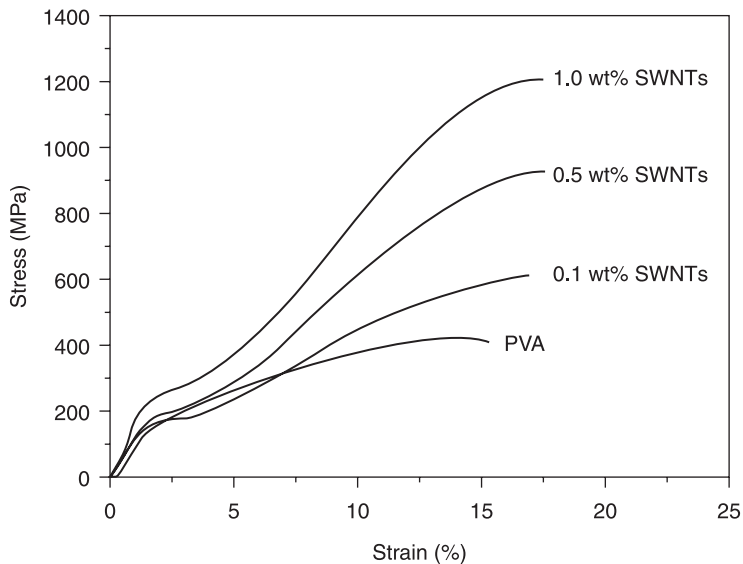
Type of CNT	Matrix	E_f (GPa)	σ_f (GPa)	Reference
SWNT	PVA	2740	116	Minus <i>et al.</i> ⁶³
SWNT	Pitch	1296	13	Andrews <i>et al.</i> ⁵⁵
SWNT	PVA	1120	45	Ciselli <i>et al.</i> ⁶¹
MWNT	UHMW-PE	868	4	Ruan <i>et al.</i> ³³
MWNT	PVA	850	–	Wang <i>et al.</i> ²⁶
MWNT	PP	732	32	Deng <i>et al.</i> ¹⁵
SWNT	PP	610	56	Kearns <i>et al.</i> ⁸⁸
SWNT	PVA	600	88	Wang <i>et al.</i> ¹³
MWNT	PP	497	5.5	Dondero <i>et al.</i> ⁸⁹
SWNT	PBO	449	19	Kumar <i>et al.</i> ¹⁶
SWNT	PVA	406	8	Zhang <i>et al.</i> ²⁵
MWNT	–	350	9	Koziol <i>et al.</i> ³⁸
MWNT	PP	305	15.3	Jose <i>et al.</i> ⁵²
MWNT	–	195	1.9	Zhang <i>et al.</i> ⁵⁴
SWNT	PA	153	36	Gao <i>et al.</i> ⁵¹
MWNT	–	150	6	Koziol <i>et al.</i> ³⁸
SWNT	PAN	149	2	Sreekumar <i>et al.</i> ⁵⁹
SWNT	PAN	149	2	Chae <i>et al.</i> ⁵⁸
SWNT	PVA	147	3	Dalton <i>et al.</i> ⁴⁹
MWNT	PAN	110	6	Chae <i>et al.</i> ⁵⁸
SWNT	PP	100	1.5	Chang <i>et al.</i> ⁹⁰
MWNT	–	65	1	Koziol <i>et al.</i> ³⁸
DWNT	PAN	61	2	Chae <i>et al.</i> ⁵⁸
MWNT	PC	48	1	Fornes <i>et al.</i> ⁵⁰

The second category of polymer fibres contains relatively small amounts of CNTs. The first report of such a fibre is by Andrews *et al.*,⁵⁵ where the modulus increased 150% and strength increased 90% after adding 5 wt% SWNT in a petroleum pitch matrix. Their fibre results in a back calculated modulus for the CNTs of 1296 GPa and strength of 13 GPa. The mechanical properties of polymer–CNT fibres based on PBO,¹⁶ PVA,^{1,13,77,81} PP^{47,56,57} and PAN,^{58,59} are investigated in the literature and are listed in Table 21.1. The great advantage of CNTs as mechanical reinforcing fibre is its extremely high tensile strength of nearly 150 GPa compared with 7 GPa for conventional carbon fibre. Modulus, on the other hand, is less of interest as a property as a Young's modulus of 1000 GPa for CNTs is less impressive when compared with that of ultimate high modulus carbon fibres of 600–800 GPa. As listed in Table 21.1, only a few studies have achieved an effective tensile strength above 10 GPa.^{13,15,29,59–63} The highest effective reinforcement in strength so far was achieved by a group led by Kumar,⁶³ where an effective strength of 116 GPa was achieved by gel spinning PVA–SWNT fibres. A slightly lower effective strength of 88 GPa was reported by Wang *et al.*¹³ earlier, where a threefold increase in strength was obtained by

adding 1 wt% SWNT in an oriented PVA matrix (see Fig. 21.4). It was concluded that a high level of dispersion, interfacial interaction and alignment of nanofillers were essential to achieve this true mechanical reinforcement in CNT-based composites.¹³

In terms of melt processed polymer–CNT fibres, it is demonstrated that better reinforcement is obtained at low filler content and low draw ratios.^{15,52} This is caused by poorer dispersion at higher filler content. As the fibres are transformed into a more organized structure at higher draw ratios, they are more sensitive to the cracks initiated by CNT bundles due to over-drawing of the system.

Another important factor to take into account is that for ultimate reinforcement the use of single-walled nanotubes (SWNTs) is essential. In terms of cost and ease of dispersion, multi-walled nanotubes (MWNTs) are the most attractive candidates to reinforce polymer composites. However, when nanotubes are used as reinforcing elements in composites, the total volume they occupy, including their hollow part, needs to be considered for their reinforcing efficiency.⁶⁴ Especially in the case of MWNTs, where the stress needs to be transferred from the outer layer to the inner layers, there are implications for their effective properties. As the interaction between individual graphene layers is known to be low, this can easily result in telescopic interlayer sliding in MWNTs, leading to a significant reduction in the effective properties of MWNTs since only the outer layers carry the load.⁶⁵



21.4 Stress–strain curves for oriented PVA–SWNT tapes with a draw ratio of 5, showing a strong increase in tensile strength with the addition of small amounts of SWNTs to the polymer. Reprinted with permission from reference 13.

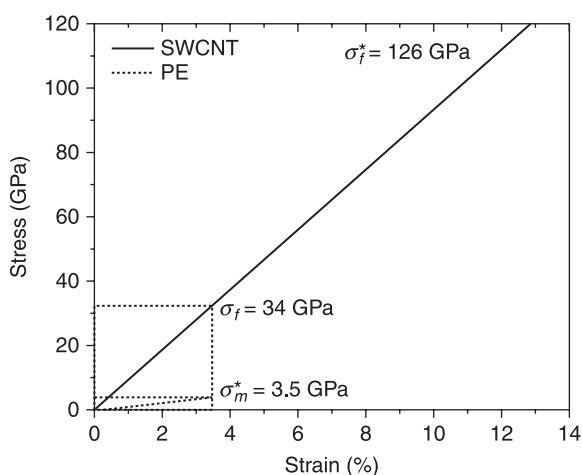
21.5 A theoretical approach to reinforcement efficiency of CNTs

From a theoretical perspective, at small $V_{f(CNT)}$ the composite properties are largely dominated by the polymer matrix. However, at a critical $V_{f(CNT)}$ the properties are dominated by the CNTs. Let us envisage a stress–strain curve for a highly aligned and therefore linear elastic PE fibre and for a single-walled CNT (PE, $E = 100$ GPa, $\sigma = 3.5$ GPa, $\varepsilon^* = 3.5\%$ ¹ and CNT, $E = 971$ GPa, $\sigma = 126$ GPa, $\varepsilon^* = 13\%$ ^{66,67}) for example (Fig. 21.5).

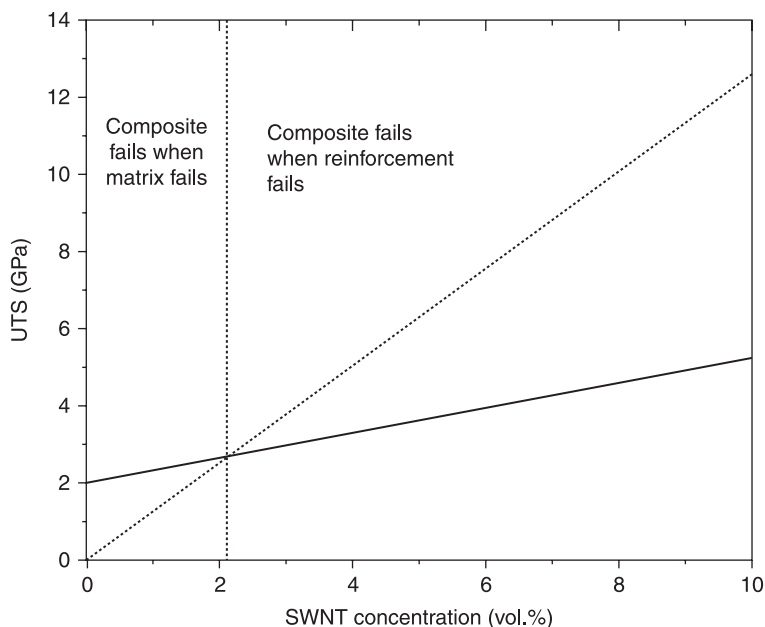
At the failure strain of the matrix (σ_m^*), a tensile stress of 34 GPa exists in the CNT. As the matrix fails, the load is transferred to the CNTs. However, if the V_f is low, the macroscopic load cannot be sustained and the composite fails. When V_f reaches a critical value, the CNTs can sustain the load (assuming load transfer remains). Therefore, a critical concentration (V_f') exists for the transition from properties which are matrix dominated to properties which are CNT dominated.

Figure 21.6 describes the failure of a polymer matrix reinforced with SWNTs. The plot describes a specific system, where the strength of the matrix and SWNT concentration is set. Then, a universal plot of E_f/E_m vs. V_f vs. $\varepsilon_f^*/\varepsilon_m^*$ yields a graph describing all reinforcing scenarios. Since we are describing only CNTs, the fibre/matrix property ratios are purely defined by the matrix choice.

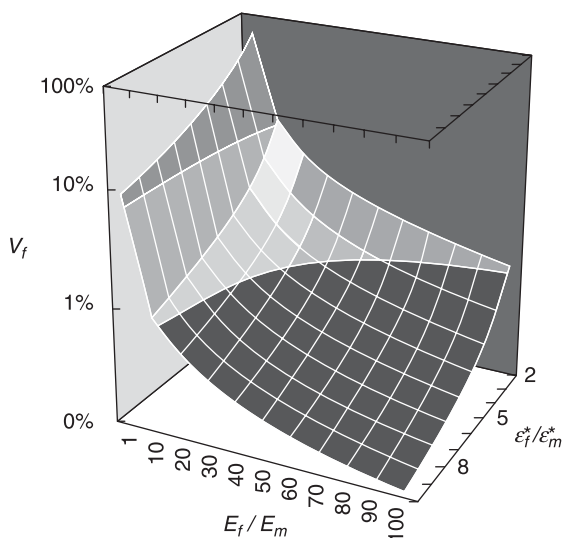
Figure 21.7 demonstrates that for SWNT composites, low strength and high strain composites benefit the most from being reinforced by CNTs. Conversely, stiff matrices with low strains – typically the characteristics of a high-performance fibre – need a large volume fraction of CNTs to fully exploit the intrinsic strength of the CNT. Take, for example, PBO (Zylon HM, Toyobo), which has a tensile



21.5 Stress–strain curves for a PE fibre and a SWNT.



21.6 Variation of composite tensile strength as a function of V_f . Below a critical volume fraction (V_f^c), the composite fails when the matrix fails, while above V_f^c the composite fails when the fracture strength of SWNTs is reached.



21.7 Variation of composite strength as a function of E_f/E_m , $\epsilon_f^*/\epsilon_m^*$ and V_f

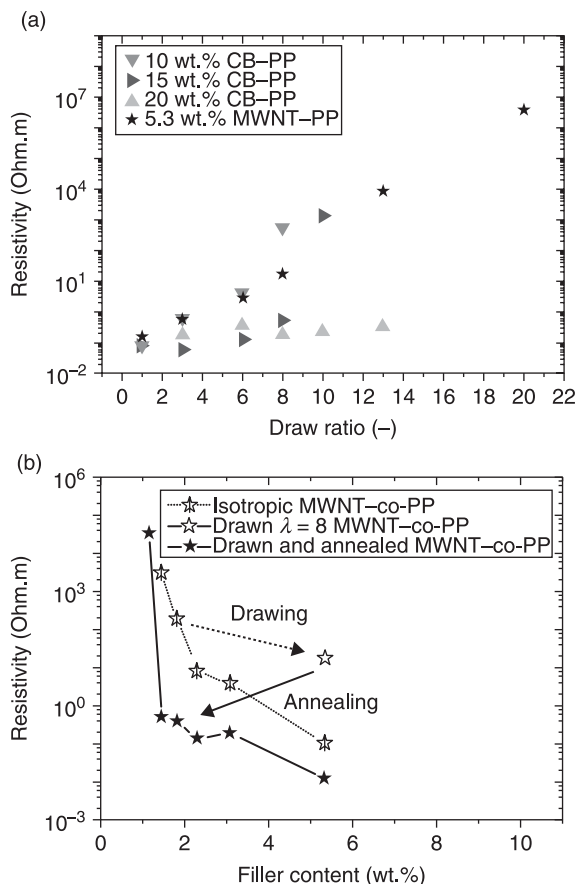
modulus of 270 GPa and failure strain of 2.5%. Here, a volume fraction of ~20% would be needed to fully exploit the potential strength of CNTs. Matrices such as *i*-PP ($E = 15$ GPa, $\sigma = 500$ MPa, $\varepsilon = 4\%$ ^{9,10,68}), however, require a far lower critical volume fraction at ~0.8%.

Wang *et al.*¹³ showed one of the highest contributions to σ_c from σ_{CNT} . The matrix here is a low draw ratio ($\lambda = 6$) PVA. It is known, however, that PVA can be drawn to more than 20 times and show an E modulus of 70 GPa and σ of 2.3 GPa.¹² Therefore, for PVA at a draw ratio of 6, V_f is ~0.16%, but this increases to ~3.4% for a more commercially interesting PVA fibre drawn to $\lambda = 21$.

Therefore, to achieve a noticeable amount of increase in fibre strength for high performance polymer fibre, relatively large amounts of CNTs are often needed. However, it is well known that dispersing large amounts of CNTs in a polymer matrix is very difficult. Many studies have investigated the dispersion qualities of carbon nanotube in different polymer matrices^{12,14,15,23,26,46,49,69} with the goal of developing composites with individually isolated carbon nanotubes. A model system for studying this dispersion is PAV as at low volumes (<1%) of CNTs, good dispersions can be achieved and it can be drawn into stiff, strong fibres.^{12,13,49} PVA has also been shown to have good interfacial interaction with CNTs.²⁶ Dispersion quality is a critical composite issue since aggregate bundles possess poor interfacial properties between adjacent tubes. Aggregation also causes a reduction in effective aspect ratio and larger aggregates are typically an entangled network of tubes which can only show poor alignment upon fibre drawing.⁴⁶ Poorly dispersed nanotube bundles may act as stress concentration points if they exceed the critical flaw size for a particular material. Current techniques can normally well disperse relatively small amounts of CNT in a polymer matrix (e.g. 1 wt% in PVA matrix),¹³ but it is still a major challenge to perfectly disperse the high CNT loadings required for highly oriented polymer fibres (typically 3–10% for high performance PVA fibres).

21.6 Electrical properties of polymer–CNT fibres

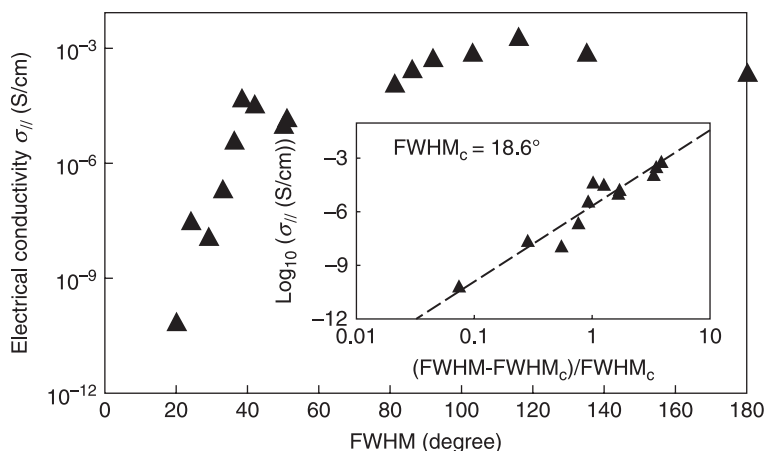
Thanks to their outstanding conductivity and exceptionally large aspect ratio, CNTs are considered one of the best conductive fillers for conductive polymer composites (CPCs). However, the conductivity of oriented polymer–CNT fibres or tapes is reported to decrease (see Fig. 21.8 (a)) upon drawing for various polymer matrixes.^{16,19,70} This is explained by the breakdown of local contacts between CNTs during solid state drawing.²⁰ The aspect ratio of the conductive filler is found to play an important role in the conductivity of the oriented composites.^{19,70} The drawing process applied to the composites is shown to align the CNT network (see Fig. 21.3). Recently, the effect of CNT orientation on the conductivity of polymer fibres was extensively studied by Du *et al.*⁷¹ They made a series of PMMA–SWNT fibres with different degrees of nanotube alignment by controlling the melt spinning conditions. The degree of alignment was



21.8 (a) The effect of solid state drawing on the resistivity of PP tapes containing MWNT or carbon black (CB); (b) the effect of solid state drawing (dashed arrows) and annealing (solid arrows) on the percolation threshold of CPCs based on co-PP and MWNTs. Reprinted with permission from references 20 and 21.

quantified using the full-width at half-maximum (FWHM) of the SWNT obtained from X-ray study, where the higher FWHM corresponds to less alignment. The conductivity decreases with increasing alignment and they form optimal orientation percolation between 20° to 40° . It also shows that intermediate levels of orientation give higher conductivity than isotropic samples (see Fig. 21.9).

The percolation threshold of highly oriented CPCs based on CNTs is relatively high (~ 5 wt%¹⁹) compared to the values obtained for isotropic systems.^{20,72,73} However, the conductivity of oriented fibres or tapes is found to increase during thermal treatments or annealing.^{18,21,22,44,49,74–77} This increase is explained by an improvement of local contacts between conductive regions caused by thermal



21.9 Electrical conductivity of a 2 wt.% SWNT–PMMA composite along the alignment direction with increasing nanotube isotropy. Nanotube alignment is assessed using X-ray scattering where FWHM = 0 is perfectly aligned and FWHM=180 is isotropic. Inset: a log–log plot of electrical conductivity vs. reduced FWHM determines the critical alignment, FWHM_c . Reprinted with permission from reference 71.

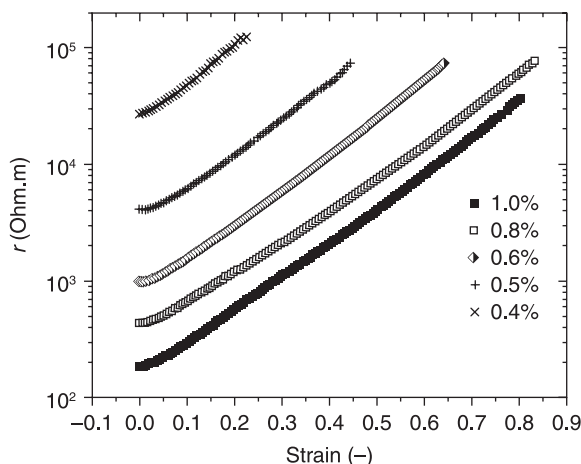
energy. Therefore, it is possible to reduce the percolation threshold in oriented systems by thermal treatment. However, thermal treatment will destroy the mechanical properties of mono-component fibres or tapes if the annealing temperatures are near or above the melting temperature of the matrix.^{18,44,77} Recently, a new concept was described by Deng *et al.*^{21,22} for the creation of multifunctional polymer nanocomposite tapes (or fibres) that combine high stiffness and strength with good electrical properties and a low percolation threshold of CNTs. The concept is based on a bicomponent tape (or fibre) construction consisting of a highly oriented polymer core and a CPC skin based on a polymer with a lower melting temperature than the core, enabling thermal annealing of these skins to improve conductivity through a dynamic percolation process while retaining the properties of the core and hence those of the tape (or fibre). The percolation threshold in the CPC skins of the highly drawn conductive bicomponent tapes could be decreased from 5.3 to 1.1 wt% after annealing (see Fig. 21.8 (b)). Such a method has provided the industry with a simple way to produce conductive fibre with high strength and conductivity. It also suggests another route to control the morphology and conductivity of the conductive network formed by nanofillers.

21.7 Sensing properties of polymer–CNT fibres

Polymer–CNT composites have been studied to sense external stimuli such as bio-molecules,⁷⁹ chemicals,^{79–82} gases,^{83,84} vapour,^{80–83} liquid,⁸⁵ mechanical

stress or strain^{23,86} and temperature.⁸⁷ The exposure of the CPCs to the external stimuli can result in changes of electrical properties, which can be considered as a signal. As shown in Fig. 21.10,²³ a mechanical strain applied to an elastomer–CNT composite can result in a clear electric signal which can be used for sensing. Applications for sensors based on polymer–CNT composites are expected in a wide range of fields, such as: building applications, smart textiles, medical applications and protective clothing.

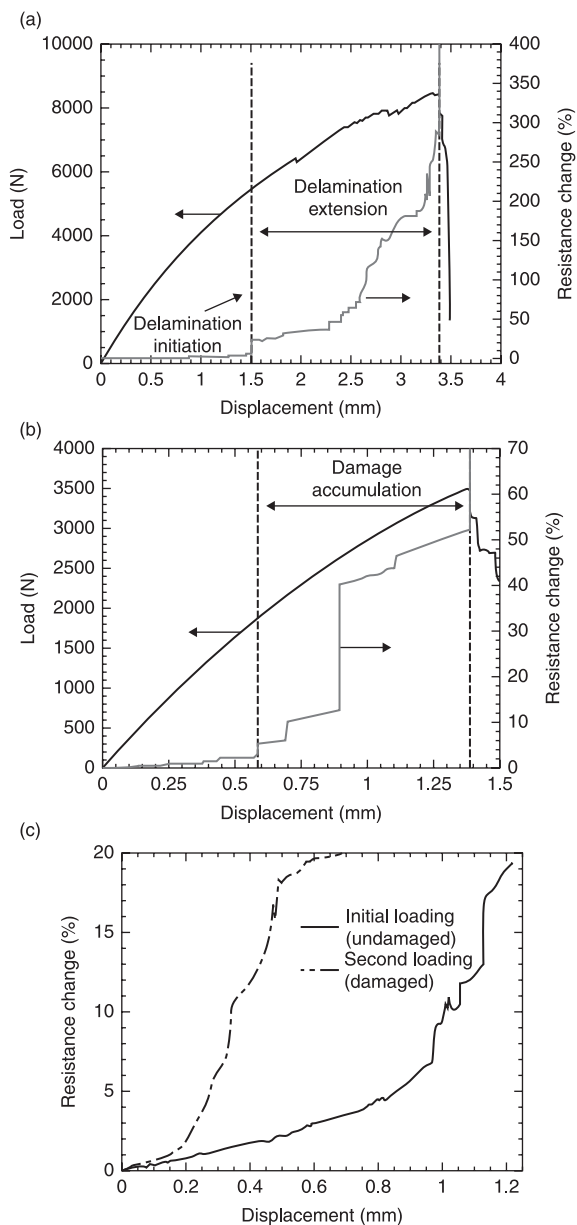
Damage sensing in structural composites is another important possible application for polymer–CNT composites.²⁴ It has been demonstrated that conducting carbon nanotube networks formed in a thermoset polymer matrix can be used as highly sensitive sensors for detecting the onset, nature, and evolution of damage in advanced polymer-based composites. The internal damage accumulation can be monitored *in situ* using electrical measurements. After the onset of damage and subsequent reloading of the damaged structure, there is a remarkable shift in the sensing curve, indicating irreversible damage (as shown in Fig. 21.11). These results demonstrate promise for evaluation of automatic self-healing approaches for polymer composites and development of enhanced life prediction methodologies.²⁴



21.10 Resistivity vs. strain for various CNT concentrations. Reprinted with permission from reference 23.

21.8 Conclusion and future trends

A general review on polymer–CNT fibres has been given and main efforts have been focused on the orientation of CNT in polymer fibres, and the mechanical and electrical properties of polymer–CNT fibres. It is demonstrated that CNTs have the potential for a wide range of applications in the polymer fibre field. Their one-



21.11 (a) Load–displacement and resistance curves for the 0° specimen with centre ply cut to initiate delamination; (b) load–displacement and resistance curves for the $0/90$ specimen; (c) resistance curves for initial loading (undamaged) and reloading (damaged) laminates. Reprinted with permission from reference 24.

dimensional character, large aspect ratio, excellent conductivity and ultra high mechanical properties make them outstanding candidates as multi-functional nanofillers.

Multi-functional polymer fibres are becoming an interesting topic in the field of polymer–CNT composites. Thanks to their intrinsic multi-functionality, CNTs have been demonstrated as able to provide polymer fibres with electrical properties, mechanical properties and sensing ability. A combination of these properties could be obtained in specific composites, whereas the properties can be tailored by engineering these materials from the nano to mm level in order to fulfil desired applications. However, due to their nano-size and large aspect ratio, there are still difficulties in dispersing them into polymer matrix, especially at higher loadings.

21.9 References

- 1 Peijs T, Jacobs MJN, and Lemstra PJ (2000) High performance polyethylene fibres, in Chou TW, Kelly A, and Zweben C (eds) *Comprehensive Composites*, vol. 1, Oxford: Elsevier Science Publishers Ltd, pp. 263–302.
- 2 Ward IM (2004) *Plastics, Rubbers and Composites*, 33: 189–194.
- 3 Kwolek SL, Morgan PW, Schaeffgen JR, and Gulrich LW (1977) *Macromolecules*, 10: 1390–1396.
- 4 Capaccio G and Ward IM (1973) *Nature-Physical Science*, 243(130): 143–143.
- 5 Smith P and Lemstra PJ (1980) *Journal of Materials Science*, 15: 505–514.
- 6 Lemstra PJ, Bastiaansen CWM, Peijs T, and Jacobs MJN (2000) in Ward I.M., CPD, Dunoulin M.M (eds) *Solid Phase Processing of Polymers*.
- 7 Ward IM and Hine PJ (2004) *Polymer*, 45, 1413–1427.
- 8 Alcock B (2004) Single polymer composites based on polypropylene: processing and properties, PhD thesis, Queen Mary University of London.
- 9 Alcock B, Cabrera NO, Barkoula NM, Reynolds CT, Govaert LE, and Peijs T (2007) *Composites Science and Technology*, 67(10), 2061–2070.
- 10 Alcock B, Cabrera NO, Barkoula N-M, Spoelstra AB, Loos J, and Peijs T (2006) *Composites: Part A*, 37, 716–726.
- 11 Loos J, Schimanski T, Hofman J, Peijs T, and Lemstra PJ (2001) *Polymer*, 42, 3827–3834.
- 12 Ciselli P, Wang Z, and Peijs T (2007) *Materials Technology*, 22, 10–21.
- 13 Wang Z, Ciselli P, and Peijs T (2007) *Nanotechnology*, 18, 455709.
- 14 Dalton AB, Collins S, Razal J, Munoz E, Ebron VH, Kim BG, Coleman JN, Ferraris JP, and Baughman RH (2004) *Journal of Materials Chemistry*, 14, 1–3.
- 15 Deng H, Bilotti E, Zhang R, and Peijs T (2010) *Journal of Applied of Polymer Science*, 118.30.
- 16 Kumar S, Dang TD, Arnold FE, Bhattacharyya AR, Min BG, Zhang X, Vaia RA, Park C, Adams WW, Hauge RH, Smalley RE, Ramesh S, and Willis PA (2002) *Macromolecules*, 35, 9039–9043.
- 17 Moore EM, Ortiz DL, Marla VT, Shambaugh RL, and Grady BP (2004) *Journal of Applied Polymer Science*, 93, 2926–2933.
- 18 Bin Y, Chen QY, Tashiro K, and Matsuo M (2008) *Physical Review B*, 77, 035419.
- 19 Bin Y, Mine M, Ai K, Jiang X, and Masaru M (2006) *Polymer*, 47, 1308–1317.

- 21 Deng H, Zhang R, Bilotti E, Loos J, and Peijs T (2009) *Journal of Applied Polymer Science*, 113(2), 742–751.
- 21 Deng H, Zhang R, Reynolds CT, Bilotti E, and Peijs T (2009) *Macromolecular Materials and Engineering*, 294(11), 749–755.
- 22 Deng H, Zhang R, Bilotti E, Loos J, and Peijs T (2009) *Synthetic Metals*, 160(5–6), 337–344.
- 23 Zhang R, Baxendale M, and Peijs T (2007) *Physical Review B*, 76, 195433–195431–195435.
- 24 Thostenson ET and Chou TW (2006) *Advanced Materials*, 18(21), 2837.
- 25 Zhang XF, Liu T, Sreekumar TV, Kumar S, Hu XD, and Smith K (2004) *Polymer*, 45, 8801–8807.
- 26 Wang W, Ciselli P, Kuznetsov E, Peijs T, and Barber AH (2008) *Phil. Trans. R. Soc. London A*, 18192168.
- 27 Naebe M, Lin T, Staiger MP, Dai LM, and Wang XG (2008) *Nanotechnology*, 19(30), 8.
- 28 Wang G, Tan ZK, Liu XQ, Chawda S, Koo JS, Samuilov V, and Dudley M (2006) *Nanotechnology*, 17(23), 5829–5835.
- 29 Pötschke P, Brunig H, Janke A, Fisher D, and Jehnichen D (2005) *Polymer*, 46, 10335–10363.
- 30 Sandler JKW, Pegel S, Cadek M, Gojny F, van Es M, Lohmar J, Blau WJ, Schulte K, Windle AH, and Shaffer MSP (2004) *Polymer*, 45(6), 2001–2015.
- 31 Perrot C, Piccione PM, Zakri C, Gaillard P, and Poulin P (2009) *Journal of Applied Polymer Science*, 114(6), 3515–3523.
- 32 Shen LM, Gao XS, Tong Y, Yeh A, Li RX, and Wu DC (2008) *Journal of Applied Polymer Science*, 108(5), 2865–2871.
- 33 Ruan S, Gao P, and Yu TX (2006) *Polymer*, 47, 1604–1611.
- 34 Ruan SL, Gao P, Yang XG, and Yu TX (2003) *Polymer*, 44, 5643–5654.
- 35 Vigolo B, Penicaud A, Coulon C, Sauder C, Pailler R, Journet C, Bernier P, and Poulin P (2000) *Science*, 290(5495), 1331–1334.
- 36 Zhang M, Atkinson KR, and Baughman RH (2004) *Science*, 306(5700), 1358–1361.
- 37 Ericson LM, Fan H, Peng HQ, Davis VA, Zhou W, Sulpizio J, Wang YH, Booker R, Vavro J, Guthy C, Parra-Vasquez ANG, Kim MJ, Ramesh S, Saini RK, Kittrell C, Lavin G, Schmidt H, Adams WW, Billups WE, Pasquali M, Hwang WF, Hauge RH, Fischer JE, and Smalley RE (2004) *Science*, 305(5689), 1447–1450.
- 38 Koziol K, Vilatela J, Moisala A, Motta M, Cunniff P, Sennett M, and Windle AH (2007) *Science*, 21, 1892–1895.
- 39 Li YL, Kinloch IA, and Windle AH (2004) *Science*, 304(5668), 276–278.
- 40 Ajayan PM, Stephan O, Colliex C, and Trauth D (1994) *Science*, 265, 1212–1214.
- 41 Loos J, Alexeev A, Grossiord N, Koning CE, and Regev O (2005) *Ultramicroscopy*, 104, 160–167.
- 42 Zhou WP, Wu YL, Wei F, Luo GH, and Qian WZ (2005) *Polymer*, 46(26), 12689–12695.
- 43 Kannan P, Eichhorn SJ, and Young RJ (2007) *Nanotechnology*, 18(23).
- 44 Bin Y, Kitanaka M, Zhu D, and Matsuo M (2003) *Macromolecules*, 36, 6213–6219.
- 45 Chae HG and Kumar S (2008) *Science*, 319, 908–909.
- 46 Ciselli P, Zhang R, Wang Z, Reynolds CT, Baxendale M, and Peijs T (2008) *European Polymer Journal*, 45(10), 2741–2748.
- 47 Coleman JN, Khan U, Blau WJ, and Gun'ko YK (2006) *Carbon*, 44, 1624–1652.
- 48 Coleman JN, Khan U, and Gun'ko YK (2006) *Advanced Materials*, 18, 689–706.

- 49 Dalton AB, Collins S, Munoz E, Razal JM, Ebron VH, Ferraris JP, Coleman JN, Kim BG, and Baughman RH (2003) *Nature*, 423, 703.
- 50 Fornes TD, Baur JW, Sabba Y, and Thomas EL (2006) *Polymer*, 47, 1704–1714.
- 51 Gao J, Itkis ME, Yu A, Bekyarova E, Zhao B, and Haddon RC (2005) *Journal of American Chemical Society*, 127, 3847–3854.
- 52 Jose MV, Dean D, Tyner J, Price G, and Nyairo E (2007) *Journal of Applied of Polymer Science*, 103, 3844–3850.
- 53 Vaisman L, Larin B, Davidi I, Wachtel E, Marom G, and Wagner HD (2007) *Composites Part A*, 38, 1354–1362.
- 54 Zhang XF, Li QW, Holesinger TG, Arendt PN, Huang JY, P.D. K, Clapp TG, DePaula RF, Liao XZ, Zhao YH, Zheng LX, Peterson DE, and Zhu YT (2007) *Advanced Materials*, 19, 4198–4201.
- 55 Andrews R, Jacques D, Rao AM, Rantell T, Derbyshire F, Chen Y, Chen J, and Haddon RC (1999) *Applied Physics Letters*, 75, 1329–1331.
- 56 Ganb M, Satapathy BK, Thunga M, Weidisch R, Pötschke P, and Jehnichen D (2008) *Acta Materialia*, 56(10), 2247–2261.
- 57 Manchado MAL, Valentini L, Biagiotti J, and Kenny JM (2005) *Carbon*, 43, 1499–1505.
- 58 Chae HG, Minus ML, and Kumar S (2006) *Polymer*, 47, 3494–3504.
- 59 Sreekumar TV, Liu T, Min BG, Guo HN, Kumar S, Hauge RH, and Smalley RE (2004) *Advanced Materials*, 16, 58–61.
- 60 Bryning MB, Islam MF, Kikkawa JM, and Yodh AG (2005) *Advanced Materials*, 17, 1186–1191.
- 61 Ciselli P (2007) The potential of carbon nanotubes in polymer composites, PhD thesis, Eindhoven University of Technology.
- 62 Valentini L, Biagiotti J, Kenny JM, and Santucci S (2003) *Composites Science and Technology*, 63, 1149–1153.
- 63 Minus ML, Chae HG, and Kumar S (2009) *Macromolecular Chemistry and Physics*, 210(21), 1799–1808.
- 64 Zalamea L, Kim H, and Pipes RB (2007) *Composites Science and Technology*, 67(15–16), 3425–3433.
- 65 Cui S, Kinloch IA, Young RJ, Noe L, and Monthieux M (2009) *Advanced Materials*, 21(35), 3591.
- 66 Yu MF, Files BS, Arepalli S, and Ruoff RS (2000) *Physical Review Letters*, 84, 5552–5555.
- 67 Yu MF, Lourie O, Dyer MJ, Kelly TF, and Ruoff RS (2000) *Science*, 287, 637–640.
- 68 Available at: www.pure-composites.com.
- 69 Zhang R, Dowden A, Deng H, Baxendale M, and Peijs T (2009) *Composites Science and Technology*, 69(10), 1499–1504.
- 70 Deng H, Zhang R, Bilotti E, Peijs T, and Loos J (2009) *Journal of Applied Polymer Science* 50, 3747–3794.
- 71 Du FM, Fischer JE, and Winey KI (2005) *Physical Review B*, 72, 121401–121404.
- 72 Pötschke P, Abdel-Goad M, Alig I, Dudkin S, and Lellinger D (2004) *Polymer*, 45, 8863–8870.
- 73 Pötschke P, Dudkin SM, and Alig I (2003) *Polymer*, 44, 5023–5030.
- 74 Deng H and Peijs T (2007) Conductive polymer composite with reduced electrical resistivity by thermal or chemical treatment. U.S. patent in application, October.
- 75 Deng H and Peijs T (2008) Conductive Polymer Composites, PCT/EP2008/064460. Patent pending.

- 76 Deng H, Skipa T, Bilotti E, Zhang R, Lellinger D, Mezzo L, Fu Q, Alig I, and Peijs T (2010) *Advanced Functional Materials*, 20(9), 1424–1432.
- 77 Miaudet P, Bartholome C, Derre A, Maugey M, Sigaud G, Zakri C, and Poulin P (2007) *Polymer*, 48, 4068–4074.
- 78 Merkoci A, Pumera M, Llopis X, Perez B, del Valle M, and Alegret S (2005) *Trac Trends in Analytical Chemistry*, 24(9), 826–838.
- 79 Bouvrée A, Feller JF, Castro M, Grohens Y, and Rinaudo M (2009) *Sensors and Actuators B: Chemical*, 138(1), 138–147.
- 80 Castro M, Lu JB, Bruzard S, Kumar B, and Feller JF (2009) *Carbon*, 47(8), 1930–1942.
- 81 Lu JB, Kumar B, Castro M, and Feller JF (2009) *Sensors and Actuators B: Chemical*, 140(2), 451–460.
- 82 Agui L, Yanez-Sedeno P, and Pingarron JM (2008) *Analytica Chimica Acta*, 622(1–2), 11–47.
- 83 Su PG, Lee CT, Chou CY, Cheng KH, and Chuang YS (2009) *Sensors and Actuators B: Chemical*, 139(2), 488–493.
- 84 Kobashi K, Villmow T, Andres T, and Pötschke P (2008) *Sensors and Actuators B: Chemical*, 134(2), 787–795.
- 85 Knite M, Ozols K, Zavickis J, Tupureina V, Klemenoks I, and Orlovs R (2009) *Journal of Nanoscience and Nanotechnology*, 9(6), 3587–3592.
- 86 Neitzert CH, Sorrentino A, Vertuccio L, Guadagno L, and Vittoria V (2009) Polymer and carbon nanotubes composite materials as low-cost temperature sensors. WO/2009/150690.
- 87 Kearns JC and Shambaugh RL (2002) *Journal of Applied Polymer Science*, 86, 2079–2084.
- 88 Dondero WE and Gorga RE (2005) *Journal of Polymer Science Part B: Polymer Physics*, 44, 864–878.
- 89 Chang TE, Jensen LR, Kisliuk A, Pipes RB, Pyrz R, and Sokolov AP (2005) *Polymer*, 46, 439–444.

Biomedical/bioengineering applications of carbon nanotube-based nanocomposites

N. DUNNE and C. MITCHELL, Queen's University Belfast, UK

Abstract: This chapter discusses the use of carbon nanotube (CNT)-based nanocomposites for biomedical applications, particularly in the areas of joint replacement surgery and dentistry. The chapter initially reviews the current issues associated with orthopaedic implants and the application of CNTs to counterbalance some of the issues described. The chapter then discusses the use of CNTs in dentistry, including dental restorative materials, periodontal dentistry and denture base resins. The next section of this chapter discusses CNTs used in the areas of regenerative medicine and tissue engineering, including targeted drug delivery systems, monitoring biological systems and biosensors. The chapter concludes by discussing issues of CNT interaction with the body.

Key words: bioactivity, biosensors, dentistry, joint replacement surgery, labelling and tracking, orthopaedics, tissue engineering.

22.1 Introduction to biomaterials and implants

Materials used for medical devices or implants must meet a number of criteria ranging from physical, mechanical, biological, toxicological and other characteristics, depending on their particular application (Davis, 2003). One of the essential properties, biocompatibility, plays a vital role in the performance of the medical device when implanted in the body (*in vivo*) (Shard and Tomlins, 2006) and has been defined as the 'ability of a material to perform with an appropriate host response in a specific application' (Williams, 1999). The biological assessment of biomaterials and medical implants is governed by a set of standards developed by the International Standards Organisation (ISO) and known as ISO Standard 10993 or, in the United States (US), as US Food and Drug Administration (FDA) blue book memorandum #G95-12, which is an adaptation of ISO 10993. Moreover, the environment should not cause any degradation or breakdown of the biomaterial or medical device that would cause loss of its physical or mechanical properties, if not required, as with biodegradable biomaterials.

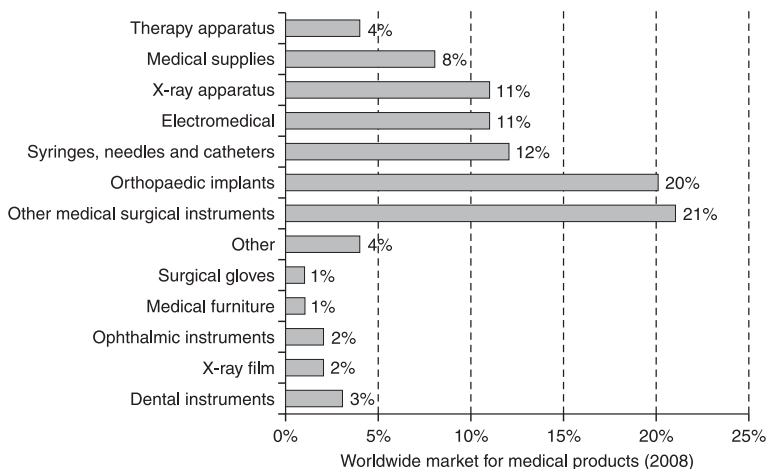
The development and manufacture of implantable medical devices have been ongoing since the early twentieth century. A common characteristic of materials used was their bio-inertness. The availability of biomaterials was a critical phase to meet the medical requirements of patients suffering from severe trauma or chronic debilitating diseases, for example, osteoarthritis, cardiovascular

dysfunction and neuro-muscular disease. In the 1970s, research and development activities progressed from bioinert to bioconductive, bioactive and bioresorbable materials for biomedical applications. By the mid-1980s, it was possible to manufacture implantable devices, causing a biological response that could induce controlled reactions under *in vivo* conditions. By the end of the 1980s, the first bioactive materials had been developed for a range of musculoskeletal applications. Initially a discipline related to mechanical engineering, technological advancements in the medical device sector (for example functional biomaterials) have shifted boundaries and mind-sets. With tissue engineering entering the traditional sector of healthcare, the conventionally distinct borders between pharmaceuticals and medical devices are merging, and information technology has added new dimensions, presenting at the same time huge opportunities and difficulties.

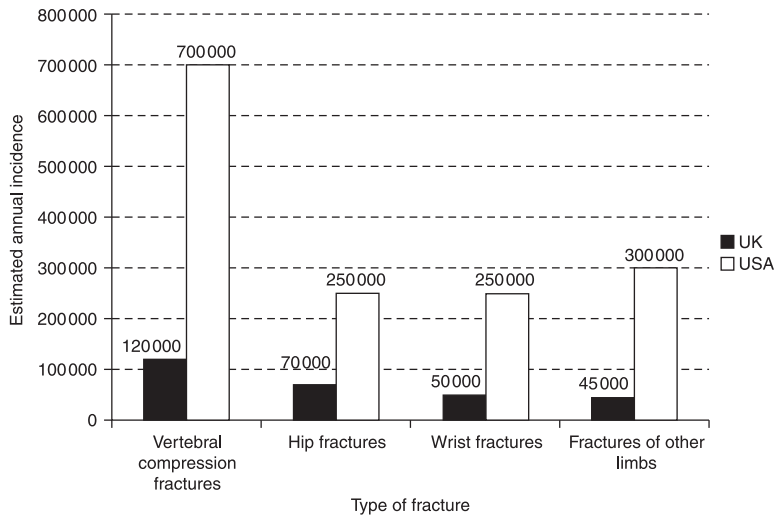
22.2 Orthopaedic implants

Because of its significance, particular attention has been given to the orthopaedic sector, which focuses on rehabilitation and prevention of deformities, injuries and other disorders associated with the musculoskeletal system. Numerous artificial prostheses are available to stabilise bone fractures, spinal deformities or fractures, or to replace articular joints (Fig. 22.1) (Taylor, 2009). Several million people are affected by orthopaedic disease or trauma (Fig. 22.2) and the market size for orthopaedic implants is in the range of US\$55 billion worldwide, with more than one million prostheses being implanted per annum (Phillips and Joshi, 2008).

The annual growth rate for hip and knee implants is estimated to be 10% and 20–25% for spinal implants, due to the growing prevalence of musculoskeletal



22.1 Worldwide market for medical products (Taylor 2009).



22.2 Prevalence of osteoporotic fractures in the United Kingdom and United States (Phillips and Joshi 2008).

diseases (for example, osteoporosis and trauma-related fractures and osteoarthritis). Other major aspects causing growth are the ageing population with their related problems as well as injuries related to increased mobility and patient demands due to changing everyday lives.

The development of orthopaedic implants has evolved over many decades, resulting in improved devices with respect to reduced complications and improved longevity. Although the devices are successful, there still remain many unanswered problems and it is anticipated that with greater demand from patients for smaller and also bone conserving implants, new devices and biomaterials are required to prevent the current issues of implant failure, allergic reactions, lack of radiopacity, wear corrosion, degradation, etc. Approximately 10% of all surgical procedures involving implants are due to failure of the implant–tissue interface. The subsequent revision of surgical procedure is demanding and takes significantly longer; recovery takes many weeks and is less successful than the primary procedure. Moreover, the cost of revision surgery is significantly greater than the cost of the initial surgical operation. The reasons for failure of the implant are multi-factorial; however, the principal cause is aseptic loosening of the implants. Approximately, 75% of all implants fail due to mechanical breakdown of the implant–tissue interface in the absence of infection (Malchau *et al.*, 2002).

Prosthetic implants and medical devices used for joint replacement surgical procedures are manufactured from almost all available material groups: metals for load-bearing applications like plates and nails for fracture fixation, rods for spinal fixation and prosthetic implants for total joint replacements. Structural ceramics find their use in articulation implants associated with total joint replacements,

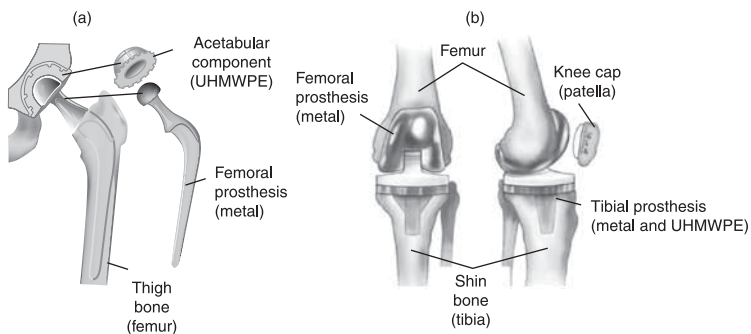
while bioactive ceramics based on calcium phosphate systems are used as bioconductive coatings and bone substitute materials. Polymers can be applied for articulation components of total hip joints and spinal implants, bone cements for stabilisation of prosthetic implants or for functioning as a temporary fixation device or scaffold, and in many other applications associated with repair of soft and hard tissue.

22.2.1 Current issues with orthopaedic implants

Although the success rate of hip joint (Fig. 22.3 (a)) and knee joint replacements (Fig. 22.3 (b)) is relatively high, a revision rate of 10% is anticipated within the first 10 years following implantation.

Loosening in the absence of infection (aseptic loosening) is the primary reason for failure and is usually a late complication often associated with an inflammatory response to wear particles from articulation of the joint replacements. Poor integration to the host bone as well as stress shielding are other reasons for failure at the implant–bone interface, resulting in aseptic loosening initially and the likelihood of peri-prosthetic fracture thereafter.

All the materials used as bearing surfaces in total joint replacement surgery are the same as, or minor modifications of, materials that have been used in clinical applications for many years. Ultra high molecular weight polyethylene (UHMWPE) has been used for the acetabular components in total hip arthroplasty, tibial components of total knee arthroplasty or the rotating component of artificial spinal discs since 1962. Metal on metal and ceramic on ceramic component combinations are in use for particular designs and primarily younger patients with more active lifestyles. All of the biomaterials currently used for joint replacement applications demonstrate limitations. Polyethylene (PE) is highly susceptible to wear, creep, degradation and fracture. Metals release ions into the surrounding tissue and bloodstream, which can cause systemic effects like hypersensitivity



22.3 Schematic diagram of (a) total hip joint replacement and (b) total knee joint replacement.

and potentially cancer. Ceramics are highly brittle and stress sensitive, therefore presenting specific loading risk and design limitations.

The anatomical stress pattern in bone is significantly changed after the implantation of a joint prosthesis or the stabilisation of a traumatic fracture. The implanted device will carry a portion of the load normally transferred through the bone, causing a change in the normal stress distribution. If the bone does not experience an appropriate load, then it will model Wolff's law (Wolff, 1891), causing bone mass loss through resorption (atrophy) or the development of highly calcified bone in areas of high stress (hypertrophy). Metallic or ceramic-based implants exhibiting a Young's modulus of 100–300 GPa are significantly stiffer than bone, which demonstrates a Young's modulus of 8–24 GPa. Bone loss is associated with stress shielding from a modulus mismatch between the bone and the implant (Levenston *et al.*, 1993) and can lead to implant loosening. This is not a serious issue when temporary devices are implanted for the stabilisation of a fracture caused by trauma; however, it is a problem for prosthetic implants that are used for replacements of diseased joints.

The unmet needs and unanswered problems for orthopaedic implants can be condensed as follows:

1. Safe and successful biocompatible materials for proposed application.
2. Facilitating stable and biomechanically sound implants that preserve as much healthy and functional tissue as possible.
3. Efficacious support between the implant and the host tissue to allow adequate stress transfer.
4. Articulating surfaces exhibiting a low coefficient of friction, thereby reducing the generation of wear particles.

22.3 Nanomaterials in medicine

Nanotechnology presents openings not only to improve materials and medical devices, but also to develop novel smart devices and technologies like intelligent drug delivery systems (Webster *et al.*, 2004). Several review papers discuss the different applications of nanomaterials and nanostructures for human healthcare (Salata, 2004; Liu and Webster, 2007). Artificial nanostructure and biomaterials have been postulated and studied for many medical applications to improve healing or replace tissue and organs (Lui *et al.*, 2007).

Being hollow nanofibres, nanotubes offer interesting characteristics. Tubes are lighter than solid structures and offer potentially higher mechanical strength. As drug carriers, tubes have the capabilities to supply and release larger quantities than surfaces. Therefore, of all the nanofibres, nanotubes are of the greatest interest for many applications in medicine. Nanotubes, particularly short nanotubes, can be produced from several materials, potentially containing therapeutic drugs. Their surfaces can also be functionalised by attaching different functional groups,

increasing their reactivity and hydrophilicity (Gojny *et al.*, 2003). The derivative tubes demonstrate enhanced properties relating to ease of dispersion, solubility, management and processability. Functionalisation can also improve the interfacial bond to the matrix, enabling better stress transfer between the carbon nanotubes (CNTs) and the matrix (Eitan *et al.*, 2006), and also making available potential sites for the attachment of chemical groups or therapeutic agents for more targeted delivery and efficacious application in medicine.

22.3.1 Biomedical applications

With their carbon composition, high aspect ratio, physical, mechanical and electrical properties, there has been significant attention in applying CNT technology to the medical and biomedical applications, for example, orthopaedic and dental implants and tissues engineered scaffolds. For several years, the number of research papers related to their use for biomedical applications has approximately doubled (Harrison and Atala, 2007). The biological activity and kinetics of any particular biomaterial depend on many variables, and the requirements and test protocols are well recognised for the conventional materials. However, because of the different physiochemical properties associated with their size, CNTs can potentially elicit a response in the human body that is very different and not directly expected from knowledge of the constituent chemical and compounds. For example, even a conventionally inert element such as gold can potentially be bioactive at the nanometre level (Goodman *et al.*, 2004).

Too many factors and conditions at the nanometre level determine CNT interaction with cells and their superior structure for any planned use. As a consequence of this enhanced complexity, the biological assessment of CNTs is not fully understood at present, even for cell cultures or small animal models. In recent years many studies relating to the toxicity and biocompatibility of CNTs have been reported, thereby increasing our understanding of these materials under biological conditions (Fiorito *et al.*, 2006).

CNTs are under investigation for potential application in many biomedical devices, given their inherent ability to interact with proteins and oligosaccharides, and their nanoscale dimensions that are comparable to those of basic biomolecules (Chen *et al.*, 2001). CNTs have potential for applications in medicine, drug and delivery areas (Harutyunyan *et al.*, 2002). There are many other possible applications of CNTs and their composites for medical applications, for example, MWCNT nanocomposites as biomimetic sensors, actuators and artificial muscles (Lee *et al.*, 2005). The capacity to change the surface chemistry and properties through the addition of functional groups on the CNT backbone has led to potential applications ranging from vascular stents (Webster, 2007), platforms for neurone growth and regeneration (Wan *et al.*, 2007), drug delivery vehicles for fighting cancer cells (Thuairé *et al.*, 2004) and a possible protection of the immune system from bacteria and viruses (Bhargave, 1999).

22.3.2 Interaction between carbon nanotubes and biological structures

When biomaterials come into contact with living cells, their surface morphology, structure, chemistry and charge dictate the biological host response. Because all biological processes, including traumatic or pathologic, are controlled and influenced by cell interactions at the nano-level (Chan *et al.*, 2006), carbon nanostructures with their extraordinary properties have been proposed for several applications in direct contact with living tissue to allow specific cell attachment or rejection. One of the most exciting medical applications for CNTs and carbon nanofibres (CNFs), aside from drug delivery systems, is tissue engineering. This involves adapting and using biomaterials for building constructs that regenerate and repair functional tissue by influencing the organisation, differentiation and growth of the appropriate cells for body functions that have been damaged as a result of disease or trauma. CNTs and CNFs offer convincing properties for such applications, but their surface chemistry usually needs to be adapted to achieve the desired biological reaction (Harrison and Atala, 2007).

Tissue engineering is of particular interest in the healing of a traumatic or disease-related wound or defect, because the surrounding tissue has inadequate ability to bridge such distances. Without scaffolding, the defect would heal within the gap to form extended scar tissue that would compromise the structure, form and function of the repaired tissue. Scaffolds can be two-dimensional (e.g. soft tissue–skin) or three-dimensional (e.g. hard tissue–bone). 2D structures are usually achieved by surface medications, like incorporation of CNTs to substrates or as nano-filler in composites. The surfaces of different materials can be structured with nano-patterns by incorporating or applying CNTs for enhanced tissue–implant interaction. Equally important as the topography is the chemistry of the surface. 3D structures that allow transmission of all forms of load are normally built up by regular or irregular fibrous structures with interconnecting pores that allow the cells to penetrate and fill the scaffold. It has been demonstrated that MWCNTs can be shaped into 3D architectures and are ideal for cell seeding and *in vitro* cell modelling, leading to the design of exciting new tissue engineered scaffolds for biological applications. For example, the growth of a mouse fibroblast cell line on a 3D porous network based on an array of MWCNTs by exerting chemically induced capillary forces on the nanotubes was demonstrated by Correa-Duarte *et al.* (2004). The porous, interconnected network supported cell attachment and growth and demonstrated sufficient structural integrity to retain its shape *in vivo*, with adequate strength to support the developing tissue. Such a nano-structured material could serve as a biocompatible matrix to restore, maintain, or reinforce damaged/weakened tissues for applications where MWCNTs are required to act as drug delivery devices.

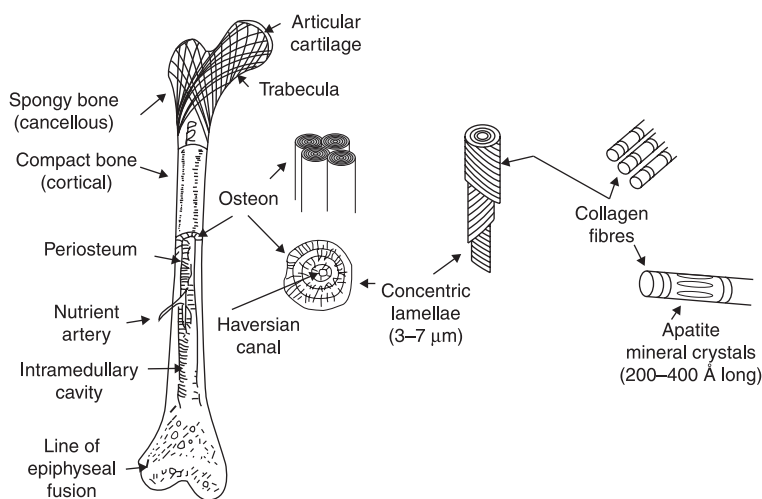
There is a clearly defined trend for medical devices to move from tissue substitution by artificial replacements to guiding and accelerating the healing

process by means of tissue engineering, which can yield enormous personal and economic benefit. Because of their unique properties, CNTs can have a major role in the development of appropriate structures and surfaces. They have also been proposed recently for use in tissue engineered dental applications, delivered as an alginate nanocomposite gel at the surgical site (Kawaguchi *et al.*, 2006).

Tissue engineering for orthopaedic applications

Bone is a natural composite material, consisting of 10% water, 20% organic material and 70% mineral matter, by weight (Shi and Xuejun, 2006). The organic matter, which provides a framework consisting of mainly type-I collagen fibrils ($\varnothing 0.1\text{--}8 \times 300\text{ nm}$), is similar in scale to carbon nanotubes. The remainder of the organic material comprises other proteins, a cement-like substance, and a cellular component, consisting of osteocytes, osteoblasts and osteoclasts, which aid in dissolution, deposition and nourishment of the bone. The inorganic mineral component, which provides strength is a calcium-deficient, carbonate-substituted apatite, containing calcium and phosphate ions, similar in structure and composition to hydroxyapatite ($\text{Ca}_{10}(\text{PO}_4)_6(\text{OH})_2$) (LeGeros and LeGeros, 1993).

Figure 22.4 illustrates the hierarchical structure of bone. Bone mineral crystals ($\varnothing 2\text{--}5 \times 20\text{--}50\text{ nm}$) are arranged between the ends of collagen fibrils, which are then rearranged into sheets called lamellae. The morphology of mineral crystals is generally agreed to be plate-like with dimensions on the scale of ten to hundreds of angstroms. The collagen lamellae are arranged either in concentric circles called tubular Haversian systems or in sheets. These sheets form the sponge-like cancellous or trabecular bone found inside the structure at the bone ends. The



22.4 Hierarchical structure of bone, example femur.

Haversian system configuration, on the other hand, leads to dense, cortical form of bone, which comprises 80% of bone mass and surrounds the cancellous bone (Lakes, 1993).

Because tissue development is controlled by events at cellular and molecular level, the surfaces for osteointegration need to be able to influence osteoprogenitor population activity and function. Recent review papers have addressed the similarities between bone and carbon nano-structures and report the application of CNTs and CNFs (Christenson *et al.*, 2006; Webster and Ah, 2006; Liu *et al.*, 2007). Significant research is currently focussed on looking at strategies for developing biomimetic tissue surfaces for prostheses; surfaces that have been engineered at the nano-scale to mimic or interact with soft or hard tissue, thereby behaving as a living surface. With the potential that nano-technology offers, many current problems in developing long-lasting, biocompatible orthopaedic devices might be solved in the future. Several applications for nanostructures and nanomaterials are already being pursued and early results are encouraging (Streicher *et al.*, 2006). The application of CNFs and CNTs has been proposed and investigated as a standalone product, either functionalised as a scaffold or as reinforcement for polymers or other composite materials for different orthopaedic applications, mostly focusing on hard tissue repair (Balasundaram and Webster, 2006; Christenson *et al.*, 2006; Webster and Ah, 2006).

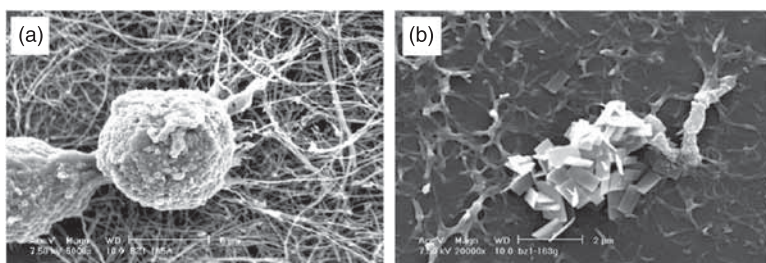
Price *et al.* (2004) compared polymer casts of consolidated typically sized and nano-sized carbon fibres, highlighting the importance of the nanostructure. This study showed significantly enhanced osteoblast adhesion to the nano-phase fibres. In a further study by Price *et al.* (2003), they produced composites with similar fibres using a polycarbonate-urethane polymer matrix. Such composites have already attracted significant attention for orthopaedic applications because of their tailored electrical and mechanical properties through the incorporation of CNFs. In these studies, Price *et al.* (2003) showed the advantage of adding 10 to 25 wt% CNFs for osteoblasts. Research groups have demonstrated selective adhesion of osteoblasts on composite structures containing CNFs, therefore making them potential candidates for prosthetic implants (Elias *et al.*, 2002). They incorporated CNFs and CNTs in a polycarbonate-urethane polymer matrix to create a nanostructure added to the structure, thereby mimicking those nano-features evident in living tissue, and assessed these nanocomposites for efficacy using cell lines *in vitro*. Selective adhesion was more pronounced with increased content of functionalised CNT-CNF; osteoblasts exhibited increased viability (Elias *et al.*, 2002; Webster *et al.*, 2004) and were preferred over fibroblasts (Price *et al.*, 2004). In another study by Khang *et al.* (2005) using the same nanocomposites, it was demonstrated that fibronectin adsorption also increased with increasing quantities of MWCNTs, a consequence of the increased surface roughness and surface energy of the nanocomposite. Osteoblasts align along CNFs with a pyrolytic outer layer, that is reduced surface energy and depose calcium phosphate mineral, which is an indicator of their viability (Khang *et al.*, 2006). All of these

phenomena would reduce fibrous tissue formation around a prosthetic implant and are advantageous for optimal osseointegration.

Shi *et al.* (2005) developed an injectable nanocomposite based on polypropylene fumarate containing unfunctionalised and functionalised SWCNTs as a potential candidate for load-bearing orthopaedic applications. They concluded from their investigations that the functionalised SWCNTs were more homogeneously dispersed within the matrix, which improved the mechanical function of the nanocomposite even at levels of loading as low as 0.1 wt% SWCNTs.

Functionalised SWCNTs have also been applied to developing hydroxyapatite (HA) based bone substitute materials and tissue promotion scaffolds for the treatment of bone fractures (Zhao *et al.*, 2005). The methodology amalgamates the osteo-conductive properties of HA with the supra-mechanical properties of CNTs, thereby improving stiffness and strength of the brittle ceramic-based bone substitute material. For this purpose, SWCNTs were chemically functionalised with various chemical groups to produce negative surface charges that attract calcium ions from the surrounding electrolyte. Some of these conjugates led to nucleation, self-assembly and orientation of the HA crystals, facilitating control of their alignment; while other groups enhanced biocompatibility of the CNTs, improving their solubility in water. This research has potential application to artificial bone with improved flexibility and strength, novel types of bone grafts and a possible local treatment of osteoporosis. This could be achieved by delivering an aqueous solution of functionalised CNTs into the bone fracture or defect, encouraging new bone tissue to grow and fill the defect. Zanello *et al.* demonstrated under laboratory conditions that osteoblast cells can grow and proliferate best on scaffolds comprising SWCNTs and MWCNTs, when the functionalisation of these CNTs can result in a neutral surface charge (Fig. 22.5) (Zanello *et al.*, 2006).

Another technique for improving the durability and biological acceptance of biomaterial surfaces, for applications as orthopaedic prostheses, is the application of coatings consisting of HA and CNTs. Balani *et al.* (2007) reported the



22.5 (a) Dividing osteoblast on MWCNTs; (b) mineralised matrix found in SWCNT cultures. (Source: Dr Laura Zanello, University of California-Riverside, US.)

improvement in the fracture toughness of a plasma-sprayed HA coating by incorporating 4 wt% MWCNTs into the HA. Additionally, they observed no adverse cellular response when in vitro biocompatibility studies were conducted on the HA–MWCNT coating. White *et al.* (2007) presented an overview of biomedical applications in the context of HA–CNT nanocomposites.

Another CNT-based nanocomposite for biomedical application can be manufactured by blending MWCNTs and poly-L-lactide (PLLA). The interaction between the polymer matrix and the MWCNTs takes place mainly through the hydrophobic C–CH₃ functional groups (Zhang *et al.*, 2006a). The conductivity of the MWCNT–PLLA nanocomposite improved as the level of MWCNT loading increased and the growth of fibroblast cells was inhibited. Potential applications of such a nanocomposite could be as a biodegradable, conductive material with selective cell interaction facility as required. Nonetheless, the important question about the fate and the biological reaction of the released CNTs from a resorbable polymer matrix needs to be fully understood.

Electrospinning can be used to produce fibres containing CNTs, for example, SWCNT-reinforced silk nanofibres (Ayutsede *et al.*, 2006) and incorporating as little as 0.8 wt% of MWCNTs to a chitosan derived biopolymer increased its tensile strength by 200% (Wang *et al.*, 2005). MacDonald *et al.* incorporated 4 wt% SWCNTs into collagen, achieving an electrically conductive composite with improved mechanical properties (MacDonald *et al.*, 2005; MacDonald and Stegemann, 2006). Such a CNT–collagen-based nanocomposite could potentially have an application as a scaffold material in tissue engineering. Correa-Duarte *et al.* applied chemically induced capillary forces to interconnect MWCNTs to a 3D network, which allowed for the successful growing of murine derived fibroblast cells within the 3D structure (Correa-Duarte *et al.*, 2004). Firowska *et al.* (2006) merged lithographic and layer-by-layer self-assembly technologies to produce a highly orientated 3D scaffold structure based on inter-crossed MWCNTs for potential application in tissue engineering.

22.4 Load-bearing implants for orthopaedic applications

A strong acetabular socket prosthesis, which is thin and compliant, but could replicate the normal transfer of load-bearing forces to the supporting bone should significantly decrease bone atrophy (loss) and provide long-term joint stability. Initial efforts using a composite based prosthesis consisting of a flexible horseshoe-shaped artificial acetabular socket were developed (Jones *et al.*, 2001a). Jones *et al.* (2001b) reported the efficacy of a polybutylene terephthalate reinforced with carbon fibre (CF) prosthesis in 50 patients over the age of 80 years after five years implantation. The initial results were positive in terms of performance; however, improvements could be made to the design. For example, if a mono-block composite acetabular socket could be developed that encourages new bone growth

on the outer surface of the prosthesis and is, in parallel wear-resistant, then this would be an exciting prospect. Analogous possibilities are available, taking into account current developments for segmental and partial joint replacement. For example, resurfacing of the hip joint, which is presently achieved using large diameter metal-on-metal articulations for young and active patients. There is currently significant interest to maintain as much natural bone as possible to facilitate bone preservation for any revision surgical procedures, as the life expectancy of the younger patient population is greater than the working life of the prosthetic implants. The pursuit of smaller implants also challenges the limits for the existing materials, and there is a need for new materials and technologies to meet the requirements of such designs. Several applications for trauma treatment, spinal repair and the treatment of degenerative diseases also require development. The application of CNTs could achieve the objective of such developments, especially when adopting all properties and not just the mechanical characteristics, and could have a major impact on new designs and implant prosthesis.

22.4.1 Carbon nanotubes in orthopaedics

To improve the mechanical strength and resistance of prosthetic implants, the reinforcement of high strength polymers with CNTs appears to be a real prospect. CNTs are highly anisotropic and due to their high strength, high aspect ratio and excellent thermal and electrical conductivity, they are currently been used as an alternative to CFs for producing composite materials. CNTs have generated significant interest, particularly as a reinforcing material for polymer matrix composite materials. CNTs are believed to improve the mechanical, electrical and thermal properties of those composites. Nevertheless, several complications related to CNT dispersion, their compatibility within the polymer matrix and the nature of the bond between the CNT and matrix material need to be understood before practical applications. To develop the unique properties of CNTs in a polymer composite, fundamental challenges need to be tackled that have proved to be a difficult issue with a number of opposing variables: including CNT production and purification, functionalisation of CNTs, alignment and dispersion of CNTs, and processing method used (Mylvaganam and Zhang, 2007; Weisenberger *et al.*, 2007).

A strong interfacial bond between the CNT and polymer matrix is required to facilitate the appropriate stress transfer between the reinforcement and matrix phases of the nanocomposite (Lau Kin-Tak, 2002). Three main load transfer mechanisms control the principal stress transfer: (1) surface topography and micromechanical interlock; (2) chemical bonding; and (3) van der Waals interaction. To achieve bonding between the reinforcement and the polymer matrix two approaches have been adopted: (1) non-covalent attachment of molecules, resulting in the formation of weak van der Waals forces; and (2)

covalent attachment of functional groups to the CNT walls. The non-covalent approach has the benefit that the perfect structure of the CNT is not altered, thus their overall mechanical properties remain unchanged. The covalent attachment of the functional groups to the CNT surface can be achieved by many chemical or physical methodologies. Adopting one of these processes has the potential to introduce defects on the CNT walls and therefore reduce the mechanical strength of the reinforcing material. It has also been demonstrated to have an influence on the stiffness of the CNT (Namila *et al.*, 2004), which needs to be considered. Notwithstanding this fact, it is thought that the interfacial shear strength of the polymer-CNT nanocomposite with non-covalent bonding can be increased over an order of magnitude by incorporating <1 wt% chemical bonds between the CNT and the polymer matrix. Another aspect is the effect of any reinforcing material on the structure of the polymer matrix. The addition of any additive during the processing of a thermoplastic semi-crystalline polymer can potentially influence the crystallinity and therefore the final properties of the polymer-CNT nanocomposite. The trade-off between strength of the polymer-CNT interface, CNT strength and the final properties of the nanocomposite material must be well balanced (Qian *et al.*, 2000).

The majority of studies have focused on the development of polymer-CNT nanocomposites that could be applied as lightweight, high strength, fibre-reinforced materials for non-medical applications, showing that, apart from the polymer, the CNTs and any potentially applied functionalisation, there is also a balance between the level of CNT loading required to achieve a significant improvement in the properties of the nanocomposite and its ability to be processed (Khare and Bose, 2005). Many different techniques have been used to attain a strong interfacial bond between various polymer matrices and the CNTs. SWCNTs and MWCNTs have been used for reinforcing thermosetting and thermoplastic based polymers (Thostenson *et al.*, 2005). Ami Eitan *et al.* (2003) have shown functionalisation of SWCNTs and MWCNTs by using a solution of nitric and sulphuric acid to form carboxylic acid groups on the surface, which are formed along the CNT walls and at the end-caps. This approach seems to be ideal for optimal transfer within the composite material. They reported that it is possible to further react with the epoxide functional group to facilitate even better interaction between the polymer matrix chains and the CNT surface of the composite.

Only a few studies to date have explored the potential use of CNT composites for load-bearing orthopaedic applications. In an effort to enhance the mechanical performance of UHMWPE, a well-accepted hydrophobic and non-polar articulation material for hip and knee joint replacements, by incorporating CNTs to the polymer matrix, reinforced composites have been manufactured by research groups from Sweden (Emami, 2007) and France (Babaa *et al.*, 2006). The French group used UHMWPE with unfunctionalised SWCNTs as a reference, which resulted in the non-covalent attachment of CNTs and the polymer matrix.

Although in this approach the structure of the SWCNTs is not changed, the mechanical properties of the nanocomposite would only be affected minimally and the low attraction forces between polymer matrix and CNTs are unfavourable (Holzinger *et al.*, 2004), as the clinical history of the same material has demonstrated (Pryor *et al.*, 1992). Babaa *et al.* (2006) also covalently bonded CNTs and polymer matrix with chemically modified SWCNTs and polyethylene (PE). This was achieved by oxidising the CNTs, forming carboxylic acid groups along the CNT walls and end-caps, and thermally oxidising the UHMWPE, forming oxygen-containing functional groups and using a di-amine to bond the oxidised PE and SWCNTs. The bi-functional molecule can react with the carboxylic acids groups attached on both the SWCNTs and PE to form a strong covalent bond. The resulting nanocomposite was formed as a film and fibres. Mechanical testing of the nanocomposite material showed significant improvements over the reference material. Another interesting aspect of applying CNTs to reinforce UHMWPE is that MWCNTs can act as radical scavengers and antioxidants (Fearon *et al.*, 2002), especially in view of the fact that the medical grade of UHMWPE is only available without any antioxidant, which tends to degrade when implanted in the body.

PEEK, a semi-crystalline high strength polymer, has been studied for many nanocomposite applications. Sandler *et al.* (2002) reported on the mechanical properties of a vapour grown 150 nm Ø CNT reinforced PEEK composite using extrusion technology to produce masterbatches. The final specimens were produced by using the injection moulding process. A linear increase in stiffness and yield strength with loading concentrations of up to 15 wt% was demonstrated, while PEEK matrix ductility was sustained to 10 wt% CNT loading. No influence of reinforcing material on the polymer matrix crystallinity was measured. Werner *et al.* (2004) studied the wear properties of PEEK–CNT nanocomposite. An exponential wear rate reduction for composites with 5–10 wt% CNT was demonstrated, depending slightly on the reinforcing material content. Werner *et al.* postulated that the CNTs demonstrated the properties of a solid lubricant, therefore decreasing the wear rate.

With the intention of manufacturing load-bearing orthopaedic prosthetic implants, Babaa *et al.* (2006) also used PEEK as a polymer matrix material and reported production of UHMWPE–CNT and PEEK–CNT nanocomposites. To obtain a covalent bond between the components, the CNTs were functionalised by using di-functional molecules for a better bonding between CNTs and the polymer matrix. With this methodology, the properties of the nanocomposite were enhanced. Bantignie (2007) attached functionalised MWCNTs and sulphonated using direct reaction bonding to sulphur group of PEEK, and demonstrated using spectroscopic methods that a covalent bonding between SWCNTs and the PEEK polymer matrix could be achieved. The direct attachment reaction bonding method is an unwieldy, labour intensive process, with limited commercial applicability. However, the functionalised CNTs have been shown to

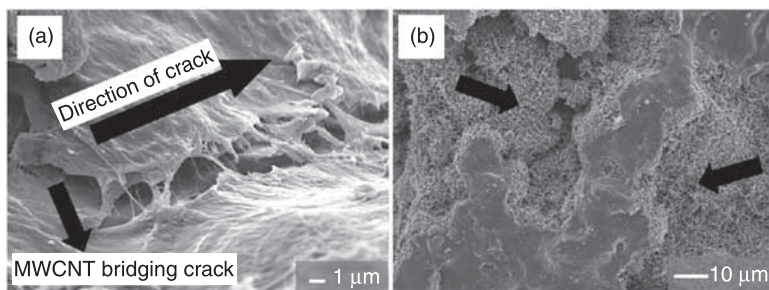
achieve a high level of bonding with functionalised PEEK, a clinically applicable material.

The premise of a PEEK–CNT nanocomposite material offers an excellent opportunity for outstanding applications of thin and high strength prosthetic implants with exceptional wear properties that could also be engineered on their interface with the host tissue to be fully integrated.

Another biomaterial used in joint replacement surgery is PMMA, which is the primary component of acrylic bone cement. It is well documented that PMMA cement is susceptible to fatigue-related cracking and impact-induced failure (Kuehn *et al.*, 2005). Active or overweight patients with implants fixed with PMMA cement are at risk from cement mantle failure, which occurs in 5% of all total joint replacements patients post-operatively. Failure rates of 67% have been reported after 16 years in patients younger than 45 years. It is postulated that the annual number of revision total knee arthroplasties performed in the US will increase 601% to 270,000 by 2030 and the number of hip arthroplasty revisions will increase 137% to 97,000, with the main cause of implant failure attributed to cement mantle failure (Marrs *et al.*, 2006). There is a plethora of literature reporting methods for improving the mechanical and physical properties of PMMA bone cement. Many of these studies have incorporated various additives into the polymer matrix with the aim of improving the mechanical properties. Specifically, PE fibres (Uzun *et al.*, 1999), glass fibres (Stipho, 1998), long macroscopic carbon fibres (Manley *et al.*, 1979), and titanium fibres (Topoleski *et al.*, 2004) have all been employed in attempts to bridge fatigue cracks and prevent, or reduce, the rate of their propagation. The involvement of these additives have been less than successful due to the poor fibre–polymer matrix bonding (and subsequent debonding), increased viscosity, poor additive distribution, and the adverse effects such materials have on the mixing of bone cement (Marrs, 2007). Marrs *et al.* (2006) investigated the influence of MWCNTs in PMMA-based bone cements. They reported moderate improvements (13–24%) in the static properties when 2 wt% MWCNTs were incorporated into the methyl methacrylate–styrene cement. Marrs *et al.* (2007) also reported significant improvements (>300%) in the dynamic properties when MWCNTs (2 wt%) were added to the same bone cement. However, both studies (Marrs *et al.*, 2006; Marrs *et al.*, 2007) used non-clinically relevant methods to ensure optimal dispersion of the MWCNTs into the cement. Additionally, it has been hypothesised that functionalisation of the MWCNTs could potentially improve the dispersion and interfacial bonding of the MWCNTs within the cement matrix, leading to further improvements in the static and dynamic properties (Gojny *et al.*, 2003; Marrs *et al.*, 2007). It has been reported that the static properties of PMMA polymer resin can be significantly improved through functionalisation of MWCNTs (Pande *et al.*, 2009). A subsequent study by Ormsby *et al.* (2010a) incorporated 0.1 wt% MWCNTS (unfunctionalised and carboxyl functionalised) into PMMA bone cement and determined the mechanical and thermal properties. They reported

the extent of the effect was dictated by the type of MWCNT, method of introduction used and the properties being quantified. Improvements in mechanical properties (2–32%) were attributed to the MWCNTs being well dispersed within the PMMA cement when the MWCNT were ultrasonically disintegrated in the liquid monomer prior to mixing with the PMMA powder, thereby arresting/retarding crack propagation through the cement (Fig. 22.6(a)). Conversely, reductions in mechanical properties were ascribed to MWCNT agglomerations occurring within the cement microstructure when the MWCNTs were dry blended into the PMMA powder prior to mixing with the liquid monomer (Fig. 22.6b). The degree of these agglomerations was dependent on the method used to incorporate the MWCNTs into the cement. Ormsby *et al.* (2010a) also reported that MWCNT-reinforced PMMA cement shrinks less and demonstrates a lower exothermic thermal reaction. The level of heat produced within the exothermic polymerisation reaction of the PMMA bone cement was significantly reduced when functionalised MWCNTs were added. The maximum temperature value reduced by 29–53% when compared to the control cement, as measured in accordance with ISO 5833: 2002. However, this reduction in maximum temperature extended the duration of the polymerisation reaction by 52–82%. Notwithstanding this fact, the reduction in exotherm translated in a decrease in the thermal necrosis index value, which is indicative of a potential reduction in hyperthermia experienced *in vivo* by polymerisation reaction of PMMA cement.

A further study by Ormsby *et al.* (2010b) investigated additional mechanical augmentation of PMMA bone cement via the incorporation of MWCNTs with varying functional groups (carboxyl and amine) at increasing wt% loadings (up to 1 wt%). The study concluded that incorporating low loadings of MWCNTs (≤ 0.25 wt%) into PMMA bone cement improved the mechanical properties of the resultant nanocomposite. Significant improvements in compressive strength ($\approx 40\%$), bending strength ($\approx 18\%$), compressive modulus ($\approx 28\%$), bending



22.6 (a) 0.1 wt% carboxyl functionalised MWCNT–PMMA cement in which MWCNT can be seen to bridge a micro-crack on the surface; (b) 1.0 wt% unfunctionalised MWCNT–PMMA cement showing an agglomeration of MWCNTs (indicated by arrows), which was the fracture initiation point for this specimen.

modulus ($\approx 14\%$) and fracture toughness ($\approx 61\%$) were observed when carboxyl functionalised MWCNTs were added to the PMMA bone cement. Higher loadings ($\geq 0.5\text{ wt}\%$) provided lesser improvements in the mechanical properties, and in some cases significant reductions were recorded. The highest loading of carboxyl functionalised MWCNTs ($1\text{ wt}\%$) significantly reduced the mechanical properties of the PMMA bone cement, giving reductions in compressive strength ($\approx 26\%$), bending modulus ($\approx 42\%$), compressive modulus ($\approx 9\%$) and bending strength ($\approx 44\%$), respectively. The incorporation of amine functionalised MWCNTs followed a similar trend with the $0.1\text{ wt}\%$ loading giving the maximum improvement in mechanical properties.

The dynamic mechanical behaviour of MWCNT–PMMA composites has also been studied (Jin *et al.*, 1998; Jin *et al.*, 2001; Wang *et al.*, 2006). Wang *et al.* (2006) showed that the storage modulus of PMMA at room temperature is doubled upon addition of $26\text{ wt}\%$ MWCNT. Subsequent studies have used smaller amounts of functionalised MWCNTs leading to significant improvements in the storage modulus of PMMA. Velasco-Santos *et al.* found that the storage modulus of PMMA at 40°C increased by 50% upon addition of $1\text{ wt}\%$ functionalised MWCNTs and by 66% upon incorporation of $2\text{ wt}\%$ functionalised MWCNTs (Velasco-Santos *et al.*, 2003). Hwang *et al.* (2004) reported that the storage modulus of PMMA increased by 1100% when $20\text{ wt}\%$ of PMMA-grafted MWCNTs were added. Building on previous studies using general purpose PMMA as the matrix material, Nien and Huang (2010) incorporated up to $0.75\text{ wt}\%$ MWCNT into PMMA bone cement and determined the effects on the static and dynamic mechanical properties. They reported an improvement in the compressive strength (21%) and tensile strength (15%) of the PMMA cement when $0.75\text{ wt}\%$ MWCNTs were added. Using dynamic mechanical analysis, they observed that the glass transition of the PMMA cement reduced by 8% for the same PMMA–MWCNT cement combination (Nien and Huang, 2010). They postulated the reduction in glass transition temperature was due to the CNT acting as a plasticiser. Improvements in the storage modulus were not demonstrated for the PMMA–MWCNT cement, on average a 7% reduction was observed irrespective of the $\text{wt}\%$ MWCNT added to the PMMA cement.

The incorporation of CNTs in PMMA cement has a significant effect in avoiding crack propagation, and could deal with one of the primary reasons for revision surgery of a cemented total joint replacement: fracture and fatigue fracture of the PMMA cement mantle. Advantageous side effects are that such reinforced PMMA cement shrinks less and demonstrates a lower exothermic thermal reaction, and that the hollow CNTs would facilitate the addition of pharmaceutical components like antibiotics, anti-inflammatory drugs and chemotherapeutic agents, etc. Potential causes for consideration may be the increase in the rheological properties and setting characteristic of such a PMMA–CNT bone cement system during application, and a possible phase separation between the PMMA cement and CNTs while filling the space between the prosthesis implant and the bone. Another

potential consequence that needs to be investigated is the interaction between the CNTs and the metal-based prosthetic implant with respect to fretting, abrasion and corrosion, particularly at higher levels of CNT loading.

Alumina–CNT nanocomposites have many potential medical applications, particularly in orthopaedic prosthetic implants. Improving the low toughness, poor bending strength of alumina by enhancing the resistance to crack propagation would allow for greater design flexibility, less risk of fracture and better wear resistance. Such improvements would be advantageous for implants manufactured from alumina, which currently have several disadvantages due to fracture risk.

Many studies have reported improvements in the properties of metal and ceramics by producing metal–CNT and ceramic–CNT nanocomposites (Zhan *et al.*, 2003; Thostenson *et al.*, 2005; Zhang *et al.*, 2006b). As a brittle material, alumina is strong in compression but is prone to fracture, that is poor flexural strength and fracture toughness. The alumina quality used for artificial hip and knee joint bearings has a typical flexural strength of 500 MPa and a fracture toughness of 4 MPa m^{1/2}. To improve the resistance to crack initiation and propagation in the microstructure of the alumina, either fibres or toughening constituents that can absorb components of the strain energy induced by the crack are employed. CNTs could have such an influence at the nanoscale level. To produce alumina–CNT nanocomposites, various approaches have been put forward (Zhan *et al.*, 2003), however, limited data is reported on the effects of incorporating CNTs into the alumina. Notwithstanding this fact, experience thus far has demonstrated difficulty in obtaining a dense and a well-dispersed structure alumina–CNT nanocomposite material.

In spite of this, Zhan *et al.* (2003) reported the successful manufacture of dense nanocrystalline alumina–SWCNT nanocomposites at sintering temperatures as low as 1150 °C by spark plasma sintering, and achieving a fracture toughness of 4 MPa m^{1/2}, nearly three times that of pure nanocrystalline alumina. Conventional alumina ceramics are sintered at temperatures above 1400 °C in an oxidising atmosphere that would burn the embedded CNTs. Therefore, the nanocomposites have to be sintered at much lower temperatures (1000 °C). It is highly unlikely that oxide ceramics meeting today's strict standards can be manufactured in this way. A possible solution to a lower sintering temperature is to allow more glassy phases between the ceramic grains, for example, by using a less pure alumina; however, this reduces the overall quality. A more promising approach to higher strength ceramics might be the application of nanostructure constituents (Tanaka *et al.*, 2002).

22.5 Carbon nanotubes in dentistry

Dental materials have to be high performance materials, to survive within the complex and hostile oral environment. They will experience a wide range of temperatures (15–68 °C), pH (6.0–7.4), chemical exposure from food and drink,

together with static and fatigue loads of up to 600 N. It is therefore essential that all restorative dental materials, whether they are to be used to restore a cavity in a tooth, or make a fixed dental prosthesis, such as a crown or bridge, or a removable dental prosthesis, such as a denture, are able to give optimum performance over a period of ideally 8–10 years before replacement is required.

CNTs have received a modest amount of research attention in dentistry as they have shown potential to increase the strength of composite materials and implants, increase cell adhesion and proliferation, effect nucleation of hydroxyapatite and provide protection against bacteria (Akasaka *et al.*, 2009).

However, the main obstacle to the widespread inclusion of CNTs in dental materials is the deep black colour that they bestow on any composite material to which they are added. Obviously, black is not going to be the colour of choice for a dental restoration, as patients require aesthetic materials that blend in with the natural colour of their teeth and gums. However, if the improvement in mechanical and physical properties is sufficiently high, it may be cost-effective to develop techniques and procedures to mask the black colour of the CNTs. This could be carried out using an aesthetically coloured coating of approximately 1–1.5 mm thickness, or by the incorporation within the composite material of other inorganic additives such as sol-gel-based opalescent fillers, or chromophoric xerogel pigment particles (Zhang *et al.*, 2008).

22.5.1 Carbon nanotubes and adhesion to tooth substance

It is important when restoring a cavity within a tooth that the replacement material bonds to the surface of the tooth to prevent microleakage of bacteria, found in saliva, between the filling material and the cavity wall. If this occurs, as it may do with current dental materials, the bacteria can enter the dental pulp, containing the nervous and vascular tissues, and cause inflammation. The inflammation in turn causes pain, and may lead to death of the pulp tissues, necessitating either tooth extraction or root canal treatment.

Sophisticated mechanisms of micro-mechanical and chemical adhesion have been developed to try and prevent this microleakage. These involve the application of acids to the surface of the tooth dentine, which demineralise the dentine, leaving collagen fibres exposed, and stripping back the smear layer exposing the dentinal tubules. Dental adhesive materials are then applied which flow into the openings of the tubules and inter-mingle with the collagen fibres creating a micro-mechanical bond. This method works satisfactorily, however, it is still vulnerable to microleakage in the long term. Therefore, constant research is being carried out to determine if the bond to tooth substances can be improved.

In early studies, CNTs were applied to tooth dentine and cementum and showed that they selectively adhered to these dental surfaces, possibly by adhering to the exposed collagen fibres (Akasaka *et al.*, 2009). Dentine contains small, thin apatite crystals embedded in a protein matrix of cross-linked collagen fibrils

(Nicholson, 2006). The interaction between the CNTs and collagen was investigated using SEM and fluorescence confocal laser scanning microscopy. Microscopy showed that the CNTs adhered to the surface of tooth dentine and cementum, but could not penetrate into the dentinal tubules. There was no interaction observed with tooth enamel, which does not contain collagen. In addition, the tooth surfaces to which the CNTs attached were observed to change colour to grey, indicating the presence of CNTs.

These findings are in agreement with those of earlier papers which also reported strong interactions between CNTs and collagen fibres in an aqueous environment (MacDonald *et al.*, 2005; Liao *et al.*, 2007). They speculated that as proteins in solution are known to adsorb CNTs via hydrophobic interactions, which the CNTs were probably interacting with the collagen fibres using the same mechanism (Karajanagi *et al.*, 2006).

Further studies by Akasaka *et al.* (2009) showed that the bond strength between the CNT-coated dentine and a resin composite dental filling material was not decreased by the presence of the CNTs. The authors speculated that further work in the area of dental bonding was warranted as CNTs can exert beneficial effects such as the nucleation of hydroxyapatite and protection against dental bacteria without decreasing the bond strength to restorative materials. The ability to protect against dental bacteria would be of particular benefit in counteracting the effects of any microleakage.

22.6 Carbon nanotubes and dental restorative materials

CNTs have been added to dental methacrylate-based resin composites used to restore cavities in teeth (Zhang *et al.*, 2008). These dental filling materials are conventionally tooth-coloured and therefore highly aesthetic and in demand by patients. However, although many significant advances have been made in the wear and physical properties, together with the dimensional stability of these materials over the last 15 years, the average life expectancy of a resin composite restoration is significantly lower than that of a conventional dental amalgam restoration (Letzel, 1989; Mjor *et al.*, 1990; Chadwick *et al.*, 2002; Lucarotti *et al.*, 2005).

Efforts therefore continue to improve, in particular, the physical properties of dental resin composites, often by the addition of nanoparticles. The use of nanoparticles within dental resin composites is increasing in popularity as the small size and wide size distribution can achieve increased filler loading, giving improved wear and reduced shrinkage on photo-polymerisation. Increases in tensile and compressive strength and fracture toughness have also been reported (Baseren, 2004; Yap *et al.*, 2004a; Yap *et al.*, 2004b; Chen *et al.*, 2006; Mesquita *et al.*, 2006).

The majority of research has focussed on the addition of tooth-coloured or white nanoparticles, such as nano-hydroxyapatite, colloidal silica, titanium dioxide or aluminium oxide nanoparticles (Jandt and Sigusch, 2009). While these have delivered

some improvements in performance, one group has added SWCNTs to dental resin composite, citing their high tensile strength and Young's modulus as the stimulus for their use. The work reported a process to deposit a thin shell of nano-silica onto the oxidised surface of SWCNTs by using a thin adlayer of 3-aminopropyltriethoxysilane, followed by modification of the layer by use of another organosilane with allyl-terminated functional groups with the aim of achieving good dispersion and integration of the nanotubes in the polymer matrix. The resultant dental resin composites gave significant increases in flexural strength (Zhang *et al.*, 2008).

The aim of this study was to help disperse the SWCNTs within the matrix, by using the silica coating as a method to prevent direct tube–tube contact, reducing agglomeration and also improving their retention in the matrix under loading, by providing a rough surface. The authors reported that TEM showed that the thickness of the coating was around 10 nm and that the structure of the allyltriethoxysilane layer provided a compatible surface for further combination with the resin matrix. They also reported that the functionalised SWCNTs appeared as single strings between the filler particles of the dental resin composite and the matrix, implying that the composites can absorb more stress under applied load (Zhang *et al.*, 2008). However, the resultant dental nanocomposites are described as being grey-black in appearance, which is obviously a major disadvantage for a dental restorative material.

22.6.1 Carbon nanotubes and apatite

The formation of the hard tissues of teeth depends on a natural process of biomineralisation. Methods have been described where clusters of needle-shaped apatite crystallites were grown on aggregated MWCNTs. The crystallites were 100 nm in width and 200–500 nm in length and were grown perpendicularly to the longitudinal axis of the nanotube and also radially, originating from a common centre of a single MWCNT (Akasaka *et al.*, 2006). The apatite crystals were grown by immersing commercially obtained, and then purified, MWCNTs of curled shape in calcium phosphate solutions at a concentration of 10 mg/l. Initially the solution underwent ultrasonication for 10 minutes, and the apatite crystallites were then grown by immersion at 37°C for various periods of time, up to 2 weeks. The authors stated that the MWCNTs may be acting as a core for the initial crystallisation of the apatites and that for nucleation to occur, an activation energy barrier must be exceeded by increasing the degree of supersaturation of the calcium phosphate solutions.

22.7 Carbon nanotubes in periodontal dentistry

Periodontal dentistry is a dental specialty concerned with maintaining the health of the gingival tissues (gums) that support and attach the teeth to the jaw bones. In periodontal disease, chronic inflammation of the gingival tissues, due primarily to the presence of dental plaque containing millions of bacteria, occurs, which may

lead to destruction of bone supporting the teeth, causing the teeth to become mobile, and eventually require extraction.

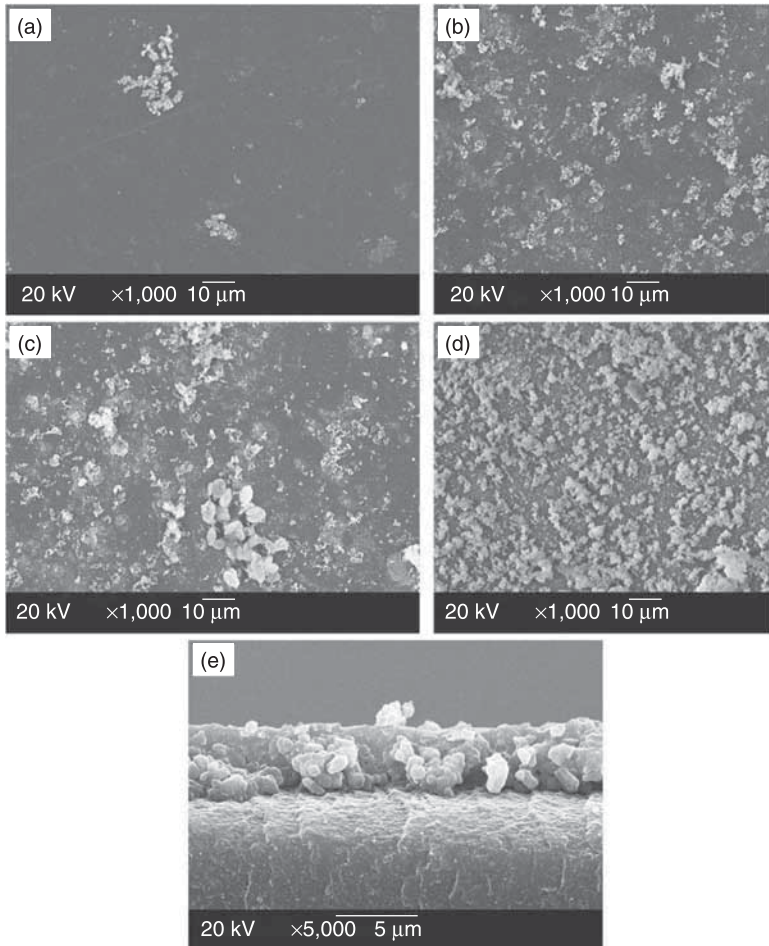
Kong *et al.* (2006) reviewed the potential use of different types of nanoparticles which may have practical applications in the treatment of periodontal disease. They speculated on the future use of CNTs for the local delivery of drugs with activity to slow or reverse the inflammatory process associated with periodontal disease together with the use of synthetic self-assembling scaffolds to replace lost bone tissue supporting the teeth. However, the use of CNTs in the possible treatment of periodontal disease has been more recently described by Mei *et al.* (2007) and Yang *et al.* (2009).

Mei *et al.* (2007) described the development of a new type of MWCNT containing composite material for use in guided tissue regeneration, where a biocompatible surface is inserted between the tooth root surface and the gingival tissue, which has lost its supporting bone through periodontal disease, with the ultimate aim of stimulating the re-formation of bone to support the teeth. The new material was a membrane created by electrospinning a suspension of poly(L-lactic acid), MWCNTs and hydroxyapatite. They found that the new membrane enhanced the adhesion and proliferation of periodontal ligament cells by 30% and inhibited the adhesion and proliferation of gingival epithelial cells by 30% also (Mei *et al.*, 2007). Clinically this may encourage the desirable regeneration and attachment of the tooth to bone, while discouraging the less desirable proliferation of gingival tissue which can interfere with reattachment of ligament cells.

Similarly, Yang *et al.* (2009) developed a new chitosan–MWCNT composite for potential use in guided tissue regeneration for the treatment of periodontal disease. MWCNTs have been shown to promote the adhesion and proliferation of osteoblasts but inhibit fibroblasts. Also, hydroxyapatite nucleates on oxidised MWCNTs functionalised with carboxyl groups. Yang *et al.* (2009) demonstrated the ability of apatite crystals to form on chitosan–MWNT composite materials. Figure 22.7 (p. 698) shows scanning electron micrographs of apatite crystals adherent to the surface of the chitosan–MWCNT composite material. The authors speculated that calcium ions bonded to negatively charged groups such as the carboxyl groups of MWCNTs, and more weakly with the amino groups of the chitosan, while phosphate ions associated with positively charged calcium ions. Apatite formation was deduced from characteristic XRD reflection peaks. They concluded that the method led to the formation of orientated nanoscopic crystallites of apatite which they assumed would enhance the bioactivity of the new material, presumably for use in guided tissue regeneration (Yang *et al.*, 2009).

22.8 Carbon nanotubes and denture-based resin

Dentures made to replace missing teeth in a dental arch are usually fabricated from PMMA. While exhibiting many advantages, such as excellent aesthetics, low density, and an ability to be repaired, it suffers from a relatively low fracture strength



22.7 SEM images of apatite-treated chitosan-multiwalled CNT composite at various numbers of treatment cycles: (a) one cycle; (b) three cycles; (c) five cycles; (d) nine cycles and (e) an overall morphology of a failure surface following nine treatment cycles (Yang *et al.*, 2009).

which renders it vulnerable to fracture, either in the mouth due to fatigue flexing, or due to accidental damage if dropped against a hard surface, such as a sink when being cleaned (Hargreaves, 1969; Jagger *et al.*, 1999). Denture repair costs represent a significant cost to patients and health services. Many attempts have been made to increase the strength of PMMA by the addition of carbon fibres, glass fibres, metal plates, wires or mesh or chemical modification of the PMMA resin by addition of rubber graft copolymers (Vallittu, 1995; Vallittu, 1996; Jagger *et al.*, 1999).

Recently work has been completed, incorporating MWCNTs into a PMMA-based denture base resin to determine if they could increase the strength and

fracture toughness (Zhou, 2009). Unfunctionalised MWCNTs, carboxyl functionalised and amine functionalised MWCNTs at varied wt% loadings (0.1, 0.25, 0.5, and 1.0) were incorporated into the liquid monomer (prior to mixing) using ultrasonic agitation, and to the acrylic powder using dry blending and ultrasonic agitation, and the resultant specimens were heat cured. Mechanical characterisation was carried out including bending modulus, bending strength, compressive strength. Plane strain fracture toughness was also determined using the Chevron-Notch Short Rod method.

The authors reported that low loadings of MWCNTs (≤ 0.25 wt%) in PMMA denture resin significantly improved the mechanical properties of the resultant nanocomposite, while higher loadings (≥ 0.5 wt%) gave only small improvements, and in some cases significant reductions were recorded. The dispersion of MWCNTs within the matrix was enhanced by adding chemical functional groups, with carboxyl-MWCNTs giving the largest improvements. It was speculated that the improvements in mechanical properties were due to the MWCNTs being well dispersed within the matrix, thereby arresting/retarding crack propagation. Although the improvements in strength were significant, a disadvantage is the resultant black colour of the denture base resin, which would require masking if it were to be used clinically.

22.9 Carbon nanotubes and targeted drug delivery for oral cancer

Squamous cell carcinoma is one of the more common types of mouth cancer and is responsible for an estimated 650,000 new cancers annually (Argiris *et al.*, 2008). Treatments that selectively target the cancer cells are required as current treatments lack specificity and can cause severe side effects. Recently oxidised SWCNTs have been bioconjugated with the anti-cancer drug cisplatin and a specific receptor ligand, epidermal growth factor (EGF) (Bhirde *et al.*, 2009). EGF has a strong affinity for a cell-surface receptor which is over-expressed in most squamous cancer cells. The SWCNTs are therefore targeted at the cancer cells improving specificity of treatment. Microscopy showed that the functionalised bioconjugated nanotubes interacted with the cell surface receptors which in turn caused endocytosis, drawing the nanotube into the cell, leading to cell death. When tested in mice, administration of the SWCNT-cisplatin-EGF bioconjugate caused a very significant reduction in tumour volume, compared to SWCNT-cisplatin control groups (Bhirde *et al.*, 2009).

22.10 Carbon nanotubes used for monitoring biological systems

Carbon nanotubes are being increasingly used in the fields of regenerative medicine and tissue engineering. As human stem cells are introduced into the body, there is

a need to be able to accurately label them and track their movement as they divide, differentiate and migrate. CNTs are proving useful in this field. In addition, CNTs are also being investigated to monitor cellular behaviour, augmenting cellular behaviour (drug delivery) and enhancing the mechanical properties of tissue scaffolds used to support newly introduced cells (Harrison and Atala, 2007).

22.10.1 Cell labelling and tracking

It initially proved difficult to track the movement of CNTs in biological systems using conventional methods such as by elemental analysis, as they only contain carbon, and also by electron microscopy due to their small size and relatively low contrast, so alternative methods were sought to overcome these disadvantages.

SWCNTs have been covalently linked to visible-wavelength fluorophores and imaged within cells (Pantarotto *et al.*, 2004; Kam *et al.*, 2004). However, Cherukuri *et al.* (2004) highlighted some potential disadvantages of this system. These were that the chemical linkage must be able to resist enzymatic cleavage, emission from the visible wavelength fluorophore must be detected above background endogenous fluorescence, and that chemical processing of the CNTs may alter their biological fate. That is, that the process of labelling the CNTs for tracking may significantly alter their behaviour in the cell and give erroneous results. To overcome these problems they proposed a method for observing pristine SWCNTs in biological systems using their intrinsic near-infrared (NIR) fluorescence. SWCNTs were incubated with cultured mouse peritoneal macrophage-like cells, in a growth medium. The incubated cells were analysed for NIR fluorescence using a spectrofluorometer and a fluorescence microscope. Fluorescence was excited by light from a 660 nm diode laser and showed distinct emission peaks arising from the semi-conducting SWCNTs. CNTs possess many desirable properties for optical detection in biological systems. They display optical transitions in the NIR spectrum between 900 and 1300 nm, which is an important optical range for biomedical applications because of the good penetration depth of light and small auto-fluorescent background, together with excellent photostability (Bruchez, *et al.*, 1998; Chan and Nie, 1998). Heller *et al.* (2009), similarly used SWCNTs as optical sensors to detect genotoxic analytes, including chemotherapeutic drugs in real time within live cells.

CNTs are useful for labelling cells as their small size means that they are less likely to cause physical damage to the cells under investigation, potentially altering their subsequent behaviour (Harrison and Atala, 2007). Chen *et al.* (2007) described the development of a single MWCNT attached to an atomic force microscope tip and functionalised with quantum dots (light-emitting nanocrystals composed of atoms from groups II–VI of the Periodic Table), by a disulphide-based linker. Penetration of cell membranes with the MWCNT was controlled by an atomic force microscope, and single-particle tracking was used to trace the movement of the quantum dots within the cell.

Tissue engineered constructs may also be monitored over time using magnetic resonance imaging (MRI). Unmodified CNTs do not contrast well against body tissue in an MRI scan, however they can be functionalised to make them more visible, for example by the addition of gadolinium heavy atoms (Hartman and Wilson, 2007; Richard *et al.*, 2008). Sitharaman *et al.* (2005) showed that nanotubes 20–100 nm long could be loaded with gadolinium through the openings at the end of the nanotubes, or defects in the walls, providing high contrast in MRI scans, enabling monitoring of the engineered tissue. Choi *et al.* (2007) described the formation of hetero-structured complexes of magnetic iron oxide nanoparticles and NIR fluorescent SWCNTs that could be used as multimodal bio-imaging agents. The resulting nanotube complexes showed near infra-red (NIR) fluorescence, Raman scattering and visible/NIR absorbance features. Macrophage cells that engulfed the nano-complexes were imaged using MRI and NIR mapping, showing that the multifunctional nanostructures could be potentially useful in bio-medical imaging.

Radiotracers have been added to CNTs to enable them to be tracked using gamma scintigraphy (Singh *et al.*, 2006). This study followed the bio-distribution of nanotubes in mice and found that functionalised SWCNTs did not accumulate in any particular organ, and were rapidly cleared in the urine.

22.11 Carbon nanotube biosensors

Tissue engineering requires not only knowledge regarding the distribution of implanted stem cells, but also of the environment and reactions occurring within the cells. The ability to monitor cellular physiology including ion transport, enzyme/cofactor interactions, protein and metabolite secretion could be used to monitor the performance of cells within engineered and normal tissues. CNTs are ideal components for nanosensors due to their small size, electrical properties and large surface area for binding to many biological compounds, including DNA and proteins (Harrison and Atala, 2007). CNT-based sensors have been used to measure the electro-oxidation process of insulin using MWCNTs. Other substances detected by CNT based sensors include amino-acids, putrescine, cholesterol, together with physiological conditions such as pH (Radosavljevic *et al.*, 2002; Xian *et al.*, 2005; Rochette *et al.*, 2005; Tan *et al.*, 2005).

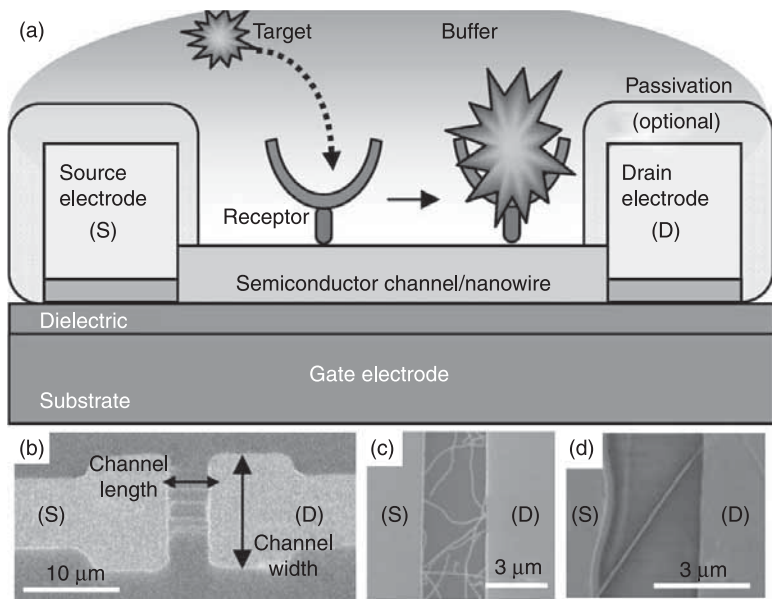
The above methods rely largely on electrochemical sensing to detect substances, but CNT-based sensors may also exploit changes in optical properties, for example, to measure the levels of β -D-glucose concentration (Barone *et al.*, 2005) by a change in the near infra-red fluorescence of the SWCNT sensor.

Kim *et al.* (2007) reviewed the use of CNTs for the electronic and electrochemical detection of biomolecules such as enzymes, proteins and DNA, together with strategies for amplifying the resultant signals to enable sensitive detection down to picomolar range. The intrinsic bandgap in the density of states of semiconducting SWCNTs allows them to act as semiconducting nanosized channels in a field-effect

transistor (FET) (Chen *et al.*, 2003; Hartman and Choi, 2006; Star *et al.*, 2006). The SWCNTs detect changes in their environment due to the specific interactions with the biomolecules of interest. FETs can be further divided into three types, dependent on the receptor type and how a signal is generated:

1. Enzyme modified FETs, which usually involve the product of a catalytic reaction, e.g. a reaction between an enzyme and its substrate.
2. Cell-based FETs which create a signal from a change in potential produced by biological cells.
3. Immunologically modified FETs and DNA-modified FETs which use surface polarisation effects or changes in the dipole moment, e.g. antigen–antibody binding or DNA hybridisation (Uno *et al.*, 2007).

Figure 22.8 from Curreli *et al.*'s (2008) review paper illustrates the structure of an FET nanobiosensor utilising either a CNT or a nanowire as the semiconductor material.



22.8 Structure of an FET nanobiosensor. (a) Cross-sectional view: source and drain electrodes bridge the semiconductor channel. The gate electrode can be used to modulate the conductivity of the semiconductor channel. A receptor molecule attached to the surface of the semiconductor material can specifically recognise and capture a target molecule from a buffer solution. (b) Top view: SEM image of a typical nano-FET. In these structures, the channel length is the S–D distance and the channel width is the S or D electrode width. Examples are shown of nano-FET fabricated at the author's research facility using either (c) carbon nanotubes or (d) indium oxide nanowires as semiconductor materials (Curreli *et al.*, 2008).

CNTs have also been used as electrodes in electrochemical-based nanobiosensors, boosting direct electron transfer to aid detection of important enzymes such as glucose oxidase, which have previously been difficult to measure using conventional methods. Kim *et al.* (2007) described the two approaches that have been used. In the first method, SWCNTs or MWCNTs are randomly deposited onto conductive surfaces in a mat configuration, or packed into a micropipette for use as electrodes. The second method involves the creation of SWCNT forests, with shortened SWCNTs standing vertically, with one end in contact with the electrode and the other exposed to the test solution (Kim *et al.*, 2007).

In conclusion, CNTs have been demonstrated to be of great use as biosensors, despite exhibiting some disadvantages such as the need to separate semiconducting nanotubes from metallic nanotubes and a non-uniform distribution of bandgaps which may lead to difficulty in fine-tuning electronic properties (Curreli *et al.*, 2008). The use of CNTs as biosensors has been well reviewed in a number of papers (Balasubramanian and Burghard, 2006; Gruner, 2006; Allen *et al.*, 2007; Kim *et al.*, 2007; Curreli *et al.*, 2008).

22.12 Bioactivity of carbon nanotubes

CNT polymer composites used for biomedical and bioengineering applications require special consideration regarding their impact on the human body. Information is required regarding the route by which CNTs and their composites are introduced into the body and how they subsequently move through the body in the short and long term.

Much of the work done to assess the biocompatibility or toxicity of CNTs used pristine, unfunctionalised CNTs that were dispersed in different media and then introduced into animal models by inhalation into the lungs or injection. The results of these tests have been very mixed with some indicating significant risks associated with specific types of CNTs and others not. However, this confusion is understandable when the large diversity of types of CNT tested is considered. Whether single-walled or multi-walled, functionalised or pristine, free within solution or as part of a polymer composite, coated or uncoated, agglomerated or dispersed, short or long, straight or tangled, they will behave differently in different experimental set-ups (Helland *et al.*, 2007). Currently there are no internationally agreed protocols for testing the biocompatibility of CNTs and several authors have highlighted the urgent need for them.

CNTs have attracted much interest among those concerned regarding the potential toxicity of nanotubes due to the physical similarity of some types of CNT fibre to asbestos fibres. The harmful effects of exposure to brown asbestos fibres are well known in the pathogenesis (development) of a type of lung cancer, a mesothelioma (Mossman and Churg 1998).

In 2005, Murr *et al.* found that exposure to SWCNTs or MWCNTs caused asbestos-like cytotoxicity determined using the MTT assay. The MTT

assay is a quantitative colorimetric method to determine cell proliferation and viability. It uses a yellow tetrazolium salt [3-(4,5-dimethylthiazol-2-yl)-2,5-diphenyltetrazolium-bromide] which is metabolized by mitochondrial succinic dehydrogenase enzyme activity from proliferating cells, producing a purple formazan reaction product. Similar results have been reported by other workers (Soto *et al.*, 2005; Jia *et al.*, 2005; Soto *et al.*, 2007).

Previous work on asbestos fibres had shown that any fibre is likely to be harmful to human lungs if it is thin enough to enter the lungs (< 3 microns), longer than the lung cells that usually remove foreign fibres (> 20 microns) and is insoluble in the lungs, and therefore likely to accumulate (Donaldson and Tran, 2004). Poland *et al.* (2008) investigated if this paradigm also applied to CNTs and found that exposing the mesothelial lining of the chest cavity in mice to long MWCNTs resulted in asbestos-like adverse effects. These included inflammation and the formation of granulomas (Poland *et al.*, 2008). The paper emphasised that, although their data showed that short CNTs did not mimic the behaviour of long asbestos, the possibility that short CNTs are also potentially harmful to humans by some other mechanism, such as intrinsic toxicity, could not be excluded. In addition, the authors stated that it is unknown whether the inflammatory and granulomatous changes in the tissues induced by the long CNTs would go on to develop a mesothelioma tumour. In addition, the degree of metal catalyst contamination of the CNTs tested has been found to be a factor in the magnitude of *in vitro* cytotoxicity displayed. Samples with higher levels of iron contamination (30%) or nickel (20%) caused significant decreases in cell viability (Kagan *et al.*, 2006; Herzog *et al.*, 2007; Shvedova *et al.*, 2010). Conversely, CNT samples containing low levels of iron were less toxic to cells (Kagan *et al.*, 2006; Herzog *et al.*, 2007). This increased cytotoxic effect may be because MWCNTs have been shown to induce cellular oxidative stress, which was removed when the CNTs were acid-treated removing the metal contaminants (Pulskamp *et al.*, 2007).

In contrast to these results, other studies have confusingly reported low cytotoxicity for raw SWCNTs with high iron contamination, purified SWCNTs with low iron content and purified MWCNTs (Worle-Knirsch *et al.*, 2006; Pulskamp *et al.*, 2007).

The potential toxicity of MWCNTs may also be influenced by the presence of structural defects in their carbon framework (Fenoglio *et al.*, 2008). Shvedova *et al.* concluded in their review paper that many physico-chemical characteristics of MWCNTs, e.g. length, width, structural defects, metal contamination, surface chemistry and zeta potential will affect the lung response. Further, they stated that until the exact parameters which contribute to their toxicity are characterised, different types of MWCNT materials will give differing biological responses (Shvedova *et al.*, 2009).

Shvedova *et al.* (2009) have suggested that these conflicting results may be more comprehensible by considering that the dye-based cell viability assays used may be interfered with by the CNTs due to light absorption and scattering. Therefore they suggest that results of cell viability studies, based on MTT dye-based assays,

should be interpreted with caution. Recent studies have investigated SWCNT uptake by different cells. Research shows that CNTs are able to cross the cell membranes of rats and therefore might have an influence on cell function (Pulskamp *et al.*, 2007). The results obtained have varied and it appears that the presence or absence of specialised signals determines the recognition and subsequent interactions of SWCNTs with cells. Overall, pristine SWCNTs carrying no recognisable signals are poorly taken up whereas those modified chemically e.g. oxidatively modified during purification and storage, or by adsorbed macromolecules such as proteins, are more readily recognised and engulfed by cells (Shvedova *et al.*, 2009). Several studies have shown that SWCNTs are not readily taken up by lung cells (Shvedova *et al.*, 2005; Herzog *et al.*, 2007; Davoren *et al.*, 2007), while others have reported uptake of both SWCNTs and MWCNTs by rat and guinea pig cells (Jia *et al.*, 2005; Dutta *et al.*, 2007; Pulskamp *et al.*, 2007).

Dutta *et al.* (2007) reported that CNTs highly adsorb albumin when placed in a serum dispersion medium. This process structurally alters the albumin which triggers scavenger receptors. Therefore the reported uptake of CNTs may be due to the altered albumin coating rather than the CNT alone. The choice of dispersion medium for CNTs is therefore important (Porter *et al.*, 2008).

22.12.1 Carbon nanotube interaction with the immune system

The potential toxicity of CNTs to the human immune system also requires consideration. Research has shown that nanoparticles can stimulate and/or suppress the immune system, and that the response is largely determined by their surface chemistry (Mitchell *et al.*, 2007; McDonald and Mitchell, 2008). Overstimulation of the human immune system may lead to inappropriate allergic-type reactions, while suppression may adversely alter the normal immune response to infections and cancer cells.

22.12.2 Carbon nanotube interference with bacterial uptake

Exposure to SWCNTs by inhalation may also interfere with the body's ability to eliminate infection. Shvedova *et al.* found that exposure to CNTs and infection by *Listeria monocytogenes* induced unusual responses in mice with mutually enhanced inflammation, together with depressed bacterial clearance (Shvedova *et al.*, 2008). Therefore exposure to CNTs through inhalation may exacerbate lung infections in susceptible populations (Shvedova *et al.*, 2009).

22.12.3 Genotoxicity and mutagenicity of carbon nanotubes

Concerns exist that materials containing CNTs could alter the genetic material of humans and other organisms, leading to the potential of carcinogenic changes.

Research has shown that both SWCNTs and MWCNTs may cause changes to the genetic material but the results obtained to date are not consistent (Shvedova *et al.*, 2009).

22.12.4 Carbon nanotube movement through the body

The movement of nanoparticles within the body after initial introduction by inhalation, intravenous injection, or ingestion, has been investigated for various nanoparticles, such as ultrafine carbon particles, and found that labelled particles were found in various organs throughout the body of rats. One study specifically investigated the translocation or movement of MWCNTs within mice. Within 10 minutes of intravenous injection of 14 C-aurine-labelled MWCNTs were found mainly accumulated in the liver and also the heart and lung, but not the brain, stomach, muscle, bone or intestines (Deng *et al.*, 2007).

22.13 Regulation of occupational exposure to carbon nanotubes

The potential for humans and the environment to be exposed to CNTs during manufacture, distribution and use/disposal of products and devices containing both SWCNTs and MWCNTs is of intense interest but little is known regarding this (Maynard and Kuempel, 2005). Air-borne levels of MWCNTs during manufacturing ranged from undetectable to 400 g/m³ (Han *et al.*, 2008). Spraying, blending or weighing produced the highest concentrations, but the implementation of controls significantly reduced levels to often non-detectable levels. Maynard *et al.* (2004) reported a field study in which airborne and dermal exposure to SWCNTs was investigated while handling unrefined material. Although laboratory studies indicated that with sufficient agitation, unrefined SWCNT material could release fine particles into the air, concentrations generated while handling material were very low with estimates of airborne concentration of nanotubes lower than 53 µg/m³ in all cases (Maynard *et al.*, 2004).

Several nanotoxicology workshops and symposia have been held to discuss the potential problem of adverse environmental and human effects of CNTs (University of Florida, 2004; Tsuji *et al.*, 2006; Balbus *et al.*, 2007). In general it is agreed that health and safety and environmental protection laws internationally lag behind the manufacture and use of CNT-containing products, devices and materials. Progress in this area has been delayed by discussion regarding whether nanoparticles with the same chemical composition of bulk or macro counterparts, such as graphite in the case of CNTs, were new materials requiring new legislation, or existing materials with a significant new use.

Research has shown that nanoparticles are more hazardous than their bulk counterparts. In addition to particle size, surface area various physico-chemical

factors including surface reactivity, solubility and shape can influence the toxicity of engineering nanoparticles (Shvedova *et al.*, 2009).

The need to proactively adopt appropriate risk management procedures for nanotubes, including CNTs, has recently been reviewed (Murashov and Howard, 2009). They highlighted the need for an adaptive approach to risk management that should exist in 'real time', by use of web-based platforms for the development of consensus-based dynamic global standards, e.g. the wiki-based project 'GoodNanoGuide' (GoodNanoGuide, 2009). Many different international organisations are developing guidelines for the safe handling of nanomaterials and the collection of risk information (Nanosafe, Institute of Occupational Medicine, SAFENANO, Institute for Work and Health, National Institute for Occupational Safety and Health, Internano, The Organisation for Economic Co-Operation and Development).

22.14 Conclusion

The requirement for new technologies and medical implants in the treatment of traumatic injuries and chronic diseases is increasing. This is due in part to an ageing population with the related degenerative processes and disease processes, and also to changing daily lifestyles with a rising need for solutions to health-related issues. Novel concept biomaterials and medical devices are urgently needed to allow less tissue damage and more tissue regeneration, likewise such materials and devices need to be implanted under minimally invasive conditions, conducive to a rapid recovery. Particularly for biomaterials and devices designed to replace a degenerated or diseased joint, bone or tooth structure, many questions need to be answered. Such devices and implants would benefit significantly from availability of a material that is multi-functional and can meet the biomechanical and biological requirements.

The conventional biomaterials available today are reaching their maximum capabilities, notwithstanding their successful application in treating and preventing different medical conditions. There is a need for the development of new biomaterials which must satisfy several requirements ranging from physical, mechanical, biological, toxicological and other characteristics, depending on the final clinical application.

Carbon is chemically inert and CNTs not only demonstrate superior mechanical, chemical and electrical properties, but also have the potential to be biocompatible particularly when functionalised. Also, encapsulation of other materials within CNTs could potentially create applications for therapeutic use in medicine.

Regardless of this interest, there are many factors and limitations to be borne in mind. The field of nanomaterials for biomedical and bioengineering applications is still very much in its early stages and many difficult questions must be addressed, including manufacturing, safety and regulatory issues. Preliminary investigations substantiate the enormous potential of CNTs for biomedical and bioengineering

applications either as a structure, coating, scaffold or composite, although most of these are only at laboratory-scale and *in vitro* testing. There is a major requirement for interdisciplinary collaboration and exchange of knowledge at many levels to effectively address the current issues, before being able to fully understand and explore the true potential of CNTs for biomedical and bioengineering applications.

22.15 References

- Akasaka T, Nakata K, Uo M and Watari F (2009) Modification of the dentin surface by using carbon nanotubes, *Biomed. Mater. and Eng.*, 19(2–3), 179–85.
- Akasaka T, Watari F, Sato Y and Tohji K (2006) Apatite formation on carbon nanotubes, *Materials Science and Engineering C: Biomimetic and Supramolecular Systems*, 26(4), 675–678.
- Allen B, Kichambare P and Star A (2007) Carbon nanotube field-effect-transistor-based biosensors, *Adv. Mater.*, 19(11), 1439–1451.
- Ami Eitan K, Dukes D, Andrews R and Schadler L (2003) Surface modification of multi-walled carbon nanotubes: towards tailoring of the interface in polymer composites, *Chem. Mater.*, 15, 3198–3201.
- Argiris A, Karamouzis M, Raben D and Ferris R (2008) Head and neck cancer, *Lancet*, 371(9625), 1695–1709.
- Ayutsede J, Gandhi M, Sukigara S, Ye H, Hsu C and Gogotsi Y (2006) Carbon nanotubes reinforced bombyx mori silk nanofibers by electrospinning, process, *Biomacromolecules*, 7, 208–214.
- Babaa R, Bantignie J, Michel T, Fiorito S, Poncharal P and Zahab A (2006) Carbon nanotubes reinforced PE and PEEK: fabrication and characterization, 20th IWPE Molecular Nanostructures, PTue5.
- Balani K, Anderson R, Laha T, Andara M, Tercero J, Crumpler E and Agarwal A (2007) Plasma-sprayed carbon nanotubes reinforced hydroxyapatite coatings and their interactions with human osteoblasts in vitro, *Biomaterials*, 28, 618–624.
- Balasubramanian K and Burghard M (2006) Biosensors based on carbon nanotubes, *Analytical and Bioanalytical Chemistry*, 385(3), 452–468.
- Balasundaram G and Webster T (2006) Nanotechnology and biomaterials for orthopaedic medical applications, *Nanomedicine*, 1(2), 169–176.
- Balbus J, Maynard A, Colvin V, Castranova V, Daston G, Denison R, Dreher K, Goering P, Goldberg A, Kulinowski K, Monteiro-Riviere N, Oberdorster G, Omenn G, Pinkerton K, Ramos K, Rest K, Sass J, Silbergeld E and Wong B (2007) Meeting report: hazard assessment for nanoparticles: report from an interdisciplinary workshop, *Environmental Health Perspectives*, 115(11), 1654–1659.
- Bantignie J (2007) Carbon nanotubes composites, 3rd CANAPE Workshop on Carbon Nanotubes for Biomedical Applications, Rome.
- Barone P, Parker R and Strano MS (2005) In vivo fluorescence detection of glucose using a single-walled carbon nanotube optical sensor: design, fluorophore properties, advantages, and disadvantages, *Analytical Chem.*, 77(23), 7556–7562.
- Baseren M (2004) Surface roughness of nanofill and nanohybrid composite resin and ormocer-based tooth-colored restorative materials after several finishing and polishing procedures, *J. Biomater. Apps.*, 19(2), 121–134.
- Bhargave A (1999) *Nanrobots: Medicine of the Future*, <http://www.ewh.ieee.org/r10/Bombay/news3/page4.html> (accessed 25 February 2010).

- Bhirde A, Patel V, Gavard J, Zhang G, Sousa A, Masedunskas A, Leapman R, Weigert R, Gutkind J and Rusling J (2009) Targeted killing of cancer cells in vivo and in vitro with EGF-directed carbon nanotube-based drug delivery, *Acs. Nano.*, 3(2), 307–316.
- Bruchez M, Moronne M, Gin P, Weiss S and Alivisatos A (1998) Semiconductor nanocrystals as fluorescent biological labels, *Science*, 281(5385), 2013–2016.
- Byon H, and Choi H, (2006) Network single-walled carbon nanotube-field effect transistors (SWNT-FETs) with increased Schottky contact area for highly sensitive biosensor applications, *J. Am. Chem. Soc.*, 128(7), 2188–2189.
- Chadwick B, Dummer P, Dunstan F and *et al.* (2002) How long do fillings last?, *Evidence-Based Dentistry*, 3, 96–99.
- Chan C, Kumar T, Liao S, Murugan R, Ngiam M and Ramakrishnan S (2006) Biomimetic nanocomposites for bone graft applications, *Nanomedicine*, 1, 177–188.
- Chan, W.C. and Nie, S. (1998) Quantum dot bioconjugates for ultrasensitive non-isotopic detection, *Science*, 281(5385), 2016–2018.
- Chen M, Chen C, Hsu S, Sun S and Su W (2006) Low shrinkage light curable nanocomposite for dental restorative material, *Dent. Mater.*, 22(2), 138–145.
- Chen R, Bangsaruntip S, Drouvalakis K, Kam N, Shim M, Li Y, Kim W, Utz P and Dai H (2003) Noncovalent functionalization of carbon nanotubes for highly specific electronic biosensors, *Proc. Nat. Acad. Sci. USA*, 100(9), 4984–4989.
- Chen R, Zhang Y, Wang D and Dai H (2001) Noncovalent sidewall functionalization of single-walled carbon nanotubes for protein immobilization, *J. Am. Chem. Soc.*, 123(16), 3838–3839.
- Chen X, Kis A, Zettl A and Bertozzi C (2007) A cell nanoinjector based on carbon nanotubes, *Proc. Nat. Acad. Sci. USA*, 104(20), 8218–8222.
- Cherukuri P, Bachilo S, Litovsky S and Weisman R (2004) Near-infrared fluorescence microscopy of single-walled carbon nanotubes in phagocytic cells, *J. Am. Chem. Soc.*, 126(48), 15638–15639.
- Choi J, Nguyen, J, Barone P, Heller D, Moll, A Patel D, Boppart S and Strano M (2007) Multimodal biomedical imaging with asymmetric single-walled carbon nanotube/iron oxide nanoparticle complexes, *Nano. Lett.*, 7(4), 861–867.
- Christenson E, Anseth K, van den Beucken J, Chan C, Ercan B, Jansen J, Laurencin C, Li W, Murugan R, Nair L, Ramakrishna S, Tuan S, Webster J and Mikos A (2006) Nanobiomaterial applications in orthopaedics, *J. Orthop. Res.*, 10, 11–22.
- Correa-Duarte M, Wagner N, Rojas-Chapana J, Morszeck C, Thie N and Giersig M. (2004) Fabrication and biocompatibility of carbon nanotubes-based 3D networks as scaffolds for cell seeding and growth, *Nano. Lett.*, 4(11), 2233–2236.
- Curreli M, Zhang R, Ishikawa F, Chang H, Cote R, Zhou C and Thompson M (2008) Real-time, label-free detection of biological entities using nanowire-based FETs, *IEEE Transactions on Nanotechnology*, 7(6), 651–667.
- Davis J (2003) *Handbook of Materials for Medical Devices*, ASM International.
- Davoren M, Herzog E, Casey A, Cottineau B, Chambers G, Byrne H and Lyng F (2007) In vitro toxicity evaluation of single walled carbon nanotubes on human A549 lung cells, *Toxicology in Vitro*, 21(3), 438–448.
- Deng X, Jia G, Wang H, Sun H, Wang X, Yang S, Wang T and Liu Y (2007) Translocation and fate of multi-walled carbon nanotubes in vivo, *Carbon*, 45, 7, 1419–1424.
- Developing Experimental Approaches for the Evaluation of Toxicological Interactions of Nanoscale Materials. Available: <http://www.nanotoxicology.ufl.edu/workshop/images/NanoToxWorkshop.pdf> [accessed 1 December 2009].

- Donaldson K and Tran C (2004) An introduction to the short-term toxicology of respirable industrial fibres, *Mutation Res.*, 553(1–2), 5–9.
- Dutta D, Sundaram S, Teeguarden J, Riley B, Fifield L, Jacobs J, Addleman S, Kaysen G, Moudgil B and Weber T (2007) Adsorbed proteins influence the biological activity and molecular targeting of nanomaterials, *Toxicological Sciences*, 100(1), 303–15.
- Eitan A, Fisher T, Andrews R, Brinson C and Schadler S (2006) Reinforcement mechanisms in MWCNT-filled polycarbonate, *Compos. Sci. Tech.*, 66(9), 1162–73.
- Elias K, Price R, Webster T (2002) Enhanced function of osteoblasts on nanometer diameter carbon fibres, *Biomaterials*, 23, 3279–97.
- Emami N (2007) Manufacturing of bionano-composites: CNT reinforced UHMWPE composite, Abstract, *Nanotech Northern Europe*.
- Fearon P, Watts C, Hsu W, Billingham N, Kroto H and Walton D (2002) Impact of carbon nanotube addition on the oxidative stability of polyolefins, *Nanotechnology in Carbon and Related Materials*.
- Fenoglio I, Greco G, Tornatis M, Muller J, Raymundo-Pinero E, Beguin, F, Fonseca A, Nagy J, Lison D and Fubini B (2008) Structural defects play a major role in the acute lung toxicity of multiwall carbon nanotubes: physicochemical aspects, *Chemical Research in Toxicology*, 21(9), 1690–1697.
- Fiorito S, Serafino A, Andreola F, Togna A and Togna G (2006) Toxicity and biocompatibility of carbon nanoparticles, *J. Nanosci. Nanotech.*, 6(3), 591–599.
- Firowska I, Olek M, Pazos-Peréz N, Rojas-Chapana J and Giersig M (2006) Highly ordered MWNT-based matrices: topography at the nanoscale conceived for tissue engineering, *Langmuir*, 22(12), 5427–5434.
- Gojny H, Nastalczyka J, Roslaniec Z and Schult K (2003) Surface modified multi-walled carbon nanotubes in CNT/epoxy-composites, *J. Chem. Phys. Lett.*, 370(5–6), 820–824.
- GoodNanoGuide. <http://goodnanoguide.org/tiki-index.php?page=HomePage> (accessed 11 November 2009).
- Goodman C, McCusker C, Yilmaz T and Rotello V (2004) Toxicity of gold nanoparticles functionalised with cationic and anionic side chains, *Bioconjug. Chem.*, 15, 897–900.
- Gruner G (2006) Carbon nanotube transistors for biosensing applications, *Analytical and Bioanalytical Chemistry*, 384(2), 322–335.
- Han J, Lee E, Lee J, So K, Lee Y, Bae G, Lee S, Ji J, Cho M and Yu I (2008) Monitoring multiwalled carbon nanotube exposure in carbon nanotube research facility, *Inhalation Toxicology*, 20(8), 741–749.
- Hargreaves A (1969) The prevalence of fractured dentures: a survey, *Br. Dent. J.*, 126(10), 451–455.
- Harrison B and Atala A (2007) Carbon nanotubes applications for tissue engineering, *Biomaterials*, 28, 344–353.
- Hartman K and Wilson L (2007) Carbon nanostructures as a new high-performance platform for MR molecular imaging, *Advances in Experimental Medicine and Biology*, 620, 74–84.
- Harutyunyan A, Pradhan B, Sumamasekera G, Korobko E and Kuznetsov A (2002) Carbon nanotubes for medical applications, *European Cells and Materials*, 3(2), 84–8.
- Helland A, Wick P, Koehler A, Schmid K and Som C (2007) Reviewing the environmental and human health knowledge base of carbon nanotubes, *Environmental Health Perspectives*, 115(8), 1125–1131.
- Heller D, Jin H, Martinez B, Patel D, Miller B, Yeung T, Jena P, Hobartner C, Ha T, Silverman S and Strano M (2009) Multimodal optical sensing and analyte specificity using single-walled carbon nanotubes, *Nature Nanotechnology*, 4(2), 114–120.

- Herzog E, Casey A, Lyng F, Chambers G, Byrne H and Davoren M (2007) A new approach to the toxicity testing of carbon-based nanomaterials: the clonogenic assay, *Toxicology Lett.*, 174(1–3), 49–60.
- Holzinger M, Steinmetz J, Samaille D, Glerup M, Paillet M, Bernier P, Ley L, and Graupner R (2004) [2+1] cycloaddition for cross-linking SWCNTs, *Carbon*, 42, 941–943.
- Hwang G, Shieh Y and Hwang K (2004) Efficient load transfer to polymer-grafted multiwalled carbon nanotubes in polymer composites, *Adv. Funct. Mater.*, 14, 487–491.
- Jagger D, Harrison A and Jandt K (1999) The reinforcement of dentures, *J. of Oral. Rehabilitation*, 26(3), 185–194.
- Jandt K, and Sigusch B (2009) Future perspectives of resin-based dental materials, *Dent. Mater.*, 25(8), 1001–1006.
- Jia G, Wang H, Yan L, Wang X, Pei R, Yan T, Zhao Y and Guo X (2005) Cytotoxicity of carbon nanomaterials: single-wall nanotube, multi-wall nanotube, and fullerene, *Environmental Science and Technology*, 39(5), 1378–1383.
- Jin L, Bower C and Zhou O (1998) Alignment of carbon nanotubes in a polymer matrix by mechanical stretching, *Appl. Phys. Lett.*, 73, 1197.
- Jin Z, Pramoda K, Xu G and Goh S (2001) Dynamic mechanical behavior of melt-processed multi-walled carbon/nanotube/poly(methyl methacrylate) composites, *Chem. Phys. Lett.*, 337, 433–7.
- Jones E, Streicher R, Field R and Rushton N (2001a) Evaluation of the role of carbon fibre composites in acetabular components, *Trans. 5th EFORT*, O669, 119.
- Jones E, Streicher R, Field R and Rushton N (2001b) Validating the limits for a PEEK composite as an acetabular wear surface, *Trans. 27th Soc. Biomat. Meeting*, 488.
- Kagan V, Tyurina Y, Tyurin V, Konduru N, Potapovich A, Osipov A, Kisin E, Schwegler-Berry D, Mercer R, Castranova V and Shvedova A. (2006) Direct and indirect effects of single walled carbon nanotubes on RAW 264.7 macrophages: role of iron., *Toxicology Lett.*, 165(1), 88–100.
- Kam N, Jessop T, Wender P and Dai H (2004) Nanotube molecular transporters: Internalization of carbon nanotube-protein conjugates into mammalian cells, *J. Am. Chem. Soc.*, 126(22), 6850–6851.
- Karajanagi S, Yang H, Asuri P, Sellitto E, Dordick J and Kane R (2006) Protein-assisted solubilization of single-walled carbon nanotubes, *Langmuir*, 22(4), 1392–1395.
- Kawaguchi M, Fukusima T, Hayakawa T, Nakashima N, Inoue Y, Takeda S, Okamura K and Taniguchi K (2006) Preparation of carbon-nanotube alginate nanocomposite gel for tissue engineering, *J. Dent. Mater.*, 25, 719–725.
- Khang D, Durbin S and Webster T (2006) Enhanced fibronectin adsorption on carbon nanotubes in polycarbonate urethane composites directs osteoblast adhesion, *Trans. 31st Soc. Biomater. Meeting*, 322.
- Khang D, Sato M and Webster T (2005) Direct osteoblasts functions on micro-aligned patterns of carbon nanofibers on a polymer matrix, *Rev. Adv. Mater. Sci.*, 10, 205–208.
- Khare R and Bose S (2005) Carbon nanotubes based composites—A review, *J. Minerals and Materials Characterization and Engineering*, 4(1), 31–46.
- Kim S, Rusling J and Papadimitrakopoulos F (2007) Carbon nanotubes for electronic and electrochemical detection of biomolecules, *Adv. Mater.*, 19(20), 3214–3228.
- Kong L, Peng Z, Li S and Bartold M (2006) Nanotechnology and its role in the management of periodontal diseases, *Periodontology* 2000(40), 184–196.
- Kuehn K, Ege W and Gopp U (2005) Acrylic bone cements: composition and properties, *Orthop. Clin. North Am.*, 36(1), 17–28.
- Lakes R (1993) Materials with structural hierarchy, *Nature*, 361, 511–514.

- Lau Kin-Tak D (2002) The revolutionary creation of newly advanced materials – carbon nanotubes composites, *Composites Part B: Engineering*, 33, 263–277.
- Lee D, Lim K and Lee M (2005) Effect of electrochemical interaction between nafen and carbon nanotubes on nanotubes' bundle size of multiwalled carbon nanotubes dispersed ionomeric nanocomposites as biomimetic artificial muscles, *Transactions 30th Society of Biomaterials Meeting*, 501.
- LeGeros R and LeGeros J (1993) *Dense Hydroxyapatite: An Introduction to Bioceramics*, L Hench, J Wilson (eds) Singapore: World Scientific.
- Letzel H (1989) Survival rates and reasons for failure of posterior composite restorations in multicentre clinical trial, *J. Dentistry*, 17(1), S10–17.
- Levenston M, Beaupre G, Shurman D and Carter D (1993) Computer simulations of stress related bone remodelling around non-cemented acetabular component, *J. Arthroplasty*, 8, 595–860.
- Liao S, Xu G, Wang W, Watari F, Cui F, Ramakrishna S and Chan C (2007) Self-assembly of nano-hydroxyapatite on multi-walled carbon nanotubes, *Acta Biomaterialia*, 3(5), 669–675.
- Liu H, Webster T (2007) Nanomedicine for implants: a review of studies and necessary experimental tools, *Biomaterials*, 28(2), 354–369.
- Lucarotti P, Holder R and Burke F (2005) Analysis of an administrative database of half a million restorations over 11 years, *J. Dentistry*, 33(10), 791–803.
- Lui Z, Cai W, He L, Nakayama N, Chen K, Sun X, Chen X and Dai H (2007) In vivo biodistribution and highly efficient tumour targeting of carbon nanotubes in mice, *Nature Nanotechnology*, 2, 47–52.
- MacDonald R, Laurenzi B, Viswanathan G, Ajayan P and Stegemann J (2005) Collagen-carbon nanotube composite materials as scaffolds in tissue engineering, *J. Biomed. Mater. Res. A*, 74, 489–496.
- MacDonald R and Stegemann J (2006) Electrically conductive biopolymers incorporating carbon nanotubes, *Trans. 31st Soc. Biomater. Meeting*, 326.
- Malchau H, Herberts P, Eisler T, Garellick G and Söderman P (2002) The Swedish Total Hip Replacement Register, *J. Bone Joint Surg. Am.*, 84–A(2), 2–20.
- Manley T, Bowman A and Cook M (1979) Denture bases reinforced with carbon fibres, *Br. Dent. J.*, 146(1), 25.
- Marrs B (2007) Carbon nanotube augmentation of a bone cement polymer, PhD Thesis, University of Kentucky, US.
- Marrs B, Andrews R and Pienkowski D (2007) Multiwall carbon nanotubes enhance the fatigue performance of physiologically maintained methyl methacrylate-styrene copolymer, *Carbon*, 45, 2098–2104.
- Marrs B, Andrews R, Rantell T and Pienkowski D (2006) Augmentation of acrylic bone cement with multiwall carbon nanotubes, *J. Biomed. Mater. Res.*, 77(2), 269–76.
- Matsudai M and Hunt G (2005) Nanotechnology and public health, *Nippon Koshu Eisei Zasshi*, 52, 923–927.
- Maynard A, Baron P, Foley M, Shvedova A, Kisin E and Castranova V (2004) Exposure to carbon nanotube material: aerosol release during the handling of unrefined single-walled carbon nanotube material, *J. of Toxicology and Environmental Health Part A*, 67(1), 87–107.
- Maynard A and Kuempel E (2005) Airborne nanostructured particles and occupational health, *J. Nanoparticle Res.*, 7, 587–614.
- McDonald J and Mitchell L (2008) Untitled, *Toxicological Sciences*, 101, 1, 181–182.

- Mei F, Zhong J, Yang X, Ouyang X, Zhang S, Hu X, Ma Q, Lu J, Ryu S and Deng X (2007) Improved biological characteristics of poly(L-lactic acid) electrospun membrane by incorporation of multiwalled carbon nanotubes/hydroxyapatite nanoparticles, *Biomacromolecules*, 8(12), 3729–3735.
- Mesquita R, Axmann D and Geis-Gerstorfer J (2006) Dynamic visco-elastic properties of dental composite resins, *Dental Materials*, 22(3), 258–267.
- Mitchell L, Gao J, Wal, R, Gigliotti A, Burchiel S and McDonald J (2007) Pulmonary and systemic immune response to inhaled multiwalled carbon nanotubes, *Toxicological Sciences*, 100(1), 203–214.
- Mjor I, Jokstad A and Qvist V (1990) Longevity of posterior restorations, *Inter. Dent. J.*, 40(1), 11–17.
- Mossman B and Churg A (1998) Mechanisms in the pathogenesis of asbestosis and silicosis, *Am. J. of Respiratory and Critical Care Medicine*, 157, 5(1), 1666–1680.
- Murashov V, & Howard J (2009), Essential features for proactive risk management, *Nature Nanotechnology*, 4, 467–470.
- Murr L, Garza KM Soto K, Carrasco A, Powell T, Ramirez D, Guerrero P, Lopez D and Venzor J (2005) Cytotoxicity assessment of some carbon nanotubes and related carbon nanoparticle aggregates and the implications for anthropogenic carbon nanotube aggregates in the environment., *International J. of Environmental Research and Public Health*, 2(1), 31–42.
- Mylvaganam K and Zhang L (2007) Fabrication and application of polymer composite comprising of carbon nanotubes, *Recent. Pat. Nanotech.*, 1, 59–65.
- Namila S, Chandra N and Shet C (2004) Mechanical behaviour of functionalised nanotubes, *Chem. Phys. Lett.*, 387, 247–52.
- Nicholson J (2006) *Biologic Considerations in Fundamentals of Operative Dentistry, A Contemporary Approach*, eds. J. Summitt, J. Robbins, T. Hilton and R. Schwartz, Third edn, Chicago: Quintessence Publishing Co, Inc, pp. 1–10.
- Nien Y and Huang C (2010) The mechanical study of acrylic bone cement reinforced with carbon nanotubes, *Mater. Sci. and Eng. B*, 169(1–3), 134–137.
- Ormsby R, McNally, T, Mitchell C and Dunne N (2010a) Incorporation of multiwalled carbon nanotubes to acrylic based bone cements: effect on the mechanical and thermal properties, *J. Mech. Behav. Biomed. Mater.*, 3, 136–145.
- Ormsby R, McNally, T, Mitchell C and Dunne N (2010b) Influence of multiwall carbon nanotube functionality on mechanical properties of PMMA/MWCNT bone cements, *J. Mater. Sci.: Mater. Med.*, 21(8).
- Pande S, Mathur B, Singhn P and Dharmi L (2009) Synthesis and characterization of multiwalled carbon nanotubes-polymethyl methacrylate composites prepared by in situ polymerization method, *J. Poly. Comp.*, 30(9), 1312–1317.
- Pantarotto D, Briand J, Prato M and Bianco A (2004) Translocation of bioactive peptides across cell membranes by carbon nanotubes, *Chemical Comm.*, 1, 16–17.
- Phillips M and Joshi K (2008) *Bone Disease, Orthopaedic Bone Cements*, Ed. Deb S, Cambridge, UK: Woodhead Publishing Ltd.
- Pienkowski A and Andrews R (2001) Polymethylmethacrylate augmented with carbon nanotubes, United States Patent 6, 872,403.
- Poland C, Duffin R, Kinloch I, Maynard A, Wallace W, Seaton A, Stone V, Brown S, Macnee W and Donaldson K (2008) Carbon nanotubes introduced into the abdominal cavity of mice show asbestos-like pathogenicity in a pilot study, *Nature Nanotechnology*, 3(7), 423–428.

- Porter D, Sriram K, Wolfarth M, Jefferson A, Schwegler-Berry D, Andrew M and Castranova V (2008) A biocompatible medium for nanoparticle dispersion, *Nanotoxicology*, 2(3), 144–154.
- Price R, Ellison K, Haberstroh K and Webster T (2004) Nanometer surface roughness and increased selected osteoblasts adhesion on carbon nanofibre compacts, *J. Biomed. Mater. Res. A*, 70, 129–138.
- Price R, Wald M, Haberstroh K and Webster T (2003) Selected bone cell adhesion on formation of formulations containing carbon nanofibers, *Biomaterials*, 24, 1877–1887.
- Pryor G, Villar R and Coleman N (1992) Tissue reaction and loosening of carbon-reinforced polyethylene arthroplasty, *J. Bone Joint Surg.*, 74-B, 156–157.
- Pulskamp K, Diabate S and Krug H (2007) Carbon nanotubes show no sign of acute toxicity but induce intracellular reactive oxygen species in dependence on contaminants, *Toxicology Lett.*, 168, 1, 58–74.
- Qian D, Andrews R and Rantell R (2000) Load transfer and deformation mechanisms in carbon nanotubes-polystyrene composites, *Appl. Phys. Lett.*, 76(20), 2868–2870.
- Radosavljevic M, Freitag M, Thadani K and Johnson A. (2002) Nonvolatile molecular memory elements based on ambipolar nanotube field effect transistors, *Nano. Lett.*, 2(7), 761–764.
- Richard C, Doan BT, Beloeil JC, Bessodes M, Toth E and Scherman D (2008) Noncovalent functionalization of carbon nanotubes with amphiphilic gd3+ chelates: toward powerful t1 and t2 MRI contrast agents, *Nano. Lett.*, 8(1), 232–236.
- Rochette J, Sacher E, Meunier M and Luong J (2005) A mediatorless biosensor for putrescine using multiwalled carbon nanotubes, *Analytical Biochemistry*, 336(2), 305–311.
- Salata O (2004) Applications of nanoparticles in biology and medicine, *J. Nanobiotechnology*, 2(1), 3–9.
- Sandler J, Werner P, Shaffer M, Demchuk V, Altstadt V and Alan H. Windle A (2002) Carbon-nanofibre-reinforced poly(ether ether ketone) composites, *Composites Part A: Applied Science and Manufacturing*, 33(8), 1033–1039.
- Scholes S, Unsworth A, Streicher R and Jones E (2002) Preliminary testing of alternative bearing material combinations for a total knee prosthesis, *Trans. Europe Soc. Biomat. Meeting*, 124.
- Shard A and Tomlins P (2006) Biocompatibility and efficacy of medical implants, *Regen. Med.*, 1(6), 789–800.
- Shi D and Xuejun W (2006) *Bioactive Ceramics: Structure, Synthesis and Mechanical Properties, Introduction to Biomaterials*, Ed. Shi D. Tsinghua, Beijing: University Press.
- Shi X, Hudson J, Spicer P, Krishnamoorti R, Tour J and Mikos A (2005) Rheological behaviour and mechanical characterisation of injectable poly(propylene fumarate)-based single walled carbon nanotubes composites, *Trans. 30th Soc Biomater. Meeting*, 66.
- Shvedova A, Fabisiaik J, Kisin E, Murray A, Roberts J, Tyurina Y, Antonini J, Feng W, Kommineni C, Reynolds J, Barchowsky A, Castranova V and Kagan V (2008) Sequential exposure to carbon nanotubes and bacteria enhances pulmonary inflammation and infectivity, *Am. J. Respiratory Cell and Molecular Biology*, 38(5), 579–590.
- Shvedova A and Kagan V (2010) The role of nanotoxicology in realizing the ‘helping without harm’ paradigm of nanomedicine: lessons from studies of pulmonary effects of single-walled carbon nanotubes, *J. Internal Medicine*, 267(1), 106–118.
- Shvedova A, Kisin E, Mercer R, Murray A, Johnson V, Potapovich A, Tyurina Y, Gorelik O, Arepalli S, Schwegler-Berry D, Hubbs A, Antonini J, Evans D, Ku B, Ramsey D,

- Maynard A, Kagan VE, Castranova V and Baron P (2005) Unusual inflammatory and fibrogenic pulmonary responses to single-walled carbon nanotubes in mice, *Am J. of Physiology-Lung Cellular and Molecular Physiology*, 289(5), L698–L708.
- Shvedova A, Kisin E, Porter D, Schulte P, Kagan V, Fadeel B and Castranova V (2009) Mechanisms of pulmonary toxicity and medical applications of carbon nanotubes: Two faces of Janus?, *Pharmacology and Therapeutics*, 121(2), 192–204.
- Singh R, Pantarotto D, Lacerda L, Pastorin G, Klumpp C, Prato M, Bianco A and Kostarelos K (2006) Tissue biodistribution and blood clearance rates of intravenously administered carbon nanotube radiotracers, *Proc. Nat. Acad. Sci. USA*, 103(9), 3357–3362.
- Sitharaman B, Kissell K, Hartman K, Tran L, Baikarov A, Rusakova I, Sun Y, Khant H, Ludtke S, Chiu W, Laus, S, Toth E, Helm L, Merbach A and Wilson L (2005) Superparamagnetic gadonanotubes are high-performance MRI contrast agents, *Chemical Comm.*, 31, 3915–3917.
- Skinner H (1988) Composite technology for total hip arthroplasty, *Clin. Orthop. Rel. Res.*, 235, 224–236.
- Soto K, Garza K and Murr L (2007) Cytotoxic effects of aggregated nanomaterials, *Acta Biomaterialia*, 3(3), 351–358.
- Soto K, Carrasco A, Powell T, Garza K and Murr L (2005) Comparative in vitro cytotoxicity assessment of some manufactured nanoparticulate materials characterized by transmission electron microscopy, *J. Nanoparticle Research*, 7(2–3), 145–169.
- Star A, Tu E, Niemann J, Gabriel JC, Joiner C and Valcke C (2006) Label-free detection of DNA hybridization using carbon nanotube network field-effect transistors, *Proc. Nat. Acad. Sci. USA*, 103(4), 921–926.
- Stipho H (1998) Effect of glass fibre reinforcement on some mechanical properties of autopolymerizing polymethyl methacrylate, *J. Pros. Dent.*, 79(5), 580–584.
- Streicher R, Schmidt M and Fiorito S (2006) Nanostructures and nanosurfaces for artificial orthopaedic implants, *Nanomedicine*, 2(6), 861–874.
- Tan X, Li M, Cai P, Luo L and Zou X (2005) An amperometric cholesterol biosensor based on multiwalled carbon nanotubes and organically modified sol-gel/chitosan hybrid composite film, *Analytical Biochemistry*, 337(1), 111–120.
- Tanaka K, Tamura J, Kawanabe K, Nawa M, Oka M, Uchida M, Kokubo T and Nakamura T (2002) Ce-TZP Al₂O₃ nanocomposite as a bearing material in total joint replacement, *J. Biomed. Mater. Res. (Appl. Biomater)* 63, 262–270.
- Taylor I (2009) *The Complete Guide to the Global Orthopaedic Market*, Espicom Business Intelligence Ltd., UK.
- Thostenson E, Li C and Chou T-W (2005) Nanocomposites in context, *Composite Sci. Tech.*, 65(3–4), 491–516.
- Thuairé A, Goujon, Gauvin R and Drew R (2004) Study of the fabrication of aluminium matrix nanocomposites reinforced with carbon nanotubes, *Microscopy and Microanalysis*, 10, 574–575.
- Topoleski L, Ducheyne, P and Cuckler J (2004) The effects of centrifugation and titanium fiber reinforcement on fatigue failure mechanisms in poly(methyl methacrylate) bone cement, *J. Biomed. Mater. Res.*, 29(3), 299–307.
- Tsuji J, Maynard A, Howard P, James J, Lam C, Warheit D and Santamaria, A (2006) Research strategies for safety evaluation of nanomaterials, part IV: risk assessment of nanoparticles, *Toxicological Sciences: Official J. of the Society of Toxicology*, 89(1), 42–50.
- Uno T, Tabata H and Kawai T (2007) Peptide-nucleic acid-modified ion-sensitive field-effect transistor-based biosensor for direct detection of DNA hybridization, *Analytical Chemistry*, 79(1), 52–59.

- Uzun G, Hersek N and Tincer T (1999) Effect of five woven fibre reinforcements on the impact and transverse strength of a denture base resin, *J. Pros. Dent. Am.*, 81(5), 616–620.
- Vallittu P (1995) A review of methods used to reinforce polymethyl methacrylate resin, *J. Prosthodontics*, 4(3), 183–187.
- Vallittu P (1996) A review of fiber-reinforced denture base resins, *J. Prosthodontics*, 5(4), 270–276.
- Velasco-Santos C, Martinez-Hernandez A, Fisher F, Rouff R and Castano W (2003) Dynamic-mechanical and thermal analysis of carbon nanotube-methyl-ethyl methacrylate nanocomposites, *J. Phys. D Appl. Phys.*, 36, 1423–1428.
- Wan K, Yang L and Padavan D (2007) Use of degradable and nondegradable nanomaterials for controlled release, *Nanomedicine*, 2(4), 483–509.
- Wang M, Pramoda K and Goh S (2006) Enhancement of interfacial adhesion and dynamic mechanical properties of poly(methyl methacrylate)/multiwalled carbon nanotubes with amine-terminated poly(ethylene oxide), *Carbon*, 44, 613–617.
- Wang S-F, Shen L, Zhang W-D and Tong Y-J (2005) Preparation and mechanical properties of chitosan/carbon nanotube composites, *Biomacromolecules*, 6, 3067–3072.
- Webster T (2007) *Nanotechnology for Generation of Soft and Hard Tissue*, Singapore: World Scientific Publishing.
- Webster T and Ah E (2006) Nanostructured biomaterials for tissue engineering bone, *Adv. Biochem. Eng./Biotech.*, 103, 275–308.
- Webster T, Waid M, McKenzie J, Price R and Ejiofor J (2004) Nanobiotechnology: Carbon nanofibres as improved neural and orthopaedic implants, *Nanotechnology*, 15, 48–54.
- Weisenberger M, Andrews and Rantell T (2007) Carbon nanotube polymer composite: Recent developments in mechanical properties, in J Mark (ed.) *Physical Properties of Polymer Handbook*, Part VI, New York: Springer.
- Werner P, Alst  d V, Jaskulka R, Jacobs O, Sandler J, Shaffer M and Windle A. (2004) Tribological behaviour of carbon-nanofibre-reinforced PEEK, *Wear*, 257, 1006–1014.
- White A, Best S and Kinloch I (2007) Hydroxyapatite-carbon nanotubes composites for biomedical applications: a review, *Int. J. App. Ceramic Tech.*, 4(1), 1–13.
- Williams D (1999) *The Williams Dictionary of Biomaterials*, Liverpool: Liverpool University Press.
- Wolff J (1891) *Das Gesetz der Transformation der Knochen*, Berlin: A Hirschwald.
- Worle-Knirsch J, Pulskamp K and Krug H (2006) Oops they did it again! Carbon nanotubes hoax scientists in viability assays, *Nano. Lett.*, 6(6), 1261–1268.
- Wright T, Astion D, Bansal M, Rimnac C, Green T, Install J and Robinson R (1998) Failure of carbon fibre-reinforced PE total knee components: a report of 2 cases, *J. Bone Joint Surg.*, 70–A, 926–932.
- Wright T, Fukubayashi T and Burstein A (1981) The effects of carbon fiber reinforcement on contact area, contact pressure and time-dependent deformation in polyethylene tibial components, *J. Biomed. Mat. Res.*, 15(5), 719–730.
- Xian Y, Zhou Y, Wang H, Zhou L, Liu F and Jin L (2005) Nanostructured electrode based on multi-wall carbon nanotubes/Pt microparticles nanocomposite for electrochemical determination of thiols in rat striatum by high performance liquid chromatography separation, *J. Chromatography B: Analytical Technologies in the Biomedical and Life Sciences*, 817(2), 239–246.
- Yang J, Yao Z, Tang C, Darvell BW, Zhang H, Pan L, Liu J and Chen Z (2009) Growth of apatite on chitosan-multiwall carbon nanotube composite membranes, *Applied Surface Science*, 255(20), 8551–8555.

- Yap AU, Wang X, Wu X and Chung S (2004a) Comparative hardness and modulus of tooth-colored restoratives: a depth-sensing microindentation study, *Biomaterials*, 25(11), 2179–2185.
- Yap S, Yap A, Teo C and Ng J (2004b) Polish retention of new aesthetic restorative materials over time, *Singapore Dent J.*, 26(1), 39–43.
- Zanello L, Zhao B, Hu H and Haddon R (2006) Bone cell proliferation on carbon nanotubes, *Nano. Lett.*, 6(3), 562–567.
- Zhan G, Kuntz J, Wan J and Mukherjee A (2003) Single walled carbon nanotubes as attractive toughening agents in alumina-based nanocomposites, *Nat. Mater.*, 2, 38–42.
- Zhang D, Kandadai M, Cech J, Roth S and Currans S (2006a) Poly(L-lactide) (PLLA)/multiwalled carbon nanotubes (MWCNT) composite: characterization and biocompatibility evaluation, *J. Phys. Chem. B: Condes. Matters Mater. Surf. Interfaces Biophys.*, 110(26), 12910–12915.
- Zhang Z, Yang X, Zhang Y, Zeng B, Wang S, Zhu T, Roden R, Chen Y and Yang R (2006b) Delivery of telomerase reverse transcriptase small interfering RNA in complex with positively charged single-walled carbon nanotubes suppresses tumor growth, *Clin. Cancer Res.*, 12, 4933–4939.
- Zhang F, Xia Y, Xu L and Gu N (2008) Surface modification and microstructure of single-walled carbon nanotubes for dental resin-based composites, *J. Biomed. Mater. Res. Part B: Appl. Biomater.*, 86(1), 90–97.
- Zhao B, Hu H, Mandal S and Haddon R (2005) A bone mimic based on the self-assembly of hydroxyapatite on chemically functionalised single-walled carbon nanotubes, *Chem. Mater.*, 17(12), 3235–3241.
- Zhou Z (2009) Augmentation of PMMA denture base materials with multi-walled nanotubes, MSc thesis, Queen's University of Belfast.

Fire-retardant applications of polymer–carbon nanotubes composites: improved barrier effect and synergism

C. DEWAGHE, C. Y. LEW and M. CLAES, Nanocyl S. A., Belgium and P. DUBOIS, University of Mons, Belgium

Abstract: Fire safety regulations are becoming more and more stringent; consequently, researchers have to develop more efficient flame-retardant polymers. In order to do so, they are investigating flame-retardant nanocomposites and, more precisely, carbon nanotubes-based nanocomposites. This chapter briefly presents the fire issues and the general state of regulation. Then the fire mechanism and the ways to counter it are discussed, followed by a section specifically on carbon nanotubes' applications. Carbon nanotubes can enhance flame-retardant properties as a unique filler of a polymer or as a synergistic agent to protect polymers in bulk, or as a filler in flame-retardant coatings which can protect many types of material.

Key words: ammonium polyphosphate, carbon nanotubes, fire test, flame retardant, polymer, protective layer, silicone, synergism.

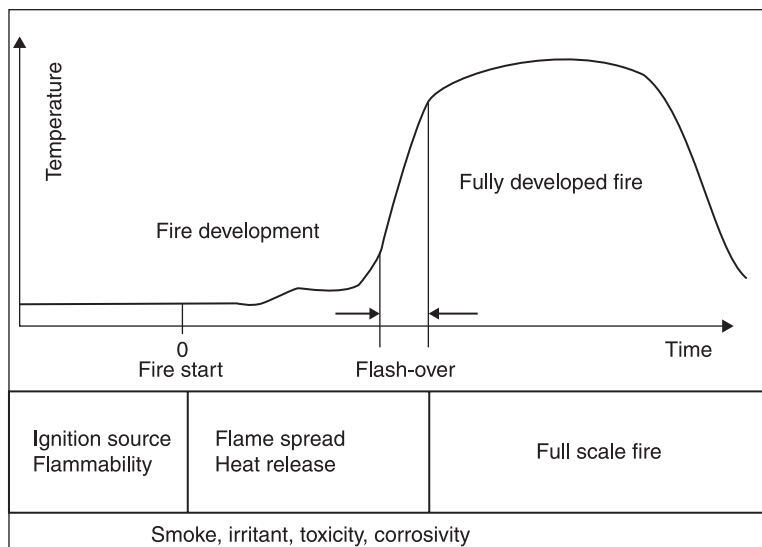
23.1 Introduction

23.1.1 Fire issues

If we just consider fire statistics: one domestic fire begins every two minutes and, unfortunately, half of the people involved are left badly injured afterwards; two out of three people who die as a result of fires, die because of smoke toxicity and not because of the flames themselves; thirty domestic fires per day, in France, are due to carelessness; one fire out of four is due to a defective electrical system; 75% of domestic fires occur at night (Comodo, France, 2009). So fire protection is a necessity and a huge challenge.

The growth of a fire can be described as follows: a fire starts, it develops quite quickly and after a few minutes, it becomes dramatically important: all vapour and heat start a general 'flash-over'. Once it reaches that stage, there is no longer any way to stop it (see Fig. 23.1).

To counter that problem, the industry has been really active in developing solutions to prevent fires starting. 'Fire-retardant' solutions are materials that will delay the flash-over due to their low contribution to fire. 'Fire-resistant' solutions are materials that will act after flash-over and that will limit the physical propagation of fire from one area to another, and keep, for example, the integrity of walls or roofs in order to protect both people trapped in fires and the firemen from building collapse.



23.1 Fire scenario.

Fire retardancy of materials is evaluated through ignitability and flammability. The different dangerous features of a fire are:

- *Flame spread* defines the size of the flames, and/or the time it takes for the flame to cover a determined distance on a sample (i.e. how long it will take the fire to grow and to reach other items).
- *Dripping* defines the presence of flaming drops which could fall on another item and set fire to it, and so spread the fire in the room.
- *Heat release* is defined as the quantity of heat that is released in the room by the burning sample, and which could involve degradation and the burning of other items.
- *Smoke opacity and toxicity* are important for the evacuation of people trapped in a fire; if the smoke opacity is too high, people and firemen will not be able to see anything or to find their way out. If smoke toxicity reaches too high a level, people will not be able to breathe and this can cause death or injury from smoke inhalation.

Fire resistancy is evaluated through stability and containment. The following are features that can delay the progress of a fire, and save lives:

- Integrity of a fireproof door, for example, which must not be destroyed during a fire, or must be destroyed as late as possible.
- Insulation of a fireproof door, to keep the same example, which has to prevent flames and smoke from entering the room, to protect people as long as possible.

- Load bearing of stainless steel beams, in buildings, which must keep their mechanical properties as long as possible to prevent walls and roof caving in or the building collapsing.

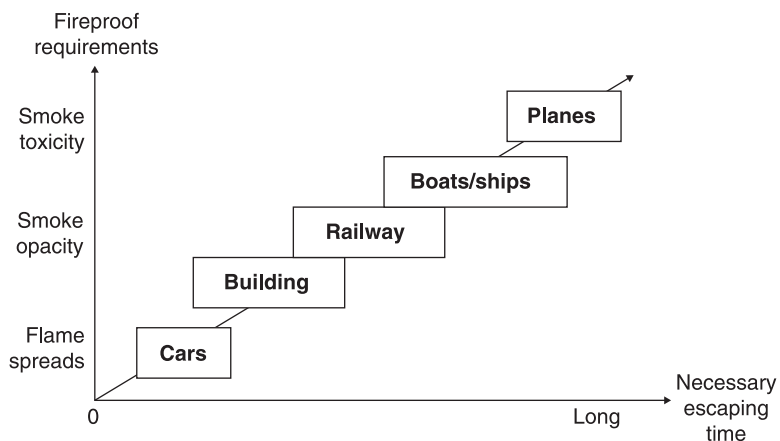
Globally, the level of flame retardancy and resistancy required is the combination of different fireproof characteristics of materials. These criteria will vary depending on the final application, and are defined by standards which are different in buildings or in transportation, for example. In transportation, the standards are not the same for all modes such as cars, trains or ships. Furthermore, the standard for the same product, in the same application, varies from one country to another. So when you develop a flame-retardant product, it is important to have an idea of the market targeted, and to have a global overview of the fireproof requirements the product will have to comply with.

As an example, in transportation, the time to escape from a burning car is really short, but in an aeroplane, this time can be longer, so it is a requirement that the smoke toxicity due to burning material used for an aeroplane must remain very low. This is not the case for the material used in a car, as people can jump out of the vehicle very quickly (Fig. 23.2).

23.1.2 Regulations and standards

The fire behaviour of products constitutes a major impact in many areas: building and construction, transport, electric and electronic engineering, furniture, etc. The issue of fire protection is the source of the largest number of standards, regulations or legislations at the national level as well as the international level.

Governments worldwide try to maintain and, where possible, improve, the fire safety of consumer products and public areas to help reduce fires. The role of fire-



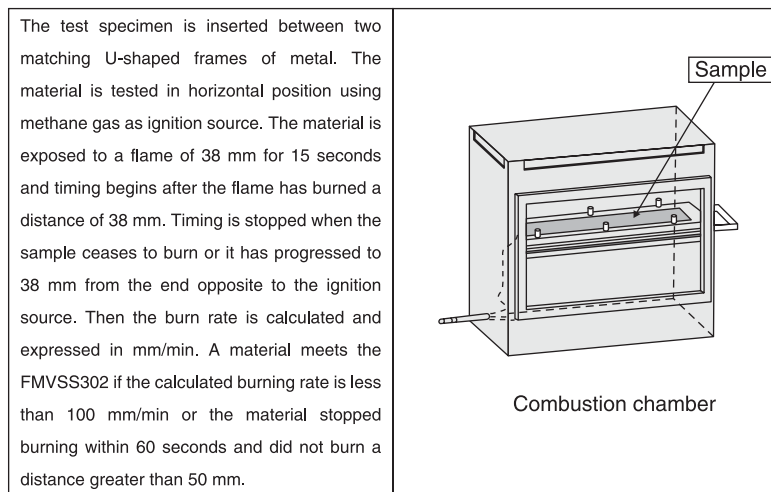
23.2 Fireproof requirements as a function of means of transport.

retardant materials in this is well recognized, but the requirements are highly dependent on the targeted application and market, as explained previously. Indeed, to ensure the fire safety of buildings, all building products, materials and furnishings need to be tested for flammability and fire resistance before they can be used in construction. Not only the construction materials but also decorative materials such as carpets, curtains and upholstery need to comply with fire standards for use in public buildings and homes.

Building materials like concrete, steel, bricks, timber and stone will all burn once they reach a sufficient temperature to start a fire. Thanks to treatment with fire-retardant chemicals or coatings, their fire resistance and fire retardant qualities can be improved. Whether for building construction, transportation equipment, industrial processes or offshore applications, understanding of fire and certifying fire standards are absolutely essential (Magma Firestop, 2009)

Here are some of the common standards:

- Cars are mainly covered by FMVSS302 and ISO3795 (see Fig. 23.3), the regulation is the same kind in the EU and the USA.
- Wires are covered by IEC 60 332-1 and 60-332-3 and ASTM E662.
- Railways have international standards Pr EN 45545 and ISO 5660, however, national regulations apply in each country.
- Concerning ships, nowadays the standard is ISO 5660 and regulation is the same all around the world (monitored by the International Maritime Organisation).
- Planes are covered by international standards JAR part 25 and FAR part 25; the regulation is the same kind in the EU and the USA.



23.3 Description of test FMVSS302. (DSM research, summary of text method, available from <http://www.dadc.nl/AD/summary/4-Flammability/37-summary-FMVSS.pdf>, accessed 15 December 2009.)

- Buildings were covered by different regulations and standards in the past, but presently Euroclass standards harmonize fire tests in Europe (EN 13501-2 and 13823).

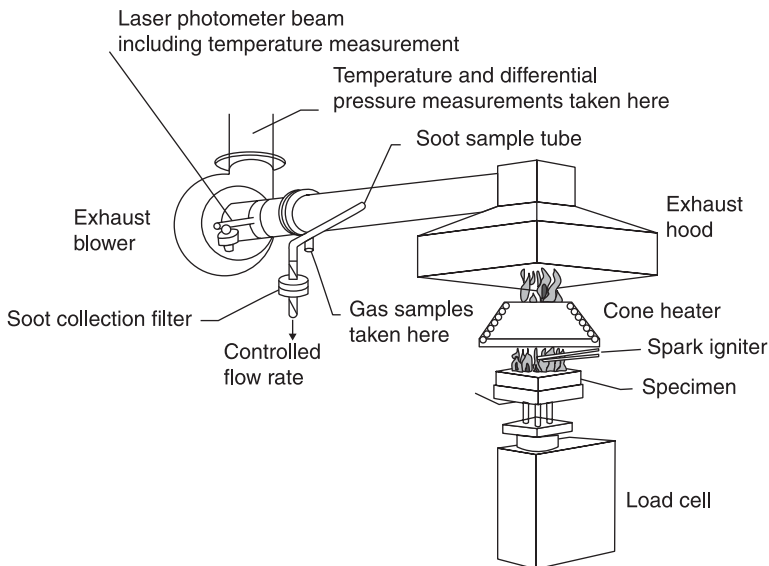
When it comes to the development of plastic products, some standard (or not standard) tests are commonly used and well recognized by flame-retardant compound developers and researchers. These tests enable a quick and efficient evaluation of flame-retardant properties of thermoplastics. These tests are classic ones and are described below.

23.1.3 Common tests to characterize flame-retardant properties

Laoutid *et al.* (2009) explain very well the principle of the main fire tests which can be performed at the laboratory scale, as discussed below.

Cone calorimetry

Cone calorimetry is one of the most effective medium-sized polymer fire behaviour tests. The principle of cone calorimetry is based on the measurement of the decreasing oxygen concentration in the combustion gases of a sample subjected to a given heat flux (in general from 10 to 100 kW/m²). Figure 23.4 illustrates the experimental set-up of a cone calorimeter. Standardized in the United States



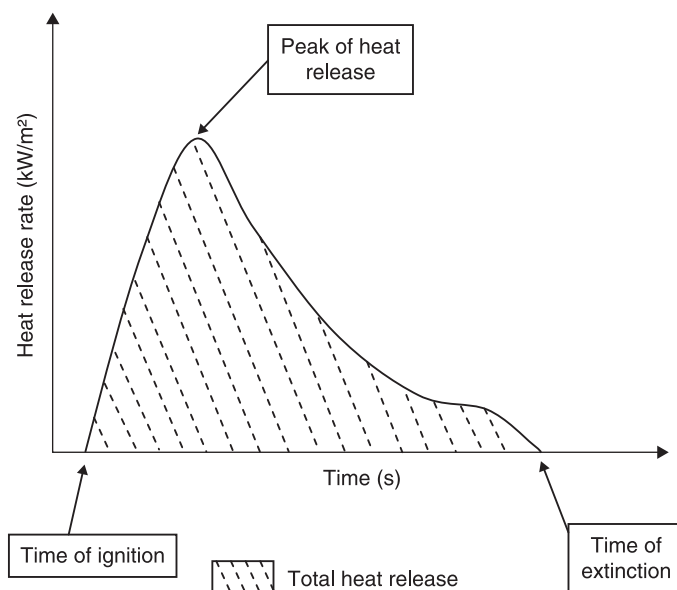
23.4 Cone calorimeter schema.

(ASTM E 1354), the cone calorimeter test is also the subject of an international standard (ISO 5660). The sample ($100 \times 100 \times 4 \text{ mm}^3$) is placed on a load cell in order to evaluate the evolution of mass loss during the experiment. A conical radiant electrical heater uniformly irradiates the sample from above. The combustion is triggered by an electric spark. The combustion gases produced pass through the heating cone and are captured by means of an exhaust duct system with a centrifugal fan and hood. The gas flow, oxygen, CO, CO₂ concentrations and smoke density are measured in the exhaust duct.

The measurements of gas flow and oxygen concentration are used to calculate the quantity of heat release per unit of time and surface area: heat release rate (HRR) is expressed in kW/m². The evolution of the HRR over time, in particular the value of its peak/maximum (pHRR or HRR_{max}), is usually taken into account in order to evaluate fire properties. The integration of the HRR vs. time curve gives the total heat release (TRR) expressed in kJ/m². In addition, this test also enables characterization of the time of ignition (TOI), time of combustion or extinction (TOF), mass loss during combustion, quantities of CO and CO₂, and total smoke released (TSR), as shown in Fig. 23.5.

Limit of oxygen index (LOI)

This test is used to indicate the relative flammability of materials. It is now subjected to an international standard (ISO 4589). The value of the LOI is defined



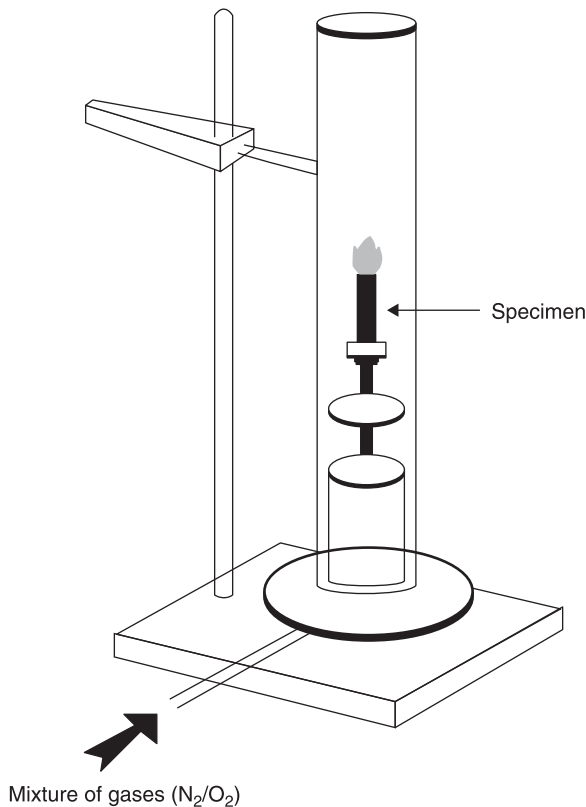
23.5 Typical cone calorimeter curve.

as the minimal oxygen concentration in the oxygen/nitrogen mixture that either maintains flame combustion of the material for 3 minutes or consumes a length of 5 cm of sample, with the sample placed in a vertical position (the top of the test sample is set on fire with a burner, see Fig. 23.6). The LOI is expressed in percentage (of oxygen).

As air contains 21% oxygen, materials with an LOI below 21 are classified as combustible, whereas those with an LOI above 21 are classified as self-extinguishing, because their combustion cannot be sustained at ambient temperature without an external energy contribution. The higher the LOI, the better the flame-retardant property.

UL94 tests

The set of UL94 tests includes a range of flammability tests (small and large flame vertical tests, horizontal test for bulk and foam materials, radiant panel flame-spread test). The most commonly used test is UL94V for measuring the ignitability



23.6 LOI schema.

Table 23.1 UL94V classification

Fire classification	
UL94 V ₀	t_1 and t_2 less than 10 sec for each specimen $t_1 + t_2$ less than 50 sec for the 5 specimens $t_2 + t_3$ less than 30 sec for each specimen No afterflame or afterglow up to the holding clamp No burning drops
UL94 V ₁	t_1 and t_2 less than 30 sec for each specimen $t_1 + t_2$ less than 250 sec for the 5 specimens $t_2 + t_3$ less than 60 sec for each specimen No afterflame or afterglow up to the holding clamp No burning drops
UL94 V ₂	t_1 and t_2 less than 30 sec for each specimen $t_1 + t_2$ less than 250 sec for the 5 specimens $t_2 + t_3$ less than 60 sec for each specimen No afterflame or afterglow up to the holding clamp Burning drops allowed

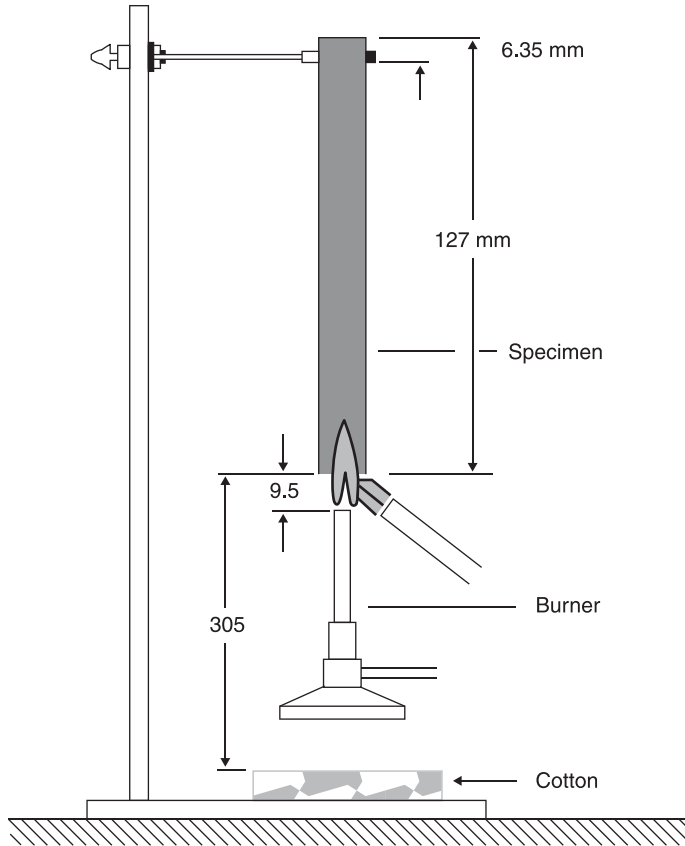
Source: Laoutid *et al.* (2009).

and flame spread of a vertical bulk material exposed to a small flame. The flame is applied to the bottom of the specimen for 10 seconds and removed. The after-flame time t_1 (time required for flame extinguishing) is noted. After extinction, the flame is applied for another 10 sec. The after-flame time t_2 is noted, together with the after-glow time t_3 (time required for the fire glow to disappear).

During the test, the presence of burning drops, causing a piece of cotton located under the sample to ignite, must be noted. The specimen will be classified V₀, V₁ or V₂ according to criteria listed in Table 23.1. The experimental set-up for the UL94 test is shown in Fig. 23.7.

23.1.4 Euroclass standards

In Europe, some fire disasters – like those in the Madrid discotheque, the Channel Tunnel, the Turin cinema, and King’s Cross tube station – have highlighted again the importance of safety in public places in the event of fire. The European Commission, supported by a Group of National Fire Regulators, proposed a completely new classification system, based partially on existing test methods, but partially, and critically for many construction products, on a completely new test, the so-called ‘single burning item’ (SBI) test. This test evaluates the potential contribution of a building product to the development of a fire, under a fire situation simulating a single burning item in a room corner near to that product. Heat and smoke release rate are measured during combustion. As a consequence, all national classes have been replaced by new European standard tests (ENs)



23.7 UL94 vertical schema. Source: Laoutid *et al.* (2009).

‘Euroclasses’, in the building area. However, the implementation in each Member State varies.

The Euroclasses became valid on the 1st January 2001 and after this date, every national classification for construction products was recognized on the national market for a period of time. At the end of this period, only European classification will be valid, at both the national and European level.

According to this European regulation, products will be rated from A to F as a function of the performance level observed. Euroclass A will cover products that do not contribute, or contribute only very slightly, to the development of a fire. Euroclass E will cover products that present an acceptable reaction to fire, i.e. they can resist ignition by a small flame for a short period. Euroclass F is for products that have shown no performance criteria. The Euroclass classification system will rate: flame spread (from class A to E), dripping (class D0 to D2) and smoke (class S1 to S3) (Magma, 2009) (Table 23.2).

Table 23.2 Simplified Euroclass classification

Level	Code	Meaning
Main class	A1 A2 B	Non combustible (over 20 min to flash-over)
	C	Moderately combustible (10 to 20 min to flash-over)
	D	Moderately combustible (2 to 20 min to flash-over)
	E	Moderately combustible
Sub class	S1	Low smoke production
	S2	Medium smoke production
	S3	High smoke production
Sub class	D0	No flaming droplets
Flaming droplet	D1	Flaming droplets which persist less than 10 s
	D2	Flaming droplets

Source: Koxka (2009) Euroclass and reaction to fire, available from <http://www.koxka.com/English/Documents/Euroclasses%20and%20reaction%20to%20fire.pdf> (accessed on 24 November 2009).

To prevent products catching fire, the first step is to understand the fire mechanism, to be able to understand the different ways for a material to resist fire, or to retard its own combustion.

Today, if the Euroclass uniformization of standards across Europe is efficient and well applied in the building area, it could be transposed to other fields of application, such as transportation.

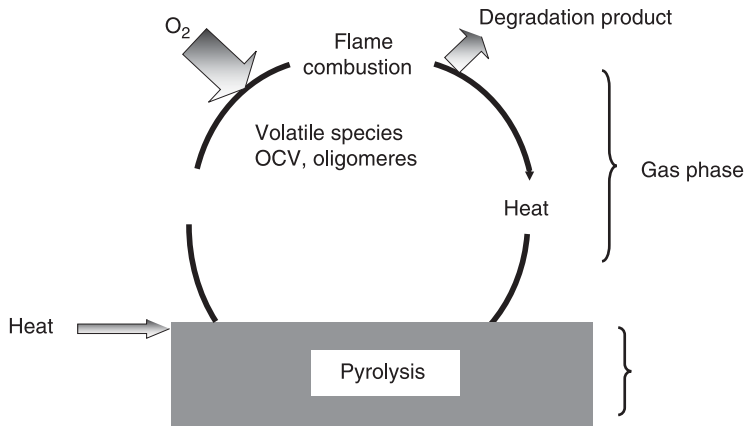
23.2 Fire protection mechanisms

23.2.1 General overview of fire and protection mechanisms

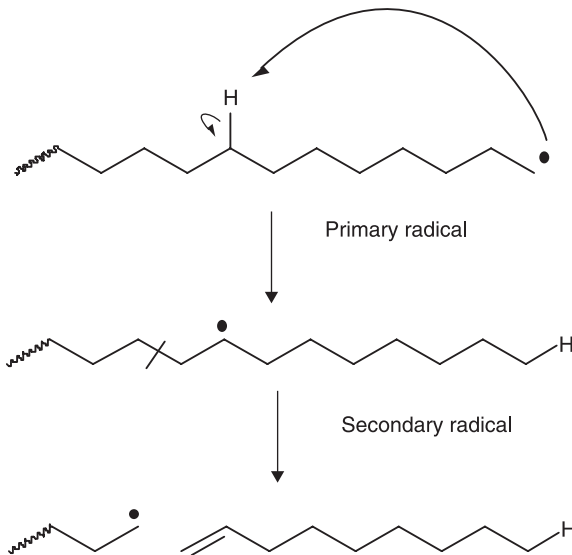
To create a fire, three elements are needed: heat, combustive element and fuel. If these elements are joined together, we can observe combustion, as shown in Fig. 23.8. The source of heat increases the temperature of the product or the polymer (depending on the intensity of heat source, and of the intrinsic characteristics of the product or the polymer). This increase in temperature involves decomposition (mainly pyrolysis) and formation of organic materials with low molecular weights (often volatile and flammable, mainly free radicals) (Fig. 23.9).

When the concentration of flammable volatile species reaches a critical level in combination with oxygen, the mixture of gaseous products (i.e. fuel) catches fire. Then the flame created becomes a heat source and maintains the decomposition of the polymer, called the condensed phase.

In order to suppress or reduce fire of polymers, we need to suppress either heat, fuel or combustion, to break the fire cycle presented in Fig. 23.9. There are different steps in this cycle, either occurring in the gas or condensed phase, which are important to understand, and when it is possible to act to achieve better flame resistant (FR) properties in polymers:



23.8 Combustion cycle. Source: Poutch (2007), courtesy of Crepim.



23.9 Decomposition: example of free radical formation. Source: Poutch (2007), courtesy of Crepim.

- As stated above, thermally induced polymer decomposition releases very reactive free radical species such as H^\bullet or OH^\bullet , which maintain the combustion in the gas phase. Adding halogenated flame retardants to the polymer formulation can slow down radical formation. Indeed, when the material is burning, this flame retardant is decomposed and releases halogenated radical species (Cl^\bullet or Br^\bullet) which neutralize (via a chemical reaction) the radical

species coming from the polymer itself. This stops the chain decomposition and therefore the combustion.

- In the gas phase it is also possible to dilute the fuel, due to the incorporation of an additive (melamine, for example) which will release inert substances during combustion. This will decrease the concentration of the reactive mixture below the limit of ignition.
- It is also possible to break the fire cycle by acting on the condensed phase by creating an endothermic reaction which will cool the polymer. In order to reach this goal, an additive, such as magnesium or aluminium hydroxides are used. These products will release molecules of water around 200–300 °C.
- In the condensed phase, another solution is to use additives which will react under high temperature to create a protective layer to insulate the underlying substrate from the heat source, as in an intumescent system (see Section 23.2.2). This ‘char’ layer limits the transfer of volatile degradation products. Furthermore, the fuel gases can be physically separated from the oxygen, which prevents the combustion process being sustained.
- A final way to limit the combustion and degradation of thermoplastics or any solid material, is to apply a flame-retardant coating to the substrate. This paint will react when submitted to high temperature and create a protective layer.

23.2.2 Intumescent systems

Of all the fire protection solutions, intumescence is very popular today, due to the increasingly severe legal requirements for fire protection. Intumescent systems can be used to protect polymers’ parts in bulk or to protect different types of solid material (like metallic beams in construction area) with a flame-retardant coating which becomes a protective layer during fire.

Intumescence is a specific way of fighting fire. The principle is the formation of a char layer that can protect the substrate and limit the degradation, isolating the surface from heat and preventing the release of degradation products. To realize such an effect, three components are necessary:

- an acid source that decomposes with temperature to release acid (e.g. ammonium polyphosphate, APP);
- a carbon source to produce a charred insulating foam (it can be the polymer itself or, for example, dipentaerythritol);
- a blowing agent (for example, ammonium polyphosphate).

The intumescent mechanism is usually described as follows: first, the acid source breaks down to yield a mineral acid, then it takes part in the dehydration of the carbon source to yield the carbon char, and finally, the blowing agent decomposes to yield a gaseous product. The latter causes the char to swell and hence provides an insulating multicellular protective layer. This shield limits at the same time the

heat transfer from the heat source to the substrate and the mass transfer from the substrate to the heat source, resulting in conservation of the underlying material (Jimenez *et al.*, 2006) (Fig. 23.10).

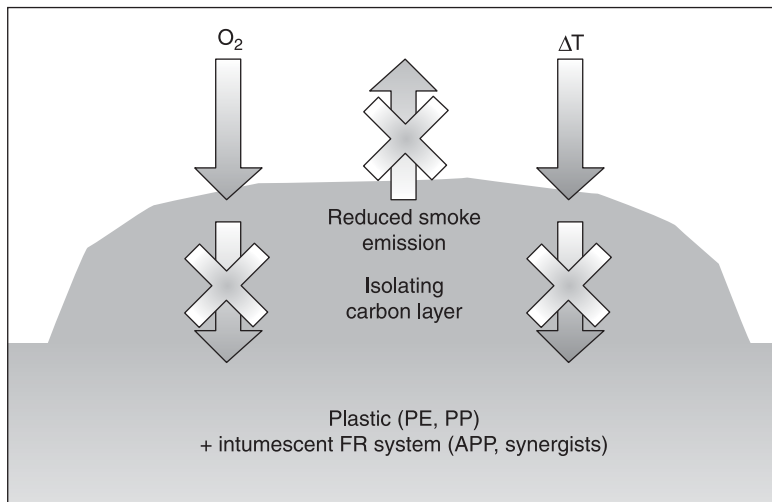
In the past few years a new type of approach has been explored as an alternative to halogenated flame retardants which are more and more sensitive to additives due to health and environment considerations: this new approach is to enhance the flame retardant properties of polymers via 'nano' fillers, particularly via carbon nanotubes (CNTs).

23.3 Using carbon nanotubes to develop fire-retardant solutions

23.3.1 Impact of carbon nanotubes on heat release rate (HRR)

Bourbigot and Duquesne (2006) explained very well the interest in flame-retardant nanocomposites. As a first step, it was pointed out that the first study which was made on the fire properties of nanocomposites showed that this type of material exhibits low flammability in terms of heat release rate (HRR). HRR is measured by a mass loss/cone calorimetry test (see Section 23.1.3). HRR is a major parameter in controlling flame propagation in fire.

Typically, with nanofillers, the peak of HRR is decreased by 50–70% in a cone calorimeter experiment. Indeed, this has been demonstrated by Kashiwagi *et al.*



23.10 Intumescent char layer. Source: Poutch (2007), Fire and its consequence on materials: what material for which application, fire resistance in plastics, 30 November – 2 December 2009, Offenbach.

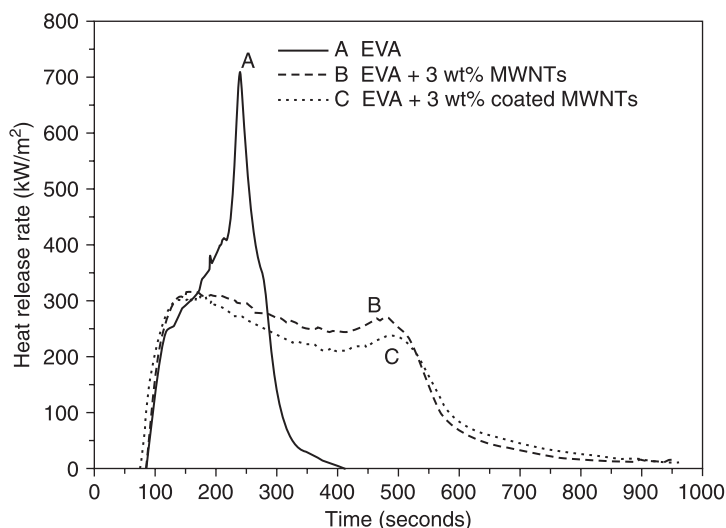
(2005) in a blend of poly(methyl methacrylate) (PMMA) and single-walled carbon nanotubes (SWNTs). The blend was prepared via dissolution of PMMA in dimethylformamide (DMF). Then nanotubes were dispersed by bath sonication for 24h. For only 0.2% by mass of SWNT in the final product, there was a decrease of the HRR by 25%.

Peeterbroeck *et al.* (2007) showed the same trend for a composite of ethyl vinyl acetate (EVA) and multi-walled carbon nanotubes (MWNTs), as shown in Fig. 23.11. For this latter case, when 3 wt% of CNT were added to EVA, the peak of HRR was decreased by 57%, and the combustion time was much longer (900s instead of 300s for virgin EVA). Dispersion of MWNT was realized by melt blending in an internal mixer. These are only two examples, many others are available in the literature. So, generally speaking, CNTs have a positive influence on the HRR of polymers, even if it is dispersed by different ways.

Another interesting phenomenon has also been observed in the case of EVA: at the end of the fire test, the formation of a cohesive char was examined for composite material. This char covered homogeneously the entire sample with no holes or cracks, which was not the case for virgin polymers.

23.3.2 Influence of dispersion quality of CNT in the matrix on FR properties of the nanocomposite

As Bourbigot and Duquesne (2006) explained in their work, the first point to be considered in FR nanocomposites is the nanodispersion. Indeed, Kashiwagi *et al.*



23.11 Cone calorimeter heat release rate versus time for unfilled EVA and EVA-based nanocomposites.

(2005) showed, based on a complete study of PMMA–SWNT blends, that in the case where the nanotubes are relatively well dispersed (almost no agglomerates or bundles), a network layer is formed without any major cracks or openings during the burning test and this covers the entire surface of the composite. However, nanocomposites with a poor dispersion or a low concentration of nanotubes (0.2% by mass or less) form numerous black discrete islands with vigorous bubbling between the islands. This study highlighted also that the peak of heat release rate of the nanocomposite that forms the network layer is about half those which form the discrete islands. This was confirmed by Bourbigot and Duquesne with MWNTs. For their experiment, they prepared a well-dispersed CNT–polystyrene (PS) nanocomposite via melt extrusion using trialkylimidazolium tetrafluoroborate (IM) as a compatibilizer, and the same blend for comparison, without IM. TEM (transmission electron microscopy) images combined with image analysis revealed that agglomerates ($\approx 1 \mu\text{m}$) of nanotubes dominate in the case of the PS–CNTs without IM, while well-dispersed SWNTs can be observed in the case of PS–CNT–IM blend. They evaluated the FR properties via adaptation of a cone calorimeter test. Here, they analysed the mass loss rate, which is as relevant as HRR. A reduction of mass loss rate for the PS nanocomposites is observed, compared to the virgin PS, but the mass loss rate of PS–CNT–IM is significantly lower than that of PS–CNT.

So we can conclude that the formation of a good layer to protect the underneath material is crucial to optimize the FR properties, especially a low HRR. This cohesive layer is highly dependent on the level of dispersion of CNT in the matrix. The number of agglomerate and bundles remaining after dispersion of CNT in the polymer matrix must be as low as possible, whichever process is used.

23.3.3 Protective layer and shield phenomenon

Formation of the protective layer

As we explained in Section 23.3.2, Kashiwagi *et al.* (2005) observed the formation of a char layer due to the presence of CNT in PMMA. The same observation was made for every nanocomposite using CNT.

According to Bourbigot *et al.* (2006), the protection mechanism involves the formation of a char layer covering the entire sample surface acting as an insulating barrier and reducing volatile vapours escaping to the flame. The formation of such a layer which does not form cracks when burning is critical to obtain a low HRR from composites.

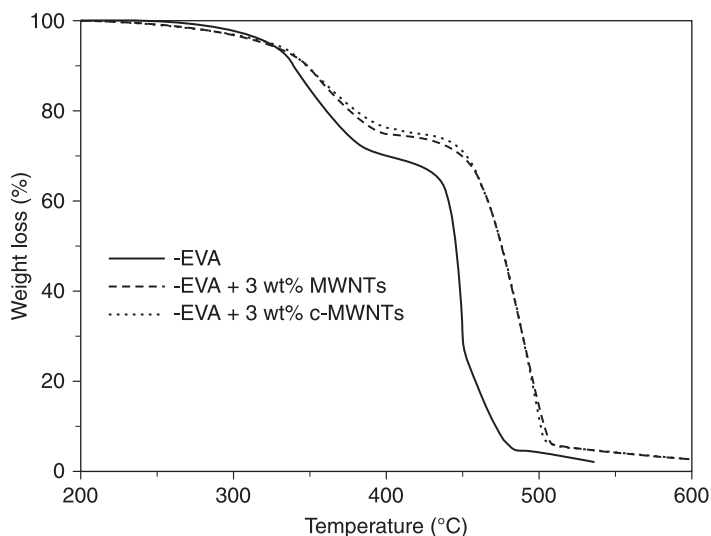
In the case of CNTs, Kashiwagi *et al.* (2005) explained the formation of a protective layer by the following mechanism. In the early stage of the burning/gasification test, the upper part of the sample is heated and starts melting. When the temperature of the sample becomes high enough, degradation starts to generate bubbles in the melt layer. The associated convection flow from the interior of the

sample toward the sample surface pushes the CNTs up to the surface to form a protective layer. But if the dispersion of nanoparticles is not good enough, the bursting of the bubbles at the surface will induce the localized accumulation of CNTs. The final residue will be formed by numerous discrete islands instead of a homogeneous layer covering the entire sample. The quality of dispersion, the concentration of CNTs as well as the temperature and the viscosity of the melt, will influence the quality of the network layer.

Shield phenomenon

Cone calorimeter tests have demonstrated that the addition of CNTs improves the flame-retardant properties of a polymer. Indeed, a significant decrease in the HRR is noted, thanks to the formation of a protective layer acting as a thermal shield. However, this layer has a secondary effect. This effect is highlighted by the influence of CNTs on the mass loss of the polymer during combustion. For example, in an EVA–CNT blend (Peeterbroeck, 2007), the presence of carbon nanotubes modified the thermal degradation of the polymer matrix (see Fig. 23.12). With CNTs, the first degradation step takes place at a higher temperature. This is probably due to a limited volatilization rate and to the production of a more thermally stable char arising from numerous cross-linking reactions.

It is assumed that the free radicals coming from the degradation of the polymer matrix are trapped in the condensed phase (involving cross-linking reactions)



23.12 Thermogravimetric analysis curves of unfilled EVA and EVA-based nanocomposites under air flow.

instead of being released in the gaseous phase. This could be due to the higher viscosity of the composites in the melt state and/or by the labyrinth effect of the interconnected fillers.

The second stage of thermo-oxidative degradation also takes place at a higher temperature in the presence of the char formed during the first degradation step which is further stabilized through π - π interactions. Indeed, when a polymer burns, it produces gaseous products, liquid products and a solid residue, as explained in Fig. 23.13.

In the presence of CNTs, the degradation route of the polymer matrix is oriented toward the solid residue formation, which is in fact a protective layer. Then less gaseous or liquid products, which feed the flame, are produced, and the fire resistance is increased. Carbon nanotubes change the burning behaviour of the polymer to residue formation.

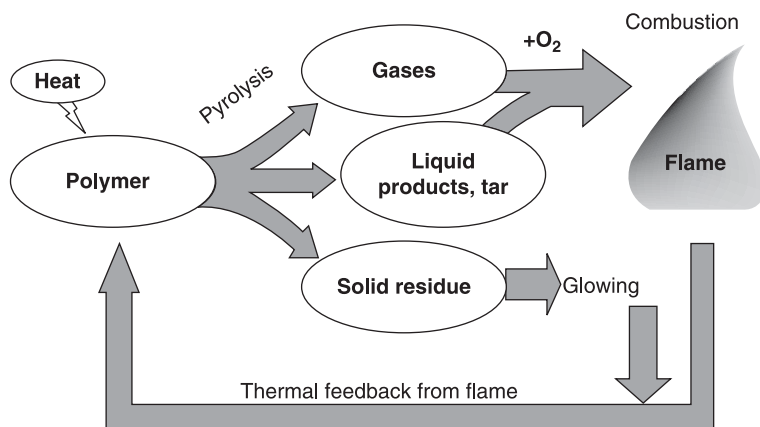
It can be assumed that the layer hinders diffusion of the volatile decomposition products as well as oxygen penetration, due to a tortuous pathway. This phenomenon is only obtained with nanofillers of a high aspect ratio, as is the case for CNTs.

Furthermore, the slower diffusion of free radical products would create a higher probability of collision and recombination (cross-linking), and build-up of a thermally insulative char layer on the surface of the burning material.

Carbon nanotubes introduced on their own in a matrix clearly enhance its FR properties. How do CNTs behave when they are used in combination with conventional flame-retardant polymers?

23.4 Synergism

It has been fully demonstrated in the literature that nanocomposites containing CNTs show improved fire behaviour: a lower heat release in cone calorimetry due



23.13 Degradation route of polymers. Source: Poutch (2007), Crepim.

to the formation of a char layer which acts as a heat shield and limits volatilization. Nevertheless, if the decrease of the HRR is a good starting point to develop a FR compound, this is not enough to pass industrial standard fire tests. The simplest standard test and the best known in FR application is the UL94 test. This test measures the ignitability and self-extinguishing time of the sample (Section 23.1.3). Most of the samples of thermoplastics–CNT nanocomposites showing good performances in cone calorimeter test fail the UL94 test.

It has been explained (Bourbigot and Duquesne, 2006) that, in UL94 testing, the nanocomposite has a relatively limited contribution to the fire associated with enhanced dripping behaviour, but it is not self-extinguishing, the ignition time is shorter and it does not reduce the flammability of the materials. During a UL94 test, the formation of a char layer can be observed on the surface of the material. Nevertheless, the carbonaceous layer is not effective enough to stop the flame and the material continues to burn slowly, failing the test.

This is the reason why CNTs have been tested in combination with other additives which in turn has highlighted the synergism effect. Indeed, in the field of flame retardancy, synergistic additives are often required in order either to sharply improve the performance of the materials or to decrease the loading of FR.

Gao *et al.* (2005) have shown a synergetic effect between nanoclays and nanotubes. In this research, clays were added to an EVA–CNT blend and fire properties were evaluated through cone calorimetry, and the carbonaceous layer was studied by X-ray diffraction analysis and scanning electron microscopy. This composite contained 2.5 phr (parts per hundred) of CNTs and 2.5 phr of clays. This material was compared to an EVA–CNT mixture (5 phr of CNTs). Composites were produced by melt extrusion of a pre-blended EVA–CNT using an internal mixer at 130 °C.

The study made by Gao *et al.* (2005) revealed that the protective layer (Section 23.3), contained graphitic and turbostratic carbons and the oxidation resistance of the char is a function of the degree of graphitization. It was assumed that CNTs act as the nucleation of this graphitization. This effect is enhanced when both CNTs and clays were mixed in the matrix. Here it has been demonstrated that the synergism between clays and CNT enhance char resistance.

This study shows that CNTs can have a synergistic effect with clay to enhance FR properties. Some research has also demonstrated the synergism between CNTs and standard flame-retardant polymers. For example, Ye *et al.* (2009) studied the synergistic effect of CNTs combined with magnesium hydroxide (MH) in EVA. They demonstrated that CNTs can considerably decrease the heat release rates and mass loss rate by about 50–60%, can prolong the combustion time to nearly double and increase the LOI values by 5%, when 2 wt% of CNTs was substituted for the MH in the EVA–MH–CNT composites. TGA data also showed that the synergistic effect of CNTs with MH increases the thermal degradation temperature and final charred residues of the EVA–MH–CNT samples. Ye *et al.* described the synergetic mechanism as follows:

- Increase of melt viscosity because of network structure formation of CNTs.
- Enhancement of thermo-oxidation stability due to the CNTs' mechanical strength and integrity of the charred layers.
- Formation of compact charred layers promoted by CNTs which provide a heat barrier and thermal insulation.

All above factors efficiently enhance the thermal and flame-retardant properties and protect the EVA–MH–CNT nanocomposite material from being burnt.

What is also very interesting in this study is by keeping the same global loading of fillers (just replace 2 wt% of MH by CNT), the FR properties are significantly enhanced. According to this, it is legitimate to assume that CNTs would enable developers to decrease the total filler loading in the material, keeping the same level for fire behaviour. This is a crucial point as the main drawback of MH is the loading. Indeed, this product must be introduced at 50–60% to make a polymer fire-retardant. This kind of concentration significantly damages the mechanical properties of the matrices. Synergism between MH and CNT could have a positive impact on that issue.

The synergistic effect of CNTs has also been demonstrated in intumescent systems. Indeed, usually, in this type of flame-retardant solutions, synergistic agents are often used to pass specific tests required by legislation. As legislation is becoming stricter, intumescent systems have to be more efficient. The mechanical properties of the intumescent shields developed in the case of a fire are particularly important since internal pressure (due to degradation products) or the external environment can easily destroy the shield, leading to a loss of insulating properties. Previously we have shown that CNTs lead to the formation of a protective layer or at least enhance its properties (Section 23.3), carbon nanotubes are very good candidates for a synergistic approach in intumescent systems.

23.4.1 Intumescent systems – synergism between ammonium polyphosphate (APP) and carbon nanotubes

Example in thermoplastic polyurethane (TPU)

Bourbigot *et al.* (2009) recently studied nanocomposites and their ability to be fireproof, with or without conventional flame retardants. This research discussed thermoplastic polyurethane (TPU). Samples of TPU–CNT (2 wt%) were produced using an internal mixer at 180 °C under nitrogen flow to avoid oxidation of polymer. Dispersion is qualified through transmission electron microscopy. It appeared that CNTs were evenly dispersed in matrix, and many single CNTs could be observed. Then, the fire properties are evaluated.

First, a cone calorimeter test confirmed that the presence of CNTs in TPU decreased the HRR of the material by 50%. Nevertheless, LOI (limit of oxygen index) and UL94 class were not enhanced (Section 23.1.3).

The same cone calorimeter test was performed on a blend containing 30 wt% of APP in TPU (TPU–APP) and in a second test less than 1 wt% of APP was replaced by CNTs (TPU–APP–CNT). (Composites are produced by the process mentioned above: in an internal mixer at 180 °C.)

The development of an intumescent layer (TPU–APP and TPU–APP–CNT) permits a decrease by 75% of the peak of HRR (pkHRR). Note that the substitution of APP by CNTs is not beneficial in terms of pkHRR, but from the 200s, HRR of TPU–APP–CNT is close to zero compared to TPU–APP, and the total HRR is lower (29 MJ/m² vs. 36 MJ/m²). This can be assigned to the higher quality of the char developed with CNTs, but the LOI of TPU–APP (30 vol.%) was not improved by the substitution of APP by CNTs. This led to a V0 rating at 3.2 mm in the UL94 test. TPU–APP exhibits a V2 rating without CNTs.

It is also important to note that incorporation of 30 wt% of APP provides the development of an intumescent layer when undergoing a heat flux. This intumescent char exhibits small holes at the surface but the substitution of a portion of APP by CNTs makes it more cohesive, i.e. without holes. Thus, there is a synergistic effect of CNTs with APP, leading to a compound with enhanced FR properties for a reduced total filler loading.

To confirm this result, a similar study was completed for polypropylene.

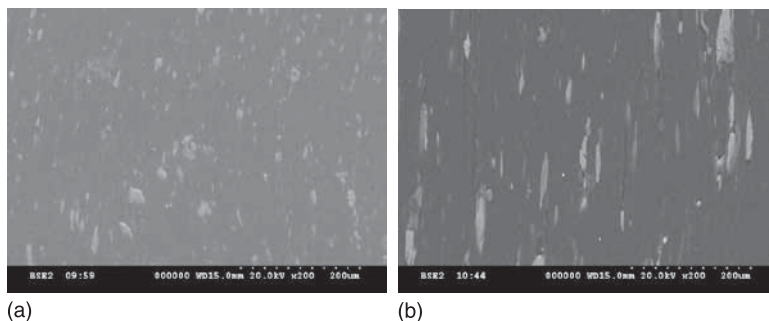
Example in polypropylene (PP)

The synergistic approach of CNTs in FR compounds has been used in polypropylene (PP). Two compounds were prepared, both by twin-screw extrusion following specific process parameters (screw profile, temperature profile), designed to achieve a high level of dispersion of carbon nanotubes.

The first compound contained only APP (PP–APP) and the second contained the same amount of APP plus less than 2 wt% of CNTs. The total filler loading rate for both samples remains below 20%. Once the materials were extruded, two types of samples were produced:

- 12.5 × 130 × 3.2 mm³ bars produced via injection moulding (material temperature set at 270 °C, and mould temperature set at 40 °C) to study fire resistance via the UL94 test at 3.2 mm of thickness and perform SEM (scanning electron microscopy) observations on the surface of these samples (see Fig. 23.14).
- 12.5 × 130 × 2 mm³ bars produced via compression moulding (190 °C, 150 bar) to study FR behaviour via the UL94 test at 2 mm of thickness and perform SEM observations on the surface of these samples (see Fig. 23.15).

The first analysis was the SEM observation prior burning test on injected samples. In the PP–APP blend (Fig. 23.14 (a)), we can see small particles of APP spread quite homogeneously in the matrix. In the PP–APP–CNT blend (Fig. 23.14 (b)), particles of APP seem to be bigger and their shape is highly oriented toward



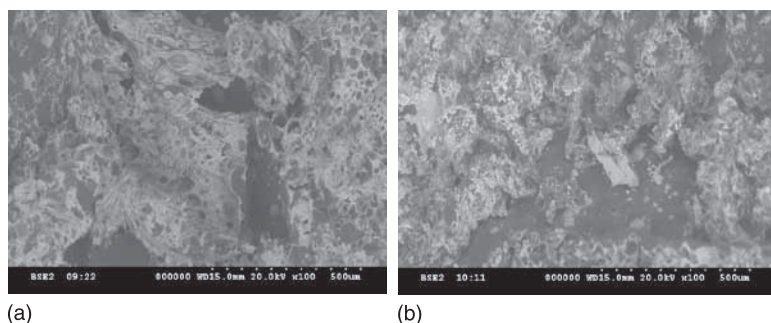
23.14 SEM images of surface of (a) PP–APP blend and (b) PP–APP–CNT blend.

injection flow. This orientation is less visible in the PP–APP blend. This difference in particles' size (i.e. dispersion) and orientation may be attributed to the increase of viscosity brought about by addition of CNTs.

The first test which was done to characterize the flame-retardant properties of these two samples was the vertical UL94 test on samples with a thickness of 3 mm. Both materials (with and without CNTs) were classified V0. As no difference in fire behaviour could be seen for such a thickness between the two samples, we chose to decrease the thickness (that is the reason why 2 mm thick samples were produced). Indeed, it is well known that the thickness is a great influence on the result of the UL94 test. The thicker the sample, the more difficult it is to ignite it during the test. Furthermore, in many applications, legislation requires UL94 V0 material for a thin sample (for example, in cables and wires, the required thickness can be 0.8 mm). Some 2 mm of thickness was thin enough to highlight a difference in behaviour between the two materials. Indeed, in this case, the PP–APP blend just reached V2 classification. Times of burning are short, but flaming droplets occurred and ignited cotton, while the PP–APP–CNT blend reached V0 (short burning times, small flames and no flaming drops). These results are already enough to show a synergistic effect of CNT when added with APP. Indeed, for the same amount of APP, the addition of a very small quantity of CNTs enhances the FR properties compared to the sample with APP only.

At the end of the test we collected the burnt samples (samples of 2 mm of thickness which showed different FR properties) and performed new SEM observations (see Fig. 23.15). We can see a structure with lots of holes in the char layer formed on PP–APP blend (Fig. 23.15 (a)), which is typical of an intumescent system. We can also see some agglomerates of needles. We can assume that these needles could be the result of some kind of 'crystallization' of phosphoric acid coming from the degradation of APP at high temperature.

When CNTs are added to the formulation (PP–APP–CNT blend, Fig. 23.15 (b)), the structure of the char layer is modified. The structures seems to be different



23.15 SEM images of surface of the char layer after burning test on (a) PP–APP blend and (b) PP–APP–CNT blend.

(the holes are less numerous and smaller) and we could not see any needles. So it seems that CNTs really act on the structure of the char layer. Today, further investigation is needed for a better understanding of the mechanisms involved.

In the case of polypropylene, a combination of CNTs with APP brings enhanced FR properties. Further study must be done to understand completely the action of CNTs in an intumescent system.

CNTs can be used to improve the flame-retardant properties of polymers in combination with ammonium polyphosphate in intumescent systems (to protect plastics in bulk). As they enhance the FR properties of the polymer, they can be considered synergist as FR properties are enhanced compared to a sample with the same loading of APP without this nanofiller. Another flame-retardant application using CNTs can be the development of flame-resistant coatings, as long as they show specific interaction with the binder.

23.5 Carbon nanotubes in flame-resistant coatings

23.5.1 Special affinity between CNTs and silicone

As we have already demonstrated, the dispersion of nanofillers in the polymer matrix is crucial (Section 23.3.2). The better the dispersion, the better the FR properties. In many cases, poor dispersion results in agglomeration or phase separation, leading to a dramatic loss of the materials' properties. To overcome this problem, a number of strategies have been developed with various degrees of success. They usually come at a high price, due to the necessity of modifying the surface of the filler.

In joint research, Nanocyl and Professor Dubois (University of Mons, Belgium) developed a combination of an optimized carbon nanotube which has been specifically developed for its strong interaction toward polysiloxane chains and a proprietary mixing method. The CNT used for this application was a unique multi-walled CNT which has been upgraded to strengthen the interface between

the CNT surface and polydimethylsiloxane (PDMS). This unique combination turns out to be the most efficient approach to impart new key properties to the silicone matrix. Viscometric, rheological and theoretical studies were performed that demonstrate the remarkable potential of dispersing a low amount of carbon nanotubes in silicone, paving the way to unexpected applications, e.g. in the field of fire endurance. These properties all rely on the nature of the nanotube–silicone interfacial interactions, which are dominated by additive CH- π interactions between the methyl groups of the polymer and the nanotube surface.

PDMS is the most common silicone elastomer owing to its ease of fabrication and advantageous chemical/physical properties, such as low surface energy, low glass transition temperature and high chain mobility. Currently, to compensate for their poor mechanical properties, silicone materials have to be reinforced by incorporation of particulate materials, silica being the most commonly used filler. However, this reinforcement still requires a relatively high mass fraction of minerals (> 10 wt%). Over the past few years, much attention has been paid to polymer nanocomposites, which represent a rational alternative to conventional filled polymers. The key point for the improvement of properties as diverse as mechanical, thermal, and barrier performance is the effective/individual dispersion of the nanofillers in the matrix. To reach this objective, the type of nanofiller, filler size and the nature of the interface formed within the matrix all have to be optimized. In this context, carbon nanotubes are of prime interest; however, they have a strong tendency to agglomerate in densely packed bundles, and their dispersion in polymers still remains a major challenge.

Classically, unfilled PDMS is a very fluid liquid. Upon adding CNTs to the unfilled matrix via mechanical blending, a huge increase in viscosity is observed, which results in a PDMS matrix that has totally lost its capacity to flow. Quite interestingly, CNTs also act as rheo-thinning agents, allowing brush-paint (poorly filled) PDMS with a very low filler content, prior to the cross-linking reaction, for any orientation of the substrate.

For comparison, PDMS filled with a needle-like magnesio-silicate nanofiller (natural sepiolite clay), or a commercially available organo-modified layered alumino-silicate clay (Montmorillonite, from Southern Clay Products, Texas: Cloisite 30B[®]) were also prepared and analyzed. From the measurements, a viscosity value of 4980 cP can be extracted for the neat matrix. (This measurement was realized in a cone-plan viscosimeter at 25 °C.) Significant differences are found between the three types of nanofillers. A very slight increase in viscosity was observed as the Cloisite 30B[®] content was increased. However, the values remain very low and do not exceed 5900 cP for a solid fraction as high as 5 wt%. In the case of natural sepiolite- filled PDMS, the increase in viscosity is more pronounced than for Cloisite 30B[®], with values reaching 7940 cP for 5 wt% loading. The most spectacular effect is observed with CNTs: the viscosity values strongly increase between 0.1 wt% (+ 25%), and 0.3 wt% (+ 280%), for which a value of 14000 cP was reached.

The rheological behavior of PDMS filled with CNTs has been studied in more detail by following viscosity as a function of shear rate for two nanofiller loadings (0.5 and 0.7 wt%). For the unfilled system, the viscosity is independent of shear rate over a broad range (5–200 s⁻¹). On the contrary, the filled systems exhibit two different regimes. As long as the shear rate is low (< 40–50 s⁻¹), the viscosity decreases with increasing shear rate; then, for higher shear rate values, the viscosity reaches a constant, minimum value. Clearly, the nanofilled silicone behaves like a thinning fluid.

The strength or density of filler–polymer interactions can be correlated to the amount of PDMS chains adsorbed per gram of CNT after a solvent extraction. This quantity is determined via ‘bound rubber’ tests. In this test the percentage of silicone resin attached to the CNT is measured.

Only PDMS composites filled with natural sepiolite or CNT show a significant amount of adsorbed polymer at the nanofiller surface after extraction. As is the case in the viscosity study, the more pronounced effects are observed with the carbon nanotubes. For example, 2.5 g of polymer per gram of nanofiller are adsorbed when natural sepiolite is the filler while the value increases to more than 20 g per gram of CNT as filler.

Since the nature of PDMS–CNT interactions are fundamental for the efficiency of the filler in reinforcing the polymer matrix, modelling studies (based on molecular dynamics (MD) simulations) were performed to assess at the microscopic level the adsorption properties of PDMS on the surface of carbon nanotubes. The simulations were carried out on a model system consisting of an armchair single-walled carbon nanotube that interacts with a single PDMS chain (ranging in size from 12 to 200 repeating units). As initial structures in the MD simulations, the polymer chains were built according to an elongated helical-like conformation (Khorasami *et al.*, 2005) and brought in van der Waals contact to the nanotube. Structure obtained after a 400 ps simulation at 300 K was in the NVT canonical ensemble. It can be clearly seen that the polymer chain completely wraps around the CNT surface. A detailed analysis of the atomic spatial distribution shows that the PDMS chains organize to form a regular radial pattern from the CNT surface: (1) a first layer of methyl groups pointing towards the CNT; (2) the oxygen and silicon atoms belonging to the polymer backbone; and (3) an outer layer formed by the remaining methyl groups. The calculations show that about one methyl group out of two binds to the CNT surface (i.e. belongs to the first layer around the CNT). Adsorption energy per repeat unit converging to $\sim 2.6 \pm 0.1$ kcal/mol in the longest chains can be extracted by averaging over the MD trajectories after equilibration. Such physical adsorption of the PDMS chains onto the CNT is mostly triggered by CH- π interactions (Nishio *et al.*, 1998) between the PDMS methyl groups and the π -electron-rich surface of the carbon nanotube. CH- π interactions are weak hydrogen bonds; they are largely due to dispersion forces and partly to charge-transfer and electrostatic forces. The calculated adsorption energy per repeating unit corresponds to roughly

three times the typical value for a CH- π interaction, which is consistent with the picture above of one methyl group per repeating unit binding to the surface. It is worth stressing that the energy destabilization induced by the change in conformation upon going from the isolated PDMS chain to the chain wrapped around the CNT is small (less than 0.6 kcal/mol per repeating unit), which, together with the presence of a high density of methyl groups amenable to CH- π bonding, explains the unique adsorption properties of PDMS on the CNT surface (Beigbeder *et al.*, 2008).

23.5.2 Fire-resistant paint

These novel reinforced PDMS exhibit a number of remarkable properties. For flame-retardant applications, they can be used as a protective coating. In order to have an idea of their performance, fire testing was performed. This test is an adaptation of ISO 2685 which evaluates the fire endurance of aluminium plates coated with a PDMS layer containing CNTs. The principle of the test is to measure the temperature reached by the unprotected side of the plate versus time, meanwhile the coated side is exposed to a flame of 1050 °C (60 kW m⁻²). The goal is to determine the heat shield properties of the coating. The better the shield properties are, the cooler the aluminium plate is. Thanks to this barrier, the plate will remain at a temperature lower than the one which would involve a loss of mechanical properties (load bearing).

So during this test, the temperature of the unprotected plate increases to 380 °C within a few minutes, which causes the fast destruction of the plate. The fire endurance times (of the order of 80 min.) of the plates coated with the PDMS–CNT mixture are much longer compared to those coated with unfilled PDMS (around 15 min) and the maximum temperature reached in the presence of the nanofillers (290 °C) is much lower than the corresponding value for neat PDMS (405 °C). These results unambiguously demonstrate the significant improvement in fire resistance of substrates protected by CNT-filled silicone. This can be attributed to the thermal percolation phenomenon where the number of thermal conductive paths increased with nanofiller content and to a very high thermal conductivity of the carbon nanotubes. Interestingly, the control of the CNT–silicone interface permits preparation of this type of formulation for very varied use, such as a sprayable paint for protecting foams or paintable coatings for composite protection and with very different silicone types.

A similar test, UL1709, has been performed on stainless steel and in this case the temperature did not go over 400 °C (the final higher temperature is due to the fact that stainless steel has a higher thermal conductivity than aluminium). So these tests demonstrated the very good ability of this PDMS–CNT coating to protect metal substrates from fire.

Further investigations have been done to show that the PDMS–CNT coating can also be used as a flame-resistant barrier on wires and cables. Samples of

electric cables were coated with the CNT–silicone dispersion (a 150 micron layer). These samples pass the UL94V0 test and the cable fire Test easily (Fig. 23.16 (a) and Fig. 23.16 (b)). The coated cable stops burning just in few seconds, as the polymer layer of the unprotected sample just burns entirely (the copper wires are fully visible at the end of the test).

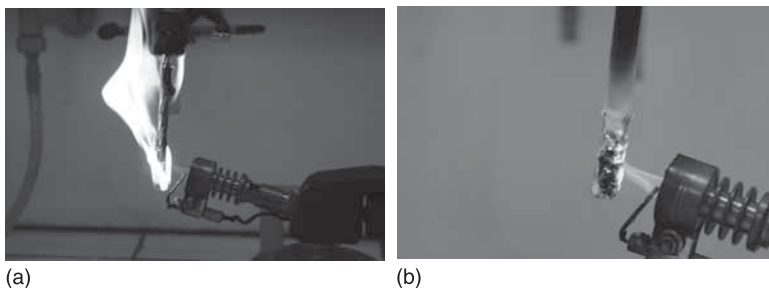
Based on these impressive results, it was decided to test the performance of the PDMS–CNT coatings on foams. Indeed, it has always been very difficult to produce flame-retardant foams which pass UL94 at V0. But it appears in this case that flexible foams, both olefinic or polyurethane (PU), can be spray coated or impregnated with PDMS–CNT paint. When spray coated, only the outer foam shell will be protected but nevertheless the foam will not burn. When a flame is applied to the unprotected foam, it just burns very quickly (the sample is totally destroyed in a few seconds). The same protocol is applied to a coated sample, which does not catch fire at all.

The very good affinity between PDMS and CNT (thanks to CH- π interactions) enables development of a coating with impressive flame-retardant properties. This coating can be applied to very different types of substrates like metal, plastic (cables and wires) or foams.

23.6 Conclusion

Understanding the wide range of fire regulations is essential for work in the flame retardancy field. Indeed, we have seen that the structure of regulations is complex, and highly dependent on the final application (railway, cable industry, buildings) and on the country (regulations differ from France to Germany, for example). Fortunately, this is moving toward uniformization, at least in Europe, thanks to Euroclasses, applicable today in the construction field.

From a technical point of view, the understanding of fire behaviour is also essential, of course, to develop FR compounds. We have explained that the fire mechanism is an endless cycle: the heat source involves the degradation of the



23.16 Cables fire test. (a) The unprotected cable burns completely; (b) with a 150 μm PDMS–CNT coating, the cable stops burning immediately, even after 30 minutes of exposure to the burner.

polymer, the degradation products may be highly reactive and constitute a fuel which burns and creates the flame, and the flame heats the polymer which continues to degrade. To counter the fire, the solution is to break this cycle. This can be done in two points, either in the condensed phase or the gaseous phase. It is important to note that the intumescent system (formation of a protective layer in the condensed phase during fire) is the most interesting, as it can handle very high temperatures. Concerning nanocomposites, carbon nanotubes can be used in the condensed phase. We have explained that adding CNTs to a polymer enhances its flame-retardant properties. More precisely, CNTs induce a significant decrease of the heat release rate (in the cone calorimeter test) due to the formation of a protective layer. This layer will limit the volatilization of degradation products and trap radical species which will induce cross-linking reactions to form a more important and cohesive solid residue at the end of the fire test. To have the best char formation, i.e. the best fire properties, it has been demonstrated that the quality of dispersion of the nanotubes in the polymer matrix is essential. With poor dispersion, the char residue will present cracks or holes in the best case, or even just discrete islands. This char layer will not be as protective.

Nevertheless, although carbon nanotubes do have a real positive influence on the fire properties of a polymer, they do not permit it to pass the fire test as a single FR additive, as in the UL94V test, for example. That is the reason why they can be used as synergistic agents in combination with ammonium polyphosphate in an intumescent system.

We have shown that adding a few percentage of this flame-retardant additive brings enhanced FR properties for a lower total filler loading, so a better retention of mechanical properties of the matrix. Such a system has been developed today in TPU and PP.

Beside this, CNT can also be used to develop flame-retardant coatings with silicone, due to their great affinity with methyl group of PDMS. This paint forms a protective layer when in contact with a flame. This layer acts as a heat shield and prevents the substrate from melting and degradation. Such paints can be applied to many types of substrates like aluminium or stainless steel parts, cables and wires, and even to foams.

So today, it is clear that CNT nanocomposites have an application in flame retardancy. Nevertheless, the chemical or physical interactions which would explain their synergistic behaviour are still not very well understood.

23.7 References

- Beigbeder A., Linares M., Devalckenaere M., Degée Ph., Claes M., Beljonne D., Lazzaroni R., Dubois Ph. (2008). CH- π interactions as the driving force for silicone-based nanocomposites with exceptional rheological and thermal properties, *Advanced Materials*, 20, 1003–1007.
- S. Bourbigot, S. Duquesne (2006) Fire retardant polymers, recent developments and opportunities *J. of Mater. Chem.*, 17, 2283–2300.

- S. Bourbigot, S. Duquesne, G. Fontaine, T. Turf, S. Bellayer, Polymer nanocomposites with and without conventional flame retardants: reaction to fire and synergy, available at: <http://www.nanocyl.com/en/CNT-Expertise-Centre/Technical-Papers/Thermal-Properties-of-CNTs/Polymer-Nanocomposites-With-and-Without-Conventional-Flame-Retardants-Reaction-to-Fire-and-Synergy> (accessed December 2009).
- Comodo, France (2009), available from: <http://www.protectionincendie.com/statistiques-incendie.html> (accessed 24 November 2009).
- F. Gao, G. Beyer, Q. Yuan (2005) A mechanistic study of fire retardancy of carbon nanotube/ethylene vinyl acetate copolymers and their clay nanocomposite, *Polymer Degradation and Stability*, 89, 559–564.
- M. Jimenez, S. Duquesne, S. Bourbigot (2006) *Ind. Eng. Chem. Res.*, 45, 4500–4508.
- T. Kashiwagi, F. Du, K. I. Winey, K. M. Groth, J. R. Shields, S. P. Bellayer, H. Kim, J. F. Douglas (2005) Flammability properties of polymer nanocomposites with single-walled carbon nanotubes' dispersion and concentration, *Polymer* 46, 471–481.
- T. Kashiwagi, M. Mu, K. Winey B. Cipriano, S. R. Raghavan, S. Pack, M. Rafailovich, Y. Yang, E. Grulke, J. Shields, R. Harris, J. Douglas (2008) Relation between the viscoelastic and flammability properties of polymer nanocomposites, *Polymer*, 49, 4358–4368.
- T. Khorasami, H. Mirzadeh, Z. Kermani (2005) Wettability of porous PDMS surface: morphology study, *App. Surf. Sci.*, 242, 339–345.
- F. Laoutid, L. Bonnaud, M. Alexandre, J.-M. Lopez-Cuesta, P. Dubois (2009) New prospects in flame retardant polymer materials: from fundamentals to nanocomposites, *Mat. Sci. and Eng.*, R63, 100–125.
- Magma Firestop (2009) Legislation and standards, available from: <http://www.magma-int.com/index.php?id=591> (accessed 24 November 2009).
- M. Nishio, M. Hirota, Y. Umezawa (1998) *The CH/ π Interaction: Evidence, Nature and Consequences*, New York: Wiley VCH.
- S. Peeterbroeck, F. Laoutid, J.-M. Taulemesse, F. Monteverde, J.-M. Lopez-Cuesta, J. B. Nagy, M. Alexandre, P. Dubois (2007) Mechanical properties and flame retardant behaviour of ethylene vinyl acetate/high-density polyethylene coated carbon nanotubes nanocomposites, *Adv. Funct. Mater.*, 17, 2787–2791.
- L. Ye, Q. Wu, B. Qu (2009) Synergistic effect and mechanism of multiwalled carbon nanotubes with magnesium hydroxide in halogen-free flame retardant EVA/MH/MWNT nanocomposites, *Polymer Degradation and Stability*, 94, 751–756.

Polymer–carbon nanotube composites for flame-retardant cable applications

G. BEYER, Kabelwerk Eupen AG, Belgium

Abstract: This chapter describes multi-walled carbon nanotubes (MWCNTs) as very efficient flame retardants at low filler contents in ethylene vinyl acetate (EVA). An optimized formulation for flame-retardant insulated wires was developed based on the filler-blend ‘multi-walled carbon nanotubes–organoclays–aluminium trihydrate’. The char was improved and strengthened by the long length/diameter ratio of the MWCNTs, resulting in better flame-retardant performances of the wires.

Key words: aluminium trihydrate, cables, carbon nanotubes, char formation, flame-retardancy, organoclays.

24.1 Introduction

Fire hazards are mainly the combination of different factors including ignitability, ease of extinction, flammability of volatiles generated, amount of heat released on burning, rate of heat release, flame spread, smoke obscuration, and smoke toxicity. The most important factors are the rate of heat release, rate of smoke production, and rate of toxic gas release.¹ An early high rate of heat release causes a fast ignition and flame spread; furthermore, it controls the fire intensity and is much more important than ignitability, smoke toxicity or flame spread. The time for people to escape from a fire is controlled by the heat release rate.² Once a fire starts in a room containing flammable materials, it will generate heat, which can heat up and ignite additional combustible materials. As a consequence, the rate at which the fire progresses increases, because more and more heat is released and a progressive increase of the room temperature is observed. The radiant heat and the temperature can rise to such an extent that all the materials within the room will be easily ignited, resulting in an extremely high rate of fire spread. This point in time, termed *flash-over*, leads to a fully developed fire. Escape from the room will then be nearly impossible, and spread of the fire to other rooms is very likely. When a fire goes to flash-over, all polymers in the fire will release roughly 20% of their weight as carbon monoxide, resulting in too much toxic smoke. Therefore, most people die in big fires, and 90% of fire deaths are the result of fires becoming too big, resulting in too much toxic smoke.³ Fire statistics report more than 12 million fires every year in the United States, Europe, Russia, and China, killing roughly 160,000 people; several hundreds of thousands of people are injured every year. Each year about 5000 people are killed by fires in Europe and more than 4000 people die in

the USA. Direct property losses by fires are roughly 0.2% of the gross domestic product in Europe and the total costs of fires are around 1% of the gross domestic product.⁴ Therefore, it is important to develop well-designed flame-retardant materials to decrease both fire risks and fire hazards and save lives.

Polymers are being used in more and more fields of applications, and specific mechanical, thermal, and electrical properties are required. One further important property is the flame-retardant behavior of polymers, which can be fulfilled traditionally by using intrinsically flame-retardant polymers like poly(vinyl chloride) (PVC) or fluoropolymers, and by flame retardants like aluminium trihydrate (ATH), magnesium dihydroxide (MDH), organic brominated compounds, or intumescent systems based on nitrogen- or phosphorus-based compounds to prevent the burning of such polymers like polyethylene (PE), polypropylene (PP), poly(ethylene-co-vinyl acetate) (EVA), polyamide (PA) or other polymers. However, these flame retardants sometimes exhibit serious disadvantages. Use of aluminium trihydrate and magnesium hydroxide in flame-retardant cables requires a very high portion of these fillers for the applied polymers EVA, PE or PP; filling levels of more than 60 wt% are necessary to achieve a suitable flame retardancy. Clear disadvantages of these filling levels are the high density and the lack of flexibility of end products, the poor mechanical properties, and the problematic compounding and extrusion steps. In Europe, at least, there are reservations about the general use of brominated compounds as flame retardants. Intumescent systems are relatively expensive and electrical requirements can restrict the use of these products.

A new class of materials, called *nanocomposites*, avoids the disadvantages of the traditional flame-retardant systems. Generally the term nanocomposite describes a two-phase material with a suitable nanofiller (usually modified layered silicates like montmorillonites (organoclays) or carbon nanotubes) dispersed in the polymer matrix at the nanometer (10^{-9} m) scale. Compared with pure polymers, the corresponding nanocomposites show tremendous improvements; the content of nanofillers within the polymer matrix is usually between 2 wt% and 10 wt%. The most important properties improved by nanocomposites are mechanical properties such as tension, compression, bending, and fracture; barrier properties like permeability; and solvent resistance, translucence, and ionic conductivity. Other highly interesting properties exhibited by these polymer nanocomposites concern their increased thermal stability and flame retardancy at very low filler levels.^{5–7} The low filler content in nanocomposites for improved thermal stability is highly attractive to the industry because the end products can be made cheaper and easier to process. Beyer discusses these improvements by nanocomposites in detail.⁸

Beyer⁹ reported at an international flame retardancy conference in 2002 for the first time on the flame retardancy of carbon nanotubes. The first convincing explanation of the flame-retardant behavior of carbon nanotubes was proposed then by Kashiwagi *et al.*^{10–12} Several of these papers described how single- and multi-walled carbon nanotubes enhance the thermal stability of polymers without

using any organic treatment or additional additives. The carbon nanotubes were at least as effective flame retardants as organoclays. PP and PMMA were investigated and the dispersion of the nanotubes within the polymer matrix was the important key parameter for good flame retardancy. Kashiwagi reported that the ideal structure of a protective surface layer (consisting of clay particles and some char) was net-like and had sufficient physical strength not to be broken or disturbed by bubbling. The protective layer should remain intact throughout the entire burning period. The formation of a continuous, network-structured protective char was easiest with high aspect ratio nanoscale particles. Kashiwagi *et al.*¹³ pointed out that in general, a variety of highly extended carbon-based nanoparticles, such as single- and multi-walled carbon nanotubes as well as carbon nanofibres, will form this kind of a network if the nanofillers formed a network structure in the polymer matrix, so that the material as a whole behaves rheologically like a gel. Also Schartel *et al.*¹⁴ reported on the flame retardancy of MWCNTs in PA-6; again, the increased melt viscosity of the nanocomposites and the fibre-network character were the dominant factors influencing the fire performance.

This chapter will review in detail results of nanocomposite-based organoclays and carbon nanotubes and the synergistic effects of these fillers with micro-sized aluminium trihydrate as a traditional flame retardant for cable applications.

24.2 Carbon nanotube-based nanocomposites

24.2.1 General properties of carbon nanotubes

Carbon nanotubes (CNTs) are tubular derivatives of fullerenes. They were first observed in arc discharge experiments, and exhibit properties, which are quite different from those of the closed cage fullerenes such as C₆₀, C₇₀ and C₇₆, etc. Special topologies are responsible for the unique and interesting properties of CNTs. As novel carbon materials, CNTs are of great interest in the field of material science research. Due to their high mechanical strength, capillary properties, and remarkable electronic structures, a wide range of potential uses is reported. Typical applications for CNTs are supports for metals in the field of heterogeneous catalysis, material for hydrogen storage, as composite materials in polymer science^{15–16} and for immobilization of proteins and enzymes. Several techniques like arc discharge, laser ablation and catalytic methods and others have been developed for the production of CNTs.¹⁶ Many material science researchers and also companies (Nanocyl, Hyperion Catalysis International, Bayer Material Science, Arkema) are working on the development of methods for large-scale production of CNTs to realize their speculated applications. CNTs can consist of one (single-walled carbon nanotubes, SWCNTs) or more (multi-walled carbon nanotubes, MWCNTs) cylindrical shells of graphitic sheets. Each carbon is completely bonded to three neighboring carbon atoms through sp² hybridization to form a seamless shell. CNTs can have a very high aspect ratio, above 1000. It

is reported¹⁷ that polymer degradation can be retarded by CNTs as measured by thermogravimetric analysis. In PVOH, a loading level of 20 wt% MWCNTs shifts the polymer degradation to higher temperatures.

24.2.2 Synthesis and purification of CNTs

Crude MWCNTs and SWCNTs were produced by catalytic decomposition of acetylene on Co-Fe/Al(OH)₃ catalysts.¹⁸ The CNTs contained catalysts and other by-products. The catalysts and support contents of the CNTs samples are shown in Table 24.1. Crude MWCNTs contained Co, Fe and alumina. Purified MWCNTs were synthesized from crude MWCNTs by dissolution of the catalyst support in concentrated NaOH, dissolution of the metal catalyst in concentrated HCl, drying at 120 °C in an air oven and additionally drying at 500 °C under vacuum. Crude SWCNTs contained Co and MgO. Purified SWCNTs were synthesized from crude SWCNTs by dissolution of the catalyst support in concentrated HCl, purification by air oxidation at 300 °C and then drying at 120 °C in an air oven.

24.2.3 Flammability of poly(ethylene-co-vinyl acetate) multi-walled carbon nanotube (EVA–MWCNT) compounds and EVA–MWCNT–organoclay compounds

It was possible to investigate for the first time worldwide the flame-retardant properties of carbon nanotube compounds by cone calorimeter.^{9,18} All compounds were melt-blended in a Brabender mixing chamber. EVA was molten within 3 minutes; then MWCNTs were added and mixed for an additional 7 minutes. The compounds were pressed to plates at 180 °C, 200 bar for 5 minutes. It is evident from the results in Table 24.2 that all the filled polymers had improved flame-retardant properties. For EVA and the EVA-based nanocomposites containing 2.5 phr of filler, the PHRR decreased as follows: EVA > organoclays ~ purified MWCNTs. For EVA and EVA-based composites containing 5.0 phr filler, the peak heat release rate (PHRR) decreased as follows: EVA > organoclays

Table 24.1 Properties of MWCNTs

Sample	Nanotubes		Catalyst		Support	
	Length (µm)	Diameter (nm)	Co (wt%)	Fe (wt%)	Al ₂ O ₃ (wt%)	MgO (wt%)
Crude MWCNTs	ca. 50	5–15	0.3	0.3	19	–
Purified MWCNTs	ca. 50	5–15	0.2	0.3	0.2	–

Table 24.2 Peak of heat release rates at heat flux = 35 kW/m² for various compounds with organoclays and multi-walled carbon nanotubes

	Sample (parts resin)	EVA (phr)	MWCNT (phr)		Organoclay	PHRR (kW/m ²)
			Purif.	Crude		
EVA	100.0	–	–	–		580
1 ^a	100.0	2.5	–	–		520
2 ^a	100.0	5.0	–	–		405
3 ^a	100.0	–	–	2.5		530
4 ^a	100.0	–	–	5.0		470
5 ^{a,b}	100.0	2.5	–	2.5		370
6a ^a	100.0	–	5.0	–		403
6b ^c	100.0	–	5.0	–		405

Note: EVA: Escorene UL 00328 with 28 wt% vinyl acetate content.

Organoclay: Nanofil 15 (dimethyl ditallow exchanged montmorillonite).

^a The screw velocity was 45 rpm and the mass temperature was 136 °C.

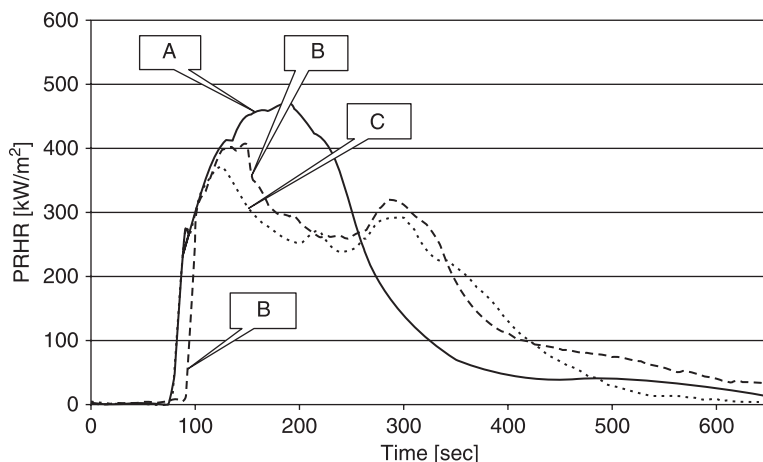
^b The nanotubes and the organoclay were premixed before their addition.

^c The screw velocity was 120 rpm and the mass temperature was 142 °C.

> purified MWCNTs = crude MWCNTs. Crude MWCNTs were as effective in the reduction of PHRR as purified MWCNTs. Increasing the filler content from 2.5 to 5.0 phr caused an additional flame-retardant effect and this improvement was most significant when purified or crude MWCNTs were used. A synergistic effect for flame retardancy between MWCNTs and organoclays was observed for the nanocomposite containing 2.5 phr of purified MWCNTs and 2.5 phr of organoclays (Fig. 24.1). The latter sample was found to be the best flame-retardant compound. The variation of the screw velocity from 45 rpm (sample A) to 120 rpm (sample B) did not change the flame-retardant properties for the composites containing 5.0 phr of crude MWCNTs. There was also no reduction in time to ignition for the MWCNT-based EVA composite, in contrast to the only organoclay-based EVA composite, which undergoes an early thermal degradation of the quaternary ammonium compound within the galleries of the organoclay.¹⁹

24.2.4 Crack density and surface results of charred MWCNT compounds

For flame-retardant EVA-based composites containing 5 phr of fillers (Table 24.2), the crack density increased in the order of purified MWCNTs < organoclays. A very important synergistic effect reducing the crack density to a very low level was observed for the nanocomposite containing both 2.5 phr purified MWCNTs and 2.5 phr organoclays (Figs 24.2 (a)–(c)). The synergistic effect for

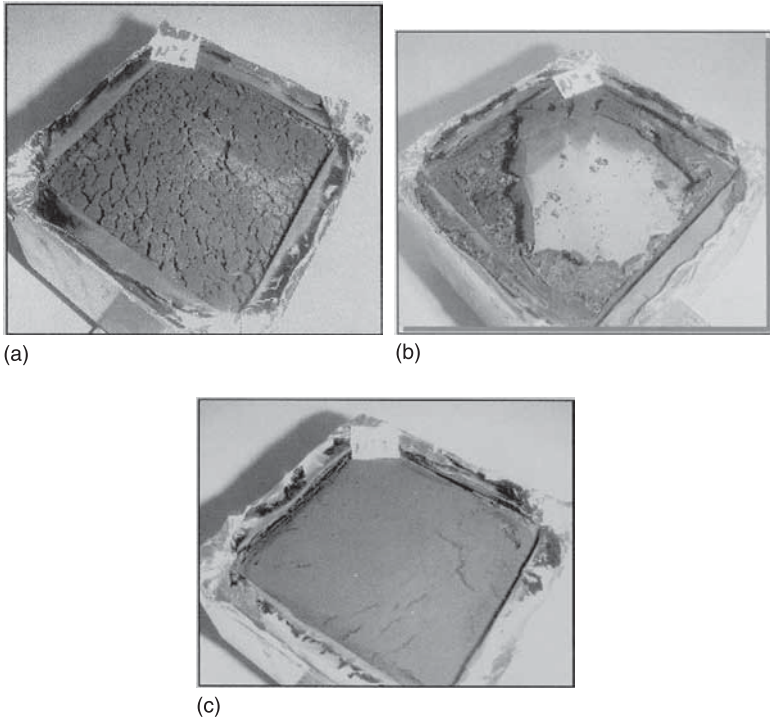


24.1 Peak of heat release rates for various EVA-based compounds with organoclays and multi-walled carbon nanotubes. A, EVA + 5.0 phr organoclays. B, EVA + 5.0 phr pure MWCNTs. C, EVA + 2.5 phr organoclays + 2.5 phr pure MWCNTs. Organoclay: Nanofil 15 (dimethyl ditallow exchanged montmorillonite). Heat flux = 35 kW/m². (From reference 18; John Wiley & Sons Limited. Reproduced with permission.)

improved flame retardancy by the filler combination MWCNTs and organoclays can be explained by the improved closed surface. The char acted as an insulating and non-burning material with reduction of emission of volatile products (fuel) into the flame area. The fewer cracks present, the better was the reduction of emission of fuel and therefore the reduction of PHRR. The fillers played an active role in the formation of this char, but obviously the MWCNTs, with their long aspect ratio, could strengthen it and made it more resistant to mechanical cracking.

24.2.5 Flammability of low-density polyethylene (LDPE) carbon nanotube compounds

Compounds of SWCNTs and MWCNTs in LDPE (BPD 8063 from INEOS) were melt blended in a Brabender mixing chamber according to the formulations indicated in Table 24.3 and Table 24.4. The corresponding cone calorimeter measurements are shown in Figs 24.3 and 24.4. The results from the cone measurements of different carbon nanotubes in LDPE demonstrated that SWCNTs did not act as flame retardants in LDPE. MWCNTs acted as flame retardants in LDPE with no reductions on time to ignition (in contrast to



24.2 (a) EVA with 5 phr organoclays after combustion. From reference 18; John Wiley & Sons Limited. Reproduced with permission. (b) EVA with 5 phr pure MWCNTs after combustion. From reference 18; John Wiley & Sons Limited. Reproduced with permission. (c) EVA with 2.5 phr pure MWCNTs and 2.5 phr organoclays after combustion. EVA: Escorene UL 00328 with 28 wt% vinyl acetate content. Organoclay: Nanofil 15 (dimethyl ditallow exchanged montmorillonite). From reference 18; John Wiley & Sons Limited. Reproduced with permission.

organoclays), and crude MWCNTs showed similar reductions for the PHRR as purified MCNTs.

24.3 Cable with the multi-walled carbon nanotube (MWCNT)–organoclay–aluminium trihydrate (ATH) flame-retardant system

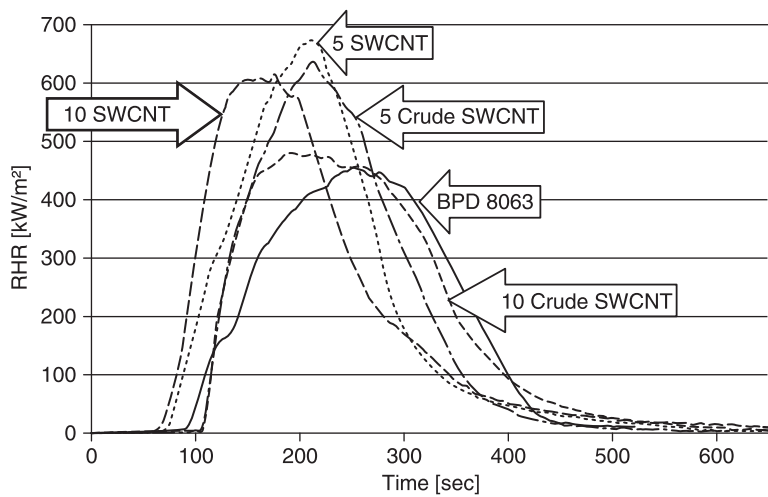
It was of interest to transform the results for the synergistic filler-based FR system ‘MWCNTs–organoclays’ into real products.²⁰ To produce a flame-retardant insulated wire by a real cable production extruder, a minimum of approximately

Table 24.3 PDE filled with SWCNTs

Sample description	LDPE (wt%)	SWCNT (wt%)	
		Purified	Crude
BPD 8063	100.0	–	–
5 SWCNT	95.0	5	–
10 SWCNT	90.0	10	–
5 Crude SWCNT	95.0	–	5
10 Crude SWCNT	90.0	–	10

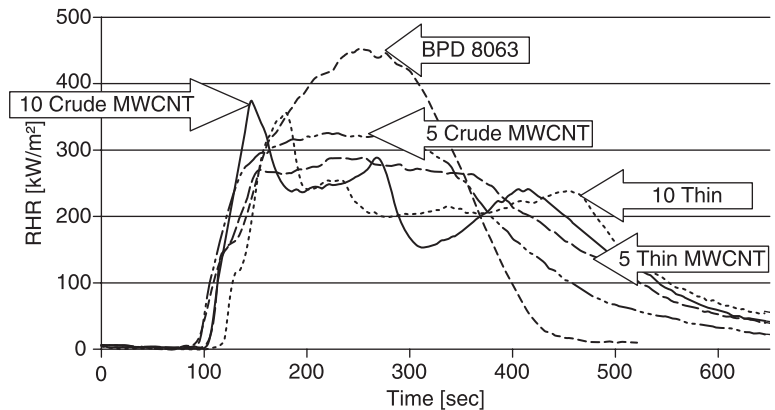
Table 24.4 LDPE filled with different MWCNTs

Sample description	LDPE (wt%)	MWCNT (wt%)	
		Purified	Crude
BPD 8063	100.0	–	–
5 MWCNT	95.0	5	–
10 MWCNT	90.0	10	–
5 Crude MWCNT	95.0	–	5
10 Crude MWCNT	90.0	–	10



24.3 Heat release rates for SWCNTs in LDPE. Heat flux = 35 kW/m². From reference 18; John Wiley & Sons Limited. Reproduced with permission.

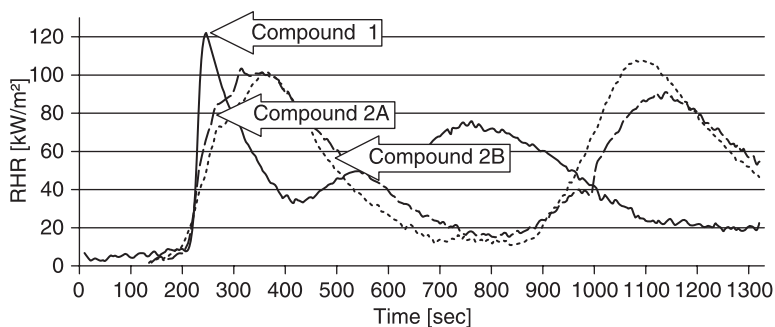
60 kg of compound was needed to fill the extruder and to run a small insulated wire production. It was checked whether the filler blend system MWCNTs–organoclays could be transformed to a real cable compound without processing problems.²⁰ A well-running only organoclay-based cable compound named compound 1 was used, and the weight ratio between these two fillers was changed stepwise. The sum of both fillers always remained constant (Table 24.5) within the cable compounds. Compounding was done on a twin-roll mill, and the reductions of PHRRs for the three compounds were measured (Fig. 24.5). The results clearly indicated that for the filler blend and the only MWCNTs-based compounds, the first PHRR was reduced maximally. The second PHRR was observed at the longest times for the two compounds 2A and 2B, indicating that the chars were less cracked (more stable in time). Therefore a 1:1 blend of MWCNTs and organoclays was used (compound 2A, see Table 24.5 for the cable



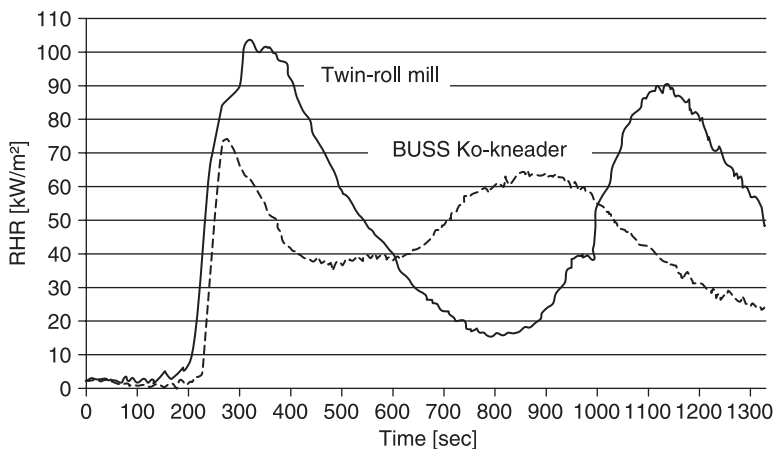
24.4 Heat release rates for MWCNTs in LDPE. Heat flux = 35 kW/m². From reference 18; John Wiley & Sons Limited. Reproduced with permission.

Table 24.5 Blends of MWCNTs and organoclays in cable compound formulations

Compound	Composition
1	Technical cable compound (EVA/PE/ATH/organoclay/processing additives)
2A	Same formulation as compound 1, but substitution of 50% organoclay by the same amount of MWCNTs
2B	Same formulation as compound 1, but substitution of 100% organoclay by the same amount of MWCNTs



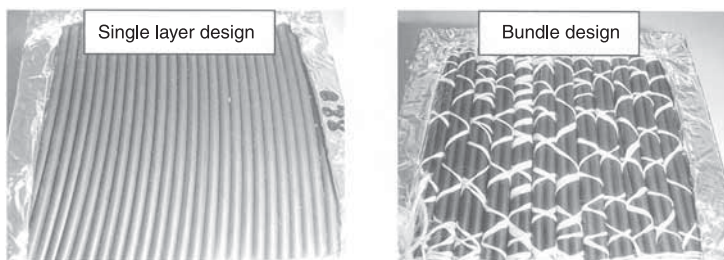
24.5 Heat release rates for compounds made by twin-roll mill with different filler blends MWCNTs–organoclays. Heat flux = 35 kW/m^2 . From reference 20; John Wiley & Sons Limited. Reproduced with permission.



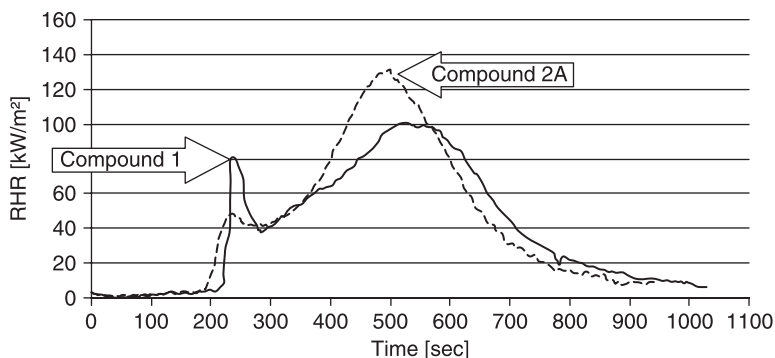
24.6 Heat release rates for cable compound 2A with the filler blend MWCNTs–organoclays by twin-roll mill and BUSS Ko-kneader. Heat flux = 35 kW/m^2 . From reference 20; John Wiley & Sons Limited. Reproduced with permission.

compound used). This allowed production of the required quantity of the cable compound. Compounding of the formulation 2A was done on an 11 L/D BUSS Ko-kneader with a 46 mm screw diameter, and 60 kg were produced without any processing problems. Processing on the BUSS Ko-kneader improved the PHRRs compared to those with the corresponding twin-roll mill compounding (Fig. 24.6), may be due to a better dispersion of the fillers.

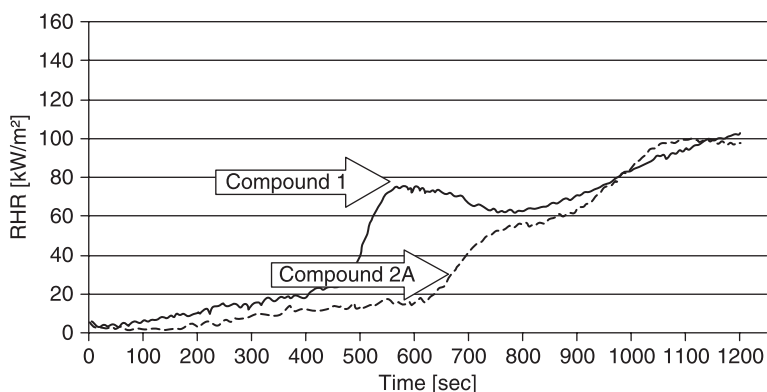
Two insulated wires with identical geometric parameters were produced on a 20-L/D single-screw cable extruder with an 80 mm screw diameter. The diameter of the copper conductor was 1.78 mm, and the wall thickness for the insulation was 0.8 mm. For one wire, the insulation was compound 1 (filler combination of ATH–organoclay) and for the other wire, the optimized compound 2A (filler combination of ATH–organoclay–MWCNTs) was used as insulation. The MWCNT-based compound 2A showed a remarkable increased viscosity over that of the standard nanocomposite compound 1, as indicated by reduced revolutions per minute of the screw and increased power take-up by the extruder motor; a high pressure capillary viscosimeter showed a higher viscosity for the compound 2A for all shear rates up to 3000 s^{-1} obviously due to the high L/D ratio of the MWCNTs and their dispersion at a nanometer level. A small fire test according to IEC 60 332-1 (the insulation was exposed to a Bunsen burner ignition source) was very similar for both insulated wires. No dripping of burning polymer was noted, and the charred lengths were identical. But the char of the insulation made with the compound 2A was far less cracked compared to the char generated from the compound 1. This may be the result of the strengthening effect by the MWCNT, with its very great L/D ratio; proposal of such a mechanism for the function of carbon nanotubes was published recently.²¹ Heat release rates and times to ignition of the two insulated wires were measured using a cone calorimeter. The wires were cut in samples of 10 cm, and the standard cone sample holder was filled with the cable pieces. Twenty-six wires were mounted by building up a single layer of wires with no gap between them and the ends of the wires were not sealed; this mounting was called a ‘single layer design’. Also, four cut wires with no sealing of the ends, simulating anunjacketed cable²² were put together. An aramid fibre binder was used to maintain the integrity of the bundles; this mounting with 24 wires/layer and totally two layers was called a ‘bundle design’ (Fig. 24.7). Both mounting designs demonstrated quite different cone calorimeter results (Figs 24.8 and 24.9). For the single layer design, the cone tests were finished



24.7 Different insulated wire mounting designs for cone calorimeter tests
From reference 20; John Wiley & Sons Limited. Reproduced with permission.



24.8 Heat release rates for the single layer design (FR wire, 2.5 mm²). Heat flux = 35 kW/m². From reference 20; John Wiley & Sons Limited. Reproduced with permission.



24.9 Heat release rates for the bundle design (FR wire, 2.5 mm²). Heat flux = 35 kW/m². From reference 20; John Wiley & Sons Limited. Reproduced with permission.

within 20 minutes. This is the flame application time for cables as defined in the new European proposal for flame tests of cables (prEN 50399). Wires insulated with the compound 1 had a higher PHRR within the first 5 minutes. For the bundle design, the duration of the cone calorimeter tests was very long, due to the insulation effect of the first charred layer on those located underneath in the second layer; therefore, the tests were stopped after 20 minutes. This mounting design is representative of many end-product applications. Wires insulated with the filler-blended compound 2A did not show any increase in the PHRR within the first 10 minutes compared to the wires insulated with the only organoclay-based compound 1.

24.4 Conclusion

MWCNTs act as very efficient flame retardants at low filler contents in EVA. An optimized formulation for flame-retardant insulated wires was developed based on the filler-blend 'multi-walled carbon nanotubes-organoclays'. Small fire tests according to IEC 60 332-1, with flames of a Bunsen burner attacking the insulation of the wire, showed that the char was strengthened by the long L/D ratio of the MWCNTs. The improved char results in better flame-retardant performances of the wires. Now there are many activities worldwide to investigate the combinations of nanostructured fillers in combination with traditional non-halogenated or halogenated traditional flame retardants for technical applications to enhance the worldwide markets for flame-retardant polymers.

24.5 References

- 1 Hirschler, M M (2000) 'Fire performance of organic polymers, thermal, decomposition, and chemical decomposition', *Polymeric Materials: Science and Engineering*, 83, 79–80, ACS Meeting, Washington, DC, August.
- 2 Babrauskas, V (1995) 'The generation of CO in bench scale fire tests and the prediction for real scale fires', *Fire and Materials*, 19, 205–213.
- 3 Hirschler, M M (2005) 'Fire safety, smoke toxicity and halogenated materials', *Flame Retardancy News*, April 2005, Business Communications Co., Norwalk, CT, USA.
- 4 Stevens, G C (2000) 'Countervailing risks and benefits in the use of flame retardants', *Proceedings of the Flame Retardants 2000 Conference*, London, UK, 8–9 February 2000, 131–145.
- 5 Beyer, G (2005) 'Nanocomposites offer new way forward for flame retardants', *Plastics Additives & Compounding*, September/October issue, 7, 32–35.
- 6 Gilman, J W, Kashiwagi, T, Giannelis, E P, Manias, E, Lomakin, S, Lichtenhan, J D, Jones, P (1998) 'Nanocomposites: radiative gasification and vinyl polymer flammability', in Le Bras, M, Camino, G, Bourbigot, S, Delobel, R (eds) *Fire Retardancy of Polymers: The Use of Intumescence*, Cambridge: Royal Society of Chemistry, pp. 203–221.
- 7 Gilman, J W, Kashiwagi, T, Lichtenhan, J D (1997) 'A revolutionary new flame retardant approach', *SAMPE J.*, 33–40.
- 8 Beyer, G (ed.) (2009) *Industry Guide to Polymer Nanocomposites*, Plastics Information Direct, ISBN: 978-1-906479-04-6.
- 9 Beyer, G (2002) 'Improvements of the fire performance of nanocomposites', in *Proceedings of the 13th Annual BCC Conference on Flame Retardancy*, Stamford, CT, USA, 3–6 June.
- 10 Kashiwagi, T, Grulke, E, Hilding, J, Harris, R, Awad, W, Douglos, J (2002) 'Thermal degradation and flammability properties of poly(propylene)/carbon nanotube composites', *Macromolecular Rapid Communications*, 23, 761–765.
- 11 Kashiwagi, T, Grulke, E., Hilding, J, Groth, K, Harris, R, Butler, K, Shields, J, Kharchenko, S, Douglas, J (2004) 'Thermal and flammability properties of polypropylene/carbon nanotube nanocomposites', *Polymer*, 45, 4227–4239.
- 12 Kashiwagi, T, Du, F, Winey, K, Groth, K, Shields, J, Bellayer, S, Kim, H, Douglas, J (2005) 'Flammability properties of polymer nanocomposites with single-walled carbon nanotubes: effects of nanotube dispersion and concentration', *Polymer*, 46, 471–481.

- 13 Kashiwagi, T, Du, F, Douglas, J, Winey, K. I, Harris, R, Shields, J (2005) 'Nanoparticle networks reduce the flammability of polymer nanocomposites', *Nature Materials*, 4, 928–933.
- 14 Schartel, B, Pötschke, P, Knoll, U, Abdel-Goad, M (2005) 'Fire behaviour of polyamide 6/multiwall carbon nanotube nanocomposites', *European Polymer Journal*, 41, 1061–1070.
- 15 Breuer, O, Sundararaj, U (2004) 'Big returns from small fibers: a review of polymer/carbon nanotube composites', *Polymer Composites*, 25, 630–645.
- 16 Tang, B. Z, Xu, H (1999) 'Preparation, alignment, and optical properties of soluble poly(phenylacetylene)-wrapped carbon nanotubes', *Macromolecules*, 32, 2569–2576.
- 17 Shaffer, M (2001) 'Carbon nanotube modified polymers', paper presented to the conference Nanostructures in Polymer Matrices, Risley Hall, Derbyshire, UK, 10–13 September.
- 18 Beyer, G (2002) 'Carbon nanotubes as flame retardants for polymers', *Fire and Materials*, 26, 291–293.
- 19 Gilman, J W, Jackson, C L, Morgan, A B, Harris, R, Manias, E, Giannelis, E P, Wuthenow, M, Hilton, D, Philipps, H (2000) 'Flammability properties of polymer-layered-silicate nanocomposites, polypropylene and polystyrene nanocomposites', *Chemistry of Materials*, 12, 1866–1873.
- 20 Beyer, G (2005) 'Filler blend of carbon nanotubes and organoclays with improved char as a new flame retardant system for polymers and cable application', *Fire and Materials*, 29, 61–69.
- 21 Beyer, G, Gao, F, Yuan, Q. A (2005) 'A mechanistic study of fire retardancy of carbon nanotube/ethylene vinyl acetate copolymers and their clay composites', *Polymer Degradation and Stability*, 89, 559–564.
- 22 Elliot, P J, Whiteley, R. H (1999) 'A cone calorimeter test for the measurement of flammability properties of insulated wire', *Polymer Degradation and Stability*, 64, 577–584.

Polymer–carbon nanotube conductive nanocomposites for sensing

J.-F. FELLER, M. CASTRO and B. KUMAR, University of
South Brittany (UBS), France

Abstract: In this chapter, recent studies on carbon nanotube conductive polymer nanocomposites (CPC) for sensing are presented. Starting from basic concepts related to CPC transducers, such as percolation, conduction mechanisms and sensing principles, this chapter successively addresses synthesis, fabrication, characterization and structure/sensing properties of these advanced materials issues. Special attention is given to conductive pathways that structure and provide an understanding of sensing behaviour. Finally, examples are given for the main fields of applications, i.e. temperature, strain, chemical sensing.

Key words: carbon nanotube, chemical sensing, conductive polymer nanocomposite transducers, strain sensing, temperature sensing.

25.1 Introduction

Carbon nanotube (CNT) smart materials (Kang *et al.*, 2006a) are being used as actuators (Baughman *et al.*, 1999), able to convert current into mechanical work and as sensors, able to convert external solicitations such as strain, temperature, chemicals, into interpretable electrical signals (Kauffman and Star, 2008). In this latter case, conductive polymer nanocomposites (CPCs) are very attractive for designing effective transducers due to their high versatility. Since their discovery (Radushkevich and Lukyanovich, 1952), carbon nanotubes (CNTs) have attracted a lot of attention (see Fig. 25.8 on p. 769) and more recently their implementation in CPCs has shown their high potential for smart applications such as chemical sensing (Castro *et al.*, 2009), temperature sensing (Lisunova *et al.*, 2007) and strain sensing (Thostenson and Chou, 2006a). After some basic concepts related to conduction in CPC, this chapter presents the different steps of CNT-filled CPCs' transducers' development: formulation, processing, characterization and properties. Guidelines are given to optimize both materials' selection and CNT dispersion in the polymer matrix for the desired sensing application. Finally, the potential of CNT-filled CPCs is shown by presenting different examples.

25.2 Basic concepts of conductive polymer nanocomposites

25.2.1 Percolation

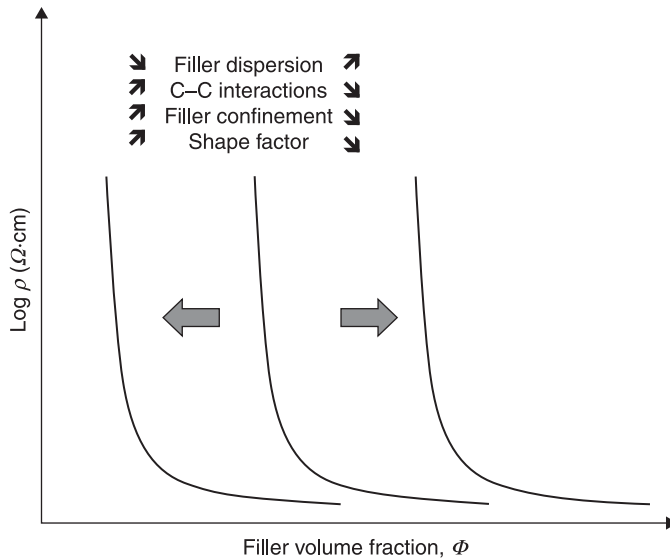
Percolation is a statistical concept, which can describe the interconnection of isolated objects. In this theory, long distance communication is possible once the number of objects becomes larger than a threshold value. On both sides of this transition considerable changes are expected which can result from only a small variation in the number of objects. Initially developed to describe crystals' growth (Broadbent and Hammersley, 1957), this scaling law has found many different applications in elasticity of gels (De Gennes, 1976), forest fires (Stauffer and Aharony, 1994), economics (Tartarin and Pajot, 1996), powder compaction (Imbert *et al.*, 1997), fluid displacement in porous media (Sahimi *et al.*, 1998), including electrical conduction in polymer composites (Feller *et al.*, 2002a, 2004) and particularly CNT-filled composites (Pötschke *et al.*, 2004a; Du *et al.*, 2004).

The statistical percolation theory is especially effective in describing electrical properties of heterogeneous media like conductive polymer composites. The dependency of conductivity on filler concentration takes the simple form of a scaling law according to Equation 25.1.

$$\rho_{CPC} = \rho_f(\Phi - \Phi_c)^{-t} \quad [25.1]$$

where ρ is the resistivity of the composite, ρ_f the scaling factor and filler resistivity, t the critical exponent, Φ the filler fraction and Φ_c its value at the percolation threshold.

Usually, experimental results are fitted by plotting $\log(\rho/\rho_0)$ versus $\log(\Phi - \Phi_c)$ and incrementally varying Φ_c until the best linear fit is obtained (Carmona, 1989). The critical exponent t is the slope of the linearized curve in the percolation zone expected theoretically to depend on the system dimensionality: $t = 1.33$ and 2 corresponding to 2- and 3-dimensional networks (Stauffer and Aharony, 1994) respectively. But as, experimentally, t values up to 6 have been reported for short carbon fibres (Carmona and Mouney, 1992; Feller *et al.*, 2002a), there is no evidence of any clear relationship between t and the conducting network morphology. Nevertheless the suddenness of the transition is inversely proportional to the distribution of the interfiller junction's nature. On the other hand, Φ_c more obviously decreases with increasing filler L/D shape factor (Celzard *et al.*, 2008) and at constant L/D is increasing with filler curvature or waviness (Dalmás *et al.*, 2006). Additionally to these geometrical considerations, Φ_c depends on dispersion level, physicochemical interactions between fillers and matrices (Bauhofer and Kovacs, 2009) and exclusion volumes (Grunlan *et al.*, 2001, 2004) as represented in Fig. 25.1. The greater the interactions between macromolecules and nanofillers, the higher the level of dispersion, and consequently the lower the conductivity



25.1 Parameters influencing percolation threshold.

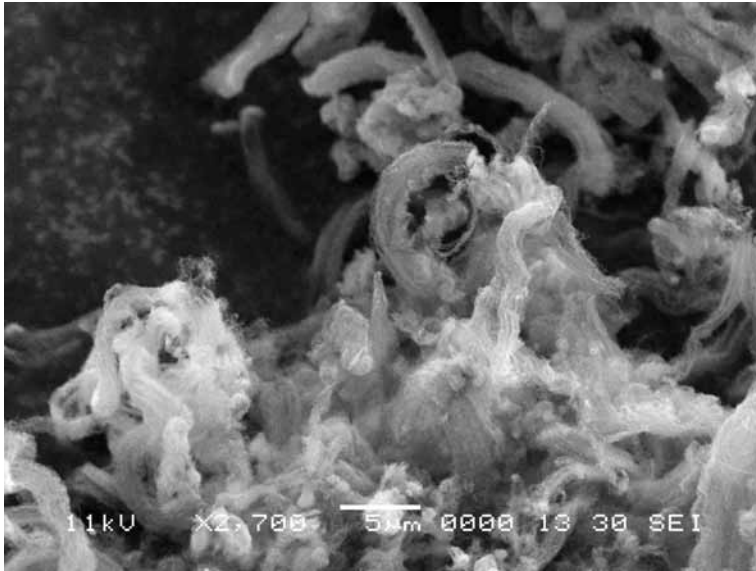
due to insulation of the filler by the polymer. Moreover, when the nanofiller has different levels of organization, like multi-walled carbon nanotubes (MWNTs) in Fig. 25.2 at both the nano and micro scale, the influence of the shape factor and dispersion on conductivity is more complicated to establish. Preferably, an intermediate level of dispersion will be targeted so that an optimum between interconnection and disaggregation of fillers will be found. In fact, this raises the question of the nature of conduction in CPCs.

25.2.2 Conduction in CPCs

Electronic conduction in conductive polymer nanocomposites is achieved through various processes, of which the most important definitely are ohmic conduction, due to direct contact between nanofillers, and tunnelling conduction, taking place when electrons can circulate through a small insulating barrier. The first step in the characterization of a conducting network architecture is the determination of current transport mechanisms operating in CPC by plotting the current/voltage (I/V) curves. Fitting curves with Equation 25.2 determines the deviation of conduction from linearity and thus evaluates the proportion of ohmic and tunnel contribution, as shown in Fig. 25.3. Thus a value of n close to 1 will mean that conduction is mainly ohmic, whereas larger values correspond to a tunnelling-dominated phenomenon.

$$I = A \cdot V^n \quad [25.2]$$

where A is a constant and n the exponent.



25.2 SEM image of entangled bundles of multi-walled carbon nanotubes (MWNTs) N7000 Nanocyl.

Nevertheless, Celzard *et al.* (1998) suggest that tunnel resistivity ρ_T expressed by Equation 25.3 is the major component in CPCs as there is almost always an insulating polymer film between two conducting fillers. This equation well expresses that by increasing voltage, electrons gain energy to cross the insulating barrier and add an increasing contribution to conduction.

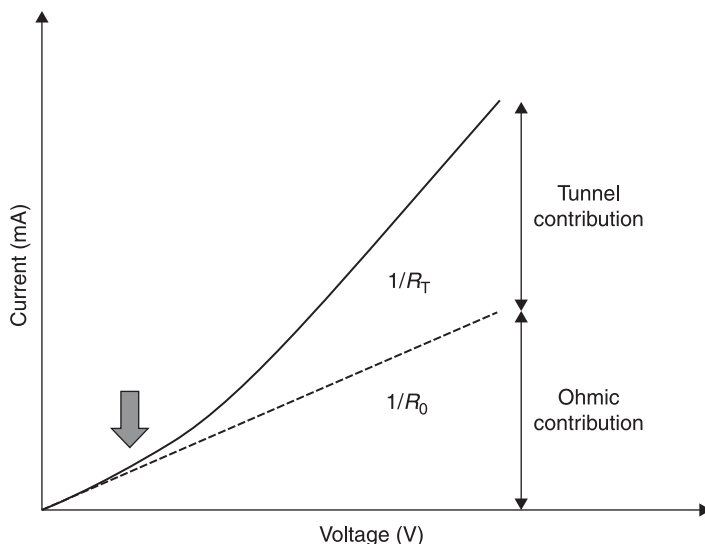
$$\rho_T = e^{\left(\frac{\pi w}{2} \sqrt{\frac{2mV_0}{(h/2\pi)^2}} \right)} \quad [25.3]$$

where m is the electron rest mass, h is Planck's constant, V_0 is the height of the barrier, and w its width.

On the other hand, for sensing applications, it is preferable to keep the transducer conductivity in ohmic mode so that any perturbation of electrons circulation will generate a detectable tunnel flow.

25.2.3 Principle of sensing with CPCs

Before going deeper into the illustration of the intelligent properties of CPC, it is worth defining some words like transducer, sensor or e-nose that will be used extensively in the following. According to an online technical encyclopedia (McGraw-Hill, 2010), a 'transducer' is 'an electronic device that changes one form of energy into electrical signals' whereas the definition for 'sensor' is 'a



25.3 Different types of conduction in CPCs. Tunnel and ohmic contributions are both proportional to the inverse of a resistance, respectively R_T and R_0 .

device that responds to a physical stimulus (as heat, light, sound, pressure, magnetism, or a particular motion) and transmits a resulting impulse (as for measurement or operating a control)'. In this chapter we will consider that a 'CPC transducer' stands for a CPC material able to transduce any chemical or physical solicitation into recordable variations of electrons motion under tension. The CPC transducer is electrically interfaced by wires or electrodes to constitute a 'CPC sensor' ready to be connected to an acquisition chain for signal processing and analysis. Additionally, an electronic nose (e-nose) or tongue (e-tongue) will be considered as being a device associating several vapour or liquid sensors (respectively) in parallel. In this case, electrical signals are analysed by pattern recognition algorithms to enable identification and quantification of chemicals. Looking now at the past, it seems that CPCs' smart properties history starts with pioneer works that early evidenced the potential of CPCs for respectively temperature (Meyer, 1973, 1974), strain (Kost *et al.*, 1983, 1984), and chemical sensing (Freund and Lewis, 1995; Lonergan *et al.*, 1996), and many CPC transducers have found various applications. But it is only recently that CNTs have been introduced into CPC formulations to develop transducers (Wei *et al.*, 2006; Du *et al.*, 2007; Castro *et al.*, 2009; Lu *et al.*, 2009a; Kumar *et al.*, 2010; Kobashi *et al.*, 2008, 2009; Pötschke *et al.*, 2009). Although the sensing principle is almost the same whatever the variable to be measured, i.e. an increase in interfiller gap, there are important differences to consider depending on the nature of the solicitation that the CPC must transduce.

Positive/negative temperature coefficient effect

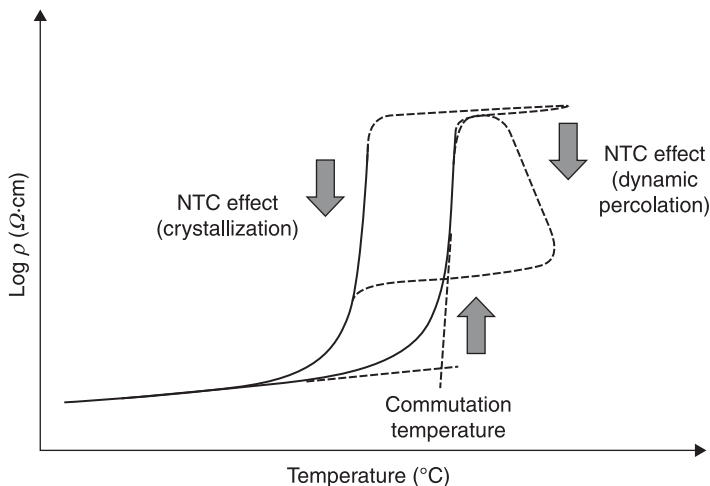
Temperature sensing with CPCs results from their original thermo-electrical behaviour upon heating/cooling. Typically, the important interfiller gap increase resulting from polymer phase volume expansion during melting will induce a resistivity rise of several decades. As described in Fig. 25.4, the commutation temperature can be determined at the beginning of the resistivity jump, known as the positive temperature coefficient (PTC) effect. This temperature coincides with the beginning of polymer crystalline phase melting (Feller *et al.*, 2002b) or the amorphous phase softening (Pillin *et al.*, 2002), although in the latter case a lower PTC amplitude is generally obtained. With single polymer phase CPCs, an undesirable phenomenon upon heating, related to reaggregation of fillers in the melt is often observed, and is called negative temperature coefficient (NTC). Cross-linking the matrix or using co-continuous polymer phases can prevent this effect, which must not be mismatched with the reversible NTC effect observed upon cooling that corresponds to normal and reversible crystallization of the polymer.

Positive/negative strain coefficient effect

Strain sensing is based on the ability of CPCs to transduce any elongations that will modify the interfiller gap and as a result generate tunnelling conduction which depends exponentially on the inter-CNT gap Z , according to

$$\rho = a e^{(bZ)} \quad [25.4]$$

where ρ is the resistivity, a and b are positive constants and Z the gap between two vicinal CNT (Gau, 2009).

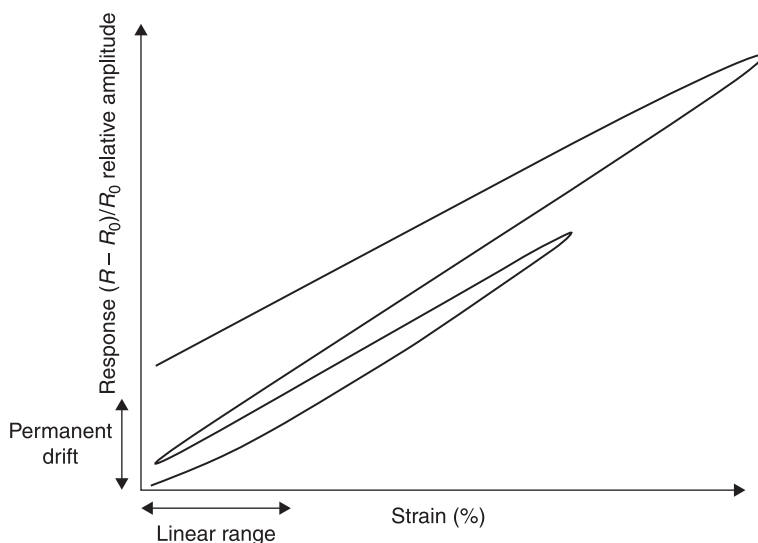


25.4 Thermo-electrical behaviour.

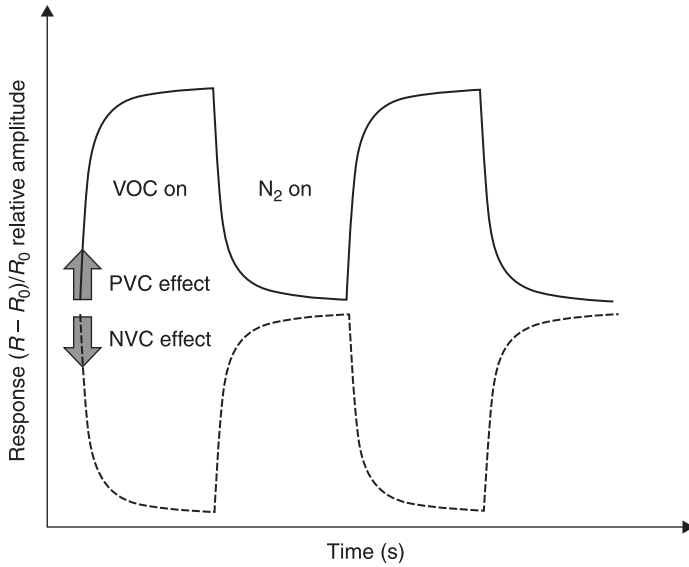
Figure 25.5 illustrates the kind of signal that can be obtained during strain sensing tests. Possible drawbacks can be non-linearity of signal due to the fact that the polymer matrix has been moved out of its linear range, which can result in permanent drift of the sensor. Thus, depending on the amplitude of the deformation to be followed, it is necessary to select a polymer matrix so that it will be always more elastic than the sample to monitor.

Positive/negative vapour coefficient effect

The chemo-electrical behaviour described in Fig. 25.6 is certainly the most complicated effect to understand. It can be used to design sensors for chemicals in both gas or liquid state but obviously the requirements will differ depending on the target. Both positive and negative vapour coefficients can be interpreted depending on the electronic conduction mechanism (Lu *et al.*, 2010). For example, the sensing mode of PaniNP transducers can be switched from the negative vapour coefficient (NVC) to positive vapour coefficient (PVC) effect by simply tuning initial conductivity through the addition of a small amount of CNTs. CPCs' chemo-electrical response to organic molecules can be interpreted and quantified from the analysis of changes in electrons' motion within the CNTs' percolated network. It is assumed that during their diffusion through the composite, vapour molecules can disconnect CNT-CNT junctions by increasing the gap between nanotubes directly by adsorbing on carbon or indirectly by relaxing macromolecules in the vicinity of the junction. Consequently, quantum-tunnelling conduction (less effective) will develop to the detriment of ohmic conduction,



25.5 Piezo-electrical behaviour of CPCs.



25.6 Chemo-electrical behaviour.

resulting in an important resistance increase even for a small amount of solvent molecules. The amplitude of this phenomenon is classically evaluated by following the evolution of A_r , the relative resistance defined by Equation 25.5.

$$A_r = \frac{R_v - R_{init}}{R_{init}} \quad [25.5]$$

where R_{init} is the initial resistance, R_v the resistance in the presence of vapour.

A_r depends on many parameters, of which at least the following must be controlled: sample thickness, temperature, initial resistance, amount of molecules in the sensor surrounding and specific interactions of analytes with macromolecules from the matrix. The Flory-Huggins intermolecular interaction parameter, calculated from Equation 25.6, is found to well predict the sensitivity of CPC transducers to volatile organic compounds (Kumar *et al.*, 2010) and organic liquids (Kobashi *et al.*, 2009):

$$\chi_{12} = \frac{V}{RT} \cdot (\delta_{Tpol} - \delta_{Tsol})^2 \quad [25.6]$$

$$\delta_T^2 = \delta_d^2 + \delta_p^2 + \delta_H^2$$

δ_T : global solubility parameter from dispersion bonds between molecules ($J^{1/2} \cdot cm^{-3/2}$)

δ_d : solubility parameter from dispersion bonds between molecules ($J^{1/2} \cdot cm^{-3/2}$)

δ_p : solubility parameter from polar bonds between molecules ($\text{J}^{1/2}\cdot\text{cm}^{-3/2}$)
 δ_H : solubility parameter from hydrogen bonds between molecules ($\text{J}^{1/2}\cdot\text{cm}^{-3/2}$)

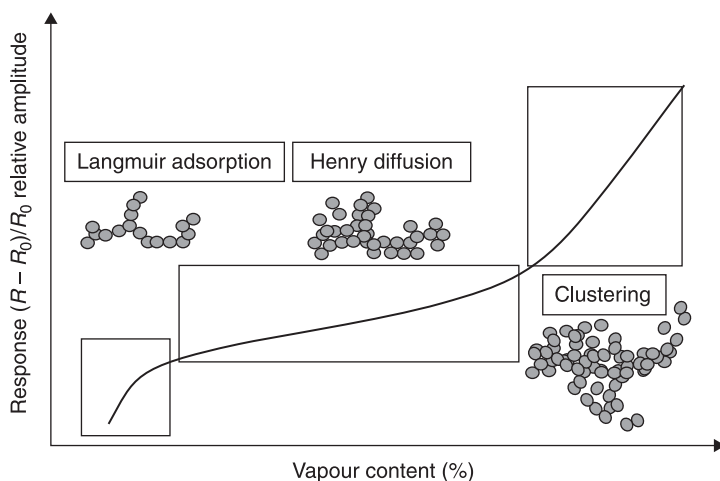
Nevertheless, there is generally no univocal relation between one CPC formulation and one vapour based on a 'key-lock' principle that prevents direct identification. To overcome this difficulty, electronic noses (e-nose) analyse a combination of electrical responses from a set of selected CPCs by mimicking the mammalian sense of olfaction (Lonergan *et al.*, 1996; Shevade *et al.*, 2003).

Additionally, dielectric permittivity and even the size of solvent molecules are also able to interpret chemical sensors' selectivity (Lu *et al.*, 2009b). Interestingly chemo-electrical responses upon volatile organic components (VOC) exposure are proportional to the amount of molecules in the vicinity of the CPC transducer, according to the Langmuir-Henry-clustering (LHC) model derived from classical sorption formalism. This model describes quite well which diffusion regime takes place in the CPC transducer: simple adsorption, diffusion, clustering, corresponding respectively to the three terms of Equation 25.7:

$$A_r = \frac{b_L \cdot (f'' - f) \cdot f}{(1 + b_L \cdot f)} + k_H \cdot f + (f - f') \cdot f^{n'} \quad [25.7]$$

where b_L is the Langmuir affinity constant, f'' is the vapour fraction over which Langmuir's diffusion is replaced by Henry's diffusion, f is the solvent fraction, k_H is Henry's solubility coefficient, n' the number of vapour molecules associated in clusters.

On the one hand, this model identifies which kind of diffusion mode is more suitable for sensing (Fig. 25.7) whereas, on the other, it makes possible the



25.7 Different diffusion mode according to the Langmuir-Henry-clustering model.

determination of organic molecules' concentration in the atmosphere, from relative amplitude measurement.

It is thanks to these remarkable properties that CPCs have attracted attention for smart materials development (Fig. 25.8), but their great sensitivity can also be a drawback if not properly exploited through the right choice of components during the formulation step.

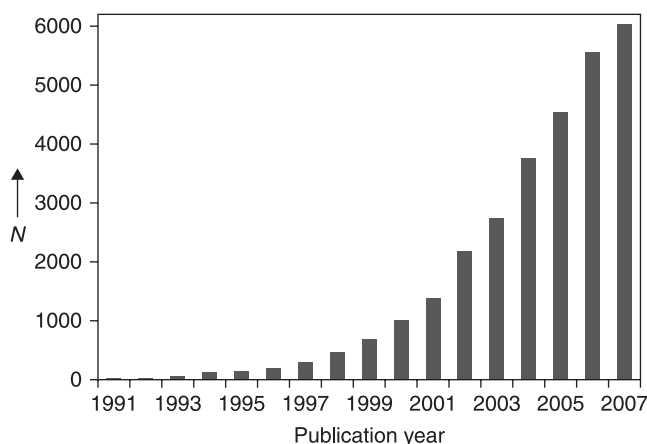
25.3 Carbon nanotube (CNT) conductive polymer nanocomposite (CPC) transducers' fabrication

25.3.1 Formulation of CPC for sensing

As with any other application, the choice of the different components of the composite formulation is crucial. This first step consists in selecting and assembling the different pieces of what will become a sensitive material. Although there is a wide range of materials potentially available, hundreds of different matrices and tens of conducting fillers, there will in the end only be a few suitable combinations.

Fillers for CPC transducers

First of all, what are the reasons why CNT should be chosen among all conducting fillers used in CPC formulations for sensing? Metal nanofillers like gold nanoparticles (AuNP) can be self-assembled with dendrimers of poly(propyleneimine) to design vapour sensors with good sensitivity to volatile organic compounds (VOC) like



25.8 Histogram detailing the number of CNT publications (N) per year between 1991 and 2007 (data obtained from ISI Web of Knowledge according to Kauffman and Star, 2008).

toluene, 1-propanol and water (Krasteva *et al.*, 2002, 2003). The resistivity can be adjusted by the number of generations of the dendrimer that will vary the interparticle gap and thus the tunnelling capability through the conducting network. Another strategy has been used with poly(electrolyte)-coated AuNP and more simply AuNP functionalized with citrates prior to dispersion in poly(styrene) (Bouvrée *et al.*, 2007). In both cases, CPC thin layers sensitive to VOC were obtained. Examples of use of iron particles in diphasic poly(ethylene)/poly(oxyethylene) systems (Mamunya *et al.*, 2007) or silver and copper particles (Boiteux *et al.*, 1999, 2006) dispersed in epoxy resin are reported to be very sensitive to temperature. Nevertheless the use of spherical fillers leads to high percolation thresholds and metal particles have also a strong tendency to aggregate since their surface energy is high, which imposes a treatment of their surface. Moreover their high density ($d_{\#20}$ for gold), high cost, and in some cases their sensitivity to oxidization are a penalty that promotes the use of carbon nanofillers in many cases. Carbon nanoparticles (CNPs), also known by the name 'carbon black', have long been used by the Chinese in inks for their colour since 2850 BC and more recently by Goodyear in rubber formulations for their reinforcement effect since the end of nineteenth century, and have been introduced in different polymer matrices for the design of e-noses (Freund and Lewis, 1995). However, one of the main advantages of CNTs among CNPs is their huge shape factor ($L/D > 1000$) resulting in percolation thresholds lower than 0.02 wt% MWCNT when dispersed in epoxy by heat shearing (Martin *et al.*, 2004), less than 0.1 wt% SWCNT when dispersed in poly(ϵ -caprolactone) in solution under sonication (Mitchell *et al.*, 2002), or less than 0.04 wt% MWCNT in PA 6.6 matrix (Krause *et al.*, 2010). Moreover, even at the same effective content (normalized towards content at percolation threshold), CNT-filled chitosan transducers were found to be more sensitive to vapours than their CNP-filled homologues, especially at low analyte concentrations (Kumar *et al.*, 2010). Despite all these advantages and although they have been successfully used to design sensors (Kauffman and Star, 2008), carbon nanotubes used on their own suffer from a lack of adjustable selectivity, due to the fact that their response mechanism is only based on the affinity of target molecules for their surface. To cope with this problem, it is necessary either to graft them with functional molecules or to associate them with a polymer matrix.

Matrices for CPC transducers

One of the major interests in CPC sensors is in the large diversity of the polymer matrices that can be associated with the conducting fillers. Depending on sensing and application targets, the choice of the polymer nature will provide a powerful adjustable capability. For temperature sensing, the driving parameter that will determine the commutation temperature, as expressed in Fig. 25.4, is the melting temperature of the polymer matrix used to disperse the conducting nanofiller. Once the temperature increases above this peculiar value, the CPC resistivity is dramatically increased which can trigger an action like an alarm. Some

examples of commutation temperatures covering the range 35–160 °C are given in Table 25.1, showing that it is rather easy to select the right polymer for the suitable target temperature range to sense. For strain sensing the polymer matrix will be chosen so that its practical extension will be in its linear elastic domain. Depending on the strain range to sense, some percentages or some tens of percentages, an amorphous matrix in its glassy or elastomeric state will be chosen respectively. An appropriate selection by the proper mechanical characterization will prevent non-reversible plastic deformation of the sensing often responsible for initial resistance drifts illustrated by Fig. 25.5. Concerning vapour sensing, the choice of matrices is wide, depending on chemical functions present on macromolecules, expected to interact with the target molecules. As there is generally no univocal relationship between a macromolecule and a solvent, it is necessary to select a set of polymers whose combination will give a unique recognition pattern. Equation 25.6 can guide the selection in a first step although some other important parameters must be taken into account such as transducer degradation or non-linearity due to extensive swelling.

The choice of the matrix is not only based on functional criteria but also on ease of processing. Thermoplastics-based transducers in the form of micronic films or fibres can be prepared via melt mixing processes, such as twin-screw extrusion (Kobashi *et al.*, 2008), internal batch mixing (Lee *et al.*, 2006) or compression moulding (Vidhate *et al.*, 2009) or melt spinning (Pötschke *et al.*, 2009). On the other hand, the preparation of nanometric layers requires the use of solution mixing. An effective dispersion of carbon nanotubes in the polymer matrix can be achieved by sonication and ultracentrifugation (Bonnet *et al.*, 2007a), different film preparation techniques like casting (He *et al.*, 2005; Pioggia *et al.*, 2007; Liu *et al.*, 2007), spin coating (Gau *et al.*, 2009b), or spray deposition (Castro *et al.*, 2009) will produce ultra thin transducers. Additionally, the use of the layer-by-layer technique initially developed by Mamedov *et al.* (2002) with polyelectrolytes

Table 25.1 Commutation temperatures of some CNT-filled CPC

T_{com} (°C)	35	40	55	55	112	120	140	137–144	160
Polymer	BPR	VMQ	VMQ	PCL	UHMWPE	HDPE	HDPE	PE	PP
CNT (wt%)	3	3	1	3	2	5.4	0.5	0.085	2.3
CNP (wt%)	0	0	0	0	0	0	25	0	0
First author	Feller	Jiang	Jiang	Lu	Mierczynska	He	Lee	Gao	Deng
Year	2009	2006	2006	2009 (a, b)	2004	2005	2006	2009	2009

BPR: biosourced polyester.

VMQ: methylvinyl silicone rubber.

PCL: poly(caprolactone).

UHMWPE: ultra high molecular weight polyethylene.

HDPE: high density polyethylene.

PP: polypropylene.

was used to build hierarchical 3D architectures by Lu *et al.* (2009b) to increase specific surface and enhance vapour transducers' sensitivity. Solution mixing has also been widely used for CNT dispersion in epoxy resins for structural composites' health monitoring strain. Filler dispersion done under stirring was improved by the use of surfactants like sodium dodecyl sulphate and controlled sonication (Park *et al.*, 2003, 2007), and high shear mixing (Zhang *et al.*, 2007). However, as sonication is suspected to alter the carbon nanotubes' structures, it has been combined with a three rolls mill calender, taking the benefit from the very high shear rate of this technique (Thostenson and Chou, 2006b; Böger *et al.*, 2008; Nofar *et al.*, 2009).

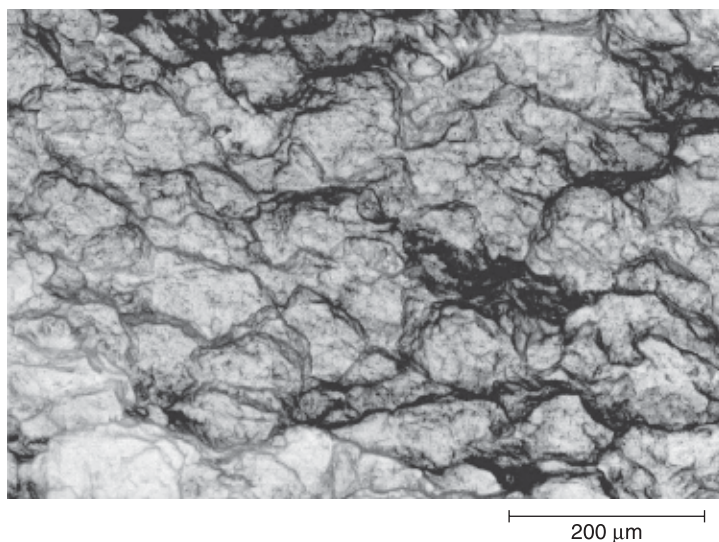
Further to filler dispersion in the matrix, CPCs are prepared via common thermoplastics or thermosets processing techniques. No doubt that this fast step is one of the most important as it will fix the morphologies at the different scales from nano to macro. Consequently, it is necessary to find strategies to control the multiscale architecture and provide the CPCs with stable and reproducible properties for sensing.

25.3.2 CNT composite architecture design

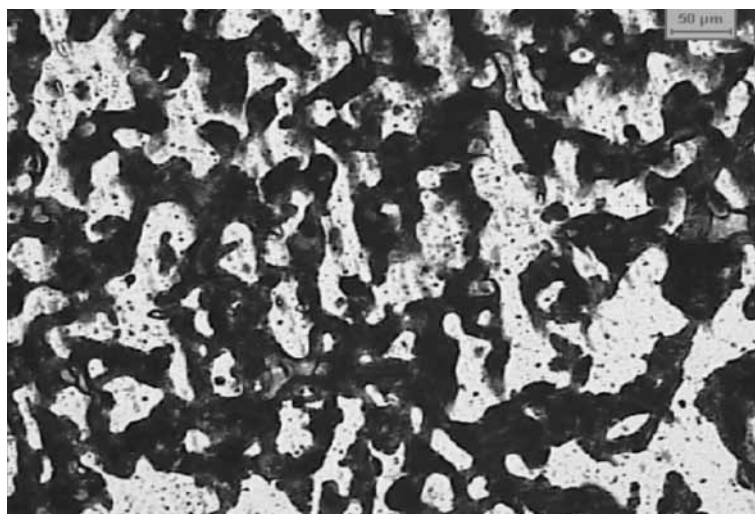
Different strategies can be used to control the conducting network structure at the different levels of organization.

Volume exclusion and segregated networks

There are many ways to use exclusion volumes to concentrate and localize the conducting fillers into confined areas by phase segregation as very well illustrated in Fig. 25.10. To prevent the complete mixing of the filler and the matrix it is possible to act on the viscosity of the matrix, or on mutual interactions. A good illustration of this method has been given by Mierczynska *et al.* (2004) and Lisunova *et al.* (2007) who associated CNT with UHMWPE power by hot compaction (Fig. 25.9), whereas Yu *et al.* (2008) confined CNT between latex microparticles from aqueous emulsions for thermoelectrical applications. Additionally, Mu *et al.* (2008) obtained conductive composite via coating of polystyrene beads with 0.5 wt% SWCNT and found higher conductivity in comparison to simply mixed composite. Besides the considerable decrease of percolation associated with this process, stable morphologies are obtained, provided that materials are not submitted to high temperature cycles. If this is the case, as in temperature sensors, the use of co-continuous structures can secure morphologies even when the conducting phase is in the liquid state. Lu *et al.* (2009a) have developed diphasic blends of polypropylene and CNT-filled poly(ϵ -caprolactone) 50PP/50(PCL-3%wCNT) for temperature sensing which were found to both stabilize sensing signal and ensure a good reproducibility upon cycling (Fig. 25.10). Although for both strain and chemical sensing there is no



25.9 Segregated network of 0.004 vol% of MWNT in UHMWPE matrix by hot compaction (Lisunova, *et al.*, 2007).

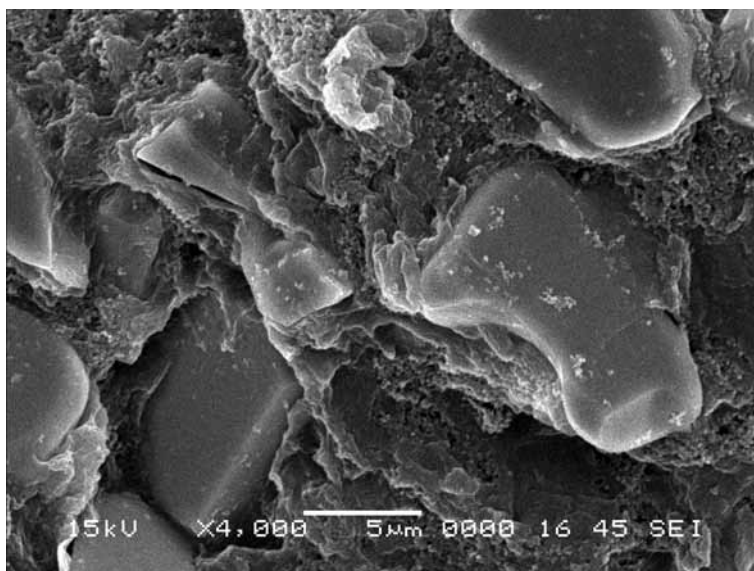


25.10 Optical microscopy image of co-continuous CPC nanocomposites, 50PP/50 PCL-3%wCNT (Lu, 2009b: 2).

strong need for co-continuous structures use, there is some reason to use the insulating polymer phase to provide the transducers with additional mechanical strength or barrier capability. Volume exclusion can also be generated by the introduction of a second filler such as clay nanoparticles (Feller *et al.*, 2004; Etika *et al.*, 2009), rubber microparticles (Zribi *et al.*, 2006) or ceramic microparticles (Droval *et al.*, 2008) that will provide additional functionality to the CPC such as stabilization of CNP dispersion by mutual adsorption, increase of electrical conductivity and increase of thermal conductivity respectively. Figure 25.11 shows an example of conducting architecture in which triple percolation, the percolation of each filler in one polymer phase associated with phase percolation of the two polymers leading to co-continuity, has been achieved to uncouple electrical and thermal conductivity. Nevertheless, any addition of any filler will also strongly modify the CPCs' rheological properties that must be addressed in the final optimization step.

Layer-by-layer assembly and hierarchical architecture

Layer by layer is a powerful protocol to develop progressively aggregated structures in 2D (Decher, 1997; Schneider and Decher, 2004). Nevertheless, Bouvrée *et al.* (2007) found that the use of polyelectrolyte to generate self-association of conducting fillers led to insufficiently conductive percolated

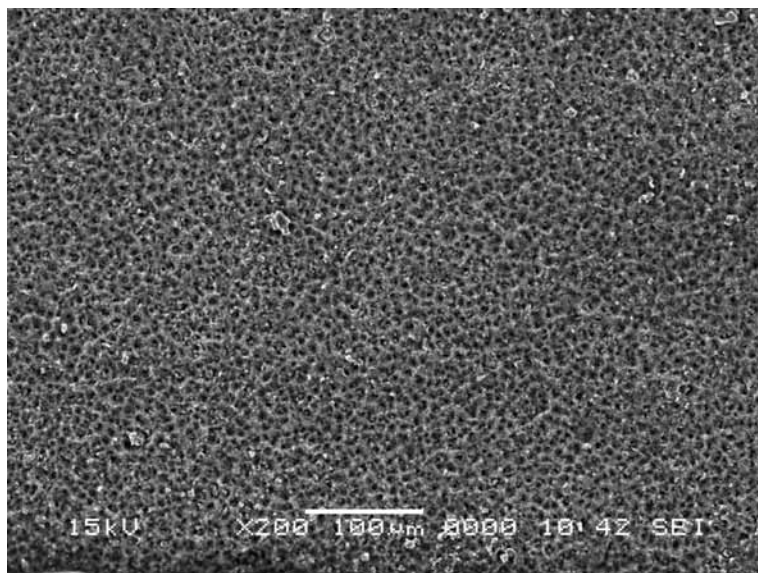


25.11 Triple percolated CPC 50(sPS-28vol% Al_2O_3)/50(HDPE-23vol%CNP) observed by SEM (Droval *et al.*, 2008).

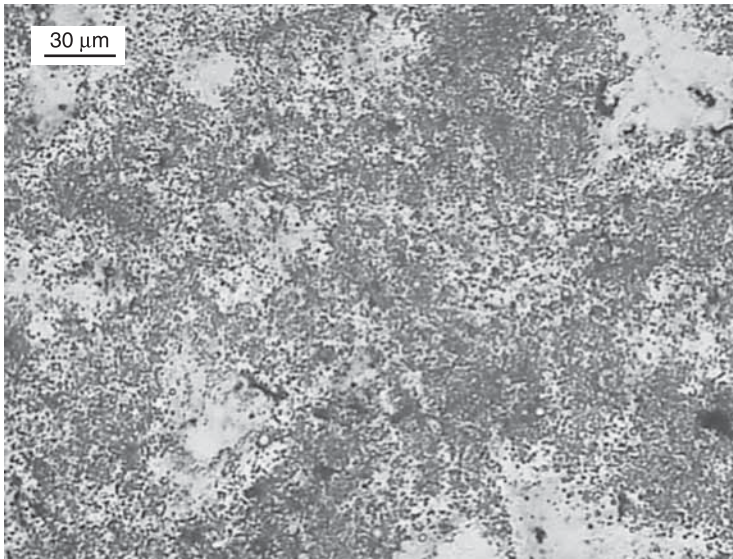
networks for sensing. This drawback was overcome by spraying layer by layer an aPS–AuNP solution which was more effective in structuring vapour transducers in 2D as represented in Fig. 25.12. Bouvrée *et al.* (2007) have extended this technique to hierarchical double-percolated PC-2wt%CNT conductive architecture of PC–CNT (Fig. 25.13) and showed that this morphology was compatible with a good dispersion of CNT in the polymer matrix at the nanoscale, evidenced by AFM, whereas, at the microscale, optical microscopy shows that polymer–CNT microdroplets formed during spraying can coalesce together upon drying inside the same layer but also between different layers in three dimensions. This process finally resulted in a hierarchically structured vapour transducer whose thickness and composition can be adjusted (by the number of layers) to tailor the chemo-electrical properties. Mamedov *et al.* (2002) and Loh *et al.* (2007) have also demonstrated the validity of this technique by dip coating to fabricate strain sensors from PVA–CNT solutions.

25.3.3 CNT composite transducers' characterization

Whatever the processing technique used for transducer fabrication, before evaluating sensing properties, the first round of characterization will be electrical and morphological observations at different scales, i.e. from nano to macro, of CNT-based composite sensor.



25.12 2D layer-by-layer sprayed aPS–AuNP transducer observed by AFM (Bouvrée *et al.*, 2007).

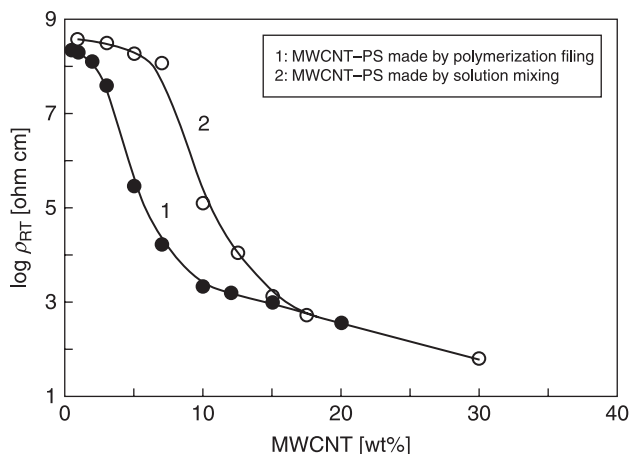


25.13 Hierarchical double-percolated PC-2wt%CNT structure observed by optical microscopy (Lu *et al.*, 2009b).

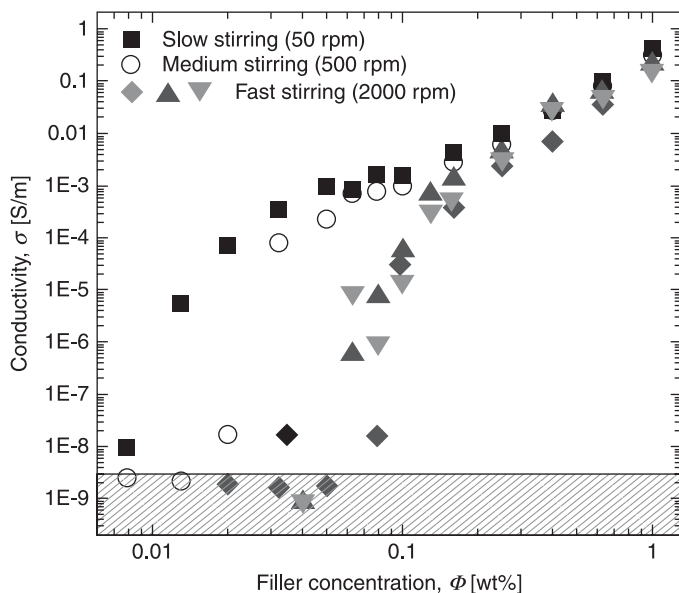
Electrical characterization

Electrical measurements in quiescent conditions obviously represent the most relevant technique for CPC transducers' initial characterization. Mainly two kind of information can be derived from such properties. First, the percolation curve expresses the quality of the conducting network in terms of interconnections' effectiveness. Ideally an optimum between CNT debundling and connectivity must be found. Figure 25.14 is a good illustration of the influence of elaboration route, polymerization filling or simple solution mixing, on CNT dispersion and finally electrical properties (Zhang *et al.*, 2005). This shift in percolation curves is expected to result from partial CNT bundles exfoliation during *in-situ* polymerization and better wetting and penetration of CNT aggregates by lower molar mass chains. Another illustration of what can be learnt from percolation curves is given in Fig. 25.15 where it is clearly seen that increasing the shear rate during CNT dispersion in epoxy resin too much leads to more insulating CPC, evidencing the existence of an optimum to reach during dispersion. There are many other outputs of percolation curves' interpretation, such as demonstrating the influence of conductive filler aspect ratio, conductive filler size, alignment of nanofillers, presence of dispersive agent, or nanofiller surface modification.

Additionally, Fig. 25.16 shows the potential of alternative current experiments to investigate percolated architecture. Cutting frequency sweep curves at low frequency gives back the percolation curve, whereas below 1%wt CNT there is a



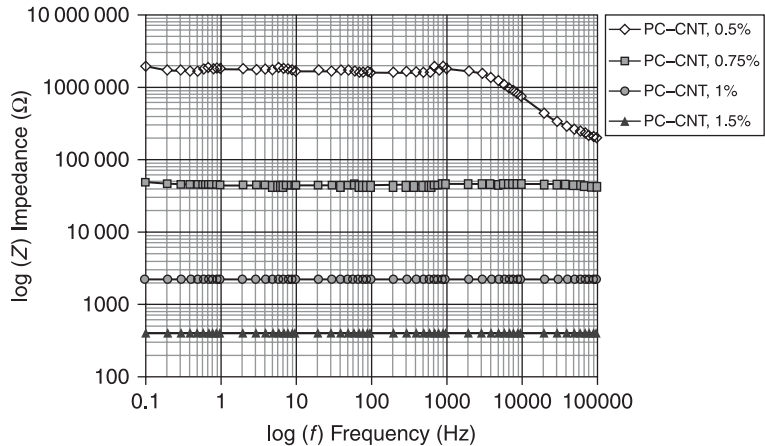
25.14 Evolution of percolation curve with synthesis route (Zhang *et al.*, 2007).



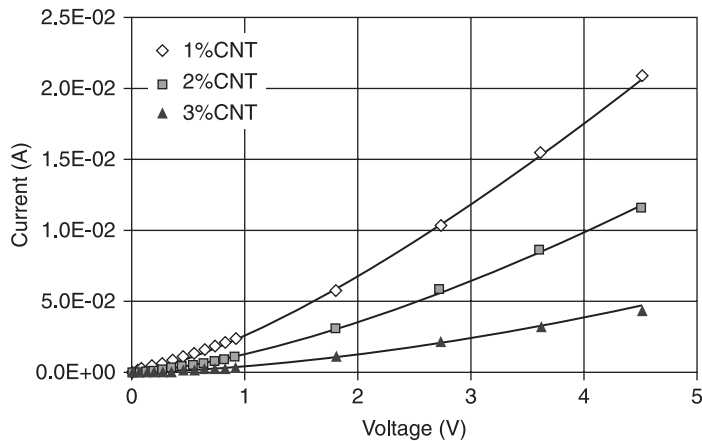
25.15 Influence of stirring speed (50, 500, 2000 rpm) on percolation curve of epoxy–CNT (Bauhofer and Kovacs, 2009).

critical frequency (around 2000 Hz), above which the current is increasing with frequency. This is another appearance of quantum tunnelling, according to Equation 25.3, i.e. only when electrons have a higher energy than the barrier value can they add their contribution to ohmic conduction.

It is finally the so-called current/voltage curves that will complete the transducers' electrical properties' characterization. In Fig. 25.17, the curves fitted with Equation 25.2 well illustrate that the divergence from linearity over 1 V induced by quantum tunnelling contribution is emphasized as filler content approaches the percolation threshold. Fitting parameters in Table 25.2 allow us to quantify this additional conduction.



25.16 Influence of filler content (wt%) on sprayed PC-CNT transducers' impedance during frequency sweep.



25.17 Typical I/V curves for PMMA-CNT transducers fitted with Equation 25.2 (Kumar *et al.*, 2009).

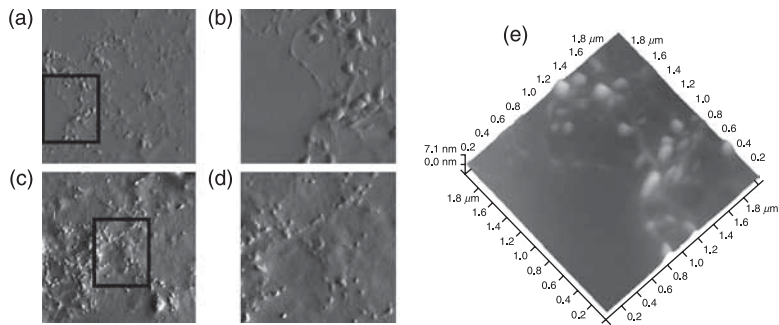
Table 25.2 Fitting parameters of PMMA–CNT transducers from Equation 25.2

PMMA	1 wt%CNT	2 wt%CNT	3 wt%CNT
A	0.0025	0.0013	0.00042
n	1.4	1.55	1.6

Morphological characterization

Electrical characterizations globalize the different phenomena responsible for conduction in CPCs. To go deeper into understanding the relationships between structure and electrical behaviour, imaging morphologies at the different scales from nano to macro are helpful and meaningful. At the microscale, optical microscopy (OM) is a pertinent technique to observe sprayed microdroplets welding (Lu *et al.*, 2009b), as presented in Fig. 25.13, or microphase co-continuous morphologies as in Fig. 25.10 (Lu *et al.*, 2009b; Liu *et al.*, 2007); CNT aggregates remaining in CPCs depending on processing conditions can also be shown by OM (Villmow *et al.*, 2008), nanofiller dispersion homogeneity can also be checked as, even if individual CNTs cannot be seen by this technique, CNT micronic aggregates are perfectly visible (Quercia *et al.*, 2005). Laser scanning confocal microscopy (LSCM) has also been successfully used to study the dispersion of carbon nanotubes in a poly(styrene) matrix by (Bellayer *et al.*, 2005).

Scanning electron microscopy (SEM), transmission electron microscopy (TEM) and also atomic force microscopy (AFM) will allow much higher magnification from submicron to nanometer, imaging details of nanofillers such as grafting and quality of dispersion at the meso scale. SEM has been extensively used to investigate the CPC network structure at the microscale (Zhang *et al.*, 2005; Li *et al.*, 2007), CNT agglomerates (Thostenson and Chou, 2006b), transducers' thickness (Song *et al.*, 2009), or composites' fractured surface (Thostenson and Chou, 2008). Using high accelerating voltage provides complementary information on the CNTs' networks, which tend to charge, leading to highly contrasted images due to enriched secondary electrons emission. (Zhang *et al.*, 2005) gave a good illustration of this technique, showing that CNT networks in a polyurethane-urea matrix looked like entangled coils rather than individual tubes. To be able to image and quantify fillers dispersion at the nanoscale, it is necessary to use the higher magnification achieved with TEM, as showed by (He *et al.*, 2005; Quercia *et al.*, 2005; Zhang *et al.*, 2005; Ferrara *et al.*, 2006; Wang *et al.*, 2007; Thostenson and Chou., 2006b; Kobashi *et al.*, 2008; Pegel *et al.*, 2009; Liu *et al.*, 2009). However, this technique requires a heavy sample preparation step and only permits visualizing nanofillers in a 2D plane which makes statistical treatment a necessity to determine not only the local but also the global state of dispersion. Since its discovery in the late 1980s, AFM has demonstrated increasing capabilities and ease of use to characterize CPCs' structure and morphology at the nanoscale. In tapping mode, forces act on the tip

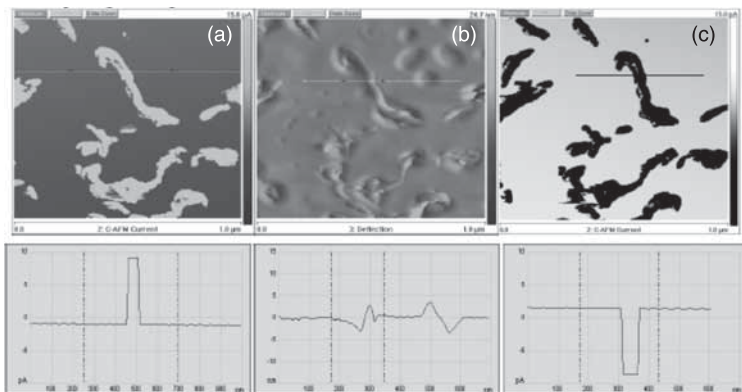


25.18 AFM images (amplitude) of PC–CNT composite on mica: (a) PC-1% CNT ($5\ \mu\text{m} \times 5\ \mu\text{m}$); (b) higher resolution of PC-1% CNT (w/w) ($2\ \mu\text{m} \times 2\ \mu\text{m}$); (c) PC-2%NT (w/w), ($5\ \mu\text{m} \times 5\ \mu\text{m}$); (d) higher resolution of PC-2% CNT (w/w) ($2\ \mu\text{m} \times 2\ \mu\text{m}$); and (e) 3D image of PC-1% CNT (w/w) (height image) (Lu *et al.*, 2009).

due to the tip–sample interactions that result in deflection or torsion of the cantilever, which are detected by a position-sensitive optical sensor. By detecting movements of the cantilever, the height differences of the surface can be resolved on a nanometric scale. Thus it is possible to measure CNTs' dimensions and dispersion level after proper conditioning of the sample by depositing it onto freshly cleaved mica substrate, as illustrated in Fig. 25.18 (Lu *et al.*, 2009b), or straight onto fractured strand surfaces (Pötschke *et al.*, 2004). Castro *et al.* (2009) also used AFM to check the efficiency of grafting by *in-situ* polymerization, or to investigate the CNT network connectivity through the thickness by using current sensing (CS) mode (Kumar *et al.*, 2009). As most CPC transducer sensing properties rely on its conducting network structure, it is particularly interesting to use the latter technique to probe its nanomorphology. In Fig. 25.19 (Kumar *et al.*, 2009) investigated the nano-electrical properties of a MWCNT-filled PMMA-based sensor material by CS–AFM in parallel with classical AFM mode distinguished from the insulating polymer matrix. The current image shows carbon nanotubes connected to the electrode, which is $15\ \mu\text{m}$ far from AFM tip, through the 3D-built CNT network within the whole volume of the sample.

25.4 Sensing properties and applications of CNT conductive polymer nanocomposites

Once transducers' electrical properties and structures have been characterized in a quiescent state, the second step consists in determining their sensing performances. The transduction mechanism responsible for the sensing ability of CNT-filled CPCs is almost always based on the disconnection of the CNTs' conducting architecture. As only some nanometers of interfiller gap fluctuations will generate large resistance variations, due to quantum tunnelling, this will make the CPCs very sensitive to



25.19 Simultaneous acquisition of ((a) and (c)) current profile (applied +500 mV and –500 mV voltage) and (b) corresponding amplitude profile with their cross-sectional analyses for PMMA–CNT composites (Kumar *et al.*, 2008).

their environment. Nevertheless the origin of this disconnection can be several, so that it is necessary to precisely control experimental conditions and possible sources of interference to make sure to really characterize the desired phenomena. Depending on which parameter has to be monitored, electrical measurements will be coupled with chemical, thermal or mechanical solicitations generally applied in loops to evaluate the sensor dynamics, reproducibility, sensitivity and durability.

25.4.1 Sensing instrumentation

Resistivity measurements are usually done by two or four points probes on the surface of samples, thanks to silver paste ensuring a smooth transition between electrodes and CPC transducer. In some cases, silver or copper threads embedded in sample bulk or copper foils glued on its surface, are used to monitor resistance changes. Depending on the targeted applications, the experimental set-up will present some particularities.

For temperature sensing, a thermal cycle is imposed on samples in a computer-controlled oven where the resistivity changes induced by temperature variations are recorded to analyse both PTC and NTC effects. The heating/cooling speeds must be adjusted to prevent artefacts related to samples' inertia. Generally the first cycle is different from the others due to the relaxation of stresses resulting from previous processing and then all the following cycles are quite superimposable, provided that no dynamic percolation has increased the fillers' aggregation and consequently decreased resistivity (Zribi *et al.*, 2006).

For chemical sensing, several devices can be used depending on the physical state of molecules to analyse, either vapour or liquid, dynamic or static mode. Static mode is the simplest protocol, which consists in injecting a defined amount

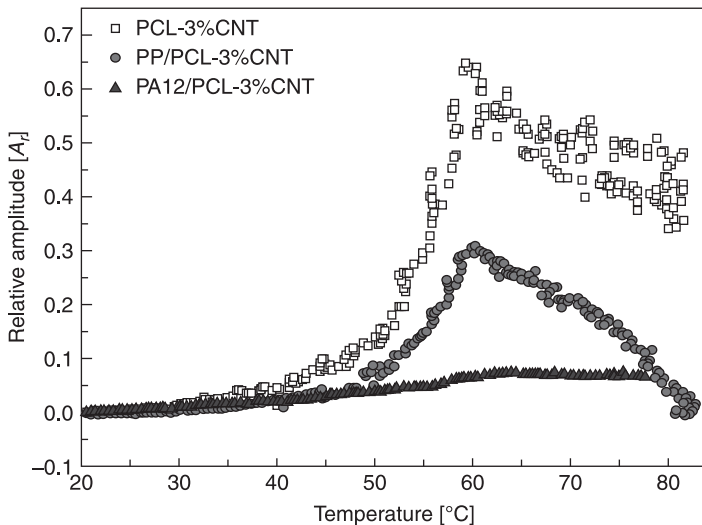
of target molecules (from several ppm to saturated conditions) into a cell of known volume. The dynamic mode is more complex to handle, as the sensor is placed into a gaseous stream of molecules, the content of which is adjusted by blending a stream of pure nitrogen (or air) with a second stream saturated with the vapour to analyse (Lu *et al.*, 2009b; Castro *et al.*, 2009). For liquid sensing characterization, immersion/drying cycles of the CPC are performed either manually or with the help of an automated device; solvent drops remaining on samples are wiped off at the beginning of drying. Different samples' geometry can be tested with suitable clamps, U-shaped films or filaments (Kobashi *et al.*, 2008, 2009).

Characterization of strain sensing properties is done classically by stretching transducers previously glued onto a substrate (metal, epoxy, etc.) with a mechanical testing machine coupled with electrical measurement. In the case of structural composites (Thostenson and Chou, 2006a) or films (Zhang *et al.*, 2007b), samples are directly tested in isolated clamps. Mechanical solicitations can be monotonic tension, three/four bending, compression, tension-compression cyclic loading, fatigue, creep. Complementary devices, like acoustic emission, have also been combined with electrical measurements to investigate damage mechanism in thermoset-based composites.

25.4.2 Temperature sensing with CNT-filled CPC transducers

The smart characteristics of CNT-based CPC sensors towards temperature are illustrated by a large positive temperature coefficient (PTC) effect of electrical resistivity. This effect can be followed by a negative temperature coefficient (NTC) effect. Mierczynska *et al.* (2004) and Lisunova *et al.* (2007) achieved a very low percolation threshold (~ 0.05 vol%) with CPCs based on the segregated network concept. They investigated the thermo-electrical behaviour of UHMWPE-2%CNT above its commutation temperature around $T_{com} = 112^\circ\text{C}$ (Table 25.1) and evidenced a PTC effect of two decades amplitude; this value is comparable to that obtained by Mironi-Harpaz and Narkis (2001) with co-continuous 70PVDF/30(UHMWPE-6%CNP) but two times less than the four decades obtained by He *et al.* (2005) with HDPE-5.4%CNT. The same authors report PTC amplitudes of seven decades with HDPE-16%CNP but interestingly using three times less the amount of CNT prevents the appearance of an NTC effect in the liquid state. This was explained by a higher stability of the CNT network than the carbon nanoparticles' (CNP) percolated structure. Correlatively (Deng *et al.*, 2009) carefully studied the influence of polypropylene matrix melting and re-crystallization in carbon-filled CPCs on the formation and destruction of the conductive network. They conclude on the higher strength of CNT network compared to CNP. Moreover, Lee *et al.* (2006) found many positive effects of the addition of only 0.5 wt% of CNT to HDPE-25%CNP CPC. The first effect was to decrease the CPC percolation threshold by about 20%, the second to increase CPC stability in the heating/cooling

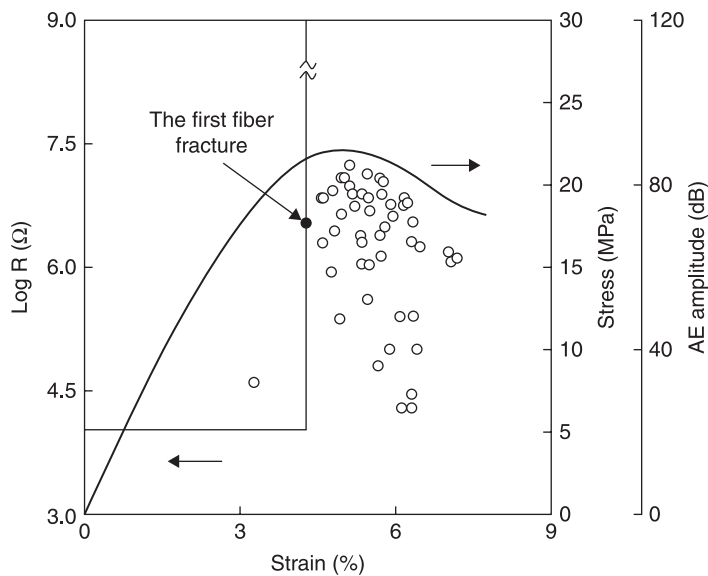
cycling, the third to enhance PTC intensity by 1.5 decade, and finally to increase HDPE crystallinity. (Gao *et al.*, 2009) confirmed the strong effect of processing conditions of segregated UHMWPE–CNT CPCs, mainly related to crystallization, on PTC characteristics like amplitude and T_{com} , which could be increased from 1.37 to 2.05 by decreasing moulding temperature from 200 to 160 °C, or increasing melting enthalpy from 133.6 J/g to 151.2 J/g by increasing isothermal treatment at 100 °C duration from 12 to 84 hrs. In complement, (Jiang *et al.*, 2006) studied the combined effects of pressure and temperature on methyl vinyl silicone rubber (VMQ) filled with γ -aminopropyl triethoxy silane (APS) modified CNT. They found that it was possible to dramatically modify VMQ-2.5%CNTs' sensing behaviour, i.e. increasing APS content from 1 to 5% enhanced sensitivity to pressure and shift T_{com} from 50 to 20 °C. Many works on temperature sensing or temperature self-regulation concern the poly(ethylene) matrix CPC due to the fact that very early, Meyer (1973) had identified its capability to generate high amplitude PTC effect, presumably thanks to its low glass transition temperature T_g . Nevertheless, high PTC amplitude is mostly interesting for self-regulation whereas temperature monitoring only needs a measurable change of relative resistance A_r . From this point of view, it is much more interesting to change T_{com} of the CPC transducer to vary the measurement range. Thus, Lu *et al.* (2009a) developed a transducer based on a CNT-filled poly(caprolactone) PCL conducting phase, with low T_{com} (Fig. 25.20) able to sense temperature rise over 50 °C, making it possible to design sensors that can trigger an alarm when the human pain threshold is reached. This can be particularly valuable for firemen's protective clothing (Fig. 25.21). Figure 25.20 shows the addition of an external matrix like PP or



25.20 Amplitude of PTC effect depending on external matrix (none, PP, PA12) associated with PCL-3%CNT conducting phase.



25.21 Possible application of PP/(PCL-CNT) textiles.



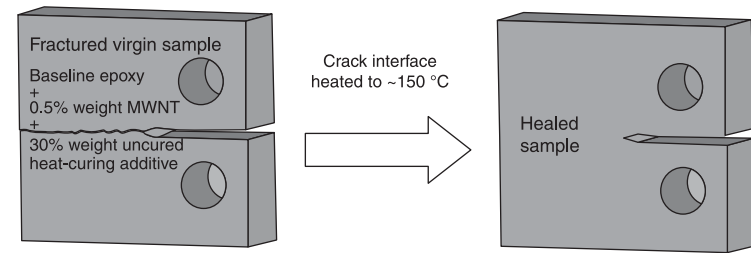
25.22 Damage sensitivity of fiber fracture of EP/CF composites with 0.1 vol% CNT (Park *et al.*, 2003).

poly(amide12) PA12 to obtain a co-continuous morphology and secure CPC thermo-electrical behaviour over PCL melting, is followed by a decrease in PTC amplitude. Although this decrease is acceptable for PP, with PA12, no significant resistance change is observed upon heating which prevents temperature sensing. A

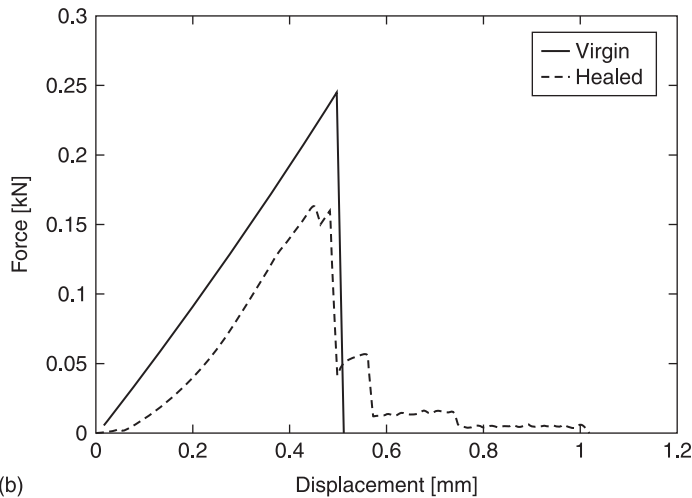
similar behaviour previously encountered with poly(butylene terephthalate)/poly(ethylene-co-ethyl acrylate)-carbon nanoparticle 60PBT/40(EEA-CNP) had been explained by the migration of CNP density at the interface between the two polymers (Feller *et al.*, 2004). Finally, PP–PCL–CNT co-continuous CPCs have been developed to design temperature transducers in either film or fibre form able to resist temperature overshoot up to 150 °C (INTELTEX, 2010). There are also possible applications in electronics. Applications for PTC composites include thermistor, circuit protection devices, and self-regulating heaters. Coupled with a wireless communication system to a computer, temperature sensors can be integrated into structures.

25.4.3 Strain sensing with CNT-filled CPCs

Since early works on health monitoring of structural composites reported by (Wang and Chung, 1997) who used the conductivity of reinforcing carbon fibres to follow dynamic strain and damage, this topic has attracted a lot of attention. (Park *et al.*, 2003) demonstrated that introducing only a small amount of carbon nanotubes (less than 0.5 vol.%) could provide an alternative way to monitor carbon fibres (CF) reinforced epoxy (EP) composites damage in a non-destructive way, just following the evolution of CPC resistance. In fact, carbon nanotubes are three orders of magnitude smaller than usual reinforcing fibres in structural composites, they can be used to create a conductive network in the polymer, penetrating the matrix-rich region surrounding the fibres, and thus allowing the direct monitoring of deformation-induced resistance changes. Moreover, Fig. 25.22 shows that the electrical signal will alert slightly in advance carbon fibres' breakage measured mechanically, which is very interesting in applications to anticipate structural composites' failure. A few years later, Thostenson and Chou (2006b) and Thostenson *et al.* (2007) reported that building carbon nanotubes conducting networks in epoxy/glass fibre (UP/GF) composites was effective to monitor damage in advanced polymer-based composites. The inherent multi-functionality of carbon nanotubes was successfully illustrated in this work to develop a 'smart materials', both charge-induced deformations and *in-situ* damage monitoring were investigated. Additionally, it was shown that the percolating carbon nanotubes network was very sensitive to initial stages of matrix-dominated failure, confirming carbon nanotubes' potential for health monitoring (Fig. 25.23). Zhang *et al.* (2007b) have also demonstrated that thanks to the CNT network, delamination defects could be detected via electrical resistance measurement in laminated composite structures and that the use of MWNT additives induces fast heating of crack interfaces allowing self-healing, i.e. reparation of damage after detection and recovery of up to 70% of the strength. Another contribution to the topic has been added by Wichmann *et al.* (2008) who developed a direction-sensitive bending strain sensor by generating a gradient in electrical conductivity throughout a single block of epoxy-CNT composite.



(a)

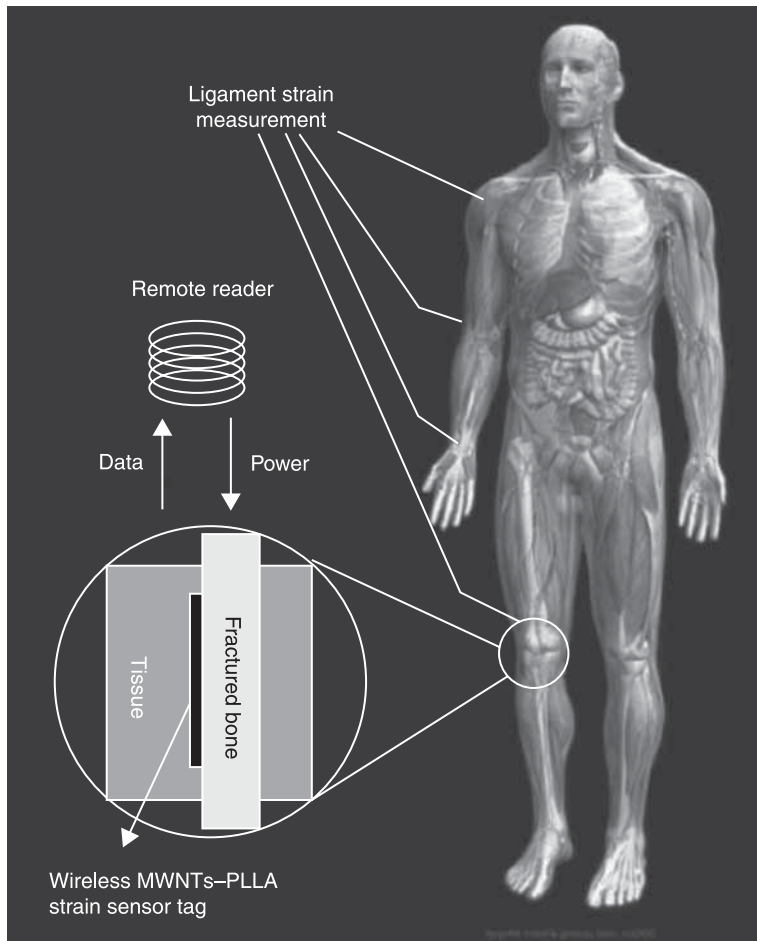


(b)

25.23 Demonstration of crack healing in (a) scheme of fractured and healed samples. (b) Load vs displacement curves of virgin (epoxy-0.5 wt% CNT) and healed (virgin + 30% uncured heat-curing additive) demonstrating 55% to 70% recovery of the ultimate failure load (Zhang *et al.*, 2007).

Electrical resistance becomes positive or negative, depending on the direction of bending deflection.

Instead of using the composite itself to monitor strain or stress, another approach has been recently proposed by Alexopoulos *et al.* (2009) who embedded CNT fibres (prepared by coagulation of CNT dispersion in a PVA solution) in glass-fibres reinforced composites. Parabolic and exponential correlations were found between mechanical stresses and the electrical responses, and it was shown that the constants thus obtained were linearly connected to the composites' previous loading history. The same kind of strategy was used by Kang *et al.* (2006b) who developed thin layers of poly(methyl methacrylate) PMMA-impregnated carbon nanotubes bucky papers to form a piezoresistive strain sensor material for health monitoring applications. Strain sensors were glued under vacuum on the surface



25.24 Experimental set-up for remote measurement of strain inside the human body with PLLA-5wt% CNT (Liu *et al.*, 2007).

of a composite cantilever beam (to overcome slippage issues and sensors' distorted responses) before impedance spectroscopy and strain testing. A linear symmetric strain response in both compressive and tensile cases was observed for the SWNT–10%PMMA sensors, even though sensitivity was lower than bucky papers sensors. Moreover, a biomimetic artificial neuron was developed by extending the length of the sensor. This long continuous strain sensor is low cost, simple to install and is lightweight, so that it may allow different target applications like crack propagation prediction in composites' structures (buildings, bridges, aircraft) or tactile sense application in artificial skin development. Zhang *et al.* (2006b) used poly(carbonate)–CNT CPC for strain sensing application and reported strain gauge factor (defined by the ratio of relative amplitude and

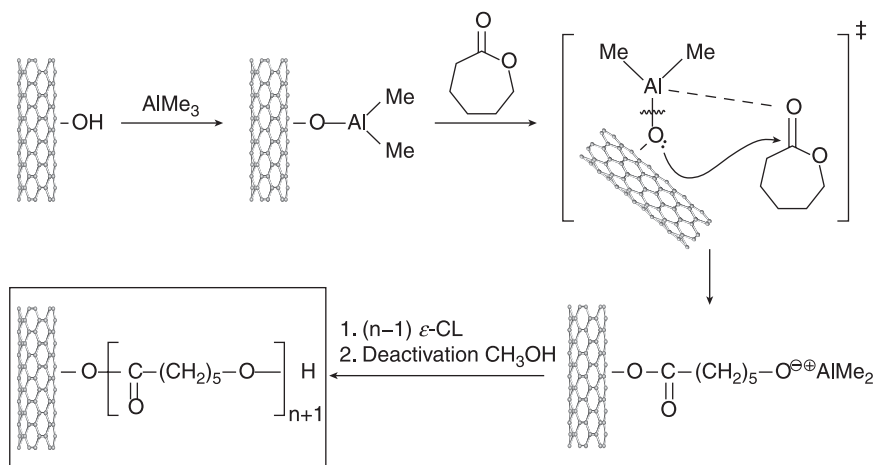
deformation, $(\Delta R/R)/\epsilon$ of 3.5 times higher than traditional ones, whereas Zhang *et al.* (2007b) have demonstrated a universal resistivity–strain dependency of poly(urethane)–urea elastomer matrix associated with amino-functionalized CNT. Knite *et al.* (2007) compared piezo-electrical properties of CPC composed of a poly(isoprene) matrix (PI) filled with either MWNTs or CNPs. They report a lower amplitude and a lack of reversibility of PI–CNT samples at large strains (40%) compared to their homologues PI–CNP, and suggest using CNT-based material only for small strain sensing applications, and preferably PI–CNP composites for large strain sensing applications. In a more recent work, Knite *et al.* (2009) show that PI–CNT can also be sensitive to pressure and chemicals. Another interesting illustration of strain sensing is given by Liu *et al.* (2007) who investigated the use of poly(L-lactic acid) PLLA (biocompatible and biodegradable) in association with CNTs for biomedical applications such as an implantable and wearable strain sensor (Fig. 25.24). They report gauge factors up to 30 soliciting sensors on a 4 points bending mode, depending on the initial resistance. Targeting long-term and large-scale infrastructure health monitoring, Loh *et al.* (2005) prepared thin CPC films, through an original layer-by-layer (LbL) assembly method. From 35 to 200 bi-layers of carbon nanotubes dispersed in either poly(vinyl alcohol) (PVA) or poly(sodium styrene-4-sulfonate) (PSS), were assembled in thin sensor films and tested upon monotonic deformation. A linear relation between resistance and strain was observed and they achieved a gauge factor (A_r/ϵ) of 4.52. On the other hand, these transducers exhibited interesting pH sensitivity, assuming promising application in corrosion monitoring.

CPC-based sensors should find many applications in manufacturing industries such as civil engineering, the automotive or aircraft industry as strain or pressure sensors for damage detection and load history. Aircraft parts are subjected to strain and pressure while in use. CPC-based sensors could impart information about surface strain state, appearance of microcracks and the evolution of strain-induced damage. Fibre-reinforced composites for structural applications are particularly concerned since microscale damages have implications on the durability and performance of the composites. Structure health monitoring is one concern but sensors can also be used upstream for *in-situ* processing monitoring. For instance, during the cooling stage of thermoset-based composites, residual stress or strain can be monitored to control the prepared parts and to prevent defects and damage propagation. CPC-based sensors could be used in civil structures like bridges, tunnels, roads or buildings to follow the ageing process and detect defects induced by fatigue, impact or corrosion. Embedded sensors could help civil engineers in structure inspections and long-term monitoring.

25.4.4 Chemical sensing with CNT-filled CPCs

Since early findings on electrical noses (Gardner and Barlett, 1992), lots of combinations of nanofillers and polymer matrices have been experimented to

design new chemical transducers with increasing sensitivity and discriminating ability. Philip *et al.* (2003) and Abraham *et al.* (2004) first showed that CNTs dispersed in a PMMA matrix could efficiently sense a set of organic vapours (dichloromethane, chloroform and acetone) and that CNT oxidation by potassium permanganate with the help of a phase transfer catalyst was effective in considerably increasing transducers' sensitivity. Since then, there has been great interest in developing carbon nanotubes-based transducers, which, compared to the more classical carbon nanoparticles, have a much larger aspect ratio and now comparable cost. Thus chemoresistive CNT-based CPCs have been used to design sensors for humidity (Chen *et al.*, 2005; Su and Huang, 2006; Su and Wang, 2007; Yu *et al.*, 2006; Kumar *et al.*, 2010), acid vapours (Bavastrello *et al.*, 2004), ammoniac (Zhang *et al.*, 2006b; Woo *et al.*, 2007), amines (Ma *et al.*, 2006; Lee *et al.*, 2008), warfare agents (Wang *et al.*, 2008; Chang and Yuan, 2009), volatile anaesthetic agent sevoflurane (Chavali *et al.*, 2008), and VOC (Zhang *et al.*, 2005; Quercia *et al.*, 2005; Sathanam *et al.*, 2005; Wang *et al.*, 2007; Wei *et al.*, 2006). Thanks to the tremendous increase in sensitivity resulting from CNT functionalization by Philip *et al.* (2003), Wang *et al.* (2007) have experimented with CNT grafting with poly(styrene), poly(4-vinylpyridine), poly(styrene-*b*-4-vinylpyridine) and poly(styrene-*co*-4-vinylpyridine) by nitroxide mediated 'living' free radical polymerization which proved to lead to effective transducers for methanol, chloroform and tetrahydrofuran. Electrical responses are synthesized by plotting sensors' sensitivity as a function of vapour content and nature, which gives a good overview of CPCs' transducer performances. More recently, Castro *et al.* (2009) used the same concept by developing *in-situ* ring opening polymerization of poly(ϵ -caprolactone) to graft CNT according to the scheme in Fig. 25.25. This CNT surface treatment was found to improve both dispersion and sensitivity of



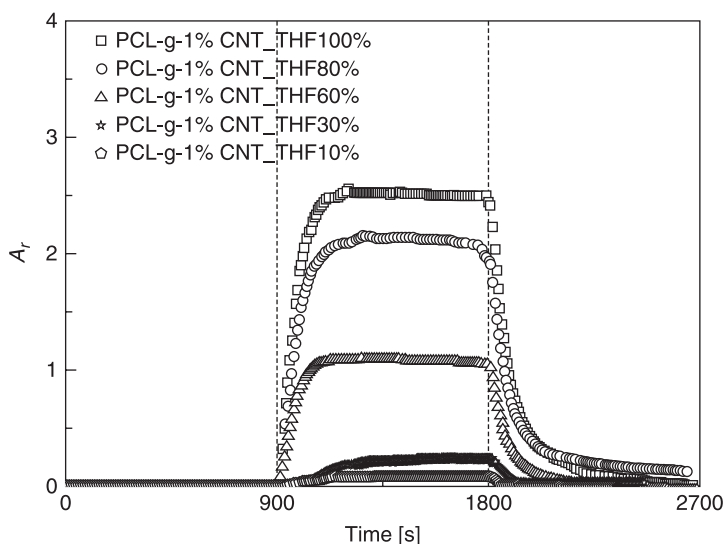
25.25 Scheme of CNT grafting by *in-situ* polymerization of poly(ϵ -caprolactone) from Castro *et al.* (2009).

transducers leading to stable, reproducible and quantitative electrical signals upon dynamic chemical solicitations as can be seen in Fig. 25.26. Interestingly, Fig. 25.27, that was obtained by taking the maximum value of A_r (the relative amplitude of the electrical response) when a stable value is reached, shows that the evolution of A_r with vapour volume fraction f (v/v) fits well with the LHC model (Equation 25.7). However, chloroform exhibits a totally different chemo-electrical behaviour. The origin of this peculiarity is well evidenced by observing in Fig. 25.28 the evolution of A_r with vapour nature, i.e. as a function of inverse of Flory-Huggins parameter χ_{12} . Experimental data fit well with Equation 25.8 that predicts an exponential evolution of A_r with the inverse of χ_{12} (Equation 25.6). Nevertheless, if the model succeeds in predicting the increase in PCL–CNT transducers' sensitivity with water, methanol, toluene and chloroform, it fails with tetrahydrofuran, suggesting the need to also take into account additional parameters like saturating pressure or size of vapour molecules to fully describe the phenomenon.

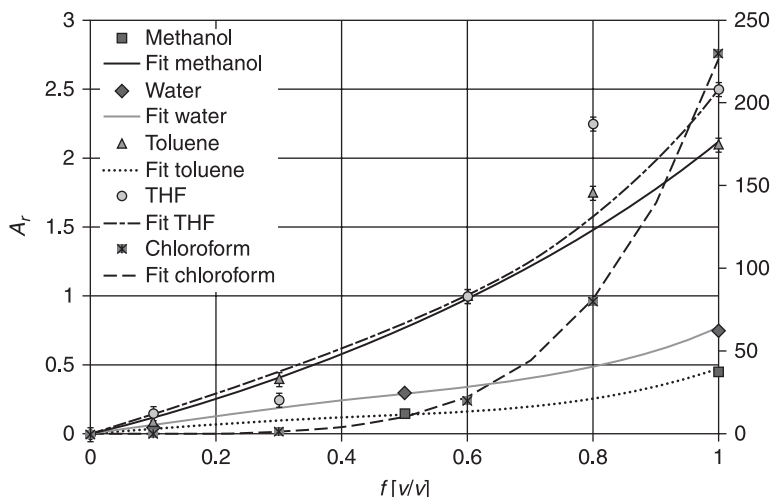
$$A_r = ae^{\frac{b}{\chi_{12}}} \quad [25.8]$$

with a and b constants.

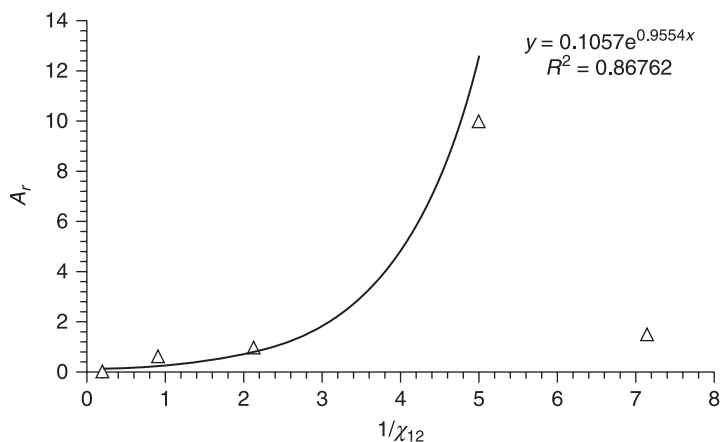
A more radical way to identify vapours is to use a statistical tool like principal component analysis (PCA) treatment developed for e-noses, which will combine all the responses of different transducers submitted to the same chemical vapours. The results presented in Fig. 25.28 clearly show the high potential of such data



25.26 Typical response of PCL-g-1%CNT to different concentrations of tetrahydrofuran (THF) in nitrogen (Castro *et al.*, 2009).



25.27 Relative amplitude A_r of PCL-g-1%CNT transducers exposed to different volume fractions of water, methanol, toluene, THF and chloroform vapours in dynamic mode. Curves were fitted using LHC model without Langmuir contribution (HC) model (Equation 25.7). The right y axis is used for chloroform which has much larger amplitude than other vapours.

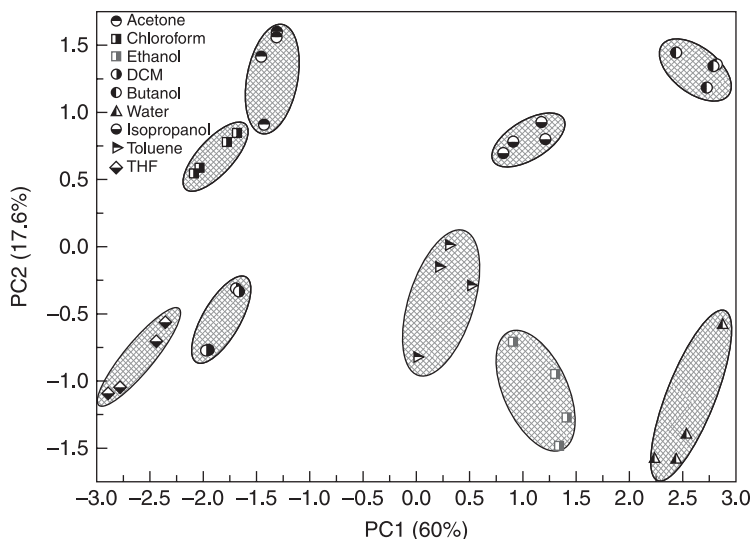


25.28 Evolution of PCL-g-CNT response with $1/\chi_{12}$ (experimental data fit with Equation 25.8).

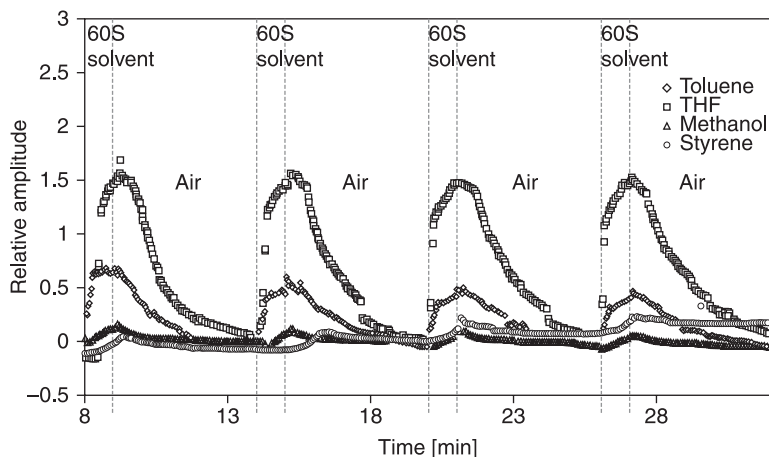
processing in providing recognition patterns for vapour identification. The common method of sensing investigations is to study each vapour separately but (Zhang *et al.*, 2008) have started to address an important issue, sensing of mixed vapours. Using a single poly(styrene)-CNT transducer they have found that unexpectedly after exposure to vapour mixtures, resistance does not decrease

as usual (PVC effect) but sharply increases (NVC effect). To explain this phenomenon, the formation of a parallel conductive water layer able to decrease sample resistivity has been assumed. Another case of the NVC effect has been reported by Li *et al.* (2007) with a PMMA–CNT transducer in the presence of methanol vapours and has been interpreted by a reduction reaction at the CNT surface which could take place due to the fact that they were chemically modified by NH_3OH and HCl . Apart from the chemical nature and composition of CPC constituents that will determine transducers' chemo-electrical properties, Lu *et al.* (2009b) have reported the influence of processing conditions that can be adjusted to tailor the sensors' characteristics. Particularly, the spray layer-by-layer (LbL) deposition process hierarchically structures the sensitive film in 3D and provides an effective way to control initial resistance and thus the transducers' sensitivity. Inkjet printing technique is another technique that has been used by Mabrook *et al.* (2008) which could be promising to fabricate thin CNT-filled CPC transducers.

To complement vapour sensing, CN-filled CPCs have also proved their ability to sense liquid chemicals. Narkis *et al.* (2000) and Srivastava *et al.* (2000) initiated interest in using co-continuous CPC filaments of PP/(PA6-CNP) and HIPS/(EVA-CNP) for liquid sensing. Later on, Segal *et al.* (2005) used co-continuous filaments of PP/TPU–CNP and PS/PANI-DBAS to sense methanol, ethanol and 1-propanol with good selectivity and sensitivity. They interpreted the sensing mechanism of these CPCs in terms of interphase debonding because the short response time of these CPCs suggested a preferential permeation through the interphase regions rather than a diffusion-controlled process through the bulk phases. Applying this principle to CNT-filled co-continuous CPC like PP/(PCL–CNT) gives the records of Fig. 25.29. Electrical responses are found to be reproducible and stable upon exposure to several organic solvents. The reason for the asymmetry of chemical cycles as compared to vapour sensing is that sorption is much quicker than desorption as molecules are invading the composite deeper and in much greater amounts than in the case of vapour, so that the clustering phase is reached, generating the matrix swelling (at least for good solvents). Nevertheless, the same kind of features as for vapour sensing have been observed by Kobashi *et al.* (2008, 2009), who recently investigated the liquid sensing properties of poly(lactic acid)/multi-walled carbon nanotube (PLA–CNT) CPC films and fibres (Fig. 25.30). Moreover, they have demonstrated the influence of the polymer matrix crystallinity on transducers' resistance changes occurring during immersion. Possible target applications for such fibres would be leakage detection in tanks or containers (Pötschke *et al.*, 2009). Another interesting issue of liquid sensing is the detection of biomolecules like glucose. (Teh and Lin, 2005) by associating dodecylbenzenesulfonate-doped poly(pyrrole) (DBS-PPy) with CNT found that transducers were responsive to oxidants, like hydrogen peroxide (H_2O_2), indirectly allowing detection of glucose ($\text{C}_6\text{H}_{12}\text{O}_6$) which in the presence of oxygen, glucose is enzymatically oxidized at the anode to yield gluconolactone ($\text{C}_6\text{H}_{10}\text{O}_6$) and hydrogen peroxide (H_2O_2).



25.29 Combination of CPC responses using PCA for vapour identification.



25.30 Liquid sensing cycling with PP/(PCL-3% CNT) film transducers exposed to toluene, tetrahydrofurane, methanol and styrene.

Finally, Pioggia *et al.* (2007a, 2007b, 2008) report the development of so-called electronic tongues. Associating conductive polymer composite transducers in arrays, they were able to associate five compounds (including hydrophilic hydrogels consisting of blends of poly(vinyl alcohol) PVA and poly(allylamine) PAA loaded with CNT) with different chemical characteristics and gustative perceptions (sodium chloride, citric acid, glucose, glutamic acid and sodium dehydrocholate for

salty, sour, sweet, umami and bitter, respectively). Impedance measurements were done at 150 Hz, during dipping in solution/drying in air cycles, and use of principal component analysis allowed a fairly good degree of discrimination.

Although many applications already use the e-noses and e-tongues principle to analyse qualitatively and quantitatively the composition of complex environments, there is still a need to develop combinations of new materials to widen the range of detectable substances. For example, in the foodstuffs industry, the sensors developed can be used for automatic quality control. Raw components are likely to undergo spoilage because of bacteria and humidity or temperatures issues and this technology offers the opportunity to follow food products during processing steps. This strategy could be used for quality control during production but also to monitor the food during storage, or even during the ageing process. Ageing in some cases is coupled with specific gas/vapour emissions that could be analysed and quantified to allow final product quality requirements. Thus, meat or seafood freshness, milk spoilage, fruit and vegetables' quality monitoring appear promising areas for carbon nanotubes-based CPC sensors. In industrial plants, e-noses can be used to monitor pollutants, toxic substances, and detection of leaks in chemicals pipes or containers. Sensors can be used to analyse exhaust gases in industrial smokestacks. In collective housing, sensors could detect gas/vapours in air conditioning distribution main pipes to prevent air contamination throughout the building. Other applications concern safety areas for detection of biological and chemical weapons, detection of drugs or explosives. Security issues regarding terrorist actions are of special concerns and nanoscale sensors' development could fulfil some military applications. Recently the study of nanostructured polymer sensor materials in the detection of potential chemical warfare agents and industrial chemical reagents like DMMP, DCM, THF, CHCl_3 , MEK and xylene was reported (Wang *et al.*, 2008; Chang and Yuan, 2009). They noticed the lack of adaptive sensors for selectivity among existing sensors, and proposed the use of MWNT-based CPC as fast-acting, inexpensive, simple to operate, sensitivity and selective sensor materials. High potential risks facilities, like airports, train stations or sport/cultural events that attract masses of people, could be equipped with such devices. Recent research has also focused on medical applications for non-invasive diagnostics (breath, urine, sweat). The objective is to detect the diseases in their early stage so that medical care can be quickly conducted. Great efforts are provided, for instance, in early stage detection of cancer markers since this disease will become one of the main causes of fatalities in the near future. One permanent challenging issue regarding these applications lies in decreasing the concentration range of the targeted molecules, i.e. from ppm to ppb.

25.5 Conclusion

The aim of this chapter was to give a quick overview of the different sensing applications of CNT-polymer composites (temperature sensors, thermistances,

vapour sensors, e-noses, e-tongues, strain sensors, durability sensors). Many applications have been and are still being discovered in this very active field of research as attested by recent reviews on sensors' materials (Huang and Choi, 2007; Kauffman and Star, 2008; Hatchett and Josowicz, 2008; Hierlemann and Gutierrez-Osuna, 2008; Bondavalli *et al.*, 2009; Qureshi *et al.*, 2009). Considering also the increasing demands related to smart functions for industrial but also domestic applications, there is still a lot of room for creativity and new developments. A good example of integration of advanced functionalities is illustrated by intelligent textiles (INTELTEX, 2010), capable of monitoring strain, temperature or chemicals, thus finding applications such as anomalous heart rate detection, real-time monitoring of body temperature or blood pressure measurement. Such smart textiles can also be used for the clothing of sportsmen operating in extreme conditions at low temperatures (mountain climbing or diving) where lightweight wearable and self-heating fabrics can be helpful. Multifunctional textiles are robust and can be used in the protective clothing of firemen or soldiers, enabling near skin temperature monitoring, detection of mechanical strain due to impact or penetration and detection of toxic volatiles in rescue or military operations conditions.

25.6 Acknowledgements

The authors would like to thank Przeyslaw Michalak for alternative current measurements and the European Commission for financial support (INTELTEX, 2010).

25.7 References

- Abraham J K, Philip B, Varadan V K and Reddy V C (2004) 'A compact wireless gas sensor using a carbon nanotube/PMMA thin film chemiresistor', *Smart Materials & Structures*, 13, 1045–1049.
- Alexopoulos N D, Bartholome C, Poulin P and Marioli-Riga Z (2009), 'Structural health monitoring of glass fiber reinforced composites using embedded carbon nanotube (CNT) fibers', *Composites Science & Technology*, 70, 12, 1733–1741.
- Baughman R H, Cui C X, Zakhidov A A, Iqbal Z, Barisci J N, Spinks G M, Wallace G G, Mazzoldi A, De Rossi D, Rinzler A G, Jaschinski O, Roth S and Kertesz M (1999) 'Carbon nanotube actuators', *Science*, 284, 1340–1344.
- Bauhofer W and Kovacs J Z A (2009) 'Review and analysis of electrical percolation in carbon nanotube polymer composites', *Composites Science & Technology*, 69, 1486–1498.
- Bavastrello V, Stura E, Carrara S, Erokhin V and Nicolini C (2004) 'Poly(2,5-dimethylaniline)–CNT nanocomposite: a new material for conductimetric acid vapours sensor', *Sensors & Actuators B*, 98, 247–253.
- Bellayer S, Gilman J W, Eidelman N, Bourbigot S, Flambard X, Fox D M, De Long H C and Trulove P C (2005), 'Preparation of homogeneously dispersed trialkyl imidazolium compatibilized multiwalled carbon nanotube/polystyrene nanocomposites via melt extrusion', *Advanced Functional Materials*, 15, 5, 910–913.

- Böger L, Wichmann M H G, Meyer L O and Schulte K (2008) 'Load and health monitoring in glass fibre reinforced composites with an electrically conductive nanocomposite epoxy matrix', *Composites Science & Technology*, 68, 1886–1894.
- Boiteux G, Boullanger C, Cassagnau P, Fulchiron R, and Seytre G (2006) 'Influence of morphology on PTC in conducting polypropylene-silver composite', *Macromolecular Symposia*, 233, 1, 246–253.
- Boiteux G, Fournier J, Issotier D, Seytre G, and Marichy G (1999) 'Conductive thermoset composites: PTC effect', *Synthetic Metals*, 102, 1–3, 1234–1235.
- Bondavalli P, Legagneux P and Pribat D (2009) 'Carbon nanotubes based transistors as gas sensors: State of the art and critical review', *Sensors & Actuators B*, 140, 304–318.
- Bonnet P, Albertini D, Bizot H, Bernard A, and Chauvet O (2007) 'Amylose/SWNT composites: From solution to film: synthesis, characterization and properties', *Composites Science & Technology*, 67, 817–821.
- Bouvée A, Feller J F, Balnois E, Salaun A C and Grohens Y (2007) 'Conductive polymer composites (CPC) transducers: Structuring of carbon and gold nanoparticles in thin layers for vapour sensing', *Transducers Proceeding*, 10–14 June, Lyon, France.
- Broadbent S R and Hammersley J M (1957) 'Percolation processes I. Crystals and mazes', *Proceedings of the Cambridge Philosophical Society*, 53, 3, 629–641.
- Carmona F (1989) 'Conducting filled polymers', *Physica A*, 157, 461–469.
- Carmona F and Mouney C (1992) 'Temperature dependent resistivity and conduction mechanism in carbon particle-filled polymers', *Journal of Material Science*, 27, 1322.
- Castro M, Lu J, Bruzard S, Kumar B and Feller J F (2009) 'Carbon nanotube/poly (ε-caprolactone) composite vapour sensors', *Carbon*, 47, 1930–1942.
- Celzard A, McRae E, Maréché J F, Furdin G and Sundqvist B (1998) 'Conduction mechanisms in some graphite-polymer composites: effects of temperature and hydrostatic pressure', *Journal of Applied Physics*, 83, 3, 1410–1419.
- Celzard A, Pizzi A and Fierro V (2008) 'Physical gelation of water-borne thermosetting resins by percolation theory: urea-formaldehyde, melamine-urea-formaldehyde, and melamine-formaldehyde resins', *Journal of Polymer Science: Part B: Polymer Physics*, 46, 971–978.
- Chang C P and Yuan C L (2009) 'The fabrication of a MWNTs-polymer composite chemoresistive sensor array to discriminate between chemical toxic agents', *Journal of Materials Science*, 44, 5485–5493.
- Chavali M, Lin T, Wu R, Luk H, and Hung S (2008) 'Active 433 MHz-W UHF RF-powered chip integrated with a nanocomposite m-MWCNT/polypyrrole sensor for wireless monitoring of volatile anesthetic agent sevoflurane', *Sensors & Actuators A*, 141, 109–119.
- Chen H, Wu R, Chan K, Sun Y and Su P (2005) 'The application of CNT-Nafion composite material to low humidity sensing measurement', *Sensors & Actuators B*, 104, 80–84.
- Dalmas F, Dendievel R, Chazeau L, Cavallé J Y and Gauthier C (2006) 'Carbon nanotube filled polymer composites: numerical simulation of electrical conductivity in three-dimensional entangled networks', *Acta Materialia*, 54, 11, 2923–2931.
- Decher G (1997) 'Fuzzy nanoassemblies toward layered polymeric multicomposites', *Science*, 277, 1232–1237.
- De Gennes P G (1976) 'On a relation between percolation theory and the elasticity of gels', *Journal de Physique Lettres*, 37, 1–3.
- Deng H, Skipa T, Zhang R, Lellinger D, Bilotti E, Alig I and Peijs T (2009) 'Effect of melting and crystallization on the conductive network in conductive polymer composites', *Polymer*, 50, 3747–3754.

- Droval G, Feller J F, Salagnac P, and Glouannec P (2008) 'Conductive polymer composites (CPC) with double percolated architecture of carbon nanoparticles and ceramics microparticles for high heat dissipation and sharp PTC switching', *Smart Materials & Structures*, 17, 025011, 1–10.
- Du D, Huang X, Cai J and Zhang A (2007) 'Amperometric detection of triazophos pesticide using acetylcholinesterase biosensor based on multiwall carbon nanotube–chitosan matrix', *Sensors & Actuators B: Chemical*, 127, 2, 531–535.
- Du F, Scogna R C, Zhou W, Brand S, Fischer J E and Winey K I (2004) 'Nanotube networks in polymer nanocomposites: rheology and electrical conductivity', *Macromolecules*, 37, 9048–9055.
- Etika K C, Liu L, Hess L A, and Grunlan J C (2009) 'The influence of synergistic stabilization of carbon black and clay on the electrical and mechanical properties of epoxy composites', *Carbon*, 47, 3128–3136.
- Feller J F (2004) 'Conductive polymer composites: influence of extrusion conditions on positive temperature coefficient effect (PTC) of poly(butylene terephthalate)/poly(olefin)-carbon black blends', *Journal of Applied Polymer Science*, 91, 4, 2151–2157.
- Feller J F, Bruzaud S and Grohens Y (2004) 'Influence of clay nanofiller incorporation on electrical and rheological properties of conductive polymer composite (CPC)', *Materials Letters*, 58, 5, 739–745.
- Feller J F, Linossier I and Grohens Y (2002) 'Conductive polymer composites (CPC): comparative study of poly(ester)-short carbon fibres and poly(epoxy)-short carbon fibres mechanical and electrical properties', *Materials Letters*, 57, 1, 64–71.
- Feller J F, Linossier I and Levesque G (2002) 'Conductive polymer composites (CPC): comparative study of poly(ethylene-co-ethyl acrylate)-carbon black and poly(butylene terephthalate)/poly(ethylene-co-ethyl acrylate)-carbon black electrical properties', *Polymers for Advanced Technologies*, 13, 10–12, 714–725.
- Ferrara M, Neitzert H C, Sarno M, Gorrasi G, Sannino D, Vittoria V, Ciambelli P (2007) 'Influence of the electrical field applied during thermal cycling on the conductivity of LLDP/CNT composites', *Physica E: Low-dimensional Systems & Nanostructures*, 37, 1–2, 66–71.
- Freund M S and Lewis N S (1995) 'A chemically diverse conducting polymer-based electronic nose', *Proceeding of National Academy of Science*, 92, 2652.
- Gao J F, Yan D X, Huang H D, Dai K and Li Z M (2009) 'Positive temperature coefficient and time-dependent resistivity of carbon nanotubes (CNT)/ultrahigh molecular weight polyethylene (UHMWPE) composite', *Journal of Applied Polymer Science*, 114, 1002–1010.
- Gardner J W, and Barlett P N (1992) *Sensors and Sensory Systems for an Electronic Nose*, Dordrecht: Kluwer Academic Publishers.
- Gau C, Ko H S and Chen H T (2009) 'Piezoresistive characteristics of MWNT nanocomposites and fabrication as a polymer pressure sensor', *Nanotechnology*, 20, 185503, 1–11.
- Gau C, Kuo C Y and Ko H S (2009) 'Electron tunnelling in carbon nanotube composites', *Nanotechnology*, 20, 395705, 1–6.
- Grunlan J C, Gerberich W W and Francis L F (2001) 'Lowering the percolation threshold of conductive composites using particulate polymer microstructure', *Journal of Applied Polymer Science*, 80, 4, 692–705.
- Grunlan J C, Mehrabi A R, Bannon M V and Bahr J L (2004) 'Water-based single-walled-nanotube-filled polymer composite with an exceptionally low percolation threshold', *Advanced Materials*, 16, 2, 150–153.

- Hatchett D W and Josowicz M (2008) 'Composites of intrinsically conducting polymers as sensing nanomaterials', *Chemical Review*, 108, 746–769.
- He X J, Du J H, Ying Z and Cheng H M (2005) 'Positive temperature coefficient effect in multiwalled carbon nanotube/high-density polyethylene composites', *Applied Physics Letters*, 86, 062112.
- Hierlemann A and Gutierrez-Osuna R (2008) 'Higher-order chemical sensing', *Chemical Review*, 108, 563–613.
- Huang X J, and Choi Y K (2007) 'Chemical sensors based on nanostructured materials', *Sensors & Actuators B*, 122, 659–671.
- Imbert C, Tchoreloff P, Leclerc B and Couarraze G (1997) 'Indices of tableting performance and application of percolation theory to powder compaction', *European Journal of Pharmaceutics & Biopharmaceutics*, 44, 3, 273–282.
- INTELTEX (2006–2010) 'Development of intelligent multi-reactive textiles integrating nano-filler based CPC-fibres', European Integrated Project supported through the 6th Framework Programme for Research and Technological Development of European Commission (NMP2-CT-2006–026626), available at: www.inteltex.eu.
- Jiang M J, Dang Z M and Xu H P (2006) 'Significant temperature and pressure sensitivities of electrical properties in chemically modified multiwall carbon nanotube/methylvinyl silicone rubber nanocomposites', *Applied Physics Letters*, 89, 182902, 1–3.
- Kang I, Heung Y Y, Kim J H, Lee J W, Gollapudi R, Subramaniam S, Narasimhadevara S and Hurd D (2006a) 'Introduction to carbon nanotube and nanofiber smart materials', *Composites: Part B: Engineering*, 37, 382–394.
- Kang I, Schulz M J, Kim J H, Shanov V and Shi D (2006b) 'A carbon nanotube strain sensor for structural health monitoring', *Smart Materials & Structures*, 15, 737–748.
- Kauffman D R and Star A (2008) 'Carbon nanotube gas and vapor sensors', *Angewandte Chemie*, 47, 6550–6570.
- Knite M, Ozols K, Zavickis J, Tupureina V, Klemenoks I and Orlovs R (2009) 'Elastomer-carbon nanotube composites as prospective multifunctional sensing materials', *Journal of Nanoscience & Nanotechnology*, 9, 6, 3587–3592.
- Knite M, Tupureina V, Fuih A, Zavickis J and Teteris V (2007) 'Polyisoprene-multi-wall carbon nanotube composites for sensing strain', *Materials Science & Engineering: C*, 27, 5–8, 1125–1128.
- Kobashi K, Tobias V, Timo A, Häußler L and Pötschke P (2009) 'Investigation of liquid sensing mechanism of poly(lactic acid)/multi-walled carbon nanotube composite films', *Smart Materials & Structures*, 18, 035008, 1–15.
- Kobashi K, Villmow T, Andres T and Pötschke P (2008) 'Liquid sensing of melt-processed poly(lactic acid)/multi-walled carbon nanotube composite films', *Sensors & Actuators B: Chemical*, 134, 787–795.
- Kost J, Narkis M and Foux A (1983) 'Effects of axial stretching on the resistivity of carbon black filled silicone rubber', *Polymer Engineering & Science*, 23, 567–571.
- Kost J, Narkis M and Foux A (1984) 'Resistivity behavior of carbon black filled silicone rubber in cyclic loading experiments', *Journal of Applied Polymer Science*, 29, 3937–3946.
- Krasteva N, Besnard I, Guse B, Bauer R E, Mullen K, Yasuda A and Vossmeier T (2002) 'Self-assembled gold nanoparticle/dendrimer composite films for vapor sensing applications', *Small*, 2, 5.
- Krasteva N, Guse B, Besnard I, Yasuda A and Vossmeier T S (2003) 'Gold nanoparticle/PPI-dendrimer based chemiresistors' vapor-sensing properties as a function of the dendrimer size', *Sensors & Actuators B: Chemical*, 92, 137–143.

- Krause B, Ritschel M, Täschner C, Oswald S, Gruner W, Leonhardt A and Pötschke P (2010) 'Comparison of nanotubes produced by fixed bed and aerosol CVD methods and their electrical percolation behaviour in melt mixed polyamide 6.6 composites', *Composites Science & Technology*, 70, 151–160.
- Kumar B, Castro M, Lu J and Feller J F (2009) 'Conducting polymer nanocomposites (CPC): nanocharacterisation of layer by layer sprayed PMMA-CNT vapour sensors by atomic force microscopy in current sensing mode (CS-AFM)', *Materials Research Society Symposium Proceeding*, 1143-KK02–06.
- Kumar B, Feller J F, Castro M and Lu J (2010) 'Conductive bio-polymer nano-composites (CPC): chitosan-carbon nanotube transducers assembled via spray layer by layer for volatile organic compound sensing', *Talanta*, 81, 908–915.
- Lee J H, Kim S K and Kim N H (2006) 'Effects of the addition of multi-walled carbon nanotubes on the positive temperature coefficient characteristics of carbon-black-filled high-density polyethylene nanocomposites', *Scripta Materialia*, 55, 1119–1122.
- Lee K, Lee J, Dong K and Ju B (2008) 'Gas sensing properties of single-wall carbon nanotubes dispersed with dimethylformamide', *Sensors & Actuators B: Chemical*, 135, 214–218.
- Li Y, Wang H and Yang M (2007) 'n-Type gas sensing characteristics of chemically modified multi-walled carbon nanotubes and PMMA composite', *Sensors & Actuators B*, 121, 496–500.
- Lisunova M O, Mamunya Y P, Lebovka N I and Melezhyk A V (2007) 'Percolation behaviour of ultrahigh molecular weight polyethylene/multi-walled carbon nanotubes composites', *European Polymer Journal*, 43, 949–958.
- Liu F, Zhang X, Li W, Cheng J, Tao X, Li Y and Sheng L (2009) 'Investigation of the electrical conductivity of HDPE composites filled with bundle-like MWNTs', *Composites A: Applied Sciences & Manufacturing*, 40, 1717–1721.
- Liu Y, Chakrabartty S, Gkinosatis D S, Mohanty A K and Lajnef N (2007) 'Multi-walled carbon nanotubes/Poly(L-lactide) nanocomposite strain sensor for biomechanical implants', *IEEE Biomedical Circuits & Systems Conference*, Montreal, Canada, pp. 119–122.
- Loh K J, J Kim, J P Lynch, Wong N, Kam S and Kotov N A (2007) 'Multifunctional layer-by-layer carbon nanotube–polyelectrolyte thin films for strain and corrosion sensing', *Smart Materials and Structures*, 16, 429–438.
- Loh K J, Lynch J P and Kotov N A (2005) 'Conformable single-walled carbon nanotube thin film strain sensors for structural monitoring', in *Proceedings of the 5th International Workshop on Structural Health Monitoring*, Stanford, CA, USA, September 12–14.
- Loneragan M C, Freund M S, Severin E J, Doleman B J, Grubbs R H and Lewis N S (1996) 'Array-based vapour sensing using chemically sensitive polymer composite resistors', *Chemistry of Materials*, 8, 9, 2298–2312.
- Lu J, Castro M, Kumar B and Feller J F (2009a) 'Thermo- and chemo-electrical behaviour of carbon nanotube filled co-continuous conductive polymer nanocomposites (CPC) to develop amperometric sensors', *Materials Research Society Symposium Proceeding*, 1143, KK05–14.
- Lu J, Kumar B, Castro M and Feller J F (2009b) 'Vapour sensing with conductive polymer nanocomposites (CPC): polycarbonate-carbon nanotubes transducers with hierarchical structure processed by spray layer by layer', *Sensors & Actuators B: Chemical*, 140, 451–460.

- Lu J, Park B J, Kumar B, Castro M, Choi H J and Feller J F (2010) 'Hybrid vapour sensor: polyaniline nanobead-carbon nanotube architecture with tuneable chemo-electrical behaviour', *Nanotechnology*, 21, 255501, 1–10.
- Ma X, Zhang X, Li Y, Li G, Wang M, Chen H and Mi Y (2006) 'Preparation of nano-structured polyaniline composite film via "carbon nanotubes seeding" approach and its gas-response studies', *Macromolecular Materials & Engineering*, 291, 75–82.
- Mabrook M F, Pearson C, Jombert A S, Zeze D A and Petty M C (2008) 'The morphology, electrical conductivity and vapour sensing ability of inkjet printed thin films of single-wall carbon nanotubes', *Carbon*, 47, 3, 752–757.
- Mamedov A A, Kotov N, Prato M, Guldi D M, Wicksted J P and Hirsch A (2002) 'Molecular design of strong SWCNT/polyelectrolyte multilayer composites', *Nature Material*, 1, 190–194.
- Mamunya Y P, Muzychenko Y V, Lebedev E V, Boiteux G, Seytre G, Boulanger C and Pissis P (2007) 'PTC effect and structure of polymer composites based on polyethylene/polyoxymethylene blend filled with dispersed iron', *Polymer Engineering & Science*, 47, 34–42.
- Martin C A, Sandler J K W, Shaffer M S P, Schwarz M K, Bauhofer W, Schulte K and Windle A H (2004) 'Formation of percolating networks in multi-wall carbon nanotube-epoxy composites', *Composites Science & Technology*, 64, 15, 1236–2309.
- McGraw-Hill (2010) *Encyclopedia of Science & Technology*, 5th edn, published online: <http://www.answers.com/library/Sci%252DTech+Encyclopedia-cid-85017>.
- Meyer J (1973) 'Glass transition temperature as a guide to selection of polymer suitable for PTC materials', *Polymer Engineering & Science*, 13, 6, 463–468.
- Meyer J (1974) 'Stability of polymer composites as positive temperature coefficient resistors', *Polymer Engineering & Science*, 14, 10, 706–716.
- Mierczynska A, Friedrich J, Maneck H E, Boiteux G and Jeszka J K (2004) 'Segregated network polymer/carbon nanotubes composites', *Central European Journal of Chemistry*, 2, 2, 363–370.
- Mironi-Harpaz I and Narkis M (2001) 'Thermo-electric behaviour (PTC) of carbon black-containing PVDF/UHMWPE and PVDF/XL-UHMWPE blends', *Polymer Engineering & Science*, 41, 205–221.
- Mitchell C A and Krishnamoorti R (2007) 'Dispersion of single-walled carbon nanotubes in poly(ϵ -caprolactone)', *Macromolecules*, 40, 5, 1538–1545.
- Mu M, Walker A M, Torkelson J M and Winey K I (2008) 'Cellular structures of carbon nanotubes in a polymer matrix improve properties relative to composites with dispersed nanotubes', *Polymer*, 49, 1332–1337.
- Narkis M, Srivastava S, Tchoudakov R and Breuer O (2000) 'Sensors for liquid based on conductive immiscible polymer blends', *Synthetic Metal*, 113, 29–34.
- Niu L, Luo Y, and Li Z (2007) 'A highly selective chemical gas sensor based on functionalization of multi-walled carbon nanotubes with poly(ethylene glycol)', *Sensors & Actuators B*, 126, 361–367.
- Nofar M, Hoa S V and Pugh M D (2009) 'Failure detection and monitoring in polymer matrix composites subjected to static and dynamic loads using carbon nanotube networks', *Composites Science & Technology*, 69, 1599–1606.
- Park J M, Kim D S, Lee J R, and Kim T W (2003) 'Non destructive damage sensitivity and reinforcing effect of carbon nanotube/epoxy composites using electro-micromechanical technique', *Materials Science & Engineering C*, 23, 971–975.
- Park J M, Kim D S, Kim S J, Kim P G, Yoon D J, and DeVries K L (2007) 'Inherent sensing and interfacial evaluation of carbon nanofiber and nanotube/epoxy composites using

- electrical resistance measurement and micromechanical technique', *Composites: Part B*, 38, 847–861.
- Pegel S, Pötschke P, Villmow T, Stoyan D and Heinrich G (2009) 'Spatial statistics of carbon nanotube polymer composites', *Polymer*, 50, 9, 2123–2132.
- Philip B, Abraham J K, Chandrasekhar A and Varadan V K (2003) 'Carbon nanotube/PMMA composite thin films for gas-sensing applications', *Smart Materials & Structures*, 12, 935–939.
- Pillin I, Feller J F, Pimbert S and Levesque G (2002) 'Conductive poly(ester)/poly(olefin)/carbon black composites: influence of glass transition temperature and crystallinity of the poly(ester) matrix on the electrical properties', *Plastics Rubbers & Composites*, 31, 78, 300–306.
- Pioggia G, Di Francesco F, Marchetti A, Ferro M and Ahluwalia A (2007a) 'A composite sensor array impedentiometric electronic tongue: Part I. Characterization', *Biosensors & Bioelectronics*, 22, 2618–2623.
- Pioggia G, Di Francesco F, Marchetti A, Ferro M and Ahluwalia A (2007b) 'A composite sensor array impedentiometric electronic tongue: Part II. Discrimination of basic tastes', 22, 2624–2628.
- Pioggia G, Di Francesco F, Ferro M, Sorrentino F, Salvo P and Ahluwalia A (2008) 'Characterization of a carbon nanotube polymer composite sensor for an impedimetric electronic tongue', *Microchimica Acta*, 163, 57–62.
- Pötschke P, Abdel-Goad M, Alig I, Dudkin S and Lellinger D (2004a) 'Rheological and dielectrical characterization of melt mixed polycarbonate-multiwalled carbon nanotube composites', *Polymer*, 45, 8863–8870.
- Pötschke P, Andres T, Villmow T, Pegel S, and Brünig H (2009) 'Liquid sensing properties of fibres prepared by melt spinning from poly(lactic acid) containing multiwalled carbon nanotubes', *Composites Science & Technology*, 70, 343–349.
- Pötschke P, Bhattacharyya A R and Janke A (2004b) 'Melt mixing of polycarbonate with multiwalled carbon nanotubes: microscopic studies on the state of dispersion', *European Polymer Journal*, 40 1, 137–148.
- Quercia L, Loffredo F, and Francia G D (2005) 'Influence of filler dispersion on thin film composites sensing properties', *Sensors & Actuators B*, 109, 153–158.
- Qureshi A, Kang W P, Davidson J L and Gurbuz Y (2009) 'Review on carbon-derived, solid-state, micro and nano sensors for electrochemical', *Diamond & Related Materials*, 18, 1401–1420.
- Radushkevich L V, and Lukyanovich V M (1952) 'About the structure of carbon formed by thermal decomposition of carbon monoxide on iron substrate', *Journal of Physical Chemistry (Moscow)* 26, 88–95.
- Sahimi M, Hashemi M and Ghassemzadeh J (1998) 'Site-bond invasion percolation with fluid trapping', *Physica A*, 260, 231–243.
- Santhanam K S V, Sangoi R and Fuller L (2005) 'A chemical sensor for chloromethanes using a nanocomposite of multiwalled carbon nanotubes with poly(3-methylthiophene)', *Sensors & Actuators B: Chemical*, 106, 766–771.
- Schneider G, and Decher G (2004) 'From functional core/shell nanoparticles prepared via layer-by-layer deposition to empty nanospheres', *Nano Letters*, 4, 1833–1839.
- Segal E, Tchoudakov R, Mironi-Harpaz I, Narkis M and Siegmann A (2005) 'Chemical sensing materials based on electrically conductive immiscible polymer blends', *Polymer International*, 54, 1065–1075.
- Shevade A V, Ryan M A, Homer M L, Manfreda A M, Zhou H and Manatt K S (2003) 'Molecular modelling of polymer composite–analyte interactions in electronic nose sensors', *Sensors & Actuators B: Chemical*, 93, 84–91.

- Song X, Liu S, Gan Z, Lu Q, Cao H and Yan H (2009) 'Controllable fabrication of carbon nanotube-polymer hybrid thin film for strain sensing', *Microelectronic Engineering*, 86, 2330–2333.
- Srivastava S, Tchoudakov R and Narkis M (2000) 'A preliminary investigation of conductive immiscible polymer blends as sensor materials', *Polymer Engineering & Science*, 40, 1522–1528.
- Stauffer D and Aharony A (1994) *Introduction to Percolation Theory*, 2nd edn, London: Taylor & Francis.
- Su P G and Huang S C (2006) 'Electrical and humidity sensing properties of carbon nanotubes-SiO₂- poly(2-acrylamido-2-methylpropane sulfonate) composite material', *Sensors & Actuators B*, 113, 142–149.
- Su P G and Wang C H (2007) 'In situ synthesized composite thin films of MWCNT/PMMA doped with KOH as a resistive humidity sensor', *Sensors & Actuators B*, 124, 303–308.
- Tartarin R and Pajot S (1996) 'A percolation model of the breakdown of a Soviet-type economy: repression, disequilibria and market diffusion', *The Transformation of Economic Systems: Discontinuous Jumps and Continuous Adaptations, Second Budapest EACES Studies Workshop*, Budapest University of Economic Sciences, 16–17 December.
- Teh K S and Lin L (2005) 'Polypyrrole-carbon nanotube nanocomposite: film deposition and characterization', *Journal of Micromechanics & Microengineering*, 15, 2019–2027.
- Thostenson E T and Chou T W (2006a) 'Carbon nanotube networks: sensing of distributed strain and damage for life prediction and self healing', *Advanced Materials*, 18, 2837–2841.
- Thostenson E T and Chou T W (2006b) 'Processing-structure-multi-functional property relationship in carbon nanotube/epoxy composites', *Carbon*, 44, 3022–3029.
- Thostenson E T, Li C and Chou T W (2007) 'Experimental and theoretical investigations on carbon nanotube-based materials for sensors and actuators', *ICCES*, 3, 1, 29–34.
- Thostenson E T and Chou T W (2008), 'Real-time in situ sensing of damage evolution in advanced fiber composites using carbon nanotube networks', *Nanotechnology*, 215713, 1–6.
- Vidhate S, Chung J, Vaidyanathan V, and D'Souza N (2009) 'Time dependent piezoresistive behavior of polyvinylidene fluoride/carbon nanotubes conductive composite', *Materials Letters*, 63, 1771–1773.
- Villmow T, Pötschke P, Pegel S, Häussler L and Kretzschmar B (2008) 'Influence of twin-screw extrusion conditions on the dispersion of multi-walled carbon nanotubes in a poly(lactic acid) matrix', *Polymer*, 49, 3500–3509.
- Wang F, Gu H, and Swager T M (2008) 'Carbon nanotube/polythiophene chemiresistive sensors for chemical warfare agents', *Journal of American Chemical Society*, 130, 5392–5393.
- Wang H C, Li Y and Yang M J (2007) 'Sensors for organic vapor detection based on composites of carbon nanotubes functionalized with polymers', *Sensors & Actuators B*, 124, 360–367.
- Wang X J and Chung D D L (1997) 'Real time monitoring of fatigue damage and dynamic strain in carbon fibres polymer matrix composite by electrical resistance measurement', *Smart Materials & Structures*, 6, 504–508.
- Wei C, Dai L, Roy A and Tolle T B (2006) 'Multifunctional chemical vapor sensors of aligned carbon nanotube and polymer composites', *Journal of American Chemical Society*, 128, 1412–1413.
- Wichmann M H G, Buschhorn S T, Böger L, Adelung R and Schulte K (2008) 'Direction sensitive bending sensors based on multi-wall carbon nanotube/epoxy nanocomposites', *Nanotechnology*, 19, 475503, 1–5.

- Woo C S, Lim C H, Cho C W, Park B, Ju H, Min D H, Lee C J, and Lee S B (2007) 'Fabrication of flexible and transparent single-wall carbon nanotube gas sensors by vacuum filtration and poly(dimethyl siloxane) mold transfer', *Microelectronic Engineering*, 84, 1610–1613.
- Xiao K Q, Zhang L C and Zarudi I (2007) 'Mechanical and rheological properties of carbon nanotube-reinforced polyethylene composites', *Composites Science & Technology*, 67, 177–182.
- Yu C, Kim Y S, Kim D and Grunlan J C (2008) 'Thermoelectric behavior of segregated-network polymer nanocomposites', *Nano Letters*, 8, 12, 4428–4432.
- Yu H, Cao T, Zhou L, Gu E, Yu D, and Jiang D (2006) 'Layer by layer assembly and humidity sensitive behaviour of poly(ethyleneimine)/multiwall carbon nanotube composite films', *Sensors & Actuators B*, 119, 512–515.
- Zhang B, Fu R W, Zhang M Q, Dong X M, Lana P L and Qiu J S (2005) 'Preparation and characterization of gas sensitive composites from multiwalled carbon nanotubes/polystyrene', *Sensors & Actuators B*, 109, 323–328.
- Zhang B, Dong X, Fu R, Zhao B and Zhang M (2008) 'The sensibility of the composites fabricated from polystyrene filling multi-walled carbon nanotubes for mixed vapors', *Composites Science & Technology*, 68, 1357–1362.
- Zhang T, Nix M B, Yoo B, Deshusses M A and Myung N V (2006a) 'Electrochemically functionalized single-walled carbon nanotube gas sensor', *Electroanalysis*, 18, 1153–1158.
- Zhang W, Suhr J and Koratkar N (2006b) 'Carbon nanotube/polycarbonate composites as multifunctional strain sensors', *Journal of Nanoscience & Nanotechnology*, 6, 960–964.
- Zhang R, Baxendale M and Peijs T (2007a) 'Universal resistivity–strain dependence of carbon nanotube/polymer composites', *Physical Review B*, 76, 195433, 1–5.
- Zhang W, Sakalkar V and Koratkar N (2007b) 'In situ health monitoring and repair in composites using carbon nanotubes additives', *Applied Physics Letters*, 91, 133102, 1–3.
- Zribi K, Feller J F, Elleuch K, Bourmaud A and Elleuch B (2006) 'Conductive polymer composites obtained from recycled poly(carbonate) and rubber blends for heating and sensing applications', *Polymers for Advanced Technology*, 17, 9–10, 727–731.

-
- acid functionalisation, 517, 634–5
 - acid treatment, 518, 536–7
 - acrylonitrile-butadiene-styrene (ABS), 498
 - activation energy, 223
 - acylation-esterification, 75–6
 - Advanced Rheometric Expansion System, 579
 - AFM *see* Atomic Force Microscope
 - agglomerate area ratio, 106, 108, 112, 115, 122, 266
 - vs applied shear stress, 109
 - vs interfacial energy, 107
 - vs mixing energy, 113
 - vs mixing speed
 - PC composites with 1 wt% Baytubes C150 HP, 112
 - vs mixing time, 114
 - vs volume resistivity, 115
 - agglomerate breakage, 94
 - agglomeration, 94, 95, 176–9, 304–7
 - build-up and destruction modelling, 307–8
 - primary agglomeration, 304–5
 - example of remaining primary agglomerates, 305
 - influence of melt mixing, 304
 - secondary agglomeration, 305–7
 - insulator-conductor transition for injection-moulded polycarbonate plates with MWNT, 307
 - TEM from polycarbonate/MWNT plates with 0.6 vol.% MWNT, 306
 - aggregation, 632–3
 - Al₂O₃, 624
 - alumina–CNT nanocomposites, 693
 - alveolar wall thickening, 627
 - amidation, 75–6
 - amine treatment, 518
 - ammonium polyphosphate (APP)
 - synergism with carbon nanotubes, 736–9
 - Andor CCD camera, 558
 - antennas, 340–1
 - arc discharge method, 403
 - area ratio *see* agglomerate area ratio
 - argon plasma, 34
 - Arrhenius activation energy, 238
 - Arrhenius equation, 223
 - asbestos
 - vs carbon nanotubes, 624–8
 - before and after agate milling, 626
 - characteristics of multiwalled CNT, 628
 - aseptic loosening, 679
 - ASTM D256, 160, 161, 181
 - ASTM D257, 581
 - ASTM D638, 160, 161
 - ASTM D790, 161
 - ASTM E662, 721
 - ASTM E 1354, 723
 - Atlas Mini-Max mixer, 526
 - atom transfer radical polymerisation, 66–8, 349
 - Atomic Force Microscope, 400
 - atomic force microscopy, 546, 779
 - ATRP *see* atom transfer radical polymerisation
 - Avrami model, 529
 - β-scission, 497
 - Bacillus subtilis*, 628
 - backbiting reaction, 497
 - batch compounding, 101–18
 - Bayblend, 298, 312, 321
 - Baytubes, 311
 - Baytubes C150HP, 103, 104, 108, 112, 606, 612, 614
 - biomaterials
 - carbon nanotube-based nanocomposites, 676–708
 - bioactivity, 703–6
 - biosensors, 701–3
 - dental restorative materials, 695–6
 - dentistry, 693–5
 - denture-based resin, 697–9
 - load-bearing implants, 686–93
 - monitoring biological systems, 699–701
 - nanomaterials in medicine, 680–6
 - occupational exposure regulation, 706–7
 - oral cancer targeted drug delivery, 699
 - orthopaedic implants, 677–80
 - periodontal dentistry, 696–7
 - biosensors, 701–3
 - FET nanobiosensor, 702
 - blue asbestos *see* crocidolite
 - Boolean model, 277
 - Brillouin scattering, 401
 - bronchial epithelial cells, 623
 - bronchoalveolar lavage examination, 625

- Brownian diffusion, 316
 'bundle design,' 756
 BUSS Ko-kneader, 755
- capillary rheology, 169
 carbon black, 331, 336
 see also carbon nanoparticles (CNP)
 carbon nanomaterials, 623–4
 carbon nanoparticles (CNP), 770, 782
 carbon nanotube-based nanocomposites
 biomedical/bioengineering applications,
 676–708
 bioactivity of CNTs, 703–6
 biomaterials and implants, 676–7
 biosensors, 701–3
 CNTs in dentistry, 693–5
 CNTs in periodontal dentistry, 696–7
 dental restorative materials, 695–6
 denture-based resin, 697–9
 load bearing implants for orthopaedic
 applications, 686–93
 for monitoring biological systems, 699–701
 nanomaterials in medicine, 680–6
 occupational exposure regulation, 706–7
 orthopaedic implants, 677–80
 targeted oral cancer drug delivery, 699
- carbon nanotube composites, 332–42
 EM shielding composites, 336–40
 EM wave absorbing material, 332–6
 other electromagnetic applications, 340–2
- carbon nanotube conductive polymer
 nanocomposites (CPC), 760–95
 basic concepts, 761–9
 conduction in CPCs, 762–3
 different types of conduction, 764
 influence parameters on percolation
 threshold, 762
 multi-walled carbon nanotubes entangled
 bundles, 763
 percolation, 761–2
- CNT composite architecture design,
 772–5, 776
 co-continuous CPC nanocomposites, 773
 2D layer-by-layer sprayed aPS–AuNP
 transducer, 775
 hierarchical double-percolated PC-2wt%
 CNT structure, 776
 layer-by-layer assembly and hierarchical
 architecture, 774–5
 segregated network of MWNT in
 UHMWPE matrix, 773
 triple percolated CPC 50, 774
 volume exclusion and segregated networks,
 772–4
- CNT composite transducers' characterisation,
 775–80, 781
 current profile and amplitude profile for
 PMMA–CNT composites, 781
 current/voltage curves for PMMA–CNT
 transducers, 778
 electrical characterisation, 776–8
 filler content influence on sprayed
 PC–CNT transducers, 778
 morphological characterisation, 779–80
 PC–CNT composite on mica, 780
 percolation curve evolution with synthesis
 route, 777
- PMMA–CNT transducers fitting
 parameters, 779
 stirring speed influence on epoxy–CNT
 percolation curve, 777
 formulation for sensing, 769–72
 CNT-filled CPC commutation
 temperatures, 771
 fillers, 769–70
 matrices, 770–2
- PCL-g-CNT
 response evolution, 791
 response to tetrahydrofuran in
 nitrogen, 790
 transducers relative amplitude, 791
- sensing principle, 763–9
 chemo-electrical behaviour, 767
 CNT publications per year
 (1991–2007), 769
 diffusion mode according to
 Langmuir–Henry-clustering model, 768
 piezo-electrical behaviour, 766
 positive/negative strain coefficient effect,
 765–6
 positive/negative temperature coefficient
 effect, 765
 positive/negative vapour coefficient
 effect, 766–9
 thermo-electrical behaviour, 765
- sensing properties and applications, 780–94
 chemical sensing with CNT-filled CPC,
 788–94
 CNT grafting by *in-situ* polymerisation of
 poly(ϵ -caprolactone), 789
 combination of CPC responses using PCA
 for vapour identification, 793
 crack healing demonstration, 786
 EP/CF composites fibre fracture damage
 sensitivity, 784
 liquid sensing cycling with PP/(PCL-
 3% CNT) film transducers, 793
 PP/(PCL–CNT) textiles possible
 application, 784
 PTC effect depending on external
 matrix with PCL-3% CNT conducting
 phase, 783
 remote measurement of strain inside
 human body with PLLA-5wt%
 CNT, 787
 sensing instrumentation, 781–2
 strain sensing with CNT-filled CPCs,
 785–8
 temperature sensing with CNT-filled CPC
 transducers, 782–5
 transducers' fabrication, 769–80
- carbon nanotube networks
 formation in PET, 579–82
 complex viscosity, storage modulus,
 Cole–Cole plots and inverse loss tangent
 variation, 580
 volume resistivity variation, 581
- carbon nanotube–polyolefin composites, 511–37
 future trends, 537
 mechanical properties, 518–26
 illustration, 519–23
 LDPE and HDPE elastic modulus, 524
 polyolefin–CNT blends, 526–33
 crystallinity, 526–30

- electrical properties, 532–3
- rheological properties, 530–2
- processing methods, 512–18
 - CNT functionalisation to manipulate dispersion and properties, 517–18
 - compatibilizers use, 516–17
 - in-situ* polymerisation, 513–14
 - melt spinning, 515–16
 - other methods, 516
 - shear mixing (melt processing), 514–15
 - solvent processing, 512–13
- thermal conductivity, 533
 - isotropic SWNT–LDPE and SWNT–HDPE composites, 534
- thermal degradation and flame-retardant properties, 534–7
 - oxidative degradation test specimens, 536
- wear behaviour, 533
- carbon nanotubes, 193–226, 331, 347, 428, 482
 - 3 phr CNT dispersion characteristics
 - CNT:ethanol = 1:10, 198
 - dry mixed, with CNT:ethanol = 1:10, 197
 - area ratio vs mixing speed
 - PC composites with 1 wt% Baytubes C150 HP, 112
 - batch compounding using small-scale mixers, 101–18
 - area ratio vs applied shear stress, 109
 - area ratio vs interfacial energy, 107
 - area ratio vs mixing energy, 113
 - area ratio vs mixing time, 114
 - area ratio vs volume resistivity, 115
 - masterbatch dilution, 116–17
 - MWCNT agglomerate dispersion in different polymers, 107
 - MWCNT dispersability, 106–8
 - MWCNT dispersion quantification, 104
 - polycarbonate processing with MWCNT materials, 101–6
 - polycarbonate with 4 wt% MWCNT melt, 106
 - polycarbonate with CNT composites diluted from a masterbatch, 116
 - processing parameters on MWCNTs
 - dispersion in polycarbonate, 112–15
 - relative change in area ratio vs mixing time, 114
 - secondary agglomeration effect, 117–18
 - bioactivity, 703–6
 - genotoxicity and mutagenicity, 705–6
 - interaction with immune system, 705
 - interference with bacterial uptake, 705
 - movement through the body, 706
 - biosensors, 701–3
 - FET nanobiosensor, 702
 - CNT functionalisation effect on epoxy–CNT composites, 232–4
 - continuous melt mixing using extruders, 118–27
 - dispersive screw configurations SC1 and SC2, 119
 - distributive screw configuration SC5, 120
 - distributive screw configurations SC3 and SC4, 119
 - electrical conductivity vs. filler content, 127
 - macrodispersion and the agglomerate size distribution, 123
 - masterbatch dilution, 125–7
 - masterbatches preparation, 118–25
 - MWCNT agglomerate size distribution, 124–5
 - MWCNT macro dispersion, 124
 - PCL composites with different MWCNT contents, 126
 - covalent functionalisation with polymers, 64–90
 - grafting-from methodology, 65–73
 - grafting-to methodology, 73–80
 - and dental restorative materials, 695–6
 - CNT and apatite, 696
 - in dentistry, 693–5
 - denture-based resin, 697–9
 - dispersion and distribution quantification
 - using microscopy techniques, 265–91
 - future trends, 291
 - light microscopy, 269–76
 - section thickness, 267
 - spatial distribution of random point pattern, 268–9
 - transmission electron microscopy, 276–90
 - dispersion characteristics
 - natural rubber samples, 219
 - sample filled with 84 phr of silica and 6 phr of CNT, 219
 - elastomer, 193–226
 - electrical properties, 667–9
 - conductivity along alignment direction with increasing nanotube isotropy, 669
 - solid state effect on resistivity, 668
 - epoxy resins and CNT effects on curing systems, 232
 - factors influencing transfer and localisation, 609–11
 - peculiarities of agglomerates, 611
 - fire-retardant solutions development, 730–4
 - functionalisation for polymer nanocomposites, 55–81
 - general properties, 748–9
 - hybrid systems based on silica filler, 216–25
 - CNT on mechanical and electrical properties, 218
 - crack growth rate vs. tearing energy, 224
 - fracture mechanical investigation, 224–5
 - SBR/BR(70:30) composites stress–strain behaviour, 218
 - styrene/butadiene with silica and addition of CNT, 217
 - temperature-dependent conductivity, 223
 - impact on heat release rate, 730–1
 - influence of material and processing parameters on polymer melts dispersion, 92–128
 - percolated and not percolated structures, 100
 - interaction with epoxy systems, 231–2
 - mechanical properties, 662–4
 - calculated effective mechanical contribution, 663
 - stress–strain curves for oriented PVA/SWNT, 664
 - melt mixing and filler dispersion, 94–7
 - particle adhesion categories, 95
 - particle size reduction, 96

- monitoring biological systems, 699–701
- cell labelling and tracking, 700–1
- multiphase polymer blends, 587–616
 - current state of polymer–carbon nanotube technology, 588–95
 - future trends, 615–16
 - localisation of CNT during melt mixing, 595–611
 - selective localisation utilisation, 613–15
 - tailoring the localisation, 611–13
- MWCNT incorporation in polycarbonates
 - different melt viscosities, 108–10
 - different molecular weights, 110–11
- natural rubber
 - dielectric properties, 222
 - quasi-static stress–strain behaviour, 220
 - with silica partially exchanges against CNT, 217–23
 - strain-dependent storage modulus, 221
- non-covalent functionalisation with polymers, 57–64
 - in-situ* polymerisation, 57–60
 - nanohybrid shish-kebabs, 62–3
 - PE/MWNT-10, PE/MWNT-25, and PE/CNF NHSK structures, 63
 - polymer wrapping, 60–2
 - supercritical- CO_2 technology, 63–4
 - transition from pull-out to fracture, 59
- occupational exposure regulation, 706–7
- orientation, 659–62
 - Raman spectra of the alignment of SWNTs, 660
 - SEM of MWNT, 661
- in orthopaedics, 687–93
- MWCNT–PMMA cement, 691
- PCL masterbatches
 - agglomerate area ratio dependence on minimum residence time, 122
 - minimum residence time, 121
 - MWCNT dispersion and specific mechanical energy input, 126
- in periodontal dentistry, 696–7
- plasma chemical functionalisation, 38–44
 - emission current density and fluorescent photos, 42
 - liquid droplets, 39
 - MWCNT transformation process
 - model, 41
 - radical addition yielding functional groups, 43
- plasma post-discharge treatment, 44–8
 - Ar + N_2 microwave discharge, 45
 - CNT with PCL islets, 47
 - polycaprolactone nanocomposites, 47
 - post-discharge chamber of Ar + N_2 μ -wave plasma, 46
- plasma treatment, 33–48
 - characteristics and principal applications, 33–5
 - overview, 33
 - plasma polymerisation, 37–8
 - plasma post-discharge treatment, 44–8
- polycarbonate with 1 wt% MWCNT
 - external diameter distributions, 105
 - melt viscosity, 108
 - molecular weights, 110
 - optical micrographs, 93, 103
 - particle size distribution, 111
 - SEM images of MWCNT materials, 103
 - TEM images, 104
- polyolefin composites by *in-situ* polymerisation, 3–22
- processing, 195–202
 - 3 phr CNT, 196
 - 3 phr CNT dispersion characteristics, 197
- CNT concentration in SBR/BR composites, 201
- dispersion on quasi-static mechanical properties and frequency dependent conductivity, 199
- elastomers dispersion characteristics, 195
- polymer type variation, 195–7
- predispersing solvents, 197–202
- SBR/BR quasi-static stress–strain curves, 200
- SBR/BR quasi-static stress–strain cycles, 203
- sensing properties, 669–70
 - resistivity vs strain, 670
- special affinity with silicone, 730–1
- structure–property relationships, 202–10
 - dynamic-mechanical properties, 204–6
 - electrical transport processes, 206–9
 - mechanical properties, 202–4
 - percolation behaviour of AC resistivity, 209
 - percolation network based on CNTs, 207
- SBR/BR dynamic-mechanical analysis, 205
- SBR/BR strain dependency of the elastic modulus, 206
- thermal transport processes, 209–10
- surface chemistry and solution-based functionalisation, 25–33, 25–49
 - covalent sidewall functionalisation reactions, 32
 - end-caps and defect-sites chemistry, 27–30
 - functionalisation reactions at ends and defect-sites, 29
 - pyramidalisation angles, 31
 - sidewall functionalisation, 30–3
- surface etching, 36–7
 - MWNTs before and after Ar microwave plasma treatment, 36
 - MWNTs before and after MMA plasma polymerisation treatment, 38
 - nodular and untreated CNT, 37
- synergism with ammonium polyphosphate (APP), 736–9
- synthesis and purification, 749
- systems with ionic liquids for increased coupling activity, 210–16
 - conductivity on the volume fraction of CNT, 214
 - ionic liquids chemical structures, 211
- S-SBR/BR dynamic-mechanical properties, 215–16
- SBR/BR matrix loaded with 3 phr CNTs, 212–13
- tailoring the localisation, 611–13
- targeted drug delivery for oral cancer, 699
- theoretical approach to reinforcement efficiency, 665–7

- failure of polymer matrix reinforced with SWNT, 666
- stress-strain curve for a PE and SWNT, 665
- SWNT composite strengths, 666
- toxicity and regulatory perspectives, 621–47
 - CNT toxicity, 628–9
 - CNT toxicology vs other particulate materials, 623–4
 - CNT vs asbestos, 624–8
 - future biological applications, 643–4
 - future trends, 644–7
 - public perception and ‘risk-versus-reward’ debate, 621–3
 - toxicity parameters, 630–43
- Cauchy-Born Rule, 388
- cell labelling, 700–1
- CF₄ plasma treatment, 38
- characteristic frequency, 208
- chemical functionalisation, 26
- chemical vapour deposition, 403, 430, 659
- chemiluminescence, 534
- chemorheology, 234–40
 - Di Benedetto’s equation, 237–8
 - glass transition temperature and degree of cure, 235
 - kinetic model, 235–6
 - kinetic model determination, 234–5
 - rheological model, 235, 238–40
- chemoviscosity, 238
- chitosan, 347, 349, 364
- cholesterol-end-capped poly(2-methacryloyloxyethyl phosphorylcholine) (CPMPC), 633
- cisplatin, 699
- Clausius-Duhem inequality, 378
- Cloisite 30B, 740
- clustering *see* secondary agglomeration
- CNTs *see* carbon nanotubes
- cold plasma, 33
- Cole-Cole functions, 208
- Cole-Cole plot, 462, 579–80
 - modified, 432, 446
- colloidal suspension, 299
- compatibilizing agents, 516
- composites *see* polymer-polymer-grafted CNTs
- condensation polymerisation, 70–2
- conductive and viscoelastic filler network, 317–21
 - electrical and rheological properties, 317–18
 - shear-induced insulator-conductor, 318
- shear rate dependence and dynamic filler network, 318–21
 - stationary values for DC conductivity, 320
 - time evolution of electrical conductivity, 319
- conductive composites, 336
- conductive filler network, 312–17
 - shear induced destruction and conductivity recovery, 312–15
 - temperature dependence of the conductivity recovery, 314
 - time-dependent conductivity measurements, 313
- steady shear conditions, 315–16
- conductivity of MWNT/PC melts
 - measured during steady shear and quiescent annealing, 316
- time-dependent conductivity measurements, 315
- steady state network, 316–17
- cone calorimetry, 722–3
 - cone calorimeter curve, 723
 - cone calorimeter set-up, 722
- continuous melt mixing, 118–27
- continuum mechanics, 378
- controlled/living radical polymerisation (CLRP), 66–8
- conventional free radical polymerisation, 65–6
- Coulomb, 299
- covalent grafting, 26, 64
- covariance, 280
- Cox-Merz rule, 456, 603
- CPC sensor, 764
- CPC transducer, 764
- crocidolite, 624, 630
- crystallinity, 568
- crystallisation temperature, 6, 14
- curing systems
 - epoxy resins and CNTs, 232
 - degree of cure of the reaction, 233
- Curv, 658
- cycloaddition, 74–5
- D Raman band, 403
- DACA, 304
 - microcompounder, 101
- Decalin, 512
- defect functionalisation, 487
- defect-site chemistry, 27–30
- degrees of dispersion, 104
- dentistry, 693–5
 - CNTs and adhesion to tooth substance, 694–5
 - dental restorative materials, 695–6
 - CNTs and apatite, 696
 - denture-based resin, 697–9
 - periodontal dentistry, 696–7
 - SEM images of ACM 10, 698
- design of experiment, 162
- Di Benedetto’s equation, 237–8
- diamond anvil cell (DAC), 406
- differential scanning calorimetry, 234–5, 550, 596
- digital image processing
 - light microscopy, 271–5
 - transmission electron microscopy, 281–90
- diglycidyl ether of bisphenol A-based epoxy resin (DGEBA), 231, 234
- dipalmitoylphosphatidylcholine, 624
- dipole polarisations, 333–4
- direct electronic impact, 45
- Dirichlet boundary conditions, 384
- discontinuous damage test, 202
- dispersion, 93, 133
 - of carbon nanotubes, quantification using microscopy techniques, 265–91
 - future trends, 291
 - light microscopy, 269–76
 - transmission electron microscopy, 276–90
- dispersion index analyzing system, 195
- displacement-controlled boundary conditions *see* Dirichlet boundary conditions

- dissociative recombination, 45
- dodecylbenzenesulfonate-doped poly(pyrrole) (DBS-PPy), 792
- DOE *see* design of experiment
- double-walled carbon nanotubes, 11
- DWCNT *see* double-walled carbon nanotubes
- dynamic deformation, 205
- dynamic mechanical analysis (DMA), 21, 353
- dynamic mechanical thermal analysis (DMTA), 413
- dynamic percolation, 306
- dynamic shear rheology, 579
- Dyneema, 657
- ϵ -caprolactam, 350
- Echelle spectrograph, 558
- effective fibre, 391
- elastomer
 - carbon nanotubes composites, 193–226
 - hybrid systems based on silica filler, 216–25
 - ionic liquids for increased coupling activity, 210–16
 - processing, 195–202
 - structure–property relationships, 202–10
 - electrical conductivity, 254–6, 295, 303, 311
 - electrical percolation threshold, 439
 - electrical resistivity, 161, 179–88
 - electrical transport, 206–9
 - electromagnetic interference (EMI), 336, 532
 - electromagnetic properties
 - electromagnetic shielding CNT composites, 336–40
 - absorption, reflection and multiple reflections within a thin slab, 337
 - multiple reflection occurring between a CNT wall, 340
 - electromagnetic wave absorbing CNT composites, 332–6
 - CNT system, 334
 - EM wave propagation through a thin slab, 333
 - MWCNT real and imaginary permittivity vs frequency, 335
 - other CNT composites' electromagnetic applications, 340–2
 - polymer–carbon nanotube composites, 329–42
 - EM wave reflection, transmission and absorption through a medium, 330
 - electromagnetic shielding (SE), 336
 - electronic displacement polarisation, 333
 - electronic nose (e-nose), 764, 794
 - electronic tongue (e-tongue), 764, 793–4
 - electrospinning, 662, 686
 - EN 13501–2, 722
 - EN 13823, 722
 - end-caps, 27–30
 - EPDM *see* ethylene propylene diene monomer rubber
 - EPDM–CNT, 194
 - EpiDerm FT, 639
 - epidermal growth factor, 699
 - epoxy–carbon nanotube composites, 230–56
 - chemorheological analysis, 240–52
 - calorimetric test in isothermal and dynamic conditions, 242
 - chemorheological model for DGEBA–1% MWNTs, 249
 - chemorheological model for DGEBA–1% MWNTs functionalised, 251
 - chemorheological model parameters, 246–7, 249, 252
 - DGEBA–MWNT, 247
 - diglycidyl ether bisphenol-A–double-walled carbon nanotube mixture (DGEBA–DWNT), 241–7
 - epoxy–SWNT functionalised and non-functionalised mixture, 247–51
 - experimental data vs chemorheological model, 246
 - experimental data vs kinetic model, 245
 - kinetic model for DGEBA–1% MWNTs, 248
 - kinetic model for DGEBA–1% MWNTs functionalised, 250
 - maximum reaction rate and reaction peak temperature for isothermal and dynamic tests, 244
 - rheological measurements, 243
 - time onsets for isothermal rheological tests, 244
 - chemorheological approach, 234–40
 - Di Benedetto's equation, 237–8
 - glass transition temperature and degree of cure, 235
 - kinetic model, 235–6
 - kinetic model determination, 234–5
 - rheological model, 235, 238–40
 - experimental materials and methods, 231–4
 - CNT and epoxy systems interactions, 231–2
 - CNT functionalisation effects, 232–4
 - effects on curing systems, 232
 - future trends, 256
 - properties, 252–6
 - chemorheological model for DGEBA–1% SWNTs
 - non-functionalised, 254
 - electric and dielectric behaviour, 254–6
 - kinetic model for DGEBA–1% SWNTs
 - non-functionalised, 253
 - parameters of chemorheological model for DGEBA–MDEA and DGEBA–1% SWNTs non-functionalised, 255
 - thermal and mechanical properties, 252–4
 - equivalent continuum, 383–7
 - molecular RVE model, 383
 - erosion-dominant mechanism, 115
 - Escherichia coli*, 628
 - ethylene-co-vinyl acetate
 - flammability, 749–50
 - peak of heat release rate, 751
 - synergistic effect reducing crack density, 752
 - ethylene propylene diene monomer rubber, 194
 - ethylene vinyl acetate copolymer composites, 501
 - Euroclass standards, 721, 725–7
 - simplified classification, 727
 - EVA composites *see* ethylene vinyl acetate copolymer composites

- FAR part 25, 721
- FEA *see* finite element analysis
- FEI Tecnai F20, 552
- fibres, 516
- filler dispersion, 94–7
- filler prelocalisation method, 532
- finite element analysis, 379
- fire-resistant paint, 742–3
- fire-resistant solutions, 718
- fire-retardant applications
 - Euroclass standards, 725–7
 - fire issues, 718–20
 - dangerous features, 719
 - features that can delay fire progress, 719–20
 - fire scenario, 719
 - fireproof requirements as function of means of transport, 720
 - fire protection mechanisms, 727–30
 - combustion cycle, 728
 - decomposition, 728
 - intumescent char layer, 730
 - intumescent systems, 729–30
- fire-retardant solutions, 718, 730–4
 - CNTs on heat release rate, 730–1
 - development using CNTs, 730–4
 - influence of CNT dispersion quality, 731–2
 - protective layer and shield phenomenon, 732–4
 - protective layer formation, 732–3
 - shield phenomenon, 733–4
- fire-retardant solutions development, 730–4
 - CNTs on heat release rate, 730–1
 - degradation route of polymers, 734
 - influence of CNT dispersion quality, 731–2
 - protective layer and shield phenomenon, 732–4
- flame-retardant properties characterisation tests, 722–5
 - cone calorimetry, 722–3
 - limit of oxygen index, 723–4
 - UL94 tests, 724–5
- improvement barrier effect and synergism, 718–44
- intumescent systems, 736–9
- regulations and standards, 720–2
 - test FMVSS302 description, 721
- synergism, 734–9
- unfilled EVA and EVA-based nanocomposites
 - cone calorimeter HRR vs time, 731
 - thermogravimetric analysis curves under air flow, 733
- flame-resistant coatings, 739–43
 - cable fire test, 743
 - fire-resistant paint, 742–3
 - special affinity between CNTs and silicone, 739–42
- flame-retardant cable applications
 - cable with MWCNT–organoclay–ATH
 - flame-retardant system, 752–8, 754–8
 - blends of MWCNTs and organoclays in cable compound formulations, 754
 - different insulated wire mounting designs for cone calorimeter tests, 756
 - carbon nanotube-based nanocomposites, 748–52, 753, 754
 - carbon nanotubes properties, 748–9
 - charred MWCNT crack density and surface results, 750–1
 - LDPE compounds flammability, 751–2
 - LDPE filled with different MWCNTs, 753
 - PDE filled with SWCNTs, 753
 - poly(EVA–MWCNT) compounds and EVA–MWCNT–organoclay compounds flammability, 749–50
 - synthesis and purification, 749
 - heat release rate
 - bundle design, 757
 - cable compound 2A with filler blend by twin-roll mill and BUSS Ko-kneader, 755
 - compounds made by twin-roll mill with different filler blends, 755
 - single layer design, 757
 - polymer–carbon nanotube composites, 746–58
- flash-over, 718, 746
- flocculation *see* secondary agglomeration
- Flory-Huggins parameter, 69, 790
- fluorination, 31
- fluoronanotubes, 31
- FMVSS302, 721
- Fourier band pass filter, 281
- Fournier equation, 303, 308
- Fourier Transform Infrared Spectroscopy, 554–8
 - band assignment for the infrared spectrum of PET and PET/10 wt% MWCNT composite, 556
 - FTIR spectra of PET, MWCNTs and PET/MWCNT composites, 555
 - plot normalised intensities of FTIR peaks, 557
- Friedel-Crafts acylation, 549
- full-width at half-maximum (FWHM), 668
- γ -aminopropyl triethoxy silane (APS), 783
- G Raman bands, 403, 406
- gap distances, 208
- gas discharge plasmas, 34
- generalised effective medium theory, 303
- geometric-mean equation, 596–7
- geometrical percolation threshold, 439
- glass transition temperature, 235, 237, 565, 596
- 'GoodNanoGuide' project, 707
- grafting-from methodology, 65–73
 - condensation polymerisation, 70–2
 - synthesising hyperbranched poly(urea-urethane)s-grafted MWNTs, 71
 - controlled/living radical polymerisation, 66–8
 - conventional free radical polymerisation, 65–6
 - other polymerisation methods, 72–3
 - ring-opening polymerisation, 68–70
 - PA6–SWNT composites synthesis, 78
 - PLLA–MWNT and PLLA–MWNT-g-PLLA composites, 69
 - SEM cross-sectional fracture images of PA6–SWNT, 79
- grafting-to methodology, 73–80
 - acylation-esterification/amidation of CNT-bound carboxyl groups, 75–6
 - condensation between oxidised CNTs and polymers, 77–80
 - PVA–MWNT-g-PVA films, 77

- cycloaddition of polymers to CNTs, 74–5
- macromolecular radical coupling, 73–4
- heating of TEMPO-end-capped P2VP chains, 73
- granuloma, 625, 631
- Guth–Gold–Smallwood equation, 203
- Haake Minilab Rheomex CTW5, 431
- Haake rheometer, 551
- half-time of crystallisation, 14
- harmonic-mean equation, 596–7
- Haversian systems, 683–4
- HDPE *see* High Density Polyethylene
- heat release rate, 723
 - impact of carbon nanotubes, 730–1
- Hi-Res TGA 2950, 577
- High Density Polyethylene, 430
- high shear extruder (HSE), 135–6
 - first and second generation, 136
- high-shear processing
 - homopolymer–CNTs composites, 139–46
 - SEM images of SBBS–CNTs nanocomposites, 140
 - polymer–carbon nanotube composites, 133–52
 - future trends, 151–2
 - polymer blends–CNTs, 146–51
 - polymer nanoblends, 136–9
 - TEM images of PC–PMMA, 137
 - TEM images of PVDF–PA11, 137
 - UV-vis transmittance spectra of pure PC, PMMA, and PC–PMMA blends, 138
 - PVDF–PA6–CNTs composites
 - electrical conductivity, 150
 - high-shear-processed sample, 147–8
 - low-shear-processed sample, 149
 - morphological representations, 150
 - stress–strain curves, 151
- hollow cathode glow discharge (HCGD), 43
- Hooke's law, 406
- hydrogenated nitrile rubber (HNBR), 196
- Hyperion nanotubes, 311
- IEC 60 332-3, 721
- IEC 60 332-1, 721, 756, 758
- IL-6, 623
- IL-8, 623
- in-line measurements
 - during extrusion, 310
 - typical set-up for laboratory-scale experiment, 310
 - during injection moulding, 310–11
 - scheme of the mould, 311
- in-situ* polymerisation, 57–60
- iPP/DWCNT composites
 - catalyst $[\text{Me}_2\text{Si}(2\text{-Me-Ind})_2]\text{ZrCl}_2/\text{MAO}$, 11
 - catalyst $\text{Me}_2\text{Si}(2\text{-Me-4Ph-Ind})_2\text{ZrCl}_2/\text{MAO}$, 12
- polyethylene–CNT composites, 9–10
 - PE–MWCNT composites synthesis, 10
 - specific conductivity, 10
- polyolefin carbon nanotube composites, 3–22
 - future trends, 21–2
 - polymer architecture by metallocene catalysis, 7–9
 - techniques, 5–7
- polypropylene–CNT composites, 11–21
 - filler and the isothermal crystallisation temperature, 19
 - iPP–DWCNT composites, 11
 - isotactic PP–CNT composites, 11–15
 - properties, 17–21
 - polypropylene polymerisation, 16
 - sPP–MWNT composites, 18
 - syndiotactic PP–CNT composites, 15–17
- in vitro* cytotoxicity screen, 636
- inductively coupled plasma mass spectrometry, 639
- injection moulding, 156–9
 - analysis, 165–88
 - 3 wt% PC–CNT volume and surface resistivities, 182
 - conditions, 180
 - electrical resistivity, 179–88
 - main effects of parameters, 165–9
 - Makrolon 2405 standard conditions, 181
 - Makrolon 2205 volume and surface resistivity values, 167
 - nanotube agglomerates in composites, 176–9
 - PC shear viscosity vs shear rate, 174
 - steady-state rheological analysis, 169–76
 - surface defects index, 172
 - tolerance for normalised main effect slopes calculation, 167
 - experiment design and materials, 159–64
 - 2^{7-k} fractional factorial DOE, 163
 - 2^{7-k} fractional factorial DOE lower and upper level values, 164
 - design of experiments, 161–4
 - injection-moulded Izod test bar, 161
 - materials and methods, 159–61
 - parameters and setpoint values, 162
 - polycarbonates, 160
 - Makrolon 2205 agglomerates
 - 3 wt% PC–CNT, 178
 - different CNT loading, 177
 - different injection melt temperatures, 179
 - Makrolon 2405 PC–CNT volume and surface resistivities
 - vs injection back pressure, 185
 - vs injection hold pressure, 186
 - vs injection hold pressure time, 187
 - vs injection melt temperature, 183
 - vs injection mould temperature, 188
 - vs injection plasticising speed, 189
 - vs injection speed, 184
 - vs wt% CNT loading, 181
- parameters
 - pinholes and spots surface defects formation, 172
 - volume and surface resistivities, 167
 - vs surface defect, pinholes index, and ρ , 170
 - vs surface defect, spots index, and ρ , 171
 - vs surface resistivity, 168
 - vs volume resistivity, 166
- PC and PC–CNT shear viscosity vs shear rate
 - 3 wt% and 15 wt%, 173
 - different CNT loading, 175
- polymer–carbon nanotubes composites, 155–91
- injection speed, 184

- inkjet printing technique, 792
- insulator–conductor transition, 303, 306
- interface polarisation, 334
- interfacial shear strength, 546
- intermolecular transfer reaction, 497
- interstitial fibrosis, 627
- interstitial granuloma, 625
- intumescence, 729
- intumescent systems, 729–30
 - char layer, 730
 - synergism between ammonium polyphosphate and CNTs, 736–9
 - images of char layer surface after burning test, 739
 - images of PP–APP blend and PP–APP–CNT blend surface, 738
 - polypropylene, 737–9
 - thermoplastic polyurethane, 736–7
- invariance of rotation, 280
- invariance of translation, 280
- ion bombardment, 40
- ionic liquids, 210–16
 - chemical structures, 211
- ionic polarisations, 333
- iPP–MWCNT composites
 - dynamic mechanical measurements, 21
 - TEM micrograph, 13
- iPP–SWCNT nanocomposites, 18
- ISO 2685, 742
- ISO 3795, 721
- ISO 4589, 723
- ISO 5660, 721
- ISO Standard 10993, 676
- isotactic PP–CNT composites, 11–15
- isothermal crystallisation, 565–8
 - DSC crystallisation and melting isotherms for PET–MWCNT composites, 567
 - PET and PET–MWCNT composites DSC characteristics, 568
 - PET glass transition temperature change, 565
- isothermal measurements, 526
- JAR part 25, 721
- Keithley 8009 resistivity test fixture, 581
- Keithley 6517A electrometer, 581
- Kelly-Tyson model, 420
- Kevlar, 657
- kinematic boundary conditions, 384
- kinetic model, 235–6
 - thermosetting systems, 236
- Kissinger method, 569, 576
- lactate dehydrogenase, 623
- Lactate Dehydrogenase assay, 636
- Langmuir–Henry-clustering (LHC) model, 768
- large amplitude oscillatory shear (LAOS), 461
- laser scanning confocal microscopy, 779
- layer-by-layer assembly, 774–5, 788, 792
- LCR meter, 310
- Leistritz ZSK-27 MAXX 48, 160
- Lewis acids, 486, 499
- Lexan 141R, 126
- light microscopy, 269–76
 - degree of dispersion, 269–71
 - digital image processing and specific examples, 271–5
 - background correction procedure, 271
 - differently melt processed composites, 274
 - feature-based algorithm for segmentation of grey scaled micrographs, 272–3
 - section thickness evaluation, 275
- limit of oxygen index (LOI), 723–4
 - schema, 724
- linear low density polyethylene (LLDPE), 353–4, 486, 489, 491
- London–van der Waals, 299
- Lotus Effect, 596
- low-density polyethylene (LDPE)
 - carbon nanotube compounds flammability, 751–2
 - filled with different MWCNTs, 753
 - heat release rate
 - MWCNTs in LDPE, 754
 - SWCNTs in LDPE, 753
- LSCM *see* laser scanning confocal microscopy
- m-Xylene, 512
- macromolecular radical coupling, 73–4
- Makrolon 2205, 159, 169
- Makrolon 2405, 159, 176
- Makrolon 2805, 159
- Makrolon 3105, 159
- masterbatch dilution, 116–17, 125–7
- masterbatches, 118–25
- MD *see* molecular dynamics
- mechanistic models, 235–6
- melt blending, 352
- melt mixing, 94–7
 - see also* continuous melt mixing
 - aspect ratio dependence of nanofiller localisation and migration behaviour, 600–2
- CNT transfer dynamics, 608–9
 - agglomerate transfer from SAN–MWNT precompound-phase, 610
 - polymer blend morphology development mechanism, 609
- selective CNT localisation in double
 - percolated polymer blends, 597–600
 - co-continuous PC–SAN blend with MWCNT Baytubes, 599
 - MWCNT selective localisation in PA6 phase, 600
 - percolated CNT network structure, 598
- selective localisation impact on rheological properties and blend morphology, 602–8
 - complex melt viscosity of PC, SAN, PC with 1wt% and PC₆₀/SAN₄₀, 607
 - phase continuity comparison, 607
 - rheological properties, viscosity ratios and phase inversion concentration prediction, 604–5
- thermodynamic driving forces, 595–7
- melt processing, 514–15, 549–51
 - and bulk material properties, 551–4
 - composite morphology, 552–4
 - composite preparation, 551–2
 - extruder torque variation, 552
 - polarised optical micrograph of PET/1 wt% MWCNT composite, 553
- melt state rheology, 447
- melting temperature, 6, 14
- mesothelioma, 630

- metallocene catalysts, 7–9, 354
- metallocene-methylaluminoxane catalysts, 4, 513–14
- metals, 336
- methyl vinyl silicone rubber (VMQ), 783
- methylaluminoxane (MAO)
 - structure, 7
- microbial cytotoxicity, 628
- micromechanical methods, 379
- microscale Raman sensing technique, 410
- microscopy techniques, 447
 - quantification of dispersion and distribution of carbon nanotubes, 265–91
 - future trends, 291
 - light microscopy, 269–76
 - transmission electron microscopy, 276–90
- Mie-Tyndall scattering, 401
- Miles equation, 602
- minimum residence time, 120
- molecular dynamics, 377–8
- multi-walled carbon nanotubes, 20, 55, 92, 97–100, 193, 347, 400, 430, 513
 - active sites for polymerisation, 5
 - before and after Ar microwave plasma treatment, 36
 - before and after MMA plasma polymerisation treatment, 38
 - agglomerate size distribution, 124–5
 - as-grown and thermally treated, 642
 - with a ball of iPP at an active site, 15
 - characterisation, 628
 - characteristic features, 102
 - detailed TEM micrograph, 14
 - flame-retardant cable applications, 748–52
 - blends with organoclays in cable compound formulations, 754
 - charred compounds crack density and surface results, 750–1
 - heat release rates for MWCNTs in LDPE, 754
 - LDPE filled with different MWCNTs, 753
 - peak of heat release rate at heat flux = 35 kW/m², 750
 - properties, 749
 - incorporation in polycarbonates
 - different melt viscosities, 108–10
 - different molecular weights, 110–11
 - macro dispersion, 124
 - and poly(ethylene terephthalate), 545–83
 - crystalline structure and crystal conformation, 554–76
 - future trends, 582–3
 - literature survey, 547–51
 - melt processing and bulk material properties, 551–4
 - rheological and electrical percolation, 579–82
 - thermal stability, 577–8
 - SEM images, 103
 - transformation process under O₂ plasma treatment, 41
- multi-walled nanotubes, 296, 311, 664
- multifocal granulomas, 626
- multiphase polymer blends
 - carbon nanotubes, 587–616
 - current state of polymer–carbon nanotube technology, 588–95
 - future trends, 615–16
 - localisation of CNT during melt mixing, 595–611
 - selective localisation utilisation, 613–15
 - tailoring the localisation, 611–13
 - multiple reflections, 337, 339
- multiscale modelling
 - composite systems Young's moduli
 - CNT lengths, 393
 - CNT volume fraction, 392
 - computational modelling tools, 377–9
 - continuum mechanics, 378
 - finite element analysis, 379
 - micromechanical methods, 379
 - molecular dynamics, 377–8
 - equivalent-continuum modelling concepts, 379–88
 - averaged scalar fields equivalence, 387–8
 - bulk metallic glass molecular model, 382
 - crystal unit cell, 381
 - equivalent continuum, 383–7
 - fibre composite microstructure, 382
 - kinematic equivalence, 388
 - molecular models length scales, 380
 - representative volume element, 379–83
 - fibre composite transverse shear modulus
 - stiff inclusions, 386
 - stiff matrix, 386
 - future trends, 394
 - polymer–carbon nanotube composites, 376–95
 - RVEs of non-functionalised and functionalised materials, 391
 - transverse Young's moduli for CNT lengths, 394
 - specific equivalent-continuum modelling methods, 388–90
 - dynamic deformation methods, 390
 - fluctuation methods, 388–9
 - static deformation methods, 389–90
- MWCNT *see* multi-walled carbon nanotubes
- MWCNT dispersion
 - different polymers, 106–8
 - 1 vol % MWCNT composites, 107
 - influence of screw configuration in masterbatches, 118–25
 - quantification, 104
 - specific mechanical energy input in PCL masterbatches, 126
- MWCNT–organoclay-ATH flame-retardant system, 752, 754–8
- MWCNT–PLLA nanocomposite, 686
- MWCNT–PMMA, 692
- MWCNTs *see* multi-walled carbon nanotubes
- N-dimethylformamide (DMF), 413
- nano-confinement, 486
- nanocomposites, 747
- Nanocyl 3150, 613
- Nanocyl 3152, 612, 613
- Nanocyl 7000, 197, 612
- Nanocyl NC7000, 102, 103, 104, 105, 126
- nanofibres
 - use of polymer–carbon nanotube, 657–72
 - micro-nanohybrid composite, 658
- nanohybrid shish-kebabs, 62–3
- nanomaterial regulation, 644–7
- NATO workshop regulation frameworks, 646

- nanomaterials, 680–6
 - biomedical applications, 681
 - carbon nanotubes and biological structure
 - interaction, 682–6
 - tissue engineering for orthopaedic applications, 683–6
 - public perception and ‘risk-*versus*-reward’ debate, 621–3
 - characterisation level, 622
- nanoradio, 341
- nanotubes, 405–21
 - liquid vs polymer interactions, 406–8
 - mechanical and spectroscopic stress–strain curves, 408
 - wavenumber-strain response embedded in PUA, 407
 - material discontinuities sensors and local stress concentrations, 408–12
 - normalised matrix stress data, 410
 - radius circular hole in infinite plate under unidirectional tensile stress, 409
 - strain mapping around a glass fibre, 412
 - molecular surface defects, 414–16
 - G band strain-induced shifts for carboxylated and pristine in PVA, 415
 - pristine Raman spectra functionalised MWCNTs, 416
 - strain effect on peak intensity ratio for pristine and COOH-SWNT, 415
- polymer stress transfer and interface
 - adhesion, 416–21
 - aligned single-walled carbon nanotube ropes image, 421
 - Raman peak shift, 417
 - stress distributions in the HMCF, 419
- natural rubber
 - dielectric properties, 222
 - quasi-static stress–strain behaviour, 220
 - with silica partially exchanges against CNT, 217–23
 - strain-dependent storage modulus, 221
- negative temperature coefficient (NTC), 765, 782
- Neumann boundary conditions, 384
- neutron activation analysis, 639
- NHSK *see* nanohybrid shish-kebabs
- nitrile rubber, 196
- non-covalent functionalisation, 26
- non-isothermal crystallisation, 568–76
 - activation energy from the Kissinger method for PET and PET/10 wt% MWCNT composite, 576
 - crystallisation exotherms for PET and PET/10 wt% MWCNT composite, 570
 - crystallisation temperatures, 574
 - graphical representation of Ozawa exponents, 575
 - Ozawa exponents for crystallisation process, 575
 - relative crystallinity changes as a function of temperature, 572
 - relative crystallinity changes as a function of time, 573
 - temperature change of PET as a function of MWCNT loading, 571
- non-Newtonian behaviour, 531, 532
- non-thermal plasma, 33
- Novocontrol impedance analyser, 308
- optical microscopic measurements, 469
- optical microscopy (OM), 779
- oral cancer, 699
- oriented polymer–CNT composite fibres, 659–62
 - Raman spectra, 660
 - SEM of MWNT/co-PP composite surface, 661
- orthopaedic implants, 677–80
 - current issues, 679–80
 - total hip joint replacement diagram, 679
 - load-bearing implants, 686–93
 - carbon nanotubes, 687–93
 - osteoporotic fracture prevalence in UK and US, 678
 - worldwide market for medical products, 677
- oscillatory shear mode test, 429
- Ozawa method, 568, 571
- PA6–SWNT composites
 - synthesis, 78
- PANalytical X’Pert PRO diffractometer, 563
- Paris plot, 224
- Payne effect, 205, 462
- PC *see* polycarbonate
- PCL *see* poly (caprolactone)
- PE–MWCNT composites, 10
- PEEK, 689–90
- percolation, 255, 761–2
- percolation theory, 223, 299–303
 - AC conductivity as a function of frequency for polycarbonate with MWNT, 302
 - concentration dependence of the DC conductivity, 301
 - DC conductivities above the percolation threshold vs reduced MWNT in polycarbonate, 302
- percolation threshold, 182, 299–300, 516, 517, 532, 533
- periodic boundary conditions, 384
- peritoneal cavity model, 627
- Perkin Elmer Spectrum 1000, 554
- permittivity, 333, 338
- phenomenological model, 235
- PLA *see* poly(L-lactic acid)
- plasma, 33
 - characteristics and principal applications, 33–5
 - radio frequency cathodic magnetron sputtering, 34
- plasma chemical functionalisation, 38–44
- plasma etching, 35
- plasma polymer, 35
- plasma polymerisation, 35
- plasma technology
 - surface treatment of carbon nanotubes, 25–49
 - plasma treatment, 33–48
 - surface chemistry and solution-based functionalisation, 27–33
- plasticising speed, 187
- PLLA *see* poly(L-lactide)
- Pluronic F127, 636
- PMMA *see* poly(methylmethacrylate)
- polarisation, 333
 - see also* specific polarisation

- polarised optical microscopy, 528, 530
- polarised Raman spectroscopy, 413
- poly (caprolactone), 118
- poly-p-phenylenebenzobisoxazole (PBO), 660, 662
- polyaniline (PANI), 498
- polycarbonate, 137, 311–12, 431–2, 437
 - injection moulding, 160
- polycarbonate-acrylonitrile butadiene styrene-CNT blends, 613–15
 - resistivity of an extruded PC-ABS, 615
 - TEM micrograph, 614
 - unstained transmission light microscopy, 615
- polycarbonate composites
 - area ratio vs mixing speed, 109
 - processing with different MWCNT materials, 101–6
- polycarbonate-styrene-co-acrylonitrile, 321
- polydimethylsiloxane (PDMS), 740–2
- polyethylene, 391–2
- polyethylene-CNT composites, 9–10
 - PE-CNT composites specific conductivity, 10
 - PE-MWCNT composites synthesis, 10
- poly(ethylene-co-vinyl acetate) multi-walled carbon nanotube
 - flammability, 749–50
- poly(ethylene glycol), 367–8
- poly(ethylene oxide), 365–6
 - stress-strain curves, 366
- polyethylene (PE), 3
- poly(ethylene terephthalate)
 - and multi-walled carbon nanotubes, 545–83
 - crystalline structure and crystal conformation, 554–76
 - future trends, 582–3
 - literature survey, 547–51
 - melt processing and bulk material properties, 551–4
 - rheological and electrical percolation, 579–82
 - thermal stability, 577–8
- poly(ethylene terephthalate)-MWCNT composites, 547–51
 - melt processing, 549–51
 - bulk material properties, 551–4
 - pre-treatment, solution mixing and *in-situ* polymerisation methods, 547–9
 - thermal stability, 577–8
 - TGA thermograms, 578
- polyethyleneimine, 637
- poly(L-lactic acid), 499
- poly(l-lactide), 69
- polymer architecture
 - metallocene catalysis, 7–9
 - methylaluminoxane, 7
 - PP microstructures, 8
 - zirconocenes structure, 9
- polymer-carbon nanotube composites
 - 2.5 wt% MWNT-HDPE0790 composite and pure HDPE0390 storage vs. loss modulus, 447
 - transient shear stress, 454
 - transient shear stress vs strain, 455
 - CNT dispersion, aspect ratio and alignment effect in polymer matrix, 447–8, 449–53
 - dynamic storage modulus for PCLCN5.0 sample, 449
 - literature investigations on rheological results, 450–3
 - storage modulus comparison for blends with f-MWNT vs p-MWNT, 449
- electromagnetic properties, 329–42
 - electromagnetic shielding CNT composites, 336–40
 - electromagnetic wave, 332–6
 - EM wave reflection, transmission and absorption through a medium, 330
 - other CNT composites' electromagnetic applications, 340–2
- fire-retardant application, 718–44
 - fire protection mechanisms, 727–30
 - fire-retardant solutions development, 730–4
 - flame-resistant coatings, 739–43
 - synergism, 734–9
- flame-retardant cable applications, 746–58
 - cable with MWCNT-organoclay-ATH flame-retardant system, 752–8
 - carbon nanotube-based nanocomposites, 748–52
- flow-induced crystallisation, 463–70
 - flow curves for pure PB400 and 0.1PB400 samples, 465
 - i-PP-PPgMA-MWCNT composite crystallisation temperature, 470
 - shear-enhanced crystallisation, 464–70
- high-shear melt processing, 133–52
 - CNTs dispersion states, 134
 - future trends, 151–2
 - homopolymer-CNTs composites, 139–46
 - polymer blends-CNTs, 146–51
 - polymer nanoblends, 136–9
 - technique, 135–6
- injection moulding, 155–91
 - analysis, 165–88
 - experiment design and materials, 159–64
- kinetic parameters for isothermal flow-induced crystallisation
 - MWNT and pure PB400 nanocomposites, 466
- linear rheological properties, 429–48
- multiscale modelling, 376–95
 - computational modelling tools, 377–9
 - equivalent-continuum modelling concepts, 379–88
 - future trends, 394
 - specific equivalent-continuum modelling methods, 388–90
- MWNT/HDPE0790 and pure HDPE0790
 - complex viscosity vs. frequency and steady shear viscosity vs. shear rate, 457
 - first normal stress difference vs. shear rate, 459
 - steady shear viscosity vs. shear rate, 456
 - storage modulus vs strain, 430
- MWNT/HDPE0390 and pure HDPE0390 composites
 - complex viscosity vs. frequency, 436
 - phase angle vs complex modulus absolute value, 438
 - storage modulus vs. frequency at 200°C, 435
 - storage modulus vs. frequency at 200°C and 260°C, 446
- MWNT/HDPE0390 composites

- loss tangent vs. nanotube concentration, 439
- storage and loss modulus vs nanotube concentration, 440
- nanotube-filled polycarbonate
 - complex viscosity, 433
 - storage modulus G' as function of loss modulus G'' , 434
 - storage modulus G' at 260°C, 433
- non-linear rheological properties, 448–63
 - dynamic properties strain dependence for S-SBR-BR blends, 462
 - elongational viscosity, 460–1
 - first normal stress difference, 458–60
 - non-linear oscillatory measurements, 461–3
 - pure PC and PC–MWCNT transient elongational viscosity, 460
 - SWNT–PMMA nanocomposites storage modulus frequency response, 448
 - transient and steady-shear viscosity, 454–8
- oscillatory shear measurements, 429–34
- pure PB400 and 0.1PB400 nanocomposite
 - isothermal flow-induced crystallisation, 467
 - storage modulus vs time, 468
- Raman spectroscopy, 400–22
 - molecules and fibres under strain, 402–3
 - Raman effect: basic principles, 401–2
 - signature on carbon nanotubes, 403–5
 - usefulness in nanotube-based composites, 405–21
- rheological percolation threshold, 434–47
 - different network types illustration, 441
 - thresholds results from reviewed publications, 442–5
- rheology, 428–70
- storage modulus vs strain
 - different frequencies for the 1 wt % MWNT–HDPE0790 composite, 431
- thermal degradation, 482–503
 - future trends, 501–2
 - mechanisms/stability improvement by CNTs, 483–6
- thermo-rheological history on electrical and rheological properties, 295–324
 - critical volume fractions of fillers at percolation threshold, 296
 - destruction and formation of electrical and rheological networks, 312–21
 - influence of processing history, 321–3
 - measuring techniques and materials, 309–12
 - thermo-rheological influence on the electrical conductivity, 297
- use in fibres, 657–72
 - electrical properties, 667–9
 - future trends, 670–2
 - mechanical properties, 662–4
 - micro-nanohybrid composite, 658
 - orientation, 659–62
 - preparation of fibres, 658–9
 - sensing properties, 669–70
 - theoretical approach to reinforcement efficiency, 665–7
- polymer matrix composites, 330
- polymer melts
 - material and processing parameters on carbon nanotube dispersion, 92–128
 - batch compounding, 101–18
 - continuous melt mixing, 118–27
 - future trends, 127–8
 - literature, 97–101
 - melt mixing and filler dispersion, 94–7
- polymer nanoblends, 136–9
- polymer nanocomposites
 - carbon nanotubes functionalisation, 55–81
 - covalent functionalisation, 64–80
 - non-covalent functionalisation, 57–64
- polymer–polymer-grafted CNTs
 - composites mechanical properties, 347–68
 - chitosan stress–strain curves, 348
 - fabrication, 352–3
 - mechanical properties, 353–68
- MWCNTs composites
 - PMMA/PMMA-grafted stress–strain curves, 361
 - PP/PP-grafted fracture surfaces SEM micrographs, 356
 - storage moduli, 355
- other polymer composites, 364–8
 - chitosan, 364
 - poly(2,6-dimethyl-1,4-phenylene oxide), 365
 - polyamide, 364
 - polybenzimidazole, 365
 - poly(ethylene oxide), 365–6
 - polyimide, 366
 - poly(L-lactide), 367
 - polyurethane, 367–8
- polymers grafting onto CNTs, 349–52
 - grafting-from method, 350–2
 - grafting-to method, 349–50
- polyolefin polymer composites, 353–8
 - chlorinated polypropylene, 357
 - CPP and CPP/CPP-grafted MWCNTs
 - stress–strain curves, 357
 - PE stress–strain curves, 354
 - poly(1-butene), 357–8
 - polyethylene, 353–5
 - polypropylene, 355–7
 - PP-g-MWCNTs lamellar thickness
 - variation and mechanical property, 356
- vinyl polymer composites, 358–64
 - poly(methyl methacrylate), 360–1
 - polystyrene, 361–2
 - poly(styrene-co-acrylonitrile), 362–4
 - poly(vinyl alcohol), 358
 - poly(vinyl chloride), 358–9
 - poly(vinylidene fluoride), 359–60
- polymer wrapping, 60–2
- polymer–carbon nanotube technology, 588–95
 - CNT localisation studies, 592–3
 - MWCNT blend of copolyamide 6/12 and ethylene and methyl acrylate, 594
 - phase morphologies combinations, 589
 - scientific research development, 590
- poly(methylmethacrylate), 38, 137, 339, 360–1, 414, 416, 495–6, 690–1
 - stress-strain curves, 361
- polyolefin–CNT blends, 526–33
 - crystallinity, 526–30

- neat PP and 5 wt% SWNT/PP composite micrographs, 529
- pure isotactic polypropylene crystallisation temperatures, 527
- electrical properties, 532–3
- rheological properties, 530–2
- MWNT content effect, 531
- polyolefin CNT composites
 - in-situ* polymerisation, 3–22
 - future trends, 21–2
 - polyethylene–CNT composites, 9–10
 - polymer architecture by metallocene catalysis, 7–9
 - polypropylene–CNT composites, 11–21
 - techniques, 5–7
- polyolefins, 3, 511
- polypropylene, 737–9
- polypropylene–CNT composites, 11–21
 - isotactic PP–CNT composites, 11–15
 - catalyst $[\text{Me}_2\text{Si}(2\text{-Me-Ind})_2]\text{ZrCl}_2/\text{MAO}$, 11
 - catalyst $\text{Me}_2\text{Si}(2\text{-Me-4Ph-Ind})_2\text{ZrCl}_2/\text{MAO}$, 12
 - detailed TEM micrograph, 14
 - SEM micrograph of MWCNT, 15
 - TEM micrograph, 13
- properties, 17–21
 - dynamic mechanical measurements, 21
 - filler type and isothermal crystallisation temperature, 19
 - sPP–MWNT composites, 18
- syndiotactic PP–CNT composites, 15–17
- propylene polymerisation after different pre-treatments, 16
- polypropylene (PP), 3, 4
 - microstructures obtained by metallocene catalysts, 8
- poly(sodium styrene-4-sulfonate) (PSS), 788
- polystyrene, 38, 107
- poly(styrene-*b*-butadiene-co-butylene-*b*-styrene), 139
- poly[styrene-*b*-(ethylene-co-butylene)-*b*-styrene], 142, 144
- poly(styrene-co-acrylonitrile), 362–4
 - storage moduli, 363
 - stress–strain curves, 363
- polyurethane acrylate, 407, 409
- poly(vinyl alcohol) (PVA), 788
- polyvinylidene fluoride, 339, 359–60
- ratios, 360
- positive temperature coefficient (PTC), 765, 782
- Pr EN 45545, 721
- predispersing solvents, 197–202
- prEN 50399, 757
- processing history, 321–3
 - electric conductivity of an injection cycle, 321
 - injection velocity, melt and mould temperature, 322
- PS *see* polystyrene
- Pseudomonas aeruginosa*, 628
- PUA *see* polyurethane acrylate
- PURE, 658
- PVDF–PA6–CNTs composites
 - electrical conductivity, 150
 - high-shear-processed sample, 147–8
 - low-shear-processed sample, 148
 - morphological representations, 150
 - stress–strain curves, 151
- Qenos, 430
- radial breathing mode (RBM), 403
- radiotracers, 701
- RAFT *see* reversible addition-fragmentation chain transfer
- Raman imaging, 100
- Raman microscopy, 636
- Raman scattering, 401, 413
- Raman spectroscopy, 447, 550, 558–63
 - FWHM and peak changes as a function of MWCNT loading, 562
 - FWHM values and weighted peak position, 560
- normalised Raman spectra for PET, MWCNTs and PET–MWCNT composites, 561
- PET, MWCNTs and PET–MWCNT composites, 559
- polymer–carbon nanotube composites, 400–22
 - molecules and fibres under strain, 402–3
 - Raman effect: basic principles, 401–2
- Raman signature on carbon nanotubes, 403–5
- SWNTs Raman spectra, 404
- usefulness in nanotube-based composites, 405–21
 - material discontinuities sensors and local stress concentrations, 408–12
 - molecular surface defects, 414–16
 - nanotube–liquid and nanotube–polymer interactions, 406–8
 - orientation in polymers, 413–14
 - stress transfer and interface adhesion, 416–21
 - thermal stress sensing, 412–13
- Raman Station spectrometer, 558
- random closed set, 277–8
- Rayleigh scattering, 401
- reactive blending method, 350
- representative volume element, 381
- resins, 339
- reversible addition-fragmentation chain transfer, 67–8, 351–2
- rheo-electricity, 308–10
 - schematic representation of rheometer, 309
- rheology
 - polymer–carbon nanotube composites melts, 428–70
 - flow-induced crystallisation, 463–70
 - linear rheological properties, 429–48
 - non-linear rheological properties, 448–63
- rheometers, 515
- ring opening polymerisation, 47, 68–70
- ROP *see* ring opening polymerisation
- Runge–Kutta method, 243
- rupture-dominant mechanism, 115
- rupture mechanism, 97
- RVE *see* representative volume element
- S-SBR–BR *see* solution-styrene-butadiene and butadiene rubber blends
- SBBS *see* poly(styrene-*b*-butadiene-co-butylene-*b*-styrene)

- SBBS–CNTs nanocomposites
 processed under shear rates 440 sec⁻¹,
 1460 sec⁻¹, 2960 sec⁻¹, 140
 stress–strain curves and strain recovery
 curves, 145
 CNT loading = 3 wt%, 141
- SBR/BR *see* styrene–butadiene–butadiene–
 rubber
- scanning electron microscopy, 348, 353, 779
- scratch tests, 533
- SEBS *see* poly[styrene-*b*-(ethylene-*co*-
 butylene)-*b*-styrene]
- SEBS–MWCNT nanocomposites
 electrical conductivity, 146
 SEM images with different nanotube
 loadings, 142
 storage modulus and tan δ temperature
 dependence, 143–4
 temperature dependence, 143–4
 secondary agglomeration, 117–18
 MWNT in the polycarbonate melt, 117
- segregated network concept, 532
- SEM *see* scanning electron microscopy
- sensor, 763–4, 794
- shape factor, 204
- shear mixing, 513
- sidewall functionalisation, 30–3
- silica filler, 216–25
- silicone
 special affinity with carbon nanotubes,
 739–42
- single burning item (SBI) test, 725
- single-walled carbon nanohorns, 643
- single-walled carbon nanotubes, 18, 55, 193,
 347, 400
 flame-retardant cable applications, 748,
 751
 heat release rate for SWCNTs in
 LDPE, 753
 PDE filled with SWCNTs, 753
 typical defects, 28
- single-walled nanotubes, 664
- sintering, 516
- small amplitude oscillatory shear data
 (SAOS), 461
- small angle neutron scattering techniques, 447
- small angle X-ray scattering (SAXS), 100–1
- smart textiles, 795
- solubilisation, 633–4
- solution processing, 512
- solution-styrene–butadiene and butadiene rubber
 blends, 462
- solvent-casting process, 456
- sonication, 513, 517
- Spectra, 657
- spherical contact distribution function, 277–9,
 290
 binarized TEM micrograph, 285
- sPP–MWCNT nanocomposites, 19
 properties, 18
- Staphylococcus epidermis*, 628
- statistical percolation theory, 761
- Stokes Raman scatter, 401
- Stone–Wales defects, 27–8
- strain-controlled rotational rheometers, 430
- strain gauged factor, 787–8
- stress concentration factors (SCF), 402
- stress-controlled rotational rheometers, 430
- structural defects, 637–8
- styrene–butadiene/butadiene–rubber, 196, 217
 3 phr CNT dispersion characteristics, 196
 CNT concentration, 201
 CNT-filled blends
 strain dependency of elastic modulus, 206
 matrix loaded with 3 phr CNTs, 212
 mechanical and electrical properties, 211
 percolation behaviour of AC resistivity, 209
 quasi-static stress–strain curves, 200
 silica filled blends
 CNT on mechanical and electrical
 properties, 218
 stress–strain behaviour, 218
 unfilled and CNT-filled samples
 dynamic-mechanical analysis, 205
 quasi-static stress–strain curves, 203
- styrene plasma, 38
- supercritical CO₂ technology, 63
- surface chemistry, 634–7
- surface etching, 36–7
- surface resistivity, 160, 168
- surfactants, 516–17
- SWCNTs *see* single-walled carbon nanotubes
- syndiotactic PP–CNT composites, 15–17
- tearing energy, 224
- tetrahydrofuran (THF), 359
- TGA *see* thermogravimetry analysis
- thermal degradation
 CNTs, 486–9
 chemically treated CNT, 487–9, 490
 impurities amount and type in nanotubes,
 486–7
 PF-functionalised MWNT synthesis, 489
 PLA molecule chain length, 490
 various functionalised carbon
 nanotubes T_{onset}, 490
- functionalised MWNTs
 synthesis and structure, 488
 TGA traces, 488
- future trends, 501–2
- mechanisms and stability improvement by
 CNTs, 483–6
 hydrogen bonding interaction between
 m-CNT and poly(ethylene
 2,6-naphthalate) matrix, 485
 polyurea TGA curve, 483
- polyamides, 492–4
 relationship between T_{onset} and MWNT
 concentration in PA11–MWNT
 composites, 494
- polyesters, 499–500
 PLA–carboxylic, PLA–hydroxy, and
 PLA–pure CN5 images, 500
- polymer–carbon nanotube composites,
 482–503
 others, 500–1
- poly(methyl methacrylate), 495–6
 PMMA–SWNT nanotubes dispersion
 effect on residues, 495
- Si–MWNT–PMMA–VTES characteristic
 thermal degradation temperature, 496
- polyolefins, 489–92, 493
 iPP–MWNT nanocomposites characteristic
 thermal degradation temperatures, 493

- styrenic polymers, 496, 497–9
 - β -cracking, 497
 - styryl-modified MWNT by esterification, 498
- thermal diffusivity, 209
- thermal gravimetric analysis, 534, 638
- thermal plasma, 33
- thermal stability
 - polymer–CNT composite, 483–6
 - barrier effect, 484
 - physical or chemical adsorption, 484
 - polymer–nanotube interaction, 484–5
 - radical scavenging action, 485–6
 - thermal conductivity, 484
- thermal stress sensing, 412–13
- thermal transport, 209–10
- thermo-rheology
 - electrical and rheological properties of
 - polymer–carbon nanotube composite, 295–324
 - critical volume fractions of fillers at
 - percolation threshold, 296
 - destruction and formation of electrical and
 - rheological networks, 312–21
 - influence of processing history, 321–3
 - measuring techniques and materials, 309–12
 - thermo-rheological influence on the
 - electrical conductivity, 297
- Thermogalactic-Grams, 560
- thermogravimetry analysis, 483
- thermoplastic polyurethane (TPU), 736–7
- thiol-coupling reaction, 350
- time-temperature superposition (TTS), 446
- TiO₂, 624
- tissue engineering, 682
 - orthopaedic applications, 683–6
 - hierarchical structure of bone and femur, 683
 - osteoblast on MWCNT and SWCNT
 - cultures, 685
- toulene, 512
- toxicity
 - carbon nanotubes, 628–9
 - basic parameters, 630
 - description of three MWCNT types, 629
 - influence of parameters, 630–45
 - length, morphology and aspect ratio, 630–2
 - level of aggregation, 632–3
 - metal catalyst residues and impurities, 638–41
 - metal content of test samples, 640
- toxicology
 - CNT vs other particulate materials, 623–4
- traction-controlled boundary conditions *see*
 Neumann boundary conditions
- transducer, 763
- transient shear viscosity, 309–10
- transmission electron microscopy, 276–90, 348, 461, 779
 - degree of dispersion, 276–7
 - volume specific fibre length determination, 276
 - digital image processing and specific
 - examples, 281–90
 - binarization scheme, 283
 - binarized TEM images of sample 4, 289
 - injection moulding parameters, 286
 - morphological quantities of the injection
 - moulded samples, 290
 - SCDF of binarized TEM micrographs, 285
 - TEM micrograph of an injection-moulded
 - PC sample, 282
 - TEM micrograph of an injection-moulded
 - sample 4, 287
 - TEM micrograph of an injection-moulded
 - sample 5, 288
 - TEM micrographs of two composites, 284
 - distribution of coefficient, 277–9
 - RCS with differently distributed line
 - segments, 278–9
 - orientation factor, 280–1
 - covariance C(r), 281
 - transmission line theory, 332
 - TS5 Laser+ Melinar, 551
 - Ts-Na, 103, 104
 - tunnelling current, 207
 - type and level of impurities, 641–3
- UL94 tests, 724–5, 726, 735
 - classification, 725
 - vertical schema, 726
- UL1709 tests, 742
- ultra high molecular weight polyethylene
 (UHMWPE), 679, 688–9
- Ultrasil 7000 GR, 217
- UL94V0 test, 743
- US Food and Drug Administration (FDA) blue
 - book memorandum #G95-12, 676
- Utracki equation, 602, 606
- van der Waals forces, 95, 348, 447
- van der Waals interaction, 403, 687
- van Gurp–Palmen plot, 437
- VE-cadherin, 623
- viscosity, 239
- volume resistivity, 158, 160, 166, 581
- wetting coefficient, 595–6
- Wicksell corpuscle problem, 266
- Wiener–Khinchin theorem, 286
- Williams–Landel–Ferry equation, 239–40
- Wolff’s law, 680
- WST-1 test, 637
- X-ray diffraction, 563–4
 - d-spacings for PET composites, 564
 - PET, MWCNTs and PET/MWCNT
 - composites, 563
- X-ray fluorescence, 638
- Young’s equation, 595
- Young’s modulus, 203, 353, 354, 355, 357, 358, 360, 364, 379, 392, 663, 680
- zirconocenes, 11
 - catalyst components for olefin
 - polymerisation, 9
- Zwick 1456, 196
- Zylon HM, 662